STRUCTURAL DYNAMICS

RECENT ADVANCES

DTIC QUALITY INSPECTED 4

20000908 138

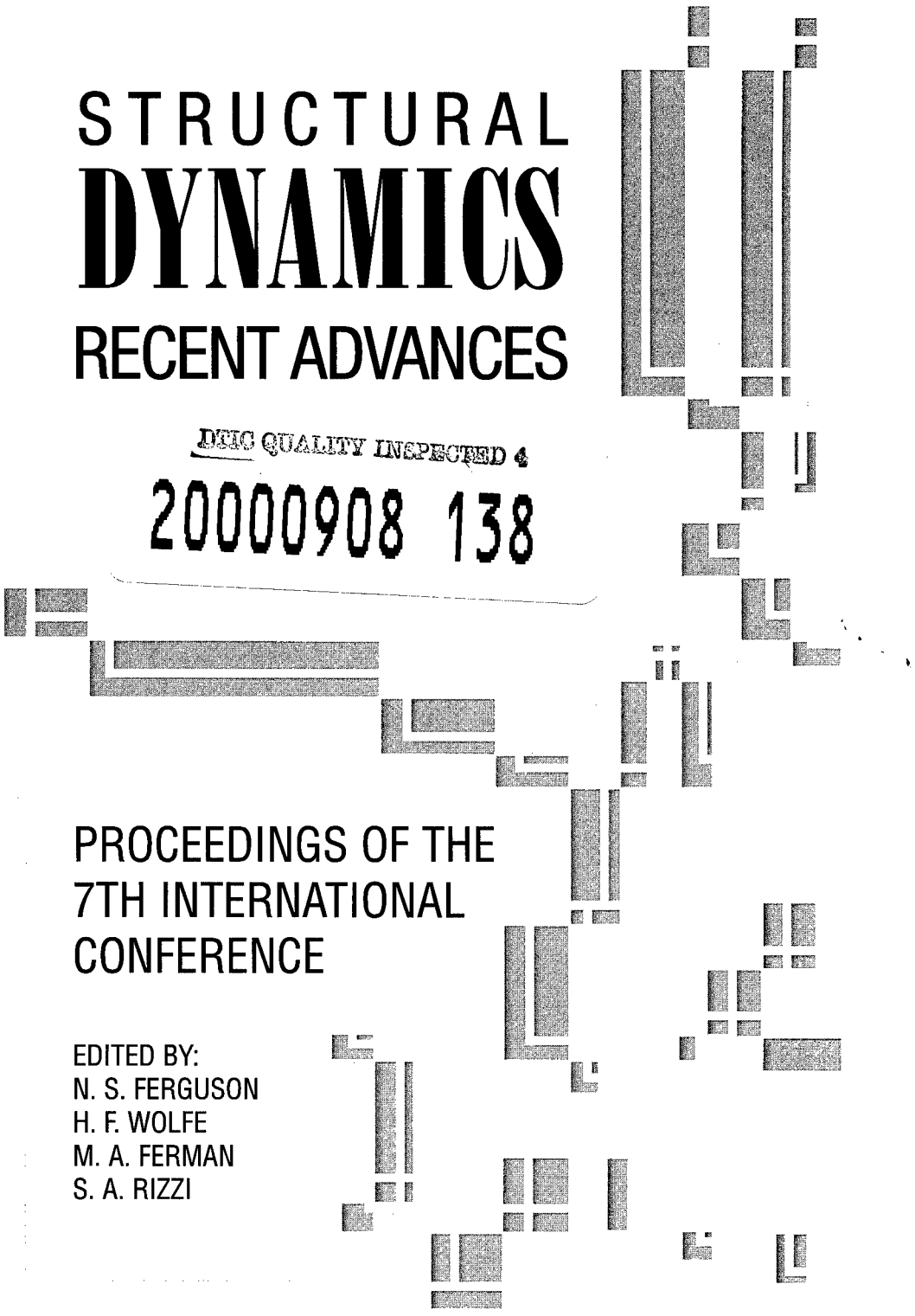

PROCEEDINGS OF THE 7TH INTERNATIONAL CONFERENCE

EDITED BY:
N. S. FERGUSON
H. F. WOLFE
M. A. FERMAN
S. A. RIZZI

REPORT DOCUMENTATION PAGE

Form Approved OMB No. 0704-0188

Public reporting burden for this collection of information is estimated to average 1 hour per response, including the time for reviewing instructions, searching existing data sources, gathering and maintaining the data needed, and completing and reviewing the collection of information. Send comments regarding this burden estimate or any other aspect of this collection of information, including suggestions for reducing this burden to Washington Headquarters Services, Directorate for Information Operations and Reports, 1215 Jefferson Davis Highway, Suite 1204, Arlington, VA 22202-4302, and to the Office of Management and Budget, Paperwork Reduction Project (0704-0188), Washington, DC 20503.

1. AGENCY USE ONLY (Leave blank)	2. REPORT DATE	3. REPORT TYPE AND DATES COVERED
	27 July 2000	Conference Proceedings

4. TITLE AND SUBTITLE

Seventh International Conference on Recent Advances in Structural Dynamics

5. FUNDING NUMBERS

F61775-00-WF065

6. AUTHOR(S)

Conference Committee

7. PERFORMING ORGANIZATION NAME(S) AND ADDRESS(ES)

University of Southampton
Highfield
Southampton SO17 1BJ
United Kingdom

8. PERFORMING ORGANIZATION REPORT NUMBER

N/A

9. SPONSORING/MONITORING AGENCY NAME(S) AND ADDRESS(ES)

EOARD
PSC 802 BOX 14
FPO 09499-0200

10. SPONSORING/MONITORING AGENCY REPORT NUMBER

CSP 00-5065

11. SUPPLEMENTARY NOTES

Two volumes.

12a. DISTRIBUTION/AVAILABILITY STATEMENT

Approved for public release; distribution is unlimited.

12b. DISTRIBUTION CODE

A

13. ABSTRACT (Maximum 200 words)

The Final Proceedings for Seventh International Conference on Recent Advances in Structural Dynamics, 24 July 2000 - 27 July 2000

Aeronautics and Flutter; Analytical Developments; Numerical Methods; Finite Element Methods; Nonlinear Vibration; Experimental techniques; Rotating Machines; Control; System Identification; Acoustic Fatigue and Thermal Effects; Power Flow Approaches and Impact Dynamics

14. SUBJECT TERMS

EOARD, Aerodynamics, Fatigue, Aeroelasticity

15. NUMBER OF PAGES

1048

16. PRICE CODE

N/A

17. SECURITY CLASSIFICATION OF REPORT	18. SECURITY CLASSIFICATION OF THIS PAGE	19. SECURITY CLASSIFICATION OF ABSTRACT	20. LIMITATION OF ABSTRACT
UNCLASSIFIED	UNCLASSIFIED	UNCLASSIFIED	UL

STRUCTURAL DYNAMICS: RECENT ADVANCES

Proceedings of the 7th International Conference

Volume I

Proceedings of the Seventh International Conference on Recent Advances in Structural Dynamics, held at the Institute of Sound and Vibration Research, University of Southampton, England, from 24th to 27th July, 2000, co-sponsored by the US Airforce European Office of Aerospace Research and Development, the Air Force Research Laboratory, Wright Patterson Air Force Base, Parks College of Engineering and Aviation, St. Louis University, and the Structural Acoustics Branch at NASA Langley Research Center.

Edited by

N.S. FERGUSON
Institute of Sound and Vibration Research,
University of Southampton, Southampton, UK.

H.F. WOLFE
Air Force Research Laboratory
Wright Patterson Air Force Base, Ohio, USA.

M.A. FERMAN
Parks College of Engineering and Aviation
St Louis University, St Louis, USA

and

S.A. RIZZI
NASA Langley Research Center
Hampton, Virginia, USA

© The Institute of Sound and Vibration Research, University of Southampton, UK.
ISBN no. 0854327215

AQF00-11-3745

PREFACE

The International Conference series on Recent Advances in Structural Dynamics enters its third decade of existence since its inception in 1980. This is the seventh conference to be held at the Institute of Sound and Vibration Research(ISVR) and it is through the continued support and sponsorship, in time and resources, of the ISVR, the Air Force Research Laboratory(Wright Patterson Air Force Base), Parks College of Engineering and Aviation(St Louis University) and NASA Langley Research Center that we have succeeded in organising the event. On this occasion there are two new co-organisers, Prof. M.A. Ferman and Dr S.A. Rizzi, who have been excellent replacements for Prof. C. Mei, who previously contributed so much. The new co-organisers have been instrumental in the organisation of new sessions, one namely Aerodynamics and Flutter, and have also continued the long standing tradition, topics and interests of the Structural Dynamics community, such as Acoustic Fatigue.

The conference has maintained its high standards by continuing to review submitted papers and thanks are directed towards the authors, Invited Speakers, paper reviewers and session chairmen for their contribution and support. Likewise the conference has a strong international participation, allowing for good technical discussion, dissemination and interchange of ideas. It is also anticipated that the published proceedings will provide a good source of material for future research activities and be a true record of the papers presented. The arrangement of the papers, in two volumes, is to accompany the programme of presentations and likewise the papers are grouped into the most appropriate sessions.

The organisers would like to thank the following for their contribution to the success of the conference: the United States Air Force European Office of Aerospace Research and Development. Personally I would like to acknowledge and thank all of the other conference organisers of the event:

Dr. H.F. Wolfe	Air Force Research Laboratory, Wright Patterson Air Force Base, USA
Prof. M.A. Ferman	Parks College of Engineering and Aviation, St Louis University, USA
Dr. S.A. Rizzi	Structural Acoustics Branch, NASA Langley Research Center, USA

Last, but not least, also tremendous thanks to Mrs. M.Z. Strickland, Conference Secretary and general assistant for all things technical and administrative.

N.S. Ferguson

Seventh International Conference on Recent Advances in Structural Dynamics

Volume I

Contents

Page No.

INVITED PAPERS

R.S.LANGLEY
The Dynamic Analysis of Uncertain Structures 1

C.R.PICKREL.
Testing for Model Validation in Structural Dynamics ~ Where Idealization Meets Reality 21

F.C.MOON
Progress in Nonlinear and Chaotic Dynamics of Structures 39

ANALYTICAL AND NUMERICAL METHODS

A.BHASKAR
Gross modifications in structural dynamics via interpolated modes 61

K.D.MURPHY and Y.ZHANG
The dynamics of a cracked translating beam 75

E.M.WEBSTER and J.F.DOYLE
A Dynamic View of Static Instabilities 87

C.W.S.TO and LINGCHUAN LI
Transient responses of non-proportionally damped structures by the group theoretic approach 101

M-L.ZHU, S-W.R.LEE, T-Y.ZHANG and P.TONG
An Analytical Method of Extension-Twisting Coupling Vibration of Piezoelectric Composite Laminates 121

A.K.BELYAEV
Benchmark study of three approaches to elastic waves in stochastic media 135

QIANG XUE
Dynamic instability of spatial frames 147

IMPACT DYNAMICS

G.DALPIAZ and A.RIVOLA
Inverse problems in mechanisms for packaging machines 159

P.VERLEYSEN and J.DEGRIECK
Determination of dynamic material model parameters by means of a combined numerical-experimental technique 173

V.I.BABITSKY and A.M.VEPRIK
Structural Dynamics of Vibro-Impact Systems 185

J-S.SEO and J.K.HAMMOND
Blind reconstruction of a mechanical impacting source signal using higher order statistics: Part I: signal restoration by cumulant maximisation (theory and simulations) 199

J-S.SEO and J.K.HAMMOND
Blind reconstruction of a mechanical impacting source signal using higher order statistics: Part II: signal restoration using optimisation by differential evolution 215

R.ADAMS and J.F.DOYLE
A general Force Identification Method for Complex Structures 225

ROTATIONAL SYSTEMS AND RELATED STUDIES

B.KLAMECKI
Journal Bearing Condition Monitoring using Vibration Measurements and a new signal enhancement technique 237

M.J.BRENNAN
Wave Motion in a Rotating Timoshenko Beam 249

KUO MO HSIAO
Free Vibration of Rotating Beam with Tip Mass 259

C.M.KROUSGRILL, A.K.BAJAJ and B.K.SERVIS
A study of modal coupling mechanisms leading to squeal vibrations 271

SUBSTRUCTURING AND COMPLEMENTARY TECHNIQUES

J-G.TSENG, K-H.HUANG, T-C.FAN and H.T.CHANG
Vibration of Air-coupled Transverse Bulkheads of A Submarine 291

N.S.FERGUSON
The Lagrange Multiplier Method Revisited for Free and Forced Vibration of a Constrained Structure 309

D.J.GORMAN
The superposition - Galerkin method for free vibration analysis of completely free rectangular plates 325

D.J.WAGG and D.P.STOTEN
Modelling the dynamics of large scale structures using numerical-experimental substructuring 341

B.R.MACE Mid-Frequency vibration analysis and application to a two-rod system 353

NONLINEAR VIBRATION

P.RIBEIRO
Even harmonics on the steady-state geometrical non-linear forced vibration of beams 365

P.RIBEIRO, J.MARINHO and L.ALVES
Experimental investigation on the occurrence of internal resonances in a clamped-clamped beam 379

E.MANOACH
Dynamic large deflection analysis of elastic-plastic beams and plates 389

L.AZRAR, R.BENAMAR and R.G.WHITE
Non-linear free and forced response of beams at large vibration amplitudes by a semi-analytical method 401

J.A.VAZQUEZ-FEIJOO, K.WORDEN and R.STANWAY
On perturbation expansion and the volterra series 415

A.Z.KAZAKOFF and K.WORDEN
Nonlinear motions of a vibration separator system 427

YU.A.ROSSIKHIN and M.V.SHITIKOVA
Transient Vibrations of a Nonlinear Spherical Shell Being in External Contact With an Elastic Isotropic Medium 441

ACTIVE AND PASSIVE CONTROL

T.L.TURNER
SMA Hybrid composites for dynamic response abatement applications 453

S.M.KIM, S.J.ELLIOTT and M.J.BRENNAN
Active vibration isolation of a multiple mount system using velocity feedback control 467

P.DE BOE and J.GOLINVAL
Identification of electromechanical coupling in piezo-structures 483

A.PATEL and J.F.DUNNE
Neural network modelling of frequency dependent automotive dampers 501

E.M.AUSTIN and D.J.INMAN
Errors in Damping Predictions due to Kinematics Assumptions for Sandwich Beams 515

Y.S.LEE, P.GARDONIO, S.J.ELLIOTT and S.DEBOST
A matched distributed piezoelectric actuator and sensor pair for control of beam motion 527

W.VARIYART and M.J.BRENNAN
A shaped PVDF modal sensor for the n = 2 propagating flexural wave in a pipe 543

G.S.AGLIETTI, R.S.LANGLEY, E.ROGERS and D.F.JOHNSON
A study of robustness of active control systems for mass loaded satellite panels 555

D.J.THOMPSON, C.J.C.JONES and T.P.WATERS
The development of a tuned damper for reducing noise from railway track 567

S.O.OYADIJI and P.SARAFIANOS
Comparing the dynamic properties of conventional and electro-rheological fluid shockabsorbers 579

AERODYNAMICS AND FLUTTER

S.L.LIGUORE, D.V.DROUIN and T.H.BEIER
Active Buffet Load Alleviation for an F/A - 18 Vertical Tail 591

M.A.FERMAN, E.W.TURNER and L.J.HUTTSELL
An experimental investigation of tangential blowing to reduce buffet response of the vertical tails of an F-15 wind tunnel model 603

J.T.VON HATTEN and M.A.FERMAN
Development of a Transient Signal Analysis Method for Flutter Testing 615

D.M.PITT and D.MANOR
Numerical Simulation of F/A - 18 A/B/C/D Limit Cycle Oscillations (LCO) and An Active Oscillation Controller (AOC) 627

J.J.OLSEN
Coupled Flight Mechanics and Aeroelasticity (the Effects of Quasi Steady Maneuvers on Supersonic Divergence and Flutter) 643

Q.ZHANG, N.POPPLEWELL and A.H.SHAH
Galloping of Bundle Conductors 659

C.ZHANG, N.POPPLEWELL, P.BANERJI and A.H.SHAH
Wind-induced instabilities of curved poles 673

WORK IN PROGRESS

S.AOKI and T.WANABE
Some Numerical Results of Analytical Solutions for Steady-State Response of a Beam with Nonlinear Boundary Conditions 689

T.AOKI and S.AOKI
Nonlinear Vibration Control Based on An Artificial Neural Network without Learning 695

L.S.KURAVSKY and S.N.BARANOV
Selection of optimal parameters for acoustic vibration suppressors 703

C.OZTURK
Practising engineer's approach to understand the effects of shell dynamics on noise radiation 715

G.V.ZURITA
Vibration Based Diagnostics of the Combustion Process in Diesel Engines 721

T.R.HOWARTH, J.F.TRESSLER, J.A.BUCARO, C.G.HORNER and W.E.ROBBINS
Acoustic actuator blanket for interior sound control 727

INVITED PAPERS

THE DYNAMIC ANALYSIS OF UNCERTAIN STRUCTURES

R.S.Langley
Department of Engineering
University of Cambridge
Cambridge CB2 1PZ, UK

ABSTRACT

Various methods for the dynamic analysis of structures with uncertain properties are described. Initially parametric uncertainties are considered, and both probabilistic (FORM) and possibilistic (interval, convex, and fuzzy analysis) methods are described. It is then shown that all of these methods can be encompassed by two algorithms, each of which represents a constrained optimisation problem. Various features of the methods are illustrated through the relatively straight forward example of a point loaded plate that has uncertain dimensions. Attention is then turned to non-parametric uncertainties, and the methods described include random matrix theory, statistical energy analysis, and hybrid techniques.

1. INTRODUCTION

In structural and mechanical design it is important to allow for the fact that uncertainties can exist in the properties of the designed system and in the applied loading. Traditionally this has been catered for through the use of factors of safety, which are developed and refined on the basis of experience and historical evidence. For systems where efficient design is of the utmost importance (for example the minimum weight design of an aircraft structure) it is possible that the traditional safety factors may be overly conservative, so that optimal efficiency cannot be achieved. Conversely, factors of safety may not be available for new design concepts or new materials. It follows that there is a need for a method (or methods) that can be applied objectively to a new design to yield information on the safety, reliability and performance of the system without reliance on established factors of safety. Such methods should ideally cater for static loading and for the full frequency range of dynamic loading. The aim of this paper is to review the various techniques that are currently available, with an emphasis on vibration problems. The methods described divide into those that employ a *parametric* model of the structural uncertainty and those that employ a *non-parametric* model. These terms are defined fully in what follows: section 2 is concerned with parametric models, and section 3 with non-parametric models.

2. PARAMETRIC UNCERTAINTIES

2.1 Statement of the Problem

The equations of motion of an N degree-of-freedom dynamic system can be written in the standard matrix form

$$\mathbf{M}\ddot{\mathbf{y}} + \mathbf{C}\dot{\mathbf{y}} + \mathbf{K}\mathbf{y} = \mathbf{F}, \tag{1}$$

where $\mathbf{y}$ is a vector containing the degrees of freedom, $\mathbf{M}$, $\mathbf{C}$, and $\mathbf{K}$ are respectively the $N \times N$ mass, damping, and stiffness matrices, and $\mathbf{F}$ is the vector of applied forces. Equation (1) may result from a finite element model of the system, a Lagrange-Rayleigh-Ritz analysis or any other approach to formulating the equations of motion in terms of a finite set of degrees of freedom. The matrices that appear in the equation depend upon the geometric, inertial, elastic, and damping properties of the structure, and many cases arise in which these properties are uncertain. The uncertainties are said to be *parametric* if the matrices can be expressed in terms of a finite number of uncertain physical parameters, $\mathbf{x}$ say, which might include material properties, structural geometry, and other such items. The force vector $\mathbf{F}$ might also be uncertain, but in this case it is important to distinguish between random loading and uncertain loading: if $\mathbf{F}$ is a stochastic process with known power spectral density and statistical properties, then the force can be considered to be "certain" in the present context – this type of randomness is encompassed by standard random vibration theory, and no other considerations are needed. If however the spectral density of the force is not known precisely, or if the force is non-stochastic, but again uncertain, then the variables $\mathbf{x}$ can be taken to include parameters that describe the force, in addition to parameters that describe the structure. Thus the terms in equation (1) can be written as $\mathbf{M}(\mathbf{x})$, $\mathbf{C}(\mathbf{x})$, $\mathbf{K}(\mathbf{x})$, and $\mathbf{F}(\mathbf{x})$.

For prescribed values of the uncertain parameters $\mathbf{x}$, equation (1) can be solved to yield the response of the structure, which can be written as $\mathbf{y}(\mathbf{x})$[1]. The problem is then to assess whether the performance of the structure meets design requirements, allowing for the fact that $\mathbf{x}$ is uncertain. Clearly this question cannot be addressed unless some description of the uncertainty is available: as discussed in the following sections, this might be a *probabilistic* description (Section 2.2), such as the probability density function of $\mathbf{x}$, or a *possibilistic* description (Section 2.3), such as a set of bounds on the possible values of $\mathbf{x}$. Various analysis methods for these cases are described in what

[1] Note that the precise description of the "response" will depend upon the nature of the loading. For stochastic loading, the response spectrum or the mean squared value might be considered, while for deterministic loading the maximum response, or the response time history might be considered. The representation $\mathbf{y}(\mathbf{x})$ relates strictly to the latter case - for ease of notation the response of an uncertain structure to stochastic loads is not given special attention here.

follows, and in Section 2.4 the possibility of treating probabilistic and possibilistic descriptions by a single analysis method is discussed.

2.2 Probabilistic Methods

The basic aim of the probabilistic approach to structural uncertainty is to derive the statistics of the response $\mathbf{y}(\mathbf{x})$ given the probability density function of the uncertain parameters $p(\mathbf{x})$. In general this is a very difficult problem, as the transformation from $\mathbf{x}$ to $\mathbf{y}$ is generally highly non-linear, and a large number of variables may be involved. A number of approaches to this problem are discussed below.

2.2.1 Monte-Carlo Simulation

This represents the most direct approach to determining the statistics of the response $\mathbf{y}$: samples of the uncertain parameters $\mathbf{x}$ are generated in accordance with the probability density function $p(\mathbf{x})$, and the equations of motion are then solved for each realisation of $\mathbf{x}$, thus allowing numerical determination of $p(\mathbf{y})$. The method is computationally intensive, although recent developments [1] have lead to sampling methods that can greatly improve efficiency. Nonetheless, the Monte-Carlo approach is often computationally unfeasible for large complex structures.

2.2.2 The Stochastic Finite Element Method

In this approach (see for example [2]) the structural uncertainties $\mathbf{x}$ are used to find the uncertainties in the properties of each element of a finite element model. The uncertainties in the assembled structural matrices are generally assumed to be small in comparison to the "certain" (or deterministic) components, and on this basis equation (1) is solved by using a first order perturbation technique. This leads to a result for the mean value and covariance matrix of the response vector $\mathbf{y}$. The approach is numerically efficient, and applicable to a very wide range of structures via the finite element modelling method. However, it is generally limited to small levels of uncertainty, and in its common form it yields only the second-order statistics of the response. Thus the approach cannot in general lead to an estimate of the probability of failure of a large complex system.

2.2.3 The First Order Reliability Method (FORM)

FORM (for example [3]) is a method of estimating the failure probability of a system whose failure state can be described by a function of the response known as the "safety margin" $M(\mathbf{y})$. The system is considered to have failed if $M(\mathbf{y})\leq 0$ and to be safe if $M(\mathbf{y})>0$; typically $M(\mathbf{y})$ might represent the amount by which a critical response (either a stress or a displacement) is exceeded by the allowable response. Since the response $\mathbf{y}$ is related to the uncertain parameters $\mathbf{x}$ via equation (1), it is possible to write the safety margin in the

form $M(\mathbf{x})$: i.e. for a prescribed value of $\mathbf{x}$, the equations of motion can be solved to yield $\mathbf{y}$, and the safety margin M can then be computed.

The probability of failure of the system can be expressed in terms of the safety margin and the statistics of $\mathbf{x}$ in the form

$$P_f = \int_{M(\mathbf{x})\le 0} p(\mathbf{x})\,\mathrm{d}\mathbf{x}, \tag{2}$$

where the integral is taken over the unsafe region. Given that $\mathbf{x}$ is generally of large dimension, it is not usually possible to evaluate equation (2) by either analytical means or direct numerical integration. In the FORM approach, the variables $\mathbf{x}$ are firstly transformed to a set of uncorrelated Gaussian random variables $\mathbf{z}$ of zero mean and unit variance. The relationship between the two sets of variables can be written as $\mathbf{z}=\mathbf{f}(\mathbf{x})$ where the function $\mathbf{f}$ is determined in accordance with the Rosenblatt transformation [4] – this transformation enables any set of random variables $\mathbf{x}$ to be transformed to a set of uncorrelated Gaussian random variables $\mathbf{z}$. The probability of failure is then written as

$$P_f \approx \Phi(-\beta), \qquad \beta = \min\left\{ \sqrt{\sum_j z_j^2} \;\middle|\; M(\mathbf{z}) = 0 \right\}. \tag{3,4}$$

Equation (4) states that β is the shortest distance between the origin and the surface $M(\mathbf{z})=0$, while the function Φ that appears in equation (3) is the cumulative normal distribution function.

The application of FORM requires the solution of the constrained minimisation problem represented by equation (4). This can be accomplished by a range of standard optimisation algorithms, providing the value of M can be computed for any specified $\mathbf{z}$. This is done by: (i) computing the associated values of $\mathbf{x}$ from $\mathbf{x}=\mathbf{f}^{-1}(\mathbf{z})$; (ii) solving the equations of motion, equation (1), given $\mathbf{x}$, to yield the response $\mathbf{y}$; (iii) computing the value of the safety margin M. Clearly, the equations of motion may need to be solved many times before convergence of the optimisation algorithm, and this can require significant computational effort. Efficient techniques known as "response surface methods" have been developed for representing the function $M(\mathbf{z})$ on the basis of limited numerical sampling points [5], and this offers the possibility of significant computational savings.

The derivation of equations (3) and (4) can be found in textbooks on reliability theory (for example [3]). The standard argument is based on transforming $\mathbf{x}$ to $\mathbf{z}$ and then linearising $M(\mathbf{z})$ about the point of closest approach to the origin – if $M(\mathbf{z})$ is actually a linear function then equation (3) is exact. In 1991 Breitung [6] noted that equation (2) is a Laplace-type integral, and thus equation (3) is a special case of a more general result that can be derived directly by employing asymptotic integral analysis. Various

refinements of the FORM approach exist, including the approximation of M to a quadratic surface (SORM) and the use of multiple failure surfaces to represent different failure mechanisms.

2.3 Possibilistic Methods

In practise it can be extremely difficult to obtain detailed statistical information regarding the uncertain variables **x**. A complex probabilistic analysis cannot be justified in the absence of detailed statistical input data, and in recent years there has been considerable debate regarding the development of alternative reliability assessment methods [7]. This has lead to a new family of non-probabilistic, or "possibilistic" methods, and three of these methods are described in what follows.

2.3.1 Interval Analysis

The application of *interval* analysis to uncertain structures was first proposed by Rao and Berke [8]. With this approach the uncertain parameters **x** are not described statistically, but rather are taken to be bounded so that

$$x_{Li} \le x_i \le x_{Ui}, \qquad i = 1,2,..,M, \tag{5}$$

where x_{Li} and x_{Ui} represent the lower and upper bounds on x_i. For static analysis or for harmonic excitation of frequency ω, the equations that govern the response of the system, equation (1), can be re-expressed in the form

$$\mathbf{A}\mathbf{y} = \mathbf{F}, \tag{6}$$

where **A** is the dynamic stiffness matrix $(-\omega^2\mathbf{M}+i\omega\mathbf{C}+\mathbf{K})$, with ω=0 for the static case. With the present notation, both **A** and **F** will be functions of the uncertain parameters **x**, and the aim of an interval analysis is to use this information to compute the bounds on the response **y**. If only one scalar response quantity is of interest then the bounds on this quantity can be determined by employing an optimisation routine, with the response quantity (or its inverse) as the objective function, and equation (6) as the set of constraints. Elishakoff [9] has coined the phrase "anti-optimisation" for the procedure used to find the least favourable response resulting from the uncertain input parameters. This type of analysis could be performed sequentially for any number of response quantities, although the computer time required could become prohibitive as the number of response quantities is increased. Alternatively the bounds on the complete response **y** could be sought by using one of the algorithms suggested by Rao and Berke [8], as described in what follows.

The simplest algorithm described by Rao and Berke [8] is a combinatorial approach whereby equation (6) is solved for each of the 2^M combinations of bounds represented by equation (5). This approach soon becomes unfeasible

with increasing M – for example, a system with M=20 would require over 1 million solutions of equation (6). An alternative approach is to employ interval arithmetic to compute the ranges of the components of $\mathbf{A}^{-1}$ and $\mathbf{F}$ and thence compute the ranges of the components of $\mathbf{y}$. As discussed by Rao and Berke [8], this method is difficult to apply to a large system, and the predicted bounds on $\mathbf{y}$ can be very conservative. Other possible methods that are targeted directly at large systems are described by Rao and Berke [8], and further progress in the development of efficient algorithms can be anticipated. Interval analysis has also been applied to eigenvalue problems [10], with the aim of computing the bounds on natural frequencies.

2.3.2 Convex Modelling

Equation (5) states that the uncertain parameters $\mathbf{x}$ lie within a hyper-cube, the vertices of which are determined by the lower and upper bounds x_{Li} and x_{Ui}. To take a two-parameter system as an example, the possible values of x_1 and x_2 can be represented by a rectangle in the x_1-x_2 plane. Were it thought unlikely that the upper (or lower) bounds on the parameters will be achieved simultaneously, then an alternative description might be an ellipse which lies within the rectangle, as shown in Figure 1 – this excludes the vertex regions of the interval description. More generally any shape of region in the x_1-x_2 plane can be defined, and if the region is convex then this approach is referred to as "convex modelling" [11]. A typical convex description of a set of M uncertain parameters would be the elliptical region defined by the equation

$$\mathbf{x}^{\mathrm{T}}\boldsymbol{\Omega}\mathbf{x} \le a, \tag{7}$$

where $\boldsymbol{\Omega}$ is a positive definite matrix and a is a positive constant. The concept of convex modelling actually predates the application of interval analysis to structures, having been pioneered by Ben-Haim and Elishakoff [11] in the late 1980s. In fact, interval analysis can be considered to be a sub-set of convex modelling in the sense that the hyper-cube description of the uncertain parameters is a particular example of a convex region.

Having described the bounds on the input parameters via an equation such as equation (7), the aim of convex modelling is to find the corresponding bounds on the system response, which might be represented by the solution $\mathbf{y}$ to equation (6) or perhaps by the solution to an eigenvalue problem. The bounds on any single response variable can be computed by using an optimisation or anti-optimisation approach, as in the case of interval analysis.

2.3.3 Fuzzy Modelling

Rao and Sawyer [12] have considered the application of fuzzy set theory to the analysis of uncertain structural systems. Central to this approach is the concept of a fuzzy number x, the properties of which are defined via a membership function $\mu(x)$, as shown for a typical "triangular" fuzzy number in

Figure 2. In some ways the membership function is analogous to a probability density function, although the meaning is much less precise. The value of the membership function, α, indicates a degree of confidence about the numerical value of x: in Figure 2, if α=1 then it is known that x has the definite (or "crisp") value c, whereas if α=0 then x lies between the bounds a and b. For intermediate values of α, x is bounded in accordance with the membership function. The fuzzy description can be considered to be a parameterised interval description, in which the interval bounds depend upon the parameter α.

For a pair of fuzzy numbers x_1 and x_2, the membership function $\alpha=\mu(x_1,x_2)$ can be plotted against the x_1-x_2 plane, or alternatively, lines of constant α can be plotted as closed contours on this plane. For M fuzzy numbers $\mathbf{x}$, a constant value of α will correspond to a closed surface bounding a region of the $\mathbf{x}$-space. If this closed set is convex then the fuzzy description is basically a parameterised convex description: for a specified value of α the values of $\mathbf{x}$ fall within a defined convex region, and this region will shrink (and possibly change shape) with increasing α. If the region is a hyper-cube at all prescribed values of α the description is a parameterised interval description (as is certainly the case for a single number x).

On the basis of the foregoing discussion, it can be seen that a fuzzy description of the uncertain variables $\mathbf{x}$ is little different from an interval description or a convex description, the only new issue being that the range of the variables can be controlled by the parameter α. At each prescribed value of α the system can be analysed by using the methods outlined for interval analysis and convex modelling, and in fact this point is made by Chen and Rao [13] who state: "since any fuzzy number can be represented in interval form, fuzzy arithmetic operations can be implemented by using interval (operation) analysis at each of the n α-levels independently", and "all the rules used for interval arithmetic are equally applicable to fuzzy arithmetic at each α-level". The output of a fuzzy analysis is a fuzzy description of the response, consisting of bounds at each prescribed α-level.

2.4 A Unified Approach to Probabilistic and Possibilistic Methods

It is clear from the previous sections that probabilistic and possibilistic methods constitute very different approaches to the analysis of uncertain structures. However, it is shown in the present section that the methods can actually be implemented via a common algorithm: the methods are then distinguished only by the numerical values and the physical meaning of the input parameters used to describe the structural uncertainties $\mathbf{x}$, and by the physical interpretation attached to the output of the analysis. In order to demonstrate this it is first necessary to consider the use of a safety margin within the context of a possibilistic analysis, as described in the following sub-section.

2.4.1 A Safety Margin Approach to Probabilistic Analysis

The three possibilistic approaches that have been outlined all describe the uncertain parameters $\mathbf{x}$ in terms of a region of permissible values: a hyper-cube in the case of interval analysis, a more general convex region in the case of convex modelling, and a parameterised region in the case of fuzzy modelling. In all cases the region can be represented in the form

$$h(\mathbf{x},\gamma) \leq \gamma\,, \tag{8}$$

where $h(\mathbf{x},\gamma)=\gamma$ represents a closed surface in $\mathbf{x}$-space, and the parameter γ is such that the volume enclosed by the region increases with increasing γ; the appearance of γ in the function $h(\mathbf{x},\gamma)$ allows for the fact that the shape (and not just the size) of the surface may change with increasing γ. It is recognised that the detailed form of $h(\mathbf{x},\gamma)$ will be complicated in the case of a hyper-cube, but nonetheless equation (8) remains valid, with γ providing a measure of the size of the cube.

Possibilistic approaches have not previously been combined with the concept of a safety margin $M(\mathbf{x})$. By recalling that $M(\mathbf{x})\leq 0$ corresponds to a failure state, it can be seen that failure will occur if $M(\mathbf{x})$ is less than zero at any point within the region described by equation (8). For this to occur, either the region $h(\mathbf{x},\gamma)\leq\gamma$ must lie completely within the region $M(\mathbf{x})\leq 0$, or the two surfaces $h(\mathbf{x},\gamma)=\gamma$ and $M(\mathbf{x})=0$ must intersect or touch. The first possibility is highly unlikely to occur in practise, since this would imply that the system is in a failure state for all possible combinations of the uncertain parameters $\mathbf{x}$. Assuming therefore that the surfaces must intersect or touch for failure to occur, it can be noted that the following statements each imply that this condition is met:

(i) $M(\mathbf{x})\leq 0$ at some point on the surface $h(\mathbf{x},\gamma)=\gamma$,
(ii) $h(\mathbf{x},\gamma)\leq\gamma$ at some point on the surface $M(\mathbf{x})=0$.

These conditions can each be re-expressed in terms of a constrained optimisation problem:

(i) for $\mathbf{x}$ on the surface $h(\mathbf{x},\gamma)=\gamma$ the minimum value of $M(\mathbf{x})$ is less than or equal to zero,
(ii) for $\mathbf{x}$ on the surface $M(\mathbf{x})=0$ the minimum value of γ_0 that satisfies $h(\mathbf{x},\gamma_0)=\gamma_0$ is such that $\gamma_0\leq\gamma$.

The second condition follows from the fact that the surface $h(\mathbf{x},\gamma)=\gamma$ expands with increasing γ: the surface $h(\mathbf{x},\gamma_0)=\gamma_0$ with minimum γ_0 is tangential to $M(\mathbf{x})=0$, and thus the surface $h(\mathbf{x},\gamma)=\gamma$ must intercept $M(\mathbf{x})=0$ for $\gamma>\gamma_0$.

The constrained optimisation problems (i) and (ii) offer numerical solution strategies that differ from existing approaches, such as interval arithmetic [8]. It is shown in the following sub-section that the algorithm associated with problem (ii) is actually identical to that employed by FORM. The alternative strategy offered by problem (i) is then considered subsequently.

2.4.2 A Probabilistic/Possibilistic Algorithm

A constrained optimisation problem of the form

$$\min\left\{ s(\mathbf{x}) \mid M(\mathbf{x}) = 0 \right\}, \tag{9}$$

where $M(\mathbf{x})$ is the structural safety margin and $s(\mathbf{x})$ is some function of the uncertain parameters $\mathbf{x}$, can be used to represent all of the analysis methods previously described. The choice of the function $s(\mathbf{x})$ determines the method, and the various options are as follows.

1. *FORM*: $s(\mathbf{x})=\beta$, where β is the distance to the origin in z-coordinates, i.e. the space in which the parameters $\mathbf{x}$ are transformed to uncorrelated Gaussian variables with zero mean and unit variance. Once β has been found, the failure probability can be estimated from equation (3).

2. *Interval analysis*: $s(\mathbf{x})=\gamma_0(\mathbf{x})$ where, in the notation of the previous sub-section, γ_0 satisfies the equation $h(\mathbf{x},\gamma_0)=\gamma_0$. For a specified point $\mathbf{x}$, $\gamma_0(\mathbf{x})$ represents the "size" of the hyper-cube that contains $\mathbf{x}$ on its surface. The hyper-cube increases in size with increasing γ_0, and $\gamma_0=\gamma$ corresponds to the actual size. The minimum value of γ_0 specifies a hyper-cube that just touches the surface $M(\mathbf{x})=0$; the structure can be considered to be safe if $\min\{\gamma_0\}>\gamma$, since in this case a hyper-cube of size γ will not intersect $M(\mathbf{x})=0$.

3. *Convex modelling*: $s(\mathbf{x})=\gamma_0(\mathbf{x})$ where γ_0 is a scaling factor on the convex region containing the uncertain parameters $\mathbf{x}$. As in the case of interval analysis, the point $\gamma_0=\gamma$ corresponds to the actual size of the region, and the structure is safe if $\min\{\gamma_0\}>\gamma$.

4. *Fuzzy modelling*: $s(\mathbf{x})=\gamma_0(\mathbf{x},\alpha)$ where γ_0 is a scaling factor on the region containing $\mathbf{x}$, and in this case the region is a function of the degree of confidence α. The analysis must be repeated at each level α to yield $\gamma_0(\alpha)$; if $\min\{\gamma_0(\alpha)\}>\gamma(\alpha)$, where $\gamma(\alpha)$ is the actual size of the region, then the structure is safe at confidence level α.

Clearly method (1) yields an estimate of the probability of failure, whereas methods (2)-(4) give a simple yes or no answer to the question of structural safety (albeit as a function of α in the case of fuzzy modelling). The amount of information yielded by methods (2)-(4) can be increased by introducing the quantity

$$\chi = (\min\{\gamma_0\} - \gamma)/\gamma, \tag{10}$$

to give some indication of the "degree" of safety.

Rather than simply assess whether a structure is safe for a given degree of uncertainty it might be desirable in some applications to compute the maximum *allowable* degree of uncertainty that yields a safe design. The level of uncertainty on the input parameters can be reduced by inspection and quality control techniques, although there will be an additional manufacturing cost associated with this; knowledge of the maximum allowable degree of uncertainty will help set quality control targets that are safe and yet not overly stringent. In the foregoing analysis, the minimum value of the scaling factor γ_0 yielded by the possibilistic methods (2)-(4) is in fact precisely the maximum tolerance that can be accepted, and hence the present algorithm can potentially be used to specify quality control requirements.

In considering quality control it should be noted that γ_0 represents a single overall scaling factor on the uncertain parameters, and the practical implications of this can be highlighted by considering an example structure consisting of a single plate. The uncertain parameters might be the plate modulus E and the thickness t, and the requirement is to find the maximum permissible tolerances on these items to maintain a safe design. It is inevitable that the answer to this question is non-unique, with many different sets of tolerances on E and t leading to a design that is "just" safe under the worst possible combination of values. Under the present approach, the relationship between the tolerances on E and t is specified in advance by the shape of the convex region $h(\mathbf{x},\gamma)$, and the maximum permissible size of the tolerances is then determined by computing the single scaling factor γ_0. In specifying the shape of $h(\mathbf{x},\gamma)$, consideration could be given to the relative cost of quality control on E and t, so that the more costly parameter is allowed a wider tolerance.

The foregoing discussion on quality control has focussed on possibilistic rather then probabilistic methods. There is no immediate counterpart of the parameter γ_0 in the probabilistic algorithm (1), although in the special case of FORM with Gaussian variables $\mathbf{x}$ a parallel can be drawn with the parameter β. If the standard deviation of *each* of the variables $\mathbf{x}$ is multiplied by a scaling factor c then the net effect is that the value of β yielded by equation (4) will become β/c. If a "target" failure probability is then specified in the form $\Phi(-\beta_0)$, then the value of c can be selected ($c=\beta/\beta_0$) to ensure that this target is met. This value of c then yields the quality control requirements for the

standard deviations of the variables **x**. If the variables **x** are not initially Gaussian then the FORM approach involves a transformation to a new set of Gaussian variables: in this case the foregoing procedure will lead to quality control requirements on the standard deviations of the transformed variables, which can be worked back to requirements on the physical variables

The various reliability assessment methods described in this section are summarised in Table 1. It is clear that in all cases the constraint function is the safety margin $M(\mathbf{x})$, while the particular method is determined by the choice of the objective function and the interpretation of the output. In the case of the three possibilistic methods, the output "safety assessment" indicates a yes or no answer to the question of structural safety.

2.4.3 A Second Probabilistic/Possibilistic Algorithm

Leaving aside the issue of tolerance specification and quality control, equation (9) provides an answer to the question "what is the probability of a structural failure?" in the probabilistic case, and "is structural failure possible within the bounds imposed on the uncertain parameters?" in the possibilistic case. As discussed previously, the possibilistic question can be posed as a constrained optimisation problem in two ways: the structure will fail if either (i) for **x** on the surface $h(\mathbf{x},\gamma)=\gamma$ the minimum value of $M(\mathbf{x})$ is less than or equal to zero, or (ii) for **x** on the surface $M(\mathbf{x})=0$ the minimum value of γ_0 that satisfies $h(\mathbf{x},\gamma_0)=\gamma_0$ is such that $\gamma_0 \leq \gamma$. The second approach forms the basis of the possibilistic algorithms described in the previous sub-section. On the other hand, the first approach states that failure will occur if

$$\min\left\{M(\mathbf{x}) \mid h(\mathbf{x},\gamma)=\gamma\right\} \leq 0. \qquad (11)$$

With the appropriate choice of $h(\mathbf{x},\gamma)$ this approach can be applied to interval analysis, convex modelling, and fuzzy modelling. The probabilistic equivalent of equation (11) within the context of FORM would be

$$\min\left\{M(\mathbf{x}) \mid \beta(\mathbf{x})=\beta_0\right\} \leq 0, \qquad (12)$$

where β is the distance to the origin in z-coordinates and β_0 is a specified value. Rather than answer the question "what is the probability of a structural failure?", equation (12) provides the answer to "is the probability of a structural failure greater than a specified value $\Phi(-\beta_0)$?".

In equations (11) and (12) the safety margin $M(\mathbf{x})$ is the objective function, while in equation (9) it forms the constraint. The calculation of $M(\mathbf{x})$ for a given value of **x** requires the solution of the equations that govern the structural behaviour, and for a complex system this will involve the use of the finite element method. The safety margin is thus a relatively complex

function of **x** when compared to the surface of a convex set, where closed-form analytical expressions are likely to be used. The optimisation problem represented by equation (9) thus involves the minimisation of a simple objective function with a complex constraint, whereas equations (11) and (12) involve the minimisation of a complex objective function with a simple constraint. The numerical problem posed by equations (11) and (12) is somewhat easier than that posed by equation (9), although this is offset by the fact that equations (11) and (12) do not lead to "quality control" information (i.e. allowable tolerances). The various analysis methods that are encompassed by equations (11) and (12) are summarised in Table 2.

2.5 Illustrative Example

The application of the foregoing algorithms to complex structures is ongoing, but some indication of the issues involved can be given by considering the response of a simply supported plate to point loading. The plate has planform dimensions $L_1 \times L_2$ and the concern is with the response w at a fixed location caused by a harmonic point load F applied at a different location. Taking the planform dimensions to be uncertain parameters, the dependency of the response on these items is shown in Figure 3. The results concern the harmonic response at a fixed frequency, and the peaks in the response correspond to combinations of L_1 and L_2 that produce a resonant frequency at the forcing frequency.

A contour plot of the response is shown in Figure 4, with the three levels drawn corresponding to $10\text{Log}(w/F)$=3.1, 3.2, and 3.3. If the structure is deemed to fail when $10\text{Log}(w/F)$=3.1, then this contour represents the safety margin boundary $M(\mathbf{x})$=0. Also shown in Figure 4 is an axis system and two convex regions. To consider initially the application of FORM to this problem, the axis system would correspond the **z**-coordinates that are employed in the method. The probability of failure is found by computing the minimum distance between the centre of the axis system and the safety margin. Three potential difficulties are apparent: (i) the safety margin is not a single continuous curve, and care will be needed to ensure that the optimisation algorithm selects the correct branch, (ii) the safety margin can be highly non-linear, and thus the FORM approximation (linearising the safety margin about the point closest to the origin) may be poor, (iii) the structure could fail on either branch of the safety margin and strictly a combined probability of failure is required – this is not given by the standard version of FORM.

To consider now the application of a possibilistic method, convex modelling, to the problem, two convex regions shown in Figure 4. These regions correspond to: (i) the convex set containing the possible values of the uncertain parameters (shown as the smaller region), (ii) a scaled version of the convex set that just touches the safety margin (shown as the larger region with a scaling factor γ_o). If the first optimisation algorithm (Table 1) is applied,

then the safety margin $M(\mathbf{x})=0$ is searched for the minimum value of γ_0, where γ_0 is defined for a point $\mathbf{x}$ on the safety margin as the scaling factor needed to place that point on the surface of the convex region. Clearly this approach faces similar computational difficulties to FORM, in that the safety margin has multiple branches and the optimisation algorithm would need to robustly locate the correct branch. Unlike FORM however, the validity of the result obtained does not depend on the linearity or otherwise of the safety margin, and the presence of multiple branches of the safety margin has no adverse effect other than the optimisation difficulty mentioned previously. If the second optimisation algorithm (Table 2) is applied, then the surface of the smallest convex region is searched for the minimum value of $M(\mathbf{x})$; the only potential difficulty here is that of locating the *global* optimal value if $M(\mathbf{x})$ displays multiple minima on the surface.

From this preliminary study it is clear that probabilistic and possibilistic methods offer different advantages and disadvantages; for vibration analysis the methods outlined in Table 2 certainly warrant further investigation.

3. NON-PARAMETRIC UNCERTAINTIES

3.1 General Comments

The analysis methods discussed in the previous section are all based on the notion that it is possible to derive a set of equations of motion that govern the structural behaviour, even though the physical parameters that underlie these equations may be uncertain. In some cases however the degree of uncertainty may be so great that it is extremely difficult to follow this procedure. If, for example, a structure is subjected to high frequency broad-band excitation then many hundreds of modes may be excited, and the structure will undergo a very complex deformation pattern that has a short structural wavelength. The development of a deterministic model of this situation may require many thousands of degrees of freedom; the model may then depend upon a very large number of uncertain physical parameters, many of which can be difficult to quantify. The methods outlined in the previous section are unfeasible in this case, and it is appropriate to seek alternatives to the idea of describing the system uncertainty via a prescribed set of physical parameters (parametric uncertainty).

If the concept of parametric uncertainty is abandoned, then there are three possible strategies that can be adopted. The first applies to the case in which it is still possible to build a deterministic model of the system, so that an equation in the form of equation (1) is taken to apply. Randomness can then be introduced into the system directly rather than via structural parameters, for example by considering the various matrix entries to be random variables with prescribed statistical properties – this type of approach is considered in section 3.2. The second strategy is to abandon the conventional form of the equations of motion and seek an alternative, more fully statistical, method of describing

the system behaviour – this approach, which includes statistical energy analysis (SEA) is discussed in section 3.3. The third strategy is to combine aspects of the first two approaches, and model some features of the response by a deterministic method (possibly with parametric uncertainty) and other features by a fully statistical approach – this is discussed in section 3.4.

3.2 Direct Randomisation of the Equations of Motion

In this case various terms that appear in the matrix form of the equations of motion are taken to be random variables. Three examples of this type of approach are as follows.

(i) Shorter and Mace [14]: the finite element equations of motion are re-cast by using modal synthesis, which involves dividing the system into a number of substructures and representing the response of each substructure in terms of blocked modes and constraint modes. The blocked modes are the modes of vibration obtained when the substructure boundaries are clamped, while the constraint modes are "static" shapes associated with motion of the subsystem boundaries. Randomness is then introduced into the model by taking the natural frequencies of the blocked modes to be random variables

(ii) Soize [15]. Here the equations of motion yielded by the finite element method are taken to give the "mean" values of the mass, damping, and stiffness matrices. The joint probability density function of the matrix entries is then derived from this information by using the principle of maximum entropy. It is interesting to note that for a scalar variable this would lead to an exponential distribution: for a random matrix the result displays exponential decay in the tails of the distribution, but the full expression for the distribution is complicated by constraining the matrix to be positive definite. Soize does in fact introduce one further parameter (referred to as λ) that determines the degree of randomness in the matrix. The resulting matrix statistics are used to perform efficient Monte-Carlo simulations of the system response. It can be noted that the matrix statistics are not derived from physical arguments, but rather by making "optimal" use of the mean values via maximum entropy considerations.

(iii) Random matrix theory [16]. This approach has not as yet been applied to response predictions for a built-up structure, but it is helpful to review the results on random matrix statistics that have been developed in the physics literature. In random matrix theory, all "deterministic" structure to a matrix is abandoned, and the matrix is considered in purely statistical terms. The most important class of random matrix is known as the Gaussian Orthogonal Ensemble (GOE) – this has the important physical property that the statistical distribution in unchanged by a rotation (i.e. an arbitrary redefinition of the degrees of freedom). The GOE has a very simple statistical structure: the

matrix is symmetric, all the entries are statistically independent and Gaussian with zero mean, and all the diagonal entries have the same variance, which is twice that of all the off-diagonal entries. A very important property of this matrix is that the spacing between consecutive eigenvalues ($\partial\omega$ say) is found to have a Rayleigh distribution so that

$$p(\partial\omega) = (\partial\omega/\sigma^2)\exp\{-(\partial\omega/\sigma)^2/2\}, \qquad (13)$$

where the parameter σ is such that the mean spacing is given by $\sigma\sqrt{(\pi/2)}$. Equation (13) is known in the literature as the Wigner surmise. Although it is not immediately clear how or why the GOE relates to an elastic system, equation (13) has been found to apply in many practical situations: most notably, Weaver [17] has shown experimentally that the natural frequencies of various aluminium blocks (with slits inserted to destroy symmetry) are in very close agreement with equation (13). This issue will be referred to again in the following section.

3.3 Statistical Energy Analysis (SEA)

A full description of SEA will not be given here, but in brief it can be noted that the method is based on vibrational energy flow and has many analogies with heat conduction and statistical physics [18,19]. In its standard form, SEA predicts the mean value of the vibrational energy in a region of a structure – here the mean is taken over the spatial extent of the region, over frequency, and over an ensemble of random structures. A major research issue in SEA is the development of a reliable method of predicting the higher order statistics of the energy, such as the variance. One of the issues behind this ongoing work is the statistics of the natural frequencies of a built-up system: early work by Lyon [20] assumed initially an exponential distribution for the natural frequency spacing and then compared the results obtained with the use of a variant of equation (13). The detailed nature of the spacing statistics was found to be important, and this has been reinforced by recent work concerning a point process model of the natural frequencies [21]. Much remains to be done in this area.

3.4 Hybrid Methods

Many practical situations arise in which a structure displays a "hybrid" behaviour, in which part of the system can be described deterministically, and part must rely on a statistical description. In such cases the ideal approach would be to model the well defined part of the behaviour by using the finite element method and then couple this to a statistical description of the uncertain part. A milestone in this area was the development of "fuzzy structure theory" by Soize [22] (not to be confused with fuzzy set theory or

fuzzy numbers). The initial motivation for this arose in part from the need to model a deterministic structure, such as a submarine hull, coupled to a very complex system, such as a large number of internal attachments and equipment items. Concepts of this type were further developed by Langley and Bremner [23] to partition out the response of modally dense and modally sparse structural components, leading to a coupled finite element/SEA analysis technique. Earlier approaches to this type of problem were suggested by Belyaev [24], and recently, Grice and Pinnington [25] have added "missing" short wavelength modes into a coarse mesh finite element model by using an impedance technique.

4. CONCUSIONS

This paper has sought to highlight a number of issues involved in modelling the dynamic response of a structure that has uncertain properties. Various analysis methods have been presented, and a distinction has been made between parametric and non-parametric models of the uncertainty. It is clear that while much has been achieved, much also remains to be done in this field before reliable and practically useful results can be obtained routinely for a large complex system.

REFERENCES

1. Pradlwarter, H.J., Schueller, G.I. and Melnik-Melnikov, P.G., Reliability of MDOF-systems. *Journal of Probabilistic Engineering Mechanics*, 1994, **9**, 235-244.
2. Der Kiureghian, A. and Ke, J.-B., The stochastic finite element method in structural reliability. *Probabilistic Engineering Mechanics*, 1988, **3**, 83-91.
3. Madsen, H.O., Krenk, S., and Lind, N.C., *Methods of structural safety.* Prentice Hall, New Jersey, 1986.
4. Rosenblatt, M., Remarks on a multivariate transformation. *The Annals of Mathematical Statistics*, 1952, **23**, 470-472.
5. Breitung, K., and Faravelli, L., Response surface methods and asymptotic approximations. In *Mathematical models for structural reliability analysis*, edited by F. Casciati and J.B. Roberts, CRC Press, New York, 1996, Chapter 5.
6. Breitung, K., Probability approximations by log likelihood maximization. *Journal of Engineering Mechanics*, ASCE, 1991, **117**(3), 457-477.
7. Elishakoff, I., Essay on uncertainties in elastic and viscoelastic structures: from A.M. Freudenthal's criticisms to modern convex modelling. *Computers and Structures*, 1995, **56**(6), 871-895.
8. Rao, S.S. and Berke, L., Analysis of uncertain structural systems using interval analysis. *AIAA Journal*, 1997, **35**(4), 727-735.

9. Elishakoff, I., An idea of the uncertainty triangle. *Shock and Vibration Digest*, 1990, **22**(10), 1.
10. Qiu, Z.P., Chen, S.H., and Elishakoff, I., Natural frequencies of structures with uncertain but nonrandom parameters. *Journal of Optimization Theory and Applications*, 1995, **86**(3), 669-683.
11. Ben-Haim, Y., and Elishakoff, I., *Convex models of uncertainty in applied mechanics.* Elsevier Science Publishers, Amsterdam, 1990.
12. Rao, S.S. and Sawyer, J.P., Fuzzy finite element approach for the analysis of imprecisely defined systems. *AIAA Journal*, 1995, 33(12), 2364-2370.
13. Chen, L., and Rao, S.S., Fuzzy finite-element approach for the vibration analysis of imprecisely-defined systems. *Finite Elements in Analysis and Design,* 1997, 27, 69-83.
14. Shorter, P.J. *Combining Finite Elements and Statistical Energy Analysis.* PhD Thesis, University of Auckland, 1998.
15. Soize, C., A nonparametric model of random uncertainties for reduced matrix models in structural dynamics. *Probabilistic Engineering Mechanics*, 2000, **15**, 277-294.
16. Mehta, M.L., *Random Matrices.* Academic Press, New York, 1991.
17. Weaver, R.L., Spectral statistics in elastodynamics. *Journal of the Acoustical Society of America*, 1988, **85**(3), 1005-1013.
18. Lyon, R.H. and De Jong, R.G., *Theory and Application of Statistical Energy Analysis.* Butterworth-Heinemann, Boston, 1995.
19. Hodges, C.H. and Woodhouse, J., Theories of noise and vibration transmission in complex structures. *Reports on Progress in Physics,* 1986, **49**, 107-170.
20. Lyon, R.H., Statistical analysis of power injection and response in structures and rooms. *Journal of the Acoustical Society of America*, 1967, **45**, 545-565.
21. Langley, R.S., A non-Poisson model for the vibration analysis of uncertain dynamic systems. *Proceedings of the Royal Society of London,* 1999, **A455**, 3325-3349.
22. Soize, C., A model and numerical method in the medium frequency range for vibroacoustic predictions using theory of structural fuzzy. *Journal of the Acoustical Society of America,* 1993, **94**(2), 849-866.
23. Langley, R.S. and Bremner, P.G., A hybrid method for the vibration analysis of complex structural-acoustic systems. *Journal of the Acoustical Society of America*, 1999, **105**, 1657-1671.
24. Belyaev, A.K., Dynamic simulation of high-frequency vibration of extended complex structures. *Mechanics of Structures and Machines,* 1992, **20**, 155-168.
25. Grice, R.M. and Pinnington, R.J., Vibration analysis of a thin-plate box using a finite element model which accommodates only in-plane motion. *Journal of Sound and Vibration,* 2000, **232**, 449-471.

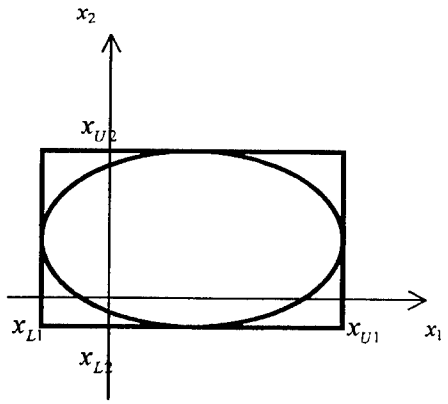

Figure 1. Interval analysis and convex modelling: the rectangle represents the admissible region for interval analysis, while the ellipse corresponds to convex modelling.

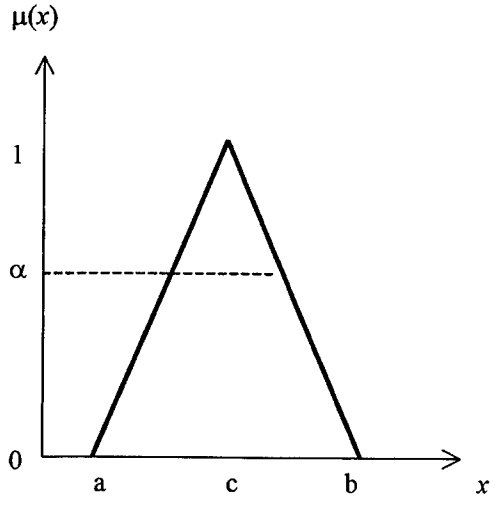

Figure 2. The membership function for a fuzzy number

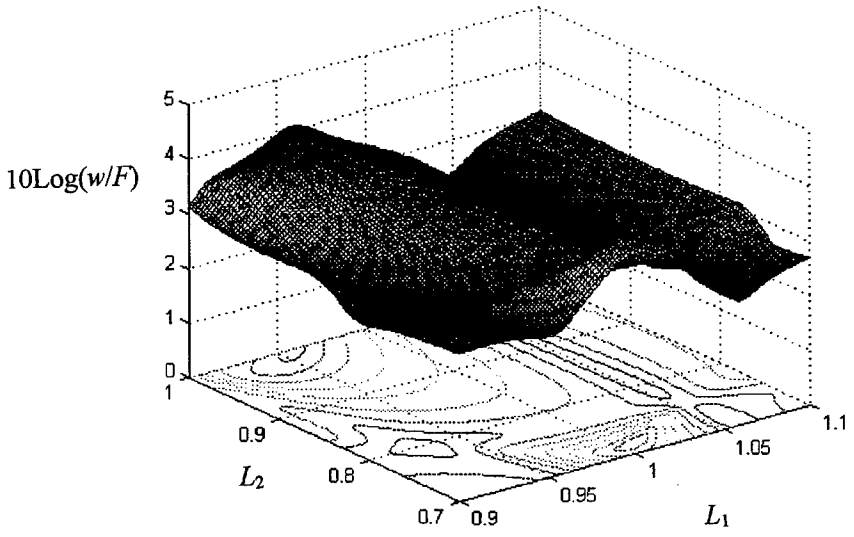

Figure 3. The response of a plate of uncertain planform dimensions to harmonic point loading.

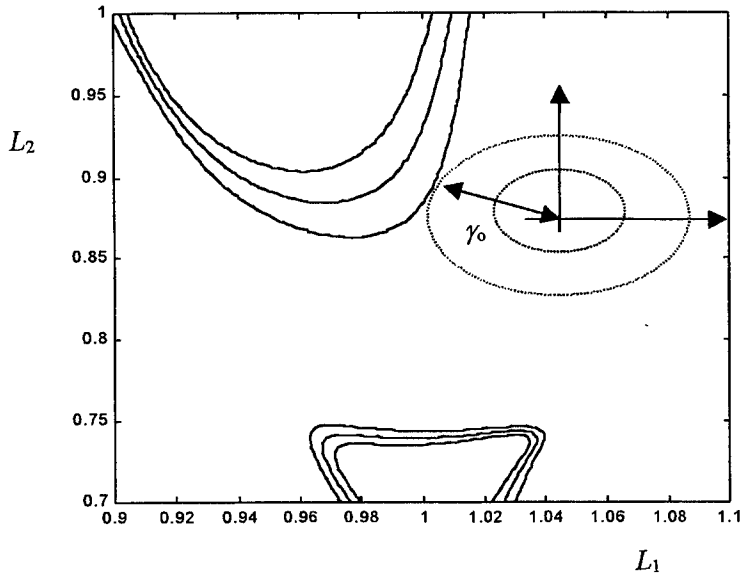

Figure 4. Contour plot of the plate response. The levels shown correspond to 10Log(w/F)=3.1, 3.2, and 3.3. The marked curve represents 10Log(w/F)=3.1.

Table 1. Summary of the algorithm options when the safety margin is a constraint.

Method	Objective Function	Constraint Function	Input	Output
FORM	Z-space radius β	Safety margin $M(\mathbf{x})$	jpdf of uncertain parameters	Probability of failure *or* allowable tolerances for a prescribed probability
Interval analysis	Hyper-cube scaling factor γ_o	Safety margin $M(\mathbf{x})$	Bounds on uncertain parameters	Safety assessment *or* allowable tolerances
Convex modelling	Convex set scaling factor γ_o	Safety margin $M(\mathbf{x})$	Convex set description	Safety assessment *or* allowable tolerances
Fuzzy modelling	Convex set scaling factor γ_o at a prescribed α level	Safety margin $M(\mathbf{x})$	Convex set description at each α level	Safety assessment *or* allowable tolerances

Table 2. Summary of the algorithm options when the safety margin is an objective function.

Method	Objective Function	Constraint Function	Input	Output
FORM	Safety margin $M(\mathbf{x})$	Z-space radius β	jpdf of uncertain parameters	Knowledge of whether reliability exceeds a specified failure probability
Interval analysis	Safety margin $M(\mathbf{x})$	Surface of hyper-cube $h(\mathbf{x},\gamma)=\gamma$	Bounds on uncertain parameters	Safety assessment
Convex modelling	Safety margin $M(\mathbf{x})$	Surface of convex set $h(\mathbf{x},\gamma)=\gamma$	Convex set description	Safety assessment
Fuzzy modelling	Safety margin $M(\mathbf{x})$	Surface of convex set $h(\mathbf{x},\gamma)=\gamma$ at a prescribed α level	Convex set description at each α level	Safety assessment

Testing for Model Validation in Structural Dynamics
~ *Where Idealization Meets Reality*

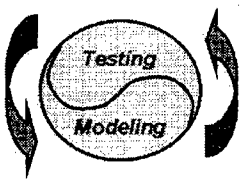

Charles R. Pickrel, Boeing Commercial Airplanes Group

Introduction

It is a remarkable fact that mathematics can and does describe the world around us. In engineering we make practical use of this fact by using mathematical models to predict system behavior, and to synthesize or design systems for desired behavior. By *model* we mean a mathematical representation which approximately describes a system or phenomenon as observed through testing. By *test*, we mean performing measurements, experiments or observations. "Testing" and "Modeling" are complementary, interacting and synergistic activities which form the basis of the scientific method. Utilizing "model" and "test" to design products or predict system behavior is an activity which is central to the practice of engineering.

Models allow us to predict behavior of a product over a broad range of operating conditions before it is built. Behavior can be predicted for conditions which cannot be tested, such as failure conditions. Model based design optimization has led to significant improvements in the operation, performance, manufacture or cost of many products. Validation of a design must often depend on both model and test. Models, in a general sense, provide the context for interpreting or understanding test results and for recognizing a "right answer" when we see one.

Testing provides empirical factors for use in models, quantifies operating environments, demonstrates the adequacy of a design, or can provide results to validate individual models or new modeling methods. Validation of designs or products is often required when product "failure" or inadequacy could impact personal safety or result in financial loss. As new modeling methods are developed, they are validated by testing.

Modeling and testing are interdependent activities. Models are dependent on test data for input, such as physical constants, and for validation or tuning. Tests are dependent on modeling in many ways: from transducer behavior and sensor location to modal analysis, data interpretation and validation. Models often bridge the gap between what we *can* test and what we *want* to test. We are reminded of a quote from Immanuel Kant, reconciling the Rationalists with the Objectivists in philosophy:

"Concepts without percepts are empty;
percepts without concepts are blind."
~ Immanuel Kant

Linearity
Time Invariance
Friction, damping
Boundary conditions
Operating environment
Engines running
Interface forces
Transonic shock waves
Reynolds number
Discretization
Mass/stiffness loading
Transducer behavior
Noise
Observability
Resources, Time, $, £...

Figure 1, Issues and complexities.

Both modeling and testing require practical simplifications and idealizations of the "real world." For example see the list in Figure 1. Validation of a model with test data provides interesting challenges, which we will explore in this paper.

We will explore many of these issues using practical examples from our experience in airplane vibration testing, including the validation of a flutter analysis for a commercial transport airplane. In this case, the "real world" consists of an airplane in flight, Figure 2. Idealized representations are symbolized by: digital drafting data sets from which the structure is manufactured; a finite element model of the structure; the spatial representation from sensor locations used in a modal test. Emphasis in this paper will be placed on validation of the structural dynamic model of the airplane the by means of a modal test, or "Ground Vibration Test" (GVT). Our airplane, of course, knows nothing of our idealizations nor of our separation of aerodynamics, structural dynamics and controls into separate disciplines or departments.

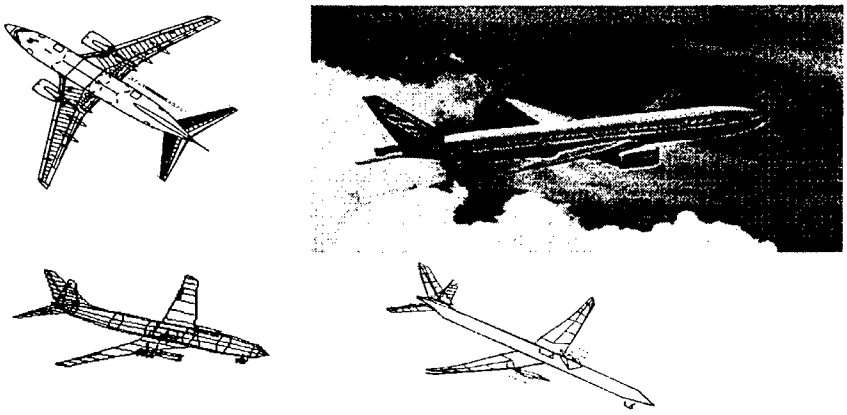

Figure 2, Idealizations *versus* Reality – An actual airplane in flight is represented by idealizations, such as CAD data sets, FE model, GVT sensor locations.

Design Validation by Model and Test

Validation of a model with test data implies that a comparison is to be made between the prediction of a model and the results from a test, as in Figure 3. The basis for comparison of structural dynamic models is often a set of modes, but could also be Frequency Response Functions (FRF's) or time responses to an input [1, 2]. Most situations are less straight forward, as in Figure 4. The behavior we wish to model and predict involves actual operation, where engines are running and many unknown inputs to our system make measurement very challenging, costly or even impossible. The structure itself is manufactured from a defining set of geometry or "CAD drawings," perhaps within some tolerance, and may exhibit variation in manufacture.

In a sense, we are trying to "get the same answer twice" using two different approaches: the first based primarily on modeling, the second based primarily on testing. Both approaches are likely to be "circuitous" and require simplification or approximation, and they are prone to various errors. The "one true answer" is usually known only through inference. We validate our design based on both model and test.

Clearly, the modeling process could be treated in greater detail. Often several modeling steps are required, sometimes performed by different people or organizations or companies. For example, multiple models of components may be assembled into a larger "model". Modeling issues will not be addressed further in this paper, which will emphasize testing issues. Another important issue which we will not discuss is model updating [3]: "When our model and test predictions do not agree within their respective confidence intervals, what changes can we make to improve the predictive capability of our model?" We leave this important topic to other authors, more versed on this topic.

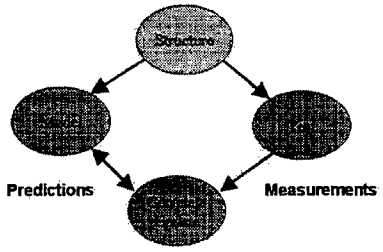

Figure 3, Conceptual Validation Map.

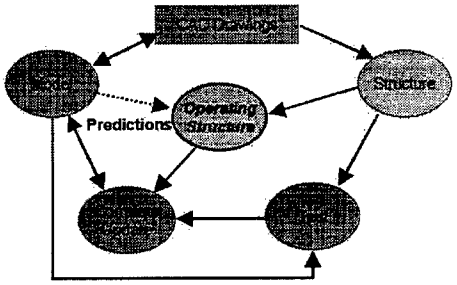

Figure 4, Typical Validation map.

Seldom can we model or test exactly what we want. The article or structure which we test may differ in many significant ways from the system in operation. It may not be practical or possible to test all or any of the conditions which must be validated for a design. We will illustrate with examples from testing transport airplanes. The airplane flutter speed must be at least 15% higher than the operating flight envelope and can not be tested directly. We can demonstrate in flight test that the airplane exhibits adequate stability, and does not flutter, at speeds to the limit of the flight envelope. A model is required to show adequate margin to the actual flutter speed.

The chart in Figure 5 depicts a simplified example of using test-validated models to predict the flutter speed of a transport airplane. The model consists of structural and

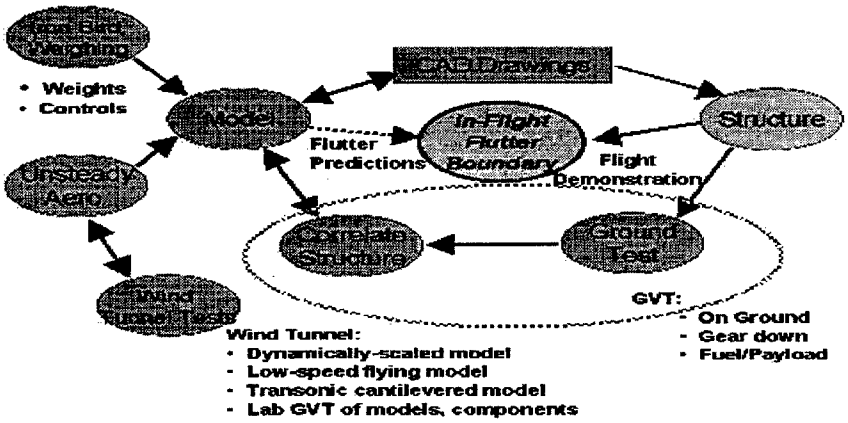

Figure 5, Validation Map for Airplane Flutter Boundary.

aerodynamic components. Ideally we would like to validate these components separately. The structural model is validated by a modal test, which we call a ground vibration test (GVT). Some mass properties are validated by weighing individual parts and components, and of course the full airplane. The dynamics of control system components are often measured on an "iron bird" in the laboratory. The aerodynamic modeling is validated by wind tunnel flutter model tests. The "Wind Tunnel Tests" bubble in Figure 5 could be expanded, in fractal fashion, to look like a reduced version of the whole figure. The flutter-model is a dynamically scaled structure which represents the actual airplane, but is simplified to make it easy to model correctly. A separate GVT is conducted on this scaled structure. In fact, different models may be used to test in subsonic and transonic flow environments.

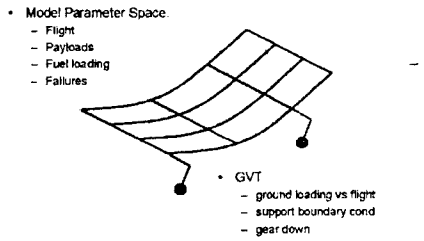

Figure 6, Tests "pin a corner" in parameter space.

Seldom can one test exactly what one wants. In this example, we wish to model an airplane in flight, but our GVT test configuration has landing gears down, and soft supported boundary conditions. A separate model is prepared to represent the specific GVT configuration. For flutter prediction, we use a family of models which represents aerodynamics at various flight conditions as well as fuel and payload mass variations, and also certain failure conditions. This is common, as in Figure 6, that a validated model or family of models is used to predict the behavior of a structure over a range of parameters (which we are calling "parameter space"). The model used for correlation with test has several parameters different from the model used for in-fight predictions. Alternate configurations can be, and sometimes are, tested: payloads, fuel loading, boundary conditions. Inevitably the modeling prediction which supports engineering designs or decisions will represent an extrapolation from the validation test data.

Modal Testing Example – Airplane GVT

We turn our attention to the validation of our structural model. This application example will bring to light many of the practical aspects of model-test correlation. We will test the first of a new airplane type as it is structurally complete, at the end of an assembly line. The cost and pressing schedule of a new airplane program motivates us to complete testing in as short a time as possible.

Our test strategy will be as follows: The airplane will be placed on "soft supports," under the landing gears, to approximate a "free-free" condition. The actual test configuration will be modeled, and we will use a modal basis for correlation. We will identify a "small signal" linear modal model, using multi-input random burst excitation. Experience has shown this small signal model (low level random excitation) is not completely representative of in flight operation, so these differences will be address using sine excitation at various levels of response amplitude.

Test Design – Leverages Pre-Test Model

We make use of our model to design the modal test to facilitate conduct of the test in the shortest possible time, and to maximize the usability of the test data for model correlation and improvement. A pre-test simulation aids in location of measurements and selection of excitation hardware [4].

We compute a set of about 30 to 50 locations for sensors which will maximize the spatial independence of our predicted mode shapes, Figure 7a [5, 6]. We then add sensors to this set to satisfy the needs of: shape visualization, symmetry, shape expansion, off-

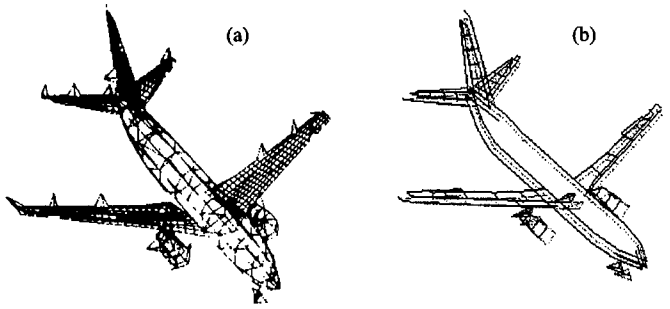

Figure 7, Sensor locations: a) Locations for effective independence, b) Full grid of for mode shape visualization.

$$PROD_i = \sqrt[N_a-1]{\prod_{n=1}^{N_a} |\phi_{ni}| * \omega_n}$$

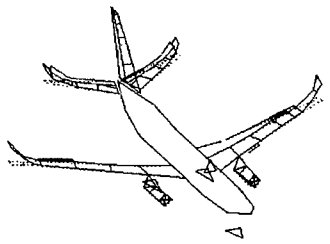

Figure 8, Product of modal coefficients shows where all modes may be excited.

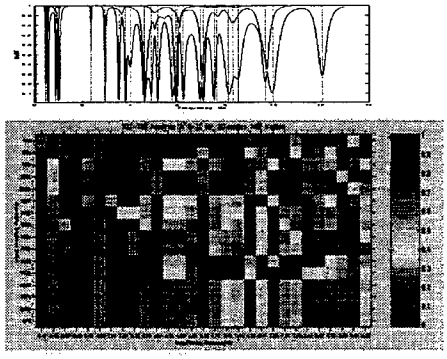

Figure 9, MvMIF shows how easily modes will be identified from candidate locations.

diagonal terms in the Modal Assurance Criterion (MAC) [7], and tradition, resulting in the set shown in Figure 7b. Subsets of sensors are identified to facilitate modal parameter estimation for different frequency bands.

The same pre-test mode shapes and synthesized FRF's are used to select input locations for shaker excitation, again with emphasis on facilitating the identification of a modal model with emphasis on the target modes. The product of all mode shapes, Figure 8, indicates locations which will excite all modes, if not equally. Mode indicator functions are computed from sets of FRF's for candidate input locations, examples of which are shown in Figure 9. Our objective is to gain assurance that we will be able to identify modes from the experimental FRF's quickly and confidently.

Another consideration for exciter location is that all modes, or a set of target modes be excited "equally" or almost equally. Consideration of cost and testing flow time often leads to compromises. In the interest of keeping the number of exciters to a minimum, we choose to emphasize the most important dozen or so structural modes (from the standpoint of predicting flutter). Certain local modes involving soft support local degrees of freedom will not be well excited. Other local modes such as control rotation will be excited independently.

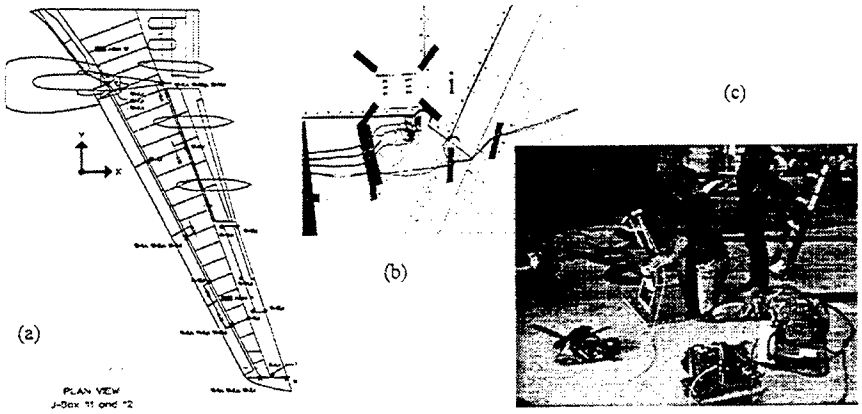

Figure 10, Sensor Locations: (a) detail drawings, (b) closeup of accelerometer installation, (c) technician positions shaker input.

Practical Considerations

Actual sensor and actuator locations must consider both model geometry and details of the physical structure. A potential source of discrepancy between model predictions and measured data arises from the position and orientation of sensors and exciters. Where compromises are necessitated by physical limitations, an interpolation or expansion must be applied to test responses (or modal coefficients) for correlation with model predictions. Detailed planning, such as the drawing in Figure 10a, helps to facilitate the sensor installation process and minimizes discrepancies.

The photograph in Figure 10b shows a close up of a tri-axial accelerometer attached to the rear spar of the vertical fin. Surface details, such as fastener rows, may prevent the sensor from being located precisely at the predetermined location. Curved surfaces can make precise directional alignment difficult in the horizontal plane. The location pictured is about 45 feet above the floor, requiring a "high-lift" for access. Binoculars are required to view this these sensors from the floor.

The photograph in Figure 10c shows a technician adjusting the alignment and location of a shaker which will apply nominally vertical excitation to an engine nacelle. Local surface contour and stiffness, or surface features such as splices or fasteners, will dictate the exact placement and direction of excitation. Directions may be deliberately skewed with respect to the model coordinate system to facilitate modal excitation.

Soft Supported Boundary Conditions

A practical means of supporting the airplane is desired, which can approximate a free-free boundary condition. The support must be quick and easy to install while imposing no threat of harm to the airplane. The photograph in Figure 11 is taken looking forward at the right hand main landing gear, which is raised about 2 inches off the floor by the soft support system (yellow). The air bags provide the desired compliant boundary condition. which is sufficient to separate the rigid body modes of the airplane from the flexible modes. The landing gear support beam slides under the gear truck, permitting quick installation of the system.

Figure 12 shows a comparison of FRF's shown for the airplane sitting on its tires and floating on the soft support system. We see that, resting on the tires, the first dozen flexible modes, which are the most critical to model well, are significantly altered by the

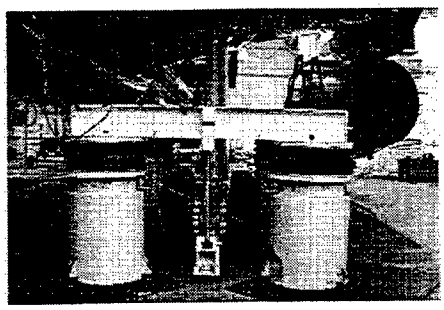

Figure 11, Rear view of soft support under right main landing gear.

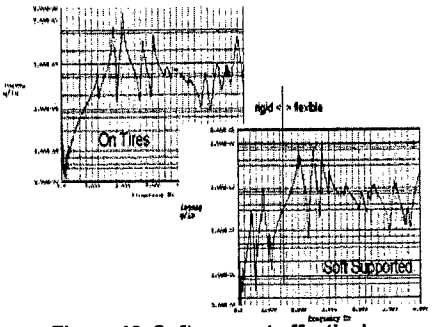

Figure 12, Soft support effectively separates rigid modes from flexible modes.

tire stiffness'. The soft support system successfully separates the rigid modes from the flexible modes.

The support system is not perfect, however, as there is significant moving mass which introduces new modes into the system. We compare the modes of the free-free airplane with the soft-supported airplane. The image in Figure 13 depicts the Modal Assurance Criteria (MAC) [7] values between two sets of mode shapes, both from the analysis model, for the flexible airplane modes from 2 to 10 Hz. On the horizontal X axis are the flexible modes with Free-Free boundary conditions, while on the vertical Y axis are the flexible modes with the soft support system included in the model. Modes numbers 7 to 35 are shown. A few new modes have been introduced, which involve local modes of the soft support. Fortunately, none of the critical mode shapes are affected by the soft support system.

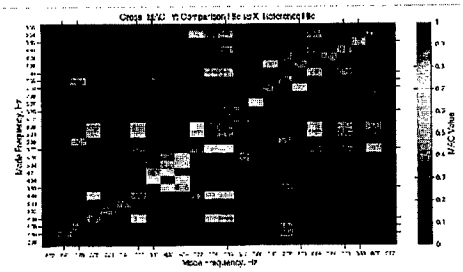

Figure 13, MAC compares analysis mode shapes for soft-supported (Y) vs free-free (X).

Measurements

Conceptually a modal test seems straight forward: one excites a structure and measures response at all the sensor locations. From this input/output data we calculate FRF's and identify modal properties [1, 2]. In practice, we must cope with transducer characteristics and various sources of noise [8]. One must arrive at an appropriate level of excitation. In Figure 14 sample FRF's are shown, from a wing tip vertical shaker input, for the frequency range from 1 to 25 Hz, measured during a four-input MIMO test using burst random excitation. The most responsive (wing tip vertical) and least responsive (body nose fore-aft) locations are shown. The response dynamic range is

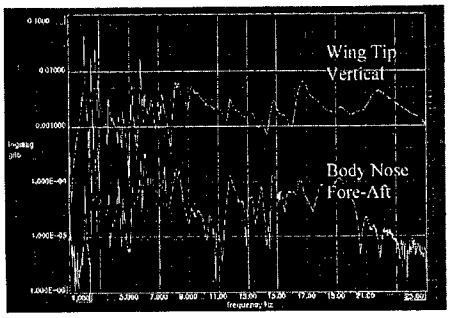

Figure 14, Typical FRF's of a transport airplane: showing highest and lowest response locations.

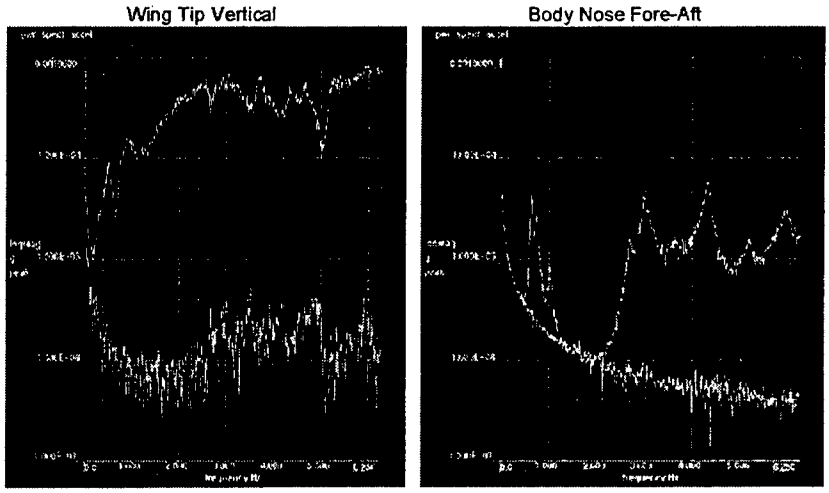

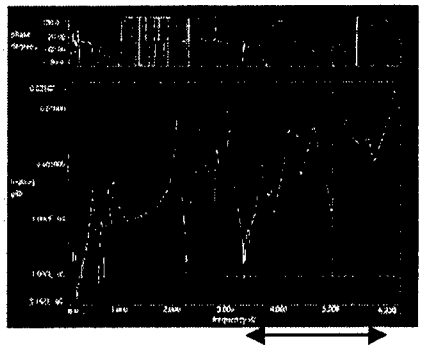

Figure 16, Reciprocal FRF's from wing tip to wing tip are nearly identical from the burst random excitation.

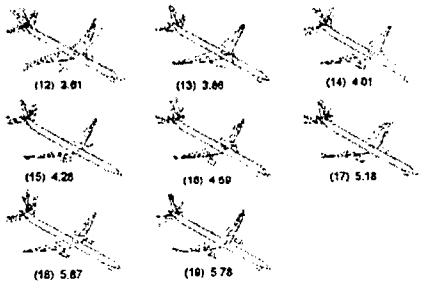

Figure 17, Mode shapes of eight modes in the frequency band from 3.4 to 6 Hz.

Figure 15, Response spectrum and noise floor.

about 4 decades, and the bottom of the graph corresponds to one micro-g per pound. The airplane has about 65 modes in this frequency range.

The noise floor can be seen in the power spectra plotted in Figure 15 which compare the same two response locations as Figure 14, in the frequency range 0 to 6.25 Hz. The upper curve shows the response during a four input random burst excitation, while the lower curve shows the noise floor with the shaker's drive signal off. On the left is a wing tip vertical sensor; on the right is the body nose fore-aft sensor. Together these span the full range of response amplitude. At this level of excitation, the signal to noise ratio varies from less than 100 to over 300. Note the wing tip sensor noise floor shows some response to environmental excitation.

Averaged FRF's from the MIMO burst random test are plotted in Figure 16, which shows two reciprocal measurements from wing tip to wing. The two measurements, are nearly

indistinguishable, revealing that the structure is substantially linear under these measurement conditions. These data are used to identify our "small signal model."

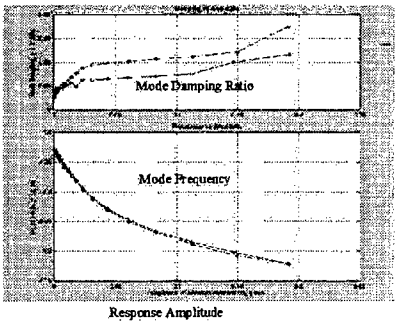

Figure 18, Variations of mode frequency and damping with response amplitude.

Departure from Linearity

From experience we know that our small-signal model, obtained from the MIMO burst random test, will not be fully representative of our in-flight airplane. We choose to represent the structure with a linear model. Departure from linearity is a significant source of uncertainty or error in this model. This was investigated in two ways: 1) A few important modes were dwelled, or "tuned," over a range of different response levels; 2) FRF's were measured across a selected frequency band using different levels of sine excitation, and a linear modal model was identified from each data set. In both cases we are considering a nominal linear model which best describes the behavior of the structure at each of several amplitudes of response.

The mode frequency and damping of an important mode exhibits variation with response amplitude, as shown in Figure 18. These trends were measured by performing a series of "mini-sweeps" in the vicinity of the mode frequency at each of several amplitude levels, from which linear modal parameters were extracted. This mode was identified at 4.28 Hz from the random data. While its shape did not change in this range, the frequency drops about 3% and the damping increases dramatically at higher amplitude. The damping values measured during the MIMO random excitation are typically very low and not representative or relevant to our operating condition. Considering the variation in both frequency and damping, one must decide "what is a relevant response amplitude?" if one

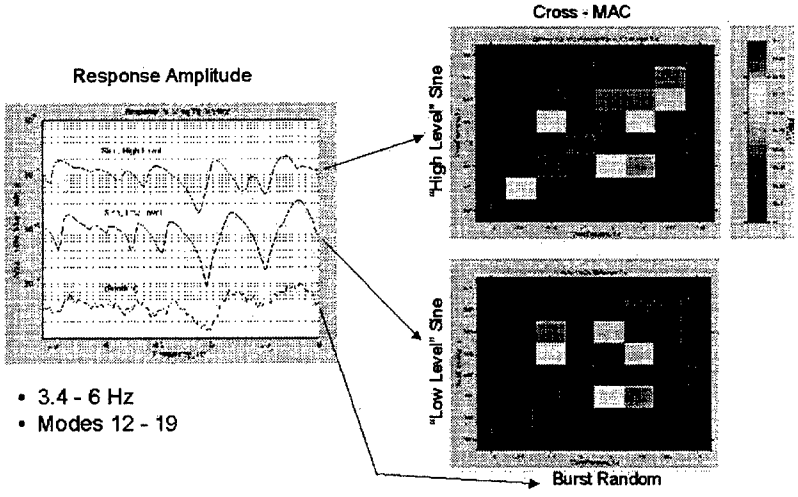

Figure 19, Comparison of mode shapes derived from measurements at different force and response amplitudes.

is to select a representative nominal linear model.

The important band of frequencies from 3.4 to 6.0 Hz, as indicated by the arrow in Figure 16, was tested with two different levels of sine excitation, and results were compared with results of the low level random excitation. The "high" amplitude sine test would have caused passengers' drinks to spill. The "low" amplitude sine test and the random test have approximately comparable overall response levels. There are 8 modes in this 3.4 to 6.0 Hz. band, whose shapes are depicted in Figure 17. (A ninth mode lies close above 6.0 Hz in the random and low-level sine data, but falls just below 6.0 Hz. In the high-level sine data). We compare the shapes of these modes as identified from each of these data sets, using the MAC, as shown in Figure 20. We find that the important structural mode shapes are unchanged by excitation level. The most noticeable change in shape occurs for the nacelle strut lateral bending mode at about 3.8 Hz (the second mode shown in Figure 19).

Contrasting Sine and Random Excitation

If the frequency and damping of structural modes is amplitude dependant, why not always perform a modal test using sine excitation at a representative response amplitude? In the case of our transport airplane, we have found that a linear modal model is much easier to identify, unambiguously from the linear data obtained during low level, MIMO random excitation. As we will see, the higher response levels result in significant departures from linearity. The resulting data is more difficult to "fit" with a linear model. Also, the sine testing requires considerably greater test time. Thus we cannot directly or conveniently measure what we want – we are forced to compromise and "piece together" our desired result.

Looking at Figure 20, we see non-linearity in the structure appears to be the dominant source of variance in mode frequency and damping for this structure. This chart compares pole estimates from the MIMO burst random data (left) with the high level stepped sine data (right) in the frequency range 3.4 to 4.8 Hz. The bottom graphs are

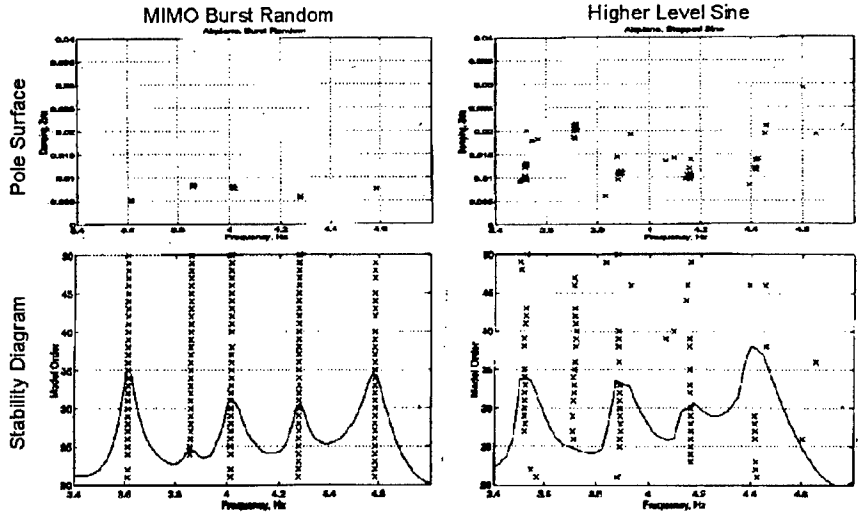

Figure 20, "Nonlinearity" dominates uncertainty in mode pole locations.

"stability diagrams" which show the pole frequencies of successively higher order models

together with the an indicator function (the log of summed FRF magnitudes) [9]. The top graphs show the same data plotted on the "pole surface" (damping ratio vs frequency). The size of the cluster of estimates for each pole is an indicator of the variance in that pole for the given data set and solution method. Clearly, the data from random excitation is "easier to fit" (to estimate unambiguously an experimental, modal model) when compared to the data from this particular sine excitation. We will take a closer look at the FRF data to see why this is so.

Numerical Data Assessment, SVD

Taking a short digression, we apply singular value decomposition (SVD) [10, 11] to reveal linear relationships in our data and assess its numerical conditioning. We start with the MIMO random FRF's, from one input location, to each of 258 response locations at frequencies in the band 3.4 to 6 Hz (lower left graph). This is the same random data which was used in Figures 19 and 20. Eight modes were found in this band, and two modes lie close outside this band. Placing the FRF's columnwise in a matrix, we use SVD to compute the singular values and the Principal Response Functions (PRF) [12, 13] as shown in Figure 21.

For these data we see the singular values in the top right graph and the PRF's in the bottom right graph. The singular values tell us the relative magnitude of the independent "linear relationships" in the FRF data, and the PRF's show us how these are distributed *vs,* frequency. Interpretation of these singular values and PRF's requires we have a "model" – by which we mean an expectation based on theory and mathematics. For a linear modal model, we expect to find a number of significant singular values equal to the number of active modes, a quickly diminishing contribution by the residual effects of modes outside this frequency band, and a noise floor due to measurement noise. In Figure 21 the singular values show perhaps 9 "significant" modes (with a condition number of about 20) and diminishing contribution from residual out-of-band modes and

$A = \{ H_{1q} H_{2Q} \ldots H_{pq} \}$

$A = U \Sigma V^H$

$U^H U = I, V^H V = I$

diagonal Σ = singular values

PRF = $U \Sigma$

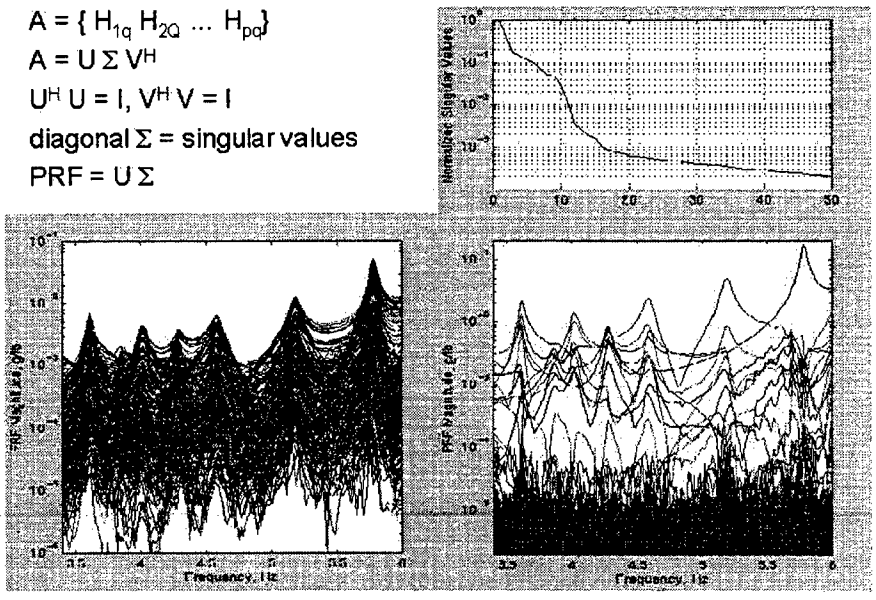

Figure 21, SVD reveals linear relationships in data.

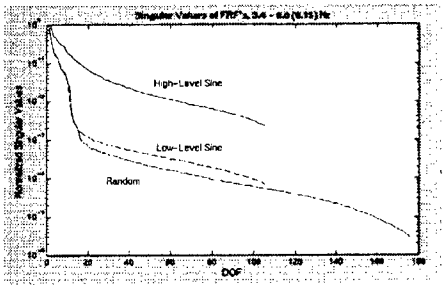

Figure 22, Normalized singular values of frfs measured under different excitation: a) Random, b) low-level stepped sine, c) higher level sine.

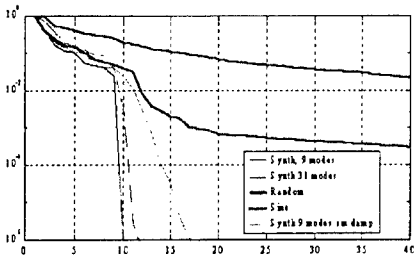

Figure 23, Normalized singular values of measured FRF's, compared with synthesized FRF's, showing effects of damping and residual modes.

non-linear response. A noise floor begins at a condition number of about 500 or so, which is consistent with our noise floor assessment above. Condition number of the matrix is the ratio of the largest singular value to the smallest [10].

Now we compare, in Figure 22, these singular values with those computed from the two stepped-sine-excitation data sets at different response (and force) amplitudes. These are singular values of the FRF's, from which the mode shapes were compared in Figure 19, using 258 responses from a single wing tip input. The low level sine is very nearly identical to the random data set, but exhibits a slightly higher noise floor. The high level sine data is very "noisy" such that the noise obscures the data from the nine modes in this frequency band. The high level excitation results in significant departure from linear behavior. Recall that the SVD is removing and separating linear relationships from our data. Many "linear relationships" are required to account for the non-linear behavior at the higher response level in this data set. When one is trying to numerically identify a linear modal model from this data, this looks like "noise."

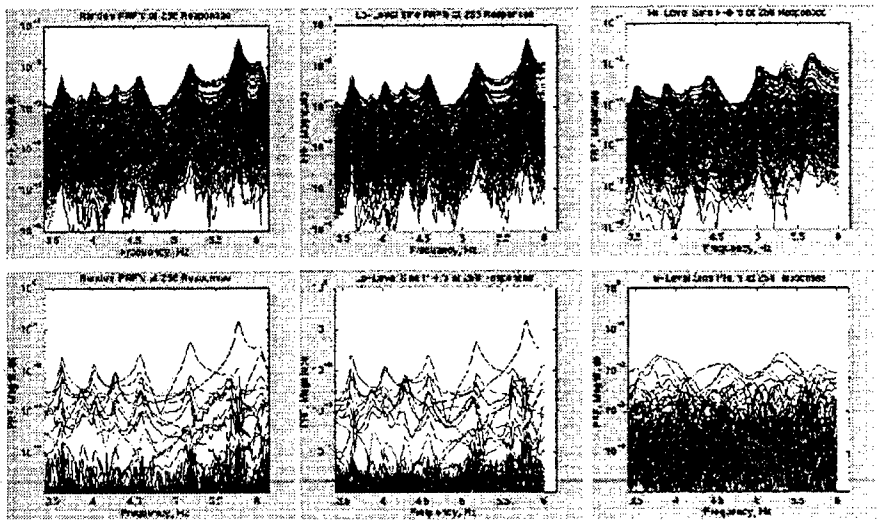

Figure 24, FRF's and PRF's for different levels of excitation: Top row, FRF's; bottom row PRF's. Left column – random; middle column – low level sine; right column – higher level sine.

(Nine modes were found in these three data sets, eight of which were shown in Figure 19. The ninth mode lies just above the 6 HZ upper limit of the middle, low level sine data set. At the higher level of response, this mode drops below 6 HZ. The random data set extends to 6.15 Hz to include this mode - which is predominantly a local soft-support mode.)

The singular values in Figures 21 and 22, derived from our test data, may not appear meaningful at first glance. It is helpful to compare them with expectations from a supporting model. We have synthesized noise free FRF's, with and without the contribution of residual out-of-band modes, using the experimental modal model. The graph in Figure 23 compares the singular values of these synthesized FRF's with the singular values of the random and high-level sine FRF data sets. The residual contribution of many out of band modes can be seen. One presumes that additional contributions to the test data curves arise from nonlinear response and from other noise and errors in the data.

There is a dramatic difference between the random and sine data. Presumably, this results from the significantly higher contribution from nonlinear response in the higher-amplitude sine data. Looking at the curve for the sine data, it appears that the smaller contribution of the more weakly excited modes is being "overwhelmed" by the non-linear response from the strongest modes. We saw in Figure 20 that this stepped sign data was more difficult to "fit" (estimate modal parameters) than the corresponding random data. That this would be so is born out by the above singular values. This sine data is "poorly conditioned" for numerical estimation because the nonlinear "noise" obscures the linear features in the data which we seek to identify.

This is further illustrated for the same three data sets, in Figure 24. The top row of graphs compare the full set of 258 FRF's from the wing tip input for each of three different excitations. The bottom row shows the Principal Response Functions, decomposed by SVD. On the left is the data set from burst random excitation. The middle column is from the low level stepped sine excitation. The right column is the high level sine excitation, which clearly shows higher damping and a much higher "noise floor."

Modal Test Strategy - Revisited

We revisit the notion that in real-world testing we seldom can test what we want - we are forced by circumstances to compromise. Then we must come to our original goal by a more circuitous route. We choose to represent our airplane with a linear, dynamic model. What we want from our GVT is a linear modal model, relevant to operating conditions, which can be readily identified from test data. The MIMO burst random excitation provides us a convenient means to identify the linear model, but the frequency and especially the damping values are not relevant to our operating condition. The sine testing gets us close to the relevant operating amplitudes, but the test time can be very expensive. So we choose to identify a linear, "small signal" model from random excitation, then do a limited amount of sine testing to "adjust" the model (frequency and damping values) to represent operating conditions.

We have seen some evidence that nonlinear behavior of our structure, at a level of response typical of operation, will limit our ability to model behavior perfectly (more closely than a few percent) with our idealized linear models. Although beyond this discussion, it can be demonstrated that this level of uncertainty is acceptable for this application, and is accommodated by conservatism and safety factors.

Limits to Correlation

We would like to use our test results to tune or improve our model, whether by numerical approach, engineering judgement or both. Often, this is done by comparing the mode frequencies of the model with those frequencies for the same modes as derived from test. If the mode shapes are not "the same" or nearly so, then we have nothing to compare on this basis. So this comparison is usually limited to about 10 to perhaps 30 modes, and inevitably falls apart at higher frequencies.

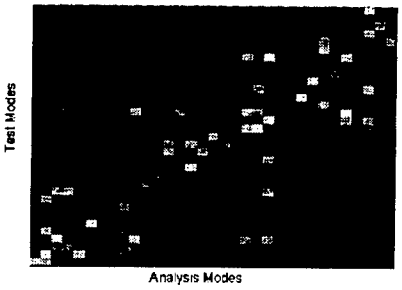

Figure 25, MAC between mode shapes of model *vs* test.

In Figure 25 the mode shapes are compared using the MAC between the predictions of the analysis model (x axis) and the test-derived mode shapes (y axis). Mode numbers 1 - 33 are shown for the frequency range 0 - 10 Hz. The important flexible modes agree quite well. For the purposes of predicting flutter, this correlation is excellent. The correlation of shapes in this example falls apart after 20 or so modes.

At even higher frequencies, we find the non-linearity of the structure renders linear modal analysis impractical. We compare modal models from two different levels of excitation, in the mid frequency range, in Figure 26. (Note: This example is taken from a different airplane test than the previous examples). The FRF's and mode shapes from a small-signal random test are compared with those derived from a higher level sine sweep test. Note the shapes compared are for mode numbers 34 to 47. Only a few of these modes have similar shapes. For the most part one would say there is no unique modal model (derived by linear modal analysis) to describe this structure at these frequencies. Similar differences in mode shape occurred when comparing data from sine sweeps at two different levels of excitation. Note that the FRF's remain substantially similar.

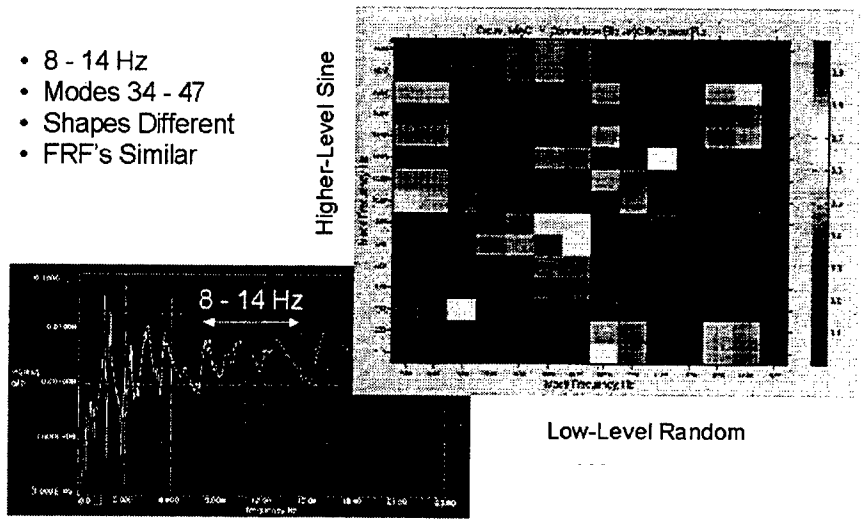

Figure 26, Modal models derived from high-level and low level excitation at mid frequencies – shapes are different, while FRF's are similar.

Operating Measurements - Flutter test results

We are challenged by a humbling taste of reality when we perform measurements on a structure in its operating environment. Here we briefly show some results from flight flutter testing, where we fly an instrumented airplane in incremental speeds up to its maximum flight speed envelope. Identification of modal parameters is again the basis for comparison between model and test, with emphasis placed upon the demonstration of adequate damping. In flight, a good deal of the damping derives from aerodynamic effects. Identifying modes is more challenging due to the presence of (unmeasured) turbulent excitation, the higher level of damping, the degree of non- linearity of the structure and the potential for time-dependent effects. In addition to these measurement challenges, we are compelled to use a minimum amount of test time due to crew safety concerns, air-traffic flight corridor issues and the extreme cost per hour of flight testing.

Using the same airplane as in Figures 14 through 24, we consider in flight measurements where excitation is provided from a sweep of the elevator control surface. In Figure 30 we see the stability diagram and pole surface from modal parameter estimation from these data, which may be compared with Figure 20. Only the frequency band from 3.2 to 6.5 Hz is shown. Of the 8 or 9 modes which were found in this band, only 3 modes are symmetric modes, which were excited and can be seen in Figure 30. Due primarily to a difference in wing fuel loading, the important mode at 4.26 Hz in Figure 17 is now found at about 3.9 Hz. The variation with Mach number of the frequency and damping of this mode is shown in Figure 31, and compared with the predictions of our model. Clearly, the variance of mode frequency and damping is much greater in flight than in the GVT.

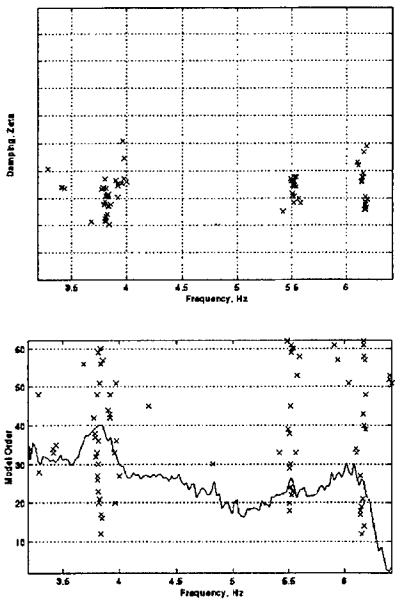

Figure 30, Pole Surface and Stability Diagram from in-flight measurements, elevator excitation.

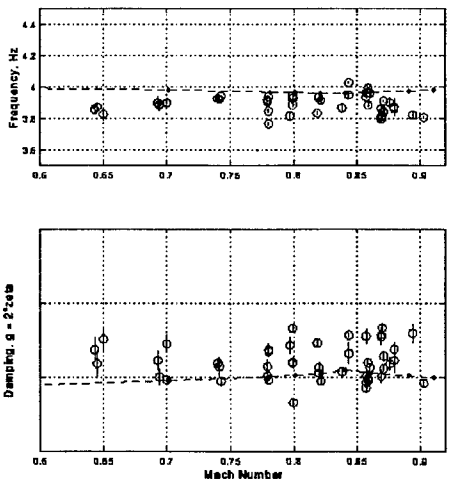

Figure 31, Comparison of predicted --- and measured O mode frequency and damping, plotted *vs* Mach number.

Vibration Trouble Shooting

We are often called upon to solve problems involving vibration. These problems manifest themselves as response: directly, due to perceived vibration or noise; or indirectly as high cycle fatigue failures. To reduce or eliminate the response, we must identify the energy source and the transmission path. To do so requires a model. Seldom do we have an FE model, but we often work with a "mental model" like the one pictured in Figure 33. Physical models provide the context for interpreting and understanding measured data. Having data without a model is like having answers without a question. The value of measurement always derives from the application of a mathematical model.

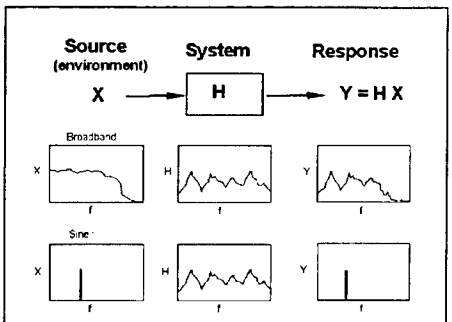

Figure 33, Source - System - Response model for vibration trouble shooting.

The source of vibration can often be deduced by the response spectrum, using "models" for source behavior, such as rotating imbalance, turbulence, vortex shedding, or impacting. Commonly an experimental model for H is measured once the source location is determined. When sufficient insight is gained, a solution can be implemented – which may consist of changing structural stiffness or damping or altering mode of operation.

Occasionally we are faced with measured data which is "inexplicable" - for which we have no model. Lacking a model, we are at a loss to define solutions to these problems, such as the source of a vibration. We illustrate with a case study example in which a turbofan engine nozzle and strut were exhibiting premature cracking and fatigue failures The illustrations in Figure 34 shows vibration and dynamic pressure measurements. A very

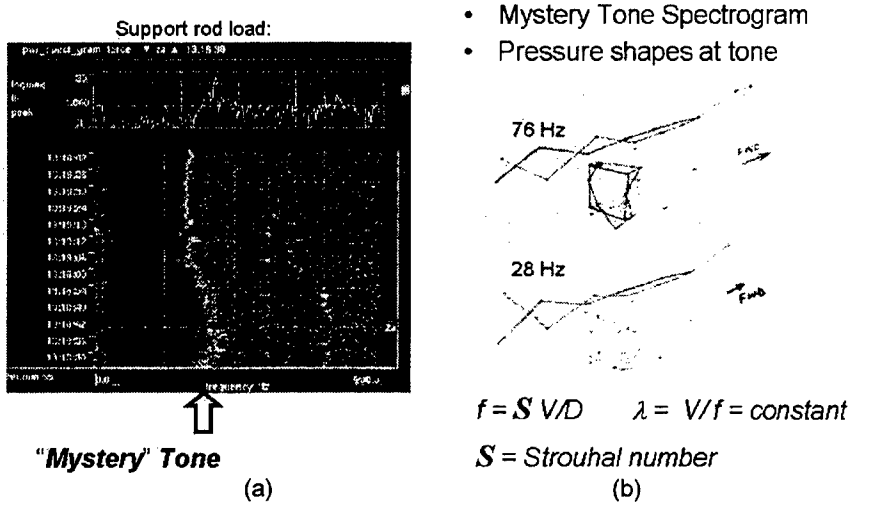

Figure 34, Tone frequency and spatial pressure variqations relate measurements to vortex shedding model.

strong tone was found (a), which at first seemed to bear no relation to engine rotation speeds. Lacking a "model" or explanation, this was called the "Mystery Tone."

As soon as an engineer noticed the tone frequency seemed to be proportional to fan duct flow velocity, the model of vortex shedding explained the tone. This "model" guided us to additional testing, which led us to the source of the tone. The dynamic pressures on either side of the aft strut fairing, at the tone frequency, can be seen in the shapes in the right hand illustration (b) with starboard side in green, port side in red. The wave length of these cyclic disturbances is seen to be independent of frequency, as expected, and points clearly to flow separation near the trailing edge of the nozzle. Additional modeling of the flow field in this area led us to a "fix."

This case is typical of the "bootstrap" interacting roles of model and test in the engineering solution of vibration problems. A disciplined approach is followed [14] which iteratively improves our understanding of the system or problem.

Conclusion

We have illustrated with examples the interdependence of modeling and testing in engineering. Practical limitations and idealizations prevent us from modeling or testing our exact (desired) operational system. The relative roles of model and test were discussed as they pertain to validation of predicted flutter boundary for a transport airplane.

Examples were shown from the GVT of a transport airplane. A pretest model of the airplane was leveraged to maximize the usefulness of the test results to validate and improve the model. Boundary condition, excitation and correlation issues were addressed. Practical measurement considerations were discussed. Departure from linearity was found to be a dominant source of uncertainty.

Interdependence of model and test is not limited to validation of FE models. Some form of physical model is required for interpretation of all test data, such as for vibration trouble shooting. We saw that great quantities of test data simply lead to increased confusion when we lack the context of an underlying model for interpretation of the data.

Models provide us with the means to calibrate and validate our measurements and to recognize a "right answer." A predictable change (from a model) in a measurement lends confidence in our measurement. We do this for every test when we calibrate our transducers and measurement systems. When repeated measurements (using our calibrated measurement system) confirm the predictions of a model, we gain confidence in the model.

Of course models are not limited to structural dynamics, or even to engineering. Predictive models are used, consciously or unconsciously, for decision making in engineering, business, economics and even interpersonal relations. Inevitably predictive models involve idealization and simplification of *reality*. We rely upon observation or measurement of *reality* to validate and revise our models. It is often challenging to observe or measure *reality* accurately, meaningfully or objectively. Gaining experience, we continually refine both our models and observations to more closely represent this *reality* [14]. Using an inaccurate or inappropriate model can be costly.

Rephrasing our quotation from Kant: *A model, not validated by test, is a speculation; Data without a model is like an answer without a question.* The reconciliation of model with test, in support of engineering predictions, is usually a significant intellectual challenge. Applying these skills to the design, prediction and validation of products is central to the practice of engineering.

References

1. Ewins, D J, *Modal Testing: Theory and Practice*, Research Studies Press, 1991.
2. Allemang, R. J., Brown, D. L., and Rost, R. W., *Experimental Modal Analysis and Dynamic Component Synthesis*, Wright Aeronautical Laboratories Report AFWAL-87-3069, 1987.
3. Friswell, M. I. and Mottershead, J. E., *Finite Element Model Updating in Structural Dynamics*, Kluwer Academic Publishers, 1995.
4. Pickrel, C. R., "A Practical Approach to Modal Pretest Design," *Mechanical Systems and Signal Processing*, V. 13, No. 2, 1999, pp. 271-295.
5. Kammer, D C, "Sensor Placement for On-Orbit Modal Identification and Correlation of Large Space Structures," *AIAA Journ of Guidance, Control and Dynamics*, Vol. 14, No. 2, pp. 251-259, 1991.
6. C. Schedlinski, M. Link, "An Approach to Optimal Pick-up and Exciter Placement," *Proceedings of the 14th International Modal Analysis Conference*, Dearborn, Michigan, 1996.
7. R. J. Allemang and D. L. Brown, "A Correlation Coefficient for Modal Vector Analysis," *Proc. 1st Intl. Modal Analysis Conf, Orlando, Florida.*, pp. 110-116, 1982.
8. McConnell, K., *Vibration Testing – Theory and Practice*, Wiley and Sons, 1996.
9. Allemang, R J, Brown, DL, and Fladung, W, "Modal Parameter Estimation: A Unified Matrix Polynomial Approach," *Proc. of the 12th Intl. Modal Analysis Conf.*, Honolulu, pp. 501-514, 1994.
10. Golub, G H, and Van Loan, C F, *Matrix Computations*, John Hopkins Univ. Press, pp. 70-84, 242-248, and 581-586, 1989.
11. Maia, Nuno M. M., "Fundamentals of Singular Value Decomposition," Proc. of IMAC 9, Florence, Italy, 1991, pp. 1515-1521.
12. Pickrel,C. R., "Estimating the Rank of Measured Response Data using SVD and Principal Response Functions," *Proc. of 2nd Intl. Conf. on Structural Dynamic Modeling*, Cumbria, U.K., 1996.
13. Pickrel, C. R., "Numerical Assessment of Test Data Using SVD," *Proc. 15th Intl. Modal Analysis Conf., Orlando*, pp. 1577-1587, 1997.
14. Ewins, D. J. "Exciting Vibrations: A Philosophical Approach to Resolving Structural Dynamics Problems," essay presented at Structural Dynamics 2000 Forum, Los Alamos, NM, April, 1999.

Progress in Nonlinear and Chaotic Dynamics of Structures

Francis C. Moon
Cornell University, Ithaca, New York, USA
June, 2000

Abstract

This paper will survey the advances in nonlinear structural dynamics in the wake of the development of modern chaos theory and nonlinear dynamical systems. Both theoretical and experimental research in the last two decades will be discussed. Among the topics reviewed will be dynamic buckling, nonlinear waves, solitary waves and spatial chaos. Nonlinearities to be discussed will include geometric terms, elasto-plastic effects, loose joints and fluid structure interactions. Methods for detecting chaos in structural systems such as the Poincare section, and time series will be discussed. The conditions for the validity of low dimensional models in nonlinear structural systems will be explored.

Introduction

This review will attempt to answer the question; When do structural systems exhibit unpredictable dynamics under deterministic forces? This is an extremely important question for structural software designers and users. Simulation capabilities have reached a high point in both hardware and software. In fact when the motions behave similar to linear vibrations of structures, it is hard to justify the application of theoretical methods to practical problems when modern structural codes with user friendly input and output capabilities are available. In the last two decades however, new phenomena in nonlinear dynamics have been discovered, including chaotic motion, which caution the uncritical use of structural codes. This is especially true when the dynamics occur over a long time scale, as contrasted with a short impulse response. These new phenomena also challenge the code designer and user to test their codes for what have now become unpredictable or parameter sensitive nonlinear behavior. In the case of structural control design, low order nonlinear models derived from modern bifurcation theory sometime offer the designer a simpler way to develop control laws.

Research on chaotic dynamics and application to structures has had a vigorous history in the last two decades in both Europe and North America. This review will use case studies from work done at Cornell University and the author apologizes for not citing all the important papers, but the list of works relating to nonlinear structural dynamics and chaos would number several hundred. Results on

classical nonlinear perturbation methods are found in the work of Nayfeh and Mook [1]. Global bifurcation methods in nonlinear dynamics are found in the seminal work of Guckenheimer and Holmes [2], and a summary of major experimental work in chaotic dynamics may be found in the one of the Author's books [3].

It should be said that even with over two decades of advances in nonlinear dynamics, there remains important unsolved problems, especially in complex, spatially distributed systems as well as dynamic energy propagation through structural joints. Also, little work has been done on chaos in elasto-plastic structures or shells and problems with fracture in structures. By *chaos* we mean motion whose time history is sensitive to initial conditions and other problem parameters even under deterministic forces. Chaotic dynamics can take the form of either transient chaos, in which the decay time is unpredictable or long time chaotic dynamics which are described by a *strange attractor*. In low dimensional systems chaos is often characterized by at least one positive *Lyapunov exponent*. There are many other types of chaos-like motions that involve a high degree of spatial complexity, especially in wave like phenomena which have yet to be fully understood, and the classical tools of chaos theory with low dimensional models may not be adequate.

Chaotic dynamics occurs in nonlinear systems and generally when more than one dynamical attractor is possible. The most common structural nonlinearites include i) geometric nonlinearites, ii) inelastic effects, iii) inertial nonlinearites, iv) uni-modal constraints, v)nonlinear force field , vi) control nonlinearites. Other types of nonlinearities not usually studied to date in chaos theory are damage effects such as fracture, fatigue, friction, wear etc. One area that has received recent attention is the nonlinear dynamics of machining and manufacturing. (See e.g. the edited volume of the Author on chaos in material processing, [4].)

Case Studies

Nonlinear structural analysis has a long history going back to the work of Euler and is summarized in the work of Love [5]. The most fundamental nonlinear effect is the coupling between in-plane stresses and lateral displacement strains as in the classical beam-column, strings, prestressed plates and shells. The classical phenomena of buckling is the result and another is the parametric vibration of structures with time periodic in-plane stresses (see Bolotin [6]). It would require a whole book to review all the research into nonlinear dynamics of structures. Therefore I will focus on a few studies in the last two decades that exhibit chaotic dynamics. These include:

a) dynamic buckling and chaos of the beam-column
b) bending-torsion chaos in the beam column
c) structures with unimodal constraints
d) fluid-structure dynamics
e) spatial-temporal chaos, and solitons in periodic structures
f) elasto-plastic structures
g) spatial chaos in the elastica

Chaos in post buckling dynamics.

The most important work here is that of P. J. Holmes [7], whose doctoral dissertation in the late 1970's was the first to show that chaos was possible in structural systems which at the time had been found in fluid dynamics. The basic model in shown in Figure 1, in which a buckled structure with two stable equilibria is forced under periodic loading. The single mode model resulted in a second order oscillator with a double well potential of the form of a Duffing equation.

$$\ddot{x} + \gamma \dot{x} - \frac{1}{2} x(1 - x^2) = f_0 \cos \omega t \qquad (1)$$

The theoretical work of Holmes was confirmed shortly thereafter in the work of Moon & Holmes (1979) [8] and Moon (1980) [9] in which the buckling forces were created by static magnetic fields. This experiment also exhibits the now classic period doubling route to chaos.

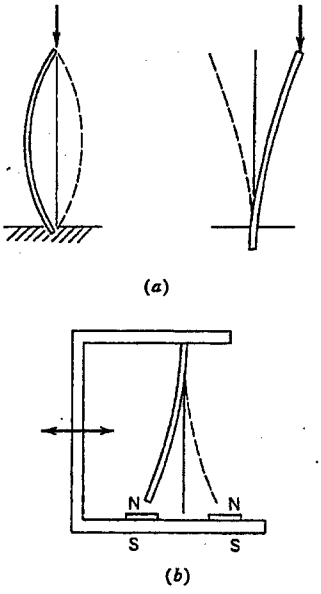

Figure 1: Buckled structures with two stable equilibrium states. Forced vibration was shown to lead to chaotic dynamics [7], [8], [9].

Another fundamental result of Holmes' original work is the derivation of a criteria for transient chaos using the work of the Russian Melnikov. This criteria provided a lower bound in the forcing amplitude-frequency plane, below which chaos would not occur.

$$f_1 = \frac{\gamma\sqrt{2}}{3\pi\omega}\cosh\left(\frac{\pi\omega}{\sqrt{2}}\right) \tag{2}$$

Later Moon and Li [10], showed that this criteria corresponded with the transition from smooth basin boundaries to fractal boundaries. The Holmes- Melnikov criteria was the first in modern nonlinear dynamics to use the idea of a homoclinic bifurcation - i.e. the intersection of stable and unstable manifolds of the Poincare map - as a method to predict the onset of chaos. This criteria could give designers a few "rules of thumb" to avoid unpredictable and chaos in systems of the type modeled by equation (1). Shortly after these early papers, there appeared a succession of both theoretical and experimental papers on nonlinear structural chaos.

One important paper at the time was that by Tang and Dowell (1990), [11], who looked at the threshold for chaos in a vibrating beam and the effect of adding more modes. They concluded that the higher modes lowered the threshold, for chaotic dynamics as found in numerical simulation.

In the 1980's, the Cornell group developed an experimental methodology to investigate chaos in nonlinear structures as well as other nonlinear systems. One of the principal tools was the use of the Poincare maps (see Moon, [3]). One recent use of the Poincare map is the control of chaos developed in the 1990's by the Maryland group of Ott, Grebogi and Yorke [12]. This technique has been used to control the chaotic motions of a buckled beam using impulse forces and nonlinear control in sync with the Poincare map. (See e.g. Moon et al [13].)

Bending torsional chaos on the beam column.

One of the principal nonlinearities of fluid mechanics is the quadratic nonlinear convection acceleration terms. In structural mechanics quadratic nonlinearities terms occur due to centripetal and Coriolis accelerations. Chaotic vibration due to inertial nonlinearities in a torsion-beam structure were reported in the dissertation of J. Cusumono at Cornell University (1987) and in the paper by Cusumono and Moon [14]. The basic model is shown in Figure 2. Vibration of the base of the thin cantilever in the weak direction can result in

spontaneous chaotic vibration near the natural frequencies as show in Figure 3. A two mode model can be derived for the as in equation 3.

$$\ddot{q}_1 + \omega_1^2 q_1 - \frac{1}{2}(\dot{q}_2)^2 \sin 2q_1 = 0$$
$$\left[\varepsilon + \sin^2 \dot{q}_1\right]\ddot{q}_2 + \varepsilon\omega_2^2 q_2 + \dot{q}_1\dot{q}_2 \sin 2q_1 = 0 \tag{3}$$

These equations have no structural geometric nonlinearities. Analysis of the higher modes have yet to be developed. For years many studies in nonlinear structures have focused on geometric nonlinearities, but these experiments show that inertial terms may sometimes be more important.

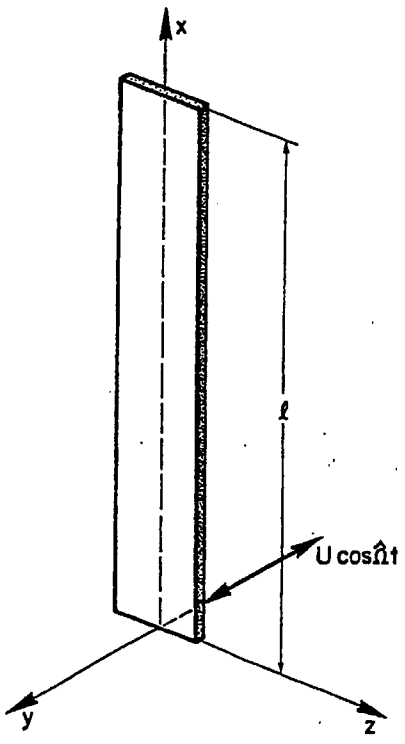

Figure 2: Forced vibration of a thin cantilever beam was shown to lead to chaotic motions with bending about the z axis and twisting about the x axis. (See [14] and Figure 3.)

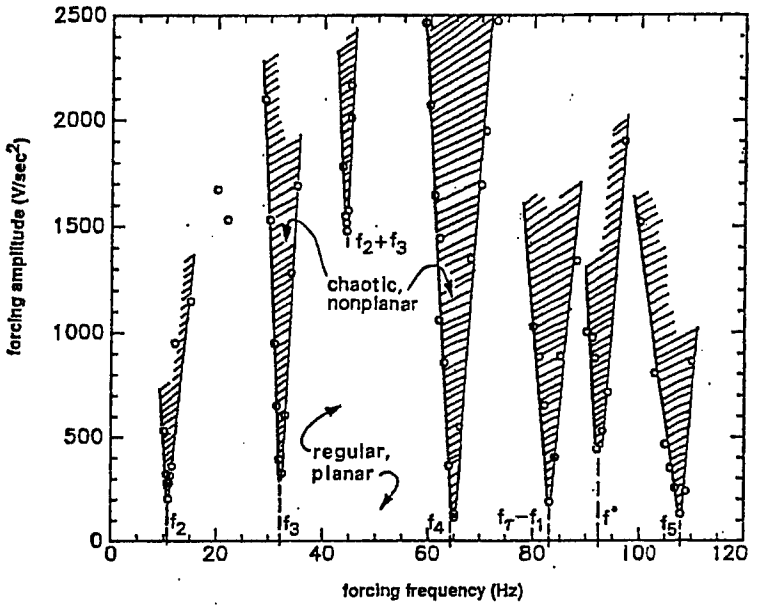

Figure 3: Regions of chaotic bending and twisting vibrations of a thin cantilever beam from Cusumano and Moon, (1995), [14].

Uni-modal constraints and nonlinear boundary conditions

When several linear substructures are attached together, nonlinearities may occur at the joints and boundary conditions, which may lead to chaos. This was illustrated in papers by Moon and Shaw,[15] Moon and Li [16], Li, Rand and Moon [17]. In the first work, the end of a cantilever is constrained in one direction but not the other direction. This problem is similar to the moored ship dynamics studied by Thompson and coworkers [18]. The experiment of Moon and Li involved a truss with loose joints. (See Figure 4.) Periodic forced vibration resulted in a broad band dynamic response. Other similar problems are boundary conditions with gaps or play in the flutter of a pipe with fluid. These problems are discussed below.

The message for practical analysts here is that even with linear structures, nonlinear boundary conditions can lead to noise and chaos, a problem that automobile manufacturers began to learn in the 1990's in part due to chaos research. Tight joints eliminate a lot of noise (or chaos) and fewer trips to the car dealer for repair.

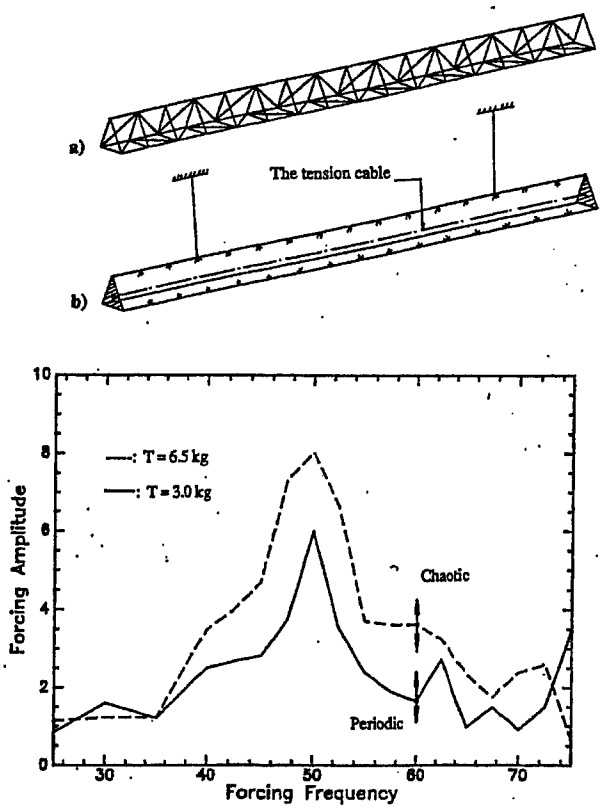

Figure 4: Regions of chaotic vibration for periodic forcing of a pin connected truss structure with center pre-tensioned cable, from Moon and Li (1990), [16].

Nonlinear fluid-structure dynamics

Fluid flowing through or around structures can result in self excited vibrations or flutter. One of the first to document chaos in flutter was Dowell [19] [20] who looked at panel flutter. Another investigator is Paidousis, [21, 22] who has documented flow induced vibrations in the power industry.

In a dissertation in my own laboratory, G. S. Copeland (1991) looked at a steady flow of water through a flexible tube. (See Copeland and Moon, [23]). In these experiments numerous regions of periodic, quasi-periodic and chaotic dynamics were observed as outlined in the Figures 5, 6. These motions corresponded to different spatial modes of the tube as well as the rigid body modes of the end mass. Copeland was able to analyze one of these modes using bifurcation theory by projecting the partial differential equations for the tube onto two spatial modes. The nonlinear analysis of two modes or a fourth order system in phase space is very difficult. Steven Wiggins of Cal Tech has published some methods to deal with such higher dimensional phase spaces [24]. Important theoretical work on nonlinear bifurcations of pipes with fluid was done by Bajaj and Sethna [25], and Steindl and Troger [26].

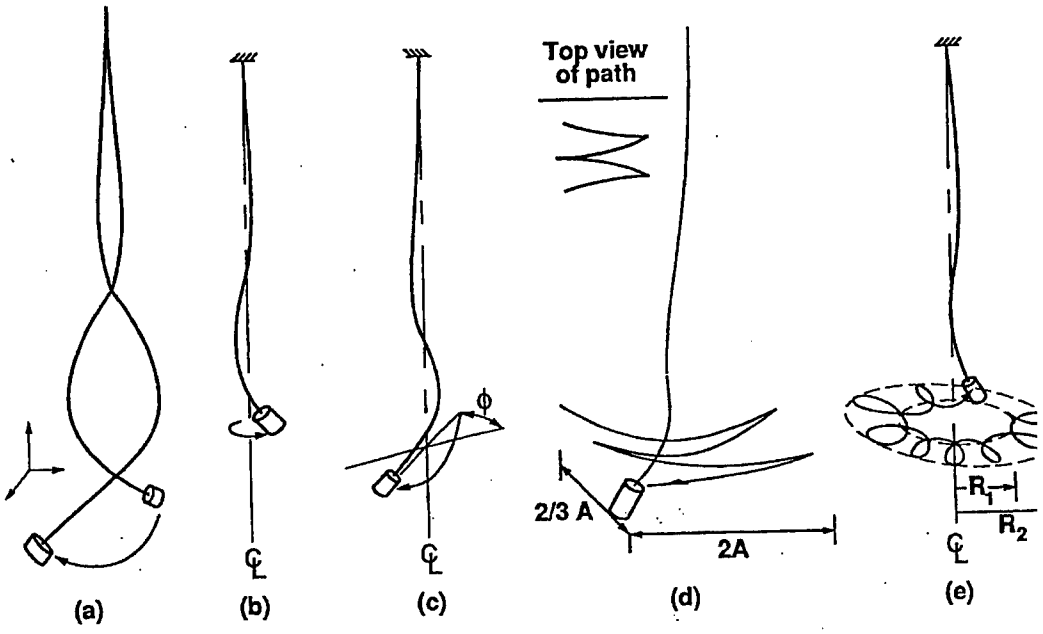

Figure 5: Multiple periodic, quasi periodic and chaotic modes of vibration of a flexible tube with steady water flow and a brass end mass from Copeland and Moon, (1992), [23].

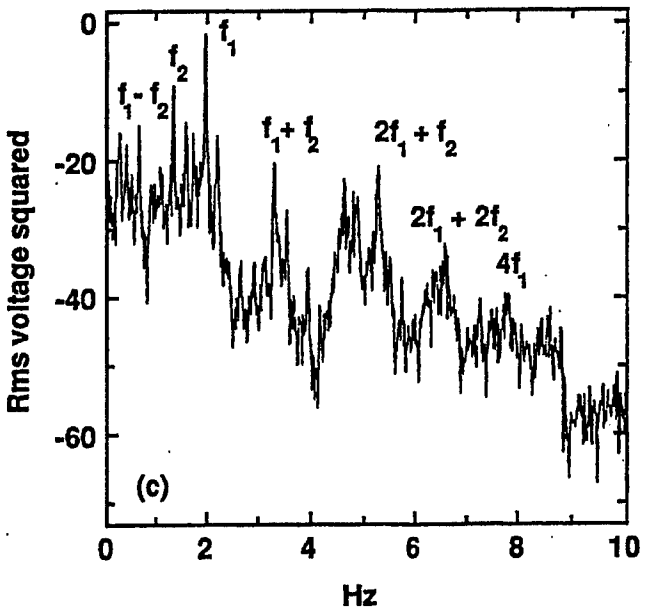

Figure 6: Power spectrum of combined quasi-periodic and chaotic vibrations of a flexible tube with steady fluid flow from Copeland and Moon, (1992), [23].

These problems illustrate the difficulty of classical chaos theory using low order models with three and fourth order phase spaces. In particular when the dynamic phenomena leads to essential motions that involve more spatial modes, as in wave-like problems, other methodologies must be used

Spatial-temporal chaos and solitons in periodic structures.

Many important structural systems involve periodic reinforcement as in ships, missiles and aircraft. (Figure 7). Analysis of such systems often involve reducing the number of degrees of freedom in each cell. One such model is the work of M. Davies in a Cornell dissertation of 1993. (See Davies & Moon [27]). The horizontal elements are arches and the vertical structures are linear beams.

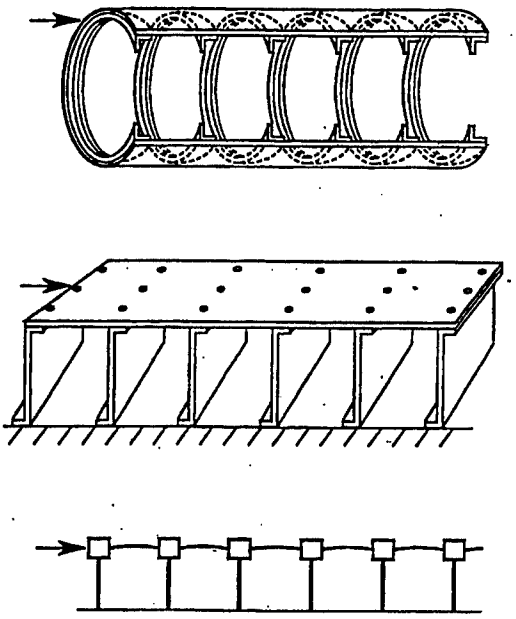

Figure 7: Top and center; periodically reinforced structures. Bottom; experimental model with horizontal structure with initial curvature and vertical cantilever structure; from Davies and Moon, (1994), [27].

This system has a weak nonlinearity for decreasing distance between neighboring masses (i.e. a weak force from the connecting arch), and a strong, almost exponential increase in force for increasing distance between masses. This model has some shell type behavior. Davies was able to approximately model the force with an exponential potential for the arch and a linear force for the vertical beam. Both experiments and analysis were performed. By using a single mode for the arch and the cantilevers, a single equation of motion for each cell was obtained.

$$m\frac{d^2x_i}{d^2t} = \frac{\gamma}{b}\left(e^{b(x_{i+1}-x_i)} - e^{b(x_i-x_{i-1})}\right) - kx_i + c\left(\frac{dx_{i+1}}{dt} - 2\frac{dx_i}{dt} + \frac{dx_{i-1}}{dt}\right) \quad (4)$$

This model has a counterpart in molecular dynamics known as a Toda lattice equation [28]. Without the linear springs to ground, the Toda lattice is known to exhibit nonlinear localized waves which preserve shape. When these waves can move through each other and preserve

energy, the nonlinear wave is known as a *soliton*. Experiments on a nine cell model show that soliton like behavior appears to be present when an impulse is put into one end of the lattice. However due to the presence of the linear springs, the waves begin to disperse and a complex spatio-temporal chaos appears. (Figure 8).

Another phenomena is the spontaneous transformation of forced nonlinear vibration of the lattice from a stationary modal state to a wave state. This effect can be observed in experiments and in simulation, and shows the difficulty of using low dimensional models in extended structural systems. The recent book by Vakakis et al [29], explores some of these problems of localization in structures that will likely not be addressed by classical low dimensional models typical of the first decades of chaos theory.

Another important phenomenon discovered by Ali Nayfeh and his group at Virginia Polytechnic Institute [30], is the transfer of vibration energy in nonlinear structures from high frequencies to low frequencies.

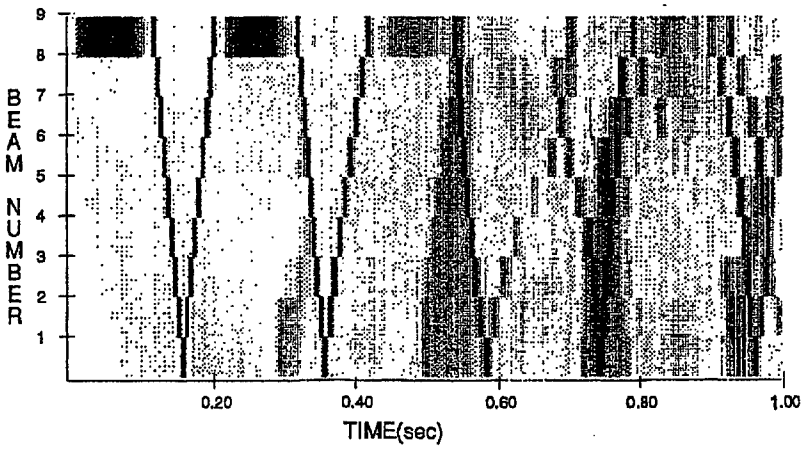

Figure 8: Numerical integration results for the structure in Figure 7, showing energy propagation through a periodic structure for an impact of mass #8. Wave propagation occurs via tension in the horizontal arched structures; from Davies and Moon, (1994), [27].

Chaos in elasto-plastic structures.

One of the important papers in the last 20 years in structural dynamics is that by Symonds and Yu of Brown University in 1985, [31]. In this study they examined the impulsive loading of an elasto-plastic beam with clamped ends. The problem was given to well known finite element experts. The results were ten different answers. In this problem, when the beam reaches the plastic state, there is plastic stretching of the mid plane so that when the dynamic energy is dissipated, the beam takes one of two shapes of an arch, up or down. Five analyses predicted the up state and five the down arch shape. What was not realized at the time was that there was no right answer - the problem was one of *transient chaos*, sensitive not only to initial conditions but to the specific numerical modeling used by the different analysts. Inspired by these results, my colleagues at Cornell, Poddar et al [32] examined a slightly different one using periodic impulsive loading. With a one element model we were able to show, using the Poincare section, that there existed a strange attractor in the time periodic loading case which lent credence to the suspicion that the Brown University paper was one of transient chaos. Since that paper there have been others by Symonds and later papers by the Cornell group (Pratap et al [33]) on dynamics and chaos in elasto-plastic beams. (Figure 9)

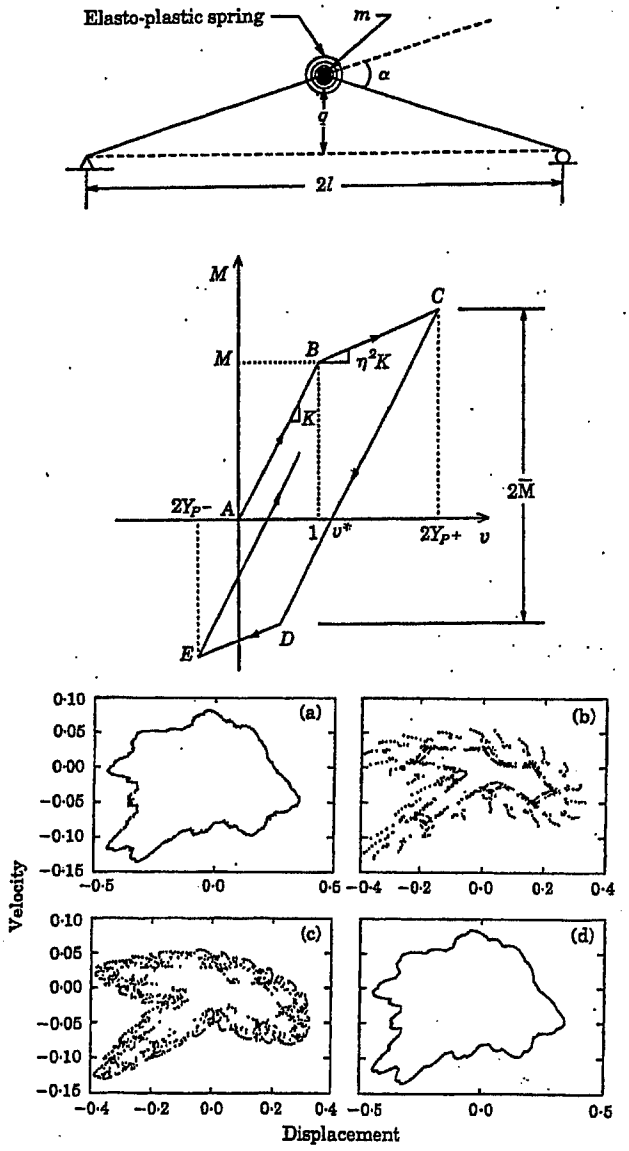

Figure 9: Nonlinear dynamics of a single element elasto-plastic oscillator. (a) - (d) show Poincare sections for forced motion and sensitivity to initial conditions. From Pratap el al (1994), [33].

These problems introduce hysteretic nonlinearities in the equations. Such terms have not received much attention from the applied mathematics community. One exception is the analysis of hysteretic electrical circuits. The important result here is that in problems with strong nonlinearities in structural dynamics, one must be wary of numerical results without checking to see how sensitive the results are to different parameters such as initial conditions and spatial loading.

Spatial chaos in the state elastica.

There is a well know analogy in mechanics between the static bending and twisting of the elastica and the dynamics of the spinning top or rigid body; this similarity is known as the Kirchhoff analogy. (see e. Love, [5]) Thus what is dynamically possible for the rigid body in time is by analogy possible for the elastica in space. Since it is known that the spinning top or rotating pendulum can be chaotic in time, then one might suspect that the static elastica structure might be chaotic in space. The coupled equations, in terms of the curvatures (κ_1, κ_2) and torsion τ, of the elastica are given by ([5],[37])

$$\begin{aligned}
\frac{dA(\kappa_1-\kappa_{1_0})}{ds} &= (B-C)\kappa_2\tau + C\kappa_2\tau_0 - B\tau\kappa_{20}, \\
\frac{dB(\kappa_2-\kappa_{2_0})}{ds} &= (C-A)\kappa_1\tau + A\tau\kappa_{10} - C\kappa_1\tau_0, \\
\frac{dC(\tau-\tau_0)}{ds} &= (A-B)\kappa_1\kappa_2 + B\kappa_1\kappa_{20} - A\kappa_2\kappa_{10}
\end{aligned} \tag{5}$$

This remarkable result has been studied by a number of authors including Thompson & Virgin (1988) [34], El Naschie and Kapitaniak (1990) [35], Mielke and Holmes (1988) [36], and Davies and Moon (1993) [37]. One example of the twisted chaotic shape of an elastica is shown in Figure 10. (Moon & Davies, [37]). Here the rod has a periodic change in shape in space corresponding to a spinning top with periodic forcing in time. This problem, although somewhat academic,

shows that spatially complex, nonlinear deformation of twisted structures are possible and are sensitive to problem parameters. One possible application of these problems is the deformation of macro molecules such as DNA. These analytic solutions present a challenge to numerical analysts of nonlinear structural deformation.

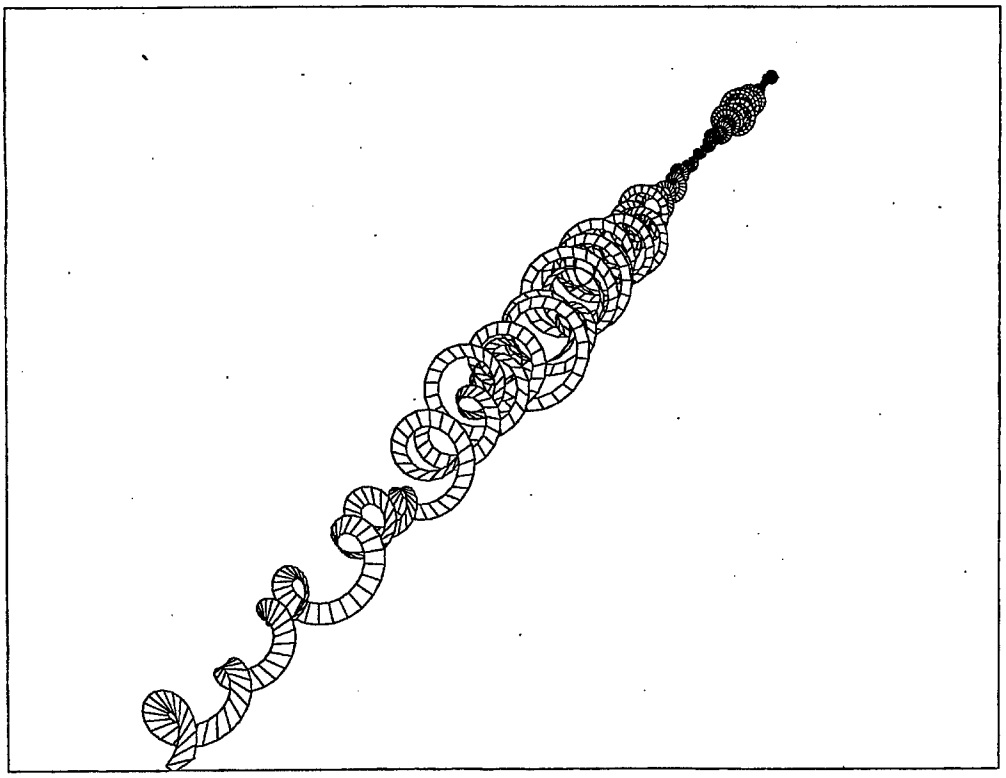

Figure 10: Numerical integration of equations (5) for initial curvatures $\kappa_{10} = \kappa_{20} = \tau_0 = 0$, and spatially varying initial modulus $B = B_0 + B_1 \cos\kappa s$. The twisted structure shows spatially static chaos; from Davies and Moon (1993), [37].

Future Directions

The early work of Holmes in 1979 clearly established the idea of unpredictable motions in deterministic structural dynamics and the experiments that followed confirmed the role of chaotic phenomena in

many structural applications. While not as ubiquitous as in fluid mechanics, the idea of chaos and even some form of spatial turbulence in structural systems is now accepted by most theorists but has not been addressed fully by the numerical simulation community in exploring the limits of predictable dynamics with existing and future codes. The other areas of future research is elasto-plastic structures and damaged and fractured structures. The need for comparison of experimental and numerical data in the chaotic regimes of these problems in structural dynamics is also an area of opportunity.

Another subject in need of new research is the interaction of random and deterministic chaotic dynamics in structures since most practical problems involve a mix of both. Also since deterministic chaos generates a probability function, it should be possible to use the tools of random vibrations if one can determine the nongaussian probability density functions for the chaotic motions.

Following the lead of fluid mechanics, there are many problems in structural systems in which there is complex spatial dynamics. The extension of the methods of *Proper Orthogonal Decomposition* (POD) from fluid mechanics to structural mechanics is one method that may be fruitful.(See e.g. Aubry et al [38].) Professor J. Cusumano of the Pennsylvania University in the USA has begun one such effort.

System identification has made great strides in linear structural dynamics. It should be expected that similar efforts in structural dynamics will develop in the next decade. The book of Abarbanel [39] of University of California, San Diego uses ideas and concepts to develop time series methods for *nonlinear system identification*. The idea is that chaotic "noise" contains important information about the nonlinear system if one can learn how to mine the data. Recent work at Cornell University in nonlinear fluid-structure dynamics uses nonlinear bifurcation theory to guide the choice of nonlinear representation fluid forces on a vibrating structure. (See Thothadri and Moon, [40]).

Finally as has been mentioned, there remains the difficult task of understanding structural dynamics in extremely complex systems such as jet engines or vehicles, robots and other complex machines. Such structural systems have sources of energy, relative motion of parts rotary motions, inertial nonlinearities, friction, intermittent contact and sometimes fluid and magnetic forces. The current method has been to take a reductionist approach to analysis and design reducing the problem to dynamics of machine elements and not always the entire flexible machine. The integration of machine and structural nonlinear dynamics is a challenging problem. There is also some evidence that a small amount of chaos in complex machines may be inevitable and

even desirable. A recent study by Steven Boedo of Borg-Warner Corporation (now at Rochester Institute of Technology) on chaos in hydrodynamic rotor bearings suggests that better performance is obtained with a small amount of chaos, [41]. Thus although the days of the study of chaos in simple mechanical systems may be in the past, the future direction of nonlinear structural dynamics will be guided by the fruit of those early studies into chaotic dynamics.

REFERENCES

1. Nayfeh. A. H., and Mook, D. T. (1979). *Nonlinear Oscillations,* John Wiley and Sons, New York.
2. Guckenheimer, J., and Holmes, P.J. (1983). *Nonlinear Oscillations, Dynamical Systems and Bifurcations of Vector Fields,* Springer-Verlag, New York.
3. Moon, F. C., (1992), *Chaotic and Fractal Dynamics,* J. Wiley & Sons, N.Y.
4. Moon, F. C. (Editor), (1998), *Dynamics and Chaos in Manufacturing Processes,* J. Wiley & Sons, N.Y.
5. Love, A. E. H. (1922). *A Treatise on the Mathematical Theory of Elasticity,* 4th ed., Dover, New York.
6. Bolotin, V. V. (1959, 1964), *The Dynamic Theory of Elastic Stability,* Holden Day.
7. Holmes, P. J. (1979, "A Nonlinear Oscillator With a Strange Attractor", *Philos. Trans. R. Soc. London* , A **292**, 419-448.
8. Moon, F. C. and Holmes, P.J. (1979). "A Magnetoelastic Strange Attractor", *J. Sound Vib.* **65**(2), 275-296.
9. Moon, F.C., "Experiments on Chaotic Motions of a Forced Nonlinear Oscillator: Strange Attractors." *Journal of Applied Mechanics,* 1980 Vol. 47. No. 3 pp. 638-644.

10. Moon, F. C. and Li, G. X., "Fractal Basis Boundaries and Homoclinic Orbits for Periodic Motion in a Two-Well Potential", *Phys. Rev. Lett*, **55**(14), 1439-1442.

11. Tang, D. M. and Dowell, E. H., "On the Threshold Force for Chaotic Motions for a Forced Buckled Beam", *Journal of Applied Mechanics*, (1990), American Society of Mechanical Engineers, New York, NY.

12. Ott, E, Grebogi, C., and Yorke, J., (1990), "Controlling Chaos", *Phys. Rev. Lett.* **64**(11), 1196-1199.

13. Moon, F. C., Johnson, M. A., and Homes, W. T., "Controlling Chaos in a Two-Well Oscillator." *International Journal of Bifurcation and Chaos*, 1996, Vol. 6, No 2, pp. 337-347.

14. Cusumano, J.P., and Moon, F. C., "Chaotic Non-Planar Vibrations of the Then Elastica, Part I: Experimental Observation of Planar Instability." *Journal of Sound and Vibration*, (1995) 179(2), pp. 185-208.

15. Moon, F.C. and Shaw, S. W., "Chaotic Vibrations of a Beam with Non-linear Boundary Conditions." *International Journal of Non-Linear Mechanics.* (1983) Vol. 18, No 6 pp. 465-477.

16. Moon, F.C. and Li, G.X., "Experimental Study of Chaotic Vibrations in a Pin-Jointed Space Truss Structure." *American Institute of Aeronautics and Astronautics Journal.* (1990) Vol. 28, No. 5, pp. 915-921.

17. Li, G. X., Rand, R. H. and Moon, F. C., "Bifurcations and Chaos in a Forced Zero-Stiffness Impact Oscillator." *International Journal of Non-Linear Mechanics*, (1990) Vol. 25, No. 4, pp. 417-432.

18. Thompson, J. M. T., and Stewart, H. B. (1986). *Nonlinear Dynamics and Chaos*, John Wiley & Sons, Chichester, England.

19. Dowell, E. H. (1982). "Flutter of a Buckled Plate as an Example of Chaotic Motion of a Deterministic Autonomous System," *J. Sound Vib.* 85(3), 333-344.

20. Dowell, E. H. and Virgin, L. N., "On Spatial Chaos, Asymptotic Modal Analysis, and Turbulence." *Transactions of the ASME,* (1990) Vol. 57, pp. 1094-1097.

21. Paidoussis, M. P. and Moon, F. C. (1988). "Nonlinear and Chaotic Fluid-elastic Vibrations of a Flexible Pipe Conveying Fluid," *J. Fluids Struct.* 2, 567-591.

22. Paidoussis, M. P., Li, G. X., and Moon, F. C. (1989). "Chaotic Oscillations of the Autonomous System of a Constrained Pipe Conveying Fluid," *J. Sound Vib.* 135(1), 1-19.

23. Copeland, G. S. and Moon, F.C., "Chaotic Flow-Induced Vibration of a Flexible Tube with End Mass." *Journal of Fluids and Structures,* (1992) 6, pp. 705-718.

24. Wiggins, S. (1990). *Introduction to Applied Nonlinear Dynamical Systems and Chaos,* Springer-Verlag, New York.

25. Bajaj, A. K., and Sethna, P. R. (1984). "Flow Induced Bifurcations to Three-dimensional Oscillatory Motions in Continuous Tubes," *SIAM J. Appl. Math.* 44(2), 270-286.

26. Steindl, A., and Troger, H. (1988). "Flow Induced Bifurcations to Three-dimensional Motions of Tubes with an Elastic Support," in *Trends in Applications of Mathematics to Mechanics,* Springer-Verlag, New York.

27. Davies, M. A. and Moon, F. C., "Transition from Soliton to Chaotic Motion During Impact of a Nonlinear Elastic Structure." *Chaos, Solitons & Fractals,* (1994) Vol. 4, No 2, pp. 275-283.

28. Toda, M. (1981). *Theory of Nonlinear Lattices,* Springer Series on Solid State Sciences, Vol. 20, Springer-Verlag, Berlin.

29. Vakakis, A. F. , Manevitch, L. I., Mikhlin, Y. V., Pilipchuk, V. N., and Zevin, A. A., *Normal Modes and Localization in Nonlinear Systems.*, (1996), John Wiley & Sons, Inc, New York, USA.

30. Nayfeh, A. H., Nayfeh, S. A., Anderson, T. A. and Balachandran, B., "Transfer of Energy From High-Frequency to Low-Frequency Modes." (1994), *Nonlinearity and Chaos in Engineering Dynamics*, pp. 39-58, Edited by Thompson, J. M. T. and Bishop, S. R., John Wiley & Sons Ltd, New York, USA.

31. Symonds, P. S., and Yu, T. X. (1985), "Counterintuitive Behavior in a Problem of Elasto-plastic Beam Dynamics", *ASME J. of Applied Mechanics*, **52**, 517-522.

32. Poddar, B., Moon, F. C., and Mukherjee, S., "Chaotic Motion of an Elastic-Plastic Beam." *Journal of Applied Mechanics*, (1988), Vol. 55 pp. 185-189.

33. Pratap, R., Mukherjee, S., and Moon, F. C., "Dynamic Behavior of a Bilinear Hysteretic Elasto-Plastic Oscillator, Part II: Oscillations Under Periodic Impulse Forcing." *Journal of Sound and Vibration*, (1994) 172(3), pp. 339-358.

34. Thompson, J. M. T., and Virgin, L. N. (1988). "Spatial Chaos and Localization Phenomena in Nonlinear Elasticity," *Phys. Lett A* 126(8,9), 491-496.

35. El Naschie, M. S., and Kapitaniak, T. 1990). "Soliton Chaos Models for Mechanical and Biological Elastic Chains," *Phys. Lett. A* 147(5,6), 275-281.

36. Mielke, A., and Holmes, P. (1988). "Spatially Complex Equilibria of Buckled Rods,: *Arch. Rational Mech. Anal.* 101(4), 319-348.

37. Davies, M. A. and Moon, F. C., "3-D Spatial Chaos in the Elastica and the Spinning Top: Kirchhoff Analogy." *Chaos*, (1993) 3(1) pp. 93-99. American Institute of Physics.

38. Aubry, N., Holmes, P., Lumley, J. L., and Stone, E. (1988). "The Dynamics of Coherent Structures in the Wall Region of a Turbulent Boundary Layer, " *Journal of Fluid. Mech.* 192, 115-173.

39. Abarbanel, H. (1996), *Analysis of Observed Chaotic Data,* Springer-Verlag.

40. Thothadri, M. and Moon, F. C., "Helical Wave Oscillations in a Row of Cylinders in a Cross-Flow." *Journal of Fluids and Structures,* (1998) 12, pp. 591-613.

41. Boedo, S. (1999), "Chaos in Offset Hydrodynamic Rotor Bearings", in *New Applications of Nonlinear and Chaotic Dynamics in Mechanics,* F. C. Moon, Editor, Kluwer Publ., The Netherlands.

ANALYTICAL AND NUMERICAL METHODS

Gross modifications in structural dynamics via interpolated modes.

Atul Bhaskar
School of Engineering Sciences,
Aeronautics & Astronautics, University of Southampton,
Highfield, Southampton, SO17 1BJ, U.K.

Abstract

Repeated analysis of a structure for a range of parameter values is often encountered in engineering design and optimisation. In this paper, the problem of approximately predicting the natural frequencies of a system, when parameters undergo gross changes, is addressed. A method of 'interpolated modes' is developed. It is shown that reasonable estimates of the natural frequencies are obtained without a recourse to exact calculations for each value of the system parameter. Illustrative examples are given.

INTRODUCTION

In many design situations, it is required to calculate the natural frequencies of a mechanical vibratory system or a structure for a large set of parameter values. A similar situation is encountered in structural optimisation studies when the objective function is related to the natural frequencies of the system. The problem becomes computationally more and more demanding as the degrees-of-freedom involved in the system increase and as the dimensionality of the parameter space increases. The parameters that describe the system or the structure could be a geometrical dimension (e.g. thickness), a lumped mass, a spring constant, modulus of elasticity etc.

Typically, complex engineering structures are analysed using a finite element (or another approximate) method and the equations of motion are written in terms of second order ordinary differential equations. The natural frequencies are associated with synchronous motion in free vibration; and imposing this condition on the type of motion to be observed leads to the following generalised eigenvalue problem

$$\mathbf{K}\mathbf{u} = \lambda \mathbf{M}\mathbf{u}. \tag{1}$$

The stiffness matrix $\mathbf{K}$ and the inertia matrix $\mathbf{M}$ are both symmetric. In addition, $\mathbf{M}$ is positive definite whereas $\mathbf{K}$, in general, is positive semi-definite to allow for rigid body modes. Square roots of the eigenvalues are the natural frequencies and the eigenvectors represent mode shapes of the system. In a computational cycle of calculating natural frequencies, it is this step of solving the eigenvalue problem (1) that is usually most expensive; setting-up matrices $\mathbf{K}$ and $\mathbf{M}$ are relatively cheaper part of the calculations. Therefore, whenever the eigenproblem (1) needs to be solved repeatedly for a large set of parameter values, the required computational resources are substantially increased. A commonly used approximation that avoids solving equation (1) repeatedly is based on Rayleigh's work [1] and is discussed now.

A change in the parameter p of the system leads to a change in the inertia and the stiffness matrices. If these changes are denoted by $\Delta\mathbf{M}$ and $\Delta\mathbf{K}$ respectively, then the perturbed eigenproblem is given by

$$(\mathbf{K}+\Delta\mathbf{K})(\mathbf{u}_i+\Delta\mathbf{u}_i) = (\lambda_i+\Delta\lambda_i)(\mathbf{M}+\Delta\mathbf{M})(\mathbf{u}_i+\Delta\mathbf{u}_i). \tag{2}$$

Here, $(\lambda_i+\Delta\lambda_i)$ and $(\mathbf{u}_i+\Delta\mathbf{u}_i)$ are the changed eigensolutions. Expanding the two sides of (2), making use of (1), premultiplying by $(\mathbf{u}_i+\Delta\mathbf{u}_i)^T$ and ignoring higher order terms in the expansion leads to

$$\Delta\lambda_i \approx \frac{\mathbf{u}_i^T(\Delta\mathbf{K}-\lambda_i\Delta\mathbf{M})\mathbf{u}_i}{\mathbf{u}_i^T\mathbf{M}\mathbf{u}_i} \tag{3}$$

for the change in the i-th eigenvalue. Note that this expression uses eigensolutions of the original (unperturbed) problem and the changes in the stiffness and mass matrices due to parameter changes. We shall refer to this approximation as the 'classical perturbation'. Based on this expression the exact rate of change of eigenvalue with respect to a parameter can be obtained. While the chassical perturbation (1) gives reasonably good answers for small perturbations, it provides poor approximations for large (or gross) changes in the parameter. This is expected since the classical perturbation formula is based on ignoring higher order terms.

Although the basic idea of perturbation of an eigenvalue problem is quite old (e.g. Rayleigh did not use the language of matrices), there have been numerous studies on specific issues. Lancaster [2] and Fox and Kapoor [3] were first to study the change in eigenvalues and eigenvectors of a matrix when the matrix is a function of a parameter. A good review on the subject, with structural dynamics as the main motivation, can be found in Brandon [4]. The issue of sensitivity and derivatives of eigensolutions is a closely related one (see, Haftka et al.,[5, 6] and other citations therein, for example). Stetson et al. [7] and Nagaraj [8] have looked into design and engineering aspects of the eigenvalue perturbation theory.

THE METHOD OF INTERPOLATED MODES

This paper is concerned with an approximation for eigenvalues (and, consequently the natural frequencies) of a system whose parameters undergo gross changes. In an earlier work, Sahu et al. [9] addressed this problem and they proposed an approximation on an interval over which a parameter takes different values. The strategy there is to interpolate between the eigenvalues that are calculated as perturbations from the two ends taking eigenvectors at the left end as the reference in the first instance; and then taking eigenvectors at the right end as the reference in the second instance. In this manner one has two estimates of the eigenvalue for each value of the parameter on the parameter axis. The final estimate is made by calculating the weighted average such that the value calculated from the eigenvector based on the end of the interval that is closer to the parameter value in question receives more weight. The approach of the present work resembles that of [9] in that it also attempts to develop an approximation for eigenvalues based on eigensolutions at the two ends of an interval. The details of the two approximations, however, are different. While [9] directly calculates an average of two different estimates, the present work employs averaging the *eigenvectors* themselves. The details of the procedure follow.

Consider an interval $p_0 \leq p \leq p_f$, where p represents a parameter that describes the system. The eigensolutions at the two ends can be found exactly:

$$\mathbf{K}_0\mathbf{u}_0 = \lambda\mathbf{M}_0\mathbf{u}_0, \quad \text{and} \quad \mathbf{K}_f\mathbf{u}_f = \lambda\mathbf{M}_f\mathbf{u}_f. \tag{4}$$

Defining a non-dimensional parameter t as

$$t = \frac{p - p_0}{p_f - p_0}, \tag{5}$$

we have $0 \leq t \leq 1$. Taking t and $(1-t)$ as the appropriate weighting factors for interpolating mode shapes to be obtained from $\mathbf{u}_0$ and $\mathbf{u}_f$, we have the following expression for the i-th interpolated mode (the subscript i has been dropped):

$$\overline{\mathbf{u}} = (1-t)(\mathbf{u}_0) + (t)(\mathbf{u}_f). \tag{6}$$

This interpolated mode is now taken as an approximation for the true mode-shape. Finally, the approximate eigenvalue $\tilde{\lambda}_i$ is calculated from the Rayleigh quotient

$$\tilde{\lambda}_i = \frac{\overline{\mathbf{u}}_i^T(\mathbf{K} + \Delta\mathbf{K})\overline{\mathbf{u}}_i}{\overline{\mathbf{u}}_i^T(\mathbf{M} + \Delta\mathbf{M})\overline{\mathbf{u}}_i}. \tag{7}$$

The natural frequencies can be calculated in the usual way by taking square root of the eigenvalues, i.e. $\omega_i = \sqrt{\tilde{\lambda}_i}$.

It may be noted that eigenvalues are not interpolated linearly and that the true non-linear dependence of the coefficient matrices $\mathbf{K}$ and $\mathbf{M}$ on the parameter p is incorporated in the Rayleigh quotient. The trial eigenvectors involved in the quotient are, however, linearly interpolated in the interval. The results are expected to be relatively better at the two ends of the interval, whereas the worst approximation errors are expected close to the centre of the interval. In the limiting case of $t = 0$ and $t = 1$, the values of $\tilde{\lambda}_i$ are exact, since the contribution in (6) is zero except due to the exact modes.

The method uses exact eigensolutions at the two end points of the interval. For calculations at the intermediate points on the parameter axis, the computational effort is considerably less: we need to set-up the coefficient matrices (assemble the finite elements) and evaluate two quadratic forms. With respect to the classical perturbation, the extra effort involved is in solving an additional eigenvalue problem. This may well be worth the effort if we require several evaluations within the interval. This would be typical in a design search or optimisation setting.

The method outlined here can be readily extended to parameter spaces that are multi-dimensional. For example, if we wish to explore the variations in the natural frequencies simultaneously with respect to two parameters, say, p_x and p_y; then the domain of interpoltion is a rectangle, say, $0 \leq p_x \leq a$, $0 \leq p_y \leq b$. Non-dimensional parameters $0 \leq t_x \leq 1$ and $0 \leq t_y \leq 1$ can be defined as

$$t_x = \frac{p_x}{a}, \quad \text{and} \quad t_y = \frac{p_y}{b}.$$

The interpolated mode (eigenvector) is then calculated as

$$\overline{\mathbf{u}}_i(p_x, p_y) = (1 - t_x)(1 - t_y)\mathbf{u}_{00} + t_x(1 - t_y)\mathbf{u}_{a0} + (1 - t_x)t_y\mathbf{u}_{0b} + t_x t_y \mathbf{u}_{ab} \tag{8}$$

where $\mathbf{u}_{rs} = \mathbf{u}_i(p_x = r, p_y = s)$. The four eigenvectors at the corners of the rectangle $[0, a] \times [0, b]$ need to be calculated exactly. It can be seen from the above equation that everywhere inside the rectangle, the interpolation is bilinear. The final step in the calculation: evaluation of the Rayleigh quotient, remains identical to the previous expression of equation (7). The approximate eigenvalues as calculated from equation (7) coincide with the exact ones at the four corners of the rectangle because the contributions to the interpolated mode from the eigenvectors of the other three corners is exactly zero.

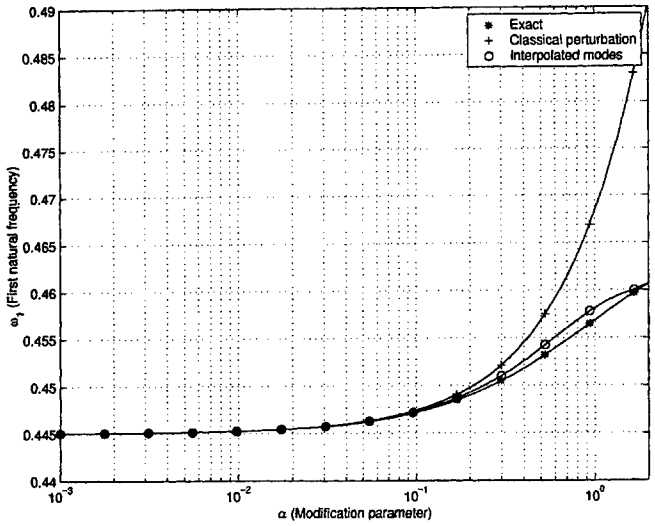

Figure 1: Variation of the first natural frequency with the modification parameter α for the three-degree-of-freedom system (Example 1), $\alpha = 2$ corresponds to 200 % change in the parameter.

EXAMPLES AND DISCUSSIONS

Two examples will be presented now to illustrate the method of interpolated modes developed in the previous section. The first example is of a three-degree-of-freedom discrete mechanical system; and the second example is a finite element model of a cantilever beam with a mass and a stiffness at the tip.

Example 1 Consider a three-degree-of-freedom system with the non-dimensional mass and the stiffness matrices given by

$$\mathbf{M}_0 = \begin{bmatrix} 1 & 0 & 0 \\ 0 & 1 & 0 \\ 0 & 0 & 1 \end{bmatrix}, \quad \text{and} \quad \mathbf{K}_0 = \begin{bmatrix} 2 & -1 & 0 \\ -1 & 2 & -1 \\ 0 & -1 & 1 \end{bmatrix}.$$

Suppose one of the stiffnesses is changed from 1 to $(1 + \alpha)$ such that the stiffness matrix changes to

$$\mathbf{K} = \begin{bmatrix} 2 & -1 & 0 \\ -1 & (2+\alpha) & -(1+\alpha) \\ 0 & -(1+\alpha) & (1+\alpha) \end{bmatrix}.$$

The mass matrix remains unchanged. Therefore α can be treated as a perturbation parameter. Clearly, $\alpha = 1$ corresponds to 100% change in the stiffness

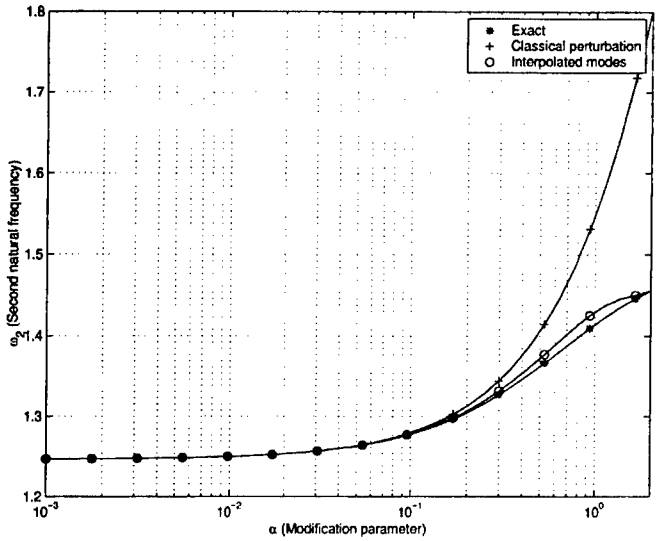

Figure 2: Variation of the second natural frequency with the modification parameter α for the three-degree-of-freedom system (Example 1), $\alpha = 2$ corresponds to 200 % change in the parameter.

parameter, $\alpha = 2$ corresponds to 200% change in the stiffness parameter, and so on.

Eigenvalues and eigenvectors were calculated exactly for $\alpha = 0$ and $\alpha = 2$. Taking $\alpha = 0$ as the 'reference design', frequencies were calculated using the classical perturbation formula (3). Approximate frequencies were also calculated using the interpolated modes as discussed in the previous section. Finally, the exact frequencies were calculated by solving the eigenvalue problem (1) at each intermediate frequency in the range $0 \leq \alpha \leq 2$. Results for the first natural frequency ω_1 are presented in figure (1). Note that the x-axis of the figure is chosen to be logarithmic, since the range of the modifications in the parameter α is reasonably large. It can be seen that the classical perturbation provides excellent approximation to the first natural frequency upto approximately 10% modification in the stiffness parameter (i.e. $\alpha = 0.1$). Beyond this, the higher order terms in the expansion of equation (2) take over and the classical perturbation formula rapidly deviates away from the curve for the variation of the exact natural frequency with respect to α.

The first natural frequency as calculated from the method of interpolated modes also starts deviating from the exact first natural frequency as α

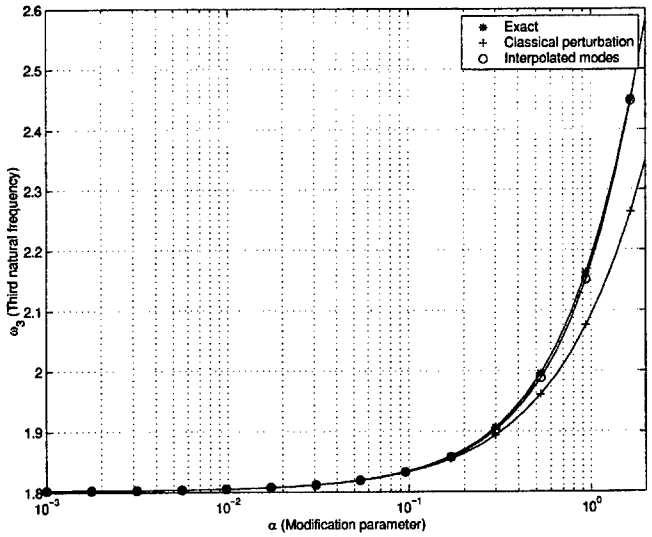

Figure 3: Variation of the third natural frequency with the modification parameter α for the three-degree-of-freedom system (Example 1), $\alpha = 2$ corresponds to 200 % change in the parameter.

increases beyond 15-20%. However, it is contained eventually as we come close to the right side end of the interval corresponding to $\alpha = 200\%$ The errors at the intermediate values can be seen to be substantially less that those obtained from the classical perturbation formula.

The second natural frequency as calculated from equation (7) shows a similar improvement over that calculated from the classical perturbation formula (3). The three curves are plotted in figure (2). Again it can be seen that the values are exact at the two ends of the interval. The third natural frequency as calculated from the perturbation formula (3) underestimates this frequency and is presented as a function of α in figure (3). The discrepancy increases with increase in the parameter α. The performance of interpolated modes, on the other hand, is exceptionally good and the curve for exact eigenvalue is almost indistinguishable from that of the frequencies calculated from the interpolated modes. This indicates that the true mode-shapes, in fact, vary linearly with α in the range shown.

Going back to figure (1), we note that the maximum absolute error in estimating ω_1 is only $\approx 0.49 - 0.461 = 0.029$. However, for a 200% change in α the total change in ω_1 is only $\approx 0.461 - 0.445 = 0.016$. Therefore, to

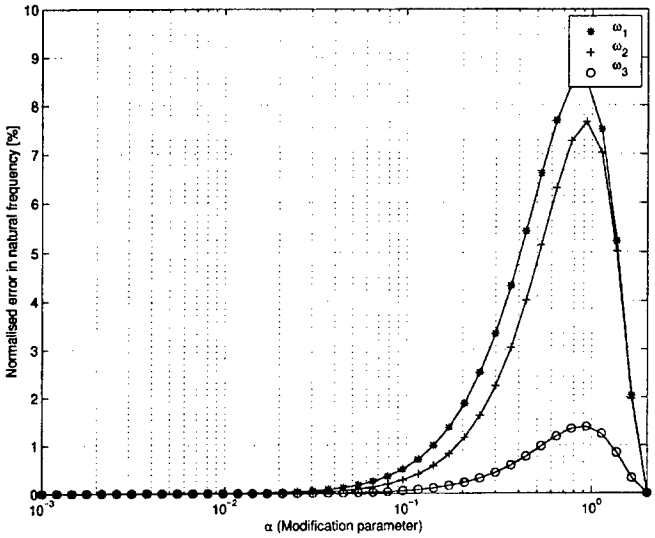

Figure 4: Normalised percentage error in estimating the three natural frequencies as a function of the modification parameter.

represent error better, a normalised error is defined as

$$\epsilon = \frac{\text{Absolute error}}{|\omega_i(p = p_f) - \omega_i(p = p_0)|}.$$

This normalised error (in percentage) is plotted for the three modes in figure (4). The general features of the three error profiles are fairly similar: errors are negligible at the two ends, and are maximum close to the centre of the interval around $\alpha = 80\% - 90\%$. The maximum error for ω_1 is less than 9%, for ω_2 it is less than 8%, and for ω_3 it is less than 2%.

To study the performance of the proposed method of interpolated modes for extremely large modifications, α was varied in the range 0-500%. Again exact calculations were carried out only at the two ends of interval. The approximate calculations and the exact calculations are presented in figure (5) for ω_1. The maximum error is observed around $\alpha = 200\%$ and its value equals approximately 40%. Elsewhere in the interval, it is substantially less. This demonstrates the usefulness of the method developed here, when one is interested only in rough estimates of natural frequencies. The possibility of integrating the method with a design search tool, therefore, exists: one could start with very rough estimates and scan a very large parameter space very cheaply. This could be followed by increasingly more accurate calculations

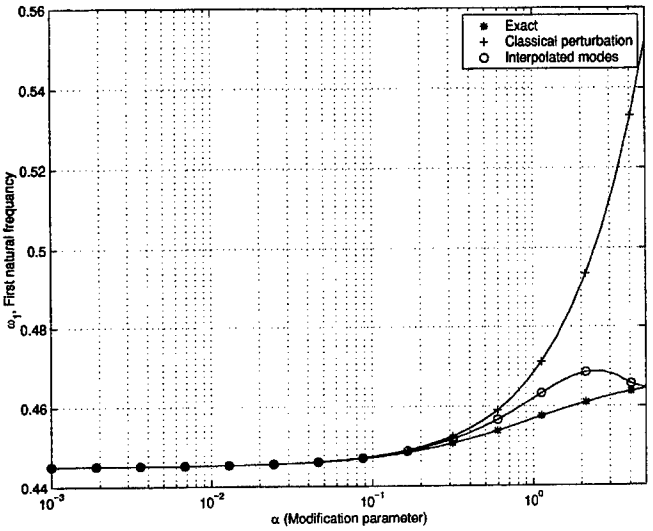

Figure 5: Variation of the first natural frequency with the modification parameter α. Note that the maximum perturbation in α is 500%.

(by reducing the interval successively) as we begin to be more and more committed to a particular design.

Yet another point to note in figure (5) is the non-monotonic nature of the curve corresponding to the interpolated modes. From one of the well-known theorems of Rayleigh [1], it follows that it is impossible to observe this trend. This is because increasing the parameter α means increasing the stiffness of the system, and therefore, natural frequencies can only increase or remain constant. Hence, it is possible to improve the performance of the method of interpolated modes further by incorporating this information that the true curve cannot cross the horizontal line passing through $\omega_1|_{p=p_f}$. Details of imposing this ceiling will not be discussed further and will be presented elsewhere. This scheme of further improvement will work only when a parameter affects *either* the mass properties *or* the stiffness properties.

Recall that the error for $\alpha = 200\%$ was zero in figure (1) because it corresponded to the right end of the interval. As the range increases it is expected that the maximum error will also increase. This variation is presented in figure (6). On the x-axis, maximum value of α (which corresponds to the right end of the interval) is plotted. On the y-axis, the maximum value of the normalised error (maximum being taken over the relevant interval) is plotted for the three natural frequencies. It is seen that the method performs better for ω_2 for relatively smaller values of α_{max} than for ω_1. This trend,

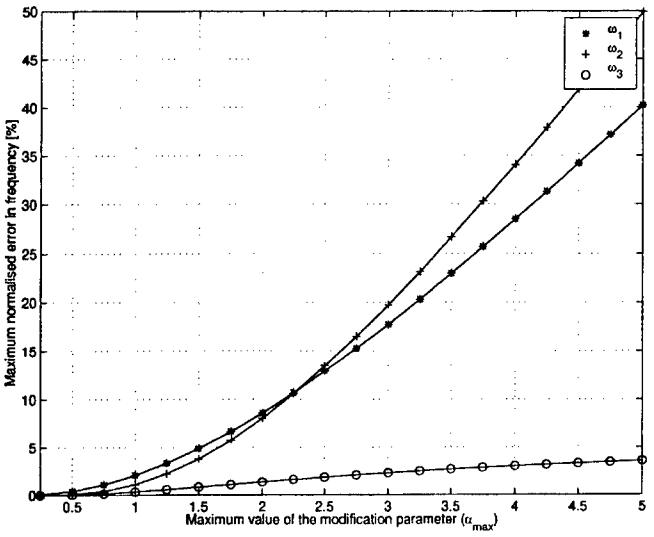

Figure 6: Maximum over interpolation range of the normalised error as a function of $\alpha_{\max}$

however, is reversed for higher values of α_{max}. The third natural frequency is consistently calculated very accurately, the worst error being less than 5% for a modification equal to 500%.

Example 2 Consider a clamped-free cantilever beam. The tip of the beam has a concentrated mass m_0 and a spring k_0. The beam is characterised by three parameters: m, the mass per unit length of the beam; EI its bending rigidity; and L the length. Non-dimensional parameters are defined as

$$m_0^* = m_0/(mL), \quad k_0^* = k_0/(EI/L^3), \quad \lambda_i^* = \lambda_i/(EI/mL^4).$$

We shall treat the two parameters m_0^* and k_0^* as modification over the reference structure which is a cantilever beam without any tip mass or tip spring. The parameter space, therefore is two dimensional.

The beam was discretised using a finite element procedure using 10 elements. Each node of an element possesses two degrees-of-freedom: one in the transverse displacement direction and one for rotation (slope).

The four corners of the domain of interpolation are defined by the points: $(m_0^* = 0, k_0^* = 0)$, $(m_0^* = 2, k_0^* = 0)$, $(m_0^* = 0, k_0^* = 2)$, and $(m_0^* = 2, k_0^* = 2)$. Percentage error is now defined as the ratio of the difference of exact eigenvalue and the eigenvalue calculated via interpolated modes to the exact value at each point in the parameter space. This error is plotted as a function

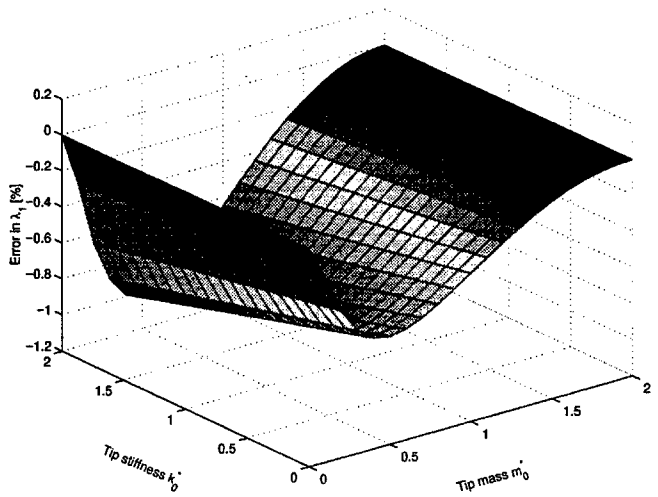

Figure 7: Percentage error in λ_1^* as a function of m_0^* and k_0^*. Maximum modification in both parameters is 200%.

of m_0^* and k_0^* for λ_1^* in figure (7). It is seen that this error is less than 1% throughout the domain when the parameters at the corner points are modified by 200%. Note the values of error at the four corners which is exactly zero, as expected. The same plot for λ_2^* is shown in figure (8). This time the maximum error is of the order of 35%.

Although the method discussed in this paper works quite well for the examples presented here, there are some unresolved difficulties. Firstly, it is recognised that eigenvectors showing sharp changes with respect to a parameter will not be properly interpolated. The results for natural frequencies calculated from such interpolated modes are likely to be fairly inaccurate. Secondly, when two eigenvalues cross each other in the the parameter space leading to reversal of the mode order, extra care needs to be taken in automating the interpolation procedure. If this is not properly done, interpolation with two different 'types' of modes will take place resulting in inaccurate estimation of the corresponding natural frequencies. Finally, the procedure needs to be adapted to systems that possess degeneracy, e.g. periodic structures. The present formulation is robust only for distinct eigenvalues.

CONCLUSIONS

A method of approximate calculation of natural frequecies of a mechanical system based on interpolated modes was presented. This method offers substantial computational saving when one is interested in approximate values

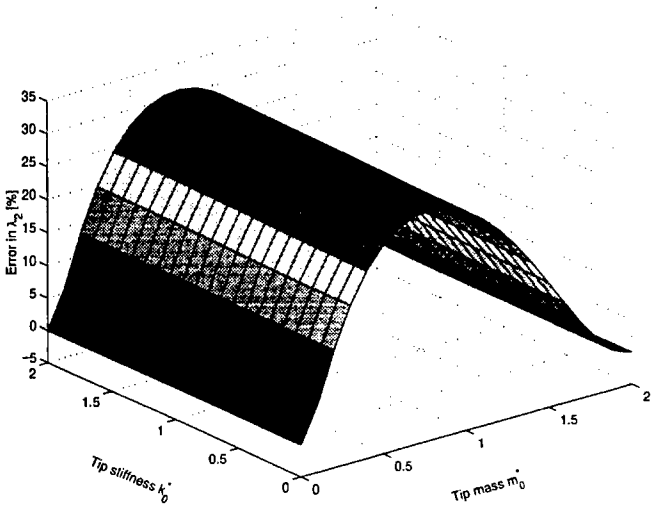

Figure 8: Percentage error in λ_2^* as a function of m_0^* and k_0^*. Maximum modification in both parameters is 200%.

at a large number of points inside an interval. The interval could be multi-dimensional. It was shown, through two simple examples, that reasonably accurate estimates of the natural frequencies are obtained for fairly large values of modification. It is believed that the method will give very useful inputs to optimisation and search porblems associated with structural dynamic design.

Acknowledgement: I thank Professor Andy J. Keane for very useful comments at an early stage of this work.

References

[1] Lord Rayleigh 1945 *Theory of Sound*, vol. 1, Dover, New York.

[2] Lancaster, P., On eigenvalues of matrices dependent on a parameter, *Numerische Math.*, 1964, **6**, 377-387.

[3] Fox, R.L. and Kapoor, M.P., Rate of Change of eigenvalues and eigenvectors, *AIAA Journal*, 1968, **6**, 2426-2429.

[4] Brandon, J.A., *Strategies for Structural Dynamic Modification*, 1990, John Wiley, New York.

[5] Adelman, H.M. and Haftka, R.T., Sensitivity analysis of discrete structural systems, *AIAA Journal*, May 1986, **24**, No. 5, 823-832.

[6] Murthy, D. V. and Haftka, R.T., Derivatives of eigenvalues and eigenvectors of a general complex matrix, *Int. J. for Num. Meth. in Eng.*, 1988, **26**, 293-311.

[7] Stetson, K.A. and Palma, G. E, Inversion of first-order perturbation theory and its application to structural design, *AIAA Journal*, 1976, **14**, No. 4, 454-460.

[8] Nagaraj, V.T., Changes in vibration characteristics due to changes in the structure, *J. Spacecraft*, 1970, **7**, No. 12, 1499-1501.

[9] Sahu, S.S., Bhaskar, A. and Nakra, B.C., Interpolation approach for gross dynamic modifications of structures, 2000, manuscript in preparation.

THE DYNAMICS OF A CRACKED TRANSLATING BEAM

Kevin D. Murphy and Yin Zhang
Department of Mechanical Engineering
University of Connecticut, Storrs, CT 06269-3139

ABSTRACT

The present study considers the influence of an elastic, open crack on the natural frequencies and stability characteristics of a simply supported, translating beam. Using Hamilton's principle and elementary fracture mechanics, the equations of motion for the beam are developed. An eigenanalysis is performed and shows that the natural frequencies ($\mathrm{Im}(\lambda)$) and stability characteristics ($\mathrm{Re}(\lambda)$) fluctuate as the crack translates with the beam between the two fixed supports. The magnitude of these fluctuations vary with the axial transport speed and are mapped in the parameter space. The implications for the free and forced responses are discussed.

INTRODUCTION

Axially moving systems have been widely studied in the literature [1], [2] and deal with applications including bandsaws, magnetic tapes, paper manufacturing etc. The present study considers the influence of a shallow crack on the vibration and stability characteristics of a translating, simply supported beam. Throughout this work it is assumed that the applied axial tension is large and that the internal bending moment is small (a reasonable assumption for small amplitude, linear motion) such that the crack always remain open. In other words, impacting conditions associated with crack closure are not considered [3], [4].

Introducing a crack into a structure produces two significant effects. First, there is a change in the stress field near the crack tip. This reduces the local stiffness of the system which, in turn, influences the dynamics of the beam. This is typically accomplished using the stress intensity factor to describe the local stress field near the crack tip. See, for example, references [5]-[7]. Alternatively, variational techniques with exponential "crack functions" have been used to obtain a consistent theoretical description of the problem [8]-[10].

The second effect, which is not commonly incorporated, involves the discontinuity in the mass per unit length of the beam produced by the

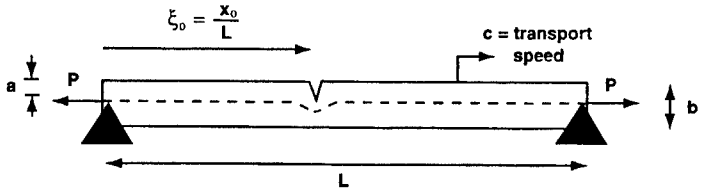

Figure 1: A schematic of the translating beam system under consideration.

presence of the crack. In a related study, Wickert and Mote [11] examined the dynamics of a translating string carrying a discrete mass (as opposed to a disruption in the mass per unit length). They showed that the mass acted to scatter harmonic waves and that the frequencies fluctuated as the mass location varied during translation.

In the present study, both effects are incorporated into a mathematical model to describe the linear vibrations, both axial and transverse, of a cracked, translating beam. The governing PDE's are discretized to a set of ODE's and the vibration and stability characteristics are examined through an eigenvalue analysis. It is shown that, like the results presented in reference [11], the natural frequencies ($\mathrm{Im}(\lambda)$) and the stability characteristics ($\mathrm{Re}(\lambda)$) fluctuate as the crack location moves. Furthermore, the influence of the transport speed on the amplitude of these fluctuations is demonstrated. The implications of these results for both the free and forced response are considered and discussed.

MODEL DEVELOPMENT

Changes in Local Stiffness Due to a Crack

Figure 1 shows a schematic of the cracked beam system being considered. The beam has length L, height b, cross sectional area A, axial transport speed c, and axial tension P. It also has a crack of depth a that is located at $\xi_o = x_o/L$ at the instant shown. The presence of the crack reduces the stiffness of the beam both in axial stretching and in bending. In other words, a given load will produce more deformation in the cracked beam than in its uncracked counterpart. This additional deformation is highly localized near the crack and not distributed evenly over the structure. In addition, the asymmetric crack causes the neutral axis to dip down from the centerline in the vicinity of the crack. This is shown schematically with a dashed line in Figure 1. This asymmetry produces an eccentric loading scenario which leads to coupling between the bending and stretching deformations.

To begin, consider the *net* effect of the crack and forget, for the moment, that the additional deformation is highly localized. In this case,

the global force-deformation relations are

$$\left\{ \begin{array}{c} d \\ \theta \end{array} \right\} = \left[C \right] \left\{ \begin{array}{c} P_1 \\ P_2 \end{array} \right\} \tag{1}$$

where d and θ are measures of the overall (global) axial and rotational deformations, respectively, $P_1 = P$ is the axial tension, $P_2 = M$ is the bending moment, and $[C]$ is the compliance matrix. In the absence of a crack, the compliance matrix is diagonal with terms $c_{11} = (L/AE)_o$ and $c_{22} = (L/EI)_o$, where the subscript indicates that this refers to the uncracked structure. The addition of the crack increases the diagonal elements and introduces off-diagonal terms coupling the axial and bending deformation:

$$\left[C \right] = \left[\begin{array}{cc} \left(\frac{L}{EA}\right)_o + \Delta c_{11} & \Delta c_{12} \\ \Delta c_{12} & \left(\frac{L}{EI}\right)_o + \Delta c_{22} \end{array} \right] \tag{2}$$

where Δc_{ij} is the change in flexibility which leads to the net increase in the global deformation variables. An appropriate expression for the change in flexibility is

$$\Delta c_{ij} = \frac{\partial^2}{\partial P_i \partial P_j} \int_0^a G(\bar{a}) d\bar{a} \tag{3}$$

where a is the depth of the crack, G is the elastic energy release rate, and the P_i are the generalized forces described previously [12], [13]. It should be noted that this description of the compliance matrix is only valid for situations where the crack remains open. If the crack should close, the compliance will experience a discontinuity (a strong nonlinearity) and a very different analysis would be required.

The global change in compliance may be computed using Equation (3) along with an appropriate expression for the energy release rate:

$$G\,(a/b) = \frac{1-\nu^2}{E} (K_I^b + K_I^s)^2 \tag{4}$$

where E is the elastic modulus, ν is Poisson's ratio, and K_I^b and K_I^s are the stress intensity factors in bending and stretching, respectively. The stress intensity factors for a beam with an edge crack in bending and stretching are found in reference [5] and take the form

$$K_I^s = \frac{p}{bt} \sqrt{\pi a}\, F_1(a/b) \tag{5}$$

$$K_I^b = \frac{6M}{b^2 t} \sqrt{\pi a}\, F_2(a/b) \tag{6}$$

where $F_1(a/b)$ and $F_2(a/b)$ are

$$F_1(a/b) = \sqrt{\frac{2b}{\pi a}\tan\left(\frac{\pi a}{2b}\right)}\,\frac{0.752 + 2.02(\frac{a}{b}) + 0.37(1-\sin(\frac{\pi a}{2b}))^3}{\cos(\frac{\pi a}{2b})} \tag{7}$$

$$F_2(a/b) = \sqrt{\frac{2b}{\pi a}\tan\left(\frac{\pi a}{2b}\right)}\,\frac{0.923 + 0.1999(1-\sin(\frac{\pi a}{2b}))^4}{\cos(\frac{\pi a}{2b})} \tag{8}$$

From this formulation, the global stiffness matrix may be computed by simply inverting the flexibility matrix, Equation (2).

Thus far, the approach taken has been a global one despite the fact that the additional deformation is known to be localized near the crack. This approach was taken because the expression for the change in compliance, Equation (3), was defined using the global deformations d and θ. To transform this global approach into a local one, two steps are taken. First, the deformation measures are changed to local measures: "stretching" strain and curvature, i.e., d and θ are replaced by $\epsilon_s(x)$ and $\kappa(x)$, respectively. As a result, the stiffness is multiplied by L. To localize the additional deformation, the changes in the stiffness, ΔK_{ij}, are are multiplied by L and the Dirac delta function centered at the location of the crack, x_o. This produces the following stiffness matrix:

$$\left[\ K\ \right] = \begin{bmatrix} (EA)_o - \Delta K_{11} L\delta(x-x_o) & \Delta K_{12} L\delta(x-x_o) \\ \Delta K_{12} L\delta(x-x_o) & (EI)_o - \Delta K_{22} L\delta(x-x_o) \end{bmatrix} \tag{9}$$

where the ΔK_{ij} are computed by inverting both the uncracked global compliance matrix and the cracked global compliance matrix, Equation (2), and subtracting the former from the latter.

Equations of Motion

Having arrived at an appropriate description for the stiffness of the beam, the governing equations of motion may be developed from Hamilton's principle. This requires expressions for the internal strain energy, the kinetic energy, and the external work.

The strain energy of the beam may be written

$$U_{SE} = \int_0^L \frac{1}{2}\,\mathbf{q}^t\,[K]\,\mathbf{q}\,dx \tag{10}$$

where U_{SE} is the strain energy, $[K]$ is the stiffness matrix defined by Equation (9), and $\mathbf{q}^t = \{\epsilon_s, \kappa\}$ is a generalized deformation vector. Here $\epsilon_s = (u_{,x} + P/EA)$ is the stretching strain. Note that the term P/EA represents a static strain resulting from the constant axial load P. As such, u represents only the dynamic axial deformation. Under the typical small

slope assumption the curvature is simply $\kappa = v_{,xx}$ with $v(x,t)$ being the transverse deflection.

Under the assumption that the crack is shallow ($a/b \leq 0.4$) and that the beam is long and thin ($b/L \approx 0.01$), the coupling terms ΔK_{12} and ΔK_{21} are less than one percent of the diagonal terms and may be ignored. Eliminating the off-diagonal terms leads to the following expression for the strain energy

$$U_{SE} = \int_0^L \left[\frac{1}{2}EIv_{,xx}^2 + \frac{1}{2}EA\left(u_{,x} + \frac{P}{EA}\right)^2\right] dx \tag{11}$$

where $EI = (EI)_o - \Delta K_{11} L\delta(x - x_o)$, $EA = (EA)_o - \Delta K_{22} L\delta(x - x_o)$, x_o refers to the location of the crack, and the ΔK_{ij} are obtained using the method described in the previous section.

The kinetic energy is given by

$$T = \frac{1}{2}\int_0^L \rho\left[(cv_{,x} + v_{,t})^2 + (c + cu_{,x} + u_{,t})^2\right] dx \tag{12}$$

where $\rho = \rho_o - m\delta(x - x_o)$ is the mass per unit length of the beam, ρ_o is the mass per unit length of the uncracked beam, m is reduction in the mass per unit length occurring at the crack location, and c is axial transport speed of beam.

These expressions for the potential and kinetic energies, along with an expression of mass conservation ($c\,\partial\rho/\partial x + \partial\rho/\partial t = 0$) are used in Hamilton's principle to obtain the following uncoupled, linear partial differential equations which govern the unforced, undamped motion of a translating beam with an open crack.

$$\rho c^2 v_{,xx} + 2\rho c v_{,tx} + \rho v_{,tt} + (EIv_{,xx})_{,xx} - (Pv_{,x})_{,x} = 0 \tag{13}$$

$$\rho c^2 u_{,xx} + 2\rho c u_{,xt} + \rho u_{,tt} - \left[EA\left(u_{,x} + \frac{P}{EA}\right)\right]_{,x} = 0 \tag{14}$$

These equations are recast using the full expressions for EI and EA, and the following dimensionless quantities: a new spatial coordinate $\xi = x/L$, two new deformation coordinates $V = v/L$ and $U = u/L$, and a dimensionless time $\tau = \sqrt{EI_o/\rho_o L^4}\, t$. The results are

$$(1 - \mu\delta)V_{,\tau\tau} + k_1(1 - \mu\delta)V_{,\xi\tau} + k_2(1 - \mu\delta)V_{,\xi\xi} -$$
$$k_3(\delta_{,\xi\xi} V_{,\xi\xi} + 2\delta_{,\xi} V_{,\xi\xi\xi} - \delta V_{,\xi\xi\xi\xi}) + V_{,\xi\xi\xi\xi} - k_4 V_{\xi\xi} = 0 \tag{15}$$

$$(1 - \mu\delta)U_{,\tau\tau} + k_1(1 - \mu\delta)U_{,\xi\tau} +$$
$$k_2(1 - \mu\delta)U_{,\xi\xi} + k_5[r\delta_{,\xi} U_{,\xi} - (1 - r\delta)U_{,\xi\xi}] = 0 \tag{16}$$

where $\mu = m/\rho_o$, $r = \Delta K_{11} L/EA_o$, $k_1 = 2c\sqrt{\rho_o L^2/EI_o}$, $k_2 = \rho_o L^2 c^2/EI_o$, $k_3 = \Delta K_{22} L/EI_o$, $k_4 = Pl^2/EI_o$, $k_5 = A_o L^2/I_o$. Furthermore, it should be understood that $\delta = \delta(\xi - \xi_o)$. Spatial derivatives of $\delta(\xi - \xi_o)$ are evaluated using the standard method [14].

Natural Frequencies and Stability

The principle objective is to develop a fundamental understanding of the system's response characteristics as the crack travels between the two supports as shown in Figure 1. This is accomplished by examining the free vibration eigenvalue problem which renders the natural frequencies ($\mathrm{Im}(\lambda)$) and the stability exponents ($\mathrm{Re}(\lambda)$).

To arrive at the eigenvalue problem, the governing equations are discretized using a Galerkin procedure with the following expansions:

$$U = \sum_{i=0}^{n} \alpha_i(\tau)\, \Psi_i(\xi) \qquad V = \sum_{i=0}^{n} \beta_i(\tau)\, \Phi_i(\xi) \tag{17}$$

where $\Psi_i(\xi) = \Phi_i(\xi) = \sin(i\pi\xi)$ for the simply supported boundary conditions under consideration here. The discretized equations are then written in matrix form:

$$[M]\ddot{\mathbf{x}} + [G]\dot{\mathbf{x}} + [K]\mathbf{x} = \mathbf{0} \tag{18}$$

where $\mathbf{x} = \{\alpha_1, \alpha_2, \ldots, \beta_1, \beta_2 \ldots\}^t$ is a vector of the modal amplitudes, $[M]$ is the mass matrix, $[G]$ is the skew-symmetric gyroscopic matrix, and $[K]$ is the linear stiffness matrix. The natural frequencies for this system are found by rewriting Equation (18) in first order form and solving the associate eigenvalue problem numerically [15].

RESULTS

Transverse Vibrations

Consider the transverse motion of a beam with a thickness to length ratio of $b/L = 0.01$, a transport speed of half its critical speed $c/c_{cr} = 0.5$, and a crack depth of $a/b = 0.1$. Figures 2a shows the imaginary part of the first and second eigenvalues as a function of the crack location. As the crack enters the domain, the natural frequencies are those of the uncracked, traveling beam (given by the dashed lines). As the crack and the accompanying discontinuities in mass and stiffness move to the right, there is a change in the frequencies. Both the first and second mode frequencies begin to increase. The first mode frequencies continue to increase until a local maximum achieved at the midspan and then it decrease monotonically

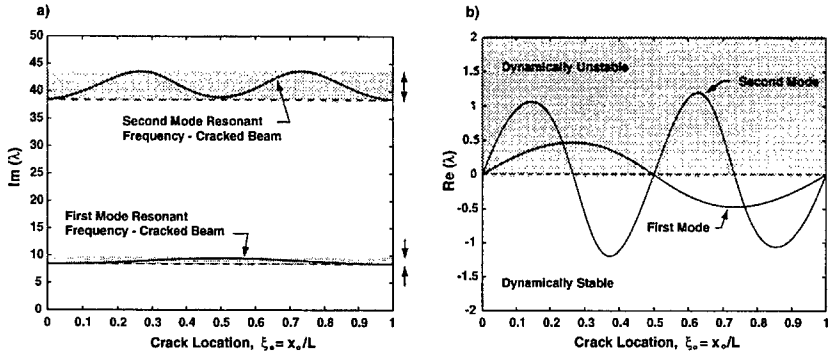

Figure 2: The imaginary (a) and real (b) parts of the first two eigenvalues for transverse motion as a function of crack location.

until the crack exits the domain at $\xi_o = 1$. The second mode eigenvalue locus experiences two local maxima and a local minimum.

There are three important observations to be made regarding Figure 2a. First, it is evident that the $\mathrm{Im}(\lambda)$ loci are symmetric about the midspan $\xi_o = 0.5$. Second, the number of local maxima in each loci is equal to the mode number associated with that loci. Finally, the fluctuations of the natural frequencies have significant implications for the forced response. Consider, for a moment, the uncracked, translating beam. That system has an infinite but countable number of resonant frequencies which should be avoided in the forced vibration problem. In the cracked beam problem, these resonant frequencies fluctuate creating *frequency bands* associated with resonance in the cracked problem (these bands are darkened in the figure). If the system is excited at a frequency in one of these bands the beam will begin to resonate as the crack translates and the natural frequency passes through the excitation frequency. Fortunately, a steady state resonance will not occur since the frequency continues to change. But a large transient may be initiated. Of course, the size of the transient depends on the transport speed which controls the duration that the natural frequency dwells near the excitation frequency.

Figure 2b shows the real parts of the eigenvalues as a function of crack location. As the crack initially enters the domain, $\mathrm{Re}(\lambda) = 0$ which is in agreement with the uncracked, undamped problem. As the crack begins to move through the domain, all of the $\mathrm{Re}(\lambda_i)$ are greater than zero indicating the system is dynamically unstable. The stability changes for the first mode as the crack moves beyond the midspan and $\mathrm{Re}(\lambda_1)$ becomes negative. The second mode fluctuates with a larger amplitude and twice the frequency of the first mode. Both loci return to zero as the crack exits the domain at $\xi_o = 1$.

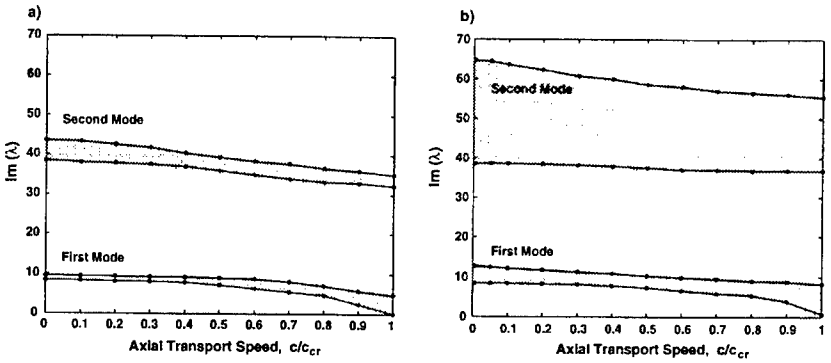

Figure 3: The resonance zones for transverse motion as a function of the transport speed for (a) a beam with a crack depth $a/b = 0.1$ and (b) a beam with a crack depth $a/b = 0.3$.

From Figure 2b, it is evident that the Re(λ) loci are anti-symmetric. As was the case for the imaginary components, the number of local maxima is equal to the mode number. Finally, as the crack enters the domain, the system is dynamically unstable (all Re(λ) increase from zero). As the crack exits the domain, the system is always dynamically stable. The extent to which the beam experiences unstable, growing transient oscillations depends on the transport speed. If the transport speed is low and the system lingers in an unstable region, a large amplitude oscillation may develop. However, if the transport speed is high, the crack will exit the dynamically unstable regime before large oscillations can develop.

Perhaps the two most important revelations about this system are that both the natural frequencies and the dynamic stability characteristics change as the crack location (which can be viewed as a parameter) changes. But how do other parameters, such as the crack depth and the transport speed, influence the size of the resonant frequency bands? Figures 3a and 3b provide some insight. These show the size of the frequency bands as a function of transport speed for crack depths of $a/b = 0.1$ and $a/b = 0.3$, respectively. Comparing 3a and 3b shows that deeper cracks lead to larger resonance bands for both modes (indeed, for all modes) at all transport speeds below c_{cr}. In both figures, the size of the first mode band does not change substantially for transport speeds below $c/c_{cr} = 0.9$. As the divergence instability is approached at $c/c_{cr} = 1$, the upper boundary of the first mode resonance zone continues to decrease mildly but the lower boundary, associated with the frequency of the uncracked beam, drops to zero and widens the band. The second mode resonance becomes more narrow with increases in the transport speed.

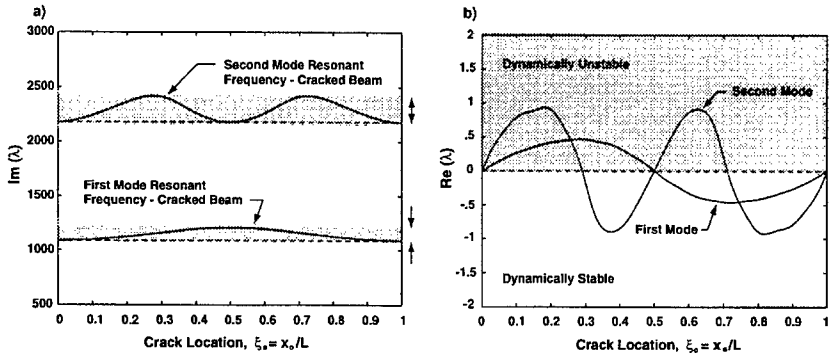

Figure 4: The imaginary (a) and real (b) parts of the first two eigenvalues for axial motion as a function of crack location.

Axial Vibrations

Axial vibrations are also influenced by the presence of an open crack. Figure 4a illustrates the behavior of the first two axial natural frequencies as the crack translates between the supports for the case $a/b = 0.1$, $c/c_{cr} = 0.5$. Many of the trends discussed for transverse vibrations also hold here. The eigenvalue loci fluctuate and the number of maxima for a given loci equals the mode number, i.e., the first mode loci has one maximum. As the crack exits the span, the frequencies again return to that of the uncracked translating beam. Of course, the absolute magnitude of the fluctuations in the axial frequencies are much larger than those associated with transverse vibrations. Relative to their respective frequency scales, there is parity. The real parts of the eigenvalues are presented in Figure 4b. Again, the behavior is qualitatively similar to the results presented for transverse motion.

As before, the size of the resonance bands increases with mode number and crack depth. As the axial transport speed is increased, the axial resonance zones also shrink mildly. However, near the critical speed there is no drastic increase in the size of the first mode resonance band since the fundamental axial frequency is never reduced to zero.

A Brief Note on Convergence

During the discretization, the expansion series given by Equations (17) were truncated. As a result, the issue of modal convergence arises. To ensure convergence of the first two eigenvalues, a convergence study was performed. This consisted of fixing the number of terms retained at n and computing the eigenvalues at four crack locations $\xi = 0.2, 0.4, 0.6,$ and 0.8. The value of n was increased and the eigenvalues were again computed.

The eigenvalues were then plotted against the number of terms retained. Once the change in *all* of the eigenvalues was below 0.5%, the system was said to be converged. Typically, ten terms ($n = 10$) were sufficient to ensure convergence of the transverse eigenvalues. The axial problem usually required many more modes to converge - usually in the range of $n = 24$.

CONCLUSIONS

The objective of this work is to study the dynamics of a translating beam containing an open crack. The mathematical framework for this problem depends on linear elastic fracture mechanics to describe the global change in the stiffness of the cracked beam. This effect is then localized in the vicinity of the crack using a delta function representation. Similarly, there is a discontinuity in the mass per unit length of the beam due to the presence of the crack. The equations governing the axial and transverse vibrations of a translating, cracked beam are developed using Hamilton's principle. These equations are nondimensionalized and then discretized using a Galerkin projection. An eigen-analysis is then carried out to ascertain the behavior of the natural frequencies ($\mathrm{Im}(\lambda)$) and the dynamic stability characteristics ($\mathrm{Re}(\lambda)$).

It is shown that as the crack translates with the beam between the fixed end supports, the imaginary and real parts of the eigenvalues fluctuate. These fluctuations are seen as eigenvalue loci plotted as a function of crack location between $0 < \xi < 1$. Turning to the natural frequencies first, these fluctuations imply that at a fixed excitation frequency in this resonance band the system will be pass through resonance at least twice. This nonstationary problem could lead to large transients oscillations. Furthermore, the size of these resonance bands increases with mode number and with crack depth. The size of the resonance band is relatively insensitive to changes in the transport speed until approximately 90% of the first critical speed, at which time the first mode band widens for the transverse case.

The real parts of the eigenvalues also fluctuate and become positive as the crack moves through the domain. This indicates that the system, at least for a portion of the motion, is dynamically unstable and free oscillations will grow. In contrast to the imaginary parts of the eigenvalues, the real parts are not substantially altered by the crack depth or the transport speed.

In general, this work sheds light on some complexities in the modeling of axially translating beams possessing an open crack. It also demonstrates some of the fundamental, yet complicated, dynamics involved in this free vibration problem and serves as a cautionary note for the forced problem.

ACKNOWLEDGEMENTS

The authors would like to thank Dr. Matthew Begley for his many helpful discussions regarding fracture mechanics. The support of the National Science Foundation (grant number CMS-9625319) is gratefully acknowledged.

REFERENCES

[1] Mote, C.D., Dynamic Stability of Axially Moving Materials. *Shock and Vibration Digest*, 1972, **4**(4), 2-11.

[2] Wickert, J.A., and Mote, C.D., Current Research on the Vibration and Stability of Axially-Moving Materials, *Shock and Vibration Digest*, 1988, **20**, 3-13.

[3] Chati, M., Rand, R., and Mukherjee, S., Modal Analysis of a Cracked Beam, *Journal of Sound and Vibration*, 1997, **207**(2), 249-270.

[4] Chu Y.C. and Shen M.-H.H., Analysis of Forced Bilinear Oscillators and the Application to Cracked Beam Dynamics, *AIAA Journal*, 1992, **30**(10), 2512-2519.

[5] Tada, H., Paris, P., and Irwin, G., *The Stress Analysis of Cracks Handbook*, 1972, Del Research Corp., Hellertown, Pennsylvania.

[6] Dimarogonas, A.D., Vibration of Cracked Structures: A State of the Art Review, *Engineering Fracture Mechanics*, 1996, **55**(5), 831-857.

[7] Sekhar, A.S., Vibration Characteristics of a Cracked Rotor with Two Open Cracks, *Journal of Sound and Vibration*, 1999, **223**(4), 497-512.

[8] Christides, S. and Barr, A.D.S., One Dimensional Theory of Cracked Euler-Bernoulli Beams, *International Journal of Mechanical Science*, 1984, **26**(11), 639-648.

[9] Shen, M.-H.H., and Pierre, C., Natural Modes of Bernoulli-Euler Beams with Symmetric Cracks, *Journal of Sound and Vibration*, 1990, **138**(1), 115-134.

[10] Chondros, T.G., Dimarogonas, A.D., and Yao, J., A Consistent Cracked Bar Vibration Theory, *Journal of Sound and Vibration*, 1997, **200**(3), 303-313.

[11] Wickert, J.A., and Mote, C.D., Linear Transverse Vibration of Axially Moving String-Particle System, *Journal of the Acoustical Society*, 1988, **84**,(3), 963-969.

[12] Dimarogonas, A.D., and Paipetis, S.A., *Analytical Methods in Rotor Dynamics*, 1983, Applied Science Publishers, London.

[13] Papadopoulos, C.A., and Dimarogonas, A.D., Coupled Longitudinal and Bending Vibrations of a Cracked Shaft, *Journal of Vibrations, Acoustics, Stress, and Reliability in Design*, 1988, **110**, 1-8.

[14] Colwell, D.J., and Gillett, J.R., A Property of the Dirac Delta Function, *International Journal of Mathematical Education in Science and Technology*, 1987, **18**, 657-658.

[15] Meirovitch, L., *Computational Methods in Structural Dynamics*, 1980, Noordhoff Publishing, the Netherlands.

A Dynamic View of Static Instabilities

Elizabeth M. Webster & James F. Doyle

PURDUE UNIVERSITY

WEST LAFAYETTE, INDIANA 47907

email: doyle@ecn.purdue.edu

1 Introduction

A common intuitive notion of stability asks the simple question: if the structure is slightly perturbed, what happens to the ensuing dynamics? That is, if the structure returns to its current state, then it is stable; otherwise it is unstable and a dynamic process ensues. The purpose of the present paper is to pursue the implications of this simple notion of stability within the context of modern computational methods.

One of the first concepts of stability was proposed by Euler. He phrased it in terms of alternate equilibrium positions existing not 'too far' from the original configuration. We take this as representative of the static view and as a basis for the discussion of the dynamic alternative. Thus, the static view of (buckling) instabilities considers the structure under monotonic loading, and when the load reaches a critical value it displaces instantaneously to a new configuration. This new configuration is a nearby equilibrium state. Reference [1] gives a good background setting for studying the stability of structures, and Reference [2] is a thorough compendium of examples and solutions. Mention should also be made of References [3, 4] which place static stability in a much broader context. Path following schemes [5] are the computational implementation of the static methods; Reference [6] gives an excellent application and discussion (with many references) of current generalized path-following procedures.

Fundamentally, the dynamic view considers instability to be synonymous with motion and large displacements, and thus requires a fully nonlinear dynamic perspective. In comparison to the static methods, we make two operational changes. First, the independent variable is time; all variables, including the load, are functions of time, and the complete state vector — both velocity and displacement — is computed and monitored. Secondly, we explicitly separate the loading associated with the fundamental path from that which initiates or interrogates the instability. There are very few papers devoted to a dynamic analysis of static instability; however, References [7, 8] give very clear discussions of the difference between the static and dynamic methods of stability analysis. An interesting dynamic computational approach is given in Reference [9] where an eigenanalysis is used to determine the displacement increment in the vicinity of a singular point and a transient solver is used to follow the subsequent

motion. The approach operates only on limit point singularities; geometries exhibiting bifurcation type singularities are converted to limit points by adding imperfections.

A schematic of the dynamic view is illustrated in Figure 1. A stable loading state (resulting from the slowly applied load $P(t)$) is illustrated by segment A; a disturbance (in the form of a short duration ping load $Q(t)$) causes oscillations about the equilibrium path, these are temporary and the structure eventually comes back to the equilibrium path. At or beyond a critical point, however, a small disturbance will cause a significant dynamic process to ensue. Depending on the particular problem, a nearby equilibrium path may or may not be found. It is worth noting that the new equilibrium path may not be statically connected to the original one; that is, we could not devise a proportional loading sequence (where the ratio of all the loads is kept constant) to connect the two equilibrium states.

As we shall show, the dynamic view has two aspects to it: monitoring the vibration eigenvalues to detect when a singularity is encountered, and using ping as agent to dynamically move the structure toward the new state. Ping plays a pivotal role and therefore we discuss its effective design.

We use the example of a rectangular plate to illustrate the main features of the dynamic view — a range of other problems including frames and shells where the dynamic view was used can be found in Reference [10]. We will look at a plate with clamped boundary conditions on the loaded edges. This plate exhibits mode jumping (secondary buckling). It is taken through a complete load/unload cycle and the dynamic approach is used to navigate through mode jumps occurring during the loading and unloading stages.

2 Implementing the Dynamic View

The dynamic view considers instability to be synonymous with motion and large displacements, and therefore requires a fully nonlinear dynamic analysis capability. This section reviews some of the underlying theory, and its implementation as part of a finite element formulation.

Dynamic Analysis

The discretized form of the equations of motion [11] are

$$[M]\{\ddot{u}\} + [C]\{\dot{u}\} = \{P\} - \{F(u)\} \tag{1}$$

where $[M]$ and $[C]$ are the mass and damping matrices, respectively; $\{P\}$ is the total applied load vector, and $\{F\}$ is the vector of internal nodal forces. Computational formulations are available for solving this equation using either an implicit or explicit scheme. Consistent with the dynamic view of instability, let us conceive of the total response and applied load as made up of the two

parts introduced in Figure 1, namely,

$$\{u(t)\} = \{u_o(t)\} + \epsilon\{\xi(t)\}, \qquad \{P(t)\} = \{P_o(t)\} + \epsilon\{Q(t)\}$$

There is the primary response $\{u_o\}$ due to $\{P_o\}$, and the smaller perturbation response $\{\xi\}$ due to the ping load $\{Q\}$. Substituting this decomposition into the equation of motion for the total response and grouping according to powers of ϵ gives the two equations

$$\epsilon^0: \qquad [M]\{\ddot{u}_o\} + [C]\{\dot{u}_o\} = \{P_o\} - \{F(u_o)\} \tag{2}$$

$$\epsilon^1: \qquad [M]\{\ddot{\xi}\} + [C]\{\dot{\xi}\} + [K_t]\{\xi\} = \{Q\} \tag{3}$$

It must be emphasized that this decomposition is only conceptual; in the discussions and results that follows, Equation (1) is treated as fully dynamic and fully nonlinear and used to generate all the responses. We see from Equation (3) that the response due to the ping (at a given load $\{P_o\}$) is that of a linear system with constant tangent stiffness $[K_t] \equiv [\partial F/\partial u_o]$. With changing deformation, governed by Equation (1), the tangent stiffness changes and clearly monitoring the spectral content of the free vibration response to $\{Q\}$ will then give information about the current tangent stiffness.

That is, look for solutions of the form

$$\{\xi(t)\} = \{\phi\}e^{i\mu t}$$

and substitute into the equation of motion to get

$$\Big[[K_t] + i\mu[C] - \mu^2[M]\Big]\{\phi\}e^{i\mu t} = 0$$

We can have non-trivial solutions only if the determinant is zero which leads to a characteristic equation to determine the eigenvalues μ_i and eigenvectors $\{\phi\}_i$. The general solution is written as a combination of

$$\{\phi\}_1 e^{i\mu_1 t}, \quad \{\phi\}_2 e^{i\mu_2 t}, \quad \cdots, \quad \{\phi\}_N e^{i\mu_N t}$$

We state our stability criterion in terms of the properties of the eigenvalues μ_i. For the system to be asymptotically stable we want

$$Imag\,[\mu] > 0 \qquad \text{since} \qquad \{\xi\}e^{i\mu t} = \{\phi\}e^{i(\mu_R + i\mu_I)t} = \{\phi\}e^{-\mu_I t}e^{i\mu_R t}$$

Thus, a negative imaginary component of μ_i would give an exponentially increasing function of time. If the criterion is not true for any one of the roots, then the system is unstable.

The static instability criterion of Euler is the case of $\mu_1 = \mu_I + i\mu_R = 0$; that is, both the real and imaginary parts are zero simultaneously. There are structural problems, however, where this criterion is insufficient. For example,

for follower-force type problems (and related problems such as aeroelastic flutter), instability occurs when the real part of μ_1 is still positive. Such situations are usually referred to as dynamic instabilities [7].

Thus, a key ingredient of the dynamic approach is to monitor the spectral behavior of $[K_t]$. This can be done by imposing a ping, and doing a Fourier analysis on the response. This is conceptually appealing and has the significant advantage of being implemented with an explicit solver for the nonlinear dynamics. Unfortunately, it is too computationally intensive for use as a continuous monitor of the system. When the tangent stiffness is available (as when using an implicit solver), a more expedient method is to do an undamped vibration eigenanalysis — we will then refer to the eigenvalues as $\mu^2 \to \omega^2$, which are real only. It should be pointed out, however, that this is generally not effective for follower-force type problems because most codes use an approximate symmetric tangent stiffness matrix. Actually, for incremental schemes using Newton-Raphson iterations, an accurate tangent stiffness matrix is not essential as verified by the success of the various modified Newton-Raphson methods. What this means is that for a given level of discretization, the tangent stiffness matrix as used in an implicit solver may give imprecise estimates of the vibration eigenvalues; it may, for example, indicate a negative eigenvalue even though the system is actually stable. Of course, we expect an accurate stiffness matrix in the limit of a fine mesh discretization, but short of that, and consistent with the dynamic view, the structure can be pinged to assess the true stability state of the structure. Thus the monitoring is a combination of a vibration eigenanalysis at regular intervals plus selective use of ping. We elaborate more on this later.

We can represent the dynamic response due to the ping using the following modal superposition

$$\{\xi(t)\} = \sum_m \{\phi\}_m \eta_m(t)$$

where $\eta_m(t)$ are the principal coordinates obtained by solving the uncoupled equations

$$\ddot{\eta}_m + 2\zeta\omega_m\dot{\eta}_m + \omega_m^2\eta_m = \{\phi\}_m^T\{Q\}$$

For a ping-like $\{Q\}$ (short duration pulse), all $\eta_m(t)$ behave like a damped oscillator and eventually tend to zero. However, at a static singular point (limit or bifurcation), we have $\omega_1 = 0$, giving

$$\ddot{\eta}_1 = \{\phi\}_1^T\{Q\}$$

This is an unconstrained motion increasing almost linearly in time (since $\{Q\}$ is of short duration). Therefore, all other things being equal, for a ping with arbitrary spatial distribution, we expect (after a short time) the shape of the deforming structure to be dominated by the first vibration mode shape at that load level.

Figure 2 shows the effect of the magnitude of ping (ranging from 10^{-1} to 10^{-5}) on the response — the last value essentially corresponds to no ping

(just numerical round-off.) We conclude that once the structure is unstable ($Imag[\mu] < 0$) that motion will eventually occur; the only effect of ping is to control when it begins. We are motivated to efficiently initiate this transition because we test for stability after each significant load stage. We can increase this control by enhancing the dominance of the first mode. This is achieved by letting the ping be designed such that

$$\{Q\} = \alpha[M]\{\phi\}_1 \tag{4}$$

where α is a proportionality factor. Then

$$\ddot{\eta}_m + 2\zeta\omega_m\dot{\eta}_m + \omega_m^2\eta_m = \{\phi\}_m^T\{Q\} = \alpha\{\phi\}_m^T[M]\{\phi\}_1 = 0\,, \qquad m \neq 1$$

Thus the motions of the higher modes are initially quiescent.

Finite Element Formulation

The program NonStaD [11] is a nonlinear finite element package for the static, dynamic, and stability analysis of thin-walled reinforced structures. The method of description is co-rotational [5] where the motion of an element is decomposed into a rigid body motion and a deformation through the use of a local coordinate system which continuously translates and rotates with the element. The strains are assumed small in the local coordinates and therefore a linear theory can be used for the element formulation. The finite elements used in the modeling are a flat-facet three-node triangular shell element and a two-node frame element, both with six degrees of freedom at each node. In the local system, the membrane behavior is that of the MRT element [12] (this has a drilling degree of freedom) and the plate bending behavior is that of the DKT element [13, 14]. The frame behavior is based on elementary beam and rod theory [15].

The equations of motion can be integrated using either an explicit or an implicit scheme. In all the results to be presented here, the implicit scheme with full Newton-Raphson (dynamic) equilibrium iterations was used. A lumped mass matrix and a mass proportional damping matrix were used.

For the present analysis, NonStaD was modified in a three ways. First, it was changed to allow two independent load histories; one corresponds to the slowly varying primary loading, and the other to the ping loading. Second, the implicit module was modified to give a vibration eigenanalysis at regular stages of the loading. Vector iteration [16, 15] was initially implemented for the eigenanalysis because it is very efficient at determining the single lowest eigenmode; it became clear, however, that we needed to monitor many of the lowest eigenvalues simultaneously and so the subspace iteration [16, 15] method was also implemented. The third significant modification was in the spatial design of ping. Three options are implemented: a single point load ping, a random (in space) ping, and a designer ping. The second of these was used to simulate ambient disturbances. The designer ping is that of Equation (4). Note

that in many cases, multiple modes can go through zero almost simultaneously. For exploring those cases, NonStaD has actually implemented a ping designed as

$$\{Q\} = \alpha_1[M]\{\phi\}_1 + \alpha_2[M]\{\phi\}_2$$

In implementing this, each eigenvector is normalized so that the largest component is unity.

3 Navigating with the Dynamic View

Our example application is a discussion of the phenomenon of mode jumping. This phenomenon received a good deal of attention after Stein reported for his plate experiments [17] that the changes of buckle pattern "occurred in a violent manner and were observed to go from 5 to 6 to 7 to 8 buckles". That it is "violent" implies it is inherently dynamic. Our objective here is to navigate through a mode jump using the dynamic view.

Secondary Buckling of Plates

A common agreement is that mode jumping is intimately associated with the interaction of two buckling modes and therefore can be very sensitive to the precise geometry and boundary conditions [18, 19]. The chosen plate has an ratio [3.4:1], is simply supported on the long edges, and is clamped on the short edges. These choices contribute to enhancing the interaction of buckling modes — the corresponding plate with simply supported conditions on all edges does not exhibit mode jumping. The implementation of the lateral simply-supported conditions actually were

$$\{u,\, v,\, w,\, \phi_x,\, \phi_y,\, \phi_z\} \Longrightarrow \{1,\, 0,\, 0,\, 1,\, 0,\, 0\}_{\text{south}}\,, \quad \{1,\, 1,\, 0,\, 1,\, 0,\, 0\}_{\text{north}}$$

where 0 means fixed, and 1 means free. This is different than the 'special' lateral conditions used in Reference [9]. Contrary to intuition, even though the geometry and loading are symmetric about the long the centerline, a full mesh must be used because there is a nonzero ϕ_x during the bifurcation dynamics.

Figure 3 shows the load and some displacement histories for a complete load/unload cycle. The load history is such that after each significant stage it remains constant until most of the dynamics associated with ping has died out, and Figure 4 shows the out-of-plane deflection contours at some of these significant times. Clearly there are drastic changes in deformed shape. Figure 5 shows the eigenvalue histories and Figure 6 the vibration mode shapes. The latter figure shows a complex evolution over time; note that because of the clamped boundary condition, the vibration mode shapes are not as 'crisp' and well defined as for the simply supported case.

For the first $10\,ms$ the behavior is close to that of a simply-supported plate. There are, however, some significant differences. First, two modes become unstable almost simultaneously and that this mode pair is quite separated from

the other modes. A second difference is that after the bifurcation, the lowest mode has significantly less stiffness than for the simply supported case.

On further increase of load, first there is a stiffening, followed by a rapid loss of stiffness which occurs at about $22\,ms$. Figure 4 shows that after the dynamics has settled down, the deformed shaped has changed significantly from a symmetric $(3,1)$ shape to an anti-symmetric $(4,1)$ shape. This singular point encountered is so sensitive that the application of ping was not necessary to cause the transition. This is the mode jump phenomenon.

Between $30\,ms$ and $34\,ms$, the load was then increased to show the stability of this new state — the four lower eigenvalues increased. On unloading, at a time of about $59\,ms$, the plate goes through another mode jump, this time from a $(4,1)$ to a $(3,1)$ shape as shown in Figure 4. This is not at the same load level as the first mode jump as can be seen more clearly in the load/deflection plots of Figure 7. After this jump, the unloading path is identical to the first post-buckling path (it is noted that for some computer runs the sense of the deflection switches). The transition through the first bifurcation is similar as for the simply-supported plate.

The load/end-shortening plot of Figure 7 shows a hysteresis loop in the post-buckling region. This non-conservative behavior indicates an energy loss, energy that was dissipated during the dynamic events.

Discussion of Plate Mode Jumps

At zero load, the vibration mode shapes have the familiar sequence for a rectangular plate. As the load increases, the sequence changes and it is the $(3,1)$ and $(4,1)$ modes that become unstable. Both modes have comparable eigenvalues. After the transition, which occurs at a load higher than the critical load, these two modes interchange positions.

As the load is increased, the $(4,1)$ mode is unchanged but there is a strong interaction between the $(3,1)$ and $(1,1)$ modes. All eigenvalues increase. The second and third modes peak first and only after they are definitely decreasing does the lowest mode peak and then decrease. It appears that it is the complicated large deflection of the plate that leads to the effective softening of the anti-symmetric mode. In the FEM formulation, the tangent stiffness matrix is constructed of two parts as

$$[K_t] = [K_E] + [K_G(\sigma_{xx}, \sigma_{yy}, \sigma_{xy})]$$

where the geometric stiffness contribution depends on the current state of the membrane stresses. Figure 8 shows the stress state during this loading stage. The numbers indicate the range of the contours; as the load changes, the shape of the contours remain essentially the same, but the range of the numbers change. Clearly, there is not a uniform membrane stress as was the case leading up to the first bifurcation. Indeed, there is a significant compressive σ_{yy} stress on the north boundary. This stress is softening the center as well as approximately the

1/4 and 3/4 areas. The vibration mode shape is reflecting this. We identify the σ_{yy} stress as the softening mechanism. Note that small changes in the boundary conditions can cause large changes in the σ_{yy} stress, and consequently large changes in the post-buckling behavior.

4 Conclusions

In line with our intuitive notion of stability, the dynamic view treats all stability problems as dynamic events and thus there is no essential difference (or complication) between bifurcations, limit points, and phenomena such as mode jumping. In a sense, it recreates a situation quite close to an experiment where "what will happen will happen" and post-buckled states not easily attained by path following methods are happened upon. The dynamic view is enhanced by implementing the following two aspects: monitoring the vibration eigenvalues to detect when a singularity is encountered, and using ping as agent to dynamically move the structure toward the new state. Both of these contribute a deeper insight into the static instability problem as well as giving some control over the loading process.

There are quite a number of issues yet to be explored. First among them is the situation when multiple modes become unstable — the question of the uniqueness of the new found equilibrium state arises. The design of ping sends the structure in a certain direction, but this may bear little relation to the final rested state. Similar issues arise with an asymmetric bifurcation point. Both of these require that we address the question of stability of motion in the large [8, 11].

Acknowledgements: This work was supported in part by a U.S. Army Multi-University Research Initiative (United States Army Grant No. DAAH04-96-10331) awarded to Purdue University.

References

[1] **Hoff, N.J.**, *The Analysis of Structures*, Wiley and Sons, New York, 1956.

[2] **Timoshenko, S.P. and Gere, J.M.**, *Theory of Elastic Stability*, McGraw-Hill, New York, 1988.

[3] **Thompson, J.M.T. and Hunt, G.W.**, *A General Theory for Elastic Stability*, Wiley & Sons, London, 1973.

[4] **Thompson, J.M.T. and Hunt, G.W.**, *Elastic Stability*, Wiley & Sons, London, 1993.

[5] **Crisfield, M.A.**, *Nonlinear Finite Element Analysis of Solids and Structures*, Wiley & Sons, New York, 1997.

[6] **Eriksson,A., Pacoste, C. and Zdunek, A.**, Numerical Analysis of Complex Instability Behavior using Incremental-Iterative Strategies, *Computer Methods in Applied Mechanics and Engineering*, **179**, pp. 265–305, 1999.

[7] **Ziegler, H.**, *Principles of Structural Stability*, Ginn and Company, Massachusetts, 1968.

[8] **Leipholz, H.**, *Stability Theory, an Introduction to the Stability of Dynamic Systems and Rigid Bodies, 2/E*, John Wiley & Sons and B.G. Teubner, Stuttgart, 1987.

[9] **Riks, E., Rankin, C.C., and Brogan, F.A.**, On the Solution of Mode Jumping Phenomena in Thin-walled Shell Structures, *Computational Methods in Applied Mechanics and Engineering*, **136**, pp. 59–92, 1996.

[10] **Webster, E.M**, *A Dynamic View of Static Instabilities*, Ph.D. Thesis, Purdue University, 1999.

[11] **Doyle, J.F.**, *Static, Dynamic and Stability Analysis of Thin-Walled Structures*, Springer-Verlag, New York, to appear 2000.

[12] **Bergan, P.G. and Felippa, C.A.**, A Triangular Membrane Element with Rotational Degrees of Freedom, *Comp. Methods in Applied Mechanics and Engineering*, Vol. 50, pp. 25–69, 1985.

[13] **Stricklin, J.A and Haisler, E.E. and Tisdale, P.R. and Gunderson, R.**, A Rapidly Converging Triangular Plate Element, *AAIA Journal*, **7**, no 1, pp. 180–181, 1969.

[14] **Batoz, J-L.**, An Explicit Formulation for an Efficient Triangular Plate-Bending Element, *International Journal for Numerical Methods in Engineering*, 1982.

[15] **Doyle, J.F.**, *Static and Dynamic Analysis of Structures*, Kluwer, The Netherlands, 1991.

[16] **Bathe, K.-J.**, *Finite Element Procedures in Engineering Analysis*, Prentice-Hall, Englewood Cliffs, NJ, 1982, 2/E 1995.

[17] **Stein, M.L.**, *Loads and Deformations of Buckled Rectangular Plates*, NASA Technical Report R-40, 1959.

[18] **Schaeffer, D. and Golubitsky, M.**, Boundary Conditions and Mode Jumping in the Buckling of a Rectangular Plate, *Comm. in Mathematical Physics*, **69**, pp. 209–306, 1979.

[19] **Holder, E.J. and Schaeffer, D.**, Boundary Conditions and Mode Jumping in the von Karman Equations, *SIAM J. Mathematical Analysis*, **15**(3), pp. 446–458, 1984.

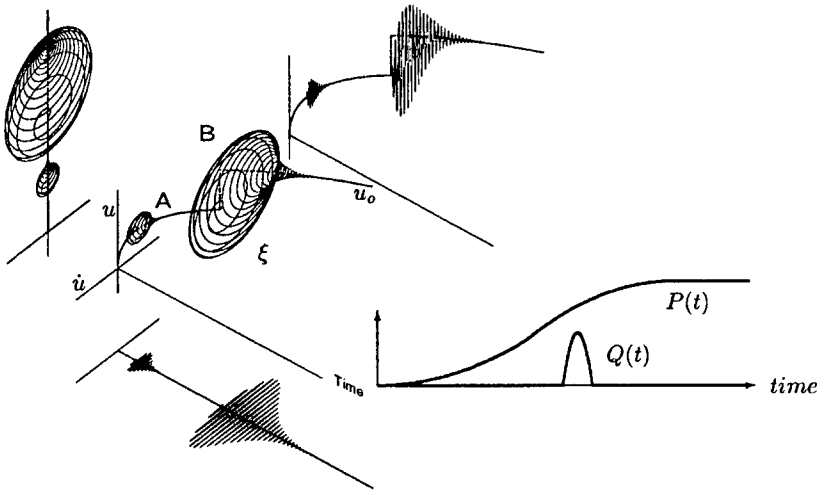

Figure 1: Dynamic view of a static instability.

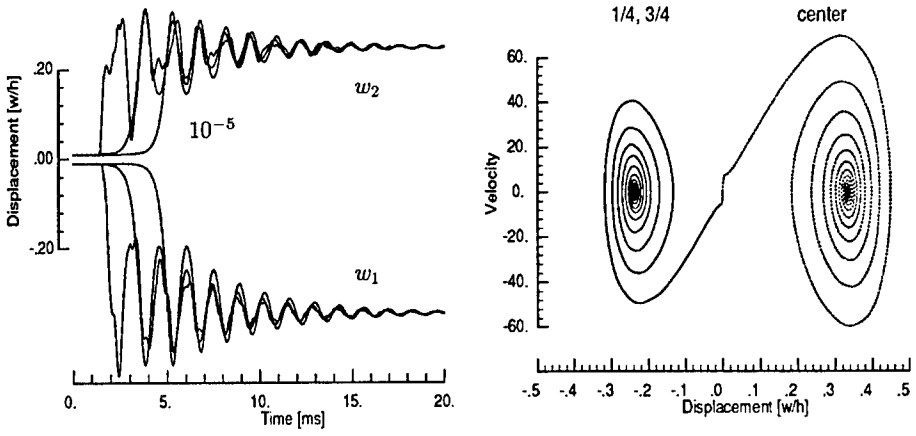

Figure 2: Effect of ping magnitude on response.

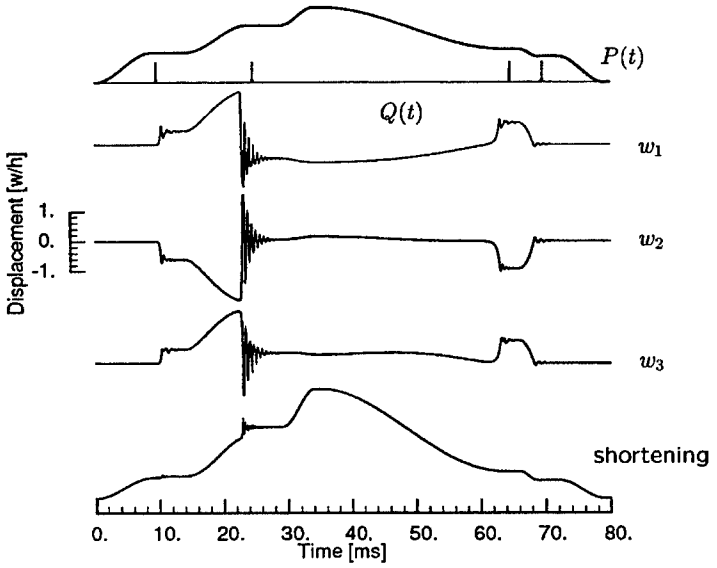

Figure 3: Displacements as a function of time.

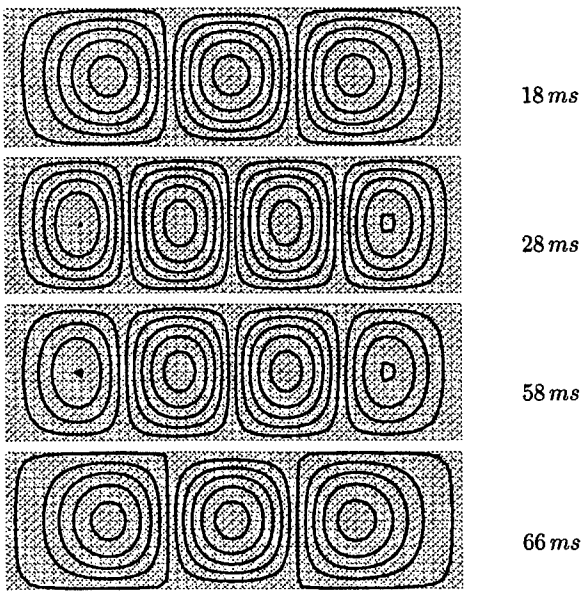

Figure 4: Contours of deformed shapes.

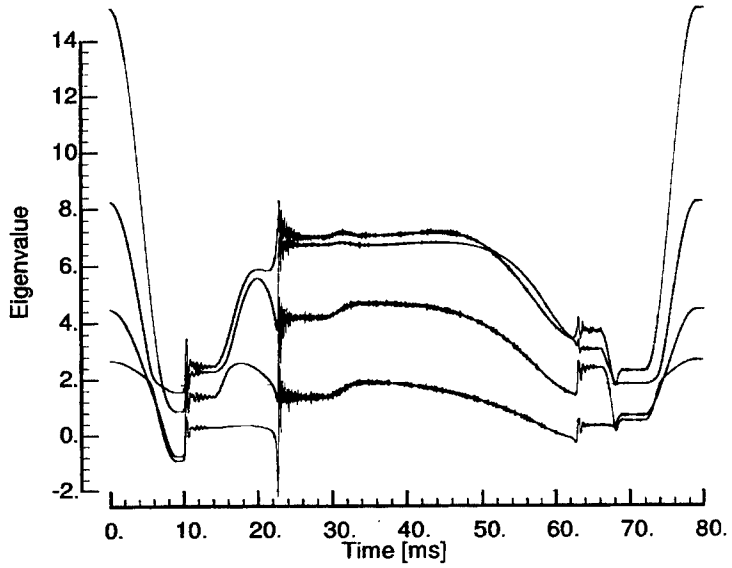

Figure 5: First four vibration eigenvalues as a function of time.

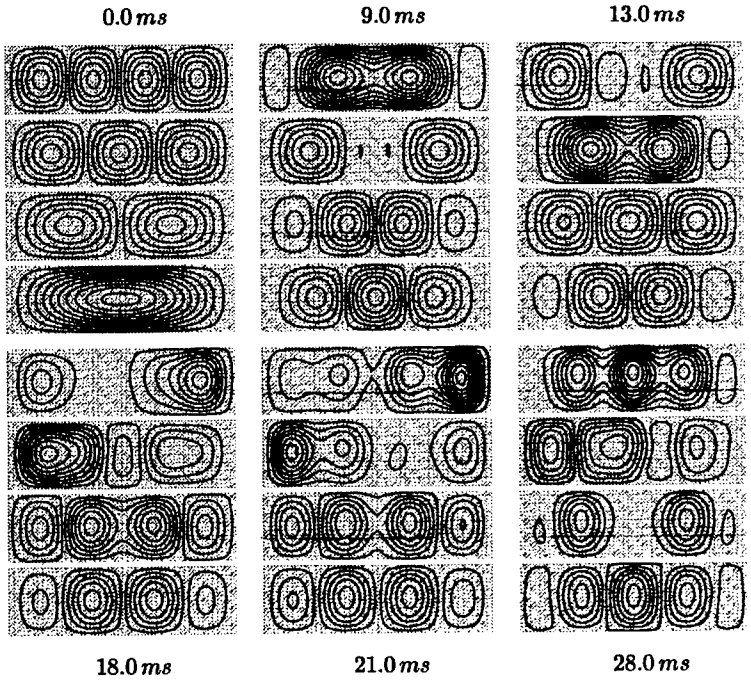

Figure 6: Sequence of vibration mode shapes.

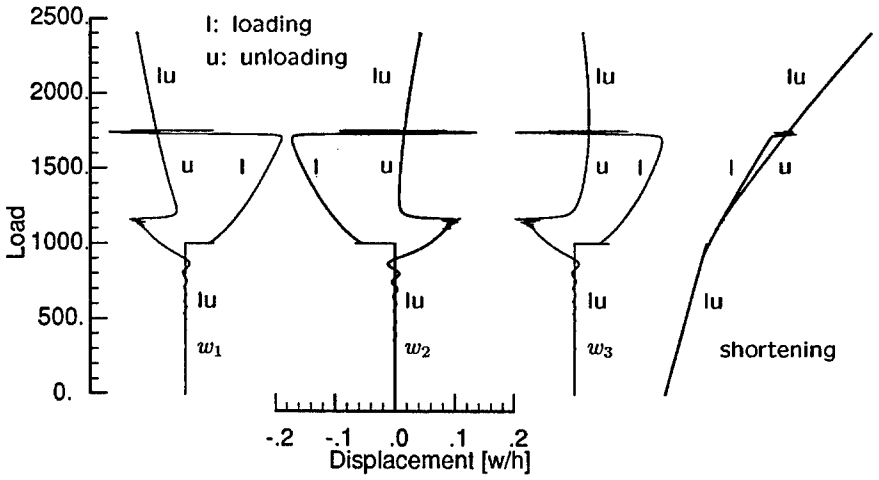

Figure 7: Load deformation plots.

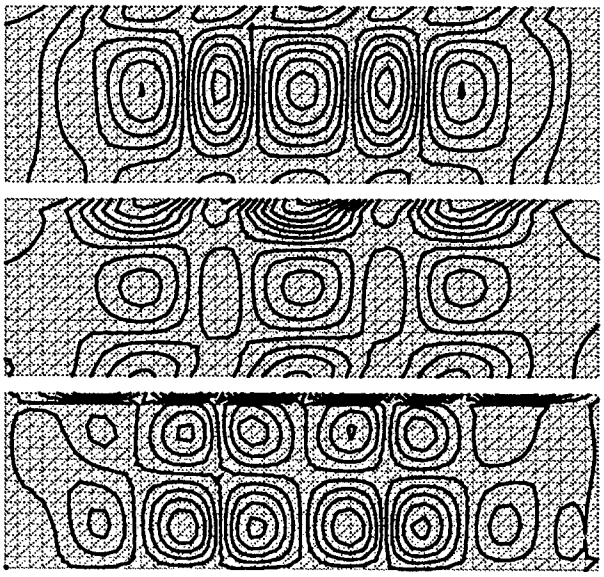

Figure 8: Contours of stress at time $t = 20\,ms$.

TRANSIENT RESPONSES OF NON-PROPORTIONALLY DAMPED STRUCTURES BY THE GROUP THEORETIC APPROACH

Lingchuan Li
KSR International Company
Engineering Department
95 Erie Street South
Ridgetown, Ontario, Canada N0P 2C0

C. W. S. To*
Department of Mechanical Engineering
University of Nebraska
Lincoln, Nebraska 68588-0656, U.S.A.
E-mail: cto2@unl.edu

ABSTRACT

Large scale dynamic finite element analysis of structural systems can be very expensive. To significantly reduce the computational cost various techniques have been developed and presented in the literature. The reduction method based on symmetry group or the so-called group theoretic approach (GTA) has been demonstrated to be a superior means for the bifurcation analysis and free vibration analysis of geometrically nonlinear systems with symmetries by Healey and associates, and others. This method has recently been extended by the authors to deal with large geometrically nonlinear static and dynamic responses of structures discretized by the finite element method. The present paper is, however, concerned with the introduction and application of the extended GTA to systems with non-proportional damping without recourse to the complex modal analysis. It is shown that the extended GTA is simple, efficient and accurate. Consequently, it can prove to be a powerful and economical method to be employed for the computation of accurate transient responses of large scale structural systems with or without non-proportional damping.

* Corresponding author.

1. INTRODUCTION

Large scale dynamic finite element analysis of complex nonlinear mechanical or structural systems can be very expensive. To reduce significantly the size and cost of such an analysis various techniques have been proposed over the last decade or so. The so-called reduced basis or modal truncation technique is a powerful and tested approach. However, it requires computation of higher order derivatives of the governing equation and therefore, it can be very costly.

For bifurcation analysis of geometrical nonlinear structural systems with symmetries, the reduction method based on symmetry group or the so-called group theoretic approach (GTA) has been applied and further developed by Healey and associates [1-5], among others. In a related study, the GTA has been applied by Whalen [4] to free vibration analysis of geometrically nonlinear systems with symmetries. Among various other advantages, the GTA is mathematically very elegant and rigorous, and the solution using GTA is exact and very efficient. This method has recently been further developed by the authors to deal with large geometrically nonlinear static and dynamic responses of structures discretized by the finite element method [6, 7]. In the investigation reported here, however, the GTA is applied to the response analysis of systems with non-proportional damping without recourse to the complex modal analysis technique. It is observed that the type of symmetry group for systems with gyroscopic matrices is different from that of systems without gyroscopic matrices. It is shown that the GTA is simple, efficient and accurate to employ. Consequently, it can prove to be a powerful and economical method for the computation of accurate transient responses of large scale structural systems with or without non-proportional dampings.

The organization of the remaining part of the paper is as follows. The statement of the problem is given in Section 2, while various elementary concepts in symmetry are included in Section 3 for completeness. Section 4 is concerned with the reduction of the problem by the group theoretic approach. Application of the concepts presented in the previous sections is made in Section 5. In particular, the case of a flexible pipe containing a steady moving medium is investigated. Section 6 presents the conclusion.

2. STATEMENT OF THE PROBLEM

A damped large scale structure discretized by the finite element method is considered in this section. The governing matrix equation of motion may be written as

$$M\ddot{u} + C\dot{u} + Ku = \lambda F \tag{1}$$

where M is the assembled mass matrix, C is the assembled damping matrix, K is the assembled tangent stiffness matrix, u is the generalized displacement vector, λ is the load multiplier which is equal to unity for linear system, F is the generalized external load vector, and the double over-dot denotes the second derivative with respect to time t. In general, damping in the system is not necessary proportional or of Rayleigh type. Thus, C can be a skew symmetric matrix, for example.

In many practical problems, the number of degrees of freedom (dof) of the discretized structure, say n, is large and the dof of the reduced problem is relatively small, say n_r. Thus, eqn (1) becomes

$$M_r\ddot{q} + C_r\dot{q} + K_r q = \lambda F_r \tag{2}$$

where

$$M_r = \Phi^T M \Phi \ , \quad C_r = \Phi^T C \Phi \ , \quad K_r = \Phi^T K \Phi \ , \quad F_r = \Phi^T F \ ,$$

and $u = \Phi q$ such that the dimension of the transformation matrix Φ is $n \times n_r$.

In linear structural dynamics the modal analysis for systems with proportional damping or complex modal analysis for those with non-proportional damping is applied to obtain the transformation matrix. However, for large scale and highly nonlinear structures such an approach is very costly because the transformation matrix has to be updated at every time step. Thus, the theory of symmetry group has recently been applied to the computation of responses of discretized structural systems with large geometrical nonlinearities by the authors [6, 7]. However, the case of systems with non-proportional damping has not been addressed in references [6, 7] and therefore the present report is concerned with such an investigation.

3. THEORY OF SYMMETRY GROUP REPRESENTATION

For simplicity, eqn (1) can be written in a more general form as

$$f(\ddot{u}, \dot{u}, u, \lambda) = h(\ddot{u}) + g_1(\dot{u},u) + g_2(u) - \lambda F = 0 \tag{3}$$

where f: $\mathbb{R}^n \times \mathbb{R} \rightarrow \mathbb{R}^n$ is a smooth function, h(ü) is the inertia force, and $g_1(\dot{u},u)$ and $g_2(u)$ are the damping and restoring forces, respectively.

Suppose that eqn (3) models a system with symmetry which is characterized mathematically by an strain-free isometric transformation of the undeformed system into a completely equivalent configuration. More precisely, let $\Omega \subset \mathbb{R}^3$ denotes the region in 3-space that is occupied by the system in the undeformed or initial state. In the present investigation Ω is the reference configuration. Recall that a 3×3 matrix Q is orthogonal if $Q^T = Q^{-1}$. Let O(3)

denotes the set of all 3×3 orthogonal matrices.

DEFINITION 1. Let $\Omega \subset \mathbb{R}^3$ be a bounded set. The *complete symmetry group* of Ω, $G(\Omega)$, is a subset of O(3), each element of which maps Ω into itself, viz., $G(\Omega) \equiv \{Q \in O(3): Q(\Omega)=\Omega\}$. A subgroup $G_s(\Omega) \subseteq G(\Omega)$ is called a symmetry group of Ω.

REMARK 1. If the region $\Omega \subset \mathbb{R}^3$ is unbounded, then translations and orthogonal transformation should be included in Definition 1 above.

By Definition 1, the complete symmetry group of the structural configuration is the set of all orthogonal transformations that map the system into an equivalent configuration. Note that in addition to the symmetry of the initial configuration Ω, the constitutive laws, the boundary conditions, and the excitation acting on the system must all agree, in some sense, with a symmetry group $G_s(\Omega)$. Naturally, one expects eqn (3) to have special properties related to $G_s(\Omega)$ that are not shared by all general equations of that form. The dimension of the state space $\mathbb{R}^n$ is not usually the same as the dimension of the space in which the model exists. Thus, it is necesary to consider an "action" of the symmetry group $G_s(\Omega)$ on $\mathbb{R}^n$.

DEFINITION 2. An orthogonal representation (*rep*) of a symmetry group $G_s(\Omega)$ on $\mathbb{R}^n$ is an n×n matrix-valued function $T: G_s(\Omega) \subseteq O(3) \rightarrow O(n)$ that satisfies the following properties:

(i) $T(Q_1)T(Q_2) = T(Q_1Q_2)$ for all $Q_1, Q_2 \in G_s(\Omega)$, where $T(Q_1)T(Q_2)$ designates matrix multiplication.

(ii) $T^{-1}(Q)=T(Q^{-1})$ for all $Q \in G_s(\Omega)$, $T^{-1}(Q)$ denotes the inverse of matrix T(Q).

(iii) $T^T(Q) = T(Q^T)$ for all $Q \in G_s(\Omega)$, where $T^T(Q)$ denotes the transpose of T(Q).

(iv) $T(I) = I$, where I is the n×n identity matrix.

Suppose that eqn (3) models a symmetric problem characterized by symmetry group $G_s(\Omega)$ on $\mathbb{R}^n$. Equation (3) is said to be *equivariant* under the action of T if

$$f(T\ddot{u}, T\dot{u}, Tu, \lambda) = Tf(\ddot{u}, \dot{u}, u, \lambda) \qquad \forall Q \in G_S(\Omega) \qquad (4)$$

where Tu or T(Q)u denotes the matrix product of an n×n matrix with column vector u, and $\forall$ designates "for all". Equation (4) has been proved in Theorem 4.1 by Healey [2].

REMARK 2. The equivalence relation (4) follows from the fact that the loading, material properties, and boundary conditions agree with the geometric symmetry of the structure. If any of these has less symmetry than the purely geometric symmetry, then an appropriate subgroup must be employed.

REMARK 3. In the present investigation, equilibrium eqn (3) is derived using the finite element method. For nonlinear systems, in general, this equation is not explicitly available. Thus, eqn (3) and its derivatives can only be evaluated numerically at solution points.

4. GROUP SYMMETRY AND REDUCTION OF PROBLEM

For completeness, the procedure of explicit construction of a reduced problem through the application of the theory symmetry group representation introduced in reference [6] is outlined in this section. The ultimate goal is to provide a computational strategy for the response analysis of discretized linear and nonlinear structures with symmetries or partial symmetries. However, during the current phase of the investigation, the main goal is confined to structures with symmetries.

Consider once again equilibrium matrix eqn (3) and assume that eqn (4) holds. If ($\ddot{u}_o$, $\dot{u}_o$, u_o,λ_o) is a solution point of eqn (3), viz., $f(\ddot{u}_o,\dot{u}_o,u_o,\lambda_o) = 0$ then by eqn (4),

$$f(T\ddot{u}_o, T\dot{u}_o, Tu_o, \lambda_o) = Tf(\ddot{u}_o,\dot{u}_o,u_o,\lambda_o) = 0 \quad \forall Q \in G_S(\Omega). \tag{5}$$

Thus, either $T(Q)\ddot{u}_o=\ddot{u}_o$, $T(Q)\dot{u}_o$ and $T(Q)u_o=u_o$ for all $Q\in G_s(\Omega)$, that is, $\ddot{u}_o$, $\dot{u}_o$ and u_o are invariant under T, or $(T\ddot{u}_o,T\dot{u}_o,Tu_o,\lambda_o)\neq(\ddot{u}_o,\dot{u}_o,u_o,\lambda_o)$ is another solution point for one or more $Q\in G_s(\Omega)$.

It should be noted that equivariance can be exploited to deliver considerably more than the foregoing. Let $G_r(\Omega)$ be any subgroup of $G_s(\Omega)$, including the possibility of $G_r(\Omega)\equiv G_s(\Omega)$.

DEFINITION 3. A subspace

$$\varphi_G \equiv \left\{\ddot{q},\dot{q},q \in \mathbb{R}^n : T\ddot{q} = \ddot{q}, T\dot{q} = \dot{q}, Tq = q \quad \forall Q \in G_s(\Omega)\right\}, \tag{6}$$

that is called the $G_r(\Omega)$-symmetric subspace of $\mathbb{R}^n$.

By eqn (4), one has

$$\begin{aligned} Tf(\ddot{q},\dot{q},q,\lambda) &= f(T\ddot{q},T\dot{q},Tq,\lambda) \quad \forall Q \in G_r(\Omega) \\ &= f(\ddot{q},\dot{q},q,\lambda) \quad \forall (\ddot{q},\dot{q},q,\lambda) \in \varphi_G \times \mathbb{R}. \end{aligned} \tag{7}$$

That is, $f: \varphi_G\times\mathbb{R}\rightarrow\varphi_G$, by virtue of eqn (5). This leads to the following important theorem.

THEOREM 1. Let f_G denote the restriction of f to $\varphi_G \times \mathbb{R}$. Then $(\ddot{q}_o, \dot{q}_o, q_o, \lambda_o) \in \varphi_G \times \mathbb{R}$ is a solution point of eqn (3) if and only if it is a solution point of the $G_r(\Omega)$-reduced problem

$$f_G(\ddot{q}, \dot{q}, q, \lambda) = 0 \ . \tag{8}$$

It should be noted that not all solutions of eqn (3) are necessarily solutions of eqn (8). Instead, the reduced problem captures only the $G_r(\Omega)$-symmetric solution points of eqn (3). The most important feature of the above theorem is that *exact* solutions of eqn (3) can be obtained by solving the lower-dimensional problem described by eqn (8). Furthermore, Theorem 1 is valid for any subgroup $G_r \in G_s(\Omega)$. Thus, it provides an elegant methodology for finding solutions of eqn (3) with various symmetries.

In order to realize the inherent reduction it is necessary to express eqn (8) relative to a basis for φ_G. To this end, let

$$span\{\phi_1, \phi_2, ..., \phi_m\} = \varphi_G, \qquad \phi_i^T \phi_j = \delta_{ij}, \tag{9}$$

be an orthogonal normal basis. It can be obtained as follows. Assume $G_r(\Omega)$ is finite with N elements, viz., $G_r(\Omega) = \{Q_1, Q_2, ..., Q_N\}$. It has been shown by Healey [1] that the dimension of φ_G is given by the non-negative integer,

$$m = \frac{1}{N} \sum_{i=1}^{N} \tau_i \tag{10}$$

where τ_i denotes the trace of matrix T.

DEFINITION 4. Let P be a linear operator on the finite dimensional inner product space V. If PP = P then P is a projection operator.

The latter has been shown by Healey [1] to be

$$P = \frac{1}{N} \sum_{i=1}^{N} T_i \ , \tag{11}$$

where T_i denotes $T(Q_i)$, and $P^T = P$ is an orthogonal projection. Equations (10) and (11) follow from the fact that $\varphi_G \subseteq \mathbb{R}^n$ is the invariant subspace under T that is associated with the irreducible identity *rep* of $G_r(\Omega)$. If $G_r(\Omega)$ is continuous, then the summations in eqn (10) and (11) have to be replaced with integrations.

Applying eqn (6) and (11), one has

$$P\Phi = \frac{1}{N} \sum_{i=1}^{N} T_i \phi_i = \Phi \qquad \forall \Phi \in \varphi_G. \tag{12}$$

Therefore, the basis in eqn (9) can be evaluated by determining the non-trivial solutions of the homogeneous system

$$(\boldsymbol{P} - \boldsymbol{I})\boldsymbol{\Phi} = \mathbf{0}, \tag{13}$$

where I is the unity matrix.

The basis can always be treated as an orthogonal normal set since P is symmetric. Vectors ϕ_i, i = 1,2,...,m, are known as symmetry co-ordinates or symmetry modes.

The symmetry modes can be calculated with the following algorithm:

(i) Let $P_1 = P$.

(ii) Let ϕ_o be the initial trial vector which contains components of the desired eigenvector.

(iii) Project ϕ_o onto subspace so that $\hat{\phi}_i = P_i \phi_o$.

(iv) Normalize ϕ_i to a unit vector: $\phi_i = \hat{\phi}_i / \| \hat{\phi}_i \|$.

(v) Deflate ϕ_i from the projection:
$P_{i+1} = P_i - \phi_i \phi_i^T$.

(vi) Repeat steps (ii) to (v) until m eigenvectors are found.

Now, the n×m transformation matrix with columns being the symmetry modes can be written as

$$\boldsymbol{\Phi} = \left[\phi_1, \phi_2, \ldots, \phi_m\right] . \tag{14}$$

Substituting eqn (14) into (2), the response of the reduced system can be obtained at every time step. It is noted that by applying the transformation matrix defined in eqn (14), eqn (2) gives an *exact* symmetric solution of eqn (1). The transformation matrix obtained in this manner is entirely different from that by applying the modal or complex modal analysis.

It may be noted that in the present investigation the central difference direct integration scheme is employed for the computation of eqn (2).

5. APPLICATIONS OF THE GROUP THEORETIC APPROACH

Three cases are considered in this section as an illustration of the application of the GTA outlined in the foregoing sections. These are: the clamped-clamped uniform beam subjected to a central transversal step force, the twenty-four bar space dome whose central node, node 4 is subjected to a vertical step load, and a pinned-pinned uniform slender pipe containing flowing water and under a vertical step point load at the central node. The latter case is one with a non-proportional damping matrix in the governing equation of motion. It may be

appropriate to note that results of large geometrically nonlinear static and dynamic analysis of the above twenty-four bar space dome was presented in reference [6] and whose symmetry modes are applied here. Furthermore, for illustration purpose, lumped element mass matrix is applied in this case while every bar is represented by one single bar finite element.

5.1 Clamped-Clamped Beam Structure

As shown in Figure 1, the clamped-clamped beam is represented by six 2-node beam elements. Every node has two dof, namely, transverse displacement and rotation about z-axis. The consistent element mass and stiffness matrices can be found in reference [8], for example. The geometrical and material properties of the beam structure are: length of each element, L = 0.127m (5 in), cross-section area; $A = 6.45 \times 10^{-4}$ m^2 (1 in^2); second moment of cross-section, $I = 3.46 \times 10^{-8}$ m^4 (0.0833 in^4); Young's modulus, $E = 2.1 \times 10^{11}$ N/m^2 (3×10^7 psi); and density, $\rho = 7800$ kg/m^3 (0.00073 lb.s^2/in^4).

In this case, comparison is made for responses obtained by the modal analysis to those computed by the and the GTA. Proportional dampings with the first two modal damping ratios are chosen: $\zeta_1 = 0.05$, $\zeta_2 = 0.10$, and the two independent coefficient of the proportional damping matrix are: $\lambda_0 = 46.22$ and $\lambda_1 = 4.69 \times 10^{-5}$. The equations for the reduced problem applying the modal analysis and GTA are numerically integrated with the central difference method. Note that in this particular problem the finite element problem has 10 dof. The natural frequencies and mode shapes are included in Tables 1 and 2, respectively. The symmetry modes for the GTA are obtained by the procedure presented in section 4 above. For brevity, the details are not included here. However, the symmetry modes for the GTA adopted in the computation are presented in Table 3. The magnitude of the vertical step load applied at the centre of the beam is F = 22.24 kN. The time step for the numerical integration is $\Delta t = 1 \times 10^{-5}$ s. The computed results are presented in Figure 2. Excellent agreement between the results applying the modal analysis and GTA is observed. Note that even for results applying the modal analysis with the first 5 modes being included in the computation, the computational time is approximately 5 times that of those employing the GTA. This is due to the fact that the mass and stiffness matrices of the discretized system must be assembled and the eigenvalue problem must be solved before the mode shapes are formed in the modal analysis, while the equivalent configurations of the system are considered to form the symmetry modes in the GTA.

5.2 Twenty-Four Bar Space Dome Structure

This relatively more complex structure is made of 24 bars and the 6 vertices are fixed so that there are 7 nodes free to move. Each node has 3 translational dof. There are 21 dof in this structure. The sketch is shown in Figure 3. The geometrical and material properties are: cross-sectional area of

each uniform bar, A = 0.1 m^2; Young's modulus, E = 2.1 × 10^{11} N/m^2; and density, ρ = 7800 kg/m^3.

This structure has 6 equivalent configurations corresponding to rotating the structure through angles of rπ/3, where r = 0,1,2,...,5, and 6. These equivalent configurations correspond to reflections of the structure across the plane through the Z-axis and the line through the origin in the XY-plane that makes a clockwise angle of rπ/6 with X-axis. Applying the procedure in Section 4, the 12 equivalent configurations can be obtained and they have been presented in reference [9]. For brevity, they are not included in this paper. However, the obtained transformation matrix of equation (2) applying the GTA is included in Table 4(a). Note that the transformation matrix is

$$\Phi = \left[\phi_1 \; \phi_2 \; \phi_3\right] .$$

For comparison purpose, the natural frequencies of this 24-bar space dome were obtained and are included in Table 4(b), but the 21 mode shapes are not presented here for brevity. Again, proportional damping is assumed and only the first two modal damping ratios are applied: ζ_1 = 0.005, and ζ_2 = 0.010. The two independent coefficient of the proportional damping matrix for this problem are: λ_o = - 3.435 and λ_1 = 1.75 × 10^{-4}.

Computed responses applying the GTA with a central transversal step load of 22.48 kN and the modal analysis are presented in Figure 4. For results applying the modal analysis method cases with 3 modes and 5 modes were also considered in addition to the 10 and 20 modes cases. The 3 modes and 5 modes cases have large error compared with the GTA results and therefore they have not been included in Figure 4. Results for the full space case, that is without reduction by the GTA, are also included for comparison. It should be noted that results obtained by the modal analysis method are approximated whereas those by the GTA are exact, insofar as the transformation is concerned.

5.3 Uniform Pinned-Pinned Pipe Containing Moving Fluid

The use of the GTA is effective for systems with symmetry and symmetric damping matrices. However, its use in the computation of responses where the damping is non-proportional and the damping matrices are not symmetric has not been investigated in details. It is nevertheless appropriate to note that an important contribution to this area is provided by Whalen [4]. In Chapter 3 and Appendix A of reference [4], it has been shown that a system with a gyroscopic matrix has the pure rotation symmetry group $\mathbb{C}_n$ instead of the structural symmetry group D_n. Note that D_n is isomorphic to $\mathbb{C}_n \times \mathbb{C}_2$. Thus, the present study makes use of the above observation. For brevity, the detailed procedure of symmetry mode computation are not included here.

In the present study, a flexible pipe containing a steady moving fluid is studied. A schematic diagram of this system is shown in Figure 5. The governing matrix equation of motion can be written as eqn (1). For this problem the consistent element mass matrix is [10]

$$[m] = \frac{(m_p + m_f)L}{420}\begin{bmatrix} 156 & . & . & . \\ 22L & 4L^2 & . & . \\ 54 & 13L & 156 & . \\ -13L & -3L^2 & -22L & 4L^2 \end{bmatrix}$$

where L is the element length while m_p and m_f are mass per unit length of the empty pipe and enclosing fluid, respectively. Note that this element matrix is symmetric and therefore only elements (entries) of the lower half of the matrix are given. The consistent element stiffness matrix can be shown to be [10]

$$[k] = [k_L] - [k_f],$$

where $[k_L]$ is the consistent element stiffness matrix for a uniform beam whereas $[k_f]$ is the component due to the flowing fluid and is symmetric. It is given as

$$[k_f] = \frac{(m_f V_f^2)}{30L}\begin{bmatrix} 36 & . & . & . \\ 3L & 4L^2 & . & . \\ -36 & -3L & 36 & . \\ 3L & -L^2 & -3L & 4L^2 \end{bmatrix},$$

where V_f is the fluid velocity.

The consistent element damping matrix is skew-symmetric and is also called the gyroscopic matrix. It is given as [10]

$$[c] = \frac{(m_f V_f)}{30}\begin{bmatrix} 0 & 6L & 30 & -6L \\ -6L & 0 & 6L & -L^2 \\ -30 & -6L & 0 & 6L \\ 6L & L^2 & -6L & 0 \end{bmatrix}.$$

Once the assembled matrices are obtained the eigenvalue problem of eqn (1) is solved with the method developed by Meirovitch [11].

The length of the uniform pipe considered in the present investigation is 3.2m [12]. Its diameter is 2.54 cm and thickness of the its wall is 1.65 mm. It is pinned-pinned at both ends. Other pertinent data are: m_p = 0.342 kg/m, m_f = 0.384 kg/m, Young's modulus of elasticity of the pipe $E = 68.9 \times 10^9$ N/m^2, area moment of the cross-section of the pipe $I = 8.64 \times 10^{-9}$ m^4, and the critical velocity for instability is V_{fc} = 39.4 m/s. For illustration purpose, the pipe is approximated by 4 elements. Its natural frequencies and mode-shapes are included in Table 5. The symmetry modes by the GTA are presented in Table 6.

A step load of 100N is vertically applied at the center node of the pipe. Representative responses in full space and in reduced sub-space by the GTA for V_f = 20 m/s and V_f = 35 m/s are presented in Figure 6. Two points should be noted. First, the case for V_f = 40 m/s was also considered but its results are not included in Figure 6 because responses of this case grow rapidly. This is what one would expect since V_{fc} = 39.4 m/s. Second, the discrepancy between the full space and reduced space solutions increases as V_f approaches V_{fc}. This has to do with the fact that in the reduced space solution only the original spatial symmetry modes are applied directly without considering the procedure proposed by Whalen [4] for systems with gyroscopic matrices.

6. CONCLUSION

The reduction method based on symmetry group or the so-called group theoretic approach (GTA) is applied to the computation of responses of non-proportionally damped systems that are approximated by the finite element method and excited by transient disturbances. An associated digital computer program written in Fortran language has also been developed.

The GTA is mathematically very elegant and rigorous. Computationally, it gives exact solutions insofar as spatial transformation from full space to reduced space is concerned. It is very efficient in that identification of greater number of equivalent configurations provides a larger dof to be reduced in the computation. With standard finite element meshes that possess symmetries, such an identification of equivalent configurations and construction of associated orthogonal matrices can be automated in the computer program. This, in turn, leads to even better computational efficiency. For instance, in the foregoing space dome structure the computional time for the reduced dynamic problem is only about 15% of that for the full space structure.

ACKNOWLEDGMENTS

The second author gratefully acknowledged support from the Natural Sciences and Engineering Research Council of Canada through the Collaborative Project Grant, CPG0181649.

REFERENCES

1. Healey, T.J., A group-theoretic approach to computational bifurcation problems with symmetry. *Comput. Meth. Appl. Mech. Engng.*, 1988, **67**, 257-295.
2. Healey, T.J., Symmetry and equivariance in nonlinear elastostatics, Part I. *Arch. Rat. Mech. Anal.*, 1988, **110**, 205-227.
3. Chang, P. and Healey, T., Computation of symmetry modes and exact reduction in nonlinear structural analysis. *Comput. Struct.*, 1988, **28(2)**, 135-142.
4. Whalen, T.M., *On the Existence of Periodic Solutions to Nonlinear Elastodynamic Systems with Symmetry.* Ph.D. Thesis, Cornell University, 1993.
5. Wohlever, J.C. and Healey, T.J., A group theoretic approach to the global bifurcation analysis of an axially compressed cylindrical shell. *Comput. Meth. Appl. Mech. Engng.*, 1995, **122**, 315-349.
6. To, C.W.S. and Li, L., Exact reduction by group theoretic approach in computational nonlinear structural dynamics. *Proc. of ASME Design Engineering Technical Conferences and Computers in Engineering Conference*, September 14-17, 1997, Sacramento, California.
7. To, C.W.S. and Li, L., Geometrically nonlinear response of beam and membrane structures by exact reduction technique. *Proc. of ASME Design Engineering Technical Conferences and Computers and Information Engineering Conference*, September 13-16, 1998, Atlanta, Georgia.
8. Cook, R.D., *Finite Element Modeling for Stress Analysis.* John Wiley and Sons, New York, 1995.
9. Li, L., *Geometrically Nonlinear Analysis of Discretized Structures by The Group Theoretic Approach.* Ph.D. Thesis, University of Western Ontario, Canada, 1999, Chapter 4.
10. To, C.W.S. and Healy, W.J., Further comment on "Vibration analysis of straight and curved tubes conveying fluid by means of straight beam finite elements. *J. Sound and Vibr.*, 1986, **105(3)**, 513-514.
11. Meirovitch, L., A new method of solution of the eigenvalue problem for gyroscopic systems. *A.I.A.A. J.*, 1974, **12(10)**, 1337-1341.
12. Blevins, R.D., *Flow-induced Vibration.* Van Nostrand Reinhold, New York, 1977.

Table 1. Natural Frequencies of Clamped-Clamped Beam Structure (in rad/s)

ω_1	ω_2	ω_3	ω_4	ω_5	ω_6	ω_7	ω_8	ω_9	ω_{10}
1454.8	4017.2	7916.2	13219.9	19834.7	30805.8	42813.7	59249.2	80814.9	104925.5

Table 2. Mode-shapes of Clamped-Clamped Beam Structure

$\bar{\Psi}_1$	$\bar{\Psi}_2$	$\bar{\Psi}_3$	$\bar{\Psi}_4$	$\bar{\Psi}_5$	$\bar{\Psi}_6$	$\bar{\Psi}_7$	$\bar{\Psi}_8$	$\bar{\Psi}_9$	$\bar{\Psi}_{10}$
0.1871	0.3885	0.5342	0.5547	0.4126	-0.2741	-0.0706	0.0871	-0.1460	0.1042
0.0620	0.0992	0.0772	-0.0168	-0.1349	0.3574	0.4752	0.5032	-0.4223	0.2411
0.5009	0.5706	0.1513	-0.3645	-0.4461	0.1384	-0.2505	-0.3111	0.0904	0.0632
0.0531	-0.0463	-0.1964	-0.1727	0.0642	-0.4217	-0.3626	0.0774	-0.5170	0.4992
0.6439	0.0000	-0.5423	0.0000	0.4654	0.0000	0.3868	0.0000	0.2227	0.0000
0.0000	-0.1514	0.0000	0.2419	0.0000	0.4472	0.0000	-0.5221	0.0000	0.5962
0.5009	-0.5706	0.1513	0.3645	-0.4461	-0.1384	-0.2505	0.3111	0.0904	-0.0632
-0.0531	-0.0463	0.1964	-0.1727	-0.0642	-0.4217	0.3626	0.0774	0.5170	0.4992
0.1871	-0.3885	0.5342	-0.5547	0.4126	0.2741	-0.0706	-0.0871	-0.1460	-0.1042
-0.0620	0.0992	-0.0772	-0.0168	0.1349	0.3574	-0.4752	0.5032	0.4223	0.2411

Table 3. Basis Vectors of Clamped-Clamped Beam Structure

ϕ_1	ϕ_2	ϕ_3	ϕ_4	ϕ_5
0.0000	-0.7071	0.0000	0.0000	0.0000
0.0000	0.0000	0.7071	0.0000	0.0000
0.0000	0.0000	0.0000	-0.7071	0.0000
0.0000	0.0000	0.0000	0.0000	0.7071
-1.0000	0.0000	0.0000	0.0000	0.0000
0.0000	0.0000	0.0000	0.0000	0.0000
0.0000	0.0000	0.0000	-0.7071	0.0000
0.0000	0.0000	0.0000	0.0000	-0.7071
0.0000	-0.7071	0.0000	0.0000	0.0000
0.0000	0.0000	-0.7071	0.0000	0.0000

Table 5(a). Natural Frequencies of the Pipe (rad/s)

ω_1	ω_2	ω_3	ω_4	ω_5	ω_6	ω_7	ω_8
27.50	107.24	249.40	486.83	775.82	1228.90	1842.69	2243.03

Table 5(b). Mode-shapes of the Pipe

$\bar{\Psi}_1$	$\bar{\Psi}_2$	$\bar{\Psi}_3$	$\bar{\Psi}_4$	$\bar{\Psi}_5$	$\bar{\Psi}_6$	$\bar{\Psi}_7$	$\bar{\Psi}_8$
-0.4439	0.5331	0.5559	0.4472	0.5739	0.5759	0.5770	0.4472
-0.3197	0.2716	0.1350	0.0000	-0.0547	-0.0504	-0.0173	0.0000
-0.3139	0.0000	-0.3931	-0.4472	-0.4058	0.0000	0.4080	0.4472
-0.4521	0.0000	-0.1909	0.0000	0.0773	0.0000	-0.0245	0.0000
0.0000	-0.5331	0.0000	0.4472	0.0000	-0.5759	0.0000	0.4472
-0.3197	-0.2716	0.1350	0.0000	-0.0547	0.0504	-0.0173	0.0000
0.3139	0.0000	0.3931	-0.4472	0.4058	0.0000	-0.4080	0.4472
0.4439	0.5331	-0.5559	0.4472	-0.5739	0.5759	-0.5770	0.4472

Table 6. Symmetry Modes of The Pipe

ϕ_1	ϕ_2	ϕ_3	ϕ_4
0.0000	0.0000	0.0000	-0.7071
0.0000	-0.7071	0.0000	0.0000
0.0000	0.0000	-0.7071	0.0000
-1.0000	0.0000	0.0000	0.0000
0.0000	0.0000	0.0000	0.0000
0.0000	-0.7071	0.0000	0.0000
0.0000	0.0000	0.7071	0.0000
0.0000	0.0000	0.0000	-0.7071

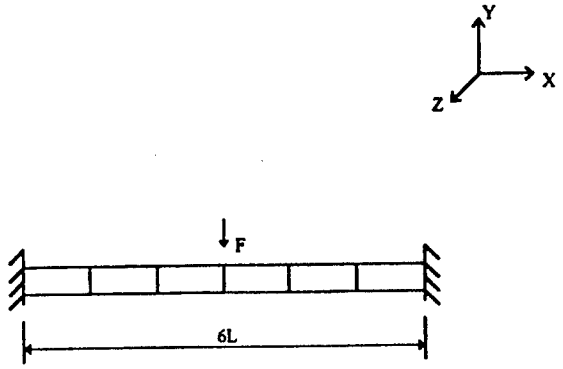

Figure 1. Discretized clamped-clamped beam structure.

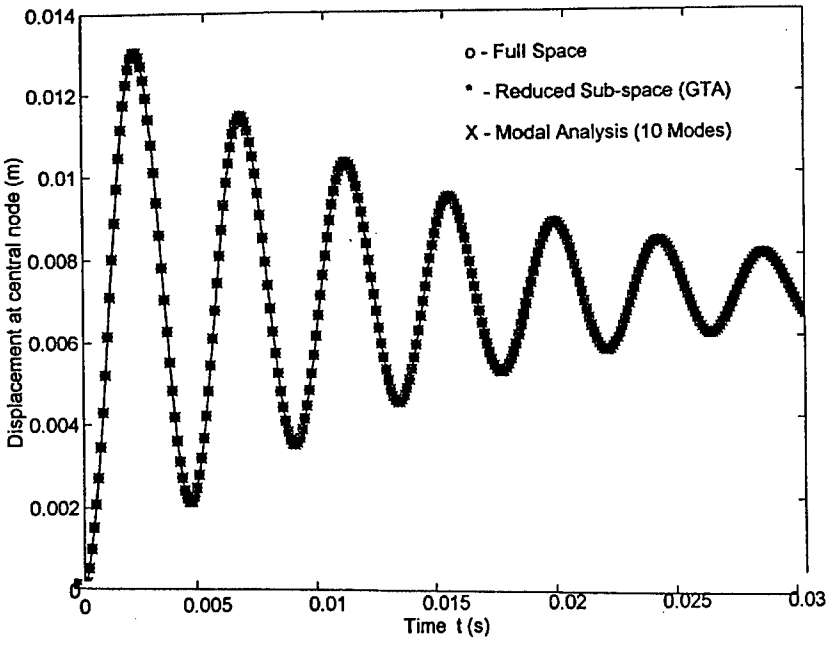

Figure 2. Comparison of time history.

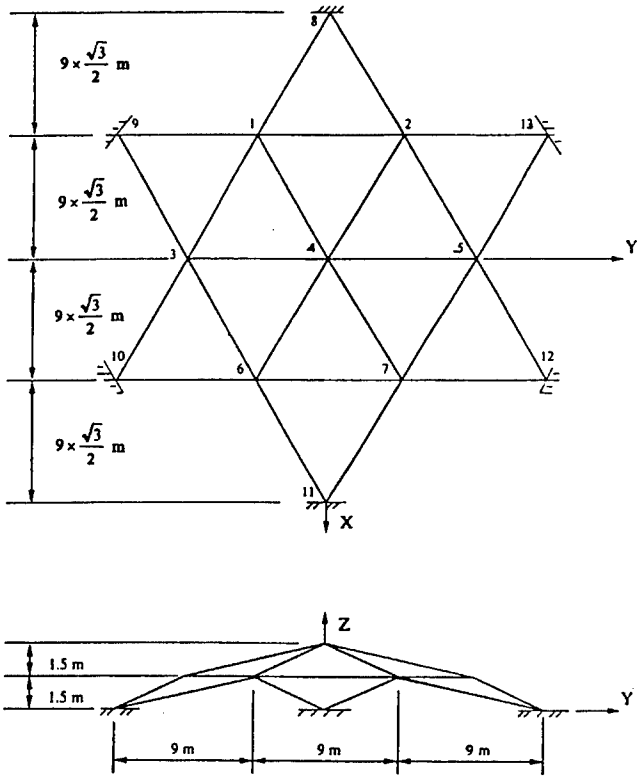

Figure 3. Twenty-four bar space dome.

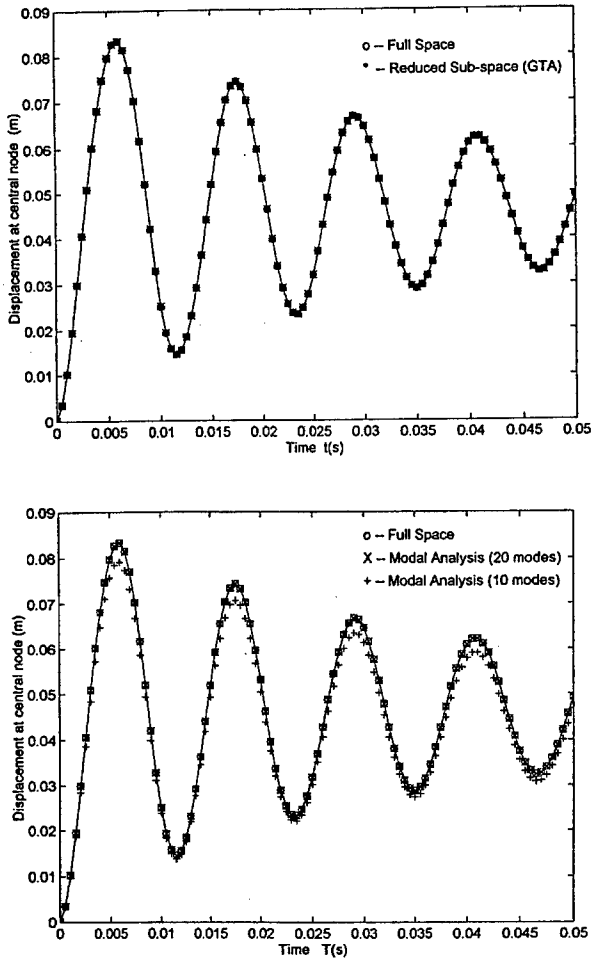

Figure 4. Response of space truss under a step load.

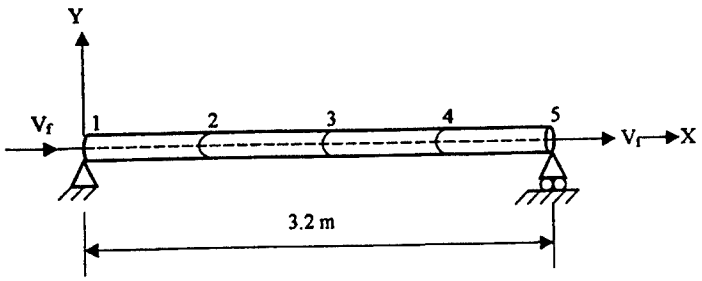

Figure 5. A fluid conveying pipe with pinned ends.

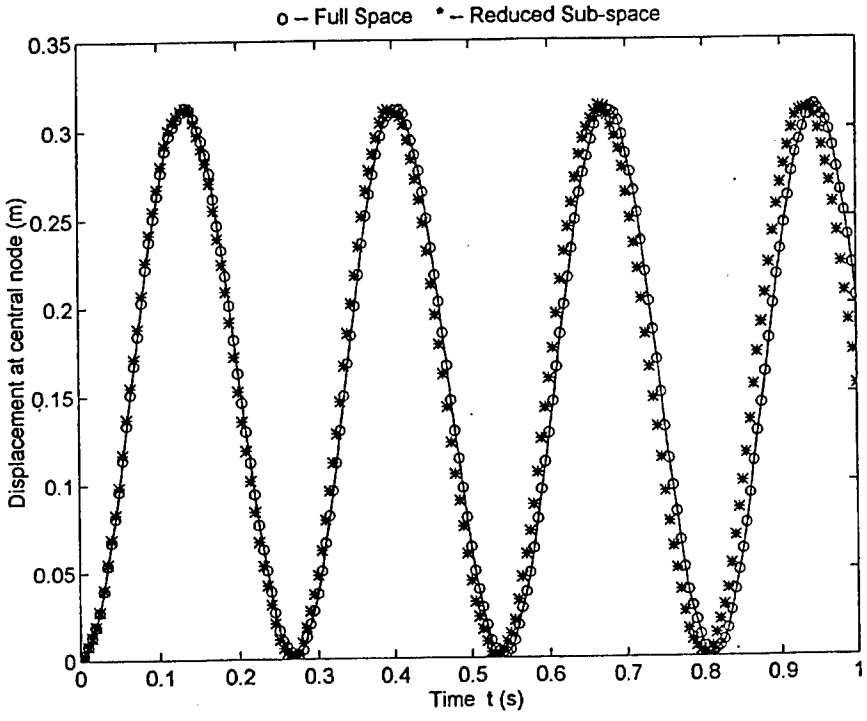

Figure 6(a). Transversal response of pipe at central node. (V_f = 20 m/s)

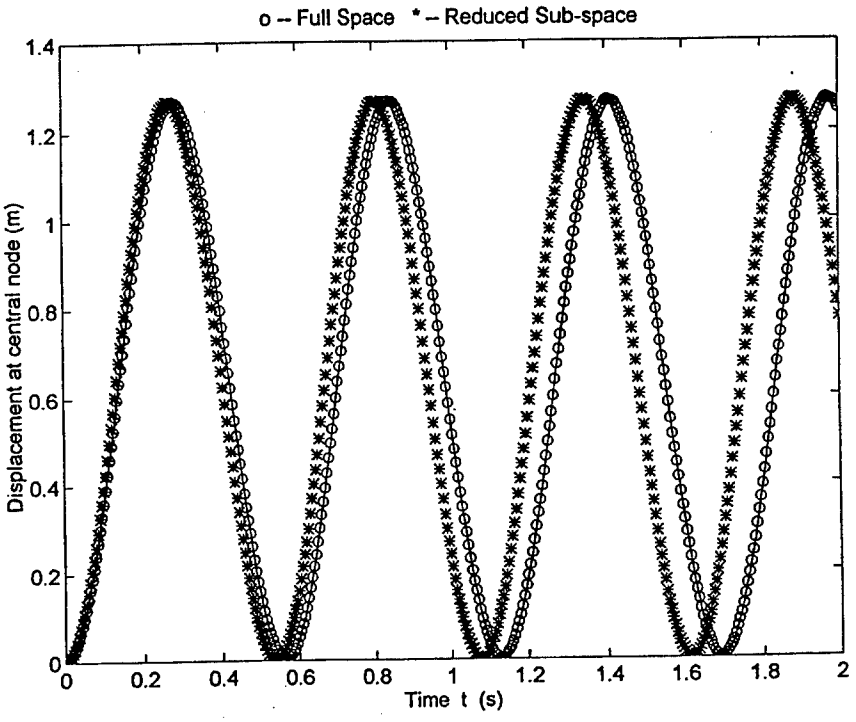

Figure 6(b). Transversal response of pipe at central node. (V_f = 35 m/s)

An Analytical Method of Extension-Twisting Coupling Vibration of Piezoelectric Composite Laminates

Mei-Ling Zhu*[1,2] Shi-Wei Ricky Lee[1] Tong-Yi Zhang[1] Pin Tong[1]

[1]Department of Mechanical Engineering
The Hong Kong University of Science and Technology
Clear Water Bay, Kowloon, Hong Kong

[2] Institute of Vibration Engineering Research
Nanjing University of Aeronautics & Astronautics
Nanjing, 210016, China

ABATRACT

This paper presents a dynamic analytical model of torsional vibration induced by extension-twisting coupling of anisotropic composite laminates with piezoelectric actuators by use of a non-conventional method (a reduced bending stiffness matrix). The aims of the method are not to require to find in-plane displacements in deriving equations of motion, and only to require to find an out-of-plane displacement of the laminate. Thus, the method changes a three-dimension problem into an one-dimension problem and none of structure complexities is lost. Finally, the model allows the analysis of anisotropic plate to be directly utilized. In addition, the Hamilton principle and the classical plate theory are used for the derivation of the model. The analytical solution of the model in the case of harmonic excitation is given. Some comparisons are presented with a finite element analysis (FEA) model. The analytical model is verified by FEA.

INTRODUCTION

Due to the demand for advanced performance in modern engineering systems, smart materials and structures have been one of the hottest research and development areas for a decade. One of the major characteristics of smart materials and structures is of their adaptability. In order to achieve this feature, the smart materials and structures must possess simultaneous sensing and actuation capabilities. Therefore, the integration of sensing/actuation and load-bearing capacity is a main subject for the research on smart materials and structures. Piezoelectric materials have relatively good performances in both of these functions. Their fast response, high energy density and the fact that these

materials generate no magnetic field make them widely utilized in actuation devices and vibration control. Sunar and Rao [1] provided a detailed a detailed review on the recent advances in sensing and control of flexible structures via piezoelectric materials technology.

Surface-bonded piezoelectric sensors and actuators and embedded piezoelectric sensors and actuators in composite laminates are commonly used smart structures. A considerable number of laminate theories, analytical approaches, numerical solutions and computational models have been reported for the analysis of laminates and structures with piezoelectric actuators or sensors for recent decades. In addition, the finite element method (FEM) is established as a powerful numerical technique which provides solutions to engineering problems and is widely used in modern engineering designs and analyses. Saravanos and Heyliger [2] and Tani et. al. [3] provided a detailed reviews of published work in the areas. Their reviews are pretty detailed and complete. In this paper, we are not ready again to review them and we are mainly concerned with the modeling of coupling vibration of laminated composite structures with piezoelectric actuators.

Mathematical models of coupling vibration of laminated composite structures with piezoelectric actuators are available in the literature. For example, Aldraihem and Wetherhold [4] proposed a shear-deformation beam theory to model the bending and twisting coupling vibration in laminated beams with a PZT/Epoxy actuator. Mass coupling and stiffness coupling are considered in their model. Shen [5] studied a mathematical model of intelligent constrained-layer (ICL) composite beams by integrating existing ICL plate models. The proposed ICL composite beam model is capable of explaining the coupling between bending, axial, and torsional vibrations of the beams. Park et al. [6] presented a static elastic model for isotropic beams of bending and torsion with induced-strain actuators. Lee and Chan [7] studied the actuation mechanism of a torsional motion induced by extension-twisting coupling for laminated composite beams with embedded piezoelectric materials. Following this, Lee and Sun [8] presented a static analysis of bending, twisting, and shearing of a beam with piezoelectric film. A one-dimensional beam theory was developed to model the piezoelectric composite beam. More recently, Lee and Li [9], employing the actuation mechanism investigated in [7], designed a rotary motor driven by an anisotropic composite lamina with piezo-ceramics as the actuator, studied the vibration control and computational modeling by use of FEA method. The structure of the driving element was a three-layer laminated plate. Due to the material anisotropy and anti-symmetric configuration, torsional vibration can be induced from in-plane strain actuation in the structure, and a rotary motor can be implemented. However, from the perspective of dynamic modeling for torsional vibration of the laminated plates, the above studies were limited to either a static analysis or finite element analyses. Therefore, an investigation by an analytical modeling for torsional vibration induced by extension-twisting coupling is in demand.

This paper will present a dynamic analytical model of torsional vibration induced by extension-twisting coupling of anisotropic composite laminates with piezoelectric actuators by use of a non-conventional method.

ANALYTICAL MODEL

In this section, consider a thin laminate as shown in Figure 1 composed of a PZT layer and two-layers of composite laminae with arbitrary in-plane orientation. The laminae are made of graphite/epoxy composite laminae that are anisotropy and anti-symmetric configuration with the center layer, while the center layer is a piezoelectric material, serving as an actuator. The composite laminate has a length of a (along the x-axis) and a width of b (along the y-axis). The thickness and density of the graphite/epoxy layer is h_c and ρ_c. The piezoelectric layer is polarized in the thickness direction and has a thickness of h_p and a density of ρ_p. Due to the material anisotropy and the anti-symmetric configuration, torsional vibration can be induced through the in-plane strain actuated by the piezoelectric layer.

Due to the material anisotropy and structural extension-twisting coupling, it may be rather difficult to achieve close–form analytical solutions of extension-twisting coupling for the aforementioned composite laminate. In the present study, we adopt a non-conventional method to present an analytic model of the laminate.

Generally speaking, a conventional method to derive vibration equation requires assumed harmonic solutions of the mid-plane displacements. The assumed harmonic solutions take the form

$$\begin{aligned} u_0(x,y,t) &= e^{i\omega t}U(x,y) \\ v_0(x,y,t) &= e^{i\omega t}V(x,y) \\ w_0(x,y,t) &= e^{i\omega t}W(x,y) \end{aligned} \tag{1}$$

where

$$\begin{aligned} U(x,y) &= \sum_{m=1}^{M1}\sum_{n=1}^{N1} E_{mn}U_{mn}(x,y) \\ V(x,y) &= \sum_{m=1}^{M2}\sum_{n=1}^{N2} F_{mn}V_{mn}(x,y) \\ W(x,y) &= \sum_{m=1}^{M3}\sum_{n=1}^{N3} H_{mn}W_{mn}(x,y) \end{aligned} \tag{2}$$

in which E_{mn}, F_{mn} and H_{mn} are undetermined coefficients, and the functions $U_{mn}(x,y)$, $V_{mn}(x,y)$ and $W_{mn}(x,y)$ are known shape functions that satisfy boundary conditions. The key to the method is to find the functions of $U_{mn}(x,y)$, $V_{mn}(x,y)$ and $W_{mn}(x,y)$ that satisfy the boundary conditions. However, in the cantilever plate we are studying, extension-twisting coupling may cause considerable difficulty in making assumptions about the in-plane solutions to boundary value problems.

Now we consider a non-conventional method. This method neglects the in-plane inertia and uses the reduced bending stiffness matrix. This matrix was mentioned in [10] and was first discussed by Reissner and Stavsky in [11]. Here our aims of the method are not to require to find in-plane displacements in deriving equations of motion, and only to required to find an out-of-plane displacement of the laminate.

Theoretical Foundation

For an isothermal process, the generalized Hamilton principle to include electroelasticity is written as by the Parton and Kudryavtsev [12]

$$\int_{t_0}^{t_1}\int_V(\delta H-\delta K)dvdt=\int_{t_0}^{t_1}[\int_V \boldsymbol{G}\delta\boldsymbol{u}dv+\int_S(\boldsymbol{f}\delta\boldsymbol{u}+q_i\delta\phi)ds]dt \tag{3}$$

where t_0 and t_1 are the two arbitrary instants, δ *is* the variation operator, H is the electric enthalpy, K is the kinetic energy, $\boldsymbol{G}$ is the body force, $\boldsymbol{f}$ is the traction along the boundary surface, q_i is the electric charge per unit area on the boundary surface, $\boldsymbol{u}$ is the displacement vector, ϕ is the electric potential, V is the entire domain of the volume, S is the boundary of the domain.

The electric enthalpy H is defined by the equation as

$$H(\{S\},\{E\})=\frac{1}{2}[\{\sigma\}^{\mathrm{T}}\{S\}-\{D\}^{\mathrm{T}}\{E\}] \tag{4}$$

where H is the function of the strain and the electric field, $\{\sigma\}$ is the stress vector, $\{S\}$ is the mechanical strain vector, $\{D\}$is the electric displacement vector, $\{E\}$ is the electric field vector.

The kinetic energy is defined as

$$K=\frac{1}{2}\{\dot{\boldsymbol{u}}\}^{\mathrm{T}}\rho\{\dot{\boldsymbol{u}}\} \tag{5}$$

where $\{\dot{\boldsymbol{u}}\}$ is the velocity vector of the laminate, and $\{\boldsymbol{u}\}=\{u\ v\ w\}^{\mathrm{T}}$ is the displacement vector, and ρ is the density of the lamina.

Constitutive Equation

The constitutive equations in the principal material coordinates for piezoelectric material under plane stress are

$$\begin{aligned}\{\sigma\}&=[\overline{Q}_p]\{S\}-[e]^{\mathrm{T}}E_3\\ D_3&=[e]\{S\}+\varepsilon_pE_3\end{aligned} \tag{6}$$

where $\{\sigma\}=\{\sigma_x\ \sigma_y\ \sigma_{xy}\}^{\mathrm{T}}$, $[\overline{Q}_p]$ is the elastic constant matrix of the piezoelectric material, $\{S\}=\{\varepsilon_x\ \varepsilon_y\ \varepsilon_{xy}\}^{\mathrm{T}}$, $[e]$ is the piezoelectric constant matrix, ε_p is the dielectric constant. Since the structure under consideration is a thin laminated plate, the polarization of the piezoelectric material is in the z direction, and an external voltage is only applied in the polarized direction. Therefore, the electric field $\{E\}$ and the electric displacement $\{D\}$ in Equation (4) are assumed to be non-zero in the z-direction only. As a results, $\{E\}=E_3$, $\{D\}=D_3$, the piezoelectric constant matrix is $[e]=[e_{31}\ e_{31}\ 0]$.

The relationship between the electric field E_3 and the electric potential ϕ is

$$E_3 = -\frac{\partial \phi}{\partial z}. \tag{7}$$

The relationship between the applied voltage $V_3(t)$ and the electric potential ϕ on the electrodes is defined as $\phi = V_3(t)$.

The constitutive equations for the graphite/epoxy composite material are

$$[\sigma] = [\bar{Q}_c][S] \tag{8}$$

where $[\bar{Q}_c]$ is the transformed reduced stiffness matrix of the graphite/epoxy lamina. In term of the reduced stiffness matrix $[Q]$ and the layer angle α between the positive direction, x, of the laminate and the fiber direction of the lamina, the transformed reduced stiffness matrix can be expressed as

$$[\bar{Q}_c] = [P_t][Q][P_t]^T \tag{9}$$

where

$$[Q] = \begin{bmatrix} Q_{11} & Q_{12} & Q_{16} \\ Q_{12} & Q_{22} & Q_{26} \\ Q_{16} & Q_{26} & Q_{66} \end{bmatrix} \tag{10}$$

$$[P_t] = \begin{bmatrix} \cos^2\alpha & \sin^2\alpha & 2\cos\alpha\sin\alpha \\ \sin^2\alpha & \cos^2\alpha & -2\cos\alpha\sin\alpha \\ -\cos\alpha\sin\alpha & \cos\alpha\sin\alpha & \cos^2\alpha - \sin^2\alpha \end{bmatrix} \tag{11}$$

in which

$$Q_{ij} = c_{ij} - \frac{c_{i3}c_{j3}}{c_{33}} \qquad i = 1, 2, 6;\ j = 1, 2, 6; \tag{12}$$

where c_{ij} is the elastic constant of material.

In particular, the constitutive equations for a piezoelectric anisotropic composite laminate with anti-symmetric configuration are

$$\begin{Bmatrix} N_x \\ N_y \\ N_{xy} \\ M_x \\ M_y \\ M_{xy} \end{Bmatrix} = \left[\begin{array}{ccc:ccc} A_{11} & A_{12} & 0 & 0 & 0 & B_{16} \\ A_{12} & A_{22} & 0 & 0 & 0 & B_{26} \\ 0 & 0 & A_{66} & B_{16} & B_{26} & 0 \\ \hdashline 0 & 0 & B_{16} & D_{11} & D_{12} & 0 \\ 0 & 0 & B_{26} & D_{12} & D_{22} & 0 \\ B_{16} & B_{26} & 0 & 0 & 0 & D_{66} \end{array}\right] \begin{Bmatrix} \varepsilon_x^0 \\ \varepsilon_y^0 \\ \varepsilon_{xy}^0 \\ \kappa_x^0 \\ \kappa_y^0 \\ \kappa_{xy}^0 \end{Bmatrix} - \left[\begin{array}{c} N_x^P \\ N_y^P \\ N_{xy}^P \\ \hdashline M_x^P \\ M_y^P \\ M_{xy}^P \end{array}\right] \tag{13}$$

Equation (13) shows that, when the composite laminate was the aforementioned configuration, the coupling between the bending and twisting does not exist in the laminate because the D_{16} and D_{26} are zero. However, the extension-twisting coupling does exist, because the B_{16} and B_{26} are non-zero. For simplicity of analysis, Equation (13) is written in the matrix form as

$$\begin{bmatrix} N \\ M \end{bmatrix} = \begin{bmatrix} A & B \\ B & D \end{bmatrix} \begin{bmatrix} \varepsilon^0 \\ \kappa^0 \end{bmatrix} - \begin{bmatrix} N^p \\ M^p \end{bmatrix} \tag{14}$$

where

$$N = \{N_x, N_y, N_{xy}\}^{\mathrm{T}} = \int_{-h/2}^{h/2} (\sigma_x^{(k)}, \sigma_y^{(k)}, \sigma_{xy}^{(k)})^{\mathrm{T}} dz \tag{15}$$

$$N^p = \{N_x^p, N_y^p, N_{xy}^p\}^{\mathrm{T}} = \int_{h_p/2}^{h_p/2} [e]^{\mathrm{T}} E_3 dz \tag{16}$$

$$M = \{M_x, M_y, M_{xy}\}^{\mathrm{T}} = \int_{-h/2}^{h/2} (\sigma_x^{(k)}, \sigma_y^{(k)}, \sigma_{xy}^{(k)})^{\mathrm{T}} z dz \tag{17}$$

$$M^p = \{M_x^p, M_y^p, M_{xy}^p\}^{\mathrm{T}} = \int_{h_p/2}^{h_p/2} [e]^{\mathrm{T}} E_3 z dz \tag{18}$$

$$\varepsilon^0 = \{\varepsilon_x^0, \varepsilon_x^0, \varepsilon_{xy}^0\}^{\mathrm{T}} = \left\{ \frac{\partial u_0(x,y,t)}{\partial x}, \frac{\partial v_0(x,y,t)}{\partial y}, \frac{\partial u_0(x,y,t)}{\partial y} + \frac{\partial v_0(x,y,t)}{\partial x} \right\}^{\mathrm{T}} \tag{19}$$

$$\kappa = \{\kappa_x^0, \kappa_y^0, \kappa_{xy}^0\}^{\mathrm{T}} = \left\{ -\frac{\partial^2 w_0(x,y,t)}{\partial x^2}, -\frac{\partial^2 w_0(x,y,t)}{\partial y^2}, -2\frac{\partial^2 w_0(x,y,t)}{\partial x \partial y} \right\}^{\mathrm{T}} \tag{20}$$

$$(A_{ij}, B_{ij}, D_{ij}) = \int_{-h/2}^{h/2} Q_{ij}(1, z, z^2) dz \tag{21}$$

in which the superscript (k) denotes the *kth* layer, $u_0(x,y,t)$, $v_0(x,y,t)$ and $w_0(x,y,t)$ are mid-plane displacements, and

$$\begin{aligned} \varepsilon_x &= \varepsilon_x^0 + z\kappa_x^0 \\ \varepsilon_y &= \varepsilon_y^0 + z\kappa_y^0 \\ \varepsilon_{xy} &= \varepsilon_{xy}^0 + z\kappa_{xy}^0 \end{aligned} \tag{22}$$

Integration of Electric Enthalpy

Substituting Equations (6) and (8) into Equation (4), and letting $\{\sigma_m\}=[\overline{Q}_p]\{S\}$ or $\{\sigma_m\}=[\overline{Q}_c]\{S\}$, the electric enthalpy for the laminate becomes

$$H = \begin{cases} \frac{1}{2}(\{\sigma_m\}^{\mathrm{T}}\{S\} - 2E_3[e]\{S\} - \varepsilon_3 E_3^2), & \text{for the PZT layer,} \\ \frac{1}{2}\{\sigma_m\}^{\mathrm{T}}\{S\}, & \text{for the graphite/epoxy layer.} \end{cases} \tag{23}$$

where, for the PZT layer, the first term on the right-hand side is the elastic strain energy of the laminate, the second term is the electromechanical coupling energy and the third term is the electric energy.

Integrating with the respect of z in Equation (23) results in

$$\int_V H dv = \frac{1}{2}\{\int_S [(N+N^p)^{\mathrm{T}}\varepsilon^0 + (M+M^p)^{\mathrm{T}}\kappa^0] ds + 2\int_S V_3[e]\varepsilon^0 ds - \int_S \varepsilon_p \frac{V_3^2}{h_p} ds\} \tag{24}$$

where $S = ab$ is the area of laminate. Substituting the constitutive Equation (14) into (24) results in

$$\int_V H dv = \frac{1}{2}\{\int_S (\varepsilon^{0\mathrm{T}} A\varepsilon^0 + 2\kappa^{0\mathrm{T}} B\varepsilon^0 + \kappa^{0\mathrm{T}} D\kappa^0) ds + 2\int_S V_3[e]\varepsilon^0 ds - \int_S \varepsilon_p \frac{V_3^2}{h_p} ds\} \tag{25}$$

It is obvious to know that Equation (25) is not only the function of the out-of-plane displacement, $w_0(x,y,t)$, and the appled voltage, V_3, but also the function of the in-plane displacements $u_0(x,y,t)$ and $v_0(x,y,t)$. Thus, as explained earlier, it is not feasible to solve such a problem with close-form analytical solutions, because, in the cantilever plate we are studying, extension-twisting coupling may cause considerable difficulty in making assumptions about the in-plane solutions to boundary value problems. In order to solve problem, we use a method mentioned in the book (Whitney, 1987) and proposed by Reissner and Stavky [1961] to rewrite Equation (14) in the following way:

By expanding Equation (14),

$$\begin{aligned} N + N^p &= A\varepsilon^0 + B\kappa^0 \\ M + M^p &= B\varepsilon^0 + D\kappa^0 \end{aligned} \tag{26}$$

Multiplying the first equation in Equation (26) by A^{-1} yields

$$\varepsilon^0 = A^{-1}(N + N^p) - A^{-1}B\kappa^0 \tag{27}$$

Substituting Equation (27) into the second term of Equation (26) results in

$$M + M^p = BA^{-1}(N + N^p) + (D - BA^{-1}B)\kappa^0 \tag{28}$$

Letting $A^* = A^{-1}$, $B^* = -A^{-1}B$ and $D^* = D - BA^{-1}B$, where, in the general case, A^* and D^* are symmetric while B^* is not, Equation (14) can be written in the semi-inverted form as

$$\begin{bmatrix} \varepsilon^0 \\ M + M^p \end{bmatrix} = \begin{bmatrix} A^* & B^* \\ (-B^*)^{\mathrm{T}} & D^* \end{bmatrix} \begin{bmatrix} N + N^p \\ \kappa^0 \end{bmatrix} \tag{29}$$

Since $D^*=D-BA^{-1}B$, D^* represents a reduction in the bending stiffness of the laminate and D^* is refer to as a reduced bending stiffness matrix. Note that none of the structure complexity is lost in reduced bending stiffness matrix since all elements of the original stiffness matrices contribute.

Now we will use the reduced bending stiffness matrix to derive the integration of electric enthalpy of the laminate. Substituting Equation (29) into (24), Equation (24) becomes

$$\begin{aligned} \int_V H dv = \frac{1}{2}\{&\int_S (N + N^p)^{\mathrm{T}} A^* (N + N^p) + \kappa^{0\mathrm{T}} D^* \kappa^0) ds \\ &+ 2\int_S V_3[e][A^*(N + N^p) + B^*\kappa^0] ds - \int_S \varepsilon_p \frac{V_3^2}{h_p} ds\} \end{aligned} \tag{30}$$

It can be known that Equation (30) only contains the out-of-plane displacement of the laminate, $w_0(x,y,t)$, and the applied voltage, $V_3(t)$, because the term $(N + N^p)$ is only a function of applied voltage. The reason is following:

According to the plate theory, if the in-plane inertia can be neglected, the

equations of motion of the in-plane are

$$\begin{cases} \dfrac{\partial N_x}{\partial x}+\dfrac{\partial N_{xy}}{\partial y}=0 \\ \dfrac{\partial N_y}{\partial y}+\dfrac{\partial N_{xy}}{\partial x}=0. \end{cases} \tag{31}$$

Expanding N_{xy} in Equation (13) results in

$$N_{xy} = A_{66}\varepsilon_{xy}^0 + B_{16}\kappa_x^0 + B_{26}\kappa_y^0 - N_{xy}^0 . \tag{32}$$

Although there exist shearing strains in the graphite/epoxy composite laminae, $\varepsilon_{xy}^0 = 0$, because the PZT is isotropic in the in-plane and there is no shearing load in the mid-plane of the PZT. Because the laminate only twists, there is no bending and κ_x^0=0 and κ_y^0=0. As a result, based on Equation (32), we know that $N_{xy} = 0$. Furthermore, based on $N_{xy} = 0$ and Equations (31), it is derived that N_x and N_y are respectively constants. Furthermore, due to no external forces and moments acted on the laminate, taking a free body of the laminate results in

$$N_x = 0,\ N_y = 0. \tag{33}$$

The piezoelectric loading N^p based on Equation (16) is

$$N^p = -V_3[e]^{\mathrm{T}} \tag{34}$$

Finally, substituting Equations (33) and (34) into (30), the integration of electric enthalpy is

$$\int_V Hdv = \frac{1}{2}\int_S (\kappa^{0\mathrm{T}} D^* \kappa^0 - V_3^2[e]A^*[e]^{\mathrm{T}} + 2V_3[e]B^*\kappa^0 - \varepsilon_p \frac{V_3^2}{h_p})ds \tag{35}$$

It is obvious that the integration of the electric enthalpy is only the function of the out-of-plane displacement of the laminate, $w_0(x,y,t)$, and the applied voltage, $V_3(t)$, and not again the function of the in-plane displacements of the laminate, $u_0(x,y,t)$ and $v_0(x,y,t)$.

Equations of Motion

In order to obtain the equations of the motion of the laminate, it is usually advantage to write the out-of-plane displacement on the mid-plane into the following function.

$$w_0(x,y,t) = \sum_i \Phi_w^i(x,y)p_w^i(t) \tag{36}$$

where $w_0(x,y,t)$ is the out-of-plane displacement on the mid-plane of the laminate, $\Phi_w(x, y)$ is the vibrational shape function that satisfies the boundary condition of the laminate, $p_w(t)$ is the generalized out-of-plane displacement variable that is a function of time, the superscript i denotes the *ith* order vibration mode (omitting the letter i in Φ^i_w and p^i_w in the following).

For the laminate, the mass force $\boldsymbol{G}$ and the traction $\boldsymbol{f}$ in Equation (3) are zero. If the in-plane inertial terms can be neglected, substituting Equations (5) and (35) into Equation (3), considering Equation (36) and carrying out the

variation of the generalized out-of plane displacement $p_w(t)$ and the applied voltage $V_3(t)$ results in the equations of the motion of the laminate. For the *ith* order vibration mode, the governing equations of motion of the laminate are

$$M_i\ddot{p}_w(t)+C_i\dot{p}_w(t)+K_ip_w(t)=\Theta_{ei}V_3(t) \tag{37}$$

$$C_eV_3(t)+\Theta_{ei}p_w(t)+Q_e=0 \tag{38}$$

where

$$\begin{cases} M_i=\int_S \rho\Phi_w^2 ds \\ C_i=2M_i\omega_n\xi_i \\ K_i=\int_S[D_{11}^*(\frac{\partial^2\Phi_w}{\partial x^2})^2+2D_{12}^*\frac{\partial^2\Phi_w}{\partial x^2}\frac{\partial^2\Phi_w}{\partial y^2}+D_{22}^*(\frac{\partial^2\Phi_w}{\partial y^2})^2+4D_{66}^*(\frac{\partial^2\Phi_w}{\partial x\partial y})^2]ds \\ \Theta_{ei}=\int_S 2e_{31}(B_{16}^*+B_{26}^*)\frac{\partial^2\Phi_w}{\partial x\partial y}ds \\ Q_e=\int_S q_3 ds \\ C_e=\int_S[e_{31}^2(A_{11}^*+2A_{12}^*+A_{22}^*)+\frac{\varepsilon_p}{h_p}]ds \end{cases} \tag{39}$$

in which

$$\rho=\int_{-h/2}^{h/2}\rho_0^{(k)}dz \tag{40}$$

$$\omega_n=\sqrt{K_i/M_i} \tag{41}$$

where M_i, K_i and C_i represent the mode mass, the mode stiffness and the coefficient of mode damping of the laminate, respectively. Note M_i, K_i and C_i are relative to boundary conditions. ξ_i is the damping factor. Also note that the damping term is artificially added. ω_n is the natural frequency of the laminate. The term Θ_{ei} represents the electromechanical coupling and describe the conversion of the applied voltage to an equivalent force on the laminate. Q_e denotes the electric charge produced on the piezoelectric layer. q_3 denotes the electric charge per unit area produced on the electrode. C_e denotes the electric capacity of piezoelectric layer.

Solution of Equation

We solve Equation (37) when the applied voltage is expressed in the form as

$$V_3(t)=V_{3m}\sin\omega t \tag{42}$$

where V_{3m} and ω is the amplitude and the frequency of the applied voltage, respectively.

Let $$r = \frac{\omega}{\omega_n}, \tag{43}$$

$$P_w = \frac{V_{3m}\Theta_i}{K_i} \tag{44}$$

where r is the ratio of the frequency of the applied voltage to the natural frequency of the laminate, and P_w is the static generalized out-of-plane displacement of the laminate. The steady-state solution $p_w(t)$ of Equation (37) are

$$p_w(t) = P_w \beta \sin(\omega t - \varphi) \tag{45}$$

where β is the magnification factor defined in the case of damped systems as

$$\beta = \frac{1}{\sqrt{(1-r^2)^2 + (2r\xi_i)^2}} \tag{46}$$

whose physical meanings is the ratio of the amplitude of dynamic displacement to static displacement. φ is the phase angle defined by

$$\varphi = \tan^{-1}\left(\frac{2r\xi_i}{1-r^2}\right) \tag{47}$$

As a result, the out-of-plane displacement of the laminate in the steady-state is

$$w(x,y,t) = \Phi_w(x,y) P_w \beta \sin(\omega t - \varphi) \tag{48}$$

.

RESULTS AND DISCUSSIONS

In the present study, a three-layer sandwiched plate as shown in Figure 1 is used for demonstration. The top and bottom layers are the graphite/epoxy composite with orientation +/- 45°. The center layer is PZT. The material properties of the lamina shown in Figure 1 are listed in Table 1.

In order to use the proposed analytical model to obtain numerical results of the laminate, first we introduce a shape function, $\Phi_w(x, y)$, which leads to an approximate solution for the excited eigenmode vibration. For the torsional vibration, we can find the following shape function in the separable form:

$$\Phi_w(x,y) = X_0(x) Y_0(y) \tag{49}$$

where

$$X_0(x) = \sin \eta x - \sinh \eta x + D(\cos \eta x - \cosh \eta x),$$

$$D = \frac{\cos \eta a + \cosh \eta a}{\sin \eta a - \sinh \eta a}, \tag{50}$$

$$\eta a = 1.875,\ Y_0(y) = y.$$

The function has satisfied the boundary conditions of the fixed side, x=0, and the free sides, x=a. For the fixed edge at x=0, $w(0,y) = 0$, $\frac{\partial w(0,y)}{\partial x} = 0$ in terms of the geometric boundary conditions; for the free edge at x = a, $w''(a,y) = 0, w'''(a,y) = 0$ in terms of no external force and moment.

A commercial code MATLAB is used to compile the analytical programs for simulation. The torsional vibration of the plate was simulated and the displacement of one of the two corners at the free end was used to represent the responses. Therefore, the twisting angle of the laminates can be calculated by dividing this displacement by the half width of the laminate. Further, in order to confirm the proposed analytical model, comparisons between the numerical results obtained from the proposed model and FEA were made. The FEA result uses the ANSYS software and uses 8-node brick element.

The numerical results of the natural frequency of the laminate between the proposed model and the FEM for the torsional vibration as shown in Figure 2, are 1622 Hz and 1616 Hz, respectively. From the result, we know that the two results obtained by the developed model and FEA agree well. Figure 3 shows the amplitudes of twisting angle of the laminate excited at different applied voltages with two different damping factors, 5% and 10%. According to the vibration theory, it is known that for $\omega = \omega_n$, the magnification factor β is equal to $1/2\xi_i$ for a damped system. From this view, if ξ_i is equal to 5%, the amplitude of the dynamic twisting angle is 10 times that of the static twisting angle in the same input voltage condition; if ξ_i is equal to 10%, the dynamic twisting angle is 5 times that of the static twisting angle. It is observed that the analytic results and the FEA static results also agree very well in this respect, where the FEA static response data come from (Lee and Chan, [7]). Moreover, it is also obviously observed that the amplitude of twisting angle is highly affected by the damping. Therefore, in order to obtain large amplitude of twisting angle, we require a small damping factor for the laminate.

It has been known that torsional vibration is produced by extension-twisting coupling. In the case that the orientation is equal to [0°/PZT/0°] or [90°/PZT/-90°], because B^*_{16} and B^*_{26} are equal to zero, there is no extension-twisting coupling. While the orientation is equal to [45°/0°/-45°], the values of B^*_{16} and B^*_{26} are maximized. As a result, this orientation [45°/0°/-45°] leads to the maximum amplitude of twisting angle of the laminates. Figure 4 shows the relationship between the amplitudes of twisting angle and the fiber orientation of laminae. The results shown in Figure 4 support the actuation principle of torsional vibration of extension-twisting coupling and also support the design of orientation [45°/PZT/-45°] for a rotary motor driven by anisotropic piezoelectric composite laminated plate (Lee and Li, [9]).

CONCLUSIONS

This paper presents a dynamic analytical model of torsional vibration induced by extension-twisting coupling of anisotropic composite laminates with piezoelectric actuators by use of a non-conventional method (a reduced bending stiffness matrix). By use of the matrix, the integration of electric enthalpy has expressed as only the function of the out-of-plane displacement of the laminate, $w_0(x,y,t)$, and the applied voltage, $V_3(t)$, and not again the function of the in-

plane displacements of the laminate, $u_0(x,y,t)$ and $v_0(x,y,t)$. Thus, the method changes a three dimension problem into a one dimension problem and none of the structure complexity is lost, because all element of the original stiffness matrices contribute. Finally, the model allows the analysis of anisotropic plate to be directly utilized. In addition, the Hamilton principle and the classical plate theory are used for the derivation of the model. The analytical solution of the model in the case of harmonic excitation has been given. Some comparisons are presented with a more accurate FEA model. The analytical model is verified by finite element analysis. The analytical model has the ability to predict the dynamic characteristics and to explain the actuation mechanism of twisting motion of piezoelectric composite laminates.

ACKNOWLEDGEMENT

The Research Grant Council of Hong Kong sponsored this study through the grant HKUST6050/97E to the Hong Kong University of Science and Technology (HKUST). The authors wish to acknowledge the support. The first author also wishes to acknowledge the support of the Alexander von Humboldt Foundation during the writing process.

REFERENCES

1. Sunar, M. and Rao, S., Recent advances in sensing and control of flexible structures via piezoelectric materials technology. Applied Mechanics Reviews, 1999, 52:1-16.
2. Saravanos, D. A. and Heyliger, P. R., Mechanics and computational models for laminated piezoelectric beams, plates, and shells. Applied Mechanics Reviews, 1999, 52: 305-319.
3. Tani, J., Takagi, T. and Qiu, J., Intelligent material systems: Application of functional materials. Applied Mechanics Reviews, 1998, 51:505-521.
4. Aldraihem, O. J., and Wetherhold, R. C., Mechanics and control of coupled bending and twisting vibration of laminated beams. *Smart Mater. Struc.*, 1997, 6:123-133.
5. Shen, Y., Bending and torsional vibration control of composite beams through intelligent constrained-layer damping treatments. *Smart Mater. Struc.*, 1995, 4:340-355.
6. Park, C., Walz, C. and Chopra, I., Bending and torsion models of beams with induced-strain actuators. *Smart Mater. Struc.*, 1996, 5:98-113.
7. Lee, S.-W. R. and Chan, K.-H. W., Actuation of torsional motion for piezoelectric laminated beams. *Dynamic response and behavior of composites, ASME.* 1995, AD-46:139-146.
8. Lee, S.-W. R. and Sun, C. T., Bending/twisting/shearing actuation and sensing of laminated composite beams with piezopolymer film. Intelligent Materials and Systems, 1995, 137-148.

9. Lee, S.-W. R. and Li, H. L., Development and characterization of a rotary motor driven by anisotropic piezoelectric composite lamina. *Smart Mater. Struc.*, 1998, 7: 327-336.
10. Whitney, J. M., *Structural analysis of laminated anistropic plates.* Technomic publishing company, Inc., 1987.
11. Reissner, E. and Starsky, Y., Bending and stretching of certain types of heterogeneous aerolotropic elastic plates. Journal of Applied Mechanics, 1962, 28:402-408.
12. Parton, V. Z. and Kudryavtsev, B. A., *Electromagnetoelasticity.* Gordon and Breach science publishers, New York, 1998.

Table 1. Material properties of piezoelectric and composite materials.

Material Properties	Graphite/Epoxy	Piezoelectric Material (PZT-5H)
E_1(GPa)	138	61
E_2(GPa)	8.96	61
G_{12}(GPa)	7.1	23.3
ν_{12}	0.3	0.31
ρ(kg/m^3)	1560	7500
d_{31}(m/V)	0	-171×10^{-12}
ε_p(F/m)	0	1.65×10^{-8}
$a \times b \times h_c$ or $\times h_p$ (mm)	25 × 90× 1	25 × 90× 1

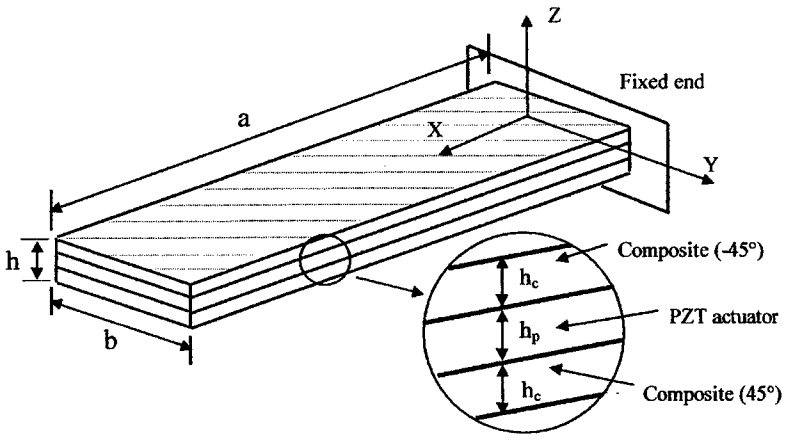

Figure 1. Configuration and dimensions of the plate under investigation

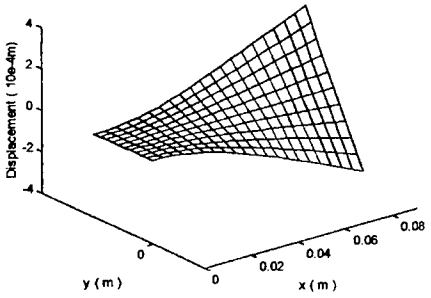

Figure2. Mode shape of the torsional vibration

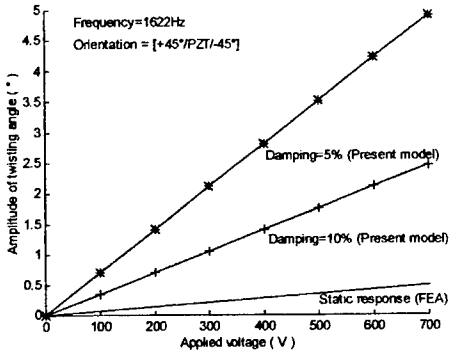

Figure 3. Amplitude of twisting angle of the laminate excited at different applied voltages with various damping factors

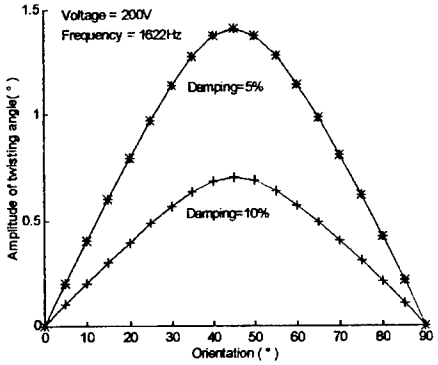

Figure 4. Relationship between amplitude of twisting angle and fiber orientation

BENCHMARK STUDY OF THREE APPROACHES TO ELASTIC WAVES IN STOCHASTIC MEDIA

A.K. Belyaev
Department of Mechanics and Control Processes, State Technical University of St. Petersburg, Polytekhnicheskaya 29, 195251, St. Petersburg, Russia.

Three approaches to the problem of 1-D wave propagation in media with random elastic and mass properties are studied: (i) method of integral spectral decomposition, (ii) Fokker-Planck-Kolmogorov equation and (iii) the Dyson integral equation. Merits and shortcomings of each approach are discussed.

1 Introduction

The approaches to stochastic wave propagation, see e.g. [1] are usually concerned with wave propagation in media with a single random function. Two random fields, namely random elastic modulus and random mass density exist in the problem of wave propagation in random elastic media.

The time-reduced one-dimensional wave equation written in terms of the displacement amplitude $\tilde{u}(x)$ is given by

$$\left(E\tilde{u}'\right)' + \rho\omega^2\tilde{u} = 0 \tag{1.1}$$

where E is Young's modulus, ρ is mass density, ω is frequency and primes denote differentiation with respect to x. Random elastic modulus and random mass density are assumed, i.e.

$$E(x) = \langle E\rangle\left[1 + \varepsilon(x)\right], \quad \rho(x) = \langle\rho\rangle\left(1 + r(x)\right) \tag{1.2}$$

where $\langle\ \rangle$ denotes the mathematic expectation of the random function and non-dimensional centred random functions ε and r describe the randomness of the mass density and the Young modulus, respectively. As the medium is assumed to be statistically homogeneous, $\langle\rho\rangle$ and $\langle E\rangle$ do not depend upon x. Two boundary conditions will be discussed: Dirichlet's boundary condition which implies a prescribed displacement H at $x=0$

$$\tilde{u}(0) = H \tag{1.3}$$

and Neumann's boundary condition with a prescribed axial stress Σ at $x=0$

$$E\tilde{u}'(0) = \Sigma \tag{1.4}$$

In what follows, both H and Σ are deterministic.

The intent of the paper is a benchmark study of the following approaches to wave propagation in random elastic media: the method of integral spectral decomposition, the Fokker-Plank-Kolmogorov equation and the Dyson integral equation. The merits and the deficiencies of each approach are discussed and they are briefly outlined in Conclusions.

2 Method of integral spectral decomposition

In the framework of this approach the medium parameters are represented in the form of the Fourier-Stiltjes integrals, e.g. [2] and [3],

$$E(x) = \langle E \rangle \left[1 + \int \Xi(k) \exp(ikx)\, dk \right], \quad \rho(x) = \langle \rho \rangle \left[1 + \int R(k) \exp(ikx)\, dk \right] \qquad (2.1)$$

where $\Xi(k)$ and $R(k)$ are the random Fourier spectra, $\langle R(k) \rangle = \langle \Xi(k) \rangle = 0$. Subsequently, $\tilde{u}$ can be represented by its spectral representation

$$\tilde{u}(x) = \langle \tilde{u}(x) \rangle + \int U(k)\, \mu(k, x) \exp(ikx)\, dk \qquad (2.2)$$

where the deterministic function $\mu(k, x)$ produces a frequency-amplitude modulation of the homogeneous stochastic process $U(k)$, $\langle U(k) \rangle = 0$. Substituting Eqs. (2.1) and (2.2) into Eq. (1.1) and taking the mean yields

$$\frac{d^2\langle \tilde{u} \rangle}{dx^2} + \lambda_0^2 \omega^2 \langle \tilde{u} \rangle + \int_{-\infty}^{\infty} S_{Eu}(k) \left[\frac{d^2\mu}{dx^2} + ik \frac{d\mu}{dx} \right] dk + \lambda_0^2 \int_{-\infty}^{\infty} S_{\rho u}(k)\, \mu\, dk = 0 \qquad (2.3)$$

where $\lambda_0 = \omega / \sqrt{\langle E \rangle / \langle \rho \rangle}$ is an "averaged" wave number. While deriving Eq. (2.3) we use the property of stochastic orthogonality of random spectra

$$\langle \Xi(k)\, U^*(k_1) \rangle = S_{Eu}(k)\, \delta(k - k_1)\,; \langle R(k)\, U^*(k_1) \rangle = S_{\rho u}(k)\, \delta(k - k_1)$$

where S_{Eu} and $S_{\rho u}$ denote the spectral densities of the random processes. Substituting Eqs. (2.1) and (2.2) into Eq. (1.1), multiplying the result with $R^*(k')$ and $\Xi^*(k')$, respectively, and taking ensemble averaging one obtains another two equations

$$\left[\frac{d^2\mu}{dx^2} + 2ik \frac{d\mu}{dx} + \mu \left(\lambda_0^2 - k^2 \right) \right] S_{Eu}(k) + \left[\frac{d^2\langle \tilde{u} \rangle}{dx^2} + ik \frac{d\langle \tilde{u} \rangle}{dx} \right] S_E(k) + \lambda_0^2 \langle \tilde{u} \rangle S_{E\rho}(k) = 0 \qquad (2.4)$$

$$\left[\frac{d^2\mu}{dx^2} + 2ik \frac{d\mu}{dx} + \mu \left(\lambda_0^2 - k^2 \right) \right] S_{\rho u}(k) + \left[\frac{d^2\langle \tilde{u} \rangle}{dx^2} + ik \frac{d\langle \tilde{u} \rangle}{dx} \right] S_{E\rho}(k) + \lambda_0^2 \langle \tilde{u} \rangle S_{\rho}(k) = 0 \qquad (2.5)$$

where the Wiener-Khinchin condition of statistical orthogonality of the spectra has been used. During the estimations, the third moments have been omitted, i.e. we introduce a closure approximation otherwise the moments are governed by an infinite hierarchy of the coupled ordinary differential equations. Therefore, the analysis is restricted to the mean field and the spectral density matrix, which is typical for the correlation theories, cf. [4].

Since Eqs. (2.3)-(2.5) are linear in $\langle \tilde{u} \rangle$ and μ, the solution is sought in the form

$$\langle \tilde{u} \rangle = B \exp(\lambda x), \quad \mu = M \exp(\lambda x) \qquad (2.6)$$

where λ is the eigenvalue. With this substitution Eqs. (2.4) and (2.5) may be solved, to give

$$M\, S_{Eu} = -B \frac{\lambda(\lambda + ik) S_E + \lambda_0^2 S_{E\rho}}{(\lambda + ik)^2 + \lambda_0^2}, \quad M\, S_{\rho u} = -B \frac{\lambda(\lambda + ik) S_{E\rho} + \lambda_0^2 S_{\rho}}{(\lambda + ik)^2 + \lambda_0^2} \qquad (2.7)$$

Substituting Eqs. (2.6) and (2.7) into Eq. (2.3) yields the characteristic

equation for λ

$$\lambda^2+\lambda_0^2-\int_{-\infty}^{\infty}\frac{\left[\lambda^2(\lambda+ik)^2S_E+2\lambda_0^2\lambda(\lambda+ik)S_{E\rho}+\lambda_0^4S_\rho\right]dk}{(\lambda+ik)^2+\lambda_0^2}=0 \tag{2.8}$$

Consider some cases. First, assume the Young modulus and the mass density to be statistically independent random functions of diffuse type with the following spectral densities

$$S_E(k)=\frac{\sigma_E^2}{\pi}\frac{\alpha_E}{k^2+\alpha_E^2},\ S_\rho(k)=\frac{\sigma_\rho^2}{\pi}\frac{\alpha_\rho}{k^2+\alpha_\rho^2},\ S_{E\rho}(k)=0 \tag{2.9}$$

where σ_ε and σ_r are the standard deviations while α_ε^{-1} and α_r^{-1} are the correlation radii. Such modelling is typical for complex engineering structures, cf. [6]. The integral in Eq. (2.8) may be evaluated by the method of contour integration to obtain the result

$$\lambda^2+\lambda_0^2-\frac{b_E^2\lambda^2(\lambda+\alpha_E)^2}{(\lambda+\alpha_E)^2+\lambda_0^2}-\frac{b_\rho^2\lambda_0^4}{(\lambda+\alpha_\rho)^2+\lambda_0^2}=0 \tag{2.10}$$

Analysis of this characteristic equation which is a polynomial of order 6 is rather laborious, see for this aim [3] where an asymptotic analysis has been briefly outlined for weakly heterogeneous media ($b_E<<1, b_\rho<<1$).

Consider the case in which the randomness in the Young modulus E and mass density ρ is fully correlated, that is

$$E(x)=\langle E\rangle\left[1+b_E\,q(x)\right],\ \rho(x)=\langle\rho\rangle\left[1+b_\rho\,q(x)\right],\ S_q(k)=\frac{\sigma^2}{\pi}\frac{\alpha}{k^2+\alpha^2} \tag{2.11}$$

where $q(x)$ is a centred exponentially correlated random function. Since this case has not yet been studied in the literature, a detailed analysis is performed. The representation (2.11) models the materials with imperfections and is rather flexible. Choosing coefficients b_E and b_ρ in a proper way one can study a broad class of the problems, e.g. to study wave propagation in a medium having only random elastic properties one put $b_\rho=0$. By means of the representation (2.11) we will see the restrictions, shortcomings and merits of the approach. Equations (2.3)-(2.5) lead to the characteristic equation

$$P(\lambda)=\left[\lambda^2+\lambda_0^2\right]\left[(\lambda+\alpha)^2+\lambda_0^2\right]-\sigma^2\left[b_E\lambda(\lambda+\alpha)+b_\rho\lambda_0^2\right]^2=0 \tag{2.12}$$

This polynomial of 4th order is reduced to a quadratic equation in $\lambda(\lambda+\alpha)$ and has 4 roots

$$\lambda_{1,2,3,4}=-\frac{\alpha}{2}\pm\sqrt{\left(\frac{\alpha}{2}\right)^2-\lambda_0^2\frac{1-\sigma^2b_Eb_\rho\pm\sqrt{\Delta}}{1-\sigma^2b_E^2}} \tag{2.13}$$

with the discriminant $\Delta=\sigma^2\left(b_E-b_\rho\right)^2+\alpha^2\lambda_0^{-2}\left(\sigma^2b_E^2-1\right)$.

In order to study the limitations of the approach, one should recall that the imaginary part of λ guarantees the wave character of the propagating disturbance. In other words, if the characteristic equation (2.12) has only real eigenvalues, the wave motion is impossible. Not complicated, but rather cumbersome analysis of the case $\sigma b_E>1$ yields finally the set of

conditions under which the wave motion does not exist

$$\sigma b_E > 1\ ;\ \lambda_0^2 < \frac{\alpha^2}{4}\frac{\sigma b_E - 1}{\sigma b_\rho + 1} \tag{2.14}$$

The case $\sigma b_E < 1$ may be analysed by analogy and results in another set of conditions

$$\sigma b_E < 1\ ;\ \sigma\left(b_E + b_\rho\right) > 2\ ,\ 4\lambda_0^2\frac{1-\sigma^2 b_E b_\rho}{1-\sigma^2 b_E^2} < \alpha^2 < \lambda_0^2\frac{\sigma^2\left(b_E + b_\rho\right)^2}{1-\sigma^2 b_E^2} \tag{2.15}$$

Inequalities (2.14) and (2.15) may be roughly viewed as follows: if the standard variation in the Young modulus is larger than its mean value ($\sigma b_E > 1$, Eq. (2.14)) or the standard variation in the mass density is larger than its mean value ($\sigma b_\rho > 1$, Eq. (2.15)), then the wave motion does not exist since these inherently positive parameters become "too often negative". This means that essentially heterogeneous media cannot be handled by means of this approach. The conditions (2.14) and (2.15) reduce to known conditions for medium with a single random field (random mass density or random Young's modulus) obtained in [2] and [3].

As we consider the waves in the positive x direction, i.e. only two eigenvalues, say λ_1 and λ_2, satisfy the Sommerfeld radiation condition, then

$$\langle\tilde{u}\rangle = \sum_{n=1}^{2} B_n \exp\left(\lambda_n x\right),\ \mu(k, x) = -\frac{S_q}{S_{uq}}\sum_{n=1}^{2} B_n \frac{b_E\lambda_n\left(\lambda_n + ik\right) + b_\rho\lambda_0^2}{\left(\lambda_n + ik\right)^2 + \lambda_0^2}\exp\left(\lambda_n x\right) \tag{2.16}$$

In order to obtain B_n we consider for example Dirichlet's boundary condition (1.4). As follows from Eq. (2.2) the boundary condition (1.4) is fulfilled and the second moments become trivial at $x=0$ if $\langle\tilde{u}(0)\rangle = H$, $\mu(k, 0) = 0$ which yields the following two equations for B_n

$$B_1 + B_2 = H,\ B_1\frac{b_E\lambda_1\left(\lambda_1 + ik\right) + b_\rho\lambda_0^2}{\left(\lambda_1 + ik\right)^2 + \lambda_0^2} + B_2\frac{b_E\lambda_2\left(\lambda_2 + ik\right) + b_\rho\lambda_0^2}{\left(\lambda_2 + ik\right)^2 + \lambda_0^2} = 0 \tag{2.17}$$

These equations can be easily solved for B_1 and B_2 that completes the solution of the problem.

The merits of the approach are (i) the approach is valid for arbitrary spectral densities and (ii) it can be easily generalised to 2-D and 3-D problems. The shortcomings are (i) only mean field and the second moments are obtained, (ii) difficult to apply to nonlinear problems and (iii) applicable only for weakly heterogeneous media.

3 The Fokker-Planck-Kolmogorov equation

This approach is based on the theory of continuous Markov processes. The state transition probability function for such processes is governed by a linear partial differential equation, knows as the Fokker-Planck-Kolmogorov (FPK) equation, cf. [5] and [6].

To begin with, we consider the case of wave propagation in medium with deterministic Young's modulus ($\varepsilon = 0$) and random mass density. Assume that in Eq. (1.3) the random function $r = \xi(x)$ is a spatial white

noise of intensity s. To apply FPK equation we introduce the new variables $v_1 = \tilde{u}$, $v_2 = \tilde{u}'$ and recast Eq. (1.1) as two first-order differential equations

$$v_1' = v_2\,,\ v_2' = -\lambda_0^2 v_1 - \lambda_0^2 \xi v_1 \tag{3.1}$$

Provided that ξ is a Gaussian random function, the state transition probability function p is governed by the FPK equation

$$\frac{\partial p}{\partial x} = -\sum_{n=1}^{N} \frac{\partial}{\partial v_n}\left[\chi_n p\right] + \sum_{n=1}^{N}\sum_{m=1}^{N} \frac{\partial^2}{\partial v_n \partial v_m}\left[\gamma_{nm} p\right] \tag{3.2}$$

In this case N=2 and the drift χ_n and diffusion γ_{nm} coefficients are given by

$$\chi_1 = v_2,\ \chi_2 = -\lambda_0^2 v_1,\ \gamma_{11} = \gamma_{12} = \gamma_{21} = 0\,,\ \gamma_{22} = \frac{s}{2}\lambda_0^4 v_1^2 \tag{3.3}$$

cf. [5]. Substituting Eq. (3.3) into the FPK equation, multiplying it consequently with v_1 and v_2 and integrating over the space of v_1 and v_2 yields the following equations for the mean values of the phase variables

$$\langle v_1\rangle' - \langle v_2\rangle = 0\,,\ \langle v_2\rangle' + \lambda_0^2\langle v_1\rangle = 0 \tag{3.4}$$

This system of equations is solved by means of the substitution $\langle v_k\rangle = V_k e^{i\lambda x}$, $k = 1, 2$ which results in the characteristic equation $\lambda^2 + \lambda_0^2 = 0$ with the roots $\lambda_{1,2} = \pm i\lambda_0$. The eigenvalue $\lambda_2 = -i\lambda_0$ satisfies the Sommerfeld radiation condition since it describes harmonic waves propagating in the positive x direction. The Dirichlet boundary condition, Eq. (1.4), yields $\langle v_1(x)\rangle = H\exp(-i\lambda_0 x)$ i.e. the mean field in stochastic medium with spatial white noise random mass density coincides with the deterministic field in the homogeneous medium.

Now we multiply the FPK equation consequently with v_1^2, $v_1 v_2$ and v_2^2 and integrate the result over the space of v_1 and v_2, to obtain the equations for the second moments

$$\langle v_1^2\rangle' - 2\langle v_1 v_2\rangle = 0,\ \langle v_1 v_2\rangle' + \lambda_0^2\langle v_1^2\rangle - \langle v_2^2\rangle = 0,\ \langle v_2^2\rangle' - s\lambda_0^4\langle v_1^2\rangle + 2\lambda_0^2\langle v_1 v_2\rangle = 0$$

To solve the latter equations we substitute $\langle v_k v_n\rangle = W_{kn} e^{\Lambda x}$, $k, n = 1, 2$, to have the following characteristic equation

$$\Lambda^3 + 4\lambda_0^2\Lambda - 2s\lambda_0^4 = 0 \tag{3.5}$$

which has one real positive root and two complex conjugated roots. Only one root of Eq. (3.5) satisfies the Sommerfeld radiation condition, namely

$$\Lambda = \lambda_0\left[-h + \frac{1}{3}h^{-1} - i\sqrt{3}\left(h + \frac{1}{3}h^{-1}\right)\right],\ h = \frac{1}{2}\sqrt[3]{s\lambda_0 + \sqrt{s^2\lambda_0^2 + 2}} \tag{3.6}$$

Boundary condition (1.4) which is $\langle v_1^2(0)\rangle = H^2$ leads to the following results

$$\langle v_1^2\rangle = H^2\exp(\Lambda x),\ \langle v_1 v_2\rangle = -H^2\frac{\Lambda}{2}\exp(\Lambda x),\ \langle v_2^2\rangle = H^2\left(\lambda_0^2 - \frac{1}{2}\Lambda^2\right)\exp(\Lambda x) \tag{3.7}$$

The latter equation indicates an exponential decay of the second moments that contradicts the equation for the mean field which states that the mean value of the stochastic waves propagates without decay, cf. [2].

For realistic modelling of the elastic and mass parameters, the spatial white noise should be pre-filtered. The further analysis is restricted to the fully correlated randomness in the Young modulus and the mass density, Eq.

(2.11), which allows us to compare the result with that of the integral spectral decomposition and draw some conclusions. Introducing the variables $v_1 = \tilde{u}, v_2 = \tilde{u}', v_3 = q$ leads to three first-order equations

$$v_1 = \tilde{u}\,,\; v_2' = \frac{\alpha b_E v_2 v_3 - \lambda_0^2\left(1 + b_\rho v_3\right) v_1}{1 + b_E v_3} - \frac{b_E v_2}{1 + b_E v_3}\,\xi\,,\; v_3' = -\alpha\, v_3 + \xi \tag{3.8}$$

where the latter equation is the filter equation and ξ is the spatial white noise of intensity $s = 2\alpha\sigma^2$. The FPK equation (3.2) has now a higher order (N=3) and is given by

$$\frac{\partial p}{\partial x} = -\frac{\partial}{\partial v_1}\left[v_2 p\right] + \lambda_0^2 \frac{\partial}{\partial v_2}\left[\frac{\alpha b_E v_2 v_3 - \lambda_0^2\left(1 + b_\rho v_3\right) v_1}{1 + b_E v_3}\, p\right] + \alpha_\rho \frac{\partial}{\partial v_n}\left[v_3\, p\right] +$$
$$\frac{\alpha\sigma^2 b_E^2}{\left(1 + b_E v_3\right)^2}\frac{\partial^2}{\partial v_2^2}\left[p v_2^2\right] - 2\alpha\sigma^2 b_E \frac{\partial^2 p}{\partial v_2 v_3}\left[\frac{v_2 p}{1 + b_E v_3}\right] + \alpha\sigma^2 \frac{\partial^2 p}{\partial v_3^2} \tag{3.9}$$

The equation obtained is much more complicated than the previous one, cf. Eqs. (3.2) and (3.3), since its coefficients are no more the polynomials but rational functions. Multiplying Eq. (3.9) consequently with $v_1, v_1 v_3$, $v_2\left(1 + b_E v_3\right)^2$ and $v_2 v_3\left(1 + b_E v_3\right)^2$ and integrating over the space of the phase variables one obtains the following equations for $\langle v_1\rangle, \langle v_2\rangle, \langle v_1 v_3\rangle$ and $\langle v_2 v_3\rangle$

$$\begin{aligned}
&\langle v_1\rangle' - \langle v_2\rangle = 0,\; \langle v_1 v_3\rangle' - \langle v_2 v_3\rangle + \alpha\langle v_1 v_3\rangle = 0,\\
&\lambda_0^2\left(1 + b_E b_\rho \sigma^2\right)\langle v_1\rangle + \lambda_0^2\left(b_E + b_\rho\right)\langle v_1 v_3\rangle + \left(1 + b_E^2\sigma^2\right)\langle v_2\rangle' +\\
&3\alpha b_E\sigma^2\langle v_2\rangle + 2b_E\langle v_2 v_3\rangle' + \alpha\langle v_2 v_3\rangle = 0\\
&\lambda_0^2\sigma^2\left(b_E + b_\rho\right)\langle v_1\rangle + \lambda_0^2\left(1 + 3b_E b_\rho\sigma^2\right)\langle v_1 v_3\rangle + 2b_E\sigma^2\langle v_2\rangle' +\\
&\alpha b_E\langle v_2\rangle + \left(1 + 3b_E^2\sigma^2\right)\langle v_2 v_3\rangle' + \alpha\left(1 + 6b_E^2\sigma^2\right)\langle v_2 v_3\rangle = 0
\end{aligned} \tag{3.10}$$

The latter equations are obtained by means of the Gaussian closure. The FPK equation delivers an infinite number of coupled partial differential equations [7], [8]. Thus, a closure is necessary to obtain a solution. The simplest closure is a Gaussian closure, i.e. one assumes that v_1 and v_2 are quasi-Gaussian. Since ξ and v_3 are Gaussian, it allows one to use the properties of the Gaussian distribution and to express unknown higher order moments in terms of lower order moments, e.g. in terms of moments up to order 2 by means of expressions $\langle v_1 v_3^2\rangle = \sigma^2\langle v_1\rangle$ etc. The vanishing determinant of the system with closure at the second order is as follows

$$\det\begin{bmatrix}
\lambda & 0 & -1 & 0\\
0 & \lambda + \alpha & 0 & -1\\
\lambda_0^2\left(1 + b_E b_\rho\sigma^2\right) & \lambda_0^2\left(b_E + b_\rho\right) & \lambda\left(1 + b_E^2\sigma^2\right) + 3\alpha b_E\sigma^2 & 2b_E\left(\lambda + \alpha\right)\\
\lambda_0^2\sigma^2\left(b_E + b_\rho\right) & \lambda_0^2\left(1 + 3b_E b_\rho\sigma^2\right) & 2b_E\sigma^2\left(\lambda + \alpha\right) & \lambda\left(1 + 3b_E^2\sigma^2\right) + \alpha\left(1 + 6b_E^2\sigma^2\right)
\end{bmatrix} = 0$$

One can see that this equation does not coincide with the characteristic equation of the integral spectral decomposition (2.12). It can be explained by the fact that we multiplied the FPK equation with the polynomials of the third and forth order, namely, $v_2\left(1+b_E v_3\right)^2$ and $v_2 v_3\left(1+b_E v_3\right)^2$. This means that the moments of third and forth order are always involved to this technique and a closure is unavoidable. The higher moments obtained were expressed via the moments up to order 2 which automatically means the accuracy reduction of the approach.

The characteristic equation of the integral spectral decomposition approach is obtained if we introduce another variables $v_1=\tilde{u}, v_2=\tilde{u}'\left(1+b_E q\right), v_3=q$ which results in three first-order stochastic differential equations

$$v_1'\left(1+b_E v_3\right)-v_2=0, v_2'+\lambda_0^2\left(1+b_\rho v_3\right)v_1=0, v_3'+\alpha v_3=\xi \tag{3.11}$$

Stochastic averaging of the first and the second equation yields

$$\langle v_1\rangle'+b_E(\lambda+\alpha)\langle v_1 v_3\rangle-\langle v_2\rangle=0,\ \langle v_2\rangle'+\lambda_0^2\left[\langle v_1\rangle+b_\rho\langle v_1 v_3\rangle\right]=0 \tag{3.12}$$

Another two equations are obtained by multiplying the first two equations (3.11) with v_3 and taking expectations

$$\begin{aligned}&\langle v_1 v_3\rangle'+b_E\sigma^2\langle v_1\rangle'+\alpha\langle v_1 v_3\rangle-\langle v_2 v_3\rangle=0,\\&\langle v_2 v_3\rangle'+\lambda_0^2\left[\langle v_1 v_3\rangle+b_\rho\sigma^2\langle v_1\rangle\right]+\alpha\langle v_2 v_3\rangle=0\end{aligned} \tag{3.13}$$

While deriving Eqs. (3.12) and (3.13) two assumptions have been done: (i) $\langle\xi v_1\rangle=\langle\xi v_2\rangle=0$ which is a standard assumption of the FPK-equation and (ii) ξ and v_3 are Gaussian and v_1 and v_2 are quasi-Gaussian which permits a Gaussian closure $\langle v_1 v_3^2\rangle=\sigma^2\langle v_1\rangle$. Since Eqs. (3.12) and (3.13) are linear in the moments, the substitution $\langle v_k v_n\rangle=W_{kn}e^{\lambda x}, k,n=1,2$ yields the characteristic equation (2.12). This means that the new variables suit better than the previous ones due to the fact that the newly introduced variable $v_2=\tilde{u}'E/\langle E\rangle$ is non-dimensional axial stress and has clear physical sense.

Let two eigenvalues which satisfy the Sommerfeld radiation condition be λ_1 and λ_2, then the general solution is $\langle v_1\rangle=A_1\exp\left(\lambda_1 x\right)+A_2\exp\left(\lambda_2 x\right)$. The Dirichlet boundary condition, Eq. (1.4) yields the following equations

$$x=0,\ \langle v_1\rangle=H, \langle v_1 v_3\rangle=0 \tag{3.14}$$

which allows one to determine the integration constants

$$A_1=H\left[1-\frac{\lambda_0^2+\lambda_1^2}{\lambda_0^2+\lambda_2^2}\frac{b_\rho\lambda_0^2+b_E\lambda_1(\lambda_1+\alpha)}{b_\rho\lambda_0^2+b_E\lambda_2(\lambda_2+\alpha)}\right]^{-1},\ A_2=H-A_1 \tag{3.15}$$

Provided that the axial stress is prescribed at $x=0$, i.e. $E\tilde{u}'(0)=\Sigma$, the Neumann boundary condition (1.5) reduces to

$$x=0, \langle v_2\rangle=\Sigma/\langle E\rangle, \langle v_2 v_3\rangle=0 \tag{3.16}$$

which results in the following system of equations for the integration constants

$$A_1 \frac{\left[b_\rho\lambda_1 - b_E(\lambda_1+\alpha)\right]}{b_\rho\lambda_0^2 + b_E\lambda_1(\lambda_1+\alpha)} + A_2 \frac{\left[b_\rho\lambda_2 - b_E(\lambda_2+\alpha)\right]}{b_\rho\lambda_0^2 + b_E\lambda_2(\lambda_2+\alpha)} = \frac{\Sigma}{\lambda_0^2\langle E\rangle}$$

$$A_1 \frac{\sigma^2 b_E\lambda_1\left[b_\rho\lambda_0^2 + b_E\lambda_1(\lambda_1+\alpha)\right] - (\lambda_0^2+\lambda_1^2)(\lambda_1+\alpha)}{b_\rho\lambda_0^2 + b_E\lambda_1(\lambda_1+\alpha)}$$

$$+ A_2 \frac{\sigma^2 b_E\lambda_2\left[b_\rho\lambda_0^2 + b_E\lambda_2(\lambda_2+\alpha)\right] - (\lambda_0^2+\lambda_2^2)(\lambda_2+\alpha)}{b_\rho\lambda_0^2 + b_E\lambda_2(\lambda_2+\alpha)} = 0 \qquad (3.17)$$

The moments $\langle v_2\rangle$, $\langle v_1 v_3\rangle$ and $\langle v_2 v_3\rangle$ can be obtained from Eq. (3.10) for each of the above boundary conditions by substituting Eq. (3.15) or (3.17) and solving the system of linear algebraic equations.

Equations for the other second moments, namely $\langle v_1^2\rangle$, $\langle v_1 v_2\rangle$ and $\langle v_2^2\rangle$ can be derived by multiplying Eq. (3.11) with v_1 and v_2 and averaging. The result is three first-order inhomogeneous ordinary differential equations

$$\langle v_1^2\rangle' - 2\langle v_1 v_2\rangle = \alpha\langle v_1\rangle\langle v_1 v_3\rangle - \langle v_1\rangle'\langle v_1 v_3\rangle - \langle v_1\rangle\langle v_1 v_3\rangle'$$

$$\langle v_1 v_2\rangle' + \lambda_0^2\langle v_1^2\rangle - \langle v_2^2\rangle =$$

$$-2b_\rho\lambda_0^2\langle v_1\rangle\langle v_1 v_3\rangle - b_E\left[\langle v_1\rangle'\langle v_2 v_3\rangle - \langle v_2\rangle\langle v_1 v_3\rangle' - \alpha\langle v_2\rangle\langle v_1 v_3\rangle\right]$$

$$\langle v_2^2\rangle' + \lambda_0^2\langle v_1 v_2\rangle = -2b_\rho\lambda_0^2\left[\langle v_1\rangle\langle v_2 v_3\rangle + \langle v_2\rangle\langle v_1 v_3\rangle\right] \qquad (3.18)$$

which is easy to solve. Because of lack of space, the solution is not included.

The main advantage of the FPK equation is that the moments of any order may be obtained. The deficiencies of the approach are as follows (i) the approach is applicable only for the random processes with rational spectral densities which are obtained by means of the white noise filtering, (ii) each filter increases the order of the system of equation, (iii) difficulties increase rapidly with the order of the system, (iii) the approach is applicable only for one-dimensional waves and (iiii) the approach appears to be accurate only for the systems with the polynomial coefficients. As the characteristic equation of both approaches coincide only weakly heterogeneous random media may be analysed by means of the FPK equation.

4 The Dyson integral equation

In contrast to the previous approaches which deal with random mass density and random Young's modulus an alternative modelling of 1-D random media is proposed, [6]. We introduce a new independent variable y and a new dependent variable U

$$y = \langle a\rangle \int_0^x \frac{d\xi}{a(\xi)}\,;\quad U(y) = \sqrt{z}\,\tilde{u}(x,\omega) \qquad (4.1)$$

where $a = \sqrt{E/\rho}$ is the velocity of sound and $z = \sqrt{E\rho}$ is the acoustic

impedance. The original problem is thus reduced to the wave propagation in elastic medium in terms of impedance and velocity of sound that seems to be much more suitable for the problems of wave propagation. In what follows a random elastic medium is modelled by a medium with the following statistically independent and statistically homogeneous random parameters: the sound speed a and the impedance z. Substituting (4.1) into (1.1) yields

$$\frac{d^2U}{dy^2}+\left[\frac{\omega^2}{\langle a\rangle^2}+e(y)\right]U=0\,,\ e(y)=-\frac{1}{\sqrt{z}}\frac{d^2\sqrt{z}}{dy^2} \tag{4.2}$$

Introducing a new centred random function $\varepsilon(y)=e(y)-\langle e\rangle$ which will be referred to as heterogeneity enables Eq. (4.2) to be written as follows

$$\frac{d^2U}{dy^2}+\left[\kappa^2+\varepsilon(y)\right]U=0\,;\ \kappa^2=\frac{\omega^2}{\langle a\rangle^2}+\langle e\rangle \tag{4.3}$$

Provided that the medium is subjected to the Neumann boundary condition $y=y_0;\quad dU/dy=1$ then the boundary value problem is equivalent to the single differential equation

$$\frac{d^2U}{dy^2}+\left[\lambda^2+\varepsilon(y)\right]U=\delta(y-y_0) \tag{4.4}$$

provided that its solution satisfies the Sommerfeld radiation condition.

$U(y)$ is the solution of Eq. (4.4) containing a delta-function in the right hand side. Hence, $U(y)=G(y,y_0)$ is the Green's function of Eq. (4.4) and $\langle U(y)\rangle=\langle G(y,y_0)\rangle$ is the averaged Green's function. The latter is known to be the solution of the Dyson integral equation, cf. [1, 9]

$$\langle G(y,y_0)\rangle=G_0(y-y_0)+\iint G_0(y-r_1)\,M(r_1,r_2)\,\langle G(r_2,y_0)\rangle dr_1dr_2\ . \tag{4.5}$$

Here Green's function for the virtual homogeneous background material is

$$G_0(y-y_0)=-\frac{e^{-i\kappa|y-y_0|}}{2\kappa i}=\frac{1}{2\pi}\int_{-\infty}^{+\infty}\frac{e^{ik(y-y_0)}}{\kappa^2-k^2}dk\,,\ \kappa>0 \tag{4.6}$$

and M denotes the kernel of an integral operator which is called the mass operator in quantum field theory and contains an infinite number of terms

$$M=\langle\varepsilon K_0\varepsilon\rangle-\langle\varepsilon K_0\varepsilon K_0\varepsilon\rangle+\langle\varepsilon K_0\varepsilon K_0\varepsilon K_0\varepsilon\rangle-\langle\varepsilon K_0\varepsilon\rangle K_0\langle\varepsilon K_0\varepsilon\rangle \tag{4.7}$$

where K_0 is an integral operator with the kernel G_0, cf. [1,12]. Even a single term in expansion (4.7) corresponds to the summation of an infinite subsequence of the series in perturbation theory. In what follows, we truncate M at its first term (so-called Bourett's approximation)

$$M(r_1,r_2)=\langle\varepsilon K_0\varepsilon\rangle=B_\varepsilon(r_1,r_2)\,G_0(r_1-r_2) \tag{4.8}$$

where $B_\varepsilon(r_1,r_2)$ is the correlation function of the random field ε.

As ε is statistically homogeneous, its correlation function depends only on the difference of the arguments, i.e. $B_\varepsilon(y_1,y_2)=B_\varepsilon(y_1-y_2)$. The Dyson equation takes the form of an integral equation with a difference kernel

$$\langle G(y-y_0)\rangle=G_0(y-y_0)+\iint G_0(y-r_1)\,B_\varepsilon(r_1-r_2)\,G_0(r_1-r_2)\langle G(r_2-y_0)\rangle dr_1dr_2$$

which is solved by means of the spatial Fourier transform, [8]. The result is

$$\left\langle \hat{G}(k) \right\rangle = \left[\hat{G}_0^{-1}(k) - 4\pi^2 \hat{G}_0(k)\, \hat{B}_\varepsilon(k) \right]^{-1} \tag{4.9}$$

The Fourier transform, is inverted to recover the averaged Green's function

$$\left\langle G(r) \right\rangle = \frac{1}{2\pi} \int_{-\infty}^{+\infty} \frac{e^{ikr}}{\kappa^2 - \int_{-\infty}^{+\infty} B_\varepsilon(\rho) G_0(\rho) e^{-ik\rho} d\rho - k^2}\, dk \tag{4.10}$$

where $r = y - y_0$ is substituted for brevity. As before, we study an exponential correlation function for the heterogeneity $B_\varepsilon(r) = \sigma^2 \exp\left(-\alpha |r|\right)$. Substituting it into Eq. (4.10) and evaluating the integral in the denominator yields

$$\left\langle G(r) \right\rangle = \frac{1}{2\pi} \int_{-\infty}^{+\infty} \frac{e^{ikr}\, dk}{\kappa^2 + \dfrac{\sigma^2}{i\kappa} \dfrac{i\kappa + \alpha}{(i\kappa + \alpha)^2 + k^2} - k^2} \tag{4.11}$$

Two poles of the integrand, namely k_1 and k_2, which satisfy Sommerfeld's radiation condition, lay in the upper half-plane

$$k_{1,2} = \frac{1}{\sqrt{2}} \sqrt{\kappa^2 - (\alpha + i\kappa)^2 \pm \sqrt{\left(\kappa^2 + (\alpha + i\kappa)^2\right)^2 + 4\, \frac{\alpha + i\kappa}{i\kappa}\, \sigma^2}}\ , \ \mathrm{Im}\, k_{1,2} > 0$$

Of special interest is the problem of the long waves in a medium with a small-scale heterogeneity ($\alpha >> \kappa$). Under the additional assumption of $\alpha \sqrt{\kappa\alpha} >> \sigma$ latter expression for the poles k_1 and k_2, reduce to

$$k_1 = -\kappa \sqrt{1 - i\, \frac{\sigma^2}{\kappa^3 \alpha}}\ , \quad k_2 = -\kappa + i\alpha \tag{4.12}$$

The contribution of the pole k_2 becomes small even within the correlation radius $R = \alpha^{-1}$, i.e. k_2 models the near field which can be neglected in case of the long travelling distances. Hence, the influence of heterogeneity is taken into account by k_1 which may be transformed to

$$k_1 = -\kappa \sqrt{1 - i\, \frac{\sigma^2}{\alpha^3 \kappa}\, \frac{\alpha^2}{\kappa^2}} \tag{4.13}$$

Inspection of this equation indicates that the imaginary part of k_1 can be considerable even for waves in weakly heterogeneous media ($\sigma << \alpha \sqrt{\kappa\alpha}$) with short range perturbations ($\alpha >> \kappa$). Considerable attenuation is explained by the accumulation of the dispersion effects. Application of the residue calculus in Eq. (4.11) renders an averaged Green's function

$$\left\langle G(r) \right\rangle = \frac{e^{ik_1 |r|}}{2ik_1}\ ; \quad k_1 = -\kappa \sqrt{1 - i\, \frac{\sigma^2 R}{\kappa^3}}\ , \ \mathrm{Im}\, k_1 > 0 \tag{4.14}$$

Equation (4.14) for the mean field may be obtained in a simpler way by setting $k=0$ in the integral over ρ in the denominator in Eq. (4.10), i.e.

$$\left\langle G(r) \right\rangle = \frac{1}{2\pi} \int_{-\infty}^{+\infty} \frac{e^{ikr}}{\kappa^2 - \int_{-\infty}^{+\infty} B_\varepsilon(\rho) G_0(\rho) d\rho - k^2}\, dk \tag{4.15}$$

Evaluation of the integral in the denominator yields

$$\langle G(r)\rangle = \frac{1}{2\pi}\int_{-\infty}^{+\infty} \frac{e^{ikr}\,dk}{\kappa^2 + \sigma^2 / \left[i\kappa\left(i\kappa+\alpha\right)\right] - k^2} \quad . \tag{4.16}$$

Provided that the random medium with short range heterogeneity ($\alpha >> \kappa$) is considered, the only pole in the upper half-plane is k_1, Eq. (4.12). In this case the residue calculus delivers Eq. (4.14). In other words, the second pole which represents a near field does not appear if one sets $k=0$ in the integral over ρ in Eq. (4.10). The substantiation is that the correlation radius R is small and it allows one to take into account only the leading term in the expansion of $e^{-ik\rho}$ in terms of $k\rho$, i.e. to set $e^{-ik\rho} = 1$.

Another correlation functions are discussed in [8]. Despite the broad variety of the correlation functions' properties the mean field equation turns out to take the form of Eq. (4.14). It allows one to study the general case of random medium with an arbitrary short range heterogeneity. To this end, we model the correlation function of the medium as follows

$$B_\varepsilon(r) = \sigma^2 \frac{\delta_R(r)}{\delta_R(0)}\,;\ \int_{-\infty}^{\infty} \delta_R(r)\,dr = 1\,;\ R = \frac{1}{2\,B_\varepsilon(0)}\int_{-\infty}^{\infty} B_\varepsilon(r)\,dr = \frac{1}{2\,\delta_R(0)} \tag{4.17}$$

where $\delta_R(r)$ is a window-function which has support only for small r, $|r| < R$. The analysis shows that when studying a random medium with the short range heterogeneity ($\alpha >> \kappa$) one must rather take into account the shift of the pole k_1 (at $k_1 = -\kappa$ if heterogeneity were supposed to vanish) to the upper half-plane caused by the heterogeneity, than the appearance of new poles.

Substituting the correlation function, Eq. (4.17) into Eq. (4.10) yields

$$\langle G(r)\rangle = \frac{1}{2\pi}\int_{-\infty}^{+\infty} \frac{e^{ikr}}{\kappa^2 + \dfrac{\sigma^2}{2i\kappa\,\delta_R(0)}\displaystyle\int_{-R}^{+R} \delta_R(\rho)\,e^{-i\kappa|\rho|}\,d\rho - k^2}\,dk \tag{4.18}$$

The case of the heterogeneity of small extend is considered, i.e. $\kappa R << 1$, that allows one to take only the leading term in the expansion of $\exp\left(i\kappa|\rho|\right)$ in a series in terms of $\kappa|\rho|$, i.e.

$$\langle G(r)\rangle = \frac{1}{2\pi}\int_{-\infty}^{+\infty} \frac{e^{ikr}}{\kappa^2 - i\,\sigma^2 R\,\kappa^{-1} - k^2}\,dk \tag{4.19}$$

The residue calculus yields Eq. (4.14) for an arbitrary heterogeneous elastic medium with short range fluctuations. Since the velocity of sound a is random, $\langle G(r)\rangle$ is still a random field which should be averaged over a. For a given probability density function for the velocity of sound, the mean field can be estimated. Averaged decay in statistically homogeneous medium $\langle d\rangle$ allows for a closed form expression

$$\langle d\rangle = -\frac{\langle a\rangle}{x - x_0}\int_{x_0}^{x} \left\langle \frac{1}{a(\xi)}\right\rangle d\xi\ \mathrm{Im}\,\kappa\sqrt{1 - i\frac{\sigma^2 R}{\kappa^3}} = -\langle a\rangle\left\langle\frac{1}{a}\right\rangle \mathrm{Im}\,\kappa\sqrt{1 - i\frac{\sigma^2 R}{\kappa^3}} > 0$$

Assuming that the decay is small leads to the following simple equation for the averaged decay

$$\langle d \rangle = \langle a \rangle \left\langle \frac{1}{a} \right\rangle \frac{\sigma^2 R}{2\kappa^2} = \frac{1}{4}\,\omega^{-2}\,\langle a \rangle^3 \left\langle \frac{1}{a} \right\rangle \int_{-\infty}^{+\infty} B_\varepsilon(r)\,dr \tag{4.20}$$

One of the main merits of the Dyson equation is that the solution method does not require the random fields to be Gaussian. This allows one to overcome the known shortcoming of the normal distribution, such as the impedance or the sound velocity may be negative. Any probability distribution function which satisfies these physical constraints with probability 1 can be taken in the framework of the present approach. Another merits are (i) the approach is applicable to essentially heterogeneous media and (ii) a closed form expression for the average attenuation is obtained. The approach shortcomings are (i) it is difficult to satisfy the boundary conditions and (ii) in order to find the standard deviation of the random fields, one should apply the Bethe-Salpeter equation, e.g. [1,9], however its solution is extremely laborious.

5 Concluding remarks

A benchmark study of the one-dimensional stochastic elastic wave shows the merits and the shortcomings of each approach which allows one to choose an appropriate based on the above conclusions. As shown above only weakly heterogeneous elastic media can be analysed in the framework of the method of integral spectral decomposition and the FPK equation. While dealing with essentially heterogeneous media, one is recommended to apply the Dyson integral equation. The approaches discussed cover all problems of the harmonic wave propagation in heterogeneous or stochastic media, thus, by means of a preliminary analysis one can find a suitable approach.

References

1. Sobczyk, K., *Stochastic wave propagation*, Elsevier, Amsterdam, 1984.
2. Makarov, B.P., *Nonlinear problems of statistical dynamics of machines and devices* (in Russian), Mashinostroenie, Moscow, 1983.
3 Náprstek, J., Propagation of longitudinal stochastic waves in bars with random parameters. In *Structural Dynamics*, eds. G. Augusti, C. Borri and P. Spinelli, A.A.Balkema, Rotterdam, 1996, pp. 51-60.
4. Yaglom, A.M., *Correlation theory of stationary and related random functions*, vol. 1, Springer-Verlag, New York, 1987.
5. Bolotin, V.V., *Random vibrations in elastic systems*, Nijhoff, The Hague, 1984.
6. Roberts, J.B. and Spanos, P.D., *Random vibration and statistical linearization*, Wiley and Sons, Chichester, 1990.
7. Dimentberg, M.F., *Statistical dynamics of nonlinear and time-varying systems*, Wiley and Sons, New York, 1988.
8. Belyaev, A.K. and Ziegler, F., Uniaxial waves in randomly heterogeneous elastic media. *J. Prob. Engng. Mech.*, 1998, **13**, 27-38.
9. Tatarsky, V.I., *Wave propagation in turbulent atmosphere* (in Russian), Nauka, Moscow, 1969.

DYNAMIC INSTABILITY OF SPATIAL FRAMES

Qiang Xue
Civil & Hydraulic Engineering Research Center, Sinotech Engineering Consultants Inc., Taipei 105, Taiwan

ABSTRACT

This paper presents a geometrically nonlinear dynamic analysis for both two and three-dimensional frames, which may be subjected to finite rotations. The finite element displacement method based on the beam-column approach is employed to derive the non-linear equations governing the behavior of spatial frames. A co-rotational formulation combined with small deflection beam theory with the inclusion of the effect of axial force is adopted. The governing dynamic equilibrium equations are obtained from the static equations by adding the inertia and damping terms. The implicit Newmark time integration with the Newton-Raphson (NR) iteration method is employed. Dynamic critical loads are defined by the Budiansky-Roth criterion. Several numerical examples are illustrated to demonstrate the effectiveness of the present method.

INTRODUCTION

The stability of plane and spatial frames under static loading has been the subject of considerable research during the past 35 years [1, 2]. However, the problem of non-linear response and stability of these structures under dynamic loads has received limited attention. A dynamic load may cause the instability of a structure even if the structure remains stable under a static load of the same magnitude as the dynamic one. When such a type of dynamic instability problem is being solved, geometrical non-linearity must also be considered in the same manner as in the static instability analysis.

The co-rotational formulation [3, 4] is employed in the present study accounting for arbitrary large joint displacements. The non-vectoral deformed rotation quantities in spatial frames have been successfully considered by the

use of Oran's joint orientation matrix [5], consisting of a triad of orthogonal unit vectors, to accommodate the arbitrary large rotations.

The implicit Newmark time integration with the NR iteration method is employed. The time-integration strategy with average acceleration (with $\beta = 1/4$ and $\gamma = 1/2$) is adopted together with a small time step for a non-linear problem.

A large class of structural problems that have received attention recently and do qualify as a category of dynamic stability is that of impulsively-loaded configurations and configurations that are suddenly loaded with loads of constant magnitude and infinite duration. Solutions to such problems started appearing in the literature in the early 1950s. Hoff and Bruce [6] considered the dynamic stability of a pinned half-sine arch under a half-sine distributed load. Budiansky and Roth [7], in studying the axisymmetric behavior of a shallow spherical cap under suddenly applied loads, defined the load to be critical when transient response increase suddenly with very little increase in the magnitude of the load. This concept was adopted by numerous investigators [8, 9] in the subsequent years because it is tractable to computer solutions. Hsu and his collaborators [10], defined sufficiency conditions for stability and instability, thus finding upper and lower bounds for the critical impulse or critical sudden load. The idea of the Liapunov's direct method [11], which attempts to provide a stability criterion for the equilibrium has also attracted the attention of many researchers [12, 13]. From all previous studies, it appears that the dynamic buckling load would be sometimes higher and sometimes lower than the static buckling load, depending on the loading history.

In this study, dynamic instability analysis is carried out based on the Budiansky-Roth criterion and the structure is subjected of step loading and assumed free of pre-loading.

FORMULATION STRATEGY

The formulation in the present study is briefly reviewed herein. Detailed derivation can be found in Ref. [14]. The members are uniform and have doubly symmetric cross-sections. Thus coupling of the torsional stiffness to the

bending stiffness and axial stiffness is excluded, and the warping effect is neglected for spatial frames. The external loads are applied at the nodes and only conservative loading is considered. The Euler-Bernoulli hypothesis is assumed to be valid and the material is assumed to be linearly elastic.

In the derivation of the non-linear equations, two types of coordinate systems are employed; a fixed global set of coordinates and local body attached coordinates, which rotate and translate with the member (Table 1). The basic member force-deformation relations are derived in the local coordinates with member deformations assumed to be small relative to them. Linear interpolation for the axial displacement and cubic interpolation for the lateral displacements are assumed for the members in each of their two principal directions. The non-linear effect of the bending distortions on the axial action is considered to manifest itself as an axial change in length due to the bowing of the beam.

Incremental Stiffness Matrix

Details of the member incremental stiffness matrix are given in Ref. [3]. The element member forces and tangent stiffness matrix with respect to the global coordinates can be obtained by the transformation from the member basic force/displacement to member intermediate (local) force/displacement, and from this to global nodal force/displacement (Table 1). The tangent stiffness matrix of the structure is then obtained by standard assembly.

Mass Matrix and Damping Matrix

It is clear that lumped mass matrices are simpler to form, occupy less storage space and require less computational effort than the consistent mass matrices. The structure damping may be expressed by the Rayleigh quotient [15].

$$C = \alpha M + \beta K \tag{1}$$

where α and β are constants to be determined from two given damping ratios that correspond to two unequal frequencies of vibration. Details can be referred to in Ref. [14].

COMPUTATIONAL ALGORITHM

The equations of motion for the non-linear dynamic analysis may be expressed by

$$\Phi(r) = P - M\ddot{r} - C\dot{r} - F = 0 \qquad (2)$$

where Φ is the unbalanced force resulting from the inertia force $M\ddot{r}$, the damping force $C\dot{r}$, the internal force due to deformation F and the external force P. The terms $\ddot{r}$ and $\dot{r}$ are the acceleration and the velocity vectors, respectively. The non-linear dynamic response of the structure is generated by the step-by-step numerical integration procedure; the Newmark procedure of average accelerations ($\beta = 1/4$ and $\gamma = 1/2$) with a Newton-Raphson type of iteration performed within each time step to satisfy the equation of motion. A weighted Euclidean norm between the unbalanced force Φ and the external force P is employed as the error measure during the equilibrium iteration. Detailed formulation and procedure of this method for non-linear use are described in Ref. [14].

Special attention must be given to spatial frames to take into account the non-vectoral rotation quantities. Use is made of the Oran's joint orientation matrix [5] in the non-linear dynamic analysis in the same way as its use in the static analysis. All translational displacements and the joint orientation matrix in spatial frame analysis must be updated properly so as to evaluate the updated tangent stiffness matrix correctly during NR iteration and updating the final displacement vector.

Critical or buckling loads for structures are determined by the Budiansky-Roth criterion [7]: The equations of motion are solved (numerically) for various values of the load parameter, thus obtaining the system response. The load parameter, at which there exists a large (finite) change in the response, is called critical. According to this, the dynamic response of a structure is monitored under increasing load levels, and a sudden increase in response due to a very small increase in the magnitude of the load is considered as an indication of dynamic instability. The dynamic buckling load is compared with the static critical load, which is determined by the incremental work criterion [3] using the arc-length method [16].

NUMERICAL EXAMPLE

A Shallow Arch

As the first step of examination, an in-plane dynamic instability of a shallow arch illustrated in Fig. 1 is analyzed and the results are compared with that given by Gregory and Plaut [17] and Masuda *et al.* [18] as presented in Table 2. The arch has two hinges and sinusoidal configuration. It is subjected to a centrally applied concentrated step loading (Fig. 1).

Response analysis of various magnitudes of the step load in the time domain is conducted. A non-dimensional average displacement δ used in the plotting is defined as the ratio of summation of the nodal deflection to that of the nodal height at the initial state. The mass density is 7.85×10^3 kgf/cm^3 and a time step of 0.001 *seconds* is adopted.

Static and dynamic buckling loads in the present analysis are obtained by using both 4 elements and 8 elements to model the structure. The maximum values of δ versus the magnitude of the step load are presented in Fig. 2. Dynamic buckling load is found to be about 78% of the static buckling load for both models. Comparisons shown in Table 2 indicated that the present results are in good agreement with that in the references as the number of elements is increased.

A Star Shaped Shallow Dome

The dynamic instability of the three-dimensional star shaped shallow dome (Fig. 3) previously analyzed under static load in Ref. [3] is studied. The structure is herein modeled with 1 element per member and subjected to a vertical concentrated load at the central node. Only step loading as shown in Fig.1 is considered. A mass density of 2400 kg/m^3 and a time step of 0.001 *seconds* are adopted. The curve of magnitude of step load versus the maximum displacement at the central node is depicted in Fig. 4. The dynamic critical load is found to be 457N, which is about 81% of the static buckling load (Fig. 5). The same structure has also been analyzed by Coan [8] and Kassimali and Bidhendi [9] as a space truss. For the same load condition, the dynamic buckling loads

were about 79% and 76% of the static buckling load for step loading in those two references.

CONCLUSION

A non-linear dynamic analysis of spatial frames with arbitrary finite rotations has been successfully implemented. It has been demonstrated by the examples that the present procedure is capable of handling the large rotations experienced in the three- dimensional frame analysis by using small linear increments in the co-rotational approach. Non-linear behavior of frames under dynamic loading can be easily obtained by the proposed integration and iteration method in time-history analysis. Dynamic critical load can be predicted accordingly with multiple processing of the program under different load levels. Without pre-loading, the dynamic buckling loads of the frames in this study under step loading are found somewhat lower than the static buckling loads.

REFERENCES

1. Argyris, J. H., Dunne, P. C. and Scharpf, D. W., On large displacement-small strain analysis of structures with rotational degrees of freedom. *Computer Methods in Applied Mechanics and Engineering*, 1978, **14**, 401-451.
2. Chan, S. L., A generalized numerical procedure for nonlinear analysis of frames exhibiting a limit or a bifurcation point. *International Journal of Space Structures*, 1991, **6**(2), 99-114.
3. Tan, H. S., *Finite element analysis of the elastic, non-linear response of frames, plates and arbitrary shells to static loads*. PhD thesis, The University of Queensland, Australia, 1985.
4. Crisfield, M. A., A consistent co-rotational formulation for non-linear, three-dimensional, beam-elements. *Computer Methods in Applied Mechanics and Engineering*, 1990, **81**, 131-150.
5. Oran, C., Tangent stiffness in space frames. *Journal of The Structural Division*, ASCE, 1973, **99**, 987-1001.
6. Hoff, N. J. and Bruce V. C., Dynamic analysis of the buckling of laterally

loaded flat arches. *J. Math. And Phys.*, 1954, **32**, 276-288.

7. Budiansky, B. and Roth, R. S., Axisymmetric dynamic buckling of clamped shallow spherical shells. *NASA Technical Notes*, 1962, **D-1510**, 597-606.
8. Coan, C. H., Dynamic stability of a lattice dome. *Earthquake Engineering and Structural Dynamics*, 1983, **11**, 269-274.
9. Kassimali, A. and Bidhendi, E., Stability of trusses under dynamic loads. *Computers and Structures*, 1988, **29**(3), 381-392.
10. Hsu, C. S., The effect of various parameters on the dynamic stability of a shallow arch. *Journal of Applied Mechanics*, 1967, **34**, 349-356.
11. Hahn, W., *Theory and Application of Liapunov's Direct Method.* Prentice-Hall, Engelwood Cliffs, New Jersey, 1973.
12. Ahmadian, M. and Inman, D. J., Structural and Dynamic Stability, on the stability of general dynamic systems using a Liapunov's direct method approach. *Computers and Structures*, 1985, **20**(1-3), 287-292.
13. Burmeister A. and Ramm E., Dynamic stability analysis of shell structures. In *Computational Mechanics of Nonlinear Response of Shells*, ed., Kratzig W. B. and Onate E., Berlin, New York, Springer-Verlag, 1990, pp. 152-162.
14. Meek, J. L. and Xue, Q., A study on the instability problem for 3d-frames. *Computer Methods in Applied Mechanics and Engineering*, 1998, **158**, 235-254.
15. Bathe, K. J., *Finite Element Procedures in Engineering Analysis.* PrenticeHall Inc., Englewood V\Cliffs, New Jersey 07632, 1982.
16. Crsfield, M. A., A fast incremental/iterative solution procedure that handles "snap-through". *Computers and Structures*, 1981, **13**, 55-62.
17. Gregory, W. E. and Plaut R. H., Dynamic stability boundaries for shallow arches, *Journal of The Engineering Mechanics Division*, ASCE, 1982, **108**(EM6), 1036-1050.
18. Masuda, N., Nishiwaki, T. and Minagawa, M., Nonlinear dynamic analysis of frame structures. *Computers and structures*, 1987, **27**(1), 103-110.

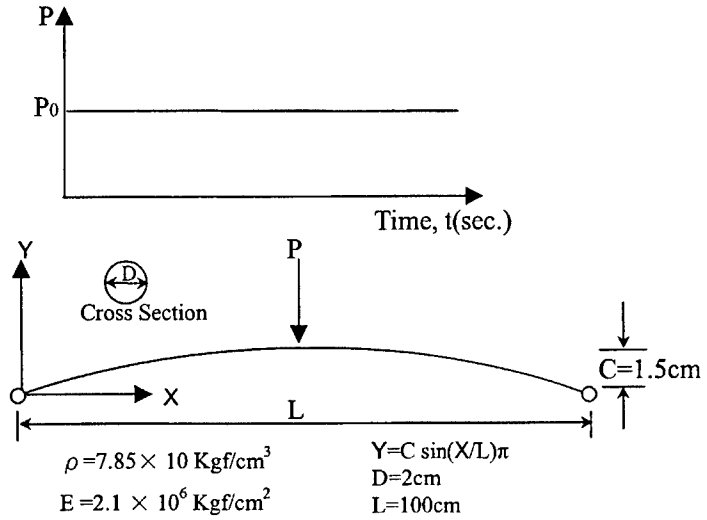

Fig.1: Geometry, material properties and load condition of the arch

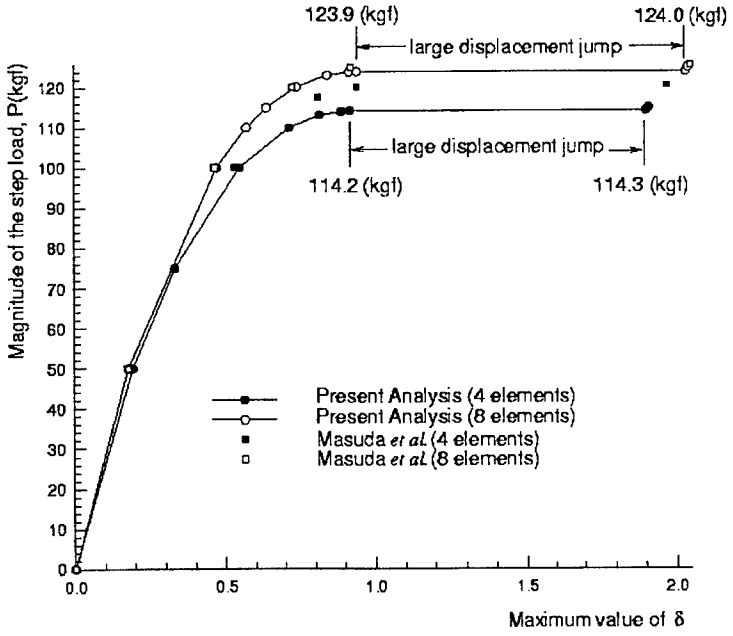

Fig. 2: Load verses maximum displacement factor δ of the arch

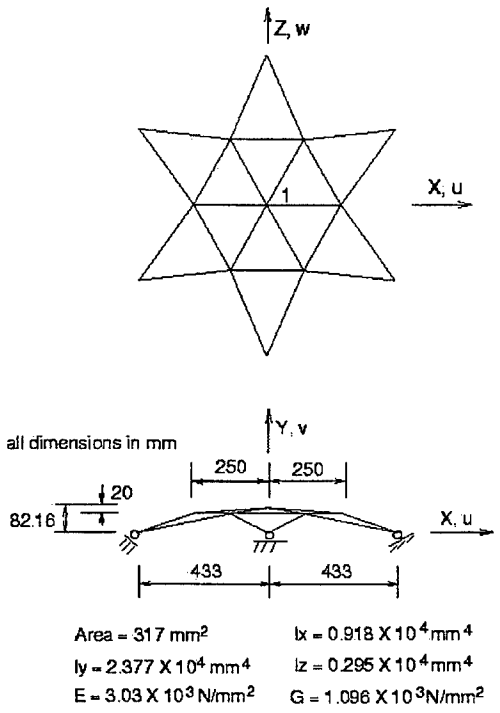

Fig. 3: Geometry, material properties and load condition of the dome

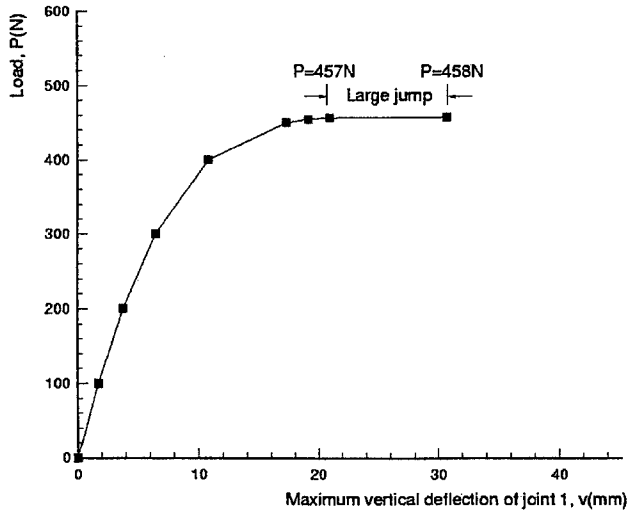

Fig. 4: Load-deflection curve for the step loading of the star shaped dome

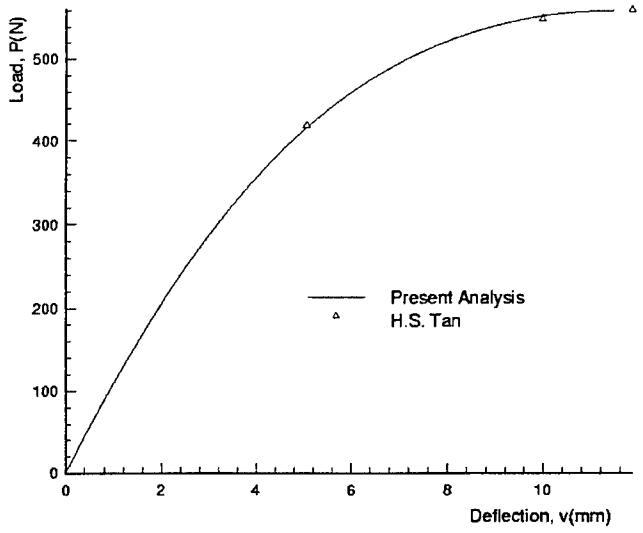

Fig. 5: Load-deflection curve under static load of the star shaped

Table 2: Comparison of the static and dynamic buckling loads of the arch

Source	Static buckling load (Kgf)	Dynamic buckling load (Kgf)
Gregory and Plaut	163.7	126.8
Masuda et al. (4 ele.)	NA	120.0-120.5
Masuda et al. (8 ele.)	NA	125.0-125.5
Present Analysis (4 ele.)	146.3	114.2
Present Analysis (8 ele.)	159.03	123.9

Table 1: Member deformation and associated forces

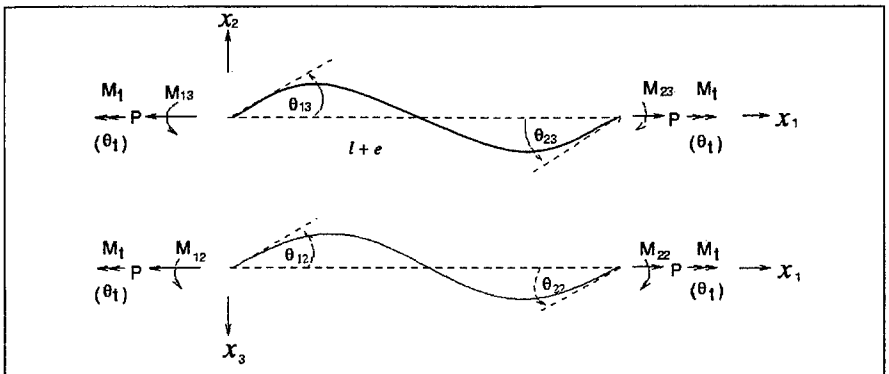

(a) Member basic displacements and forces

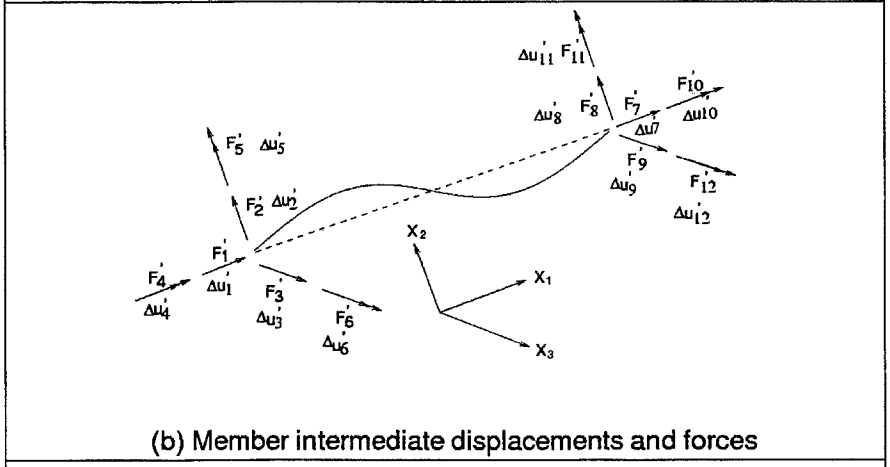

(b) Member intermediate displacements and forces

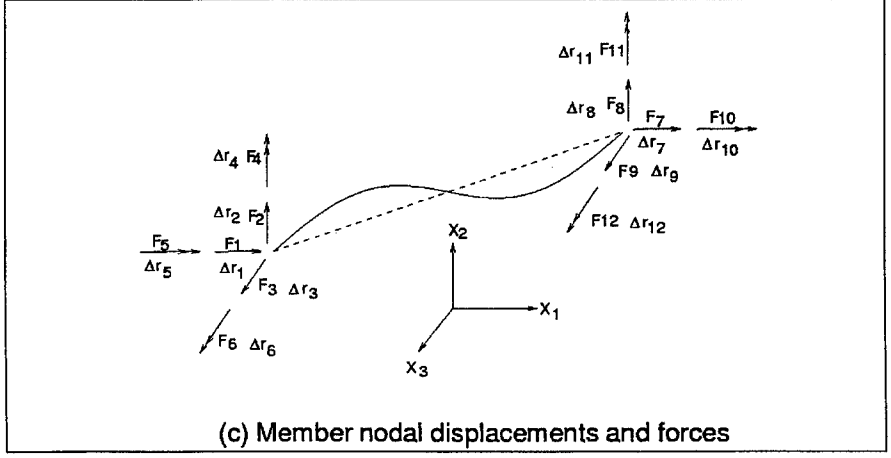

(c) Member nodal displacements and forces

IMPACT DYNAMICS

INVERSE PROBLEMS IN MECHANISMS FOR PACKAGING MACHINES

G. Dalpiaz and A. Rivola
University of Bologna - DIEM
Viale Risorgimento 2, I-40136 Bologna, Italy.
E-mail: giorgio.dalpiaz@mail.ing.unibo.it

Abstract

An inverse-filtering technique for the in-service recovery of mechanism motion from casing response measurements is presented. Different processing options are discussed based on experimental results. In particular, the capability of some FRF estimators and cepstral smoothing is pointed out. The results are satisfactory.

1. INTRODUCTION

Vibration analysis is widely used in the field of condition monitoring and fault diagnostics of machinery, with applications in predictive maintenance, quality control and automation. This paper deals with diagnostics in automatic packaging machines of high performances. These machines are composed of sub-assemblies, each embodying one or more mechanisms for reciprocal or intermittent motion, designed to achieve the proper motion of the output link, acting on the product. Unfortunately, due to mechanism vibrations, the actual motion may be quite different from the theoretical one. These vibrations are excited by variable forces, such as inertia forces, and internal shocks which occur in the kinematic pairs with backlash when contact forces reverse [1-3]. Joint wear causes backlashes to increase and more intense shocks to take place. These effects may produce stronger deviations of the actual motion from the theoretical one and, consequently, unacceptable product quality and poor production; in addition, higher accelerations and dynamic overloads may arise. In this kind of mechanism, mechanical breakage is very infrequent, so the predominant aim of condition monitoring is preventing the mechanism from the above improper conditions.

In this context, the best strategy would be to measure the output motion, which can be directly related to the mechanism functional limits and to the actual inertia forces. Moreover, mathematical models of the mechanism can be easily used as a diagnostic tool [3].

However, in automatic machines, as well as in many other engineering applications, it is practically impossible to mount

transducers on the mechanism links during machine operation; as a matter of fact, monitoring and diagnostics are generally performed by analysing the machine casing vibrations [4, 5].

It is noteworthy that casing vibrations are excited by the forces transmitted by the mechanisms, whose dynamic behaviour is the result of numerous factors, including the kinematic and dynamic properties of the mechanism itself, external forces, parametric excitations, friction, backlash effects in joints and faults. However, the casing response is generally distorted with respect to mechanism forces because machine structures have complicated transfer functions, due to dispersion, multi-path transmission and reverberation phenomena. The effect of the transfer function (TF) between mechanism components and casing can be so important that information about faults might be partially or completely hidden in the casing vibration [6, 7], i.e. low sensitivity to faults and poor diagnostic capability might be the result. Besides, to correlate the casing vibration parameters to machine condition may be difficult, because of the result scattering between nominally identical machines in analogous health conditions [8, 9].

For the mentioned reasons, it is desirable to recover the actual quantities of interest - i.e. mechanism forces or motion - from the casing response. This can be carried out by means of an inverse-filtering technique [10], that consists of the experimental estimation of the TF between these quantities and the casing vibration. The TF estimate can be used in production to recover the desired functional quantities from the measurement of the casing vibration. Different approaches and implementations can be found in literature, including applications to reciprocating machinery [7, 9, 10], gear systems [11-13] and cam mechanisms [3-5, 14].

In the specific case of automatic machines, previous works [3-5] have shown that the actual motion of one of the mechanisms embodied in a sub-assembly can be satisfactorily recovered, but in some cases poor results may be produced by errors affecting the TF estimation. In particular, difficulties were found for sub-assemblies containing two mechanisms [14]. This work is a contribution to overcome the above mentioned problems and to assess an effective inverse-filtering technique. To this end, some estimators of the inverse filter have been considered and developed for the application to the specific case. The results are compared on the basis of experimental tests carried out on a subassembly containing two mechanisms, both in sound and faulted conditions. The capability of the TF estimators is firstly compared; the application of cepstral-smoothing [7, 9, 10] is then discussed for assessing the effectiveness of these techniques in order to increase the robustness of the inverse-filtering process.

2. INVERSE-FILTERING PROCESS

2.1. General outline. The various sources of excitation in the machinery produce both output link motion and casing vibrations. With reference to a specific sub-assembly embodying only one cam mechanism, the actual motion of the output link can be considered as the response of the mechanism to the input motion imposed by the curve manufactured on the cam working surface. On the other hand, the casing vibration can be considered as the response of the machine structure to the same excitation, though the path is now more complicated. Therefore, two transfer functions exist between the cam curve and, respectively, the output motion and the casing vibration: $H'(f) = Y_m(f) / X_0(f)$, and $H''(f) = Y_c(f) / X_0(f)$, where $X_0(f)$, $Y_m(f)$ and $Y_c(f)$ are the Fourier transforms of the cam curve, the output link acceleration and the casing acceleration at a specific location, respectively. Consequently, the TF between the acceleration of the output link and the casing, $H(f)$, can be defined as the ratio between $H''(f)$ and $H'(f)$:

$$H(f) = Y_c(f) / Y_m(f) = H''(f) / H'(f) . \qquad (1)$$

The complex inverse of this TF, $H_{inv}(f)=1/H(f)$, is the filter function (or inverse filter) [10] needed in order to recover the output acceleration by filtering the casing acceleration: $Y_m(f) = H_{inv}(f)\, Y_c(f)$.

Since the exact filter function $H_{inv}(f)$ is not known and its estimation is required, the following recovering technique was proposed [3, 14]. Preliminarily, the inverse filter is estimated for each individual machine, for example at the installation stage [Fig. 1(a)]: both the output link acceleration, $y_m(t)$, and the casing acceleration at a properly selected location, $y_c(t)$, are experimentally achieved; as an estimate of $H(f)$, the Frequency Response Function (FRF), $\hat{H}(f)$, is then evaluated considering the output link acceleration as the input; finally, the filter function estimate, $\hat{H}_{inv}(f)$, is obtained by complex inversion of the FRF. During machine working life this filter function is used for recovering the output acceleration [Fig. 1(b)]: only the acceleration of the selected point on the casing is periodically or continually picked up; the output link acceleration spectrum, $\hat{Y}_m(f)$, is then computed based on the casing acceleration spectrum, $Y_c(f)$, and the inverse filter estimate; finally, the time pattern of the output acceleration, $\hat{y}_m(t)$, can be recovered and analysed for monitoring and diagnostic purposes. This recovering operation is possible in any health condition on the reasonable hypothesis that the filter function is practically independent

of the faults that may take place.

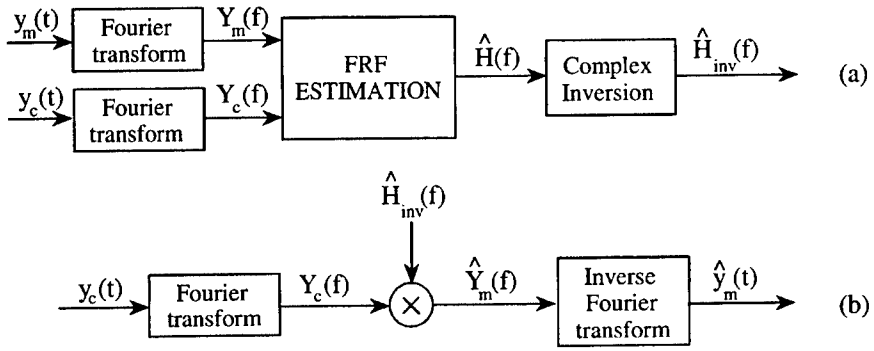

Fig. 1 - Inverse-filtering process. (a) Inverse filter estimation in the preliminary stage; (b) use of the inverse filter for the mechanism motion estimation in production.

It was noted in [3] that the above described technique is unable to properly restore the first cam revolution harmonics due to the fact that the casing response is generally very low in that frequency range and consequently the FRF estimation is poor. However, it was found that the first harmonics are almost insensitive to mechanism conditions; in fact, they essentially describe the theoretical pattern of output acceleration, while the superposed vibrations are due to higher-frequency components. Thus, the output acceleration spectrum can be recovered by copying lower components from an output acceleration spectrum measured and stored in the preliminary stage, and by recovering only higher components by the above described process of Fig. 1(b), see [3]. In the case considered in this paper, this copying operation concerns the range 0 to 40 Hz, containing the first four revolution harmonics.

2.2. Transfer function estimation. FRF measurements are the base of several techniques for the frequency domain identification of the dynamic characteristics of structural systems. They are employed to such technologies as experimental modal analysis, structural systems identification, and force determination to name a few. In the strict sense of the term, the FRF can be defined only for a linear, time invariant system, so it cannot be defined for the system under consideration. However, since the purpose is not the accurate system identification but the approximate signal recovery, the use of the FRF can be admissible. An additional cause of errors is that the casing response is generally affected by vibrations due to other mechanisms,

as occurs in particular when two or more mechanisms are embodied in the same sub-assembly [14]. Also, measurement and computational errors are present.

For a generic linear time invariant system, in the case of single input and single output (SISO), the true FRF is defined as $H_0(f)=Y(f)/X(f)$, where $X(f)$ and $Y(f)$ are respectively the Fourier transforms of the input and output signals [15]. Several FRF estimation techniques have been proposed in literature in order to minimize the error effects: estimates obtained with Least Square techniques (i.e. H_1 and H_2), with Total Least Square Techniques (i.e. H_v) and by means of Average Methods (i.e. H_3 and H_4) [16-18]. The most popular estimation methods for uncorrelated input and output noise are [16]

$$H_1(f)=\frac{S_{xy}(f)}{S_{xx}(f)}, \qquad H_2(f)=\frac{S_{yy}(f)}{S_{yx}(f)}, \tag{2}$$

where $S_{xx}(f)$ and $S_{yy}(f)$ are the autopower spectra of the input and output, respectively, $S_{xy}(f)=E[X^*(f)Y(f)]$ is the crosspower spectrum (the symbol $E[\cdot]$ denotes the expectation operator) and $S_{yx}(f)$ the complex conjugate of $S_{xy}(f)$. The estimator H_1 is the least square solution for the true FRF which minimises the bias effects of output noise; conversely, the estimator H_2 minimises the effects of input noise [16]. It should be noted that the estimator H_2 is more accurate at the resonances because the output signal to noise ratio (SNR) is high, so that the noise to be minimised is that which affects the excitation. On the contrary, at the anti-resonances the better estimator is H_1 and H_2 overestimates the true FRF substantially.

As the assumption that errors are confined to the input or the output signal is usually unrealistic, other techniques have been proposed. Among them, the H_V technique [17] aims to minimize the total squared error on both input and output and proved to be effective in many circumstances. Besides, according to the observation that H_1 and H_2 are respectively a lower and upper bound estimators of H_0, new estimators defined as their arithmetic mean, H_3, and geometric mean, H_4, were proposed [16, 18]:

$$H_3(f)=\left(H_1(f)+H_2(f)\right)/2, \qquad H_4(f)=\sqrt{H_1(f)\cdot H_2(f)}. \tag{3}$$

It is worth noting that the phase of estimators H_1 and H_2 is the same and, consequently, this phase is also the one of estimators H_3 and H_4.

Since the H_V estimator reduces to H_4 for SISO systems [17], and the application of other estimators proposed in literature does not

seem suitable in the present case, only the results obtained by using estimators H_1, H_2, H_3 and H_4 were compared in this work.

2.3. Cepstral smoothing. The cepstral smoothing [9, 10] of a signal is performed by applying a window to the signal complex cepstrum, $c(\tau)$ - i.e. the inverse Fourier transform of the logarithm of the signal spectrum - in order to extract from the signal only the low-quefrency information. In details, the smoothed complex cepstrum, $c_{sm}(\tau)$, is obtained as: $c_{sm}(\tau)=c(\tau)\cdot w(\tau)$, where $c(\tau)$ is the complex cepstrum computed on the signal spectrum $X(f)$, after phase unwrapping, and $w(\tau)$ is the cepstral window which eliminates the high-quefrency components. By coming back to the frequency domain, a smoothed version of the spectrum, $X_{sm}(f)$, is obtained, as windowing the cepstrum is equivalent to a smoothing operation in the frequency domain. The use of a window function other than the rectangular one is needed in order to avoid discontinuity in the cepstrum and related spectrum errors at high frequencies [9]. If only smoothed magnitude is required, the original phase must be used.

Cepstral smoothing was applied in literature both to the TF and the casing response [7, 9, 10, 13] in order to improve the robustness of the inverse filter. In the case of automatic machines, it was found [14] that the complex inversion of the FRF may produce poor results at those frequencies where the amplitude is very low; in this case, cepstral smoothing could make it possible to overcome the problem.

3. EXPERIMENTAL RESULTS AND DISCUSSION

Tests were carried out on a sub-assembly mounted on a complete machine, set-up for normal operation. This sub-assembly contains two cam mechanisms acting on the same output link, in order to give it two motions: a reciprocal translating motion and a reciprocal rotational motion around the link axis. Thus the motions of both mechanisms contribute to the case vibration, possibly causing difficulties in recovering one of the motions, as indicated by the results presented in [14]. This paper only concerns the recovery of the translating motion. Such a motion is obtained by means of the mechanism of Fig. 2, made up of a cylindrical cam and a follower system composed of a lever with two rollers which engage the cam rib, a small connecting rod and the output link acting on the product.

The results deal with two health conditions: sound condition and artificially increased backlash between the cam and rollers of the mechanism for the translating motion. The backlash in the latter condition - simulating the typical fault of this type of machines, i.e.

wear in joints - was about twelve times greater than in the first: it was judged to be a limit condition for production, so that maintenance is required as soon as possible.

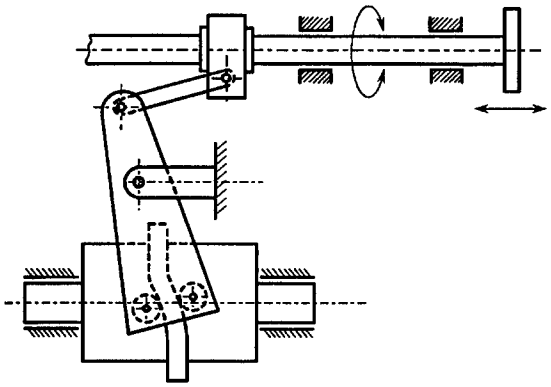

Fig. 2 - Schematic of the mechanism for reciprocal translating motion.

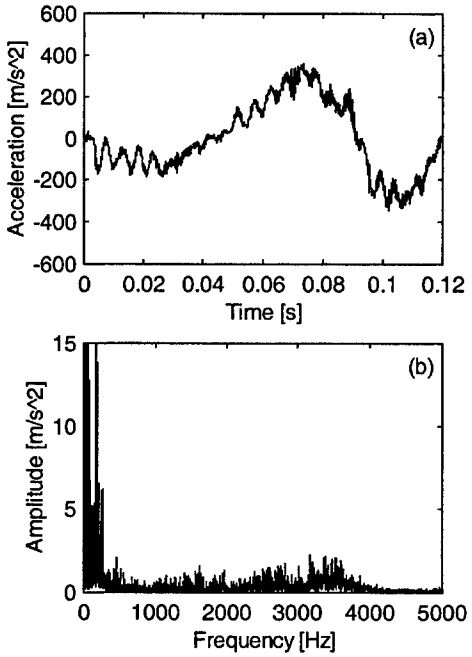

Fig. 3 - Measured output link acceleration in sound conditions. (a) Time pattern; (b) amplitude spectrum.

The output link acceleration was measured using an accelerometer, mounted at the extremity of the output link with its

sensitivity axis coincident with the link axis, while the casing acceleration was picked up next to the lever bearings by means of a second accelerometer; moreover a one-per-cam revolution tachometer signal was collected by an inductive proximity probe.

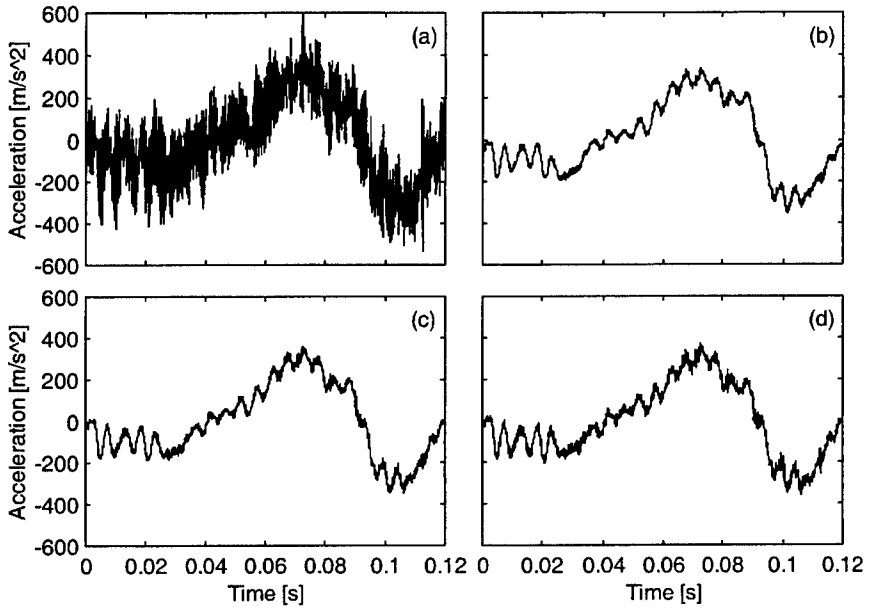

Fig. 4 - Output link acceleration in sound conditions recovered by means of inverse filters estimated through various algorithms: (a) H_1, (b) H_2, (c) H_3, (d) H_4.

Figure 3(a) shows the time pattern of the measured output link acceleration, corresponding exactly to one machine cycle (one cam revolution) and beginning at the bottom of the output link stroke. It is worth noting the presence of oscillations superimposed to the theoretical acceleration, produced by the internal shocks occurring when the roller hits the cam surface; this happens at the beginning of the motion and, during the motion, when the inertia force direction reverses (at about 50 and 95 ms), the backlash is traversed and the contact side between rollers and cam rib changes. Figure 3(b) shows the amplitude spectrum of the same signal, computed over a time pattern corresponding exactly to five cam revolutions with rectangular window (as well as the other spectra presented in this paper). The low-frequency components exceed the diagram amplitude range, as the scale is set with the aim of showing the high-frequency components more clearly.

The recovery procedure described in Sect. 2.1 was applied. The FRF between the output link acceleration and the casing acceleration was estimated for the mechanism in sound condition by means of the autopower and crosspower spectra evaluated over 20 averages, in the range 0-5 kHz, using Hanning window and frequency resolution of 1.5 Hz (blocksize of 8192 points). Since only data acquired at the maximum cam speed of 500 rpm were employed, the inverse-filtering process may give bad results at different speeds. However, properly recovering the output link motion only at one particular speed, taken as reference, may be enough for diagnostics. In other tests [3], on the contrary, these spectra were evaluated by averaging data relative to several cam speeds, in order to obtain an inverse filter useful for different speeds, with the drawback of longer test time.

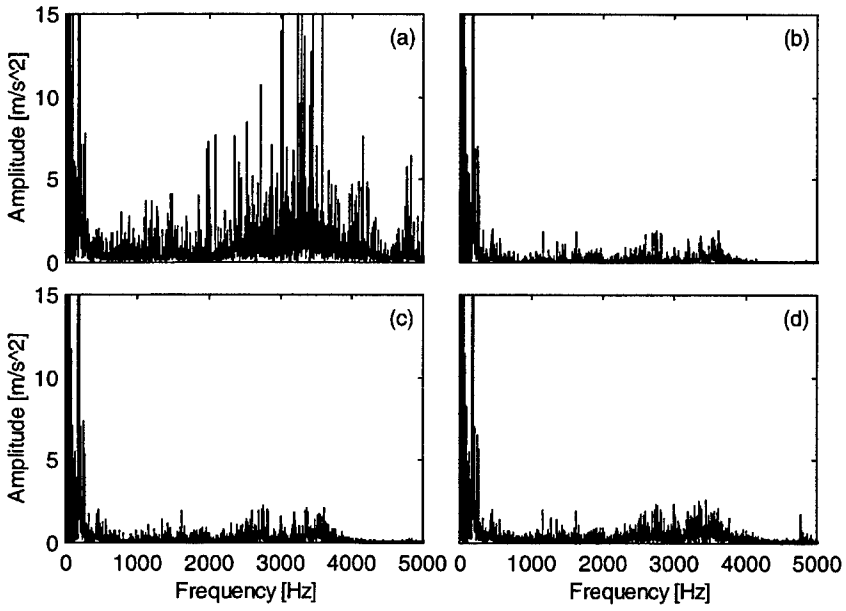

Fig. 5 - Amplitude spectrum of the output link acceleration in sound conditions, recovered by means of inverse filters estimated through various algorithms: (a) H_1, (b) H_2, (c) H_3, (d) H_4.

The capability of the FRF estimators mentioned in Sect. 2.2 is assessed by comparing the output link acceleration recovered by means of the related inverse filters (Figs. 4 and 5) to the acceleration directly measured in sound conditions (Fig. 3). Estimator H_1 produces completely unsatisfactory recovery [Fig. 4(a)] because the FRF is underestimated and consequently causes the inverse filter and the

recovered spectrum to assume incorrectly high amplitude over wide frequency ranges [Fig. 5(a)]. The other estimators give better results. The recovered acceleration waveforms [Figs. 4(b)-(d)] are quite good; deviations from the measured waveform are observable mainly at 35 to 50 ms, where the recovered waveforms exhibit oscillations of higher amplitude. Moreover, the amplitude relationships between the oscillations at 0 to 25 ms and 95 to 120 ms are altered by using H_2, while a satisfactory recovery is obtained through H_3, in spite of a slight disagreements in the oscillation amplitude. In addition, the high-frequency vibrations superimposed to the time pattern are rather well recovered only by means of H_4; in fact, the amplitude spectra recovered by H_2 and H_3 are globally underestimated, while the spectrum obtained through H_4 is rather good [Figs. 5(b)-(d)]. As general results, the application of H_4 gives the most satisfactory recovery in sound conditions, while the use of H_3 produces results of intermediate quality between H_2 and H_4.

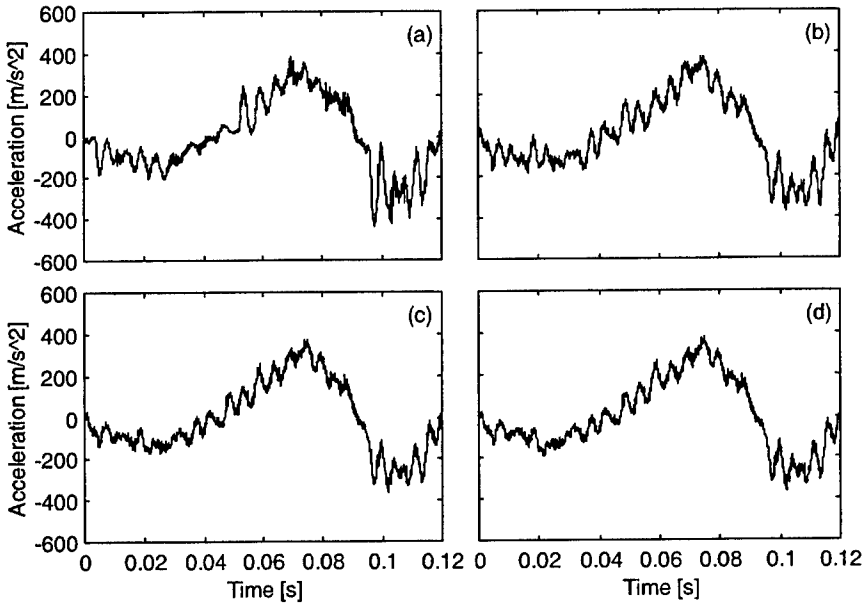

Fig. 6 - Output link acceleration in the case of increased backlash. (a) Measured pattern. Recovered patterns using algorithm H_4: (b) without smoothing; (c) with 1/2-blocksize cepstral smoothing; (d) with 1/4-blocksize cepstral smoothing.

Similar results about the applications of the estimators were found in the case of increased backlash; however the recovery is not so

good as in sound conditions, as shown by Figs. 6(a)-(b), comparing the measured output member acceleration and the recovered one by means of H_4. In particular, the important oscillations that take place at about 50 ms and between 90 to 115 ms are recovered with lower amplitude; in addition, the amplitude of the oscillations at about 18 ms, between 30 to 50 ms and 80 to 90 ms is overestimated in the recovered pattern. These deviations are produced by inverse filter errors which mainly affect the frequency range 150 to 270 Hz, that appears to be a resonance band of the mechanism [Figs. 7(a)-(b)].

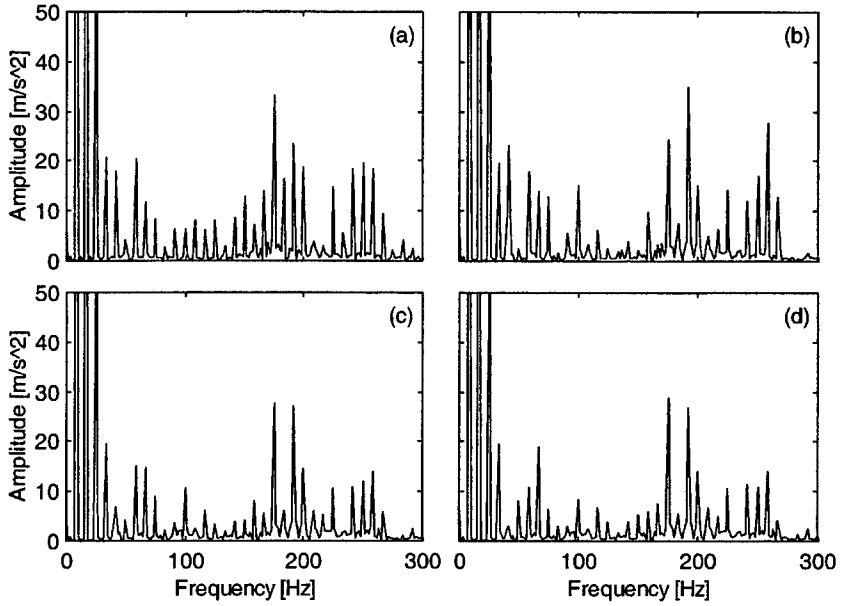

Fig. 7 - Amplitude spectrum of the output link acceleration in the case of increased backlash. (a) Measured pattern. Recovered patterns using algorithm H_4: (b) without smoothing; (c) with 1/2-blocksize cepstral smoothing; (d) with 1/4-blocksize cepstral smoothing.

The cepstral smoothing was applied in [9] with the aim of evaluating a robust inverse filter, able to recover waveforms of rather simple shapes, and scarcely affected by the TF variability among nominally identical machines, as well as errors in transducer locations. In that work, not only the TF is smoothed, but also the casing response spectrum employed for the source waveform recovery; in addition, a quite narrow cepstral window seems to be used. On the other hand, the application considered in the present paper has different needs, as the objective is to accurately recover a link motion pattern of

complicated shape; so the evaluation of the inverse filter for each individual machine is required and the use of the measured casing response - without smoothing - is suitable. Thus, according to the procedure described in Sect. 2.3, the cepstral smoothing of the magnitude of the FRF estimated in sound condition through algorithm H_4 has been carried out, in order to eliminate only the narrow peaks and dips, which may be affected by localized but important estimation errors.

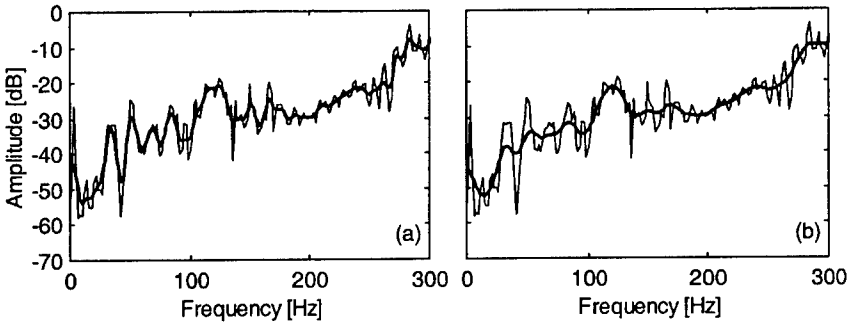

Fig. 8 - FRF estimated by means of algorithm H_4 in sound conditions. (a) Without smoothing (thin line) and using 1/2-blocksize cepstral smoothing (thick line); (b) without smoothing (thin line) and using 1/4-blocksize cepstral smoothing (thick line).

The length of the cepstral window must be properly set, taking into account that too narrow windows would cause the loss of meaningful information and, consequently, unacceptable alterations of the recovered waveform. Figure 8 compares the original FRF with the smoothed versions obtained applying Hanning cepstral windows of length equal to 1/2 and 1/4 of the blocksize (4096 and 2048 points, respectively). The two smoothed FRF's exhibit meaningful differences only in the low frequency range 0-160 Hz, where quite wide peaks and dips are present; the use of 1/2-blocksize window appears to be suitable, while the 1/4-blocksize window seems to introduce excessive simplifications in the low-frequency range. This is verified by considering the effects of the cepstral smoothing on the recovered signals. In the case of increased backlash, the 1/2-blocksize smoothing produces significant improvement in the time waveform [Fig. 6(c)], reducing the overestimation of the oscillation amplitude at about 18 ms and in the zones 30 to 50 ms and 80 to 90 ms; this is the consequence of the improvement of the spectrum recovery [Fig. 7(c)] chiefly in the range 150 to 270 Hz. On the other hand, the 1/4-blocksize smoothing does not introduce further improvements, but it conversely gives

errors in the 40 to 80 Hz range of the recovered spectrum [Fig. 7(d)], where the relationships between component amplitude are strongly altered with respect to the measured spectrum; the reason is that the FRF is excessively smoothed in that range. In sound conditions it has been shown that the recovery without smoothing is satisfactory; the cepstral smoothing does not introduce meaningful changes, but only a slight improvement at 25 to 50 ms. Besides, the phase smoothing does not give significant advantages in the considered tests.

4. CONCLUSIONS

This paper presents an inverse-filtering technique for the in-service recovery of the motion of the output link in mechanisms for reciprocal or intermittent motion, used in high performance packaging automatic machines. In this case, waveforms of complicated shape have to be accurately recovered - taking into account TF differences between nominally identical machines - in order to directly assess health condition and obtain diagnostic information.

On the basis of experimental results concerning a sub-assembly embodying two cam mechanisms, the effectiveness of different processing options is discussed with the aim of improving the robustness of inverse filter and reducing estimation errors. In particular, the capability of some FRF estimators is firstly compared and the application of cepstral smoothing is then discussed. Satisfactory recovery both in sound and in faulted conditions is obtained by means of algorithm H_4, while the cepstral smoothing of the FRF magnitude produces significant improvement, particularly in faulted conditions, on condition that the length of the cepstral window is properly set. In fact, too narrow windows may cause the loss of meaningful information and consequent alterations of the recovered waveform.

As a final remark, the proper selection of the FRF estimation technique appears to be essential for correct waveform recovery, while cepstral smoothing may give significant improvement, but it may not compensate relevant errors due to FRF estimation.

The application of the proposed technique to other mechanisms presenting faults of different severity is needed in order to establish its general effectiveness.

REFERENCES

1. Dresner, T.L. and Norton, R.L., Cam Dynamics and Modeling. In *Modern Kinematics: Developments in the Last Forty Years*, ed. A. G. Erdman, John Wiley, New York, 1993, 305-312.

2. Koster, M.P., *Vibrations of Cam Mechanisms*, MacMillan, London, 1974.
3. Dalpiaz, G. and Maggiore, A., Monitoring Automatic Machines. *Mechanical Systems and Signal Processing*, 1992, **6**, 517-534.
4. Dalpiaz, G. and Rivola, A., Fault Detection and Diagnostics in Cam Mechanisms. *Proceedings of the 2nd International Symposium on Acoustical and Vibratory Surveillance Methods and Diagnostic Techniques, Senlis, France*, 1995, 327-338.
5. Dalpiaz, G. and Rivola, A., Condition Monitoring and Diagnostics in Automatic Machines: Comparison of Vibration Analysis Techniques. *Mechanical Systems and Signal Processing*, 1997, **11**, 53-73.
6. McFadden, P.D. and Smith, J.D., Effect of Transmission Path on Measured Gear Vibration. *Journal of Vibration, Acoustics, Stress, and Reliability in Design*, 1986, **108**, 377-378.
7. McCarthy, D.J. and Lyon, R.H., Recovery of Impact Signatures in Machine Structures. *Mechanical Systems and Signal Processing*, 1995, **9**, 465-483.
8. Dalpiaz, G. , Maggiore, A. and Meneghetti, U., Monitoring Cam Mechanisms by Vibration Analysis. *Atti XI Congresso Nazionale AIMETA, Meccanica delle macchine, Trento, Italy*, 1992, 133-138. (In Italian).
9. Kim, J.T. and Lyon, R.H., Cepstral analysis as a tool for robust processing, deverberation and detection of transients. *Mechanical Systems and Signal Processing*, 1992, **6**, 1-15.
10. Lyon, R.H., *Machinery Noise and Diagnostics*, Butterworths, Boston, 1987.
11. Umezawa, K., Houjoh, H. and Maki, H., Estimation of the Vibration of In-Service Gears by Monitoring the Exterior Vibration. *JSME Int. Journal*, 1988, **31**, 588-592.
12. Dalpiaz, G. and Meneghetti, U., Monitoring Fatigue Cracks in Gears. *NDT&E International*, 1991, **24**, 303-306.
13. Chai, J. and Lyon, R.H., Determination of Component Motions in a Motor-Operated Valve Using Housing Vibration. *Mechanical Systems and Signal Processing*, 1996, **10**, 113-123.
14. Dalpiaz, G., Rivola, A. and Meneghetti. U., Use of Filtering Function for Machine Health Monitoring. *Proceedings of an International Conference on Condition Monitoring, Swansea, UK*, 1994, 217-228.
15. Oppenheim, A.V. and Schafer, R.W., *Discrete-time Signal Processing*, Pretice-Hall Int., 1989.
16. Mitchell, L.D., Improved Methods for the Fast Fourier Transform (FFT) Calculation of the Frequency Response Function. *Journal of Mechanical Design*, 1982, **104**, 277-279.
17. Rocklin, G.T., Crowley, J. and Vold, H., A Comparison of H_1, H_2, and H_v Frequency Response Functions. *Proceedings of the 3rd International Modal Analysis Conference, Orlando, FL*, 1985, 272-278.
18. Zhang, L. and Yao, Y., Advances of Frequency Resonse Function Estimation in Modal Analysis. *Proceedings of the 6th International Modal Analysis Conference, Kissimmee, FL*, 1988, 107-112.

Determination of dynamic material model parameters by means of a combined numerical-experimental technique

Patricia VERLEYSEN[1] and Joris DEGRIECK[2]

[1] *Doctor-Assistent, Ghent University, Faculty of Engineering, Department of mechanical Construction and Production, Sint-Pietersnieuwstraat 41, 9000 Gent, Belgium*
[2] *Full Professor, Ghent University, Faculty of Engineering, Department of mechanical Construction and Production.*

abstract

A material model to describe the dynamic tensile behaviour of quasi brittle materials, as concrete, was developed within the framework of damage mechanics. The constitutive equations contain some material parameters. The presented contribution deals with the determination of these parameters. An automatic procedure has been worked out. By means of a combined experimental-numerical technique the start-values of the parameters are optimized. The experimental results, needed for the determination of the material constants, are obtained by split Hopkinson bar tests. For the numerical simulations the constitutive equations describing the dynamic material behaviour have been implemented in a finite element program.

1. Introduction

For the development of the material models or the determination of material constants experimental results are needed. In medium to high strain rate (strain rates from 1 to 5000 s^{-1}) material testing [1] split Hopkinson bar setups [2] (or Kolsky apparatus[3][4]) are often used. This is because practical test execution is relatively simple and because Hopkinson tests give rise to straightforward interpretation of the test results [5][6]. The test method was originally designed for metallic materials; materials showing large deformations upon rupture. Under some conditions the stress and the deformation in metallic specimens during an experiment are assumed to be uniaxial and homogenous. As can be proved, in that case the history of stress, strain and strain rate in the specimen during an experiment can be obtained very easily.

However, for non-metallic materials the test technique has some limitations. When used for (quasi-)brittle materials the experimental setup and the extraction of the signals have to be adapted. One reason for this is the low

accuracy of the test method in the region of small strains [7]. Another reason is a consequence of the softening behaviour exhibited by quasi-brittle materials; the deformation will be highly localised in a small zone of the specimen. Consequently test conditions deviate from ideal Hopkinson bar test conditions. In such case the classical test setup and treatment of the signals do not provide information concerning the actual distribution of stress and deformation along the specimen. The classical treatment of the signals does not allow verification of the assumptions made on behalf of the stress and deformation in the specimen. Verification of the assumptions is only possible by measuring on the specimen itself to obtain the deformation over the length of the specimen or by performing a wave analysis in the specimen by means of numerical simulations. We chose the latter method. By means of the finite element method we simulated the deformations and stresses in the specimen. Time histories of stresses and strains at different places in a specimen were obtained by means of dynamic simulations with an appropriate material model and well-determined material constants.

After a short review of the split Hopkinson bar test technique and the constitutive equations used to describe the dynamic tensile behaviour of quasi-brittle materials, attention is focussed on the extraction of the material constants.

2. Test method

2.1. The split Hopkinson bar setup

Figure 1 provides a schematic representation of a typical split Hopkinson bar setup for tensile testing. The experimental setup of a split Hopkinson bar test consists of two long bars, an input bar and an output bar, between which a specimen is sandwiched. In the setup used for our experiments, the input bar has a length of 2.25 m, the output bar is 1.45 m long. Both Hopkinson bars are aluminium bars with a diameter of 25 mm. The choice of the Hopkinson bar material and dimensions is based on numerical simulations [8].

The anvil at the outer end of the input bar is hit by an impactor, which is generally pneumatically accelerated. A tensile strain wave ε_i, the so-called incident wave, is thus generated and propagates along the input bar towards the specimen. Upon reaching the specimen the wave is partly reflected back to form the reflected wave ε_r, and is partly transmitted to form the transmitted wave ε_t. The strains associated with the waves ε_i, ε_r and ε_t are most often measured by means of strain gauges. These strain gauges are located at well chosen points on the bars, away from the specimen.

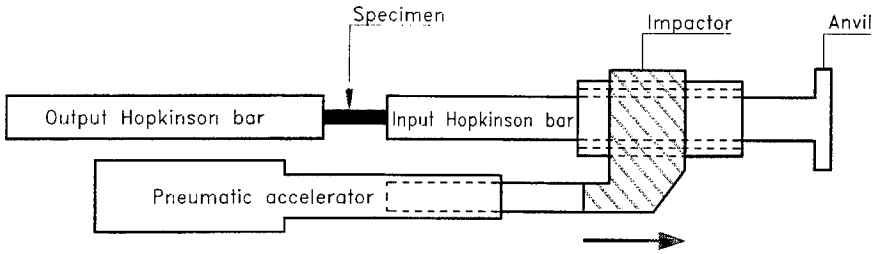

Figure 1

Experimental setup of a typical split Hopkinson pressure bar device. It consists of an input bar, the specimen and an output bar. Strain gages are used to measure the incident, reflected and transmitted waves.

2.2. Treatment of the signals

The strain signals have to be shifted, forward or backward, towards the interface planes with the specimen, in order to obtain forces and displacements at both ends of the specimen. It is very common to assume that the stresses and deformations are uniaxial and homogenous in the specimen [3][4]. In that case the history of the stress σ, the strain ε and the strain rate $\dot{\varepsilon}$ in the specimen can be obtained by :

$$\sigma(t) = \frac{A_s E_s}{A_p} \varepsilon_i(t) \tag{1}$$

$$\varepsilon(t) = -\frac{2 C_s}{L_p} \int_0^t \varepsilon_r(\tau) d\tau \tag{2}$$

$$\dot{\varepsilon}(t) = -\frac{2 C_s}{L_p} \varepsilon_r(t) \tag{3}$$

with A_s (A_p) the area of a section of the Hopkinson bars (specimen),
E_s the modulus of elasticity of the Hopkinson bars,
C_s the longitudinal wave propagation velocity in the Hopkinson bars,
L_p the specimen length.

The validity of formulas (1) to (3) limits the choice of test conditions, such as the specimen geometry and the length of the incident wave. In some cases the assumptions of homogenous stress and deformation in the specimen are never

fulfilled. Such is often the case when testing heterogenous materials as concrete or fibre reinforced materials; the specimen dimensions have to be large compared to the granulate or fibre size.

3. Numerical modelling

It is not the purpose of this paper to give a full description of the material model used to describe the dynamic behaviour of quasi brittle materials, only an overview of the implemented constitutive equations is given. More details concerning the material model can be found in [7].

The material model to describe the dynamic tensile behaviour of materials as concrete is developed within the framework of damage mechanics [9][10][11]. A *damage parameter* D is introduced; D describes the gradual degradation of the stiffness the material :

$$E = E_0(1-D) \;, \quad D = 1 - \frac{E}{E_0} \tag{4}$$

with E_0 the stiffness of the undamaged material and E the stiffness reduced by damage of the material. The value of D varies from 0 for the undamaged material to 1 when the stiffness of the material is completely lost. The stress can be calculated from :

$$d\sigma = E_0(1-D)d\varepsilon - E_0\varepsilon d(D) \tag{5}$$

where dε is the strain increment and d(d) the increase of the damage.
The evolution of the damage parameter is described by a *damage law*. When examining the damage mechanisms in quasi-brittle materials it seems a proper approach to split the damage evolution into two parts : a part describing the nucleation of damage and a part describing the growth of existing damage. For the nucleation of the damage as a function of the stress σ the following function is proposed :

$$\dot{D}_{nucleatie} = \frac{\partial D_{nucleatie}}{\partial t} = C1\left[\left(\frac{\sigma}{\sigma_{max}}\right)^2 - \left(\frac{\sigma_{stat}}{\sigma_{max}}\right)^2\right] > 0 \tag{6}$$

C1 is a material constant. σ_{stat} is the value of the so-called *static curve*. The static curve gives the relation between the stress and damage during a static tensile test. σ_{max} is the maximum value of the stress reached in a static experiment. During a dynamic experiment the value of the stress σ accorded with a certain damage can be greater than the value of σ_{stat} of the static curve;

the point (D, σ) is above the static curve. The damage development can't follow the stress; in that case the damage will grow. The higher the strain rate, the higher the difference between σ_{stat} and σ, so the higher will be the damage growth. Thus, although the strain rate does not appear explicitly in the constitutive equations the proposed material model is strain rate dependent.
The propagation term is quite similar to the nucleation term :

$$\dot{D}_{propagatie} = \frac{\partial D_{propagatie}}{\partial t} = C7 \cdot \left[\left(\frac{\sigma}{\sigma_{max}} \right)^2 - \left(\frac{\sigma_{stat}}{\sigma_{max}} \right)^2 \right] \cdot D > 0 \qquad (7)$$

C7 is a dynamic material parameter.
The total damage growth consists of the sum of the nucleation (formula (6)) and propagation (formula (7)) term :

$$\dot{D} = \dot{D}_{nucleatie} + \dot{D}_{propagatie} \qquad (8)$$

The constitutive equations (5) and (8) describing the dynamic material behaviour have been implemented in a finite element program called "IMPACT". IMPACT is a one dimensional program using an unconditionally stable algorithm for the time integration [7]. The program allows simulation of one-dimensional wave propagation problems as arise in the Hopkinson experiment : the two Hopkinson bars and the specimen are modelled and the incident wave $\varepsilon_i(t)$ is applied to the beginning of the input bar.

4. Combined numerical-experimental technique

With numerical simulations knowledge of the dynamic characteristics of the specimen can only be obtained in an indirect way. Indeed, to simulate the wave propagation in the specimen during a Hopkinson test, knowledge of the constitutive equations is necessary. But, in most cases the experiments are performed to derive these constitutive equations.

This problem can be solved by a so-called "numerical-experimental" method [12][13][14]. This alternative procedure for the interpretation of the test results consists generally of the following steps :

1. suitable constitutive equations are assumed with well-chosen start-values of the constants,
2. during the experiment as much information as possible is gathered; velocities at the surface, histories of strain, ... Also the boundary conditions have to be precisely known,

3. with the assumed constitutive equations and constants a numerical simulation of the experiment is performed,
4. the numerical results are compared with the experimental observations. When the agreement is insufficient, step 3 and 4 have to be repeated with improved values of the constants used in the constitutive equations,
5. to verify the obtained constants and constitutive equations, other experimental configurations or other experimental observations can be simulated with the same material law.

The constitutive equations presented in section 3 contain two unknown constants : C1 and C7. With guess-values of those constants a numerical simulation of a Hopkinson experiment is performed. In the simulation the measured incident wave is applied on the beginning of the 1.45 m-long input bar with diameter 25 mm. These dimensions correspond with the real dimensions of the bar. With the considered length the extraction of the reflected wave is straightforward. In line of the first bar a specimen (with a length of 10 mm and diameter of 25 mm) and the output Hopkinson bar is modelled. The length of the output bar in the simulation is 1m, this is sufficiently long : during the time the incident tensile wave interacts with the specimen no other waves reach the specimen. A length of 1 m also allows the transmitted wave to be extracted from the simulation results in a direct way, without interference with other waves.

The incident wave, the wave reflected by and the wave transmitted through the specimen are measured during a Hopkinson experiment. All information (the strain rate, the strain and the stress in the specimen) derived directly from these signals using formulas (1) to (3) is based on assumptions concerning the homogeneity of stresses and deformations in the specimen and thus subject to errors. Therefor it is recommended not to use the stress, the strain or strain rate obtained by these formulas to implement the combined numerical-experimental method, but use directly the transmitted or reflected wave.
The information in the reflected wave is directly connected with the deformation of the specimen (see formula (3)). Together with the incident wave, the reflected wave allows the extraction of the stress history in the specimen. After all when the stress is homogeneous in the specimen, the following equation gives the same results as equation (1) :

$$\sigma(t) = \frac{A_s E_s}{A_p}(\varepsilon_i(t) + \varepsilon_r(t)) \qquad (9)$$

Since the reflected wave is connected with the deformation *and* stress in the specimen, we used the reflected wave to optimize the values of the material model parameters. The use of the reflected wave has another important advantage, explained in the next paragraph.

When testing plain microconcrete the process of the degradation of the specimen until fracture consumes very little time (± 50 μsec). After the specimen is broken the incident wave (which has a duration of ≈ 200 μsec) is completely reflected on the fracture surface. Only the part of the reflected wave corresponding to the time during which the specimen is not completely broken was used to optimise the parameters. The part of the wave after fracture of the specimen can be used to synchronise the simulated and experimentally measured waves. Figure 2 shows those two waves; when t>0.52 ms the specimen is broken, between t=0.47 ms and t=0.52 ms the specimen is degrading. The simulation is performed with start-values of the material parameters. This explains the bad correspondence between the simulated and experimental wave in the beginning.

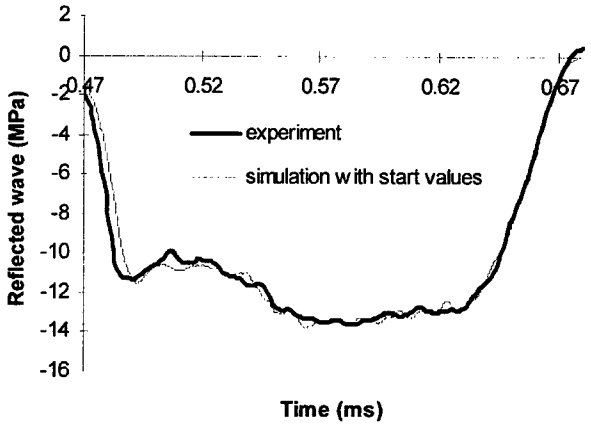

Figure 2
Measured and simulated history of the wave reflected by the specimen during a split Hopkinson bar experiment.

Figure 3 gives the part of reflected wave used for optimisation of the material constants. The experimental wave, the wave simulated with start values of the parameters, and the result after optimisation of the parameters is presented in this figure.

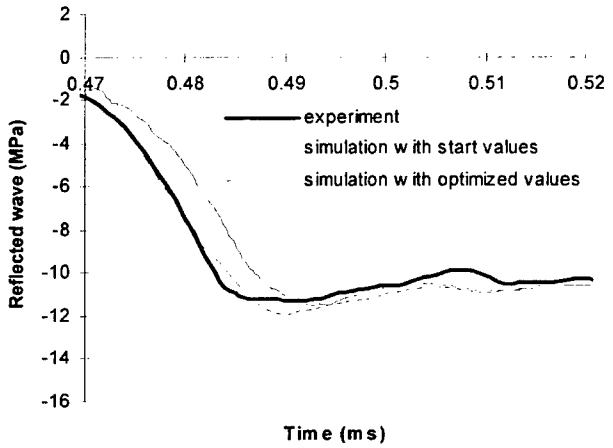

Figure 3
Part of the measured reflected wave taken into account for the extraction of the material parameters. Also simulations of that part of the reflected wave are presented; one is performed with start values of the parameter, the other with the values of the parameters after optimisation.

The optimisation of the constants is performed automatically; initial values of the constants are optimised without intervention of the operator. Therefore the program IMPACT for the simulation of the Hopkinson tests is incorporated in ODRPACK [15]. ODRPACK is a package of routines written for the iterative optimisation of constants and is based on the least squares method. Figure 4 gives the procedure schematically. After a first simulation with guess-values of the material constants a so-called goal function is calculated. This goal function is here the quadratic deviation between the simulated and the experimentally measured reflected wave. Subsequent simulations with adapted values of the constants are performed, every time the goal function is calculated, new values for the constants are proposed, ... that until the goal function reaches an acceptable minimum and thus the agreement between the experiment and the simulation is as good as possible. Afterwards, with the finally obtained values of the constants, the simulated transmitted wave is compared with the transmitted wave measured during the experiment.

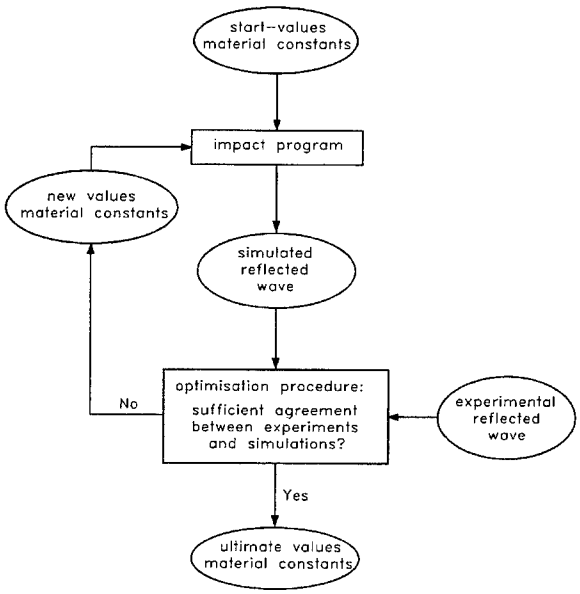

Figure 4
Schematic representation of the optimisation method of the material constants.

5. Results

5.1. Material

There are indications that the material model presented in section 3 can be used for quite a lot of quasi-brittle materials. It is sufficient to use the static curve for the considered material in equation (6) and (7). Also the combined numerical-experimental technique presented in section 4 is not bounded with a specific material. The material considered for the results of the technique presented in this contribution is microconcrete. Microconcrete is a concrete on scale : the size of the granulates is limited (in our case < 3 mm).

5.2. Parameters

Table 1 gives the values of the constants C1 and C7 extracted from four experiments with the above described automatic procedure. The experiments 1 to 4 were executed with different histories of the strain rates during the experiment. As can be seen the value for C1 and C7 does not vary much from experiment to experiment. The final simulations to obtain the stresses, strains,

strain rates, damage, ... in the specimen were performed with mean values of C1 and C7.

experiment	C1	C7
exp1	11777	45358
exp2	10676	48321
exp3	13727	37461
exp4	14727	53823
mean value	12726	46240

Table 1

Values for C1 and C7 obtained with the automatic extraction procedure for four experiments.

Figure 5 gives the stress as a function of strain obtained with the equations (1) and (2) and the simulated curve. As can be seen, the agreement between the numerical simulation and the experimental result is very good. More simulations and more details of these simulations are presented in [7].

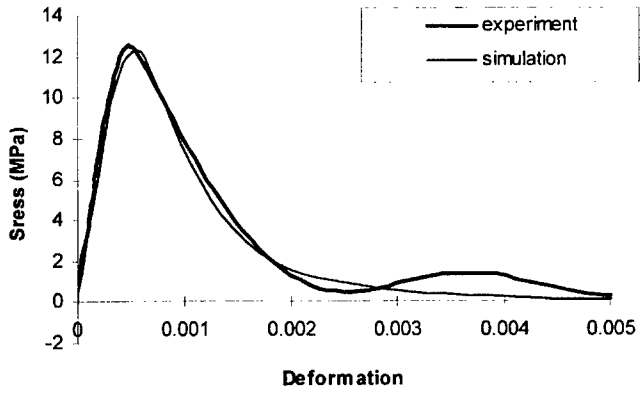

Figure 5

Simulated and experimental history of the stress as a function of the deformation in a specimen during a split Hopkinson bar tensile experiment.

6. Conclusions

In this contribution a combined numerical-experimental method is presented. It has been found that the combination of experiments and numerical simulations is an adequate and essential tool for material modelling. The technique allows an optimal use of experimental data.

The necessary experimental results are here provided by split Hopkinson bar tests. After a short description of the test method, the constitutive equations needed to model the dynamic behaviour of some quasi-brittle materials are given.

The connection between experiments and simulations allows determination of material model parameters. An algorithm was worked out to optimise the parameters automatically. The results of this algorithm are given for a microconcrete. With the so-determined values of the parameters an excellent agreement between experiments and simulations is obtained. So, it can be concluded that the presented constitutive equations with the material parameters give a valid description of the material behaviour for the considered range of strain rates.

Once the parameters are determined the numerical simulations provide a valuable source of information; information of the material behaviour can be obtained in other circumstances than the experiment.

7. References

1. Davies, E., A Critical study of the Hopkinson pressure bar. Philosophical Transactions A, 1948, **240**, 375-457.

2. Hopkinson, B., A method of measuring the pressure in the deformation of high explosives by the impact of bullets. Phil. trans. Roy. Soc. of London, 1914, Series A, **213**, 437-452.

3. Kolsky, H., An investigation of the mechanical properties of materials at very high rates of loading. Proc. Phys. Soc., 1949, Sec. B, **62**, 676-700.

4. Kolsky, H., Stress waves in solids. New York Dover Publications Inc., 1963.

5. Ruiz, C. and Mines, R.A.W., The Hopkinson pressure bar : an alternative to the instrumented pendulum for Charpy tests. International Journal of Fracture. 1985, **29**, 101-109.

6. Zhao, H., Analyse de l'essai aux barres d'Hopkinson-Application à la mesure du comportement dynamique des matériaux. Thèse doctorale de

l'Ecole nationale des Ponts et Chaussées, 1992.

7. Verleysen, P., Experimental investigation and numerical modelling of the dynamic behaviour of quasi-brittle materials and fibre reinforced quasi-brittle materials. Doctoral dissertation University of Gent, 1999 (in Dutch).

8. Verleysen P, Degrieck J. Dynamic simulation of radial stress histories in Hopkinson test specimens. Proceedings Acomen 98 1, 1-12, 1998.

9. Kachanov, L.M., On the creep rupture time. Izv. AN SSSR, Otd. Tekhn. Nauk., 1958, **8**, 26.

10. Krajcinovic,D, Damage mechanics. Mech. mat. 1989, **8**, 117-197.

11. Rice, J.R., Continuum mechanics and thermodynamics of plasticity in relation to microscale deformation mechanisms, in A.S. Argon, ed.. Constitutive Equations in Plasticity, MIT Press, Cambridge, MA, 23.

12. Zukas, J.A., Nicholas T., Swift, H.F., Greszczuk, L.B. and Curran, D.R., Impact Dynamics, John Wiley and Sons, 1982, 452 p..

13. De Wilde, W.P., Identification of the rigidity of composite systems by a mixed numerical/experimental method. Mechanical identification of composites, Ed. Vautrin A., Sol H., Elsevier, 1990, 448 p..

14. Sol, H., Identification of the complex moduli of composite materials by a mixed numerical/experimental method. Composite Materials, Design and Analysis, Ed. De Wilde W.P., Blain W.R., Springer-Verlag, 1990, 576 p..

15. Boggs, T.P., Byrd, R.H., Rogers, J.E. and Schnabel, R.B., User's reference guide for ODRPACK version 2.01 software for weighted orthogonal distance regression. U.S. Department of Commerce National Institute of Standards and Technology. Gaithersburg, MD 20899, 1992.

STRUCTURAL DYNAMICS OF VIBRO-IMPACT SYSTEMS

V.I. Babitsky, A.M. Veprik
Department of Mechanical Engineering, Loughborough University
Loughborough, Leicestershire, LE11 3TU, England.

The systematic impact interactions within mechanical structures can excite their complex nonlinear resonant responses. An introduction of special functions, called periodic Green's functions, allows the regular analysis of these phenomena based on structural presentations without reference to differential equations. The paper reviews some results on the application of periodic Green's functions for analysis of resonances in vibro-impact structures. The results of analysis are supported by physical experiments.

INTRODUCTION

Multiple impact interactions of components of mechanical structures have a severe influence on their vibration and noise activity and load capacity. The collisions arise under variable load as a result of intermittent unilateral contact in connections, due to the backlashes in joints and kinematic pairs, during opening and closing of cracks etc. In some systems, an introduction of special impact structures: stops, bumpers, impact dampers is an effective method of vibration control.

Embedding of impact pairs into mechanical structures transforms the latter into strongly nonlinear systems. The systematic impact interactions of solids can excite complex nonlinear resonant responses of structures. The specific features of these resonances are concentration of high harmonics in their waveforms, dependence of the behaviour on parameters and initial conditions, and generation of essential forces of interaction.

An effective approach to analysis of these phenomena was developed with the use of special functions called *periodic Green's functions* (PGF) [1-3]. These are steady-state responses of interacting linear structures on periodic impulse excitation. The application of PGF makes it possible to obtain an exact solution for the problem of periodic impact interaction of linear substructures, to reveal the main features of their specific resonant behaviour and to develop efficient approximations for more complex substructures.

The *stitching method* used traditionally for the analysis of systems with impact interactions necessitates the knowledge of the *general solutions* for appropriate differential equations describing the motion between impacts [4]. Contrary to this, the PGF method produces similar solutions without referring to differential equations and can be applied even when the full mathematical model of the system is unknown. An exercise of the method requires the knowledge of frequency characteristics of contacting elements only, that can be obtained experimentally. If the mentioned differential equations of the system are available, their *particular solution* is enough for the total solution of periodic nonlinear problem.

FORMULATION OF THE PROBLEM

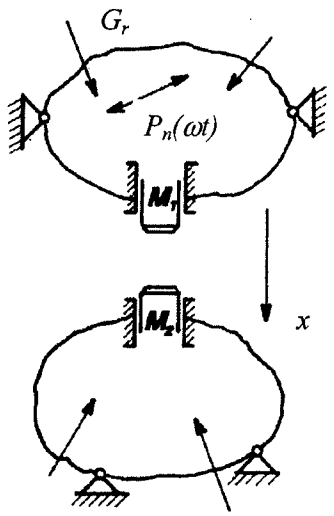

Figure 1

Let us consider two linear stationary structures 1,2 (Figure 1) loaded by constant forces G_r. The structures contact through the rigid bodies M_1 and M_2. The bodies perform one-dimensional T-periodic movements with collisions under external T_l periodic excitation $P_n(\omega t)\,(T_l = T/l = 2\pi/\omega$, where ω is an angular frequency, l is multiplicity of sub-periodic regime) applied to the arbitrary point of the systems. Let $L_1(j\omega)$ and $L_2(j\omega)$ be receptances of bodies in contact points, Δ is initial gap (the negative Δ corresponds to interference) resulted under action of static forces.

The force characteristic of vibro-impact interaction is defined by the function $\Phi[x(t),\dot{x}(t)]$, where $x(t)$ is the relative movement of impact pair elements. For periodic vibro-impact interaction with period $T = 2\pi l/\omega$ and the most intensive single impact interaction per period, we can present the force of impact interaction as a Fourier series:

$$F(t) = \Phi[x(t),\dot{x}(t)] = \sum_{m=-\infty}^{\infty} F_m \exp\left(\frac{jm\omega}{l}t\right), \tag{1}$$

where coefficients of Fourier series are as follows

$$F_m = \frac{1}{T}\int_0^T F(t)\exp\left(-\frac{jm\omega}{l}t\right)dt \tag{2}$$

The operator equations for absolute displacements of the contact elements can be written in the form:

$$x_1(t) = \sum_r L_{1r}(0)G_{1r} + \sum_n L_{1n}(s)P_{1n}(t) - L_{10}(s)F(t)$$

$$x_2(t) = \sum_r L_{2r}(0)G_{2r} + L_{20}(s)F(t), \quad s = j\omega.$$

Here the terms under the summation sign describe the static deformation of the elements. Subtracting the second equation from the first and initiating time from an impact, we obtain

$$x(t) = \vartheta(t+\tau) - L(s)F(t) \tag{3}$$

where $\vartheta(t) = \sum_r L_{1r}(0)G_{1r} - \sum_r L_{2r}(0)G_{2r} + \sum_n L_{1n}(s)P_{1n}(t)$,

$L(s) = L_{10}(s) + L_{20}(s)$, τ is time shift of the excitation relative to impact.

With taking (1) into account

$$x(t) = \vartheta(t+\tau) - \sum_{m=-\infty}^{\infty} L\left(\frac{jm\omega}{l}\right) F_m \exp\left(\frac{jm\omega}{l} t\right). \tag{4}$$

Putting (2) into (4) and changing the sequence of summation and integration, yields

$$x(t) = \vartheta(t+\tau) - \int_0^T \chi(t-\varsigma)\Phi[x(\varsigma), \dot{x}(\varsigma)]d\varsigma, \tag{5}$$

where

$$\chi(t) = \frac{1}{T}\sum_{m=-\infty}^{\infty} L\left(\frac{jm\omega}{l}\right)\exp\left(\frac{jm\omega}{l} t\right) \tag{6}$$

is *periodic Green's function.* This is a steady-state response of linear system on periodic excitation

$$\delta^T(t) = \sum_{\nu=-\infty}^{\infty} \delta(t - \nu T)$$

where $\delta(t)$ is Dirac function.

For stationary linear system with fractional-rational operator

$$L(s) = \frac{h_0 s^{2n-2} + h_1 s^{2n-3} + ... + h_{2n-2}}{d_0 s^{2n} + d_1 s^{2n-1} + ... + d_{2n}} = \frac{R(s)}{D(s)}$$

it is possible to sum the series (6) and obtain a finite function

$$\chi(t) = \sum_{k=1}^{2n} \frac{R(s_k)}{D'(s_k)} \frac{\exp(s_k t)}{1 - \exp(s_k T)} \qquad t \in (0, T]$$

where s_k are simple roots of characteristic equation $D(s) = 0$ [5].

ANALYTICAL SOLUTION

Examining the integral on the right-hand side of equation (5), we find using mean value theorem and assuming continuity of periodic Green's functions

$$\int_0^T \chi(t-\varsigma)\Phi[x(\varsigma), \dot{x}(\varsigma)]d\varsigma = \int_0^{\varepsilon} \chi(t-\varsigma)\Phi[x(\varsigma), \dot{x}(\varsigma)]d\varsigma =$$

$$= \chi[t - \varepsilon\theta(t)]\int_0^{\varepsilon} \Phi[x(\varsigma), \dot{x}(\varsigma)]d\varsigma = J\chi[t - \varepsilon\theta(t)], \quad 0 < \theta(t) < 1.$$

Here J is impulse of contact force, ε is small parameter.

Noting that $\varepsilon\theta(t) << T$, we have for continuous periodic Green's functions $\chi[t - \varepsilon\theta(t)] \approx \chi(t)$. For a momentary impact defined by Newton's hypothesis, the relation becomes an exact one and we have instead of (5) the finite expression

$$x(t) = \vartheta(t+\tau) - J\chi(t) \tag{7}$$

Supposing, for example, that $\vartheta(t+\tau) = a\cos(\omega t + \varphi)$, we find the unknown values of phase φ and impulse J from the impact condition:

$$x(0)=\Delta,\quad (1+R)M\dot{x}_{-}(0)=J, \tag{8}$$

where Δ is static gap (interference), R is restitution coefficient, $M=M_1M_2(M_1+M_2)^{-1}$, $\dot{x}_{-}(0)$ is a velocity just before an impact.

Applying conditions (8) to (7), we find

$$a\cos\varphi=\Delta+J\chi(0),\quad a\sin\varphi=-\frac{J}{\omega}\left[\dot{\chi}_{-}(0)+\frac{1}{(1+R)M}\right]$$

The solving of these equations yields

$$J=\frac{-\Delta\chi(0)\pm\sqrt{a^2\chi^2(0)-\frac{1}{\omega^2}\left[\dot{\chi}_{-}(0)+\frac{1}{(1+R)M}\right]^2(\Delta^2-a^2)}}{\chi^2(0)+\frac{1}{\omega^2}\left[\dot{\chi}_{-}(0)+\frac{1}{(1+R)M}\right]^2}, \tag{9}$$

$$\sin\varphi=-\frac{J}{\omega a}\left[\dot{\chi}_{-}(0)+\frac{1}{(1+R)M}\right],\quad \cos\varphi=\frac{\Delta+J\chi(0)}{a}. \tag{10}$$

Neglecting the damping in the system, we have from (9)

$$J=\frac{\Delta\pm a}{\chi(0)}.$$

STABILITY ANALYSIS

The disturbed motion can be written as follows

$$x(t)=a\cos\left[\omega t+\tilde{\varphi}(t)\right]-\tilde{J}(t)\chi(t), \tag{11}$$

where $\tilde{\varphi}(t),\tilde{J}(t)$ are slowly changing functions of time.

Using the first expression (10) as the reduced condition for the balance of work between the dissipative and exciting forces, we will formulate the energy condition for stability of periodic motion as follows [2]

$$\frac{d}{d\tilde{J}}\left\{\frac{\tilde{J}}{\omega a}\left[\dot{\chi}_{-}(0)+\frac{1}{(1+R)M}\right]+\sin\tilde{\varphi}\right\}_{\tilde{J}=J}>0 \tag{12}$$

Introducing two arbitrary slow functions in place of one, we will link them by an expression similar to the second equation in (10). Differentiating (12) and using this link, we obtain, taking account of (10)

$$J>\frac{-\Delta\chi(0)}{\chi^2(0)+\frac{1}{\omega^2}\left[\dot{\chi}_{-}(0)+\frac{1}{(1+R)M}\right]^2}. \tag{13}$$

Comparing (9) with the equation obtained, we can establish that the stability condition is satisfied only with the solution, which has the positive sign before the radical.

TWO COLLIDING BODIES

In the case of two colliding bodies under periodic excitation (Figure 2) two resonant modes were revealed as a result of analysis and confirmed by physical experiments (Figure 3) [6]. The motions of the bodies are shown in Figure 3 with thick line as $x_1(t)$ and thin line as $x_2(t)$.

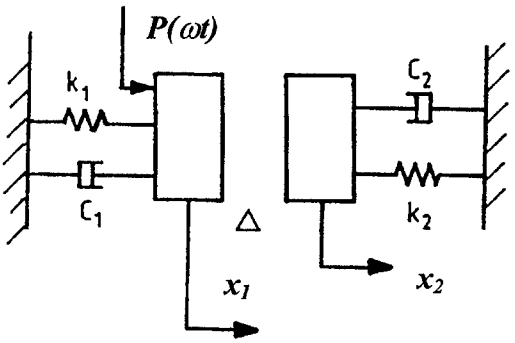

Figure 2

In the first mode, termed as *grazing resonance* (Figure 3,a), both bodies follow the same direction of movement with one weak contact during the period. The frequency of this resonance is independent of excitation amplitude and disposed in the vicinity of the natural frequency of the first subsystem. In the second mode, named as *clapping resonance* (Figure 3,b), the bodies move in the opposite direction with one strong impact per cycle. The clapping resonance is affected by amplitude of excitation and demonstrates typical non-linear behaviour with pulling and jump phenomena. Its frequency band is in the vicinity of the double frequency of the excited body.

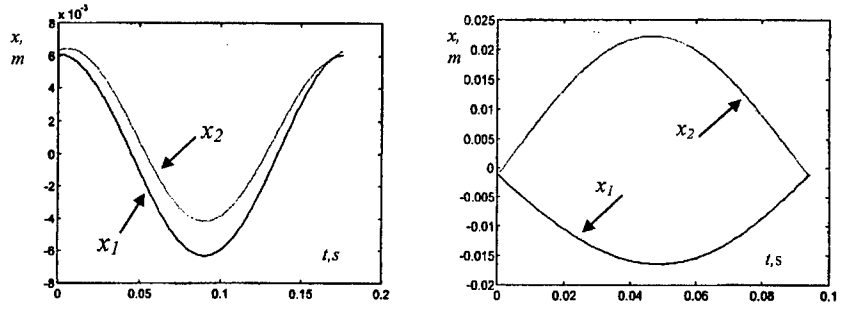

a) **b)**

Figure 3

SYSTEMS WITH MULTIPLE IMPACT PAIRS

The procedure described can be generalised when searching for resonant regimes in systems with *multiple one-dimensional impact pairs* [2]. The integral equation in this case is

$$\mathrm{x}(t) = \Theta(t+\tau) - \int_0^T \mathrm{X}(t-\varsigma)\Psi[\mathrm{x}(\varsigma), \dot{\mathrm{x}}(\varsigma)]d\varsigma \qquad (14)$$

where $\mathrm{x}(t)$ is vector of the relative disposition of the elements in pairs, $\Psi(\mathrm{x}, \dot{\mathrm{x}})$ is the vector of force characteristics of the impacting pairs, $\Theta(t)$ is the vector of relative vibration of elements of the impacting pairs when impact interaction is neglected, $\mathrm{X}(t)$ is the matrix of periodic Green's functions for the linear part of the system

$$\mathrm{X}(t) = \frac{1}{T}\sum_{m=-\infty}^{\infty} \Lambda(jm\omega)\exp(jm\omega t),$$

where $\Lambda(j\omega)$ is the receptance matrix.

In systems of the type examined it is possible to observe impacting modes of vibration, characterised by *simultaneous* impacts in almost all pairs. The number of impact pairs sharing vibration in various modes can vary.

For the regimes described, called as *cooperative modes*, we find from (14)

$$\mathrm{x}(t) \approx -\mathrm{X}(t)\bar{J}, \qquad (15)$$

where $\bar{J}$ is vector of impact impulses. From the impact conditions $\mathrm{x}(0) = \bar{\Delta}$, where $\bar{\Delta}$ is vector of gap (interference) arrangements, we find

$$\mathrm{x}(t) \approx \mathrm{X}(t)\mathrm{X}^{-1}(0)\bar{\Delta}. \qquad (16)$$

The existence conditions for regimes of type (16) and unknown phase of excitation are found from an energy balance of the dissipative and excitation forces in these solutions

$$\int_0^T \{\Lambda^{-1}(s)\} \cdot \dot{\mathrm{x}}(t)dt = \int_0^T \{\Lambda^{-1}(s)\mathrm{x}(t)\} \cdot \dot{\mathrm{x}}(t)dt + \sum_i \frac{(1-R_i)J_i^2}{2(1+R_i)M_i}. \qquad (17)$$

Here i is the index of the impact pair under consideration, R_i is the coefficient of restitution for the i- th pair, J_i is their impact impulse, M_i is the reduced mass.

EXPERIMENTAL VERIFICATION OF COOPERATIVE MODE

Figure 4 demonstrates an experimental rig for the verification of existence of

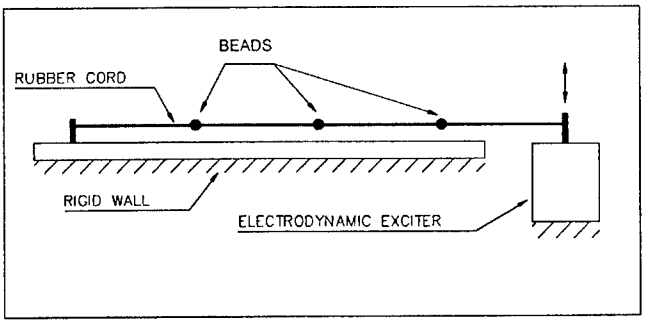

Figure 4

mode with simultaneous impacts in multiple pairs [7]. A rubber cord with three fixed plastic beads was stretched between the pin of the force transducer on the left end and the pushrod of an electrodynamic shaker producing transverse excitation of the cord.
The beads had unilateral rigid limitation of displacement with the possibility to register the instant of contact. The pictures of co-operative mode were taken by using stroboscope flashes synchronised with the voltage applied to the exciter.
Figure 5 demonstrates the cooperative mode described when the set of beads impacts their limiters simultaneously.

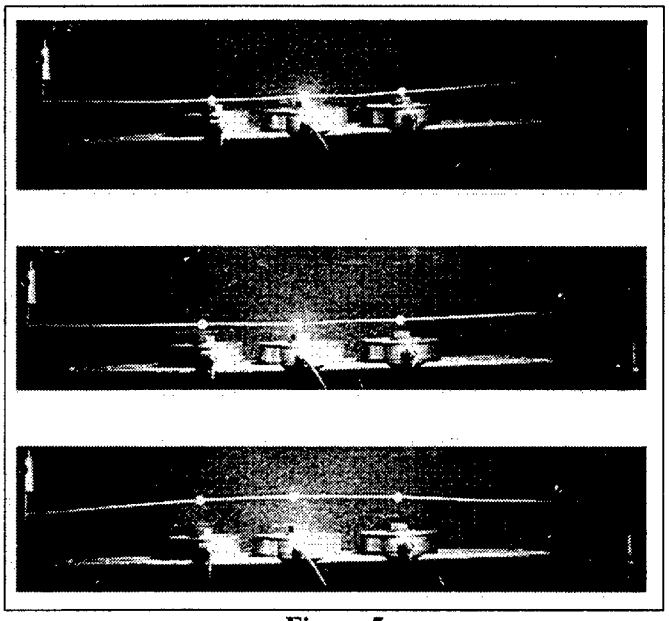

Figure 5

Figure 6 confirms the existence of cooperative mode by registration of measuring signals. Here 1,2,3 are the signals of the contact pick-ups of the limiters, 4 is the force transducer signal, 5 is the pushrod vibration signal.
The set of beads involved in the cooperative mode of vibration behaves like an impact oscillator with single degree of freedom [2]. It demonstrates *frequency pulling* , i.e. preservation of mode due to variation of the exciting frequency and *amplitude pulling* as a preservation of mode due to movement of the limiter. Both type of pulling finish their existence with a jump from cooperative vibro-impact mode to linear mode of vibration without touching the limiters. There is opportunity of transition from cooperative vibro-impact mode to linear mode of vibration without impacts and vice versa by means of *hard excitation* (additional triggered impulse). The frequency band of the cooperative modes is located in the right-hand vicinity of the natural frequencies of the linear system.

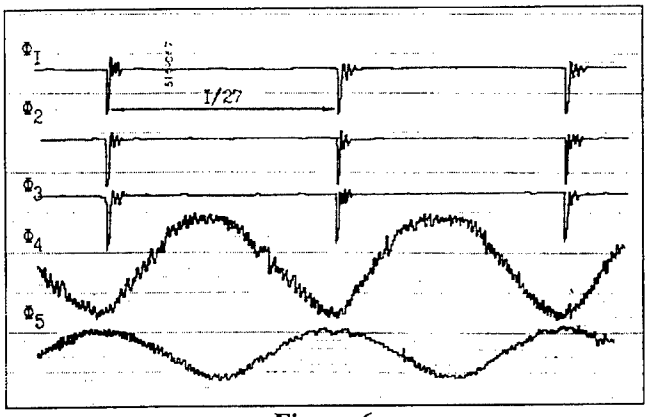

Figure 6

LOCALISED NONLINEAR STANDING WAVES

During the above experiments there were discovered *localised* vibro-impact

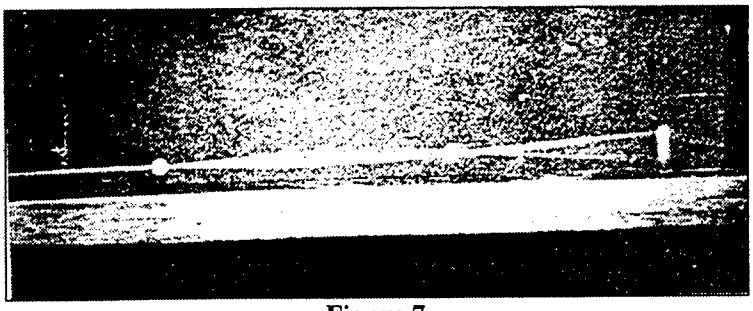

Figure 7

modes of vibration (Figure 7) when only one of the beads vibrates with impacts against a limiter and others beads keep a very small amplitude of vibration [7].

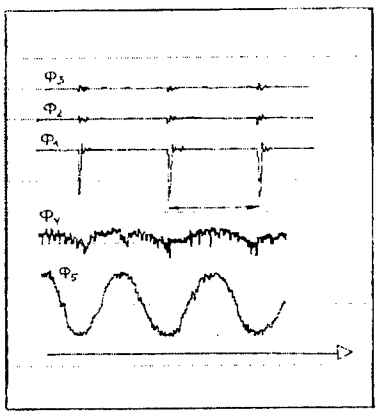

Figure 8

Figure 8 indicates the corresponding readings of the pick-ups. The localised mode is disposed behind the frequency of the last linear mode of the system with lumped parameters and can be explained as a nonlinear transformation of this mode at frequency pulling. Such type of localisation can be realised with any of the beads. This mode demonstrates also both frequency and amplitude

pulling. The conditions of existence of the localised mode can be calculated similarly with the help of the proper periodic Green's functions.

EXCITATION OF SPACIAL VIBRO-IMPACT MODES IN SOLIDS

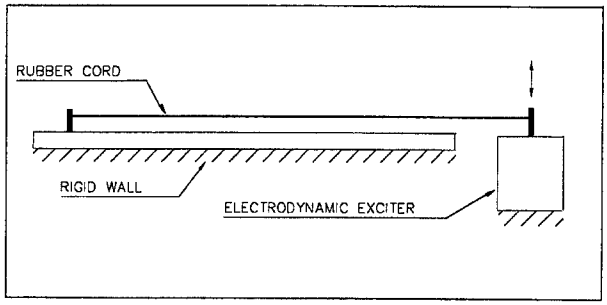

Figure 9

The study of vibro-impact processes in the extended one-dimensional systems leads to investigation of the impact pair as a system with *distributed* parameters [8]. In such systems a significant variable length of continuous vibrating element may be involved into vibro-impact interaction with the neighbouring elements or a rigid wall.

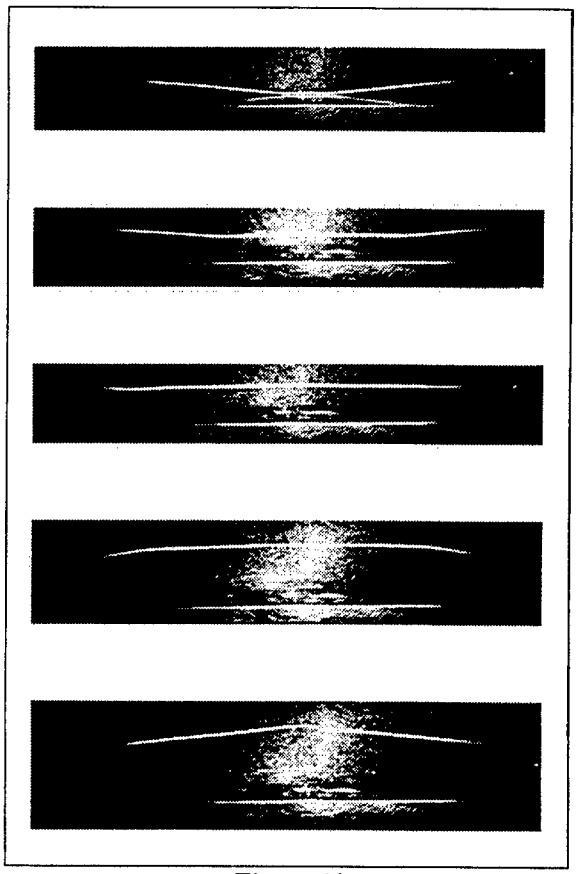

Figure 10

The object of experimental study was the axially stretched rubber cord (Figure 9) located in parallel with a rigid wall that limited the transverse deflections of the cord.

As the frequency of excitation exceeded the frequency of the first resonance of linear system (the cord without motion limiter) the nonlinear mode of cord vibration took a trapezoidal form with simultaneous impact of entire plane part against

the limiter (Figure 10).
The dynamic behaviour of the cord in such type *slapping mode* is similar to that of single degree of freedom impact oscillator [2]. It demonstrates frequency and amplitude pulling as well as transition from slapping mode to linear mode (vibration without contact with limiter) and vice versa under action of additional impulse.

ANALYSIS OF SLAPPING MODES

The straight uniform beam of length L is stretched parallel to the rigid limiter by axial force N (Figure 11). The following definitions will be used for description of the system: ρ is the density of beam material, E, G are elastic and shear moduli, S is cross sectional area of the beam, I is area moment of inertia, ε is small parameter.
The beam is exposed to the action of distributed external force of density $\varepsilon P(x,t)$. It vibrates in the plane and can collide with a straight obstacle displaced parallel to the beam with a clearance Δ relative to the position of static equilibrium of the beam.

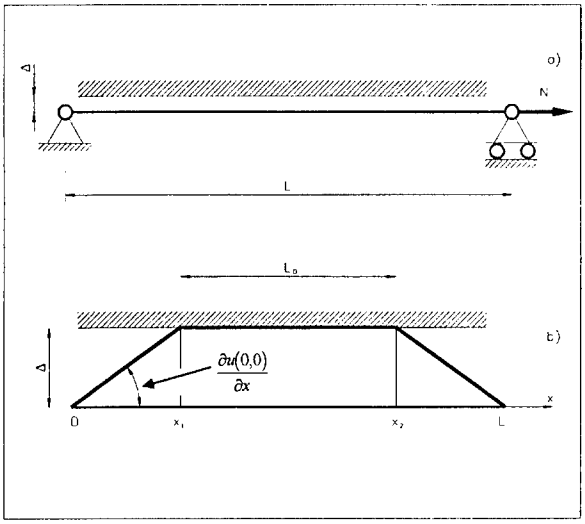

Figure 11

The subsequent analysis follows to the reference [8]. The Timoshenko beam equations are used:

$$\rho S\frac{\partial^2 u}{\partial t^2}-(\alpha SG+N)\frac{\partial^2 u}{\partial x^2}+\alpha SG\frac{\partial y}{\partial x}+\hat{\Phi}(u)=\varepsilon P(x,t)$$
$$K\frac{\partial^2 y}{\partial x^2}-\alpha SG\left(y-\frac{\partial u}{\partial x}\right)-\frac{I\rho}{S}\frac{\partial^2 y}{\partial t^2}=0 \qquad (18)$$

with boundary conditions:

$$u(0,t)=u(L,t)=\frac{\partial u(0,t)}{\partial x}=\frac{\partial u(L,t)}{\partial x}=0. \tag{19}$$

Here: $u(x,t)$ is the shape of the beam transverse deflections at instant t, $y(x,t)$ is the shape of the beam cross section rotation at instant t relative to the neutral line, $K=EI$ is a bending stiffness, α is a form factor, $\hat{\Phi}(u)$ is a density of impact forces containing δ-functions.

Equations (18) permit solutions with non-smooth shape of deflections and discontinuous distribution of velocities along the beam. Such modes can be described by means of *generalised functions*. An application of such functions causes an appearance of δ-functions in the left-hand side of the first equation (18) that compensate impact force containing δ-functions as well.

For the T- periodic motions with single impact over the one period of excitation (slapping modes), the impact force density may be presented in the time domain as follows:

$$\hat{\Phi}(u)=\hat{J}(x)\delta^{T}\left[t-\varphi(x)\right], \tag{20}$$

where $\hat{J}(x)\geq 0$ and $\varphi(x)$ are distributions of density of impact impulse and the phase of impact respectively.

The beam vibration in a first slapping mode (as described in experiment) can be analysed with the following impact conditions (see Figure 11)

$$u_{-}(x,0)=u_{+}(x,0)=u(x,0)=\begin{cases}\dfrac{\Delta}{x_1}x, & x\in[0,x_1)\\ \Delta, & x\in[x_1,L-x_1]\\ \dfrac{\Delta}{x_1}x+\Delta+\dfrac{\Delta}{x_1}(L-x), & x\in(L-x_1,L]\end{cases} \tag{21}$$

$$\frac{\partial u_{-}(x,0)}{\partial t}=\begin{cases}V_0, & x\in[x_1,L-x_1]\\ 0, & x\notin[x_1,L-x_1]\end{cases},\ \frac{\partial u_{+}(x,0)}{\partial t}=-R\frac{\partial u_{-}(x,0)}{\partial t} \tag{22}$$

As a result:

$$\begin{aligned}&\hat{J}(x)=(1+R)\rho S\,V_0=\hat{J}=const, \quad x\in[x_1,L-x_1]\\ &\varphi(x)=const=0, \quad x\notin[x_1,L-x_1]\end{aligned} \tag{23}$$

Analysis of slapping modes can be carried out by means of application of energy balance to the generative solution of conservative problem. For T-periodic free vibration $(\varepsilon=0, R=1)$ with single elastic impact over the excitation period:

$$u(x,t)=-\int_0^L\int_0^T\chi(x,z,t-s)\hat{\Phi}\left[u(z,s)\right]ds\,dz, \quad t\in(0,T], \quad x\in[0,L] \tag{24}$$

where $\chi(x,z,t)$ is a T-periodic Green's function representing a steady state response of the section x on periodic impulses of unit density applied to the section z.

The periodic Green's function can be expressed by using the transfer receptance of the linear system $L(x,z,j\omega)$ between sections x and z as follows:

$$\chi(x,z,t)=\frac{2}{T}\sum_{k=1}^{\infty}L(x,z,kj\omega)\cos(k\omega t). \tag{25}$$

In a number of cases it is possible to neglect the rotary inertia of the cross sections and ignore, therefore, the last term in the second equation of (18). Under such assumption, the expression for the receptance can be presented in the form of the infinite series:

$$L(x,z,j\omega)=-\frac{2}{\rho Sl}\sum_{m=1}^{\infty}\frac{\sin\frac{\pi mx}{l}\sin\frac{\pi mz}{l}}{\omega^2-\Omega_m^2} \tag{26}$$

with the natural frequencies Ω_m defined as follows

$$\Omega_m=\sqrt{\frac{\left(\frac{\pi m}{l}\right)^2\left[\alpha KSG\left(\frac{\pi m}{l}\right)^2+NK\left(\frac{\pi m}{l}\right)^2+\alpha NSG\right]}{\rho S\left[K\left(\frac{\pi m}{l}\right)^2+\alpha NSG\right]}}.$$

Substituting (26) into the (25) and using the finite expression for the Fourier series on the interval of periodicity, we find

$$\chi(x,z,t)=\frac{1}{\rho Sl}\sum_{m=1}^{\infty}\frac{\sin\frac{\pi mx}{l}\sin\frac{\pi mz}{l}\cos\Omega_m\left(t-\frac{T}{2}\right)}{\Omega_m\sin\frac{\Omega_m T}{2}},\ x\in[0,l],\ t\in(0,T]. \tag{27}$$

After substituting (20), (23) and (27) into (24) and integrating we have

$$u(x,t)=\frac{2\hat{J}}{\pi\rho S}\sum_{m=1}^{\infty}\frac{(-1)^{m+1}}{\Omega_{2m-1}(2m-1)}\sin\frac{\pi(2m-1)l_0}{2l}\sin\frac{\pi(2m-1)x}{l}\frac{\cos\Omega_{2m-1}(t-T/2)}{\sin\Omega_{2m-1}T/2}$$

$$x\in[0,l],\ t\in(0,T]. \tag{28}$$

In the expression (28) the unknown values $\hat{J}$ and $l_0=2l-x_1$ are functions of vibration period T. For the first nonlinear impact mode (as shown in Fig. 11,b), from the condition of impact of the middle point of the beam with coordinate $x=l/2$ involved in the impact, we have

$$u(l/2,0)=\frac{2\hat{J}}{\pi\rho S}\sum_{m=1}^{\infty}\frac{1}{\Omega_{2m-1}(2m-1)}\sin\frac{\pi(2m-1)l_0}{2l}\cot\frac{\Omega_{2m-1}T}{2}=\Delta \quad \text{or}$$

$$\hat{J}=\frac{\pi\rho S\Delta}{2\sum_{m=1}^{\infty}\frac{1}{\Omega_{2m-1}(2m-1)}\sin\frac{\pi(2m-1)l_0}{2l}\cot\frac{\Omega_{2m-1}T}{2}}. \tag{29}$$

From Fig. 11,b it follows also that $l_0 = l - 2x_1 = l - \dfrac{2\Delta}{\tan \partial u(0,0)/\partial x}$. For a small vibration $\left(\tan \partial u(0,0)/\partial x \approx \partial u(0,0)/\partial x\right)$ we find finally an equation for defining l_0:

$$l_0 = l\left[1 - \frac{l\Delta\rho S}{\hat{J}\sum_{m=1}^{\infty}\frac{(-1)^{m+1}}{\Omega_{2m-1}}\sin\frac{\pi(2m-1)l_0}{2l}\cot\frac{\Omega_{2m-1}T}{2}}\right] \tag{30}$$

By substituting (29) into (30), we have the following transcendental equation for the non-dimensional variable $\lambda = l_0 / l$

$$\lambda = 1 - \frac{2}{\pi}\frac{\sum_{m=1}^{\infty}\frac{1}{\Omega_{2m-1}(2m-1)}\sin\frac{\pi(2m-1)\lambda}{2}\cot\frac{\pi\Omega_{2m-1}}{\zeta\Omega_1}}{\sum_{m=1}^{\infty}\frac{(-1)^{m+1}}{2m-1}\sin\frac{\pi(2m-1)\lambda}{2}\cot\frac{\pi\Omega_{2m-1}}{\zeta\Omega_1}}. \tag{31}$$

Here $\zeta = 2\pi / T\Omega_1$ is non-dimensional frequency of vibration.

In order to estimate the condition of existence for the slapping mode (28) a force of excitation distributed in accordance with the first linear mode $P(x,t) = q\sin(\pi x / l)\cos(\omega t + \varphi)$ was considered, where q is intensity, φ is the phase of excitation relative to impact. The generative solution (28) with values of $\lambda(\zeta)$ and $\hat{J}(\zeta)$ being evaluated numerically according to (29), (31), was substituted into the first equation from (18). Then both parts of the equality obtained were multiplied by the function $\partial u(x,t)/\partial t$ produced analytically from (28). The equality prepared in such manner was integrated along the length of the beam and over the period of vibration $T = 2\pi / \omega$. As a result the equation of energy balance between excitation and dissipation was estimated:

$$\int_0^L\int_0^T \hat{\Phi}(u)\frac{\partial u(x,t)}{\partial t}\,dxdt = \varepsilon\int_0^L\int_0^T P(x,t)\frac{\partial u(x,t)}{\partial t}\,dxdt \tag{25}$$

Because a considerable part of the beam is involved in simultaneous collision, the energy loss can be calculated as the impact of a rigid body with coefficient of restitution R such as $1 - R \sim \varepsilon$:

$$\int_0^l\int_0^T \hat{\Phi}(u)\frac{\partial u(x,t)}{\partial t} = \left(\hat{J}l_0\right)^2\frac{1-R}{2l_0(1+R)\rho S} \approx \hat{J}^2 l_0\frac{\varepsilon}{4\rho S}.$$

After substituting in the right side of equation (25) the excitation and integrating, the equation of energy balance was finally yielded:

$\sin\varphi = \dfrac{\pi\hat{J}\lambda\left(\Omega_1^2 - \omega^2\right)}{8q\omega\sin(\pi\lambda/2)}$. The condition of existence of the slapping mode is $|\sin\varphi| \le 1$.

The PGF method provides also a natural way for the analysis of regular and random perturbations of periodical motion for vibro-impact systems with the use of an averaging technique [3,9].

CONCLUSIONS

- The synchronisation of structure vibration by multiple impact interactions leads to the temporal and spatial localisation of mechanical energy due to resonant excitation of vibro-impact modes.
- The spatial vibro-impact modes demonstrate the behaviour of impact oscillator with a single degree of freedom.
- Method of periodic Green's functions provides effective procedures for analysis of vibro-impact resonances in complex mechanical structures.

REFERENCES

1. Babitsky V.I., Kolovsky M.Z. On the investigation of resonances in vibro-impact systems. *Mechanics of Solids*, 1976, No. 4. (in Russian).
2. Babitsky V.I. *Theory of Vibro-Impact Systems and Applications.* Springer, Berlin, 1998 (Revised translation from Russian, Nauka, Moscow, 1978).
3. Babitsky V.I., Krupenin V.L. *Vibration of Strongly Nonlinear Systems.* Springer, Berlin (in preparation, Revised translation from Russian, Nauka, Moscow, 1985).
4. Kobrinsky A.E. *Dynamics of Mechanisms with Elastic Connections and Impact Systems.* Iliffe Books Ltd., London, 1969 (Translation from Russian, Nauka, Moscow, 1964).
5. Rosenwasser E.N. *Oscillations of Nonlinear Systems.* Nauka, Moscow, 1969 (in Russian).
6. Kember S.A., Babitsky V.I. Excitation of vibro-impact systems by periodic impulses. *Journal of Sound and Vibration*, 1999, v.227, No. 2.
7. Babitsky V.I., Veprik A.M., Krupenin V.L. Vibro-impact phenomena due to limited oscillations of one-dimensional elastically connected particles. *Proceedings of Soviet Academy of Sciences*, 1988, v.300, No. 3.
8. Veprik A.M., Krupenin V.L. About resonant oscillations of system with distributed impact element. *Machine Studies*, 1988, No. 6 (in Russian).
9. Kovaleva A.S. *Optimal control of mechanical oscillations.* Springer, Berlin, 1999 (Translation from Russian, Nauka, Moscow, 1990).

BLIND RECONSTRUCTION OF A MECHANICAL IMPACTING SOURCE SIGNAL USING HIGHER ORDER STATISTICS
PART I, SIGNAL RESTORATION BY CUMULANT MAXIMISATION (THEORY AND SIMULATIONS)

J-S Seo and J.K. Hammond

Institute of Sound and Vibration Research
University of Southampton

ABSTRACT

This paper addresses the problem of reconstructing an impacting (non-Gaussian) signal from a measured signal where the transmission path from the impacting point is unknown and the measurement may include a Gaussian 'noise' component arising from other sources. Restoration of the input signal is described using Higher Order Statistics (HOS); specifically two normalised cumulants of third and fourth order. The use of cumulants ensures that the Gaussian interference is suppressed. The method uses an optimisation procedure which relies on the non-Gaussianity of the impacting signal. The optimisation process is performed through both constrained and normalised higher order cumulants based on a generalised Wiener approach. Different inverse systems are employed with the emphasis on the performance of a Finite Impulse Response (FIR) filter including consideration of selection of the length of the inverse filter. Examples are presented for simulated data.

1. INTRODUCTION

In many situations in engineering, science, geophysics, etc, the cause of an observed phenomenon is not directly measurable. The determination of this cause from output variables is an inverse problem. These problems can sometimes be straightforward when the system through which the cause passes is known. For certain physical situations, however, it is impractical to assume the availability of the system characteristics and we require restoration of the original input signal solely from the measured (observed) signal. In this case, the restoration is called *blind inversion*.

In Figure 1.1, a process consists of an input signal (unobservable) and an unknown linear time invariant system which produces a measured signal which is noise corrupted.

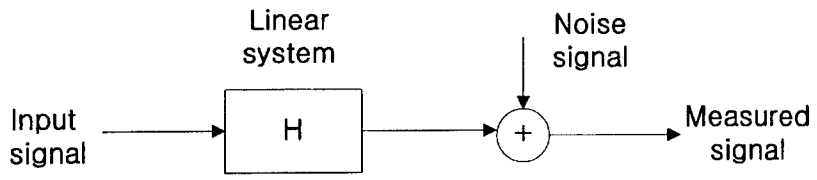

Figure 1.1 Linear Time-Invariant (LTI) system and signals

The aim here is to determine the *input signal* from the *measured signal* alone. A practical example is that of the condition monitoring, which requires the identification of the 'cause' of a mechanical imbalance or impacting. To retrieve the input signal, the higher order statistical properties of the measured signal (greater than second order) are considered in this work.
Recently, higher-Order ($\geq$ 3) statistics (HOS) [1], [2] have been considered to find optimum linear inverse filters to restore the original input signal. Cumulants not only display the degree of higher-order correlation but also provide us with a measure of the "departure" from the Gaussianity which is inherent in impacting type systems [3]. The advantages of HOS are due to their ability to carry the phase information of a signal or a system and to suppress any (white or coloured) Gaussian additive noise [4].

For non-Gaussian, independent, identically, distributed (i.i.d.) signals, Donoho [5] has shown that the probability distribution of the linear combinations of these signals tend to become 'closer' to the Gaussian (this is sometimes referred to as *partial order*) than that of the individual components. Based on this concept, the idea of blind deconvolution is based on selecting the inverse system that can simply decrease the Gaussianity of the output of the inverse system. This is achieved by *maximising* an appropriately selected function (which represents the degree of the Gaussianity) with respect to the coefficients of the linear inverse system used to achieve blind deconvolution.

Wiggins[6] has proposed a normalised *objective function* which consists of two cumulants (i.e., fourth-order cumulant divided by squared second-order cumulant; the *kurtosis*) which can be related to the partial order described by Donoho. When the kurtosis of any signal is greater than 3 (or greater than zero, depending on the definition), this is referred to the 'super-Gaussianity' or when smaller than 3 it is known as 'sub-Gaussianity'. For both cases, *maximisation* of the absolute value of the objective function has been used as an estimate of

the input signal. Claerbout [7] has suggested another objective function, which is named entropy. Figure 1.2 illustrates the various objective functions in use. For any of the methods described above, by driving the objective functions toward their maxima (by adjusting the inverse filter coefficients) one attains blind deconvolution (equalisation). The procedure of obtaining the coefficients of the inverse filter from which we can reconstruct the unknown input signal has been done by (nonlinear) iterative calculation (Nandi) [8] and by the iterative techniques based on the stochastic gradient of the objective function by Cadzow[9].

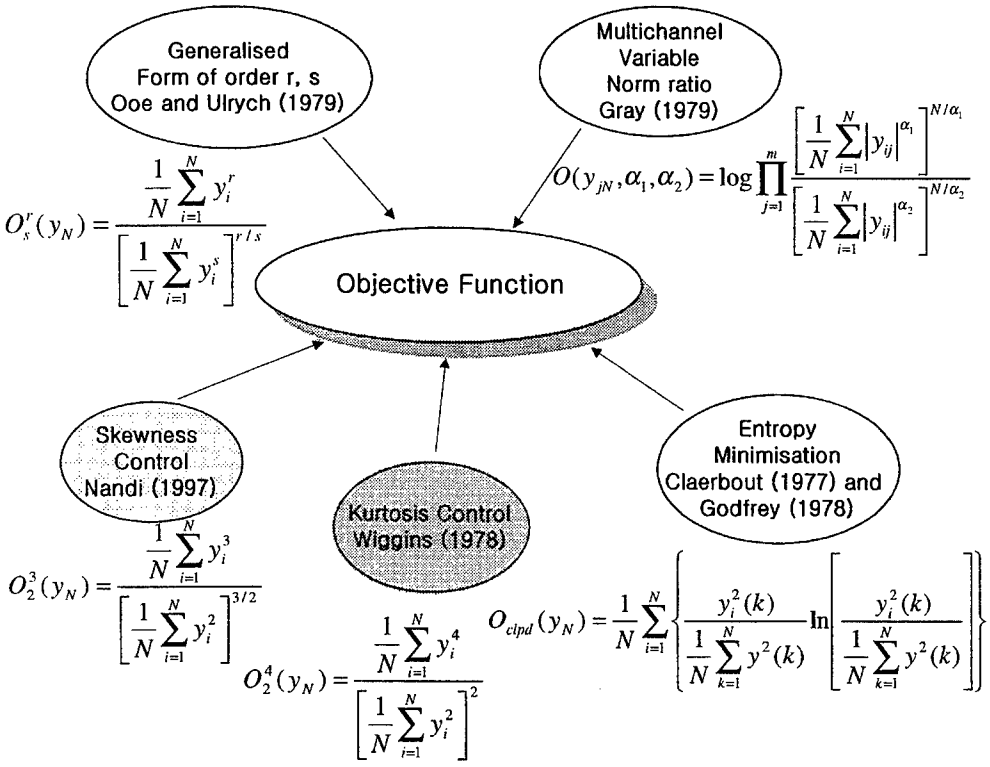

Figure 1.2 The objective functions

Section 2 provides a theoretical background to blind inversion via Higher Order Statistics (HOS). In Section 3, three different inverse filter types (MA, AR, and ARMA systems) are introduced and their performances are compared. The effect of the choice of initial inverse

filter coefficients and determining the optimal length of the filter length are included. Some concluding remarks are presented in section 4 and suggestions for further research are presented at the end of the companion paper (part II).

2. SUMMARY OF BLIND DECONVOLUTION PROBLEM USING HOS

The nth order moment of random variable X is

$$E\{X^n\} = \int_{-\infty}^{\infty} x^n p(x)dx \quad , \quad \text{for } n = 1,2,3,\ldots, \tag{2.1}$$

where the symbol E denotes the expected value operator and $p(x)$ is the probability density function. The symbol $m_n^{\ x} = E\{X^n\}$ is commonly used for the n-th moment.

The *Fourier transform* of the probability density function of X is

$$\begin{aligned} \phi_X(\omega) &= \int_{-\infty}^{\infty} e^{j\omega x} p(x)dx \\ &= E\{e^{j\omega x}\} \end{aligned} \tag{2.2}$$

which is the *moment generating function* [2] of random variable X. The natural logarithm of the moment generating function is the *cumulant generating function* and is

$$\psi_X(\omega) = \ln[\phi_X(\omega)] = \ln[E\{e^{j\omega X}\}] \tag{2.3}$$

Using a Taylor expansion of the moment generating function, the cumulants of the random variables X are related to its moments by

$$\begin{aligned} c_1 &= Cum[X] = m_1 \\ c_2 &= Cum[X,X] = m_2 - m_1^{\ 2} \\ c_3 &= Cum[X,X,X] = m_3 - 3m_2m_1 + 2m_1^{\ 3} \\ c_4 &= Cum[X,X,X,X] = m_4 - 4m_3m_1 - 3m_2^{\ 2} + 12m_2m_1^{\ 2} - 6m_1^{\ 4} \end{aligned} \tag{2.4}$$

Using their relationships, consider the random variables v_i composed of the sum of each random variables x_i and n_i

$$v_i = x_i + n_i, \quad i = 1, 2, 3,\ldots \tag{2.5}$$

The joint probability density function of $\{x_1, x_2, x_3\}$ is non-Gaussian and that of $\{n_1, n_2, n_3\}$ is jointly Gaussian and independent from $\{x_1, x_2, x_3\}$. Assuming $E\{x_i\} \neq 0$, $E\{n_i\} \neq 0$ for $i = 1,2,3$

$$cum[v_1, v_2, v_3] = cum[x_1, x_2, x_3] + cum[n_1, n_2, n_3] \tag{2.6}$$

If the set of random variables $\{n_1, n_2, n_3\}$ is jointly Gaussian, then all the joint cumulants of order n>2 are identically to zero. Hence if the interfering signals are Gaussian their cumulants above 3rd-order are zero [2]. Then

$$cum[v_1, v_2, v_3] = cum[x_1, x_2, x_3] \tag{2.7}$$

On the other hand,

$$\begin{aligned} Mom[v_1, v_2, v_3] = & Mom[x_1, x_2, x_3] + Mom[n_1, n_2, n_3] \\ & + Mom[x_1, n_2, x_3] + Mom[n_1, x_2, x_3] \\ & + Mom[n_1, n_2, x_3] + Mom[x_1, x_2, n_3] \\ & + Mom[x_1, n_2, n_3] + Mom[n_1, x_2, n_3] \end{aligned} \tag{2.8}$$

This demonstrates the key motivations behind the use of cumulants in signal processing problems; namely, [i] their ability to suppress noises (n_i) which are additive and Gaussian and [ii] non-Gaussianity is manifested in the non-zero lag cumulants of order ≥ 3.

Suppose a random variable y can be expressed as a linear combination of p statistically *independent* random variables $\{x_1, x_2, \ldots, x_p\}$ which are *independent identically distributed* (*i.i.d.*). This linear combination takes the form

$$y = a_1 x_1 + a_2 x_2 + \cdots + a_p x_p \tag{2.9}$$

where $a_1, a_2, \ldots, a_p$ are constants. Using the properties above the cumulant generating function can be expressed as

$$\psi_y(\omega) = \psi_{x1}(a_1\omega) + \psi_{x2}(a_2\omega) + \cdots + \psi_{xp}(a_p\omega) \tag{2.10}$$

From this, the kth order cumulant of random variable y is

$$c_y(k) = a_1^{\,k} c_{x1}(k) + a_2^{\,k} c_{x2}(k) + \cdots + a_p^{\,k} c_{xp}(k) \tag{2.11}$$

We now apply this to the response of a linear system. The output signal y is related to the input signal x as

$$y(n) = \sum_{k \in K} h_k x(n-k), \quad -\infty < k < \infty \tag{2.12}$$

where h_k is the impulse response sequence of linear operator and x is the excitation input sequence. If $x(n)$ is an i.i.d sequence then

$$\phi_y(\omega) = \prod_{k \in K} \phi_x(h_k \omega) \tag{2.13}$$

The associated cumulant generating function becomes

$$\psi_y(\omega) = \sum_{k \in K} \psi_x(h_k \omega) \tag{2.14}$$

Using (2.14), the cumulant of order p can be expressed

$$C_y(p) = C_x(p) \sum_k (h_k)^p \tag{2.15}$$

i.e., the response cumulant of order p is seen to be the product of the excitation cumulant of order p with the sum of the linear operator's unit-impulse response elements raised to the pth power [1].

Blind deconvolution is the problem of restoring the input signal from the measured (observed) signal alone (Figure 2.1). For our problem assumptions are; i) the input signal to be restored is non-Gaussian, ii) the unknown transmission path is linear, iii) the additive noise is Gaussian and independent of the input signal.
Starting from those assumptions, the blind deconvolution (BD) process is illustrated in the figure below:

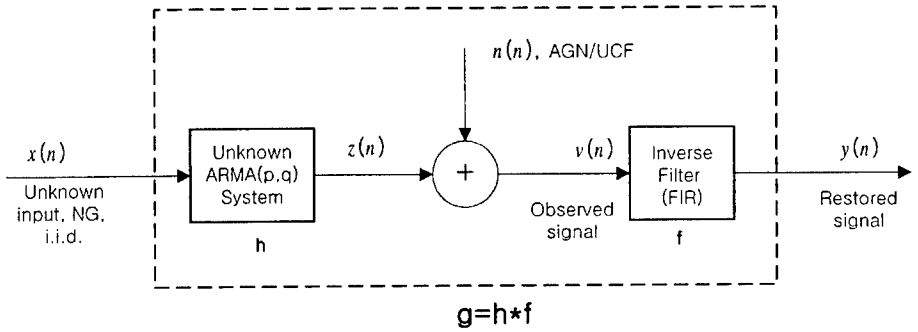

Figure 2.1 The process of convolution-deconvolution in the blind source reconstruction problem. [NG: Non-Gaussian; i.i.d.: Independent Identically Distributed; AGN: Additive Gaussian Noise; UCF: Unknown Covariance Function.]

The *partial order* (Donoho, 1981) [5] at each signal stage can be expressed as

$$\mathbf{x} \cdot \geq \mathbf{h} * \mathbf{x} \cdot \geq \mathbf{v} \cdot \geq \mathbf{f} * \mathbf{v} \cdot \geq G \tag{2.16}$$

where G is any Gaussian signal. The notation $\cdot \geq$ is called the partial order of a random variable. $X \cdot \geq Y$ means Y is more Gaussian than X.

From above relationship, the combined convolution-deconvolution filter **g** may act to increase the Gaussianity of the restored signal **y** unless a certain condition is imposed. This condition is that the inverse filter $\hat{\mathbf{f}}$ should make the output of a filtered version of **v** "less Gaussian" i.e.

$$\hat{\mathbf{f}} * \mathbf{v} \cdot \geq \mathbf{x} \cdot \geq \mathbf{v} \tag{2.17}$$

which leads to

$$\hat{\mathbf{f}} = arg \max_{\hat{\mathbf{f}}} O(\mathbf{y}) \tag{2.18}$$

provided that the O agrees with the partial order $\cdot \geq$. O is called an objective function. Normally, the necessary condition which gives a *local* maximum is obtained by differentiating the objective function with respect to the filter coefficients and equating to zero.

In subsequent pages we construct the inverse filters by maximising both constrained and normalised cumulants of the measured signal.

In the absence of constraints unbounded filter coefficients result. The constraint can limit the behaviour of the inverse filter while optimising the appropriated objective function. The constraint used ensures that the Frobenius norm of the FIR inverse filter coefficient is unity.

$$\|\mathbf{f}\|_2 = 1 \tag{2.19}$$

(which means the variance of the input and output of the inverse system is the same for an i.i.d. input).

As an example, the objective function for the fourth-order statistics

$$\begin{aligned} O_y(\mathbf{f}) &= E\{\mathbf{y}^4\} - 3E\{\mathbf{y}^2\}^2 \\ &= \frac{1}{N}\sum_{i=0}^{N-1}(y_i - m_y)^4 - 3\left[\frac{1}{N}\sum_{i=0}^{N-1}(y_i - m_y)^2\right]^2 \end{aligned} \tag{2.20}$$

where E[•] denotes expectation, m_y is the mean value of **y**, N is the number of total data samples observed. The constraint function is

$$g(\mathbf{f}) = 1 - \frac{\frac{1}{N}\sum_{i=0}^{N-1}(y_i - m_y)^2}{\frac{1}{N}\sum_{i=0}^{N-1}(v_i - m_v)^2} = 0 \tag{2.21}$$

in which m_v is the mean of the signal **v**. Combining above two equations, the final cost function for the BD process takes the form

$$J(\mathbf{f}) = O_y(\mathbf{f}) + \lambda g(\mathbf{f}) \tag{2.22}$$

where λ represents the Lagrange multiplier. The optimisation proceeds by maximising J which satisfying the constraint (refer to J. S. Seo [10] for details of the iterative Wiener solution).

An alternative to constraining the inverse filter coefficients is to maximise a *normalised* objective function (normalised response cumulant $O_y(r,s;\mathbf{f})$), where s is any positive even integer less than r which can be any constant when the cumulant of order s of signal y (c_s^y) is nonzero. For example, the objective function for the normalised fourth-order statistics takes the form (kurtosis)

$$O_y(\mathbf{f}) = \frac{c_4^y}{(c_2^{\,y})^{4/2}} = \frac{E[(y-m_y)^4]}{(\sigma_y^{\,2})^2} = \frac{\frac{1}{N}\sum_{i=0}^{N-1}(y_i - m_y)^4}{\left[\frac{1}{N}\sum_{i=0}^{N-1}(y_i - m_y)^2\right]^2} \tag{2.23}$$

where σ_y^2 is the variance of **y** (r=4, s=2 and refer to A. K. Nandi [8] for the iterative Wiener solution).

An example of restored signals from both constrained and normalised objective function maximisation are compared: The input is impulsive in nature and highly non-Gaussian (2.2 a). Figure 2.2 b is a filtered and Gaussian noise contaminated signal. Figure 2.2 c and d are restored signals following two procedures described earlier.

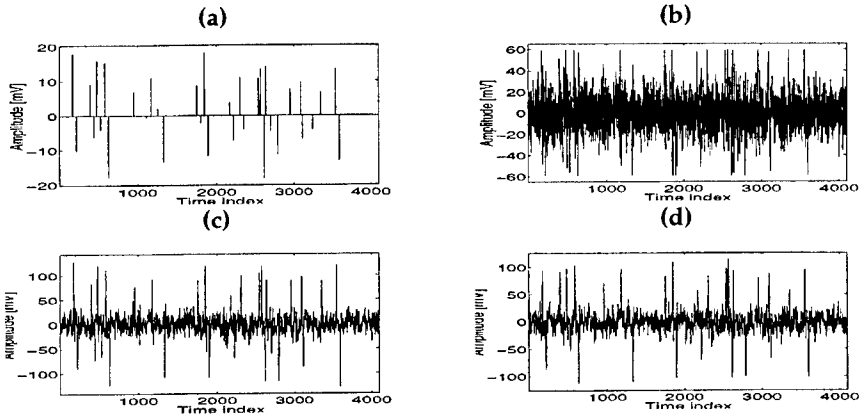

Figure 2.2 Input, measured and restored signal from the fourth-order method, (a): Unknown input signal, (b): measured signal, (c): restored signal from 4th order cumulant and unit norm filter coefficient constraint, and (d): restored signal from 4th order normalised cumulant.

Table 2.1 Comparison of the inverse filter and restored signal from two different optimisation methods

	Constraint	Normalised	Remarks
Frobenius norm of the inverse filter coefficient	$\|\mathbf{f}\|_2 = 1$	$\|\mathbf{f}\|_2 = 0.93$	L=21, FIR inverse filter
Variance of the restored signal	1.60	1.38	Ratio of the variance of measured signal
skewness	0.42 (0.128)	0.36 (0.128)	( ) is the skewness of measured signal
kurtosis	11.53 (4.82)	10.66 (4.82)	( ) is the kurtosis of measured signal

3. PROPERTIES OF THE OBJECTIVE FUNCTION AND OPTIMISATION METHODS

In Figure 2.2 only an MA inverse system (FIR) was used. However, depending on filter h in Figure 2.1 the inverse system could be AR, MA or ARMA. This section thus demonstrates the behaviour of the objective function along with the coefficients of the different inverse filters. The three different inverse filters are MA, AR and ARMA filters and their performances are compared.

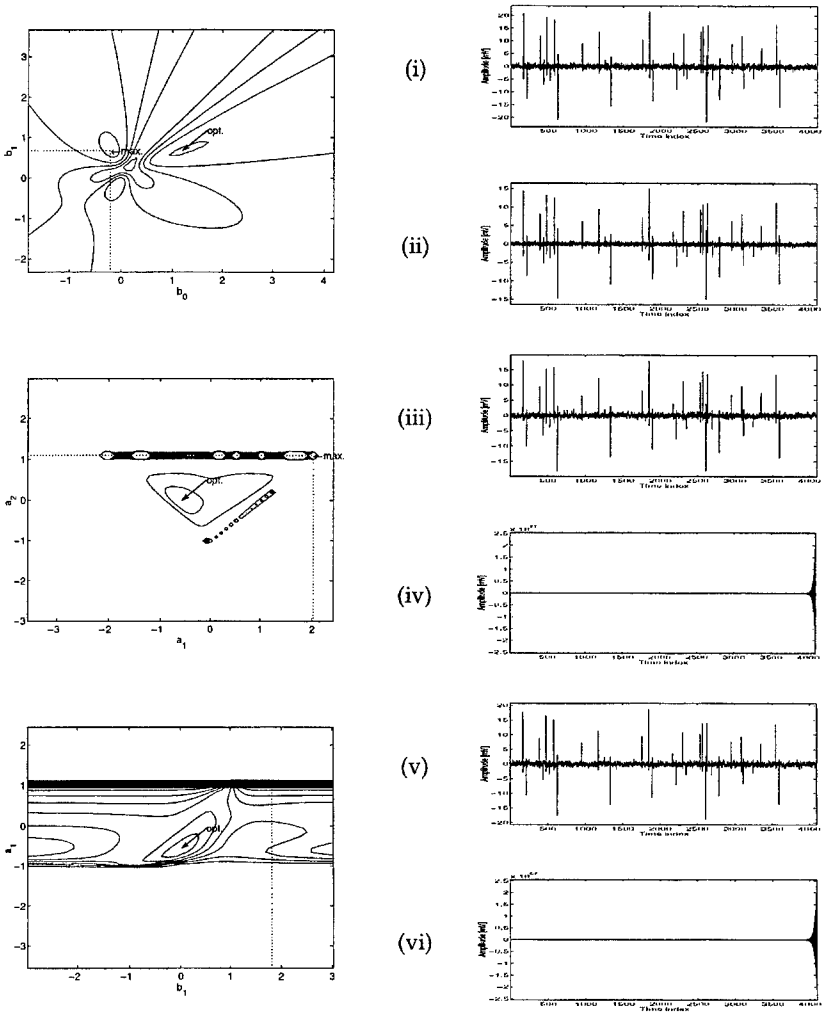

Figure 3.1 The Objective function of the 4th order statistics, right top: objective function shape of MA(2), middle: AR(2), bottom: ARMA(2,2) inverse filter, left column : restored signals from 'opt' and 'max' point for each filters

As a simple demonstration, to restore the signal shown in Figure 2.2, each inverse filter MA, AR or ARMA is assumed to have order 2 (q=2, p=2). The objective function is kurtosis (fourth order normalised cumulant), which is plotted for two coefficients of the three inverse filter types in Figure 3.1. From the Figures, we see there can be several local maxima for both MA and AR inverse filters. Thus, it is evident that the Wiener solution may end up at a local maximum. Note the intersection of the dotted line (denoted 'max') points maximum Objective value and arrow mark (denoted 'opt') points calculated filter coefficient values. As can be seen in the top of the Figure 3.1, for the MA filter case, the inverse filter from the max point can also yield the signal restoration successfully (see the two restored signal in right side of top row (i) and (ii) are identical except the scale, which can happen due to the scale –including sign reversal- and delay ambiguity in the blind deconvolution problem). However, for the AR and ARMA inverse filter case, the filter coefficients that give the maximum point of the objective function value does not reveal correct restoration (note the unrealistic signals in (iv) and (vi) of Figure 3.1) whereas the filter coefficients from the 'opt' point can give correct signal restoration (referring to signals in (iii) and (v) of the Figure 3.1).

In the iterative solution of the Wiener type equation the first stage of maximising the objective function for the blind deconvolution procedure is the selection of the initial inverse filter. This can affect the performance of input signal reconstruction procedure. Three initial filter setting are selected (a) a random set, (b) an impulse, and (c) a delayed impulse (centred) are shown in Figure 3.2 below.

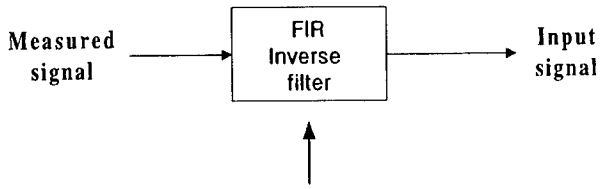

f_a_ini=[random number of filter coefficient]
=[0.75 0.2 −0.3 1.1 −0.12 .....0.25]

f_a_ini=[Impulse type initial filter coefficient]
=[1 0 0 .....0]

f_a_ini=[Centered impulse initial filter type]
=[0 0..1..0 0]

Figure 3.2 Different types of initial inverse filter for deconvolution

According to the relationship between the partial order and linear filtering, the effect of the selection of the above initial inverse filter is demonstrated. The left of following Figure 3.3 illustrates the change of the objective function values with three different initial inverse filter types for up to 8-14 iterations. The dotted line implies the kurtosis value of the measured signal itself.

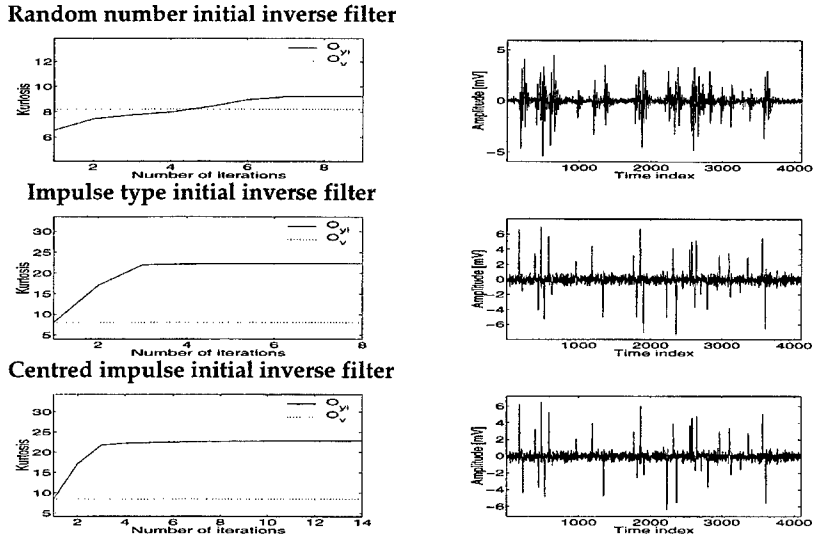

Figure 3.3 The comparison of the objective function values and the restored signals from three different initial inverse type. O_{yi}: Value of the objective function of output of the inverse filter in each iteration, O_v: Value of the objective function of measured signal (unchangeable).

As can be seen in the top, left of the figure, when the random initial inverse filter was selected the objective function value of the first iteration (first point of the solid line) is smaller than that of the measured signal (dotted line). This means that the randomly selected initial inverse filter could make the output of the inverse filter *closer to Gaussian*, which in return results difficulties for the convergence of the filter coefficient to the desired optimal points, thus the restored signal is degraded (top, right). On the other hands, the initial unit impulsive initial filter (middle) and the centred unit impulsive initial filter (bottom) give *significantly* better results. Gray (1979) [3] was the first to report the use of an impulsive initial condition so that the first output

of the filter is the same as the input and makes the convergence better as the iteration proceeds.
The results reflect the importance of selecting the initial inverse filter type on the blind deconvolution process.

Another key question is the selection of inverse filter length for a FIR inverse. Without the knowledge of the driving system (**h** in Figure 2.1) nor the variance of the additive noise, the FIR inverse filter may take any length. Proper selection of the inverse filter now to be established depending on certain criteria. We consider three major aspects that can affect the choice of the length of the inverse filter.
The algorithm employed here concentrates on a performance index defined as difference of the normalised higher order cumulant value (e.g., skewness or kurtosis) of the restored signal and the observed signal. This is a measure of the success the deconvolution. Thus the performance index

$$P = \left| O_y^i - O_v \right| \tag{3.1}$$

where O_y, O_v designates the normalised higher cumulant value of restored signal **y** and observed signal **v**, and i means their values for i filter length.

Another criteria for selecting the length of the inverse filter possibly be given by using the *Generalised Gaussian Distribution* (Miller and Thomas, 1972) [11].
This Generalised Gaussian Distribution (GGD) can generally represent the probabilistic shape of the random signal x, which is expressed via two parameters as,

$$f(x,\beta,\alpha) = \frac{\alpha}{2\beta\Gamma(\frac{1}{\alpha})} e^{-(\frac{|x|}{\beta})^{\alpha}} \tag{3.2}$$

where

$-\infty < x < \infty$ is a random signal
$\Gamma(\bullet)$ is the gamma function
$\beta > 0$ is the scale parameter
$\alpha > 0$ is the shape parameter.

Hence, by examining the α value, we can 'measure' the performance of the deconvolution for a spiky signal reconstruction. This may be monitored against filter length.

The observed signal is normally considered as the signal which contains an unknown system's smoothing effect (i.e. **h** in Figure 2.1) and is corrupted by Gaussian noise. For the problem of seeking an impacting signal from the smoothed and noise corrupted observed signal, the status of deconvolution process can be monitored by checking the probabilistic characteristics of each signal. The impacting signal to be restored is one with several randomly located large events separated by many near-zero events which can be interpreted as noise. Under the certain constraint that the variance of the observed signal and its estimated impacting signal (deconvolved signal) should be equal, then the deconvolved signal will have less entropy (Gray, 1979) [3]. The entropy of the signal **x** is calculated from its probability function as,

$$E = -\int_{-\infty}^{\infty} f(x) \ln f(x) dx \qquad (3.3)$$

in which the log is the natural logarithm. The shape of this entropy curve of the restored signal along with the different inverse filter length has a similar shape to that of the α curve.

Considering above three parameters, the optimal length of the inverse filter is determined by balancing the performance index and entropy curve whilst keeping the shape parameter (α) as small as possible. Figure 3.4 is the graphical illustration of optimal inverse filter selection scheme.

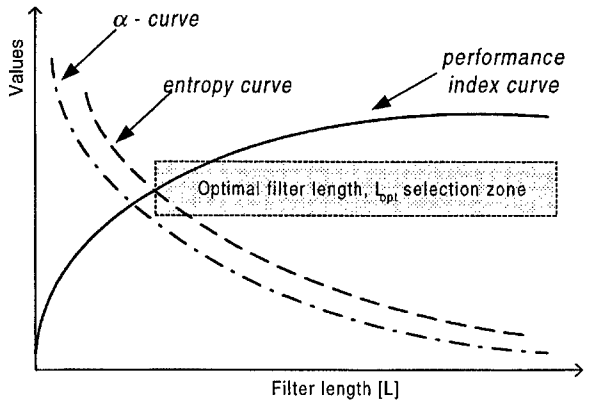

Figure 3.4 Graphical illustration of optimal inverse filter length selection.

An example of restored signals from optimal inverse filter selection criterion using third-and fourth order for normalised objective function maximisation are compared:

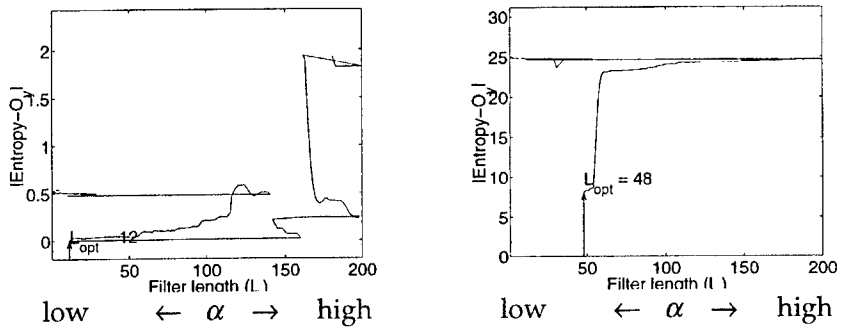

Figure 3.5 The shape of the entropy-performance curve for filter length selection for 3rd, 4th order case.

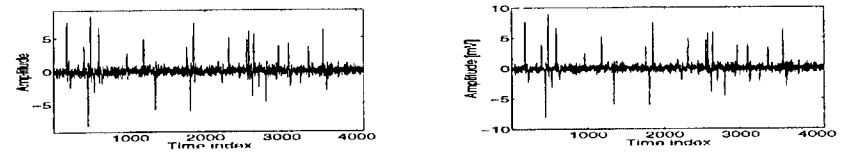

Figure 3.6 The shape of restored signals via 3rd, 4th order deconvolution methods with optimal length.

4. DISCUSSIONS

Considering the changes of degree of Gaussianity along with the linear filtering blind signal reconstruction has been demonstrated. The higher order cumulants – i.e., constrained or normalised zero lag higher order (order 3, 4) cumulant of the output signal of the inverse filter - named as an objective function has been employed for the restoration of the impacting signal (restoration of unknown source signal, see Figure 2.2). The compactness of the recursive (AR or ARMA) inverse system in blind deconvolution is seen provided that instability (see Figure 3.1) of the filter can be suppressed. For instance, confining the position of poles inside the unit circle at each iteration can control the filter instability.

The effect of the initial condition of the inverse system (Figure 3.3) has been explored on the basis of the partial order.

A criterion on the choosing the length of the FIR inverse system has been suggested (Figure 3.4) monitoring the performance index, shape parameter, and entropy of the restored signals. The maximisation of the defined objective function from the iterative solution of a Generalised Wiener approach sometimes falls into one of the local maxima. Hence, in conjunction with the work carried out here, another optimisation methods are recommended to be considered expecting to find the global maximum. This provides the starting point for the companion paper Part II.

REFERENCES

[1] Jerry M. Mendel, "Tutorial on Higher-Order Statistics (Spectra) in Signal Processing and System Theory : Theoretical Results and Some Applications," Proceedings of *IEEE* Vol 79, No. 3, pp 278-305, March 1991.

[2] C. L. Nikias and A. P. Petropuou," *Higher-Order Spectra Analysis - A Nonlinear signal processing framework -*," Prentice-Hall International, Chapter 7,1993.

[3] W. Gray, "Variable norm deconvolution", PhD. Thesis, Stanford University, Stanford, CA, 1979.

[4] C. L. Nikias and M. R. Raghuveer, "Bispectrum estimation : A digital signal processing frame work," Proceedings of *IEEE* Vol 75, pp 869-891, July 1987.

[5] D. Donoho, *On minimum entropy deconvolution*, In Applied Time series Analysis II ed., D. Findley, Academic Press, New York, pp 556-608, 1981.

[6] R. A. Wiggins, *Minimum entropy deconvolution*, Elsevier Scientific publishing Geoexploration, 16, pp 21-35, 1978.

[7] J. F. Claerbout, "Parsimonious deconvolution", Stand. Exploration Project, Vol. 13, pp 1-9, 1977.

[8] A.K. Nandi, D. Mampel, and B. Roscher, "Blind Deconvolution of Ultrasonic Signals in Nondestructive Testing Applications", IEEE Transactions on Signal processing, Vol 45, No. 5, May, 1997.

[9] James A. Cadzow, "Blind Deconvolution via Cumulant Extrema", IEEE Signal Processing Magazine, pp 24-42, May. 1996.

[10] J. S. Seo," Blind fault detection and source identification using Higher Order Statistics for impacting systems", PhD. Thesis 2000, ISVR, University of Southampton, UK (in preparation).

[11] J. H. Miller and J. B. Thomas," Detector for Discrete-Time Signals in Non-Gaussian Noise," IEEE Transactions on Information Theory, Vol. 18 No. 2 pp 241-250, March 1972.

BLIND RECONSTRUCTION OF A MECHANICAL IMPACTING SOURCE SIGNAL USING HIGHER ORDER STATISTICS
PART II, SIGNAL RESTORATION USING OPTIMISATION BY DIFFERENTIAL EVOLUTION

J-S Seo and J.K. Hammond

Institute of Sound and Vibration Research
University of Southampton

ABSTRACT

This paper consists of two sections complementing Part I including (i) extension of local optimisation to global optimisation. This global maximisation method is known as Differential Evolution (DE). And (ii) applying the methods described in both Part I and II to experimental data.

1. INTRODUCTION

In section 2, we reconsider the optimisation problem described in Part I, this time seeking global optimisation schemes. The purpose of global optimisation is to find a solution for with the objective function obtains its least (or largest) value. When the objective function has many local maxima, local optimisation techniques are likely to miss the global maximum, so a search tool is needed to find the global maximum. The approach we use is known as the Differential Evolution (DE) algorithm. Differential Evolution is basically very similar to conventional Genetic Algorithms (GA) [1], [2]. The differences are in the way the mechanisms of mutation and crossover are performed using real floating point numbers instead of long strings of zeros and ones. In particular, the concept of perturbing a vector with the difference of two other parameter vectors is borrowed from the reflection, expansion and contraction processes of the Nelder and Mead's downhill simplex optimisation algorithm [3].

In section 3, simulations and experimental data are used to illustrate the methodology of both Part I and Part II.

2. DIFFERENTIAL EVOLUTION (DE)

Suppose we have a function of a vector **x** of parameters $f(\mathbf{x})$ and need to find the extreme value of $f(\mathbf{x})$ as we iterate **x**. With a given number of random guesses of **x** (named the initial population), we attempt to improve the value of $f(\mathbf{x})$ retaining a number of best guesses as the process continues. The initial vector population is chosen randomly and should cover the entire parameter space (as a rule, a uniform probability distribution for all random decisions will be employed unless otherwise stated). The improvement (evolution) is carried out by forming the next (child) population by mating pairs of the initial (parents) population, based on random search (mutation and crossover). In comparison with GA, the basic difference lies in the scheme for generating trial vectors [4]. Figure 2.1 shows schematically the basic operations of DE working on optimisation of a hypothetical multi-parameter system. The parameter vectors considered here are composed of five parameters x_{Di} (D=1,2,...,5 and i is the entry number of population up to p). Hence, there are two D x p (in this case, D=5) which represent the generations of the parameters. This means the algorithm starts with an initial pool of 5 dimensional parameter vectors with p population (candidates or ancestors) drawn from a certain probability distribution. Normally the uniform probability distribution ensures that the parameter vectors generated will span the parameter space equally. The initial pool acts as the first generation from which the whole evolution operation starts. Thus, the top table represents the generation whose members will evolve according to the mechanisms of the differential evolution.

In the bottom table each newly evolved member will be placed according to the positions which its predecessor was holding in the top table. The bottom table is called a new generation.

As can be seen in the Figure 2.1, the member $[x_{11}, x_{21}, \ldots, x_{51}]^T$ of the first table (top) is evolved to the descendant $[x_{1tr}, x_{2tr}, \ldots, x_{5tr}]^T$ that holds the leftmost position in the bottom table. The performance index or cost value corresponding to each parameter vector is displayed in the corresponding row of the two tables. The detailed processes between the top and bottom table are featured and described as follows;

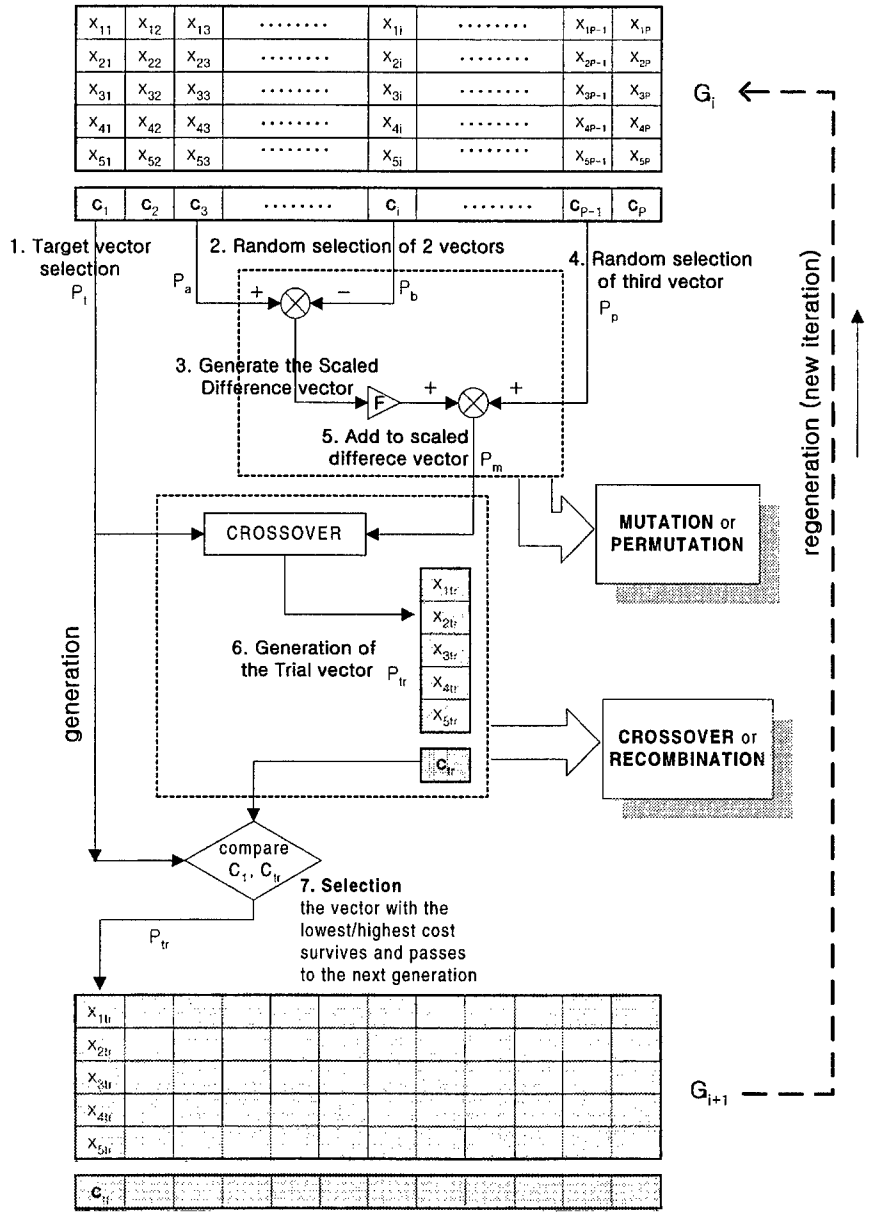

Figure 2.1 Schematic representation of differential evolution operations

Step 1: Target vector selection
The first left parameter vector of the top table is selected and denoted Target vector P_t . Note that the steps of differential evolution in Figure 2.1 are applied in parallel to all the rest vectors of the top table toward the right hand side during the differential evolution single run (one iteration). All the (parallel) applied target vectors form the basis of ancestors to be compared to the generated descendants and leave their positions to newly generated ones that can fill the bottom table. At the end of each run the improved generation in the bottom table is passed to the top table in order to play the role of new ancestors.

Step 2: Random selection of two vectors
Two parameter vectors denoted P_a, P_b are selected among the top table which should not be the same as the target vector P_t.

Step 3: Generate the scaled difference vector
From the randomly selected parameter vectors P_a and P_b in the previous step, the difference of two parameter vectors are multiplied by a user defined constant F ($F \in [0,1]$) to create the scaled difference vector.

Step 4: Random selection of third vector
The third parameter vector denoted P_b is selected randomly. This vector also should not be either the target vector P_t or two randomly selected parameter vectors P_a, P_b.

Step 5: Add to scaled difference vector (mutation)
Differential evolution mutates (perturbs) by using two randomly selected and one separately selected vector (i.e. the third vector). This process creates a new mutated parameter vector P_m. While in Figure 2.1 the perturbation process is portrayed in the top dashed box, the visual interpretation of this process is shown in the Figure 2.2.

Step 6: Generation of the Trial vector (crossover)
The next operation of the differential evolution is crossover. The mutated parameter vector P_m recombines with the target vector P_t in order to generate a new trial vector P_{tr}. The P_{tr} consists of parameters obtained from both P_m and P_t. In the context of Genetic algorithms, P_m and P_t are known as the parents and the newly generated parameter vector P_{tr} is known as their child. The actual parameter components of every vector P are known as genes. Differential evolution implements recombination by using the chance of occurrence applied to the

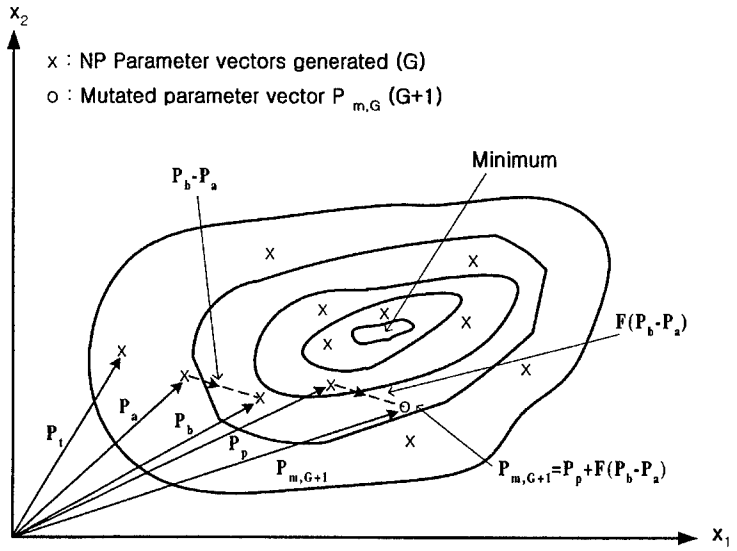

Figure 2.2 Perturbation (mutation) process of differential evolution for two dimensional cost function and the process for generating mutated parameter $P_{m,G+1}$ [4]

selection of the genes from the parents to the child. The likelihood that governs the inheritance of the parameter vector P_{tr} is determined by a constant parameter designated as the crossover ratio (CR). The graphical illustration is given in the Figure 2.3 followed by the explanation about the operation.

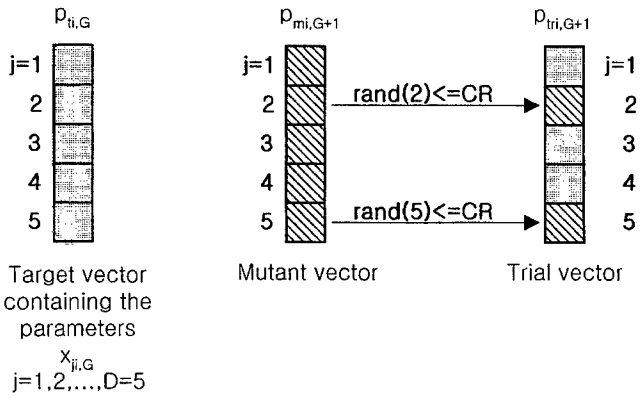

Figure 2.3 Illustration of the crossover process for D=5 parameters [4]

As can be seen in Figure 2.3, the process of crossover creates a new parameter vector named the trial vector (right) by exchanging the elements (gene) of the target parameter vector (left) and the mutant vector (middle). This gene recombination based on the random search from which as many explorations for the improved generation as possible is given by the following rule.

$$P_{tr,ij,G+1} = \begin{cases} P_{m,ij,G+1} & \text{if } \text{rand(j)}\big|_{at\ j} \le CR \quad \text{or} \quad j=\text{perm}(1,2,\ldots,D)\big|_{at\ j} \\ P_{t,ij,G} & \text{if } \text{rand(j)}\big|_{at\ j} > CR \quad \text{and} \quad j \ne \text{perm}(1,2,\ldots,D)\big|_{at\ j} \end{cases} \quad (2.1)$$

where $\text{rand(j)}\big|_{at\ j}$ is the j-th evaluation of a uniform random number generator with outcome $\in [0,1]$, CR is the crossover constant $\in [0,1]$, and $\text{perm}(1,2,\ldots,D)\big|_{at\ j}$ is a randomly chosen index $\in [0,1]$ which ensures that $P_{tr,ij,G+1}$ gets at least one parameter from $P_{m,ij,G+1}$.

Step 7: Selection
By comparing the cost value of the target parameter vector and that of the trial vector obtained from the crossover process, the lowest or highest cost value of parameter vector survives and passes in the next generation depending on the optimisation scheme (e.g., minimisation or maximisation). The chosen parameter vector and its cost value is then placed in the same position of the bottom table.

Repeating the steps for every target vector in the top table creates a new generation which fills the bottom table and takes the role of the previous generation for each iteration. Since the selection of the target vector is done from the leftmost to the right direction, this procedure as called the parallel search method. The iteration halts when a stopping criterion is satisfied. Usually this criterion is set as either a user defined cost value or a maximum number of iterations or both.

An example of the impacting signal restoration from measured signal using both Wiener Optimisation (denoted 'WO') and Differential Evolution (DE) method when an MA(2) inverse filter is applied is compared in the Figure 2.4. This rather 'simple' example in using only an MA(2) filter is used for illustration purposes. As can be seen in Figure 2.4 (c), The optimal point of DE marked by 'opt. (DE)' coincides with the 'max' point whereas the optimal point of Wiener optimisation marked by 'opt. (WO)' is at a different point on the objective function surface, which is identified as a local maximum. The signal restoration results, however, are similar (only a sign reversal) for both methods as

the objective function has little difference between the 'opt' point of Wiener optimisation and 'max' point. We can conclude that the Wiener optimisation may well also be a feasible method for blind signal restoration provided that the previously considered inverse filter's requirements (e.g. select an initial inverse type by an impulsive coefficients) are satisfied. This is reassuring considering that the computational loads in employing DE become nontrivial for large order filters. (refer to J. S. Seo [5] for details of the DE process).

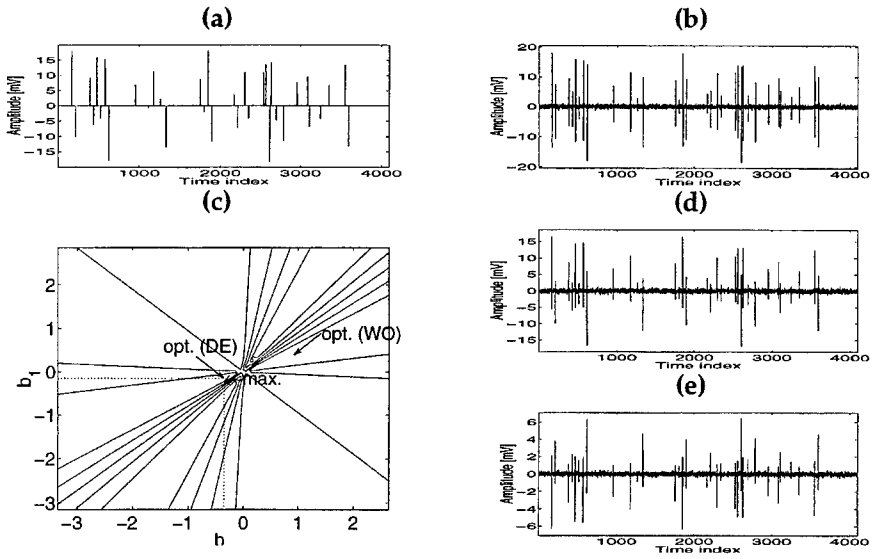

Figure 2.4 Restoration of signal from fourth-order Wiener solution, and DE method, (a): unknown input signal, (b): measured signal, (c): Global maximum and local maxima for both methods. (d): restored signal by using Wiener optimisation, and (e): restored signal by using DE optimisation method.

3. EXPERIMENTAL VERIFICATION FOR THE BLIND DECONVOLUTION OF IMPACTING SIGNAL

This section provides the practical application of considerations developed in the previous section and in Part I. Using both Wiener optimisation and the Differential Evolution method, we considered the reconstruction of an impacting signal from an experimental test assuming only a single measurement data of accelerometer is available.

The experimental lay out is shown in Figure 3.1 in which a cantilever beam is driven by a broad band Gaussian excitation. Impacting is induced by placing an end stop restricting the motion of the beam (at the beam tip). The Gaussian excitation signal is produced from a signal analyser (Ch.1) and fed to the exciter. The signal from the exciter (Ch.3) is responsible for the movement of the beam. The impacting signal (Ch. 2) is generated by the end stop incorporating a force transducer which is placed 1.5 mm behind from the beam steady state position. The accelerometer is attached at the free end of the cantilever beam to collect the signal (Ch. 4) mixed with the vibration signal of the beam and impacting signal caused by the end stop. Note the impacting signal (Ch. 2) is captured so as to assess the performance of the inversion process – normally of course this would be unavailable.

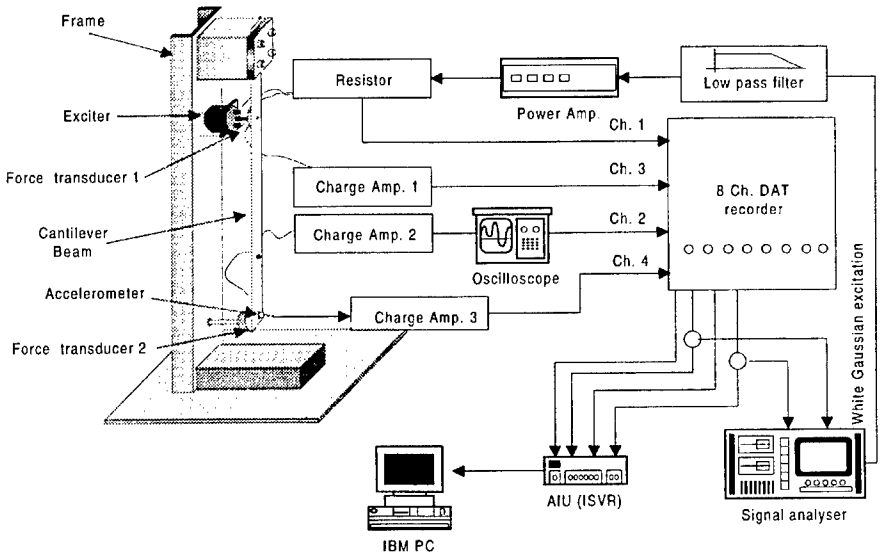

Figure 3.1 Experimental set-up for blind signal reconstruction

From the measured signal, the impacting signal has been reconstructed blindly. Suppose we have measured the motion of the beam from only the accelerometer point. From this measured data, the impacting signal is to be reconstructed using the higher-order cumulant of the measured signals. The ARMA(2,7) inverse system has been selected for both Wiener approach and DE method in this blind deconvolution of impacting signal problem.

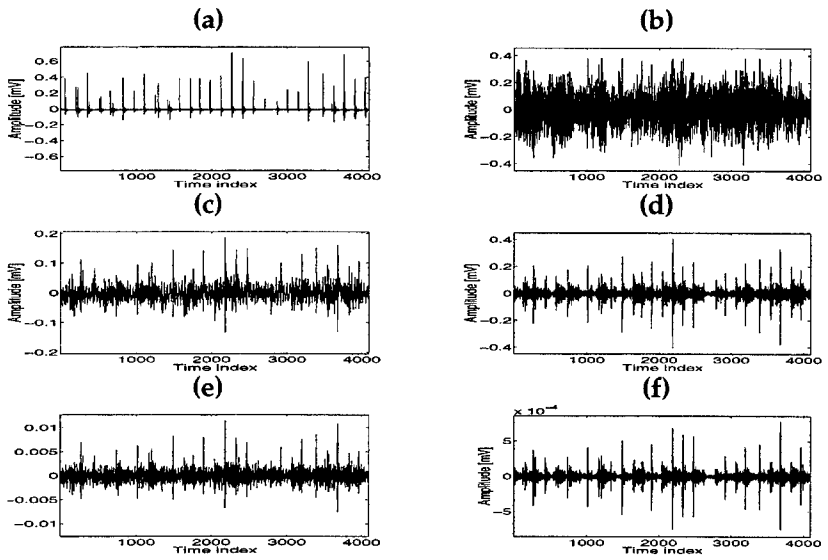

Figure 3.2 The result of signal restoration for experimental impacting signal; (a): impacting signal, (b) measured signal (from accelerometer), (c) restored signal from 3rd order method (Wiener approach), (d): restored signal from 4th order method (Wiener approach), (e): restored signal from 3rd order method (DE method), and (f): restored signal from 4th order method (DE method).

Table 3.1 Numerical comparison of the restored signals of the Figure 3.2

Methods / Values	Wiener approach		DE method		observed signal
	Third order	Fourth order	Third order	Fourth order	
α **coefficient**	0.83	0.65	0.76	0.59	2.02 (0.33)*
Entropy	2.93	2.52	2.79	2.53	3.60 (1.15)
Skewness	0.815	0.04	0.81	-0.07	0.066 (9.45)
Kurtosis	8.19	13.10	9.44	16.28	2.98 (128.5)

*: values in ( ) corresponds to the input signal

4. CONCLUDING REMARKS

Since the Wiener approach is believed to yield only one of the local maxima, the restoration of impacting signal using the global optimisation method has been carried out and compared to the Wiener optimisation method. One noticeable point to be mentioned here is that even through the Wiener optimisation method results generally in a local maximum, the reconstruction seems very comparable to the global optimisation.

There still exist some other aspects to the problem of restoring the impacting signal for both including the choice of filter length for both Wiener optimisation and Differential Evolution.
Following from this work possible future research could include

(i) The stabilisation of the IIR (AR and ARMA) inverse filters,
(ii) The use of multi-channel data and joint cumulant approach, and
(iii) Detection of the existence of non-Gaussian impacting signal.

REFERENCES

[1] D. E. Goldberg," *Genetic Algorithms in Search, Optimization and Machine Learning*," Addison-Wesley, 1989.
[2] L. Ingber and B. Rosen," Genetic Algorithms and Very Fast Simulated Reannealing: A Comparison," *Journal of Mathematical and Computer Modelling* 16 (11), pp 87-110, 1992
[3] J. A. Nelder and R. Mead," A Simplex method for function optimisation," *Computer J.* 7 pp 308-313, 1965.
[4] Rainer Storn and Kenneth Price," Differential Evolution – A Simple and Efficient Heuristic for Global Optimisation over Continuos Spaces," *Journal of Global Optimizatiion* 11 pp 341-359, 1997.
[5] J. S. Seo," Blind fault detection and source identification using Higher Order Statistics for impacting systems", PhD. Thesis 2000, ISVR, University of Southampton, UK (in preparation).

A General Force Identification Method for Complex Structures

Robert Adams & James F. Doyle
PURDUE UNIVERSITY
WEST LAFAYETTE, INDIANA 47907
email: doyle@ecn.purdue.edu

1 Introduction

The response $u(x,t)$ of a general linear structural system to a single excitation load $P(t)$ can be written as

$$u(x,t) = \int_0^t G(x,t-\tau)P(\tau)\,d\tau$$

where $G(x,t)$ is the system response function. The force identification problem is posed as: Given some measurements $u(t)$ (perhaps imperfectly), and knowledge of the system function $G(x,t)$ (perhaps imperfectly), determine the load $P(t)$. This problem is difficult for two quite separate reasons. The first is that it is a highly ill-conditioned problem which means that small errors in the measurements or the modeling can cause very large variances in the identified forces. Second, the need to know the system function in analytical form has meant that most structural systems analyzed were relatively simple.

Reference [1] gives an excellent summary of the literature on force identification as well as an overview of the subject itself; more recent citations can be found in Reference [2]. A variety of methods have been used, but the most common solution scheme has been some form of deconvolution. References [2, 3, 4, 5] used Fourier methods because of the relative simplicity of the inversion and because it is suitably matched to the spectral element approach. Each of these are quite limited in that they are restricted to relatively simple geometries. The beginnings of a deconvolution method coupled with a general finite element approach was given in Reference [6] which used an FEM program to generate wavelet solutions which could be synthesized in the inverse solution.

A quite different approach was pioneered in References [7, 8]. This approach uses ideas from dynamic programming, but what sets it apart from the above references is that it deals with the discretized form of the governing equations. This makes it suitable for coupling with a finite element modeling of the structure. However, as pointed out in Reference [7] "one of the disadvantages of the method is that the amount of computations increases dramatically as the order of the model increases". This necessitated the authors to introduce a modal

reduction scheme. The final size of the problem studied in References [7, 8] was nine degrees of freedom. More details and applications can be found in the Monograph [9].

It is the goal of this paper to develop a method for force identification that is robust enough to be applied to complex structures, but whose computational costs scale as for a forward finite element analysis. Furthermore, we wish to be able to determine multiple isolated forces as well as distributed pressures and tractions. After developing the main ingredients of the method, we illustrate its attributes using experimental data from the impact of a 3-D shell.

2 The Essential Difficulty

Using the discretization afforded by the finite element method [10], the governing dynamic equations for our general complex (but linear) structure can be discretized in space as

$$[\,M\,]\{\ddot{u}\} + [\,C\,]\{\dot{u}\} + [\,K\,]\{u\} = \{P\} = [\,B_g\,]\{g\} \tag{1}$$

In this, $\{u\}$ is the vector of all the free degrees of freedom and is of size $\{m_u \times 1\}$, $[\,K\,]$ is the $[m_u \times m_u]$ stiffness matrix, $[\,C\,]$ is the $[m_u \times m_u]$ damping matrix, $\{P\}$ is the $\{m_u \times 1\}$ vector of all applied loads (some of which are zero), $\{g\}$ is the $\{m_g \times 1\}$ subset of $\{P\}$ vector of non-zero applied loads, and $[B_g]$ is the $[m_u \times m_g]$ matrix that associates these loads with the degrees of freedom. Let these governing equations be discretized in time as the recurrence relations

$$\{u\}_{n+1} = [\,A\,]\{u\}_n + [\,B\,]\{g\}_n \tag{2}$$

In this, n is the subscript over the discretized time; $\{u\}$ now contains the state vectors (at least displacement and velocity) and is of size $m \geq 2m_u$; the vector of forcing terms, $\{g\}$, is of size $\{m_g \times 1\}$; and $[\,B\,]$ is the $[m \times m_g]$ matrix that associates the forces with the DoF. Some specific forms for $[\,A\,]$ and $[\,B\,]$ are given in References [11, 12]

In the forward problem, given the initial conditions as $\{u\}_1 = \textit{known}$ and the applied loads histories $\{g\}$, we can solve for the response recursively from Equation (2). In the inverse problem of interest here, the applied loads are unknown but we know some information about the responses; we wish to use this information to determine the applied loads. In particular, assume we have a vector of measurements $\{d\}$ of size $\{m_d \times 1\}$ which are related to the structural DoF according to

$$\{d\}_n \Leftrightarrow [\,Q\,]\{u\}_n$$

Note that the $[m_d \times m_u]$ matrix $[\,Q\,]$ could be a difference relation as would be the case for strains. We want to find the forces $\{g\}$ that make the system best match the measurements. Consider the general least squares error given by

$$E(u,g) = \sum_{n=1}^{N} \left[\{d - Qu\}_n^T [\,W\,]\{d - Qu\}_n \right], \qquad \{u\}_{n+1} = [\,A\,]\{u\}_n + [\,B\,]\{g\}_n$$

where $[\,W\,]$ could be a general weighting array on the data although we will take it as diagonal. Our objective is to find the set of forces $\{g\}$ that minimize this error functional.

It is possible to establish a global system of simultaneous equations by the usual procedures for minimizing the least squares. That is, we arrange Equation (2) to form

$$[\,\bar{A}\,]\{u\} = [\,\bar{B}\,]\{g\}, \quad \{u\} = \{\{u\}_1, \cdots, \{u\}_N\}^T, \quad \{g\} = \{\{g\}_1, \cdots, \{g\}_N\}^T$$

Solve for $\{u\}$ in terms of $\{g\}$. That is, first decompose $[\,\bar{A}\,]$ and then solve $[\,G\,]$ as the series of back-substitutions

$$[\,\bar{A}\,][\,G\,] = [L^T DU][\,G\,] = [\,\bar{B}\,]\{u\} = [\,G\,]\{g\}$$

The matrix $[\,G\,]$ is the collection of forward solutions for unit loads applied for each of the unknown forces. Substitute $\{u\} = [\,G\,]\{g\}$ into the error equation and minimize with respect to $\{g\}$. The resulting system is

$$[G^T Q^T W Q G]\{g\} = [QG]^T[\,W\,]\{d\}$$

This naive scheme is not practical for two very important reasons.

Consider our dynamic problems where there are m_u degrees of freedom at N time steps; this would lead to the very large system array $[\,\bar{A}\,]$ of size $[(m_u \times N) \times (m_u \times N)]$. A system with 10,000 DoF over 2000 time steps has nearly 100×10^6 unknowns and a system size of $[\,\bar{A}\,]$ that is the square of that. Clearly, this approach to solving the problem does not scale very well and the procedure is restricted to very small problems only.

There is an even more insidious reason why the above scheme will not work even if we could afford the computational cost — the established system of equations are notoriously ill-conditioned. That is, any small perturbations in the input data or system parameters will cause significant changes in the estimated parameters.

The two key factors we must address are therefore size and ill-conditioning. In the following, the ill-conditioning is handled by the introduction of regularization terms [13]. We cope with the problem of size by adapting ideas from Kalman filtering that allows a sequential (in time) solution of the problem.

3 Well-Posed Problems

The usual least squares procedure is posed in the form of finding the set of discretized unknowns $\{u\}$ given the set of data $\{d\}$ so that the positive functional $\mathcal{A} = \chi^2$ is a minimum; that is,

$$\textit{minimize}: \qquad \mathcal{A} = [Au - d]^T[Au - d]$$

The number of data is typically larger than the number of unknowns and therefore minimizing wit respect to the unknown $\{u\}$ gives a determinate system of equations. These problems, however, are actually very difficult to get robust answers even when there is an excess of data since they are highly ill-conditioned.

Our situation is even more complicated in that we possibly could have many more unknowns than data. For example, we may be interested in finding a traction distribution on a surface with an unknown force associated with each node on the surface — if the FEM discretization is fine, then there will be many more nodes (hence unknown forces) than measurements.

We now paraphrase some of the discussion of regularization as given in Reference [13]. A key point has to do with degenerate minimization principles. If $[\ A\ ]$ has fewer rows than columns then minimizing $\mathcal{A}(u)$ will not give a unique solution for $\{u\}$. However, if we add any multiple λ times a nondegenerate quadratic form $\mathcal{B}(u)$, for example, a function formed as $\{u\}^T\{u\}$ then minimizing $\mathcal{A}[u] + \lambda\mathcal{B}[u]$ will lead to a unique solution for $\{u\}$.

Thus the essential idea in our inverse theory is the objective

$$\text{minimize:} \qquad \mathcal{A} + \lambda\mathcal{B} = \{Au - d\}^T\{Au - d\} + \lambda\{u\}^T[\ H\ ]\{u\}$$

for various values of $0 < \lambda < \infty$ along the so-called trade-off curve. There are two positive functionals, $\mathcal{A}$ and $\mathcal{B}$. The first measures something like the agreement of a model to the data; when $\mathcal{A}$ by itself is minimized, the agreement with the data becomes very good but the solution becomes unstable, oscillating wildly. This reflects that $\mathcal{A}$ alone typically defines a highly ill-conditioned minimization problem. The second term $\mathcal{B}$ is introduced to overcome this problem; it measures something like the "smoothness" of the desired solution, or sometimes a quantity reflecting *a priori* judgments about the likelihood of a solution. This function is called the regularizing operator. Minimizing $\mathcal{B}$ by itself gives a solution that is "smooth" or "stable" or "likely". Note that this has nothing at all to do with the measured data — only our *a priori* biases. We settle on a "best" value of λ by some criterion ranging from fairly objective to entirely subjective.

The regularization method we will discuss is generally called Tikhonov[14] regularization. Typically, the functional $\mathcal{B}$ involves some measures of smoothness that derive from first or higher derivatives.

Consider a normal traction distribution represented by the collection of forces $g(x) \Rightarrow \{g\}$. Suppose that our *a priori* belief is that, locally, $g(x)$ is not too different from a constant. Then a reasonable functional to minimize is associated with the derivative

$$\mathcal{B} \propto \int (\frac{dg}{dx})^2\, dx \propto \sum_{m=1}^{M-1} [g_m - g_{m+1}]^2 = \{g\}^T[\ D\ ]^T[\ D\ ]\{g\} = \{g\}^T[\ H\ ]\{g\}$$

since it is nonnegative and equal to zero only when $g(x)$ is constant. The matrix $\{D\}$ is the $[(M-1) \times M]$ first difference matrix and $[\ H\ ]$ is the $[M \times M]$

symmetric matrix formed from it. They are given by

$$[\,D\,] = \begin{bmatrix} -1 & 1 & 0 & \cdots \\ 0 & -1 & 1 & \cdots \\ 0 & 0 & -1 & \cdots \end{bmatrix}, \qquad [\,H\,] = [\,D\,]^T[\,D\,] = \begin{bmatrix} 1 & -1 & 0 & \cdots \\ -1 & 2 & -1 & \cdots \\ 0 & -1 & 2 & \cdots \end{bmatrix}$$

This is called first order regularization. This choice of $[\,D\,]$ is only the simplest in an obvious sequence of derivatives.

The above schemes are for regularization along a line — an edge traction, for example. A 2-D pressure distribution on a shell or plate is handled slightly differently because the pressure first acts on the element and we impose regularization of the pressure between neighboring elements.

4 Recursive Formulation of the Problem

Consider the general least squares error given by

$$E(u,g) = \sum_{n=1}^{N} \Big[\{d - Qu\}_n^T [\,W\,] \{d - Qu\}_n + \lambda \{g\}_n^T [\,H\,] \{g\}_n \Big]$$

where the summation is over all the time steps as discussed before. The main idea to be developed is to perform the minimization recursively, rather than globally, working from the last time step.

In the type of structural dynamics problem we are interested in, the system parameters do not change over time. As a result, many of the arrays in the recursive relations also do not change over the increments in time; this leads to the possibility of formulating the equations in terms of changes of quantities rather than the quantities themselves. The following equations for an efficient formulation are due to Kailath[15] who discusses it in good detail. Derivations can also be found in Reference [9].

The solution is in the form of the recursion relations:

$$\begin{aligned}
[D_{n-1}^{-1}] &= [D_n^{-1}] - 2[B^T Y_n][L_n][Y_n^T B] \\
[D_{n-1}] &= [D_{n-1}^{-1}]^{-1} \\
[L_{n-1}] &= [L_n] + 2[L_n Y_n^T B][D_{n-1}][B^T Y_n L_n] \\
[Y_{n-1}] &= [A^T]\Big[Y_n - 2K_n B^T Y_n\Big] \\
[K_{n-1}] &= [K_n] - \Big[Y_n - 2K_n B^T Y_n\Big][L_n Y_n^T B][D_{n-1}] \\
\{S_{n-1}\} &= -2[Q^T W]\{d\}_{n-1} + [A^T]\Big\{\{S_n\} - 2[K_n B^T]\{S_n\}\Big\}
\end{aligned}$$

It is clear that these computations can be sequenced so that many of the partial products can be re-used. When doing this, the carry-over arrays should be

chosen to be the small ones. One such possible scheme is given in Reference [11]. The initial conditions for the recursive variables are

$$\begin{aligned}
[D_N^{-1}] &= 2\lambda[\,H\,] + 2[B^T Q^T][\,W\,][QB] \\
[D_N] &= [D_N^{-1}]^{-1} \\
[Y_N] &= [A^T][Q^T] \\
[K_N] &= [Q^T W][QB][D_N] \\
[L_N] &= -[\,W\,] + 2[\,W\,][QB][D_N][B^T Q]^T[\,W\,] \\
\{S_N\} &= -2[Q^T W]\{d\}_N
\end{aligned}$$

We are now in a position to complete the solution.

During the backward phase of the computations, we store the quantities

$$[D_n B^T]\{S_n\}\,, \qquad [K_n^T]$$

either to disk or in-core. These can then be used in the forward calculations. The forward stage of the computations is given by

$$\begin{aligned}
\{g\}_n &= -[K_{n+1}^T][\,A\,]\{u\}_n - [D_{n+1}B^T]\{S_{n+1}\} \\
\{u\}_{n+1} &= [\,A\,]\{u\}_n + [\,B\,]\{g\}_n
\end{aligned} \tag{3}$$

This form of the recursive relations deals with arrays of size

$$\begin{aligned}
[D_n^{-1}] &= [m_g \times m_g] \quad \text{symmetric} \\
[D_n] &= [m_g \times m_g] \quad \text{symmetric} \\
[L_n] &= [m_d \times m_d] \quad \text{symmetric} \\
[Y_n] &= [m \times m_d] \\
[K_n] &= [m \times m_g] \\
\{S_n\} &= [m \times 1]
\end{aligned}$$

The largest arrays are of size $[m \times m_d]$ and $[m \times m_g]$, and since both m_d and m_g are significantly less than m, we have a huge reduction in the storage requirements.

Both the Ricatti and time invariant equations were incorporated into a program called `Inverse`. Implicit and explicit versions of the time integrations are selectable. Existing finite element code to produce the stiffness, mass, and damping arrays of 3-D thin-walled shell structures with reinforcements was modified and incorporated into `Inverse`; consequently it can handle the same problems as the original finite element program. The model of the structure is created using the mesh generating program associated with the finite element program.

Through the matrix $[\,Q\,]$, any number of mixed sensors can be used. In the case of the implicit scheme, the accelerometer data can be used directly; in the explicit scheme it needs to be integrated once to be put in the form of velocity.

Through the matrix $[B_g]$, any number of forces and moments can be determined. As seen in the equations of Appendix I, we actually determine the rate of force and not the force itself. This has the effect of adding regularization in the time direction.

The system array $[\ A\ ]$ is very large and therefore it is to our advantage to give special treatment to its manipulations. We never do actually assemble the $[\ A\ ]$ matrix but instead retain the individual component matrices. The storage used for the array is then

$$[(2m_u + m_g) \times (2m_u + m_g)] \quad \Longleftrightarrow \quad [m_u \times b + 2m_u]$$

This affords a substantial reduction for large systems. The vector product $\{w\} = [\ A\ ]\{v\}$ is accomplished by breaking $\{v\}$ into three parts and then adding the separate products with the only expensive computation being the product $[\ K\ ]\{v_1\}$ and this is accomplished in banded form. In this way, both the storage and computational cost of manipulating the system array $[\ A\ ]$ is reduced considerably. As is the case with the forward finite element problem, the largest array is the stiffness matrix. More details on the program can be found in Reference [11].

5 Application to 3-D Shell

In order to exercise the program and determine some of the metrics, we first apply it to a shell problem using synthetic data. This will be used to demonstrate the ability of the program to handle large problems, and to demonstrate the necessity of regularization. We conclude with an experimental study of a cylindrical shell.

Synthetic Data

This example, shown in Figure 1, presents a complex problem in that it is three dimensional with a large number of degrees of freedom. The elements used are such that there are six degrees of freedom at each node — three displacements, and three rotations. The total number of DoF for the mesh shown is 3456 and this translates into total system size (state vector plus unknown forces)

$$\begin{array}{lllll} \text{implicit:} & Size = 10375\,, & \Delta t = 5.0\,\mu s\,, & N = 400 \\ \text{explicit:} & Size = 6375\,, & \Delta t = 0.4\,\mu s\,, & N = 2000 \end{array}$$

These numbers are on the order of those presented in the introductory discussion.

The distributed load along the west edge is comprised of seven unknown forces. The sensors are not distributed in any particular optimized manner for calculating these forces — indeed we purposely, for the results to be shown, did not use any sensors in the immediate location of the unknown force.

The timings for the solution are: 53 minutes for the implicit scheme and 10.6 hours for the explicit scheme. The relative cost between the backward

and forward portions of the solution is approximately 8:1 for both integration schemes. The difference between the two schemes is that the implicit method can use a time step related to the frequency content of the excitations, whereas the step size for the explicit method is dictated by the element size. In this instance, the advantage lies with the implicit method.

The force reconstructions are shown in Figure 2. The most significant aspect to the force reconstruction is that they depend significantly on the amount of regularization. That is, for λ greater than about 1.0×10^{-19} the results can be meaningless even though perfect, uncorrupted, data is being used. The results on the right are for $\lambda = 4.0 \times 10^{-19}$ which is about the threshold of somewhat meaningful results. The reconstructions on the left are for $\lambda = 1.0 \times 10^{-16}$ and show excellent agreement with the input values.

These results highlight the ill-conditioned aspect of the identification problem — even perfect data, in good quantity, may not be sufficient to get a robust solution when regularization is not used.

Experimental Setup

The setup for the experiment is shown in Figure 3. The 51 mm (2 in.) long cylinder was constructed with 3 mm (1/8 in.) thickness throughout. Accelerometers were placed on the top (90 deg), and 180 deg from the impact site as shown in Figure 3 and attached using bees wax. The specimen was suspended by strings and impacted midway 25 mm (1 in.) along the length.

Data for the experiments were collected by means of an Omega Instruments DAS-58 data acquisition card installed in a PC computer. The DAS-58 is a 12-bit card capable of 1 Mhz sampling rate and storing up to 1M data points in the on-board memory. For this experiment, four channels were sampled at 250 khz, or a 4 μs time step.

Accelerometers (PCB 309A) and a modified (PCB) force transducer were used to collect the data. The connections between the accelerometers and the computer were through the use of an Omega Instruments BNC-58 multiplexing unit. The accelerometer outputs were converted to velocity by the simple trapezoidal integration rule

$$v_{n+1} = v_n + \tfrac{1}{2}(a_n + a_{n+1})\Delta t$$

Because of slight offsets in the acceleration voltages, a trend is usually observed in the velocity. This trend is estimated and subtracted; we refer to the detrended data as the raw data.

Inverse Study

Correct inverse analysis is predicated on a high fidelity finite element model of the structure being analyzed. That is, this model must correspond accurately to the real experimental situation in terms of material properties (Young's modulus,

mass density), dimensions (diameter, thickness) and sensor locations. Therefore, before any solution to an inverse problem is attempted, the model must be verified by doing a forward problem.

A convergence study was performed to determine the proper element size for the finite element model. A model was created similar to that of Figure 1. The data from the force transducer provided the input force history for this study. From the results of the convergence study, it was determined that $3\,mm$ (1/8 in.) modules would be an acceptable size for the `Inverse` analysis. The number of elements for the resulting model was 704 folded plate elements. This creates a problem with a system size of 2243 degrees of freedom.

The force reconstructions from the experimental velocity inputs are shown in Figure 4. It is pleasing to note that the double impact is detected. Accelerometer #2 on its own does a good job but the same is not true for Accelerometer #1. At first sight, this might appear to indicate that somehow this data is seriously corrupted. However, the fact that using both accelerometers together gives somewhat improved results does not bear this out. If accelerometer #1 was indeed contaminated, then mixing both acceleration data would also show the contamination. A more reasonable conjecture is that position #1 is very sensitive, in an ill-conditioning sense, to slight errors in the data. Our conjecture has important implications for inverse methods so we decided to further investigate the nature of the discrepancy by manipulating synthetic data in a couple of ways and comparing the performance of positions #1 and #2.

First, the sensitivity due to the positioning of the accelerometer in relation to the node used in the `Inverse` analysis was examined. These results demonstrated that, for a given misalignment, the 90 deg position is more sensitive than the 180 deg position. However, the symptom of the error (a constant frequency superposition) does not reflect the symptom shown in the experimental results.

As a second study, approximately the same amount of drift seen in the experimental velocities was added to the velocities generated synthetically. Again, these adjusted velocities were used to reconstruct the force from the response at the nominal 90 deg and 180 deg positions. These results are as an inset in Figure 4. Again, the 90 deg position is more sensitive to slight deviations in the input data. This time the symptom is similar to that of the experimental results. It is noted that using both accelerometers does not give a simple average but gives a result that is better than the individual results.

These studies indicate a concern that is quite crucial in inverse studies and is different from the experimental issues of position accuracy and signal fidelity. When doing an inverse analysis, the location of the sensor(s) and not just its accuracy is very important. The implication is that multiple sensors must be used, and that they be combined through the use of regularization. Both of these aspects are part of the program `Inverse`.

6 Discussion

This paper brings together a number of technologies to solve the force identification problem on complex structures. At the core, is the embedding of the finite element modeling of complex structures. Consequently, structures as complex as is usually modeled with the finite element method can be handled conveniently. Special effort was made to insure that the computational costs scale in a manner similar to the forward problem using the finite element method. The problem of ill-conditioning is handled through regularization. This alleviates the burden of proper sensor placement and as a result, the difficult problem of traction and pressure distributions can be solved. This opens up the exciting possibility of solving problems with unknown boundary conditions or using subdomains for the modeling. A preliminary investigation of these are given in Reference [11].

Acknowledgement: This work was supported in part by a U.S. Army Multi-University Research Initiative (United States Army Grant No. DAAH04-96-10331) awarded to Purdue University.

References

[1] **Stevens, K.K.**, Force Identification Problems: An Overview, *Proceedings of SEM Spring Meeting*, Houston, pp. 838–844, 1987.

[2] **Martin, M.T. and Doyle, J.F.**, Impact Force Identification from Wave Propagation Responses, *International Journal of Impact Engineering*, **18**, pp. 65–77, 1996.

[3] **Doyle, J.F.**, Further Developments in Determining the Dynamic Contact Law, *Experimental Mechanics*, 24, pp. 265–270, 1984.

[4] **Rizzi, S.A. and Doyle, J.F.**, A Spectral Element Approach to Wave Motion in Layered Solids, *Journal of Vibration and Acoustics*, **114**, pp. 569–577, 1992.

[5] **Danial, A.N. and Doyle, J.F.**, A Massively Parallel Implementation of the Spectral Element Method for Impact Problems in Plate Structures, *Computing Systems in Engineering*, **5**, pp. 375–388, 1994.

[6] **Doyle, J.F.**, A Wavelet Deconcolution Method for Impact Force Identification, *Experimental Mechanics*, **37**, pp. 404–408, 1997.

[7] **Busby, H.R. and Trujillo, D.M.**, Solution of an Inverse Dynamics Problem using an Eigenvalue Reduction Technique, *Computers & Structures*, **25**(1), pp. 109–117, 1987.

[8] **Hollandsworth, P.E. and Busby, H.R.**, Impact Force Identification using the General Inverse Technique, *International Journal of Impact Engineering*, **8**, pp. 315–322, 1989.

[9] **Trujillo, D.M. and Busby, H.R.**, *Practical Invere Analysis in Engineering*, CRC Press, New York, 1997.

[10] **Doyle, J.F.**, *Static and Dynamic Analysis of Structures*, Kluwer, The Netherlands, 1991.

[11] **Adams, R.A.**, *Force Identification in Complex Structures*, M.S. Thesis, Purdue University, 1999.

[12] **Adams, R.A. and Doyle, J.F.**, Force Identification in Complex Structures, *Experimental Mechanics*, to appear, 1999.

[13] **Press, W.H., Flannery, B.P., Teukolsky, S.A. and Vetterling, W.T.**, *Numerical Recipes, 2nd ed.*, Cambridge University Press, Cambridge, 1992.

[14] **Tikhonov, A.N. and Arsenin, V.Y.**, *Solutions of Ill-Posed Problems*, Wiley and Sons, New York, 1977.

[15] **Kailath, T.**, Some New Algorithms for Recursive Estimation in Constant, Linear, Discrete-Time Systems, *IEEE Transactions on Information Theory*, AC–19(4), pp. 83–92, 1973.

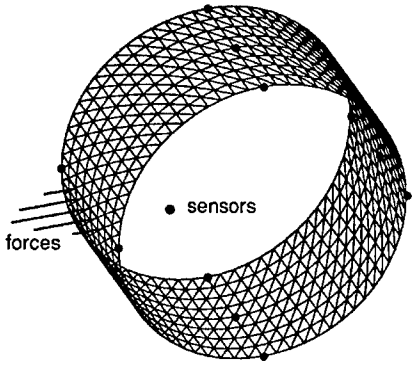

Diam: 3.5 in

Length: 2.0 in

Thick: .125 in

Aluminum

Figure 1: Shell mesh with parameters.

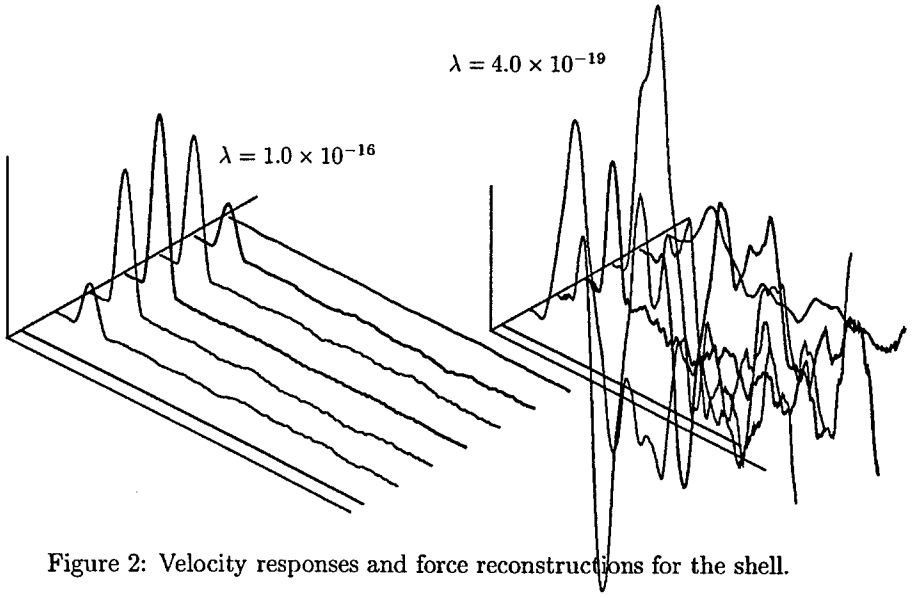

Figure 2: Velocity responses and force reconstructions for the shell.

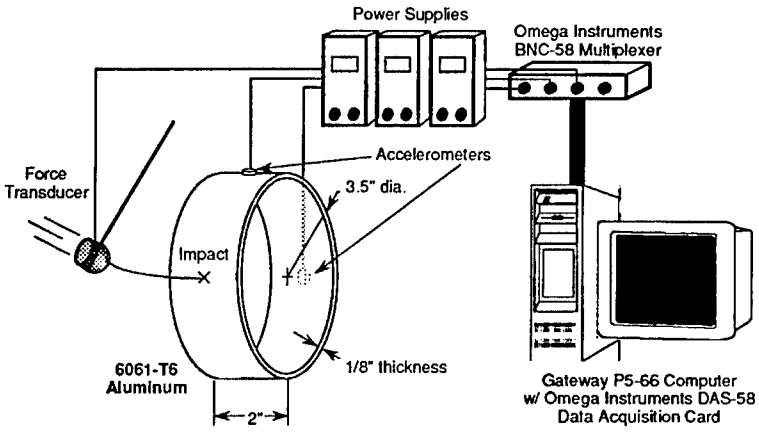

Figure 3: Experimental setup.

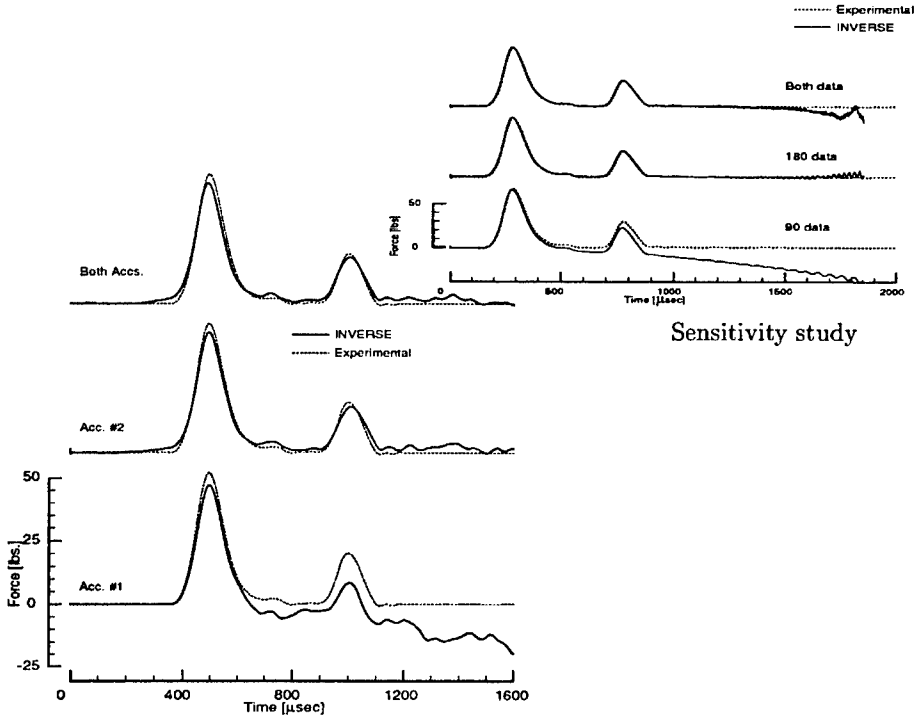

Figure 4: Comparison of results from `Inverse` and force transducer data for the shell experiment.

ROTATIONAL SYSTEMS AND RELATED STUDIES

JOURNAL BEARING CONDITION MONITORING USING VIBRATION MEASUREMENTS AND A NEW SIGNAL ENHANCEMENT TECHNIQUE

Barney E. Klamecki
Department of Mechanical Engineering, University of Minnesota,
Minneapolis, MN 55455-0111 USA

ABSTRACT

Vibration measurements were made using two accelerometers mounted on the block of a four-cylinder, spark ignition engine. A large number of tests were run with varying sensor location, engine speed, oil grade and bearing wear simulated by machining away material from bearing surfaces. Results show that changes in bearing wear and oil grade produce easily seen patterns in the time series signals. Frequency spectra were dominated by the engine firing frequency and so individual cylinder events are not easily identified in signal spectra. The enhancement of spectra peaks associated with individual cylinder firing events by adding noise to accelerometer signals (stochastic resonance) was demonstrated in numerical experiments using actual accelerometer signals.

Introduction

Intermittent or continuous monitoring of machines during operation is an attractive opportunity for machine maintenance based on the actual condition of a machine rather than on a pre-defined, fixed schedule. If the condition of components can be deduced during operation, maintenance can be performed only if needed. Also, if mechanical models (in contrast to statistical models) are available along with performance records over time, predictions of future system performance and predictive maintenance are possible. And, if accurate measures of bearing and other machine component operation are available, machine and component analysis and design can be improved.

Accelerometers have many desirable characteristics for machine monitoring, e.g., high sensitivity, durability and ease of mounting on bearing cases. Also, the wide bandwidth of signals implies the possibility of monitoring several machine elements. However, accelerometers are not typically used for journal bearing condition monitoring. Evidently, the relatively high fluid film compliance compared to rolling element bearings and the desirability of mounting accelerometers away from the bearing suggest low signal to noise ratio

measurements. Part of the work reported here demonstrates that accelerometers mounted on the outside surface of internal combustion engines can be used to measure bearing wear

Improvements in measurement systems can be sought in use or development of better sensors. An alternate approach is to attempt to extract more information from available signals. Signal enhancement is a concept that is different from signal manipulation. In contrast to transforming the data into different forms such as in calculating signal frequency spectra of time series data, the intent is to add useful content to the signal. A surprising result in signal enhancement is described in the second part of this paper. Recently it has been shown that the addition of noise (an additional random input) to the input to nonlinear systems can produce an increase in certain portions of spectra calculated from system output. This signal enhancement is called stochastic resonance. Numerical experiments were performed using accelerometer data and stochastic resonance was observed. This is apparently the first demonstration of stochastic resonance, albeit in numerical experiments, in mechanical systems.

PROBLEMS CONSIDERED

Two problems were addressed. One was the assessment of the usefulness of engine vibration signals for monitoring main journal bearing wear in internal combustion engines. Previous research has shown that bearing failure can be identified, but measuring bearing wear and predicting failure remain open problems. The other part of the work was a study of the potential of stochastic resonance for vibration measurement enhancement.

BACKGROUND

The use of accelerometers to measure machine vibration and signal analysis using frequency spectra are well established, widely used and may be considered to be standard measurement techniques. These topics are not reviewed here other than to note that accelerometers are not typically used to monitor journal bearing operation. Harker and Sandy[1] summarized expected problems due to poor transmission of shaft related vibration across the fluid film to the bearing casing.

Recently there have been a few demonstrations that the addition of a randomly varying input to the signal acquisition system of biological and physical systems can increase or enhance detection of certain low level parts of the original system input. Enhancement of low level components of signals in this way is being called stochastic resonance.

Douglass, et al. [2] measured signal reception in mechanoreceptor cells in crayfish. Low level signal components were increased when an optimal value of noise was added to the system input signal. Demonstrations of stochastic resonance in crayfish and in electrical circuits are presented by Wiesenfeld and Moss [3]. Fauve and Heslot [4] produced stochastic resonance in a Schmitt trigger circuit. McNamara and Weisenfeld. [5] measured improved signal-to-noise ratio when noise was injected into a bidirectional ring laser. Benzi, et al. [6] and Winograd *et al.*[7] explained recurrent ice ages using periodic and stochastic forces in a climate model.

Benzi et al. [8] and Nicolis [9] studied climatic change and provided a mathematical foundation showing that in systems subjected to periodic forcing, random perturbation may produce enhanced response in certain ranges of the power spectrum of the system output signal. Development of the concept by McNamara and Wiesenfeld [10] showed weak parts of signals can be increased by noise in systems that have a threshold above which a signal is defined. This represents the very large group of measurements systems which have inherent thresholds or in which a threshold can be set.

Monitoring Bearing Wear

Experimental Setup and Tests

The engine used is a four-cylinder, 1.8 liter displacement spark ignition engine mounted on a 1600 kg concrete slab that is supported on soft springs at its corners. Bearing wear was simulated by machining 0.15 mm from a bearing face and installing this bearing as the lower half of the second bearing from the front of the engine. Accelerometers were mounted on studs threaded into existing tapped holes on the side of the engine block at about the height of the main bearings. One accelerometer was mounted ahead of the first crankshaft main bearing and is called sensor a. The other accelerometer, sensor b, was mounted near the center of the second cylinder and about 40 mm behind (toward the rear of the engine) the second main bearing. So, sensor a was about 200 mm along the engine length from the test bearing while the accelerometer b was about 40 mm from the test bearing.

Each of the two data acquisition channels consisted of an accelerometer, a low pass anti-aliasing filter and an amplifier. The accelerometers have an essentially flat response of less than 2% deviation over the 20 Hz – 10 kHz bandwidth. All data was obtained using a 5,000 samples/second sampling rate. Frequency spectra of the time series data were calculated using a mathematical software package. Vibration signals are shown in terms of volts which was the

directly measured quantity and which is directly proportional to acceleration. All tests were run at the same data acquisition system settings and so all results are directly comparable. Data is displayed as a function of the data point number.

Tests were run under no load conditions. The engine was allowed to come to a stable operating condition indicated by constant oil and coolant temperatures before measurements were made. Engine speed was varied between 800 rpm and 2700 rpm and. SAE 10, SAE 30 and SAE 40 oils were used.

Effect of Bearing Wear on Accelerometer Signals and Signal Spectra

Figure 1 contains typical accelerometer b signals and spectra from tests with new bearings, left column, and a worn bearing.

The tests were with, SAE 10 oil at engine speeds of about 2100 rpm and 2660 rpm. The general signal pattern is periodic with frequency of twice the engine rotation speed, which is the engine firing frequency for the four cylinder, four stroke engine. In the 2100 rpm, new bearings test results show that there is an every-fourth peak which is slightly higher than the other three peaks in the engine firing sequence. This higher peak shows the ability to identify individual cylinder firing events, presumably from the cylinder nearest the accelerometer. The signal is less uniform in the 2090 rpm test. The larger forces in this higher speed case mean that engine firing events in cylinders farther away from the accelerometer are seen in the signal. For the large number of tests run over the wide ranges of test conditions used, it was observed that there was an engine speed range in which events related to individual cylinder firing were most clearly seen in accelerometer signals. The clearest indication of individual cylinder firing was obtained in the speed intermediate range of 1800 rpm– 2100 rpm.

Comparison of the accelerometer signals from tests with new and worn bearings shows a drastic difference in signals and the ability to easily identify a worn bearing condition. The every-fourth peaks in the time series data for the 2100 rpm, worn bearing case are about two to three times higher than the corresponding peaks in the signal from the test with new bearings. This clear pattern indicating a worn bearing is not seen in the 2660 rpm tests. This again shows the dependence of signal characteristics on engine speed described above.

The accelerometer signal frequency spectra in Figure 1 show three relevant results. The first is that the engine firing frequency of twice the engine rotation speed dominates the spectra. The second important result follows from the first and is that there are only weak indications of the individual cylinder firing frequency in the spectra. The individual cylinder events occur at one-fourth the engine firing

frequency and there are only small peaks in the spectra at this frequency. The third result is the implication that the spectra are less useful for monitoring bearing wear than the time series data

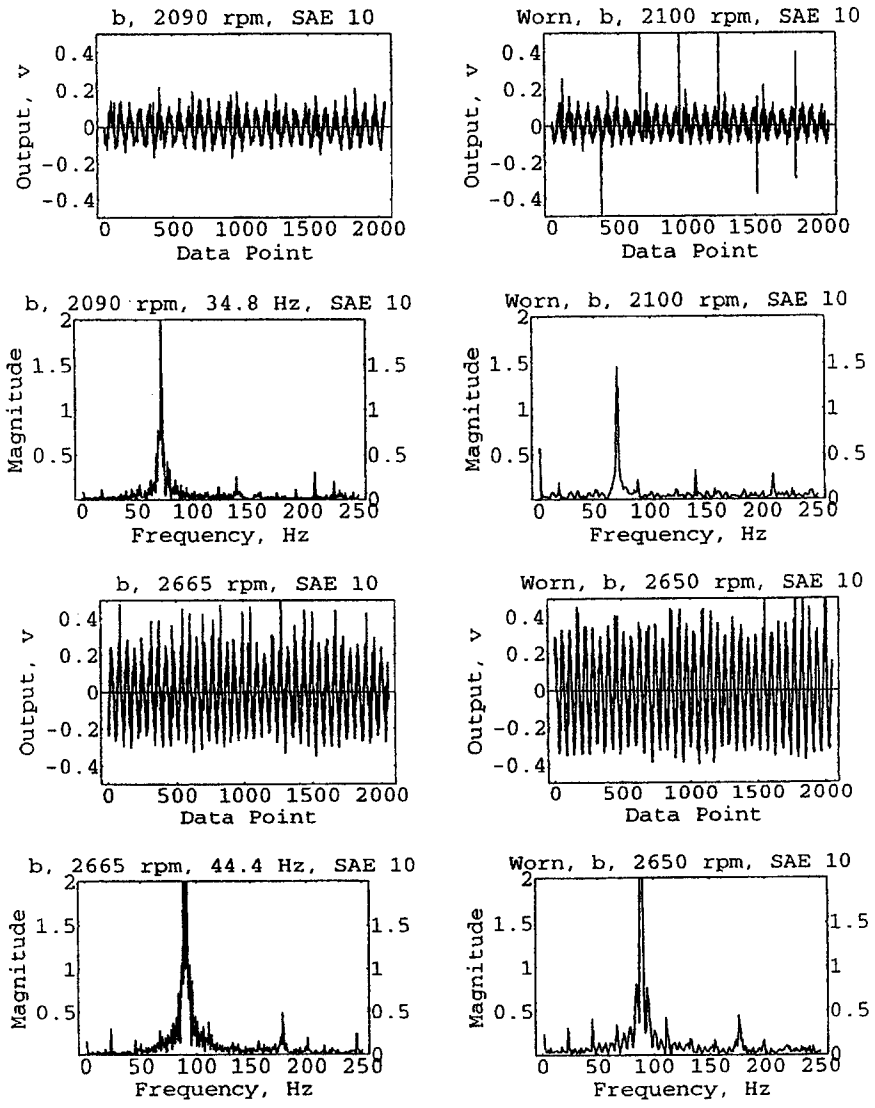

Figure 1. Accelerometer signals from sensor b for new and worn bearings.

Effect of Accelerometer Location and Oil Grade

The effects of sensor location and engine oil grade on accelerometer signals are summarized in the typical results presented in Figure 2.

The accelerometer signals in the top row show the general result that the accelerometer nearer the event of interest produced an easier to interpret signal, again in an appropriate range of engine speed. In these tests using SAE 10 oil and a worn bearing, the individual cylinder firing peaks are two to five times higher in the sensor b signal than in the signal from accelerometer a which was located about five times as far from the worn bearing.

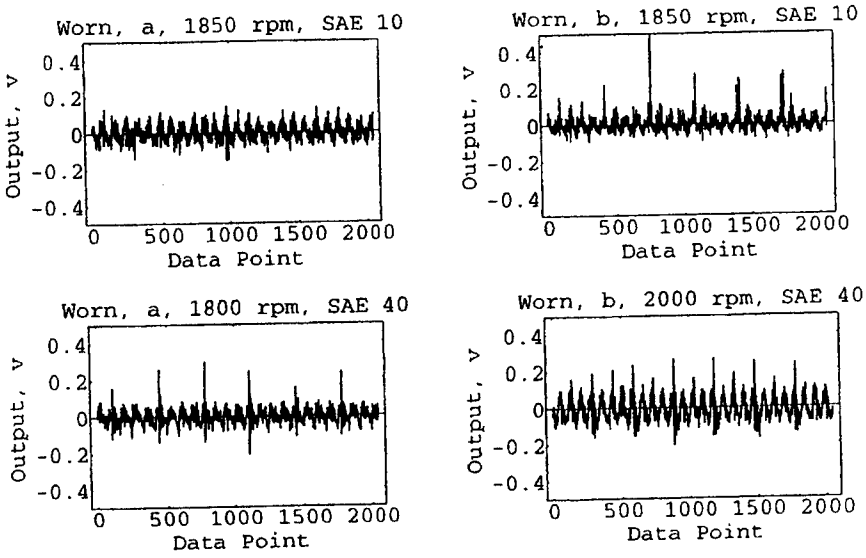

Figure 2. Accelerometer signals for sensors a and b for SAE 10 and SAE 40 oils.

Using a higher grade number, higher viscosity (0.004 PaSec and 0.0085 PaSec for SAE 10 and SAE 40 oils at 100 C) oil produced two effects. The accelerometer a signals in the left column of Figure 2 show the general result that using higher grade number oil resulted in much higher signal peaks associated with individual firing events. In this case these peaks are about twice as high and more easily identified in the SAE 40 oil test results compared to the SAE 10 test signal in which they are not at all clear.

The second result is that while the individual cylinder firing, every-fourth peaks are higher for sensor a, in the SAE 40 oil tests, the overall signal levels of the rest of the signals are about the same. For

sensor b which is much closer to the worn bearing the use of SAE 40 oil resulted in an increase in overall signal level.

The implications of these results are that higher viscosity oil produces larger mechanical effects in journal bearings and individual cylinder events are more clearly seen in the accelerometer signals.

Signal Enhancement

Method

Signal enhancement by stochastic resonance was investigated by producing new frequency spectra from accelerometer signals. In physical systems the random noise is an input to the forced system. A system model is shown in Figure 3a.

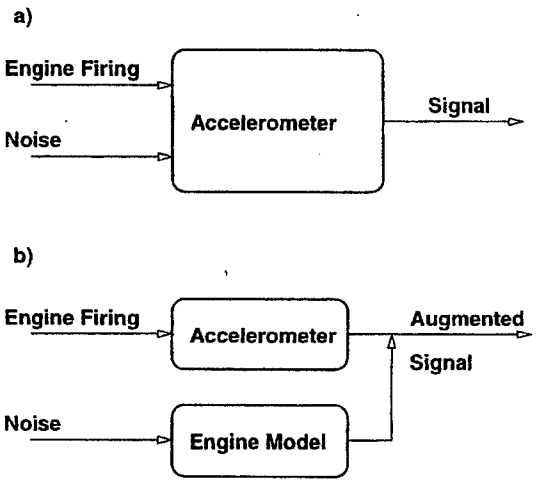

Figure 3. System model for numerical experiments

Engine firing and worn bearing effects drive the accelerometer and an engine generated noise is included. In this investigation the random noise input was modeled as an addition to the accelerometer signal. The engine is assumed to be a linear system and so the form of the physical, mechanical noise is constant while its magnitude may change as it is transmitted through the engine to the accelerometer. The system model is shown in Figure 3b. In essence, noise in the physical system is modeled by the addition of a random component to the measured accelerometer signals.

In the numerical experiments new signal spectra were produced in a four-step process. First random, uniformly distributed values were added to the original accelerometer data points. Second, a threshold

level was set for the augmented signal. Third, a new signal was formed from the values of the augmented signal that exceeded the threshold. Finally, the frequency spectrum of this last signal was calculated.

The variables studied in a series of signal enhancement tests were the maximum magnitude of the random signal component and the threshold level for formation of a new signal.

Results

Figure 4 shows the kind of results obtained.

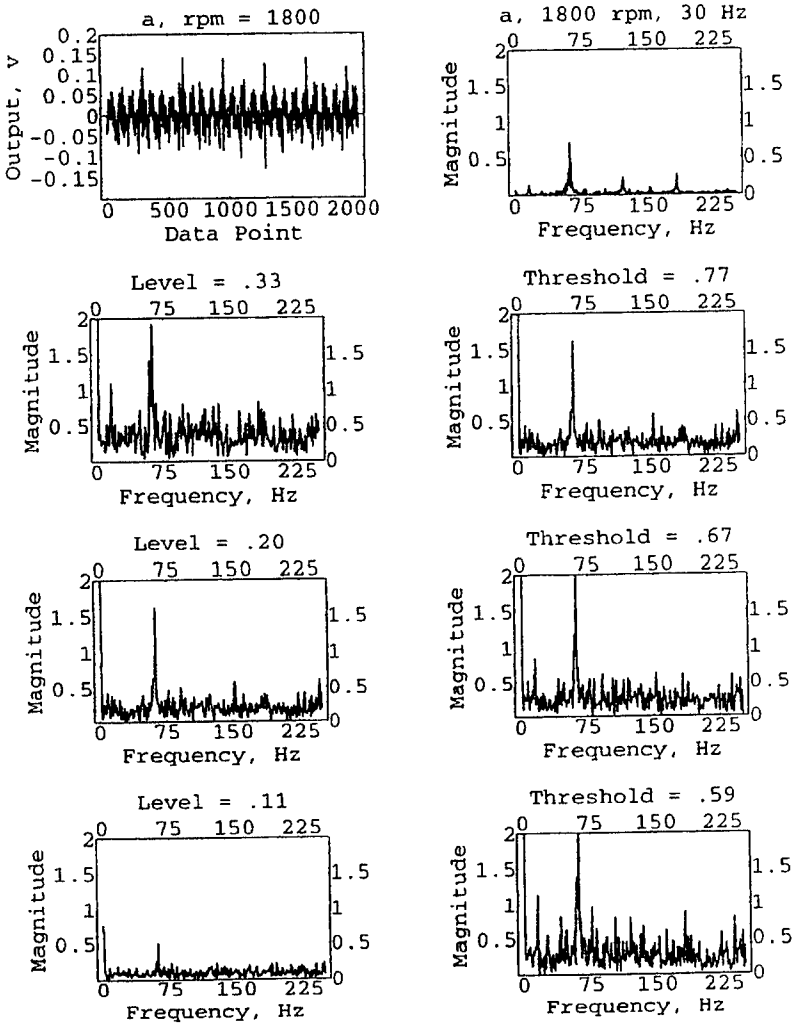

Figure 4a. Frequency spectra for varying added noise level and threshold, Trial 1.

Original time history data and its spectrum from a 1800 rpm, unworn bearing test are shown at the top of the columns. The spectrum of this signal displays a small one-fourth firing frequency peak and is typical of all the test results.

The lower part of Figure 4a contains spectra from signals modified using the procedure described above. The left column contains results for different maximum noise level additions given as fraction of the maximum original signal level. The right column shows results from numerical experiments in which the threshold was varied. The general result seen is that the initially small peak at one-fourth the firing frequency in the original data spectrum can be enhanced by the addition of a random component to the original accelerometer signal.

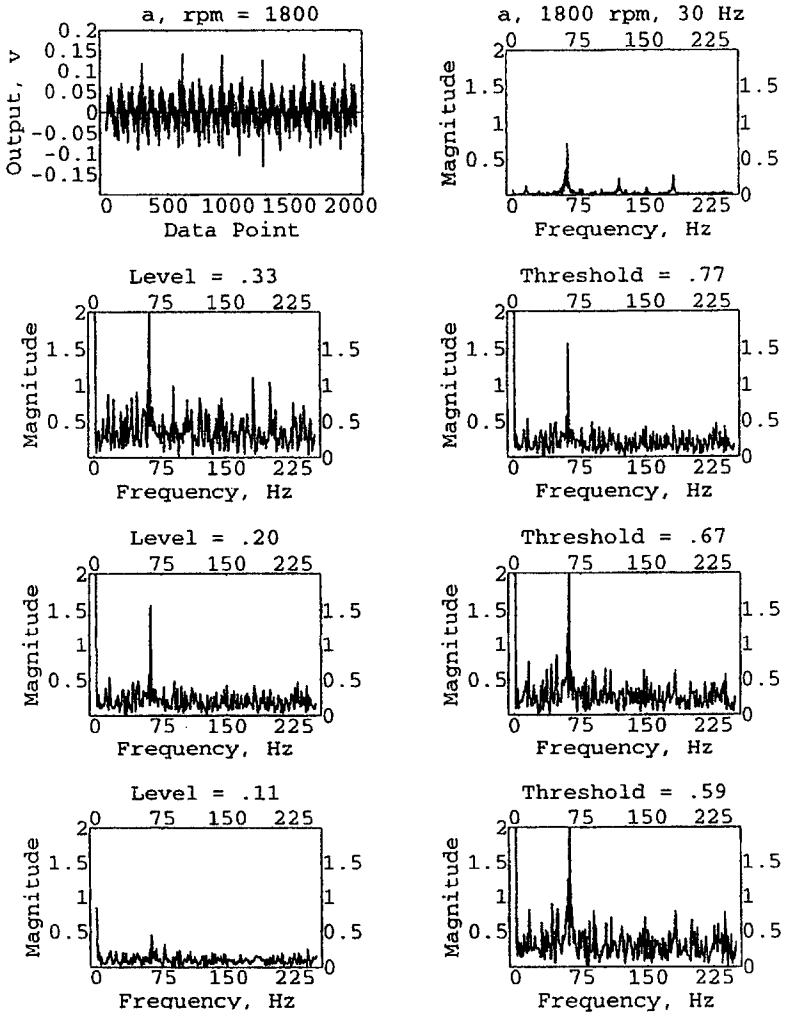

Figure 4b. Frequency spectra for varying added noise level and threshold, Trial 2.

The results of another trial are shown in Figure 4b. Since the signal enhancement procedure adds a random component to the original signal, the results will vary from test to test. In this case the magnitudes of the spectra peaks are different but the overall result is the same.

For the particular cases shown there are relative increases of the one-fourth firing frequency peak for added noise level of one-third the maximum original signal level and for thresholds of 0.59 and 0.67 times the maximum original signal level. In summary, certain parts of the augmented signal spectra contain higher peaks and the signal enhancement depends on the noise level and the threshold value.

There are many ways to define the differences between the original and enhanced signal spectra. A reasonable measure of signal enhancement is the ratio of the magnitude of the frequency peak of interest to the average magnitude of the spectra in the regions immediately surrounding the peak. This measure was used to show signal enhancement as it depends on the level of random noise used. Results of a series of one hundred tests are shown in Figure 5. An optimum noise level for signal enhancement is suggested by this limited series of tests.

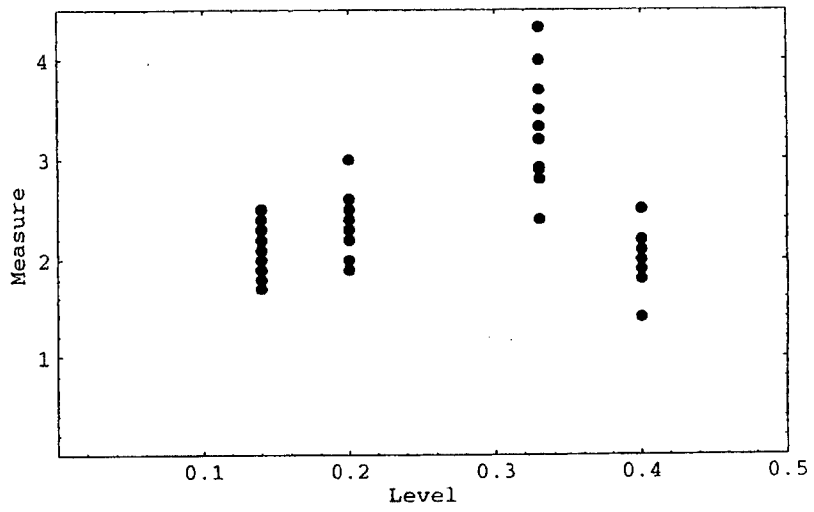

Figure 5. Signal enhancement measure for varying added noise level.

Summary

The results generated in this work lead to four general, definite conclusions. First, engine main bearing operation and condition can be deduced from signals from accelerometers mounted at convenient locations on the outside surface of the engine. Differences in individual cylinder firing effects due to main bearing wear are easy to pick out of time series accelerometer signals. Since the frequency spectra are dominated by engine firing frequency, spectral peaks related to individual cylinder firing are small and spectra may not be useful for monitoring events related to individual cylinders.

Second, engine operating conditions influence the accelerometer signals and so the indication of bearing wear in the signals. The use of higher viscosity oil produced larger signal components related to bearing wear. This indicates that vibration signals may be useful for monitoring bearing operating characteristics other than wear.

Third, sensor-source distance has a large effect on accelerometer signals. Sensors close to mechanical event generation locations contain large signal components related to individual cylinder firing events.

Fourth, stochastic resonance was produced in numerical experiments using actual accelerometer signals. This is apparently the first demonstration of the effect in mechanical systems, albeit partially numerical.

References

1. Harker, G. G. and Sandy, J. L., Rolling Element Bearing Monitoring and Diagnostics Techniques, *ASME Journal of Engineering for Gas Turbines and Power*, 1989, **111**, 251-263.
2. Douglass, J. K., Wilkens, L., Pantazelou, E. and Moss, F., Noise Enhancement of Information Transfer in Crayfish Mechanoreceptors by Stochastic Resonance, *Nature*, 1993, **365**, 337-340.
3. Weisenfeld, K and Moss, K., Stochastic Resonance and the Benefits of Noise: From Ice Ages to Crayfish and SQUIDs, *Nature*, 1995, **373**, 33-36.
4. Fauve, S. and Heslot, F., 1983, Stochastic Resonance in a Bistable System, *Physics Letters*, 1983,. **97A**, 5-7.
5. McNamara, B., and Wiesenfeld, K., Stochastic Resonance in a Ring Laser, *Physical Review*, 1989, **A39**, 48-53.
6. Benzi, R., Parisi, A., Sutera, A. and Vulpiani, A., Stochastic Resonance in Climatic Change, *Tellus*, 1982, **34**, 10-18.
7. Winograd, I. J., Coplen, T. B., Landwehr, J. M., Riggs, A. C., Ludwig, K. R., Szabo, B. J., Kolesar, P. T. and Revesz, K. M.,

Continuous 500,000-Year Climate Record from Vein Calcite in Devils Hole, Nevada, *Science*, 1992, **258**, 255-260.
8. Benzi, R., Sutera, A. and Vulpiani, A., The Mechanism of Stochastic Resonance, *Journal of Physics A*, 1981, **14**, L453-L457.
9. Nicolis, C., Stochastic Aspects of Climatic Transitions – Response to a Periodic Forcing, *Tellus*, 1982, **34**, 1-9.
10. McNamara, B., Wiesenfeld, K. and Roy, R., Observation of Stochastic Resonance in a Ring Laser, *Physical Review Letters*, 1988, **60**, 26-29.

WAVE MOTION IN A ROTATING TIMOSHENKO BEAM

M.J. Brennan

Institute of Sound and Vibration Research, University of Southampton, Hampshire, SO17 1BJ, United Kingdom. e-mail: mjb@isvr.soton.ac.uk

1. INTRODUCTION

In recent years the upper speed limits of rotating shafts have increased, because a higher performance of machinery is demanded, and this trend is likely to continue. For a low speed shaft the dynamic behaviour can be modelled as an Euler-Bernoulli beam with two orthogonal planes of vibration. A high speed rotating shaft can be modelled as a Timoshenko beam with two orthogonal planes of vibration.

Many modelling methods have been used in the past to predict the behaviour of rotating shafts, and an excellent review on these methods is given by Nelson [1]. As shown in Nelson's paper, many of these methods involve finite element analysis, and all of them involve the study of finite systems. Although these models can give adequate predictions of dynamic behaviour, they do not all facilitate physical insight into such behaviour. Some recent work by Raffa and Vatta [2], and Bonello [3], have recently derived wavenumbers for the synchronous vibration of a rotating shaft, where the shaft has been modelled as a rotating Timoshenko beam. These wavenumbers contain much information about the way in which the system behaves, as discussed by Cremer and Heckl [4] and Fahy [5]. To the author's knowledge, the wavenumbers for a rotating Timoshenko beam, where vibration is not restricted to be synchronous with the shaft speed, have not been investigated previously, and thus this is the subject of this paper. Non-dimensionalised wavenumbers are derived for the rotating beam (shaft), and the way in which these wavenumbers differ from a stationary shaft are investigated. To aid understanding the wavenumbers are compared to the Euler-Bernoulli bending wavenumber, the shear wavenumber and the longitudinal wavenumber.

The main aim of this paper is to investigate the way in which waves propagate on a rotating Timoshenko beam, and the wavenumbers are used to gain physical insight into the behaviour of a high speed shaft. The paper is organised as follows. Following this introduction, the wavenumbers are derived in section 2, which is followed in section 3 by a physical interpretation of the effects of rotation on the wavenumbers. Finally the paper is closed with some general conclusions in section 4.

2. DERIVATION OF WAVENUMBERS

The basic coupled equations of motion of a circular shaft of radius of gyration r_o rotating at angular speed Ω which is shown in **figure 1** are given by [6]:

$$EI\frac{\partial^4 x}{\partial z^4}-mr_o^2\left(1+\frac{EI}{\kappa AGr_o^2}\right)\frac{\partial^4 x}{\partial z^2\partial t^2}+m\frac{\partial^2 x}{\partial t^2}+\frac{m^2r_o^2}{\kappa AG}\frac{\partial^4 x}{\partial t^4}-2mr_o^2\Omega\frac{\partial^3 y}{\partial t\partial z^2}+\frac{2m^2r_o^2\Omega}{\kappa AG}\frac{\partial^3 y}{\partial t^3}=0 \quad \text{(1a)}$$

$$EI\frac{\partial^4 y}{\partial z^4}-mr_o^2\left(1+\frac{EI}{\kappa AGr_o^2}\right)\frac{\partial^4 y}{\partial z^2\partial t^2}+m\frac{\partial^2 y}{\partial t^2}+\frac{m^2r_o^2}{\kappa AG}\frac{\partial^4 y}{\partial t^4}+2mr_o^2\Omega\frac{\partial^3 x}{\partial t\partial z^2}-\frac{2m^2r_o^2\Omega}{\kappa AG}\frac{\partial^3 x}{\partial t^3}=0 \quad \text{(1b)}$$

where E, G, A, ρ, $m=\rho A$, $I=Ar_o^2$ are the elastic modulus, the shear modulus, the cross-sectional area, the density, the mass per unit length and the second moment of area of the shaft respectively. κ is the Timoshenko shear coefficient whose value depends upon the shape of the cross-section [7]. It can be seen that it is the last two terms on the left-hand side of the equations that couple them together. These are gyroscopic terms which are dependent upon the rotational speed of the shaft and the polar moment of inertia per unit length $I_p=2mr_o^2$. If a harmonic solution is assumed then the following matrix equation results:

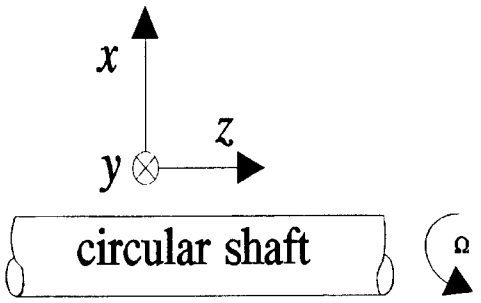

Figure 1 Shaft and coordinate system

$$\begin{bmatrix} \bar{\beta}^4+\bar{k}_f^4(1+\bar{s}^2)\bar{\beta}^2-\bar{k}_f^4\left(1-\bar{s}^2\bar{k}_f^4\right) & -j2\bar{k}_f^4\bar{\Omega}\left(\bar{\beta}^2+\bar{k}_f^4\bar{s}^2\right) \\ j2\bar{k}^4\bar{\Omega}\left(\bar{\beta}^2+\bar{k}_f^4\bar{s}^2\right) & \bar{\beta}^4+\bar{k}_f^4(1+\bar{s}^2)\bar{\beta}^2-\bar{k}_f^4\left(1-\bar{s}^2\bar{k}_f^4\right) \end{bmatrix}\begin{bmatrix} A \\ B \end{bmatrix}=\begin{bmatrix} 0 \\ 0 \end{bmatrix} \quad \text{(2)}$$

where A and B are constants, $j=\sqrt{(-1)}$ and:

$\bar{\beta}=\beta r_o$ is the non-dimensional wavenumber

$\bar{k}_f=\left(\frac{m}{EI}\right)^{\frac{1}{4}}\omega^{\frac{1}{2}}r_o$ is the non-dimensional Euler-Bernoulli beam flexural wavenumber, where ω is circular frequency

$\bar{s}^2 = \dfrac{EI}{\kappa A G r_o^2}$ is the non-dimensional flexural rigidity

$\bar{\Omega} = \dfrac{\Omega}{\omega}$ is the non-dimensional rotational speed

For a non-trivial solution of equation (2) the determinant of the matrix must be zero. This results in the eighth order equation:

$$\left\{\bar{\beta}^4+\bar{k}_f^4(\bar{s}^2+1-2\Omega)\bar{\beta}^2-\bar{k}_f^4\left(1-(1-2\Omega)\bar{s}^2\bar{k}_f^4\right)\right\}\left\{\bar{\beta}^4+\bar{k}_f^4(\bar{s}^2+1+2\Omega)\bar{\beta}^2-\bar{k}_f^4\left(1-(1+2\Omega)\bar{s}^2\bar{k}_f^4\right)\right\}=0 \quad (3)$$

The solutions to this equation yield the eight wavenumbers for the rotating shaft:

$$\bar{\beta} = \pm\bar{\beta}_a,\ \pm j\bar{\beta}_b,\ \pm\bar{\beta}_c,\ \pm j\bar{\beta}_d \qquad \textbf{(4a-h)}$$

where

$$\bar{\beta}_a = \bar{k}_f\left\{-\frac{\bar{k}_f^2}{2}(\bar{s}^2+1-2\bar{\Omega})+\sqrt{\frac{\bar{k}_f^4}{4}(\bar{s}^2-1+2\bar{\Omega})^2+1}\right\}^{\frac{1}{2}} \qquad \textbf{(5a)}$$

$$\bar{\beta}_b = \bar{k}_f\left\{\frac{\bar{k}_f^2}{2}(\bar{s}^2+1-2\bar{\Omega})+\sqrt{\frac{\bar{k}_f^4}{4}(\bar{s}^2-1+2\bar{\Omega})^2+1}\right\}^{\frac{1}{2}} \qquad \textbf{(5b)}$$

$$\bar{\beta}_c = \bar{k}_f\left\{-\frac{\bar{k}_f^2}{2}(\bar{s}^2+1+2\bar{\Omega})+\sqrt{\frac{\bar{k}_f^4}{4}(\bar{s}^2-1-2\bar{\Omega})^2+1}\right\}^{\frac{1}{2}} \qquad \textbf{(5c)}$$

$$\bar{\beta}_d = \bar{k}_f\left\{\frac{\bar{k}_f^2}{2}(\bar{s}^2+1+2\bar{\Omega})+\sqrt{\frac{\bar{k}_f^4}{4}(\bar{s}^2-1-2\bar{\Omega})^2+1}\right\}^{\frac{1}{2}} \qquad \textbf{(5d)}$$

3. PHYSICAL INTERPRETATION

To gain physical insight into the behaviour of the waves it is necessary to see how the wavenumbers vary as a function of both speed and frequency. If the speed of the shaft is set to zero then the wavenumbers become those of a stationary Timoshenko beam. At low frequencies when a flexural wavelength

is greater than about six times the diameter of the shaft then a Timoshenko beam behaves like an Euler Bernoulli beam [4]. A basic assumption of Euler-Bernoulli beam theory is that there is no shear deformation, which implies an infinite shear stiffness. In the formulation presented here this means that $\bar{s}=0$ and when $\bar{k}_f \ll 1$ then equations **(5a-d)** collapse to $\bar{\beta}_{a,b,c,d}=\bar{k}_f$. This means that there are four waves in each of the *xz* and *yz* planes; two evanescent and two propagating waves as described in reference [4].

Increasing frequency, but keeping the shaft stationary, means that the effects of a finite shear stiffness and rotational inertia (terms two and four on the left-hand sides of equations **(1a,b)**) can be investigated. For a stationary shaft at high frequencies, when $\bar{s}=0$ and $\bar{k}_f \gg 1$ equations **(5a-d)** can be approximated to:

$$\bar{\beta}_a = \bar{\beta}_c = \mathrm{j}\bar{k}_f^2, \qquad \bar{\beta}_b = \bar{\beta}_d = \bar{s}\,\bar{k}_f^2 \qquad \textbf{(6a-d)}$$

These can be rewritten as:

$$\beta_a = \beta_c = \mathrm{j}k_l\,, \qquad \beta_b = \beta_d = k_s\,\kappa^{-\frac{1}{2}} \qquad \textbf{(7a-d)}$$

where $k_l = \sqrt{(\rho/E)}\,\omega$ is the longitudinal wavenumber for a slender uniform bar and $k_s = \sqrt{(\rho/G)}\,\omega$ is the shear wavenumber.

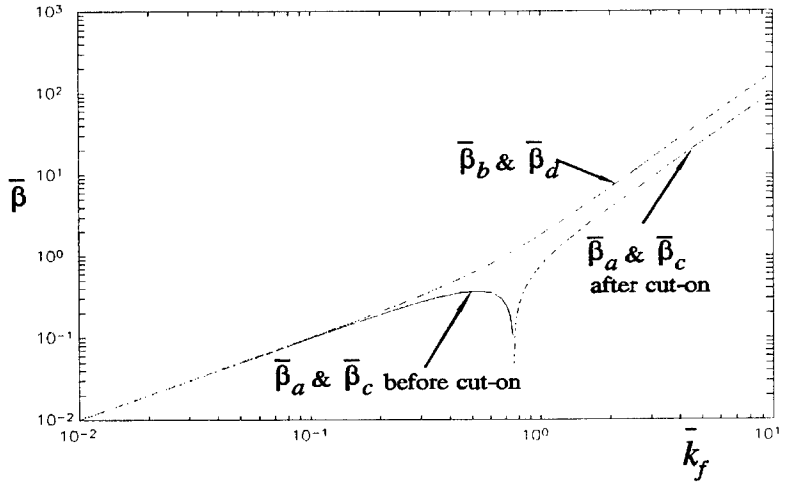

Figure 2 *Non-dimensional wavenumbers of a stationary shaft as a function of the non-dimensionalised Euler-Bernoulli bending wavenumber for* $\bar{s}=3$*, A solid line denotes an evanescent wave and a dashed lines denotes a propagating wave.*

The wavenumbers for a stationary shaft are plotted in **figure 2** for $\bar{s}=3$, which is representative of a solid steel shaft. It can be seen that at low frequencies both wavenumbers are the same as for an Euler Bernoulli beam as discussed above. $\bar{\beta}_a$ and $\bar{\beta}_c$ are evanescent waves and $\bar{\beta}_b$ and $\bar{\beta}_d$ are propagating waves. At high frequencies the waves $\bar{\beta}_a$ and $\bar{\beta}_c$ are no longer evanescent, but are non-dispersive propagating waves with the speed of a longitudinal wave. Moreover, the flexural propagating waves $\bar{\beta}_b$ and $\bar{\beta}_d$, which are dispersive at low frequencies, propagate non-dispersively with a phase speed similar to a shear wave. The frequency at which the evanescent waves cut-on and start to propagate can be determined by setting $\bar{\Omega}=0$, and the term inside the large curly brackets in equation **(5a)** to zero, i.e.,

$$\frac{\bar{k}_f^2}{2}(\bar{s}^2+1)+\sqrt{\frac{\bar{k}_f^4}{4}(\bar{s}^2-1)^2+1}=0 \tag{8}$$

which simplifies to:

$$\bar{k}_f^2\bar{s}=1 \tag{9}$$

Substituting for the non-dimensional variables $\bar{k}_f$ and $\bar{s}$ gives a frequency of:

$$\omega_{\text{cut-on}}=\sqrt{\frac{GA\kappa}{\rho I}} \tag{10}$$

This frequency agrees with that given by Graff [8] and can be interpreted as a resonance of the shear stiffness per unit length (multiplied by a shape factor) divided by the rotary inertia per unit length. It could be viewed as the frequency at which the rotary inertia overcomes the shear stiffness and thus the wave starts to propagate. The motion of the wave is shown in **figure 3** [8], where it can be seen that this wave is an in-plane wave; it has no out of plane motion unlike the evanescent wave.

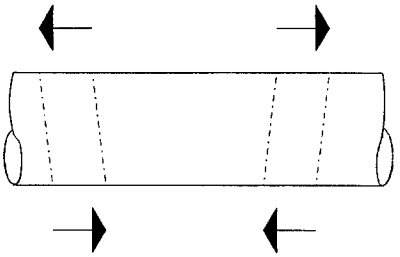

Figure 3 Motion of the in-plane waves after cut-on

In summary it can be seen that at high frequencies there are four free-waves (two right-going and two left going) on a stationary (non rotating) shaft in each of the *xz* and *yz* planes. They are both non-dispersive and two waves contribute to the out-of-plane vibration. These waves propagate like left and right-going shear waves as described by Fahy [5].

Having established the wave behaviour of a stationary shaft it is appropriate to investigate the way in which rotation of the shaft influences this behaviour. Because it is the gyroscopic forces that modify the dynamic behaviour, the rotation of the shaft will only have an effect at high shaft speeds and at high frequencies. With these conditions equations **(5a,b)** become:

$$\bar{\beta}_a = \bar{k}_f^2 (2\bar{\Omega} - 1)^{\frac{1}{2}}, \qquad \bar{\beta}_b = \bar{s}\bar{k}_f^2 \tag{11a,b}$$

Equation **(5c)** becomes:

$$\bar{\beta}_c = j\bar{k}_f^2 (2\bar{\Omega} + 1)^{\frac{1}{2}}, \qquad \bar{\Omega} \le \frac{\bar{s}^2 - 1}{2}$$

$$\bar{\beta}_c = j\bar{s}\bar{k}_f^2, \qquad \bar{\Omega} > \frac{\bar{s}^2 - 1}{2} \tag{11c,d}$$

and equation **(5d)** becomes:

$$\bar{\beta}_d = \bar{s}\bar{k}_f^2, \qquad \bar{\Omega} \le \frac{\bar{s}^2 - 1}{2}$$

$$\bar{\beta}_d = \bar{k}_f^2 (2\bar{\Omega} + 1)^{\frac{1}{2}}, \qquad \bar{\Omega} > \frac{\bar{s}^2 - 1}{2} \tag{11e,f}$$

The non-dimensionalised wavenumber $\bar{\beta}_a$ calculated using equation **(5a)** with $\bar{s} = 3$ is plotted in **figure 4**. Referring to this figure and equation **(11a)**, it can be seen that the shaft rotation has an effect on the wavenumber. For $\bar{\Omega} < 0.5$ the wave still cuts on, but the rotational speed affects the frequency at which it starts to propagate. The cut-on frequency increases with rotational speed until $\bar{\Omega} = 0.5$ after which the wave remains evanescent, but the wavenumber still increases with rotational speed. The cut-on frequency is, in fact, the "static" cut-on frequency given by equation **(10)**, divided by $(1 - 2\bar{\Omega})^{0.5}$. The reason for this behaviour can be seen by examining equation **(1b)**. The rotational inertia due to the gyroscopic forces (the fifth term on the left-hand side of the equation) is of opposite sign to the rotational inertia due to vibration (the second term on the left-hand side of the equation). As discussed above, the evanescent wave starts to propagate when the rotational inertia overcomes the restraining shear stiffness. Because the gyroscopic effects oppose this inertia, the frequency at which the wave will cut-on is affected. When the inertia terms are the same which occurs at $\bar{\Omega} = 0.5$ there is no inertia effect and the wave will remain evanescent.

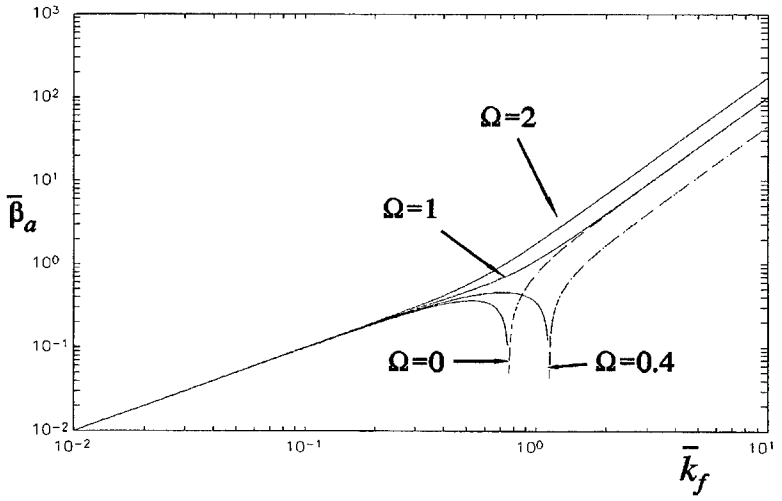

Figure 4 *Non-dimensionalised wavenumber* $\bar{\beta}_a$ *plotted as a function of the non-dimensionalised Euler-Bernoulli bending wavenumber for* $\bar{s}=3$ *and various* $\bar{\Omega}$*, A solid line denotes an evanescent wave and a dashed lines denotes a propagating wave.*

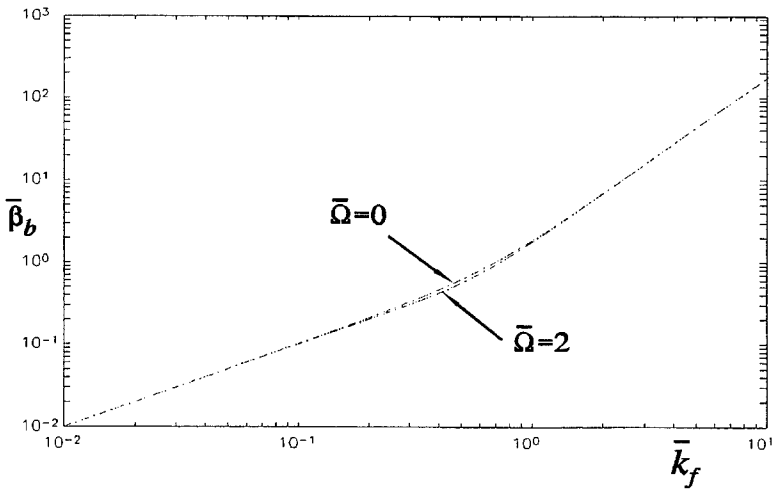

Figure 5 *Non-dimensionalised wavenumber* $\bar{\beta}_b$ *plotted as a function of the non-dimensionalised Euler-Bernoulli bending wavenumber for* $\bar{s}=3$ *and various* $\bar{\Omega}$*, A dashed lines denotes a propagating wave.*

The non-dimensionalised wavenumber $\bar{\beta}_b$ calculated using equation **(5b)** with $\bar{s}=3$ is plotted in **figure 5**. Referring to this figure and equation **(11b)**, it can be seen that the rotation of the shaft has very little effect on the $\bar{\beta}_b$ wavenumber. It propagates at all frequencies and exhibits Euler-Bernoulli dispersive behaviour at low frequencies and shear-like behaviour at high frequencies. The rotation has practically no effect at low and high frequencies, only having a marginal effect at frequencies close to the cut-on frequency of the $\bar{\beta}_a$ wave. This wave is unaffected by shaft rotation because it behaves as a shear wave at high frequencies, and because the gyroscopic forces largely affect the rotational inertia of the shaft, this has a negligible affect on this wave.

The non-dimensionalised wavenumber $\bar{\beta}_c$ calculated using equation **(5c)** with $\bar{s}=3$ is plotted in **figure 6**.

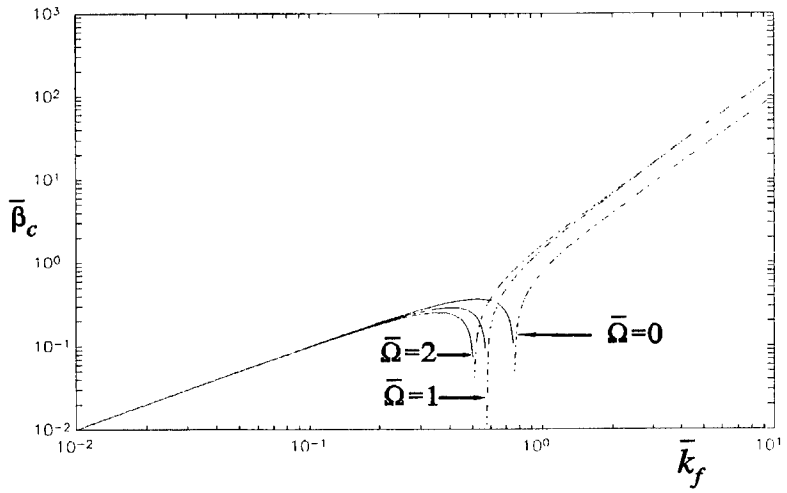

***Figure 6** Non-dimensionalised wavenumber $\bar{\beta}_c$ plotted as a function of the non-dimensionalised Euler-Bernoulli bending wavenumber for $\bar{s}=3$ and various $\bar{\Omega}$, A solid line denotes an evanescent wave and a dashed lines denotes a propagating wave.*

Referring to **Figure 6** and equations **(11c,d)**, it can be seen that the rotation of the shaft has an affect on the frequency at which this wave cuts on, which is given by the "static" cut-on frequency (equation **(10)**) divided by $(1+2\bar{\Omega})^{0.5}$. It can be seen that it starts to propagate at a lower frequency as the speed of the shaft increases. This is because, the rotational inertia due to

the gyroscopic effects adds to the rotational inertia due to the vibration, as can be seen in equation **(1a)**. Thus the effective inertia is higher and the wave cuts on at a lower frequency. At high frequencies and high shaft speeds when the wave is cut-on the rotation of the shaft has no effect on the wavenumber as can be seen in equation **(11d)**.

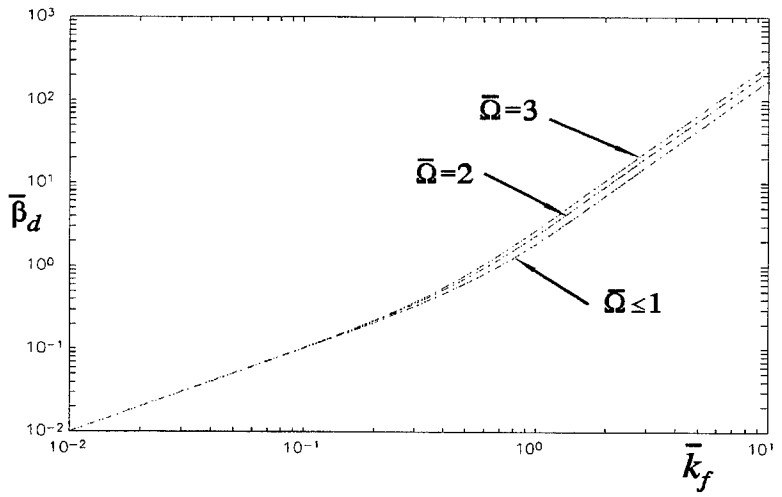

Figure 7 Non-dimensionalised wavenumber $\bar{\beta}_d$ plotted as a function of the non-dimensionalised Euler-Bernoulli bending wavenumber for $\bar{s}=3$ and various $\bar{\Omega}$, A dashed line denotes a propagating wave.

The non-dimensionalised wavenumber $\bar{\beta}_d$ calculated using equation **(5d)** with $\bar{s}=3$ is plotted in **figure 7**. It can be seen in this figure and equations **(11e,f)** that the rotation of the shaft has no effect on the wavenumber when $\bar{\Omega}$ is small but at high speeds there is a small effect. These effects can again be attributed to the fact that this wave is predominantly a shear wave at high frequencies and thus the gyroscopic effects are marginal.

4. CONCLUSIONS

The free flexural wave behaviour of a rotating shaft has been investigated in this paper. Non-dimensional wavenumbers have been derived from first principles and the way in which they behave at low and high frequencies have been investigated. The complicated expressions for the wavenumbers reduce to the simple Euler-Bernoulli bending wavenumber at low frequencies, and simplify to relatively small expressions at high frequencies. The way in which

the rotation of the shaft affects the wavenumbers has also been investigated. It has been shown that the main effect of shaft rotation is due to the gyroscopic forces which change the frequencies at which the flexural evanescent waves cut-on and start to propagate. The cut-on frequency for one of these waves increases as the rotational speed of the shaft increases, and when the non-dimensional speed is equal to 0.5 or greater the rotation of the shaft prevents the wave from propagating. The other evanescent wave, which is orthogonal to this wave cuts on at lower and lower frequencies as the speed of the shaft increases. This effect is attributed to the rotational inertia due to gyroscopic effects combining with the rotational inertia due to flexural vibration.

REFERENCES

1. Nelson, H.D., Rotordynamic modelling and analysis procedures: A review. *JSME International Journal,* Series C Vol **41**, No 1-12, 1998.
2. Raffa, F.A. and Vatta, F., The dynamic stiffness method for linear rotor-bearings systems. *Transactions of the ASME, Journal of Vibration and Acoustics*, Vol 118, 332-338, 1996.
3. Bonello, P., Predicting the response of a multi-span coupled rotor-bearing-foundation system by the mechanical impedance technique. *MSc Dissertation, University of Southampton,* 1999.
4. Cremer, L., Heckl, M. and Ungar, E.E., *Structure-Borne Sound*, Springer-Verlag, 1973.
5. Fahy, F.J., *Sound and Structural Vibration: Radiation, Transmission and Response*, Academic Press, 1985.
6. Dimentberg, F.M., *Flexural Vibrations of Rotating Shafts*, Butterworths, 1961.
7. Blevins, R.D., *Formulas for Natural Frequency and Mode Shape*, Kreiger Publishing Company, 1993.
8. Graff, K.F., *Wave Motion in Elastic Solids*, Clarendon Press, 1975.

FREE VIBRATION OF ROTATING BEAM WITH TIP MASS

Kuo Mo Hsiao
Department of Mechanical Engineering, National Chiao Tung University,
Hsinchu, Taiwan, Republic of China

ABSTRACT

The objective of this paper is to investigate the effect of tip mass on the natural frequency of the rotating beam with tip mass.

The equations of motion for rotating Euler beam are derived by the d'Alembert principle and the virtual work principle. In order to capture all inertia effect and coupling between extensional and flexural deformation, the consistent linearization of the fully geometrically non-linear beam theory is used in the derivation. A method based on the power series solution is proposed to solve the natural frequency.

Numerical examples are studied for the natural frequency of rotating beams with different tip mass, angular velocity, setting angle, and slenderness ratio.

INTRODUCTION

Rotating beams are often used as simple models for propellers, turbine blades, and satellite booms. In many structural designs, tip mass are utilized. The free vibration frequencies and mode shapes of rotating beams have been extensively studied [1-7]. Rotating beam differs from a non-rotating beam in having additional centrifugal force and Coriolis effects on its dynamics. However, most studies have neglected the Coriolis effects. In order to capture correctly all inertia effects and coupling among bending and stretching deformations of the beam, the equations of motion of beam might be derived by the fully geometrically non-linear beam theory [8]. However, in most existing literature, the governing equations for the bending vibrations of rotating beam are derived using linear beam theory.

The objective of this paper is to derive an exact expression for linear vibration equations of a rotating Euler beam, and investigate the effect of tip mass on the natural frequency of the rotating beam with tip mass. The equations of motion for rotating Euler beam are derived by the d'Alembert principle and the virtual work principle. In order to capture all inertia effect and coupling between extensional and flexural deformation, the consistent linearization [8] of the fully geometrically non-linear beam theory is used in the derivation. A method based on the power series solution is proposed to solve the natural frequency.

Numerical examples are studied for the natural frequency of rotating beams with different tip mass, angular velocity, setting angle, and slenderness ratio.

FORMULATION

Description of problem

Consider a uniform Euler beam with tip mass rigidly mounted on the periphery of rigid hub with radius R which rotates about the hub axis fixed in space at a constant angular speed Ω as shown in Fig. 1. The deformational displacements of the beam are defined in a rotating rectangular Cartesian coordinate system, which is rigidly tied to the hub. The origin of this coordinate system is chosen to be the intersection of the centroid axes of the hub and the undeformed beam. The X_1 axis are chosen to coincide with the centroid axis of the undeformed beam, and the X_2 and X_3 axes are chosen to be the principal directions of the cross section of the beam at the undeformed state. In this paper all vectors are referred to this coordinate system. The angular velocity of the hub may be given by

$$\Omega = \{0, \Omega \sin\beta, \Omega \cos\beta\} \tag{1}$$

where the symbol { } denotes a column matrix , which is used through the paper; β, the angle between the hub axis and the X_3 axis, is the setting angle of the beam.

Here it is assumed that the beam is only deformed in the X_1-X_3 plane. It is well known that the beam sustains a static axial deformations (time independent displacement) induced by constant rotation. In this study the vibration (time dependent displacement) of the beam is measured from the position of the steady-state axial deformation, and only infinitesimal free vibration is considered. Here the engineering strain and stress are used for the measure of the strain and stress. It is assumed that the strains are small strains and the stress-strain relationships are linear.

Kinematics of Euler beam

Let P (see Fig. 2) be an arbitrary point in the beam element, and Q be the point corresponding to P on the centroid axis. The position vector of point P in the undeformed and deformed configurations may be expressed as

$$\mathbf{r}_0 = \{R + x,\ y,\ z\}, \tag{2}$$

$$\mathbf{r} = \{R + x + \bar{u}(x,t) - z\sin\theta,\ y,\ w(x,t) + z\cos\theta\} = r_i \mathbf{e}_i, \tag{3}$$

$$\bar{u}(x,t) = u_s(x) + u(x,t), \tag{4}$$

where t is time, $u_s(x)$ is the static axial deformations (time independent displacement) induced by constant rotation, $u(x,t)$ and $w(x,t)$ are the infinitesimal displacements of point Q in the X_1 and X_3 directions,

respectively, caused by the free vibration, $\theta = \theta(x,t)$ is the infinitesimal angle measured from the X_1 axis to the tangent of the deformed centroid axis, $\mathbf{e}_i$ (i = 1, 2, 3) denote the unit vectors associated with the X_i axes.

The only nonzero component of the engineering strains for the Euler beam may be approximated by

$$\varepsilon = \varepsilon_0 - z\theta_{,x} = \varepsilon_0 - zw_{,xx}, \tag{5}$$

where ε_0 is the unit extension of the centroid axis. Making use of the assumption of small strain, ε_0 may be approximated by

$$\varepsilon_0 = \bar{u}_{,x} + \frac{1}{2}(\bar{u}_{,x}{}^2 + w_{,x}{}^2) \tag{6}$$

Equations of motion

The equations of motion for rotating Euler beam are derived by the d'Alembert principle and the virtual work principle. The consistent linearization of the fully geometrically non-linear beam theory is used in the derivation.

Figure 3 shows a portion of the deformed centerline of the beam. Here the generalized displacements are chosen to be $\bar{u}$, w, and θ defined in equation (3). The corresponding generalized forces are F_1, F_3, and M, the forces in X_1-, X_3-directions, and moment about negative X_2-axis. F_{1j}, F_{3j}, and M_j (j = 1, 2) in Fig. 3 denote the values of F_1, F_3, and M at sections j.

For linear elastic material, the virtual work principle may be written as

$$\delta W_{ext} = \delta W_{int} \tag{7}$$

$$\begin{aligned}\delta W_{ext} &= (F_1\delta\bar{u} + F_3\delta w + M\delta\theta)\Big|_1^2 \\ &= \int_1^2 \frac{d}{dx}(M\delta\theta + F_1\delta\bar{u} + F_3\delta w)dx \\ &= \int_1^2 \left(M_{,x}\delta\theta + M\delta\theta_{,x} + F_{1,x}\delta\bar{u} + F_1\delta\bar{u}_{,x} + F_{3,x}\delta w + F_3\delta w_{,x}\right)dx\end{aligned} \tag{8}$$

$$\delta W_{int} = E\int_{V_{12}} \delta\varepsilon^t\,\varepsilon\,dV + \rho\int_{V_{12}} \ddot{\mathbf{r}}^t\,\delta\mathbf{r}\,dV \tag{9}$$

where δW_{ext} and δW_{int} are the virtual work of the external forces and the internal stresses, respectively, $()\Big|_1^2$ is the value of ( ) at node 2 minus the

value of ( ) at node 1, $\delta\varepsilon$ is the variation of ε given in equation (5), $\delta\mathbf{r}$ is the variation of $\mathbf{r}$ given in equation (3), and $\ddot{\mathbf{r}} = d^2\mathbf{r}/dt^2$ is the absolute acceleration. In this paper, the symbol ($\dot{}$) denotes differentiation with respect to time t. E is Young's modulus, G is shear modulus, ρ is the density, V_{12} is the volume of the undeformed beam between sections 1 and 2. The differential volume dV may be expressed as $dV = dAdx$, where dA is the differential cross section area of the beam.

The exact expression of δW_{int} may be very complicated. However, due to the assumption of infinitesimal vibration, the quantities u, w, and θ defined in equation (3), and their derivatives with respect to x and t are all infinitesimal. For convenience, they are called infinitesimal quantities in this study. Thus only the terms up to the first order of infinitesimal quantities are retained in δW_{int}. However, in order to retain all terms up to the first order of infinitesimal quantities in δW_{int}, all terms up to the first order of infinitesimal quantities are retained for $\delta\varepsilon$ ε $\delta\mathbf{r}$ $\ddot{\mathbf{r}}$ in equation (9). Note that the static axial deformations $u_s(x)$ in equation (4) and its derivatives with respect to x are small finite quantities, not infinitesimal quantities.

From equations (3), and (5)-(9), using $\int_A z\,dA = 0$, $\int_A yz\,dA = 0$, and the approximations $1 + \bar{u}_{,x} \approx 1$ and $\theta \approx w_{,x}$, and retaining all terms up to the first order of infinitesimal quantities by consistent linearization, one obtains

$$F_{1,x} = \rho A[\ddot{u} + 2\dot{w}\Omega\sin\beta - (R + x + \bar{u})\Omega^2], \tag{10}$$

$$F_{3,x} = \rho A(\ddot{w} - 2\dot{u}\Omega\sin\beta - w\Omega^2\sin^2\beta), \tag{11}$$

$$M_{,x} + F_3 = \rho I(\ddot{w}_{,x} - w_{,x}\Omega^2\cos^2\beta) + EA\bar{u}_{,x}w_{,x}, \tag{12}$$

$$M = EI\theta_{,x} = EIw_{,xx}, \tag{13}$$

$$F_1 = EA\bar{u}_{,x}, \tag{14}$$

where $I = \int_A z^2\,dA$ is the moment of inertia of the cross section.

Equations (10)-(12) are equations of motion, and equations (13) and (14) are constitutive equations.

Substituting equations (11), (13), and (14) into equations (10), and (12), one obtains

$$AE\bar{u}_{,xx} = \rho A[\ddot{\bar{u}} + \underline{2\dot{w}\Omega\sin\beta} - (R + x + \bar{u})\Omega^2], \tag{15}$$

$$EIw_{,xxxx} = AE(u_{s,x}w_{,x})_{,x} + \underline{\underline{\rho I(\ddot{w}_{,xx} - w_{,xx}\Omega^2\cos^2\beta)}} - \rho A(\ddot{w} - \underline{2\dot{u}\Omega\sin\beta} - w\Omega^2\sin^2\beta), \tag{16}$$

where the single underlined terms in equations (15) and (16) are Coriolis force, and the double underlined term in equation (16) is the rotary inertia term.

The boundary conditions for a fixed end at $x = 0$ and for a free end at $x = L$ are given by

$$u_s(0) = u(0,t) = 0, \quad w(0,t) = 0, \quad w_{,x}(0,t) = 0, \tag{17}$$

$$F_1(L,t) = -m_t a_1(L,t), \quad F_3(L,t) = -m_t a_1(L,t), \quad M(L,t) = -m_t h^2 \ddot{w}_{,x}(L,t) \tag{18}$$

where m_t is the mass of tip mass, a_1 and a_3 are the absolute accelerations of the tip mass in the X_1 and X_3 directions, and h is the radius of gyration of the tip mass.

Static axial deformations

For the static axial deformations, $\overline{u}(x,t) = u_s(x)$, $u(x,t) = w(x,t) = 0$. Thus equations (15)-(18) can be reduced to

$$Eu_{s,xx} = \rho(R + x + u_s)\Omega^2, \tag{19}$$

$$u_s(0) = 0, \qquad EAu_{s,x}(L) = m_t\Omega^2(l + R). \tag{20}$$

Let

$$k = \Omega L\sqrt{\rho/E}. \tag{21}$$

When $k << 1$, The solution of equations (19) and (20) may be approximated by

$$u_s(x) = \frac{\rho\Omega^2}{E}\left[\frac{-x^3}{6} - \frac{Rx^2}{2} + \frac{L^2x}{2} + RLx + \frac{m_t}{\rho A}(L + R)x\right]. \tag{22}$$

Free vibration

The vibration of the beam is measured from the position of the static axial deformation. From equations (4), (15), (16), (19), and (22), the governing equations for free vibration may be expressed as

$$U_{,\xi\xi} = \frac{\rho L^2}{E}[\ddot{U} + \underline{2\dot{W}\Omega \sin\beta} - \Omega^2 U], \tag{23}$$

$$W_{,\xi\xi\xi\xi} = \eta N_{,\xi} W_{,\xi} + \eta N W_{,\xi\xi} + \underline{\underline{\frac{\rho L^2}{E}(\ddot{W}_{,\xi\xi} - W_{,\xi\xi}\Omega^2 \cos^2\beta)}} - \frac{\rho A L^4}{EI}(\ddot{W} - \underline{2\dot{U}\Omega \sin\beta} - W\Omega^2 \sin^2\beta) \tag{24}$$

where

$$N = -k^2[\frac{1}{2}\xi^2 + (r+\frac{1}{2})\xi - \frac{1}{2}r - \frac{3}{8} + M(r+1)] \tag{25}$$

$$N_{,\xi} = -k^2(\xi + r + \frac{1}{2}), \tag{26}$$

$$\mu = \frac{\mu_0}{\eta}, \qquad \eta = \frac{AL^2}{I}, \qquad \xi = \frac{x}{L} - \frac{1}{2}, \qquad M = \frac{m_t}{\rho AL}$$

$$U = \frac{u}{L}, \qquad W = \frac{w}{L}, \qquad r = \frac{R}{L}, \tag{27}$$

We shall seek a solution of equations (23) and (24) in the form

$$\mathbf{U}(\xi,t) = \left(\mathbf{U}_R(\xi) + i\mathbf{U}_I(\xi)\right)e^{i\omega t} \tag{28}$$

$$\mathbf{U}(\xi,t) = \{U,W\}, \quad \mathbf{U}_R(\xi) = \{U_R, W_R\}, \quad \mathbf{U}_I(\xi) = \{U_I, W_I\}, \tag{29}$$

where $i = \sqrt{-1}$, and ω is the natural frequency to be determined.

Introducing equation (28) into equations (23) and (24), we obtain $U_I = U_R$, $W_R = -W_I$ and

$$U_{R,\xi\xi} + (K^2 + k^2)U_R + 2kKW_I \sin\beta = 0, \tag{30a}$$

$$W_{I,\xi\xi\xi\xi} + (K^2 + k^2\cos^2\beta - \eta N_\xi)W_{I,\xi\xi} - \eta N'_\xi W_{I,\xi} - 2\eta kKU_R \sin\beta - \eta(K^2 + k^2\sin^2\beta)W_I = 0 \tag{30b}$$

$$K = \omega L\sqrt{\rho/E} \tag{31}$$

Power series solution

From equations (25), (26) and (30), it can be seen that equation (30) is a set of linear ordinary differential equations with variable coefficients. The solution of equation (30) can be expressed as a power series in the independent variable ξ:

$$\mathbf{A}(\xi)=\begin{Bmatrix}U_R\\W_I\end{Bmatrix}=\sum_{n=0}^{\infty}\begin{Bmatrix}C_n\\D_n\end{Bmatrix}\xi^n=\sum_{n=0}^{\infty}\mathbf{C}_n\xi^n\,, \tag{32}$$

where C_n and D_n are undetermined coefficients.

Substituting equation (32) into equation (30) and equating coefficients of like power of ξ, we obtain the recurrence formula

$$C_2=-\frac{1}{2}\{a\quad b\}\begin{Bmatrix}C_0\\D_0\end{Bmatrix},\quad C_3=-\frac{1}{6}\{a\quad b\}\begin{Bmatrix}C_1\\D_1\end{Bmatrix} \tag{33a}$$

$$\mathbf{C}_n=\sum_{j=1}^{4}\mathbf{A}_n^j\mathbf{C}_{n-j}\,,\quad n\geq 4 \tag{33b}$$

$$\mathbf{A}_n^1=\frac{-1}{n}\begin{bmatrix}0&0\\0&d\end{bmatrix},\qquad \mathbf{A}_n^2=\frac{-1}{n(n-1)}\begin{bmatrix}a&b\\0&c\end{bmatrix}$$

$$\mathbf{A}_n^3=\frac{-1}{n(n-1)(n-2)}\begin{bmatrix}0&0\\0&e\end{bmatrix},\qquad \mathbf{A}_n^4=\frac{1}{n(n-1)(n-2)(n-3)}\begin{bmatrix}0&0\\\eta b&f\end{bmatrix} \tag{34}$$

where $a=K^2+k^2$, $b=2kK\sin\beta$, $c=K^2+k^2\cos^2\beta-\eta k^2\left(\frac{1}{2}r+\frac{3}{8}\right)$,

$d=k^2\left(r+\frac{1}{2}\right)$, $e=\eta d(n-3)$, $f=\eta(K^2+k^2\sin^2\beta)-\frac{1}{2}\eta k^2(n-3)(n-4)$.

Substituting equation (33) into equation. (32), one may obtain

$$\mathbf{A}(\xi)\;=\mathbf{E}\mathbf{C}\,, \tag{35}$$

$$\mathbf{E}=\begin{bmatrix}\mathbf{E}_1&\mathbf{E}_2&\mathbf{E}_5\end{bmatrix},\qquad \mathbf{C}=\{C_0\quad D_0\quad C_1\quad D_1\quad D_2\quad D_3\} \tag{36}$$

$$\mathbf{E}_1=\mathbf{I}+\xi^2\mathbf{D}_a+\sum_{n=4}^{\infty}\xi^n\left(\mathbf{Y}_0^n+\mathbf{Y}_2^n\mathbf{D}_a\right)$$

$$\mathbf{E}_2=\xi\mathbf{I}+\xi^3\mathbf{D}_b+\sum_{n=4}^{\infty}\xi^n\left(\mathbf{Y}_1^n+\mathbf{Y}_3^n\mathbf{D}_b\right)$$

$$\mathbf{E}_3=\xi^2\mathbf{I}+\sum_{n=4}^{\infty}\xi^n\mathbf{Y}_2^n\,,\qquad \mathbf{E}_4=\xi^3\mathbf{I}+\sum_{n=4}^{\infty}\xi^n\mathbf{Y}_3^n\,,$$

$$\mathbf{E}_5=\begin{bmatrix}\mathbf{E}_3\mathbf{e}_2&\mathbf{E}_4\mathbf{e}_2\end{bmatrix}. \tag{37}$$

$$\mathbf{Y}_i^n=\sum_{j=1}^{4}\mathbf{A}_n^j\mathbf{Y}_i^{n-j}\qquad,\ i=0,\ 1,\ 2,\ 3\ ,\ n\geq 4 \tag{38}$$

$$\mathbf{Y}_i^j = \begin{cases} \mathbf{I} & if \ \ i = j \\ \mathbf{0} & if \ \ i \neq j \end{cases} \qquad i, j = 0,\ 1,\ 2,\ 3 \tag{39}$$

$$\mathbf{D}_a = -\frac{1}{2}\begin{bmatrix} a & b \\ 0 & 0 \end{bmatrix}, \ \mathbf{D}_b = -\frac{1}{6}\begin{bmatrix} a & b \\ 0 & 0 \end{bmatrix}, \ \mathbf{e}_2 = \begin{Bmatrix} 0 \\ 1 \end{Bmatrix} \tag{40}$$

where $\mathbf{I}$ and $\mathbf{0}$ are unit matrix and zero matrix of order 2×2, respectively.

From the boundary conditions given in equations (17) and (18), and equations (12)-(14), (27)-(29) and (35)-(40), one can obtain

$$\mathbf{K}(K)\mathbf{C} = \mathbf{0}, \tag{41}$$

and $\mathbf{K}(K)$ denotes $\mathbf{K}$ is function of K given in equation (31).

For a nontrivial $\mathbf{C}$, the determinant of the 6×6 matrix $\mathbf{K}$ in equation (41) must be equal to zero. The values of K which make this determinant vanish are called eigenvalues of matrix $\mathbf{K}$ and give the natural frequencies of the rotating Euler beam through equation (31). The bisection method is used here to find the eigenvalues.

NUMERICAL EXAMPLES

To demonstrate the accuracy and efficiency of the present formulation and investigate the effects of the tip mass on the natural frequency of the rotating beam, the rotating beam with slenderness ratio $\sqrt{\eta} = 100$ is studied.

With the consideration of the Coriolis force, except $\beta = 0$ or $k = 0$, the axial and lateral vibrations are coupled in the vibration modes. However, for convenience, in this study the terms lateral vibration and axial vibration only denote that the vibrations are lateral vibration and axial vibration, respectively, at $k = 0$.

The natural frequencies of the rotating beams with different values of the tip mass and rotary inertia of the tip mass for setting angle $\beta = 0$, and 0.5π are listed in Table 1 and Table 2, respectively. In Table 1 and 2, (A) denotes that the corresponding free vibration is axial vibration. As can be seen that at $k = 0$, the vibration mode correspond the fourth natural frequency is lateral vibration for all cases. However, at k = 0.05, 0.1, the vibration mode correspond the fourth natural frequency is axial vibration for case M = 0.5, h/L = 0, and at k = 0.1, the vibration mode correspond the fourth natural frequency is axial vibration for case M = 1, h/L = 1.

CONCLUSIONS

In this paper, the correct linearized governing equations for the linear vibration of a rotating uniform Euler beam with tip mass are derived. The

vibration of the beam is measured from the position of the static axial deformation, and only infinitesimal free vibration is considered. The equations of motion for rotating Euler beam are derived by the d'Alembert principle and the virtual work principle. It is seen that even for linear vibration of a rotating Euler beam, the exact governing equations might be derived by the consistent linearization of the fully geometrically non-linear beam theory. The effects of the Coriolis force and rotary inertia on the natural frequency of the rotating beam are considered. A method based on the power series solution is proposed to solve the natural frequency.

The results of numerical examples show that the effect of the tip mass on the natural frequencies of the rotating Euler beam may be considerable.

REFERENCES

1. Hoa, S. V., Vibration of a rotating beam with tip mass. *Journal of Sound and Vibration*, 1979, **67**, 369-381.
2. Bhat, R. B., Transverse vibrations of a rotating uniform cantilever beam with tip mass as predicted by using beam characteristic orthogonal polynomials in the Rayleigh-Ritz method. *Journal of Sound and Vibration*, 1986, **105**, 199-210.
3. Khulief, Y. A., Vibration frequencies of a rotating tapered beam with end mass. *Journal of Sound and Vibration*, 1989, **134**, 87-97.
4. Lee, H. P., Vibration on an inclined rotating cantilever beam with tip mass. *Journal of Vibration and Acoustics*, 1993, **115**, 241-245.
5. Bruch, J. C. Jr. and Mitchell, T. P., Vibration of a mass-loaded clamped-free Timoshenko beam. *Journal of Sound and Vibration*, 1988, **114**, 341-345.
6. Khulief, Y. A. and Yi, L., Lead-lag vibrational frequencies of a rotating beam with end mass. *Computers & Structures* , 1988, **29**, 1075-1085.
7. Low, K. H., Vibration analysis of a tip-loaded beam attached to a rotating joint. *Computers & Structures*, 1994, **52**, 955-968.
8. Simo, J.C. and Vu-Quoc, L, The role of non-linear theories in transient dynamic analysis of flexible structures. *J. of Sound and Vibration*, 1987 **119**, 487-508.

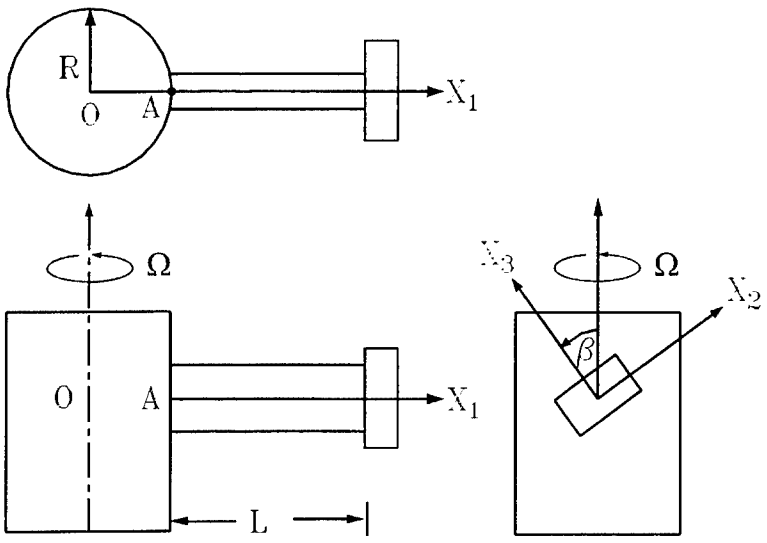

Fig. 1 A rotating Euler beam with tip mass

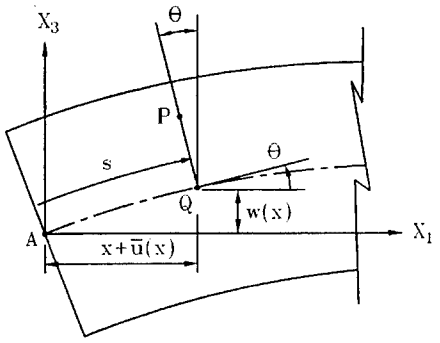

Figure 2 Kinematics of deformed beam

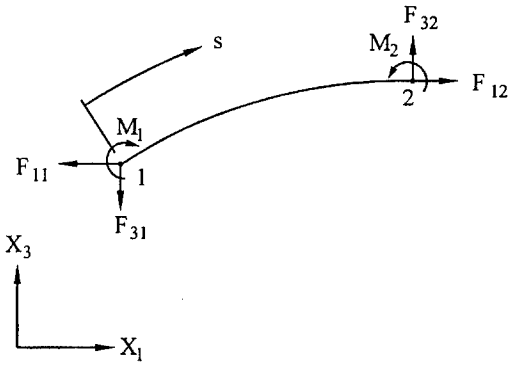

Figure 3 Forces and moments on a differential beam element

Table 1 Dimensionless frequencies for rotating Euler beam
($r = 0, \beta = 0, \sqrt{\eta} = 100$)

k	M	h/L	$K_1(10^{-1})$	$K_2(10^{-1})$	$K_3(10^{-1})$	K_4
0.00	0	0	0.35152	2.19988	6.14601	1.20047
	0.5	0	0.20161	1.68885	5.15805	1.05542
	0.5	0.5	0.17021	0.59752	2.55620	0.64876
	1	1	0.08679	0.33905	2.40015	0.63312
0.05	0	0	0.64476	2.54041	6.49528	1.23684
	0.5	0	0.57073	2.36918	5.97477	1.07563(A)
	0.5	0.5	0.46058	0.77827	3.10734	0.72334
	1	1	0.22373	0.62461	3.22000	0.74796
0.10	0	0	1.11988	3.35835	7.43558	1.33924
	0.5	0	1.06425	3.71092	7.92453	1.07214(A)
	0.5	0.5	0.73511	1.17299	4.33211	0.90835
	0.5	1	0.38336	1.13170	4.31364	0.90733
	1	1	0.31825	1.10058	4.85666	0.85445(A)

Table 2 Dimensionless frequencies for rotating Euler beam
$(r = 0, \beta = 0.5\pi, \sqrt{\eta} = 100)$

k	M	h/L	$K_1(10^{-2})$	$K_2(10^{-1})$	$K_3(10^{-1})$	K_4
0.00	0	0	3.51520	2.19988	6.14601	1.20047
	0.5	0	2.01614	1.68885	5.15805	1.05542
	0.5	0.5	1.70213	0.59752	2.55620	0.64876
	1	1	0.86789	0.33905	2.40015	0.63312
0.05	0	0	4.06560	2.49028	6.47564	1.23579
	0.5	0	2.74165	2.31498	5.95329	1.08026(A)
	0.5	0.5	2.40888	0.70662	3.06694	0.72154
	1	1	1.42986	0.40877	3.17979	0.74619
0.10	0	0	5.00969	3.20350	7.36612	1.33531
	0.5	0	3.58429	3.56825	7.85812	1.09067(A)
	0.5	0.5	3.23210	0.88636	4.21038	0.90242
	1	1	1.99573	0.51065	4.74464	0.87754(A)

A STUDY OF MODAL COUPLING MECHANISMS LEADING TO SQUEAL VIBRATIONS

C. M. Krousgrill
A. K. Bajaj
B. K. Servis

School of Mechanical Engineering
Purdue University
West Lafayette, Indiana 47907-1288
USA

ABSTRACT

In this paper, the stability of steady sliding of a braking system is investigated. An emphasis is placed on understanding the influence of the friction-moment coupling on the development of squeal oscillations. The equations of motion for small oscillations about the engaged configuration of the brake system are expressed in terms of the linear modes of the individual system components. A consequence of the friction-moment coupling is a non-symmetric contribution to the stiffness matrix, typical of circulatory systems. A variation method applied on a Rayleigh-type quotient is used for determining the critical values of friction needed for the onset of squeal. Unstable oscillations from single-mode coupling within the drum and mixed-mode coupling within the drum and between the drum and shoes are observed. Simpler rigid-drum and rigid-shoe models are used to interpret the results and to provide a qualitative understanding of the different mechanisms of squeal generation observed in the study.

INTRODUCTION

Squeal oscillations in braking systems are friction-induced oscillations resulting in the generation of noise with a frequency content ranging from a few hundred Hz to several thousand Hz. Early work in the field focused on the nature of the friction coefficient at the braking surface that leads to friction oscillations, either in a simple friction model with a higher static coefficient than the dynamic or in a friction model with a negative slope in the friction-relative velocity curve. Experiments ([Felske et al., 1980], [Kusano et al., 1985], [Lang and Newcomb, 1989]), however, have shown that squeal oscillations can be observed even for conditions of relatively constant friction coefficients. Work appearing in the 1970's ([Spurr, 1971], [Earles and Soar, 1971], [Earles and Lee, 1976], [Milner, 1976a, 1976b]) were pioneering efforts that featured frictional coupling of the natural modes of the system at the braking surface as being the primary mechanism for the generation of squeal oscillations under conditions of constant friction coefficients. With these models, squeal oscillations occurred for system parameters for which a positive net energy flow existed from the rotating source into components of the braking system. A number of other works have

subsequently appeared which have successfully used models incorporating the frictional coupling of natural modes for the prediction of squeal (e.g., [Nishiwaki, 1993], [Hulten, 1994], [Hulten, 1995], [Adams, 1995], [Kido et al., 1996]). Some excellent review articles have also recently appeared ([Nishiwaki, 1990], [Ibrahim, 1994a], [Ibrahim, 1994b]) that discuss the contemporary views on brake squeal and other mechanisms of friction-induced oscillations.

In reviewing existing squeal models for drum brakes, Hulten (1994, 1995) has observed that there are two primary sources of modal coupling that can lead to friction-induced oscillations: friction force coupling and friction moment coupling. The friction force coupling is geometric in nature and results from a kinematic constraint between the radial and transverse components of deformation of the drum and shoes at the braking surface. This coupling is increased as the radius of the drum is reduced. Friction moment coupling results from the coupling of the bending moments at the braking surface due to the friction force acting at a distance from the neutral axis of bending of the drum and/or shoes. This coupling is generally increased by an increase in the thickness of the friction material of the brake lining. In this work, Hulten offers some physical insight as to how these two different types of coupling can lead to the transfer of rotational energy of the wheel hub into a growth of vibrational energy in the drum and shoes.

Typically, a set of non-conservative, linearized equations of motion are produced from these modal coupling models that govern the free vibration of an engaged braking system. The onset of squeal is predicted when a pair of natural frequencies corresponding to the equations of motion coalesce and subsequently become complex. Generally, any number and types of modal pairs are capable of merging, depending on model parameters such as component stiffnesses and sliding coefficient of friction. For models possessing a large number of degrees of freedom, it becomes quite difficult to understand why certain modes will couple to create squeal and other do not, thereby creating obstacles to design engineers in their attempts to reduce the propensity of squeal vibrations.

In this present investigation, a focus is placed on the understanding of the ability of different modal pairs to produce squeal vibrations. In particular, the moment-coupling mechanism observed by Hulten is explored through simplified bending models for the drum and shoes. Linearized equations of motion are developed for these models, and the influence of lining stiffness and sliding

friction coefficient on the onset of squeal is studied. A Rayleigh quotient-based approach is used to directly compute the critical values of the stiffness and friction coefficient parameters from the eigenvalue and adjoint eigenvalue problems. A particular emphasis of this investigation is to see which drum and/or shoe modes are likely to be responsible for the creation of squeal oscillations.

MATHEMATICAL MODEL

For this model, the rotating drum ("body 3") will be considered to be a thin ring with flexural rigidity $\mathcal{E}I_3$, mass per length of ρ and cross-sectional area of $\mathcal{A}_3$. The two shoes ("bodies 1 and 2") will be assumed to be thin, curved beams having mass per length ρ, flexural rigidities of $\mathcal{E}I_1$ and $\mathcal{E}I_2$, and cross-sectional areas of $\mathcal{A}_1$ and $\mathcal{A}_2$, respectively. In this work, we will study the coupling between circumferential modes of the drum and purely bending modes of the shoes. With this in mind, the models for the drum and shoes will be further reduced to that of thin, straight beams having lengths of $\mathcal{L}_1$, $\mathcal{L}_2$ and $\mathcal{L}_3$ for bodies 1 through 3, respectively, as shown in Figure 1. The transverse displacements of bodies 1 through 3 are to be denoted as $u_j(x_j)$ $(j = 1,2,3, \textit{respectively})$. Simply-supported boundary conditions are to be applied to shoes, whereas periodic boundary conditions are to be applied to the drum (that is, continuity of displacement u_3, and all of its spatial derivatives at $x_3 = 0$ and $x_3 = \mathcal{L}_3$). The beam model for the drum has a sliding speed of v relative to shoes 1 and 2 with a sliding coefficient of friction μ at the interface of the drum with the lining material. The speed of the drum will be considered to be small compared to structural wave speeds of the drum and shoes. As a consequence of this assumption, the relative sliding between the x_j $(j = 1,2)$ and x_3 coordinates will be ignored when establishing the equations of motion for the system. The inertia and bending resistance of the friction material will be considered negligible compared to that of the beams, and as a result, the friction material will be treated as a distributed elastic foundation with a stiffness per unit length of k for the friction material on each shoe.

The response for each of the three structural components will be expanded in terms of their "non-engaged" modal functions (i.e., modes of each component in the absence of the coupling due to the friction material) as:

$$u_j(x_j,t) = \underline{\psi}_j^T(x_j)\,\underline{q}_j(t) \quad ; \; j = 1,2,3 \tag{1}$$

where

$$\begin{aligned}
\underline{\psi}_j^T(x_j) &= \sqrt{\frac{2}{\rho A_j L_j}}\left\{\sin\pi\frac{x_j}{L_j}, \sin 2\pi\frac{x_j}{L_j}, \ldots, \sin \mathcal{N}_j\pi\frac{x_j}{L_j}\right\} \quad ; \; j = 1,2 \\
\underline{\psi}_3^T(x_3) &= \sqrt{\frac{2}{\rho A_3 L_3}}\left\{\cos 2\pi\frac{x_3}{L_3}, \ldots, \cos \mathcal{N}_3\pi\frac{x_3}{L_3}, \sin 2\pi\frac{x_3}{L_3}, \ldots, \sin \mathcal{N}_3\pi\frac{x_3}{L_3}\right\}
\end{aligned} \tag{2}$$

Employing the modeling assumptions described above, the kinetic and potential energy of the braking system become:

$$\mathcal{T} = \frac{1}{2}\sum_{j=1}^{3}\rho_j A_j \int_0^{L_j}\left[\underline{\psi}_j^T\,\dot{\underline{q}}_j\right]^2 dx_j = \frac{1}{2}\,\dot{\underline{p}}^T\,\dot{\underline{p}} \tag{3}$$

$$\begin{aligned}
\mathcal{U} &= \frac{1}{2}\sum_{j=1}^{3} EI_j \int_0^{L_j}\left[\frac{d^2\underline{\psi}_j^T}{dx_j^2}\,\underline{q}_j\right]^2 dx_j + \frac{1}{2}\,k\sum_{j=1}^{2}\int_0^{L_j}\left[\underline{\psi}_j^T\,\underline{q}_j - \underline{\psi}_3^T\,\underline{q}_3\right]^2 dx_j \\
&= \frac{1}{2}\,\underline{p}^T[\mathcal{K}]\,\underline{p} + \frac{1}{2}\,k\,\underline{p}^T[\mathcal{A}]\,\underline{p}
\end{aligned} \tag{4}$$

respectively, where $\underline{p}^T = \left\{\underline{q}_1^T, \underline{q}_2^T, \underline{q}_3^T\right\}$, *[K]* is a diagonal matrix of the square of the non-engaged ($k = 0$) natural frequencies of the components, and:

$$[\mathcal{A}] = \begin{bmatrix} [\mathcal{A}^{11}] & [0] & -[\mathcal{A}^{13}] \\ [0] & [\mathcal{A}^{22}] & -[\mathcal{A}^{23}] \\ -[\mathcal{A}^{31}] & -[\mathcal{A}^{32}] & [\mathcal{A}^{33}] \end{bmatrix} \tag{5}$$

$$[\mathcal{A}^{jm}] = \int_0^{L_j}\underline{\psi}_j\,\underline{\psi}_m^T\,dx_j \quad ; \quad (j,m) = (1,1), (1,3), (3,1), (2,2), (2,3), (3,2) \tag{6}$$

$$[\mathcal{A}^{33}] = \int_0^{L_1}\underline{\psi}_1\,\underline{\psi}_3^T\,dx_1 + \int_0^{L_2}\underline{\psi}_2\,\underline{\psi}_3^T\,dx_2 \tag{7}$$

Owing to the assumption of only transverse vibrations of the components, the virtual work done by the friction forces at the interfaces of the drum with the friction material arises through a distributed bending moment per unit length of (see Figure 2):

$$m_{f3} = \mu k_j h_3 \left[u_j(x_j, t) - u_3(x_3, t) \right] \tag{8}$$

on the drum and of:

$$m_{fj} = \mu k_j h_j \left[u_j(x_j, t) - u_3(x_3, t) \right] \tag{9}$$

on each shoe, where h_j is the distance from the neutral axis of body j to the friction interface. With equations (8) and (9), the virtual work done by friction can be written as:

$$\begin{aligned} \delta W_f &= \sum_{j=1}^{2} \left[\int_0^{L_j} m_{fj} \delta \left(\frac{\partial u_j}{\partial x_j} \right) dx_j + \int_0^{L_j} m_{f3} \delta \left(\frac{\partial u_3}{\partial x_3} \right) dx_j \right] \\ &= -\mu k \delta \left(\underline{p}^T \right) [\mathcal{B}] \underline{p} \end{aligned} \tag{10}$$

where

$$[\mathcal{B}] = \begin{bmatrix} [0] & [0] & -\left[\mathcal{B}^{13}\right] \\ [0] & [0] & -\left[\mathcal{B}^{23}\right] \\ \left[\mathcal{B}^{31}\right] & \left[\mathcal{B}^{32}\right] & \left[\mathcal{B}^{33}\right] \end{bmatrix} \tag{11}$$

$$\left[\mathcal{B}^{jm}\right] = h_j \int_0^{L_j} \frac{d\underline{\psi}_j}{dx_j} \underline{\psi}_m^T \, dx_j \quad ; \quad (j,m) = (1,3), (3,1), (2,3), (3,2) \tag{12}$$

$$\left[\mathcal{B}^{33}\right] = h_3 \int_0^{L_1} \frac{d\underline{\psi}_1}{dx_1} \underline{\psi}_3^T \, dx_1 + h_3 \int_0^{L_2} \frac{d\underline{\psi}_2}{dx_2} \underline{\psi}_3^T \, dx_2 \tag{13}$$

Applying Lagrange's equations with equations (3), (4), (6) and (10) produces the following equations of motion for the system:

$$\ddot{\underline{p}} + \left[\mathcal{K} + k[\mathcal{A}] + \mu k[\mathcal{B}] \right] \underline{p} = \underline{0} \tag{14}$$

Equation (14) represents a set of $\mathcal{N} = \mathcal{N}_1 + \mathcal{N}_2 + \mathcal{N}_3$ differential equations of motion for the coupled system describing small oscillations about an equilibrium deformation state created by an engagement of the drum with the friction material on the two shoes. The [A] matrix in equation (14) accounts for the stiffness contribution to the system by the compression of the friction material. This stiffness coupling is symmetric, characteristic of *conservative* coupling forces. The [B] matrix in equation (14) arises from the virtual work done by the friction forces at the interface of the friction material with the moving drum. The stiffness contribution of [B] provides non-symmetric coupling for the system components, characteristic of non-conservative "circulatory forces" [Huseyin, 1978].

ANALYSIS

The homogeneous equations of motion in equation (14) above represent the free response of an engaged brake system. With the coefficient matrices in equation (14) being constant, the character of the response is dictated by its eigenvalues and eigenvectors. In this section, the influence that the lining stiffness and friction properties have on the eigenvalues and eigenvectors as well as on the propensity for squeal in the braking system.

The eigenvalue and adjoint eigenvalue problems corresponding to the equations of motion (14) can be written as:

$$\left[-\omega^2[I]+[\mathcal{K}]+k[\mathcal{A}]+\mu k[\mathcal{B}]\right]\underline{R}=\underline{0} \tag{15}$$

$$\left[-\omega^2[I]+[\mathcal{K}]+k[\mathcal{A}]+\mu k[\mathcal{B}]^T\right]\underline{L}=\underline{0} \tag{16}$$

respectively, where ω are the natural frequencies, and $\underline{R}$ and $\underline{L}$ are the right- and left-eigenvectors, respectively. Two independent coupling parameters exist in the eigenvalue problem: the friction material stiffness, k, and the coefficient of sliding friction, μ.

When $\mu = 0$, the equations of motion are coupled only through the lining stiffness matrix *[A]*. For $k = 0$ (non-engaged braking system), the natural frequencies are those of the individual brake components (shoe 1, shoe 2 and the drum), and these natural frequencies are contained in the elements of the diagonal stiffness matrix *[K]*. Since the cosine-sine mode pairs for the drum model were used for the drum trial functions, the natural frequencies for the

drum will appear in repeated pairs. As the lining stiffness parameter k is increased, the individual natural frequencies for the braking system will either increase or remain unchanged. The repeated natural frequency pairs corresponding to the cosine-sine mode pairs for the drum will tend to separate, with the amount of separation depending on the shoe lengths, ℓ_1 and ℓ_2 , and the shoe spacing, $2a$. However, since the stiffness matrices $[K]$ and $[A]$ are symmetric, the natural frequencies will remain real for $\mu = 0$ and stable oscillations of the system will result [Huseyin, 1978].

For $\mu > 0$, a variation of k can lead to complex natural frequencies resulting in unstable oscillations about the equilibrium state. This instability, common in systems with circulatory forces, results from "coupled-mode flutter" appearing as a result of the merging (and subsequent splitting) of a pair of natural frequencies and mode shapes in the system.

It can be shown [Huseyin, 1978] that the coalescence of a pair of natural frequencies that leads to the flutter instability occurs when the corresponding left- and right-eigenvectors are related by:

$$\underline{\mathcal{L}}^T \underline{\mathcal{R}} = 0 \quad . \tag{17}$$

That is, a critical set of parameters $k = k_{cr}$ and $\mu = \mu_{cr}$ exists when the corresponding left- and right-eigenvector pair forms an orthogonal set. This relation will be used to determine the combination of parameters that leads to unstable sliding of body 3 with respect to the friction material. To this end, premultiply the eigenvalue problem (15) by $\underline{L}^T$:

$$-\omega^2 \underline{\mathcal{L}}^T \underline{\mathcal{R}} + \underline{\mathcal{L}}^T \left[[\mathcal{K}] + k[\mathcal{A}] \right] \underline{\mathcal{R}} + \mu k \underline{\mathcal{L}}^T [\mathcal{B}] \underline{\mathcal{R}} = \underline{0} \quad . \tag{18}$$

Applying the coalescence condition (17) and solving for μ gives:

$$\mu_{cr} = - \frac{\underline{\mathcal{L}}_{cr}^T \left[[\mathcal{K}] + k[\mathcal{A}] \right] \underline{\mathcal{R}}_{cr}}{k \underline{\mathcal{L}}_{cr}^T [\mathcal{B}] \underline{\mathcal{R}}_{cr}} \triangleq Q\left(\underline{\mathcal{L}}_{cr}, \underline{\mathcal{R}}_{cr} \right) \quad . \tag{19}$$

The parameter Q defined in (19) can be thought of as a "Rayleigh quotient" for the critical value of the parameter μ leading to a flutter-type unstable response. For an arbitrary pair of N-vectors $\underline{u}$ and $\underline{v}$, it can be shown [Huseyin, 1978] that the quotient $Q(\underline{u},\underline{v})$ takes on a stationary value when $\underline{v} = \underline{L}_{cr}$ and $\underline{u} = \underline{R}_{cr}$; that is,

$$dQ \Big|_{\underline{u} = \underline{\mathcal{R}}_{cr},\ \underline{v} = \underline{\mathcal{L}}_{cr}} = 0 \tag{20}$$

In order to determine the stationary value of Q in (20), a set of vectors $\underline{u}$ and $\underline{v}$ will be written as linear combinations of the (linearly independent) eigenvectors $\underline{\phi}^{(j)}$ ($j = 1, 2, \ldots, N$) _corresponding to $\mu = 0$:

$$\underline{u} = \sum_{j=1}^{\mathcal{N}} \underline{\phi}^{(j)} a_j = [\Phi]\, \underline{a} \tag{21}$$

$$\underline{v} = \sum_{j=1}^{\mathcal{N}} \underline{\phi}^{(j)} b_j = [\Phi]\, \underline{b} \tag{22}$$

where the modes have been normalized such that:

$$[\Phi]^T [\Phi] = [I] \tag{23}$$

The coefficients $\underline{a}$ and $\underline{b}$ are chosen in such a way that $\underline{u}$ and $\underline{v}$ satisfy the coalescence condition of equation (17):

$$\underline{u}^T \underline{v} = \underline{a}^T [\Phi]^T [\Phi] \underline{b} = \underline{a}^T \underline{b} = 0 \quad . \tag{24}$$

The stationary value of Q is then found by solving the constrained problem of:

$$dQ + \lambda\, d\left(\underline{a}^T \underline{b}\right) = 0 \tag{25}$$

where λ is a to-be-determined Lagrange multiplier.

Substituting equations (21) and (22) into equation (25) produces:

$$\left[\mu_{cr}\, k [\Phi]^T [\mathcal{B}]^T [\Phi] + [\mathcal{N}] + \lambda [I] \right] \underline{a} = \underline{0} \tag{26}$$

$$\left[\mu_{cr}\, k [\Phi]^T [\mathcal{B}] [\Phi] + [\mathcal{N}] + \lambda [I] \right] \underline{b} = \underline{0} \tag{27}$$

where $[N]$ is a diagonal matrix containing the square of the $\mu = 0$ natural frequencies, ν_j ($j = 1, 2, \ldots, N$). Simultaneous solution of equations (24), (26) and (27) produces the critical value of the friction coefficient, μ_{cr}, for a given value of lining stiffness k.

In summary, the investigation of the onset of squeal vibrations for the braking system modeled presented here is reduced to a two-parameter problem in the μ-k plane. Combinations of values for μ and k that satisfy equations (24), (26) and (27) correspond to the merging of free vibration modes of the engaged and rotating brake system. Solution of the constrained eigenvalue problem in these equations produces a direct method for the calculation of stability boundaries within the μ-k plane. Usage of this method allows for the study of

which drum and shoe modes contribute to the production of squeal oscillations. The results of such a study are presented in the following section.

RESULTS AND DISCUSSION

Here, three situations will be studied: a) rigid shoes and compliant drum, b) compliant shoes and rigid drum, and c) compliant shoes and drum.

a) Rigid shoe model

If the flexibility of the shoes is ignored, only the on-diagonal block matrices in the lower right hand corner of the system matrices in equation (14) remain. Furthermore, if the elastic foundation for the drum exists over its entire length ($L_1 + L_2 = L_3$), the eigenvalue problem (15) reduces to a set of $\mathcal{N}_3/2$, (2×2) blocks having the form of:

$$\begin{bmatrix} -\omega^2+\nu_j^2 & \mu k\mathcal{B}_{ij}^{33} \\ -\mu k\mathcal{B}_{ij}^{33} & -\omega^2+\nu_j^2 \end{bmatrix} \underline{\hat{R}}=\underline{0} \quad . \tag{28}$$

It is easily shown from equation (28) that the critical value of the friction coefficient for squeal is zero. That is, for a complete support of the drum by an elastic foundation, the steady sliding is unstable for ANY non-zero value of μ. This observation is consistent with results from other models of friction-induced oscillations having uniform stiffness supports [Adams, 1995].

Thus it can be concluded that nonuniformity of the support stiffness for the drum is a stabilizing factor. For non-uniform stiffness of interest in this work, a variation in the lining stiffness k initially separates the coincident cosine-sine mode frequency pairs of the elastic drum. Introduction of $\mu > 0$ will tend to draw the frequency pairs back together, potentially leading to the onset of the flutter instability.

Two types of mode-coupling instabilities are observed in this drum model. The first corresponds to (Di,Di) modal coupling[1]. As shown in Figure 3 for (D3,D3), the stability boundary is initially brought to the stiffness axis as k is increased (stiffness destabilizing) followed by movement of the stability boundary away from the stiffness axis (stiffness stabilizing). At the intersection of the stability boundary with the stiffness axis, $\mu_{cr} = 0$, and therefore steady

1 Here, the notation of Dj and Si refers to the jth drum mode and ith shoe mode, respectively, for $\mu = k = 0$.

sliding is unstable for ALL values of $\mu > 0$, as was seen for the uniform support stiffness case. The second type of mode-coupling has the stability boundary moving initially toward the stiffness axis but turning away without crossing the $\mu = 0$ axis. However, this stability boundary changes from (Di,Di) to (Di,Dj) for I $\neq$ j (mixed-mode coupling). In Figure 4, a change from (D2,D2) to (D1,D2) modal coupling is seen as the lining stiffness is varied. It is seen that the (D1,D2) eventually intersects the stiffness axis and moves away, similar to the single-mode coupling in Figure 3. The single-mode coupling tends to be "less unstable" than the mixed-mode coupling in that the imaginary/real ratio of the unstable natural frequencies tend to be much smaller than for the mixed-mode coupling. Small amounts of structural damping are likely to suppress the single-mode flutter instabilities, particularly for those corresponding to the higher modes of the drum.

b) Rigid drum model

If the flexibility of the drum is ignored, the motion of each shoe is uncoupled from the other. From equation (11), it can be seen that the on-diagonal blocks of the *[B]* matrix are zero for the shoes. That is, the friction moment is not capable of coupling the shoe modes when the lining acts against a rigid drum. As a result, the equations of motion of a braking system mode with a rigid drum are those of a conservative system, and the natural frequencies are real for all values of lining stiffness and friction coefficient. Therefore, squeal oscillations are not possible in the limiting case of a rigid drum.

c) Combined flexible shoe and drum model

A simultaneous solution of equations (24), (26) and (27) shows that several types of single-mode and mixed-mode couplings that lead to the squeal instabilities for the combined flexible shoe/drum model. Shown in Figures 5-7 are the single-mode mergings of (D2,D2), (D3,D3) and (D4,D4), as well as mixed-mode couplings of (D2,S2), (D3,S3) and (D4,S4). Several key observations can be made from these stability diagrams. First, single-mode flutter of (D2,D2), (D3,D3) and (D4,D4) stability boundaries have been found for low values of the stiffness parameter k. These "v-shaped" stability boundaries result from the drum-mode coupling discussed in the context of the rigid shoe model. The

critical value of μ corresponding to $k \approx 0$ appears to decrease with increasing mode number. This can be explained by considering the fact that the effect of the stiffness non-uniformity of the lining is diminished in the higher modes. As discussed before, stiffness uniformity is a destabilizing factor for the drum-mode coupling. A second observation is that stability boundaries corresponding to (D2,S2), (D3,S3) and (D4,S4) mixed-mode coupling occurs, as seen in Figures 5-7. These mixed-mode stability branches join the (D2,D2), (D3,D3) and (D4,D4) single-mode branches, respectively, for friction values outside the range given in these figures. The joining of these different types of branches is similar to that seen for the single-mode and mixed-mode drum branches seen in Figure 4 for the rigid shoe model. With its unique shape, the (D2,S2) stability boundary of Figure 5 appears to be equally influenced by both the drum and shoe modes.

For the parameter ranges studied here, the ratio of imaginary/real parts of the unstable natural frequencies for the mixed-mode instabilities are considerably larger than those for the single-mode instabilities of the drum. For the higher modes, this ratio is typically small enough that the introduction of only a small amount of damping can raise the critical value of μ to values larger than those of the mixed-mode. Because of this, it is felt that the mixed-mode instabilities are of a more serious concern than the single-mode instabilities of the drum.

CONCLUSIONS

A study has been performed to determine the influence lining stiffness and friction properties on the stability of steady sliding in a compliant braking system. For the model chosen here, the motion of the drum component was written in terms of its set of spatially-periodic, cosine-sine mode shapes, and the motion of the shoes was written in terms of a set of simply-supported mode shapes. In the absence of the coupling due to the brake lining, the natural frequencies of the drum appear in terms of stable, coincident pairs, and the natural frequencies of the shoes are finitely separated. The influence of lining stiffness is to shift the natural frequencies for the drum and shoes. Since the friction couple acts to couple sympathetic modes into unstable motion, the sliding of the drum against a uniform lining on a rigid shoe was found to be unstable for any non-zero friction. Non-uniformities and compliance of the shoe were seen to be stabilizing influences. However, unstable sliding due to single-

mode coupling in the drum was found to persist at low stiffness values, particularly for the higher modes of the drum. Mixed-mode coupling among the different drum modes and between drum and shoe modes was found to lead to unstable sliding conditions, particularly at higher stiffnesses of the lining.

It can been shown that the curvature-coupling ignored in this drum-brake system will produce components to the friction-coupling matrix [B] similar to those detailed here for the moment-coupling. Therefore it is felt that many of the observations made here for the moment-coupling will be valid for the curvature-coupled mechanisms. A detailed study that compares these two mechanisms is left for future investigation.

The ultimate goal of this work is to produce a fundamental understanding of which modes in a braking system will lead to a squeal response. With many modes appearing in models with large numbers of degrees of freedom, the task of predicting the onset of squeal is enormous and tedious. Only with a good qualitative understanding of modal coupling will come design modifications and new designs of brake components for which squeal response can be avoided.

REFERENCES

Adams, G.G., 1995, "Self-Excited Oscillations in Sliding with a Constant Friction Coefficient", *1995 Design Engineering Technical Conference*, Vol 3 - Part A, pp. 1171-1177.

Earles, S.W.E. and Soar, G.B., 1971, "Squeal Noise in Disc Brakes", *Pro. Instn. Mech. Engrs. Vibration and Noise in Motor Vehicles*, pp. 61-69.

Earles, S.W.E. and Lee, C.K., 1976, "Instabilities Arising from Friction Interaction of a Pin-Disc System Resulting in Noise Generation", *Journal of Engineering for Industry*, Vol. 98, Series B, No. 1, pp. 81-86.

Felske, A., Hoppe, G. and Matthai, H., 1980, "A Study on Drum Brake Noise by Holographic Vibration Analysis", SAE Paper 800221.

Hulten, J., 1994, *Some Mechanisms Generating Drum Brake Squeal*, Ph.D. Thesis, Chalmers University, Goteborg, Sweden.

Hulten, J., 1995, "Some Drum Brake Squeal Mechanisms", SAE Paper 951280.

Huseyin, K., 1978, *Vibrations and Stability of Multiple Parameter Systems*, Sijthoff and Noordhoff.

Ibrahim, R.A., 1994a, "Friction-Induced Vibration, Chatter, Squeal and Chaos, Part I: Mechanics of Contact and Friction", *Applied Mechanics Review.* , Vol. 47, No. 4, pp. 209-226.

Ibrahim, R.A., 1994b, "Friction-Induced Vibration, Chatter, Squeal and Chaos, Part II: Dynamics and Modeling", *Applied Mechanics Review.* , Vol. 47, No. 4, pp. 227-253.

Kido, I. Kurahachi, T. and Makato, A., 1996, "A Study of Low-Frequency Brake Squeal Noise", SAE Paper 960993.

Kusano, M., Ishidou, H., Matsumura, S. and Washizu, S., "Experimental Study on the Reduction of Drum Brake Noise", SAE Paper 851465.

Lang, A.M., and Newcomb, T.P., 1985, "An Experimental Investigation into Drum Brake Squeal", I.Mech.E. Paper C382/051.

Meirovitch, L., 1980, *Computational Methods in Structural Dynamics*, Sijthoff and Noordhoff.

Milner, N., 1976a, *A Study of the Squeal of Drum Brakes*, Ph.D. Thesis, University of Leeds, Leeds, England.

Milner, N., 1976b, "A Theory of Drum Brake Squeal", I.Mech.E. Paper C39/76.

Spurr, R.T., 1971, "Brake Squeal", *Pro. Instn. Mech. Engrs.* C95/71, pp. 13-16.

Nishiwaki, M., 1993, "Generalized Theory of Brake Noise", *Pro. Instn. Mech. Engrs.* , Vol. 207, pp. 195-202.

Nishiwaki, M., 1990, "Review of Study of Brake Squeal", *JSAE Review.* , Vol. 11, No. 4, pp. 48-54.

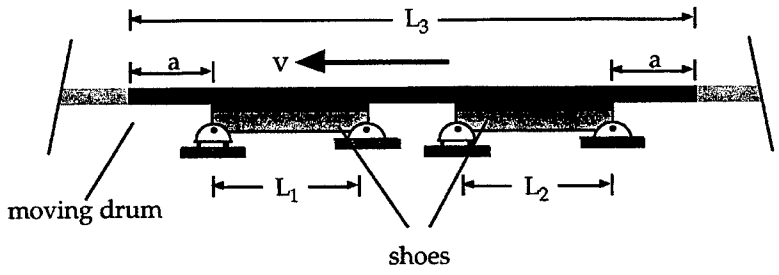

Figure 1. Model of drum-brake system showing the geometry of moving drum component over shoe components (periodic boundary conditions at ends of drum).

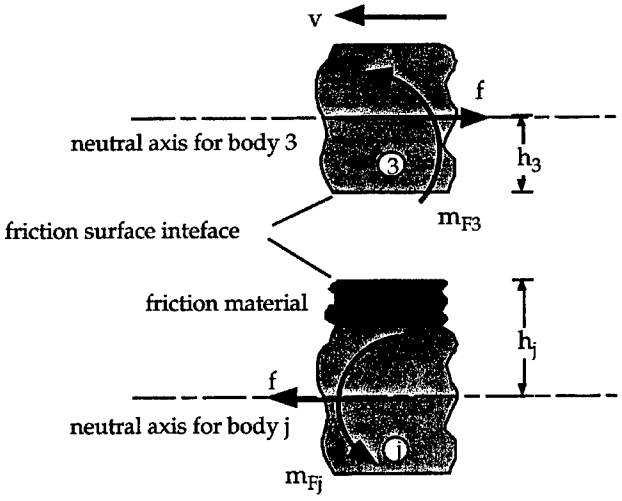

Figure 2. Model of drum-brake system showing the friction forces and moments at friction interface (as seen from a side-view of the drum-lining material interface).

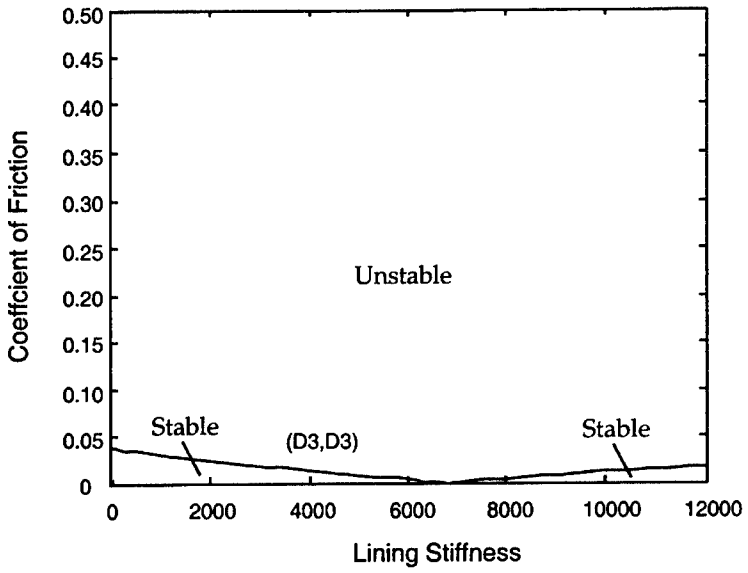

Figure 3. Stability boundaries for the merging of the third cosine-sine modes of the drum (rigid shoe model).

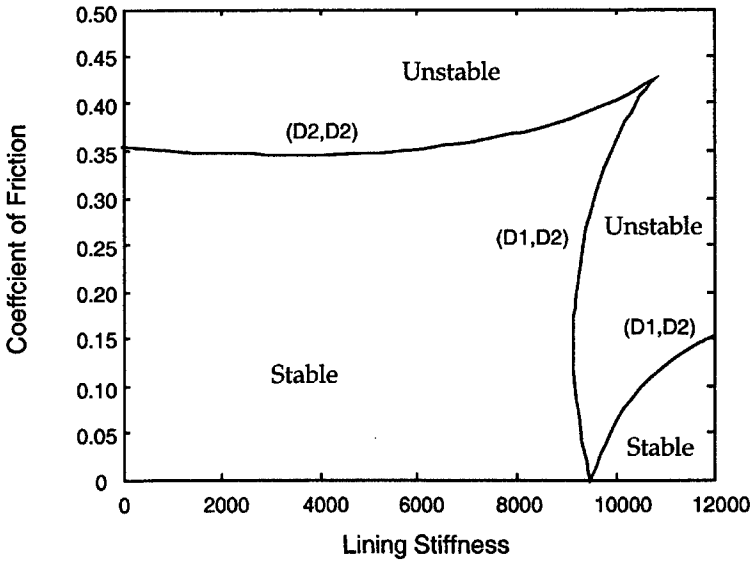

Figure 4. Stability boundaries for the merging of the first and second cosine-sine modes of the drum (rigid shoe model).

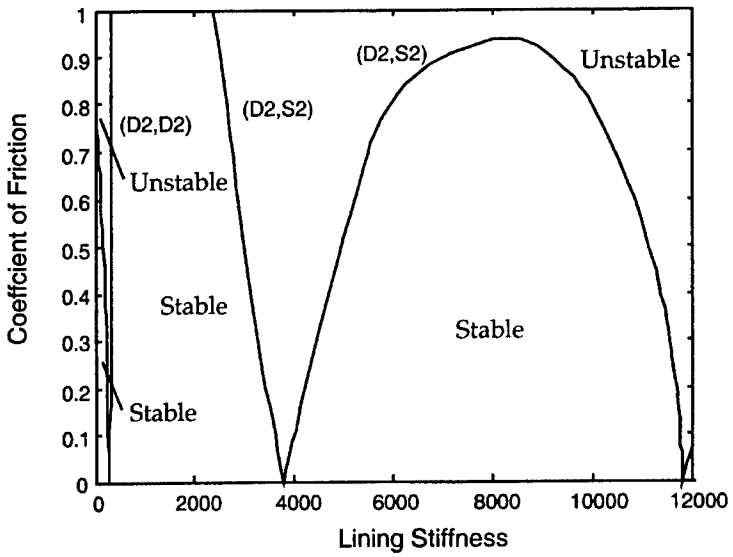

Figure 5. Stability boundaries for the merging of the second cosine-sine modes of the drum and the second drum and shoe modes.

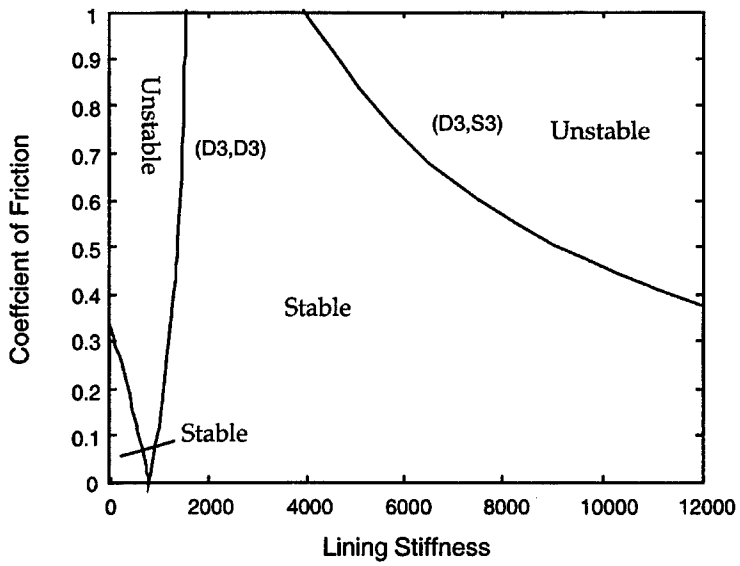

Figure 6. Stability boundaries for the merging of the third cosine-sine modes of the drum and the third drum and shoe modes.

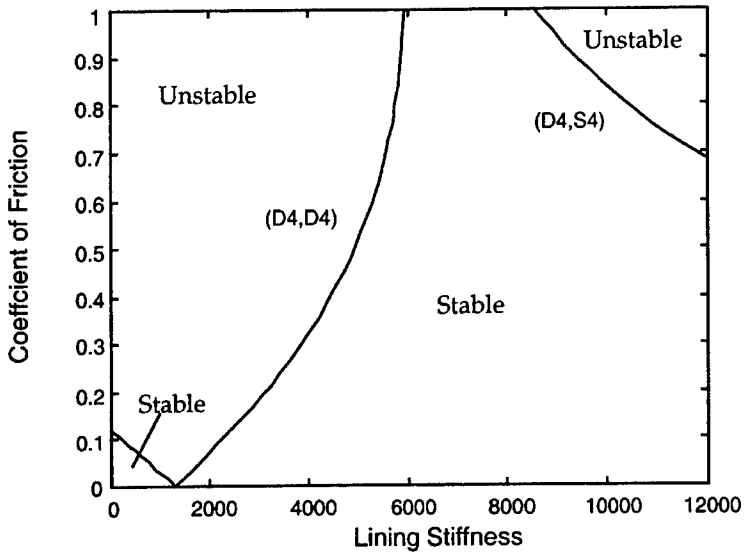

Figure 7. Stability boundaries for the merging of the fourth cosine-sine modes of the drum and the fourth drum and shoe modes.

SUBSTRUCTURING AND COMPLEMENTARY TECHNIQUES

Vibration of Air-coupled Transverse Bulkheads of A Submarine

J.-G. Tseng, K.-H. Huang, and T.-C. Fan
Department of Naval and Mechanical Engineering
H.-T. Chang
Department of Marine Science and Technology
Chinese Naval Academy

ABSTRACT

Noise and vibration control is the most basic and important requirement for a submarine [1] to survive and win the battle. To better understand the airborne and structure borne noise and vibration of a submarine, a simplified model is first attempted by considering the major structure, transverse bulkheads, and the air coupling effect, which has been neglected from other analysis. Vibration of a submarine's watertight compartments, line up in the rigid cylindrical pressure shell, in which adjacent bulkheads (treated as thin plates) couple weakly through air cavities, is investigated through theoretical methods. Such air coupling manifests itself through separated natural frequencies, and system-level modes in which bulkheads in the array vibrate in- or out-of-phase to each other at closely-spaced frequencies. Compared to each mode of the single plate, there exist one in-phase mode and $N-1$ combinations of out-of-phase system modes for a N-plate array. A vibration model comprising of N classical thin plates that couple through the three dimensional acoustic fields established in the circular cavities between plates is developed, and its results are shown in splitting the natural frequencies. In order to solve for the system modes, plate alone and air alone expansion functions are obtained in advance by considering clamped circular plate and rigid cylindrical acoustic cavity, separately. Green's theorem is applied for the rigid air cavity in transforming the velocities of the transverse air particles, adjacent to plate surfaces, into the

[1]Key words: submarine, transverse bulkheads, air-coupled, cylindrical pressure shell, system-level modes, in-phase modes, out-of-phase modes.

coupled air potential equations. Galerkin weighted residual method and Ritz discretization are employed to set up the foundation for the numerical calculation.

INTRODUCTION

The demand of a extremely quite underwater cruise for a submarine may be more important than higher speed and operating depth capability [1]. The success of each attack and the surviving conditions are all depending on the necessity of detecting and identifying the enemy's submarines before they do [2]. Therefore, the acoustic signature must be reduced to the possible lowest level and the strict noise control must be executed in design and manufacturing phases by reducing the structural and airborne noise from the propulsion system [3]. This task will be easier to achieve if the designers are aware of the dynamic behavior of the coupled air and structure system, hence, the fluid-structure interaction is brought to interest in this analysis. In a specific submarine, as shown in Fig. 1 [4], the watertight compartments are separated by the transverse bulkheads in the pressure hull and air is filled within the compartments. As a prototype approach, this theoretical study is simplified by only considering the coupling between the air and the major structure bulkheads (Fig. 2) which is treated as classical thin plates fixed onto the rigid cylindrical pressure hull; and ignoring the design feature of the girder, frames, decoration divider, etc. Also, the fluid outside the pressure hull is not included in the study. Historically, such plate/hull assemblies have been designed from the viewpoint of a collection of *in vacuo* plate that are isolated in vibration from one another. However, with increasing performance requirements, models of greater fidelity, in which coupling between adjacent or separated plates is incorporated, are becoming increasingly important. Swamidas [5] and Orgun and Tonguc [6], for instance, discussed vibration coupling and mode localization in stacked disk systems in which the neighboring plates are coupled through discrete springs. Insofar as such plates operate in the interior of cylindrical hull, the present study emphasizes acoustoelastic interactions in a typical stacked plate array.

A rich and historical literature is available on acoustic-structure interaction. A general introduction is available in the book written by Junger and Feit [7], from which several

commonly-used approaches to analyze vibration, wave propagation, and sound radiation [8] can be identified. Gladwell and Zimmermann [9] formulated the combined acoustic and structural vibration problem by using a complementary energy method, with applications to both membranes and plates. Finite element methods are available to handle coupled plate and acoustic interaction [10, 11], and have been applied to problems involving irregularly-shaped cavities [12]. Investigations of single plates that couple with an acoustic cavity [13] date to the development of aeroelasticity theory in the 1960's. Predictions of the interior sound fields created by flexible wall motion are developed in Dowell's work [14], where full coupling between a panel and a cavity is treated. Analysis of coupled structural and acoustic modes is another effective way of evaluating sound-structure interaction [15]. Tseng and Wickert [16] studied the acoustic effects between the coupled annular plates in computer disk stack assemblies. The purpose of this research is to investigate the vibration of acoustically coupled stacked array of clamped circular plates inside a rigid cylindrical pressure hull through theoretical methods.

VIBRATION ANALYSIS

As shown in Fig. 3, the prototypical plate (bulkhead) array problem comprises N circular plates, clamped at rigid cylindrical shell, coupled with $N-1$ air cavities. Although the plates can have small different dynamic characteristic due to the manufacturing imperfection, eccentricity while mounted with clearance on the spindle [17], and periodically variation of the pressure and stiffness associated with clamping collar's bolt pattern [18], the plates are assumed to have identical set of *invacuo* natural frequencies. Further more, the plates are treated as having identical dimensions and material properties and the cavities between them as having uniform depth. Insofar as those simplification are admissible, the plates are modeled as being ideally clamped at the edge ($r = 1$, which is the nondimensional quantity).

Assuming that all length are non-dimensionalized with respect to b (radius of the plate), time with respect to the wave speed in the plate, and pressure with respect to its ambient value, the non-dimensional variables are listed as follows:

$$r = \frac{r^*}{b}, \quad \nabla^4 = b^4 \nabla^{*4}, \quad u^{(i)} = \frac{u^{(i)*}}{b}, \tag{1}$$

$$p^{(i)} = \frac{p^{(i)^*}}{p_0}, \quad t = \sqrt{\frac{D}{\rho_p h_p b^4}}\, t^* \tag{2}$$

The transverse displacement for each plate is denoted as $u^{(i)}$, with $1 \leq i \leq N$ and in the context of classical thin plate theory, they satisfy the equation of motion

$$u^{(i)}_{,tt} + \nabla^4 u^{(i)} = (\rho v)\left(p^{(i)} - p^{(i-1)}\right) , \tag{3}$$

where the comma-subscript denotes partial differentiation and the biharmonic operator ∇^4 is expressed as follows:

$$\nabla^4 = \left(\frac{\partial^2}{\partial r^2} + \frac{1}{r}\frac{\partial}{\partial r} + \frac{1}{r^2}\frac{\partial^2}{\partial \theta^2}\right)^2 . \tag{4}$$

Two dimensionless parameters, the wave speed ratio v and the cavity-to-plate inertia ratio ρ, in Eq. (3) define the model:

$$v^{(i)} = \sqrt{\frac{\frac{Bb^2}{\rho_a}}{\frac{D}{\rho_p h_p}}}, \quad \rho = \frac{\rho_a b}{\rho_p h_p} \tag{5}$$

where

$$D = \frac{E h_p^3}{12(1-\nu^2)} \tag{6}$$

is the plate's flexural rigidity; E, ν, ρ_p, and h_p are its elastic modulus, Poisson ratio, density, and thickness; B and ρ_a are the bulk modulus and density of air in the cavity.

The boundary conditions for the plates are clamped at the edge ($r = 1$).

$$u^{(i)}(1,\theta,t) = 0, \;\; u^{(i)}_{,r}(1,\theta,t) = 0, \;\; i = 1,2,...,N \tag{7}$$

The variables $p^{(i)}$ and $p^{(i-1)}$ are the three dimensional air pressure fields within the cavities on either side of the i^{th} plate, and they are evaluated at its lower and upper faces, respectively, in Eq. (3). Acoustic radiation from the plate array is not considered, and so the upper- and lower-most surfaces of the stack are treated as being exposed to vacuum with the corresponding pressure terms $p^{(0)}$ and $p^{(N)}$ vanishing.

When the pressures are expressed in terms of the velocity potentials $\phi^{(i)}$ such that

$$p^{(i)} = -\left(\frac{\rho v D}{p_0 b^3}\right) \phi^{(i)}_{,t} , \tag{8}$$

the governing equations for the acoustic fields become

$$\phi^{(i)}_{,tt} - v^2 \nabla^2 \phi^{(i)} = 0 , \quad 1 \leq i \leq N-1, \tag{9}$$

Each $\phi^{(i)}$ satisfies the concomitant boundary conditions for a rigid wall at $r = 1$ and of having compatible plate and air particle velocities at each plate surface. The non-dimensional boundary conditions of the fluid cavities are as follows:

$$\begin{aligned} \phi^{(i)}_{,r}(1,\theta,z) &= 0 \\ \phi^{(i)}_{,z}(r,\theta,\frac{h^{(i)}_a}{2}) &= \frac{1}{v}u^{(i)}_{,t} \\ \phi^{(i)}_{,z}(r,\theta,\frac{-h^{(i)}_a}{2}) &= \frac{1}{v}u^{(i+1)}_{,t} \end{aligned} \tag{10}$$

where $h^{(i)}_a$ is the air cavity thickness.

This distributed parameter model is discretized globally through the method of weighted residuals. Following Morse and Ingard [19] and Dowell [14], the neighboring problems that are chosen to select the expansion functions for the $u^{(i)}$ and $\phi^{(i)}$ are taken as those of the plate and cavity when considered alone. The corresponding normalized and orthogonal eigensolutions are denoted by (U_k, ω_{pk}), and (Φ_k, ω_{ak}), respectively. The field variables are expanded in the *NP*- and *NA*-term separable series

$$u^{(i)}(r,\theta;t) \approx u^{(i)}_{NP} = \sum_{k=1}^{NP} q^{(i)}_{pk}(t) U_k(r,\theta) \tag{11}$$

$$\phi^{(i)}(r,\theta,z;t) \approx \phi^{(i)}_{NA} = \sum_{k=1}^{NA} q^{(i)}_{ak}(t) \Phi_k(r,\theta,z) \tag{12}$$

in terms of the generalized coordinates $\underline{q}^{(i)}_p$ and $\underline{q}^{(i)}_a$ for each plate and cavity.

The wave equation Eq. (9) and its boundary conditions can be transformed into a set of ODEs in time by using Green's Theorem in the form

$$\int_V (\phi^{(i)} \nabla^2 \Phi^{(i)}_m - \Phi^{(i)}_m \nabla^2 \phi^{(i)})\, dV = \int_A (\phi^{(i)} \frac{\partial \Phi^{(i)}_m}{\partial n} - \Phi^{(i)}_m \frac{\partial \phi^{(i)}}{\partial n})\, dA \tag{13}$$

After applying the Galerkin's method [14] along with Eq. (11) and Eq. (12), the coupled plate-cavity equation set is obtained:

$$\underline{M}\ddot{\underline{q}} + \underline{G}\dot{\underline{q}} + \underline{K}\underline{q} = 0 \tag{14}$$

of $(N)(NP) + (N-1)(NA)$ ordinary differential equations, in which the terms $\underline{G}$ that couple elements of the displacement and pressure state vector

$$\underline{q} = \left\{ \underline{q}^{(1)T}_p, \ \cdots, \ \underline{q}^{(N)T}_p; \ \underline{q}^{(1)T}_c, \ \cdots, \ \underline{q}^{(N-1)T}_c \right\}^T \tag{15}$$

are skew-symmetric [15].

The case of three-plate coupled system, $N = 3$, is chosen for the theoretical representation of the system matrices to avoid showing large amount of the elements in the matrix. All different choice of number of plates and cavities assemblies can be down easily.

$$\underline{M} = \text{Diag}\,(\underline{I}, \underline{I}, \underline{I}, \rho\underline{I}, \rho\underline{I}) \tag{16}$$

in which the first three block identity matrices are of dimension $NP \times NP$ and the fourth and fifth are of dimension $NA \times NA$,

$$\underline{G} = \rho v \begin{bmatrix} 0 & 0 & 0 & \underline{P}_1^{(1)T} & 0 \\ 0 & 0 & 0 & -\underline{P}_3^{(1)T} & \underline{P}_1^{(2)T} \\ 0 & 0 & 0 & 0 & -\underline{P}_3^{(2)T} \\ -\underline{P}_1^{(1)} & \underline{P}_3^{(1)} & 0 & 0 & 0 \\ 0 & -\underline{P}_1^{(2)} & \underline{P}_3^{(2)} & 0 & 0 \end{bmatrix} \tag{17}$$

where the superscript T denotes transposition, and

$$\underline{K} = \text{Diag}\left(\underline{\Omega}_p, \underline{\Omega}_p, \underline{\Omega}_p, \rho\underline{\Omega}_a, \rho\underline{\Omega}_a\right) \tag{18}$$

where $\underline{\Omega}_p = \text{Diag}(\omega_{pk}^2)$ and $\underline{\Omega}_a = \text{Diag}(\omega_{ak}^2)$ comprise the frequencies of the uncoupled plates and cavity.

Since both $\underline{M}$ and $\underline{K}$ is diagonal owing to the choice of expansion functions, coupling between the displacements and potential function occurs only through $\underline{G}$, the elements of which are given by the projections

$$\begin{aligned} P_1^{(i)} &= \pm \int_A \Phi_m^{(i)} U_n^{(i)} dA_1^{(i)} \\ P_3^{(i)} &= \pm \int_A \Phi_m^{(i)} U_n^{(i+1)} dA_3^{(i)} \end{aligned} \tag{19}$$

of the plate and cavity expansion functions onto one other, with $1 \leq m \leq NA$ and $1 \leq n \leq NP$. In Eq. (19), the sign is chosen during integration over the argument z at either the upper or lower surface of the cavity. As expected, when ρ or v vanishes, the plate stack decouples, and responses for the plate-alone or cavity-alone are obtained.

Eq. (14) is then transferred into state space representation:

$$\underline{A}\dot{\underline{X}} + \underline{B}\underline{X} = \underline{0} \tag{20}$$

where

$$\underline{X} = \begin{Bmatrix} \dot{\underline{q}} \\ \underline{q} \end{Bmatrix} \tag{21}$$

Synchronous solutions $\underline{q}(t) = \underline{q}_0 e^{i\omega t}$, with ω real, for the fully five coupled plates ($N = 5$) and Eq. (14) were found numerically using the values $NP = NA = 40$ and available subroutine libraries. The choice of 40 lower modes is verified with convergence tests.

DISCUSSION

With the problem's symmetry in mind, the pairs of split frequencies correspond to system-level modes in which each plate maintains identical values of m and n, but vibrates either exactly in- or out-of-phase relative to the others; these modes are identified by the number "N" appended to the designation (m,n). For the particular geometry considered, the modes indicated as (m,n), where m and n denote the number of nodal circles and diameters, respectively. In Fig. 4, the predicted natural frequencies [2] of the plate stack described in Fig. 3 are shown as a function of the air cavity depth between plates. There is strong coupling between the acoustic and structural modes in the high frequency region. The solid lines correspond to frequencies of the coupled plates and cavity, which are coupled from a plate alone mode, denoted by $P(m,n)$, and the cavity alone mode, denoted $A(l,m,n)$; these are the expected asymptotes in the limit of large h_a. In the latter case, the index l identifies the number of nodal z-coordinate planes, and m and n retain their usual meanings. As one can easily see that there exist sets of four loci around each cavity alone modes because it contains four cavity regions in accompany with the five plate system. Curve veering phenomenon also exist at several intersections between $P(1,1)SC$, and $A(l,0,1)SC$ mode. The symbols S and C represent Sine and Cosine mode, respectively. For the present problem, the modes denoted by $P(m,n)SC$ or $A(l,m,n)SC$ indicates that the sine and cosine modes have same frequency because of geometric symmetry. Fig. 5 shows the zoom region of Fig. 4, say, in the range of $h_a \leq 1$, the loci with $0 \leq m \leq 1$ and $0 \leq m \leq 3$ includes, in fact, five sets of loci

[2] The parameters values are chosen as $E = 70 \times 10^9$ N/m^2; $\nu = 0.3$, $\rho_p = 2.69 \times 10^3$ kg/m^3, $h_p = 1.9$ mm, $B = 1.26 \times 10^5$ N/m^2, and $\rho_a = 1.19$ kg/m^3.

from $P(0,0)$ to $P(0,3)$ modes plus one acoustic group modes: $A(0,0,1)SC$. In $P(m,n)$ modes, each set contains N closely-spaced frequencies, denoted as (m,n)-N ($1 \leq N \leq 5$ for this case) associated with in- and out-of-phase modes of each plate for a N-coupled plate system. The group of one nodal diameter $P(0,1)$ system modes, for instance, comprised of $P(0,1)$-1 to $P(0,1)$-5 modes with the increasing order of the natural frequencies. The only in-phase mode is $P(0,1)SC$-5 mode, which shows the highest frequency in this group and remain the same frequency as a single disk vibrates *in vacuo*. All the other modes in the $P(0,1)SC$ mode group consist of different combination of out-of-phase mode and decreased monotonically with the spacing. The mode shapes of $(0,0)$-N group are shown in Fig. 6 for the illustration of in- and out-of-phase modes. All the plates are shown as out-of-phase to each other in $(0,0)$-1 mode. Plate #1, #2 pair and #4, #5 pair are out-of-phase to one another while plate #3 keeps flat in $(0,0)$-2 mode. In $(0,0)$-3 mode, plate #2, #3, and #4 are in-phase to each other and so do plate #1 and #5, but these two subgroup are out-of-phase to each other. Two upper plates and two lower plates are out-of-phase without varying the displacement of the middle plate is the situation of mode $(0,0)$-4. Again, all plates are shown in-phase to each other in $(0,0)$-5 mode. Some other predicted mode shapes of the lowest frequencies, i.e., (m,n)-1 mode, in each group are also shown in Fig. 7. For each nodal diameter mode shown in Fig. 4 and Fig. 5, the frequency of the in-phase $(0,n)$-5 mode remains essentially independent of the plate-to-plate spacing, and all the other out-of-phase mode's frequency, $(0,n)$-1 to $(0,n)$-4, decreases with cavity depth, this effect becoming most pronounced for spacings of $h_a \leq 1$. A "back of the envelope" mass conservation calculation [16] demonstrates that the velocity of the air, proportional to $\phi^{(1)}_{,r}$, is greater than the plate's velocity by a multiplicative factor of $\mathcal{O}(1/h_a)$. Notwithstanding the relatively small mass of air within the cavity, the effective inertia, or contribution provided to the system-level kinetic energy by the acoustic layer, becomes $\mathcal{O}(\rho_a/\rho_p h_a^2)$, which does become large as the plate-to-plate spacing decreases. If the plates are not identical, for instance, one plate is much thinner than the others, the mode localization phenomenon occurs and breaks up the system in-phase and out-of-phase modes.

SUMMARY

Weak coupling between neighboring bulkheads can contribute to the system-level vibration characteristics of stacked bulkheads fixed on a rigid cylindrical pressure shell, including beating and split vibration modes. While the motivating applications can involve an arbitrary number of bulkheads with both acoustic and structural coupling mechanisms being present, the examples discussed in this investigation concentrate on the case of five circular bulkheads which couple through four air cavities. The interesting results from the acoustic coupling between the transverse bulkheads can be employed for the future design of modern submarines.

In short, (i) frequencies that are repeated for each plate when they are considered alone split into distinct values under the influence of acoustic coupling; (ii) the frequency difference for each set of split modes increases as the cavity depth is decreased; (iii) the highest frequency of each set remains essentially constant at the *in vacuo* value; and (iv) the rest of lower frequencies decreases monotonically with depth. The distinction between the in- and out-of-phase components of a split mode set, in which the out-of-phase mode has lower frequency, is attributed to an inertia contribution that derives from oscillatory air flow for those modes. This effect grows with diminishing cavity depth, and, at least over the range of parameters considered, has little influence on the in-phase modes.

ACKNOWLEDGMENT

This material is based (in part) upon work supported by the National Science Council of Taiwan, R.O.C., under Grant Number NSC-89-2212-E-012-001.

REFERENCES

1. Tan, H.-L. 1995, "Design Consideration for A Submarine", R.O.C. Naval Academy Monthly Review, Vol. 25 (8), pp. 32 - 41.

2. Yen, C.-C. 1997, *Submarine's Design and Construction*, printed by R.O.C. Naval Mil-

itary Academy Golden Anchor Price.

3. Schultz, H., 1995, "Type 212 - The German Navy Heading for the Next Generation of Submarines," *The German Submarine Consortium - SUBCON*, Special Issue, pp. 8 - 10.

4. Gillmer, T.C., 1963, *Fundamentals of Construction and Stability of Naval Ships*, U.S. Naval Institute Annapolis, Maryland.

5. Swamidas, A.S.J., 1975, "Free Vibration of Elastically Connected Circular Plate Systems," *Journal of Sound and Vibration*, Vol. 39, pp. 229-235.

6. Orgun, C.O. and Tongue, B.H., 1994, "Mode Localization in Coupled Circular Plates," *ASME Journal of Vibration and Acoustics*, Vol. 116, pp. 286-294.

7. Junger, M. and Feit, D., 1972, *Sound, Structures, and Their Interaction*, MIT Press.

8. Takahashi D., 1983, "Sound Radiation From Periodically Connected Double-Plate Structures," *Journal of Sound and Vibration*, Vol. 90, pp. 541-557.

9. Gladwell, G.M.L. and Zimmermann, G., 1966, "On Energy and Complementary Energy Formulations of Acoustic and Structural Vibration Problems," *Journal of Sound and Vibration*, Vol. 3, pp. 233-241.

10. Craggs, A., 1971, "The Transient Response of a Coupled Plate-Acoustic System Using Plate and Acoustic Finite Elements," *Journal of Sound and Vibration*, Vol. 15, pp. 509-528.

11. Aggarwal, K.R., Sinhasan, R. and Grover, G.K., 1983, "Dynamics of Coupled Fluid-Structure Multiplate Systems," *ASME Journal of Vibration, Acoustics, Stress, and Reliability in Design*, Vol. 105, pp. 505-511.

12. Petyt, M., Lea, J. and Koopman, G.H., 1976, "A Finite Element Method for Determining the Acoustic Modes of Irregularly Shaped Cavities," *Journal of Sound and Vibration*, Vol. 45, pp. 495-502.

13. Lyon, R.H., 1963, "Noise Reduction of Rectangular Enclosures with One Flexible Wall," *The Journal of The Acoustical Society of America*, Vol. 35, pp. 1791-1797.

14. Dowell, E.H., Gorman, III, G.F. and Smith, D.A., 1977, "Acoustoelasticity: General Theory, Acoustic Natural Modes and Forced Response to Sinusoidal Excitation, Including Comparisons with Experiment," *Journal of Sound and Vibration*, Vol. 52, pp. 519-542.

15. Bokil, V.B. and Shirahatti, U.S., 1994, "A Technique for the Modal Analysis of Sound-Structure Interaction Problems," *Journal of Sound and Vibration*, Vol. 173, pp. 23-41.

16. Tseng, J.-G. and Wickert, J.A. 1998, "Split Vibration Modes in Acoustically-Coupled Disk Stacks," *ASME Journal of Vibration and Acoustics*, Vol. 120 (1), pp 234-239.

17. Tseng, J.-G. and Wickert, J.A., 1994a, "Vibration of an Eccentrically Clamped Annular Plate," *ASME Journal of Vibration and Acoustics*, Vol. 116, pp. 155-160.

18. Tseng, J.-G. and Wickert, J.A., 1994b, "On the Vibration of Bolted Plate and Flange Assemblies," *ASME Journal of Vibration and Acoustics*, Vol. 116, pp. 468-473.

19. Morse, P.M. and Ingard, U.K., 1968, *Theoretical Acoustics*, McGraw-Hill.

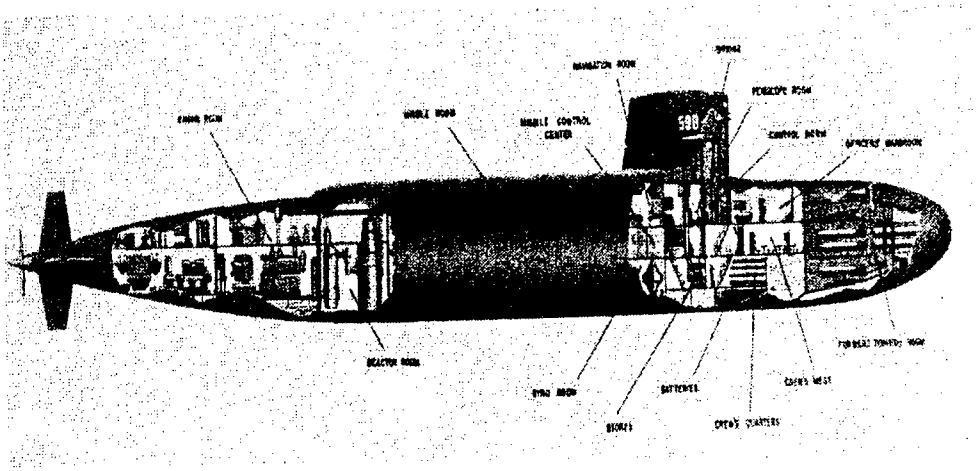

Figure 1: Cutaway profile of modern submarine USS George Washington (Courtesy Thomas C. Gillmer, Fundamentals of Construction and Stability of Naval Ships, 1963)

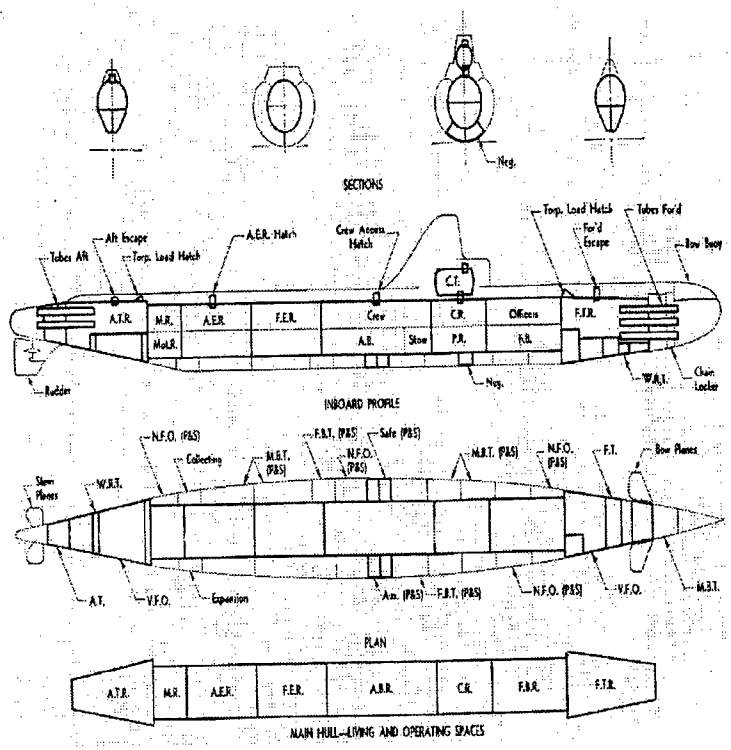

Figure 2: A typical submarine structure in which the watertight compartments are separated by the transverse bulkheads (Courtesy Thomas C. Gillmer, Fundamentals of Construction and Stability of Naval Ships, 1963)

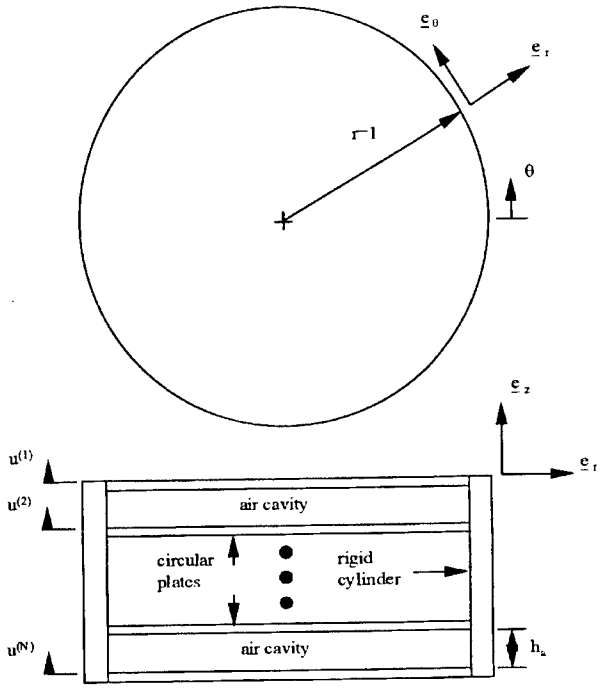

Figure 3: Vibration model for a array of N clamped circular plates that are coupled in vibration through acoustic cavities. The pressure hull on the edge is treated as rigid cylindrical shell.

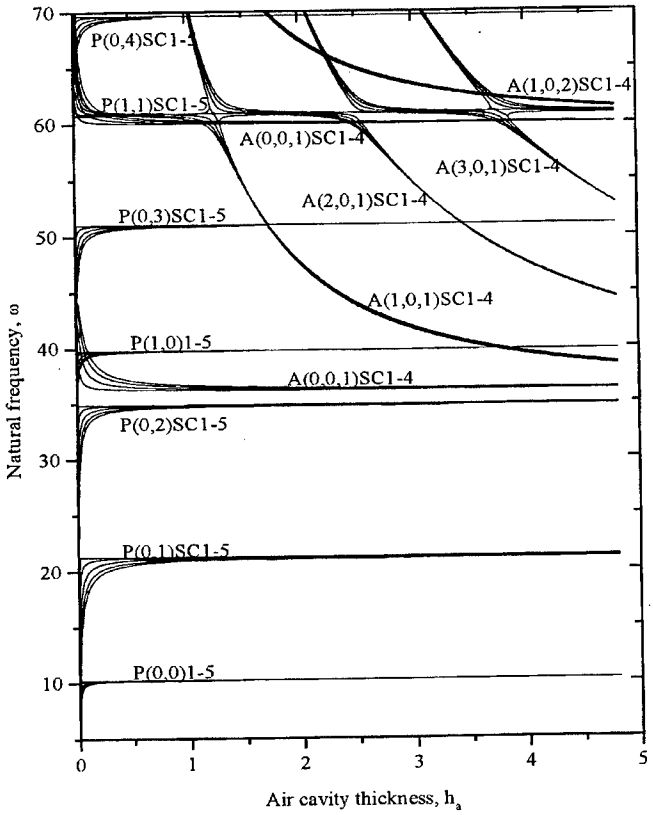

Figure 4: Predicted natural frequencies of five acoustically-coupled plates as a function of the air cavity's depth.

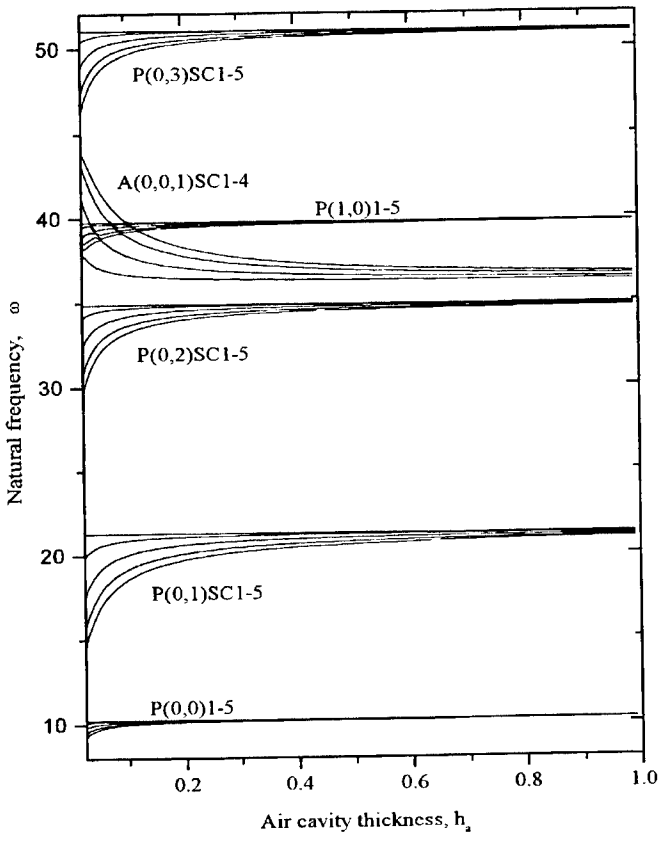

Figure 5: Predicted lower natural frequency groups as a function of air cavity thickness.

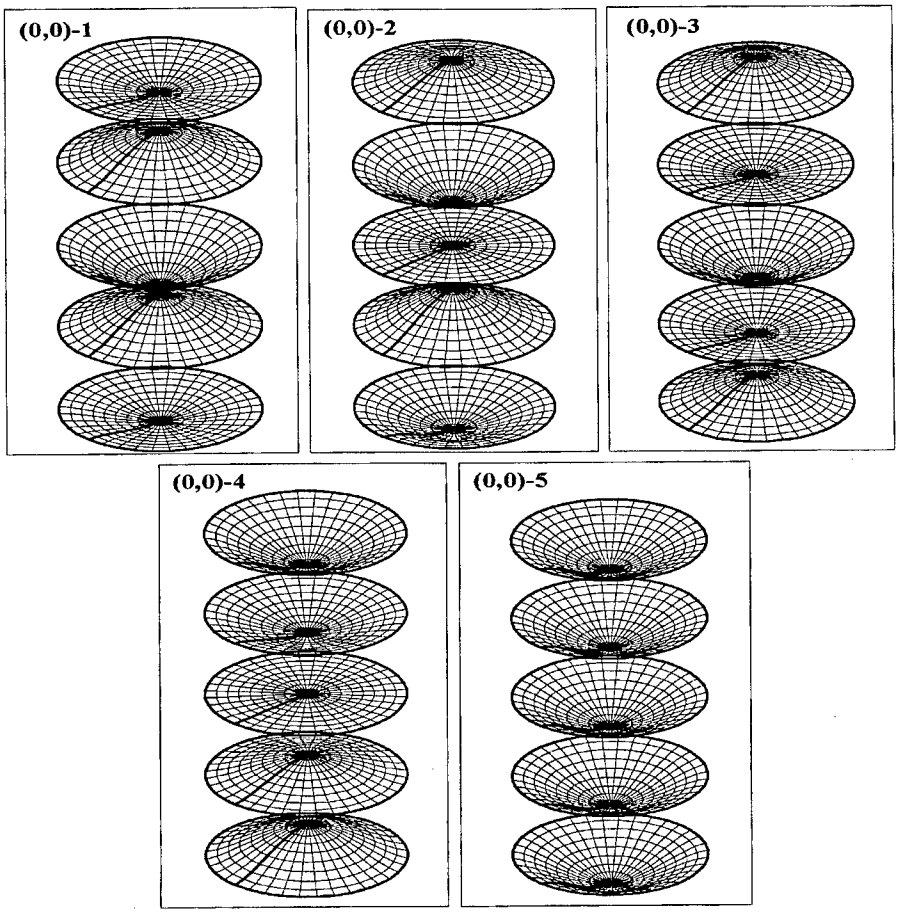

Figure 6: Predicted $(0,0) - N$ group mode shapes of the five coupled bulkheads, where N is the number used to represent different phase condition.

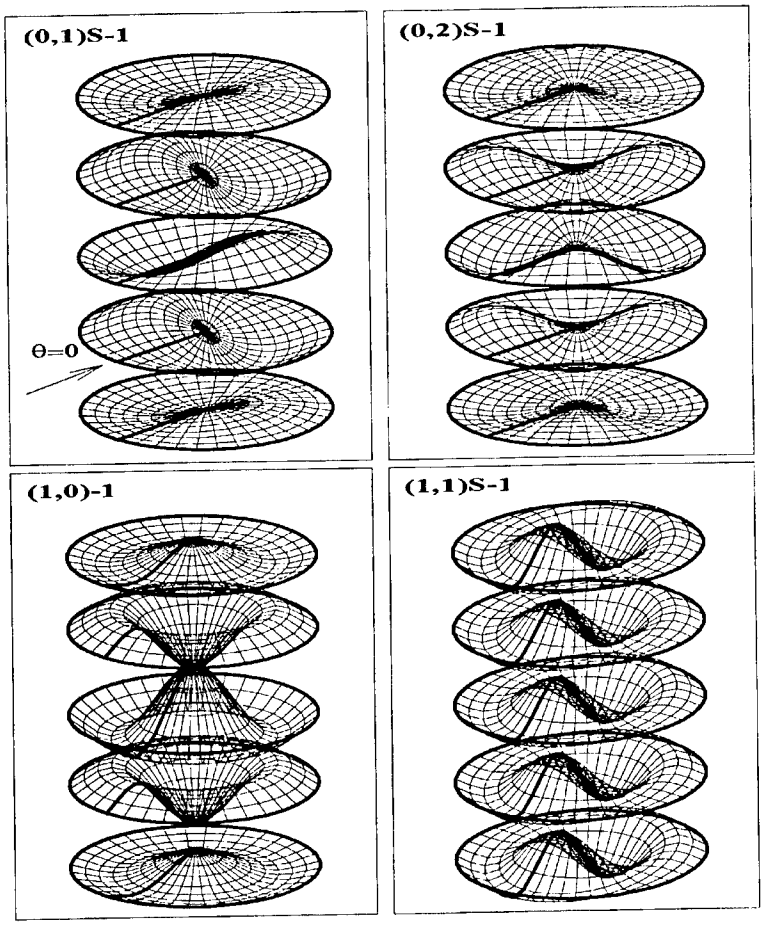

Figure 7: Predicted one or two nodal diameter and/or nodal circle mode shapes for the cases of $N = 1$.

The Lagrange Multiplier Method Revisited for Free and Forced Vibration of a Constrained Structure

N.S. Ferguson

ISVR, University of Southampton

Abstract

Efficient methods have been and are continuously being developed to analyse the free and forced vibration of structures. For example, a recent study showed a very numerically efficient procedure for analysing an elastic system with a number of discrete lumped elements, where the order of the eigenvalue problem was a determinant of a matrix of order $s \times s$, where s is the number of discrete attachments. Alternatively, in the Lagrange multiplier approach, where an unconstrained structure is described in terms of spatial functions or component modes, the constraints are applied to produce constraint equations, resulting in equations of motion which are generally complex to solve but the final results are very concise. Not surprisingly, the same simpler determinant problem can also be obtained from the Lagrange multiplier approach.

This study will revisit the free vibration of structures using the Lagrange multiplier approach and also show that it is completely analogous and equivalent to other approaches, such as using a mobility or impedance approach, and the results are as originally formulated by Lord Rayleigh in "The Theory of Sound". Forced vibration problems have generally not been examined using this technique but it will be shown that the forced response can be calculated directly, without the need to resort to the formulation in terms of the global free vibration modes. An example, to be shown in detail, is for a finite multi-supported beam excited by an acoustic field. The contribution of the response in the component modes will be examined and comments on the 'single mode formula', as used for acoustic fatigue calculations, will be examined.

1.0 Introduction

Many methods have been developed for the attachment of simple lumped parameter systems to multi-degree-of-freedom or continuous systems (see [1] for a

list of further references). Some of the simplest conceptual models are based on impedance or mobility approaches [2] or the use of the modes of the continuous or multi-degree of freedom system, resulting in the latter case in modal equations of motion [3]. The actual problem is a generalisation of that considered by Rayleigh [4] who examined the effect of discrete masses attached to a uniform string, free to vibrate in flexure and fixed at its ends. Although the formulation is slightly different from other much later investigations [1, 5-7], the result, in terms of the expression for the frequency equation, is actually identical as will be shown in the following section.

The latest approach by Cha [1] produces equations in matrix form that, starting with N original modes of the system without attachments, reduce from an $N \times N$ diagonal matrix to a matrix of size $s \times s$, s being the number of attachments. The natural frequencies of the combined system are then obtained from the frequencies corresponding to the zeros of the reduced characteristic determinant of size $s \times s$. The reduction in algebra, due to the diagonal nature of the original equations of motion, produces a frequency equation result that is identical to that obtained by the Lagrange multiplier method [5-7]. Cha restricted the examples presented to point attached masses or springs, but there are possible extensions to line connected subsystems or the attachment of continuous systems and this paper will discuss these examples and will also show that the forced response of the combined system can be calculated in terms of the original unconstrained modes, in addition providing a physical insight to how the forced response in particular modes is affected by the attached system(s).

2.0 Theory

The original theory, applying the Lagrange multiplier method for free vibration of structures, was clearly presented by Dowell [5] (also indirectly by Bishop [2]) and later it was shown that the physical interpretation of the constraints are that they correspond to the physical forces (or moments) required to impose the constraint on the original structure. A brief presentation of the method is given below for an example where an additional point of a structure is constrained to have zero displacement or rotation. The important assumptions used are that the analysis requires the modes of the original structure, $\phi_s(x,y)$, in order to formulate the response and the constraint equations. The form of the resulting matrix equation for the Lagrange multiplier provides a route for the solution of the free vibration natural frequencies of the constrained structure, and the values of the frequencies

obey the well-known results by Rayleigh [4, 7]. The attachment of two structures, or a structure with a simple component system such as a point mass, spring, etc., can similarly be analysed using the techniques whereby the constraint equations impose the continuity conditions at the attachment point. Initially, the free vibration problem is presented below and previously the normal approach of solving the forced vibration, using the 'new' modes of the constrained system in a modal summation, could be envisaged. An example is shown where the forced response of the structure is calculated in terms of the unconstrained original modes of the original structure.

2.1 Free vibration of connected structures with point connections

Consider the arbitrary structures, with normal modes $\phi_s(x,y)$ and $\psi_t(x,y)$, connected at, say, one arbitrary point (x_0,y_0). The constraint equation of equal displacement at the connection point can be formulated as:

$$f_1 = \sum_s q_s\phi_s(x_0,y_0) - \sum_t p_t\psi_t(x_0,y_0) = 0 \qquad (2.1.1)$$

q_s, p_s are the corresponding modal generalised coordinates. Using Lagrange's equations, the following equations of free vibration are obtained, with λ_1 equal to the single Lagrange multiplier.

$$M_s\ddot{q}_s + k_s q_s - \lambda_1\phi_s(x_0,y_0) = 0 \qquad s = 1...S \qquad (2.1.2)$$

$$M_t\ddot{p}_t + k_t p_t + \lambda_1\psi_t(x_0,y_0) = 0 \qquad t = 1...T \qquad (2.1.3)$$

Assuming free harmonic vibration, then

$$q_s = \frac{\lambda_1\phi_s(x_0,y_0)}{M_s(\omega_s^2 - \omega^2)} \qquad (2.1.4)$$

$$p_t = \frac{\lambda_1\psi_t(x_0,y_0)}{M_t(\omega_t^2 - \omega^2)} \qquad (2.1.5)$$

The constraint equation then becomes

$$\lambda_1\left[\sum_s \frac{\phi_s^2(x_0,y_0)}{M_s\left(\omega_s^2-\omega^2\right)}+\sum_t \frac{\psi_t^2(x_0,y_0)}{M_t\left(\omega_t^2-\omega^2\right)}\right]=0 \qquad (2.1.6)$$

$\sum_s \frac{\phi_s^2(x_0,y_0)}{M_s\left(\omega_s^2-\omega^2\right)}$ and $\sum_t \frac{\psi_t^2(x_0,y_0)}{M_t\left(\omega_t^2-\omega^2\right)}$, respectively, are the point receptances of the two individual unconnected structures at the point of attachment, i.e.

$$\alpha_{11}+\beta_{11}=0\,, \qquad (2.1.7)$$

which corresponds to the well-known result in terms of the frequency equation of connected structures in terms of point receptance [2]. The physical interpretation of λ_1 and the expression in the square bracket in equation (2.1.6) as constraint force and influence coefficient, or in this case, point receptance of the combined system, is clear.

The analysis can be extended to structures connected by a finite number of point connections, or an assembly of structures where some, not necessarily all, are connected together at some point. This latter case is considered in the forced vibration example.

2.2 Forced vibration example: multiple supported beam excited by harmonic acoustic plane wave

Dowell [5] considered a similar problem for a multi-bay panel for flutter investigations and also a beam-stiffened rectangular plate [6]. The approach was based on using the unconstrained modes of the original panel, expanding the response of the stiffeners in terms of their unconstrained modes and applying, for each stiffener, the imposition of equal displacement of the beam and plate along the attachment line. Using plate modes, expanded in terms of beam-type modes, with attachments all parallel to one side, the line constraints individually are represented by single constraint equations. So using N spanwise plate modes, with R attached beam stiffeners, the final eigenvalue equation is reduced to solving for the zeros of the determinant of a square matrix of size R times N [6].

The problem analysed below is the forced vibration of a beam on multiple simple supports, but instead of imposing the constraints to the full length beam, the analysis will consider each bay as an individual component, with its own

component modes, that are then connected to the adjoining components through the constraint equations at its ends. The reason for considering this representation is to examine the assumption used for acoustic fatigue predictions where the calculations are often simplified by using, say, the individual panel modes of a multi-bay panel fuselage in isolation from the adjoining structure, calculating the excitation and response in the individual bay alone and performing subsequent fatigue calculations on that bay [8]. Using the component modes it will be shown that there is a quantifiable contribution from other modes, that the individual mode contributes to modes of the whole structure and that one can express the forced contribution as a part that is due to the external excitation, in that mode alone, and a part that is due to excitation of other parts of the structure that are then coupled to the mode through the constraint equation.

Consider a uniform beam on multiple simply-supported supports such that there are N_{bays}, corresponding to $N_{bays} + 1$ supports. For simplicity, one will assume that each bay is of the same length ℓ but this is not necessary in general. Each bay will be represented by N_{modes} of a simply-supported beam, although again one could have a different number of modes used for each bay, if required. Let bay i have a local coordinate system x_i, so bay i is connected to bay $i + 1$ through a constraint equation relating the continuity of slope, i.e.

$$N^{th}\text{ bay has displacement } \sum_{i=1}^{N\text{modes}} q_i \Phi_i(x_i) = \sum_{i=1}^{N\text{modes}} q_i \sin\frac{i\pi x}{\ell} \tag{2.2.1}$$

$$N+1^{th}\text{ bay has displacement } \sum_{j=1}^{N\text{modes}} p_j \sin\frac{j\pi x}{\ell} \tag{2.2.2}$$

The continuity of slope between i^{th} and $i+1^{th}$ bay is given by

$$\sum_{i=1}^{N\text{modes}} q_i\left(\frac{i\pi}{\ell}\right)\cos i\pi = \sum_{j=1}^{N\text{modes}} p_j\left(\frac{j\pi}{\ell}\right), \tag{2.2.3}$$

equivalently, in this case,

$$\sum_{i=1}^{N\text{modes}} q_i(i)(-1)^i = \sum_{j=1}^{N\text{modes}} p_j(j) \tag{2.2.4}$$

The constraint equations can be expressed in general modal terms as

$$\sum_{i=1}^{N\text{modes}} q_i^N \phi_i^N(\ell)' - \sum_{i=1}^{N} q_i^{N+1} \phi_i^{N+1}(0)' = 0 \qquad (2.2.5)$$

or $$f_i = \sum_u q_u \beta_u = 0 \qquad (2.2.6)$$

and $$\sum_{i=1}^{N\text{modes}} q_i^N \phi_i^N(0)' - \sum_{i=1}^{N\text{modes}} q_i^{N-1} \phi_i^{N-1}(\ell)' = 0 \qquad (2.2.7)$$

or $$f_{i-1} = \sum_u q_u \beta_{i-1u} = 0 \qquad (2.2.8)$$

where ' represents derivative with respect to the local x_i coordinate and the superscript denotes the bay number. u is the global number of the generalised coordinate.

The total number of equations of motion is N_{modes} times N_{bays}, with (N_{bays} - 1) constraints on slope of adjacent bays at their attachment.

Consider the excitation to be due to a harmonic acoustic plane wave, whose direction of propagation is at an angle of θ degrees to the normal of the beam surface. The acoustic trace wavelength, k_t, on the surface of the beam is given by $k\sin\theta$, where k is the acoustic wavenumber equal to $\frac{\omega}{c_0}$. The derivation of the equations of motion for the generalised coordinates for the individual bays follows the derivation using Lagrange's equations, with constraints included in the Lagrangian, as before, but each mode also has external excitation acting. Considering the global coordinate x to be zero at the left-hand end of the whole beam, then for the i^{th} mode in the N^{th} bay, one has the generalised force equal to

$$F_i = \int_{x_i=0}^{\ell} P_0 e^{j(\omega t - k_t x)} \sin\frac{i\pi x_i}{\ell} dx_i \qquad (2.2.9)$$

where x_i is the local bay coordinate and
$x = (N-1)\ell + x_i$ is the global coordinate.

For acoustic fatigue purposes, assuming total reflection of the incident pressure wave, then P_0 represents twice the amplitude of the incident acoustic wave [8], assuming negligible effect of re-radiated sound from the vibrating structure.

The form of the generalised force F_i is such that one can evaluate the forces in the modes in the first bay and then use an iterative procedure for the other bays as

$$\int_{x_i=0}^{\ell} P_0 e^{j(\omega t - k_i[(N-1)\ell + x_i])} \sin\frac{i\pi x_i}{\ell} dx_i = P_0 e^{j(\omega t - k_i(N-1)\ell)} \int e^{jk_i x_i} \sin\frac{i\pi x_i}{\ell} dx_i \qquad (2.2.10)$$

$$\Rightarrow F_{i+N_{modes}} = e^{-jk_i(N-1)\ell} F_i \qquad (2.2.11)$$

i.e., equal amplitude but different phase, as would be expected.

For the i^{th} mode in the N^{th} bay one then has the following equation of motion, with two constraints if $1 < N < N_{modes}$ and one constraint if in the first or last bay.

The equation of motion for an internal bay, excluding the first and last bays, is then

$$M_i \ddot{q}_i^N + K_i q_i^N - \lambda_i \beta_{ii} - \lambda_{i-1} \beta_{i-1i} = F_i^N \qquad (2.2.12)$$

where $\beta_{ii} = \phi_i^N(\ell)'$, $\beta_{i-1i} = \phi_i^N(0)'$ and the superscript on the generalised coordinate and force corresponds to the bay number for the i^{th} generalised coordinate.

Assuming harmonic steady state response, at the excitation frequency, then the equations of motion (N_{modes} times N_{bays}), and the constraint equations (N_{bays} - 1) can be expressed in matrix form as

$$\left[\begin{array}{cccc|c} \omega_1^2 - \omega^2 & 0 & 0 & \cdots & \vdots \\ & \omega_2^2 - \omega^2 & 0 & 0 & \vdots \\ & & \ddots & 0 & \cdots \\ & & & \ddots & \vdots \\ \hline & & & & \vdots \\ & & & & \vdots \\ & & & & [0]_{(NBAYS-1)\times(NBAYS-1)} \end{array}\right] \left[\begin{array}{c} q_1^1 \\ \vdots \\ q_{NMODES}^1 \\ \vdots \\ q_{NMODES}^{NBAYS} \\ \lambda_1 / M_1 \\ \vdots \\ \lambda_{NBAYS-1/MNMODES} \end{array}\right] = \left[\begin{array}{c} F_{1/M_1} \\ F_{2/M_2} \\ \vdots \\ \vdots \\ F_{NMODES}^{NBAYS} / M_{NMODES} \\ 0 \\ \vdots \\ 0 \end{array}\right] \qquad (2.2.13)$$

where the matrix on the left-hand side is produced by the equations of motion, each equation divided by the modal mass, the remaining (N_{bays} - 1) rows are given by the constraint equations and the matrix is symmetric, i.e. the last (N_{bays} - 1) columns are the transpose of the (N_{bays} - 1) last rows. Rather than solving for the Lagrange

multipliers and then the generalised coordinates, it is possible to solve these equations directly and obtain the modal contribution for the excited and constrained system directly.

Considering a particular mode of an internal bay, then the steady-state response, given by solving equation (2.2.12) is

$$q_i = \frac{F_i^N + \lambda_i \beta_{ii} + \lambda_{i-1} \beta_{i-1i}}{M_i \left[\omega_i^2 - \omega^2 \right]} \tag{2.2.14}$$

$$= \frac{F_i^N}{M_i \left[\omega_i^2 - \omega^2 \right]} + \frac{\left(\lambda_i \beta_{ii} + \lambda_{i-1} \beta_{i-1i} \right)}{M_i \left[\omega_i^2 - \omega^2 \right]} \tag{2.2.15}$$

Although the generalised coordinate is dependent upon the values of the Lagrange multipliers, this form clearly shows that the modal response is given by the sum of one term, which is effectively the mode contribution from excitation applied to it individually, i.e. uncoupled and unconstrained, and the addition of the response due to excitation through the constraints. One can quantify the 'single mode response' as well as the contribution due to the 'substructure' or connected structure.

The modes of the constrained structure, in general, will not be the same as the modes of the individual components. See latter comments for further clarification. Examining the analytical expressions, they show that if the modes are well separated, then near the original component mode natural frequencies, i.e. ω close to ω_i for some ω_i, the single mode may dominate the response and the question arises whether the component due to the constraint is significant. Some numerical results presented will show relative contributions but it is not clear whether it can be generalised. Likewise, an individual component mode is not restricted to contribute solely to one of the modes of the complete structure, as will be shown by the simulations.

For numerical evaluation two alternatives have been considered.

(i) Direct solution of the matrix equations given by (2.2.13), or

(ii) Solution for the Lagrange multipliers and then substitution into the equations for the generalised coordinates (2.2.15). In this latter case, one uses the

relationships for the generalised coordinates, in terms of the Lagrange multipliers and generalised forces to substitute into the constraint equations.

i.e. equation (2.2.15) for q_i into the constraint equations given by (2.2.8). One then has

$$[C_{rv}]\begin{bmatrix}\lambda_1\\ \vdots \\ \lambda_R\end{bmatrix}=\left[-\sum_u \frac{F_u\beta_{1u}}{M_u\left(\omega_u^2-\omega^2\right)} \quad \vdots\right]$$

where the notation used by Dowell has been adopted [5], as the left-hand side is the set of equations for the free vibration solution.

$$C_{rv}=\sum_u \frac{\beta_{ru}\beta_{vu}}{M_u\left(\omega_u^2-\omega^2\right)} \qquad u = 1 \ldots N_{modes} \times N_{bays}$$

Solving the case of $F_u = 0$, for all modes equivalent to having $\left|[C_{rv}]\right| = 0$, gives the natural frequencies of the complete structure [5-7].

The direct solution has been adopted for the results in the following section.

3.0 Results for Multi-supported Beam under Plane Wave Acoustic Excitation

The approach in section 2.2 has been adopted for the numerical example of a three bay beam system, on simple supports. For these provisional results each bay is identical in length (0.5 m) thickness and material properties (EI = 172.5 Nm^2, ρA = 0.0785 kg/m) but this is not an essential requirement. The investigation and results show the influence of:

- number of modes used for each bay response and convergence effects;
- the effect of the angle of incidence;
- comparison of the single mode response versus the combined effect of the constraints on the response.

Figure 1 shows the effect of increasing the numbers of modes used for each bay for 10, 20 and 50 modes per bay, respectively. The response of the middle bay of the three bays is primarily dominated by the first sinusoidal mode shapes up to 2500 radians/s and the summation is shown cumulatively to show how, increasing the number of modes, there is a slight reduction in the relative contribution of the fundamental mode to the response at higher frequencies. The first three natural frequencies of the middle bay alone on simple supports are 1850, 7402 and 16644 radians/s and so the main response in the fundamental modes is at or close to its natural frequency whilst the other two frequencies below 5000 radians/s are modes of the complete three bay system. The reason for the presence of the natural frequency at 1850 radians/s is that the three bay system can exhibit the half sinewave mode shape for each bay with a phase shift of π between each bay and no constraining effects of the bays on one another. Significantly, though, the modes of the complete system at approximately 2500 radians/s and less so at approximately 3500 radians/s contain a significant contribution from the fundamental mode for each bay.

Figure 2 shows, for grazing incidence, the forced response in the middle of the centre bay with the single mode contribution (the first term in equation (2.2.15)), the constraint contribution (the second term in equation (2.2.15)) and the total response. It is only by including the constraint terms that one can obtain the response in the system at the whole system resonances (approximately 2500 and 3500 radians/s). Figure 3 clearly shows the effect of the angle of incidence on the contribution of the first three modes of the centre bay for the acoustic field incident at 0° (normal) to the beam where response in the second mode (one full sine wave for each beam) cannot occur. Figure 4 compares the total response for the two extreme cases 0° and 90° incidence, showing that the second mode of the complete system does not respond in the former case. Note also that the fundamental response for 0° incidence is also lower as effectively excitation in adjacent bays is self-cancelling but with three bays there is no total cancellation. Figure 5 gives a better insight into the response for 90° excitation with the first mode of the whole system dominated by the fundamental individual beam modes, the second and third individual bay modes contribute to the second and third modes of the complete system although at frequencies well below their individual natural frequencies.

4.0 Conclusions

The Lagrange multiplier technique appears to be a very valuable approach for analysing constrained structures in terms of the modes of the unconnected substructures. Whilst the number of modes required for convergence is reasonably high, the numerical solution is very efficient and the forced response can be separated. This latter property provides a very useful insight into how the structural response can be from direct subsystem excitation or excitation due to the constraint effects of other attached structures which are also excited. Hence a development of the approach for acoustic fatigue investigations may be a very useful consequence. Likewise, one can change part of a combined structure and reformulate the problem in a very straightforward manner.

Future developments may include predictions for non-linear response calculations or the coupling of a linear and non-linear structure together.

References

1. Cha, P.D. and Wong, W.C., A novel approach to determine the frequency equations of combined dynamical systems. *Journal of Sound and Vibration*, 1999, **219**(4), 689-706.
2. Bishop, R.E.D., Gladwell, G.M.L. and Michaelson, S., *The Matrix Analysis of Vibration*, Cambridge University Press, London, 1965.
3. Meirovitch, L., *Analytical Methods in Vibrations*, MacMillan Company, New York, 1967.
4. Rayleigh, *Theory of Sound*, Volume 1, MacMillan Company, 1877.
5. Dowell, E.H., Free vibrations of a linear structure with arbitrary support conditions. *Journal of Applied Mechanics*, 1971, **38**, 595-600.
6. Dowell, E.H., Free vibrations of an arbitrary structure in terms of component modes. *Journal of Applied Mechanics*, 1972, **39**, 727-732.
7. Dowell, E.H., On some general properties of combined dynamical systems. *Journal of Applied Mechanics*, 1979, **46**, 206-209.
8. ESDU International, London, Series on Vibration and Acoustic Fatigue.

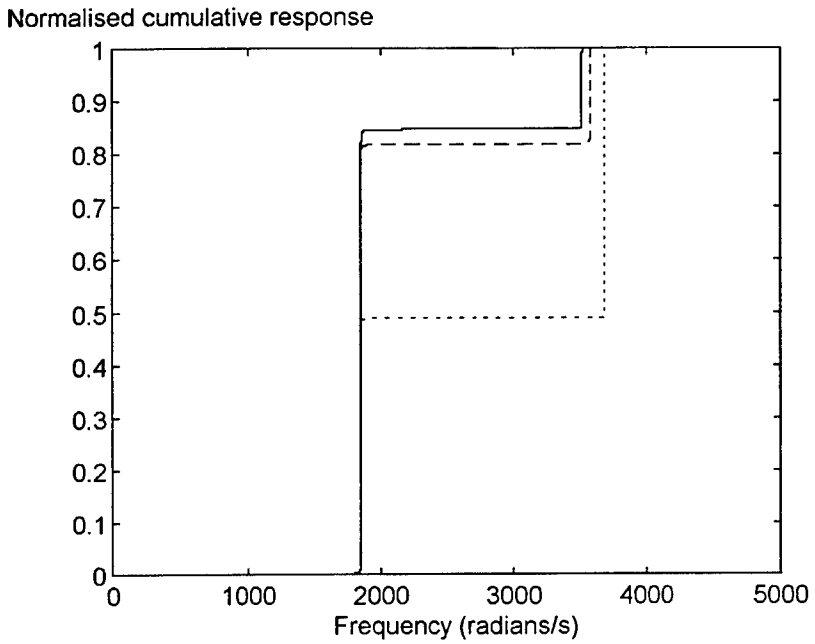

Figure 1: Comparison of the normalised cumulative fundamental mode contribution to the mean square response when using 10(dotted line), 20(dashed line) and 50(solid line) modes per bay for a three bay multi-supported beam. Beam properties EI = 172.5 Nm^2, ρA = 0.0785 kg/m and bay length equal to 0.5 m. Excitation is acoustic plane wave at 90° to the beam normal (grazing incidence).

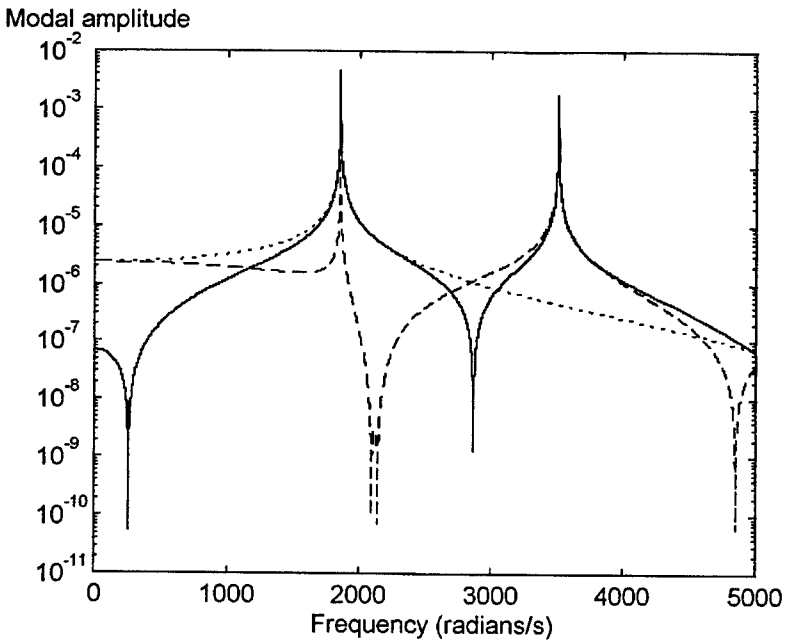

Figure 2: Comparison of the fundamental mode contribution without constraint(dotted) to the constrained fundamental mode contribution(dashed) and the total response in the centre of the middle bay, using 50 modes per bay for a three bay multi-supported beam. Beam properties EI = 172.5 Nm^2, ρA = 0.0785 kg/m and bay length equal to 0.5 m. Excitation is acoustic plane wave at 90° to the beam normal (grazing incidence). Note that the second mode of the complete system at approximately 2350 radians/s exhibits a node at this position.

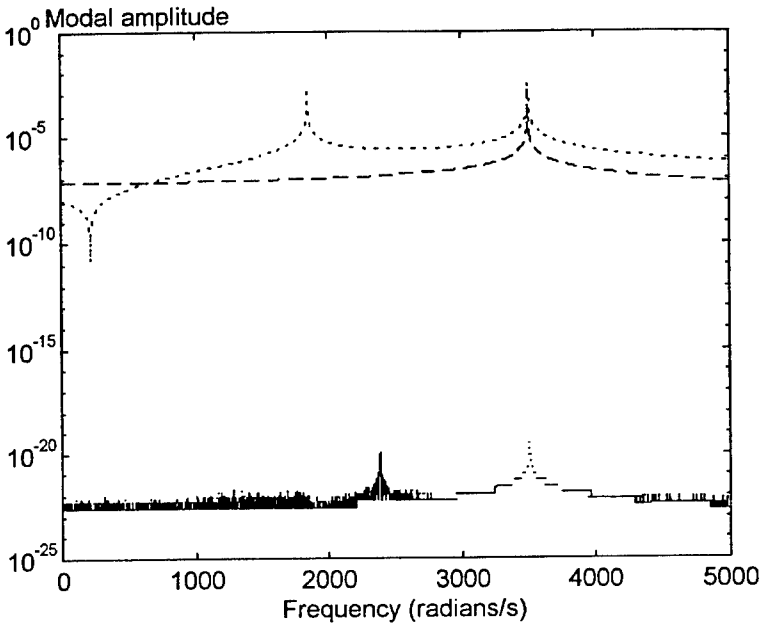

Figure 3: Comparison of the fundamental mode contribution(dotted) to the second mode contribution(solid) and the third mode(dashed) in the middle bay using 50 modes per bay for a three bay multi-supported beam. Beam properties EI = 172.5 Nm^2, ρA = 0.0785 kg/m and bay length equal to 0.5 m. Excitation is acoustic plane wave at 0^{o} to the beam normal (normal incidence). Note that the second mode is not excited directly by the acoustic excitation in this direction, only through the coupling introduced in the constraint equations.

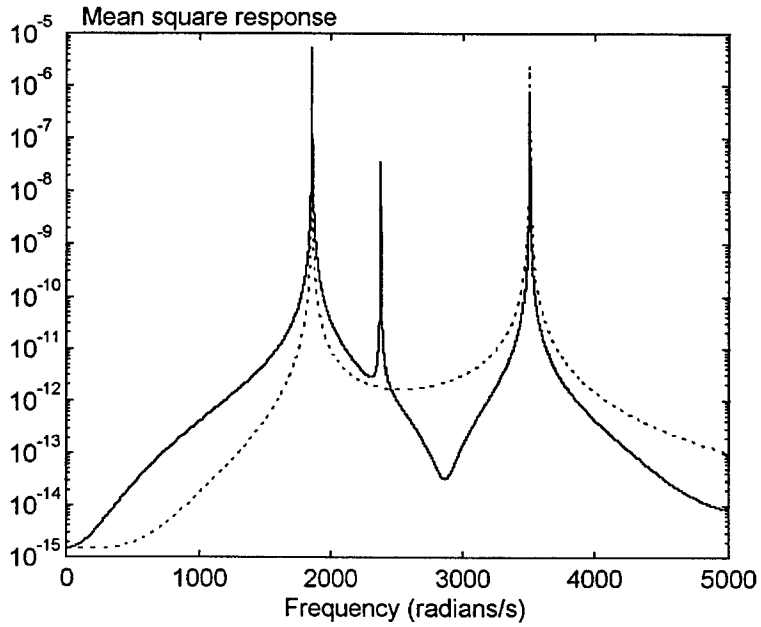

Figure 4: Comparison of the spatial and temporal mean square displacement response of the middle bay, using 50 modes per bay for a three bay multi-supported beam, for acoustic excitation normal to the beam(dotted) and at grazing incidence(solid). Beam properties EI = 172.5 Nm^2, ρA = 0.0785 kg/m and bay length equal to 0.5 m. Note that the second mode is not excited directly by the acoustic excitation in the former case.

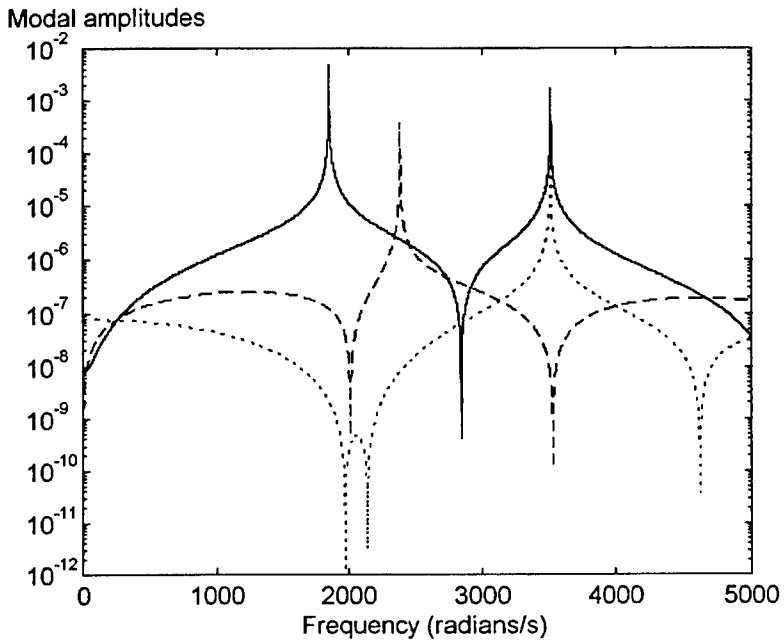

Figure 5: Comparison of the fundamental mode amplitude(solid) to the second mode (dashed) and the third mode(dotted)amplitudes in the middle bay, using 50 modes per bay for a three bay multi-supported beam. Beam properties EI = 172.5 Nm^2, ρA = 0.0785 kg/m and bay length equal to 0.5 m. Excitation is acoustic plane wave at 90° to the beam normal (grazing incidence).

THE SUPERPOSITION – GALERKIN METHOD FOR FREE VIBRATION ANALYSIS OF COMPLETELY FREE RECTANGULAR PLATES

By

D. J. Gorman
Department of Mechanical Engineering
University of Ottawa
Ottawa, Canada, K1N 6N5

1. Introduction

It is now well accepted that the superposition method provides a highly accurate means for obtaining the free vibration frequencies and mode shapes of rectangular plates. It has been successfully applied to both isotropic and orthotropic thin plates with various combinations of classical edge conditions [1][2]. It has also been utilized to analyze thick plates and laminated plates utilizing the Mindlin Theory[3].

It remains a fact, nevertheless, that work involved in applying this method increases significantly when we move from thin isotropic to orthogonal plates. An even much more significant increase in work is encountered when moving to the analysis of plates utilizing the Mindlin Theory. This is because of the much greater number of possible forms of solution for the force driven "building blocks" employed, when the Mindlin Theory is utilized.

It was in recognition of these observations that the author, some years ago, introduced the superposition-Galerkin method. This latter method differs from the traditional superposition method only in the means whereby solutions are obtained for the force driven building blocks. Now, instead of solving directly the governing differential equation controlling building block response, the same response is obtained by means of the Galerkin method. The savings in the work required was found to be dramatic for the orthographic thin plate problems and plate problems resolved by means of the Mindlin theory. Results of investigations of both of these types of problems are to be found in reference [4].

It will be noted that the work of these references pertained to plates with combinations of clamped-simply supported edge conditions, only. It was found that, unfortunately, completely free plates could not be analysed at that time by the superposition-Galerkin method. This was because of the requirement of the Galerkin method that each term in the series representing the building block response must satisfy

all prescribed boundary conditions. It was found impossible to meet these conditions when analyzing completely free plates because of the mixed derivatives which appeared along the boundaries of the force driven building blocks. Accordingly, an attempt to analyze completely free plates by the superposition-Galerkin method was reluctantly abandoned.

It is now found that by an alternate and judicious choice of building blocks, none of which contains mixed derivatives along its driven edge, an analysis of the completely free plate is achievable by the superposition-Galerkin method. This is found to be true for both the thin plate problems and problems requiring the Mindlin theory. The objective of this paper is to explain how these goals were achieved.

2. Mathematical Procedure

2.1 The completely free thin orthotropic plate.

It was decided to choose the orthotropic plate for demonstration purposes as it includes the isotropic plate as a special case. In the interest of being concise we will examine only the fully symmetric modes for this plate problem. It will be obvious to the reader that other modes in the set are easily handled.

Analysis of this plate vibration problem by the traditional superposition method is achieved by following steps described in detail in Ref,[5]. In this earlier publication we described the analysis of the completely free orthotropic plate resting on point supports. It will be obvious that if we simply delete the portion of the eigenvalue matrix related to the concentrated point supports we will have the matrix related to the present problem.

Fully symmetric modes are analyzed by means of a superposition of the building blocks shown in Figure 1. where only one quarter of the full plate is analyzed. Edges with adjacent small circles are given slip-shear support, i.e., there is zero vertical edge reaction along these edges and slope taken normal to them is also zero.

The first building block has zero vertical edge reaction along its driven edge. This edge is driven by a distributed harmonic moment represented schematically in the figure. The amplitude of this distributed moment is represented in dimensionless form as,

$$\frac{\mathbf{Mb}^2}{\mathbf{aD}} = \sum_{\mathbf{m}=0,1,2}^{\infty} \mathbf{F}_{\mathbf{m}} \cos(\mathbf{m}\pi\xi) \tag{1}$$

The solution for the amplitude of the building block response is expressed as,

$$\mathbf{W}(\xi,\eta) = \sum_{\mathbf{m}=0,1,2}^{\infty} \mathbf{Y}_{\mathbf{m}}(\eta)\cos(\mathbf{m}\pi\xi) \tag{2}$$

Substituting equation 2. Into the governing differential equation the space variables are separated and we obtain,

$$\mathbf{Y}_m^{IV}(\eta) + \alpha_1 \mathbf{Y}_m^{II}(\eta) + \alpha_2 \mathbf{Y}(\eta) = \mathbf{0} \tag{3}$$

where the Roman superscripts indicate the order of differentiation with respect to the coordinate η. The coefficients α_1 and α_2 are given by

$$\alpha_1 = -2DHY\phi^2(m\pi)^2 \text{ and } \alpha_2 = DXY\phi^4\{(m\pi)^4 - \lambda^4\}$$

This is a fourth order ordinary differential equation for which the form of the possible solutions, which depend on the coefficients in the equation, are well known. Each form of the solution contains four unknowns which must be evaluated, two of these unknowns are eliminated in view of the fact that functions $Y_m(\eta)$ must be symmetric with respect to the ξ axis. The possible forms of solution become,

$$\begin{aligned}
&\mathbf{Y}_m(\eta) = \mathbf{A}_m \cosh\beta_m\eta + \mathbf{B}_m \cos\gamma_m\eta \\
&\mathbf{Y}_m(\eta) = \mathbf{A}_m \cosh\beta_m\eta + \mathbf{B}_m \cosh\gamma_m\eta \\
&\textbf{and} \\
&\mathbf{Y}_m(\eta) = \mathbf{A}_m \sin R\eta \sinh S\eta + \mathbf{B}_m \cos R\eta \cosh S\eta
\end{aligned} \tag{4}$$

where all symbols are as defined in reference.[5]. Two boundary conditions are available for establishing the unknowns, Λ_m, and B_m. They are, using the known expressions for plate vertical edge reaction, and bending moment, as well as equations 1 and 2,

$$\mathbf{Y}_m'''(\eta) + \nu^* \phi^2 \mathbf{Y}_m'(\eta) = \mathbf{0}/_{\eta=1} \tag{5}$$

and

$$\mathbf{Y}_m''(\eta) + \nu\phi^2 \mathbf{Y}_m(\eta) = -\mathbf{E}_m \tag{6}$$

Enforcing the boundary conditions as expressed by equations 5 and 6, one can readily eliminate the unknowns from equations 4 and thus obtain the response of the first building block in terms of the driving coefficients, E_m , [5]. Solution for the second building block is inferred from the first through a proper interchange of co-ordinates and one is now ready to complete the free vibration analysis of the plate by the superposition method. This involves superimposing the two building block solutions, expanding the net bending moment along the edges, η=1, and ξ=1, in a cosine series, and requiring each term in these two series to vanish. We thus arrive at the required set of homogeneous algebraic equations relating the unknown driving coefficients, E_m, from which the eigenvalue matrix for the problem is constructed. Eigenvalues and mode shapes are obtained by following well established procedures[5].

Let us turn now to the problem of obtaining the forced response of the moment driven building blocks by the Galerkin method. Returning to equation 2 we wish to

expand the functions $Y_m(\eta)$ in series form, where each term in the series must satisfy exactly the prescribed boundary conditions. There is no problem choosing a series whose terms are symmetric about the origin. The insurmountable difficulty arises when we try to select this same series so that each term satisfies equations 5 and 6. It is the problem of meeting these conditions that so far has precluded application of the superposition–Galerkin method to analysis of the completely free plate.

Let us now focus attention on the set of building blocks of figure 2. Here, the first and second pair of building blocks, respectively, replace the first and second building blocks of figure 1.

The first building block of figure 2 is driven by an applied harmonic moment, however, unlike the first block of figure 1, lateral displacement along the edge, $\eta=1$, is forbidden. The second building block of figure 2 is driven by a distributed harmonic vertical edge reaction along the edge, $\eta=1$, slope taken normal to this edge is forbidden. This latter condition is indicated in the figure by two solid dots joined by a straight line.

Two important observations are to be made here. One is that no mixed derivatives are encountered when enforcing boundary conditions along the driven edge of either building block. A Galerkin type solution can therefore be obtained for the forced response of each building block. Secondly, the two building blocks compliment each other as follows. The first building block permits the application of any desired moment to the driven edge even though it will leave some residual vertical edge reaction along this boundary. The second building block permits the application of any desired vertical edge reaction along the driven edge but will leave some residual bending moment along this boundary. It will be appreciated, however, that by superimposing the two building blocks we can ultimately impose a condition of zero net bending moment and zero net vertical edge reaction along the edge, $\eta=1$, of the superimposed set. We are thus ready to solve the problem of free vibration analysis of the completely free orthotropic plate by the superposition-Galerkin method.

Solutions for both building blocks are taken in the form of equation 2. The applied bending moment is expressed as in equation 1. Using established formulations for dimensionless bending moments and vertical edge reactions, the boundary conditions to be applied at the driven edge of the first building block become,

$$\mathbf{Y}_m(\eta)/_{\eta=1} = \mathbf{0} \tag{7}$$

and

$$\mathbf{Y}_m^*(\eta)/_{\eta=1} = -\mathbf{E}_m \tag{8}$$

For the second building block the corresponding boundary conditions become,

$$\mathbf{Y}_m^{'}(\eta)/_{\eta=1} = \mathbf{0} \tag{9}$$

and

$$Y_m''(\eta)/_{\eta=1} = -E_m \tag{10}$$

One can, of course, obtain the exact solution for the response of the above building blocks following the procedure described earlier. Corresponding solutions can be obtained for the third and fourth building blocks of Figure 2. and all four superimposed in order to obtain the eigenvalues for the completely free orthotropic plate. This, in fact, has been done and it was found that the eigenvalues obtained using either set of building blocks (those of figure 1, or those of figure 2) were identical.

We turn now to the main objective of the paper, i.e., demonstrating how solutions for the building blocks of figure 2 can be obtained by the Galerkin method. We recall that each term in the proposed series must be symmetic with respect to the origin. Consider for the functions $Y_m(\eta)$ associated with the first building block the series expansion

$$Y_m(\eta) = \sum_{i=1,3,5}^{\infty} E_i \frac{\cos(i-1)\pi\eta}{2} + E_m\left[\frac{1}{2} - \frac{\eta^2}{2}\right] \tag{11}$$

It will be noted that with addition of the polynomial terms at the end of equation 11, all of the required boundary conditions (eqns. 7 and 8) are satisfied by each term in the series.

Turning to the second building block it is found that the following series representation also fullfills the required conditions,

$$Y_m(\eta) = \sum_{i=0,1,2}^{\infty} E_i \cos i\pi\eta + E_m\left[\frac{\eta^2}{12} - \frac{\eta^4}{24}\right] \tag{12}$$

From here on the standard Galerkin procedure is followed to establish the unknown coefficients, E_i, as a function of E_m, for any term $Y_m(\eta)$ of the response. Concentrating on the first building block of figure2, we differentiate equation 11, term-by-term and substitute in the governing differential equation(3). Let us say we utilize kk terms in the series of equation 11. There will then be kk unknowns, E_i, in the quantity, Q_m, obtained upon carrying out the above substitution. We then expand this quantity, Q_m, which will be a function of η, in an appropriate series of kk terms and set each coefficient in this new series equal to zero. Here, it is appropriate to utilize a series identical to that of equation 11, for this latter expansion. In this way we take advantage of orthogonality of the trigonometric terms in the series. We thus arrive at a set of kk non-homogenous algebraic equations relating the quantities, E_i, and the driving coefficient E_m. Utilizing standard computer subroutines we can solve these equations and obtain a linear relationship between each E_i, and E_m. The response of the building block

to any driving term, E_m, is thus known. In a similar manner the response of the second building block is obtained. The Galerkin procedure as employed here is described in detail in an earlier publication [4].

Again, the response of the third and fourth building blocks of figure 2 are obtained by means of the above procedure after introducing changes in coordinates, etc., as discussed earlier.

With the solutions known the four building blocks are superimposed and the eigenvalue matrix is obtained by expanding the net bending moments and vertical edge reaction along the edges, $\eta=1$, and $\xi=1$, in appropriate series and requiring the coefficients in these new series to vanish. Verification of the present superpostion-Galerkin method has been obtained by comparing results obtained in this manner with results obtained by means of exact solutions to the building block responses as discussed earlier. Advantages of the present method will be discussed later.

2.2 **Analysis of the completely free Mindlin plate.**

A thorough analysis of this plate problem by the traditional superposition method was presented in reference[3]. It is therefore not necessary to repeat a description of this analysis here. Only a brief outline of the related mathematical procedure will be provided for the sake of completeness.

Let us suppose we wish to analyze the fully symmetric modes of this problem. We may accomplish this by utilizing the building blocks represented in figure1. Now, however, the building block responses are considered to be governed by the three Mindlin differential equations. These equations, in dimensionless form, are reproduced below.

$$\frac{\partial^2 W}{\partial \xi^2} + \frac{1}{\phi^2}\frac{\partial^2 W}{\partial \eta^2} + \frac{\partial \psi_\xi}{\partial \xi} + \frac{1}{\phi}\frac{\partial \psi_\eta}{\partial \eta} + \frac{\lambda^4 \phi_h^2}{\nu_3} W = 0, \tag{13}$$

$$\frac{\partial^2 \psi_\xi}{\partial \xi^2} + \frac{\nu_1}{\phi^2}\frac{\partial^2 \psi_\xi}{\partial \eta^2} + \frac{\nu_2}{\phi}\frac{\partial^2 \psi_\eta}{\partial \eta \partial \xi} - \frac{\nu_3}{\phi_h^2}\left(\psi_\xi + \frac{\partial W}{\partial \xi}\right) + \frac{\lambda^4 \phi_h^2}{12}\psi_\xi = 0, \tag{14}$$

$$\frac{\partial^2 \psi_\eta}{\partial \xi^2} + \frac{1}{\phi^2 \nu_1}\frac{\partial^2 \psi_\eta}{\partial \eta^2} + \frac{\nu_2}{\phi \nu_1}\frac{\partial^2 \psi_\eta}{\partial \xi \partial \eta} - \frac{\nu_3}{\phi_h^2 \nu_1}\left(\psi_\eta + \frac{1}{\phi}\frac{\partial W}{\partial \eta}\right) + \frac{\lambda^4 \phi_h^2}{12\nu_1}\psi_\eta = 0, \tag{15}$$

where $\phi_h = h/a$, $\nu_1 = (1-\nu)/2$, $\nu_2 = (1+\nu)/2$ and $\nu_3 = 6\kappa^2(1-\nu)$.

Associated shear forces, bending moments and twisting moments may be written as,

$$\mathbf{Q}_{\xi} = \psi_{\xi} + \frac{\partial \mathbf{W}}{\partial \xi}, \mathbf{Q}_{\eta} = \psi_{\eta} + \frac{1}{\phi}\frac{\partial \mathbf{W}}{\partial \eta},$$

$$\mathbf{M}_{\xi} = \frac{\partial \psi_{\xi}}{\partial \xi} + \frac{\nu}{\phi}\frac{\partial \psi_{\eta}}{\partial \eta}, \mathbf{M}_{\eta} = \frac{\partial \psi_{\eta}}{\partial \eta} + \nu\phi\frac{\partial \psi_{\xi}}{\partial \xi}, \mathbf{M}_{\xi\eta} = \frac{\partial \psi_{\eta}}{\partial \xi} + \frac{\mathbf{1}}{\phi}\frac{\partial \psi_{\xi}}{\partial \eta}.$$

Focusing on the first building block it is again considered to be driven by a distributed harmonic bending moment. The driven edge is free of transverse shear force and twisting moment. The other three edges have conditions of zero rotation of the plate cross-section running along the edge, as well as zero transverse shear force and zero twisting moment, imposed.

Amplitude of the dimensionless driving moment is expressed as,

$$\frac{\partial \psi_{\eta}}{\partial \eta} + \nu\phi\frac{\partial \psi_{\xi}}{\partial \xi} = \sum_{m=0,1}^{\infty} E_m \cos(m\pi\xi) \tag{16}$$

The dimensionless plate lateral displacement and plate cross-sectional rotations are expressed respectively as,

$$W(\xi,\eta) = \sum_{m=0,1}^{\infty} X_m(\eta)\cos(m\pi\xi), \psi_{\xi}(\xi,\eta) = \sum_{m=1,2}^{\infty} Y_m(\eta)\sin(m\pi\xi),$$
$$\psi_{\eta}(\xi,\eta) = \sum_{m=0,1}^{\infty} Z_m(\eta)\cos(m\pi\xi). \tag{17}$$

Here, it is found advantageous to consider response to driving terms E_m separately for the situation when m is equal or greater than 1, and when m equals 0.

Looking first at the situation when $m \geq 1$, and substituting equations 17 into the governing differential equations 13-15, it is found that the variables η and ξ are separable and a set of three ordinary differential equations involving the function $X_m(\eta)$, $Y_m(\eta)$ and $Z_m(\eta)$ are obtained. This set of coupled ordinary homogeneous equations is expressed in matrix form below as,

$$\begin{Bmatrix} X_m'' \\ Y_m'' \\ Z_m'' \end{Bmatrix} + \begin{bmatrix} 0 & 0 & a_{m1} \\ 0 & 0 & a_{m2} \\ a_{m3} & a_{m4} & 0 \end{bmatrix} \begin{Bmatrix} X_m' \\ Y_m' \\ Z_m' \end{Bmatrix} + \begin{bmatrix} b_{m1} & b_{m2} & 0 \\ b_{m3} & b_{m4} & 0 \\ 0 & 0 & b_{m5} \end{bmatrix} \begin{Bmatrix} X_m \\ Y_m \\ Z_m \end{Bmatrix} = \begin{Bmatrix} 0 \\ 0 \\ 0 \end{Bmatrix}. \tag{18}$$

where coefficients a_{m1}, a_{m2}, etc., are defined in reference[3].

By operating on this set of equations with judiciously selected operators and adding and subtracting the resultant equations, as required, the functions $X_m(\eta)$, $Y_m(\eta)$ etc., can be separated out and solutions for each function obtained. For each value of "m" a total of six unknowns appear, three of which are eliminated because symmetry for plate lateral displacement required with respect to the ξ axis.

Other unknowns are evaluated by means of boundary conditions to be imposed along the driven edge. The reader will already appreciate that much work is required here to separate the functions and to enforce the boundary conditions. It is found that four forms of solution are possible for the functions with $m \geq 1$. It will be seen that all of this work is eliminated with introduction of the superposition Galerkin method.

Computation of the building block response to the driving term with m=0, is a little less burdensome. This is really a "strip" solution and only two governing differential equations, which govern the parameters $W(\xi,\eta)$ and $\psi_\eta(\xi,\eta)$, apply. Two possible forms of solution for the response are found to exist. With the response of the building blocks known, that of the second building block obtained again through a transformation of coordinates, the building blocks are superimposed and eigenvalues and mode shapes are obtained following the procedures as described in reference[3].

It is important to note that again, solution for response of the above building blocks cannot be obtained by the much simpler Galerkin method because of the mixed derivatives appearing in boundary conditions to be enforced along the driven edges.

We next look into the analysis of the same problem by means of the building blocks of figure 3. The first three building blocks of this set replace the first one of the previous set. All building blocks have slip shear conditions as defined above, imposed on their non-driven edges.

We focus attention now on the first of the three building blocks. Lateral displacement and cross-section rotations are again expressed in series form as in equations 17. We begin by considering the case where $m \geq 1$. Moments and shear force acting along the driven edge are expressed as,

$$\mathbf{M}_\eta = \frac{\partial \psi_\eta}{\partial \eta} + \nu\phi \frac{\partial \psi_\xi}{\partial \xi} \tag{19}$$

$$\mathbf{Q}_\eta = \psi_\eta + \frac{1}{\phi}\frac{\partial \mathbf{W}}{\partial \eta} \tag{20}$$

$$\mathbf{M}_{\xi\eta} = \frac{\partial \psi_\eta}{\partial \xi} + \frac{\mathbf{1}}{\phi}\frac{\partial \psi_\xi}{\partial \eta} \tag{21}$$

We now control driving moment along the edge, $\eta=1$, by prescribing the first term on the right had side of equation 19, only, thus

$$\frac{\partial \psi_\eta}{\partial \eta} = \sum_{m=0,1}^{\infty} E_m \cos(m\pi\xi) \tag{22}$$

Instead of setting Q_η and $M_{\xi\eta}$, of equations 20 and 21, equal to zero we demand that only $(\partial W/\partial\eta)$ and $(\partial\psi_\xi/\partial\eta)$ of equations 20 and 21, respectively, should vanish. Obviously there will be residual shear force and twisting moment left along the driven edge of the first building block. These will be taken out later by the second and third building blocks. It is important to note that the boundary conditions described immediately above involve no mixed derivatives. A Galerkin type solution is therefore achievable for this building block.

The following series, each term of which satisfies exactly the prescribed boundary conditions, have been utilized to permit a Galerkin type solution for the first building block.

$$X_m(\eta) = \sum_{i=1,2} E_i \cos(i-1)\pi\eta \tag{23}$$

$$Y_m(\eta) = \sum_{j=1,2} E_j \cos(j-1)\pi\eta \tag{24}$$

and

$$Z_m(\eta) = \sum_{l=1,2} E_l \sin(2l-1)\frac{\pi}{2}\eta + E_m\eta \tag{25}$$

The same quantities of equations 19-21, involving no mixed derivatives, are prescribed for the second and third building blocks. For the second building blocks the quantity $(\partial W/\partial\eta)$ is prescribed in a series form Identical to that of equation 22. For the third building block the quantity $(\partial\psi_\xi/\partial\eta)$ is prescribed as,

$$\frac{\partial \psi_\xi}{\partial \eta} = \sum_{m=1,2}^{\infty} E_m \sin(m\pi\xi) \tag{26}$$

The remaining prescribed quantities are set equal to zero.

For the second building block the following series representations meet the Galerkin requirements,

$$X_m(\eta) = \sum_{i=1,2}^{\infty} E_i \cos(i-1)\pi\eta + E_m\frac{\eta^2}{2} \tag{27}$$

$$Y_m(\eta) = \sum_{j=1,2}^{\infty} E_j \cos(j-1)\pi\eta \tag{28}$$

and

$$Z_m(\eta) = \sum_{l=1,2}^{\infty} E_l \sin(2l-1)\frac{\pi}{2}\eta \tag{29}$$

Series representations utilized for the third building block functions are,

$$X_m(\eta) = \sum_{i=1,2}^{\infty} E_i \cos(i-1)\pi\eta \tag{30}$$

$$Y_m(\eta) = \sum_{j=1,2}^{\infty} E_j \cos(j-1)\pi\eta + E_m\frac{\eta^2}{2} \tag{31}$$

$$Z_m(\eta) = \sum_{l=1,2}^{\infty} E_l \sin(2l-1)\frac{\pi}{2}\eta \tag{32}$$

Computation of building block response for any driving coefficient, E_m, is easily achieved by following standard Galerkin procedures. The above serries are differentiated term-by-term, as discussed earlier, and substituted into the three differential equations. We thereby obtain three quantities , each a function of η, which we may designate as Q_{m1}, Q_{m2}, and Q_{m3}. These quantities are each expanded in an approriate series of "KK" terms. Setting each coefficient of the new series equal to zero gives rise to a set of 3 KK non-homogeneous algebraic equations involving the 3 KK unknowns, E_i, E_j, etc., and the driving coefficient E_m. We are thus able to obtain these unknowns as linear functions of E_m. The reader may wish to examine reference[4] where a solution was obtained in a similar fashion for the fully clamped Mindlin plate. It will be observed that the main coefficient matrix associated with the left hand side of the above sets of non-homogeneous equations is identical for each building block, for any value of "m". It need be computed only once.

Returning to equations 17 and the situation prevailing when, m=0, it is found that only the first two building blocks are involved. We are now considering a strip solution.

The driven edge moment and shear force are expressed as,

$$M_\eta = \frac{\partial \psi_\eta}{\partial \eta} \tag{33}$$

and

$$Q_\eta = \psi_\eta + \frac{1}{\phi}\frac{\partial W}{\partial \eta} \tag{34}$$

For the first building block we again prescribe the quantity $(\partial\psi_\eta/\partial\eta)$ as given by equation 22, along the driven edge. We also set the quantity $(\partial W/\partial\eta)$ equal to zero.

These conditions are met by utilizing the following series for $X_m(\eta)$ and $Z_m(\eta)$,

$$X_m(\eta) = \sum_{i=1,2}^{\infty} E_i \cos(i-1)\pi\eta \tag{35}$$

and

$$Z_m(\eta) = \sum_{j=1,2}^{\infty} E_j \sin(2j-1)\frac{\pi}{2}\eta + E_m\eta \tag{36}$$

For the second building block we prescribe the quantity $(\partial W/\partial\eta)$ by means of a series identical to that of equation 22. The quantity $(\partial\psi_\eta/\partial\eta)$ is set equal to zero.

The following series are then utilized for the functions of equations 3 and 36 so that required boundary conditions will be satisfied,

$$Y_m(\eta) = \sum_{i=1,2}^{\infty} E_i \cos(i-1)\pi\eta + E_m\frac{\eta^2}{2} \tag{37}$$

and

$$Z_m(\eta) = \sum_{j=1,2}^{\infty} E_j \sin(2j-1)\frac{\pi}{2}\eta \tag{38}$$

The evaluation of the quantities E_i, E_j, above in terms of the driving coefficient E_m, is now achieved following steps described for the case with $m \geq 1$.

In all of the solutions discussed for fully symmetric mode vibration of Mindlin plates it is known that functions representing $W(\xi,\eta)$ and $\Psi_\xi(\xi,\eta)$ must be symmetric with respect to the ξ axis. Functions representing the quantity $\Psi_\eta(\xi,\eta)$ must be anti-symmetric. It is seen that all these conditions are satisfied.

Finally, to obtain eigenvalues and mode shapes for the Mindlin plate by means of the superposition-Galerkin method, solutions for the last three building blocks of figure 3 must be obtained by an interchange of co-ordinates as discussed earlier. All six building blocks are then superimposed and conditions of zero net bending moment, transverse shear force, and twisting moment are enforced along the edges, η=1, and ξ=1, of the quarter plate. The required eigenvalue matrix is thus obtained.

The reader will appreciate that it is also possible to solve the above problem, utilizing the building blocks of figure 4, by means of the traditional superposition method where exact solutions for the building block responses are obtained. This has, in fact, been done and results have been compared with those obtained by the superposition Galerkin method, as described immediately above.

3. Discussion of results and conclusions

Two distinct problems have been resolved here for the first time by means of the superposition-Galerkin method. They constitute analysis of the fully symmetric free vibration modes of the thin orthotropic completely free plate and a corresponding analysis for the completely free Mindlin plate. In each case, one quarter of the plate has been analyzed. It will be obvious to the reader that by adding other sets of building blocks driven along the edges, $\eta=0$, and $\xi=0$, of the original plate, a general analysis of the modes of vibration of these plates is readily achievable. Solutions for the additional building blocks required are easily inferred from the solutions discussed above. Furthermore, as discussed in reference[3], the elements of the eigenvalue matrix related to these additional building blocks are easily obtained from those already computed for the building blocks of Figure 3.

It should be pointed out that on utilizing the superposition-Galerkin method one must not only chooze the number of building block driving coefficients "K", to be utilized but one must also chooze a value for "KK", the number of terms to be utilized in the Galerkin series, both values must be selected so as to give the desired number of significant digits in the computed eigenvalues. In work reported here it is found that values of "K" equal to about seven are usually sufficient to give the required convergence. Values of the quantity "KK" equal to several times "K" are usually required.

Highly accurate eigenvalues for each of the two main problems discussed were already available from the studies conducted by the traditional superposition method. In both cases, solutions, based on building block sets selected for use in the superposition-Galerkin method, (Figures 2 and 3) were also obtained by the traditional method simply for verification purposes. It is gratifying to report that very good agreement was obtained when all results, including those the superposition-Galerkin method, were compared. Some of these computed results are tabulated in Table 1.

	Orthotropic Plate				**Mindlin Plate**			
	DHX = DHY				Φ_n			
	1.0		**1 / 2**		**0.02**		**0.2**	
Mode	**A:**	**B:**	**A:**	**B:**	**A:**	**B:**	**A:**	**B:**
1	4.806	4.806	4.800	4.800	4.805	4.805	4.648	4.648
2	6.106	6.106	6.048	6.048	6.103	6.104	5.863	5.863
3	15.69	15.69	10.74	10.74	15.60	15.66	13.73	13.73

Table 1. Comparison of Eigenvalues obtained for Fully Symmetric Modes of Thin Orthotropic Square Plates (A - traditional superposition method, B - superposition - Galerkin method)

It is of critical importance to note that the superposition-Galerkin method offers vast computational advantages which become much more pronounced when we move from the thin orthotropic plate to the Mindlin plate. These advantages, particularly as they relate to Mindlin plate problems, have been discussed in reference[4]. They may be summarized briefly for this later family of problems as follows,

1. The numerous possible forms of solution to the differential equations are not needed as these equations are not solved directly.
2. The vast manipulations involved in uncoupling the coupled ordinary differential equations is completely avoided.
3. The vast operations related to enforcing boundary conditions, after solutions to the equations governing building block response have been solved, are completely eliminated
4. Only trigonometric functions and low power polynomial terms are involved when employing the superposition-Galerkin method. Computational problems which sometimes arise as a result of hyperbolic functions appearing in solutions obtained by the traditional superposition method are eliminated.

The reader will be aware that many problems related to free vibration of laminated plates are solved by the Mindlin approach. Completely free plate problems in this later family are now amenable to solution by the superposition-Galerkin method.

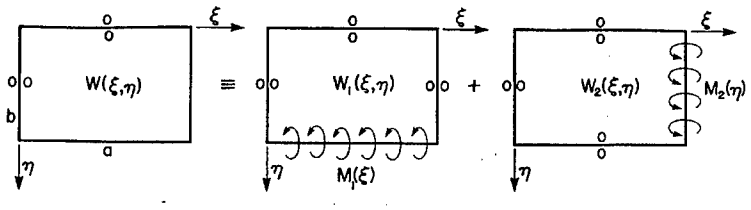

Figure 1. Schematic Representation of Building Blocks Utilized in Analysis of the Completely Free thin Orthotropic Plate by the Traditional Superposition Method

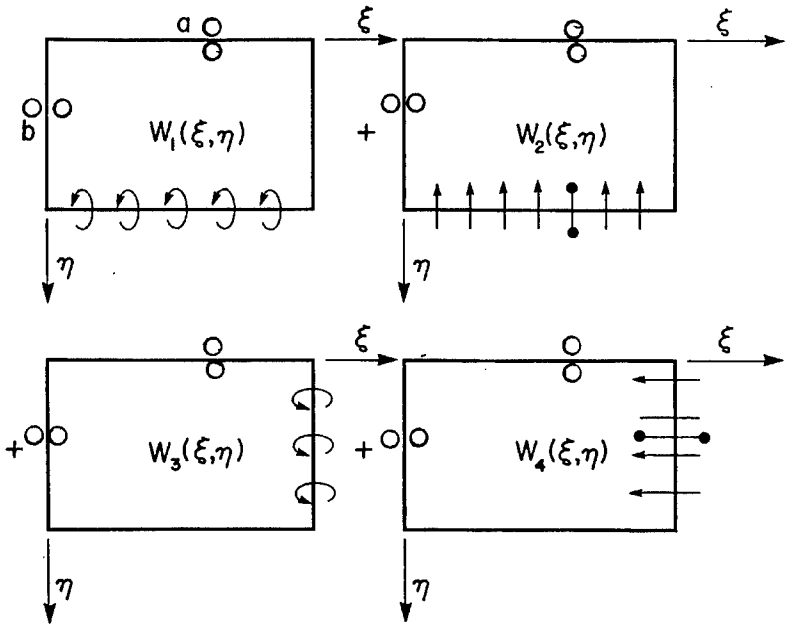

Figure 2. Building Blocks Utilized in Analysis of the Completely Free thin Orthotropic Plate by the Superposition-Galerkin Method

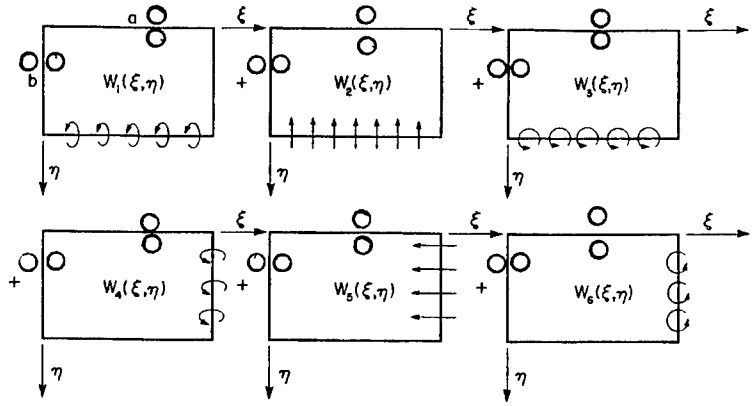

Figure 3. Building Blocks Utilized in Analysis of the Completely Free Mindlin Plate by the Superposition-Glerkin Method

References

1. D. J. Gorman, 1982, "Free Vibration Analysis of Rectangular Plates", Elsevier North Holland Inc.

2. D. J. Gorman, 1999, "Vibration Analysis of Plates by the Superposition Method", World Scientific Publishing Co. Inc.

3. D. J. Gorman, and Wei Ding, 1996, "Accurate Free Vibration Analysis of the completely Free rectangular Mindlin Plate", Journal of Sound and Vibration, 189(3), 341-353.

4. D. J. Gorman, and Wei Ding, 1996, "The Superposition-Galerkin Method for Free Vibration Analysis of rectangular Plates", Journal of Sound and Vibration, 194(2), 187-198.

5. D. J. Gorman, 1994, "Free Vibration Analysis of Point-Supported Orthotropic Plates", Journal of Engineering Mechanics, American Society of Civil Engineers, 120(1), pp 58-74.

Nomenclature

a,b	edge lengths of quarter plate
D	flexural rigidity of Mindlin plate
D_x, D_y	flexural rigidities associated with x- and y- directions, respectively of orthotropic plate
D_t	torsional rigidity of orthotropic plate
DHX	$= H/D_x$
DHY	$= H/D_y$
DXY	$= D_x/D_y$
h	plate thickness
H	$2H = \nu_x D_x+\nu_y D_y+4 D_t$
M	bending moment
M_ξ, M_η	dimensionless bending moments associated with ξ and η directions, respectively, of Mindlin plate
W	plate lateral displacement divided by "a".

x,y	distances along plate edges in ξ and η directions
ξ	$=x/a$
η	$=y/b$
λ^2	eigenvalue = $\omega a^2\sqrt{\rho/D_x}$ for orthotropic plate, $\omega a^2\sqrt{\rho/D}$ for Mindlin plate
ω	circular frequency of vibration
ρ	mass of plate per unit area
ν	Poisson's ratio
ν^*	$=(2 - \nu)$
κ^*	Mindlin shear correction factor
ν_x,ν_y	Poisson ratios associated with x and y directions, respectively, of orthotropic plate
ϕ	$=b/a$
ϕ_h	$=h/a$
ψ_ξ,ψ_η	plate cross section rotations associated with ξ and η directions, respectively

Modelling the dynamics of large scale structures using numerical-experimental substructuring

D. J. Wagg *and D. P. Stoten†

Faculty of Engineering, University of Bristol, Queens Building, University Walk, Bristol BS8 1TR.

September 27, 1999

Introduction

In this paper we consider modelling the dynamics of large scale structures using a numerical-experimental substructuring technique. The size and complexity of many structures often makes accurate predictive modelling of dynamic behaviour difficult. This is particularly true for large scale civil engineering structures such as bridges and dams. For such structures design engineers often use experimental model testing of the structure in addition to theoretical and numerical modelling. However, because of size and weight limitations full scale dynamic testing is impossible for most large structures. As a result, complex experimental test results have to be interpreted with the additional problem of scaling between the model and the prototype.

For numerically simulating modular structures, or those with a high degree of self similarity, the technique of *substructuring* has been developed to reduce the computational workload (see for example [1]). This concept involves subdividing the overall structure into smaller substructures, and can be used to create a model where one (or more) of the subdivided parts is a physical test specimen. Thus the model of the overall structure is a combination of a numerical and an experimental model. To produce such a combined numerical–experimental model some part of the two systems

*Department of Civil Engineering and Department of Mechanical Engineering, University of Bristol, Queens Building, University Walk, Bristol BS8 1TR, U.K.

†Department of Mechanical Engineering, University of Bristol, Queens Building, University Walk, Bristol BS8 1TR, U.K.

must be synchronised using a control algorithm. In this work we use the "minimal control synthesis" (MCS) adaptive control algorithm, developed at Bristol, which can be used without having to carry out any system identification [2]. We demonstrate how the MCS algorithm can be used to implement substructuring.

Numerical-experimental substructuring is particularly suitable to structures where a design critical element can be identified. Critical elements are those which are most difficult to characterise, or most likely to fail during dynamic loading, and as such are of primary interest to the design engineer. In this case the critical element would be modelled using a physical test specimen while the remainder of the structure is modelled numerically. The advantage of this method over scale model testing is that the critical element is tested at full size and the problems associated with scaling are eliminated.

For systems which generate dynamic forces by inertia, such as shaking tables, substructuring must be implemented in real time. We discuss how this can be achieved using the MCS algorithm for a small scale experimental system. We demonstrate the concepts associated with substructuring using a numerical-experimental example. Finally we consider how numerical-experimental substructuring can be applied to modelling soil-structure interaction problems, often encountered in earthquake engineering.

1 The substructuring concept

Substructuring is a method used to divide a large structure into several smaller structures. Often this has computational benefits, and can be used to speed up simulations of an otherwise complex structure. Numerical–experimental substructuring extends this basic concept by modelling one (or more) of the substructures experimentally. In this current work we will deal with systems which have only a single substructure. Thus we refer to the *structure* as the overall system we wish to model, the *substructure* as the experimental system, and the *numerical model* as the remaining substructures. We refer to the numerical-experimental model for the structure as the *substructured* model.

Numerical-experimental already exist in the form of *pseudo-dynamic* testing [3, 4]. In this approach delayed time scales are used, so that loading is applied to the structure quasi-statically. The concept of pseudo-dynamic testing has been extended to real time scales for single degree of freedom systems (without substructuring) [5] by using a dynamic actuator, for the purpose of testing velocity dependent components. In real time substructuring, such as this current work, all the tests are carried out in real time [6].

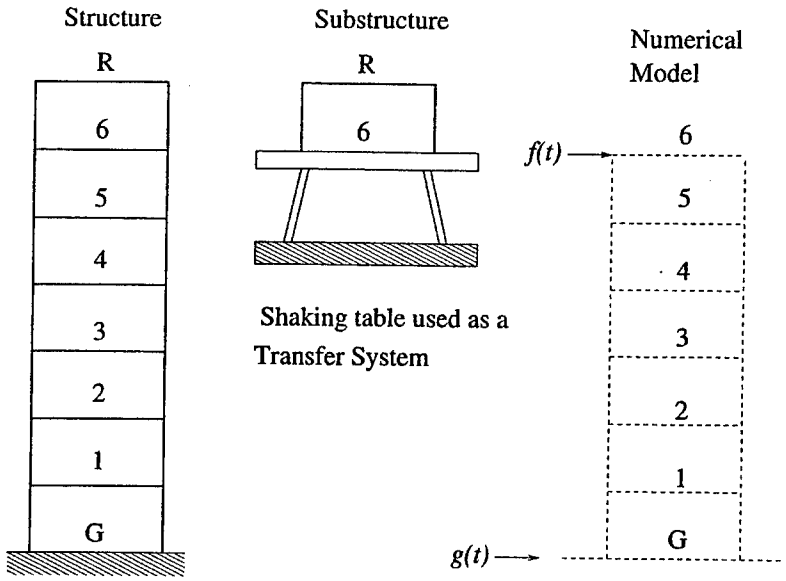

Figure 1: Schematic representation of numerical–experimental substructuring of a multi-storey building.

For numerical–experimental substructuring to be effective, there must be an interaction between the numerical and experimental parts of the model. This is achieved using a *transfer system*, which for structural testing would typically be a shaking table, reaction wall or similar test facility. The motion of the transfer system must be controlled to follow the output of the numerical model.

An example of modelling a multi-storey building is shown in figure 1. Here the response of the substructured model subject to some base excitation $g(t)$ is required, and the dynamics of the roof is the area of particular interest. Thus an experimental model of the top storey is mounted on the transfer system, which in this case is a shaking table. The rest of the structure is modelled numerically. The sixth floor of the structure is where the numerical model and substructure "join". To provide realistic modelling the motion of the transfer system must be controlled to follow the motion of the sixth floor from the numerical model. The interaction between the sixth floor and the roof, is represented by the feedback force $f(t)$, which is measured experimentally, and used in the numerical computations. Thus the motion of the sixth floor is a function of $f(t)$ and $g(t)$, such that the motion of the substructure has an effect on the dynamics at the interface. Depending on the complexity of the modelling, $f(t)$ would typically be a vector containing forces and moments for each axis of excitation.

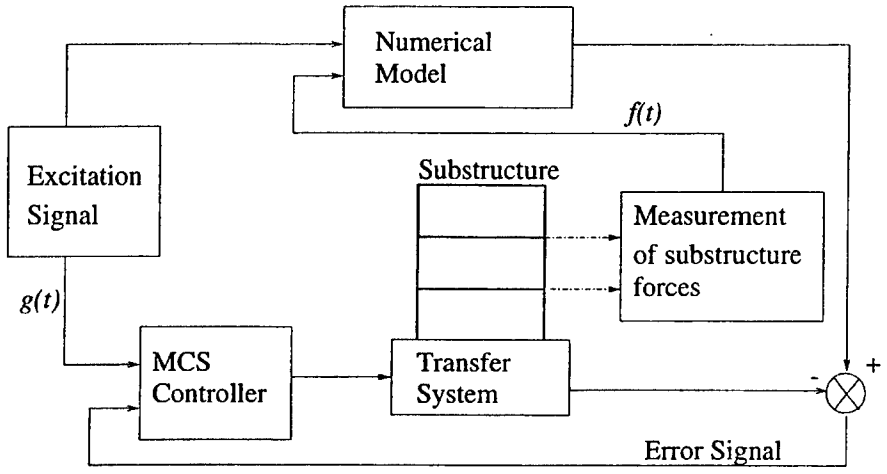

Figure 2: Schematic representation of numerical–experimental substructuring using MCS controller.

2 Control Strategy

With conventional dynamic testing of structures, the excitation signal $g(t)$ is applied directly to the model being tested. In this case the task of the controller is to track $g(t)$ as closely as possible. However, in a substructuring test, the required motion of the transfer system cannot be known in advance, as it is dependent on the numerical model and feedback force $f(t)$. As a result the demands on the controller cannot be studied in advance. Thus the use of an adaptive controller, which can respond to a wide range of possible demand signals is highly desirable. In addition the substructuring process means that the transfer system must follow the output from a numerical model. This is very similar to the "model reference" adaptive control technique [7].

As a result we have chosen to use the MCS algorithm which is a model reference adaptive control algorithm. MCS has the additional benefits of requiring no system identification prior to use, and can be used in a decentralised form [8].

The standard MCS algorithm can be altered to control the transfer system during a substructuring test. A schematic representation of a substructured model using MCS is shown in figure 2. Here we see that the MCS controller uses the excitation signal $g(t)$ and the error signal as the inputs to the feed-forward and feedback components of the control signal respectively. The key alteration of the method is that the standard reference model is replaced with the numerical part of the substructured model. Then the relevant part of the numerical model (selected to have the same

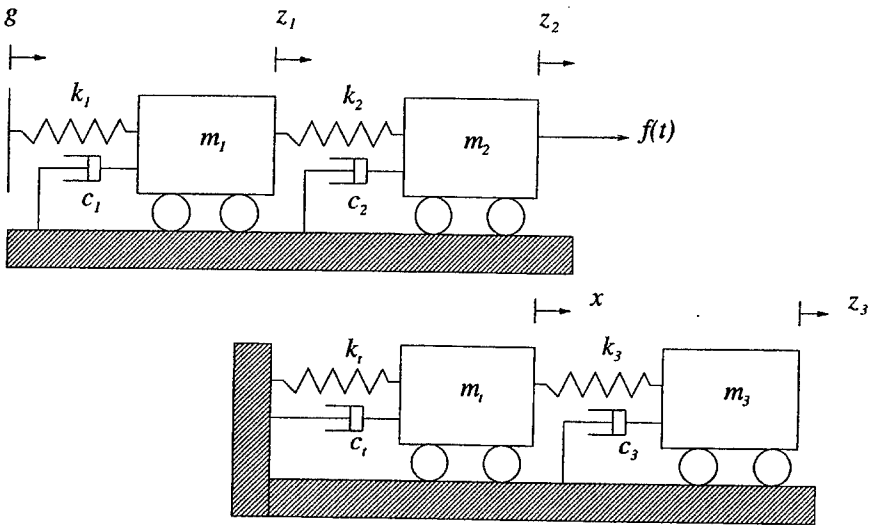

Figure 3: Schematic representation of substructured model of a three mass oscillator.

dimension as the transfer system) is used as the reference for the MCS controller. The effect of the additional dynamics from the coupled nature of the numerical model and the feedback force $f(t)$ is accounted for as a disturbance to the system.

3 Small scale experimental example

We can demonstrate the substructuring concept using a small scale experimental example. The idea of using small scale experimentation is to demonstrate the *concept* of numerical-experimental substructuring, as a viable modelling technique. This process also highlights some of the complexities of modelling a structure via substructuring.

In this example, we wish to model the dynamics of a three mass oscillator, which is one of the simplest linear system we can use to demonstrate the concept. We select one of the masses to be the substructure, with the remaining two masses modelled numerically. A schematic representation of the substructured model for this system is shown in figure 3.

In this figure we have two systems of two coupled masses. The first is the numerical model with coordinates z_1 and z_2. This is acted on by the excitation signal $g(t)$ and the feedback force $f(t)$. The second set of two masses represents the transfer system, with coordinate x, to which the substructure, coordinate z_3, is connected. The masses m_i, are connected by springs of stiffness k_i and damped by viscous dampers, with damping

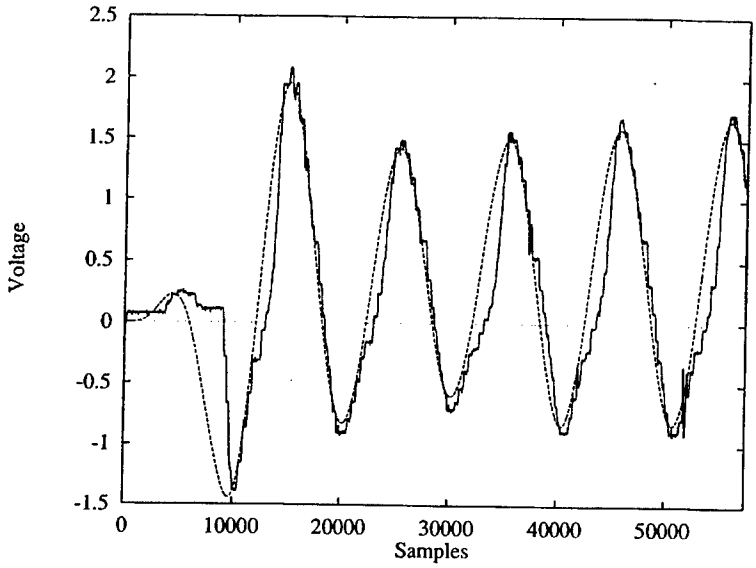

Figure 4: Experimental results from the substructured three mass system. Dashed line, output from numerical model z_2. Solid line, displacement of the transfer system x. Calibration 15mm/Volt. System Properties $m_i = m_t = 0.515$kg, $k_i = k_t = 2.43$N/m and $c_i = c_t \approx 2.4$Ns/m.

coefficients c_i, for $i = 1, 2, 3$. The coupling in this example occurs only via the springs, the dampers being connected to the ground as an aid to simplicity. The transfer system material properties are denoted by m_t, k_t and c_t, and would typically (although not in this simple example) be quite different from the model properties. For the experimental part of the system we have used a two mass apparatus, mounted on a linear bearing, and connected via springs. For this apparatus the masses and spring forces are equal, such that $m_i = m_t$ and $k_i = k_t$.

For this example to achieve effective modelling, we must *synchronise* the motion of z_2 and x using the control algorithm. If this is achieved then the substructured system will be a close representation of a three mass system. The issues of controller stability and effective synchronisation have been discussed in detail by [9]. The substructuring system can be shown to be stable using the passivity concept [10]. Here, we will assume that the control algorithm is suitably stable and robust for our purposes.

The experimental system was controlled using simple and inexpensive hardware. A 486 Personal Computer running RedHat Linux 5.1 provided the computational interface. The displacement and velocity of each mass was recorded using LVDT transducers and tachometers respectively. These signals were read via a Amplicon PC30AT card, which was also used to

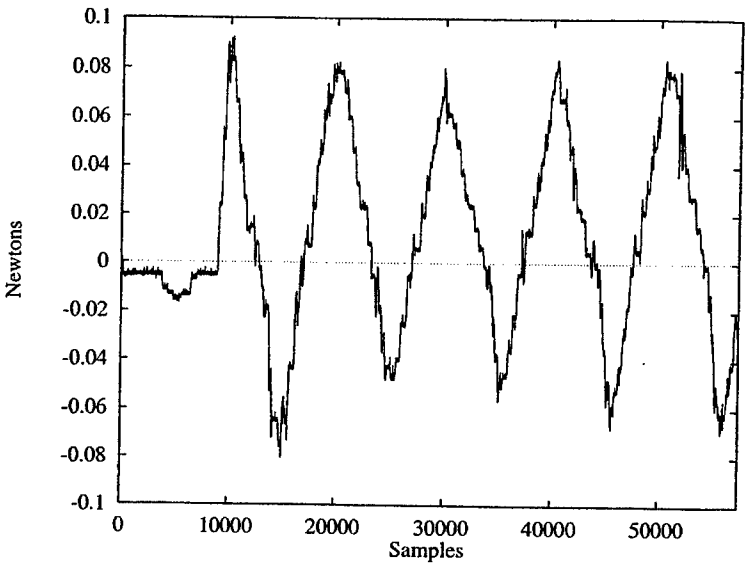

Figure 5: Experimental results from the substructured three mass system. Dashed line, output from numerical model z_2. Solid line, displacement of the transfer system x.

output the control signal. The substructuring algorithm ran at a sampling rate of 512Hz, using the Linux real-time clock. At each sampling interval, the displacement and velocity values were read. The feedback force $f(t)$ was then computed using the relation

$$f(t) = k_3(z_3 - x) + c_3 z_3, \tag{1}$$

although in practise, the actual measured interaction force would be used. The numerical model was then integrated forward one time step using the Runge-Kutta algorithm, and the control algorithm applied to the output.

A typical set of results are shown in figure 4. Here, the excitation signal is a sine wave $0.1\cos(0.1t)$, and the output from the numerical model (dashed line) has the form of a harmonic function. The frequency of the excitation signal is very low, this was to remain within the limitations of our control hardware. The feedback force, $f(t)$, computed during this test is shown in figure 5.

Thus we see via this simple demonstrative example that it is possible to form a numerical-experimental model of a dynamical system. We envisage that the use of powerful modern computers and digital acquisition systems will enable the substructuring technique to be applied to a wide range of structural modelling situations.

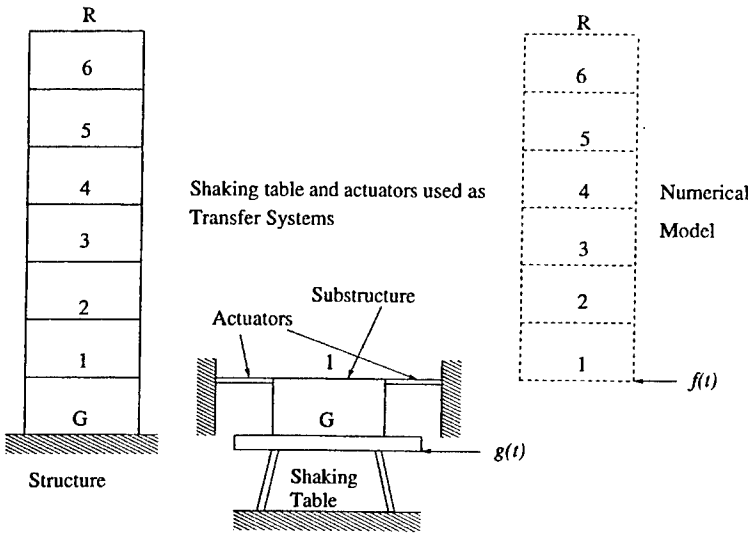

Figure 6: Schematic representation of numerical–experimental substructuring of a multi-storey building using two transfer systems.

4 Large scale modelling applications

We now discuss some possible future applications for numerical-experimental substructuring. It is interesting to note that for the three mass example, our choice of substructure (the end mass) simplified the problem significantly. If we had required the middle mass to be the substructure we would need two transfer systems. For example, consider the multi-storey building problem again. If we are interested in the dynamics of any other than the top storey, we need two transfer systems. This is shown in figure 6. Here, one transfer system is the shaking table, as before, but in addition a set of actuators is required as a second transfer system. The use of two transfer systems has applications for testing where multiple support input is required [11].

This is also encountered in a typical soil-structure interaction problem. In figure 7 we show a single transfer system method for modelling a simple soil-structure interaction problem. However, it is more likely that the design engineer is interested in the dynamics of the soil, and so this should be modelled experimentally. This scenario is shown in figure 8. This type of test could be carried using a shear stack apparatus [12], which can be used to test soils on a shaking table. In this arrangement the building is represented as a plate on the soil, attached to actuators mounted from above. The building is modelled as a simple rigid block, although more complex models could be incorporated. For example, individual pile foundations

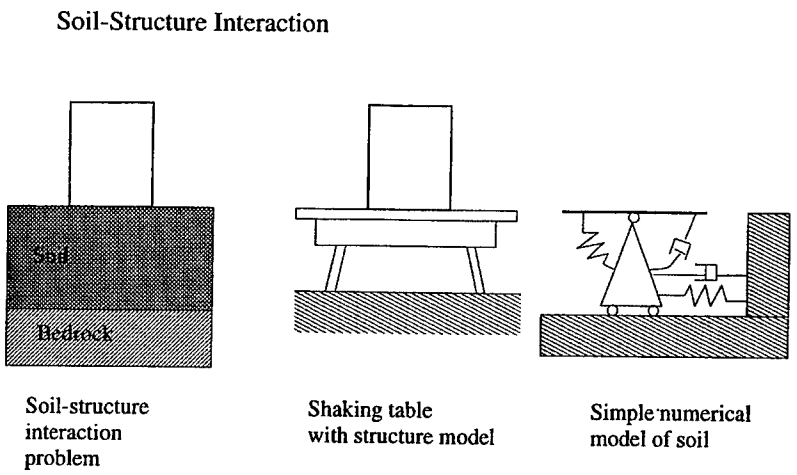

Figure 7: Experimental results from the substructured three mass system. Dashed line, output from numerical model z_2. Solid line, displacement of the transfer system x.

could be attached to actuators to represent the soil-structure interaction.

The advantage of using a shaking table for these tests is that inertial forces are developed in the experimental structure (in this case a soil mass), rather than being estimated as in the pseudo-dynamic tests. Thus it is intended that the initial proof of concept work on numerical-experimental substructuring presented here, will be extended to shaking table facilities [13]. This will allow us to gain valuable insight into the behaviour of structural elements within large scale structures, when subjected to dynamic forces.

5 Conclusions

In this paper we have discussed the concept of numerical-experimental substructuring. This technique can be used to model the dynamics of critical elements in structures. To do this we require the use of a model reference adaptive control algorithm. The technique has been demonstrated using a small scale experimental model. Future applications to modelling large scale structures, particularly soil-structure interaction problems, have been discussed.

One key point requiring future research, is determining the accuracy of the substructured model. In other words, how do we know if the the substructured model is a close representation of the overall structure? Essentially we need to use the error signal from the control algorithm as a monitoring technique. Developing this technique, and the application of

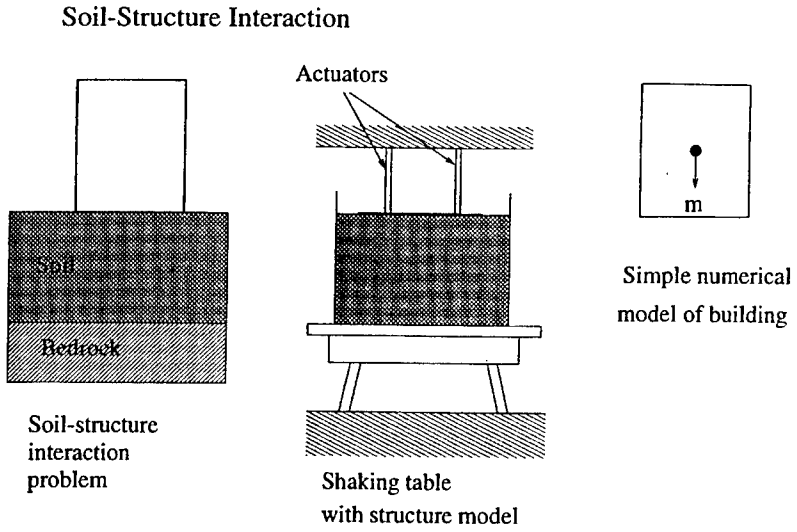

Figure 8: Experimental results from the substructured three mass system. Dashed line, output from numerical model z_2. Solid line, displacement of the transfer system x.

substructuring to shaking table testing will form the basis of our future research on this subject.

References

[1] J. S. Prezemieniecki. *Theory of matrix structural analysis.* McGraw-Hill, 1968.

[2] D. P. Stoten. An overview of the minimal control synthesis algorithm. In *I. Mech. E. Conference on Aerospace Hydraulics and Systems*, London, 1993. Paper C4474-033.

[3] P-S. Shing and S. A. Mahin. Cumulative experimental errors in pseudodynamic tests. *Earthquake Engineering and Structural Dynamics*, 15:409–424, 1987.

[4] J. Donea, P. Magonette, P. Negro, P. Pegon, A. Pinto, and G. Verzeletti. Pseudodynamic capabilities of the elsa laboratory for earthquake testing of large structures. *Earthquake Spectra*, 12(1):163–180, 1996.

[5] M. Nakashima, H. Kato, and E. Takaoka. development of real-time pseudo dynamic testing. *Earthquake Engineering and Structural Dynamics*, 21:779–92, 1992.

[6] T. Horiuchi, M. Inoue, T. Konno, and Y. Namita. Real-time hybrid experimental system with actuator delay compensation and its application to a piping system with energy absorber. *Earthquake Engineering and Structural Dynamics*, 28:1121–1141, 1999.

[7] Y. D. Landau. *Adaptive control:The model reference approach.* Marcel Dekker:New York, 1979.

[8] H. Benchoubane and D. P. Stoten. The decentralized minimal controller synthesis algorithm. *International Journal of Control*, 56(4):967–983, 1992.

[9] D. P. Stoten and H. Benchoubane. Robustness of a minimal controller synthesis algorithm. *International Journal of Control*, 51(4):851–861, 1990.

[10] S. P. Hodgson and D. P. Stoten. Passivity-based analysis of the minimal control synthesis algorithm. *International Journal of Control*, 63(1):67–84, 1996.

[11] A. A. Dumanoglu and R. T. Severn. Seismic response of modern suspension bridges to asynchronous vertical ground motion. *Proceedings of the Institution of Civil Engineers. Part 2*, 83:701–730, 1987.

[12] C. A. Taylor, A. R. Dar, and A. J. Crewe. Shaking table modelling of seismic geotechnical problems. In *10th European Conference on Earthquake Engineering*, pages 441–446. Balkema: Rotterdam, 1995.

[13] D. P. Stoten and E Gómez. Recent application results of adaptive control on multi-axis shaking tables. In *Proceedings of the SECED international conference on seismic design practice into the next century*, Oxford, 1998.

MID-FREQUENCY VIBRATION ANALYSIS AND APPLICATION TO A TWO-ROD SYSTEM

Brian Mace

Department of Mechanical Engineering, The University of Auckland,
Private Bag 92019, Auckland, New Zealand.

In the mid-frequency range, small differences in the properties of different realisations of a structure lead to different vibrational responses. A stochastic approach to vibration analysis is thus required, the aim being to predict the response statistics. In this paper a local modal perturbational (LMP) method is described, the response statistics being found for very little cost above that required to perform the analysis of the baseline system. A system comprising two coupled rods in axial vibration is considered as an application. The discrete frequency and frequency average behaviours of a sample of systems are compared to the baseline response and to SEA predictions.

1. UNCERTAINTY AND MID-FREQUENCY VIBRATIONS

Different physical realisations of a manufactured product, while similar, inevitably differ in detail. This inherent variability in the properties of the system produces consequent variability in dynamic response. The dynamic variability becomes larger at higher frequencies, especially in complex, built-up structures, because of the increasing sensitivity of the dynamic behaviour to even small variations in system properties. A number of factors can cause this variability. These include normal manufacturing variations in component dimensions, material properties, joint properties etc., variations in environmental conditions such as ambient temperature, aging, wear, and variations in operating conditions. In a similar manner, numerical predictions are subject to uncertainty in the physical and geometric properties or the boundary conditions of a given system: these cannot be known exactly.

The effects of uncertainty and variability influence the engineer's choice of analysis method. At "low frequencies" the effects of variability are small and a deterministic method of vibration analyses is normally used: this typically involves a global modal analysis of the system, often using finite element analysis (FEA) with the properties of the system assumed to be known exactly. The result of this deterministic analysis is an estimate of the "exact" system

response. At "high frequencies", on the other hand, the effects of variability are large and a stochastic approach, such as statistical energy analysis (SEA) [1], should be adopted. In SEA the system properties are assumed to have a high degree of uncertainty, and estimates are made of the average response, the average being taken over system properties, amongst other things.

In the "mid-frequency" range neither approach is entirely satisfactory: a single, "exact", deterministic analysis is not able to describe the behaviour of all possible realisations of the system with acceptable accuracy, but high frequency methods are too broad-brush and lose all detail of the behaviour. A stochastic approach is required but some detail must be retained. The aim is to predict the statistics of the responses of similar, but different, realisations of the system, the properties of which vary randomly but with only a moderate degree of uncertainty. These statistics include the response of the baseline system (the engineer's "best guess"), the mean, variance and so on.

Thus, in this context, the low-, mid- and high frequency regimes are related to the degree of dynamic variability that exists, and the appropriate analysis methodology varies accordingly.

In this paper a local modal perturbational (LMP) approach to mid-frequency vibration analysis is described with specific application to a system comprising two end-coupled rods in axial vibration. In the next section some aspects of low- and high frequency vibration analysis are reviewed and the example system described. Then the LMP method is outlined. The discrete frequency and frequency average behaviours of a sample of systems are compared to the baseline response and to SEA predictions. Ensemble statistics are estimated: these statistics include the mean response, percentiles, etc.

2. LOW AND HIGH FREQUENCY ANALYSIS

2.1. Low frequency analysis of the baseline system: global modes and CMS. The deterministic, low frequency analysis of the baseline system follows the steps indicated in Figure 1(a). It is computationally efficient to use component mode synthesis (CMS) [2]: the system is divided into subsystems which are modelled in terms of their local modes; the baseline response is found by assembling the subsystems and solving for the global modes of vibration. This subsysteming approach is quite natural in built-up structures and is in-keeping with the SEA philosophy. As will be seen below, using CMS has a further advantage when uncertainty is included, because variations in the properties of the individual subsystems are usually statistically

independent, the subsystems being manufactured by different processes or manufacturers and then later assembled.

In this paper the subsystem modes are of two types: the *fixed interface component modes* are the (mass normalised) modes of vibration when the interfaces are clamped, while the *constraint modes* are the deformed shapes when each boundary degree of freedom (DOF) is given a unit displacement (or rotation), with the other boundary DOFs remaining fixed. The constraint modes are required to couple together the motions of the subsystems. The component modes will often be found using FEA. The physical response is approximated by assuming that only a finite number of these modes give significant contributions to the total response in the frequency range of interest. This usually leads to a substantial reduction in the number of degrees of freedom of a subsystem, especially when a (possibly large) FE model is used to calculate the component modes.

The global modes are found by assembling the local modal models. A vector $\mathbf{q}$ of component modal DOFs is defined. This contains the fixed interface and constraint modes for all subsystems. The components of $\mathbf{q}$ are here ordered so that $\mathbf{q}$ can be partitioned as

$$\mathbf{q} = \left[\mathbf{q}_f{}^T \quad \mathbf{q}_c{}^T\right]^T \qquad (1)$$

where $\mathbf{q}_f$ are the fixed interface modal DOFs and $\mathbf{q}_c$ are the constraint modes. The equations of free vibration can then be written in the form

$$\mathbf{M}\ddot{\mathbf{q}} + \mathbf{K}\mathbf{q} = \mathbf{0} \qquad (2)$$

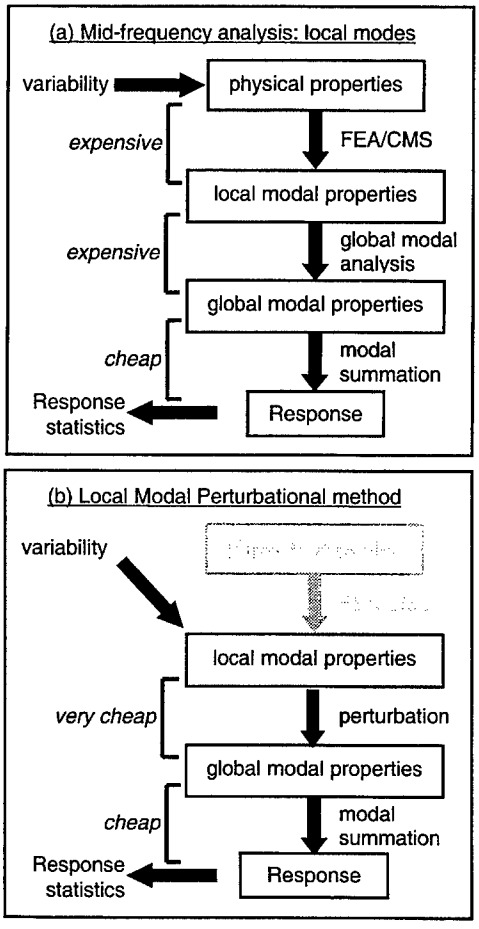

Figure 1. Mid-frequency analysis using (a) local and global modes and (b) LMP method.

where the mass and stiffness matrices are

$$\mathbf{M}=\begin{bmatrix} \mathbf{I} & \mathbf{m}_{fc} \\ \mathbf{m}_{fc}{}^{T} & \mathbf{m}_{cc} \end{bmatrix};\ \mathbf{K}=\begin{bmatrix} diag\left(\lambda_j^{(i)}\right) & \mathbf{0} \\ \mathbf{0}^{T} & \mathbf{k}_{cc} \end{bmatrix} \tag{3}$$

The submatrices are as follows: $\mathbf{m}_{fc}$ is a coupling mass matrix, $\mathbf{m}_{cc}$ and $\mathbf{k}_{cc}$ are constraint mass and stiffness matrices, $\lambda_j^{(i)}$ is the jth fixed interface modal eigenvalue (square of the local natural frequency) of the ith subsystem ordered in an appropriate way, *diag(.)* represents a diagonal matrix, **I** is the identity matrix and **0** is a matrix of zeros of appropriate dimension.

The global modal properties follow from equation (2). The eigensolution results in the global eigenvalues λ_j and the global mode shapes ϕ_j, which relate the component modal DOFs **q** to the global modal DOFs. The forced response is then found in terms of a sum of modal contributions in the normal way.

2.2. High frequency analysis: SEA. In an SEA model [1] the system is divided into subsystems and the response described in terms of the time and (for broadband excitation) frequency averaged subsystem energy *E*. The average is also implicitly taken over an ensemble of systems with different properties and over all possible excitation points. Various approximations are made, most notably those required to express the coupling power between two subsystems in terms of the coupling loss factor η_{ij}.

SEA provides broad-brush, average predictions, giving no information about either the spatial distribution of energy within a subsystem, the detailed variation of this energy with frequency or the dependence of this energy on spatial distribution of the excitation.

2.3. The two-rod system. Figure 2 shows the system comprising two end-coupled rods. Each rod forms one subsystem and undergoes axial

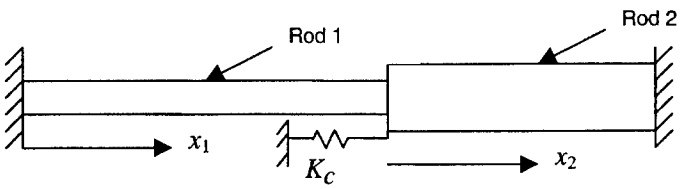

Figure 2. System comprising two rods undergoing axial vibration.

vibration. The density, cross-sectional area, length and elastic modulus of each rod are ρ_i, A_i, l_i and E_i respectively. The properties of the baseline system for which numerical results are presented are given in Table 1. The two rods are identical except for their lengths. Time harmonic excitation acts on rod 1 at x_1 = 0.245 l_1 and the response found is the velocity of rod 2 at $x_2 = 0.745\, l_2$. These points are such that all the local modes whose natural frequencies lie in the frequency range under consideration are excited or respond (although some very weakly).

$E_1A_1 = E_2A_2$	1
$\rho_1A_1 = \rho_2A_2$	1
l_1	$\pi\sqrt{26}/8$
l_2	$\pi\left(1-\sqrt{26}/8\right)$
η	0.01
K_c	40

Table 1. Physical and geometric properties of baseline system (arbitrary units).

A spring of stiffness K_c is attached to the junction between the rods. Its stiffness is such that the impedance of the coupling spring equals the characteristic impedance of the rods at a frequency $\omega = 20$.

2.3.1. CMS of the two-rod system. The jth fixed interface (mass normalised) mode shape and natural frequency for the ith rod are given by

$$s_j^{(i)}(x_i) = \sqrt{\frac{2}{\rho_i A_i l_i}}\ \sin\frac{j\pi x_i}{l_i};\quad \omega_j^{(i)} = \sqrt{\frac{E_i}{\rho_i}}\left(\frac{j\pi}{l_i}\right);\quad i = 1,2 \tag{4}$$

More details can be found in [3]. The constraint mode shapes are

$$s_{c,0}^{(i)} = 1 - x_i/l_i\,;\ s_{c,l}^{(i)} = x_i/l_i \tag{5}$$

and are found by prescribing a unit displacement at the end $x_i = 0$ and $x_i = l_i$ respectively. For this system the vector of component modal degrees of freedom $\mathbf{q}$ (equation(1)) is defined by

$$\mathbf{q} = \left[\mathbf{q}_f^{(1)T}\quad \mathbf{q}_f^{(2)T}\quad q_c\right]^T \tag{6}$$

where $\mathbf{q}_f^{(1)}$ and $\mathbf{q}_f^{(2)}$ are the amplitudes of the fixed interface modes in rods 1 and 2 respectively, only a finite number of these modes being retained. Also q_c is the displacement of the interface where the two rods are connected, this being where the end of subsystem 1 at $x_1 = l_1$ is

connected to the end of subsystem 2 at $x_2 = 0$. The submatrices of **M** and **K** can be found straightforwardly (e.g. [3]).

2.3.2. *SEA of the two-rod system.* Each rod forms one subsystem, with the parameters in a conventional SEA model [1] being

$$\eta_{ij} = \frac{T^2}{2\pi n_i \omega (1 - T^2/2)}; \quad n_i = \frac{l_i}{\pi}\sqrt{\frac{\rho}{E}}; \quad T^2 = \frac{1}{1+\mu^2}; \quad \mu = \frac{K_c}{2A\sqrt{E\rho\omega}} \tag{7}$$

where η_{ij} is the coupling loss factor, ω the centre of the frequency band under consideration, $n_i(\omega)$ the modal density of subsystem i, T^2 the power transmission coefficient of the coupling and the parameter μ the ratio of the impedances of the spring and rod

2.3.3. *Numerical examples.* Following the component mode synthesis, 72 and 42 fixed interface subsystem modes were retained for rods 1 and 2 respectively. Thus there are 115 elements in the global component modal vector **q** of equation (6). The global modes were found using Matlab and 60 retained for later response calculations.

The response (magnitude of the velocity squared) of the baseline system is shown in Figure 3. Clear resonances can be seen in the discrete frequency response. The asymptotic modal density of the system is $n(\omega) = 1$, while the bandwidth of the jth mode is $\Delta_j = \omega_j \eta \approx j\eta$. Thus the modal overlap $M = n\Delta = 0.01\omega$ is smaller than 1 in the frequency range shown. The general level of the response tends to be lower in certain frequency bands. First, these may be where the excitation point is close to an integer multiple of half a wavelength from the fixed end at $x_1 = 0$: now the excitation point tends to lie close

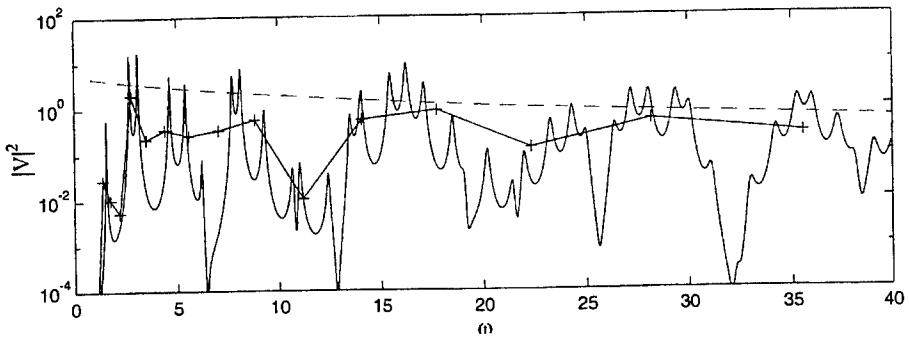

Figure 3. Response of baseline system: discrete frequency and (+) third octave averages; - - - SEA predictions.

to nodal points of the modes which are resonant in these frequency ranges. These frequency ranges are around integral multiples of ω = 6.5. Secondly, similar mode shape coherence effects occur around integral multiples of ω = 11 when the response point is close to an integer multiple of half a wavelength from the fixed end at $x_2 = l_2$. Third octave band frequency averaging removes the resonant behaviour at higher frequencies, when more modes are contained in each band.

SEA predictions for this system are smooth, showing no resonant detail whatsoever. SEA overpredicts the response (i.e. it predicts the wrong average, the system being strongly coupled), and fails to predict broad trends with frequency.

3. MID-FREQUENCY LMP ANALYSIS

In the mid-frequency range there is uncertainty in the system's properties. In principle, a Monte Carlo simulation can be performed: the properties are allowed to vary randomly and the CMS of the previous section is repeated many times to estimate the statistics of the response. The computational cost would normally be immense.

The most computationally expensive steps in the analysis are indicated in Figure 1(a) and are: (1) solving the subsystem eigenvalue problems for the component modes and (2) solving the assembled model for the global modes of vibration. In the LMP approach indicated in Figure 1(b) these steps are removed and the response statistics estimated in the following ways:

1) Variability is assumed to exist in the *local modal properties* of each subsystem rather than in their physical properties (i.e. material and geometric properties) directly. Of course the two are related, since the physical properties uniquely define the local modal properties. However, including variability in this manner avoids having to re-solve for the local modes each time.
2) A *perturbational relationship* is found that relates the global and local modal properties. This avoids having to solve the global eigenvalue problem for every member of the sample.
3) A Monte Carlo simulation is then used to estimate the statistics.

The LMP approach is described in more detail in [3] and [4] with regard to the estimation of frequency response functions and energy influence coefficients. It is computationally very efficient. Once the analysis of the baseline system is performed, the response of each

member of the sample and the response statistics can be estimated at very little cost.

3.1. Variability in subsystem properties. The modal properties in each subsystem are assumed to vary randomly with some assumed statistical distributions, mean values, variances, covariances and so on. Here the following assumptions are made. It is reasonable to assume that the properties of one subsystem are independent of those of the other subsystems, since typically the subsystems are manufactured by different processes and then later assembled. In many practical cases, it is also reasonable to assume that the properties of the interfaces are deterministic (i.e., $\mathbf{m}_{cc}$ and $\mathbf{k}_{cc}$ are deterministic) and that the subsystem coupling mass matrices $\mathbf{m}_{fc}$ are deterministic. Thus the constraint modes are assumed deterministic. The subsystem component modal natural frequencies, however, are assumed to vary randomly. Consequently in equation (3) the mass matrix **M** is deterministic and so, too, are all the elements of **K** except for those diagonal entries which correspond to the fixed interface eigenvalues $\lambda_j^{(i)}$.

For simplicity, it is assumed here that, for each member drawn from the ensemble, the jth eigenvalue in the ith subsystem is given by

$$\lambda_j^{(i)} = \overline{\lambda_j^{(i)}}\left(1+\varepsilon^{(i)}\right)\left(1+\varepsilon_j^{(i)}\right) \tag{8}$$

where the mean value $\overline{\lambda_j^{(i)}}$ is the value assumed for the baseline system and where $\varepsilon^{(i)}$ and $\varepsilon_j^{(i)}$ are small random variables with zero mean, Gaussian distribution and with specified variances. The perturbation of $\lambda_j^{(i)}$ in equation (8) arises from two sources. First, there are fully-correlated variations in all the fixed interface eigenvalues for subsystem i as defined by $\varepsilon^{(i)}$. Physically this might arise, for example, because of uncertainties in the elastic modulus of the material from which the subsystem is constructed, the result of which is that all the eigenvalues of that subsystem change by the same proportion. Secondly, there are uncorrelated variations in the individual eigenvalues as defined by the j random variables $\varepsilon_j^{(i)}$. These might perhaps arise from spatially dependent variations in geometric or materials properties within a subsystem. It is not known how realistic these assumptions are: certainly in general one must define variances and covariances between all the subsystem eigenvalues.

3.2. First order perturbation. Suppose there is a variation $\delta\mu$ in some parameter μ on which **M** and **K** in equations (2,3) depend. In [5] it is shown that, to first order, the variation in the kth global eigenvalue is

$$\delta\lambda_k = \phi_k^T \left[\frac{\partial \mathbf{K}}{\partial \mu} - \lambda_k \frac{\partial \mathbf{M}}{\partial \mu} \right] \phi_k \ \delta\mu \tag{9}$$

where ϕ_k is the kth eigenvector. Now let $\delta\mu = \delta\mu_j$ be a perturbation in the jth component modal eigenvalue. Under the previous assumptions, none of the elements of **M** or **K** vary except for that diagonal element of **K** which corresponds to the jth component modal eigenvalue. Thus the total perturbation in the kth global eigenvalue is

$$\delta\lambda_k = \sum_j (\phi_k)_j^2 \ \delta\mu_j \tag{10}$$

Similarly a perturbation in the jth component modal eigenvalue produces a perturbation in the kth global eigenvector given by [5]

$$\delta\phi_k = \left(\sum_{r \neq k} \frac{(\phi_k)_j (\phi_r)_j}{\lambda_k - \lambda_r} \phi_r \right) \delta\mu_j \tag{11}$$

The total first-order perturbation in ϕ_k is given by summing the contributions from perturbations in each component mode.

3.3. Monte Carlo simulation. A Monte Carlo simulation is finally used to estimate the statistics of the responses of the ensemble by choosing at random a sample of systems. For each member in the sample the parameters ε are chosen at random, the component modal eigenvalues found and the perturbation relations used to estimate the global eigenvalues and eigenvectors. The global response is then found by summing contributions from the perturbed global modes.

3.4. Numerical examples. A Monte Carlo simulation was performed using a sample of 200 members. All the parameters ε are assumed to be Gaussian with zero mean and standard deviations equal to 0.02. The standard deviation of the uncertainty $\delta\omega_j$ in the jth global natural frequency ω_j is then approximately $\delta\omega_j \approx 0.02\omega_j$. This amount of variability has been chosen to demonstrate the effects of variability in system properties and to show the transition from low to high frequency behaviour.

The discrete frequency responses of 20 members of the sample are shown in Figure 4(a). At low frequencies the responses of all members are almost the same: this is the low frequency region where a deterministic analysis of the baseline system provides acceptably accurate estimates of the responses of all possible systems. At higher frequencies the dynamic variability increases substantially. However, there are still broad trends in the response at higher frequencies. Figure 4(b) shows third octave averages. If frequency averages are taken the variability persists, but is substantially reduced. The variability at low frequencies can be attributed primarily to the fact that very few modes lie in each band, at moderate frequencies also to dynamic variability, but at higher frequencies is very much less than for discrete frequency response because there are many modes in each third octave band.

An "acoustic limit" or "uncertainty horizon" can be identified as the frequency above which the typical uncertainty in a specific natural frequency (say, plus or minus one standard deviation) becomes equal to the average modal spacing. For this system, this occurs at around the 25th natural frequency. Here, for example, the 25th natural frequency of one member system may occur at a higher frequency than the 26th natural frequency of another member of the ensemble.

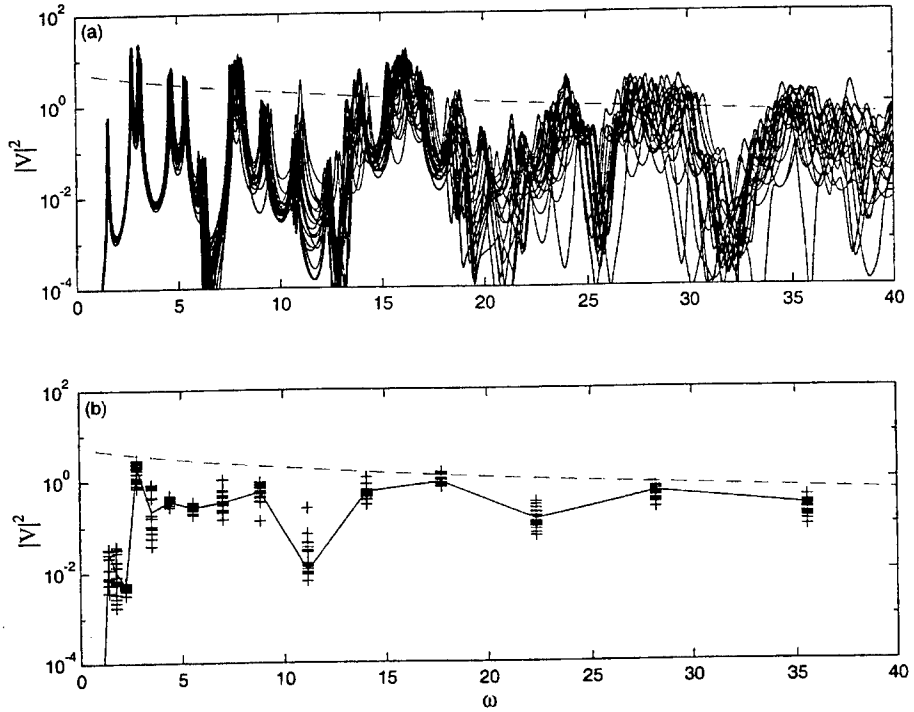

Figure 4. Responses of 20 different realisations of the system: (a) discrete frequency; (b) third octave averages; - - - SEA predictions.

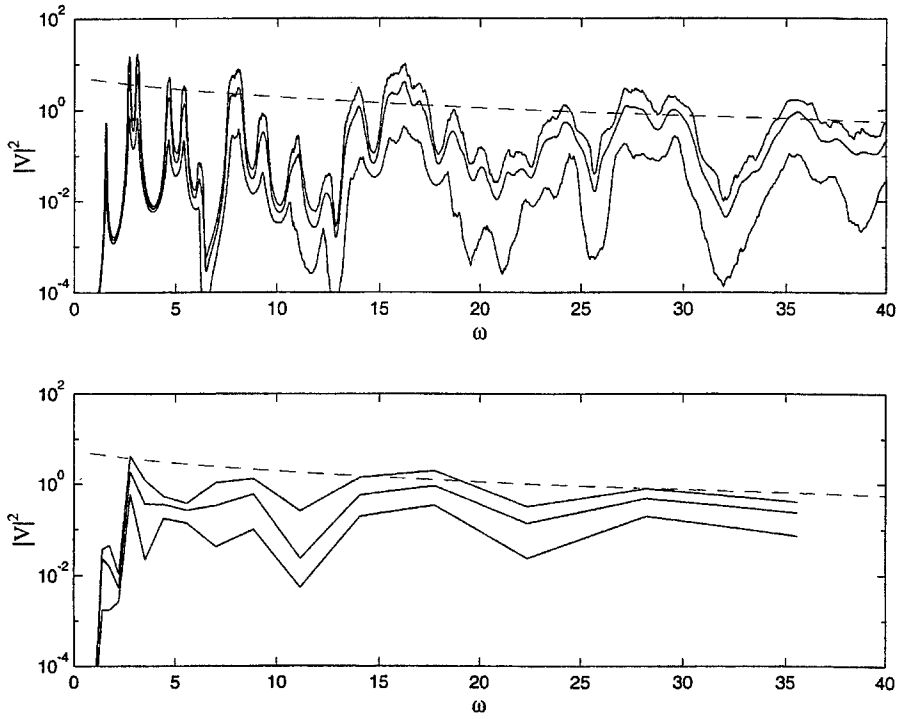

Figure 5. Ensemble statistics: (a) discrete frequency: mean, 10th and 90th percentiles; (b) third octave averages: mean, minimum and maximum; - - - SEA predictions.

Beyond the acoustic limit the amount of variability in the ensemble is large enough (in a dynamic sense) for there to be no real value in making deterministic predictions.

Figure 5 shows estimates of various response statistics obtained using the LMP method. The LMP estimates agree very closely with those based on 200 full global modal analyses (not shown) but are obtained for very little cost. The mean and quartiles in particular show very close agreement. The main differences arise in estimating the 'tails' of the distribution of discrete frequency responses, for example their minimum and maximum values. This is due to the difficulty in capturing the outlying resonant and antiresonant responses equally with a sample of only moderate size (200 members), since these responses occur rarely. The variability in discrete frequency response increases with increasing frequency because the dynamics become increasingly sensitive to uncertainty in the system's parameters, the

modal overlap being fairly small. At higher frequencies the resonant frequencies of individual systems become more spread out, so that the ensemble statistics as a whole do not show distinct resonant peaks, even though every single ensemble member does so.

Figure 5(b) shows some statistics for third octave averages. The absence of resonant-like behaviour in the ensemble statistics at higher frequencies can be attributed also to the fact that each third octave now contains a significant number of modes. However, there is still a significant spread of responses and noticeable differences between SEA predictions and the mean third octave response.

4. CONCLUDING REMARKS

Different analysis methods are appropriate in different frequency regimes because of uncertainties in the properties of the system. In the mid-frequency range a stochastic method is required. The LMP approach described in this paper provides estimates of ensemble response statistics at very little cost above that of the analysis of the baseline system. While some variability in the properties of the system is assumed, the variability is not as large as that assumed in a high frequency, statistical method such as SEA: some of the broader features of the systems' responses are retained. The method is particularly appropriate if all subsystems have small or moderate variability.

REFERENCES

1. Lyon, R.H. and DeJong, R. *Theory and Applications of Statistical Energy Analysis*. 2nd edition. Butterworth-Heinemann, 1995.
2. Craig R R Jr. Substructure methods in vibrations. *Trans A.S.M.E.* 1995, **117**, 207-213.
3. Mace, B.R. and Shorter, P.J. A local modal/perturbational method of estimating frequency response statistics of built-up structures with uncertain properties. *Submitted to J Sound Vib*, 2000.
4. Shorter, P.J. and Mace, B.R. Stochastic energy flow models from component mode synthesis. *In preparation.*
5. Plaut, R H and Huseyin, K. Derivatives of eigenvalues and eigenvectors in non-self-adjoint systems. *AIAA J*, 1973, **11**, 250-252.

NONLINEAR VIBRATION

EVEN HARMONICS ON THE STEADY-STATE GEOMETRICAL NON-LINEAR FORCED VIBRATION OF BEAMS

P. Ribeiro
DEMEGI, Faculdade de Engenharia, Universidade do Porto,
Rua dos Bragas, 4050-123 Porto, Portugal.
e-mail: *pmleal@fe.up.pt*

ABSTRACT

Most analytical and numerical investigations on the transverse vibration of beams with large displacements, and subjected to transverse harmonic forces, only find odd harmonics in the response. However, experimental research indicates that the second harmonic is also excited and in this paper an explanation for its excitation is sought. Two possibilities are explored. The first is to consider the longitudinal inertia, usually neglected, and, therefore, quadratic and cubic non-linearities will coexist in the equations of motion. The second, is to add small perturbations, characteristic of experimental work, to the harmonic excitation and analyse the ensuing vibration.

1. INTRODUCTION

As the amplitude of vibration displacement of a beam with fixed ends increases, the stiffness increases due to the effect of the longitudinal forces and the beam vibrates in the non-linear regime. Multi-frequency response to harmonic excitation, variation of the natural frequency and of the normal mode with the vibration amplitude are well-known consequences of geometrical non-linearity [1-8].

The geometrical non-linear vibration of thin beams has been widely studied. In reference [2] large vibration amplitudes of beams clamped at both ends (cc) were investigated by applying Hamilton's principle. Harmonic motion was assumed and the displacement was expanded in the form of a finite series. In reference [3] the non-linear vibration of beams was studied using the finite element method (FEM), and 1:3 internal resonances were found. In reference [4] the hierarchical finite element method (HFEM) was applied, and it was demonstrated that this method requires far fewer degrees of freedom than the *h*-version of the FEM, a major advantage in non-linear analysis. 1:3 and 1:5 internal resonances were detected in cc and simply supported (ss) beams. Only odd harmonics are present in the response in references [2-4], and many other references where the same occurs could be added to this list.

In reference [5] the FEM and a time domain numerical integration scheme were used, and it was found that the vibration of ss and cc beams in their first non-linear mode can be defined by an expansion of its odd, symmetric, linear modes. The longitudinal inertia was neglected in works [2-5]; consequently, the

equations of motion constitute a system of Duffing's equations (i.e., with a cubic non-linearity).

References [2-5] lead one to conclude that the geometrical non-linear vibration of cc and ss beams only includes odd harmonics, and that in the neighbourhood of the first non-linear mode, the shape of vibration is symmetric. However, in an experimental investigation of the geometrical non-linear vibration of a beam clamped at both ends [1], it was found that the second harmonic is also excited. Moreover, the response of the beam to a transverse harmonic force applied in the middle of its span was influenced by higher order even, thus antisymmetric, modes of vibration. A numerical investigation including the second harmonic was carried out, only to find out that its amplitude is zero. Again, equations of the Duffing type were used.

In this work, an explanation for the presence of even harmonics in the geometrical non-linear vibrations of beams is sought. When the excitation is purely harmonic, the second harmonic is not present in the solution of Duffing's equation [6]. This suggests two possibilities to explore. The first one, is to consider the in-plane or longitudinal inertia, which is usually neglected. In this way, equations of motion with quadratic and cubic non-linearities are obtained. The second, is to consider excitations not purely harmonic. In fact, due to the characteristics of experimental work, a small constant, offset, force and/or a longitudinal excitation may be attached to the harmonic force.

2. BEAM EQUATIONS OF MOTION

The principle of virtual work, d'Alembert's principle, and the HFEM are applied to derive the equations of motion in the time domain. The HBM is used to map these equations into the frequency domain [4].

A beam, its local and global co-ordinate systems are shown in Figure 1. Only vibrations of the beam in the plane x-z are analysed. ξ is a non-dimensional element, or local, co-ordinate; x, y and z are global co-ordinates. The full beam is modelled with only one element, therefore the relation between and x is given by:

$$\xi = \frac{2x}{L} \tag{1}$$

Elastic and isotropic beams with uniform thickness h are investigated. Low order modes are analysed, and thus transverse shear deformations and rotatory inertia are neglected. The transverse displacement, w, is large when compared with the beam thickness - leading to geometrical non-linearity - but is very small compared with the length, L, of the beam. Hence, the beam analogue of von Kármán's plate theory [7] can be applied, i.e., the in-plane, or longitudinal, displacement, u, and the transverse displacement w are given by

$$u(x,z,t) = u^0(x,t) - zw^0_{,x} \text{ and } w(x,z,t) = w^0(x,t), \tag{2}$$

In this equation the superscript ^{0} denotes the middle plane and "$_{,x}$" the derivative with relation to x.

The strain-displacement relationship is:

$$\varepsilon_x = u^0_{,x} + \frac{1}{2}\left(w^0_{,x}\right)^2 - zw^0_{,xx} \tag{3}$$

where $u^0_{,x}$ is the linear in-plane strain, $1/2\left(w^0_{,x}\right)^2$ is the non-linear in-plane strain and $w^0_{,xx}$ is the curvature of the beam. The vector $\{d\}$, formed by the displacement components u^0 and w^0, is expressed as a function of the in-plane, $\lfloor N^u \rfloor$, and out-of-plane, $\lfloor N^w \rfloor$, hierarchical shape functions:

$$\{d\} = \begin{Bmatrix} u^0 \\ w^0 \end{Bmatrix} = \begin{bmatrix} \lfloor N^u \rfloor & 0 \\ 0 & \lfloor N^w \rfloor \end{bmatrix} \begin{Bmatrix} q_p \\ q_w \end{Bmatrix}. \tag{4}$$

where $\{q_p\}$ and $\{q_w\}$ are, respectively, the vectors of generalised in-plane (or longitudinal) and transverse nodal displacements. The set of shape functions used is given in [4]. Neglecting, for the moment, the work of the damping forces, the principle of virtual work can be written as:

$$\delta W_{in} + \delta W_V + \delta W_{ex} = 0, \tag{5}$$

where δW_{in}, δW_V and δW_{ex} are, respectively, the work done by the inertia, internal elastic forces and external forces.

The virtual work of the inertia forces – defined following d'Alembert's principle – is given by:

$$\delta W_{in} = -\rho h b \int_L \{\delta d\}^T \left\{\ddot{d}\right\} dL = -\{\delta q\}^T [M] \left\{\ddot{q}\right\}, \tag{6}$$

where ρ is the mass per unit volume, b is the width of the beam, $\{q\}$ is the vector of generalised displacements and $\left\{\ddot{q}\right\}$ is the vector of generalised accelerations. The mass matrix $[M]$, formed by the in-plane $[M_p]$ and bending $[M_b]$ mass matrices [8].

The variation δW_V is the symmetric of the variation of the elastic potential energy, and may be expressed as

$$\delta W_V = -\{\delta q\}^T \left([K_1] + [K_2] + [K_3] + [K_4]\right)\{q\}, \tag{7}$$

where $[K_1]$ is the linear stiffness matrix formed by the in-plane, $[K_{1p}]$, and bending, $[K_{1b}]$, linear stiffness matrices; the non-linear stiffness matrices $[K_2]$ and $[K_3]$ are linear functions of the generalised transverse displacements, and $[K_4]$ is a quadratic function of those displacements.

If $\overline{P}_{0j}(t)$ represents a concentrated transverse force acting at the point $x=x_j$, $\overline{P}_{0d}(x,t)$ a transverse distributed force, $\overline{P}_{tj}(t)$ a concentrated longitudinal force acting at the point $x=x_j$, and $\overline{P}_{td}(x,t)$ a longitudinal distributed force, the virtual work of the external forces is given by

$$\begin{aligned}\delta W_{ex} &= \int_L \left[\overline{P}_{0j}(t)\delta(x-x_j)+\overline{P}_{0d}(x,t)\right]\delta w(x,t)dL \\ &+ \int_L \left[\overline{P}_{tj}(t)\delta(x-x_j)+\overline{P}_{td}(x,t)\right]\delta u(x,t)dL = \{\delta q_w\}^T\{\overline{P}_w(t)\}+\{\delta q_p\}^T\{\overline{P}_p(t)\}.\end{aligned} \tag{8}$$

where $\{\overline{P}_w(t)\}$ and $\{\overline{P}_p(t)$ are the vectors of generalised external forces applied in, respectively, the transverse and longitudinal directions and $\delta(x-x_j)$ is a spatial Dirac delta function.

Damping will be assumed to be mass proportional and hysteretic. It depends on the damping factor β, which is given by

$$\beta = \omega_{l1}^2 \times \alpha, \tag{9}$$

where ω_{l1} is the fundamental linear frequency and α the loss factor.

Inserting equations (6), (7) and (8) in equation (5), and adding mass proportional hysteretic damping, the following two coupled systems of equations of motion are obtained:

$$[M_p]\{\ddot{q}_p\}+\frac{\beta}{\omega}[M_p]\{\dot{q}_p\}+[K_{1p}]\{q_p\}+[K_2]\{q_w\}=\{\overline{P}_p\}, \tag{10}$$

$$[M_b]\{\ddot{q}_w\}+\frac{\beta}{\omega}[M_b]\{\dot{q}_w\}+([K_{1b}]+[K_4])\{q_w\}+[K_3]\{q_p\}=\{\overline{P}_w\}. \tag{11}$$

Because the longitudinal inertia was not neglected, the equations of motion have quadratic - $[K_2]\{q_w\}$ and $[K_3]\{q_p\}$ - and cubic - $[K_4]\{q_w\}$ - non-linearities.

Periodic response is of the form:

$$\begin{Bmatrix} q_p \\ q_w \end{Bmatrix} = \sum_{i=0,1,2}^{k} \{w_{ci}\}\cos(i\omega t)+\{w_{si}\}\sin(i\omega t), \tag{12}$$

where k is the number of harmonics used. Equation (12) is inserted into the equations of motion (10) and (11) and the HBM is employed in order to derive the equations of motion of in the frequency domain. These are of the form:

$$\{F\} = \left(-\omega^2[M]+[C]+[KL]+\left[KNL(\{w\})\right]\right)\{w\} - \{P\} = \{0\}, \qquad (13)$$

where $[M]$ represents the mass matrix, $[C]$ the damping matrix, $[KL]$ the linear stiffness matrix and $\left[KNL(\{w\})\right]$ the non-linear stiffness matrix. The equations of motion (13) are solved by a continuation method [3-4]. The total number of degrees of freedom of the model is $n=(2k+1)p_o+(2k+1)p_i$, where p_o and p_i are, respectively, the numbers of out-of-plane and in-plane shape functions used.

3. STABILITY STUDY

Since only the stable solutions are physically meaningful, the stability of the steady-state solutions should be investigated. To carry out this study, a small disturbance is added to the solutions

$$\{\tilde{q}\} = \begin{Bmatrix} \tilde{q}_p \\ \tilde{q}_w \end{Bmatrix} = \begin{Bmatrix} q_p \\ q_w \end{Bmatrix} + \delta \begin{Bmatrix} q_p \\ q_w \end{Bmatrix} \qquad (14)$$

and the evolution of $\delta\{q\}=\delta\{q_p,q_w\}$ is analysed. If it increases with time, then the solution is unstable [6].

Inserting the disturbed solution (14) into equations (10) and (11), expanding the non-linear terms by means of Taylor series around $\{q_p\}$ and $\{q_w\}$ and ignoring terms of order higher than $\delta\{q_p$ and $\delta\{q_w\}$, the following coupled systems of equations are obtained:

$$[M_p]\delta\{\ddot{q}_p\}+\frac{\beta}{\omega}[M_h]\delta\{\dot{q}_p\}+[K_{1p}]\delta\{q_p\}+\frac{\partial([K_2]\{q_w\})}{\partial\{q_w\}}\delta\{q_w\}=\{0\}. \qquad (15)$$

$$[M_h]\delta\{\ddot{q}_w\}+\frac{\beta}{\omega}[M_h]\delta\{\dot{q}_w\}+[K_{1h}]\delta\{q_w\}+\frac{\partial([K_3]\{q_p\})}{\partial\{q_w\}}\delta\{q_w\} \qquad (16)$$
$$+\frac{\partial([K_3]\{q_p\})}{\partial\{q_p\}}\delta\{q_p\}+\frac{\partial([K_4]\{q_w\})}{\partial\{q_w\}}\delta\{q_w\}=\{0\}.$$

It is quite complex to obtain the evolution of $\delta\{q_p,q_w$ from the system of equations (15) and (16) and a simplification will be suggested. Because the transverse displacements are more important than the longitudinal, only the system of equations (16) is considered. Also, since the variation $\delta\{q_p\}$ is of a lower order than $\delta\{q_w\}$, the term $\left[\partial([K_3]\{q_p\})/\partial\{q_p\}\right]\delta\{q_p$ is neglected. Consequently, the approach proposed in the following paragraphs should be used with caution when the vibration displacements are large. With these assumptions equation (16) results in:

$$[M_b]\delta\{\ddot{q}_w\}+\frac{\beta}{\omega}[M_b]\delta\{\dot{q}_w\}+[K_{1b}]\delta\{q_w\}+\frac{\partial([K_3]\{q_p\})}{\partial\{q_w\}}\delta\{q_w\} \quad (17)$$
$$+\frac{\partial([K_4]\{q_w\})}{\partial\{q_w\}}\delta\{q_w\}=\{0\}.$$

Matrices $\partial([K_4]\{q_w\})/\partial\{q_w\}$ and $\partial([K_3]\{q_p\})/\partial\{q_w\}$ are periodic functions of time and can be expanded in a Fourier series. If $\{q_w\}$ is of the form (17) with k=3, then we have the following expansions:

$$\frac{\partial([K_4]\{q_w\})}{\partial\{q_w\}}=[pk_{40}]+[pk_{41}]\cos(\omega t)+[pk_{42}]\sin(\omega t)+[pk_{43}]\cos(2\omega t) \quad (18)$$
$$+[pk_{44}]\sin(2\omega t)]+[pk_{45}]\cos(3\omega t)+[pk_{46}]\sin(3\omega t),$$

$$\frac{\partial([K_3]\{q_p\})}{\partial\{q_w\}}=[pk_{30}]+[pk_{31}]\cos(\omega t)+[pk_{32}]\sin(\omega t)]+[pk_{33}] \quad (19)$$
$$\cos(2\omega t)+[pk_{34}]\sin(2\omega t)+[pk_{35}]\cos(3\omega t)+[pk_{36}]\sin(3\omega t),$$

where $[pk_{4i}]$ and $[pk_{3i}]$ are Fourier coefficients.

Multiplying equations (17) by the transpose of the modal matrix $[B]$ and using modal co-ordinates $\{\xi\}$, one arrives at:

$$\left\{\delta\ddot{\xi}\right\}+\frac{\beta}{\omega}[I]\left\{\delta\dot{\xi}\right\}+\left[\omega_j^2\right]\{\delta\xi\}+[B]^T([pk_{40}]+([pk_{41}]+[pk_{31}])\cos(\omega t) \quad (20)$$
$$+([pk_{42}]+[pk_{32}])\sin(\omega t)+([pk_{43}]+[pk_{33}])\cos(2\omega t)+([pk_{44}]+$$
$$[pk_{34}])\sin(2\omega t)+([pk_{45}]+[pk_{35}])\cos(3\omega t)+([pk_{46}]+[pk_{36}])$$
$$\sin(3\omega t))\,[B]\{\delta\xi\}=\{0\}$$

where $\left[\omega_j^2\right]$ is the diagonal matrix of linear natural frequencies.

The solution of (20) is of the form:

$$\{\delta\xi\}=e^{\lambda t}\left(\sum_{i=0}^{k}\{b_i\}\cos(i\omega t)+\sum_{i=1}^{k}\{a_i\}\sin(i\omega t)\right) \quad (21)$$

Inserting (21) into (20) and applying the HBM results in an eigenvalue problem which defines the characteristic exponents λ. If the real part of any λ is positive, then the solution is unstable.

4. NUMERICAL RESULTS AND DISCUSSION

The geometrical non-linear vibrations of aluminium beams clamped at both ends are analysed. Their Young modulus is $E=7\times10^{10}$ N/m^2 and the mass density is $\rho=2778$ Kg/m^3. All the beams have the same width and length, which are, respectively, $b=20$ mm and $L=580$ mm. Following the convergence studies carried out in reference [8], four out-of-plane and eight in-plane shape functions will be used. These are enough to investigate the first two modes of vibration and give a reasonable approximation for the third and fourth modes. The model has 84 degrees of freedom.

The longitudinal inertia is more important when the thickness of the beam is larger. Therefore, beams with the following different thicknesses will be investigated: $h_1=2$ mm (Beam 1), $h_2=20$ mm (Beam 2) and $h_3=50$ mm (Beam 3). Beam 3 is quite thick and is studied here in order to ascertain the effect of longitudinal inertia; however, a correct analysis of Beam 3 might require the use of Timoshenko's beam theory. The first linear natural frequencies, $\omega_{\ell 1}$, of these beams are respectively 192.755 rad/s, 1927.55 rad/s and 4818.87 rad/s. With $p_o=4$, the relation between $\omega_{\ell 2}$ and $\omega_{\ell 1}$ is $\omega_{\ell 2}/\omega_{\ell 1}=2.757$ and the relation between $\omega_{\ell 3}$ and $\omega_{\ell 1}$ is $\omega_{\ell 3}/\omega_{\ell 1}=5.704$.

Applying purely harmonic forces, transversely and concentrated in the middle of the beams, Figure 2, which represents the amplitude of the first harmonic, was obtained. The amplitudes of those forces are 0.05 N, 150 N and 10^4 N, in Beams 1, 2 and 3, respectively.

Regardless off the thickness of the beams, only the first and the third harmonics are present in the response. As an example, Figures 3 and 4 represent the deformations of Beam 2 associated with these harmonics. Both harmonics have symmetric shapes and the influence of the longitudinal inertia is negligible. The same occurs in Beams 1 and 3. Because the frequency is not a parameter in the continuation method, results are not always compared at exactly the same frequencies.

Although it is not shown here for the sake of conciseness, the first and the third harmonics are also the only harmonics present in the response when the beams are excited by transverse harmonic forces at a quarter of their length (position defined by $x=L/4$).

In a second analysis, a transverse excitation with a constant term of 30 N and a harmonic term with amplitude equal to 300 N, referred to as 'constant plus harmonic excitation', was applied in the middle of Beam 2. The variation of the amplitude of the first harmonic with the frequency of excitation is displayed in Figure 5. The constant term and the first three harmonics were excited. The shapes at three different frequencies of vibration are shown in Figure 6, where it is visible that the longitudinal inertia has a negligible effect. The constant term and the first harmonic, have a shape similar to the first linear mode. The second harmonic has a shape that is initially similar to the first linear

mode, but afterwards it is also influenced by the third linear mode. The third harmonic is determined by both the first and third modes. All the harmonics have a symmetric shape.

Finally, an excitation with transverse and longitudinal components, both harmonic, was applied in the middle of Beam 2. The relation between F_2 and F_1 is F_2=0.1 F_1; this occurs in an experimental analysis if the direction of excitation has a small misalignment (6°) with relation to the transverse direction. Figures 7-10 represent the deformations of the constant term, the first, second and third harmonics. The influence of the longitudinal inertia is negligible in the calculation of the first harmonic. There is an expected constant deformation, but the second harmonic is also excited. Both the constant term, the second harmonic and, for larger amplitudes, the third harmonic have different values if the longitudinal inertia is and is not considered. In the Figures shown, the constant term and the second harmonic have a shape similar to the second mode shape and at some frequencies of vibration a shape similar to the fourth mode shape was encountered. Thus, with this type of external force, antisymetric modes are excited. The excitation of the second mode occurred after ω/ω_{f1}=1.38, indicating that its excitation occurs because the frequency of the second harmonic is close to the second natural frequency ($(\omega_{f2}/\omega_{f1})/2$=2.757/2=1.38).

In Figure 11, a result of a stability study is displayed, and one can see that for moderate amplitudes of vibration (around half the thickness of the beam) the simplified approach proposed in section 3 gives plausible results. However, this is not true for larger vibration amplitudes.

For larger amplitudes of vibration, information from the approach proposed in section 3 and from the signal of the Jacobian matrix determinant, as in [4], can be used to carry out an accurate stability study. This method was applied to obtain Figure 12. The unstable solutions on the upper part of the curve are instabilities of second order [6]: they occur on the neighbourhood of $\omega_{f2}/2$ and the characteristic exponents are complex conjugates with a positive real part.

5. CONCLUSION

It was demonstrated that when the excitation is transverse and harmonic, only odd harmonics occur in the geometrical non-linear response of Bernoulli-Euler beams. This happens even when considering the longitudinal inertia of quite thick beams. On the other hand, if the excitation is a transverse harmonic and with a small constant term, an expected constant term and the second harmonic are present in the response. In both of the former cases, the longitudinal inertia can be neglected. Consequently, the longitudinal displacements can be obtained from equation (10) and the system of equations (11) results in a system of equations of the Duffing type.

When the excitation has a transverse and a small longitudinal term the response includes a constant term (or constant deformation), odd and even harmonics. With an excitation frequency close to the first natural frequency, the constant term and the even harmonics have an antisymetric shape, whilst the odd harmonics' shape is symmetric. When the excitation has a transverse and a longitudinal term, and if accurate solutions are needed, the longitudinal inertia should not be neglected and thus the equations of motion have quadratic and cubic non-linearities.

One possible explanation for the appearance of even harmonics in experimental analyses was hence found: not purely transverse or not purely harmonic excitations.

A simplified study of the stability, where both the longitudinal and the transverse displacements are considered, was proposed. It gives accurate results for moderate non-linearities, namely for vibration displacements of the order of half the beam's thickness.

REFERENCES

1. Bennouna M.M., White R.G., The effects of large vibration amplitudes on the fundamental mode shape of a clamped-clamped uniform beam. *J. of Sound and Vibr.*, 1984, **96**, 309-331.
2. Benamar R., Bennouna M.M., White R.G., The effects of large vibration amplitudes on the mode shapes and natural frequencies of thin elastic structures. Part I: simply supported and clamped-clamped beams. *J. of Sound and Vibr.*, 1991, **149,** 179-195.
3. Lewandowski R. Non-linear free vibrations of beams by the finite element and continuation methods. *J. of Sound and Vibr.*, 1994, **170**, 577-593.
4. Ribeiro P., Petyt M., Nonlinear vibration of beams with internal resonance by the hierarchical finite element method. *J. of Sound and Vibr.*, 1999, **224**, 591-624.
5. Shi Y. and Mei C., A finite element time domain modal formulation for large amplitude free vibration of beams and plates. *J. of Sound and Vibr.*, 1996, **193**, 453-464.
6. Szemplinska-Stupnicka W., *The Behaviour of Non-linear Vibrating Systems*, Kluwer Academic, Dordretch, 1990.
7. Chia, C.Y. *Nonlinear Analysis of Plates*, McGraw-Hill, New York, 1980.
8. Ribeiro P. Geometrical Nonlinear Vibration of Beams and Plates by the Hierarchical Finite Element Method. Ph.D. Thesis, University of Southampton, 1998.

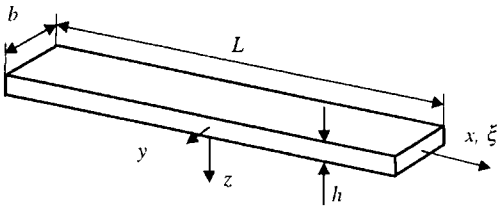

Figure 1. Beam, local and global co-ordinate systems

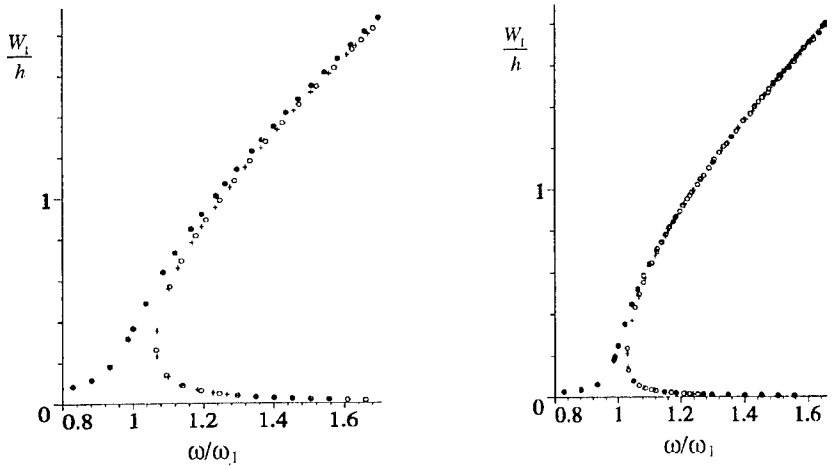

a) Beam 1

b) Beam 2

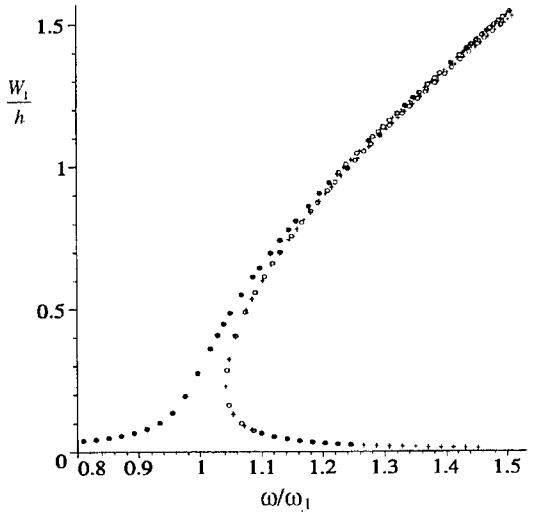

c) Beam 3

Figure 2. Response to transverse harmonic excitation at x=0, with (+) and without (o) in-plane inertia.

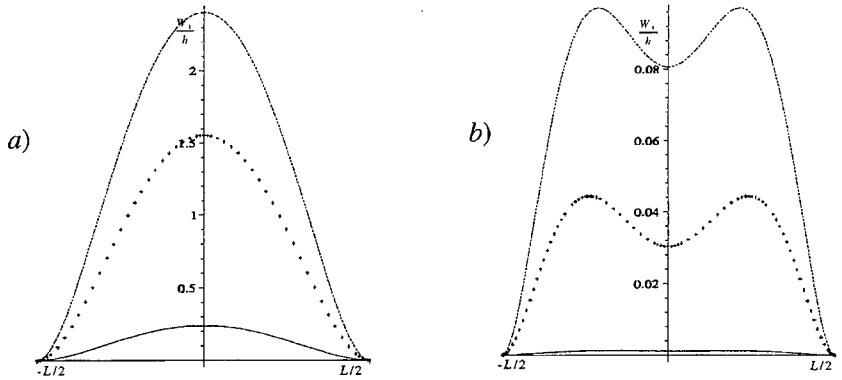

Figure 3. First, *a*), and third, *b*), harmonics of Beam 2, at ω/ω_{f1}=1.0014, ω/ω_{f1}=1.5155 and ω/ω_{f1}=2.0310, without in-plane inertia. Harm. excitation.

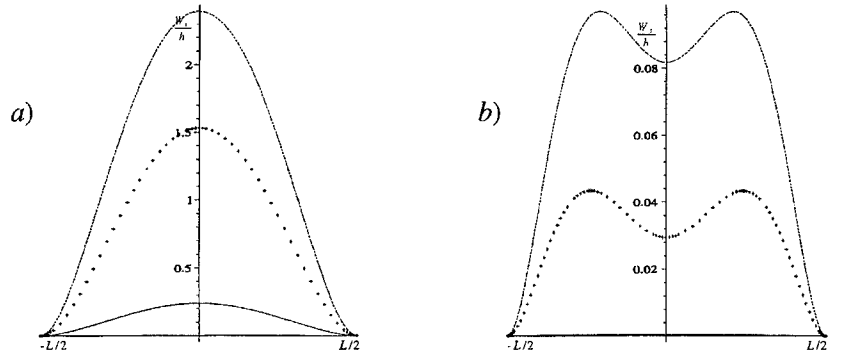

Figure 4. First, *a*), and third, *b*), harmonics of Beam 2 at ω/ω_{f1}=1.0014, ω/ω_{f1}=1.5040, ω/ω_{f1}=2.0247, with in-plane inertia. Harmonic excitation.

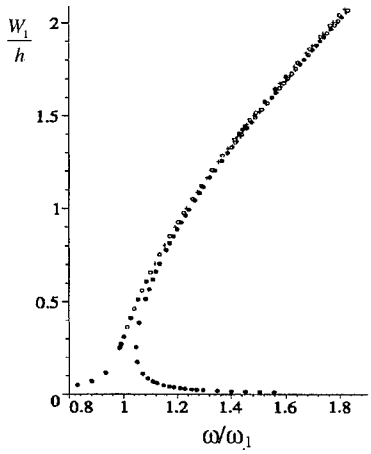

Figure 5. Response to harmonic plus constant excitation, at x=0, Beam 2, with (+) and without (o) in-plane inertia.

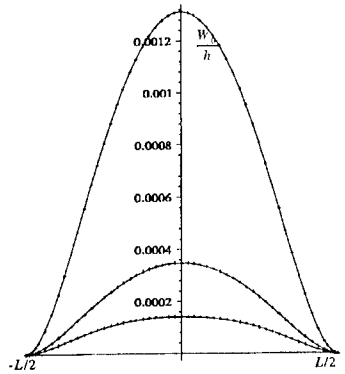

a) Constant term

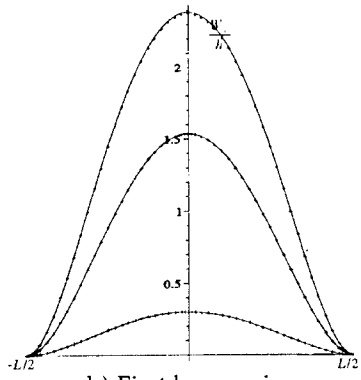

b) First harmonic

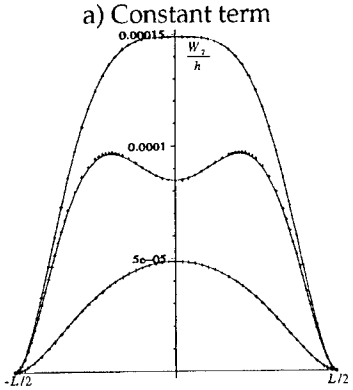

c) Second harmonic

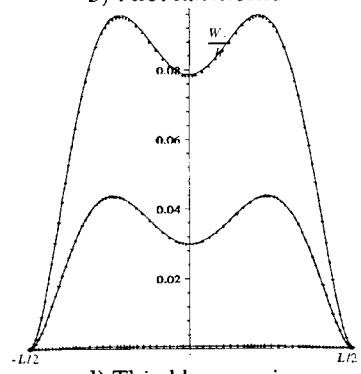

d) Third harmonic

Figure 6. Harmonic coefficients' of Beam 2 in the following orders:

a) and c) ω/ω_1=1.0016, ω/ω_1=2.0194, ω/ω_1=1.5046

b) and d) ω/ω_1=1.0016, ω/ω_1=1.5046, ω/ω_1=2.0194

with (++) and without (-) in-plane inertia, constant plus harm. excitation.

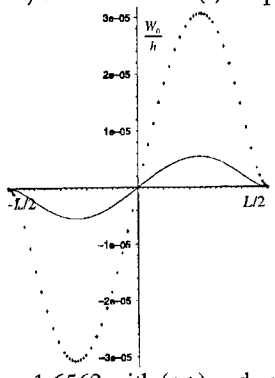

a) ω/ω_1=1.6563 with (++) and without ω/ω_1=1.6562 (-) in-plane inertia

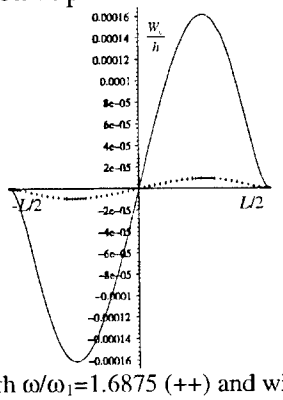

b) with ω/ω_1=1.6875 (++) and without ω/ω_1=1.6876 (-) in-plane inertia

Figure 7. Constant term of Beam 2, transverse and longitudinal harmonic excitation.

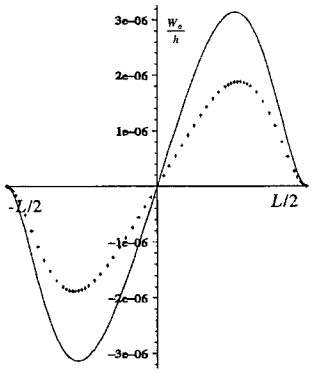

c) with ω/ω_{f1}=1.8128 (+) and without ω/ω_{f1}=1.8212 (-) in-plane inertia

Figure 7. Constant term, Beam 2, transverse plus longitudinal harm. excit.

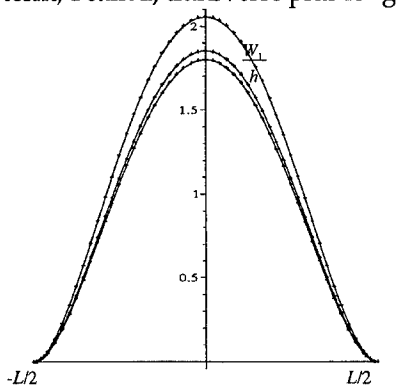

Figure 8. First harmonic at ω/ω_{f1}=1.6563, ω/ω_{f1}=1.6875, ω/ω_{f1}=1.8212, Beam 2 with (++) and without (-) in-plane inertia, harmonic transverse and longitudinal excitation.

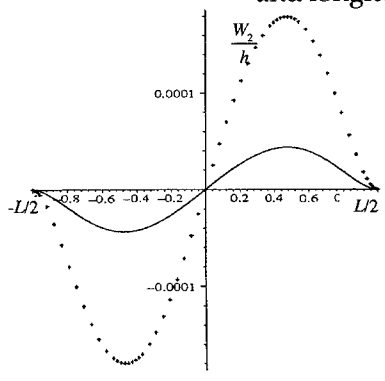

a) ω/ω_1=1.6563

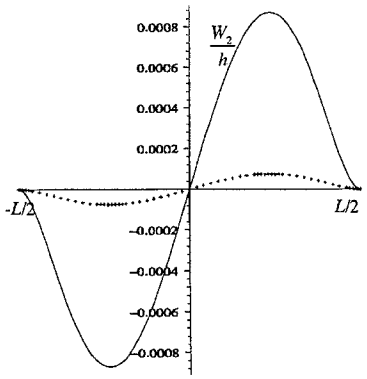

b) ω/ω_1=1.6875.

Figure 9. Second harmonic, Beam 2 with (++) and without (-) in-plane inertia, transverse and longitudinal harmonic excitation.

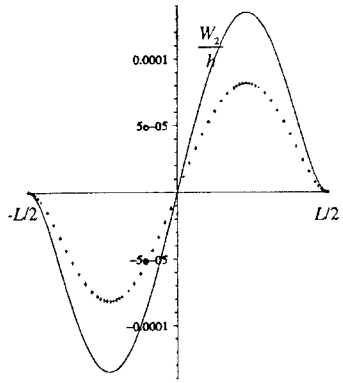

Figure 9 c). As in Figure 9, but $\omega/\omega_{f1}=1.8212$.

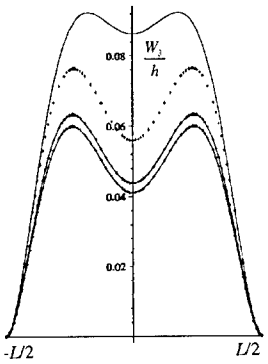

Figure 10. Third harmonic $\omega/\omega_{f1}=1.6563$, $\omega/\omega_{f1}=1.6875$, $\omega/\omega_{f1}=1.8212$, Beam 2 with (+) and without (-) in-plane inertia, transv. and longitud. exc.

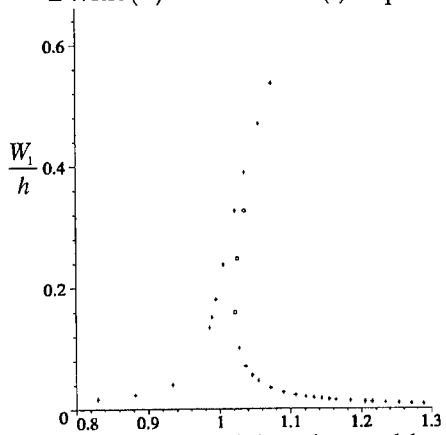

Figure 11. Stable (+) and unstable (o) solutions.

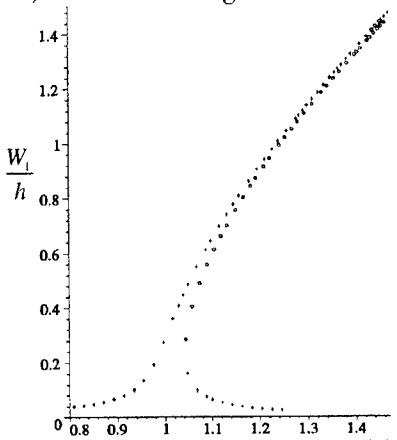

Figure 12. Stable (+) and unstable (o) solutions.

EXPERIMENTAL INVESTIGATION ON THE OCCURRENCE OF INTERNAL RESONANCES IN A CLAMPED-CLAMPED BEAM

P. Ribeiro, J. Marinho and L. Alves
DEMEGI, Faculdade de Engenharia, Universidade do Porto,
Rua dos Bragas, 4050-123 Porto, Portugal. e-mail: *pmleal@fe.up.pt*

ABSTRACT

The geometrical non-linear vibration of an aluminium beam clamped at both ends, is experimentally investigated with the goal of verifying the occurrence of internal resonances. The beam is excited transversely with a harmonic excitation and the deflection of the first and higher harmonics analysed in order to detect the mode shapes involved. 1:3 and 1:5 internal resonances between the first and higher order modes and between the second and higher order modes are found.

1. INTRODUCTION

The non-linear mode shape of a beam vibrating with large displacements and clamped at both ends changes with the amplitude of vibration because of two main reasons. The first is the fact that the longitudinal forces stiffen the beam, causing a smooth variation of the mode shape. Several authors have demonstrated this, both theoretically and experimentally [1-4]. The second reason is modal coupling. The response of a non-linear beam excited at a certain frequency involves the frequency of excitation and some of its harmonics. Because the natural frequencies change with the vibration amplitude, they can become commensurate (i.e., related by $m_1\omega_1+m_2\omega_2+ \ldots + m_n\omega_n\cong 0$, where m_i are integers) and energy can be interchanged between different modes of vibration. If this phenomenon, known as internal resonance, occurs, then the vibration is defined by the coupled modes and the non-linear mode shape changes considerably along the period of vibration.

Internal resonances between the first mode and higher order modes have been detected in numerical and analytical analyses of the geometrical non-linear vibration of beams [1, 5, 6]. The multi-modal vibrations and strong variation of the mode shape during the period of vibration, which result from internal resonance, were also clearly demonstrated by analytical and numerical methods [1].

In this work, the geometrical non-linear vibration of an aluminium beam clamped at both ends is investigated, with the goal of experimentally verifying the occurrence of internal resonances.

2. MEASUREMENTS AND ANALYSIS

2.1 Experimental details

Experimental work was carried out on a slender beam of dimensions 585×30×3 mm, made of an aluminium alloy. This beam was clamped at its ends in two steel blocks, which were screwed to a heavy steel table. An electromagnetic exciter was attached to the beam by means of a drive rod and of a force transducer. The signal sent to the shaker was generated by the analyser and amplified by a power amplifier. Figure 1 represents the experimental set-up.

A slow frequency sweep was performed to identify the non-linear phenomena of interest. In order to avoid transients, some time was given before collecting data after each increment in frequency. The beam was divided into seventeen points (Figure 2). However, due to the symmetry of the system, most often measurements were only taken along half span (points 1 to 9).

The resonance frequencies change with the amplitude of vibration, and sub-harmonic and super-harmonic resonances may be important. Therefore, it may be misleading to try to detect which modes are involved in the response with a basis on the power spectra alone. By measuring the shapes associated with each harmonic, the modes involved in the response were detected with more certainty.

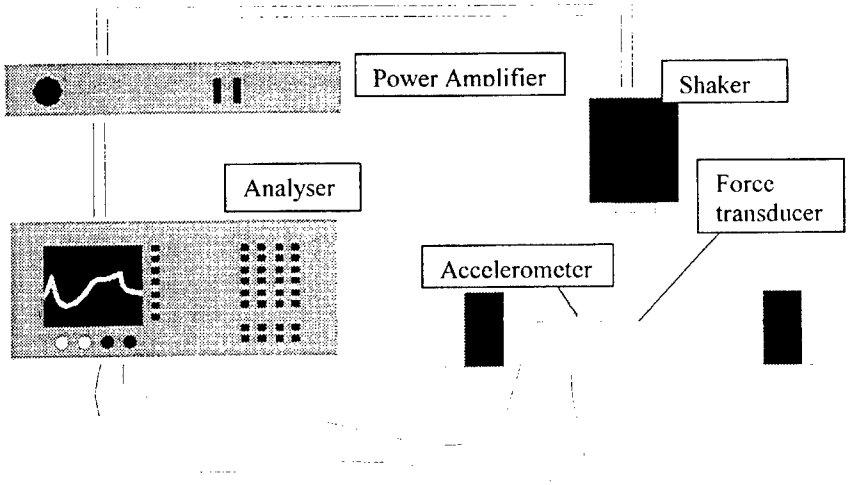

Figure 1. Experimental set-up.

Figure 2. Measurement points.

The accelerometer mass is 4.8 g and the force transducer's is 30 g (part of its weight is supported by the shaker though). Since the weight of the portion of the beam between clamps is 147.6 g, the mass of the transducers has a meaningful influence on the results. This is reflected on the different estimations obtained for the natural frequencies using a hammer - therefore without a force transducer connected to the beam - and using the electromagnetic exciter (Table 1). The position of the transducers also influenced the natural frequencies, and thus the ones tabulated are average ones.

Table 1. Natural Frequencies (Hz).

Natural Frequency (rad/s)	Hammer	Electromagnetic exciter
$\omega_{\ell 1}$	47	39.5
$\omega_{\ell 2}$	126	118
$\omega_{\ell 3}$	245	232.5
$\omega_{\ell 4}$	-	366.9

The first four linear modes and the seventeen points where the accelerometer was fixed are represented in Figure 3.

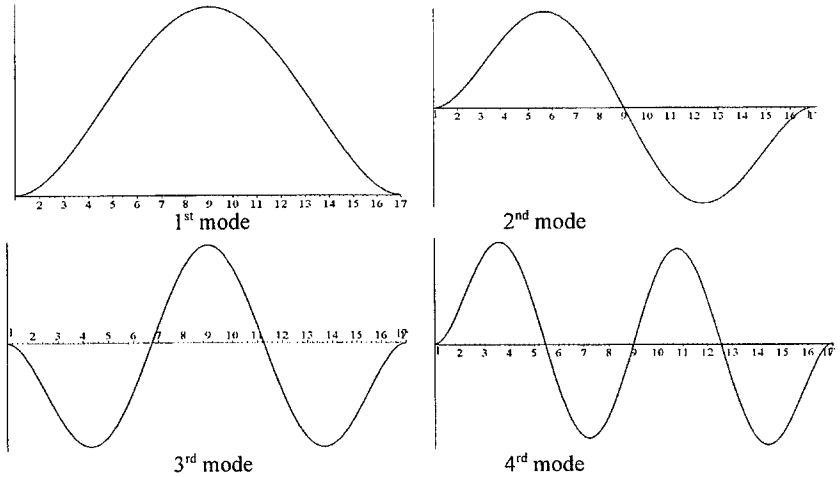

Figure 3. First four linear mode shapes

2.2 Modal coupling between the first and higher order modes

In order to detect modal coupling between the first and higher order modes, the beam was excited transversely at its mid span with sine excitations. Three excitation amplitudes were applied: 0.25, 0.5 and 0.8 N.

These values should be considered as approximated ones, because there was no closed-loop system to absolutely guarantee that the force applied by the shaker was constant during the frequency sweep and because of the force transducer's inertia.

Figures 4-6 represent the displacement amplitudes of the first, third and fifth harmonics of the response, when the excitation amplitude is respectively 0.25, 0.5 and 0.8 Newton. The displacements are shown at point 9, which is located at the middle of the beam, and at point 5, where the amplitudes of the second and third mode shapes are large (Figure 3). *h* represents the thickness of the beam.

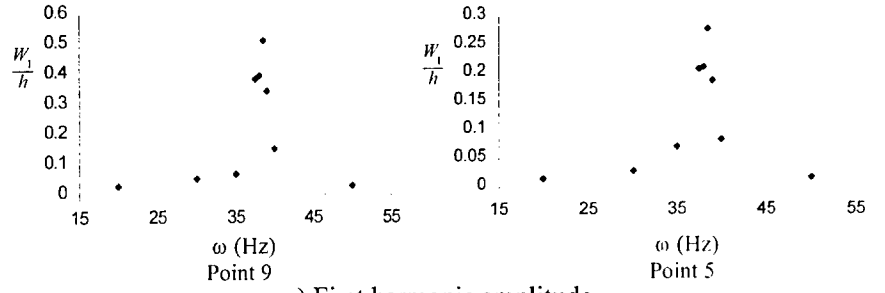

a) First harmonic amplitude.

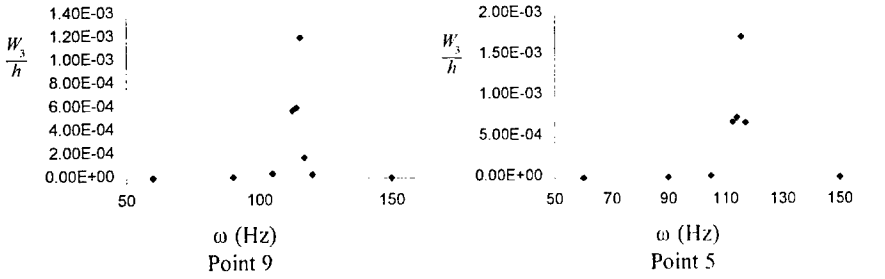

b) Third harmonic.

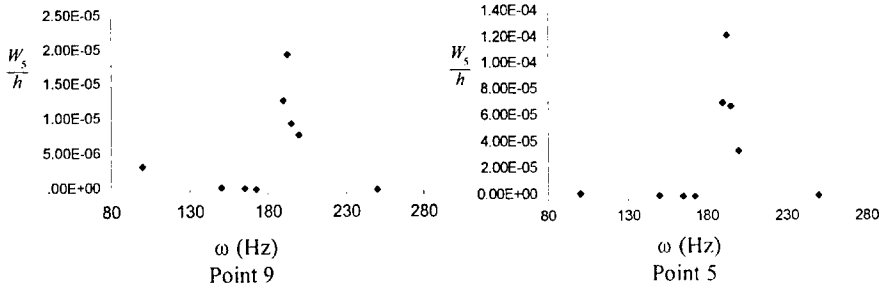

c) Fifth harmonic

Figure 4. First three harmonic's amplitude, excitation amplitude F= 0.25 N.

Analytical and numerical analyses of geometrical non-linear beam vibration, under the action of a transverse harmonic force, only predict odd harmonics in the response, and we will concentrate on these ones. However, it should be pointed out that there are actually some even harmonics in the response. Probably, this occurs because it is very difficult to apply a force that is purely harmonic and apply it exactly in the transverse direction. Small deviations from an exact harmonic and transverse excitation cause the appearance of even harmonics in the response [7].

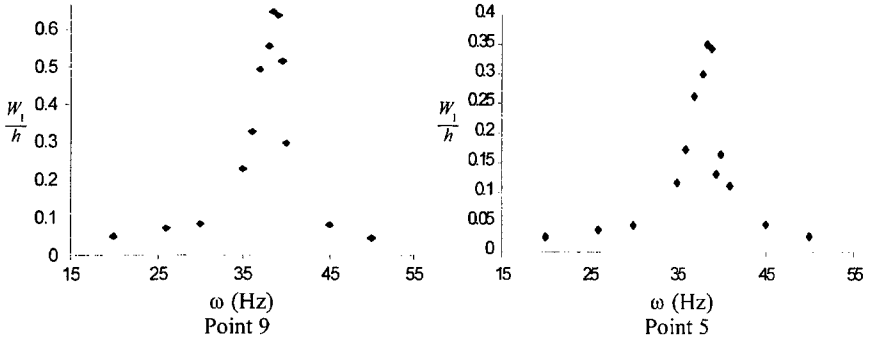

a) First harmonic.

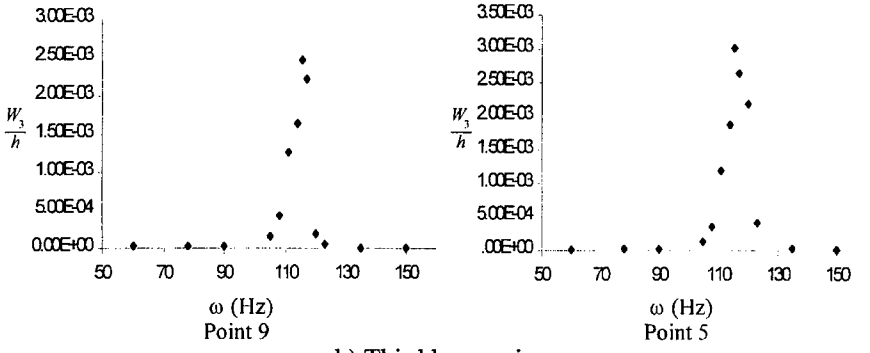

b) Third harmonic.

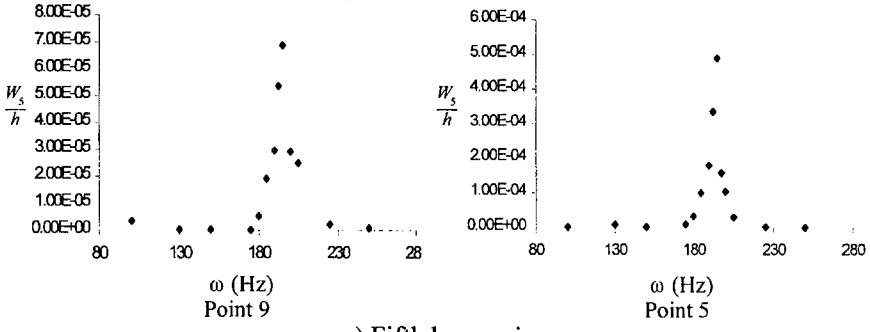

c) Fifth harmonic

Figure 5. First three harmonic's, F=0.5 N.

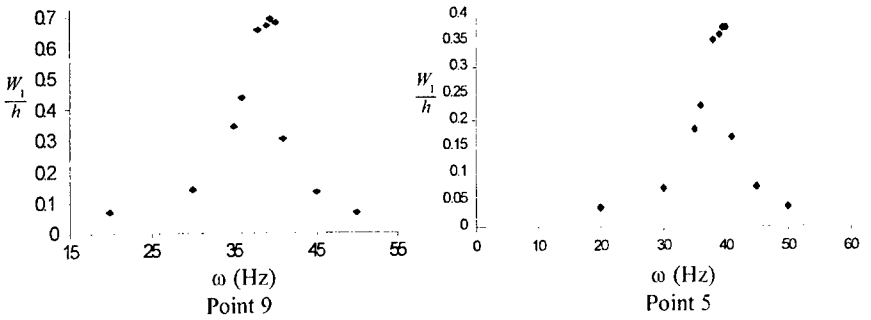

a) First harmonic's amplitude.

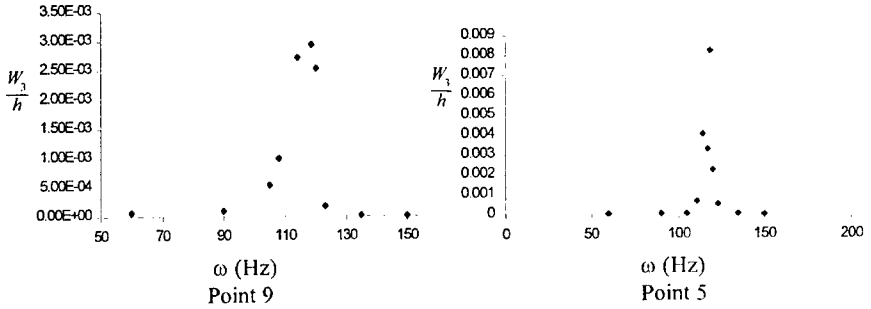

b) Third harmonic.

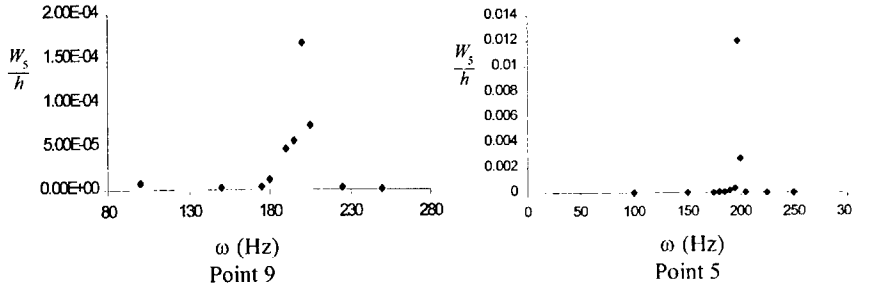

c) Fifth harmonic

Figure 6. First three harmonic's, F=0.8 N.

The first harmonic increases slightly with the force amplitude. On the other hand the third and fifth harmonics increase very much. The "bending" of the curve, a characteristic of non-linearity, is particularly visible in Figure 6a. Due to hard spring effect, this bending occurs towards the right.

In Figure 7a the shapes assumed by the first and third harmonics, when the excitation frequency is equal to 38.5 Hz and the excitation amplitude is 0.25 N, are shown. Since the modes are symmetric or antisymmetric, only one half of the beam is displayed. The first harmonic's shape is similar to the first linear mode shape and the third harmonic's shape seems to be defined by the second mode and by the first one.

Figure 7b displays the shape of the same harmonics, when the excitation frequency is equal to 40 Hz and the excitation amplitude is 0.8 N. The first harmonic's shape is similar to the first linear mode shape. The third harmonic's shape is defined by the second mode (the maximum amplitude of vibration occurs at point five) and by the first one, but the importance of the second mode is much greater now than in Figure 7a.

When the excitation frequency is 38.5 Hz (Figure 7a) and 40 Hz (Figure 7b), the third harmonic occurs at, respectively, 118.5 Hz and 120 Hz, i.e., close to the second linear frequency. Due to this and to the coupling caused by the non-linearity, the second mode of vibration is excited by the first. Since the non-linearity increases with the amplitude of excitation, the second mode is more excited in the second case.

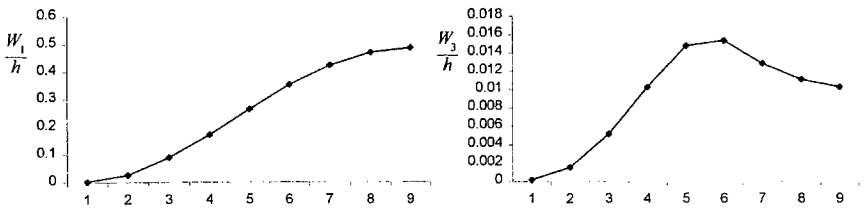

a) First harmonic. b) Third harmonic.

Figure 7a. Shapes of the first and third harmonics. Excitation amplitude F=0.25 N and excitation frequency ω=38.5 Hz

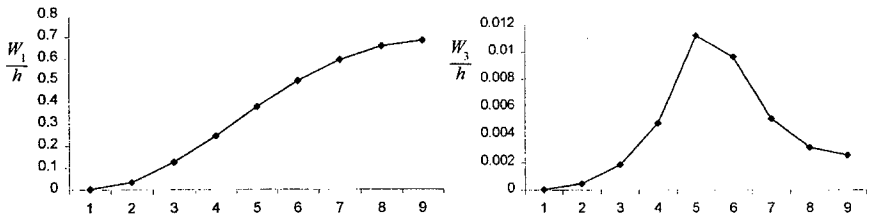

a) First harmonic. b) Third harmonic.

Figure 7b. Shapes of the first and third harmonics. F=0.8 N, ω=40 Hz.

In Figure 8 the shapes assumed by the first harmonic at 39.5 Hz and by the fifth harmonic at 197.5 HZ, when the excitation amplitude is 0.8 N are shown. The first harmonic's shape is similar to the first linear mode shape. The fifth harmonic's shape seems to be defined mainly by the third (the maximum amplitude of vibration occurs at point four) and first modes. The third linear natural frequency of vibration occurs

around 220 Hz, i.e. close to the fifth harmonic. When the beam is vibrating with large displacement amplitudes, the non-linearity has a substantial effect, and the third mode of vibration is strongly excited by the first mode due to a 1:5 internal resonance. In terms of displacements this is slightly more important than the 1:3 internal resonance formerly discussed. The 1:5 internal resonance has a much greater effect than the 1:3 one, if we consider the accelerations instead.

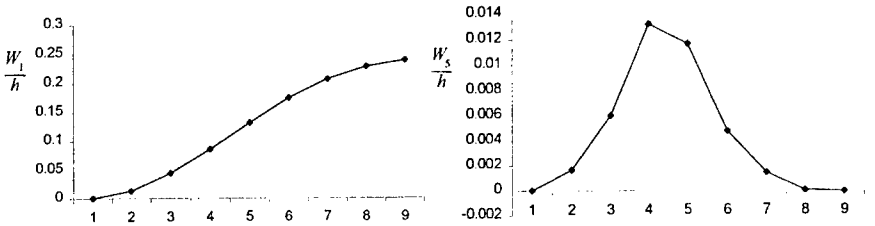

a) First harmonic. b) Fifth harmonic.

Figure 8. First and fifth harmonics along one half of the beam, F=0.8 N.

2.3 Modal coupling between the second and higher order modes

In order to detect modal coupling between the second and higher order modes, the beam was transversely excited at point five, with a harmonic excitation and with frequencies around the second natural frequency. The displacements associated with the first and higher harmonics were analysed.

In Figure 9 the frequency spectra of the response when the excitation amplitude is 0.25 N (as before, this value is approximated) is shown.

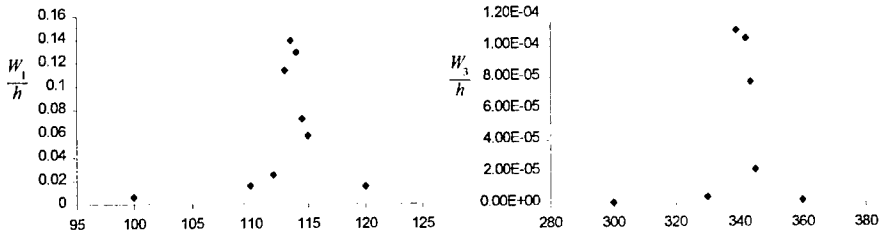

Figure 9. First and third harmonic's, F 0.25 N, point 9.

Figure 10 shows the shape of the first and third harmonics, for a frequency of excitation equal to 113 Hz. The first harmonic is linked with the second mode, and the third with the fourth mode. With this frequency of excitation the third harmonic is 339 Hz, and consequently

the fourth mode is excited by the second due to a 1:3 internal resonance.

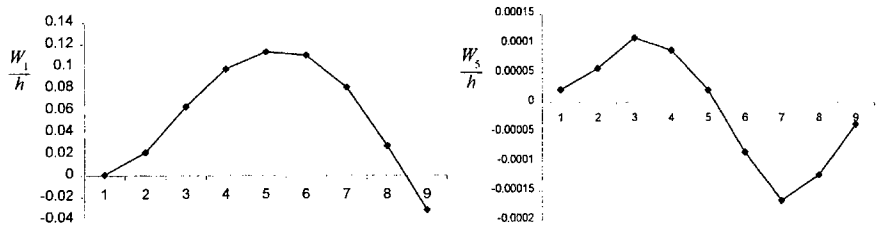

a) First harmonic. b) Third harmonic.

Figure 10. Shapes of the first and third harmonics along one half of the beam, F=0.25 N.

3. CONCLUSIONS

A clamped-clamped beam was excited transversely with a sine excitation and the deflection of the first and higher harmonics analysed in order to detect the modes involved in the response.

A 1:3 internal resonance between the first and second modes and a 1:5 internal resonances between the first and third modes were found. A 1:3 internal resonance between the second and fourth mode was also detected. These results qualitatively agree with the ones from reference [1], with the exception of the 1:3 internal resonance between the first and second modes, which was not predicted in that reference.

The internal resonances occur due to the coupling caused by the non-linearity. The non-linearity increases with the vibration amplitude, and, as expected, the internal resonance effect is more important for larger vibration amplitudes.

However, it is apparent that internal resonances occur quite easily, and they are already present at moderate amplitudes of vibration. This confirms that caution is necessary in analytical works, when assuming that the dynamic behaviour of a structure may be modelled by a very restricted number of linear modes.

It was found that internal resonance of order n may exist when the ratio of the natural frequencies of the interacting modes is close, but slightly different, from n. By other words, $\omega_{\ell k2}/\omega_{\ell k1} \cong n$, where the subscripts $k1$ and $k2$ represent two different modes, but there is some margin in the signal "$\cong$". Possibly, the explanation for this lies in the fact that one should add to the coupling caused by the non-linearity, some coupling caused by damping.

ACKNOWLEDGMENTS

Mr. Hernâni Lopes' introduction to the equipment in the laboratory is gratefully acknowledged.

REFERENCES

1. Ribeiro, P. and Petyt, M., Non-linear vibration of beams with internal resonance by the hierarchical finite element method. *J. of Sound and Vibr.*, 1999, **224**, 591-624.

2. Benamar, R., Bennouna, M.M. and White, R.G., The effects of large vibration amplitudes on the mode shapes and natural frequencies of thin elastic structures. Part I: simply supported and clamped-clamped beams. *J. of Sound and Vibr.*, 1991, **149**, 179-195.

3. Bennouna, M.M. and White, R.G., The effects of large vibration amplitudes on the fundamental mode shape of a clamped-clamped uniform beam. *J. of Sound and Vibr.*, 1984, **96**, 309-331.

4.Wolfe, H., An experimental investigation of nonlinear behaviour of beams and plates excited to high levels of dynamic response. Ph.D. Thesis, University of Southampton, 1995.

5. Lewandowski, R., Non-linear free vibrations of beams by the finite element and continuation methods. *J. of Sound and Vibr.*, 1994, **170**, 577-593.

6. Nayfeh, A. H. and Balachandran, B., Modal interactions in dynamical and structural systems. *Applied Mechanics Review* 1989, **42**, S175 - S201.

7. Ribeiro, P., Even harmonics on the steady-state geometrical, non-linear forced vibration of beams. In *Proceedings of the 7th International Conference - Structural Dynamics: Recent Advances.* Southampton, England, 2000.

DYNAMIC LARGE DEFLECTION ANALYSIS OF ELASTIC-PLASTIC BEAMS AND PLATES

E. Manoach
Bulgarian Academy of Sciences
Institute of Mechanics
Acad. G. Bonchev Str. Bl. 4; 1113 Sofia, Bulgaria
Phone: + 359 2 717186 Fax: + 359 2 707498 e - mail: manoach@bgcict.acad.bg

Abstract

An investigation of large deflections of elastic-plastic beams and plates are investigated by the pseudo-normal mode superposition method is presented. The geometrical nonlinear versions of the Mindlin plate theory and the Timoshenko beam theory was used in the analysis. The results obtained numerically for the responses of beams and circular plates were compared with published experimental and numerical results as well as with existing analytical solutions.

1. Introduction

The problems of the response of thin-walled structures such as beams and plates subjected to large dynamic loads are important in engineering practice. Their detailed investigations are a research subject for many investigators. The correct solution of these problems requires accounting for the material nonlinearities as well as the geometrical effects at the modeling of the deformation process.

For moderately thick beams and plates subjected to large dynamic loads, which lead to arising of plastic strains, the transverse shear forces exert an important influence on the behavior of the structures. Some of the often used small deflection theories which take into account the shear deformation and rotatory inertia are the Timoshenko beam theory and the Mindlin plate theory.

The objective of this study, being an extension of [1]- [3], is to specify the influence of large transverse deflections on the dynamic response of moderately thick elastic-plastic beams and plates within the context of the nonlinear versions of the Timoshenko beam theory and the Mindlin plate theory.

The pseudo-normal mode superposition technique was used in [1] to investigate the axisymetrically forced vibrations of circular plates described by the small deflections Mindlin plate theory. The yield criterion used in this paper is expressed in terms of bending moments only, thus neglecting the influence of the shear forces in the plastic yielding. Moreover, this assumption does not allow to observe the propagation of the plastic zone along plate thickness, which could be important for many applications.

This disadvantage was overcome in [2] where this method was adopted for solving the dynamic response of thick elastic-plastic beams. Two types of yield conditions have been considered there: when the yield surface is a function of the bending and transverse shear stresses, and when the yield surface is a function of the bending stresses only.

In [3] the pseudo-normal mode superposition method was extended for a large deflection analysis of elastic-plastic Mindlin circular plates but assumed that the relationships between the in-plane stress resultants and the strains remain elastic.

In this paper the internal inconsistency of the model used in [3] is overcome, and the method is developed for large deflections of beams and plates taking into account elastic-plastic relationship between all stresses and strains. Damping coefficients, which are assumed to be proportional to the mass terms, are also introduced into the governing equations.

The developed algorithm and computer programs are used to investigate the forced vibrations of elastic-plastic beams and plates subjected to pulse loading. The comparisons with existing numerical and experimental solutions are provided in order to estimate the method's applicability. Some comparisons are made with the exact formulas for rigid plastic solutions [4] for the impulse loaded plates.

2. Basic equations

2.1. Plate equations

The governing equations, describing the motion of a moderately thick circular plate with radius R subjected to a pulse load $p(r,t)$ symmetrically disposed about an axis perpendicular to the plate and passing through its center may be written in the form

$$\frac{\partial N_r}{\partial r}+\frac{N_r-N_t}{r}-c_1\frac{\partial u}{\partial t}-\rho h\frac{\partial^2 u}{\partial t^2}=0$$

$$\frac{\partial M_r}{\partial r}+\frac{M_r-M_t}{r}-Q_r-c_2\frac{\partial \psi}{\partial t}-\frac{\rho h^3}{12}\frac{\partial^2 \psi}{\partial t^2}=0 \quad r<R,\ t>0; \qquad (1\text{ a-c})$$

$$\frac{\partial Q_r}{\partial r}+\frac{Q_r}{r}+N_r\left(\frac{\partial^2 w}{\partial r^2}+\frac{1}{r}\frac{\partial w}{\partial r}\right)+\frac{\partial N_r}{\partial r}\frac{\partial w}{\partial r}-c_1\frac{\partial w}{\partial t}-\rho h\frac{\partial^2 w}{\partial t^2}=-p(r,t)$$

In Eqns (1), N_r and N_t are the radial and the circumferential stress resultants per unit length in the mid-plane of the plate respectively, M_r and M_t are the corresponding bending moments, Q_r is the transverse shear force per unit length, u and w are the radial and transverse displacements, ψ is the angular rotation, ρ is the material density, h is the plate thickness, r is the radial distance of points in the middle plane and t is the time. With c_1 and c_2 are denoted the damping coefficients which are assumed to be proportional to the mass terms ρh and $\rho h^3/12$, respectively.

The strain and curvature-displacements relationships associated with the mid-plane, which consider large displacements and shear can be expressed as

$$\varepsilon_r^0 = \frac{\partial u}{\partial r} + \frac{1}{2}\left(\frac{\partial w}{\partial r}\right)^2, \quad \varepsilon_t^0 = \frac{u}{r}, \quad \varepsilon_{rz}^0 = \psi + \frac{\partial w}{\partial r}, \quad .$$

$$\kappa_r^0 = \frac{\partial \psi}{\partial r}, \quad \kappa_t^0 = \frac{\psi}{r} \qquad \text{(2a-e)}$$

2.2 Beam equations

The governing equations, used for describing the motion of a beam with length L, thickness h and width b are

$$\frac{\partial N}{\partial x} - c_1 \frac{\partial u}{\partial t} - \rho F \frac{\partial^2 u}{\partial t^2} = 0$$

$$\frac{\partial M}{\partial x} + Q - c_2 \frac{\partial \psi}{\partial t} - \rho I \frac{\partial^2 \psi}{\partial t^2} = 0 \qquad 0<x<L,\ t>0 \qquad \text{(3 a-c)}$$

$$\frac{\partial Q}{\partial x} + N\left(\frac{\partial^2 w}{\partial x^2}\right) + \frac{\partial N}{\partial x}\frac{\partial w}{\partial x} - c_1 \frac{\partial w}{\partial t} - \rho F \frac{\partial^2 w}{\partial t^2} = -p(x,t)$$

where $F=bh$ is the area of the beam cross-section and $I=bh^3/12$.

The strain and curvature-displacements relationships associated with the mid-axes of the beam which consider large displacements and shear can be expressed as

$$\varepsilon_x^0 = \frac{\partial u}{\partial x} + \frac{1}{2}\left(\frac{\partial w}{\partial x}\right)^2, \quad \varepsilon_{xz}^0 = \psi + \frac{\partial w}{\partial x}, \quad \kappa^0 = \frac{\partial \psi}{\partial x} \qquad \text{(4 a-c)}$$

2.3. Constitutive equations

Taking into account the circumstance that the beam equations can be considered as a variant of the plate equations further the equations concerning the plate will be shown mainly.

Denoting by **S** the stress vector $\mathbf{S} = \{\sigma_r, \sigma_t, \sigma_{rz}\}^T$ and by ε the vector of strains $\varepsilon = \left\{\varepsilon_r^0 + zk_r^0, \varepsilon_t^0 + zk_r^0, f(z)\varepsilon_{rz}^0\right\}^T$, the constitutive equations for the plate can be presented in the following form:

$$\mathbf{S}=[\mathrm{D}]\,\varepsilon \qquad (5)$$

where in the case of an elastic material

$$[D] = [D^e] = \begin{bmatrix} A & \nu A & 0 \\ \nu A & A & 0 \\ 0 & 0 & kG \end{bmatrix} \qquad (6)$$

is the elastic matrix, f(z) is a function describing the distribution of the shear strains along the thickness, G is the shear modulus and k is a constant. In all following considerations it is accepted that $f(z) = 1-4z^2/h^2$.

The bending moments, the shear force and in-plane stress resultants are expressed by the stresses as follows

$$M_r = \int_{-h/2}^{h/2} \sigma_r z\, dz, \quad M_t = \int_{-h/2}^{h/2} \sigma_t z\, dz, \quad Q_r = \int_{-h/2}^{h/2} \sigma_{rz}\, dz$$
$$N_r = \int_{-h/2}^{h/2} \sigma_r\, dz \quad N_t = \int_{-h/2}^{h/2} \sigma_t\, dz \tag{7}$$

Based on the von Mises criterion the yield surface including the shear and the bending stresses is expressed as

$$\phi(\mathbf{S}) = \left\{\sigma_r^2 + \sigma_t^2 - \sigma_r\sigma_t + 3\sigma_{rz}^2\right\}^{1/2} - \sigma_p \geq 0, \tag{8}$$

where σ_p is the yield stress in simple tension.

After yielding, during infinitesimal increment of the stresses, the changes of strains are assumed to be divided into elastic and plastic parts

$$\Delta\varepsilon = \Delta\varepsilon^e + \Delta\varepsilon^p \tag{9}$$

where

$$\Delta\varepsilon^e = \left[D^e\right]^{-1}\Delta\mathbf{S} \tag{10}$$

By using Eqns (8), (9) and the associated flow rule [5], following Yamada and others [6], the following explicit expression between increments of stresses and strains is obtained

$$\Delta\mathbf{S} = \left[D^{ep}\right]\Delta\varepsilon \tag{11}$$

where $\left[D^{ep}\right]$ is the elastic-plastic matrix:

$$\left[D^{ep}\right] = \left[D^e\right] - \left[D^e\right]\left\{\frac{\partial\phi}{\partial\mathbf{S}}\right\}\left\{\frac{\partial\phi}{\partial\mathbf{S}}\right\}^T\left[D^e\right]\left[H + \left\{\frac{\partial\phi}{\partial\mathbf{S}}\right\}^T\left[D^e\right]\left\{\frac{\partial\phi}{\partial\mathbf{S}}\right\}\right]^{-1} \tag{12}$$

2.4. Boundary and initial conditions

The dynamic plate (beam) response is studied in the case of two kinds of boundary conditions:

$$u(0,t)=u(R,t)=w(R,t)=0 \text{ and } M(R,t)=0 \tag{13 a-d}$$

for a simply supported in-plane fixed plate and

$$u(0,t)=u(R,t)=w(R,t)=0 \text{ and } \psi(R,t)=0 \tag{14 a-d}$$

for a clamped, in-plane fixed plate.

The initial conditions are:

$$w(r,0)=w^0(r), \quad \dot{w}(r,0) = \dot{w}^0(r),$$
$$\psi(r,0)=\psi^0(r), \quad \dot{\psi}(r,0) = \dot{\psi}^0(r) \tag{15 a-d}$$

3. Solution of the problem

3.1. Reorganizing of equations of motion

Let the total time interval T on which the dynamic response is desired, be divided into sequence of time increments $[t_i, t_{i+1}]$ and $l = t_{i+1}-t_i$. Making Eqn (1) dimensionless as regards R - $\bar{r} = r / R$, $\bar{u} = u / R$, $\bar{w} = w / R$, and then omitting the bars, neglecting the mid-plane inertia effects and by using Eqns (3)-(7), the governing equations can be written in the following form:

$$\frac{\partial^2 u}{\partial r^2}+\frac{1}{r}\frac{\partial u}{\partial r}-\frac{u}{r^2}=G_u^p$$

$$\frac{\partial^2 \psi}{\partial r^2}+\frac{1}{r}\frac{\partial \psi}{\partial r}-\frac{\psi}{r^2}-\beta\left(\frac{\partial w}{\partial r}+\psi\right)-d_2\frac{\partial w}{\partial t}-\alpha\lambda^2\frac{\partial^2 \psi}{\partial t^2}=G_1^p, \quad (16\text{ a-c})$$

$$\beta\left(\frac{\partial^2 w}{\partial r^2}+\frac{1}{r}\frac{\partial w}{\partial r}+\frac{\partial \psi}{\partial r}+\frac{\psi}{r}\right)-d_1\frac{\partial w}{\partial t}-\lambda^2\frac{\partial^2 w}{\partial t^2}=-\bar{p}+G_2^p+G_2^L$$

where $\alpha=h^2/12R^2$, $\lambda^2=\rho hR^4/D$, $\beta=k^2GhR^2/D$, $D=Eh^3/[12(1-\nu^2)]$, $\bar{p}=pR^3/D$, $d_1=c_1R^2/D$, $d_2=c_2R^2/D$ and $k^2=5/6$. In Eqns (16) G_u^p denotes the expression

$$G_u^p(r,t_{i+1})=-\frac{1-\nu}{2r}\left(\frac{\partial w}{\partial r}\right)^2+\frac{\partial w}{\partial r}\frac{\partial^2 w}{\partial r^2}+$$

$$\frac{1-\nu^2}{Eh}\sum_{j=0}^{i}\left[\frac{\partial}{\partial r}\left(\Delta N_r^e-\Delta N_r^{ep}\right)^{j+1,j}+\frac{\left(\Delta N_r^e-\Delta N_r^{ep}+\Delta N_t^e-\Delta N_t^{ep}\right)^{j+1,j}}{r}\right] \quad (17)$$

and by G_2^L, G_1^p, G_2^p are denoted the components of the vectors $\mathbf{G}_L(0,G_2^L)$ and $\mathbf{G}_p(G_1^P,G_2^P)$ which may be called nonlinear force vectors due to finite displacements and inelastic strains, correspondingly.

They are presented as:

$$G_2^L(r,t_{i+1})=-\frac{R^2}{Dr}\sum_{j=0}^{i}\left(N_r^j\frac{\partial \Delta w^{j+1,j}}{\partial r}+\Delta N_r^{j+1,j}\frac{\partial w^{j+1}}{\partial r}\right)-$$

$$\frac{R^2}{D}\sum_{j=0}^{i}\left[N_r^j\frac{\partial^2 \Delta w^{j+1,j}}{\partial r^2}+\Delta N_r^{j+1,j}\frac{\partial^2 w^{j+1}}{\partial r^2}+\frac{\partial N_r^j}{\partial r}\frac{\partial \Delta w^{j+1,j}}{\partial r}+\frac{\partial \Delta N_r^{j+1,j}}{\partial r}\frac{\partial w^{j+1}}{\partial r}\right]$$

$$\mathbf{G}_p(r,t_{i+1})=\sum_{j=0}^{i}\int_{-h/2}^{h/2}\Delta\mathbf{G}_p^{j+1,j}dz, \quad (18\text{ a-c})$$

$$\Delta\mathbf{G}_p^{j+1,j}=\mathbf{L}([D^e]\Delta\varepsilon^{j+1,j})-\mathbf{L}([D^{ep}]\Delta\varepsilon^{j+1,j})$$

where $\Delta\varepsilon^{i+1,i}=\varepsilon(r,t_{i+1})-\varepsilon(r,t_i)$, etc. and by $\mathbf{L}$ the differential operator is denoted on the left hand side of Eqns (1b,c), multiplied by D^{-1}. In Eqn (17) by N^e is denoted in-plane stress resultant obtained by using elastic matrix $[D^e]$ and by N^{ep} - stress resultant obtained by using elastic matrix $[D^{ep}]$

The corresponding governing equations for beams are:

$$\frac{\partial^2 u}{\partial x^2} = G_u^p$$

$$\frac{\partial^2 \psi}{\partial x^2} + \beta\alpha^{-1}\left(\frac{\partial w}{\partial x} + \psi\right) - d_2 \frac{\partial w}{\partial t} - \lambda^2 \frac{\partial^2 \psi}{\partial t^2} = G_1^p, \qquad \text{(16 a-c)}'$$

$$\beta\left(\frac{\partial^2 w}{\partial x^2} + \frac{\partial \psi}{\partial x}\right) - d_1 \frac{\partial w}{\partial t} - \lambda^2 \frac{\partial^2 w}{\partial t^2} = -\bar{p} + G_2^p + G_2^L$$

where, $\lambda^2 = \rho L^2/E$, $\beta = kG/E$, $\bar{p} = pL/EF$, $d_1 = c_1 L^2/EF$, $d_2 = c_2 L^2/EI$.

$$G_u^p(r, t_{i+1}) = -\frac{\partial w}{\partial x}\frac{\partial^2 w}{\partial x^2} + \frac{1}{EF}\sum_{j=1}^{i}\frac{\partial}{\partial x}\left(\Delta N^e - \Delta N^{ep}\right)^{j+1,j} \qquad (17)'$$

$$G_2^L(r, t_{i+1}) = -\frac{1}{EF}\sum_{j=0}^{i}\left(\Delta N^{j+1,j}\frac{\partial^2 w^j}{\partial x^2} + N^{j+1}\frac{\partial^2 \Delta w^{j+1,j}}{\partial x^2}\right) \qquad (18a)'$$

3.2. Use of mode superposition

Regarding G_u^p as a known function, Eqn (16 a) and (16 a)' can be solved directly and its solutions are:

$$u(r) = \frac{r}{2}\left[K + \int_0^r G_u^p(\xi)d\xi\right] - \frac{1}{2r}\int_0^r \xi^2 G_u^p(\xi)d\xi \qquad (19)$$

and

$$u(x) = x\left[K + \int_0^x G_u^p(\xi)d\xi\right] - \int_0^x \xi G_u^p(\xi)d\xi, \qquad (19)'$$

correspondingly, where the constant K is determined from the boundary condition $u(1,t)=0$.

The l.h.s. of Eqns (16 b,c) are linear forms and therefore the mode superposition method can be used for their solution.

Thus, the generalized displacements vector $\mathbf{v} = \{\alpha\psi, w\}^T$ is expanded as a sum of the product of the vectors of pseudo-normal modes v_n and the time dependent functions $q_n(t)$ as

$$\mathbf{v}(r,t) = \sum_n \mathbf{v}_n(r) q_n(t). \qquad (20)$$

Substituting Eqn (20) into Eqns (16 b,c), multiplying by $v_m(r)$, integrating the product over the plate surface, invoking the orthogonality condition (see [1] and [2]) and assuming a proportional damping i.e. $\left(2\pi\int_0^1 (d_1\psi_n^2 + d_2 w_n^2) r dr = 2\xi_n \omega_n\right)$ the equations for $q_n(t)$ will uncouple in the form:

$$\ddot{q}_n(t) + 2\xi_n \omega_n \dot{q}_n + \omega_n^2 q_n(t) = F_n(t), \tag{21}$$

where ω_n are the natural frequencies of the linear elastic (undamped) Mindlin circulate plate (Timoshenko beam), ξ_n are modal damping parameters and

$$F_n(t) = 2\pi\lambda^{-2} \int_0^1 \mathbf{v}_n^T(r)\ [\mathbf{P}(r,t) + \mathbf{G}(r,t)]\ rdr$$

$$\mathbf{P}(r,t) = (0,-\overline{p})^T, \quad \mathbf{G} = \mathbf{G}_p + \mathbf{G}_L \tag{22a-c}$$

The initial conditions defined by Eqns (15) are transformed also in terms of $q_n(0)$, and $\dot{q}_n(0)$

$$q_n(0) = q_n^0, \quad \dot{q}_n(0) = \dot{q}_n^0,$$

$$q_n^0 = 2\pi \int_0^1 (w^0 w_n + \alpha\psi^0 \psi_n) rdr, \quad \dot{q}_n^0 = 2\pi \int_0^1 (\dot{w}^0 w_n + \alpha\dot{\psi}^0 \psi_n) rdr \tag{23a-d}$$

Using the methodology developed by Kukreti and Issa [7] the pseudo-load vector $\{\mathbf{P} + \mathbf{G}\}$ is interpolated by a quadratic polynomial of time, i.e.

$$\mathbf{P}(r,\tau)+\mathbf{G}(r,\tau)=\mathbf{A}(r)+\mathbf{B}(r)\tau+\mathbf{C}(r)\tau^2, \quad 0\le\tau\le l \tag{24}$$

where $\tau = t_{i+1} - t_i$. Denoting

$$\mathbf{P}_0(r) = \mathbf{P}(r,0), \quad \mathbf{P}_1(r) = \mathbf{P}(r,ml), \quad \mathbf{P}_2(r) = \mathbf{P}(r,l)$$

$$\mathbf{G}_0(r) = \mathbf{G}(r,0), \quad \mathbf{G}_1(r) = \mathbf{G}(r,ml), \quad \mathbf{G}_2(r) = \mathbf{G}(r,l) \qquad 0<m<1$$

the expressions for constants **A**, **B** and **C** are developed in terms of $\mathbf{P}_i$, $\mathbf{G}_i$ (i=1÷3). The general solution of Eqn (21) is :

$$q_n(\tau) = E_{1n} q_n^0 + E_{2n} \dot{q}_n^0 + F_{1n} a_n + F_{2n}\, b_n + F_{3n} c_n \tag{25}$$

where

$$E_{1n} = k_n(\omega_{nd} \cos\omega_{nd}\tau + \gamma_n \sin\omega_{nd}\tau),$$

$$E_{2n} = k_n \sin\omega_{nd}\tau,$$

$$F_{1n} = -k_n \omega_n^{-2}(\omega_{nd} \cos\omega_{nd}\tau + \gamma_n \sin\omega_{nd}\tau - k_n^{-1}) \tag{26a-e}$$

$$F_{2n} = 2k_n\gamma_n\omega_n^{-4}(\omega_{nd} \cos\omega_{nd}\tau + \gamma_n \sin\omega_{nd}\tau - k_n^{-1}) - k_n\omega_n^{-2}(\sin\omega_n\tau - \tau k_n^{-1})$$

$$F_{3n} = 8k_n\gamma_n^2\omega_n^{-6}(k_n^{-1} - \omega_{nd} \cos\omega_{nd}\tau - \gamma_n \sin\omega_{nd}\tau) +$$

$$2k_n\omega_n^{-4}\left[\omega_{nd} \cos\omega_{nd}\tau + 3\gamma_n \sin\omega_{nd}\tau - (1 + 2\gamma_n\tau)k_n^{-1}\right] + \tau^2\omega_n^{-2}$$

$$\gamma_n = \xi_n\omega_n, \ \omega_{nd}^2 = \omega_n^2 - \gamma_n^2 = \omega_n^2(1-\xi_n^2), \tag{27 a-c}$$

$$k_n = e^{-\alpha_n\tau} / \omega_{nd}$$

and

$$a_n = 2\pi \int_0^1 \mathbf{v}_n^T \mathbf{A}\, rdr, \quad b_n = 2\pi \int_0^1 \mathbf{v}_n^T \mathbf{B}\, rdr, \quad c_n = 2\pi \int_0^1 \mathbf{v}_n^T \mathbf{C}\, rdr. \tag{28 a-c}$$

The numerical algorithm used in the present paper is a natural extension of the one used in [3] and will be briefly presented in this paper.

At every time-step $[t_i, t_{i+1}]$ using the initial conditions obtained from the previous time-step, the vectors of displacements **u** and strains **ε** are evaluated. At the first iteration we assume that the strain changes are purely elastic, and

the deflection w is described by the small deflection theories. Then trial stresses are computed and the resulting stress state is checked for yielding. For the points that have yielded the vector $\mathbf{G}_p$ is formed and for all points $G_u(r)$ is evaluated. At the following iteration steps one computes vector $\mathbf{G}_L$, based on the obtained from the previous iteration step displacements **u** and on the membrane forces N obtained by a numerical quadrature. The criterion for convergence of the iteration process is:

$$\left\|\mathbf{G}^{k+1}(r,\tau)-\mathbf{G}^{k}(r,\tau)\right\| / \left\|\mathbf{G}^{k}(r,\tau)\right\| < tolerance, \quad \tau = ml, \tau = l \qquad (29)$$

where $\|\mathbf{G}\|$ denotes the Euclidean norm of the vector **G** while k+1 and k are the numbers of the current and the previous iteration, respectively.
The integrals of Eqns (7), (19), (22), (23) and (28) are evaluated by numerical quadrature following the Simpson rule.

4. Results and discussion

In previous works [1-3], a number of numerical calculations were accomplished for beams and plates subjected to rectangular and triangular pulses. In those examples pulse durations were comparable or larger than the first period of free vibrations and the elastic part of the total strain was considerable. It transpires that the application of mode-superposition approach for such kind of problems yield fast and economic solutions.

In this paper a considerable part of the numerical calculations proposed, concerns short pulses with large amplitudes, which could be interpreted as impulse loading. It transpires that for loading it is necessary to consider a large number of modes in the expansion Eqn (20), very small time steps and therefore considerable machine resources. In spite of that, numerical examples of problems for which numerical or experimental results exist were accomplished in order to verify the method extension proposed here. The numerical calculations were realized by a specially created FORTRAN computer code.

A comparison between the dynamic response of the plate center obtained experimentally by T. Duffey and S. Key in [8] and those obtained by the approach proposed here is shown in Fig. 1.
The object is a very thin (h/R = 0.0208, R= 0.762 m) 1022 steel plate ($E=2.1\text{x}10^8$ kPa, $\nu=0.3$, $\sigma_0 = 5.58\text{x}10^5$ kPa , $\rho= 7.85\text{x}10^3$ kg/m^3) loaded by a large pulse load on the internal circle with radius r' = R/3. The plate material is elastic-plastic with linear strain hardening (H/E=0.015). The load is modeled as a rectangular pulse with amplitude $p= 1.07895\text{x}10^5$ kPa and duration $\tau=$ 0.000001 s. The damping is assumed to be 12 % of the critical damping, and 15 pseudo-normal modes are included into expansion Eqn (20). The load applied causes deflections with a magnitude more than five times larger than the plate thickness. The results obtained in the case of an equivalent impulse with V_0=87.63 m/s show a discrepancy and a pour convergence of the numerical

algorithm due to the omission of the higher modes in the model. Neglecting the mid-plane inertia effect, in our opinion, could lead also to discrepancies compared to experimental results.

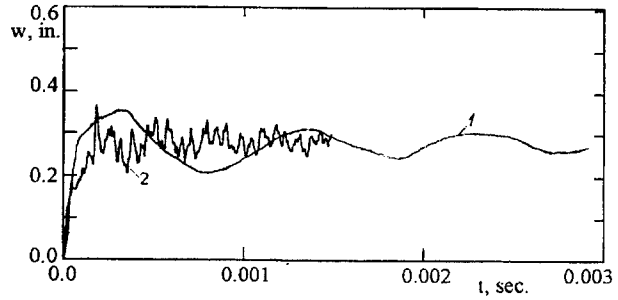

Figure 1. Time history of the plate center deflection obtained: 1 – experimentally by Duffy and Key [8]; 2 - obtained by present solution .

In Fig. 2 a comparison is shown of the plate center deflections, obtained by using small deflection plate theory, large deflection plate theory with damping, large deflection plate theory without damping, and rigid-plastic large deflection solution [3]. The calculations are accomplished for thick mid-steel simply-supported plate ($E=2{,}06.10^8$ kPa, $\nu=0.3$, $\rho= 7{,}85.10^3$ kg/m^3, $\sigma_0 =4{,}88.10^5$ kPa $H/E=0.02$) with $h/R=0.15$ ($R = 1$ m), loaded by a rectangular pulse with duration $\tau_0=0.0002$ s and amplitude $p_0 = 200000$ kPa. The damping is 20 % of the critical damping.

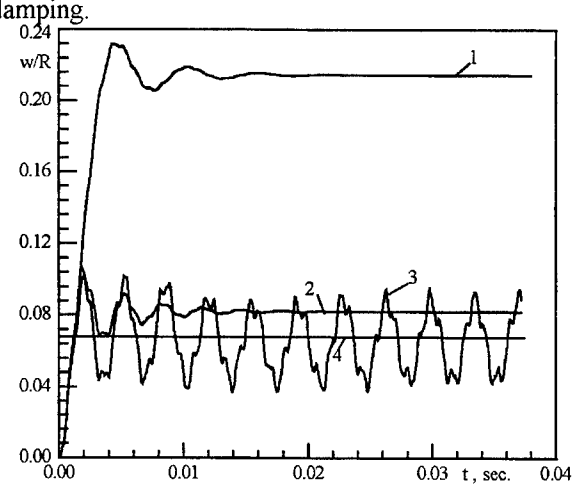

Figure 2. A comparison of the plate center deflection obtained: 1 - by SDPT; 2 - LDPT (damped solution); 3 - LDPT (undamped solution); 4 - rigid-plastic solution.

The rigid-plastic solution is obtained by using the formula:

$$w_f / h = \left\{(1+2\lambda/3)^{1/2} - 1\right\} / 2$$

where

$$\lambda = \rho h V_0^2 R^2 / M_0 h, \quad M_0 = \sigma_0 h^2 / 4$$

and initial velocity V_0 is connected with pulse parameters as $V_0=p_0t_0/\rho h$.

It could be considered that the agreement between the analytical solution and numerical results is good and this conclusion confirms the applicability of rigid-plastic methods of analysis of such kind of loaded structures. The comparison between curves 1 and 2 shows the importance of taking into account the geometrical nonlinearity at the modeling. The inclusion of damping is very important as well as it can be seen comparing curves 2 and 3.

In Figure 3 a comparison can be made between the present solution, " inconsistency " solution [3] and the analytical rigid-plastic solution. The plate material and the geometrical parameters are the same as in the above example but the pulse duration is larger and the pulse amplitude is smaller - τ_0=0.0005 s, p_0 = 93575 kPa. The damping is 11 % of the critical damping. It must be noted that the agreement between the rigid-plastic solution and the present solution is better than the rigid-plastic solution and "inconsistency" solution. The discrepancy between these solutions is larger for shorter pulses with large amplitude.

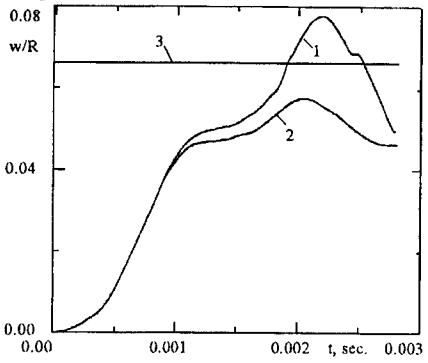

Figure 3. A comparison of the plate center deflection obtained by: 1 - present solution, 2 - "inconsistency" solution [3]; 3 - rigid-plastic solution

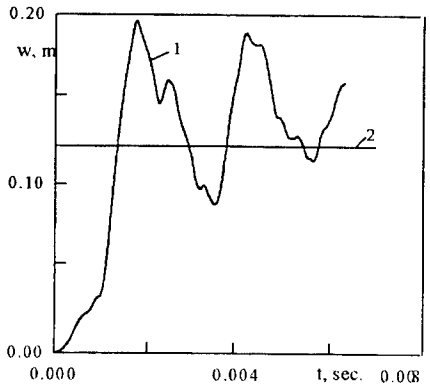

Figure 4. Plate center deflection for simply supported aluminum plate. 1 - the present solution; 2 – the rigid plastic solution.

The results for central deflection obtained for moderately thick simply-supported aluminum plate (E= 6,86.10^7 kPa, ν=0.3, ρ= 2,733.10^3 kg/m^3, σ_0 = 2.426 . 10^5 kPa, H/E=0.5) with h/R=0.66 obtained by the method proposed - 1 and rigid-plastic solution - 2 can be seen in Figure 4. The plate is subjected to a pulse load with duration τ_o=0.0004 s and pulse amplitude p_0 =25000 kPa.

The influence of the plate thickness on the maximal elastic and elastic-plastic deflections obtained by small deflections plate theory (SDPT) and large

deflection plate theory (LDPT) can be seen in Figure 5. Plates with five different thickness are considered and each of them is loaded with step-pulses with five different dimensionless amplitudes. The results show that with increasing pulse magnitude, the difference between elastic and elastic-plastic solutions increases but the difference between the results obtained by SDPT and LDPT decreases. This effect could be explained with the fact that for thicker plates the influence of the membrane forces on the response is smaller than the influence of the bending moments and transverse shear.

The results obtained for beams are compared with those obtained in [9] by a modified form of the central difference predictor scheme. They concern small deflection beam theory. A simply supported beam is subjected to a step pressure of $0.625p_0$, where p_0 is the static collapse load of the beam. Young modulus is $E= 2.068 \times 10^8$ kPa, $\nu=0.3$, $\rho= 7.8 \times 10^3$ kg/m^3 and $\sigma_0 = 3.44737 \times 10^5$ kPa.

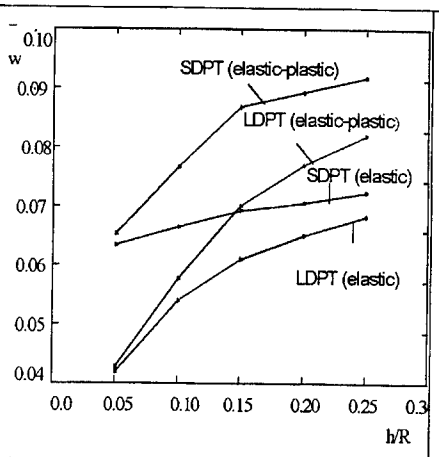

Figure 5. The influence of the plate thickens on the maximal elastic and elastic-plastic deflections obtained by SDPT and LDPT

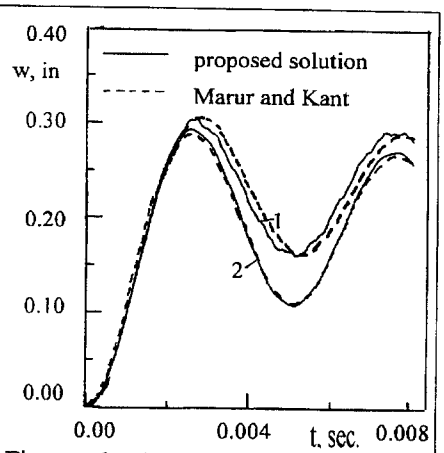

Figure 6. A comparisons between elastic-perfect plastic (Curve 1) and elastic- plastic with linear strain-hardening (Curve 2) responses obtained by present solution and Marur & Kant solutions

The curves denoted with 1 concern elastic perfectly plastic material and curves denoted with 2 refer to elastic-plastic material with linear strain hardening and H/E=0.25. The damping is 5% of the critical damping. The good agreements between the solutions confirm the applicability of the approach proposed to predict responses of elastic-plastic beams dynamically loaded.

5. CONCLUSIONS

The pseudo-normal mode superposition method was used for studying the behavior of elastic-plastic circular plates and beams subjected to a pulse load within the context of geometrically nonlinear version of the Mindlin plate theory and the Timoshenko beam theory.

The method used herein was based on the analytical definition of the vibration modes of an "assumed linear elastic undamped" structure, on the exact solving of the ordinary differential equations as regards time, and on an iterative procedure for determination of nonlinear load-vectors. In this paper the internal inconsistency of the elastic-plastic model proposed in [3] is overcome. Numerical examples of highly nonlinear problems are provided and a comparably good agreement with existing results is observed. For such problems, however, the method requires very small time step and large number of eigen modes to be included in the calculations and the attractivity of the method decreases.

REFERENCES

1. E. Manoach, Dynamic response of elastoplastic Mindlin plate by mode superposition method. *Journal of Sound and Vibration* **162,** (1993), 165-175 .
2. E. Manoach and D. Karagiozova, Dynamic response of thick elastic-plastic beams. *International Journal of Mechanical Sciences.* **35,** (1993), 909-919.
3. E. Manoach, Dynamic large deflection analysis of elastic-plastic beams and plates *International Journal of Non-Linear Mechanics* **29**, (1994), 723-735
4. N. Jones, *Structural Impact*, Cambridge University Press (1989).
5. R. Hill, *Mathematical Theory of Plasticity,* Oxford University Press, London (1950).
6. Y. Yamada, N. Yoshimura and T. Sakurai, Plastic stress-strain matrix and its application for the solution of elastic-plastic problems by the finite elements, *International Journal of Mechanical Sciences* **10**, (1968), 343-354.
7. A. R. Kukreti and H.I. Issa Dynamic analysis of nonlinear structures by pseudo-normal mode superposition method. *Computers and Structures* **19**, (1984), 653-663
8. T.A. Duffey and S.W. Key. Experimental-theoretical correlations of impilsively loaded clamped circular plates. *Experimental Mechanics* **9**, (1969), 241-269 .
9. S.R. Marur and T. Kant. A modified form of the central difference predictor scheme for damped nonlinear systems. *Computers and Structures* **50**, (1994), 615-618

NON-LINEAR FREE AND FORCED RESPONSE OF BEAMS AT LARGE VIBRATION AMPLITUDES BY A SEMI-ANALYTICAL METHOD

L. AZRAR *, R. BENAMAR ** and R. G. WHITE***

(*)Laboratoire SDTAS, Faculté des Sciences et Techniques de Tanger, Université, Abdelmalek Essaadi, BP 416 Tanger, Morocco

(**) Laboratoire LERSIM, E.G.T. E.M.I., Université, Mohammed V, BP 765 Agdal, Rabat, Morocco

(***) Department of Aeronautics and Astronautics, University of Southampton, Highfield Southampton S09 5NH, England

ABSTRACT

The main purpose of this paper is the presentation of a semi-analytical method for the prediction of the non-linear forced response of beams to harmonic excitation forces using a multi-mode approach. Various types of excitation forces such as distributed and concentrated are considered. The governing equation of motion is obtained and can be considered as a multidimensional form of the Duffing equation. Using the harmonic balance method, the equation of motion is converted into non-linear algebraic form. Numerical solutions are obtained using iterative-incremental procedures. The non-linear frequency and the non-linear modes are determined at large amplitudes of vibration. The basic function contribution coefficients to the displacement response for various beam boundary conditions are calculated. The percentage of participation for each mode in the response is presented in order to appraise the relation to higher modes contributing to the solution.

INTRODUCTION

The use of beams and plates is extensive in various engineering structures and they are often subjected to dynamic loading. Dynamic loads are sometimes harmonic in nature or they may be idealized as harmonic excitations. The steady-state response under these loads is of great interest in aerospace and mechanical engineering and other related fields. The study of the free and forced vibration of geometrically nonlinear beams involves obtaining solutions of the governing non-linear partial differential equations for which exact solutions are not available. Numerical methods are the only alternative to obtain general

solutions. A review of literature and a survey of various approaches for non-linear vibration analysis of beams and plates has been recently presented by Azrar, Benamar and Wolfe in a review paper [1].
In the study of linear vibration, the technique of modal analysis is an appropriate and an efficient procedure. The use of eigenmodes leads to a system of uncoupled differential equations that can be treated separately. For non-linear vibration, multimode analysis leads to a coupled non-linear system involving the contribution of various modes. Using the harmonic balance method, Benamar, Bennouna and White [2,3] reduced the non-linear free vibration problem to a set of non-linear algebraic equations. However, although the above model succeeded well in analyzing the effect of large vibration amplitudes on the mode shapes of beams and plates, it was restricted in a sense that only the free response problem was considered in the formulation. A semi-analytical approach for the non-linear dynamic forced response has been developed and applied to large amplitude forced vibrations of beams [4,5,6].

Based on the investigations presented in [6], the present paper concerns the contribution of higher modes to the non-linear deflection shapes and the bending moment in the free and forced cases. Solution techniques are also presented in order to obtain an automatic algorithm for various resonance curves. The mathematical formulation for the dynamic response of beams leading to a multidimensional Duffing equation has been presented in [5] and is briefly reviewed here. The use of the harmonic balance method permitted conversion of the equation of motion into a non-linear algebraic system. Solution techniques based on continuation methods have been presented. Various types of excitation such as uniformly distributed and concentrated forces are considered. Numerical solution enabled the non-linear frequency response function to be derived as the beam response spatial distribution across its whole span, depending on the level of excitation, and involving the deformation of the deflection shape, due to the nonlinearity. The percentage participation for each mode to the non-linear deflections and bending moments is presented in order to appraise the relation to the higher modes contributing to the solution.

FORMULATION

The non-linear effect, produced by large transverse vibration amplitudes, is axial stretching of the mid-plane of the beam. This effect is modeled by a non-linear strain-displacement relationship of the von Karman type. The axial strain ε and the curvature K are defined as:

$$\begin{cases} \varepsilon = \dfrac{\partial U}{\partial x} + \dfrac{1}{2}\left(\dfrac{\partial W}{\partial x}\right)^2 \\ K = \dfrac{\partial^2 W}{\partial x^2} \end{cases} \qquad (1)$$

where U and W are the axial and the transverse displacements respectively. For immovable beams, if one neglects the in-plane inertia, the non-linear stretching force N can be written in terms of transverse displacement, W, alone. The total strain energy of the beam is given by the following formulation [2,5,6]:

$$V = \frac{ES}{8L}\left[\int_0^L \left(\frac{\partial W}{\partial x}\right)^2 dx\right]^2 + \frac{EI}{2}\int_0^L \left(\frac{\partial^2 W}{\partial x^2}\right)^2 dx \qquad (2)$$

Neglecting the axial inertia, the kinetic energy is given by:

$$T = \frac{1}{2}\rho S \int_0^L \left(\frac{\partial W}{\partial t}\right)^2 dx \qquad (3)$$

The out of plane displacement field, W, is assumed to be of the form of the modal transformation:

$$W(x, t) = \sum_{i=1}^{n} q_i(t)\, w_i(x) \qquad (4)$$

where $w_i(x)$ are the basic functions, chosen in the present work as the beam linear modes of vibration. The modal coefficients $q_i(t)$, are time dependent generalized coordinates.

Assume that the structure is excited by a force $F(x,t)$ distributed over the spatial range Ω (Ω is the length of the beam or a part of it). The physical force $F(x,t)$ excites the modes of the structures via a set of generalized forces $F_i(t)$ depending on the expression for the force F, the excitation point when F is a concentrated force, the excitation length for distributed forces, and the mode considered. The generalized forces $Fi(t)$ are given by:

$$Fi(t) = \int_\Omega F(x,t)\, w_i(x)\, dx \qquad (5)$$

in which $w_i(x)$ is the i^{th} mode shape of the structure considered.
Using Lagrange's equation and matrix formulation, the nonlinear differential system governing the forced dynamic behaviour of the beams is:

$$[M]\{\ddot{q}\} + [K]\{q\} + 2\,[B(q)]\{q\} = \{F\} \qquad (6)$$

where $[M]$, $[K]$, $[B]$, $\{q\}$ and $\{F\}$ are the mass matrix, the linear rigidity matrix, the nonlinear rigidity tensor, the vector of generalized parameters and the vector of generalized forces respectively.

It appears that the model presented above and summarized in equation (6) can be considered as a multidimensional form of the Duffing equation very often encountered in nonlinear vibration analysis of structures. It is worth noting here that the theory presented in [5] provides a means of calculating the cubic nonlinearity coefficient in the approximate one dimensional Duffing equation for beams with various boundary conditions. This could allow numerical solutions to be obtained for engineering purposes, which would be valid as far as the single mode assumption is valid.

ALGEBRAIC MODEL

Consider a beam excited by a concentrated harmonic force $F^c(x,t)$ applied at the point x_0, and also the case of a beam excited by a distributed harmonic uniform force $F^d(x,t)$. The corresponding generalized forces $F_i^c(t)$ and $Fi^d(t)$ for each case are given by:

$$\begin{cases} F_i^c(t) = F^c\, wi(x_0)\, cos(\omega t) = f_i^c\, cos(\omega t) & \text{(7-a)} \\ F_i^d(t) = F^d\, cos(\omega t) \int_0^L w_i(x)\,dx = f_i^d\, cos(\omega t) & \text{(7-b)} \end{cases}$$

The dynamic equation representing the forced vibration of beams is obtained by introducing the generalized forces (7) into equation (6). Numerical solution of this equation yields the steady state motion of beams for various excitations and boundary conditions.

Following the approach developed in [5,6] the nonlinear response is assumed here to be harmonic, which leads to:

$$q_i(t) = a_i\, cos(\omega t) \qquad \text{for i=1 to n} \qquad (8)$$

Introducing (8) into equation (6) and applying the harmonic balance method leads to [6]:

$$\begin{cases} ([K] - \omega^2 [M])\{A\} + \frac{3}{2}[B(A)]\{A\} = \{F\} & (9) \\ A = \{a_1, a_2, \ldots, a_n\}^t \end{cases}$$

In order to obtain a non dimensional formulation, the nonlinear parameters have been defined as follows:

$$\begin{cases} w_i(x) = R\, w_i^*(x^*),\ x^* = \frac{x}{L},\ R^2 = I/S,\ \omega^2/\omega^{*2} = EI/\rho SL^4 \\ k_{ij}/k_{ij}^* = EIR^2/L^3,\ m_{ij}/m_{ij}^* = \rho SR^2 L,\ b_{ijkl}/b_{ijkl}^* = EIR^2/L^3 \end{cases} \qquad (10)$$

where k_{ij}^*, m_{ij}^*, b_{ijkl}^* and ω^* are the nondimensional generalized parameters.

The dimensionless generalized forces $f^c i^*$ and $f^d i^*$ corresponding to the concentrated force at x_0 and to the uniformly distributed force on the whole beam respectively are given by:

$$f^c i^* = F^c \frac{L^3}{EIR}\, w_i^*(x_0^*) = FOR_C\, w_i^*(x_0^*) \qquad \text{(11-a)}$$

$$f^d i^* = F^d \frac{L^4}{EIR} \int_0^1 w_i^*(x^*)\,dx^* = FOR_D \int_0^1 w_i^*(x^*)\,dx^* \qquad \text{(11-b)}$$

By substituting notations (10, 11) in equation (9) one obtains the following nonlinear algebraic equation:

$$([K^*] - \omega^* [M^*])\{A\} + \frac{3}{2}[B^*(A)]\{A\} = \{f^*\} \qquad (12)$$

To solve the nonlinear equation (12), incremental-iterative methods will be used. Some continuation methods are well established and developed and applied in structural engineering. The most popular ones, based on the Newton-Raphson procedure, are the load control, the displacement control and arc length methods [7,8]. The governing equation of nonlinear forced vibrations of beams presented above is written as:

$$G(A, \omega^*) = [K^*].\{A\} - \omega^{*2} [M^*].\{A\} + \frac{3}{2}[B^*(A)]\{A\} - \{f^*\} = \{0\} \qquad (13)$$

where G is the residual vector. This equation represents n relations between (n+1) unknowns $(a_1, a_2, a_3,..., a_n, \omega^*)$. In order to solve this problem, an extra equation, noted $g(A, \omega^*) = 0$, can be introduced to complete the system. A numerical solution of the following extended system by using the Newtonian algorithm has to be carried out.

$$G(A, \omega^*) = 0, \qquad g(A, \omega^*) = 0 \qquad (14)$$

Iterative-incremental methods must be invariably used to solve the nonlinear problem (14). The solution path is followed incrementally proceeding from a known solution $({}^1A, {}^1\omega^*)$ to an adjacent configuration. Two strategies are usually followed to achieve equilibrium. The first one is called prediction, being a procedure from a known configuration to the next one; and the second, called correction, consists on an improvement of the predicted solution. These configurations presenting the prediction-correction solution are generally performed following the Newton-Raphson procedure.

$$K_t . \Delta A = G({}^1A, {}^1\omega^*) + \frac{\partial G}{\partial \omega}({}^1A, {}^1\omega^*). \Delta\omega^* \qquad (15)$$

where ΔA and $\Delta\omega^*$ are the increments. The tangent matrix K_t and the derivative $G_{,\omega}$ are given by:

$$\begin{cases} -K_t = K^* - {}^1\omega^{*2} M^* + \frac{3}{2}[B^*({}^1A, {}^1A, .) + B^*({}^1A, ., {}^1A) + B^*(., {}^1A, {}^1A)] \\ \frac{\partial G}{\partial \omega}({}^1A, {}^1\omega^*) = -2\,{}^1\omega^* M^* . {}^1A \end{cases} \qquad (16)$$

where $B^*({}^1A, {}^1A, .) = \sum_{i=1}^{n}\sum_{j=1}^{n} b^*_{ijkl}\, {}^1a_i\, {}^1a_j$; $B^*({}^1A, ., {}^1A) = \sum_{i=1}^{n}\sum_{k=1}^{n} b^*_{ijkl}\, {}^1a_i\, {}^1a_k$

and $B^*(., {}^1A, {}^1A) = \sum_{j=1}^{n}\sum_{k=1}^{n} b^*_{ijkl}\, {}^1a_j\, {}^1a_k$

The last formulations can be simplified by using the symmetry of the tensor b^*_{ijkl}. Various strategies of resolution proposed in the literature for non-linear static problems correspond to particular choices for equation $g(A, \omega^*) = 0$ [6-9].

For the load control method, which is termed here frequency control, the additional constraint equation is $g(A, \omega^*) = \omega^* - C = 0$, where C denotes a fixed frequency. For displacement control, we specify a value of one component of the vector A, say aj, so that, $g(A, \omega^*) = a_j - \bar{a}_j$. The displacement component, which should be controlled, is a_j. $\bar{a}_j$ is the value of the prescribed component of the displacement. The frequency control method or the displacement control method fail when a frequency limit or a displacement limit exists. Using alternatively the increments of the amplitude of the displacement or the frequency permits successful determination of backbone curves of a complex shape [6]. The shortcoming of the latter method is the necessity for modification of the tangential matrix during an iteration process. The arc-length methods are intended to enable solution algorithms to pass limit points. For these methods, various formulations of the constraint equation $g(A, \omega^*) = 0$ are possible. The most popular methods keep a specific arc-length constant, which is defined by Euclidean norm of the general displacement and frequency [6-9]. They are, however, not always appropriate for all problems. The particular choice for the additional equation enjoys a great popularity in view of the wide range of applications.

NUMERICAL RESULTS

There are many parameters that can be varied in non-linear forced vibrations of beams, so that it would be very difficult to present and compare results in all cases. Only a few typical cases are selected to illustrate the effectiveness of the method. Numerical solution of equation (12) gave the non-linear frequency and the contribution of each mode involved in the analysis. Making use of these contributions, the non-linear mode shape and bending moment are easily obtained across the whole span of the beam . Results presented in Table 1 were obtained for non-linear free vibrations of a C-C beam using six linear beam functions (3 Symmetric and 3 anti-symmetric). These results compare well with Shi and Mei's results [10], obtained using a finite element time domain formulation.

The contributions of higher modes appear to be relatively small. However, their effects on the curvatures, and hence on the nonlinear bending moment estimates may not be negligible, since they intervene via their second derivatives, which involve multiplication by v_i^2, the v_i's being the beam parameters [2,5,6] (For a C-C beam, v_i are solutions of

$ch(v_i)\cos(v_i) = 1$). In order to examine that effect, a formulae was used to estimate the percentage of participation of a given beam function, to the curvature, as follows:

$$\text{Participation of the } i^{th} \text{ beam function} = 100\, a_i v_i^2 / \sum_{i=1}^{n} |a_i| v_i^2 \qquad (17)$$

Percentages of the participation to the curvature of the first nonlinear mode obtained using (17) are summarized in table 2. It can be seen that while the percentage of participation of the first beam function to the first nonlinear mode given in table 1 remains predominant and greater than 98% for values of the dimensionless amplitude w/R up to 4, its percentage of participation to the curvature is only 86.72% for w(centre)/R =4 and decreases for large amplitudes. This shows that the influence of higher modes increases with the amplitude of vibration and the necessity to take into account various modes for more accurate results. The bending moments associated with free vibration of a C-C beam at various amplitudes are presented in Figure 1. This figure shows clearly the influence of the non-linear effects especially in the region of the clamps. In Figure 2 results corresponding to a clamped-simply supported beam are presented for very large amplitudes.

In Table 3, the nonlinear forced response of a C-C beam excited at a quarter span of the beam is considered using three symmetric and three anti-symmetric beam functions and taking FOR_C =200. The ratios of the nonlinear excitation frequencies to the linear frequency and the modal participation to the response of each involved beam basic function are given for positive and negative amplitudes. The deflection moments and modal participations using relationship (17) are presented in Table 4 for the same amplitudes as in Table 3. The influence of the higher modes appears clearly in these tables. The nonlinear deflection shapes of a C-C beam corresponding to the same amplitudes and excitations as in table 3 are presented in Figure 3 for negative amplitudes. The evolution of the behaviour of the beam from the first to the second resonance is demonstrated.

The most important advantage of the method is that it enables the non-linear forced response to be obtained easily, not only in the vicinity of the first resonance but also the higher ones. Also, the nonlinear response obtained involves contributions of many modes, which allows nonlinear effects, such as deformation of deflection shapes and higher rate of increase in bending stresses, compared with that predicted by the linear theory, to be taken into account. In figure 4, the first, the second, and the third forced resonance curves of a C-C beam under a concentrated harmonic force at the centre are presented. These results have been obtained automatically by solving equation (14) using a iterative-incremental procedure based on the Newton-Raphson algorithm with a control parameter.

REFERENCES

[1] L. AZRAR, R. BENAMAR and WOLFE. Nonlinear vibration analysis of beams and plates. A review of the literature and a survey of methodological approaches. To be submitted to JSV

[2] R. BENAMAR, M.M.K. BENNOUNA and R.G. WHITE 1991 Journal of Sound and Vibration 149(2),179-195. The effects of large vibration amplitudes on the mode shapes and natural frequencies of thin elastic structures. Part I: Simply supported and clamped-clamped beams

[3] R. BENAMAR, M.M.K. BENNOUNA and R.G. WHITE 1993 Journal of Sound and Vibration 164, 399-424. The effects of large vibration amplitudes on the mode shapes and natural frequencies of thin elastic structures. Part II: Fully clamped rectangular isotropic plates

[4] L. AZRAR and R. BENAMAR 1995 5ème Colloque Maghrébin sur les Modèles Numériques de l'Ingénieur, E.M.I., Rabat, Maroc, Vol. II, 594-599. Etude des vibrations non linéaires forcées des poutres par une méthode semi-analytique.

[5] L. AZRAR, R. BENAMAR and R. G. WHITE 1999, Journal of Sound and Vibration, 224(2), 183-207. A semi-analytical approach to the nonlinear dynamic response problem of S-S and C-C beams at large vibration amplitudes. Part I: General theory and application to the single mode approach to free and forced vibration analysis.

[6] L. AZRAR, R. BENAMAR and R. G. WHITE, submitted to Journal of Sound and Vibration. A semi-analytical approach to the nonlinear dynamic response problem of S-S and C-C beams at large vibration amplitudes. Part II: General theory and application to the single mode approach to free and forced vibration analysis.

[7] M. A. CRISFIELD 1983 International Journal for Numerical Methods and Engineering 19, 1269-1289. An arc-length method including line searchers and accelerations.

[8] E. RIKS 1984 Computer Methods in Applied Mechanics and Engineering 47, 219-259. Some computational aspects of the stability analysis of non-linear structures.

[9] R. LEWANDOWSKI 1994 Journal of Sound and Vibration , 170(5), 577-593. Nonlinear free vibrations of beams by the finite element and continuation methods.

[10] Y. SHI and C. MEI 1996 Journal of Sound and Vibration 193(2), 453-464. A finite element time domain modal formulation for large amplitude free vibrations of beams and plates.

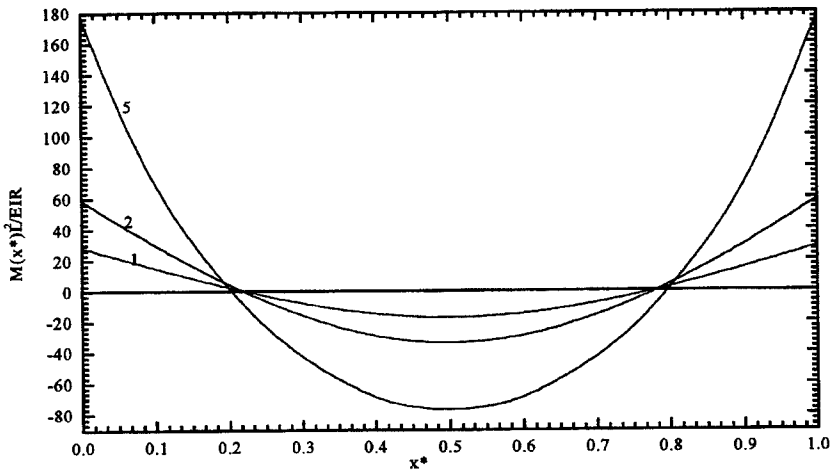

Figure 1. Non-linear free vibration deflection moments of a fully clamped beam at amplitudes Wmax/R = 1, 2 and 5.

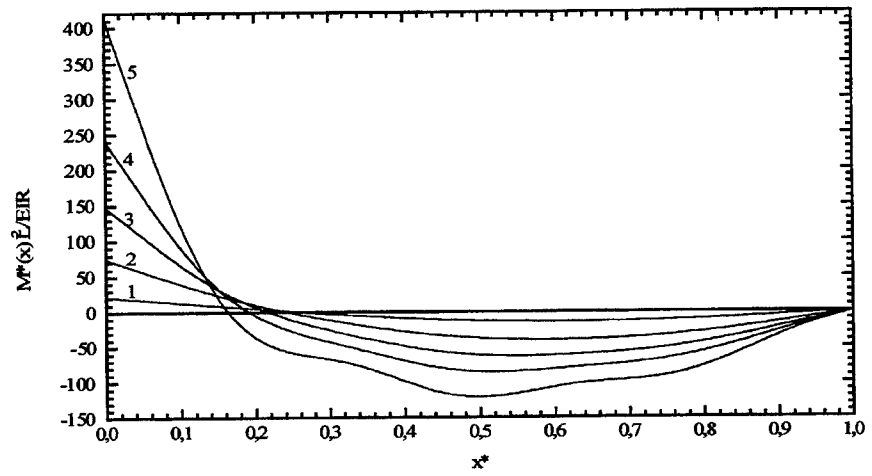

Figure 2: Non-linear free vibration deflection moments associated with the first non-linear mode shape of a clamped–simply supported beam at various amplitudes: 1: w(centre)/R= 1, 2: w(centre)/R= 3, 3:w(centre)/R= 5, 4: w(centre)/R= 7, 5: w(centre)/R= 10.

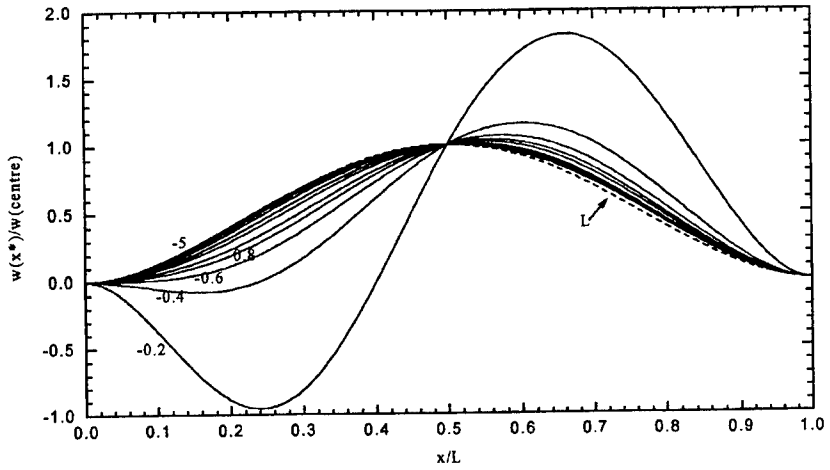

Figure 3. Linear and non-linear forced vibration deflection shapes of a fully clamped beam under a harmonic concentrated force at L/4 at "negative amplitudes". (FOR_C=200. L: First linear mode, the other curves correspond to the numerical results given in table 3 for w(centre)/R variant from -5 to -0.2.

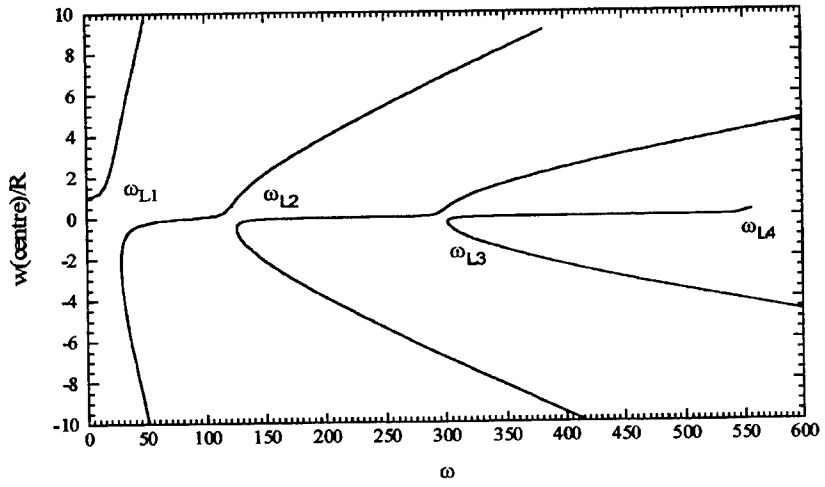

Figure 4. The first, the second and the third resonance curves of a C-C beam under a concentrated harmonic force at the beam centre (FOR_C = 200)

Table 1. Frequency-ratios of free vibration and the modal participation of a C-C beam at various amplitudes. Case of three symmetric and three anti-symmetric modes

Present analysis		Modal participation (%) (&)			Shi and Mei [10]	Modal participation (%) (&)		
W(centre)/R	ω^*/ω_L^*	a_1	a_3	a_5	ω^*/ω_L^*	a_1	a_3	a_5
1.00003	1.02220	99.8598	.124537	.156724E-01	1.0221	99.84	0.15	1.5E-2
1.50004	1.04922	99.6889	.275959	.351365E-01	1.0484	99.61	0.34	4.3E-2
2.00003	1.08578	99.4574	.480423	.621478E-01	1.0854	99.59	0.33	7.9E-2
2.50002	1.13086	99.1723	.731219	.964637E-01	1.1339	99.17	0.59	0.25
3.00001	1.18336	98.8415	1.02075	.137769	1.1842	98.66	1.17	0.16
3.50000	1.24224	98.4733	1.34102	.185677	1.2439	98.12	1.5	0.30
4.00001	1.30652	98.0761	1.68416	.239731	1.3020	98.00	1.66	0.34

Table 2. Bending moments and modal contributions at various amplitudes of free vibration of a C-C beam

			Modal participation (%) (&&)					
W(centre)/R	M*(0)	M*(1/2)	$a_1v_1^{**2}$	$a_2v_2^{**2}$	$a_3v_3^{**2}$	$a_4v_4^{**2}$	$a_5v_5^{**2}$	$a_6v_6^{**2}$
1.0001	28.501	-17.036	98.963	.66708	.20733	.89408E-01	.46269E-01	.26718E-01
1.5000	43.346	-25.387	97.71	1.4621	.45983	.19922	.10335	59764E-01
2.0000	58.892	-33.552	96.053	2.5085	.80175	.34959	.18196	.10543
2.5000	75.337	-41.483	94.046	3.7500	1.2227	.53742	.28090	.16317
3.0000	92.863	-49.147	91.771	5.1272	1.7110	.75923	.39883	.23235
3.5000	111.62	-56.520	89.306	6.5821	2.2543	1.0112	.53424	.31229
4.0000	131.74	-63.593	86.719	8.0631	2.8405	1.2895	.68564	.40230

(&) Participation of mode i = $100\,a_i / \sum_{i=1}^{n} |a_i|$ (&&) Participation of the i^{th} beam function to the curvature = $100\,a_i v_i^2 / \sum_{i=1}^{n} |a_i| v_i^2$

Table 3. Frequency-ratios of non linear forced vibrations of a C-C beam under a harmonic concentrated force at a quarter of the beam using three symmetric and three antisymmetric modes and FOR_C=200.

(FOR_C = 200).		Modal participation (%) (&)					
W(centre)/R	ω^*/ω_L^*	a_1	a_2	a_3	a_4	a_5	a_6
1.0003	.71789	86.103	10.557	2.6151	.38717	-.14099	-.19618
1.5002	.86345	90.067	7.4445	2.0005	.27741	-.74802E-01	-.13576
2.0001	.95491	92.243	5.6394	1.7745	.21852	-.22341E-01	-.10231
2.5004	1.0321	93.520	4.4445	1.7451	.18162	.28158E-01	-.80751E-01
3.0000	1.1056	94.270	3.5915	1.8361	.15615	.80632E-01	-.65610E-01
3.5000	1.1793	94.712	2.9513	2.0084	.13726	.13681	-.54353E-01
4.0001	1.2546	94.943	2.4548	2.2373	.12245	.19728	-.45660E-01
4.5001	1.3319	95.022	2.0609	2.5055	.11033	.26209	-.38764E-01
5.0004	1.4112	94.992	1.7430	2.8002	.10005	.33109	-.33180E-01
-5.0000	1.4855	-95.738	1.8180	-1.9223	.10267	-.38480	-.33664E-01
-4.5000	1.4193	-95.879	2.1634	-1.4800	.11356	-.32502	-.39428E-01
-4.0001	1.3586	-95.928	2.5978	-1.0292	.12652	-.27152	-.46591E-01
-3.5001	1.3048	-95.851	3.1555	-.56970	.14246	-.22527	-.55687E-01
-3.0001	1.2597	-95.592	3.8919	-.097859	.16296	-.18748	-.67573E-01
-2.5000	1.2260	-94.306	4.8676	.39543	.18942	-.15853	-.83104E-01
-2.0001	1.2082	-92.318	6.2745	.93250	.22773	-.14224	-.10518
-1.5000	1.2152	-89.308	8.5318	1.5864	.28977	-.14374	-.13982
-1.0000	1.2701	-83.824	12.826	2.5661	.40648	-.17554	-.20262
-.80003	1.3205	-79.974	15.911	3.1793	.48703	-.20420	-.24494
-.60007	1.4076	-73.906	20.859	4.0701	.60769	-.25019	-.30731
-.40004	1.5795	-62.768	30.218	5.4844	.79969	-.32540	-.40432
-.20004	2.0698	-34.662	56.275	7.1678	1.0031	-.39844	-.49365

Table 4. Deflection moments and modal contributions at various amplitudes of forced vibrations of a C-C beam under concentrated harmonic force at a quarter.

(FOR_C =200)

				Modal participation (%) (&&)					
W(centre)/R	ω/ωL	M*(0)	M*(1/2)	$a_1v_1{}^{**2}$	$a_2v_2{}^{**2}$	$a_3v_3{}^{**2}$	$a_4v_4{}^{**2}$	$a_5v_5{}^{**2}$	$a_6v_6{}^{**2}$
1.0002	.71782	42.866	-13.794	62.240	21.039	10.217	2.5004	-1.3603	-2.6435
1.5000	.86339	57.650	-22.202	70.690	16.109	8.4858	1.9452	-.78375	-1.9862
2.0006	.95500	72.826	-30.492	75.903	12.788	7.8898	1.6059	-.24469	-1.5686
2.5004	1.0321	88.595	-38.596	78.784	10.321	7.9445	1.3667	.31663	-1.2678
3.0000	1.1056	105.15	-46.497	80.035	8.4052	8.4238	1.1843	.91348	-1.0382
3.5004	1.1794	122.67	-54.201	80.424	6.9068	9.2168	1.0411	1.5509	-.86007
4.0002	1.2546	141.19	-61.680	80.203	5.7159	10.214	.92403	2.2241	-.71886
4.5002	1.3319	160.82	-68.960	79.551	4.7557	11.335	.82505	2.9282	-.60481
5.0001	1.4111	181.58	-76.050	78.598	3.9759	12.520	.73955	3.6551	-.51173
-5.0000	1.4855	-158.17	81.252	-81.260	4.2535	-8.8174	.77842	-4.3584	-.53252
-4.5000	1.4193	-136.30	74.390	-82.706	5.1442	-6.8992	.87509	-3.7414	-.63389
-4.0000	1.3586	-115.58	67.335	-83.947	6.2667	-4.8669	.98903	-3.1706	-.75992
-3.5000	1.3048	-95.987	60.064	-84.866	7.7016	-2.7254	1.1267	-2.6614	-.91897
-3.0000	1.2596	-77.481	52.565	-85.300	9.5735	-.47153	1.2990	-2.2323	-1.1239
-2.5000	1.2260	-59.981	44.832	-81.851	11.645	1.8545	1.4686	-1.8361	-1.3443
-2.0000	1.2082	-43.384	36.878	-76.583	14.348	4.1805	1.6876	-1.5746	-1.6263
-1.5000	1.2152	-27.522	28.723	-69.495	18.300	6.6706	2.0142	-1.4925	-2.0277
-1.0001	1.2701	-12.118	20.407	-58.704	24.758	9.7106	2.5428	-1.6404	-2.6446
-.80002	1.3205	-5.9423	17.049	-52.389	28.731	11.255	2.8500	-1.7850	-2.9905
-.60007	1.4076	.42428	13.686	-44.019	34.247	13.100	3.2333	-1.9885	-3.4115
-.40004	1.5795	7.5403	10.339	-32.234	42.777	15.220	3.6686	-2.2299	-3.8700
-.20003	2.0698	20.937	7.1367	-13.754	61.559	15.371	3.5558	-2.1098	-3.6510

ON PERTURBATION EXPANSION AND THE VOLTERRA SERIES

J.A.Vazquez-Feijoo, K.Worden & R.Stanway
Dynamics Research Group
Department of Mechanical Engineering
University of Sheffield
Mappin Street
Sheffield S1 3JD
United Kingdom

Abstract

The connection between the perturbation series and Volterra series for a SDOF Duffing oscillator is sketched and a number of Associated Linear Equations (ALEs) are derived. It is shown how these constructs can be useful in proving properties of both forward and inverse Volterra systems.

INTRODUCTION

There are numerous methods for analysing nonlinear systems available to the structural dynamicist. Unfortunately, none of these methods has universal applicability. Rather, the dynamicist relies on a 'toolbox' of approaches and selects the appropriate tool for a given job. One popular approach which can be applied for weak nonlinearities at low levels of excitation is the perturbation approach [1, 2]. Another method valid in the same regime is Volterra expansion [3]. As one might expect, two series techniques with similar domains of validity turn out to be rather closely related and this paper explores some of the simpler consequences of this relationship.

It is shown that the components of the Volterra series are related to each other via a sequence of linear differential equations - the *associated linear equations* or ALEs. These linear equations prove to be useful tools in proving results for both forward and inverse Volterra systems and their use is illustrated here by constructing the inverse Volterra system for a Single Degree-Of-Freedom (SDOF) Duffing oscillator.

The layout of the paper is as follows: Section Two introduces the Volterra series. Section Three derives the first two of the ALEs for the Duffing oscillator and Section Four shows how all the ALEs follow from the perturbation expansion in this case. Section Five illustrates the theory by constructing the inverse system for the Duffing oscillator and the paper concludes with some discussion in Section Six.

THE FORWARD AND INVERSE VOLTERRA SERIES

It is known that many nonlinear systems (those satisfying appropriate smoothness and convergence criteria) or input-output process $x(t) \longrightarrow y(t)$ or $y = \boldsymbol{H}[x]$ can be realised as a *Volterra series* or mapping [3],

$$y(t) = y_1(t) + y_2(t) + y_3(t) + \ldots + y_n(t) + \ldots \tag{1}$$

which contains a potentially infinite number of terms where,

$$y_n(t) = \int_{-\infty}^{+\infty} \ldots \int_{-\infty}^{+\infty} d\tau_i \ldots d\tau_n \; h_n(\tau_1, \ldots, \tau_n) x(t-\tau_1) \ldots x(t-\tau_n) \tag{2}$$

and the functions h_n are referred to as the *Volterra kernels.* The terms in the series will also be denoted by $\boldsymbol{H}_n[x] = y_n$.

As in the linear case, there exists a dual frequency-domain representation for nonlinear systems based on the *Higher-order Frequency Response Functions* (HFRFs) or *Volterra kernel transforms*, $H_n(\omega_1, \ldots, \omega_n)$, $n = 1, \ldots, \infty$ which are defined as the multi-dimensional Fourier transforms of the kernels.

$$H_n(\omega_1, \ldots, \omega_n) = \int_{-\infty}^{+\infty} \ldots \int_{-\infty}^{+\infty} d\tau_1 \ldots d\tau_n \; h_n(\tau_1, \ldots, \tau_n) e^{-i(\omega_1\tau_1 + \ldots + \omega_n\tau_n)} \tag{3}$$

Suppose that the terms in the series (1) are generalised such that,

$$y_n(t_1, \ldots, t_n) = \int_{-\infty}^{+\infty} \ldots \int_{-\infty}^{+\infty} d\tau_1 \ldots d\tau_n \; h_n(\tau_1, \ldots, \tau_n) x(t_1-\tau_1) \ldots x(t_n-\tau_n) \tag{4}$$

(there is a minor abuse of notation here, but the meaning of the terms will always be clear from context) so that,

$$y_n(t) = y_n(t_1, t_2, \ldots, t_n)|_{t_1=t_2=\ldots=t_n=t} \tag{5}$$

and the multi-dimensional output Fourier transform is defined by,

$$Y_n(\omega_1, \ldots, \omega_n) = \int_{-\infty}^{+\infty} \ldots \int_{-\infty}^{+\infty} dt_1 \ldots dt_n \; y_n(t_1, \ldots, t_n) e^{-i(\omega_1 t_1 + \ldots + \omega_n t_n)} \tag{6}$$

then it can be shown [3], that,

$$Y_n(\omega_1, \ldots, \omega_n) = H_n(\omega_1, \ldots, \omega_n) X(\omega_1) \ldots X(\omega_n) \tag{7}$$

where $X(\omega)$ is the input spectrum.

The series $y = \boldsymbol{H}[x]$ is the *forward* Volterra series for the process $x(t) \longrightarrow y(t)$. The corresponding *inverse* series will have the property $x = \boldsymbol{K}[y]$ so that $\boldsymbol{K}$ o $\boldsymbol{H}$ is the identity operator or $x = \boldsymbol{K}[\boldsymbol{H}[x]]$. (In general it is only possible to construct inverse systems up to a given order of nonlinearity. However, in the example given here it will prove possible to construct an exact inverse with a finite Volterra series so the restricted definition above will be used.)

ASSOCIATED LINEAR EQUATIONS

From this point on, the analysis will be restricted to the SDOF Duffing oscillator system, i.e. $x(t)$ and $y(t)$ are related by the equation of motion,

$$m\ddot{y} + c\dot{y} + ky + k_3 y^3 = x(t) \tag{8}$$

and this system has a convergent Volterra series for low enough levels of excitation i.e. for low values of the RMS of $x(t)$. The question of convergence is usually an important issue; however, in the example considered her, the final result is not dependent on the convergence of the series. The Volterra kernels can be computed, but the kernel transforms are easier to find and they are the objects of interest here. Using the method of harmonic probing [4], it can be shown that [5],

$$H_1(\omega) = \frac{1}{-m\omega^2 + ic\omega + k} \tag{9}$$

$$H_3(\omega_1, \omega_2, \omega_3) = -k_3 H_1(\omega_1) H_1(\omega_2) H_1(\omega_3) H_1(\omega_1 + \omega_2 + \omega_3) \tag{10}$$

The first ALE is obtained from the Duhamel relation,

$$y_1(t) = \int_{-\infty}^{\infty} d\tau \; h_1(\tau) x(t - \tau) \tag{11}$$

or in the frequency-domain (by convolution),

$$Y_1(\omega) = H_1(\omega) X(\omega) \tag{12}$$

Working back from (12) to the time-domain using (9) gives,

$$m\ddot{y}_1 + c\dot{y}_1 + ky_1 = x(t) \tag{13}$$

which is the first Associated Linear Equation or ALE.

The second ALE starts from the third-order version of equation (7). (Because there is no even term in the nonlinearity in (8), all the even-order Volterra kernels and HFRFs vanish [5].)

$$Y_3(\omega_1,\omega_2,\omega_3) = H_3(\omega_1,\omega_2,\omega_3)X(\omega_1)X(\omega_2)X(\omega_3) \tag{14}$$

Substituting for H_3 from (10) gives,

$$Y_3(\omega_1,\omega_2,\omega_3) = -k_3H_1(\omega)H_1(\omega_1)H_1(\omega_2)H_1(\omega_3)X(\omega_1)X(\omega_2)X(\omega_3) \tag{15}$$

where $\omega = \omega_1 + \omega_2 + \omega_3$. From (12) it follows that,

$$Y_3(\omega_1,\omega_2,\omega_3)H_1(\omega)^{-1} = -k_3Y_1(\omega_1)Y_1(\omega_2)Y_1(\omega_3) \tag{16}$$

or by (9),

$$(-m\omega^2 + ic\omega + k)Y_3(\omega_1,\omega_2,\omega_3) = -k_3Y_1(\omega_1)Y_1(\omega_2)Y_1(\omega_3) \tag{17}$$

Now, change variables to $\omega = \omega_1 + \omega_2 + \omega_3$, $\mu_1 = \omega_2 + \omega_3$, $\mu_2 = \omega_3$ and (17) becomes,

$$(-m\omega^2 + ic\omega + k)Y_3(\omega - \mu_1, \mu_1 - \mu_2, \mu_2) = -k_3Y_1(\omega - \mu_1)Y_1(\mu_1 - \mu_2)Y_1(\mu_2) \tag{18}$$

and according to equation (6.3-12) of [3],

$$Y_3(\omega) = \frac{1}{(2\pi)^2}\int_{-\infty}^{\infty}\int_{-\infty}^{\infty} d\mu_1 d\mu_2\ Y_3(\omega - \mu_1, \mu_1 - \mu_2, \mu_2) \tag{19}$$

so multiplying the LHS of (18) by $1/(2\pi)^2$ and integrating with respect to μ_1 and μ_2 yields,

$$(-m\omega^2 + ic\omega + k)Y_3(\omega) \tag{20}$$

and the inverse Fourier transform of this is,

$$m\ddot{y}_3 + c\dot{y}_3 + ky_3 \tag{21}$$

The same sequence of operations on the RHS of (18) gives,

$$\frac{-k_3}{(2\pi)^3}\int_{-\infty}^{\infty}\int_{-\infty}^{\infty}\int_{-\infty}^{\infty} d\omega d\mu_1 d\mu_2\ e^{i\omega t}Y_1(\omega - \mu_1)Y_1(\mu_1 - \mu_2)Y_1(\mu_2) \tag{22}$$

and changing variables back to $(\omega_1,\omega_2,\omega_3)$ gives (the Jacobian is unity),

$$\frac{-k_3}{(2\pi)^3}\int_{-\infty}^{\infty}\int_{-\infty}^{\infty}\int_{-\infty}^{\infty} d\omega_1 d\omega_2 d\omega_3\ e^{i(\omega_1+\omega_2+\omega_3)t}Y_1(\omega_1)Y_1(\omega_2)Y_1(\omega_3) \tag{23}$$

and the integral factors and becomes simply,

$$-k_3 y_1^3 \tag{24}$$

Equating (24) with the LHS in (21) gives the second ALE,

$$m\ddot{y}_3 + c\dot{y}_3 + ky_3 = -k_3 y_1^3 \tag{25}$$

The extraction of (24) was rather cumbersome and the derivations become more complicated for higher-order ALEs. Fortunately, there is a much more direct route via perturbation analysis as is shown in the next section.

If the nonlinearity is on the input, the situation is somewhat simpler. Consider the system,

$$m\ddot{y} + c\dot{y} + ky = f(x) \tag{26}$$

where f is an analytic function, i.e.,

$$f(x) = \sum_{i=1}^{\infty} a_i x^i \tag{27}$$

(it is assumed that there is no constant term, this will be dealt with in a later publication). The associated ALEs are simply,

$$m\ddot{y}_i + c\dot{y}_i + ky_i = a_i x^i \tag{28}$$

For example, the system,

$$m\ddot{y} + c\dot{y} + ky = a_1 x + a_3 x^3 \tag{29}$$

has ALEs,

$$m\ddot{y}_1 + c\dot{y}_1 + ky_1 = a_1 x, \qquad m\ddot{y}_3 + c\dot{y}_3 + ky_3 = a_3 x^3 \tag{30}$$

Now, by linearity of the differential operator on the LHS,

$$m(\ddot{y}_1 + \ddot{y}_3) + c(\dot{y}_1 + \dot{y}_3) + k(y_1 + y_3) = a_1 x + a_3 x^3 \tag{31}$$

and comparing this with (29), uniqueness of the solution of differential equations [7] gives,

$$y(t) = y_1(t) + y_3(t) \tag{32}$$

as required for this system.

PERTURBATION ANALYSIS

The connection between the Volterra series and perturbation analysis is known, see for example [6]. However, the analysis is given here for completeness and also to derive the required results for the Duffing oscillator example.

Assuming that k_3 in (8) is small enough to act as an expansion parameter, then the solution of the equation can be expressed as an infinite series,

$$y(t) = y^{(0)}(t) + k_3 y^{(1)}(t) + k_3^2 y^{(2)}(t) + \dots \tag{33}$$

Once (33) is substituted into (8), the coefficients of each k_3^i can be projected out to yield equations for the $y^{(i)}$. To order k_3^2, one has,

$$\begin{aligned} k_3^0 &: \; m\ddot{y}^{(0)} + c\dot{y}^{(0)} + k y^{(0)} = x(t) \\ k_3^1 &: \; m\ddot{y}^{(1)} + c\dot{y}^{(1)} + k y^{(1)} + y^{(0)3} = 0 \\ k_3^2 &: \; m\ddot{y}^{(2)} + c\dot{y}^{(2)} + k y^{(2)} + 3y^{(0)2} y^{(1)} = 0 \end{aligned} \tag{34}$$

The perturbation method is iterative. The first step is to solve the order k_3^0 equation. This is the standard SDOF linear equation and the solution is simply,

$$y^{(0)}(t) = \int_{-\infty}^{\infty} d\tau \; h_1(\tau) x(t-\tau) \tag{35}$$

where $h_1(\tau)$ is the impulse response of the underlying linear system.

The frequency content of the expansion is summed up by,

$$Y(\omega) = Y^{(0)}(\omega) + k_3 Y^{(1)}(\omega) + k_3^2 Y^{(2)}(\omega) + \dots \tag{36}$$

and so to order k_3^0, one has,

$$Y^{(0)}(\omega) = H_1(\omega) X(\omega) = Y_1(\omega) \tag{37}$$

where $Y_1(\omega)$ is the first term in the Volterra expansion for the spectrum.

The next equation is to order k_3^1 from (34). Note that the nonlinear term y_0^3 is actually known from the k_3^0 calculation, and the equation has a forced linear SDOF form,

$$m\ddot{y}^{(1)} + c\dot{y}^{(1)} + k y^{(1)} = -y^{(0)3} \tag{38}$$

and this has solution,

$$y^{(1)}(t) = -\int_{-\infty}^{\infty} d\tau \; h_1(t-\tau) y^{(0)3}(\tau) \tag{39}$$

so substituting (35) yields,

$$y^{(1)}(t) = -\int_{-\infty}^{\infty} d\tau\ h_1(t-\tau)\left(\int_{-\infty}^{\infty} d\tau_1\ h_1(\tau-\tau_1)x(\tau_1)\right)\times$$

$$\left(\int_{-\infty}^{\infty} d\tau_2\ h_1(\tau-\tau_2)x(\tau_2)\right)\left(\int_{-\infty}^{\infty} d\tau_3\ h_1(\tau-\tau_3)x(\tau_3)\right) \tag{40}$$

or,

$$y^{(1)}(t) = -\int_{-\infty}^{\infty}\int_{-\infty}^{\infty}\int_{-\infty}^{\infty} d\tau_1 d\tau_2 d\tau_3 \times$$

$$\left(\int_{-\infty}^{\infty} d\tau h_1(t-\tau)h_1(\tau-\tau_1)h_1(\tau-\tau_2)h_1(\tau-\tau_3)\right) x(\tau_1)x(\tau_2)x(\tau_3) \tag{41}$$

so, comparing with equation (2), it appears that,

$$y_3(t) = k_3 y^{(1)}(t) \tag{42}$$

so,

$$h_3(t-\tau_1, t-\tau_2, t-\tau_3) = -k_3\int_{-\infty}^{\infty} d\tau h_1(t-\tau)h_1(\tau-\tau_1)h_1(\tau-\tau_2)h_1(\tau-\tau_3) \tag{43}$$

setting $t = 0$,

$$h_3(-\tau_1, -\tau_2, -\tau_3) = -k_3\int_{-\infty}^{\infty} d\tau h_1(-\tau)h_1(\tau-\tau_1)h_1(\tau-\tau_2)h_1(\tau-\tau_3) \tag{44}$$

and finally letting $t_i = -\tau_i; i = 1, \ldots, 3$, one obtains

$$h_3(t_1, t_2, t_3) = -k_3\int_{-\infty}^{\infty} d\tau h_1(-\tau)h_1(\tau+t_1)h_1(\tau+t_2)h_1(\tau+t_3) \tag{45}$$

As a check it is useful to see what is happening in the frequency-domain. The appropriate transformation is (from (3)),

$$H_3(\omega_1, \omega_2, \omega_3) = -k_3\int_{-\infty}^{+\infty}\int_{-\infty}^{+\infty}\int_{-\infty}^{+\infty} dt_1 dt_2 dt_3\ e^{-i(\omega_1 t_1+\omega_2 t_2+\omega_3 t_3)}\times$$

$$\left(\int_{-\infty}^{\infty} d\tau h_1(-\tau)h_1(\tau+t_1)h_1(\tau+t_2)h_1(\tau+t_3)\right) \tag{46}$$

Now, this expression factors,

$$H_3(\omega_1, \omega_2, \omega_3) = -k_3\int_{-\infty}^{\infty} d\tau h_1(-\tau)\left(\int_{-\infty}^{\infty} dt_1 e^{-i\omega_1 t_1}h_1(t_1+\tau)\right)\times$$

$$\left(\int_{-\infty}^{\infty} dt_2 e^{-i\omega_2 t_2}h_1(t_2+\tau)\right)\left(\int_{-\infty}^{\infty} dt_3 e^{-i\omega_3 t_3}h_1(t_3+\tau)\right) \tag{47}$$

and using the Fourier transform shift theorem to take the sequence of transforms gives,

$$= -k_3 H_1(\omega_1)H_1(\omega_2)H_1(\omega_3)H_1(\omega_1+\omega_2+\omega_3) \tag{48}$$

which agrees with the harmonic probing result (10) as it should.

Carrying the calculation to higher orders is straightforward but tedious, After evaluating $y^{(2)}(t)$ and $y^{(3)}(t)$ it becomes clear that,

$$y_{2n+1}(t) = k_3^n y^{(n)}(t) \tag{49}$$

so the higher-order ALEs can be taken directly from (34).

THE INVERSE VOLTERRA SERIES FOR THE DUFFING OSCILLATOR

In this section, the ALEs will be used to prove an interesting result regarding the inverse Volterra series for the Duffing oscillator. As discussed in Section One, this is the series which satisfies $\boldsymbol{x} = \boldsymbol{K}[y]$ for the system in (8). In diagrammatic form,

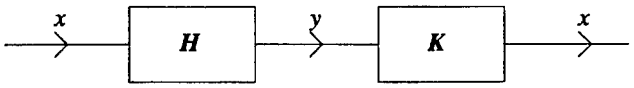

or, breaking the signals down into the relevant components,

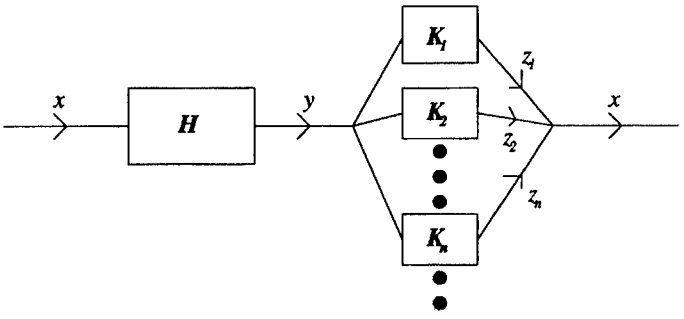

so,

$$z_i = \boldsymbol{K}_i[y] \tag{50}$$

and,

$$\boldsymbol{x} = \sum_{i=1}^{\infty} z_i \tag{51}$$

It transpires that only z_1 and z_3 are needed, and according to [3], the corresponding components of $\boldsymbol{K}$ are given by,

$$\boldsymbol{K}_1 = \boldsymbol{H}_1^{-1} \tag{52}$$

and,

$$\boldsymbol{K}_3 = -\boldsymbol{K}_1 \circ \boldsymbol{H}_3 \circ \boldsymbol{K}_1 \tag{53}$$

Considering z_1: according to the first ALE for the Duffing oscillator (13),

$$y_1 = \boldsymbol{H}_1[x] \Longrightarrow x = \boldsymbol{K}_1[y_1] = m\ddot{y}_1 + c\dot{y}_1 + ky_1 \tag{54}$$

and therefore,

$$z_1 = \boldsymbol{K}_1[y] = m\ddot{y} + c\dot{y} + ky = x - k_3 y^3 \tag{55}$$

by equation (8). The third ALE for the system (25) illustrates the decomposition,

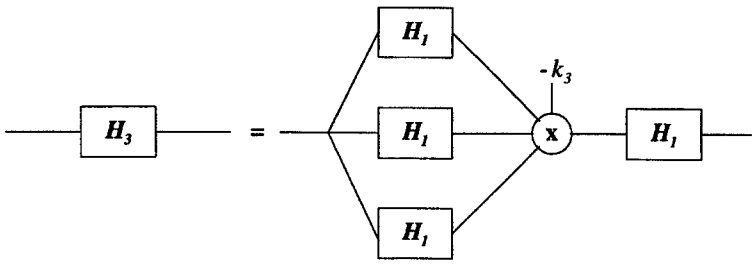

which gives a breakdown for z_3 according to (53),

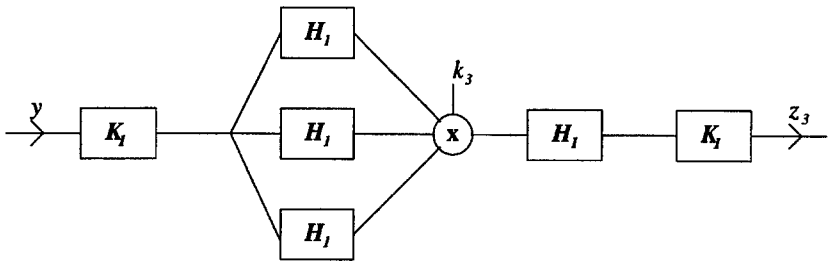

and according to (52) this collapses to,

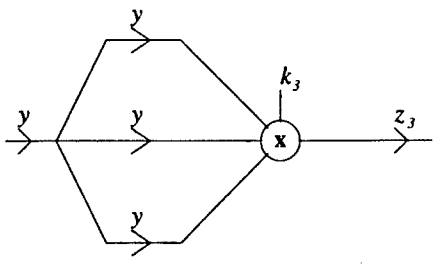

or,

$$z_3 = k_3 y^3 \tag{56}$$

So, adding (55) and (56), one finds that,

$$z_1 + z_3 = x \tag{57}$$

and the Volterra inverse therefore terminates at order three. Equations (55) and (56) further show that the inverse can be implemented in block form using only P and D operations, i.e.,

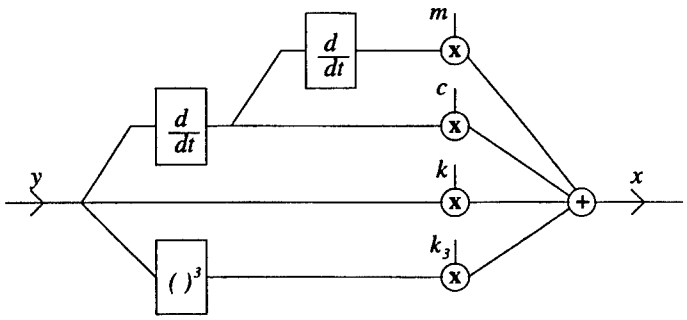

and it is clear from this representation, that the inverse system is valid for all levels of excitation of the original Duffing oscillator, even if the said oscillator does not have a convergent Volterra representation.

It is shown above that the third ALE is equivalent to a breakdown of $\boldsymbol{H}_3$ into $\boldsymbol{H}_1$ components. In fact, the n^{th} ALE gives the corresponding decomposition for $\boldsymbol{H}_n$. For example, the fifth ALE (from (34)),

$$m\ddot{y}_5 + c\dot{y}_5 + ky_5 = -3k_3^2 y_1^2 y_3 \tag{58}$$

gives,

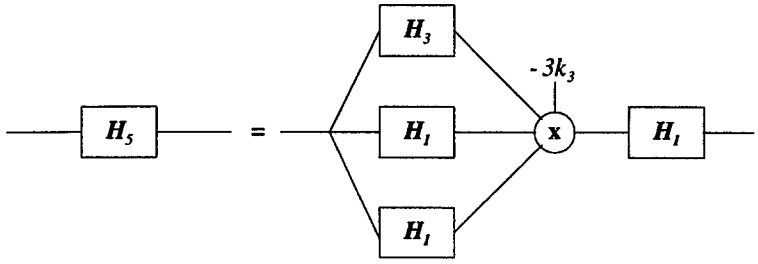

where the decomposition of $\boldsymbol{H}_3$ is already known.

CONCLUSIONS

The conclusions from this paper are simple. A decomposition of a nonlinear system into a system of associated linear equations (ALEs) is proposed on the basis of the Volterra representation of the system. No new results are presented here; however, it is argued that the ALEs allow simpler demonstrations of established results and also lend themselves to a diagrammatic representation which facilitates analysis. Further work will show how the ALEs are used in the generation of new results; namely in the analysis of inverse systems for oscillators with DC terms and for the analysis of inverses of discrete systems.

References

[1] Nayfeh, A.H. & Mook, D.T., *Nonlinear Oscillations*, Wiley Interscience, 1979.

[2] Nayfeh, A.H., *Perturbation Methods*, Wiley, New York, 1973.

[3] Schetzen, M., *The Volterra and Wiener Theories of Nonlinear Systems*, Kreiger, 1980.

[4] Bedrosian, E. & Rice, S.O., The output properties of Volterra systems driven by harmonic and Gaussian inputs, *Proceedings IEEE*, 1971, **59** pp.1688-1707.

[5] Worden, K & Tomlinson, G.R., *Nonlinearity in Structural Dynamics*, Adam Hilger (In Press), 2000.

[6] Ibrahim, R.A., Functional-perturbational type approach for random vibration analysis, *Preprint, Department of Mechanical Engineering, Wayne State University.*

[7] Simmons, G.F., *Differential Equations.* McGraw Hill, 1974.

NONLINEAR MOTIONS OF A VIBRATION SEPARATOR SYSTEM

A.B.Kazakoff & K.Worden
Dynamics Research Group
Department of Mechanical Engineering
University of Sheffield
Mappin Street
Sheffield S1 3JD
United Kingdom

Abstract

This paper presents a case study of a vibration separator system with vertical sieve surfaces. Under excitation by an unbalance force from an eccentric axle, the system displays multi-frequency vibrations. The analysis here considers a two-dimensional model and states the extension to three-dimensions and the expected results. Cubic and quadratic nonlinearities for the system arise as a result of interactions between the coordinates of the motion. An experiment is performed on a real separator and subharmonic behaviour is observed.

INTRODUCTION

This paper is concerned with a case study of a three-dimensional dynamical system which has been proposed and patented as a vibration separator with vertical sieve surfaces [1]. In addition to providing insight into the behaviour of the system, the analysis is of pedagogical interest as the equations of motion incorporate both a time-varying mass, and nonlinearity as a result of interactions between spatial coordinates.

The separator was designed for use removing sand from clay solution in the porcelein industry; however, it is applicable in any situation where sediment must be removed from a fluid. The machine functions by vibration separation of solid materials through vertical sieve surfaces. The vibrations are induced using an unbalanced axle. A schematic for the separator is given in Figure 1.

It was shown in [2], that multi-frequency vibrations could be obtained under single frequency excitation from several unbalanced axles rotating at a certain multiple of the resonant frequency. The main result of this paper is the observation that multi-frequency vibrations can be obtained under excitation by a single unbalance force in a real mechanical system, namely the separator; part of the analysis is outlined in support of the experimental results.

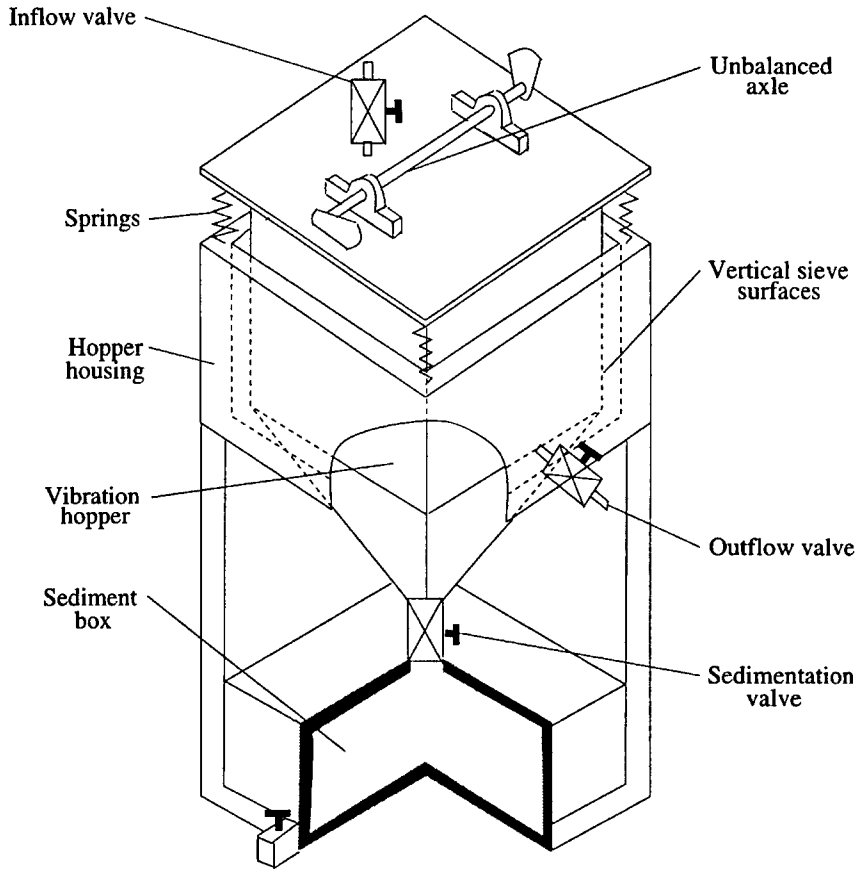

Figure 1. The vibration separator.

This paper is part of a longer-term investigation; there are essentially three stages to the overall programme of study:

1. An investigation into the spatial movement of a single mass system in two-dimensions. First with constant mass and then with a time-varying mass. The results of this investigation were reported in [4].

2. An investigation on the mechanisms for transferring energy between the coordinates via the nonlinear linkages. A look at possible exploitation of the nonlinearity to supress components of the multi-frequency response. A proposed method for the control of the vibration separator and the analysis of the multi-frequency response has also been the subject of a patent [3].

3. An attempt at experimental confirmation of the analytical results.

This paper partially addresses phase 3 of the programme above. The layout of the paper is as follows: Section Two introduces the ideas behind the vibration separator and discusses a simplified two-dimensional model, steady-state vibration results are presented from numerical simulation in Section Three. In Section Four, the three-dimensional model is discussed in a truncated form. In Section Five, the actual separator system is described and the results of the experimental study are presented.

THE TWO-DIMENSIONAL MODEL

Following the philosophy of [5], the system shall be regarded as a single-mass dynamical system subject to spatial stiffness and damping forces which restore equilibrium on excitation by an external force. In this section, a two-dimensional approximation to the motion will be explored, and a schematic for the system is shown in Figure 2.

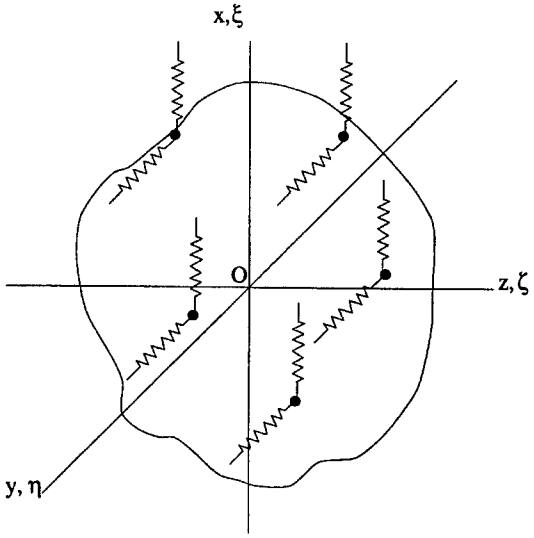

Figure 2. Two-dimensional spatial model.

The body is considered rigid of mass M, the general motion will be with respect to fixed coordinates (y, z) in two dimensions. (For the moment, angular motion is not considered so the sense of rotations is unimportant.) Motion is relative to an origin O. Where needed, a coordinate system (η, ζ) moving with the mass M could be employed.

The equations of motion for the mass moving in the plane (y, z), are (retaining terms up to cubic-order) derived using Lagriangian methods in [5, 6],

$$\ddot{y} + \frac{c_y}{m}\dot{y} + \omega_y^2 y + \frac{1}{r}\omega_y^2 yz - \frac{1}{r^2}(\omega_y^2 + \omega_z^2)yz^2 +$$

$$\frac{1}{2r^2}\omega_y^2 y^3 + \frac{1}{2r}\omega_z^2 z^2 = \frac{F}{m}\sin(\omega t) \tag{1}$$

$$\ddot{z} + \frac{c_z}{m}\dot{z} + \omega_z^2 z + \frac{1}{r}\omega_z^2 yz - \frac{1}{r^2}(\omega_y^2 + \omega_z^2)y^2 z +$$

$$\frac{1}{2r^2}\omega_z^2 z^3 + \frac{1}{2r}\omega_y^2 y^2 = \frac{F}{m}\cos(\omega t) \tag{2}$$

where the excitation is an unbalance force of magnitude F arising from an unbalanced axle rotating in the (y, z) plane with circular frequency ω, c_y and c_z are the total viscous dampings associated with the coordinates y and z, ω_y and ω_z are natural frequencies associated with the coordinates via the total stiffnesses k_y and k_z i.e. $\omega_y^2 = k_y/m$ and $\omega_z^2 = k_z/m$. The length of the elastic elements (springs) is r. Note that the springs are linear, the nonlinearity in the equations arises as a result of projecting the motion of the springs onto the two coordinate axes. For a complete analysis, the equations (1) and (2) would be supplemented by an equation for the angular degree of freedom θ, this is,

$$I\ddot{\theta} + c_\theta\dot{\theta} + k_\theta\theta + m(\ddot{y}z - y\ddot{z}) = M \tag{3}$$

where I is the moment of inertia and M is a driving moment. However, it was found in [6] that the influence of the angular variable in the two-dimensional system was small and could therefore be neglected safely. Note that when the angular variable is included, the simulation problem also becomes rather more complicated due to the presence of the spatial accelerations in its equation of motion.

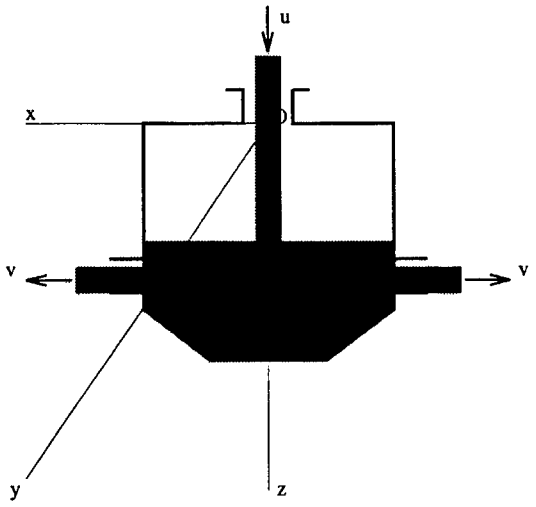

Figure 3. Schematic of two-dimensional model of separator.

The particular system under study here is the vibration separator; a schematic for the two-dimensional motion is given in Figure 3, the actual three-dimensional system is shown in Figure 1.

Fluid flows in at the top with an inflow velocity u and out at the base with outflow velocity $v = \sqrt{2gh}$, where g is the acceleration due to gravity and h is the vertical distance between the free surface of the fluid and the outflow openings. As a result, the system has a time-varying mass $m(t)$. There are essentially three modes of movement:

Filling up. The mass of the system increases steadily as a result of the fluid influx i.e. $u > v$ until equilibrium is reached with outflow equal to inflow.

Equilibrium Inflow equal to outflow $v = u$ i.e. $h = u^2/2g$. (The areas of the openings for inflow and outflow are assumed equal.)

Pure Outflow Fluid influx is zero and the separator empties to the level of the outflow.

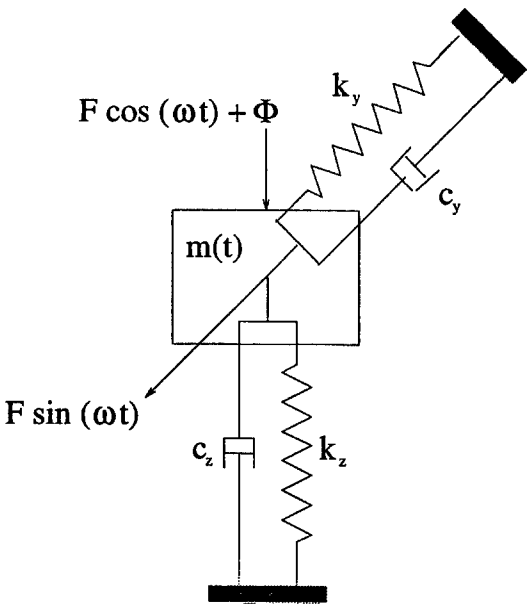

Figure 4. Minimal form of two-dimensional model of separator.

Figure 4. shows the model adopted for the separator incorporating the time-varying mass and reactive force as derived in [4]. After adjusting the equations (1) and (2) accordingly, they were not soluble analytically. In order to proceed, it was necessary to use numerical methods or adopt further simplifications. The former course was chosen. The equations (1) and (2) became (for inflow),

$$\ddot{y} + \frac{c_y}{m(t)}\dot{y} + \omega_y(t)^2 y + \frac{1}{r}\omega_y(t)^2 yz - \frac{1}{r^2}(\omega_y(t)^2 + \omega_z(t)^2)yz^2 + \frac{1}{2r^2}\omega_y(t)^2 y^3 + \frac{1}{2r}\omega_z(t)^2 z^2 = \frac{F}{m(t)}\sin(\omega t) \quad (4)$$

$$\ddot{z} + \frac{c_z + u\rho A}{m(t)}\dot{z} + \omega_z(t)^2 z + \frac{u(u-v)A^2\rho}{m(t)A_s} - \frac{u^2 A\rho}{m(t)} + \frac{1}{r}\omega_z(t)^2 yz - \frac{1}{r^2}(\omega_y(t)^2 + \omega_z(t)^2)y^2 z + \frac{1}{2r^2}\omega_z(t)^2 z^3 + \frac{1}{2r}\omega_y(t)^2 y^2 = \frac{F}{m(t)}\cos(\omega t) \quad (5)$$

NUMERICAL SIMULATIONS OF THE 2D MODEL

A number of simulations were performed in [4] to illustrate the full nonlinear and time-varying nature of the system. For completeness, some of the results are repeated here. The situation considered in the experimental study later is for the steady-state of the separator when it is either empty of fluid or in equilibrium between the inflow and outflow stages. Note that the full inflow/steady-state/outflow sequence was simulated in [4]. In order to carry out the simulations, the following parameter values were adopted as representative of the separator system (only those relevant for the steady-state motions are given here). The stifnesses were roughly estimated by testing the full separator system and relating the forces applied to the observed amplitudes.

Quantity	Symbol	Value	Units
Initial mass of separator	m_0	121	kg
Mass of added fluid	m_t	185	kg
y spring constant	k_y	1.844×10^6	Nm^{-1}
z spring constant	k_z	1.844×10^6	Nm^{-1}
y damping constant	c_y	298.7	Nsm^{-1}
z damping constant	c_z	298.7	Nsm^{-1}

Table 1: Parameter values for 2D simulations

The damping values were computed using the steady-state mass and stiffness values to give a damping ratio of 0.01 or 1% of critical.

The first of the simulations from [4] are reproduced here for completeness. In order to simplify matters, the set of simulations shown were made during the steady state, i.e. with the mass constant at 306 kg. The relevant equations are essentially (1) and (2). The simulations were carried out using a standard fourth-order Runge-Kutta algorithm as specified in [7].

The first simulation was for the system with a sinusoidal force of magnitude 2000 N and a frequency of 12.355 Hz. This is the natural frequency of both degrees of freedom as $k_y = k_z$. The sampling frequency was chosen as 500 Hz - well above the Nyquist limit even allowing for multiple harmonics in the response. A segment of the time response for y after the steady-state had been reached is given in Figure 5a. There appears to be no appreciable harmonic distortion; however, if the spectrum of the signal is computed (Figure 5b), the harmonics characteristic of a nonlinear system response are clearly present. As the nonlinear restoring force has both a quadratic and cubic part, both odd and even harmonics are present.

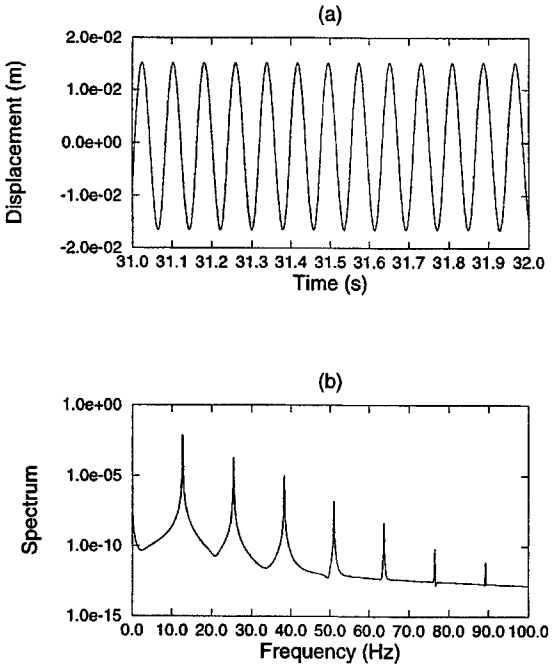

Figure 5. Response of 2D stationary system. Input at the natural frequency.

The second simulation used the same system parameters, amplitude of vibration and sampling frequency, but adjusted the excitation frequency

to 24.71 Hz, i.e. twice the natural frequencies. A segment of the time response (same interval as before) is given in Figure 6a. As before, there is no apparent harmonic distortion but the frequency is clearly twice that of the response in Figure 5a. Figure 6b shows the spectrum and again reveals the harmonic content, this time at multiples of 24.71 Hz. There is also evidence of subharmonic activity at 12.355 Hz.

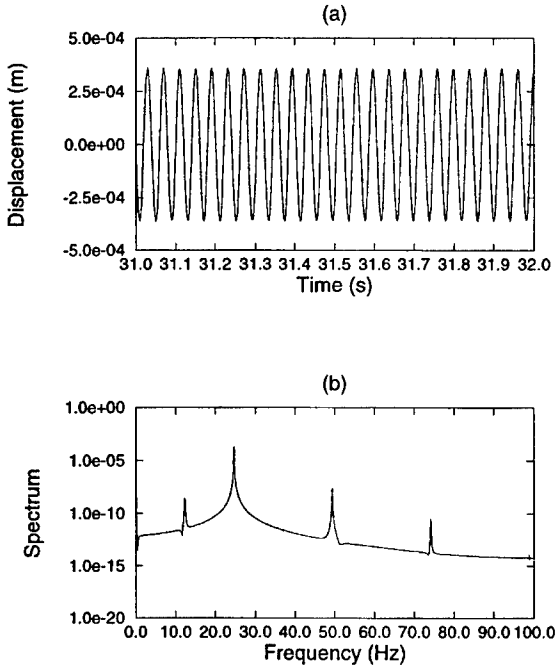

Figure 6. Response of 2D stationary system. Input at twice the natural frequency.

The objective of these simulations is to show that a multi-frequency response is obtained in the two-dimensional model when values for the stiffnesses and dampings are adopted which are representative of the true three-dimensional system. The harmonics in the response are a result of the nonlinearities in the equations of motion, which are in turn a result of the nonlinear relationships between the actual motions of the system and the projections onto the coordinate axes. If similar nonlinear terms are present in the full three-dimensional model, the same multi-frequency responses can be expected from that model and from the real system.

THE THREE-DIMENSIONAL MODEL

Three-dimensional spatial vibrations of the separator system are generated by driving the system with an unbalanced axle as shown in

Figure 7. The unbalance masses are at a relative angle of 90 degrees. This excitation forces elliptical motions (in the linear regime) in the $y-z$-plane and the remaining coordinates are excited as a result of the nonlinear geometrical linkages.

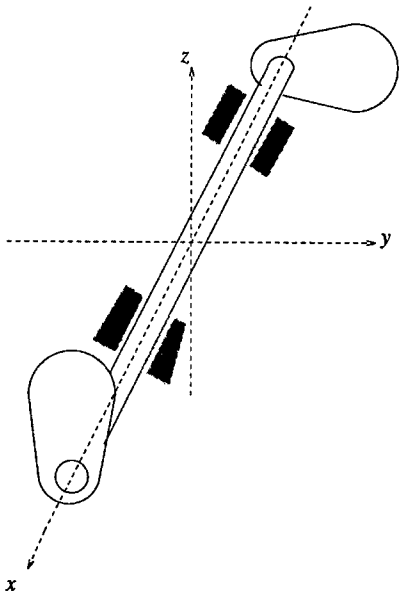

Figure 7. Unbalanced axle.

The equations of motion are rather complex, they are given here only up to second-order and only for the steady-state in order to show the difficulty of the problem,

$$m\ddot{x} + c_x\dot{x} + \omega_x^2 x = H_x \tag{6}$$

$$m\ddot{y} + c_y\dot{y} + \omega_y^2 y = H_y + F\sin(\omega t) \tag{7}$$

$$m\ddot{z} + c_z\dot{z} + \omega_z^2 z = H_z + F\cos(\omega t) \tag{8}$$

$$I_\theta\ddot{\theta} + c_\theta\dot{\theta} + a_{44}\theta = M_x - I_\phi\ddot{\phi}\psi - I_\phi\dot{\phi}\dot{\psi} - m(y\ddot{z} - \ddot{y}z) \tag{9}$$

$$I_\psi\ddot{\psi} + c_\psi\dot{\psi} + a_{55}\psi = M_y + I_\phi\ddot{\phi}\theta + I_\phi\dot{\phi}\dot{\theta} - m(z\ddot{x} - \ddot{z}x) + M\sin(\omega t) \tag{10}$$

$$I_\phi\ddot{\phi} + c_\phi\dot{\phi} + a_{66}\phi = M_z + I_\theta\ddot{\theta}\psi + I_\phi\dot{\theta}\dot{\psi} - (I_\psi - I_\phi)\dot{\psi}\theta + m(x\ddot{y} - \ddot{x}y) + M\cos(\omega t) \tag{11}$$

where F and M are the magnitudes of the force and torque respectively induced by the axle. I_θ, I_ψ and I_ϕ are the mass moments of inertia. a_{44}, a_{55} and a_{66} are constants induced by the geometry analogous to the parameter r in the two-dimensional equations of motion (1) and (2) (the notation a_n is from [5]). H_x, H_y, H_z, M_x, M_y and M_z and quantities describing the

nonlinear interactions between the coordinates. The simplest of these is H_x which is (only to second-order),

$$H_x = a_{15}\psi + a_{111}xz + a_{120}z\psi + a_{126}\theta\phi \tag{12}$$

where again the numbers refer to the notation of [5]. Clearly these equations are far too complicated to allow any analytical progress and the only course of action is computation. This exercise will be pursued in another publication, the point to note now from the equations above is that they are nonlinear in the coordinates in a similar fashion to the two-dimensional model and will be expected to generate the same nonlinear behaviour. Because both odd and even nonlinearities are present in the full equations, odd and even superharmonics and subharmonics might be expected in the responses. That this occurs is illustrated in the next section by experiment.

EXPERIMENTAL RESULTS

The full three-dimensional system is essentially that presented in Figure 1. The excitation was provided by the unbalanced axle of Figure 7 driven by a Bruel and Kjær sine-wave generator and standard power amplifier. Two Bruel and Kjær accelerometers placed on the hopper housing were used to measure the responses. The experiments were repeated three times with the sensors oriented along a different coordinate in each case. For each experiment, the sensors were placed a small distance apart and the angular responses were obtained by passing two accelerometer readings into a signal differencer. The Fourier transforms were carried out using a Bruel and Kjær spectrum analyser.

Coordinate	Natural Frequency (Hz)
x	$f_x = \omega_x/(2\pi) = 12.5$
y	$f_y = \omega_y/(2\pi) = 12.5$
z	$f_z = \omega_z/(2\pi) = 16.0$
θ	$f_\theta = \omega_\theta/(2\pi) = 18.5$
ψ	$f_\psi = \omega_\psi/(2\pi) = 14.5$
ϕ	$f_\phi = \omega_\phi/(2\pi) = 24.0$

Table 2: Natural frequencies of unadjusted system

The first set of data were obtained with the separator hopper full and the natural frequencies for the various coordinates were as given in Table 2.

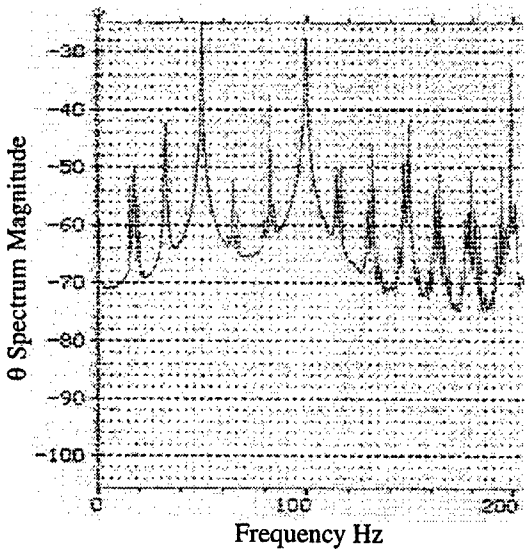

Figure 8. θ-spectrum of unadjusted system.

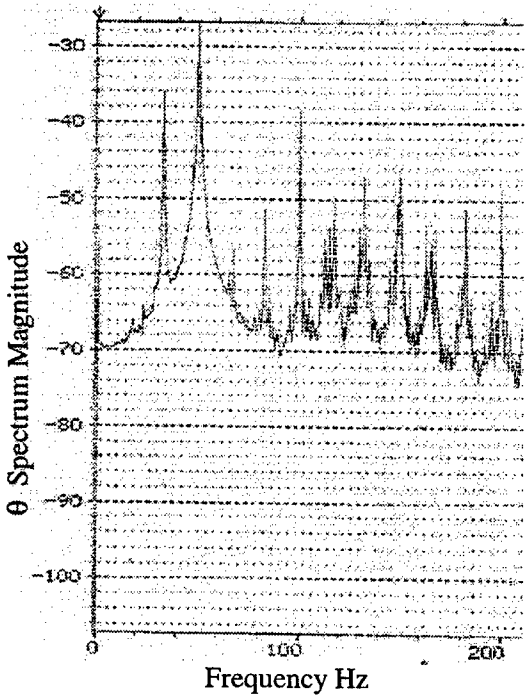

Figure 9. θ-spectrum of adjusted system.

The full separator was excited with a sinusoidal force at 50 Hz. The resulting vibrations showed a marked subharmonic and superharmonic content. The results are shown in Figure 8 for the θ coordinate spectrum, the

third-order subharmonic components at 16.7 Hz and 33.3 Hz are evident. This shows clearly the nonlinear nature of the system resulting from the geometrical couplings between the coordinates.

A similar response is obtained from the empty hopper. If the natural frequencies of the empty hopper are adjusted by the method given in [6] whereby mass is added in order to change, predominantly, the natural frequencies of the θ and ψ coordinates, the natural frequencies are as given in Table 3.

Coordinate	Natural Frequency (Hz)
x	$f_x = 19.3$
y	$f_y = 19.3$
z	$f_z = 19.3$
θ	$f_\theta = 19.9$
ψ	$f_\psi = 19.9$
ϕ	$f_\phi = 29.0$

Table 3: Natural frequencies of adjusted system

and the θ-spectrum is given in Figure 9. Note that the effect of the mass adjustment has been to suppress the 1/3 subharmonic at the expense of amplifying the 2/3 subharmonic. This shows that the mass adjustment procedure in [6] offers the possibility of amplifying or suppressing signal components from three-dimensional rigid body motions.

The experiment thus confirms the qualitative predictions from the model simulations, namely that the separator produces superharmonic and subharmonic responses as a result of nonlinear geometrical relationships between the coordinates.

CONCLUSIONS

The purpose of this paper has been to illustrate the fact that spatial rigid body motions are intrinsically nonlinear due to the geometrical couplings between coordinates. Two demonstrations are made: one on a two-dimensional simulated system and the second on a three-dimensional experiment. The theory for the three-dimensional system is rather complicated as discussed above and this will be reported elsewhere; however, samples of the full equations of motion are given here in order to show their qualitative similarity to those of the two-dimensional model. The separator study also indicates that mass adjustments which change the coordinate natural frequencies can potentially suppress or amplify signal components from the forced vibrations.

References

[1] Tcherneva, Z.T. and Kazakoff, A.B., Method and device for vibrations separation of materials through vertical sieve surfaces. *Patent of Bulgaria, 28/08/82*, **No.36088**, 1982.

[2] Bauman, V.A. and Bichovski, I.I., *Vibration, Machines and Processes in Building.* Vishaia Shkola (in Russian), 1977.

[3] Tcherneva, Z.T. and Kazakoff, A.B., Method and device for vibrations separation of materials through vertical sieve surfaces - for polyfrequency three-dimensional motion generation. *Patent of Bulgaria, 21/05/87* **No.79825**.

[4] Kazakoff, A.B. and Worden, K., Nonlinear motions of a model vibration separator system, *in Proceedings of 1st International Conference on the Integration of Dynamics, Monitoring and Control, Manchester*, pp.267-275, 1999.

[5] Ganiev, R.F. and Kononenko, V.O., *Vibrations of a Rigid Body.* Nauka Moscow (in Russian), 1976.

[6] Kazakoff, A.B., Theoretical and experimental investigations of spatial vibrations of a single mass dynamical systems with applications in vibration technology. *Ph.D. Thesis, Technical University of Sofia*, 1991.

[7] Press, W.H., Flannery, B.P., Teukolsky, S.A. and Vetterling, W.T., *Numerical Recipes - The Art of Scientific Computing* Cambridge University Press, 1986.

Transient Vibrations of a Nonlinear Spherical Shell Being in External Contact With an Elastic Isotropic Medium

Yu. A. Rossikhin and M. V. Shitikova

Department of Theoretical Mechanics, Voronezh State Academy of Construction and Architecture, ul.Kirova 3-75, Voronezh 394018, Russia

Transient vibrations of an isotropic nonlinearly elastic spherical shell being in external smooth contact with an elastic isotropic medium are considered. At the initial instant of time, the internal surface of the shell is subjected to the snap-action velocity vector components which are dependent on the coordinates on the shell's middle surface. The solution of the problem is accomplished in three stages. At the first stage, the solution is constructed for a spherical cavity whose boundary is subjected to a given velocity vector at the initial instant of time. As a result, two types of shock waves, quasilongitudinal and quasitransverse waves, begin to propagate in the surrounding medium with the speeds of elastic waves. Behind the wave fronts, the functions to be found are determined in terms of ray series constructed by virtue of the theory of discontinuities. At the second stage, the solution to the problem on transient vibrations of a spherical shell is sought in terms of power series with respect to time with indeterminate coefficients dependent on the coordinates on the shell's middle surface. At the third stage, the solutions obtained on the first two stages are matched with each other using the conditions of contact and initial conditions. As a result of the procedure described, the time dependence of the shell deflection and contact force can be obtained and the stress and displacement velocity fields can be constructed in the domain adjacent immediately to the contact zone.

INTRODUCTION

The problems connected with nonstationary interactions of thin shells with a surrounding medium belong to the contact dynamic problems and are of practical significance. These problems are the topical problems just

as from the view point of fundamental investigations dealing with the contact dynamic problems, so also in the view of their applications to various fields of modern production. One is up against such problems in mining art when investigating the interaction of a working with a support, in petroleum extractive and refining industry in storage of oil and petroleum products in spherical subsurface vessels, in seismology and seismic survey when cavities of the Earth's crust interacting with incident and reflected waves may play the role of resonators increasing the energy of wave fields in the vicinity of these cavities, and so on.

Mathematical methods used for solving contact dynamic problem are of a great variety, among them the method of invariant-functional solutions suggested by V.N. Smirnov and S.L. Sobolev, the Wiener-Hopf method, the integral transform method, the generalized Volterra and Hadamard methods, the method of characteristics, various numerical methods, as well as the ray method. The advantage of the last named method over other mentioned methods is in its pictorial compatibility with the intuitive notion of wave propagation generally and light waves specifically, in the ease of interpretation of the results obtained, as well as in its versatility, since the ray series, which are the basis of this method, may be successfully applied both for solving the problems connected with the generation of harmonic vibrations and waves and for tackling the problems dealing with the origination of transient vibrations and waves.

Rossikhin [1] was the first to use the ray method for solving contact dynamic problems when studying transient vibration of a plate resting on an elastic anisotropic half-space. Then it was generalized by Shitikova [2] for investigating different problems of such a kind. A comprehensive review of papers, wherein dynamic contact problems were solved by the ray method based on the theory of discontinuities, can be found in [3].

The ray method, which has been advantageously applied in the above enumerated papers for solving linear problems, has been extended further to the solution of the problems dealing with nonlinear thin bodies. Thus, the transient vibrations of a nonlinear elastic plate resting on an elastic isotropic half-space have been studied in [4], but the transient vibrations of a nonlinearly elastic infinite cylindrical shell of constant thickness being in external contact with an elastic isotropic surrounding medium have been investigated in [5].

In the present paper, the dynamic contact problem for the interaction of a nonlinearly elastic spherical shell with an elastic isotropic medium contacting with the shell's external surface, when its internal surface is subjected to nonstationary excitations, is solved by the ray method.

1 Problem Formulation

Let us consider transient vibrations of a nonlinearly elastic isotropic spherical shell of the thickness h and radius R being in external smooth contact with an unbounded elastic isotropic medium; in so doing the stress-strain relations and the bending strain-displacement relations for the shell are considered to be linear while the membrane strain-displacement relations are nonlinear.

The equations of axisymmetric vibrations of such a shell in the cylindrical coordinate system (Fig.1) have the form [6]

$$D\Delta^4 w - \frac{1}{R}\Delta^2\Phi - L(w,\Phi) + \varrho_1 h\frac{\partial^2 w}{\partial t^2} = q, \tag{1a}$$

$$\Delta^4\Phi = -\frac{E_1 h}{R}\Delta^2 w - \frac{E_1 h}{2}L(w,w), \tag{1b}$$

where

$$L(w,w) = 2\frac{1}{\rho}\frac{\partial^2 w}{\partial\rho^2}\frac{\partial w}{\partial\rho}, \quad L(w,\Phi) = \frac{1}{\rho}\left(\frac{\partial^2 w}{\partial\rho^2}\frac{\partial\Phi}{\partial\rho} + \frac{\partial w}{\partial\rho}\frac{\partial^2\Phi}{\partial\rho^2}\right),$$

$$\Delta^2 = \frac{1}{\rho}\frac{\partial}{\partial\rho}\left(\rho\frac{\partial}{\partial\rho}\right), \quad D = \frac{E_1 h^3}{12(1-\nu_1^2)},$$

w is the shell middle surface deflection, ρ is the polar radius, q is the external loading components along the shell's radius, ϱ_1, E_1, and ν_1 are the material density, the Young's modulus, and Poisson's ratio, respectively, and t is the time.

The dynamic behaviour of the unbounded elastic isotropic medium surrounding the spherical shell is described in the spherical system of coordinates r,θ,φ by the following set of equations:

$$\frac{1}{r^2}\frac{\partial(r^2\sigma_{rr})}{\partial r} + \frac{1}{r\sin\theta}\left(\frac{\partial(\sigma_{r\theta}\sin\theta)}{\partial\theta} + \frac{\partial\sigma_{r\varphi}}{\partial\varphi}\right) - \frac{\sigma_{\varphi\varphi}+\sigma_{\theta\theta}}{r} = \varrho\frac{\partial^2 u_r}{\partial t^2},$$

$$\frac{1}{r^3}\frac{\partial(r^3\sigma_{r\theta})}{\partial r} + \frac{1}{r\sin\theta}\left(\frac{\partial(\sigma_{\theta\theta}\sin\theta)}{\partial\theta} + \frac{\partial\sigma_{\theta\varphi}}{\partial\varphi}\right) - \frac{\operatorname{ctg}\theta}{r}\sigma_{\varphi\varphi} = \varrho\frac{\partial^2 u_\theta}{\partial t^2}, \tag{2}$$

$$\frac{1}{r^3}\frac{\partial(r^3\sigma_{r\varphi})}{\partial r} + \frac{1}{r\sin^2\theta}\frac{\partial\left(\sigma_{\theta\varphi}\sin^2\theta\right)}{\partial\theta} + \frac{1}{r\sin\theta}\frac{\partial\sigma_{\varphi\varphi}}{\partial\varphi} = \varrho\frac{\partial^2 u_\varphi}{\partial t^2},$$

where σ_{ij} and u_i $(i,j{=}r,\theta,\varphi)$ are the stress tensor and displacement vector components, respectively, and ρ is the density of the surrounding medium.

The generalized Hooke's law for the isotropic medium has the form:

$$\sigma_{rr} = 2\mu e_{rr} + \lambda e, \quad \sigma_{\varphi\varphi} = 2\mu e_{\varphi\varphi} + \lambda e, \quad \sigma_{\theta\theta} = 2\mu e_{\theta\theta} + \lambda e,$$

$$\sigma_{r\varphi} = 2\mu e_{r\varphi}, \quad \sigma_{r\theta} = 2\mu e_{r\theta}, \quad \sigma_{\varphi\theta} = 2\mu e_{\varphi\theta}, \tag{3}$$

where $e = e_{rr} + e_{\varphi\varphi} + e_{\theta\theta}$ is the relative bulk deformation, the strain tensor components e_{ij} $(i, j{=}r, \theta, \varphi)$ have the form

$$e_{rr} = \frac{\partial u_r}{\partial r}, \quad e_{\theta\theta} = \frac{1}{r}\frac{\partial u_\theta}{\partial \theta} + \frac{u_r}{r}, \quad e_{\varphi\varphi} = \frac{1}{r\sin\theta}\frac{\partial u_\varphi}{\partial \varphi} + \frac{u_r}{r} + \operatorname{ctg}\theta\frac{u_\theta}{r},$$

$$e_{r\theta} = \frac{1}{2}\left(\frac{1}{r}\frac{\partial u_r}{\partial \theta} + \frac{\partial u_\theta}{\partial r} - \frac{u_\theta}{r}\right), \quad e_{r\varphi} = \frac{1}{2}\left(\frac{1}{r\sin\theta}\frac{\partial u_r}{\partial \varphi} + \frac{\partial u_\varphi}{\partial r} - \frac{u_\varphi}{r}\right), \tag{4}$$

$$e_{\varphi\theta} = \frac{1}{2}\left(\frac{1}{r\sin\theta}\frac{\partial u_\theta}{\partial \varphi} + \frac{1}{r}\frac{\partial u_\varphi}{\partial \theta} - \frac{u_\varphi \operatorname{ctg}\theta}{r}\right).$$

and λ and μ are Lame's parameters.

The shell and surrounding medium are in smooth contact at $r = R$, i.e.,

$$\sigma_{r\varphi} = \sigma_{r\theta} = 0, \quad \sigma_{rr} = q, \quad w(\rho, t) = u_r. \tag{5}$$

The initial condition on all the surface of the shell

$$\frac{\partial w}{\partial t} = V_0(\rho), \tag{6}$$

where $V_0(\rho)$ is the given function, should be added to Eqs.(1)-(5).

SOLUTION FOR THE SPACE WITH A SPHERICAL CAVITY

As a result of snap-action application of displacement velocity (6) to the boundary of the spherical cavity, two surfaces of strong discontinuity propagate in the elastic isotropic medium. Behind the wavefronts the solution for a certain function $Z(r, \theta, \varphi, t)$ to be found is constructed in the form of a series in terms of powers $y_{(\alpha)} = t - (r - R)G^{(\alpha)^{-1}} \geq 0$, *i e*, the ray series,

$$Z(r, \theta, \varphi, t) = \sum_{\alpha=1}^{2}\sum_{k=0}^{\infty}\frac{1}{k!}\left[Z_{,(k)}^{(\alpha)}\right]\Big|_{y_{(\alpha)}=0} y_{(\alpha)}^k H(y_{(\alpha)}), \tag{7}$$

where $\left[Z_{,(k)}^{(\alpha)}\right] = \left(\partial^k Z^{(\alpha)}/\partial t^k\right)^+ - \left(\partial^k Z^{(\alpha)}/\partial t^k\right)^-$ are the jumps in the kth time derivatives of the function $Z^{(\alpha)}(r, \theta, \varphi, t)$ on the fronts of the shock waves, the signs "+" and "-" denote that the given function is calculated immediately ahead of and behind the wavefront, respectively, α signifies the ordinal number of the wave: $\alpha = 1$ for the quasilongitudinal wave and $\alpha = 2$ for the quasitransverse wave, respectively, $G^{(\alpha)}$ are the shock wave velocities, and $H(y_{(\alpha)})$ are the unit Heaviside functions.

To determine the coefficients of the ray series (7) for the desired functions σ_{ri} and u_i $(i = r, \varphi, \theta)$, we differentiate Eqs.(2) k times and Eqs.(3)

and (4) $k+1$ times with respect to time, take their difference on the different sides of each of the wave surfaces, and apply the condition of compatibility for discontinuities of the $(k+1)$th derivatives, which, as it has been shown in [7], for the physical components of a certain vector or tensor takes the form

$$G\left[\partial Z_{,(k)}/\partial r\right] = -\left[Z_{,(k+1)}\right] + \delta\left[Z_{,(k)}\right]/\delta t, \tag{8}$$

where $\delta/\delta t$ is the Thomas δ-derivative [8].

As a result of straightforward calculations, we obtain the recurrent relationships in terms of the discontinuities in the partial time derivatives of the displacement velocities v_r, v_φ and v_θ

$$\left(\varrho G^2 - (\lambda+2\mu)\right)[v_{r,(k+1)}] = -2(\lambda+2\mu)\left(\frac{\delta[v_{r,(k)}]}{\delta t} + \frac{G}{r}[v_{r,(k)}]\right)$$

$$-\frac{G}{r}(\lambda+\mu)\left(\cot\theta[v_{\theta,(k)}] + \frac{\partial[v_{\theta,(k)}]}{\partial\theta} + \frac{1}{\sin\theta}\frac{\partial[v_{\varphi,(k)}]}{\partial\varphi}\right) + L_{k-1}, \tag{9}$$

$$\left(\varrho G^2 - \mu\right)[v_{\theta,(k+1)}] = -2\mu\left(\frac{\delta[v_{\theta,(k)}]}{\delta t} + \frac{G}{r}[v_{\theta,(k)}]\right) - \frac{G}{r}(\lambda+\mu)\frac{\partial[v_{r,(k)}]}{\partial\theta} + M_{k-1}, \tag{10}$$

$$\left(\varrho G^2 - \mu\right)[v_{\varphi,(k+1)}] = -2\mu\left(\frac{\delta[v_{\varphi,(k)}]}{\delta t} + \frac{G}{r}[v_{\varphi,(k)}]\right) - \frac{G}{r}\frac{(\lambda+\mu)}{\sin\theta}\frac{\partial[v_{r,(k)}]}{\partial\varphi} + N_{k-1}, \tag{11}$$

where the functions L_{k-1}, M_{k-1} and N_{k-1} have the form

$$\begin{aligned}
L_{k-1} &= (\lambda+2\mu)\left(\frac{\delta^2[v_{r,(k-1)}]}{\delta t^2} + 2\frac{G}{r}\frac{\delta[v_{r,(k-1)}]}{\delta t} - 2\frac{G^2}{r^2}[v_{r,(k-1)}]\right) \\
&+ \frac{G^2}{r^2}\mu\left(\cot\theta\frac{\partial[v_{r,(k-1)}]}{\partial\theta} + \frac{\partial^2[v_{r,(k-1)}]}{\partial\theta^2} + \frac{1}{\sin\theta}\frac{\partial^2[v_{r,(k-1)}]}{\partial\varphi^2}\right) \\
&+ \frac{G}{r}(\lambda+\mu)\left(\cot\theta\frac{\delta[v_{\theta,(k-1)}]}{\delta t} + \frac{\partial}{\partial\theta}\frac{\delta[v_{\theta,(k-1)}]}{\delta t} + \frac{1}{\sin\theta}\frac{\partial}{\partial\varphi}\frac{\delta[v_{\varphi,(k-1)}]}{\delta t}\right) \\
&- \frac{G^2}{r^2}(\lambda+3\mu)\left(\cot\theta[v_{\theta,(k-1)}] + \frac{\partial[v_{\theta,(k-1)}]}{\partial\theta} + \frac{1}{\sin\theta}\frac{\partial[v_{\varphi,(k-1)}]}{\partial\varphi}\right),
\end{aligned}$$

$$\begin{aligned}
M_{k-1} &= \mu\left(\frac{\delta^2[v_{\theta,(k-1)}]}{\delta t^2} + 2\frac{G}{r}\frac{\delta[v_{\theta,(k-1)}]}{\delta t} + \frac{G^2}{r^2}\frac{1}{\sin^2\theta}\frac{\partial^2[v_{\theta,(k-1)}]}{\partial\varphi^2}\right) \\
&+ \frac{G^2}{r^2}(\lambda+2\mu)\left(\cot\theta\frac{\partial[v_{\theta,(k-1)}]}{\partial\theta} + \frac{\partial^2[v_{\theta,(k-1)}]}{\partial\theta^2} - \frac{1}{\sin^2\theta}[v_{\theta,(k-1)}]\right) \\
&+ \frac{G}{r}(\lambda+\mu)\frac{\partial}{\partial\theta}\frac{\delta[v_{r,(k-1)}]}{\delta t} + 2\frac{G^2}{r^2}(\lambda+2\mu)\frac{\partial[v_{r,(k-1)}]}{\partial\theta} \\
&- \frac{G^2}{r^2}(\lambda+3\mu)\frac{\cot\theta}{\sin\theta}\frac{\partial[v_{\varphi,(k-1)}]}{\partial\varphi} + \frac{G^2}{r^2}\frac{(\lambda+\mu)}{\sin\theta}\frac{\partial^2[v_{\varphi,(k-1)}]}{\partial\theta\partial\varphi},
\end{aligned}$$

$$N_{k-1} = \mu\left(\frac{\delta^2[v_{\varphi,(k-1)}]}{\delta t^2} + 2\frac{G}{r}\frac{\delta[v_{\varphi,(k-1)}]}{\delta t}\right) + \frac{G^2}{r^2}\frac{(\lambda+2\mu)}{\sin^2\theta}\frac{\partial^2[v_{\varphi,(k-1)}]}{\partial\varphi^2}$$
$$+ \frac{G^2}{r^2}\mu\left(\cot\theta\frac{\partial[v_{\varphi,(k-1)}]}{\partial\theta} + \frac{\partial^2[v_{\varphi,(k-1)}]}{\partial\theta^2} - \frac{1}{\sin^2\theta}[v_{\varphi,(k-1)}]\right)$$
$$+ \frac{G}{r}\frac{(\lambda+\mu)}{\sin\theta}\frac{\partial}{\partial\varphi}\frac{\delta[v_{r,(k-1)}]}{\delta t} + 2\frac{G^2}{r^2}\frac{(\lambda+2\mu)}{\sin\theta}\frac{\partial[v_{r,(k-1)}]}{\partial\varphi}$$
$$+ \frac{G^2}{r^2}(\lambda+3\mu)\frac{\cot\theta}{\sin\theta}\frac{\partial[v_{\theta,(k-1)}]}{\partial\varphi} + \frac{G^2}{r^2}\frac{(\lambda+\mu)}{\sin\theta}\frac{\partial^2[v_{\theta,(k-1)}]}{\partial\theta\partial\varphi}.$$

From Eqs.(9)-(11) at k = -1, 0, 1, 2 we determine the velocities of two types of waves: compressive $G^{(1)} = \sqrt{(\lambda+2\mu)/\varrho}$ and shear $G^{(2)} = \sqrt{\mu/\varrho}$, as well as the values $[v_{i,(k)}]^{(\alpha)}$ $(i = r, \varphi, \theta)$ on the first wave at $\alpha = 1$ within the accuracy of the arbitrary functions $f_{(k)}(\varphi,\theta)$, and on the second wave at $\alpha = 2$ with the accuracy of the arbitrary functions $g_{(k)}(\varphi,\theta)$ and $h_{(k)}(\varphi,\theta)$, respectively. Hereafter we restrict ourselves to four terms of the ray series. Thus, on the first wave we obtain

$$[v_{r,(0)}] = \frac{f_{(0)}}{r}, \quad [v_{\theta,(0)}] = [v_{\varphi,(0)}] = 0,$$

$$[v_{\theta,(1)}] = -\frac{G}{r^2}f_{(0),\theta}, \quad [v_{\varphi,(1)}] = -\frac{G}{r^2}\frac{1}{\sin\theta}f_{(0),\varphi},$$

$$[v_{r,(1)}] = \frac{f_{(1)}}{r} - \frac{1}{2}\frac{G}{r^2}\left\{f_{(0),\theta\theta} + \cot\theta f_{(0),\theta} - 2f_{(0)} + \frac{1}{\sin^2\theta}f_{(0),\varphi\varphi}\right\},$$

$$[v_{\theta,(2)}] = -\frac{G}{r^2}f_{(1),\theta} + \frac{1}{2}\frac{G^2}{r^3}\left\{f_{(0),\theta\theta\theta} + \cot\theta f_{(0),\theta\theta} - \frac{1}{\sin^2\theta}f_{(0),\theta}\right.$$
$$\left. + \frac{1}{\sin^2\theta}f_{(0),\varphi\varphi\theta} - \frac{2\cot\theta}{\sin^2\theta}f_{(0),\varphi\varphi}\right\},$$

$$[v_{\varphi,(2)}] = -\frac{G}{r^2}\frac{1}{\sin\theta}f_{(1),\varphi} + \frac{1}{2}\frac{G^2}{r^3}\frac{1}{\sin\theta}\left\{\frac{1}{\sin^2\theta}f_{(0),\varphi\varphi\varphi} + f_{(0),\theta\theta\varphi} + \cot\theta f_{(0),\varphi\theta}\right\},$$

$$[v_{r,(2)}] = \frac{f_{(2)}}{r} - \frac{1}{2}\frac{G}{r^2}\left\{f_{(1),\theta\theta} + \cot\theta f_{(1),\theta} - 2f_{(1)} + \frac{1}{\sin^2\theta}f_{(1),\varphi\varphi}\right\}$$
$$+\frac{1}{8}\frac{G^2}{r^3}\left\{f_{(0),\theta\theta\theta\theta} + 2\cot\theta f_{(0),\theta\theta\theta} + \frac{1}{\sin^4\theta}f_{(0),\varphi\varphi\varphi\varphi}\right.$$
$$-(8+\cot^2\theta)f_{(0),\theta\theta} + \frac{2}{\sin^2\theta}f_{(0),\varphi\varphi\theta\theta} - \frac{2\cot\theta}{\sin^2\theta}f_{(0),\varphi\varphi\theta}$$
$$\left. - \cot\theta(5-\cot^2\theta)f_{(0),\theta} - \frac{4(1-\cot^2\theta)}{\sin^2\theta}f_{(0),\varphi\varphi}\right\}, \qquad (12a)$$

and on the second wave

$$[v_{r,(0)}] = 0, \quad [v_{\theta,(0)}] = \frac{g_{(0)}}{r}, \quad [v_{\varphi,(0)}] = \frac{h_{(0)}}{r},$$

$$[v_{r,(1)}] = \frac{G}{r^2}\left\{g_{(0),\theta} + \cot\theta g_{(0)} + \frac{1}{\sin\theta}h_{(0),\varphi}\right\},$$

$$[v_{\varphi,(1)}] = \frac{h_{(1)}}{r} - \frac{1}{2}\frac{G}{r^2}\left\{h_{(0),\theta\theta} + \cot\theta h_{(0),\theta} + \frac{1}{\sin^2\theta}\left(h_{(0),\varphi\varphi} - h_{(0)}\right) + \frac{2\cot\theta}{\sin\theta}g_{(0),\varphi}\right\},$$

$$[v_{\theta,(1)}] = \frac{g_{(1)}}{r} - \frac{1}{2}\frac{G}{r^2}\left\{g_{(0),\theta\theta} + \cot\theta g_{(0),\theta} + \frac{1}{\sin^2\theta}\left(g_{(0),\varphi\varphi} - g_{(0)}\right) - \frac{2\cot\theta}{\sin\theta}h_{(0),\varphi}\right\},$$

$$[v_{r,(2)}] = \frac{G}{r^2}\left\{g_{(1),\theta} + \cot\theta g_{(1)} + \frac{1}{\sin\theta}h_{(1),\varphi}\right\}$$
$$-\frac{1}{2}\frac{G^2}{r^3}\left\{g_{(0),\theta\theta\theta} + 2\cot\theta g_{(0),\theta\theta} - (2+\cot^2\theta)g_{(0),\theta} + \frac{\cot\theta}{\sin^2\theta}\left(\sin^2\theta g_{(0)} + g_{(0),\varphi\varphi}\right)\right.$$
$$\left. + \frac{1}{\sin^2\theta}g_{(0),\varphi\varphi\theta} + \frac{1}{\sin\theta}h_{(0),\theta\theta\varphi} + \frac{1}{\sin^3\theta}\left(h_{(0),\varphi\varphi\varphi} + h_{(0),\varphi}\right) - \frac{\cot\theta}{\sin\theta}h_{(0),\varphi\theta}\right\},$$

$$[v_{\varphi,(2)} = \frac{h_{(2)}}{r} - \frac{1}{2}\frac{G}{r^2}\left\{h_{(1),\theta\theta} + \cot\theta h_{(1),\theta} + \frac{1}{\sin^2\theta}\left(h_{(1),\varphi\varphi} - h_{(1)}\right)\right.$$
$$\left. + \frac{2\cot\theta}{\sin\theta}g_{(1),\varphi}\right\} + \frac{1}{8}\frac{G^2}{r^3}\left\{h_{(0),\theta\theta\theta\theta} + 2\cot\theta h_{(0),\theta\theta\theta} - (2+3\cot^2\theta)h_{(0),\theta\theta}\right.$$
$$+ \cot\theta(5+3\cot^2\theta)h_{(0),\theta} + \frac{1}{\sin^4\theta}\left(h_{(0),\varphi\varphi\varphi\varphi} - 2h_{(0),\varphi\varphi} - 3h_{(0)}\right)$$
$$+ \frac{2}{\sin^2\theta}\left(h_{(0),\varphi\varphi\theta\theta} - \cot\theta h_{(0),\varphi\varphi\theta}\right) - \frac{4(2+\cot^2\theta)}{\sin\theta}g_{(0),\varphi\theta}$$
$$\left. + \frac{4\cot\theta}{\sin\theta}g_{(0),\varphi\theta\theta} + \frac{4\cot\theta}{\sin^3\theta}\left(g_{(0),\varphi} + g_{(0),\varphi\varphi\varphi}\right)\right\},$$

$$[v_{\theta,(2)}] = \frac{g_{(2)}}{r} - \frac{1}{2}\frac{G}{r^2}\left\{g_{(1),\theta\theta} + \cot\theta g_{(1),\theta} + \frac{1}{\sin^2\theta}\left(g_{(1),\varphi\varphi} - g_{(1)}\right)\right.$$
$$\left. - \frac{2\cot\theta}{\sin\theta}h_{(1),\varphi}\right\} + \frac{1}{8}\frac{G^2}{r^3}\left\{g_{(0),\theta\theta\theta\theta} + 2\cot\theta g_{(0),\theta\theta\theta} - 3(2+\cot^2\theta)g_{(0),\theta\theta}\right.$$
$$+ \cot\theta(1+3\cot^2\theta)g_{(0),\theta} + \frac{1-3\cot^2\theta}{\sin^2\theta}g_{(0)} + \frac{1}{\sin^4\theta}g_{(0),\varphi\varphi\varphi\varphi}$$
$$+ \frac{2}{\sin^2\theta}g_{(0),\varphi\varphi\theta\theta} - \frac{2\cot\theta}{\sin^2\theta}g_{(0),\varphi\varphi\theta} - \frac{2(\cot^2\theta-1)}{\sin^2\theta}g_{(0),\varphi\varphi}$$
$$\left. - \frac{4\cot\theta}{\sin\theta}h_{(0),\varphi\theta\theta} + \frac{4\cot^2\theta}{\sin\theta}h_{(0),\varphi\theta} - \frac{4\cot\theta}{\sin^3\theta}\left(h_{(0),\varphi} + h_{(0),\varphi\varphi\varphi}\right)\right\}, \qquad (12b)$$

where $r = R + Gt$, a low index after a comma denotes the derivative with respect to the corresponding curvilinear coordinate, and the ordinal number of the wave

is omitted for simplicity. Note that the values $[v_{i,(3)}]^{(\alpha)}$ $(i = r, \varphi, \theta)$ are rather cumbersome, so they are not presented here.

Knowing the values $[v_{i,(k)}]^{(\alpha)}$ defined by (12), one can obtain at each fixed instant of the time the desired values u_i and σ_{ri} $(i = r, \varphi, \theta)$ behind the fronts of the shock waves up to the contact boundary as follows:

$$u_i(r,\theta,\varphi,t) = \sum_{\alpha=1}^{2}\sum_{k=1}^{5}\frac{1}{k!}\left[v_{i,(k-1)}^{(\alpha)}\right]\Big|_{y_{(\alpha)}=0} y_{(\alpha)}^{k} H(y_{(\alpha)}), \tag{13}$$

$$\sigma_{ri}(r,\theta,\varphi,t) = \sum_{\alpha=1}^{2}\sum_{k=0}^{4}\frac{1}{k!}\left[\sigma_{ri,(k)}^{(\alpha)}\right]\Big|_{y_{(\alpha)}=0} y_{(\alpha)}^{k} H(y_{(\alpha)}), \tag{14}$$

where

$$G[\sigma_{rr,(k+1)}] = -(\lambda+2\mu)[v_{r,(k+1)}] + (\lambda+2\mu)\frac{\delta[v_{r,(k)}]}{\delta t}$$
$$+\lambda\frac{G}{r}\left(2[v_{r,(k)}] + \cot\theta[v_{\theta,(k)}] + \frac{\partial[v_{\theta,(k)}]}{\partial\theta} + \frac{1}{\sin\theta}\frac{\partial[v_{\varphi,(k)}]}{\partial\varphi}\right),$$

$$G[\sigma_{r\varphi,(k+1)}] = \mu\left(-[v_{\varphi,(k+1)}] + \frac{\delta[v_{\varphi,(k)}]}{\delta t} - \frac{G}{r}[v_{\varphi,(k)}] + \frac{G}{r}\frac{1}{\sin\theta}\frac{\partial[v_{r,(k)}]}{\partial\varphi}\right),$$

$$G[\sigma_{r\theta,(k+1)}] = \mu\left(-[v_{\theta,(k+1)}] + \frac{\delta[v_{\theta,(k)}]}{\delta t} - \frac{G}{r}[v_{\theta,(k)}] + \frac{G}{r}\frac{\partial[v_{r,(k)}]}{\partial\theta}\right).$$

A NONLINEAR SOLUTION FOR A SPHERICAL SHELL

Let us seek the stress function entering into Eqs.(1a) and (1b) in the form of a power series

$$\Phi(\rho,t) = \sum_{k=1}^{n}\frac{1}{k!}\phi_{(k)}(\rho)t^k. \tag{15}$$

To construct the solution for a spherical shell, the ray series for the values u_r (13) and σ_{ri} $(i = r, \varphi, \theta)$ (14) need first to be written on the contact boundary, *ie*, at $r = R$, with due account for the relationships (12). Then substituting them into the three conditions of contact (5), for each k one obtains three linear algebraic equations which allow one to express two functions $g_{(k)}$ and $h_{(k)}$ in terms of $f_{(0)}$, $f_{(1)}$, ..., $f_{(k-1)}$. Substituting further the found values $u_r|_{r=R} = w$ and $\sigma_{rr}|_{r=R} = q$, as well as the function Φ defined by (15) into the equations of shell motion (1a) and (1b), and equating the coefficients for like powers of t, we determine the functions $\phi_{(k)}$ $(k = 1, 2, ...)$, and all functions $f_{(k)}$ beginning from $k = 1$ we express in terms of $f_{(0)}$, which, in its turn, can be found from the initial condition (6). As a result of such a procedure, we obtain the net relationship for the shell's deflection w in the form

$$w = \frac{f_{(0)}}{R}t - \frac{\varrho G^{(1)}}{\varrho_1 h}\frac{f_{(0)}}{R}\frac{t^2}{2}$$

$$+\left\{\left[\left(\frac{\varrho G^{(1)}}{\varrho_1 h}\right)^2+\frac{\lambda-2\mu}{\varrho_1 hR}-\frac{E_1}{\varrho_1 R^2}\right]\frac{f_{(0)}}{R}-\frac{D}{\rho_1 hR}\Delta^4 f_{(0)}\right\}\frac{t^3}{6}$$

$$-\left\{\frac{\varrho G^{(1)}}{\varrho_1 h}\left[\left(\left(\frac{\varrho G^{(1)}}{\varrho_1 h}\right)^2+\frac{2(\lambda-2\mu)}{\varrho_1 hR}-\frac{E_1}{\varrho_1 R^2}\right)\frac{f_{(0)}}{R}-\frac{2D}{\rho_1 hR}\Delta^4 f_{(0)}\right]\right.$$

$$+\frac{\varrho G^{(1)^3}}{\varrho_1 hR^3}\left[\frac{\lambda}{\lambda+2\mu}\left(1-2\frac{G^{(2)}}{G^{(1)}}\right)+2\frac{G^{(2)}}{G^{(1)}}\left(1-\frac{G^{(2)}}{G^{(1)}}\right)-\frac{1}{2}\right]\left(f_{(0),\theta\theta}+\operatorname{ctg}\theta f_{(0),\theta}\right)$$

$$\left.-\frac{1}{\varrho_1 hR}\left(F_{(0),\rho\rho}\phi_{(1),\rho}+F_{(0),\rho}\phi_{(1),\rho\rho}\right)\frac{1}{\rho}+\frac{\varrho G^{(1)^3}}{\varrho_1 hR^3}f_{(0)}\right\}\frac{t^4}{24}, \tag{16}$$

where

$$F_{(0)}(\rho)=F_{(0)}(R\sin\theta)=f_{(0)}(\theta),\quad \phi_{(1),\rho}=-\frac{E_1 h}{R^2\rho}\int\rho F_{(0)}(\rho)d\rho.$$

From formula (16) it is seen that the deflection of the nonlinear spherical shell represents the sum of linear and nonlinear terms, in so doing nonlinearity begins to manifest itself only in the terms involving the time t in the fourth power and above. So if the time interval on which the transient vibrations are investigated is modest, then the surrounding medium being in contact with the nonlinear spherical shell can be considered as a linearly elastic medium.

Note that the truncated ray series (16) is valid for small time intervals, *ie*, it has an asymptotic character, and that is why it has all advantages and disadvantages which are inherent to the asymptotic expansions.

Choosing the function $V_0(\rho)$ entering into the initial condition (6) in the following form

$$V_0(\rho)=\pm C\sqrt{1-\frac{\rho^2}{R^2}}, \tag{17}$$

where C is a certain constant, the time dependence of the shell's displacement w can be written as

$$w=C\left\{yt-y\frac{\varrho G^{(1)}}{\varrho_1 h}\frac{t^2}{2}+\left[\left(\left(\frac{\varrho G^{(1)}}{\varrho_1 h}\right)^2+\frac{\lambda-2\mu}{\varrho_1 hR}-\frac{E_1}{\varrho_1 R^2}\right)y\right.\right.$$

$$\left.+\frac{D}{\rho_1 hR^4}\left[\frac{5}{y^3}+21\frac{1-y^2}{y^5}+15\frac{(1-y^2)^2}{y^7}\right]\right\}\frac{t^3}{6}$$

$$-\left[\left(\frac{\varrho G^{(1)}}{\varrho_1 h}\right)^3 y+\frac{\varrho G^{(1)}}{\varrho_1 h}\left(\frac{2(\lambda-2\mu)}{\varrho_1 hR}-\frac{E_1}{\varrho_1 R^2}\right)y+\frac{8\varrho G^{(1)}G^{(2)^2}}{\varrho_1 hR^2}\left(1-\frac{G^{(2)}}{G^{(1)}}\right)y\right.$$

$$\left.\left.-\frac{2}{3}\frac{E_1}{\varrho_1 R^3}C+\frac{\varrho G^{(1)}}{\varrho_1 h}\frac{2D}{\rho_1 hR^4}\left[\frac{5}{y^3}+21\frac{1-y^2}{y^5}+15\frac{(1-y^2)^2}{y^7}\right]\right]\frac{t^4}{24}\right\}, \tag{18}$$

where $y=\pm\sqrt{1-\rho^2/R^2}$.

Reference to the formula (18) shows that the terms of the truncated series beginning from the third one have the singularity at $y = 0$, which, as calculations show for further terms, may increase. In other words, the asymptotic expansion of the function w at $y \to 0$ becomes unvalid. To make the truncated ray series (18) to be uniformly valid [9] at the fixed small t in the region $0 \le y \le 1$, we can represent the variable y in the following form:

$$y = s + \Sigma(s)t^2, \tag{19}$$

where s is the new variable, and $\Sigma(s)$ is an unknown function yet.

To eliminate the terms involving singularities from (18), we substitute (19) into Eq.(18) in a such a way that these terms should be vanished. As a result we obtain the uniformly valid relationship for w

$$w = Cs\left\{t - \frac{\varrho G^{(1)}}{\varrho_1 h}\,\frac{t^2}{2} + \left[\left(\frac{\varrho G^{(1)}}{\varrho_1 h}\right)^2 + \frac{\lambda - 2\mu}{\varrho_1 h R} - \frac{E_1}{\varrho_1 R^2}\right]\frac{t^3}{6}\right.$$

$$-\frac{\varrho G^{(1)}}{\varrho_1 h}\left[\left(\frac{\varrho G^{(1)}}{\varrho_1 h}\right)^2 + \frac{2(\lambda - 2\mu)}{\varrho_1 h R} - \frac{E_1}{\varrho_1 R^2}\right.$$

$$\left.\left.-\frac{2}{3}\frac{E_1 h C}{\varrho G^{(1)} R^3}\,\frac{1}{s} + \frac{8\varrho G^{(1)} G^{(2)2}}{\varrho_1 h R^2}\left(1 - \frac{G^{(2)}}{G^{(1)}}\right)\right]\frac{t^4}{24}\right\}, \tag{20}$$

as well as the function $\Sigma(s)$

$$\Sigma(s) = -\frac{1}{6}\,\frac{D}{\varrho_1 h R^4}\left[\frac{5}{y^3} + 21\frac{1 - y^2}{y^5} + 15\frac{(1 - y^2)^2}{y^7}\right]. \tag{21}$$

If we substitute (21) into (19) and put $y = 0$, then we are led to the equation

$$s - \frac{1}{6}\,\frac{D}{\varrho_1 h R^4}\left[\frac{5}{y^3} + 21\frac{1 - y^2}{y^5} + 15\frac{(1 - y^2)^2}{y^7}\right]t^2 = 0, \tag{22}$$

which defines the lower boundary of the value s by the formula

$$s_0 = \left(\frac{15}{6}\,\frac{D}{\varrho_1 h R^4}\right)^{1/8} t^{1/4}. \tag{23}$$

To find the upper boundary of the value s, it is a need to put $y = 1$ in Eq.(19).

For numerical investigations it is more convenient to rewrite Eq.(20) in the dimensionless form

$$w^* = s\left\{t^* - æ\frac{t^{*2}}{2} + æ\left[æ + k\left(1 - 4\frac{G^{(2)2}}{G^{(1)2}}\right) - k^2\delta\right]\frac{t^{*3}}{6}\right.$$

$$\left.-æ\left[æ^2 + æk\left(1 - 4\frac{G^{(2)2}}{G^{(1)2}}\right) - æk^2\delta + 8æk^2\frac{G^{(2)2}}{G^{(1)2}}\left(1 - \frac{G^{(2)}}{G^{(1)}}\right)\right.\right.$$

$$-\frac{2}{3}\frac{1}{s}k^3\delta C^*\Big]\frac{t^{*4}}{24}\Big\}, \tag{24}$$

where the dimensionless time t^*, deflection w^* and initial velocity C^* are connected with the corresponding dimension values as

$$t^* = t\,\frac{G^{(1)}}{h}, \quad w^* = w\,\frac{G^{(1)}}{Ch}, \quad C^* = \frac{C}{G^{(1)}},$$

and $æ = \varrho/\varrho_1$, $k = h/R$, $\delta = E_1/(\lambda + 2\mu)$.

The t^*-dependence of the dimensionless deflection w^* is presented in Fig.2 for $æ = 1.2$ (solid line) and $æ = 0.8$ (dashed line) at $s = 1$, $k = 0.1$, $\delta = 1$, and $C^* = 0.01$. Reference to Fig.2 shows that a relatively light shell ($æ > 1$) vibrates faster and with a smaller amplitude then a relatively heavy shell ($æ < 1$) does.

CONCLUSIONS

The ray method put forward enables one to solve, with considerable success, dynamic problems on the snap-action interaction of both linearly elastic and nonlinearly elastic thin-walled bodies with a surrounding medium. The analytical character of the solution obtained both for the shell and the medium is one of the merits of this method.

ACKNOWLEDGMENTS

This work is supported in part by the Russian Foundation for Basic Research under Grant No.98-15-96001.

REFERENCES

1. Rossikhin, Yu.A., On nonstationary vibrations of a plate on an elastic foundation, *J. Appl. Math. Mech.*, 1978, **42**, 347-353.

2. Shitikova, M.V., Ray method in the problems of dynamic contact interaction of elastic bodies (in Russian), DSc Thesis, Minsk Polytechnic Academy, Minsk, 1994 (English Abstr. published in *J. of Acoust. Soc. Amer.*, 1995, **97**(2), 1345).

3. Rossikhin, Yu.A. and Shitikova, M.V., Ray method for solving boundary dynamic problems connected with propagation of wave surfaces of strong and weak discontinuities, *Appl. Mech. Reviews*, 1995, **48**(1), 1-39.

4. Rossikhin, Yu.A. and Shitikova, M.V., Nonstationary vibrations of a nonlinear plate resting on an elastic isotropic half-space. In *Proc. Int. Conf. on Nonlinear Theory and Its Application (NOLTA'96)*, Oct.7-9, 1996, Kochi, Japan, pp. 412-424.

5. Rossikhin, Yu.A. and Shitikova, M.V., Nonlinear nonstationary vibrations of an elastic cylindrical shell embedded into an elastic isotropic medium. In *Proc. Int. Conf. on Vibration, Noise and Structural Dynamics'99*, April 28-30, 1999, Venice, Italy, pp. 378-385.

6. Birger, I.A. and Panovko, Ya.G. (eds), *Handbook: Strength, Stability, Vibrations* (in Russian), **3**, Mashinostroenie, Moscow, 1968.

7. Rossikhin, Yu.A. and Shitikova, M.V., The ray method for solving boundary problems of wave dynamics for bodies having curvilinear anisotropy, *Acta Mech.*, 1995, **109**(1-4), 49-64.

8. Thomas, T.Y., *Plastic Flow and Fracture in Solids*, Academic Press, 1961.

9. Nayfeh, A.H., *Perturbation Methods*, Wiley, N.Y., 1973.

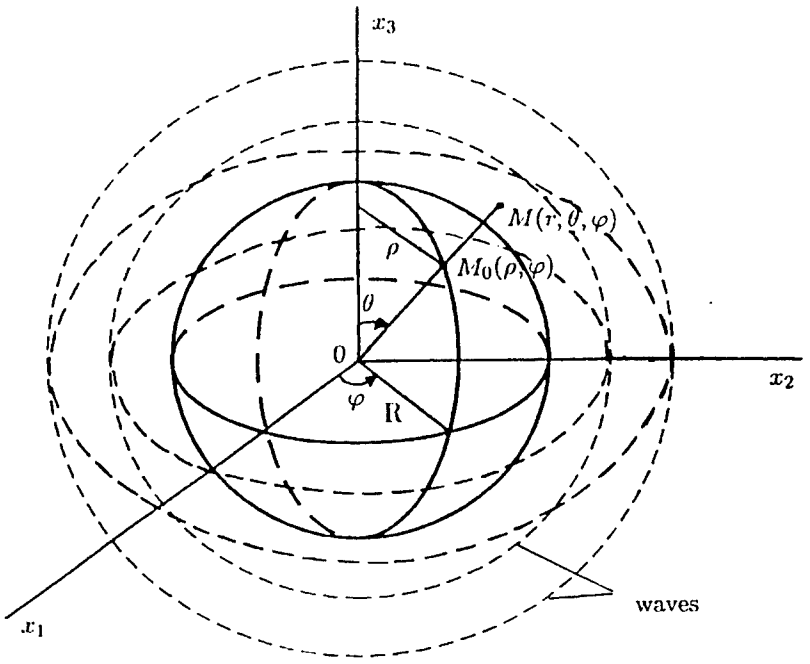

Figure 1. A scheme of the shell and wavefronts

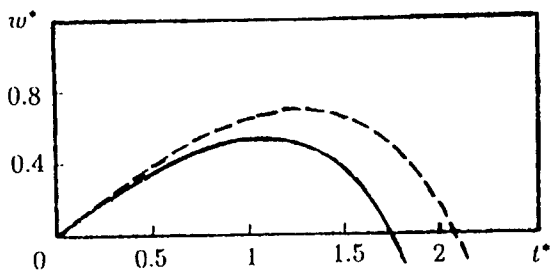

Figure 2. The dimensionless time dependence of the dimensionless deflection

ACTIVE AND PASSIVE CONTROL

SMA HYBRID COMPOSITES FOR DYNAMIC RESPONSE ABATEMENT APPLICATIONS

Travis L. Turner
Structural Acoustics Branch, MS 463
NASA Langley Research Center
Hampton, VA 23681–2199

ABSTRACT

A recently developed constitutive model and a finite element formulation for predicting the thermomechanical response of SMA hybrid composite (SMAHC) structures is briefly described. Attention is focused on constrained recovery behavior in this study, but the constitutive formulation is also capable of modeling restrained or free recovery. Numerical results are shown for glass/epoxy panel specimens with embedded Nitinol actuators subjected to thermal and acoustic loads. Control of thermal buckling, random response, sonic fatigue, and transmission loss are demonstrated and compared to conventional approaches including addition of conventional composite layers and a constrained layer damping treatment. Embedded SMA actuators are shown to be significantly more effective in dynamic response abatement applications than the conventional approaches and are attractive for combination with other passive and/or active approaches.

INTRODUCTION

Excitation levels for many aerospace vehicle structures are high due to engine noise and turbulent boundary layer fluctuating pressures. The ever-increasing need for weight-efficient structures leads to significant sonic fatigue and interior noise issues. Conventional aerospace structures typically employ passive treatments such as structural stiffening, constrained layer damping, and acoustic absorption materials to reduce the structural response and interior acoustic levels. These treatments typically suffer from substantial weight penalty and are often limited to relatively low temperatures and/or high frequencies. Smart materials may enable new structural design paradigms for high performance structures. There are many smart materials concepts, but some involving shape memory alloys (SMAs) appear to have significant advantages for applications involving adaptive stiffening and structural shape control.

Shape memory alloys are a class of smart materials that exhibit a martensitic phase transformation when cooled through the transformation temperature range $M_s \rightarrow M_f$ from the austenitic state, see figure 1. The shape memory effect (SME) can be described in simple terms in the following manner. A SMA can be easily deformed in the low temperature martensitic condition and can be returned to its original configuration by heating through the reverse transformation temperature range $A_s \rightarrow A_f$. This type of SME is termed free recovery. Conversely, in a constrained recovery configuration the SMA element is prevented from recovering the initial strain and a large tensile stress (recovery stress) is induced. A situation in which the specimen performs work (deforms under load) is called restrained recovery. Extensive work has been done to characterize these materials, both qualitatively through theoretical models [1–4] and quantitatively for particular alloys [5,6]. Compilations of papers have also been published, most recently

by Otsuka and Wayman [7]. Birman [8] gave a review of work done in the areas of alloy characterization, constitutive modeling, and applications.

Although there are several alloy systems that exhibit the SME, Nitinol has the most engineering significance. The recovery stress (constrained recovery) for Nitinol is a function of initial strain (prestrain) and temperature, see figure 2 [5]. The yield strength of the austenitic phase is about ten times that of the corresponding martensitic phase. The austenitic Young's modulus is also three to four times that of the martensite, see figure 3 [5].

Shape memory alloys have been investigated for a variety of applications since their discovery [9–12]. The concept of embedding SMA actuators in a composite laminate, termed a shape memory alloy hybrid composite (SMAHC), was introduced by Rogers and Robertshaw [13]. Subsequent studies have considered SMA actuators, external to the structure, for active vibration control [14–16] and shape control [17] of cantilevered beams. Other studies have proposed SMA actuators for vibration control of space structures [18] and presented analytical formulations to demonstrate the vibration/structural acoustic control of SMAHC panels [19,20]. Studies of thermal post-buckling [21] and random dynamic response [22] suppression of SMAHC panels were presented using a thermoelastic FE formulation. A different approach was offered by Ro and Baz [23–25], where thermal, static, and dynamic analyses were developed for the case of SMA actuators passing through sleeves in composite plates. Birman [26] investigated optimal distributions of SMA actuators in sleeves to improve the buckling performance of sandwich panels under mechanical loading.

SMAHC structures incorporating prestrained actuators are of particular interest in this study because of the potential for structural control due to tensile recovery stresses that are generated (constrained recovery) when the structure is placed in its service environment. In this way, an inherently elevated temperature (e.g. many aerospace applications) can be used to control structural response without control electronics or auxiliary power. The purpose of the present work is to demonstrate the dynamic response performance of SMAHC panels in comparison to conventional response abatement approaches.

FORMULATION

Constitutive Modeling

Constitutive theories for SMAHC structures can be developed from the previously mentioned shape memory models [1–4], as was done by Boyd and Lagoudas [27] and Birman [28]. However, these models are difficult to use in practice. An alternative approach is to employ a constitutive model which makes use of experimental measurement of fundamental engineering properties. A new model of the latter type was recently developed by Turner [29]. This model casts the uniaxial thermoelastic constitutive relation for a SMA actuator, along the axis of the actuator, in terms of an effective coefficient of thermal expansion (CTE):

$$\sigma_{1a} = E_a\left[\epsilon_1 - \int_{T_o}^{T} \alpha_{1a}(\tau)d\tau\right] \tag{1}$$

where E_a is the Young's modulus of the SMA, ϵ_1 is the mechanical strain in the 1–direction, and α_{1a} is the "effective" (nonlinear) CTE. Note that this expression is

valid for constrained, restrained, or free recovery applications; only the empirical method of obtaining the thermal strain changes. A measure of the nonlinear CTE $\alpha_{1a}(T)$ over the temperature range of concern would be appropriate for free or restrained recovery applications. For constrained recovery applications, however, one must resort to measurement of the recovery stress and modulus.

It can be shown that, for constrained recovery behavior, the nonlinear thermal strain in Equation (1) can be modeled by linear thermal expansion below the austenite start temperature and can be related to the SMA recovery stress σ_r and modulus by the equation

$$\sigma_r = -E_a \int_{T_0}^{T} \alpha_{1a}(\tau)d\tau \qquad \text{or} \qquad \int_{T_0}^{T} \alpha_{1a}(\tau)d\tau = -\frac{\sigma_r}{E_a} \tag{2}$$

at temperatures above A_s. Note that in this case, the nonlinear thermoelastic nature of the SMA is still captured, albeit in a different way, because measurements of recovery stress and modulus versus temperature are inherently cumulative (integrated). Also, note that an experimental approach could be devised to measure appropriate recovery stress σ_r quantities for restrained recovery applications as an alternative to direct measurement of $\alpha_{1a}(T)$. The uniaxial SMA constitutive relation for the transverse direction has a form analogous to Equation (1). However, $\alpha_{2a}(T)$ is not related to the recovery stress, but is still nonlinear due to the differing martensitic and austenitic properties.

Governing Equations

The governing equations for the thermomechanical response of a structure subjected to combined steady-state thermal and out-of-plane dynamic mechanical loads can be derived through the use of a variational principle. The resulting finite element system of equations can be written in the following form [29]

$$\begin{bmatrix} M_b & 0 \\ 0 & M_m \end{bmatrix} \begin{Bmatrix} \ddot{A}_b \\ \ddot{A}_m \end{Bmatrix} + \left(\begin{bmatrix} K_b & K_B \\ K_B^T & K_m \end{bmatrix} - \begin{bmatrix} K_{\Delta T} & 0 \\ 0 & 0 \end{bmatrix} + \frac{1}{2} \begin{bmatrix} N1_b + (N1_b)_B & N1_{bm} \\ N1_{mb} & 0 \end{bmatrix} + \frac{1}{3} \begin{bmatrix} N2_b & 0 \\ 0 & 0 \end{bmatrix} \right) \begin{Bmatrix} A_b \\ A_m \end{Bmatrix} = \begin{Bmatrix} F_b(t) \\ 0 \end{Bmatrix} + \begin{Bmatrix} P_{b\Delta T} \\ P_{m\Delta T} \end{Bmatrix} \tag{3}$$

or in compact notation as

$$[M]\{\ddot{A}\} + \left([K] - [K_{\Delta T}] + \frac{1}{2}[N1] + \frac{1}{3}[N2]\right)\{A\} = \{F(t)\} + \{P_{\Delta T}\} \tag{4}$$

where $[M]$ and $[K]$ are the usual system mass and linear stiffness matrices; $[K_{\Delta T}]$ is the geometric stiffness matrix due to the thermal in-plane force vector $\{N_{\Delta T}\}$; $[N1]$ and $[N2]$ are the first- and second-order nonlinear stiffness matrices which depend linearly and quadratically upon displacement $\{A\}$, respectively; $\{F(t)\}$ is the mechanical excitation load vector, and $\{P_{\Delta T}\}$ is the thermal force vector. The subscripts b and m denote bending and membrane components, respectively, and the subscript B indicates that the corresponding stiffness matrix is due to the laminate bending-membrane coupling stiffness matrix $[B]$. Note that the stiffness matrices $[K]$, $[K_{\Delta T}]$, $[N1]$, $[N2]$ and the thermal force vector $\{P_{\Delta T}\}$ are all temperature dependent.

Three types of analyses are required to study the response of structures to thermal and dynamic mechanical loads, governed by Equations (4): (1) thermal buckling analysis, (2) thermal post-buckling analysis, and (3) dynamic analysis. Details of the constitutive model, FE formulation, and solution procedures can be found in Turner [29]. A Rayeigh's integral approach was used to calculate radiated acoustic quantities and transmission loss, see Turner et al. [30].

RESULTS AND DISCUSSION

The results presented in this study are intended to demonstrate the performance of SMAHC structures in comparison to conventional treatments. The results will focus on a single SMA actuator prestrain level of 5% because changes in SMA volume fraction have a more significant effect, the SMA volume fraction is more easily varied/controlled in fabrication, and the fatigue performance of Nitinol actuators degrades substantially at prestrain levels greater than 5%. The material system considered in this work consists of a E-glass/epoxy matrix material with Nitinol actuators embedded within the laminae along the direction of the glass fibers. The following material properties were used to generate the results presented in this section.

Glass/Epoxy		Nitinol	
E_1	53.78 GPa	σ_r	from figure 2
E_2	17.93 GPa	E	from figure 3
G_{12}	8.62 GPa	ν	0.3
ν_{12}	0.25	ρ	6450 kg/m^3
ρ	2031.8 kg/m^3	α_{1a}	6.61×10^{-6} /°C, $T<A_s$
α_1	5.4×10^{-6} /°C		from equation 2, $T\geq A_s$
α_2	30.6×10^{-6} /°C	α_{2a}	6.61×10^{-6} /°C, $T<A_s$
			11.0×10^{-6} /°C, $T>A_f$
			interpolation, $A_s\leq T\leq A_f$

Recall figure 2 characterizing the recovery stress for the Nitinol considered in this study [5]. The reverse transformation (austenitic) characteristic temperatures, under free recovery conditions, for the material represented in this plot are $A_s \approx$35°C (95°F) and $A_f \approx$50°C (120°F). Note from figure 2 that A_f is increased by mechanical constraint and increasing prestrain, while A_s is not significantly affected by either. Furthermore, the "knee" in the recovery stress curve becomes less distinct with increasing prestrain. These are well known phenomena and are attributable to stress increasingly inhibiting the formation of austenite and completion of the reverse transformation. These insights will be useful in later discussions.

SMAHC Performance

Consider a glass/epoxy panel with dimensions of 0.36x0.25x0.001 m (14x10x0.045 in.) and (45/0/-45/90/0/90/-45/0/45) lamination. The reason for the middle 0°–layer will be made clear subsequently. Static and dynamic performance results for a conventional (baseline) and two SMAHC laminates with clamped boundary conditions are shown in table 1 for ambient 21°C (70°F) and elevated temperature 82°C (180°F) conditions. The

SMAHC laminates in this table have a SMA volume fraction of 22%. The dynamic response is forced by normally-incident, random acoustic pressure with an overall sound pressure level (OASPL) of 120 dB (ref 20 μPa) and a bandwidth of 10–400 Hz. A uniform modal critical damping ratio of 1% was used in the dynamic calculations.

Some general comments about this data are as follows. The buckling and resonance behavior of the SMAHC panels relative to baseline panel at ambient temperature is attributable to differences in material properties, primarily in the 2–direction in principal material coordinates. Discussion of these differences is omitted here for brevity. Comparison of the two SMAHC panels, one with SMA in all layers and the other containing SMA in the outer 0° layers and in the 90° layers, indicates some small performance gain is achieved by concentrating the embedded SMA in only a few layers. This approach is attractive from a fabrication point of view, particularly for automated fabrication where it is easy to imagine replacing strategic spools of prepreg with SMA ribbon in a continuous consolidation process. The middle 0°–layer is necessary to separate the two 90° layers containing a substantial SMA volume fraction, thereby avoiding consolidation problems during cure. The remaining results/discussions will focus on SMAHC laminates with embedded SMA concentrated in the outer 0° layers and in the 90° layers.

It can be seen that activation of the embedded SMA has strong effects on the critical buckling temperatures, resonance frequencies, and RMS dynamic responses. The maximum displacement response power spectral density (PSD) of the SMAHC panel is shown in comparison to that of the baseline panel in figure 4. It is clear that the embedded SMA has little effect at ambient temperature. At 82 (180°F, ΔT=61°C), however, substantial benefit from the SMA recovery stress is evident in shifting the fundamental frequency, shifting other modes out of bandwidth, and reducing peak responses. Thus, performance can be enhanced by shifting resonance out of the excitation bandwidth and by response reduction within the excitation bandwidth.

The data in table 1 also indicates that SMAHC panels can exhibit two critical buckling temperatures (ΔT_{cr} for inactive and active SMA states), as was previously reported [22,29]. This occurs for cases in which A_s is greater than ambient temperature. This phenomenon is exemplified in figure 5, where the normalized, maximum post-buckling deflection versus temperature increase is shown for SMAHC laminates with varying SMA volume fraction. It can be seen that a volume fraction of 4% is insufficient to eliminate thermal post-buckling, but its effect in reducing the deflection is clearly observed. As little as 13% SMA will eliminate thermal post-buckling over a small range of temperatures; higher concentrations of SMA (e.g. 22%) can greatly extend the temperature range. This behavior can be explained as follows. Thermal expansion may induce buckling at temperatures below A_s. The SMA is activated at A_s and the recovery stress rapidly increases with temperature, which overcomes the compressive thermal stress and reduces the thermal deflection (potentially rendering the structure flat again). At higher temperatures, the rate of increase of the recovery stress with temperature diminishes and may be surpassed by the rate of increase in matrix compressive thermal stress. Further increases in temperature will cause net-compressive stress development, eventually leading to a second incidence of thermal buckling. Note that this effect can be easily avoided in practice by selecting an alloy with slightly higher Nickel content [9], which can lower A_s to ambient temperature or below and result in a single, high-temperature buckling event.

The thermal post-buckling observations have strong implications for the panels' dynamic response. An example is shown in figure 6, where the maximum displacement PSD of the SMAHC panel (v_a=22%) is shown at ambient and two elevated temperatures. At 82°C (180°F, ΔT=61°C), substantial benefit of the embedded SMA is evident, while further heating to 121°C (250°F, ΔT=100°C) greatly diminishes the performance (RMS W_{max}=0.0927e-3 m) because continued thermal expansion has partially overcome the beneficial effects of the recovery stress. This particular material system, glass/epoxy matrix with 22% Nitinol volume fraction at 5% prestrain, achieves its "optimal" dynamic response at approximately 82°C (180°F), which corresponds to the "knee" in the recovery stress curve, see figure 2. This result also holds for analogous SMAHC panels (v_a=22%) with embedded Nitinol having 3% and 4% prestrain, which exhibit "optimal" dynamic performance at their respective "knee" temperatures of 54°C (130°F) and 66°C (150°F). The optimal temperature for dynamic performance will be designated by A_o and is governed by the same thermoelastic balance as that described in the thermal post-buckling discussion. In general, with a different material system or at higher prestrain levels (in the absence of a distinct "knee"), A_o must be determined numerically or by comparing the slope of the recovery stress curve with that of the matrix thermal stress versus temperature.

Selection of an alloy composition and processing combination that will place A_o near the application temperature is obviously recommended for dynamic control applications. An alternate approach to achieve similar performance would entail increasing the SMA volume fraction and/or prestrain, which will result in a less efficient and/or durable design. The above discussions imply potential for a delicate balance between avoiding thermal buckling by imposing A_s to be less than ambient temperature and "optimizing" dynamic performance by specifying A_o to be near the application temperature. Thermal buckling can also be avoided by boundary expansion, a common approach for aerospace structures, so A_s can be neglected in such cases and A_o should be used to guide efficient design.

SMAHC vs. Conventional

The performance of the SMAHC laminate will now be compared with conventional approaches including increased stiffness through additional composite layers and a constrained layer damping (CLD) treatment. The conventional approaches were analyzed at ambient temperature to simulate the conditions of boundary expansion, i.e. no thermal buckling. No attempt was made to account for changes in matrix properties with temperature. A variety of dynamic response performance characteristics are compiled in table 2 for convenience of comparison. The SMAHC panel achieves a 77% RMS displacement response reduction, relative to the baseline 9–layer glass/epoxy panel, with a 48% mass increase. A conventional composite laminate of 13 layers (45/0/-45/90/45/0/90/0/45/90/-45/0/45) exhibits a similar mass increase (44%), but only achieves a 61% RMS displacement reduction. A RMS displacement response of 0.0474e-3 m (nearly equivalent to that of the SMAHC panel) can be achieved with a 16–layer $(45/0/-45/90)_{2s}$ conventional laminate, but at the expense of a 78% mass increase. A typical CLD treatment was modeled as a 19.16 N/m^2 (0.2 lbf/ft^2) weight addition and a uniform modal critical damping ratio of 6%, which are considered to be representative values. This treatment also happens to result in a mass increase (42%) similar to that of the SMAHC, but the RMS displacement response reduction of 63% is again inferior to the SMAHC. Additional insights are more clear from comparisons of the displacement response spectra.

A comparison of the respective maximum displacement response PSDs is shown in figure 7. As anticipated, the means by which the three systems achieve dynamic response reduction is quite different. The SMAHC achieves a much more weight-efficient stiffening effect relative to that of adding layers, while the CLD treatment achieves reduction primarily by damping enhancement. The weight-efficient stiffening effect of the embedded SMA is advantageous for combination with other passive treatments, which are typically more effective at higher frequencies. SMAHCs are also attractive for combination with control approaches involving piezoelectric actuators, which typically exhibit actuation authority roll-off below 200 Hz. Such combined active-passive approaches could achieve enormous dynamic response reductions by using the embedded SMA to shift resonance frequencies and provide peak response control by stiffness enhancement, while the active approach would provide enhanced damping at resonances still within the excitation bandwidth.

The dynamic response results have direct implication for sonic fatigue life prediction. Consider an analogous acoustic pressure loading condition with an OASPL of 150 dB (ref 20μPa). It is clear that linear dynamic response analysis is no longer valid, but its use at high response levels is still common practice in the aerospace industry for sonic fatigue design. This condition is more representative of a sonic fatigue environment and will produce more realistic life predictions, while it is understood that conservative estimates will be obtained. A representative strain-life (S-N) relationship for glass/epoxy laminates was modeled by $\epsilon = 7385e^{-6}(N)^{-0.1551}$ and the maximum RMS normal strain was taken as the failure criterion. In all cases, the maximum strain was the transverse normal strain at the mid-span of the long boundary. Under these conditions, the baseline panel has an expected life of 63.7k cycles. The corresponding life predictions for the SMAHC, 13–layer conventional, and CLD panels are 205M, 2.84M, and 37.8M cycles, respectively. These estimates are in direct relation with the corresponding peak displacements in figure 7. It is intuitive that measures to further attenuate the SMAHC peak response would result in excellent sonic fatigue performance. The previously mentioned active-passive system, for example, might be a particularly attractive solution.

A plot of the transmission loss (TL) versus frequency for the SMAHC panel at two temperatures is shown in comparison to the baseline panel in figure 8. The main effect of the embedded SMA in its most effective state at 82°C (180°F) is a vast increase in the stiffness-controlled portion of the TL. This improvement is diminished at higher temperatures (e.g. 121°C) for the same reasons as stated above for the dynamic response. Although the stiffness-controlled TL for the SMAHC panel shows dramatic improvement, the TL over the 400 Hz bandwidth is actually diminished because the mass-law effect has been moved to higher frequencies. The TL for the SMAHC panel at 82°C (180°F) is shown in comparison to that for the two conventional approaches in figure 9. It can be seen that the SMAHC panel is superior over a 200 Hz bandwidth, but not as effective at mid-range (resonance-controlled) frequencies due to the shift in mass-law effects. Combination of the SMAHC with other passive and/or active approaches is again an attractive alternative for this frequency range. At high frequencies (mass controlled) the three approaches will produce nearly equivalent TL.

CONCLUSIONS

A recently developed thermoelastic constitutive model and a finite element formulation for predicting the thermomechanical response of shape memory alloy (SMA) hybrid

composite structures (SMAHC) have been briefly described. Constrained recovery behavior of embedded SMA actuators is the focus of this study, but the constitutive formulation is also capable of modeling restrained or free recovery behavior. The constitutive model captures the material nonlinearity of the SMA with temperature. The constitutive and finite element formulations are in a form that is amenable to implementation in a commercial finite element code.

Results are shown for SMAHC panels consisting of a glass/epoxy matrix material system with embedded Nitinol actuators having a prestrain of 5% subjected to uniform thermal and acoustic pressure loads. Performance gains can be achieved by concentrating the SMA actuators in specific layers, which is also driven by fabrication considerations. SMAHC panels can exhibit two critical buckling temperatures for $A_s > T_o$, which can be avoided by proper alloy composition selection. SMAHC structures exhibit an "optimal" operating temperature (A_o) for dynamic response performance. A_o is a function of the matrix material and SMA composition, volume fraction, and prestrain level. The implied conflict between specifying $A_s < T_o$ to avoid thermal buckling and $A_o \approx T$ to "optimize" dynamic response can be resolved by taking the conventional approach of allowing boundary expansion to prevent buckling and using $A_o \approx T$ to guide structural design.

The performance of a SMAHC panel was compared to that of a baseline panel and two conventional approaches including additional conventional composite layers and a constrained layer damping (CLD) treatment. The three response abatement approaches have similar added mass relative to the baseline panel, but the SMAHC panel exhibits superior dynamic response and sonic fatigue behavior. The SMAHC panel also exhibits superior transmission loss (TL) characteristics in the low frequency, stiffness controlled region; up to 200 Hz in this case. The SMAHC panel is less effective for TL at higher frequencies due to the shift in mass-law effects. However, the weight-efficient stiffening effect of the embedded SMA makes it ideal for low frequency noise transmission abatement and for combination with other passive or active approaches, which are typically more effective at higher frequencies. These combined approaches have significant implications for dynamic response/sonic fatigue also.

REFERENCES

1. Tanaka, K. and Nagaki, S.: "A Thermomechanical Description of Materials with Internal Variables in the Process of Phase Transformation," *Ingenieur-Archiv*, vol. 51, pp. 287–299, 1982.
2. Liang, C. and Rogers, C. A.: "One-Dimensional Thermomechanical Constitutive Relations for Shape Memory Materials," *J. of Intell. Matl. Syst. and Struct.*, Vol. 1, April, 1990, pp. 207–235.
3. Brinson, L. C.: "One Dimensional Constitutive Behavior of Shape Memory Alloys: Thermomechanical Derivation with Non-Constant Material Functions," *J. of Intell. Matl. Syst. and Struct.*, Vol. 4:2, pp. 229–242, 1993.
4. Boyd, J. G. and Lagoudas, D. C.: "A Thermodynamical Constitutive Model for Shape Memory Materials – Part I: The Monolithic Shape Memory Alloy", *Int. J. of Plasticity*, 12:805–842, 1996.
5. Cross, W. B.; Kariotis, A. H.; and Stimler, F. J.: "Nitinol Characterization Study," NASA CR-1433, 1969.

6. Jackson, C. M.; Wagner, H. J.; and Wasilewski, R. J.: "55–Nitinol The Alloy with a Memory: Its Physical Metallurgy, Properties, and Applications," NASA SP-5110, 1972.
7. Otsuka, K. and Wayman, C. M. (Editors): *Shape Memory Materials*, Cambridge University Press, Cambridge, CB2 2RU, UK, 1998.
8. Birman, V.: "Review of Mechanics of Shape Memory Alloy Structures," *Applied Mechanics Reviews*, 50(11):629–645, 1997.
9. Buehler, W. J. and Wang, F. E.: "A Summary of Recent Research on the Nitinol Alloys and Their Potential Application in Ocean Engineering," *Ocean Engineering*, vol. 1, pp. 105–120, 1968.
10. Wayman, C. M. and Shimizu, K.: "The Shape Memory ("Marmem") Effect in Alloys," *Metal Science Journal*, vol. 6, pp. 175–183, 1972.
11. Wayman, C. M.: "Some Applications of Shape-Memory Alloys," *Journal of Metals*, pp. 129–137, June 1980.
12. Otsuka, K. and Shimizu, K.: "Pseudoelasticity and Shape Memory Effects in Alloys," *International Metals Reviews*, vol. 31, no. 3, pp. 93–114, 1986.
13. Rogers, C. A. and Robertshaw, H. H.: "Shape Memory Alloy Reinforced Composites," *Engineering Science Preprints 25*, Society of Engineering Science, Inc., ESP25.8027, 1988.
14. Rogers, C. A.: "Active Vibration and Structural Acoustic Control of Shape Memory Alloy Hybrid Composites: Experimental Results", *J. of the Acoustical Society of America*, 88(6):2803–2811, 1990.
15. Baz, A.; Imam, K.; and McCoy, J.: "Active Vibration Control of Flexible Beams Using Shape Memory Actuators", *J. of Sound and Vibration*, 140(3):437–456, 1990.
16. Srinivasan, A. V.; Cutts, D. G.; and Schetky, L. M.: "Thermal and Mechancical Considerations in Using Shape Memory Alloys to Control Vibrations in Flexible Structures", *Metallurgical Transactions A*, 22A:623–627, 1991.
17. Chaudhry, Z. and Rogers, C. A.: "Bending and Shape Control of Beams Using SMA Actuators", *J. of Intell. Syst. and Struct.*, 2:581–602, 1991.
18. Maclean, B. J.; Patterson, G. J.; and Misra, M. A.: "Modeling of a Shape Memory Integrated Actuator for Vibration Control of Large Space Structures", *J. of Intell. Mater. Syst. and Struct.*, 2:72–94, 1991.
19. Rogers, C. A.; Liang, C.; and Jia, J.: "Structural Modification of Simply-Supported Laminated Plates Using Embedded Shape Memory Alloy Fibers", *Computers and Structures*, 38(5/6):569–580, 1991.
20. Liang, C.; Rogers, C. A.; and Fuller. C. R.: "Acoustic Transmission and Radiation Analysis of Adaptive Shape Memory Alloy Reinforced Laminated Plates", *Journal of Sound and Vibration*, 145(1):23–41, 1991.
21. Zhong, Z. W.; Chen, R. R.; Mei, C.; and Pates, C. S.: "Buckling and Postbuckling of Shape Memory Alloy Fiber-Reinforced Composite Plates", *Symposium on Buckling and Postbuckling of Composite Structures*, ASME AD-Vol. 41/PVP-Vol. 293, pp.115–132, 1994.
22. Turner, T. L.; Zhong, Z. W.; and Mei, C.: "Finite Element Analysis of the Random Response Suppression of Composite Panels at Elevated Temperatures Using Shape Memory Alloy Fibers," AIAA-94–1324–CP, *Proceedings of the 35th Structures, Structural Dynamics, and Materials Conference*, Hilton Head, SC, April 18–21, pp. 136–146, 1994.

23. Ro, J. and Baz, A.: "Nitinol-Reinforced Plates: Part I. Thermal Characteristics", *Composites Engineering*, 5(1):61–75, 1995.
24. Ro, J. and Baz, A.: "Nitinol-Reinforced Plates: Part II. Static and Buckling Characteristics", *Composites Engineering*, 5(1):77–90, 1995.
25. Ro, J. and Baz, A.: "Nitinol-Reinforced Plates: Part III. Dynamic Characteristics", *Composites Engineering*, 5(1):91–106, 1995.
26. Birman, V.: "Stability of Functionally Graded Shape Memory Alloy Sandwich Panels", *Smart Materials and Structures*, 6:278–286, 1997.
27. Boyd, J. G. and Lagoudas, D. C.: "A Thermodynamical Constitutive Model for Shape Memory Materials – Part II: The SMA Composite Material", *Int. J. of Plasticity*, 12(7):843–873, 1996.
28. Birman, V.: "Micromechanics of Composites with Shape Memory Alloy Fibers in Uniform Thermal Fields", *AIAA Journal*, 34(9):1905–1912, 1996.
29. Turner, T. L.: "A New Thermoelastic Model for Analysis of Shape Memory Alloy Hybrid Composites", *J. of Intell. Matl. Syst. and Struct.*, In Press.
30. Turner, T. L.; Singh, M. P.; and Mei, C.: "A Spectral Analysis Approach for Acoustic Radiation from Composite Panels," AIAA-95–1303–CP, *Proceedings of the 36th Structures, Structural Dynamics, and Materials Conference*, New Orleans, LA, April 10–13, pp. 1262–1271, 1995.

Table 1: Results for conventional and SMAHC panels.

SMA Layer Content	T=21°C, Inactive SMA			T=82°C, Active SMA		
	ΔT_{cr}, °C	f_1, Hz	RMS W_{max}, m	ΔT_{cr}, °C	f_1, Hz	RMS W_{max}, m
None	4.99	87.48	0.2062e-3	4.99	—	—
All	5.29	71.11	0.1899e-3	113.6	173.5	0.0482e-3
Outer 0°, 90°	5.43	87.57	0.2058e-3	122.1	226.4	0.0476e-3

Table 2: Results from baseline, SMAHC, and panels with conventional response abatement treatments.

Case	Added Mass	f_1, Hz	RMS W_{max}, m	TL, dB	Max RMS $\mu\epsilon$ @ 120dB	Life @ 150 dB
Baseline	0%	87.48	0.2062e-3	17.9	42.0	63.7e+3
SMAHC @ 82°C	48%	226.4	0.0476e-3	14.3	12.0	205e+6
13-Layer	44%	128.3	0.0805e-3	19.1	23.3	2.84e+6
16-Layer	78%	158.6	0.0474e-3	20.2	16.8	23.4e+6
Baseline-CLD	42%	73.4	0.0768e-3	27.4	15.6	37.8e+6

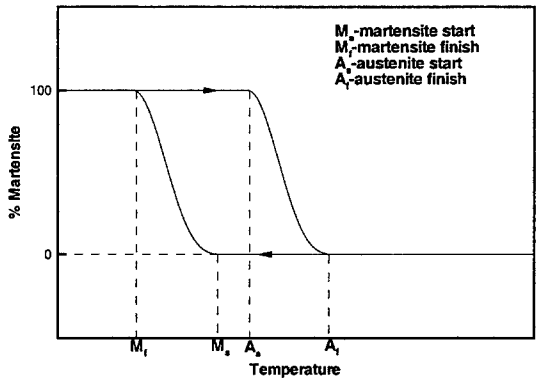

Figure 1: Martensitic and reverse transformation temperature schematic [20].

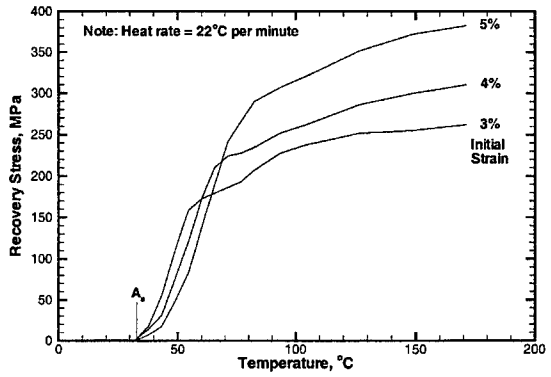

Figure 2: Nitinol recovery stress versus temperature and initial strain [5].

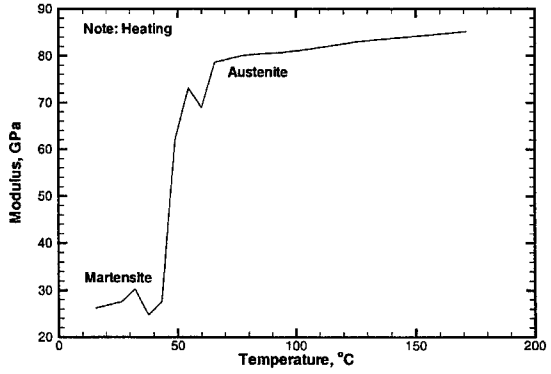

Figure 3: Nitinol Young's modulus versus temperature [5].

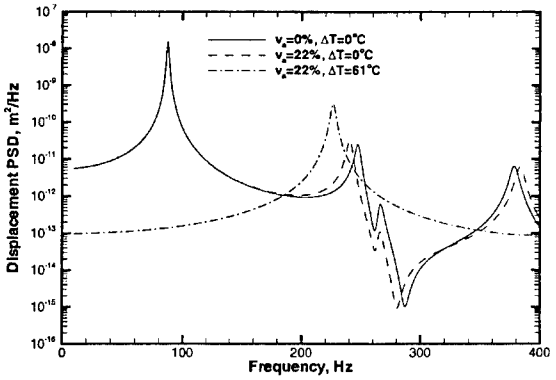

Figure 4: W_{max} PSD for the baseline and SMAHC laminates.

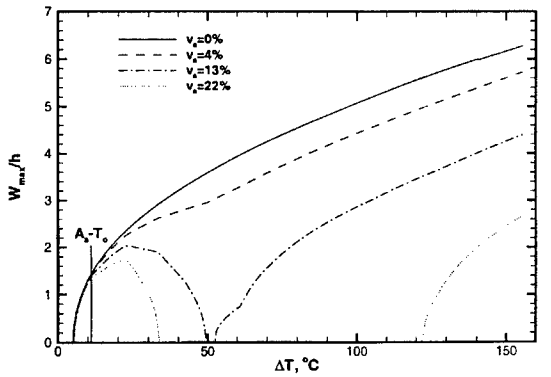

Figure 5: Post-buckling deflection of SMAHC laminates versus ΔT and v_a.

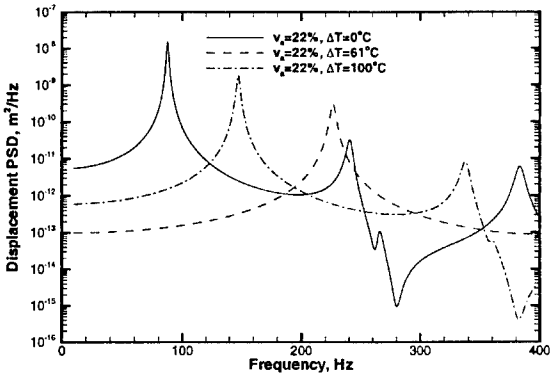

Figure 6: W_{max} PSD for a SMAHC laminate at three temperatures.

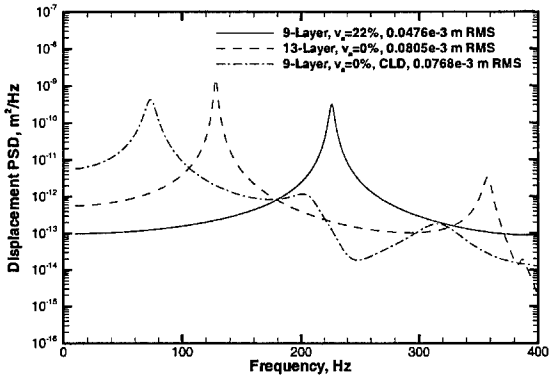

Figure 7: W_{max} PSD comparison of two SMAHCs with conventional treatments.

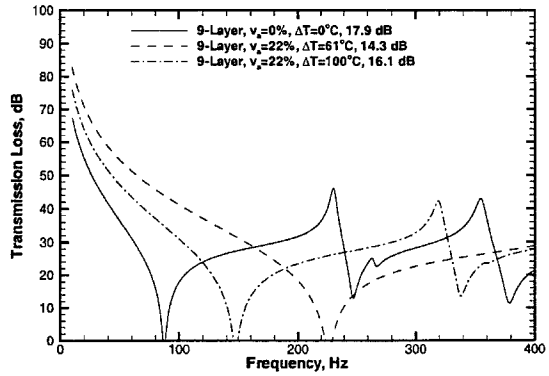

Figure 8: TL versus frequency for the baseline and SMAHC laminates.

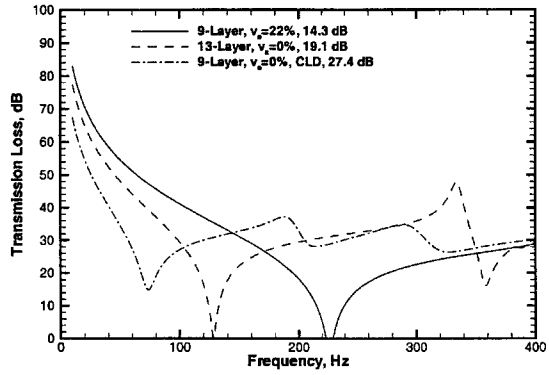

Figure 9: TL comparison of two SMAHCs with conventional treatments.

ACTIVE VIBRATION ISOLATION OF A MULTIPLE MOUNT SYSTEM USING VELOCITY FEEDBACK CONTROL

Sang-Myeong Kim, ksm@kjist.ac.kr
Mechatronics Dept, Kwang-Ju Institute of Science and Technology(KJIST), Kwangju, 500-712, Korea

Steve J. Elliott and Mike J. Brennan, sje, mjb@isvr.soton.ac.uk,
ISVR, University of Southampton,
Highfield, Southampton, SO17 1BJ, UK

Abstract

This paper describes a theoretical and experimental investigation into an active vibration isolation system in which four electromagnetic actuators are installed in parallel with each of four passive mounts placed between a piece of equipment and a vibrating base structure. *Decentralised velocity feedback control* is employed, where each actuator is operated *independently* by feeding back the absolute equipment velocity at the same location. Although one end of each actuator acts at the sensor positions on the equipment, the control system is *not* collocated because of the reactive forces acting on the flexible base structure, whose dynamics are strongly coupled with the mounted equipment. Isolation of low frequency vibration is considered where the equipment can be modelled as a rigid body and the mounts as lumped parameter springs and dampers. Control mechanisms are discussed, and some experimental and simulation results are reported.

1. Introduction

Anti-vibration mounts (also called isolators) are generally required to protect a piece of delicate equipment in a severe vibration environment. These mounts may be modelled as a combination of both resilient and energy dissipating elements, and are widely used to support the equipment and isolate it from base vibration. However, with such passive mounts there is a trade-off between low and high frequency isolation performances depending on the damping on the mount. Low mount damping results in poor performance at low frequencies, while high damping results in poor performance at high

frequencies[1]. Thus, to further improve isolation performance it is often required to introduce extra power sources that can actively reduce vibration transmission through the mounts at all frequencies. Active vibration isolation has been of great interest in various engineering fields as reviewed in [2,3].

Although active isolators can be constructed by feeding back the full state variables commonly seen in active suspension systems, for example [4,5], a more practical and simple way may be direct output feedback control. The absolute velocity responses of a plant structure measured by sensors are often used as the feedback quantity. In particular, when the actuators are collocated with the sensors, then the multichannel control system is proven to be asymptotically stable[6,7]. In this case, the electric control gain used can be analogously transformed to a virtual mechanical skyhook damper [8]. Using this idea, Serrand[9] conducted an experimental study on a two-mount active isolation system, and experimentally showed that decentralised control is capable of globally reducing equipment vibration at all frequencies of interest.

The work presented here is an extension to a four-mount active vibration isolation system for a three-dimensional piece of equipment. Electromagnetic actuators are used as the control actuators, and are installed in parallel with each of four mounts. The control strategy used is *decentralised velocity feedback control*[10,11], where each of the four actuators is operated *independently* by feeding back the equipment absolute velocity response at each control location. The special feature of this control configuration is that, although one end of each actuator acts at a sensor position, the control system is *not* collocated in the sense of [6,7] because of the reactive force acting at the other end of each actuator on the base structure. Stability issues of this control system were discussed by Kim et al[12], and they demonstrated that the decentralised velocity feedback control system is unconditionally stable, provided that stiffness effects of the equipment and inertial effects of the mounts are negligible. Thus isolation of low frequency vibration is considered where the equipment behaves as a rigid body and the mounts as springs and dampers. The aim of this work is to clarify the control mechanisms associated with decentralised velocity feedback control of the four-mount vibration isolation system using structural-borne reactive actuators. The basic concepts and mechanisms of velocity feedback control are discussed in Section 2 initially with a single-mount vibration isolation system. The impedance method [13,14] is employed for the mechanical analysis of both passive and active vibration isolation systems. The active four-mount system is discussed in Section 3. Experiment results are presented in Section 4 and are compared with simulation results.

2. Active isolation of a single mount system

Consider a single mount isolation system where an equipment structure is connected to a flexible base structure via a single mount. If only vertical motions are considered and the mount is assumed to be massless, the whole system can be represented in terms of impedance as shown in Figure 1(a),

where Z_e, Z_m, and Z_b denote the impedances of the equipment, mount, and base, respectively. The base structure with velocity v_b is excited by a primary force f_p, and direct velocity feedback control is applied to reduce the equipment velocity v_e using a pair of control forces f_c via the controller with a gain $-H$. The control forces f_c represent the action and reaction forces of an electromagnetic actuator which is installed in parallel with the mount between the equipment and base structures. As a simple illustration of the single mount system, Figure 1(b) shows a two d.o.f system where an inertial equipment, $Z_e = j\omega m_e$, is installed on a single d.o.f vibrating base structure, $Z_b = j\omega m_b + c_b + k_b/j\omega$, through a single mount consisting of a spring and damper, $Z_m = c_m + k_m/j\omega$. It is convenient to interpret the system as a coupled one connecting the mounted equipment and the base structure, where the mounted equipment is the combination of the equipment and the mount.
Let the total force acting through the mount be f_m, then the dynamic equations of the mounted equipment can be written in the frequency domain as

$$Z_e v_e = f_m \tag{1}$$

$$f_m = f_c + Z_m(v_b - v_e) \tag{2}$$

and, the base structure can be described as

$$Z_b v_b = f_p - f_m \tag{3}$$

where frequency dependency of all the variables are assumed. By combining equations (1-3), the complete system can be represented in the matrix form as

$$\begin{bmatrix} Z_e + Z_m & -Z_m \\ -Z_m & Z_b + Z_m \end{bmatrix} \begin{Bmatrix} v_e \\ v_b \end{Bmatrix} = \begin{Bmatrix} f_c \\ f_p - f_c \end{Bmatrix} \tag{4}$$

When direct velocity feedback control is applied as shown in Figure 1(a) with the control force given by

$$f_c = -Hv_e \tag{5}$$

where H is the positive control gain, the feedback active system can be written as

$$\begin{bmatrix} Z_e + Z_m + H & -Z_m \\ -(Z_m + H) & Z_b + Z_m \end{bmatrix} \begin{Bmatrix} v_e \\ v_b \end{Bmatrix} = \begin{Bmatrix} 0 \\ f_p \end{Bmatrix} \tag{6}$$

Note that, because of the additional force acting on the base, the whole system impedance matrix is now non-symmetric. Thus, the stability of the system can not be assessed by simply using the definiteness property (positive or negative) of the impedance matrix as in collocated control [6,7]. In addition, the mechanical analogy of a skyhook damper [8] is no longer a correct interpretation, as far as the dynamics of the complete coupled system is considered. The system was proven analytically to be unconditionally stable regardless of the degree of coupling between the mounted equipment and the base, provided the equipment is rigid and the mount is massless[12]. Thus, the responses $\{v_e \quad v_b\}^T$ can be obtained by inverting the system impedance matrix.

As a measure of control performance, transmissibility is widely used and is given for the system shown in Figure 1(a) by[8]

$$T = \frac{v_e}{v_b} = \frac{Z_m}{Z_e + Z_m + H} \tag{7}$$

The equation suggests that, as far as the relative equipment motion is concerned, the control gain H is exactly analogous to a passive skyhook damper. When the feedback gain is very large so that $H >> |Z_e + Z_m|$ in equation (7), the transmissibility is greatly improved i.e. $T \approx 0$. The control force in this case becomes

$$f_{co} \approx -Z_m v_b \tag{8}$$

It is interesting to note that the control force for an infinite gain is not infinity, but is bounded and is in fact the *perfect control force* for the feedforward controller using the base response as the reference signal. Actuator saturation would not occur as long as the allowable force of the actuator is bigger than $|Z_m v_b|$. If the perfect control force f_{co} is applied, equation (6) becomes

$$v_e \approx 0, \qquad v_b \approx Y_b f_p \tag{9}$$

where $Y_b = 1/Z_b$. Perfect control of equipment vibration can be achieved approximately, and the base behaves as if no mounted equipment were attached. This implies that the control force *uncouples* the mounted equipment from the base.

The active system in equation (6) can be further simplified when the mounted equipment structure is weakly coupled to the base structure. Since the reaction force from the mount is negligible compared with the primary force i.e., $|f_m| << |f_p|$ in equation (3), equation (6) for *weak coupling* becomes

$$\begin{bmatrix} Z_e + Z_m + H & -Z_m \\ 0 & Z_b \end{bmatrix} \begin{Bmatrix} v_e \\ v_b \end{Bmatrix} = \begin{Bmatrix} 0 \\ f_p \end{Bmatrix} \tag{10}$$

The system can now be regarded as collocated control whose stability analysis is trivial [6,7], and the control gain can thus be equivalently transformed to a skyhook damper. The criterion for weak coupling can be judged by comparing dynamic characteristics of the uncoupled systems at the connection point v_b, and is given by [13,14]

$$|Z_{me} Y_b| << 1 \tag{11}$$

where the input impedance to the mounted equipment is $Z_{me} = Z_m Z_e / (Z_m + Z_e)$.

The two d.o.f system shown in Figure 1(b) whose dynamics are well known [15], are considered to illustrate the basic coupling mechanisms during active control. The upper single d.o.f mounted equipment system was assumed to be of mass $m_e = 1\ kg$, natural frequency $f_n = 20\ Hz$ and damping ratio $\varsigma = 0.05$, and the lower single d.o.f base system was assumed to be of mass $m_b = 1\ kg$, natural frequency $f_n = 30\ Hz$ and damping ratio $\varsigma = 0.01$. The results are

shown in Figure 2 both before and after control. Due to the strong coupling, the natural frequencies of the coupled system are different from the uncoupled natural frequencies; 20 Hz and 30 Hz. In addition, in Figure 2(b) there is a sharp anti-resonance at the uncoupled natural frequency of the mounted equipment since it acts as a dynamic neutraliser at this frequency [16]. Figure 2(a) shows the maximum velocity reduction is not at the natural frequency of the uncoupled mounted equipment unlike the transmissibility T in equation (7) suggests, but at the natural frequencies of the coupled system. Transmissibility is a good performance measure for a weakly coupled system, however, in a strongly coupled system the denominator v_b of T changes after attachment as well as a change of control gain. Thus the equipment absolute velocity is preferable in this case [1], and for multiple degree-of-freedom(d.o.f) equipment structures the kinetic energy of the equipment may be a good performance measure. Figure 2(a, b) clearly demonstrate that the controller *uncouples* the mounted equipment from the base as the gain increases, since both equipment and base responses approach those of the uncoupled systems. The uncoupled equipment velocity to base excitation is zero, and so its response is not shown in Figure 2(a).

3. Active vibration isolation of a multiple-mount system

Consider a three-dimensional piece of rigid equipment installed on a flexible base structure via four massless mounts as shown in Figure 3. The impedance approach described in the previous section can be applied to this case but with some care because the number of mounts(four) is not the same as the number of degrees of freedom of the equipment structure(three). The co-ordinate transformations between the mounting point (nodal) and modal co-ordinates are given by

$$\mathbf{v}_e = \mathbf{Q}\mathbf{a}, \qquad \mathbf{a} = \mathbf{R}\mathbf{v}_e \tag{12,13}$$

where $\mathbf{a} = \{\dot{w} \quad \dot{\theta} \quad \dot{\phi}\}^T$ is the modal velocity vector consisting of the derivatives of heave, pitch and roll motions at the mass centre, and $\mathbf{v}_e = \{v_{e1} \quad v_{e2} \quad v_{e3} \quad v_{e4}\}^T$ is the velocity vector at the mounting points. Since equation (12) is over-determined, the pseudo-inverse of $\mathbf{Q}$ can be obtained from its least square solution to account for measurement errors in the velocity signals so that $\mathbf{R} = (\mathbf{Q}^T\mathbf{Q})^{-1}\mathbf{Q}^T$ [17,18]. The dynamic equations can be written in a similar way as those for the single mount system given in equation (1-3). The dynamic equations of the equipment structure can be written in terms of the modal velocity vector $\mathbf{a}$ similarly as equation (1), as

$$\overline{\mathbf{Z}}_e\mathbf{a} = \mathbf{g}_m, \tag{14}$$

where the modal impedance matrix of the equipment is $\overline{\mathbf{Z}}_e = j\omega\mathbf{J}_e$ in which $\mathbf{J}_e$ is the diagonal inertia matrix of the equipment whose diagonal terms are the mass of the equipment M, and the moment of inertia quantities to pitch and

roll motions I_θ and I_φ. Note this is an over-determined case, and theoretically the corresponding physical domain description of equation (14) does not exist. The generalised force vector acting through the mounts $\mathbf{g}_m$ is given by

$$\mathbf{g}_m = \mathbf{Q}^T\mathbf{f}_m \tag{15}$$

where the mount force vector in physical co-ordinates $\mathbf{f}_m = \{f_{m1} \quad f_{m2} \quad f_{m3} \quad f_{m4}\}^T$. By extending equation (2), $\mathbf{f}_m$ can be written as

$$\mathbf{f}_m = \mathbf{f}_c + \mathbf{Z}_m(\mathbf{v}_b - \mathbf{v}_e), \tag{16}$$

where the impedance matrix of the mounts $\mathbf{Z}_m$ is a (4×4) diagonal matrix whose diagonal terms are the impedances of each mount, $\mathbf{f}_c$ is the control force vector $\mathbf{f}_c = \{f_{c1} \quad f_{c2} \quad f_{c3} \quad f_{c4}\}^T$, and $\mathbf{v}_e$ and $\mathbf{v}_b$ are the velocity vectors of the equipment and base structures at the mount locations. Also by extending equation (3), the base response can be written as

$$\mathbf{Z}_b\mathbf{v}_b = \mathbf{d}_p - \mathbf{f}_m, \tag{17}$$

where $\mathbf{d}_p = \mathbf{Z}_b\mathbf{Y}_{bp}\mathbf{f}_p$ in which $\mathbf{Z}_b$ and $\mathbf{Y}_{bp}$ are the impedance and mobility matrices of the uncoupled base structure due to the mount force vector $\mathbf{f}_m$ and the primary force vector $\mathbf{f}_p$, respectively. Combining equations (14-17) gives

$$\begin{bmatrix} \overline{\mathbf{Z}}_e + \overline{\mathbf{Z}}_m & -\mathbf{Q}^T\mathbf{Z}_m \\ -\mathbf{Z}_m\mathbf{Q} & \mathbf{Z}_b + \mathbf{Z}_m \end{bmatrix} \begin{Bmatrix} \mathbf{a} \\ \mathbf{v}_b \end{Bmatrix} = \begin{Bmatrix} \mathbf{g}_c \\ \mathbf{d}_p - \mathbf{f}_c \end{Bmatrix} \tag{18}$$

where the generalised control force vector is $\mathbf{g}_c = \mathbf{Q}^T\mathbf{f}_c$, and $\overline{\mathbf{Z}}_m = \mathbf{Q}^T\mathbf{Z}_m\mathbf{Q}$ is the modal mount impedance matrix which is the transformed form of the nodal mount impedance matrix $\mathbf{Z}_m$. When velocity feedback control with the control gain matrix $\mathbf{H}$ is applied, the control force vector is written as

$$\mathbf{f}_c = -\mathbf{H}\mathbf{v}_e \tag{19}$$

Since $\mathbf{g}_c = \mathbf{Q}^T\mathbf{f}_c$ and $\mathbf{v}_e = \mathbf{Q}\mathbf{a}$, the modal gain matrix is written as

$$\overline{\mathbf{H}} = \mathbf{Q}^T\mathbf{H}\mathbf{Q} \tag{20}$$

Using equations (18-20), the active system can be written as

$$\begin{bmatrix} \overline{\mathbf{Z}}_e + \overline{\mathbf{Z}}_m + \overline{\mathbf{H}} & -\mathbf{Q}^T\mathbf{Z}_m \\ -(\mathbf{Z}_m + \mathbf{H})\mathbf{Q} & \mathbf{Z}_b + \mathbf{Z}_m \end{bmatrix} \begin{Bmatrix} \mathbf{a} \\ \mathbf{v}_b \end{Bmatrix} = \begin{Bmatrix} \mathbf{0} \\ \mathbf{d}_p \end{Bmatrix} \tag{21}$$

Equation (21) is a compact description of the four-mount active vibration isolation system in term of impedances. Note this is also a simple extension form of the single mount system in equation (6). If the control system is stable, the solution of equation (21) can be obtained by inverting the impedance matrix. Similarly as the single mount case, the equipment modal velocity vector $\mathbf{a}$ obtained is related with the performance of the isolator. If the perfect control force vector $\mathbf{f}_{co} = -\mathbf{Z}_m\mathbf{v}_b$ is applied, it uncouples the mounted equipment from the vibrating base structure so that the active system becomes similar to equation (9).

Rather than implementing a complex 4-input 4-output fully coupled control system, it is interesting to consider the simplified system when four separate

SISO (single-input-single-output) control systems are used. In this case the control gain matrix **H** in equation (20) becomes diagonal. This is termed as *decentralised control* [10,11] where each of the four actuators is controlled *independently* by feeding back the corresponding equipment absolute velocity response at each control location. For the symmetrically installed equipment structure as shown in Figure 3, the transform matrices are given by

$$\mathbf{Q}=\begin{bmatrix} 1 & -l_\theta & -l_\phi \\ 1 & +l_\theta & -l_\phi \\ 1 & +l_\theta & +l_\phi \\ 1 & -l_\theta & +l_\phi \end{bmatrix}, \qquad \mathbf{R}=\frac{1}{4}\begin{bmatrix} 1 & 1 & 1 & 1 \\ -1/l_\theta & +1/l_\theta & +1/l_\theta & -1/l_\theta \\ -1/l_\phi & -1/l_\phi & +1/l_\phi & +1/l_\phi \end{bmatrix} \tag{22,23}$$

If it is assumed that the installation of the equipment is statically balanced [1] so that $\overline{\mathbf{Z}}_\mathbf{m}$ is diagonal, then for the symmetrical system shown in Figure 3 the impedances of each mount are the same, which may be denoted Z_m. If it is further assumed that the gains of each controller are the same H, the equipment dynamic equation given in the (1,1) term of equation (21) becomes diagonal, and is given by

$$\overline{\mathbf{Z}}_\mathbf{e}+\overline{\mathbf{Z}}_\mathbf{m}+\overline{\mathbf{H}}=\begin{bmatrix} j\omega M+Z_m+H & 0 & 0 \\ 0 & j\omega J_\theta+(Z_m+H)l_\theta^2 & 0 \\ 0 & 0 & j\omega J_\phi+(Z_m+H)l_\phi^2 \end{bmatrix} \tag{24}$$

The equipment dynamic equations are uncoupled even after control, and the gain H is simply added to the mount impedance Z_m in all three motions. This means that, for the statically balanced symmetric structure shown in Figure 3, the use of a single common gain for decentralised control (*equi-decentralised control*) results in the modal controller which equally damps all modes (*equi-modal control*). Each of four control forces has the same effect as a skyhook damper, as far as the relative equipment motions are concerned, as discussed earlier. The four skyhook dampers at each mount location can equivalently reduce every rigid body mode of the equipment structure. Consider the general case when the equipment structure is non-symmetric but statically balanced as is preferred in practice [1]. Even in this case, equi-modal control can again be achieved by making the modal control gain matrix $\overline{\mathbf{H}}$ diagonal similarly as $\overline{\mathbf{Z}}_\mathbf{m}$.

As suggested in the previous section, the kinetic energy can be conveniently employed as a performance measure for the three-dimensional equipment structure, and can be written as

$$E_k=\frac{1}{2}\mathbf{a}^\mathbf{H}\mathbf{J}_\mathbf{e}\mathbf{a} \tag{25}$$

where **a** is the modal velocity vector and $\mathbf{J}_\mathbf{e}$ is the inertia matrix of the equipment.

4. Experimental implementation

4.1 System description

Decentralised direct velocity control was experimentally implemented with a statically balanced four-mount system similar to that shown in Figure 3. The experimental set-up is shown in Figure 4(a) where a piece of symmetrical equipment is located on top of a free-free-clamped-clamped rectangular base plate via four identical mounts. Two opposite sides of the base plate were bolted on stiff frames to realise the clamped-clamped boundary conditions. The large shaker underneath the plate was the primary force actuator, and the four small electromagnetic actuators fixed on the thick equipment plate were the control actuators at each mount position. The equipment structure was the combined structure between the four actuators and a thick aluminium plate of thickness 20 mm. The plan view of the set-up is shown in Figure 4(b) where the dimensions of the base plate is $L_x \times L_y$, and f_p is denoted at the primary force. The locations of the numbers denote the locations of each mount, and they are referred as Nodes 1, 2, 3, and 4 for convenience. The heave w, pitch θ, and roll ϕ motions are denoted at the mass centre of the symmetric equipment structure. The flexible base structure was excited by white noise from the primary force f_p. Figure 5 shows the structure of a single channel of the decentralised control system. The acceleration of the equipment $\dot{v}_e$ was first measured and passed through an integrator to obtain the velocity response v_e, which was then fed back to the actuator via a power amplifier for the gain control. Each actuator was fixed on top of the thick equipment plate at each mount location as shown in Figure 5, and a stinger was connected between the actuator and the mount foot through the mount. The cylindrical mounts were made from natural rubber. The integrator was contained in a commercial charge amplifier (B&K type 2635) which also had high- and low-pass filter modules. The highpass filter cutoff frequency was set to be 1 Hz to avoid low frequency instability, and the lowpass filter cutoff frequency was set to be 1 kHz to filter out any measurement of flexible modes within the equipment structure. Only isolation of low frequency vibration, under 200 Hz, was considered where the equipment structure could be modelled as a rigid body and each mount as a parallel connection of spring k_m and damper c_m, as shown in Figure 3. The physical and geometric properties of the experimental set-up are summarised in Tables 1 and 2. They were used for a series of simulations, the results of which are compared with the experimental results.

The experimental model was first identified and compared with the theoretical model calculated from the procedure described in Section 3. To measure the plant response, the actuator input voltage V_{in} in Figure 5 was used as the input signal instead of the input force because the input voltage at low frequencies is approximately proportional to the force input [19]. The mounted equipment structure was first installed on a rigid base structure to identify the uncoupled characteristics. Figure 6(a) shows the measured plant response at Mount 1

excited by the actuator at the same location. For comparison, experimental (solid line) and simulation (dashed line) results are shown together. The three rigid body modes were heave motion at 26 Hz, pitch motion at 29 Hz, and roll motion at 24 Hz, and whose passive damping ratios were around 5 %. The mounted equipment structure was then installed on the flexible structure as shown in Figure 4, and the plant response at Mount 1 excited by the actuator at the same location was measured. The plant response is now a coupled response between the mounted equipment and base structures, and the experimental (solid) and simulation (dashed) results are shown in Figure 6(b). The first three dominant peaks correspond to heave motion at 15.8 Hz, pitch motion at 21.3 Hz, and roll motion at 22.5 Hz. Some discrepancies over 30 Hz were due to the imperfect physical realisation of the clamped-clamped boundary condition.

4.2 Control performance

The experimental rig was excited by white noise from the primary force, and the four-channel decentralised control system whose single channel structure is shown in Figure 5 was tested. Control performances according to the change of the common gain H were examined and compared with simulations. The velocities of the equipment at the mounting points of the experimental plant are shown in Figure 7, in which the responses before control are shown with solid lines and those after control are shown with dashed lines. In Figure 7(a) for Mount 1, the highest response (solid line) is the response before control, and the others (dashed lines) correspond to feedback gains of 110, 320, 1000. It clearly shows that, as the gain increases, the vibration amplitude is gradually reduced almost all over the frequency range. This trend is the same for Mount 2, 3, and 4. Some amplification near 30 Hz at Mount 2 could be due to the redundancy of the controller configuration that used four actuators to control three rigid body modes. Higher gains could not be applied to the experimental plant because there was an instability occurring at about 1 Hz which was the cutoff frequency of the highpass filter used in conjunction with the integrator. The causes of instability was found to be phase advances at very low frequencies in the commercial power amplifier and the integrator used[12].

From the performances at the mounting points in Figures 7, the modal performances can be calculated by first using the co-ordinate transform matrix in equation (13) and then substituting into the kinetic energy equation in (25). The total kinetic energies of the experimental and simulation models are shown in Figure 8(a,b) respectively. Since the theoretical model implicitly assumes that the power amplifier and the integrator are ideally operating, it is unconditionally stable[12] so that some higher gains 3350 and 10000 were also tested. It can be seen that as the gain increases, the total energy is reduced gradually in the whole frequency range without any amplification. It means that, although there is some amplification in nodal responses due to the redundancy of actuators, the actuators are operating in a way to reduce the overall kinetic energy of the equipment at all frequencies. The control

performance of both the simulations and experiments are tabulated in Table 3 according to the feedback gain values used. The gains H are transformed to skyhook damping values, and are compared with the values of the passive damping in a single mount c_m, as given in Table 1. The skyhook damping and damping ratio calculated based on heave motion can be compared with the passive damping ratios, which are about 5 %. The overall kinetic energy of the experiment was calculated from 5 Hz to avoid accounting for the amplification region. Both simulation and experiment results show a kinetic energy reduction of more than 14 dB for the gain 1000.

In order to investigate the control mechanism, the base velocity underneath Mount 1 was also calculated and measured during control. The simulation and experimental results are shown in Figure 9(a,b) respectively. As the gain increases, the original base response(solid line) approaches the uncoupled base response(dotted line), that is the base response without the mounted equipment attached. Dashed lines correspond to the base responses for each control gain. This clearly demonstrates that the mechanism of the active isolation system is that the controller uses the reactive actuators to uncouple the mounted equipment from the base structure.

5. Conclusions

This paper has investigated both theoretically and experimentally a statically balanced four-mount active vibration isolation system where electromagnetic actuators are installed in parallel with each of four mounts placed between a piece of equipment and a vibrating base structure. Decentralised velocity feedback control was used for active vibration isolation at low frequencies where the equipment behaves as a rigid body and the mounts as springs and dampers. The impedance method has been used to analyse both passive and active isolation systems. Analytical studies show that equi-gain-decentralised control for a statically balanced symmetric equipment is the same as equi-gain-modal control, which reduces all vibration modes equally. The control mechanism is shown to be that the actuators uncouple the mounted equipment from the base structure as the gain increases. Experimental results show that up to 14 dB reduction in the kinetic energy of the equipment can be achieved in practice. When very high gains were used, however, instability was encountered in the experimental rig at about 1 Hz due to undesirable phase advances in the electrical equipment used.

References

1. C.E. Crede and J.E. Ruzicka,1996, Shock and Vibration Handbook (C.M. Harris, editor) New York: McGraw-Hill. Ch.30 Theory of vibration isolation
2. L. Meirovitch, 1990, Dynamics and control of structures, John Wiley & Sons, Inc.
3. C.R. Fuller, S.J. Elliott and P.A. Nelson, 1996, Active control of vibration, Academic Press.
4. D. Hrovat and M. Hubbard, 1981, Journal of Dynamic systems, Measurement, and Control, Vol. 103, 228-236, Transactions of the ASME, Optimal Vehicle suspensions minimizing RMS rattlespace, sprung-mass acceleration and jerk.
5. A. Hac, 1986, Journal of Dynamic systems, Measurement, and Control, Vol. 108, 106-110, Transactions of the ASME, Stochastic optimal control of vehicles with elastic body and active suspension
6. M.J. Balas, 1979, Journal of Guidance and Control, Vol. 2, 252-253, Direct velocity feedback control of large space structures
7. S.M. Joshi, Journal of Guidance and Control, 1986, Vol.9, pp.85-91, Robustness properties of collocated controllers for flexible spacecraft
8. D. Karnopp, M.J. Crosby and R.A. Harwood, 1974, Journal of Engineering for Industry, pp. 619-626, Vibration control using the semi-active force generators
9. M. Serrand, 1998, MSc Dissertation, University of Southampton, Active isolation of base vibration
10. S. Skogestad and I. Postlethwaite, 1996, Multivariable feedback control; Analysis and design, John Wiley & Sons, Inc.
11. M. Morari and E. Zafiriou, 1989, Robust process control, Prentice-Hall, Inc.
12. S.M. Kim, S.J. Elliott and M.J. Brennan, 1999, Active vibration isolation of a 3-dimensional structure using velocity feedback control, ISVR Technical Memorandum No. 845
13. S.M. Kim and M.J. Brennan, 1999, Journal of Sound and Vibration, (223), pp.97-113, A compact matrix formulation using the impedance and mobility approach for the analysis of structural-acoustic systems
14. S.M. Kim 1998, PhD Thesis, University of Southampton, Active control of sound in structural-acoustic coupled systems
15. F.S. Tse, I.E. Morse and R.T. Hinkle, 1978, Mechanical Vibrations: Theory and Applications, Allyn and Bacon, Inc.
16. D.J. Mead, 1999, Passive vibration control, John Wiley & Sons Ltd.
17. B. Noble and J.W. Daniel, 1988, Applied Linear Algebra, Prentice-Hall, Inc.
18. F.B. Hilderbrand, 1965, Methods of applied mathematics, Prentice-Hall, Inc. 2nd.
19. M.Z. Ren, K. Seto and F. Doi, 1997, Journal of Sound and Vibration, 205, 57-80, Feedback structural-borne sound control of a flexible plate with an electromagnetic actuator: the phase lag problem

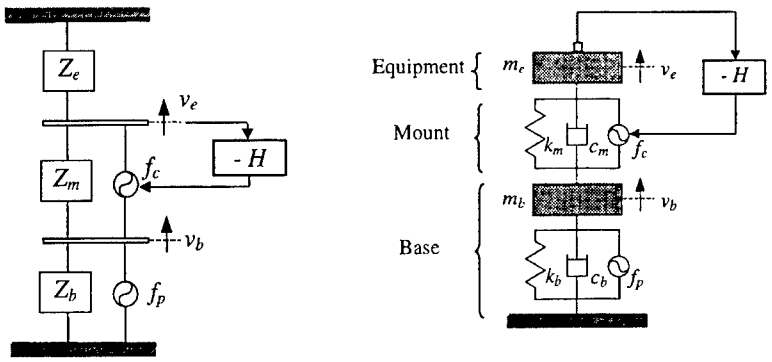

(a) Impedance diagram (b) two degrees of freedom system

Figure 1. A single mount vibration isolation system

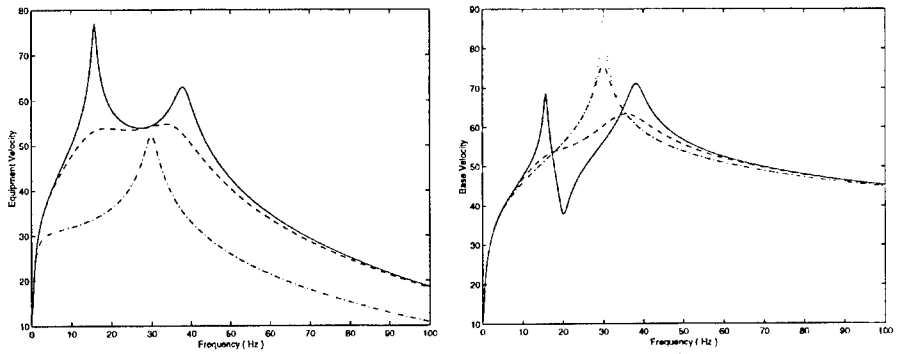

(a) Absolute equipment velocity (b) Absolute base velocity

Figure 2. Active vibration isolation in a two d.o.f system; before control but coupled (solid) and uncoupled (dotted), after control with $H=10c_m$ (dashed) and $H=100c_m$ (dash-dotted). (dB ref.=10^{-5} m/s)

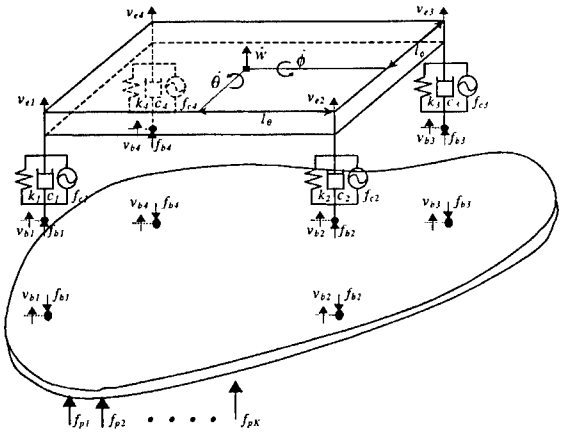

Figure 3. A 3-dimensional rigid equipment structure supported upon four mounts

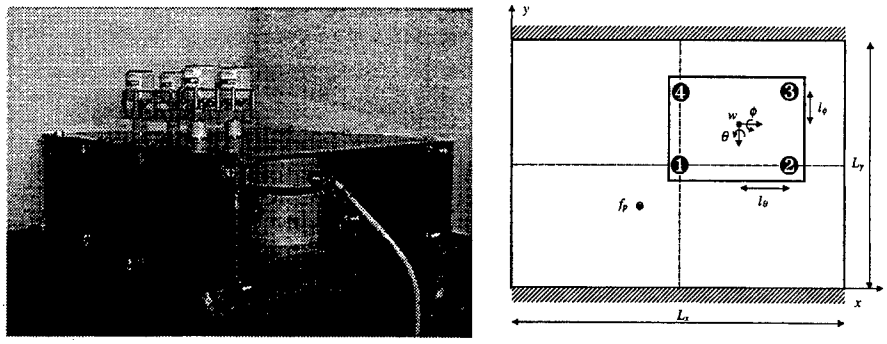

(a) set-up (b)schematic diagram

Figure 4. Experimental set-up for the active isolation system on a free-free-clamped-clamped base plate structure. The locations of the four mounts are marked as Nodes 1,2,3, and 4.

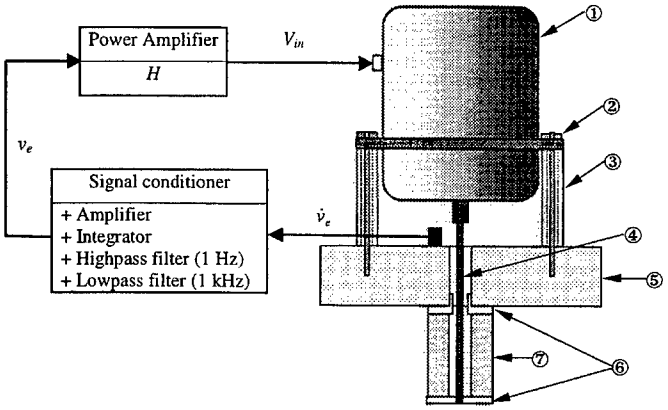

Figure 5. Structure of the active isolator; ① Electromagnetic Actuator, ② Bolt, ③ Support (height = 40 mm) , ④ Stinger , ⑤ Equipment Structure (Al), ⑥ Upper and Lower Adapters (Al), ⑦ Rubber Mount (height = 30 mm, outer dia. = 30mm, inner dia. = 10 mm).

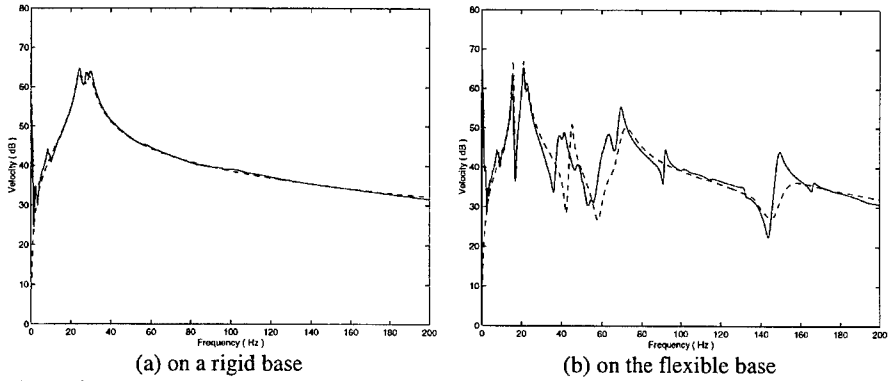

(a) on a rigid base (b) on the flexible base

Figure 6. Plant responses at Mount 1 when only the actuator at Node 1 is active; experiment (solid) and simulation (dashed). (dB ref.=10^{-5} m/s)

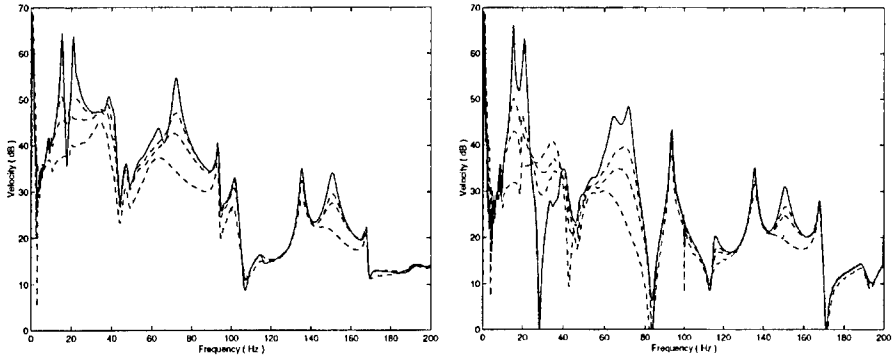

(a) Node 1 (b) Node 2

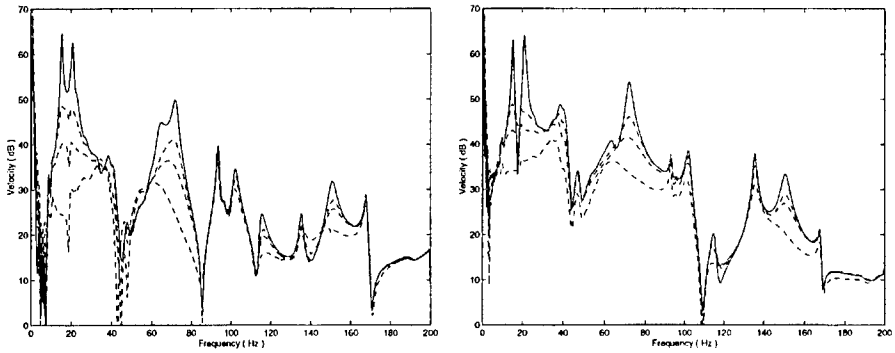

(c) Node 3 (d) Node 4

Figure 7. Experimental results of the equipment responses at the mounting points as a function of feedback gain H; without control(solid) and with control(dashed). (dB ref.=10^{-5} m/s)

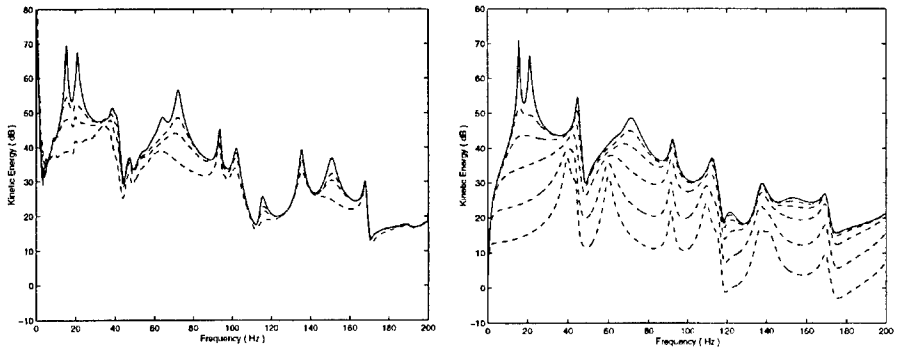

(a) Experiments (b) Simulations

Figure 8. The total kinetic energies of the equipment structure according to the gains H; without control(solid) and with control(dashed). (dB ref.=10^{-10} J)

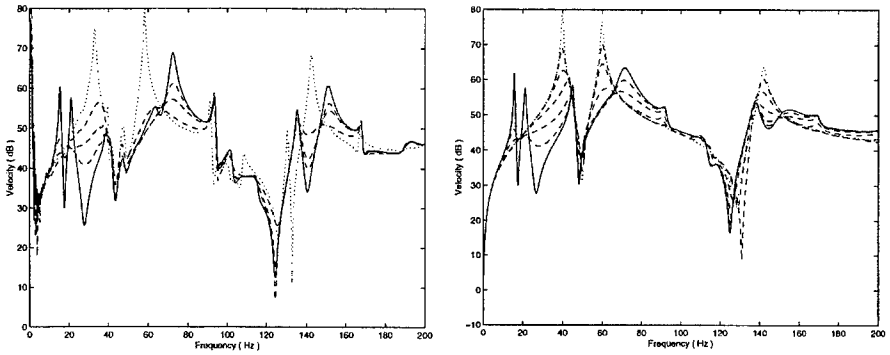

(a) Experiments (b) Simulations

Figure 9. Base response at Node 1 according to the gains H; without control but coupled(solid) and uncoupled(dotted), and with control(dashed).

Table 1. Physical properties

Equipment Structure	M_s, Mass	6.232 kg
	I_θ, Moment of inertia to pitch motion	0.0685 kgm^2
	I_ϕ, Moment of inertia to pitch motion	0.0162 kgm^2
	Material of the equipment plate	Aluminium
Mount	k_m, Spring constant of each mount	4.2×10^4 N/m
	c_m, Damping of each mount	25.6 Ns/m
Base Plate	Material	Steel
	ζ, Damping ratio	0.01

Table 2. Geometric data

($L_x \times L_x \times t$), Dimensions of the steel base plate (mm)	$(700 \times 500 \times 2)$
($L_x \times L_x \times t$), Dimensions of the aluminium equipment plate (mm)	$(300 \times 160 \times 20)$
Mount locations on the equipment (mm)	$l_\theta = 117,\ l_\theta = 47$
Location of the primary force (mm)	(320, 270)
Location of Node 1	$(L_x/2, L_y/2)$

Table 3. Comparison of the control performances. (Skyhook damping and its ratio are calculated based on the heave motion, and $c_m = 25.6$ Ns/m)

Gains			Energy ratio J_o/J_i (%)		Overall reduction(dB)	
Absolute Value, H	Skyhook Damping	Skyhook Damping Ratio	Theory	Experiment	Theory	Experiment
110	$4.3 \times c_m$	0.215	18.82	19.59	-7.3	-7.1
320	$12.5 \times c_m$	0.626	8.14	10.31	-10.9	-9.9
1000	$39.1 \times c_m$	1.955	3.21	4.0	-15.0	-14.0
3350	$130.9 \times c_m$	6.548	1.52	.	-18.2	.
10000	$390.6 \times c_m$	19.546	0.82	.	-20.9	.

Identification of electromechanical coupling in piezo-structures

Pascal De Boe[1], Jean-Claude Golinval[2]

LTAS – Vibrations et Identification des Structures,
Université de Liège, B-4000 Liège, Belgium.
[1] *pdeboe@ulg.ac.be*, [2] *jc.golinval@ulg.ac.be, http://www.ulg.ac.be/ltas*

Abstract

An identification method based on a structural model updating procedure may be used to improve the knowledge of a piezoelectric tested structure and to determine the coupling coefficients of the piezoelectric material. This procedure starts with the modal analysis of the open-loop instrumented structure. Let the target modes be a subset of the model modes; a selection of sensor locations is then performed by determining the smaller subset such that the H_2 modal norm is as close as possible to the modal norm of the original full set. In most cases, experimental testing with the selected sensor set will give acceptable information to identify target modes. These data, coupled with electrical sensing at the piezoelectric element level, will then be used to perform modal analysis of the piezo-structure. A pole-residue development of the open-loop piezo-structure shows that conventional algorithms may be used to estimate the mechanical modal parameters and the electromechanical coupling matrix.

The second step of the procedure is to perform model updating itself by improving the initial finite element piezoelectric model with stiffness corrections. The corrections are split in their mechanical and electromechanical contributions. It is then possible to separate mechanical modelling errors from electromechanical coupling errors. The problem becomes a classical model updating problem which may be solved using well established techniques. This will result not only in a model behaving like the measures, but also in an improved knowledge of the structure behaviour without loosing physical insight. From a numerical point of view, it will be shown that ill-conditioning inherent to the presence of piezoelectric elements presents some difficulties at different steps of the model correction procedure.

A clamped-free plate instrumented with piezo-laminates is used to illustrate the selection of measurement points and the model updating approach. Experimental identification data will then be used as inputs for the model correction procedure and the behaviour of the updated model will be compared with the initial model dynamics.

Introduction

The current trend to design light-weight structures is generally antagonist to the mechanical requirement in terms of vibrational stability and accuracy. Active control of such flexible structures is a solution to overcome this problem. Modelling field, which use often the finite elements method (*FEM*), has then been improved in order to have a satisfactory prediction of the dynamic. The performance of the model is important because it could condition the ability of an implemented active system to follow the dynamic behaviour of the actual structure. Unfortunately, a numerical model contains some uncertainties inherent to the boundary conditions and to the physical properties of structural materials. Errors are also induced by the discretisation and by the condensation of the actual structural degrees of freedom to an acceptable size for the controller.

A model correction procedure, called model updating, could be then useful in order to improve the structural dynamic prediction. One way is to correct the estimated masses and stiffness (damping correction will not be considered in this work) . The idea is then to update the initial model in order to minimise the distance between the numerical prediction and the measured data; whether in the modal or frequency domain.

Literature exhibits several hundred papers on the model updating of conventional 'passive' structures. Ewins [0] and, later, Maia et al. [1] summarise the various published techniques in this field, but none of them are applied on *'smart'* structures. This paper will show the application of the frequency domain updating technique on *'smart'* structures fitted with piezoelectric elements.

Piezoelectric elements are very popular in the field of active control. Their light-weight and distributed properties are very attractive to overcome the structural vibration suppression challenge. There are two fundamental electromechanical effects associated with piezoelectricity, namely the direct effect and the converse effect. Direct effect can be detected when applying a force on a piezoelectric material and monitoring the electrical voltage or charge generated. Inversely, to emphasise the converse effect, an electric field can be applied to the material which will induce stress or strain. Piezoelectricity is used for a large number of applications in the field of electromechanical engineering, e.g. waves-sound generators, echo-graphic probes, micro-positioner, accelerometer transducers, pressure transducers,... Thin piezoelectric laminates are widely used as distributed sensors and

distributed actuators and are very well adapted for the control of elastic shells or plates.

Modal analysis of a piezo-structure

The modal testing of a structure fitted with distributed piezoelectric sensor/actuator is described by Saunders et al. [2]. The pole-residue model is developed by remembering the modal decomposition of a viscously damped and linear passive structure :

$$\boldsymbol{M} \cdot \ddot{\boldsymbol{x}} + \boldsymbol{D} \cdot \dot{\boldsymbol{x}} + \boldsymbol{K} \cdot \boldsymbol{x} = \boldsymbol{f} \qquad (1)$$

with
- $\boldsymbol{M}$ $n \times n$ mass matrix, symmetric and definite positive,
- $\boldsymbol{D}$ $n \times n$ damping matrix,
- $\boldsymbol{K}$ $n \times n$ stiffness matrix, symmetric and definite positive,
- $\boldsymbol{f}$ $n \times 1$ vector of structural forces,
- $\boldsymbol{x}$ $n \times 1$ vector of structural degrees of freedom.

The resolution of the eigenvalues problem associated with (1) yields n pairs of complex conjugate eigenvalues :

$$p_i = -\zeta_i \cdot \omega_i \pm j \cdot \omega_i \cdot \sqrt{1 - \zeta_i^2} \qquad i = 1, 2, \ldots n \qquad (2)$$

associated with n complex eigenvectors $\Phi = [\phi_1 \ \ \phi_2 \ \ \ldots \ \ \phi_n]$ (nxn). In the case of proportional or diagonal damping the p_i eigenvalues are linked to the solutions ω_i of the associated non-damped system and with the modal critical damping ζ_i (see Géradin and Rixen [3]).

For a force applied at the spatial position l and for a response measured at the spatial position k, the frequency response function (*FRF*) is expressed by :

$$\frac{x_k}{f_l} = \alpha_{kl} = \sum_{i=1}^{n} \left\{ \frac{\phi_{ki} \cdot \phi_{li}}{m_i \cdot [j \cdot \omega - p_i]} + \frac{\phi_{ki}^* \cdot \phi_{li}^*}{m_i \cdot [j \cdot \omega - p_i^*]} \right\} \qquad (3)$$

with m_i the modal mass associated with the ith mode ϕ_i.

In the case of a structure fitted with a piezoelectric sensor/actuator, electromechanical relationship are added to the previous system (1) to represent contributions of the electrical degrees of freedom linked to the piezoelectric actuator and sensor :

$$\begin{aligned} \boldsymbol{M}\cdot\ddot{\boldsymbol{x}} + \boldsymbol{D}\cdot\dot{\boldsymbol{x}} + \boldsymbol{K}\cdot\boldsymbol{x} &= \boldsymbol{f} + \Theta^{a}\cdot\boldsymbol{v}_{a} \\ \Theta^{s^{T}}\cdot\boldsymbol{x} + \boldsymbol{C}_{p}\cdot\boldsymbol{v}_{s} &= \boldsymbol{q} \end{aligned} \qquad (4)$$

The first equation is commonly called the actuator equation and the second, the sensor equation. The actuator equation exhibits the force generated by the piezoelectric actuator through the electromechanical coupling actuator matrix Θ^{a} and the electrical potentials applied at each electrode of the elements. On the other hand, the sensor equation shows the relationship existing between the mechanical degrees of freedom $\boldsymbol{x}$ and the electrical charges $\boldsymbol{q}$ or potentials $\boldsymbol{v}_{s}$ through the electromechanical coupling matrix $\Theta^{s^{T}}$ and the capacitance $\boldsymbol{C}_{p}$ of sensor.

In the case of a force applied on a system only fitted with a piezoelectric sensor, and by forcing the electrode potentials to zero with a short-circuit (e.g. : physically, by means of a perfect charge amplifier), we can write :

$$\begin{aligned} \boldsymbol{M}\cdot\ddot{\boldsymbol{x}} + \boldsymbol{D}\cdot\dot{\boldsymbol{x}} + \boldsymbol{K}\cdot\boldsymbol{x} &= \boldsymbol{f} \\ \Theta^{s^{T}}\cdot\boldsymbol{x} &= \boldsymbol{q} \end{aligned} \qquad (5)$$

The first thing to observe is that the presence of the piezoelectric sensor do not modify the dynamic behaviour of the structure (same eigen-frequencies, modes and modal critical damping and masses). On the other hand, remembering (3), it is easy to find the relation between the electrical sensing and the applied force decomposed in a summation of modal participation weights :

$$\frac{\boldsymbol{v}_{s}}{\boldsymbol{f}_{l}} = \sum_{i=1}^{n}\left\{\frac{\Theta^{s^{T}}\cdot\phi_{i}\cdot\phi_{li}}{\boldsymbol{m}_{i}\cdot\left[j\cdot\omega - \boldsymbol{p}_{i}\right]} + \frac{\Theta^{s^{T}}\cdot\phi_{i}^{*}\cdot\phi_{li}^{*}}{\boldsymbol{m}_{i}\cdot\left[j\cdot\omega - \boldsymbol{p}_{i}^{*}\right]}\right\} \qquad (6)$$

This last relation is very important because it induces that the determination of the electromechanical coupling matrix Θ^{s} is theoretically possible by means of an experimental modal analysis and an adequate set of measurements.

Extraction of the modes, eigen-frequencies, modal damping and modal masses could be performed with conventional modal analysis algorithms applied on experimental structural ***FRF***s. Note that correct estimation of modes needs measurement at a driving point, i.e. where excitation and response are measured at the same position and in the same direction (see Maia, Silva et al. [1]).

Once dynamic parameters are extracted, it is easy, by (6), to retrieve the electromechanical coupling matrix Θ^{s^r}. Estimation of the actuator electromechanical coupling matrix Θ^a can also be estimated with the same method by simply using the actuator in sensor mode. Unfortunately, complete estimation of Θ^{s^r} is only possible if all mechanical degrees of freedom in common with the piezoelectric element are monitored, which could be practically difficult. This implies that the knowledge of the piezoelectric elements will be only partial unless a structural model (generally a finite element model which contains errors due to simplifications and material uncertainties), improved by experimental data, is available. The structural model improvement (namely : model updating) will depends of the selected frequency range (it is obviously false to believe that an updated model will be valid from 0 Hz to ∞ Hz) and of the quality of the available measurements. It is then important that experimental data set is rich enough to afford a correct identification of all the modes existing in the selected frequency range of interest.

Excitation and measurement points selection for experimental modal analysis

The selection of the optimal positions of excitation and sensing is not a simple task. Without any criteria, engineer judgement and various trials are needed to obtain an acceptable set of data able to perform a correct identification of modes in the frequency range of interest. This procedure is time-consuming and not very effective. The problem of actuator and sensor placement have been already investigated in literature. Kammer [4] proposes the selection of the best signal to noise ratio position. In Gawronski [5], the procedure is based on the monitoring of the observability and controllability Grammians to choose optimal excitation and sensor locations.

Controllability is a means to measure the ability of a particular excitation configuration to control all the states of the system : if it is possible to transfer the state of a system $x(0)$ to its origin $x(t_1) = 0$ with t_1 finite. Conversely, observability measures the ability of a sensor configuration to estimate all the states of a system : if it is possible to determine the state of system $x(t_1)$ from the sensor configuration $y(t)$, $t \in [t_0, t_1]$ and where t_1 is a finite time.

To apply the theory of controllability and observability, which has been developed in the theory of control, it is convenient to express the generalised (multi-excitations and outputs) system nodal representation (1) in the form :

$$\begin{aligned} M \cdot \ddot{x} + D \cdot \dot{x} + K \cdot x &= B_0 \cdot f \\ y &= C_{0x} \cdot x + C_{0\dot{x}} \cdot \dot{x} \end{aligned} \tag{7}$$

where y is defined as the output vector and depends linearly of the structural displacements and velocity.
The state space-form can then be written as :

$$\begin{aligned} \dot{Z} &= A \cdot Z + B \cdot f \\ y &= C \cdot Z \end{aligned} \tag{8}$$

where we define :

$$Z = \begin{Bmatrix} x \\ \dot{x} \end{Bmatrix} \tag{9}$$

the state-space vector of size $N = 2 \cdot n$ which includes the system displacements and velocities. Elementary manipulations link the expression of the system nodal representation (1) to the nodal state space form (8) :

$$A = \begin{bmatrix} 0 & I \\ -M^{-1} \cdot K & -M^{-1} \cdot D \end{bmatrix}, \quad B = \begin{bmatrix} 0 \\ M^{-1} \cdot B_0 \end{bmatrix}, \quad C = \begin{bmatrix} C_{0x} & C_{0\dot{x}} \end{bmatrix} \tag{10}$$

In classical control theory (see Kwakernaak and Sivan [6]), a linear time invariant system (A, B, C) is fully controllable if and only if the constructed matrix :

$$C = \begin{bmatrix} B & A \cdot B & A^2 \cdot B & \dots & A^{N-1} \cdot B \end{bmatrix} \tag{11}$$

has rank N. In the same way, a linear time invariant system (A, B, C) is fully observable if and only if the matrix :

$$O = \begin{bmatrix} C \\ C \cdot A \\ \vdots \\ C \cdot A^{N-1} \end{bmatrix} \tag{12}$$

has rank N. As clearly explained in Gawronski [5], these criteria, although simple, are not at all efficient :

- the level of controllability or observability is not quantified; but these criteria give an answer in term of yes or no.
- The computation of C or O is prohibitive in case of system with realistic size.

These two drawbacks bring us to prefer expressing the system properties in term of Grammians. The controllability and observability Grammians are defined as follows :

$$W_c(t) = \int_0^t e^{A \cdot t} \cdot B \cdot B^T \cdot e^{A^T \cdot t}\, dt, \quad W_o(t) = \int_0^t e^{A^T \cdot t} \cdot C^T \cdot C \cdot e^{A \cdot t}\, dt \quad (13)$$

The controllability Grammian reflects the ability of a perturbation f to perturb the state of the system. The observality Grammian reflects the ability of a state Z to affect the output y of a system. In the case of a time invariant system, the stationary solutions of (13) are given by the Lyapunov equations :

$$A \cdot W_c + W_c \cdot A^T + B \cdot B^T = 0, \quad A^T \cdot W_o + W_o \cdot A + C^T \cdot C = 0 \quad (14)$$

The singular values of the Grammians product are invariant under linear transformation and are called the Hankel singular values $\gamma_i = \sqrt{\lambda_i(W_c \cdot W_o)}, \quad i = 1 \ldots N$.

The order N of the nodal representation can become very huge when the number of degrees of freedom of the finite element model is very large. A convenient approach is to use a modal representation. Defining the state variables as the modal displacement and velocities :

$$Z_m = \begin{Bmatrix} x_m \\ \dot{x}_m \end{Bmatrix} \quad (15)$$

the modal state-space form is then defined by the following triple :

$$A = \begin{bmatrix} 0 & I \\ -\Omega^2 & -2 \cdot Z \cdot \Omega \end{bmatrix}, \quad B = \begin{bmatrix} 0 \\ B_m \end{bmatrix}, \quad C = \begin{bmatrix} C_{mx} & C_{m\dot{x}} \end{bmatrix} \quad (16)$$

where $\Omega = diag(\omega_1, \omega_2, \ldots \omega_n)$ is natural frequencies matrix associated with the $(n \times n_m)$ modal matrix $\Phi = \begin{bmatrix} \phi_1 & \phi_2 & \ldots & \phi_{n_m} \end{bmatrix}$. The modal mass, damping (assuming proportional damping for convenience) and stiffness diagonalized matrix are obtained by the modal projection on K, D, M :

$$M_m = \Phi^T \cdot M \cdot \Phi, \quad D_m = \Phi^T \cdot D \cdot \Phi, \quad K_m = \Phi^T \cdot K \cdot \Phi$$
$$Z = \frac{1}{2} \cdot M_m^{-1} \cdot D_m \cdot \Omega^{-1} \qquad (17)$$

In the same way, the modal input, displacement and velocity outputs matrices are introduced by :

$$B_m = M_m^{-1} \cdot \Phi^T \cdot B_0, \quad C_{mx} = C_{0x} \cdot \Phi, \quad C_{m\dot{x}} = C_{0\dot{x}} \cdot \Phi \qquad (18)$$

By simply rearranging the columns and lines of (16) in order to organise the state components as :

$$\left\{ x_{m1} \quad \dot{x}_{m1} \quad \cdots \quad x_{mn_m} \quad \dot{x}_{mn_m} \right\}' \qquad (19)$$

the modal state-space representation is characterised by a block diagonal structure :

$$A_m = diag(A_{mi}), \quad B_m = \begin{bmatrix} B_{m1} \\ \vdots \\ B_{mn_m} \end{bmatrix}, \quad C_m = \begin{bmatrix} C_{m1} & \cdots & C_{mn_m} \end{bmatrix} \qquad (20)$$

The dimension of this modal state-space representation $(2 \cdot n_m \times 2 \cdot n_m)$ is then more economic than the nodal state-space representation $(2 \cdot n \times 2 \cdot n)$ since $n_m << n$ for a modal truncated system. An other important advantage of the modal state representation is that the resulting controllability and observability Grammians are diagonally dominant (see Gawronski [5]) :

$$W_c \cong diag(w_{ci} \cdot I_{2\times 2}) \quad W_o \cong diag(w_{oi} \cdot I_{2\times 2}) \qquad (21)$$

Diagonal entries of (21) and Hankel singular values could be then obtained as follows :

$$w_{ci} = \frac{\|B_{mi}\|_2^2}{4 \cdot \zeta_i \cdot \omega_i} \quad w_{oi} = \frac{\|C_{mi}\|_2^2}{4 \cdot \zeta_i \cdot \omega_i} \quad \gamma_i \cong \frac{\|B_{mi}\|_2 \cdot \|C_{mi}\|_2}{4 \cdot \zeta_i \cdot \omega_i} \qquad (22)$$

The transfer function of this system is given by :

$$G(\omega) = C \cdot (j \cdot \omega \cdot I - A)^{-1} \cdot B \qquad (23)$$

Transfer function norms $H_2, H_\infty, H_{hankel}$ serve as a measure of the controlling ability of an actuator / sensor configuration applied on a system defined by (A, B, C). In this paper, only the H_2 norm, defined by :

$$\|G\|_2 = \frac{1}{2 \cdot \pi} \cdot \int_{-\infty}^{+\infty} tr\left(G^*(\omega) \cdot G(\omega)\right) d\omega = tr\left(C^T \cdot C \cdot W_c\right) = tr\left(B \cdot B^T \cdot W_o\right) \qquad (24)$$

will be considered.

For flexible systems in the modal state representation, H_2 norm can be expressed in terms of the norms of the modes. This modal decomposition affords then a visibility on each modal contributions. Taking the transfer function of the i^{th} mode :

$$G_i(\omega) = C_{mi} \cdot (j \cdot \omega \cdot I - A_{mi})^{-1} \cdot B_{mi} \qquad (25)$$

the H_2 norm of the i^{th} mode can be estimated (see Gawronski [5]) by :

$$\|G_i\|_2 \cong \frac{\|B_{mi}\|_2 \cdot \|C_{mi}\|_2}{2 \cdot \sqrt{\zeta_i \cdot \omega_i}} = \frac{\|B_{mi}\|_2 \cdot \|C_{mi}\|_2}{\sqrt{\Delta\omega_i}} \cong \gamma_i \cdot \sqrt{2 \cdot \Delta\omega_i} \qquad (26)$$

where $\Delta\omega_i = 2 \cdot \zeta_i \cdot \omega_i$ is the half-power frequency at the i^{th} resonance. By (24) and since the Grammians are diagonally dominant in the modal state-space representation, the H_2 norm of the complete system is estimated by the *rms* sum of the modal norms :

$$\|G\|_2 \cong \sqrt{\sum_{i=1}^{n_m} \|G_i\|_2^2} \qquad (27)$$

Equations (26) and (27) are the bases for actuator and sensor placement strategy.

The procedure starts with the selection of the best actuators position. Assuming that all degrees of freedom are monitored, we compute the placement index σ_{2ki} that evaluates the importance of the k^{th} actuator at the i^{th} mode on the global transfer function H_2 norm :

$$\sigma_{2ki} = w_{ki} \cdot \frac{\|G_{ki}\|_2}{\|G\|_2} \qquad (28)$$

where w_{ki} is an user weight reflecting the accorded importance on the mode and the actuator in application. A placement indices matrix can then be constructed by varying B_0 and with C fixed :

$$\Sigma_2 = \begin{bmatrix} \sigma_{211} & \cdots & \sigma_{21n} \\ \vdots & \ddots & \vdots \\ \sigma_{2n_m1} & \cdots & \sigma_{2n_mn} \end{bmatrix} \Leftarrow i^{th}\,mode \qquad (29)$$

$$\Uparrow$$

$$k^{th}\,actuator$$

which clearly shows the ability of the k^{th} actuator position to affect the i^{th} mode. Once the actuator positions selected (B_0 optimized), the same procedure can be repeated by constructing a sensor placement indices matrix, helping the selection of the best sensors positions.

Illustrative example : experimental modal analysis on a clamped free plate

A 0.16 x 0.08 x 0.001 m clamped-free stainless steel plate, fitted with one commercial piezoelectric laminate on each face will be studied to illustrate the method. These two 0.0508 x 0.0254 x 0.0004 m piezoelectric (PZT) laminates are placed near the clamped side of the plate. Figure 1 presents the geometry of the experiment.

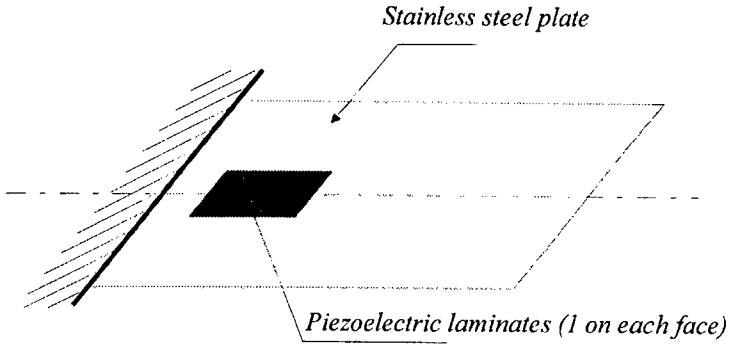

Figure 1 : *Experiment geometry*

The first step is to perform a finite element model of the clamped plate and the two piezo-laminates. This model uses 3-D solid finite elements. Due to the excessive strain energy stored in the thickness direction, this kind of element has a poor efficiency when meshes don't approach the cubic shape. Model / actual structure differences will be then essentially due to meshing errors. The five computed eigen-frequencies were estimated at :

- 33 Hz : first flexion mode,
- 168 Hz : first mode of torsion,
- 206 Hz : second mode of flexion,
- 529 Hz : second mode of torsion,
- 569 Hz : third mode of flexion.

The support plate is discretized in 918 mechanical degrees of freedom. The two laminates are discretized in 90 mechanical degrees of freedom and 1 electrical potential for each electrodes.

The second step of the procedure begins with the selection of the best actuator position using (29). Figure 2 shows a graphical representation of the actuator placement indices for the 5 first modes.

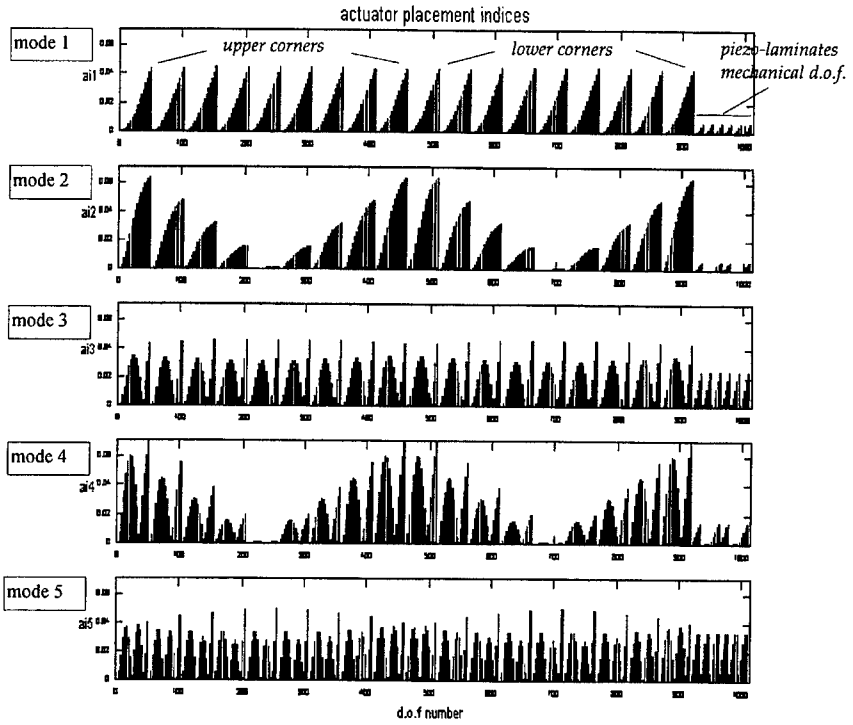

Figure 2 : *Actuator placement indices*

As expected, controllability of actuator position is best at the two corners, situated at the opposite of the clamping side. Direction of excitation is of course perpendicular to the plate.

Once selected the excitation point, the sensor placement indices matrix have also been constructed for the selection of the best sensor positions (see figure 3). As for the excitation selection, the best sensor position are given at the plate corner.

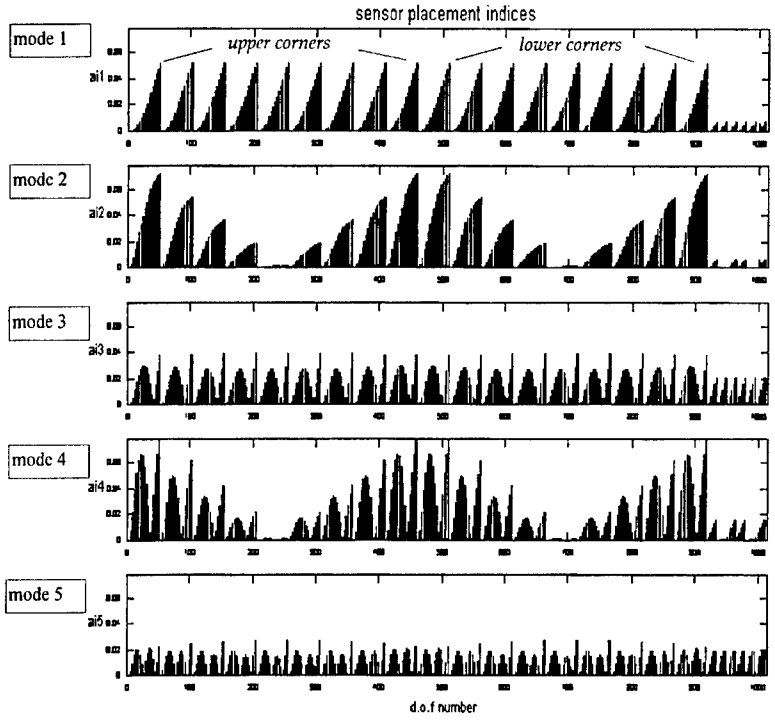

Figure 3 : *Sensor placement indices*

In order to increase the visibility in the case of graphical animation, 32 sensor locations have been equally spaced on the plate.

*FRF*s (motion/force and laminates electrical signal/force) have then been monitored by exciting the structure by means of an impulse hammer.

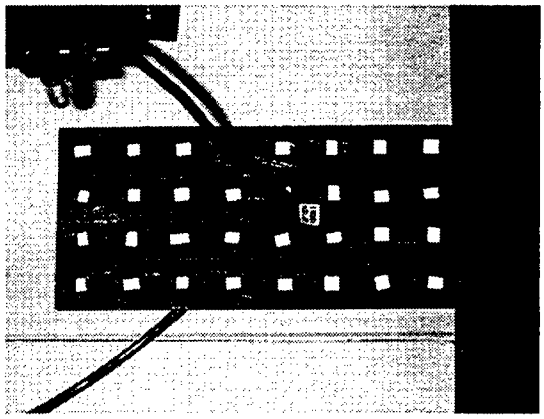

Figure 4 : *Experimental set-up*

Due to the light weight of the structure, non-contact measurement technique, by means of a LASER vibrometer, has been preferred (see figure 4). Figure 5 presents the experimental *FRF*s where a good coherence was achieved around the structural resonances.

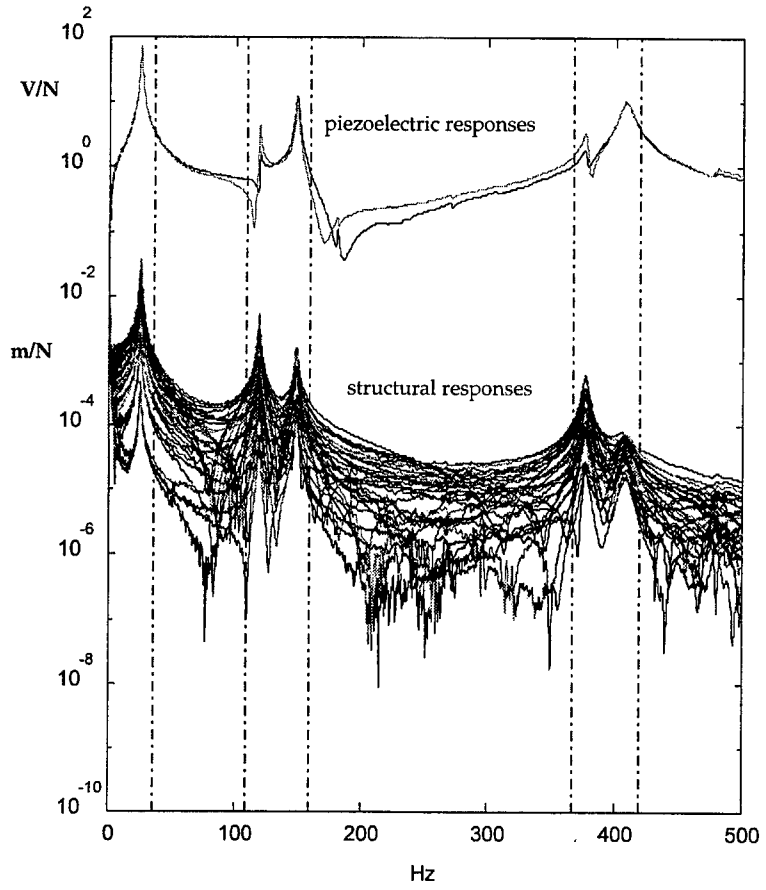

Figure 5 : *Experimental FRFs*

Modal extraction with a classical circle fitting algorithm (see Maia, Silva et al.[1]) has been performed on *FRF*s measurement. Figure 6 presents the achieved modal identification.

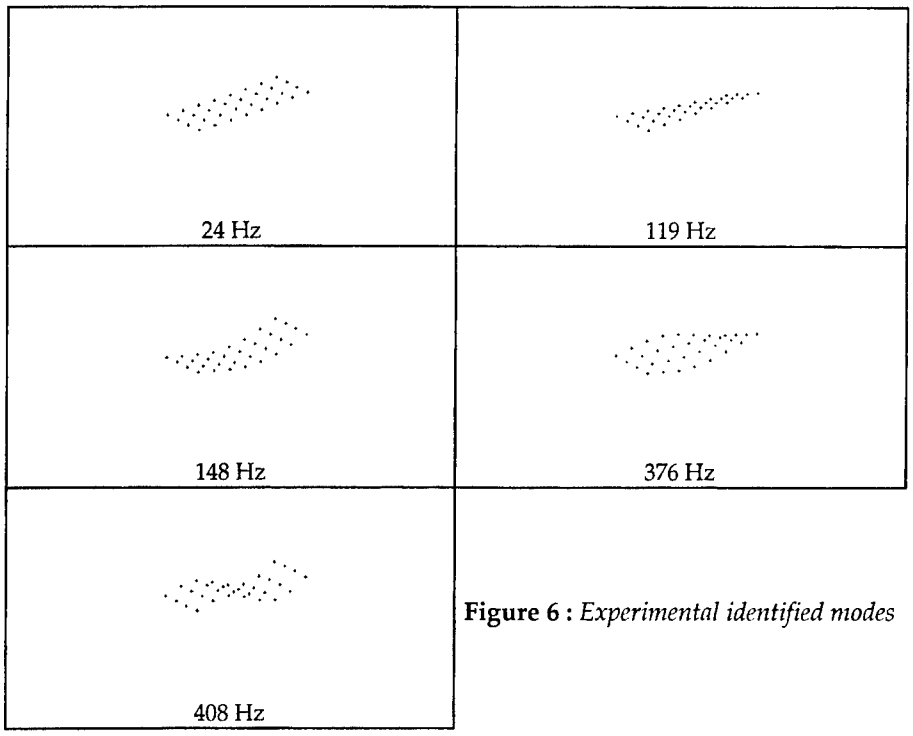

Figure 6 : *Experimental identified modes*

Model updating : theory and application on experimental data

In the previous chapters, we have seen how to choose optimal actuator and sensor locations and how to perform modal analysis on piezoelectric structures. In this chapter, we will attempt to improve an initial finite element model so to fit experimental data with modelling results.

Iterative, sensitive methods are very popular in the model updating community. These methods are based on the minimisation of a residue vector expressing the difference between the experimental data and modelling results. A combination of resonance frequency differences and frequency response function is favourable in most cases (see Heylen et al. [7]).

Resonant frequencies sensitivities are based on the first order terms of a Taylor expension :

$$\omega_{Xj}^2 = \omega_{Aj}^2 + \sum_{i=1}^{N_p} \frac{\partial \omega_{Aj}^2}{\partial p_i} \cdot p_i \qquad (30)$$

where p_i is the i[th] updating parameters $(1 \ldots N_p)$,

ω_{Xj} is the j[th] experimental resonant pulsation.

ω_{Aj} is the j[th] corresponding analytical resonant pulsation associated with the mode ϕ_{Aj}, solution of :

$$K_A \cdot \phi_{Aj} = \omega_{Aj}^2 \cdot M_A \qquad (31)$$

By differentiating (31) versus p_i, and assuming no structural damping, it is possible to develop the eigenvalues sensitivities by :

$$\frac{\partial \omega_{Aj}^2}{\partial p_i} = \frac{\phi_{Aj}^T \cdot \left(\frac{\partial K_A}{\partial p_i} - \omega_{Aj}^2 \cdot \frac{\partial M_A}{\partial p_i} \right) \cdot \phi_{Aj}}{\phi_{Aj}^T \cdot M_A \cdot \phi_{Aj}} \qquad (32)$$

In the same way, the difference frequency response function of the system to an excitation at point k is given by :

$$G_A(\omega) \cdot \sum_{i=1}^{N_p} \left(\frac{\partial K_A}{\partial p_i} - \omega^2 \cdot \frac{\partial M_A}{\partial p_i} \right) \cdot \{G_X(\omega)\} = \{G_A(\omega)\}_k - \{G_X(\omega)\} \qquad (33)$$

where $G_A(\omega) = \left(K_A - \omega^2 \cdot M_A \right)^{-1}$ is the global matrix of analytical transfer functions at pulsation ω,

$\{G_A(\omega)\}_k$ is the k[th] column of $G_A(\omega)$,

$\{G_X(\omega)\}$ is the experimental vector of frequency response function of the structure submitted to a force applied on the k[th] degree of freedom.

In the most cases, there will be an incompatibility between the size of the finite element model and the size of experimental data : the number of degrees of freedom of the model most often exceeds the number of measured degrees of freedom. Matching can be made by experimental data expansion or model reduction. Literature presents various solution (see Maia et al.[1] or Heylen et al [7]). In this paper, the dynamic reduction is used since it gives an exact representation of the system at a given pulsation ω_{test}.

The system formed by equations (30) and (33) has to be solved, for the identified resonances ω_{Xj} and at the tested frequencies ω_{tested}, by least square technique (since the number of relations is usually higher than the number of updating parameters p_i). The choice of the updated parameters is very important and not straightforward : bad parameters choice could give a solution which is acceptable on a

mathematical point of view but not physically realist. Moreover, in the case of piezoelectric structure, the orders of magnitudes of the different coupling matrices are very spread : $\boldsymbol{K} \div 10^{10}$, $\Theta^{s} \div 10^{0}$ and $C_p \div 10^{-10}$. This numerical ill-conditioning requires then some cares when matrix inversions are required :

- at the model matching level,
- for the resolution of the least square problem.

Singular value decomposition may be used to improve these steps. For example, a matrix $\boldsymbol{A}$ can be factored as $\boldsymbol{A} = \boldsymbol{U} \cdot \Sigma \cdot \boldsymbol{V}^{t}$ where $\boldsymbol{U}$ and $\boldsymbol{V}$ are orthogonal matrices which contain the left and right singular vectors and Σ is a diagonal matrix that contains the singular values σ_i of $\boldsymbol{A}$. Some singular values σ_i will tend to zeros if some rows of $\boldsymbol{A}$ are not totally independent. A criterion of rejection could be then established to reject small singular values by comparing them, for example, to a threshold proportional to the singular values average :

$$\sigma_{threshold} = 10^{-th} \cdot \frac{1}{N} \cdot \sum_{i=1}^{N} \sigma_i \qquad (34)$$

where th is an user defined integer.

A model updating procedure has then been applied on the finite element model of the piezoelectric plate described in the previous section. In figure 5, straight lines point the selected frequencies for the updating (note that frequencies were taken away from resonances in order to avoid damping effects). The correction procedure have also been performed on the five resonance frequencies identified during experimental modal analysis. The number of updating parameters has been carefully chosen : the Young modulus and shear coefficients of the plate material and piezo-laminates material have been taken into account. Moreover, a correction on the piezoelectric global electromechanical coupling matrices have been performed independently on each laminates. Figure 7 presents graphically the achieved model corrections. It can be seen that correction differences appears between the two piezoelectric laminates, as expected with the gap existing between the two laminates responses visible on figure 5.

Finally, figure 8 shows the comparison between the experimental modes and the updated system modes by means of the extensively used *Modal Assurance Criterion* (MAC) which is defined as follows :

$$MAC(\phi_{X_i}, \phi_{A_j}) = \frac{\left|\phi_{X_i}^{T} \cdot \phi_{A_j}\right|^2}{\left(\phi_{X_i}^{T} \cdot \phi_{X_i}\right) \cdot \left(\phi_{A_j}^{T} \cdot \phi_{A_j}\right)} \qquad (35)$$

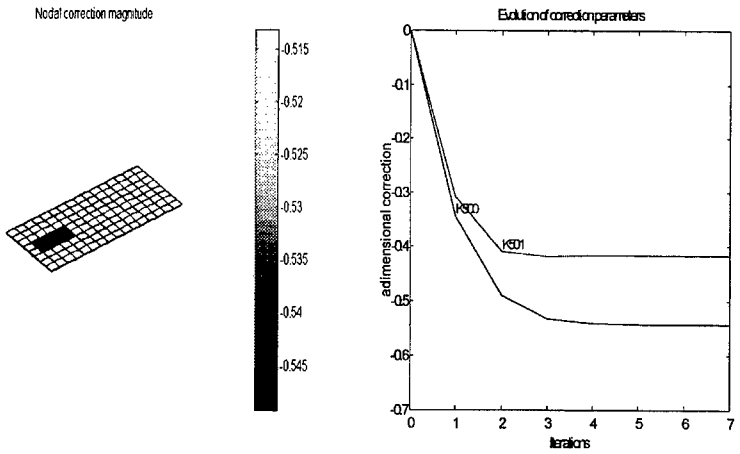

Figure 7 : *Mechanical (on left) and piezoelectric (on right) model correction*

The MAC always lies between 0 (no correlation between modes) and 1 (modes are perfectly correlated). Figure 8 shows a very good achieved correlation but resonant frequencies of mode 3 and 5 are not perfectly fitted with the experimental identified eigen-frequencies.

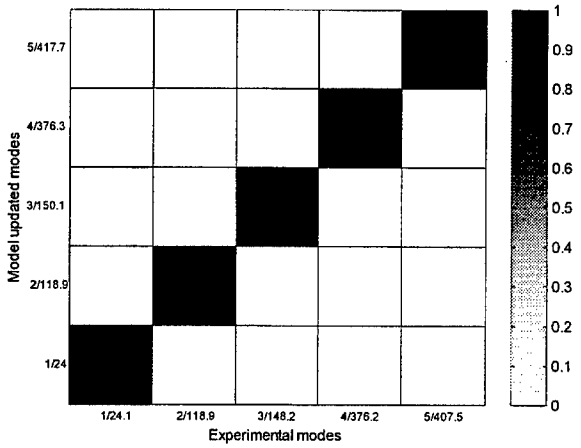

Figure 8 : *MAC matrix between experimental and model updated modes*

Conclusion

The described method for the identification of a piezoelectric system has been applied on an experimental case. Based on the observability and controllability Grammians, the procedure begin by

the selection of the best excitation and sensing points in order to ensure a good experimental identification. Modal extraction performed, an initial finite element model is improved by using the sensitivities on eigen-frequencies and *FRF*s. Achieved results are very encouraging but could be certainly more improved by a better selection of udpating parameters.

Acknowledgement

This work has been financed by the *Région Wallonne* of Belgium under the contract *RW-ULG 9613500.*

References

0. Ewins, D.J., *Modal testing : theory and practice,* Research Studies Press LTD., England, 1984.

1. Maia, Silva , He, Lin, Skingle, To, Urgueira, *Theoretical and experimental modal analysis,* Research Studies Press LTD., Taunton, England, 1997.

2. Saunders, W.R., Cole, D.G., Robertshaw, H.H., Experiments in piezostructure modal analysis for MIMO feedback control, *Smart Mater. Struct.*, 1994, **3**, 210-218.

3. Géradin, M., Rixen, D., *Mechanical vibrations, Theory and application to structural dynamics,* Wiley, Chichester, England, 1993.

4. Kammer, D.C., Sensor placement for on-orbit modal identification and correlation of large space structures, *Journal of Guidance Control and Dynamics*, **14**, 251-259.

5. Gawronski, W.K., *Dynamics and control of structures : a modal approach,* Springer-Verlag, New-York, 1998

6. Kwakernaak, H.K., Sivan, R., *Linear optimal control systems,* Wiley, 1972

7. Heylen, W., Lammens, S., Sas, P., *Modal analysis theory and testing,* Katholieke Universiteit Leuven , PMA, 1998

NEURAL NETWORK MODELLING OF FREQUENCY DEPENDENT AUTOMOTIVE DAMPERS

by

A. Patel and J. F. Dunne

School of Engineering and Information Technology
University of Sussex, Falmer, Brighton UK BN1 9QT.

ABSTRACT

An Artificial Neural Network is used to model a highly nonlinear frequency dependent automotive damper. Using constant temperature displacement-force measurements, a Recurrent Multi-Layer Perceptron is trained using twin-tube damper data obtained under combined-harmonic, and fully-random broad-band test conditions. The network trained on these two types of data, is compared in its ability to predict forces arising in different random conditions, and in a deterministic 'step-down' ramp-input displacement corresponding to a 'pothole' condition. By comparison with measured data, the paper shows that training under fully random conditions, is significantly more appropriate in this application, than training using combined-harmonic data.

1. INTRODUCTION

There is increasing interest in structural dynamics in the use of accurate nonlinear dynamic models for simulation of prototype engineering systems [1]. One area of particular importance is in the field of automotive engineering for rapid tuning of vehicle suspension systems. A modern suspension system carefully combines mass, springs, and dampers, to serve several important functions, particularly in maintaining high vehicle stability, and for achieving adequate ride comfort. Dampers play a significant role in meeting these desired performance objectives, provided passive damper control settings are appropriately chosen. The factors which influence this choice are however not easily established other than through extensive vehicle testing, or possibly through computer simulation. Vehicle testing is both time consuming and tedious, whereas a (much preferred) wholly simulation-based approach demands use of a very accurate suspension model for the required optimisation. This requires a very good, but simple mathematical model of the damper, which for the most part, is still lacking. Therefore much emphasis still continues on

extensive road testing for tuning damper-suspension systems. Any improvements in a damper model enabling simulation to be used for tuning purposes would reduce the road testing period, and would clearly be of major benefit to automotive manufacturers.

The physical design principles of a modern automotive damper are both advanced and complex [2]. These are typically either of mono-tube or twin-tube construction, in which the flow and compressibility properties of a viscous fluid and a working gas are exploited to achieve the desirable characteristics in 'bump' and 'rebound' motion. Different types of valves which serve to 'bleed' and 'restrict' flow create appropriate nonlinear behaviour, which also exhibits strong dependence on displacement frequency and fluid temperature. The most serious modelling difficulty arising with automotive dampers is this unfortunate triple combination of strong nonlinearity, frequency, and temperature dependence, often further exacerbated by additional nonlinear effects arising in the total suspension system. There is in general, little evidence available to suggest the existence of an accurate method of handling this combination in computer simulations with realistic broad-band road surface conditions. There are however seemingly good nonlinear models available at least for isothermal use at low discrete frequencies [2].

Classical mathematical damper models have been in widespread use for design and simulation purposes using semi-empirical differential equations to account for different nonlinear effects - the simplest (and crudest) being a viscous type equivalent linear damper [3]. The main problem with use of more sophisticated classical models however, for example those obtained directly from the laws of physics, is in practice they prove very difficult to obtain in the first place, and since they typically depend on many parameters, they are often very complex for detailed design and control purposes. The earliest attempts to construct a detailed model of a damper, by rigorously synthesising the inner workings, was reported by Lang [4], and Segal and Lang [5]. In an attempt to characterise observed frequency dependence, the resulting model required 82 parameters. To exploit such models for simulation and design purposes, Wallaschek [3] proposed use of statistical linearisation applied directly to real data. Serious limitations were however identified with use of a linear model. Alternative nonlinear functional series modelling approaches were developed and applied to real data by Surace et al [6]. In general, their findings suggested use of random data as perhaps most appropriate for complete characterisation, but to do this accurately a vast amount of data is needed. Cafferty et al. [7] also attempted to model the combination of nonlinearity and frequency dependence using a restoring force surface method but found the surfaces were largely corrupted by small stochastic components. Alternative attempts to use both parametric and nonparametric models have met with varying degrees of success, for example Reybrouck [8], and Duym et al [9]-[11]. In recent years, attention has refocused

on models which characterise the detailed inner physical behaviour of the damper. A good example of this is the work of Lee [12], whose model gives good agreement for stroke velocities of less than ±1m/s. This model however, requires many parameters and a large number equations to be solved for different damper conditions. Very recently, Reybrouck and Duym [2] have constructed a physical model with 10 tuneable parameters to account for nonlinearity, frequency, and temperature dependence. This model shows remarkable promise in testing at low discrete frequencies, although evidence is yet to be shown of the robustness of the model under broad-band loading conditions with temperature variations. Artificial neural networks (ANN's) seem an ideal alternative 'black box' modelling approach to account for the triple complexity including temperature variation. But there are few reports of of ANN applications using real damper data. Some early work has been reported by Giacomin [13] who used the back-propagation algorithm to train a Multilayer Perceptron MLP model of a damper. This network required 4 inputs (displacement and velocity at adjacent times) to predict the output damper force via two hidden layers. The network was trained on measured harmonic data over a frequency range 1–30Hz and then imported to ADAMS code. This was used to simulate a vehicle front suspension system passing over an obstacle. Predictions were qualitatively reasonable though not generally accurate. Recently in a related study, Hardier [14] designed a Recurrent Radial Basis Function RBF network for detection of automotive damper wear using incomplete noisy kinematic measurements. The network was designed to predict unmeasured damper force characteristics from which the wear condition of the damper could be established. To emulate a real damper, in various states of wear, simulated data was obtained for training and test purposes using an assumed hydraulic damper model which formed part of a quarter vehicle suspension system. Test results showed, using short sections of simulated noisy data at a single input frequency, that damper wear could indeed be successfully detected using this network. Application of ANN modelling using real damper data however, appears still to be in a relatively early stage.

Both the MLP and the RBF network are proven universal approximators (but of fundamentally different type). One can always find an MLP to replicate an RBF network and vice versa. Both have relative merits, for example the MLP can often generalise more successfully to areas of the input space where there is limited training data, whereas the RBF network is capable of fast learning. It is known however that to construct a smooth nonlinear mapping an RBF network may need a very large number of radial-basis functions. And moreover, although the MLP usually requires two hidden layers, if a single hidden layer can be used (with an optimum number of neurons) then fast MLP training may also be possible giving the MLP an advantage over an RBF network. In this paper important results of modelling an automotive damper are presented. A Recurrent MLP with a single-hidden-layer is designed to model a real damper.

This has been chosen for its generalising capability and its relatively small number of neurons. Training and testing of the network has used real isothermal experimental data obtained from a modern twin-tube damper. Predictions are compared for a network trained using different data, with the prime objective of establishing an appropriate type of data to use in training. The particular issues discussed in the paper initially focus on: experimental evidence of frequency dependence, neural network training requirements for fast convergence, and thereafter showing evidence of the flexibility and accuracy of an RMLP based damper model.

2. AN ARTIFICIAL NEURAL NETWORK DAMPER MODEL

There has been a great need in recent years to look carefully at the use of accurate but more flexible alternative damper models, such as Artificial Neural Networks (ANNs). The main initial difficulty is in selecting an appropriate network architecture, and choosing an efficient procedure for training. These two issues are now discussed briefly before describing training data generation.

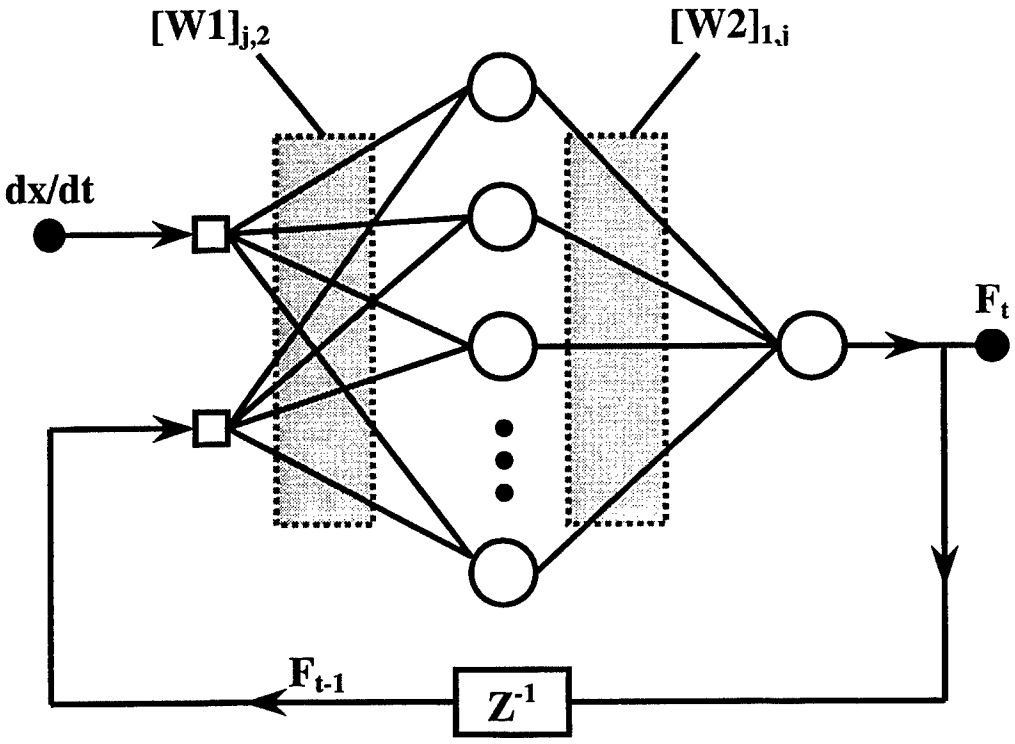

Figure 1. The RMLP Architecture for the damper model

2.1 The Neural Network Architecture

The neural network architecture used is essentially a recurrent multi-layer perceptron RMLP comprising one hidden-layer of neurons with one input and one output. The activation functions chosen for the hidden layer are standard hyperbolic-tangent-sigmoid functions, whereas linear functions are used for the output neurons. When working in a predictive mode, the *input* information to the network is the velocity at time *t*. The predicted force at time *t-1* is obtained by feeding back the time-delayed output, as shown in figure 1, using the fixed weight matrices [W1] and [W2] obtained via training. This figure shows the architecture of the network and feedback path in simplified form, indicating that the trained network predicts force F at time *t*.

2.2 Training the network

The network is trained using displacement-force data obtained from a series of experimental tests using the rig described in section 3. Velocity components are obtained directly by numerically differentiating the (clean) measured displacement signals. The Levenberg-Marquardt algorithm is used for training the network to reach a minimum error goal and thereby fixing weights in [W1] and [W2]. The training data presented to the network is supplied in exactly the same form as when used in a predictive mode but there is no feedback since the measured rather than predicted force is used at time *t-1*. Training stops when the network has reached the error goal.

3. EXPERIMENTAL MEASUREMENT PROGRAMME

The experimental test rig is now described, followed by details of the test programme. From the data obtained, sample histories show clear evidence of combined strong nonlinearity and frequency dependence in the damper characteristic. This evidence will be shown shortly before moving on to ANN training and prediction.

The Test Rig

Three different types of test were made using an advanced damper test facility shown schematically in figure 2. The machine used for these tests is known as a Hybrid Model 849 MTS Test System (Mechanical Testing and Simulation system). The mechanical components of the MTS system comprise: a load unit, hydraulic power supply accumulators, a load cell transducer, specimen fixing arrangements, an hydraulic actuator, and an hydraulic power supply. In our experiments, a rear *M100 Daewoo Matiz* twin-tube damper was used throughout for data generation. The data control and capture features of the test facility shown in figure 2 comprised a host computer, installed with commercial shock test control software. This controlled the procedure for executing and running the tests on the MTS machine. The information collected from the rig during the programme included displacement and force histories, and sampling

frequency for each data set. Temperature was monitored to ensure an isothermal test programme. The data was arranged to cover as wide a range of frequencies and amplitudes as allowed within the technical limitations of the system. Tests were made to accumulate regular harmonic data, multi-sinewave data, step-input, ramp-input and fully random data. The analogue console included advanced function generation capabilities, and the host computer saved information derived from the 'best' data run. This in turn, was supplied to the storage computer – this machine was networked with the analogue console, allowing ASCII format data files to be exported for use in training and prediction.

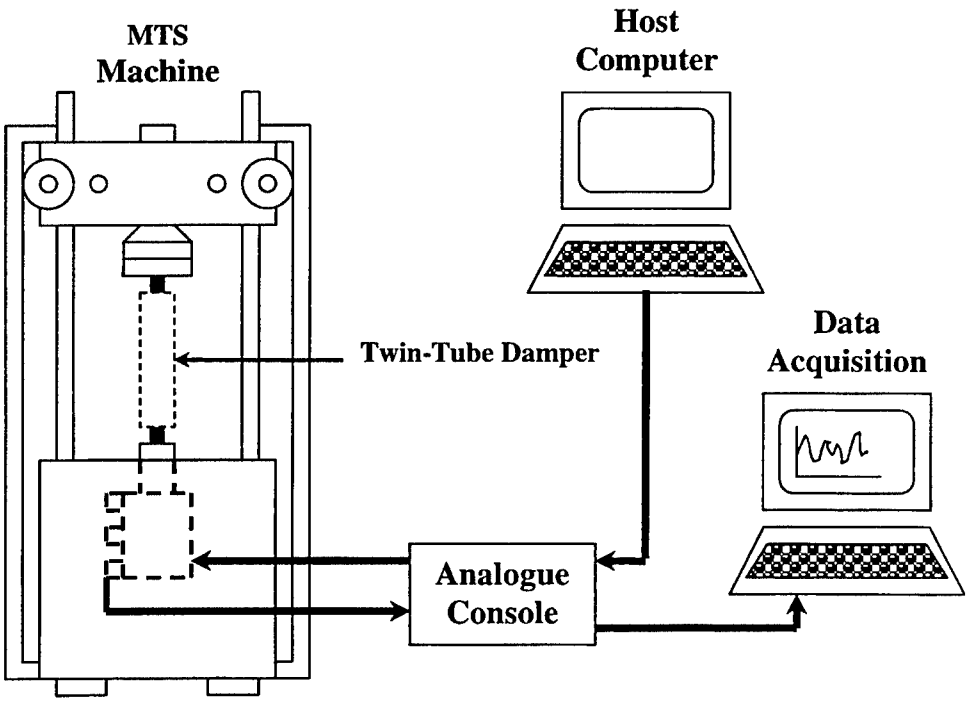

Figure 2. Damper test rig in schematic form.

The Measurement Programme

The input displacement of the damper served as the control input variable and the corresponding force as output. The input displacements were selected as being: i) purely harmonic; ii) Pavé (namely a broad-band random displacement to represent the cobblestone surfaces which can typically be found in most European cities); and iii) a rapid step-down ramp displacement input (corresponding to the wheel of a vehicle moving at speed dropping down into a 'pot-hole' in the road). In terms of the frequency domain, these cases represent discrete deterministic, broadband random, and deterministic broadband.

Temperature can play a very significant role in changing the characteristics of a damper – so these tests were designed to maintain static temperature conditions throughout. This was confirmed by monitoring the temperature of the damper during the short test runs. However, in practice a real damper will generate considerable heat, which is largely dissipated through draught cooling of the moving vehicle. Operating conditions of a real damper will involve a wide temperature range – this is one reason why a neural network model may ultimately prove most robust for modelling and control purposes. Support for this conjecture stems from the known universal approximation capabilities of MLP and RBF networks which require no fundamental change in approach as conditions become more testing. Whereas the more sophisticated classical models need to become, the more detailed knowledge of the damper is needed with an ever increasing number of free parameters to be re-calibrated for each particular operating condition.

Figure 3 shows the displacement-force loci for the purely harmonic tests at frequency 2Hz, 6Hz, 10Hz and 14Hz showing clear evidence of nonlinearity and frequency dependence. The objective of these tests was to establish the most appropriate type of data to use for training the neural network, namely that which required the least amount of data, and therefore one that would require the shortest duration on the test facility. This was the most likely way to maintain reasonably constant temperature conditions during collection of test data. The network was trained in a batch mode on: i) data containing the four discrete frequencies in a single contiguous section, and ii) on one section of the fully random data. The two differently trained networks, were then used to examine predictive capability on: a) the fully random data and b) step-down ramp input data. Note, it is well known that in testing a broad range of frequencies it is not possible to maintain constant input displacement amplitude, since at high frequency the forces involved are considerable and consequently input displacements are very much smaller than at low frequency. The harmonic data was sampled at 250 Hz, except for the 14Hz histories which were captured at 500Hz, the same sampling rate as used for capturing the fully random and step-down data.

4. THE NEURAL NETWORK MODEL PREDICTION CAPABILITIES

Some brief details are initially given in table 1 below of training the ANN described in section 3, via the Levenberg-Marquardt algorithm using data collected in the test programme of section 3.2.

Table 1. Neural Network Damper Model Training details

Input Type	SS Error	Epochs	Relative training time
Combined-Harmonic	0.5903	5000	1
Random	1.4978	5000	7.4

Note the term 'combined-harmonic' is used to avoid confusion since the network was trained in a batch mode on all of the data i.e. using data containing four contiguous discrete frequencies in a single section rather than separate single harmonic frequencies. Table 1 shows that training times using fully random data are significantly higher than those using combined-harmonic data.

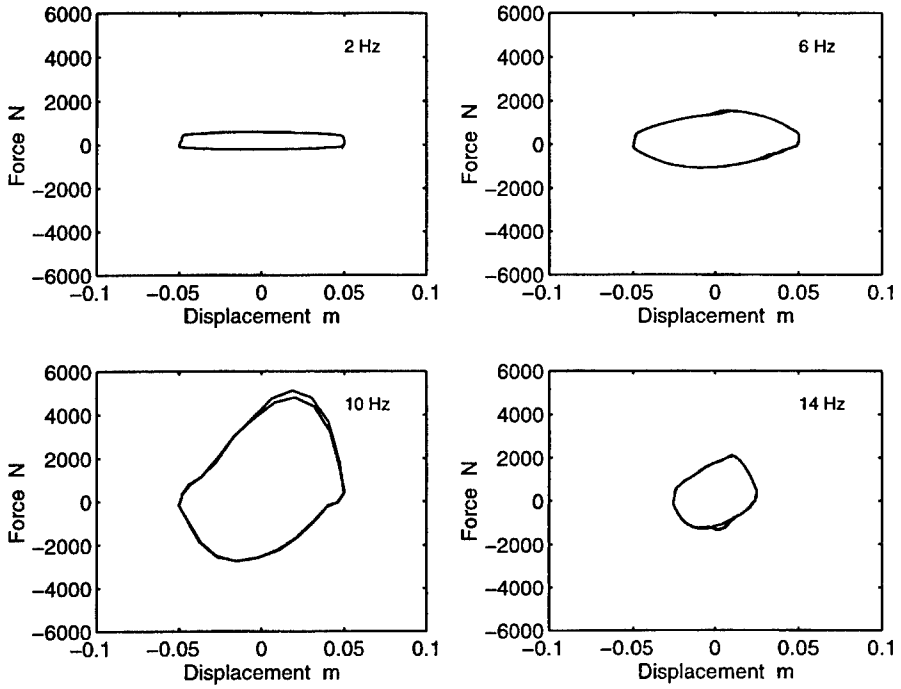

Figure 3. Measured displacement-force loci for harmonic input: a) 2Hz, b) 6 Hz, c) 10Hz, d) 14 Hz.

Prediction using combined-harmonic data for training

Figure 4 shows the contiguous set of harmonic training data and the corresponding ability of the network to predict precisely the same data it has been trained on. The measured force histories are shown throughout as solid lines. One would expect the network to perform very well in this role, since it is being required only to predict information that it has been trained on. Figures5a-d show in much greater detail the network being used to predict sections at single frequencies. Predictive agreement can clearly be seen to be extremely good, but not perfect. Figure 6 by contrast shows the network trained on the harmonic data in figure 4 being used to predict fully random Pavé data. Again agreement is reasonably good, but it can be seen that the network is failing to adequately predict high frequency information evident in the time histories.

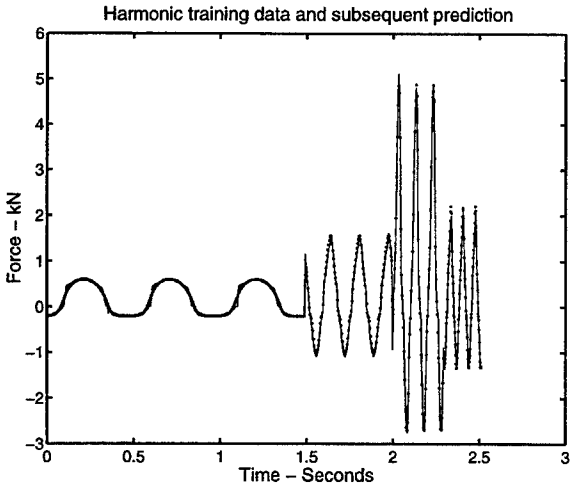

Figure 4. Harmonic input training data and ANN prediction (•)

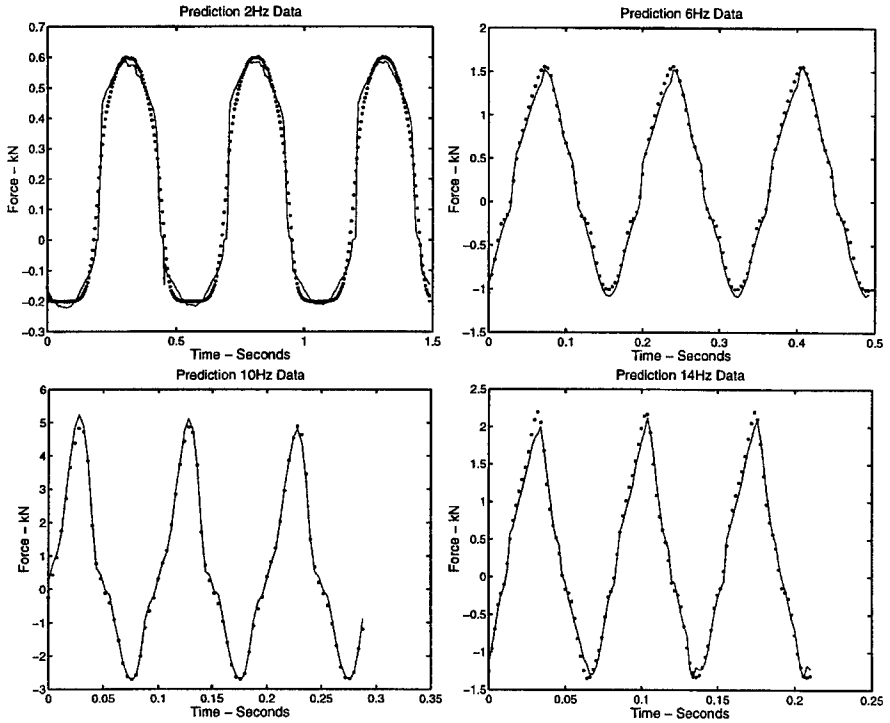

Figure 5. Predicted Force compared with measured: a) 2Hz, b) 6 Hz, c) 10Hz , d) 14 Hz. (ANN prediction •)

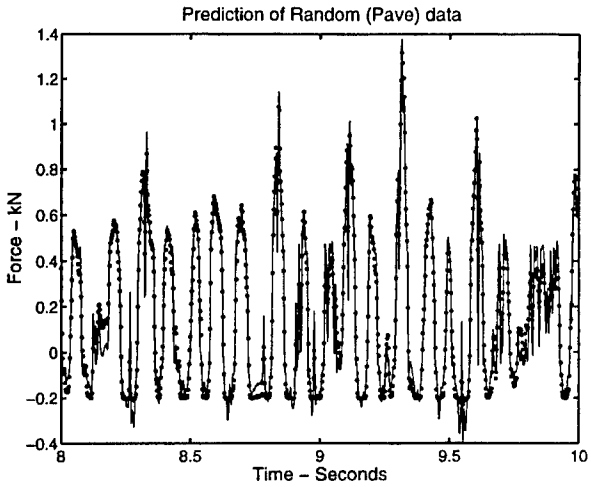

Figure 6. Prediction of Pavé data using harmonically trained network (ANN prediction •)

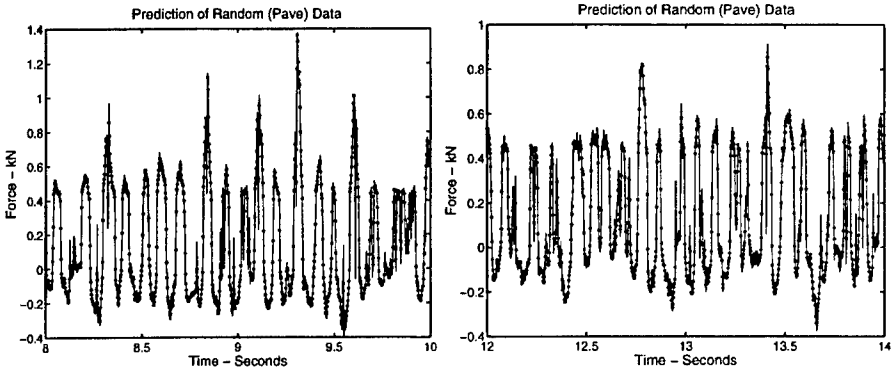

Figure 7. Prediction of Pavé data using random data a) training data; b) prediction of different section of Pavé data. (ANN prediction •)

Figure 7a shows the network predicting the force when trained on the same section of Pavé data. Here again, one would expect good agreement. Figure 7b by contrast, shows the same network used to predict a totally different section of Pavé data. Here the predictive ability of the network is remarkably good. Finally figure 8 shows the ability of the network to predict 'pothole' step-down data when trained using the data in figure 4, compared with the network trained using the data in figure 6. Interestingly the harmonically trained network seems not to perform very well at all, whereas the network trained on random data is still extremely good.

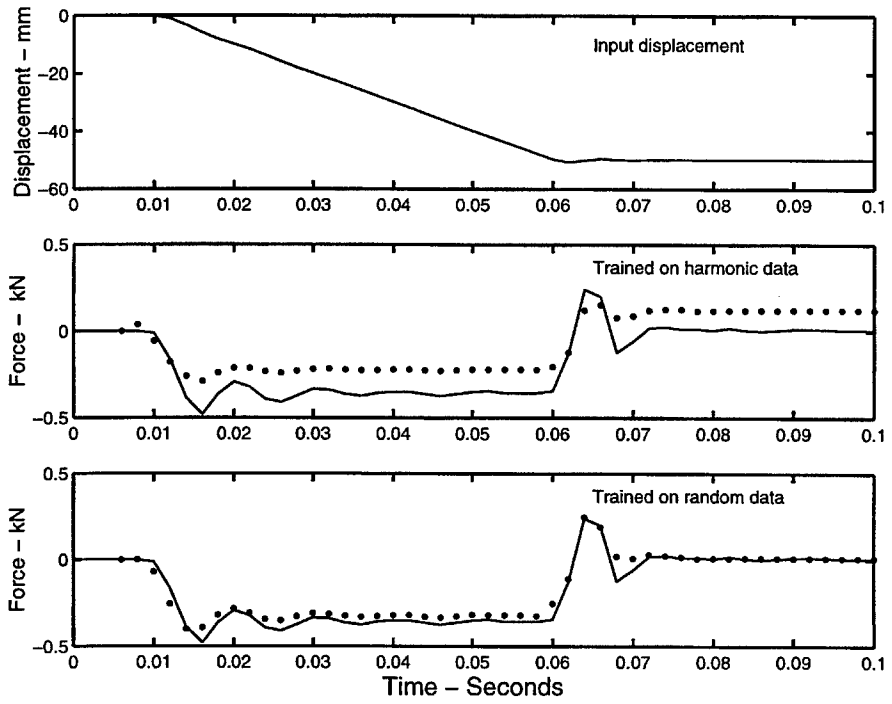

Figure 8. a) Step-down displacement history; Prediction of 'pothole' response using network trained on: b) harmonic data; c) Pavé data. (ANN prediction •)

Discussion of Results

We begin our discussion by drawing attention to the damper data in figure 3 showing raw displacement-force loci at discrete frequencies 2 – 14Hz. These figures show both nonlinearity and frequency dependence in a useful qualitative way which is perhaps easier to see than with use of power spectra. Frequency dependence is clearly evident from the different magnitudes of force for each frequency, whereas nonlinearity is evident from the departure from pure elliptical behaviour of each locus.

Turning attention to the predictive capability of the network, it is evident that in order to model broad-band damper behaviour, whether it be fully random or deterministic, it is essential that the training data adequately covers the entire bandwidth. This requirement is clear from figure 6 and figure 8. The harmonically trained network is failing to predict high frequency as shown by figure 6; and is also failing to predict low frequency behaviour as shown in figure 8b. By contrast, the network trained on fully random broad-band data (figure 7a) is clearly fulfilling its purpose very well as confirmed by the results in figure 7b and figure 8c. This finding fully concurs with the conclusions

drawn in [6]. With the ability to accurately model a damper under isothermal conditions, it remains to be seen whether a neural network will be capable of modelling the triple combination of nonlinearity, frequency, and temperature dependence.

5. CONCLUSIONS

A Recurrent Multi-Layer Perceptron neural network, trained on two different types of data, has been compared for prediction of different random and deterministic broad-band response. The paper shows that in modelling highly nonlinear frequency dependent dampers, the training data must span the band-width of the required prediction. When this requirement is fully met, a neural network has been shown to very accurately model the characteristics of a modern twin-tube damper under isothermal loading conditions.

Acknowledgements
The authors wish to acknowledge the considerable support given to the project by the DWTC (Daewoo Worthing Technical Centre) Worthing, West Sussex, UK, who supplied both raw data and project guidance.

REFERENCES

[1] Paez, T. L, Tucker, S, and O'Gorman C, 1997. 'Simulation of Nonlinear Random Vibrations using Artificial Neural Networks', 6th *International Conference on Recent Advances in Structural Dynamics*, ISVR , Southampton, pp1613-1627.
[2] Duym, S, and Reybrouck, K, 1998, 'Physical Characterization of Nonlinear Shock Absorber Dynamics', *European Journal of Mechanical and Environmental Engineering*, 43, no. 4, pp 181-188
[3] Wallaschek, J, 1990, 'Dynamics of Non-Linear Automobile Shock-Absorbers', *Non-Linear Mechanics*, 25, no. 2/3, pp 299-308
[4] Lang, H. H, 1977, 'A Study of the Characteristics of Automotive Hydraulic Dampers at High Stroking Frequencies', Ph. D. Thesis, University of Michigan
[5] Segal, L, and Lang, H. H, 1981, 'The Mechanics of Automotive Hydraulic Dampers at High Stroking Frequencies', *Vehicle System Dynamics*, 10, pp 79-83
[6] Surace, C, Worden, K, and Tomlinson, G, 1992, 'On the Non-linear Characteristics of Automotive Shock Absorbers', IMechE, *Journal of Automobile Engineering*, 206, pp 3-16
[7] Cafferty, S, Worden, K, and Tomlinson, G, 1995, 'Characterisation of Automotive Shock Absorbers Using Random Excitation', IMechE, *Journal of Automobile Engineering*, 209, pp 239-248

[8] Reybrouck, K, 1994, 'A Non Linear Parametric Model of an Automotive Shock Absorber', *Vehicle Suspension Advancements* - SAE Paper 940869, pp 74-86.
[9] Duym, S, Stiens, R, and Reybrouck, K, 1996, 'Fast Parametric and Nonparametric Identification of Shock Absorbers', ISMA21 - *Noise and Vibration Engineering*, pp 1157-1169
[10] Duym, S, 1997, 'An alternative Force State Map for Shock Absorbers', IMechE, *Journal of Automobile Engineering*, 211, pp 175-179
[11] Duym, S, Stiens, R, and Reybrouck, K, 1997, 'Evaluation of Shock Absorber Models', *Vehicle System Dynamics*, 27, pp 109-127
[12] Lee, K, 1997, 'Numerical Modelling for the Hydraulic Performance Prediction of Automotive Monotube Dampers', *Vehicle System Dynamics*, 28, pp 25-39
[13] Giacomin, J, 1991, 'Neural Network Simulation of an Automotive Shock Absorber', *Engineering Applications of Artificial Intelligence*, 4, pp 59-64
[14] Hardier, G, 1998 ' Recurrent RBF networks for suspension system modelling and wear diagnosis of a damper'. *IEEE International conference on Neural Networks*, Vol 3. pp 2441-2446.

Errors in Damping Predictions due to Kinematics Assumptions for Sandwich Beams

Eric M. Austin*and Daniel J. Inman

Abstract

It is commonplace in academia to base models of constrained-layer damping treatments on the assumption that the outer layers displace identically during transverse (out-of-plane) vibrations. This assumption is valid for a large range of problems, particularly for problems common in the era when damping was achieved by applying foil-backed treatments to thin panels. With the introduction of the modal strain energy method for damping design in 1981, new classes of applications have emerged for both passive and active constraining layers. This paper illustrates some of the pitfalls of applying the equal-displacement assumption for seemingly benign-looking structures.

1 Introduction

The primary goal of this paper is to show that a particular set of kinematic assumptions often used in modeling viscoelastic sandwich beams can lead to inaccurate predictions of damping for even simple cases. This is shown by comparing the simplified modeling with a higher order approach for beams with very simple, benign-looking geometries. Here higher order refers to displacement fields of order higher than the linear variations in Euler-Bernoulli beam theory. Beams are targeted since they are commonly used as vehicles for research on passive and active constrained-layer damping technologies.

In 1959, Kerwin [1] presented the first general analysis of viscoelastic material constrained by another metal layer. His target structures were thin-skin beams or plates, and the damping treatments consisted of a viscoelastic material prepackaged with a thin metal backing. Kerwin applied

*the authors are Research Scientist (austine@vt.edu) and G.R. Goodson Professor and Director (dinman@vt.edu), Center for Intelligent Material Systems and Structures, Department of Mechanical Engineering, Mail Code 0261, Virginia Polytechnic Institute & State University, Blacksburg, VA 24061, USA

both prepackaged damping tapes and made-up constrained-layer damping treatments to long, thin (914.4 mm × 50.8 mm) aluminum bars with thicknesses of 1.60, 3.18, and 6.35 mm. DiTaranto [2] developed sixth-order equations of motion in terms of axial displacements, and Mead and Markus [3] developed sixth-order equations of motion in terms of transverse displacements. Both works used Kerwin's basic set of assumptions, of which the key assumptions, as stated by Mead [4], were

1. the core carried shear, but no normal stress, was linearly viscoelastic and had complex shear modulus $G_c(1 + i\beta)$; and
2. all points on a normal to the plate moved with the same transverse displacement;

In particular we are interested in the second item: the equal-displacement assumption. Douglas [5] termed the full set of assumptions the *Mead and Markus* (MM) model, and this term will be used for the remainder of this paper.

Since the 1950's, there have been many hundreds of papers published on the modeling and application of constrained-layer damping (CLD). While many researchers used Kerwin's basic model, others made modifications to investigate the validity of the assumptions, look for other loss mechanisms, or suit the needs of individual applications. Many of these studies produced minor changes done during an era when finite element analysis was not economical and closed-form approximations were generally sought. The equal-displacement assumption simplified the sandwich model by essentially eliminating one of the two beams (by linking them) and creating a state of simple shear in the core viscoelastic material. Excellent reviews on these first-generation modeling techniques for CLD have been written by Nakra [6], Torvik [7], and Mead [4].

Much has changed in the world since the above-cited reviews of CLD modeling, and many current-generation constrained-layer damping treatments bear little resemblance to the thin-panel treatments for which Kerwin developed his assumptions. Examples are the equipment racks and stiffened panels reported by Ikegami et al. [8] and Staley and Stahle [9]. These are cases where constraining layers range from composite materials to C- and I-shaped structural members. Ross et al. [10] summed up the apparent view of constraining layer in early damping treatments with the statement, "It is true of almost all practical applied damping treatments that the extensional stiffness of the layer adjoining the base plate is very small compared to that of the base plate itself, and that the stiffness of a constraining layer is at most one-fourth or one-fifth that of the plate to be damped." By stiffness they mean extensional stiffness per unit width, i.e., Young's modulus times thickness. Contrast this with the previous examples as well as Johnson's 1995 statement in a review of passive damping designs, "Instead

of a constraining layer, the VEM could be sandwiched between the base structure and built-up sections (I-beams, C-channels, hat sections, etc.)." Perhaps the first example of this concept is given by Miles [11] in a design to reduce cabin noise on the Boeing 747 aircraft.

The goal of this paper is to demonstrate pitfalls of using MM modeling to design CLD treatments for simple beams, with a particular emphasis on partial-coverage treatments. We do this by comparing how various levels of modeling predict the distribution of modal strain energy between the layers. In the end we conclude that much happens near the ends of the constraining layer, and these effects are easily masked by assuming equal transverse displacements for all layers. Many papers have been published where models using the MM assumptions are exercised to optimize the performance of both full- and partial-coverage damping treatments. It is not the intention of this paper to refute this body of work as a whole. Rather, the intention is to raise questions in the minds of scientists seeking to squeeze more and more performance out of passive and active damping treatments.

2 Modeling Comparisons

Finite element analysis (FEA) was chosen for the modeling so that the analyses could extend outside of the realm where exact elasticity solutions exist. Using FEA also provides an important link between academic work and industry problems. A FEA code was written to analyze plane strain and plane stress sandwich beams with several different options for elements and kinematic assumptions. Both lower order models using the MM assumptions and higher order models using C^0 elements with as many as 20 nodes were implemented.

Authors (e.g., Baz [12]) have used the Mead and Markus assumptions to create a single element representing the layers of a three-layer sandwich beam. The constraining layer is assumed to have the same transverse translational and rotational displacements as the Euler-Bernoulli base layer. The eight degrees of freedom needed for a 2-D "MM element" are the axial, transverse, and rotational displacements of the base layer along with only the axial displacement of the constraining layer, as contained in the element degree-of-freedom vector $\{a\} = \{u_1 \;\; w_1 \;\; \theta_1 \;\; u_4 \;\; u_2 \;\; w_2 \;\; \theta_2 \;\; u_3\}^T$ and shown in Fig. 1. One approach would be to define the axial displacement fields within the base and constraining layers over an element as

$$u_b(x, z_b) = \hat{u}_b(x) - (z_b - h_b/2)\ \partial w(x)/\partial x$$
$$u_c(x, z_c) = \check{u}_c(x) - (z_c + h_c/2)\ \partial w(x)/\partial x$$

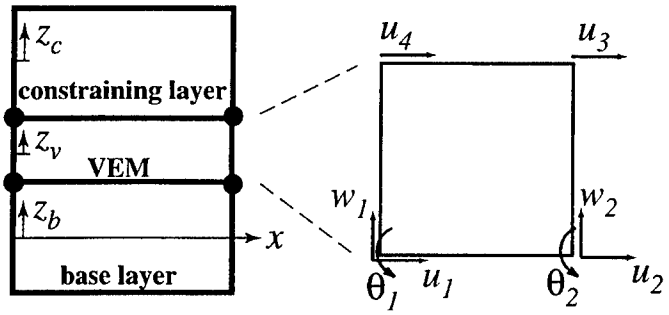

Figure 1: Degrees of freedom for the Mead and Markus model.

where $\hat{u}_b(x)$ and $\check{u}_c(x)$ are the axial displacements of the base and constraining layers at the interface with the VEM layer, $z_b \in [-h_b/2, h_b/2]$, and $z_c \in [-h_c/2, h_c/2]$.

An alternate approach also investigated is to allow the base and constraining layers to be independent Euler-Bernoulli beams with the VEM core divided into four-noded elements through the thickness. Miles and Reinhall [13] published this in 1986 for full-coverage beams with a linear displacement field for the core. Had they used finite elements, this would correspond to a single element through the thickness of the core.

2.1 Qualification of Higher Order Modeling

If higher order modeling is to be used as the basis for comparisons, the first logical question is, "how high is enough?" The approach discussed here is based around C^0 elements, i.e., elements where only the displacements, not the slopes, are continuous at element boundaries. Following many authors in the past, we use Pagano's 1969 [14] solution to the cylindrical bending problem as a baseline. The structure is a simply supported, plane-strain, layered beam subjected to a static load in the shape of a sine function. Even though this is a static analysis, it lends insight on how well various modeling schemes reproduce elasticity results. Austin [15] compared Pagano's distributions of strain energy with those predicted using C^0 elements with between 4 and 20 nodes per element. The study showed that the 20-node (as some with fewer nodes) match the elasticity solution very well, so this C^0 is used to produce the baseline results for the remainder of this paper.

The relationship between damping and energy was noted by Ungar and Kerwin [16], and in 1981 Johnson, Kienholz, and Rogers [17] published an important work on using the modal strain energy (MSE) method as an economical way of designing damping treatments by finite element methods. Morgenthaler [18] documented that the MSE method tends to underpredict

natural frequencies and overpredict levels of damping. Nonetheless, Austin [15] showed that is a valid indicator of modeling accuracy. The crux of the following arguments is that accurate distributions of strain energy in the structure are a necessary condition for accurate predictions of damping effectiveness.

Table 1 shows the MSE predicted in the soft middle layer of a three-layer sandwich. The layers have equal thicknesses, and the core is represented by a real-valued material with shear modulus 50 psi and Poisson's ratio 0.49. The first entry for each modeling approach corresponds to a high element aspect ratio, and the second line is a mesh refined to the point of convergence. The table shows that both the C^0 and MM modeling approaches do a good job for the beams with aspect ratios of 40 and 400, but the MM approach is inaccurate for the beam with aspect ratio of 4. Also shown is the modeling approach, labeled MR, used by Miles and Reinhall [13]. It is essentially the same as the MM approach, except Miles and Reinhall recognized that the base and constraining layers should be allowed to deform independently. The points to be made here are 1) a mesh of 20-node C^0 elements (C0-20) reproduces elasticity results very well, even at an element aspect ratio of 1200, 2) the Mead and Markus assumptions work well for full-coverage as long as the beam aspect ratio is not too small, and 3) the MR approach is nearly as good at the C0-20 element, as a fraction of the cost in degrees of freedom.

Table 1: Percent strain energy in the middle layer of a full-coverage,three-layer sandwich beam. Comparison with Pagano's closed-form results for various elements for beams with aspect ratios of 4, 40, and 400.

		beam AR† = 4		beam AR = 40		beam AR = 400	
element	DOF	AR_e‡	%SE	AR_e	%SE	AR_e	%SE
Pagano	∞	n/a	16.4122	n/a	13.1835	n/a	37.8897
C0-20	575	12	16.4121	120	13.1830	1200	37.9317
	913	3	16.4123	30	13.1835	300	37.9575
MR	22	3	17.0117	30	13.4305	300	35.3694
	382	0.19	17.2516	1.9	14.5168	18.8	35.6651
MM	15	3	0.1668	30	13.8886	300	35.7721
	255	0.19	0.1754	1.9	14.5033	18.8	35.6587

†ratio of base beam length to maximum total beam thickness
‡ratio of element length to thickness

2.2 Effect of MM Assumption

The benign-looking beams referred to earlier were chosen to be 508 mm (20 inches) long and 3.175 mm (0.125 inches) thick. The damping treatments reported here are the four possible combinations of 0.127- and 1.270-mm-thick (5 and 50 mils) viscoelastic materials and 0.254- and 3.175-mm-thick (10 and 125 mils) constraining layer. The damping treatments were applied symmetrically with percentages of coverage ranging between 25% and 100%.

Figure 2 shows the percent difference in the VEM's modal strain energy predicted using the MM assumptions and that predicted using a mesh comprised entirely of 20-node C^0 elements. For clarity, the curves are

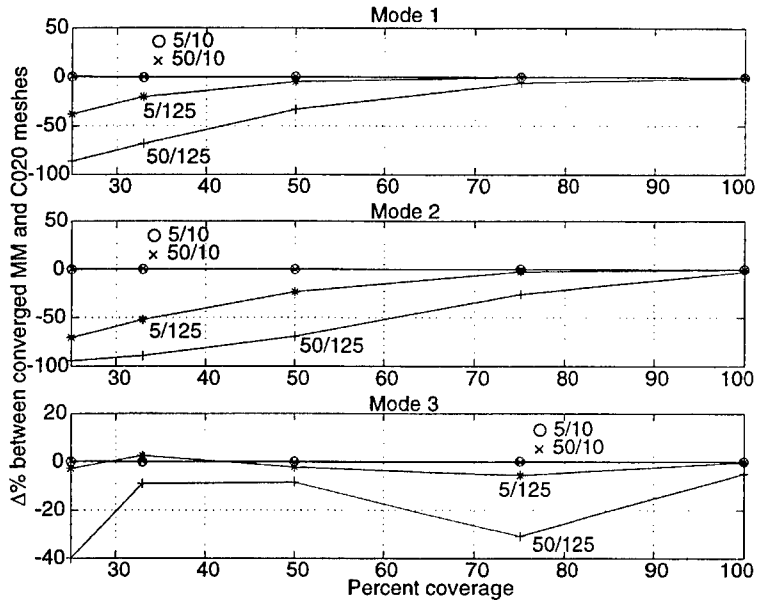

Figure 2: Error in predictions of modal strain energy vs. percent coverage for the first three modes using the Mead-Markus approach.

labeled by VEM thickness/constraining layer thickness in mili-inches. The individual meshes have been refined sufficiently so that differences that show up here are not due simply to poor convergence. The modes were extracted in separate runs to account for the frequency dependence of the VEM shear modulus.

The results in Fig. 2 confirm that the MM assumptions are best for the flexible (thin) constraining layers on a stiff (thin) VEM and worst for the stiff (thick) constraining layers on a soft (thick) VEM. There is no significant difference between the VEM MSE (modal strain energy in the viscoelastic material) over all coverages and modes studied for the two cases with 0.254-mm-thick (10 mils) constraining layers (labeled as 5/10 and 50/10). However, the error in the MM predictions for the 3.175-mm-thick constraining layers (125 mils) increases monotonically as the percent coverage decreases, except an anomaly in the third mode at 75% coverage which will be discussed later.

Figure 3 shows a symmetric half of the first mode for 25% coverage. Visually, it is difficult to see any difference in the mode shapes with and without the equal-displacement constraint. Close inspection of the bottom

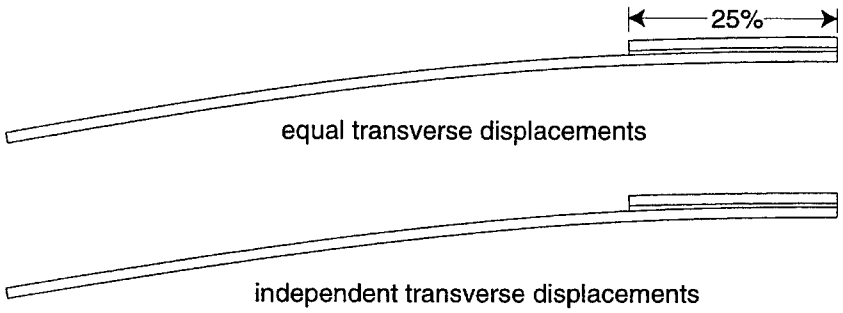

Figure 3: First mode (symmetric boundary condition) for 25% coverage (50/125) with and without the assumption of equal transverse displacements.

mode shape shows the constraining layer peeling away slightly from the base layer at the free end of the constraining layer. This small difference accounts for the -86% error in VEM MSE (0.548% with the MM constraint and 3.962% without it) shown in Fig. 2. The MR approach differs by only 0.3% from the the baseline C0-20 predictions, thus showing the value of releasing the equal-displacement constraint.

The trends for the second mode are almost identical to those of the first mode. Figure 4 shows this mode with 75% coverage with and without the assumption of equal transverse displacements. The magnified portions of this exaggerated mode shape show that the constraining layer wants to peel up in the absence of the constraint. Here the constrained model predicts 6.65% MSE and the unconstrained predicts 8.99%, and this accounts for the -26% error shown in Fig. 2. Here the MR models differs from the baseline by only 0.4%. The full models were run for this mode to avoid the complication of an asymmetric boundary condition for the beams having only one axis of symmetry.

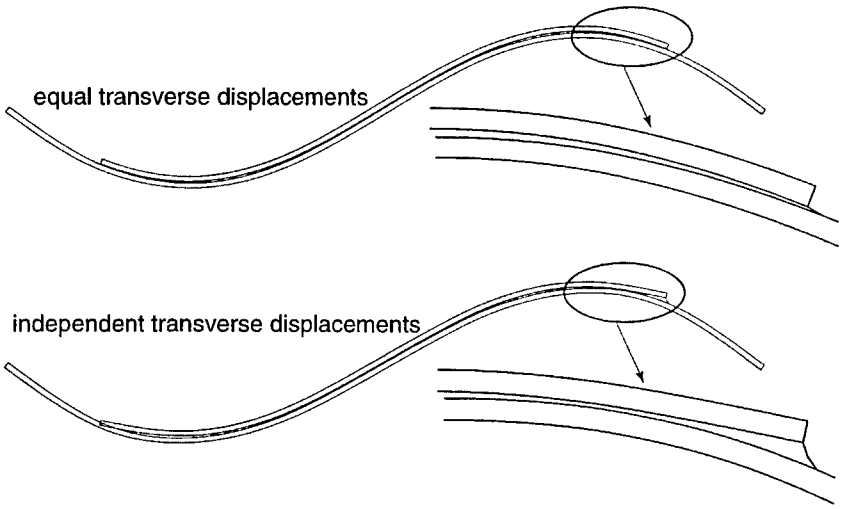

Figure 4: Second mode for 75% coverage (50/125) with and without the assumption of equal transverse displacements.

The MSE predictions under the MM assumptions do not get worse uniformly for the third mode as they do for the first two modes. Figures 5 and 6 show a symmetric half of the third mode for 50% and 75% coverage (50/125 case) both with and without the assumption of equal transverse displacements. The 50% case is better than the 75% case since the "floating" end of the damping treatment is at a location of low curvature in the base beam.

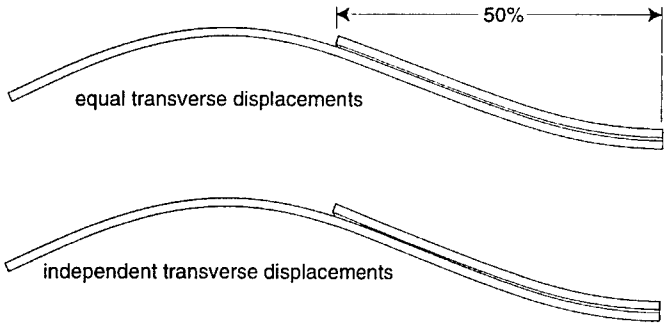

Figure 5: Third mode (symmetric boundary condition) for 50% coverage (50/125) with and without the assumption of equal transverse displacements.

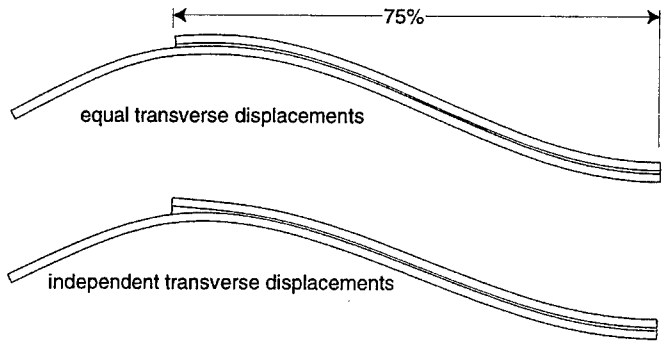

Figure 6: Third mode (symmetric boundary condition) for 75% coverage (50/125) with and without the assumption of equal transverse displacements.

3 Summary and Conclusions

Representing physical problems with mathematical models is a large part of an engineer's responsibility, and mathematical modeling always involves assumptions at some level. Engineers in industry use models to investigate candidate damping designs, and researchers in academia use models to try out new techniques, materials, and configurations for damping treatments. Models based on the Mead and Markus assumptions yield an appropriate tool for many important problems and interesting research topics. Nonetheless, engineers and researchers alike must recognize that the limits of their applicability lie within the realm of benign-look beams, particularly for partial coverage damping treatments.

The accuracy of the Mead and Markus modeling assumptions were investigated on a 508-mm-long by 3.175-mm-thick, simply supported, 2-D beam with a set of four damping treatments covering between 25% and 100%. A 20-node C^0 element was used to produce the basis for comparisons after showing that it reproduces Pagano's elasticity solution very well. A variation on the MM approach where the base and constraining layers are allowed to deform independently was also reported. The full-coverage implementation of this, credited to Miles and Reinhall, reproduced the baseline results very well.

At the heart of the MM assumptions is the constraint that the base and constraining layers undergo the same transverse displacements. While (Fig. 6) the effect on the mode shapes seems insignificant, hidden from the engineer are the forces necessary to enforce this constraint and the effect on the distribution of modal strain energy. The later point is shown in

Fig. 2 for various amounts of partial coverage. In contrast, the maximum errors for these same cases allowing the constraining layer to deform independently of the base layer were on the order of only 1%. The primary conclusions of the paper are as follows:

1. The Mead & Markus assumptions work best with the combination of relatively weak constraining layer and relatively stiff core.

2. Simply allowing the facesheets to deform independently is a vast improvement over MM. This carries only a small additional cost in degrees of freedom for finite element analysis, but the mathematics of closed-form solutions is more complicated (not shown here).

3. Prevention of peeling at the ends of the damping treatment is the main cause of error in the MM predictions.

There are several ongoing issues connected with this problem. First is the question of what is gained by removing the equal-displacement assumptions and thus complicating the models. The answer depends on the type of constrained-layer damping treatment being designed. The damping from thin-panel treatments like those in use for the past 40 years is predicted fine using the MM assumptions. It is a fact of modern life that the engineer often has to increase the damping in a structure as much as possible while only having access to a portion of the structure. This motivates research on both passive and active partial-coverage damping treatments. By demonstrating some pitfalls of the Mead and Markus assumptions for certain classes of damping treatments, the authors intent is that researchers reexamine their own modeling assumptions for applicability to their research.

The peeling at the ends carries its own set of issues. Are the significant geometric and or material nonlinearities? How useful are viscoelastic material properties measured only in shear (typical)? These questions form the bases of ongoing research.

Acknowledgement

The authors wish to recognize the support of the US Army Research Office grant number DAAG–98–1–0030, under the direction of Dr. Gary Anderson, and NSF grant CMS–9713453–001.

References

[1] Kerwin, E. M. Damping of flexural waves by a constrained visco-elastic layer. *Journal of the Acoustical Society of America*, **31**, 952–962 1959.

[2] DiTaranto, R. A. Theory of vibratory bending for elastic and viscoelastic layered finite-length beams. *ASME Journal of Applied Mechanics*, **32**, 881–886 December 1965.

[3] Mead, D. J. and Markus, S. The forced vibration of a three-layer, damped sandwich beam with arbitrary boundary conditions. *ASME Journal of Vibration and Acoustics*, **10**(2), 163–175 1969.

[4] Mead, D. J. A comparison of some equations for the flexural vibration of damped sandwich beams. *Journal of Sound and Vibration*, **83**(3), 363–377 1982.

[5] Douglas, B. E. and Yang, J. C. S. Transverse compressional damping in the vibratory response of elastic-viscoelastic-elastic beams. *AIAA Journal*, **16**(9), 925–930 1978.

[6] Nakra, B. C. Vibration control with viscoelastic materials – III. *Shock and Vibration Digest*, **16**(5), 17–22 May 1984.

[7] Torvik, P. J. The analysis and design of constrained layer damping treatments. *Proceedings ASME Winter Annual Meeting — Damping Applications for Vibration Control*, 85–112 1980.

[8] Ikegami, R., Beck, C. J., and Walker, W. J. Application of damping to improve reliability of IUS-type satellite equipment — RELSAT program. *Vibration Damping 1984 Workshop Proceedings*, TT1–TT15 November 1984.

[9] Staley, J. A. and Stahle, C. V. Damping in support structures for satellite equipment reliability — RELSAT. *Vibration Damping 1984 Workshop Proceedings*, UU1–UU26 November 1984.

[10] Ross, D., Ungar, E. E., and Kerwin, E. M. Damping of plate flexural vibrations by means of viscoelastic laminae. *Structural Damping — a colloquium on structural damping held at the ASME annual meeting*, 49–87 December 1959.

[11] Miles, R. N. Beam dampers for skin vibration and noise reduction in the 747. *Vibration Damping 1984 Workshop Proceedings*, PP1–PP18 1984.

[12] Baz, A. and Ro, J. Optimum design and control of active constrained layer damping. *Journal of Mechanical Design and Journal of Vibration and Acoustics*, **117 (B)**, 135–144 1995. ASME 50th Anniversary Design Engineering Division.

[13] Miles, R. N. and Reinhall, P. G. An analytical model for the vibration of laminated beams including the effects of both shear and thickness deformation in the adhesive layer. *Journal of Sound and Vibration*, **108**, 56–64 1986.

[14] Pagano, N. J. Exact solutions for composite laminates in cylindrical bending. *Journal of Composite Materials*, **3**, 398–411 1969.

[15] Austin, E. M. *Influences of Higher Order Modeling Techniques on the Analysis of Layered Viscoelastic Damping Treatments*. Ph.D. thesis, Virginia Polytechnic Institute and State University November 1998.

[16] Ungar, E. E. and Kerwin, E. M. Loss factors of viscoelastic systems in terms of energy concepts. *Journal of the Acoustical Society of America*, **34**, 954–957 1962.

[17] Johnson, C. D., Kienholz, D. A., and Rogers, L. C. Finite element prediction of damping in beams with constrained viscoelastic layers. *The Shock and Vibration Bulletin*, **51**(1), 71–81 May 1981.

[18] Morgenthaler, D. R. The absolute value modal strain energy method. *Damping '91*, **II**, FDB1–FDB16 February 1991.

A MATCHED DISTRIBUTED PIEZOELECTRIC ACTUATOR AND SENSOR PAIR FOR CONTROL OF BEAM MOTION

Y.S. Lee, P Gardonio, S.J. Elliott and S Debost[+]

ISVR, University of Southampton and [+]Thompson Sintra

Abstract

This paper presents a theoretical and experimental study of a matched triangularly shaped piezoelectric PVDF actuator and sensor pair bonded on either sides of a cantilever beam for the control of vibration at the tip position of the beam. The distributed piezoelectric sensor only detects the velocity at the tip of the beam and the distributed piezoelectric actuator only generates a force at the tip of the beam. The generated force and the detected velocity are thus, in principle, collocated and the transfer function between the two transducers should correspond to a driving point mobility and have an entirely positive real part. A simple feedback controller connected between these two transducers should thus be unconditionally stable so that large attenuations of tip velocity disturbances should be possible. This type of "smart beam" could be used for high precision positioning control in many applications and could allow the construction of very simple and compact "smart robotic arms" whose bending vibration at the tip can be actively controlled. The measured transfer function between the two transducers on an experimental beam shows unexpected behaviour characterised by an overall rising trend with frequency. A detail study of this behaviour has uncovered two main causes: first, coupling between the actuator and the sensor via in-plane vibration of the beam, and second effects generated by the non-perfect and non-identical shaping of the two PVDF elements. It may be possible to compensate for the in-plane coupling effect by subtracting out the effects of the in-plane dynamics of the beam, which can be modelled as an axial spring at low frequencies. The second problem can be solved by increasing the accuracy of the manufacturing for such a smart structure.

1. Introduction

Piezoelectric materials have been widely used in active control systems for detection and suppression of vibration [1-4], for the control of sound radiation and transmission [5-7], and for the position control of flexible beams [8]. The geometry of such transducers can be varied from small patches to distributed sheets bonded on the surface of a structure. Collocated and matched piezoelectric sensor and actuator

pairs, with the same size and material, have been used to detect and control the vibration of structures [7, 9].

This paper presents a study of a matched and collocated piezoelectric PVDF actuator/sensor pair bonded on either side of a cantilever beam for active tip position control. The piezoelectric actuators and sensors have a triangular shape to produce a transverse force at the tip [10] and to detect the tip position of the beam. The transfer response between the two transducers should thus be proportional to the *driving point* mobility [11] of the beam tip, which has an entirely positive real part. A feedback control system connected to such a system is guaranteed to be unconditionally stable, and so can greatly attenuate any tip vibration, generated by slewing of the beam for example. This type of a "smart beam" could be used for high precision positioning and pointing control in many robotics applications. The novelty of the system presented in this paper is given by the matched and collocated actuator/sensor pair for tip position control of a beam. This solution allows the construction of very simple and compact smart robotic arms whose bending vibration at the tip can be actively controlled using a relatively simple analogue velocity feedback controller.

Many studies have assumed that this sensor/actuator pair is coupled only by the bending motion of a beam onto which the pair is bonded. It is demonstrated in this paper that the piezoelectric actuator and sensor elements are, in fact, coupled via both in-plane and bending motions of the structure. This is an important problem that could limit both the control effectiveness of collocated and matched sensor/actuator pair and the stability of a feedback control system. Therefore for the design of active vibration control (AVC) and active structural acoustical control (ASAC), it is very important to take into account both the *in-plane* and *out-of-plane* coupling effects of collocated sensor and actuator pairs. In order to cancel in-plane coupling in a matched and collocated sensor/actuator pair, Yang and Huang [9] suggested the use of a double pair arrangement using a pair of actuators and a pair of sensors, which could provide a way of detecting and actuating only out-of-plane motion. However, this paper suggests a different way of avoiding these problems, by compensating for the in-plane coupling.

2. Matched piezoelectric actuator and sensor pair with triangular shape

The cantilever beam used in the experiments and illustrated in Figure 1 is made of aluminium and it is 1 mm thick ($2h_s$) with dimensions 200×30 mm ($L_x \times L_y$). Two triangularly shaped PVDF films are symmetrically bonded on either side of the beam. Each PVDF film is 0.5

mm (h_{pe}) thick, 200 mm long, and 30 mm wide. The triangular shaped sensor and actuator can detect and excite the out-of-plane vibration at the tip position of the cantilever beam as will be described below. Two insulation layers consist of two copper foils and one polyimid foil are bonded together as illustrated in Figure 1. One of the two identically designed PVDF films is for an actuator and the other is for a sensor. The total thickness of the beam structure is thus about 3 mm, which has been greatly exaggerated in Figure 1 for clarity.

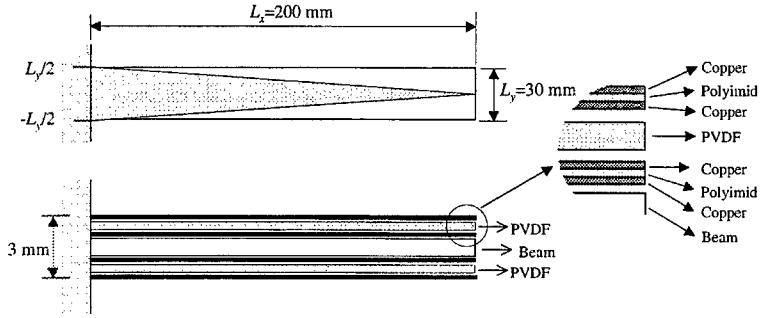

Figure 1. Arrangement of a collocated piezoelectric actuator/sensor pair coupled with a cantilever beam.

2.1. Response of a piezoelectric triangularly shaped sensor

It is assumed that the clamped-end is at $x=0$ and the free-end is at $x=L_x$ and the out-of-plane position at x is $w(x)$ so that $w(0)=0$ and $w'(0)=0$. For the triangular sensor considered in Figure 1, the spatial sensitivity weighting function $S(x)$ of the triangularly shaped piezoelectric sensor can be defined for $x=0$ to L_x by

$$S(x)=-k(x-L_x), \tag{1}$$

where $k=L_y/(2L_x)$ is the slope of the triangular shaped sensor.

If the beam is subject only to out-of-plane vibration, the charge output $q_{oop}(t)$ of the piezoelectric sensors can be written as

$$q_{oop}(t)=-e_{31}h_{sen}\int_0^{L_x} S(x)\frac{\partial^2 w(x,t)}{\partial x^2}dx, \tag{2}$$

where e_{31} is piezoelectric stress constant, and $h_{sen}=h_s+h_{pe}/2$ is the distance between the neutral axis of the beam and the sensor. After some manipulation equation (2) can be solved using the boundary

conditions of the sensor and the beam. The charge output of the sensor due to the pure out-of-plane motion of the beam can be expressed by

$$q_{oop}(t) = -2e_{31}h_{sen}kw(L_x,t), \tag{3}$$

where $w(L_x,t)$ is out-of-plane displacement at the tip of the beam. Therefore the current generated by the charge output is proportional to the tip velocity $\dot{w}(L_x,t)$ representing the time derivative of the tip displacement of the beam and is equal to

$$i_{oop}(t) = dq_{oop}(t)/dt = -2e_{31}h_{sen}k\dot{w}(L_x,t). \tag{4}$$

If the out-of-plane position of the beam is expressed in terms of modal expansion as $w(x,t) = \sum_n B_n(t)\phi_n(x)$, then the charge output $q_{oop}(t)$ by the sensor can be written as

$$q_{oop}(t) = -2e_{31}h_{sen}k\sum_n B_n(t)\phi_n(L_x). \tag{5}$$

2.2. Excitation due to a piezoelectric triangularly shaped actuator

A triangularly shaped piezoelectric PVDF actuator bonded to one side of the cantilever beam as shown in Figure 1 with the same dimensions as the sensor is considered here. For the analysis of the actuation mechanism, both the beam and the actuator are regarded as two-dimensional elements. The forced out-of-plane motion equation for the beam-actuator assembly with a spatial sensitivity $S(x,y)$ of the actuator can be written as [7]

$$\begin{aligned}&[D_s + D_{pe}(x,y)]\left(\frac{\partial^4 w}{\partial x^4} + 2\frac{\partial^4 w}{\partial x^2\partial y^2} + \frac{\partial^4 w}{\partial y^4}\right) + m\frac{\partial^2 w}{\partial t^2}\\ &= -h_{act}V_3(t)\left(e_{31}\frac{\partial^2 S(x,y)}{\partial x^2} + 2e_{36}\frac{\partial^2 S(x,y)}{\partial x\partial y} + e_{32}\frac{\partial^2 S(x,y)}{\partial y^2}\right)\end{aligned} \tag{6}$$

where $h_{act} = h_s + h_{pe}/2$ (h_s is half thickness of the beam and h_{pe} is thickness of the actuator), m is the mass per unit length of the assembly, $V_3(t)$ is the applied voltage to the piezoelectric actuator to the out-of-plane direction , and D_s and $D_{pe}(x,y)$ are the out-of-plane stiffnesses of the beam and the actuator. After some manipulation, the inside of the parentheses in the forcing function of the right hand side of equation (6) can be expressed using the Macauley notation as [10]

$$
\begin{aligned}
& e_{31}\frac{\partial^2 S(x)}{\partial x^2}+2e_{36}\frac{\partial^2 S(x)}{\partial x\partial y}+e_{32}\frac{\partial^2 S(x)}{\partial y^2} \\
&= e_{31}(< x >^{-2} - < x-L_x >^{-2})(< y-kx+L_y/2 >^{0} - < y+kx-L_y/2 >^{0}) \\
&\quad -2ke_{31}(< x >^{-1} - < x-L_x >^{-1})(< y-kx+L_y/2 >^{-1} + < y+kx-L_y/2 >^{-1}) \\
&\quad +(k^2e_{31}+e_{32})(< x >^{0} - < x-L_x >^{0})(< y-kx+L_y/2 >^{-2} - < y+kx-L_y/2 >^{-2}).
\end{aligned} \tag{7}
$$

If only the out-of-plane vibration of the beam is considered, then equation (7) indicates that the beam is excited by a concentrated force f_t at the tip $x=L_x$ and two forces, f_r at the corners where the beam is clamped. Also line moments m_1 and m_2 also act along the edges of the triangular actuator as shown in Figure 2. The amplitudes of these force and moment excitations are given by [10]

$$
\begin{aligned}
& f_t(t)=4ke_{31}h_{act}V_3(t), && f_r(t)=2ke_{31}h_{act}V_3(t), \\
& m_1(t)=(k^2e_{31}+e_{32})h_{act}V_3(t), && m_2=e_{31}h_{act}V_3(t).
\end{aligned} \tag{8}
$$

The effect of the out-of-plane excitations f_r and m_2 along the two lateral edges of the triangular actuator can be ignored since they are located at the clamped end. Therefore it can be concluded that the out-of-plane excitation of the beam is just given by f_t and x-directional component of m_1 as illustrated in Figure 2.

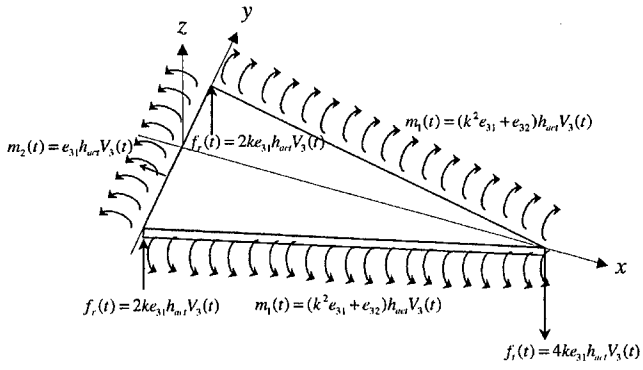

Figure 2. Distribution of out-of-plane *force* due to a triangularly shaped actuator bonded to a beam.

3. Measured transfer functions

Two frequency responses of the *driving point* mobility (velocity/force) [11] at the tip of the cantilever beam were measured on the

experimental beam and are shown in Figure 3. In the first measurement in Figure 3(a), the input force applied at the beam tip by a shaker (Ling Dynamic Systems model V201) has been measured with a force transducer (B&K Type 8200) connected to a spectrum analyser (Advantest R9211C FFT analyser) via a charge amplifier (B&K Type 2635). The velocity at the tip of the beam was measured by an accelerometer (B&K Type 4375) also connected to the spectrum analyser via another charge amplifier (B&K Type 2635) using its internal integrator.

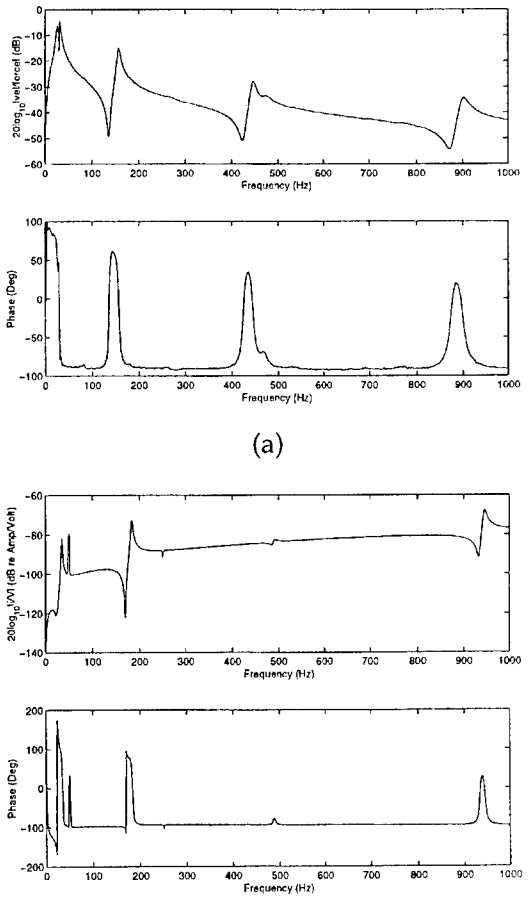

Figure 3. Comparison of two measured mobility responses. (a) Shaker input and accelerometer output. (b) PVDF actuator voltage input and sensor current output.

Figure 3(b) shows the measured mobility response between the triangularly shaped PVDF actuator/sensor pair bonded to the beam, measured with the spectrum analyser. The input signal to the actuator element was white noise in the frequency range between 0 and 1kHz and has been amplified to around 100 V using a power amplifier (PCB AVC 790 series). The current output $i(\omega)$ taken from the sensor element has been measured with a B&K charge amplifier Type 2635. The current output from the sensor element was designed to be proportional to the out-of-plane velocity at the tip of the beam as in equation (4) and the force generated by the actuator element was designed to be proportional to the input voltage, as in equation (8). Hence the frequency response between the piezoelectric triangular actuator and sensor pair in Figure 3(b) was expected to be equal to that measured in Figure 3(a).

Figure 3(a) shows a typical feature of driving point mobility of a cantilever beam. The resonances are alternated by anti-resonances which occur at frequencies quite close to the following resonance. Also the phase response lies between $\pm 90^{\circ}$ and the amplitude tends to decrease with frequency [12]. However, Figure 3(b) shows an unexpected rising trend with frequency which indicates a behaviour quite different than that of Figure 3(a). The origin of this mismatching between the two measurements will be described at the next section through the analysis on the actuation and detection mechanism of the PVDF elements.

4. In-plane coupling between the actuator and sensor

A piezoelectric material such as PVDF film subject to an electric field can only be extended or contracted in the in-plane direction. That is, the piezoelectric material alone can only induce a purely in-plane force only. The out-of-plane forces in equation (8) and Figure 2 are originated by these in-plane forces acting over the distance between the piezoelectric material and the neutral axis of the beam. The in-plane forces will also generate in-plane strains in the beam, although these are small and would not normally be detected by an accelerometer for example. If a piezoelectric sensor is used, however, its output will be strongly affected by the in-plane strain and this will cause additional coupling between the actuator and sensor, as pointed out by Yang and Huang [9]. This in-plane coupling is analysed below.

If the beam is under pure in-plane vibration, the in-plane charge output $q_{ip}(t)$ of the triangularly shaped piezoelectric sensor on the beam can be written as

$$q_{ip}(t) = e_{31}\int_0^{L_x} S(x)\frac{\partial u(x,t)}{\partial x}dx$$
$$= e_{31}\sum_n A_n(t)\int_0^{L_x} S(x)\frac{\partial \psi_n(x)}{\partial x}dx, \tag{9}$$

where the in-plane displacement u is expressed in terms of modal expansion as $u(xt) = \sum_n A_n(t)\psi_n(x)$. For the in-plane motion of a cantilever beam, whose mode shapes are given $\psi_n(x) = \sin\frac{(2n-1)\pi}{2L_x}x$ [13], then after some manipulation the in-plane charge output $q_{ip}(t)$ can be expressed for the spatial sensitivity $S(x)$ of the sensor element given by equation (1) as

$$q_{ip}(t) = e_{31}\sum_n A_n(t)\frac{2L_y}{(2n-1)\pi}\left[1-\cos\frac{(2n-1)\pi}{2}\right]. \tag{10}$$

Therefore, the measured charge output of the sensor will be the sum of both the out-of-plane charge output $q_{oop}(t)$ and the in-plane charge output $q_{ip}(t)$.

If the purely in-plane excitation of the PVDF actuator element is considered, the in-plane line forces can be obtained by dividing the line bending moments m_1 and m_2 in equation (8) by h_{act}. The resulting in-plane line forces f_1 and f_2 can be decomposed into components of f_{1x}, f_{1y}, f_{2x}, f_{2y} and for the cantilever beam clamped at $x=0$, the in-plane and the out-of-plane components can be expressed by

$$f_{1x}(t) = k^2 e_{31}V_3(t)\sin\theta \qquad f_{1y}(t) = e_{32}V_3(t)\cos\theta$$
$$m_{1x}(t) = k^2 e_{31}h_{act}V_3(t)\sin\theta \qquad m_{1y}(t) = e_{32}h_{act}V_3(t)\cos\theta, \tag{11}$$

where θ is the slope of the piezoactuator given by $\tan\theta = k$. Thus, the total force applied to the cantilever beam by the actuator are given by a concentrated force f_t at tip of the actuator, the components of the in-plane force and the out-of-plane force f_{1x}, f_{1y}, m_{1x}, and m_{1y} along the each gradient of the spatial sensitivity $S(x,y)$ as shown in Figure 4. Thus the triangular actuator can induce in-plane motion as well as out-of-plane motion of the cantilever beam.

4.1. Overall coupling

The analytical model of the PVDF actuator-beam-PVDF sensor system has been shown that the mobility in this case is composed of individual out-of-plane and in-plane contributions.

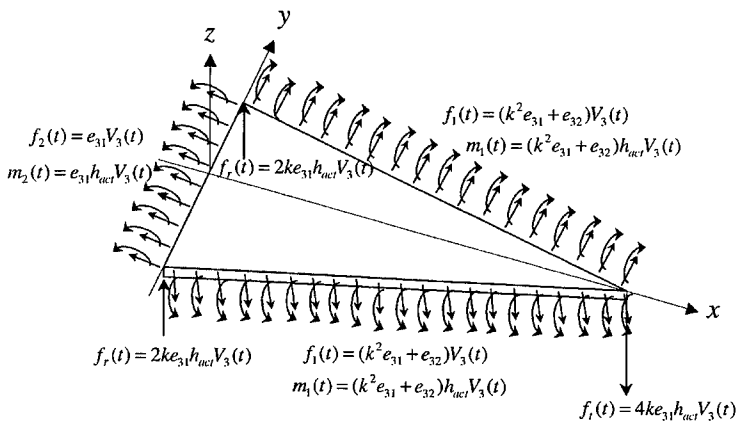

Figure 4. Distribution of the in-plane and the out-of-plane forces due to a triangularly shaped actuator bonded on a cantilever beam.

The out-of-plane motion $w(x,t)$ of the cantilever beam due to the distributed and uniform out-of-plane force component $m_{1x}(t)$ and the concentrated tip force $f_t(t)$ as given in equations (8) and (11) can be expressed for steady state frequency response as

$$w(x,t) = \sum_n \frac{\phi_n(x)\left[2\int_0^{L_x} m_{1x}(t)\phi_n'(x)dx + f_t(t)\phi_n(L_x)\right]}{\rho A L_x[\omega_n^2(1+j\eta) - \omega^2]}, \tag{12}$$

where η is a loss factor. The out-of-plane mobility representing input voltage to the actuator element to tip velocity detected by the sensor element can be thus be expressed as

$$\frac{\dot{w}(L_x)}{V_3(t)} = -j\omega \frac{e_{31}\{\sin(\tan^{-1}k) + 2\}h_{act}L_y}{\rho A L_x^2} \cdot \sum_n \frac{\phi_n^2(L_x)}{[\omega_n^2(1+j\eta) - \omega^2]}. \tag{13}$$

The out-of-plane mobility transfer function T_{oop} can be written with the current output $i_{oop}(t) = dq_{oop}(t)/dt$ as

$$T_{oop} = \frac{i_{oop}(t)}{V_3(t)} = j\omega \frac{e_{31}^2\{2k^2\sin(\tan^{-1}k) + 4k\}h_{sen}h_{act}L_y}{\rho A L_x^2} \cdot \sum_n \frac{\phi_n^2(L_x)}{[\omega_n^2(1+j\eta) - \omega^2]}. \tag{14}$$

The in-plane motion $u(x,t)$ of the cantilever beam due to the distributed and uniform in-plane force component $f_{1x}(t)$ as given in equation (11) can be expressed as

$$u(x,t) = \sum_n \frac{\psi_n(x)\int_0^{L_x} f_{1x}(t)\psi_n(x)dx}{\rho A L_x[\omega_n^2(1+j\eta)-\omega^2]}. \tag{15}$$

The in-plane mobility transfer function T_{ip} representing input voltage to the actuator element by output current detected by the sensor element can be given as

$$T_{ip} = \frac{i_{ip}(t)}{V_3(t)} = j\omega \frac{4e_{31}^2 k^2 \sin(\tan^{-1} k) L_y}{\rho A \pi^2} \cdot \sum_n \frac{\left[1-\cos\frac{(2n-1)}{2}\pi\right]^2}{(2n-1)^2[\omega_n^2(1+j\eta)-\omega^2]}. \tag{16}$$

The total measured mobility for the PVDF actuator and sensor pair is thus given by

$$T_{total} = T_{oop} - T_{ip}. \tag{17}$$

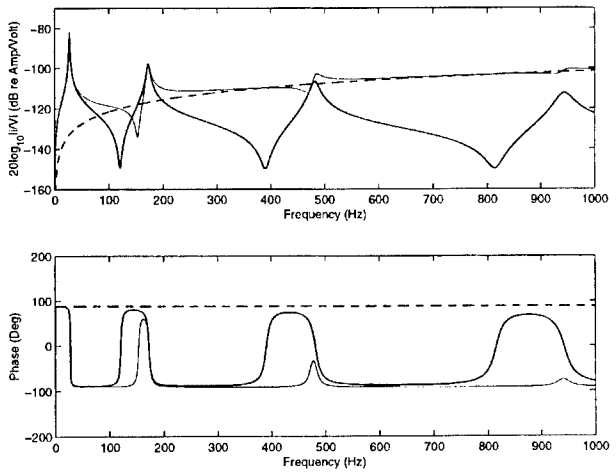

Figure 5. Calculated mobility responses of the piezoelectric sensor and actuator: pure out-of-plane response (thick line), pure in-plane response (dashed line), and the coupled motion (thin line).

Based on the above analytical modelling, the unexpected measured mobility response in Figure 3(b) could be understood and decoupled into in-plane and out-of-plane responses. The individual mobility responses calculated using equations (14) and (16) are plotted in Figure 5 together with their sum. This total calculated mobility is now similar to the measured one in Figure 3(b). This means the understanding the in-plane behaviour of a beam coupled with single piezoelectric actuator/sensor pair is crucial understanding its overall behaviour.

4.2. Compensation to in-plane coupling effect

The pure out-of-plane mobility could be extracted from the total response by eliminating the in-plane response. The first estimated natural frequency of in-plane mode is around 6000 Hz for the experimental beam and so the frequency range of interest (below 1000 Hz) is located within the *stiffness controlled range* of in-plane response. The mobility of the cantilever beam within the *stiffness controlled range* can be expressed as $M_k = j\omega/k_{in}$ [14], where k_{in} is the in-plane stiffness. Thus the in-plane mobility could be plotted as an almost straight line in a linear scale or a parabolic curve in a logarithmic scale as shown in Figure 5. The in-plane mobility can be expressed in the frequency range of interest as

$$M_k = j\omega s, \tag{18}$$

where $s = 1/k_{in}$ is a constant. If the value of s could be determined, the in-plane mobility could be subtracted from the coupled mobility.

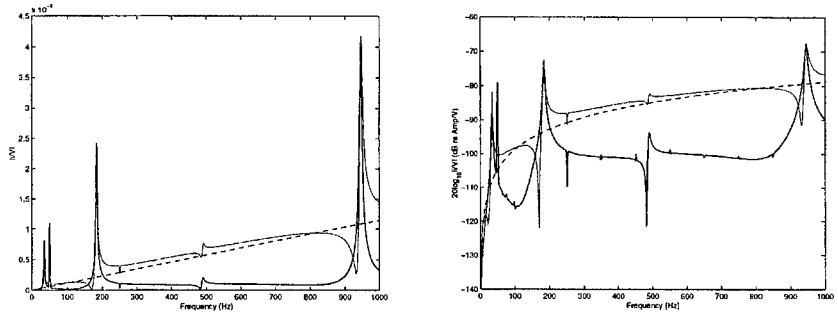

(a) (b)

Figure 6. Extraction of pure out-of-plane mobility (thick line) from the measured mobility (thin line) by subtracting out the estimated in-plane mobility component (dashed line). (a) A linear scale. (b) A logarithmic scale.

In the case of the measured response in Figure 3(b), s has been estimated to be 1.2×10^{-8} and the resulting in-plane mobility is plotted as the dashed line in Figure 6. The solid thick line in Figure 6 is the out-of-plane mobility response calculated by compensating the measured mobility (thin line) with the estimated in-plane mobility.
The extracted pure out-of-plane mobility in Figure 6 shows a similar response and trend with frequency to the measured mobility using shaker-accelerometer in Figure 3(a). However, the extracted pure out-of-plane in Figure 6 shows the unexpectedly strong out-of-plane resonances at the second and fourth modes. These resonances occur at even modes, which suggest that they could be caused by the piezoelectric actuator and sensor shaping error, as discussed below.

5. Sensitivity to shaping errors of the two layers of PVDF

Lee and Moon [2] showed that the response of modal actuators and sensors was sensitive to small errors in the shapes of the transducers, particularly affecting the high frequency response. After some investigation of the shaping errors of the PVDF actuator and sensor used here it was found that the two PVDF elements are not identical and not perfectly collocated. The actuator and sensor elements are bonded about 4mm and 2mm away from the clamped end of the beam respectively with some minor cutting errors especially in the sharp edges at the tip position.

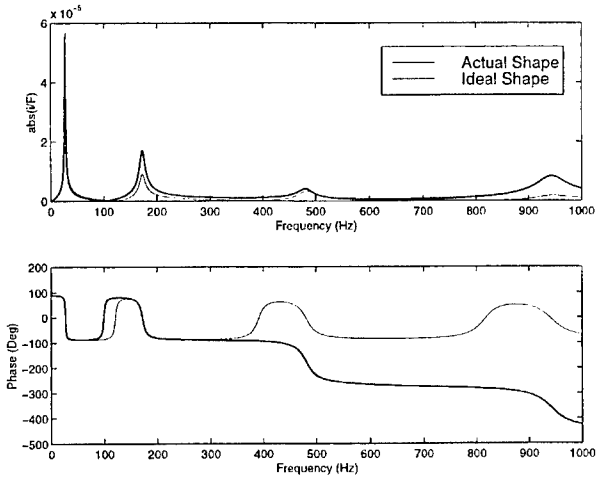

Figure 7. A computer simulation for the shaping error effect in out-of-plane mobility of the beam.

A computer simulation with the analytical model developed in the previous sections gave a response for the actual transducer shapes as shown in Figure 7. The even modes could thus be amplified by shaping error of the PVDF actuator/sensor elements comparing with those of the ideally shaped elements.
Therefore, the shaping errors in the PVDF elements could represent a serious problem in excitation and detection for this smart beam. This is one of the possible shortcomings of piezoelectric actuator/sensor system and it can be more amplified with the more complex shaping of the actuator/sensor as pointed out by Preumont et al [15]. The two pairs of piezoelectric actuators/sensors suggested for the compensation of the in-plane coupling by Yang and Huang [9] could increase the danger of this shaping and collocation errors. Hence more careful workmanship is required for construction of these shaped piezoelectric actuator/sensor systems.

6. A possible feedback controller

If a smart structure was constructed with a piezoelectric actuator and sensor pair which was free from shaping errors, the out-of-plane behaviour of the structure could be actively controlled using the above in-plane compensation method. For example, tip position control for a flexible beam with a pair of piezoelectric actuator and sensor may be possible by compensating the in-plane coupling expressed in equation (17). The in-plane compensation part could be implemented with a first order filter in the position active control system which could be adaptive. Velocity feedback control could then be implemented for the tip position control. The schematic diagram for the active control with compensating the in-plane coupling is shown in Figure 8.

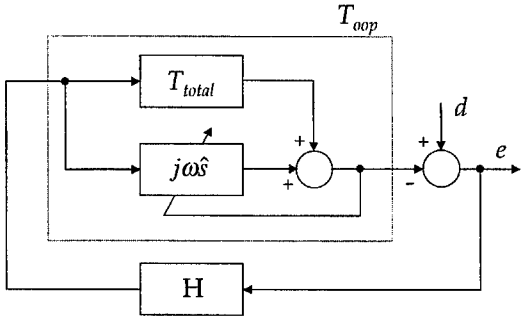

Figure 8. The schematic diagram for the active control with compensating the in-plane coupling.

7. Conclusion

This paper presents a study of a collocated triangularly shaped piezoelectric PVDF actuator and sensor pair bonded on either sides of a cantilever beam for the control of vibration at tip position of the beam. The two piezoelectric elements allow both the excitation and the detection of bending vibration at the tip position of the beam. The measured mobility using the PVDF actuator/sensor pair has been shown to be affected by in-plane coupling due to not a pure bending from the actuator. The analytical model was developed to decompose the response into an in-plane contribution and an out-of-plane contribution. A compensation method to cancel the in-plane coupling was suggested. However, unwanted strong out-of-plane resonances were appeared at even modes even after the in-plane compensation. These were caused by the errors in the shaping of the PVDF actuator and sensor. A computer simulation with erroneous shapes showed a similar mobility function to the measured one. These shaping errors could be removed with careful construction process in piezoelectric actuator/sensor. Therefore, if the beam is free from the PVDF shaping error, the out-of-plane behaviour could be actively controlled with an in-plane compensating filter. Velocity feedback control could then be implemented for the tip position control since the control force and measured response would be collocated. This type of "smart beam" could be used for high precision positioning control in many applications and could allow the construction of very simple and compact "smart robotic arms" whose bending vibration at tip can be actively controlled.

Acknowledgements

The contents of this paper arose partly out of a Brite-Euram project supported by EU under the contract BRPR-CT96-0154 DAFNOR, "Distributed Active Foils for NOise Reduction". The authors also would like to thanks Mr G Roux who built the cantilever beam with the triangularly shaped actuator and sensor shown in Figure 1.

References

1. Burke, S.E. and Hubbard Jr., J.E., Active vibration control of a simply supported beam using a spatially distributed actuator, *IEEE Control systems magazine*, 1987, 25-30.
2. Lee, C.K. and Moon F.C., Modal sensor/actuators, *Journal of Applied Mechanics*, 1990, **57**, 434-441.
3. Fuller, C.R., Elliott, S.J., and Nelson, P.A., *Active Control of Vibration*, Academic Press, London, 1996.

4. Brennan, M.J., Elliott, S.J., and Pinnington, R.J., The dynamic coupling between piezoceramic actuators and a beam, *Journal of Acoustical Society of America*, 1997, **102**(4), 1931-1942.
5. Clark, R.L. and Fuller, C.R., Active structural acoustical control with adaptive structures including wavenumber considerations, *Journal of Intelligent Material Systems and Structures*, 1992, **3**(2), 296-315.
6. Johnson, M.E. and Elliott, S.J., Active control of sound radiation using volume velocity cancellation, *Journal of Acoustical Society of America*, 1995, **98**(4), 2174-2186.
7. Gardonio, P., Lee, Y.S., Elliott, S.J., and Debost, S., Active control of sound transmission through a panel with a matched PVDF sensor and actuator pair, *Proceedings of Active 99*, 1999, 341-354.
8. Lee, Y.S. and Elliott, S.J., Active position control of a flexible beam, submitted to *Journal of Sound and Vibration*, 1999.
9. Yang, S.Y. and Huang, W.H., Is a collocated piezoelectric sensor/actuator pair feasible for an intelligent beam, *Journal of Sound and Vibration*, 1998, **216**(3), 529-538.
10. Sullivan, J.M., Hubbard Jr, J.E. and Burke, S.E., Modeling approach for two-dimensional distributed transducers of arbitrary spatial distribution, *Journal of Acoustical Society of America*, 1996, **99**(5), 2965-2974.
11. Gardonio, P. and Elliott, S.J., Driving point and transfer mobility matrices for thin plates excited in flexure, ISVR Technical Report No.277, University of Southampton, 1998.
12. Ewins, D.J., Modal Testing: Theory and Practice, John Wiley & Sons, Chichester, England, 1984.
13. Bishop, R.E.D. and Johnson, D.C., *The Mechanics of Vibration*, Cambridge University Press, 1960.
14. Cremer, L. and Heckl, M. Structure-Borne Sound, 2nd edn (trans. E.E. Ungar), Springer-Verlag, 1988.
15. Preumont, A., Francois, A., and Debru, S., Piezoelectric array sensing for real-time, broad-band sound radiation measurement, *ASME Journal of Vibration and Acoustics*, 1999, **121**, 446-452.

A shaped PVDF modal sensor for the n = 2 propagating flexural wave in a pipe

W. Variyart and M. J. Brennan,
DG, ISVR, University of Southampton
Highfield, Southampton, SO17 1BJ, England

Abstract

In pipe vibration the n=2 (ovalling mode) wave causes a large increase of strain in the pipe wall at the cut-on frequency when the wave starts to propagate. Hence from a fatigue perspective this wave is of major concern. It would be of interest, therefore, to design a control system to suppress this wave. A vital part of this system is the sensor, and thus the design of a shaped PVDF modal sensor to target this wave is investigated in this paper.

Using Flugge's shell theory, the sensitivity of the sensor to the n = 2 mode is desired and the cross-sensitivity of the sensor to higher order circumferential modes is established. It is shown that for an acceptable level of the performance in terms of cross-sensitivity the width of the sensor has to be less than one third of the wavelength of the n = 2 flexural wave at the ring frequency.

Theoretical predictions of the modal sensor sensitivity were successfully validated by some experimental work.

1. Introduction

In many processing and chemical industries, and in ships and aircraft, pipework is important for transporting fluids, i.e. gas, cooling water and hydraulic fluid. A piping system can be excited by many sources connected to the structure or internal fluid such as compressors, pumps, or valves. In the system, the propagating wave of the n=2 mode (ovalling mode) causes a large vibration in the pipe wall at the cut-on frequency and may result in excessive noise radiation or in failure of the system due to fatigue. There is the motivation to actively control this wave and part of such a control system would be a sensor to detect this wave. In this paper the design of a shaped PVDF modal sensor to sense this wave is investigated.

The modal sensor was first introduced by Lee and Moon [1], who applied it on a beam, and included an analysis of the modal sensor for a plate as

well. It was extended in theory and practice for a plate by Gu et al [2]. The analysis of a PVDF sensor bonded to a shell was developed by Tzou [3]. Factors that affect the output of the segmented PVDF, i.e. thickness of the PVDF and shell, the curvature of the shell, were investigated by Tzou and Bao [4]. However, the sensors for a pipe in both pieces of work were not discussed in the context of a modal sensor. A modal sensor for an semi-infinite pipe was used in the work of Fuller and Brevart [5]. Since, the shapes of the modal sensors need to be accurate; otherwise they cannot be used in an active control system to completely cancel undesired modes, Callahan and Baruh [6] preferred to use segmented PVDF patches (rectangular shape) with the sensor output cancellation technique. However, this technique risks the ill-conditioning of the modal coordinate matrix and it takes some time to converge to the desired mode. Therefore, the modal sensor for the pipe in the work reported here still uses the PVDF in the form of sine and cosine functions, which is a similar sensor arrangement to that of Fuller and Brevart [5].

To derive the modal sensor equation, it is important to understand the behaviour of a pipe. Once it is established, the experiment is carried out to verify this equation.

2. In vacuo dynamic behaviour of a pipe

For a thin walled pipe, structural waves propagate in the axial direction along a pipe and in a circumferential direction forming a helical pattern as shown in figure 1 (Fahy [7]) where $\hat{r}, \hat{\theta}$ and $\hat{x}$ are the unit vectors in the asial, radial and tangential directions, respectively. The wavenumber of the helical wave, k_s, is the vector combination of the waveguide components in both directions, the axial wavenumber, k_x, and circumferential wavenumber, k_θ, which gives

$$k_s^2 = k_x^2 + k_\theta^2$$

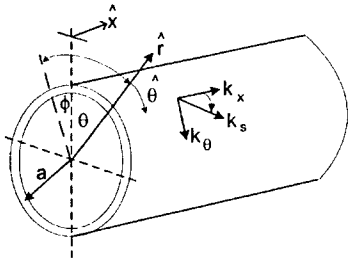

Figure 1: Diagram showing a semi-infinite cylinder and axial, circumferential and helical wavenumbers.

The axial wavenumber is thus given by

$$k_x = \sqrt{k_s^2 - k_\theta^2}$$

It can be seen that k_x is only real and hence propagating when $k_s^2 \geq k_\theta^2$. Otherwise, the wave is evanescent. Due to the closure of the pipe in the circumferential direction the wave propagation must be continuous in this direction, and hence the circumferential deformation takes the form of sine or cosine functions of $k_\theta a\theta$, where $k_\theta = n/a$, n is the mode number, a is the radius of a pipe, θ is the azimuthal angle and ϕ is the orientation

angle (azimuthal reference angle). In other words, two equally helical waves in opposite direction interfere in circumferential to form a standing wave giving such functions around the pipe. With the form of such a function in the circumferential direction shown in figure 2, at n= 0 (also known as the breathing mode) there is only stretching or contracting of the pipe wall, while at n = 1 (bending mode) and n ≥ 2 (lobar modes), the pipe cross section is in-extensional.

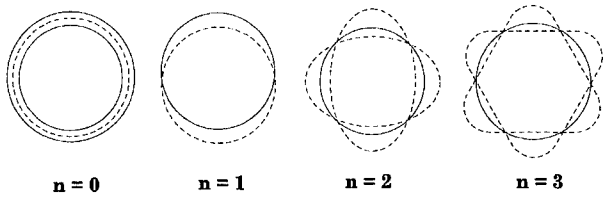

Figure 2: Forms of mode deformation of a pipe.

Table 1: Pipe data

E (N/m²)	ρ (kg/m³)	ν	a (mm)	h (mm)	η
3.55*10⁹	1430	0.4	33	1.9	0.025

Note : E is the Young's modulus, ρ is the density, ν is the Poisson's ratio, a is the radius, h is the thickness and η is the loss factor.

With the circumferential mode shapes formed in the pipe wall, the lobar modes propagate with the axial waveguide with wavenumber, k_x. For frequency less than the ring frequency, ω_r, the non-dimensional axial wavenumber, $k_{nb} = k_x a$, can be obtained from the equation (Variyart and Brennan [9])

$$\Omega^2 = \frac{\beta^2 (k_{nb}^2 + n^2)^2 (k_{nb}^2 + n^2 - 1)^2 + (1-\nu^2) k_{nb}^4}{(k_{nb}^2 + n^2)(k_{nb}^2 + n^2 + 1)}$$

where $\Omega = \omega/\omega_r$, $\beta^2 = h^2/12a^2$ and h is the thickness of the pipe. Since the interest of this work is the propagation of the n= 2 wave, only the axial wavenumbers for this mode are presented. Using the pipe data from Table 1, the real and imaginary wavenumbers are calculated for $\Omega < 1$ and are shown in figure 3. Before the cut-on frequency, all waves are decaying standing waves and after the waves cut on, there are two

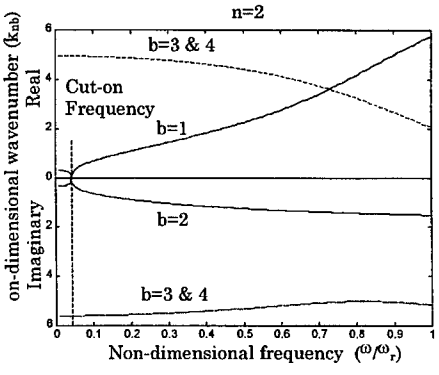

Figure 3: Dispersion curve of n = 2 mode

decaying standing waves (b = 3 & 4) of equal but opposite sign which was first shown by Fuller and Fahy [8], a near field flexural wave (b = 2) and a flexural wave (b = 1). Because the decaying standing and near field waves are evanescent, only the flexural wave can potentially propagate. The radial shell displacement w for a semi-infinite pipe is given by (Variyart and Brennan [9])

$$w(s,\theta,t) = \sum_{n=1}^{\infty}\sum_{b=1}^{4} W_n \left(\lambda_1 \cos(n\theta) + \lambda_2 \sin(n\theta)\right) e^{j(k_{nb}s-\omega t)}$$

where W_n is the radial amplitude of the n^{th} mode, $\lambda_1 = \cos(n\phi)$, $\lambda_2 = \sin(n\phi)$ and $s = x/a$.

3. Modal sensor for a pipe

A schematic diagram of a composite section of a pipe, which consists of an inner layer of pipe and an outer layer of sensor, is shown in figure 4. Generally, the mid-surface of the pipe itself is changed due to increasing thickness from a PVDF, however since the distributed PVDF sensor is very thin, it is assumed that the mid-surface of the pipe is unchanged. The assumption, that the sensor is perfectly bonded on the pipe, is also made so that the strain is continuously distributed through the composite pipe. It is well known that the PVDF sensor uses the direct piezoelectric effect, which converts mechanical strain to an electrical charge (Lee [10]). Without a skew angle, which is the angle between axes of the sensor and of the pipe, the effect in terms of an electric displacement may be represented (Lee [10] and Lee and Moon [1]) as

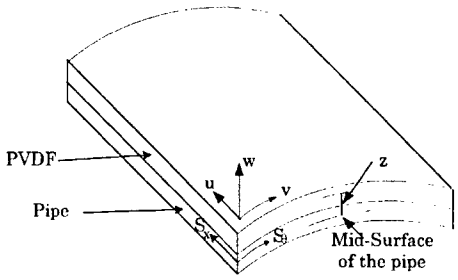

Figure 4: Schematic diagram (Not to scale) of composite section of a pipe

$$D_3 = \varepsilon_{33}E_3 + e_{31}S_\theta + e_{32}S_x \qquad \ldots(1)$$

where S_x and S_θ are the axial and circumferential strains, respectively, ε_{33} is the permittivity at constant stress (F/m), E_3 is the electric field (V/m) and e_{31} and e_{32} are the piezoelectric stress constants (C/m^2). The piezoelectric stress constants are given by

$$\begin{bmatrix} e_{31} \\ e_{32} \end{bmatrix} = \begin{bmatrix} E_{pv}/(1-\nu_{pv}^2) & \nu_{pv}E_{pv}/(1-\nu_{pv}^2) \\ \nu_{pv}E_{pv}/(1-\nu_{pv}^2) & E_{pv}/(1-\nu_{pv}^2) \end{bmatrix} \begin{bmatrix} d_{31} \\ d_{32} \end{bmatrix} \qquad \ldots(2)$$

where E_{pv} is Young's modulus of PVDF (N/m^2), ν_{pv} is Poisson's ratio of PVDF, and d_{31} and d_{32} are the piezoelectric strain constants (C/N).

Following Flugge's shell theory (Leissa [11], Flugge [12]), the axial (S_x) and circumferential (S_θ) strains at an arbitrary distance z from the mid-surface of a pipe may be expressed in terms of the pipe strain combination between stretching (extensional deformation) and bending (in-extensional deformation) strains of the mid-surface of the pipe. It is shown in figure 2 that the extensional deformation dominates the motion of the pipe for the n = 0 mode, while the deformation of n = 1 or higher modes is in-extensional (Flugge [12] and Timoshenko and Woinowsky-Krieger [13]). Since the main aim of this work is to develop a modal sensor for the n = 2 mode of the pipe, in which the stretching strain is equal to zero, only the bending strains in the axial and circumferential directions represent the motion of the pipe. Because one of the conditions for in-extensional deformation (Timoshenko and Woinowsky-Krieger [13]) is $\frac{\partial v}{\partial \theta} = -w$ and the ratio of the thickness to the radius of the pipe may be neglected in comparison with unity, and hence the axial and circumferential strains may be expressed as

$$S_x = -z\frac{\partial^2 w}{\partial x^2} \text{ and } S_\theta = -\frac{z}{a^2}\left(\frac{\partial^2 w}{\partial \theta^2} + w\right) \text{ for } n \geq 1 \qquad \ldots(3\text{ a, b})$$

In the case that the width of the sensor is much smaller than the wavelength of a propagating wave, the axial strain is approximately constant over the width of the sensor. The assumption will be justified later in terms of the maximum width of the sensor. Assuming the strains discussed above, the electric displacement given in equation (1) becomes

$$D_3 = \varepsilon_{33} E_3 - e_{31}\frac{z}{a^2}\left(\frac{\partial^2 w}{\partial \theta^2} + w\right) + e_{32} S_x \qquad \ldots(4)$$

In order to measure the charge generated from the PVDF sensor, a closed-circuit arrangement (Lee [10] and Callahan and Baruh [6]), in which the surface electrodes of both sides of the sensor are short-circuited, is employed so that the electric field E_3 is zero. With such an arrangement, the generated charge is approximately the average of the electric displacement integrated over the area of both sides of the effective surface electrodes. So

$$q(t) = \frac{1}{2}\left(\iint_{A_p(z=z_o+h_{pv}/2)} D_3 a\,dx\,d\theta + \iint_{A_p(z=z_o-h_{pv}/2)} D_3 a\,dx\,d\theta\right) \qquad \ldots(5)$$

where A_p is the effective surface area of the PVDF, h_{pv} is the thickness of the PVDF, $z_o = (h + h_{pv})/2$ is the distance from the mid-plane of the pipe to the mid-plane of the PVDF.

After some mathematical manipulation, the generated charge in the frequency domain of a cosine function modal sensor for the n = 2 mode is given by

$$q_c = 4\pi\lambda_1\left(A_2 \sum_{b=1}^{4} \frac{1}{k_{2b}} W_2 J_1(k_{2b} p_s) e^{jk_{2b}s_c} - A_6 \sum_{b=1}^{4} \frac{1}{k_{6b}} W_6 J_3(k_{6b} p_s) e^{jk_{6b}s_c} + \ldots \right) \ldots (6)$$

where s_c is the central location of a modal sensor normalised by the radius of a pipe, p_s,is the ratio of a half of width of the sensor to the radius of the pipe, $A_n = z_0 e_{31}(n^2-1)$ and $J_m()$ is the Bessel function of order m. The sensor detects a series of mode displacements, which are n = 2, 6, 10 and so on. In this work, the investigation is up to the n = 6 mode because the frequency range of interest is below the ring frequency, in which the maximum mode is n = 7 ($n_r \cong \sqrt{12}$ a/h; Fahy [7]).

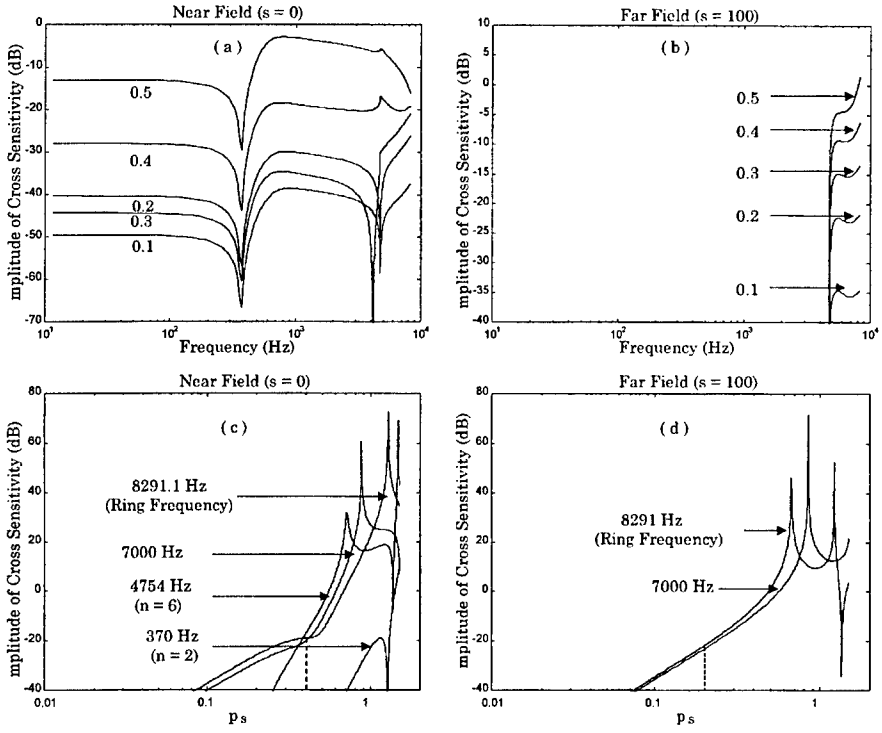

Figure 5: Cross sensitivities of the responses of the n = 6 mode to those of the n = 2 mode for various p_s (in (c) and (d), the frequency at 7000 Hz is chosen only to show a trend of the response).

Since the responses of the n = 2 and n = 6 modes depend upon p_s, it is therefore interesting to evaluate the cross sensitivity of the n = 2 sensor, which is its response to the n = 6 mode to that of n = 2 mode, for various

p_s. Using the pipe data given in Table 1, numerical assessments of the cross sensitivity in the near and far fields of an excitation force at the free end of the pipe are shown in figure 5. As expected, the cross sensitivity in the near field shown in figure 5a largely reduces at 370 Hz where the waves of the n = 2 mode cut on. This does not occur in the far field because there is no motion of the n = 6 mode before it cuts on. Figure 5b clearly shows that the cross sensitivity increases with increasing p_s. Using a criteria of –20 dB cross sensitivity, it illustrates in figure 5c and 5d that, with p_s up to 0.4 in the near field of the vibration source and to 0.2 at the far field, the responses of the n = 6 modes are insignificant. So, equation (6) can be reduced to the first term, which is the response of the n = 2 mode. To simplify it, the Bessel function of first order can be expanded as (Arfken [14])

$$J_1(k_{2b}p_s) = \frac{k_{2b}p_s}{2} - \frac{(k_{2b}p_s)^3}{2^3 2!} + \frac{(k_{2b}p_s)^5}{2^5 2!3!} - \ldots$$

where ! is the factorial. If the product of $k_{2b}b_s$ is less than unity, then higher orders can be ignored. Having the maximum wavenumber of the n = 2 mode at the ring frequency shown in figure 3 equal to approximately 6, p_s should be less than 0.16 to satisfy the above requirement. Hence, the generated charge becomes

$$q_c = 2\pi\lambda_1 p_s z_o e_{31}(n^2-1)\sum_{b=1}^{4} W_2 e^{jk_{2b}s_c} \qquad \text{for } n = 2 \qquad \ldots(7)$$

Since $p_s = p_w/2a$, where p_w is the width of the modal sensor, and the non-dimensional wavenumber of the n = 2 mode at the ring frequency $k_{2b} = 2\pi a/\lambda_{2r}$, where λ_{2r}, is the wavelength of the n = 2 wave at the ring frequency, the criterion for determining the width of the sensor is thus given by

$$p_w < \frac{\lambda_{2r}}{\pi} \approx \frac{1}{3}\lambda_{2r}$$

Since only the flexural wave can potentially propagate, it means that, if the width of the modal sensor is less than one third of the wavelength of the n = 2 flexural wave at the ring frequency, it only senses the response of the n = 2 mode. This width formula of the modal sensor for the pipe is similar to that done by Gu et al [2], who evaluated it for a flat plate.

Because the orientation of the wave is unknown, the sine shaped modal sensor is also required. To derive its modal sensor equation, the same procedure to obtain the expression of the generated charge for the cosine function shape is applied and it is given by

$$q_s = 2\pi\lambda_2 p_s z_o e_{31}(n^2-1)\sum_{b=1}^{4} W_2 e^{jk_{2b}s_c} \qquad \text{for } n = 2 \qquad \ldots(8)$$

The total generated charge, q_t, for a mode with an arbitrary orientation can be obtained by combining the amplitude from both sine and cosine shaped sensors in terms of the square root of the sum of the squares and is given by

$$q_t = 2\pi p_s z_o e_{31}(n^2-1)\sum_{b=1}^{4} W_2 e^{jk_{2b}s_c} \qquad \text{for } n = 2 \qquad \ldots(9)$$

The orientation angle can be determined as

$$\phi = \frac{1}{n}\tan^{-1}\left(\frac{\lambda_2}{\lambda_1}\right) = \frac{1}{n}\tan^{-1}\left(\frac{q_s}{q_c}\right) \qquad \ldots(10).$$

With a radial excitation force applied at the end of the pipe, the measured responses of the modal sensor are in the form of the transfer function, Coulomb/ Newton. Now, the amplitude of the n^{th} circumferential mode, W_n, of a semi-infinite pipe is given by (Variyart and Brennan [9])

$$\sum_{b=1}^{4} W_n e^{jk_{nb}s_c} = -\frac{j\varepsilon_n \Omega^2 F_o}{2\pi\omega^2 \rho h a^2}\sum_{b=1}^{4} A_b e^{jk_{nb}s_c} \qquad \ldots(11)$$

where $\varepsilon_n = 1$ for $n = 0$ and $\varepsilon_n = 2$ for $n \geq 1$, F_o is the amplitude of the excitation force and

$$A_b = \frac{(k_{nb}^2 + n^2)^2}{4\,k_{nb}\left[2\beta^2(k_{nb}^2+n^2)(k_{nb}^2+n^2-1)(k_{nb}^2+n^2-\frac{1}{2}) + (1-\nu^2)k_{nb}^4 - \Omega^2(k_{nb}^2+n^2+\frac{1}{2})\right]}$$

Hence, by combining equation (8) and (11) the transfer functions of the n = 2 sine and cosine shaped modal sensors are given by

$$T_{qc} = \frac{q_c}{F_0} = -\frac{j6\lambda_1 p_s z_0 e_{31}\Omega^2}{\omega^2 \rho h a^2}\sum_{b=1}^{4} A_b e^{jk_{2b}s_c} \quad \text{and}$$

$$T_{qs} = \frac{q_s}{F_0} = -\frac{j6\lambda_2 p_s z_0 e_{31}\Omega^2}{\omega^2 \rho h a^2}\sum_{b=1}^{4} A_b e^{jk_{2b}s_c} \qquad \ldots(12\ a,b)$$

Using equation (9) and equation (12a, b), the total transfer function is given by

$$T_q = \frac{q_t}{F_0} = -\frac{j6 p_s z_0 e_{31}\Omega^2}{\omega^2 \rho h a^2}\sum_{b=1}^{4} A_b e^{jk_{2b}s_c}\,. \qquad \ldots(13)$$

4. Experimental Setup and Procedure

Experimental work was conducted to calidate the theory presented in section 2 and 3. Modal sensors were fabricated by cutting 52 μm thick PVDF in the shape of a sine function with p_s = 0.009 approximately (both sine and cosine function modal sensors are the same but there are placed at a 90^0 circumferential angle to each other on the pipe, which is similar arrangement to Fuller and Brevart's experiment work [5]). The poling of the patches is arranged as shown in figure 6 and they were electrically connected together. Since the PVDF sheet has piezoelectric strain constants, $d_{31} = 23*10^{-12}$ m/V and $d_{32} = 3*10^{-12}$ m/V, with $E_{pv} = 2*10^9$ N/m^2 and $\nu_{pv} = 1/3$, then the piezoelectric stress constants are $e_{31} = 54*10^{-3}$ C/m^2 and $e_{32} = 24*10^{-3}$ C/m^2. A schematic diagram of the experimental setup is shown in figure 7. The 2.7 m plastic pipe, whose properties are given in Table 1, was suspended by cords. It was free at one end and had an anechoic termination at another end to ensure that its behaviour was as a semi-infinite pipe, which was confirmed by the experiment work done by Variyart and Brennan [9]. Both modal sensors shaped as sine and cosine functions were placed close together, 300 mm and 310 mm respectively from the excitation point. The pipe was excited at the free end by a small shaker, which was driven by a random signal supplied by an HP 3566A Signal Analyzer.

Figure 6: Arrangement of modal sensor

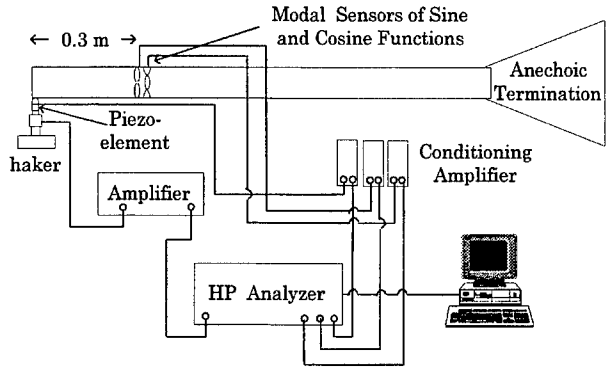

Figure 7: Experimental setup for evaluation of the modal sensor.

5. Results and Discussion

The total response of the n = 2 modal sensor, which is shown in figure 8, agrees reasonable well with the theory except at low frequencies, where the pipe behaves as a mass. Other discrepancies between the predicted

and measured results may also be due to inaccuracy in the shapes of the modal sensors and the significant response of the pipe at the cut-on frequencies of other modes, where there are large reflected waves.

Before the waves cut on, the pipe has very small displacements, so the orientation angle of the pipe of 13^0 shown in figure 9 was determined from equation (10) after the wave cut on at about 370 Hz.

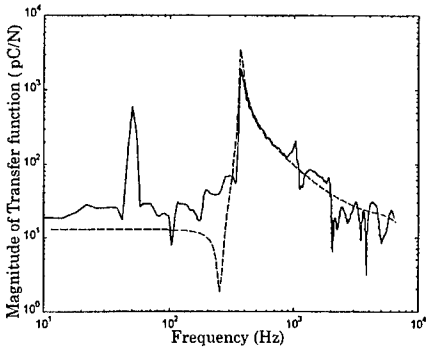

Figure 8: Amplitude of the total response measured by the modal sensors; —measured result; --- equation (13)

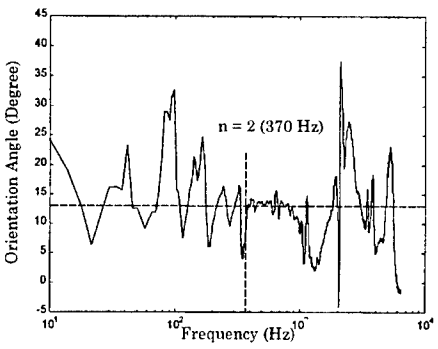

Figure 9: Orientation angle of the pipe with respect to the force position

6. Conclusions

This paper has described a theoretical and experimental investigation into a modal sensor for the n = 2 mode of a pipe. Based on Flugge's shell theory, the relationship between the charge generated from a PVDF sensor and the combination of the axial and circumferential bending strains has been established for the case of in-extensional deformation. By using the Bessel function to describe the pipe strains induced on the surface of a modal sensor, it was found that the modal sensor is sensitive to higher order modes as well as the n=2 mode. This is because the circumferential strain is coupled with the axial strain via the Poisson's ratio of the pipe. If the axial strain over the surface of the modal sensor is not constant, the higher order modes can be detected by the sensor. The cross-sensitivity is dependent upon the ratio of one half of the modal sensor width to the radius of the pipe (p_s). However, if p_s is small enough to keep the axial strain constant over its surface, the modal sensor will only be sensitive to the circumferential bending strain of the pipe so that it is only sensitive to the n = 2 mode. This means that the performance of the modal sensor in detecting only the n = 2 mode increases with the decrease of its sensitivity because of its surface area reduced. It is found

that to keep the axial strain of n = 2 mode constant over the frequency range of interest, the width of the modal sensor has to be less than one third of the wavelength of the n = 2 flexural wave at the ring frequency and hence it only senses the response of the n = 2 mode.

References

1. Lee, C.-K., and Moon, F.C., Modal sensors/actuators, ASME Journal of Applied Mechanics, 1990, **57**, pp. 434-441.
2. Gu Y., Clark R. L., Fuller C. R. and Zander A. C., Experiments on active control of plate using piezoelectric actuators and polyvinylidene fluoride (PVDF) modal sensors, ASME J. of Vibration and Acoustics, 1994, **116**, pp. 303-308.
3. Tzou H. S., A new distributed sensor and actuator theory for intelligent shells, J. of Sound and Vibration, 1992, **153**(2), pp. 335-349.
4. Tzou H. S. and Bao Y., Parametric study of segmented transducers laminated on cylindrical shells, Part 1 : Sensor patches, J. of Sound and Vibration, 1996, **197**(2), pp. 207-224.
5. Fuller C. R. and Brevart B. J., Active control of coupled wave propagation and associated power in fluid-filled elastic long pipes, Active 95, July 1995, pp. 3-14.
6. Callahan J. and Baruh H., Modal sensing of circular cylindrical shells using segmented piezoelectric elements, Smart Materials and Structures, 1999, No. 8, pp. 125-135.
7. Fahy F. J., Sound and structural vibration: radiation, transmission and response, Academic Press, 1985, pp.200-204.
8. Fuller C. R. and Fahy F. J., Characteristics of wave propagation and energy distributions in cylindrical elastic shells filled with fluid, J. Sound and Vibration, 1982, **81**(4), pp. 501-518.
9. Variyart W. and Brannan M. J., Measurement of flexural propagating waves in pipes using shaped PVDF modal sensors, ISVR Technical Memorandum, 1999, No. 847.
10. Lee C. K., Theory of laminated piezoelectric plates for the design of distributed sensors/actuators. Part I: Governing equations and reciprocal relationships, J. Acoust. Soc.Am., 1990, **87**(3), pp. 1144-1158.
11. Leissa A. W., Vibrations of shells, NASA SP-288, Washington DC: U.S. Gov Printing Office, 1973, pp. 7-13.
12. Flugge W., Stresses in shells, 2nd Edn., Springer-Verlag, 1962, pp. 210-216.
13. Timoshenko S. and Woinowsky-Krieger S., Theory of plates and shells, 2nd Edn., McGraw-Hill Book Company, INC, 1956, pp. 501-507.
14. Arfken G., Mathematical methods for physicists, 3rd Edn., Academic Press, INC., 1985, pp. 573-584.

A STUDY OF ROBUSTNESS OF ACTIVE CONTROL SYSTEMS FOR MASS LOADED SATELLITE PANELS

G. S. AGLIETTI[1], R. S. LANGLEY[2], E. ROGERS[3], and D. F. JOHNSON[2]

[1]School of Engineering Sciences, University of Southampton, Southampton SO17 1BJ, UK
[2]Department of Engineering, University of Cambridge, Trumpington Street, Cambridge CB2 1PZ, UK
[3]Department of Electronics and Computer Science, University of Southampton, Southampton SO17 1BJ, UK.

ABSTRACT

A Lagrange-Rayleigh-Ritz (LRR) model of a mass loaded satellite panel is developed to enable the effect of structural uncertainties on the stability of an active control system to be studied. The control is achieved via piezoelectric sensors and actuators and these elements are incorporated within the model. The effect of structural uncertainties is investigated via the Monte-Carlo method, and also via the FORM (First Order Reliability Method) approach to reliability assessment. Good agreement between the two methods is reported for an example system in which the Linear Quadratic Gaussian (LQG) control algorithm is employed, and the relative efficiency of the FORM approach is highlighted.

1. INTRODUCTION

Sensitive equipment on board spacecraft must often be mounted on structural panels where vibrations are induced by the functioning of other equipment. Microgravity experiments or accurately targeted optical instruments are, in fact, frequently mounted on panels where reaction wheels, crycoolers and other subsystems, act as vibration sources [1]. A typical satellite structure is subjected to vibration disturbances [2] at frequencies ranging from 1 –1000 Hz arising from items such as reaction wheels, gyroscopes, thrusters, and electric motors, and passive damping technology is often not an efficient or even a feasible way of reducing the induced vibration to acceptable levels. For this reason there has been much interest in the use of active vibration control systems. The current paper is concerned with aspects of such an active control system for an equipment loaded satellite panel.

Active feedback control of vibrations (both on spacecraft and more general systems) has attracted much attention in recent years [3], and much effort has been expended in the development of effective and robust control algorithms [4]. The need for robustness arises from the uncertainties which inevitably occur in a mathematical model of a real system. Such uncertainties may arise from modelling errors, or more fundamentally from a lack of knowledge of the detailed properties of the system, such as material constants, dimensions, and boundary conditions. Control engineers represent such effects as either structured or unstructured uncertainties, and modern control algorithms are intended to maintain robustness and stability under such perturbations. It can often be difficult to confirm that the control system does in fact perform well under realistic perturbations, due mainly to the lack of a suitable model for the exploration of these effects. Such a model is presented here for an actively controlled satellite panel.

The authors have previously developed an efficient Lagrange-Rayleigh-Ritz (LRR) model [5] of a mass loaded panel that is actively controlled through the use of piezoelectric patches as both sensors and actuators. When compared to the conventional Finite Element Method (FEM) [6] of structural modelling, the LRR approach requires relatively few degrees of freedom while retaining the essential physical characteristics of the real system. Thus the LRR approach provides a convenient way of assessing various control algorithms and strategies. Furthermore, it is shown in the present paper that the model enables statistical studies of the effects of uncertainties in the system properties. The model can be used in conjunction with Monte-Carlo simulations to estimate the probability of an unstable plant, or alternatively the FORM [7] (First Order Reliability Method) approach can be used to yield a more efficient (albeit more approximate) estimate of this probability. Each method is illustrated here by application to a Linear Quadratic Gaussian (LQG) controller.

2. MATHEMATICAL MODEL

In this work, attention is restricted to a mass loaded panel which is an acceptable compromise between problem complexity and the need to gain useful insights as to the benefits (and limitations) of linear active control schemes. A schematic diagram of the arrangement considered is shown in Figure 1, where the equipment mounted on the panel is modelled as lumped masses and the disturbances as point forces. The sensors and actuators for the active control system to be designed and

implemented are twin patches of piezoelectric material [8] bonded onto opposite faces of the panel, Figure 2.

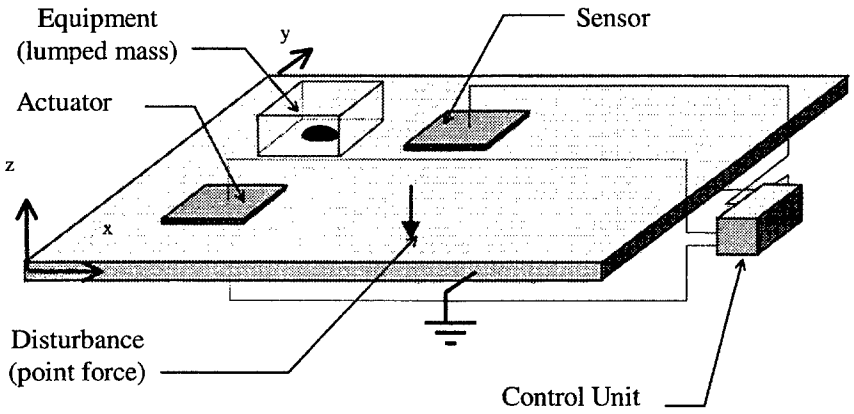

Figure 1: Mass loaded panel

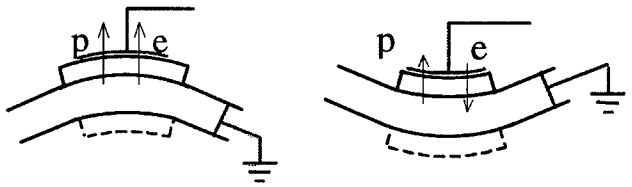

Figure 2: Piezoelectic patch and panel deformation

The Lagrange Rayleigh Ritz (LRR) procedure used to model this system is based on Lagrange's equations of motion which in the general case take the form:

$$\frac{d}{dt}\left(\frac{\partial T}{\partial \dot{q}_i}\right)-\frac{\partial T}{\partial q_i}+\frac{\partial U}{\partial q_i}=Q_i \qquad (1)$$

Here T and U are the kinetic and potential energies of the system, and q_i and Q_i are respectively the i-th generalised co-ordinate and generalised force. In this case the kinetic energy and potential energy (elastic and electric) can be expressed as

$$T = T_{pl} + T_{lm} + T_{pz}$$
$$U = U_{pl} + U_{pz_{elast}} + U_{pz_{elastelect}} + U_{pz_{elect}} \qquad (2a,b)$$

where T_{pl} , T_{lm} and T_{pz} are respectively the kinetic energy of plate, lumped masses and piezoelectric patches, U_{pl} is the elastic energy stored in the plate, $U_{pz\ elast}$ is the elastic energy stored in the piezoelectric patches, $U_{pz\ elastelect}$ represents the additional energy due to the voltage driven piezoelectric effect, and $U_{pz\ elect}$ is the electric energy stored due to the dielectric characteristics of the piezoelectric material.

The displacement field (out-of-plane displacement w) is described as a superposition of shape functions $S_{m,n}$ (consisting of the first *Nm,Nn* modes of the bare panel), multiplied by the time dependent modal co-ordinates $\phi_{m,n}$

$$w(x,y,t) = \sum_{m=1}^{Nm}\sum_{n=1}^{Nn} S_{m,n}(x,y)\phi_{m,n}(t) = \mathbf{s}^t\boldsymbol{\phi} \qquad (3)$$

where the *Nm*Nn*×1 column vectors **s** and $\boldsymbol{\phi}$ contain the shape functions and modal co-ordinates, respectively.

The external excitation consists of *Nf* point forces F_j acting on the panel at arbitrary locations, and therefore the generalised forces will have the form:

$$Q_i = \sum_{j=1}^{Nf} F_j \frac{\partial w}{\partial \phi_i} \quad \text{or} \quad \mathbf{Q} = \mathbf{S}_f\mathbf{f} \qquad (4)$$

where **f** is the Nf×1 column vector of forces and $\mathbf{S}_f$ is a matrix whose columns are the modal shape vectors $\mathbf{s}_f^t$ evaluated at corresponding force locations.

It is now necessary to compute each of the terms in (2), starting with kinetic energies. Each of these can be calculated using standard formulae [9], and their final forms in terms of the corresponding inertia matrices are:

$$T_{pl} = \frac{1}{2}\dot{\boldsymbol{\phi}}^t\mathbf{M}_{pl}\dot{\boldsymbol{\phi}} \qquad T_{pz} = \frac{1}{2}\dot{\boldsymbol{\phi}}^t\mathbf{M}_{pz}\dot{\boldsymbol{\phi}} \qquad T_{lm} = \frac{1}{2}\dot{\boldsymbol{\phi}}^t\mathbf{M}_{lm}\dot{\boldsymbol{\phi}} \qquad (5a,b,c)$$

The potential energy of the system is stored as the elastic energy of the plate and the elastic/electric energy of the piezoelectric patches. For the plate, using standard formula:

$$U_{pl} = \frac{1}{2}\phi^t \mathbf{K}_{pl} \phi \tag{6}$$

where $\mathbf{K}_{pl}$ is the plate stiffness matrix:

$$\mathbf{K}_{pl} = \iiint_{pl} \frac{E_{pl} z^2}{2(1-\nu^2)} \left(\frac{\partial^2 \mathbf{s}}{\partial x^2}\frac{\partial^2 \mathbf{s}^t}{\partial x^2} + \frac{\partial^2 \mathbf{s}}{\partial y^2}\frac{\partial^2 \mathbf{s}^t}{\partial y^2} + + 2\nu \frac{\partial^2 \mathbf{s}}{\partial x^2}\frac{\partial^2 \mathbf{s}^t}{\partial y^2} + 2(1-\nu)\frac{\partial^2 \mathbf{s}}{\partial x \partial y}\frac{\partial^2 \mathbf{s}^t}{\partial x \partial y} \right) dx dy dz \tag{7}$$

By using the same procedure for the piezoelectric patches it follows that

$$U_{pz\,elast} = \frac{1}{2}\phi^t \mathbf{K}_{pz\,elast} \phi \tag{8}$$

where $\mathbf{K}_{pz_{elast}}$ is the stiffness matrix associated with the patches, which is fully populated.

The additional stress which arises in the i-th piezoelectric patch when an electric field **e** is applied across the material, can be expressed as:

$$\sigma_{elect} = \begin{pmatrix} \sigma_{x_{elect}} \\ \sigma_{y_{elect}} \end{pmatrix} = \frac{E_{pz}}{1-\upsilon_i^2} \begin{pmatrix} d_{xz} + \nu_i d_{yz} \\ d_{yz} + \nu_i d_{xz} \end{pmatrix} e \tag{9}$$

Here d_{xz} and d_{yz} are the piezoelectric constants of the material, which is assumed to have pole direction z perpendicular to the plate. This additional stress, multiplied by the assumed stain, defines $U_{pz\,elastelect}$, which can be calculated by substituting (9) into the expression:

$$\mathbf{U}_{pz_{elastelect}} = \iiint_{pz} \frac{1}{2}\, \sigma^t_{elect} \varepsilon \; dx\, dy\, dz \tag{10}$$

where pz denotes the piezoelectric patches. Therefore it is possible to write the elastoelectric potential energy stored in the *Np* patches as:

$$U_{pz_{elastelect}} = \mathbf{v}^t \boldsymbol{K}_{pz_{elastelect}} \phi \tag{11}$$

where **v** is the column vector which contains the *Np* patch voltages.

Also the energy stored in the piezoelectric material as electric energy can be expressed as:

$$U_{pz_{elect}} = \iiint_{pz_i} \frac{1}{2} e\, d\, dx\, dy\, dz \tag{12}$$

where e is the electric field and d is the electrical displacement (charge/area). For each patch the electrical displacement is

$$d_i = \varepsilon_{pz_i} \mathbf{p}_i^t \mathbf{v} \tag{13}$$

where ε_{pzi} is the dielectric constant of the piezoelectric material of the i-th patch and and $\mathbf{p}_i$ is a vector with $1/h_{pz\,i}$ in the position of the i-th piezoelectric patch and zeros in all the other positions. Hence, an equivalent expression for the stored electric energy is

$$U_{pz_{elect}} = \frac{1}{2} \mathbf{v}^t \mathbf{K}_{pz_{elect}} \mathbf{v} \tag{14}$$

where the elements of the matrix $\mathbf{K}_{pz\ elect}$ are the capacitances of the piezoelectric patches.

All the energy terms are now available as functions of the generalised co-ordinates ϕ and $\mathbf{v}$. Hence it is a straight forward task to apply Lagrange's equations of motion (1) to yield:

$$\begin{aligned} &(\mathbf{M}_{pl} + \mathbf{M}_{pz} + \mathbf{M}_{lm})\ddot{\phi} + (\mathbf{K}_{pl} + \mathbf{K}_{pz_{elast}})\phi + \mathbf{K}^t_{pz_{elastelect}} \mathbf{v} = \mathbf{Q} \\ &\mathbf{K}_{pz_{elastelect}} \phi + \mathbf{K}_{pz_{elect}} \mathbf{v} = 0 \end{aligned} \tag{15a,b}$$

Equation (15a) results from differentiating the energy terms with respect to the modal co-ordinates ϕ and (15b) by differentiating these terms with respect to the voltages $\mathbf{v}$. This procedure has assumed that all modal co-ordinates and voltages are degrees of freedom of the system. In the case when all patches act as actuators, their voltages v_i are externally driven and hence equation (15b) is redundant. If all patches are to be used as sensors equation (15b) can be used to write an expression for the voltages as a function of the modal co-ordinates. This expression can then be substituted into equation (15a) to produce a complete set of equations in the unknown ϕ. The most general case arises when some of the patches act as actuators and others as sensors, and it is necessary to partition the matrix $\mathbf{K}_{pz}$ elastelect to separate out actuator and sensor contributions. To do this, let $\mathbf{v}_a$ and $\mathbf{v}_s$ be the sub vectors of the voltages at the actuators and sensors respectively, and denote the corresponding partitions of the matrix $\mathbf{K}_{pz}$ elastelect by $\mathbf{K}_{pza}$ elastelect and $\mathbf{K}_{pzs}$ elastelect respectively. Then equation (15a) can be rewritten as

$$\mathbf{M}\ddot{\phi} + \mathbf{C}_s\dot{\phi} + \left(\mathbf{K}_{elas} + \mathbf{K}_{pzs}\right)\phi = -K^t_{pza\ elastelect}\,\mathbf{v}_a + \mathbf{s}^t_f f \tag{16}$$

where all the inertia elements are included in the matrix **M** and the stiffness due to the elasticity in $\mathbf{K}_{elas}$. Also

$$\mathbf{K}_{pzs} = -K^t_{pzs_{elastelect}}\,\mathbf{K}^{-1}_{pzs_{elect}}\,K_{pzs_{elastelect}} \tag{17}$$

represents the contribution to the stiffness from the piezoelectric energy stored in the patches acting as sensors, where $\mathbf{K}_{pzs\ elect}$ is the partition of $\mathbf{K}_{pz\ elect}$ corresponding to the sensors. The presence of the term $\mathbf{C}_s\dot{\phi}$ also shows that damping has been introduced into the overall system.

Extensive verification of this modelling technique has been done by comparing the results produced with those obtained by modelling the same mass loaded panel using the FEM. Complete details of this verification can be found in [5].

3. CONTROL SYSTEM

The mathematical model developed in the previous section can be written in state space form to provide a standard mathematical basis for control studies [10]. The model in its final form is:

$$\begin{aligned}\dot{\mathbf{x}} &= \mathbf{A}\mathbf{x} + \mathbf{B}_v\mathbf{v}_a + \mathbf{B}_f\,\mathrm{f}\\ \mathbf{v}_s &= \mathbf{C}_v\mathbf{x}\\ \mathbf{w}_{out} &= \mathbf{C}_w\mathbf{x}\end{aligned} \tag{18a,b,c}$$

where:

$$\mathbf{x} = \begin{pmatrix}\phi\\ \dot{\phi}\end{pmatrix} \quad \mathbf{A} = \begin{bmatrix}\mathbf{0} & \mathbf{I}\\ -\mathbf{M}^{-1}(\mathbf{K}_{elas}+\mathbf{K}_{pzs}) & -\mathbf{M}^{-1}\mathbf{C}_s\end{bmatrix} \quad \mathbf{B}_v = \begin{bmatrix}\mathbf{0}\\ \mathbf{M}^{-1}K^t_{pza_{elastelect}}\end{bmatrix} \quad \mathbf{B}_f = \begin{bmatrix}\mathbf{0}\\ \mathbf{M}^{-1}\mathbf{s}^t_f\end{bmatrix}$$

$$\mathbf{C}_v = \left[-\mathbf{K}^{-1}_{pzs_{elect}}K_{pzs_{elastelect}} \quad \mathbf{0}\right] \qquad \mathbf{C}_w = \left[\mathbf{s}^t_{out} \quad \mathbf{0}\right] \tag{19 a,b,c,d,e,f}$$

$\mathbf{w}_{out}$ is the output displacement vector and $\mathbf{s}_{out}$ is the vector of the mode shapes evaluated at the output location. Given this state space description, it is possible to design a controller whose objective is to minimise the displacement at a specified point on the panel in the presence of point force disturbances acting at other location(s). The aim of the controller is the minimisation of the performance index:

$$J = \int_0^\infty (\mathbf{w}_{out}{}^t\mathbf{Q}\mathbf{w}_{out} + \mathbf{v}_a{}^t\mathbf{R}\mathbf{v}_a)dt \qquad (20)$$

where **Q** (positive semi definite) and **R** (positive definite) are weighting matrices of compatible dimensions to be selected by the designer. Appropriate selection of the entries in the weighting matrices **Q** and **R** allows a balance between minimisation of the output of the plant $\mathbf{w}_{out}$, (which is our main objective), and the minimisation of the control effort. The strength of the actuators as well as the power available for their functioning will in fact be limited (in any real application) and there is nothing to be gained in designing for a performance level which can be achieved, in theory, using the control system, if the result is an unrealistic control effort.

In practice the design of the controller is performed by solving an LQG problem, and once a satisfactory controller has been designed by this method it is applied to the actual plant. The frequency response of the plant with and without control is shown in Figure 3.

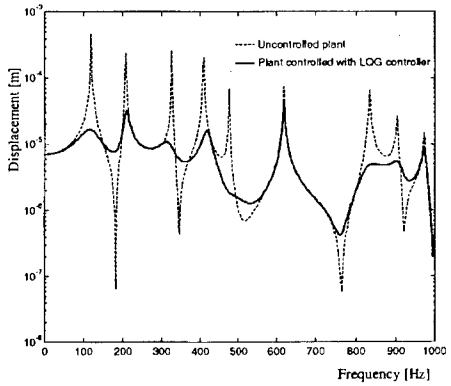

Figure 3: Frequency response to 1N input disturbance force for nominal plant with and without active control

4. MONTE-CARLO SIMULATIONS

As mentioned in the earlier sections, the physical properties of an engineering system can be subject to a degree of uncertainty. In the present case the material properties of piezoelectric patches and panel, could differ from the nominal design values. The panel boundary conditions may differ from the ideal simple supports which are assumed in the present analysis. Also the panel dimensions, and the locations of the piezoelectric patches are subject to a certain degree of

uncertainty. In this work, variation in the system dimensions is intended to make an allowance for uncertainties in the boundary conditions as well as uncertainties in the actual dimensions, since both these factors produce changes in the natural frequencies and mode shapes. It is of interest to study the effect of these uncertainties on the performance of an active controller which has been designed on the basis of the nominal plant, and this issue is addressed in the present section via Monte Carlo simulations. The statistical properties of various physical parameters have been specified, and these properties have then been used in conjunction with a random number generator to produce an ensemble of structures. By applying an active controller (designed on the basis of the nominal system) to each member of the ensemble, it is possible to determine the probability of an unstable system.

5. FORM ANALYSIS

The Monte-Carlo technique described in the previous section tends to be computationally intensive, since a large ensemble of random plants needs to be analyzed to ensure a statistically accurate result, particularly when the probability of an unstable plant is relatively low. An alternative approach is to employ the FORM (First Order Reliability Method) approach, in which the uncertain parameters (the system dimensions, damping etc) are considered to be components of a vector $\mathbf{X}$, and the 'safety' of the system is described by a function referred to as the 'safety margin' $g(\mathbf{X})$ [7]. The system is considered to have failed if

$$g(\mathbf{X}) \leq 0. \tag{21}$$

In the present application $g(\mathbf{X})$ can be taken to be the negative of the real part of the least stable pole. The "exact" probability of failure is given by the integral of the joint probability density function of $\mathbf{X}$ over the failure region. In general this integral is a very difficult quantity to compute, due to the fact that $\mathbf{X}$ can be of high dimension and $g(\mathbf{X})$ can have a complex geometry. The FORM approach seeks an approximate probability of failure by transforming the variables $\mathbf{X}$ to a set of uncorrelated Gaussian variables $\mathbf{Z}$, each of which has zero mean and unit standard deviation. The probability of failure is then estimated as

$$P_f = \Phi(-\beta), \qquad (22a,b)$$

$$\beta^2 = \min\{Z^T Z \mid g(X) = 0\}$$

where Φ is the cumulative normal distribution function. Geometrically, β is the shortest distance between g(**Z**) and the origin, as shown in Figure 4. Equation (22a) is exact if the safety margin g(**Z**) is a linear function; otherwise the result is an approximation which is based upon linearising the safety margin about the point of closest approach to the origin. Equation (22b) represents a constrained optimisation problem, which can be solved numerically providing g(**X**) can be evaluated for a specified value of **X** – the present LRR approach provides an efficient way of doing this.

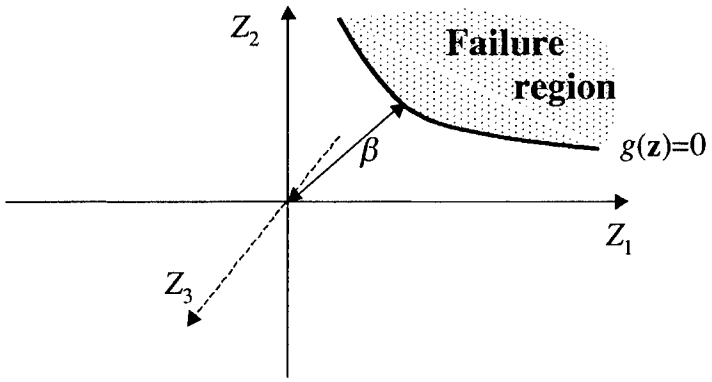

Figure 4: Geometric Problem

6. RESULTS

The nominal system considered is the simply supported mass loaded aluminium panel (305mm by 203mm with thickness 1.52mm) shown in Figure 1, with piezoelectric patches acting as sensors and actuators, full details can be found in reference 4. The panel length, breadth, and thickness have been taken to be Gaussian random variables with standard deviations of respectively 0.33mm, 0.33mm, and 0.066mm. The damping has also been taken to be random, with a standard deviation of 3% of the nominal value. It can be noted that the relatively large variation in the system dimensions is intended to make an allowance for uncertainties in the boundary conditions as well as uncertainties in the actual dimensions.

In the Monte Carlo simulations, an ensemble of 1700 plants was considered, and it was found that 20 were unstable, giving a failure

probability of 0.0118. The poles yielded by a sample of 550 of the simulations are shown in Figure 5; the poles of both the controlled and the uncontrolled plant are shown in the figure. It can be seen that some of the poles of the controlled plant have a very high degree of variability, e.g. pole number 18 becomes unstable, for some perturbed plants.

The FORM analysis yielded β=2.27, which corresponds to a failure probability of around 0.012. The failure point (i.e. the point satisfying equation (34)) lies on the portion of $g(\mathbf{X})$ that is associated with pole 18, and thus both the probability of failure and the mode of failure are in good agreement with the Monte Carlo results. This analysis required a small fraction of the computer time needed for the Monte Carlo studies (typically 30 to 60 calls to the function $g(\mathbf{X})$), and thus the combination of FORM with the present LRR modelling technique provides a very efficient method of studying the robustness properties of an active control system.

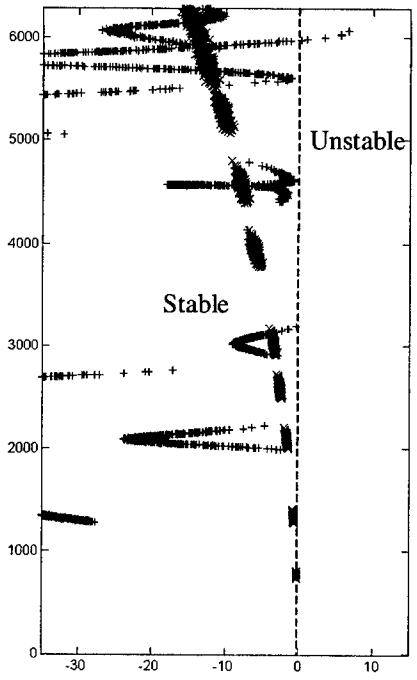

Figure 5: Poles of the plant (x open loop, + closed loop).

7. CONCLUSIONS

The present paper has presented a mathematical model of an actively controlled mass loaded spacecraft panel, which was then used to investigate the robustness of the active control system. The mathematical model captures the essential physics of the system in a realistic way, while avoiding the use of an excessive number of degrees of freedom. The efficiency of the model is such that various control strategies can rapidly be assessed, and furthermore it is feasible to perform Monte-Carlo simulations to investigate the effect of random perturbations in the system properties. Furthermore, FORM can be employed to yield an even more efficient assessment of the system robustness. The results reported here are of a preliminary nature and are designed to illustrate the methodology rather than provide a definitive assessment of a particular controller for a specific system. The present approach can clearly aid control system design both in terms of algorithm development and in the application of an algorithm to a specific system.

REFERENCES

[1] H.R. Stark, C. Stavrinidis, *"ESA microgravity and microdynamics activities - An overview,"* Acta Astronautica **34**, pp. 205-221, 1994.

[2] S. J. Dine, D. E. L. Tunbridge, P. P. Collins, *"The vibration environment on a satellite in orbit,"* IEE Colloquium on "High Accuracy Platform Control in Space", 1993.

[3] C.R Fuller, P.A. Nelson, S.J. Elliott, *"Active Control of Vibrations"*, London, Academic Press, 1996.

[4] K. Zhou, J. Doyle, K. Glover, *Robust and optimal control*, Prentece Hall, 1996.

[5] G.S.Aglietti, S.B.Gabriel, R.S.Langley, E.Rogers, *"A Modelling Technique For Active Control Design Studies With Application To Spacecraft Microvibrations"*, J. of The Acoustical Society of America, 102 (4), pp 2158-2166, (1997).

[6] O. C. Zienkiewicz, *The Finite Element Method*, (McGraw-Hill, London) 1977.

[7] H.O. Madsen, S. Krenk, N.C. Lind *Methods of Structural Safety*, Prentice-Hall, New Jersey, 1986.

[8] D.J. Jones, S.E. Prasad, J.B. Wallace, Piezoelectic materials and their applications, Key Engineering Materials, Vols.122-124, 1996.

[9] S Timoshenko, "Vibrational Problems in Engineering" 4th Edition.

[10] B. D. O. Anderson, J. B. Moore, *Optimal Control Linear Quadratic Methods*, (Prentice Hall, Englewood Cliffs) 1989.

THE DEVELOPMENT OF A TUNED DAMPER FOR REDUCING NOISE FROM RAILWAY TRACK.

D.J. Thompson, C.J.C. Jones and T.P. Waters
Institute of Sound and Vibration Research, University of Southampton,
Highfield, Southampton SO17 1BJ, UK

ABSTRACT

Rolling noise from railways is produced by vibrations of both the wheel and the track. A promising means to reduce the component of noise radiated by the track is to increase the damping experienced by the rail. This reduces the length over which vibrations are transmitted along the rail and thereby the noise radiated. To achieve this, a tuned mass-spring absorber system has been designed. To cover a wide range of frequencies, multiple tuning frequencies are used along with a material with a high loss factor. Suitable materials have been found from tests on samples and prototypes of the damper have been built and tested, both in the laboratory and in the field. Results are very promising with reductions of the track component of noise of the order of 6 dB.

1. INTRODUCTION

The most important source of environmental noise from railway operations in many countries is rolling noise. Even where locomotive noise or warning horns produce higher maximum levels, the longer duration associated with the rolling noise of the rest of the train means that it remains a very important source for the overall average level. The usual counter-measure adopted in recent years is to install high noise barriers alongside the track. These are costly and intrusive. Reduction of noise at the source can be more attractive, but this requires a thorough understanding of the mechanisms.

Rolling noise is generated by the excitation of the wheels and track by the combined roughness of their running surfaces. The vibration response of the wheels, the rails and the sleepers beneath them all contribute significantly to the overall spectrum of noise. The relative importance of these different sources depends on the design of wheels and track, the roughness spectrum and the speed of the train. In many situations the rail is the greatest overall source. A theoretical model, 'TWINS', for the generation of this noise has been available for some time [1, 2]. This has led to the investigation of a number of noise-reducing technologies. This paper describes the development and testing of a rail damping device for reducing the vibration of the rail.

Figure 1 shows a typical one-third octave band spectrum of the sound power predicted for a single wheel and the associated track vibration. This prediction is for a train speed of 100 km/h and a roughness spectrum for tread-braked rolling stock, which are typical for freight traffic in Europe. In this case, the sleeper is the dominant source of noise below 400 Hz and the wheel is the major source in the 1600 Hz band and above. Overall the rail is the greatest

source here, being responsible for the broad peak in the spectrum from the 500 Hz to the 2000 Hz band. This also coincides with the peak in the roughness excitation. It can be seen that the sound radiation from the vertical vibration of the rail is greater than that from the lateral component.

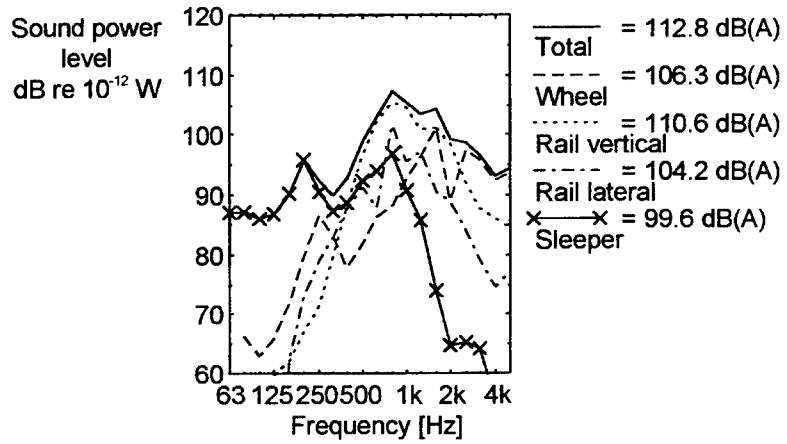

Figure 1. Predicted rolling sound power generated per wheel for a standard 920 mm freight wheel running on a standard track at 100 km/h.

For the noise from the track, it has been shown that the stiffness of the rail pads, located between the rail and sleepers, has a strong influence on the levels of noise. It controls the balance of the vibration response of the rail and sleeper and the rate of decay of vibration along the rail [3, 4]. The sound power produced by the rail in a particular frequency band is inversely proportional to the decay rate Δ in dB/m, since a high decay rate implies a short radiating length. An optimum stiffness of rail pad exists at which the rail and sleeper components of sound are equal, However, this is very stiff compared to the pad stiffnesses now commonly adopted. Low stiffness pads have become standard in the rail industry as they reduce high frequency forces transmitted to the sleepers and to the ballast. This reduces track component damage and the tamping-related costs of track maintenance. Furthermore there is evidence that such stiff pads may be counter-productive for noise by leading to an increase in the roughness of the rail head.

The starting point for reducing the rail noise has therefore been taken as a typical ballasted track with UIC 60 rails, monobloc concrete sleepers and a rail pad stiffness of 200 MN/m per pad. The spectra presented in Figure 1 have been calculated for this track. A preliminary study showed that constrained layer damping treatments would only be effective above 2 kHz. In order to obtain high damping of the rail at lower frequencies, a damped mass-spring absorber system has been considered. An initial parameter study is used to show its effectiveness and to identify the optimal configuration. This is followed by more detailed analysis of a practical implementation.

2. INITIAL STUDIES OF TUNED ABSORBERS

2.1 Methodology

Initially the concept of a tuned absorber system was studied using a simple track model to identify appropriate parameters. Within the TWINS software a number of track models exist. For these initial studies, a model is used in which the rail is represented as a Timoshenko beam on a continuous spring-mass-spring foundation representing the rail pad, sleeper and ballast.

The effect of damping devices on the rate of decay of vibration along the rail has been calculated using a two step approach. Firstly, the effect of the damping treatment on the rail vibration is calculated for an unsupported rail. This frequency-dependent decay rate is then added to that for the untreated rail in track. The sound power is calculated by modifying the component associated with each wave according to the difference in combined decay rate.

Figure 2 shows the effect of a single continuous mass/spring system. This is tuned to a frequency of 800 Hz, has a mass per unit length of 17.5 kg/m and a loss factor of 0.35. It is compared with decay rates measured on a rail *in situ*.

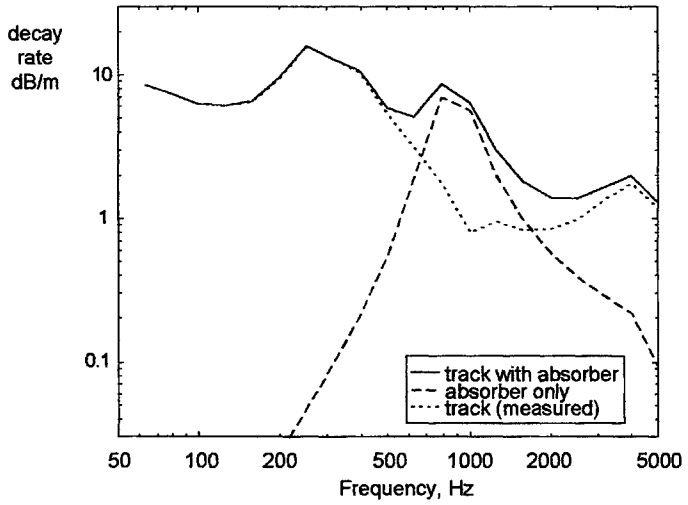

Figure 2. Track decay rates for vertical vibration of the reference track with a continuous tuned absorber system added.

For the untreated rail in track, at low frequencies, the waves in the rail have a high rate of attenuation because of the stiffness of the foundation. Around 400 Hz, for vertical vibration, a resonance of the track occurs in which the rail vibrates on the stiffness of the pad. Above this frequency, wave propagation occurs freely and the decay rate for the untreated track declines rapidly. This dip corresponds to the peak in the rail noise spectrum, and an effective rail damper has to increase the decay rate in this frequency region.

2.2 Single frequency system for vertical and lateral motion

The computation represented by Figure 2 for the decay rates of vertical and lateral bending waves in the track is efficient and has been implemented within an automatic procedure to vary the parameters of tuning frequency and damping for the absorber. The dynamic model of the track, which is a relatively quick part of the overall noise calculation procedure, was used to calculate the decay rates for a large number of parameter combinations. The corresponding components of the rail sound power were predicted using TWINS for a baseline case, and the change in each has then been estimated from the change in their decay rates obtained from the track model. The mass/spring system is assumed to operate at the same frequency for both vertical and lateral waves.

Figure 3 shows the variation of predicted rail noise reduction as a function of the tuning frequency of the absorber for different train speeds. Here a mass of 10 kg per metre of rail has been assumed. The figure shows that the best tuning frequency is around 900 Hz for 100 km/h and is not strongly dependent on the train speed.

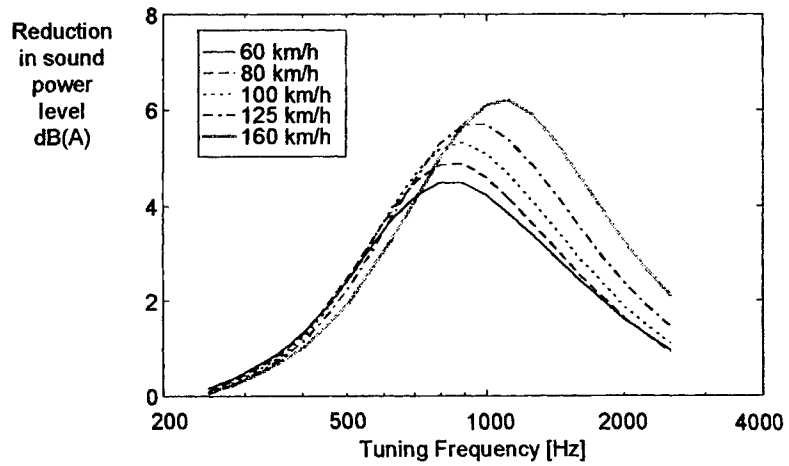

Figure 3. Reduction in rail noise from the reference track for an absorber of mass 17.5 kg/m and loss factor 0.35 as a function of tuning frequency.

Figure 4(a) shows the effect of loss factor of the damper for a train speed of 100 km/h. The benefit increases with loss factor for values up to about 0.35 but, above this, little extra noise reduction is expected. The variation of the sound reduction with the active mass of the absorber is shown in Figure 4(b). It can be seen that there is no optimum mass, but improved noise reduction is obtained as the mass is increased. The practical limit of the mass of the absorber is about 17.5 kg/m due to space constraints as will be seen later. This gives a reduction of 5.3 dB.

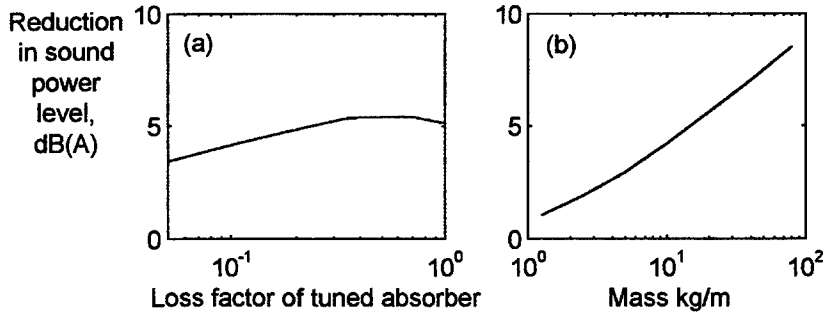

Figure 4. Effect of parameters of single tuned absorber on reduction in rail noise for tuning frequency of 900 Hz. (a) Effect of loss factor for mass of 17.5 kg/m. (b) Effect of absorber mass for a loss factor of 0.35.

2.3 Two-frequency systems

Increasing the damping loss factor broadens the peak in the decay rate in Figure 2, but also reduces its height. Another method of broadening the peak is to use multiple tuning frequencies. The same procedure as above has been used to study the noise reduction for a system with two tuning frequencies. The total added mass allowable is assumed to be constant at 17.5 kg/m. The system is described by three parameters that can vary: its first natural frequency, the ratio of the two tuning frequencies and the ratio of the two masses. Identical tuning frequencies are assumed to act in both vertical and lateral directions. Figure 5 indicates the combinations of parameter values considered. Where a noise reduction greater than 5.5 dB is found this is indicated by a plus sign and the optimum configuration is shown by a circle. The optimum configuration gave a noise reduction of 5.9 dB(A), a gain of 0.6 dB over a single-frequency absorber. Moreover, a two-frequency system is more robust for variations in train speed, train type or temperature which will affect the stiffnesses.

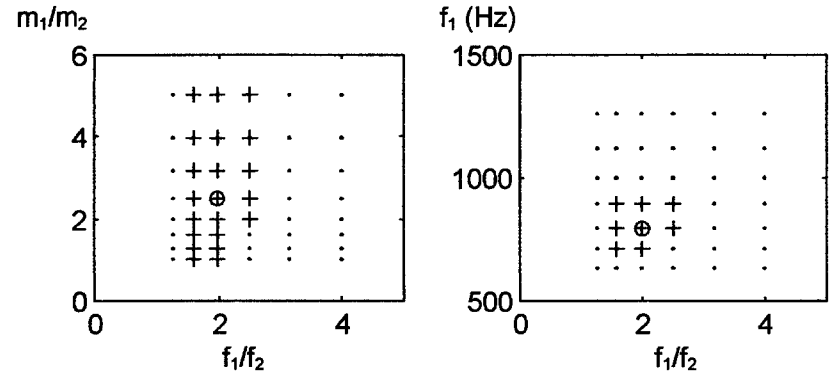

Figure 5. Range of parameter study for two separate absorbers: + indicates noise reductions greater than 5.5 dB(A), o indicates optimum configuration.

A three-frequency system was also studied in the same way, with variations allowed in five parameters. However it was found to give much smaller improvements over the two-frequency system for the same overall mass. This benefit was considered to be insufficient to justify the added cost of a three-frequency system.

Although the two-frequency system could be produced using two separate single-degree-of-freedom systems, an alternative was explored in which a two-degree-of-freedom system is added to the rail. Not all combinations of frequency and mass ratios are possible, as shown in Figure 6, but the optimum system that was found corresponds closely to the optimum of the two SDOF systems, and the noise reduction is identical.

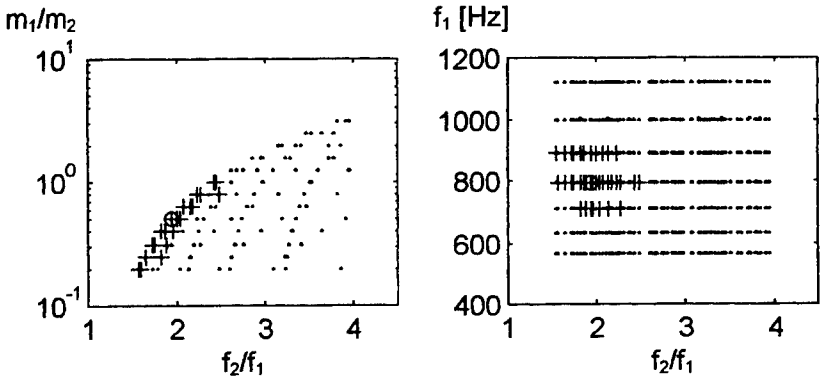

Figure 6. Range of parameter study for stacked two-frequency absorbers. +: noise reductions greater than 5.5 dB(A), o: optimum configuration.

In summary, the parameter study indicates an optimum system with tuning frequencies at 800 Hz and 1600 Hz operating both for vertical and lateral directions. It has subsequently been discovered that the decay rates used for track (Figure 2) were affected by the measurement having been taken at about 5°C; for a higher temperature the pad stiffness would be lower. In order for the solution to be robust for a range of temperatures, a modified system is considered with tuning frequencies at 630 Hz and 1350 Hz.

3. IMPLEMENTATION

Railway track is designed with the criteria of safety, low cost of maintenance and standardisation as the highest priorities. For new methods of achieving noise reduction to be accepted in the short or medium term, they must be capable of being fitted to the established infrastructure design with minimal change to railway practice. Therefore, the present development has concentrated on a design of rail damper that may be fitted to the standard UIC60 rail section, either at manufacture or as a retro-fit. It is confined to a space that does not interfere with the handling machinery for track laying and

maintenance, nor with the rail clips. The allowable envelope for a continuous absorber is shown in Figure 7.

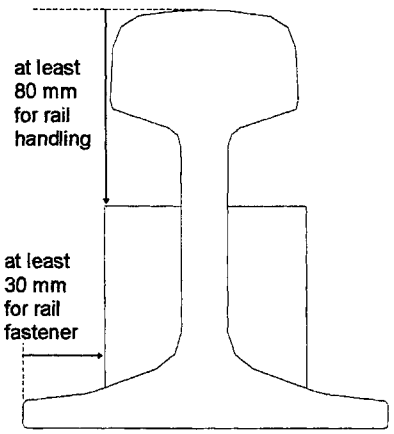

Figure 7. The UIC 60 rail section showing the space occupied by the absorber that allows normal track construction and maintenance.

A rail absorber was designed having a total mass per unit length of 17.5 kg/m, with two masses on each side of the rail, separated from each other and from the rail by layers of an elastomeric material. The design was made symmetrical in order to avoid introducing cross-coupling between the vertical and lateral dynamics of the rail. The system has two resonances in the vertical direction in the desired ratio, but this was not possible for the frequencies in the lateral direction. However, the vertical rail vibration is the dominant noise source for this track (see Figure 1).

Finite element models of the rail and absorber cross-section were used to study the design in detail. These led to the specification for an elastomer having a Young's modulus of around 16 MNm^{-2} and a loss factor greater than 0.35. The desired material properties should be achieved over a suitable working temperature range. The specification was sent to a number of suppliers and materials were developed by measuring the dynamic Young's modulus and loss factor of a number of material samples over the frequency range from 300 Hz to 3000 Hz, thereby guiding the suppliers toward the most suitable material. In addition, a number of test samples of 15 cm lengths of rail were assembled with the absorber using the different materials. These were tested to ensure that the expected tuning frequencies were obtained in practice.

Figure 8 shows the temperature dependence of the material parameters for one of the materials found to be acceptable and which was used in subsequent prototypes. It can be seen that, in order to meet the requirement for a high loss factor, the transition between the glassy and rubbery phases of the elastomer occurs in the working temperature range. There is therefore a high dependence of both parameters with frequency and temperature.

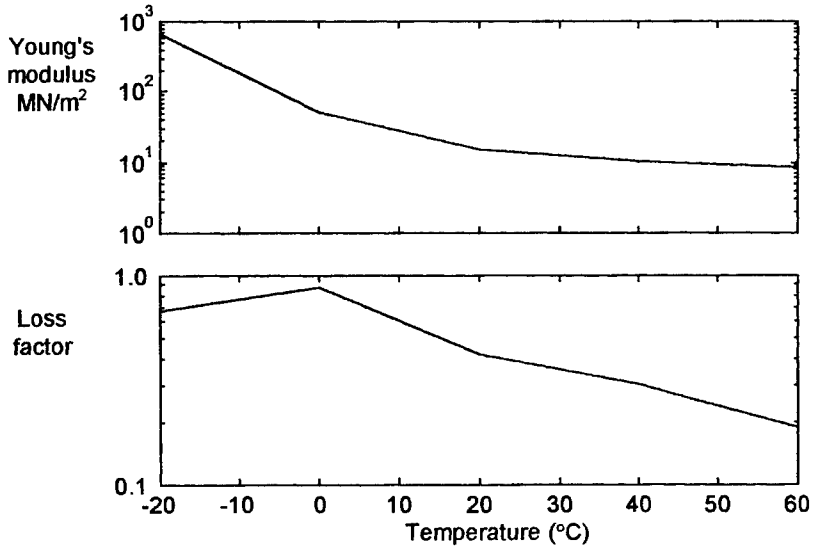

Figure 8. The temperature dependent Young's modulus and loss factor of the elastomer.

4. DETAILED MODELLING

For the detailed evaluation of the specific design, a periodic structure model of the track is used [5]. In this, a 10 mm slice of the rail cross-section and damper are modelled using finite elements. The slice is then assumed to be repeated to form an infinite structure on which the modes of vibration of the cross-section propagate as waves with complex wave numbers.

For this purpose the finite element mass, stiffness and damping matrices for the rail cross-section with the absorber were obtained using 8-noded hexahedral elements. The damping matrix was assembled using the element stiffness matrices, each multiplied by an appropriate element loss factor. In this way the model was able to account for the different material damping of the elastomeric and steel components of the composite cross-section.

The decay rates were calculated using three sets of material properties of the elastomer, that are valid at different frequencies. An interpolation scheme was then used between the three curves obtained to give the decay rates corresponding to the stiffness that applies at intermediate frequencies. The resulting predicted curves for the vertical and lateral decay rates of the free rail with absorbers are presented in Figure 9.

A 4 m length of rail was fitted with the absorber and measurements of the decay of vibration in the rail were made. At low frequencies the decay rate was measured indirectly by modal analysis. At frequencies above about 700 Hz, where this was no longer possible due to very high modal damping, the decay rate was sufficient for it to be measured directly within the 4 m length. The

measured vertical and lateral decay rates are given in Figure 9 for comparison with the predictions. At high frequency the measured decay rates are a little higher than those predicted for the pure bending waves because of the participation of wave types corresponding to deformation of the rail section in the measured response of the rail.

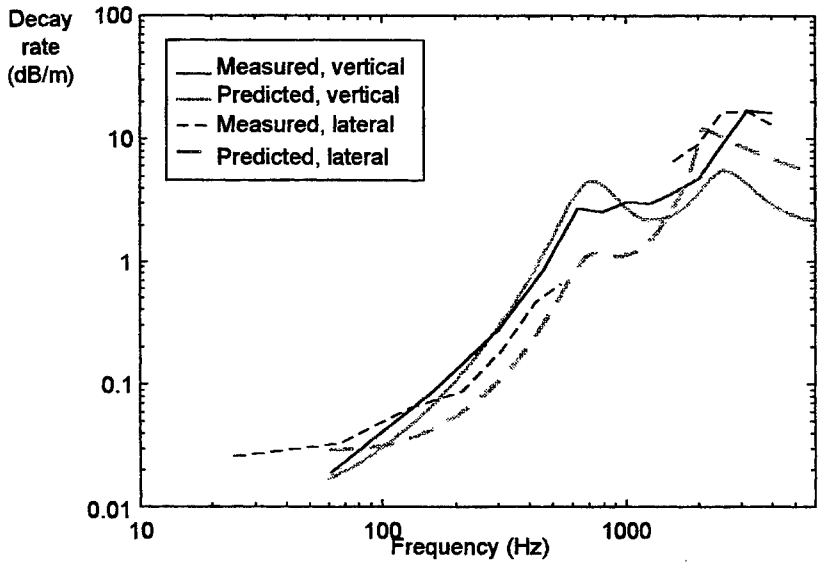

Figure 9. Predicted decay rates compared to measurements on a 4 m length of freely suspended rail.

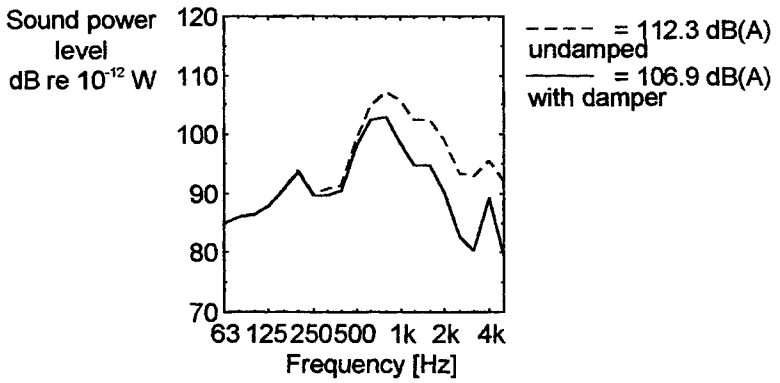

Figure 10. Predicted rail sound power with and without the absorbers.

The predicted noise reduction for these decay rates can be seen in Figure 10. The decay rates measured on the 4 m samples have been used in this prediction. Thus at a rail temperature of 20°C a reduction of the rail noise of 5.4 dB(A) is expected. From the predicted performance at this temperature the

reduction is 5.6 dB(A). Estimates of the sound power radiated by the active masses themselves suggest that the noise reduction would be compromised by less than 1 dB(A) by this source, due to the high loss factor and small area.

A prediction of the decay rates for the elastomer properties at 0°C has also been made. This shows that, due to the stiffening of the material and consequent raising of the operating frequencies of the absorber, its benefit would be reduced to 3.4 dB(A). This effect must be taken into account in further refinement of the absorber for production. However, it must also be offset against the changes in decay rate of the untreated track with temperature.

5. FIELD MEASUREMENTS

Field measurements on a track fitted with a prototype rail absorber were conducted in May 1999 as part of the 'Silent Track' project [6]. The decay rates in the track were measured using impact excitation and rolling noise measurements were made using a test train. The rail temperature was in excess of 30°C, which meant that the rail pads were softer than was the case in the previous decay rate measurements (Figure 2), and the rail noise component would be higher. On the other hand, the rail damper elastomer would also have a lower stiffness and therefore a lower tuning frequency. From Figure 3 it can be seen that this will reduce the performance of a single frequency damper, and the same is the case for the two-frequency damper.

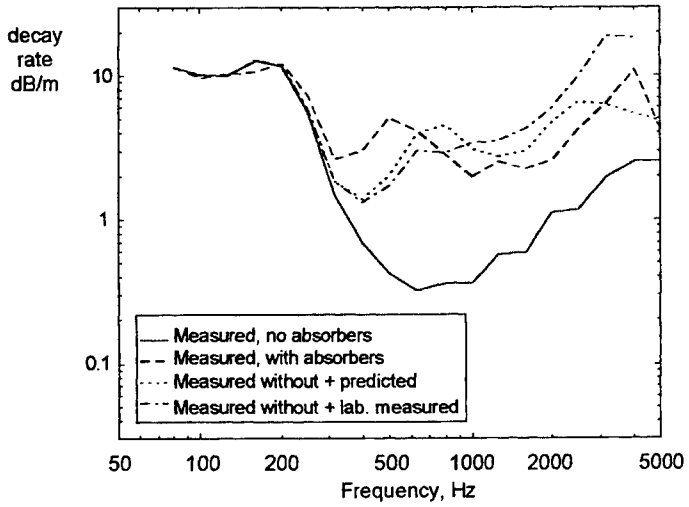

Figure 11. Measured decay rates in track compared to predictions and laboratory measurements.

The measured decay rates for vertical bending waves at the field test site are shown in Figure 11. The decay rate for the track without absorbers is lower than that in Figure 2 due to the higher temperature. It is used here as the basis to which either the predicted or laboratory measurements of decay rate

for the freely supported rail (Figure 9) have been added. In both cases, results corresponding to 20°C have been used. The decay rates achieved (measured with absorbers) compare well with those predicted using either method. However the first frequency of the absorber can be seen to occur at a lower frequency in the track measurements (around 500 Hz) due to the higher temperature.

For the noise measurements, a weighted average of the sound pressure at three microphones, 3 m from the near rail at different heights, was used. The levels measured from a test train passing at 100 km/h with and without the absorbers are shown in Figure 12. The measurement shows an overall reduction of 5.6 dB(A).

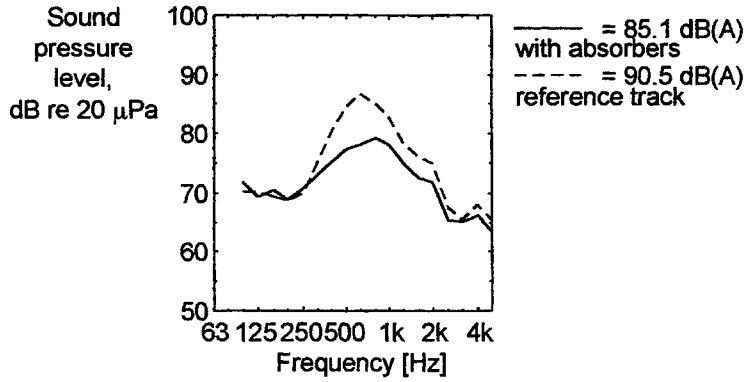

Figure 12. Results of measurements of rolling noise at 100 km/h using a vehicle fitted with a noise reducing wheel. Average from three microphones at 3 m from near rail.

In order to show the reduction in track noise most clearly, these results are for a low-noise wheel [7,8]. This had no effect on the track component of noise. However, the overall measured noise is influenced significantly by the noise from the wheel in the 1600 Hz band and above. The full reduction of the track noise is therefore not seen in these bands. Estimates in which the wheel noise is removed indicate a reduction of 6.0 to 6.2 dB(A) in the track noise due to the absorber. These results are consistent with the predictions.

6. SUMMARY

The stages in the development of a damping device to reduce the rail component of rolling noise have been described. A damped tuned absorber has been chosen to give a broad band reduction in noise in the region 500 to 2000 Hz. An initial parameter study using an efficient method was used to obtain the main parameters which were realised in a design using steel masses and an elastomer formulated to a specification. Samples were tested in the laboratory using a combination of modal analysis and direct decay rate

measurements. This confirmed the results of detailed modelling, which takes account of the temperature- and frequency-dependence of the material. This modelling can therefore be used as an accurate design tool for further development and refinement of the absorber. Field tests of a prototype absorber have demonstrated that it reduces rail noise by about 6 dB(A) for a modern track design with soft rail pads. At 0°C the benefit is expected to be about 3 dB(A), but this can be improved by alterations to the material specification. For a track with a stiffer pad the reduction will be much smaller, but the design has been optimised for soft pads as they are likely to become more widely used for other reasons. Apart from the additional weight, a rail fitted with the absorber can still be handled using conventional machinery.

7. ACKNOWLEDGEMENT

This work was undertaken as part of the Silent Track project funded by the European Union (Brite Euram project BE 96-3017, contract BRPR-CT96-0258). Collaboration with Corus Rail is gratefully acknowledged.

8. REFERENCES

1 Thompson, D.J., Hemsworth, B. and Vincent, N., Experimental validation of the TWINS program for rolling noise, part 1: description of the model and method. *J. Sound. Vib.*, 1996, **193**(1), 123 - 136.

2 Thompson, D.J., Fodiman, P. and Mahé, H., Experimental validation of the TWINS program for rolling noise, part 2: results. *J. Sound. Vib.*, 1996, **193**(1), 137 - 148.

3 Vincent, N., Bouvet, P., Thompson, D.J., and Gautier, P.E., Theoretical optimisation of track components to reduce rolling noise, *J. Sound. Vib.*, 1996, **193**(1), 161 - 172.

4 Jones, C.J.C., and Edwards, J.W., Development and testing of wheels and track components for reduced rolling noise from freight trains. *Proc. Internoise '96*, Liverpool, 1996, 403 - 408.

5 Thompson, D.J., Wheel-rail noise generation part III: rail vibration. *J. Sound. Vib.*, 1993, **161**, 421 - 446.

6 Castel, L. and Bird, W., The Silent Track project. *Second Int. Workshop on Abatement of Railway Noise Emissions - Freight Transport*, Berlin, 1998.

7 Jones, C.J.C., Thompson, D.J., Frid, A., Wallentin, M.O., Design of a railway wheel with acoustically improved cross-section and constrained layer damping. *To be presented at Internoise 2000,* Nice, France.

8 Bouvet, P., Vincent, N., Coblentz, A., Demilly, F., Rolling noise from freight railway traffic: reduction of wheel radiation by means of tuned absorbers. *To be presented at Internoise 2000,* Nice, France.

COMPARING THE DYNAMIC PROPERTIES OF CONVENTIONAL AND ELECTRO-RHEOLOGICAL FLUID SHOCK ABSORBERS

S O Oyadiji and P Sarafianos
Division of Mechanical Engineering
Manchester School of Engineering
University of Manchester
Manchester M13 9PL, U.K.

ABSTRACT

Procedures for characterising the dynamic properties of standard hydraulic oil-filled (SHO) and electro-rheological fluid (ERF)-filled shock absorbers are presented. The conventional shock absorber has fixed settings of stiffness and damping ratings, whereas for the ERF shock absorber, these parameters can be varied via an applied electric field. It is shown that the SHO shock absorber is relatively soft in compression but relatively hard in extension. Conversely, it is shown that the present design of ERF shock absorber is relatively hard in compression but relatively soft in extension.

1 INTRODUCTION

The selection of shock absorbers for vehicles is an optimisation problem. This is because of the conflicting demands of the stiffness and damping characteristics of the suspension system imposed by the requirements for ride comfort and vehicle handling [1]. For ride comfort, a soft shock absorber is required but this leads to poor handling. Conversely, for good handling, a hard shock absorber is needed which results in poor ride comfort conditions. Using conventional hydraulic oil-filled shock absorbers, the optimum shock absorber is selected by a trial-and-error subjective approach. This involves fitting of shock absorbers of various stiffness and damping coefficients to a vehicle. The vehicle is test-driven and the performance of the shock absorbers, in terms of ride comfort and handling, are judged qualitatively. This process is repeated until a suitable set of shock absorbers of appropriate stiffness and damping values are selected.

Obviously, this trial-and-error approach is not satisfactory. Also, the selected shock absorber is optimal only for the same types of loading and road surface conditions used in the tests. To overcome this problem, there is the need for an adaptive or active approach. A number of active and semi-active suspension systems have been developed. These include self-levelling, semi-active, and fully-active suspension systems [2]. In the self-levelling suspension systems, the conventional suspension components, namely the springs and dampers, are replaced with air springs. Self-levelling air suspension systems are used on heavy trucks and in some luxury cars. Semi-

active suspension systems consist of a spring and a damper with the damping properties being altered using a solenoid-controlled valve attached to the damper. Fully-active suspension systems are essentially hydraulic actuators which rely on hydraulic pumps and servo-valves for their operation. Semi-active and fully-active suspension systems are more complicated and more expensive than their passive counterparts. Also, their performance, especially their response time, is often limited. One of the means for overcoming these limitations is the use of an electrorheological (ER) fluid instead of hydraulic oil in shock absorbers.

ER fluids consist of suspensions of dielectric particles in an electrically insulating fluid medium [3-5]. When placed in an electric field, the dynamic properties of the fluids are altered by varying the applied electric field strength. As the electric field strength is increased from zero, the ER fluid becomes more viscous. At sufficiently high field strength, the ER fluid becomes a gel-like soft solid. However, when the electric field is switched off, the ER fluid reverses to its original fluid state. Thus, the use of an ER fluid in a shock absorber will enable the continuous tuning of the stiffness and damping coefficients of the shock absorber to desired values. This will eliminate the trial-and-error subjective approach for selecting passive shock absorbers of optimum dynamic properties. It will also overcome the limitations inherent in the semi-active and fully-active suspension systems based on existing dampers filled with hydraulic oil. In addition, using ER fluids will enable the continuous optimisation of the properties of the shock absorber for various loading and road surface conditions.

In this paper, the results of the experimental characterisation of the non-linear dynamic characteristics of both a conventional and an ERF shock absorbers are presented. It is shown that the conventional shock absorber is soft in compression but hard in extension, whereas the ERF shock absorber is soft in extension but hard in compression. Furthermore, it is shown that increasing the electric field strength applied to the ERF shock absorber significantly increases the magnitude of the restoring compression force produced but only slightly increases the magnitude of the restoring extension force.

2 MODELS FOR CHARACTERISING DYNAMIC PROPERTIES

For a multi-degree of freedom system, the output response vector of amplitudes $\{Y(\omega)\}$ in the frequency domain is related to the input excitation vector $\{X(\omega)\}$ by

$$\{Y(\omega)\} = [H(\omega)]\{X(\omega)\} \qquad (1)$$

where $[H(\omega)]$ is the frequency response function (FRF) matrix. For example, $\{X(\omega)\}$ could be the vector of dynamic excitation forces applied to the four

wheels of a car mounted on a four pillar test rig, while $\{Y(\omega)\}$ is the vector of response amplitudes measured at various points on the vehicle body. In such a case, the FRF matrix $[H(\omega)]$ will contain the dynamic characteristics of any component along the transmission path such as the tyres and shock absorbers. To obtain the dynamic properties of a shock absorber alone, a single input-single output relationship is used. The shock absorber is subjected to an input excitation $x(t)$ and its output response $y(t)$ is measured. The characteristics of the shock absorber are obtained from

$$Y(\omega) = H(\omega)X(\omega) \tag{2}$$

where $X(\omega)$ and $Y(\omega)$ are the Fourier transforms of $x(t)$ and $y(t)$ respectively, and $H(\omega)$ is the frequency response function which contains the dynamic characteristics of the shock absorber.

For a viscous damper, the output restoring force $f_d(t)$ generated when it is subjected to a input relative velocity $\dot{x}(t)$ is given by

$$f_d(t) = c\dot{x}(t) \tag{3}$$

where c is a constant known as the damping coefficient. The damper characteristics represented by Eq.(3) is linear. These characteristics can be simply expressed by the constant damping coefficient c.

However, for a shock absorber, the output restoring force $f_d(t)$ generated is generally a non-linear function of input relative displacement $x(t)$ and relative velocity $\dot{x}(t)$ expressed as

$$f_d(t) = f\{x(t), \dot{x}(t)\} \tag{4}$$

The non-linear characteristics represented by Eq.(4) can be represented by a polynomial equation and/ or graphically using force-displacement and force-velocity curves. Also, a three-dimensional map which is known as the restoring force surface (RFS) is used to depict the non-linear variation of the restoring force with displacement and velocity. The RFS method is a non-parametric technique for identification of non-linear dynamical systems [6]. The non-linear restoring force $f(x, \dot{x})$ is plotted as a surface over the state plane $(x, \dot{x})$.

3 EXPERIMENTAL TEST PROCEDURES

A standard hydraulic oil-filled (SHO) shock absorber for a medium range British car, and an equivalent electrorheological fluid (ERF) shock absorber were developed. The SHO shock absorber was obtained from the Ford Motor

Company while the ERF shock absorber was developed at the University of Manchester [7]. Each of the shock absorbers was fixed, in turn, in an Instron hydraulic test machine. The lower end of the shock absorber was fixed to the actuator of the test machine by means of a set of clamps operating at 30 bar. The other end of the shock absorber, the piston rod of the shock absorber, was fixed to a similar set of clamps which were connected to the frame of the test machine via a force transducer. Thus, the shock absorber was constrained to vertical motion. Further details of the shock absorbers, the experimental apparatus, and of the composition and dynamic properties of the electrorheological fluid used can be found elsewhere [7-10].

The shock absorbers were excited sinusoidally at various frequencies within the range of 0.5 Hz to 25 Hz, and at various amplitudes within the range ±0.05 mm to ±28.0 mm. As the frequency was increased, the maximum amplitude of excitation achievable was reduced due to the power limitations of the actuator of the test machine. For each test, the input displacement excitation and the output force response were measured using a linear voltage displacement transducer (LVDT) and a force transducer respectively. Both the displacement-time and the force-time data sets were averaged in order to reduce random effects. Also, the displacement-time data was differentiated numerically in order to obtain the velocity-time data. Thus, the data triplet $(f, x, \dot{x})$, which comprises of the restoring force, displacement and velocity was obtained for each of the test conditions. In addition, the ERF shock absorber was tested at electric field voltages of 0 kV and 4 kV.

4 COMPARISON OF MEASURED CHARACTERISTICS

Because of space constraints, the dynamic properties of the standard hydraulic oil and the electrorheological fluid absorbers are presented at a selected excitation frequency of 0.5 Hz and at dynamic amplitudes of up to ±28.0 mm. In all the results, positive displacements, velocities and forces denote extension, while negative displacements, velocities and forces denote compression.

Figure 1 shows the displacement, velocity and force histories of the SHO shock absorber at an excitation frequency of 0.5 Hz and dynamic amplitude of 28.0 mm. Whereas the displacement and velocity histories are sinusoidal, the figure shows that the force history is sinusoidal in the extension or rebound stroke but non-sinusoidal in the compression or jounce stroke. It is also seen that the peak force in the extension stroke is about 170 N, whereas the peak force in the compression stroke is about 50 N. Thus, the shock absorber is relatively soft in compression but relatively hard in extension. The corresponding force-displacement and force-velocity characteristics of the shock absorber are shown in Figure 2. These characteristics again show the soft compression hard extension behaviour of the shock absorber.

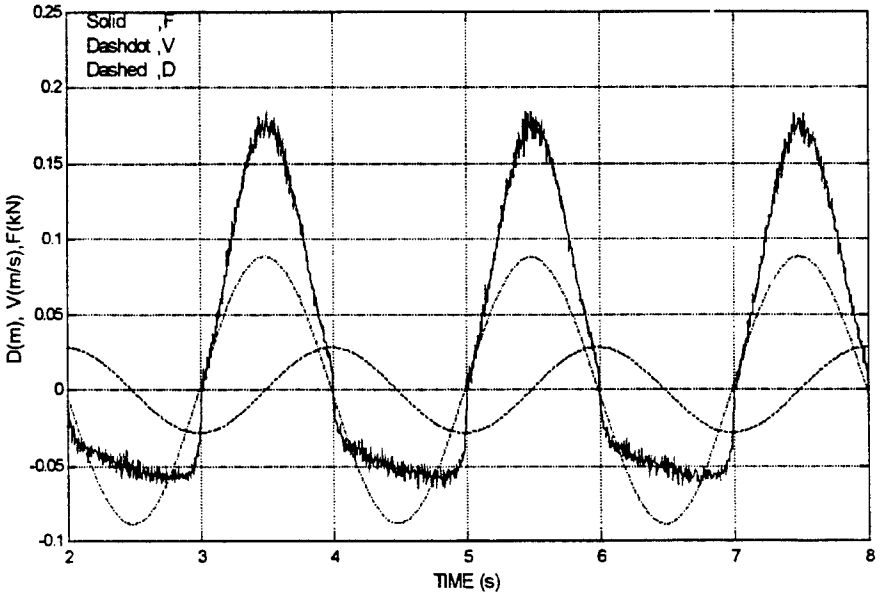

Figure 1: Displacement, Velocity and Force Histories of Standard Hydraulic Oil Shock Absorber at 0.5 Hz Excitation and 28.0 mm Dynamic Amplitude.

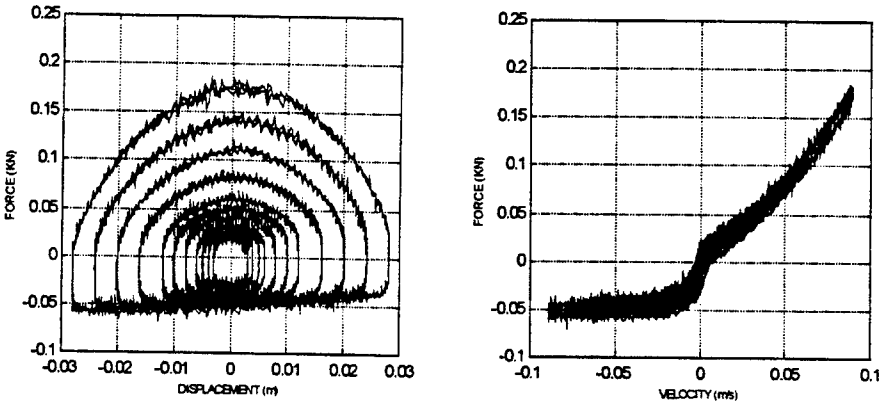

Figure 2: Force-Displacement and Force-Velocity Characteristics of Standard Hydraulic Oil Shock Absorber at 0.5 Hz and Amplitudes of up to 28.0 mm.

In the case of the ERF shock absorber, Figure 3 shows its displacement-time, velocity-time and force-time characteristics at an excitation frequency of 0.5 Hz, dynamic amplitude of 28.0 mm, and at 0.0 kV electric field. It is obvious that both the displacement and velocity input excitations are sinusoidal. However, the output force response is distorted and non-linear in both the compression and extension strokes. The sharp discontinuities in the restoring force as the velocity passes through a value of zero, where it changes sign, indicates some sticktion effects. In addition, the peak force in the compression stroke is about 270 N, while the peak force in the extension stroke is about 190 N. Therefore, it can be inferred that the shock absorber is relatively hard in compression but relatively soft in extension. The corresponding force-displacement and force-velocity characteristics of the shock absorber are shown in Figure 4. These characteristics again show the hard compression but soft extension behaviour of the ERF shock absorber. The sticktion effects in the neighbourhood of $\dot{x} = 0$ are clearly seen in the force-velocity characteristics.

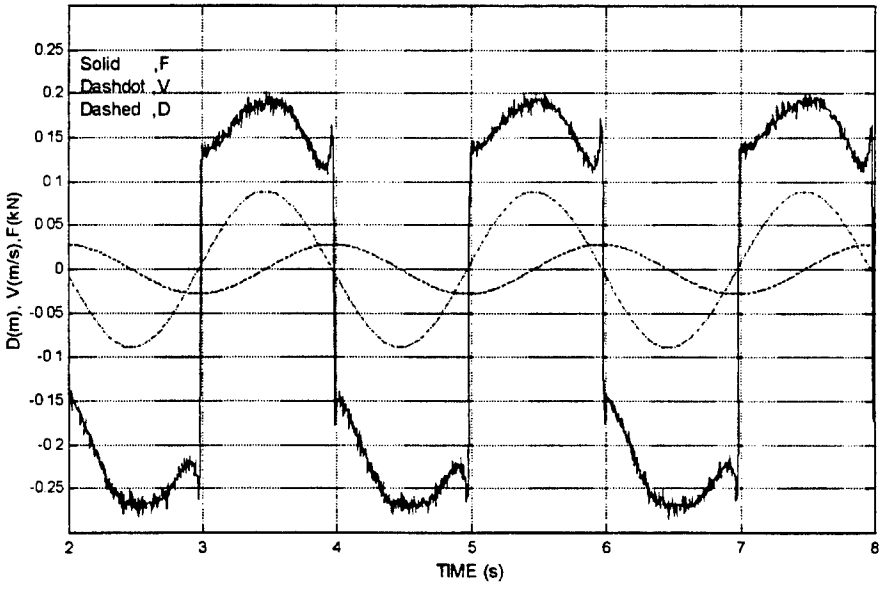

Figure 3: Displacement, Velocity and Force Histories of ER Fluid Shock Absorber at 0.5 Hz and 28.0 mm Dynamic Amplitude.

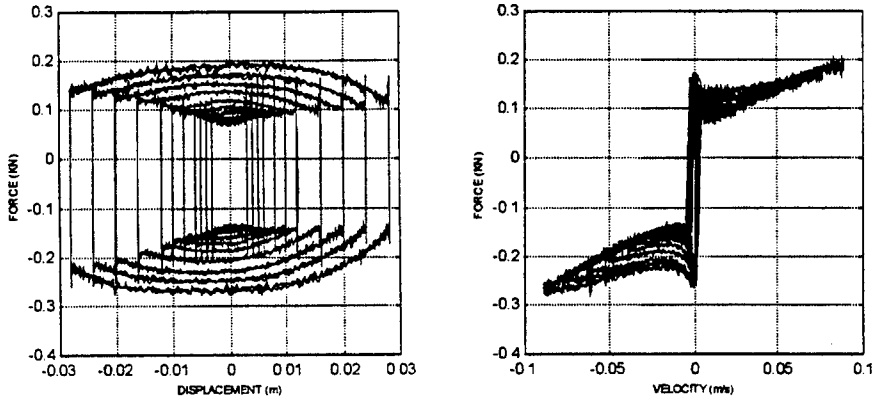

Figure 4: Force-Displacement and Force-Velocity Characteristics of Standard Hydraulic Oil Shock Absorber at 0.5 Hz and Amplitudes of up to 28.0 mm.

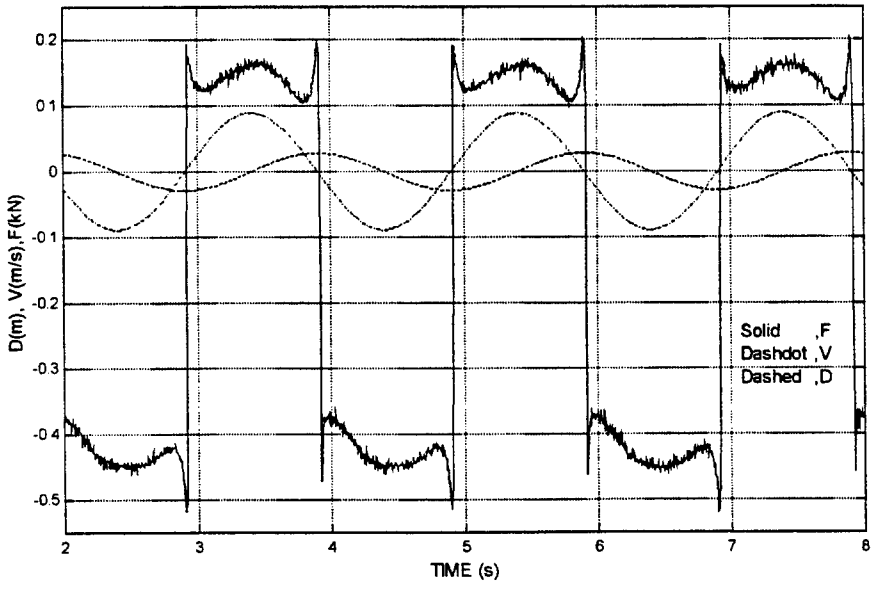

Figure 5: Displacement, Velocity and Force Histories of Standard Hydraulic Oil Shock Absorber at 0.5 Hz and 28.0 mm Dynamic Amplitude.

The displacement-time, velocity-time, force-time, force-displacement and force-velocity characteristics of the ERF shock absorber at an excitation frequency of 0.5 Hz, dynamic amplitude of 28.0 mm, and at 4.0 kV electric field are shown by Figures 5 and 6. From Figure 5, it is seen that both the displacement and velocity input excitation are sinusoidal. However, the output force response is highly distorted and highly non-linear in both the compression and extension strokes. The sharp discontinuities in the restoring force, in the neighbourhood of $\dot{x} = 0$, are much more pronounced. Also, the peak force in the compression stroke is now about 500 N, while the peak force in the extension stroke is about 200 N. This gives a ratio of compressive-to-tensile force of 2.5 which is much higher than the ratio of 1.4 obtained when there was no applied electric field. Hence, it is can be inferred that the shock absorber becomes relatively harder in compression as the applied electric field potential is increased. In addition, the magnitude of the sticktion effects increases as the magnitude of the applied electric field potential is increased.

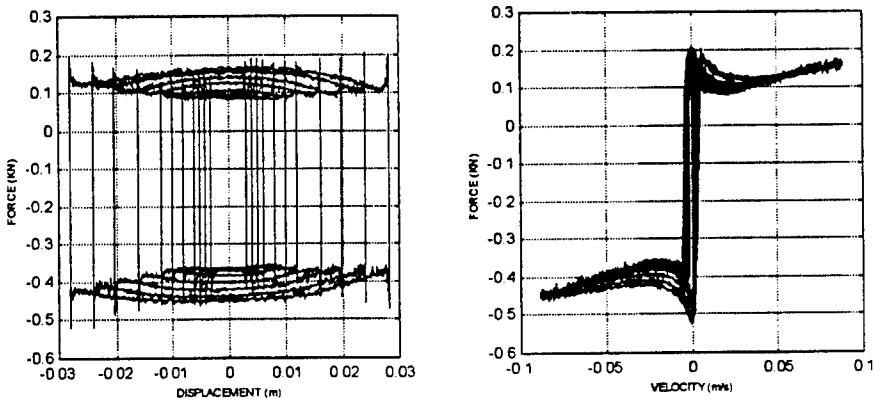

Figure 6: Force-Displacement and Force-Velocity Characteristics of Standard Hydraulic Oil Shock Absorber at 0.5 Hz and Amplitudes of up to 28.0 mm.

The force-velocity characteristics of the SHO shock absorber and of the ERF shock absorber at excitation frequency of 0.5 Hz and at dynamic amplitudes of 0.2, 2.0 and 20.0 mm are compared in Figure 7. The ERF shock absorber was subjected to electric field potentials of 0.0 kV and 4.0 kV. The figure shows that at very low amplitudes of vibration, the force-velocity characteristics of the SHO shock absorber are approximately linear. However, as the excitation amplitude is increased, the characteristics of the SHO shock absorber become more and more non-linear and the magnitudes of the restoring force produced also increase. The figure also shows that force-velocity characteristics of the

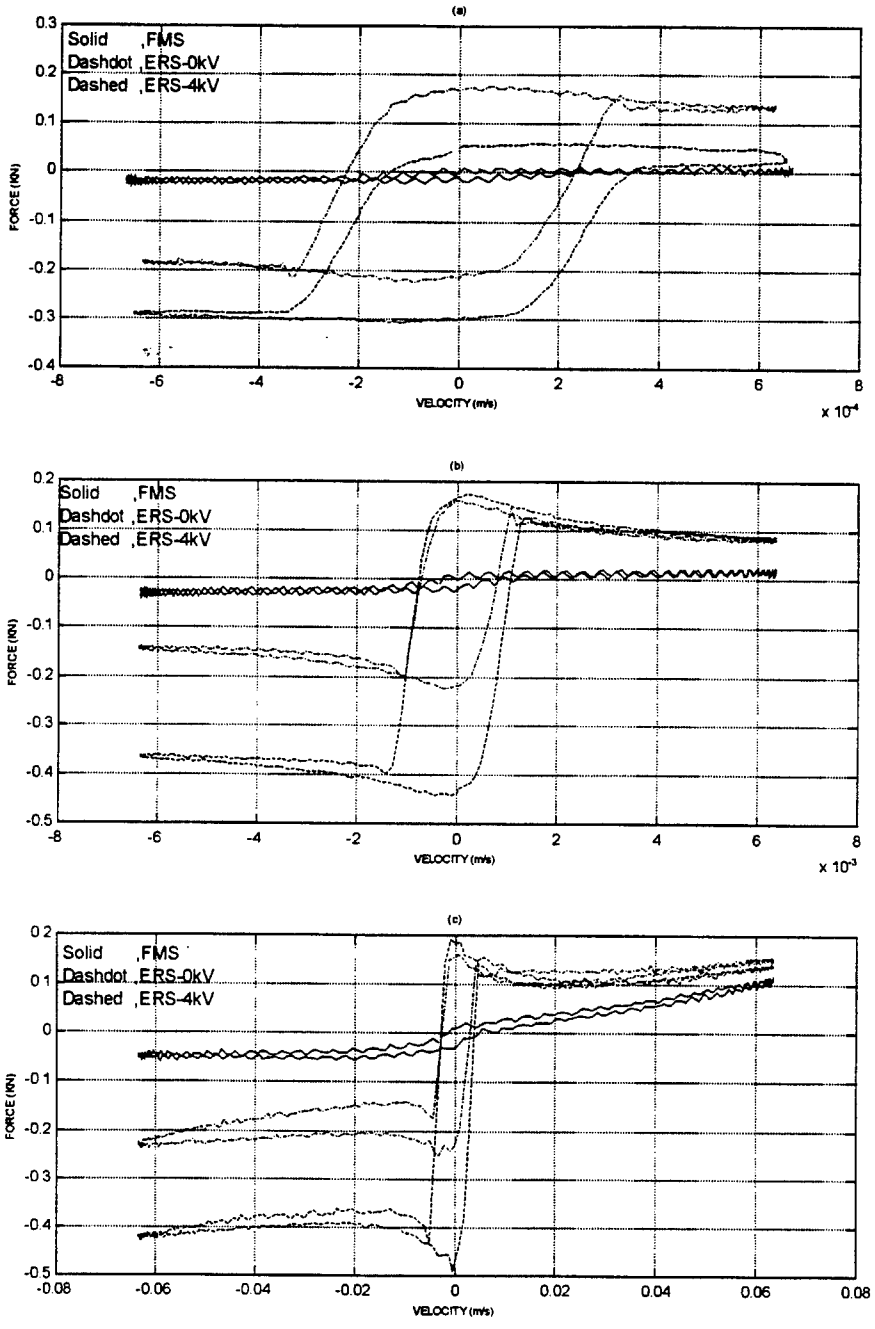

Figure 7: Force-Velocity Characteristics of Hydraulic Oil and ER Fluid Shock Absorbers at 0.5 Hz and Amplitudes of (a) 0.2 (b) 2.0, and (c) 20.0 mm.

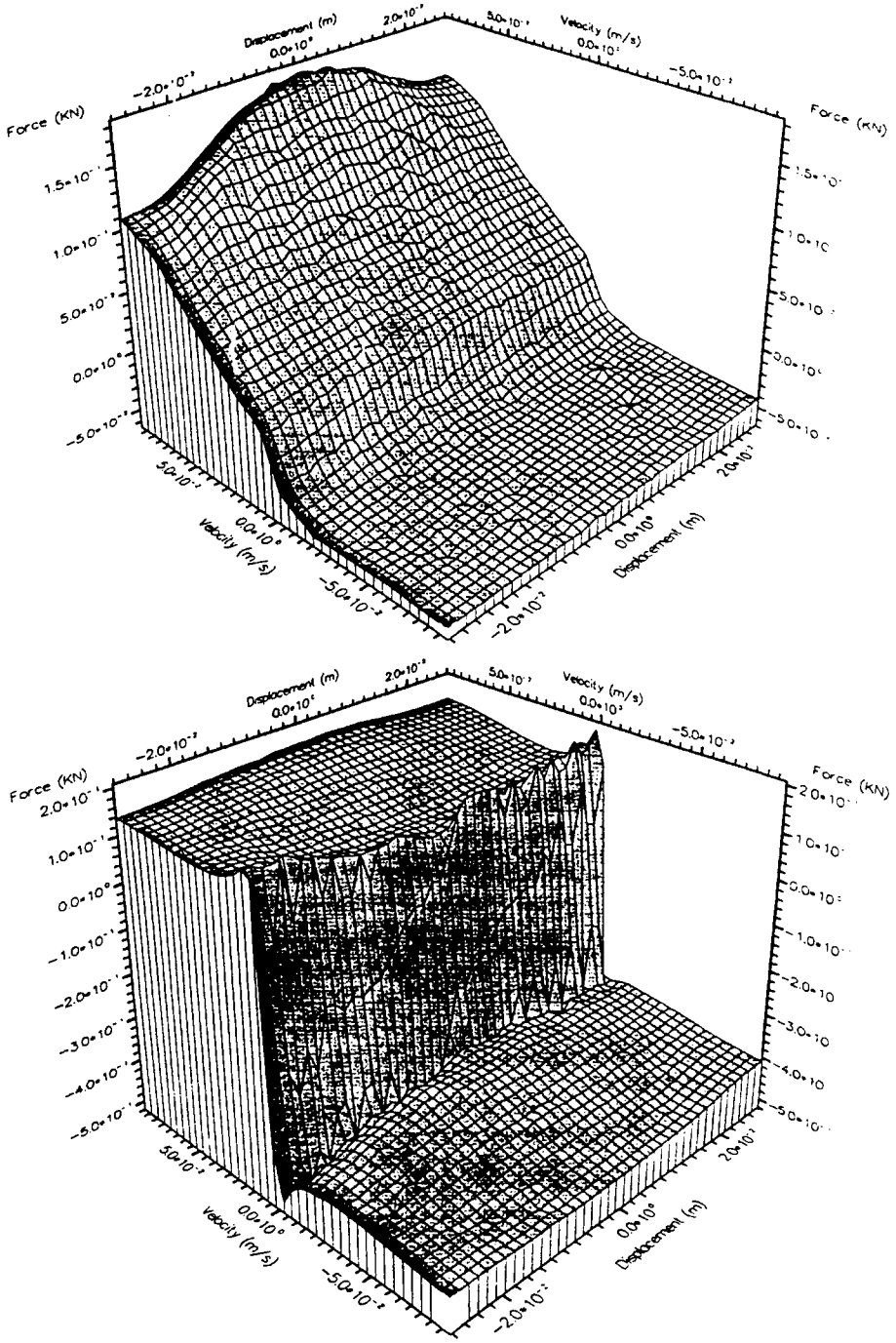

Figure 8: Restoring Force Surface Characteristics of Hydraulic Oil and ER Fluid Shock Absorbers at 0.5 Hz and Amplitudes of up to 28.0 mm.

ERF shock absorber are non-linear at very low as well as at very high amplitudes of vibration. Furthermore, it is seen that the magnitudes of the restoring forces generated, and the areas of the hysteresis loops produced are significantly increased as the amplitude of excitation is increased, and as the electric field potential is increased.

In Figure 8 is shown a comparison of the restoring force surface characteristics of the SHO shock absorber and the ERF shock absorber at 0.5 Hz excitation frequency and at a range of amplitudes from 0.1 to 28.0 mm. An electric potential of 4.0 kV was applied to the ERF shock absorber. The figure shows the smooth transition of the restoring force characteristics of the SHO shock absorber from relatively high positive values to relatively low negative values. This again implies a soft compression and hard extension behaviour. Conversely, there is an abrupt transition of the restoring force characteristics of the ERF shock absorber from relatively low positive values to relatively high negative values. That is, the ERF shock absorber exhibits a hard compression and a low extension behaviour. Also, both restoring force surfaces show that the dynamic properties of the two shock absorbers are highly non-linear.

6 CONCLUSIONS

The procedures for characterising the dynamic properties of shock absorbers have been presented. It has been shown that the standard hydraulic oil-filled shock absorber is relatively soft in compression but relatively hard in extension. This property of the SHO shock absorber is as desired, namely: in the compression stroke, when a shock is absorbed, the restoring force needs to be relatively small. But in the extension stroke of the shock absorber, when the shock energy is dissipated, the restoring force needs to be relatively high. Conversely, it was shown that the present design of an electrorheological fluid shock absorber is relatively hard in compression but relatively soft in extension. This behaviour is contrary to that desired. Thus, the design of the ERF shock absorber needs to be improved in order to re-distribute the restoring force characteristics in a more favourable way.

7 ACKNOWLEDGEMENT

The authors wish to thank Mr Julian Hetherington, Ford Motor Company Ltd, Halewood, Liverpool for the manufacture of a major component of the ER fluid shock absorber. The authors also wish to thank Mr Philip Hand and Mr Ian Crawford, Advanced Vehicle Engineering, Ford Motor Company Ltd, Basildon, Essex for providing some standard hydraulic oil-filled shock absorbers.

8 REFERENCES

1. Petek N. K., Romstadt D. J., Lizell M. B. and Weyenberg T.R., 1995, Demonstration of an Automotive Semi-active Suspension using Electrorheological Fluids, SAE 950586.
2. Gillespie T. D., 1992, Fundamentals of Vehicle Dynamics, Society of Automobile Engineers, ISBN 1-56091-199-9.
3. Hill J. C. and Van Syeenkiste T. H., 1991, Response Times of Electrorheological Fluids, Journal of Applied Physics D, vol 70, pp 3.
4. Conrad H., Fisher M. and Specher A. F., 1990, Electrorheological Fluids, Proceedings of the Second International Conference on ER Fluids, Carlson J. D., Specher A. F. and Conrad H. (Eds), Technomic Publ. Co., Lancaster-Basel, p63.
5. Gandhi M., 1989, Electrorheological Fluids: Application Begin to Gel, Journal of Composite Materials, vol 23, pp 1232-1255.
6. Masri S. F. And Caughey T. K., 1979, A Nonparametric Identification Technique for Nonlinear Dynamical Problems, Journal of Applied mechanics, vol 46, pp 433-447.
7. Mistry D., 1996, Electrorheological Fluid Vehicle Shock Absorber, BSc-MEng Thesis, Manchester School of Engineering, University of Manchester.
8. Sarafianos P., 1998, Characteristics of Hydraulic Oil and Electrorheological Fluid Shock Absorbers, MPhil Thesis, Manchester School of Engineering, University of Manchester.
9. Oyadiji S. O., 1996, Electric Field Strength, Temperature and Frequency Dependency of the Dynamic Properties of an Electro-Rheological Fluid, Proceedings of Sensors and Actuators Conference, Manchester, pp 138-146.
10. Oyadiji S. O., 1996, Characterisation of the Complex Shear Modulus Properties of Electro-Rheological Fluids by the Direct Stiffness and Master Curve Techniques, International Journal of Modern Physics B, v.10, n. 23&24, pp 3227-3236

AERODYNAMICS AND FLUTTER

Active Buffet Load Alleviation for an F/A-18 Vertical Tail

Salvatore L. Liguore
Donald V. Drouin
Theodor H. Beier
The Boeing Company
St. Louis, MO 63166-0516

Abstract

A wind tunnel experiment using a 15% scaled F/A-18 model was performed to demonstrate the use of the rudder to control dynamic response during buffeting. For the test, a flexible left-hand vertical tail was used with a rigid fuselage model. The vertical tail was designed with a movable rudder (+/-14 ° max.) that was controlled using a hydraulic actuator. Nominal control of +/-8° produced 25% RMS reduction while the maximum rudder motion of +/-14° produced an average RMS bending moment reduction of 42%. In addition, it was found that control of the tail's first torsion mode is feasible with a 20% RMS reduction in torsion moment response. Based on these results, the dynamic fatigue life can be significantly improved, 4 to 10 times the current life.

Background

Modern fighter aircraft fly at high angles of attack (AoA) to gain maneuvering advantages over opponents. They achieve this high lift by use of vortices, generated by lifting surface features that produce lift after the wing has stalled. At high AoA, these vortices burst ahead of the empennage resulting in the empennage being engulfed in a region of turbulent and swirling flow producing strong unsteady pressures. The effect of these unsteady pressures is buffet, which is defined as random loading that arises from the pressure fluctuations. The F/A-18 exhibits this type of buffet, (Figure 1). Buffet has been studied for many years by several researchers on the F/A-18. The dynamic loads, which are caused by unsteady vortex breakdown, have characteristic frequencies that can excite structural modes. The magnitude and frequency spectrum of this pressure field depends on the angle of attack, flight speed, and wing/leading edge extension configuration.

The characteristics of these buffet loads are highly dependent on flight conditions. Previous research has investigated the statistics of buffet in flight and has shown that if the aircraft is flying at a constant altitude and airspeed, the response is reasonably stationary (1)(2). As expected, when the aircraft is rapidly changing altitude and airspeed, i.e. maneuvering, then the buffet response changes accordingly. In wind tunnel tests, data are collected at a constant angle of attack and dynamic pressure. In flight test, data are measured at specified conditions to verify wind tunnel data; however, the

aircraft can maintain a constant condition for only 1.5 seconds, as kinetic energy is lost. In actual usage, pull-up maneuvers may occur at pitch rates up to 30 degrees per second in typical buffeting flight, and any alleviation system must be able to respond to these rapidly changing conditions.

The effect of pitch rate is to delay vortex burst to higher AoA. Under dynamic pull-up conditions, the vortex burst occurs at a point further downstream than under static conditions. The delayed bursting results in a buffet condition equivalent to static conditions at lower AoA (3).

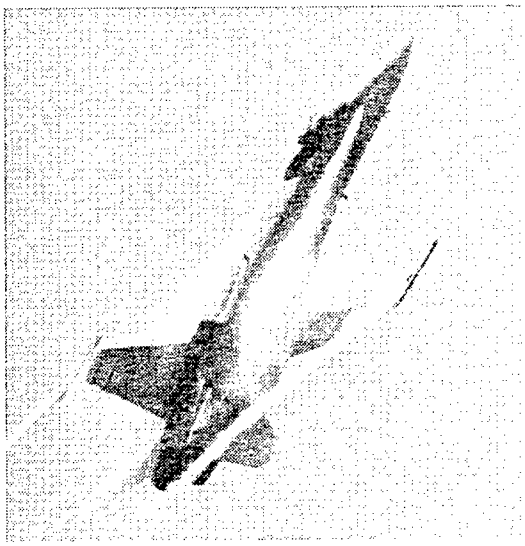

Figure 1. F-18 at High Angle-of-Attack Showing Vortices

Previous Research

Various methods for alleviating empennage buffeting have been explored. Perhaps the most common one is strengthening the structure. This lengthens the fatigue life of the structure but increases weight and is very likely to move the fatigue failures to un-strengthened adjacent structure. On the F-15, a Boron/Epoxy patch was used to stiffen the main torque box (4). This technique was effective at reducing the load in the upper torque box by shifting the second bending frequency from the peak buffet forcing frequencies and by introducing a new load path through the patch instead of the substructure. The F/A-18 C/D employed a fence mounted on the leading edge extensions to re-direct the vortex and control the burst point. This technique reduced tail buffeting from 450 g's to 200 g's at the cost of slightly reduced aircraft performance. Passive damping has also been studied for use on the F/A-18 C/D vertical tails and horizontal tail (5)(6)(7). In these studies, various constrained viscoelastic layer-damping treatments were analyzed and tested. Full-scale tests were performed on an F/A-18 C/D horizontal tail

using a graphite/epoxy-damped patch. The patch was effective in adding damping into the structure, but the damping performance was temperature sensitive and did not match analytic predictions. In other studies on the vertical tail, internal treatment using spacers and an integrally damped composite skin showed great promise in adding significant damping into the primary modes of the vertical tail.

Several investigations have demonstrated active load alleviation systems using "smart" materials distributed over the vertical tail structure to control the first few structural modes (8)-(12). The analytical and experimental results from these programs show that piezoelectric driven skins may reduce the transmitted buffet load that causes fatigue at all flight conditions.

The active rudder concept was first studied at McDonnell Aircraft in the late 1970's for use on the F-15. In 1990, the RANN Corporation studied the use of control surfaces (i.e., the rudder and tip vanes) for controlling buffet response. RANN performed studies on both the F-15 and F/A-18 (8). They concluded that for the F/A-18 the concept looked quite promising due to its larger rudder surface area compared to the overall fin surface area. Boeing and NASA/LaRC are investigating this concept. NASA has performed various wind tunnel experiments using an active rudder on a 16% scale F/A-18 C/D vertical tail and has been successful (9)-(10). This paper summarizes the Boeing program using this concept and the extension of the effect to include pitch rate effects.

Wind Tunnel Experiment

Testing was performed in the Boeing Mini-Speed Wind Tunnel (MSWT) test Facility in St. Louis, MO. The model was configured with a dynamically scaled flexible vertical tail, mounted on the left-hand side of the model. All other parts on the model were "rigid". Instrumentation was installed on the flexible vertical tail to monitor internal dynamic loads and accelerations due to vortex impingement.

The wind tunnel model was a rigid 15% aerodynamics model. The basic model components include: fuselage with flow through ducts, wing leading edge extensions, basic wing, wing tip mounted AIM-9 sidewinder missiles, rigid horizontal tails, one rigid vertical tail, and one flexible vertical tail with an hydraulically controlled movable rudder. The leading edge slats were deflected to typical angles for in-flight maneuvers, (Figure 2). The flexible tail is a flutter model design with aluminum spar and balsa wood cross sections. The balsa wood sections are non-structural and give the tail its aerodynamic shape. A hydraulic actuator is incorporated into the tail to move the rudder during the controlled runs. The flexible vertical tail is instrumented with strain gages and accelerometers for quantifying the bending moment and for providing real-time feedback to the active control system.

The MSWT is a continuous flow wind tunnel, which can be configured as a closed or open circuit. The open jet test section is 15 feet high, 20 feet

wide and 20 feet long. Subsonic flight can be obtained up to Mach 0.11 at atmospheric pressure with Reynolds number of 0.75 million per foot. This translates into speeds up to 126 feet/second at Q=18 psf. For this test, the tunnel was configured as a closed circuit. Tests were performed at dynamic pressures of 1.5, 3.5, 5.2, 7.0 and 10.0 pounds per square foot (psf), which is 66-psf to 444-psf full-scale at sea level. The model was pitched up to 7 deg/sec at each dynamic pressure in addition to the static (constant AoA) tests. Pitching the model was accomplished by using a hydraulic actuator mounted to the aft end of the model.

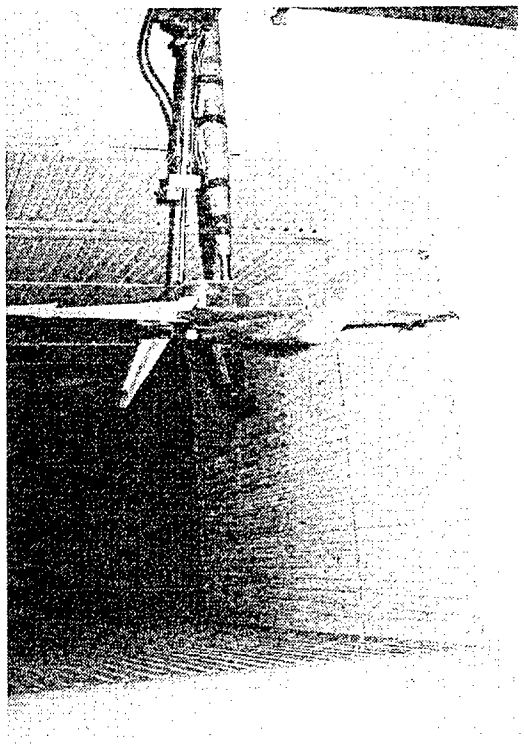

Figure 2. F/A-18 15% Wind Tunnel Model is shown in its inverted installation.

A vibration modal test was performed to verify the dynamic characteristics of the F/A-18 15% flexible vertical tail. The natural frequencies of the first five vertical tail modes were identified. The frequencies are shown in Figure 3 with a comparison to the full aircraft results.

Mode Shape	Model Hz	Aircraft Hz
First Bending	16	16
Rudder Rotation	22	32
First Torsion	41	54
Second Bending	60	58
Second Torsion	75	86

Figure 3. Modal Test Summary

Control System Implementation

For this project, Neural Predictive Control (NPC) was used (11)-(12) to control the hydraulic actuator for active rudder positioning to reduce buffet. A 133 MHz Pentium based PC was used to provide the processing power for the NPC digital controller running at 400Hz; as well as, real time data logging and graphical plotting. The PC was also equipped with a plug-in SHARC board containing 8 RISC processors useful for modeling the plant in real time. Analog-to-Digital and Digital-to-Analog boards working at ± 10 volts mounted within the PC were used for data I/O.

The test plan called for controlling only the first bending mode, then controlling only the torsion mode. Root bending strain was used and the control input for the bending mode. The inboard torsion strain gauge was used for torsion mode control. Another issue examined was controller performance as a function of maximum allowed deflection. It is important that buffet reduction not interfere with flight performance. Controller performance at ± 8 ° and ± 14° maximum rudder defection was examined. The neural controller was trained at one specific static AoA for each band of interest, (Figure 4).

In many systems, it is desirable to generate modeling data under disturbance free conditions. In this case the control surface of the rudder used aerodynamic forces to oppose aerodynamic forces. Accordingly, the model to be used for control had to be created under quite noisy conditions, in some cases the signal to noise ratio could be as low as 1-to-10. To complicate matters, the amount of authority available due to aerodynamic forces is a function of Q and AoA. It was postulated that a suitable model for control could be developed at each Q since data was collected at a low enough angle of attack to limit the amount of noise due to buffet. To train the neural network, the rudder-to-strain transfer function was obtained at an AoA of 7°, where buffeting is very low. After a neural network model of the tail and rudder has been trained, it was then ready to be used within the predictive control framework. There were two modes of interest in this test - first mode bending response at 16 Hz and a torsion mode response at 41 Hz.

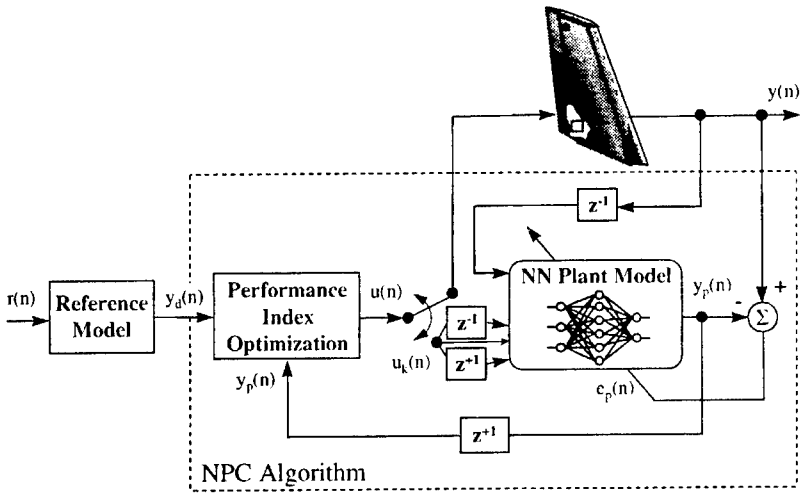

Figure 4. Neural Predictive Control Buffet Load Alleviation System

As stated previously, the objective is to control the torsion mode of the tail as well as the bending mode. As can be seen in Figure 5, authority as measured by the Rotational Variable Displacement Transducer (RVDT), was sharply curtailed beginning at about 35Hz. Although mode 2 authority was reduced by a factor of four, there was still enough bandwidth to attempt control of the torsion mode. Results from the Boeing 1996 wind tunnel test entry show that the rudder is more effective at lower tunnel speeds. Hence, it was expected that different Neural Predictive Models would be required for different Q's but not for AoA variations, (Figure 6).

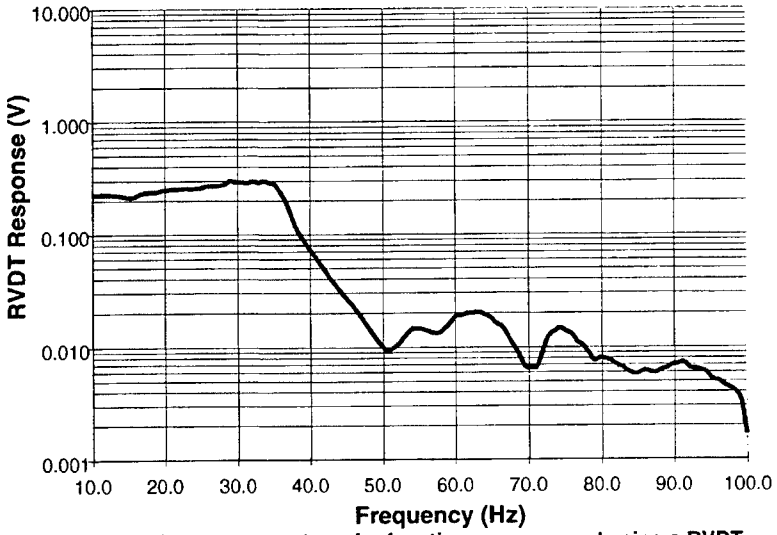

Figure 5. Rudder response transfer function as measured using a RVDT

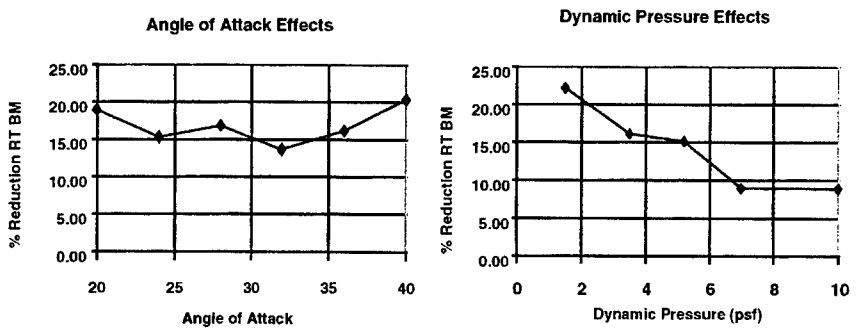

Figure 6. 1996 WT Test Results: Average Response Reductions as a Function of Q and AOA

Test Results

As mentioned, the test was conducted at dynamic pressures of 1.5, 3.5, 5.2, 7.0 and 10.0 pounds per square foot (psf), which equates to 66 psf to 444 psf at full scale and at pitch rates of 0, 1, 3, 5 and 7 degrees per second. A strain gage placed at the root of the main vertical tail spar was used to measure the bending moment. Strain was measured directly. The bending moment was derived from calculations derived from calibration runs where known weights were hung from the vertical tail. Since a control surface (rudder) is being used, the amount of rudder control authority (RCA) was regulated to +/- 8° and +/- 14°. Mode I control of the buffet response was very successful. A 25% reduction of Mode I RMS (Root Mean Squared) response was achieved for a nominal rudder deflection, Figure 7. However, a 42% RMS response average reduction was measured for a maximum allowed deflection of 14°, Figure 8. Mode II active control was also successful. Initial results indicate Mode II RMS response reductions ranging from 10-29%, (Figure 9).

	Angle of Attack							
Q	**26**	**28**	**30**	**32**	**34**	**36**	**38**	**Avg.**
2.3	40	24	27					22
2.7		31	27	7				22
3.1			23	26	19			22
3.5		31	25	29	21	21	28	26
Avg.	40	29	20	21	20	21	28	25

Figure 7. Mode I Control: 1st Bending RMS % Reduction for +/- 8 deg RCA.

	Angle of Attack							
Q	26	28	30	32	34	36	38	Avg.
2.3								
2.7		51	42					46
3.1			43	44	38			40
3.5				38	36	39		37
Avg.		51	43	39	37	39		42

Figure 8. Mode I Control: 1st Bending RMS % Reduction for +/- 14 deg RCA.

The active rudder was able to reduce RMS bending moment by 25% to 42% during steady state tunnel conditions. During dynamic pitching test conditions, the dynamic response of the vertical tail was lower, and the peak response tended to shift to higher AoA, (Figure 10). During controlled runs, the response improvement was similar to the static (steady state) controlled runs with some mixed results at various AoA/Q's, Figure 11.

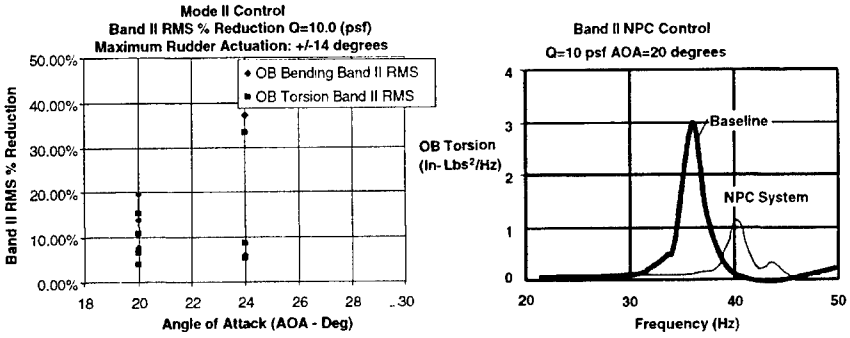

Figure 9. Response Reduction for Band II Control

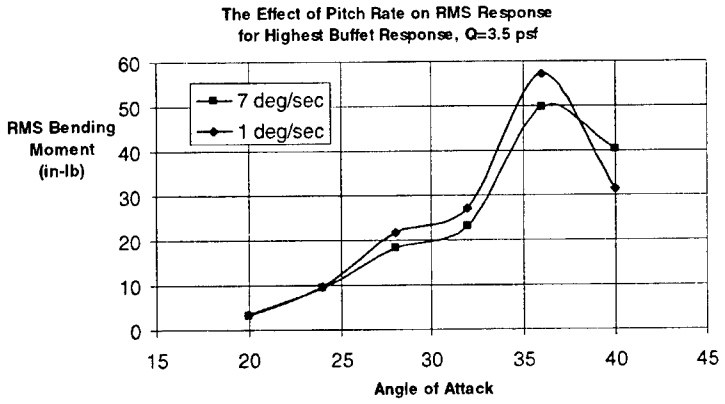

Figure 10. Root Bending Moment Response vs. AoA at Pitch Rate

Q/AoA	20	24	28	32	36	40	Avg.
3.5	12.4	2.7	15.6	14.4	12.9	-29.0	4.8
5.2	-19.6	8.3	12.9	13.6	9.4	11.2	5.6
7.8	-4.0	2.8	-3.4	-9.8	-18.2	8.3	-4.1
10.	-15.3	-15.0	26.2	3.5	-1.8	13.6	1.9
Avg.	-6.6	-0.3	12.8	5.4	0.6	1.0	2.2

Figure 11. Comparison Between Static and 7º /sec Pitch Rate Runs

During these tests, baseline and controlled tests were performed at +/- 5° rudder offset, where + 5° is outboard and –5° is inboard with two important results. The first being that the mean load decreases by 20% when the rudder is deflected 5° (Outboard) and has little effect when deflected -5° (Inboard) as compared to the 0° condition, (Figure 12). At these AoA, the vortex is primarily outboard and there is a strong suction pressure on the tail in that direction. Deflecting the rudder outboard helps to create a bending moment that counters the vortex suction. Hence, this suggested that the rudder could be used to control the static portion of the buffet loading. The RMS bending moment did not change appreciably when the rudder was fixed inboard or outboard with an average of 29% overall RMS reductions, Figure 13. However, the mean bending moment increases by 8% over the open loop fixed rudder runs, Figure 12.

	UnControlled		Controlled	
Rudder Offset Deg.	AoA=30	AoA=32	AoA=30	AoA=3
5	7.1	7.7	7.9	8.3
0	9.3	9.8		
-5	9.4	10.1	9.4	10.5

Figure 12. Mean Signal Bending Moment

	UnControlled		Controlled	
Rudder Offset Deg.	AoA=30	AoA=32	AoA=30	AoA=32
5	27.3	32.9	20.1	23.4
0	28.3	36.3		
-5	27.7	35.1	19.4	25.6

Figure 13. RMS Signal Bending Moment

Fatigue Life Improvement

For the vertical tail, fatigue is broken down into damage caused by maneuver and static pressure loads and those caused by dynamic buffeting. But, the dynamic fatigue damage is a lower percentage of the total fatigue life in the lower tail and increases in percentage in the outboard portion of the tail. The most expensive damage occurs in the root rib and spar caps. The approximate damage percentages in the root area (Spar and Former Flanges) of the tail are 26% due to mode I and 33% due to mode II, and 41% due to maneuver and static pressures. A large portion of the static load is attributable to the suction pressure caused by the vortex on the tail. Hence, the tail is under a condition of combined dynamic and static loading. An effective load alleviation system would be able to reduce both portions of the response.

In order to determine the effect of the active rudder on the fatigue of the airframe other data must be used. The first is percentage of damage per mode for the entire flight envelope. For fleet tracking purpose, this data is available as a table in terms of AoA vs. Q. For the F/A-18, the flight region of interest lies between Q= 75 to 400 psf and AoA = 20 to 45 deg. The second piece of data required is the Usage Data (or time spent at condition.) Again this data is generated from date from fleet fatigue tracking systems and is also a table of Time (seconds) as function of Q and AoA. From this information, a reference fatigue prediction can be made. Assuming that damage is defined as

$$D_i = \frac{n_i}{N_i}$$

Where, D_i is the damage, n_i is the number of damage cycles per 1000 hrs, and N_i is the cycles to failure. The D_i's come from Percentage Damage Table, and the n_i's come from the Usage Data Table. Hence, a table of N_i's can be calculated. 6000 hour A/C fatigue life and 16 Hz center frequency were assumed. The table of N_i's was calculated by converting the n_i's into cycles multiply by 6 (6000 hrs /1000 hrs) and 16 Hz, and then dividing by the percent damage, D_i, for that Q & AoA.

The next step was to determine the reference RMS Strain level associated with these N_i's. These were determined by assuming a power law fatigue relationships for a typical aluminum alloy. The lower spar fitting was made of AL-7050. The following relationship was used to calculate the RMS Strain where a= 5.448 and b=-0.3163.

$$\varepsilon(N_i) = 10^{a\log(N_i)^b}$$

The next step was to determine the RMS strain levels adjusted for active control based on the wind tunnel test data, (Figure 7 and Figure 8). The wind tunnel results were measured at different Q's and AoA's.

From the test data, 25% reduction was achieved with the rudder set at +/-8° and 42% at +/-14°. The previous calculations were then run in reverse, using the reduction factors from the test and multiplying those by the

reference RMS strain. The cycles to failure, N_i, were calculated. Finally, the damage, D_i, per Q & AoA block can be calculated from the ratio of the $D_i = n_i/N_i$. In summing these damages, D_i, the answer was 4.43% versus 26% for the baseline. This is a dynamic LIF of 26/4.43 = 5.8 for the (+/- 8°) control tests. The results for the (+/-14°) is 0.8 % or a dynamic LIF of 26/0.8 = 32.5!

The goal of the buffet load alleviation system was to reduce dynamic response and eliminate fatigue damage. Based on these test results, some indication of fatigue life improvement (LIF) can be determined. If only Mode I is considered then the LIFs are 5.8 and 32 for the +/-8 and +/-14 degree rudder maximum rotations, respectively. When the Mode II dynamics and maneuver loads are considered, then these LIF reduce to 1.27 and 1.33, Figure 14. Based on the Mode II active control results, an average of 20% reduction were achieved during worst case buffet. This translates into a LIF of 4.6 in Mode II damage. Combine this with the Mode I LIF of 5.8 equates to a Total LIF of 1.9. This still assumes 41% damage due to steady state. The steady state load was a major portion of the fatigue life associated with the root locations, and greater life improvements could be realized if the NPC controller was allowed to also command static deflections. If an 18% reduction in maneuver loads is achievable based on the test results, then the Total LIF is 3.63 or an additional 15,818 flight hrs.

	Baseline Damage	Mode I	Mode I & II	Mode I, II & Maneuver
Mode I	0.26	0.044	0.044	0.044
Mode II	0.33	0.33	0.071	0.071
Maneuver	0.41	0.41	0.41	0.16
Total Damage		0.784	0.525	0.275
Total LIF		1.27	1.904	3.636
Total Hrs		7653	11428	21818
Hrs Increase		1653	5428	15818

Figure 14. Predicted Fatigue LIF Improvement Factors based on Different Combined Control Techniques

Summary

Dynamic fatigue in the vertical tail is caused by the first bending and torsion buffet response of the tail. Since a control surface (rudder) was being used, the amount of rudder control authority to +/- 8° and +/- 14° was regulated. A 25% reduction of Mode I RMS (Root Mean Squared) response was achieved for a nominal 8° rudder deflection. A 42% RMS response reduction was measured for a maximum allowed deflection of 14°. Initial results indicate Mode II RMS response reductions ranging from 10-29%. Finally, the active rudder enabled RMS bending moment reduction during transient conditions of about 16% for the highest pitch rates conditions tested. Active control was generally better at lower dynamic pressures where the vortex is positioned for

maximum buffet on the tail. The variation in rudder control authority did not in general change with Angle of Attack.

For the fixed rudder offset runs, these results would suggest that the rudder concept may have the added benefit of controlling the static as well as the dynamic loads on the tail increasing the fatigue life improvement factors by 10 to 30 times those using only dynamic loads control. This must be kept in mind when comparing rudder control versus PZT control approaches, since the rudder produces a static bending moment when deflected into the air stream.

References

1. Zimmerman, N.H. and Ferman, M.A., "*Prediction of Tail Buffet Loads for Design Applications*," NADC Report, NADC-88043-60, July 1987.
2. Zimmerman, N.H., Ferman, M.A., et. al., "*Predictions of Tail Buffet Loads for Design Applications*," April 3-5, 1989, Mobile, Alabama.
3. Liguore, S.L. and Drouin, D.V., "*Time Varying Effects on the Buffet Response of Scaled F/A-18 Vertical Tail*," AIAA-98-1958.
4. Ferman, M.A. and Liguore, S.L., "*Composite Exoskin Doubler Extends F-15 Vertical Tail Fatigue Life*," 34th SDM Conference, April 19-22, 1993, LaJolla, CA.
5. Ferman, M.A., Patel, S.R., et. al. " A Unified Approach to Buffet Response of Fighter Aircraft Empennage," AGRAD/NATO 20th Symposium, Sorrento Italy, 2-4 April 1990.
6. Yurkovich, R. N., "Application of Constrained Layer Damping on F/A-18 Horizontal tail", Presented at Damping '89, West Palm Beach, February 1989.
7. Liguore, S.L., Ferman, M., and Yurkovich, R., "Integral Passive Damping of Primary Aircraft Structure," Presented at Damping '91, February 13-15, 1991.
8. Rock, S. M., Ashley, H., et. al. "Active control for fin buffet alleviation," Proceedings from AIAA Guidance, Navigation and Control Conference, 1993, pp. 1051-1056.
9. Moses, R.W., "Vertical Tail Buffeting Alleviation Using Piezoelectric Actuators - Some Results of the Actively Controlled Response of Buffet-Affected Tail (ACROBAT) Program", *Proceeding of the SPIE Smart Structures and Materials Conference*, 1997.
10. Moses, R.W., "Vertical Tail Buffeting Alleviation Using Piezoelectric Actuators And Rudder", *High Angle of Attack Technology Conference* September 17-19, 1996 NASA LaRC, Hampton VA.
11. Pado L.E., Liguore S. L., Lichtenwalner P.F., and Drouin D., "Neural Predictive Control for Active Buffet Alleviation", Proceedings, SPIE Symposium on Smart Structures and Materials, Vol. 3326, San Diego, CA, 1998.
12. Pado L.E. and Lichtenwalner P.F., "Neural Predictive Control for Active Buffet Alleviation", AIAA SDM Conference, St. Louis, MO. 1999, AIAA- 99-1319.

AN EXPERIMENTAL INVESTIGATION OF TANGENTIAL BLOWING TO REDUCE BUFFET RESPONSE OF THE VERTICAL TAILS OF AN F-15 WIND TUNNEL MODEL

BY
M.A. Ferman*, E.W. Turner, and L.J. Huttsell****

ABSTRACT

A concept employing tangential blowing was investigated experimentally as a possible means for mitigating buffet response of fighter aircraft empennage. Wind tunnel tests of a 4.7 % scale model of the F-15 Fighter were run in the Subsonic Aerodynamics Research Laboratory (SARL), WPAFB, OH. Tangential blowing was introduced from three points: (a) the nose, (b) the wing root leading edge, and (c) the gun bump, using symmetric blowing from both sides of the model. Individual blowing from each of the three locations was used, as were all combinations, and results were compared to baseline data without blowing. The model was equipped with one flexible tail and one rigid tail, and instrumented so that oscillatory pressures could be measured on both tails, and vibratory root bending and torsion moments and tip acceleration on the flexible tail. Angles of attack (AOA) from 0 to 32 degrees, and yaw angles of -4, 0, +4 degrees were investigated. Two dynamic pressures (Q) were employed, 30 and 56 psf, both to check on data scaling, and to assess the blowing effectivity at two Q's.

Generally, an influence of blowing was seen in the response and the pressures, but it is difficult to cite complete general trends in a simple statement. Most cases showed some reduction in response from blowing, though the broadband and narrowband results differed as to the degree and trend, especially bending response as compared to torsion, and especially depending on the combination of AOA and yaw angle considered. In some cases, blowing actually increased response slightly. The wing blowing position was the most effective, the gun position was the next most effective, while the nose was the least effective. This type of tangential blowing appears to reflect a Coanda effect, since the blowing was injected well upstream of the empennage, but closely followed the model surfaces until reaching the tails. The results suggest further investigation and application is merited.

This work was sponsored by the Air Force Research Laboratory (AFRL) under their Unsteady Aerodynamics Integrated Product Team (IPT) effort. The results of the tests, data acquisition, data reduction, and the evaluation of the effectivity of the blowing are detailed in a three volume Report, [1]-[3]. This paper is a brief summary of that work, and extends a earlier paper, [4] which gave a status report of work through Fall 1997. A separate effort under this IPT employed pizeoelectric actuators and modern control methods as another means for mitigating buffet response on the empennage of this model.

BACKGROUND AND APPROACH

A number of modern fighter aircraft attain high angle-of-attack maneuvering capability through vortex lift. At the lower angles of attack, the vortex core is tightly wound and convects aftwards, producing an additional static (steady-state) lift effect, with little or no associated vibratory loading effects. At the higher AOA's, these vortices exhibit what is called, breakdown, where a turbulent characteristic appears to be superimposed on the

* Prof. Aerospace/Mech. Engr. Dept, Parks College , St. Louis University, St. Louis MO
** Aerospace Engineers, AFRL, WPAFB, OH

calmer vortex core. Thus, in addition to the principal lifting effect, a strong vibratory loading, or buffeting, is present from the burst vortices. While the burst vortex still convects aftwards, it is wider and generally touches, or comes closer to the empennage than did the original vortex core. Thus, Buffeting pressures are able to induce strong excitation of the empennage, leading to severe structural strains occurring at frequencies whereby a large numbers of cycles could be quickly accumulated, potentially causing overstress, cracking or foreshortened fatigue life. Several twin tailed aircraft, The F-14, F-15, and F/A-18 have experienced these buffeting loads, and engineers have had to consider these effects in their designs for safe flight operation. Techniques to reduce buffet have used structural stiffening, addition of composite doublers, and inclusion of fences or vents, see [5]-[10]. A wide range of researches into the use of pizeoelectric dampers and other new concepts have been initiated by many investigators.

The concept considered herein attempted to alter these turbulent flows by employing airflow injected tangentially along the fuselage and wing, but upstream, of the empennage of a modern fighter aircraft. These controlled airflows are often referred to as "blowing". Since the F-15 Fighter operates at high angles of attack, and since it has experienced buffet from vortical flow breakdown, a wind tunnel model of scale 4.7 % of the F-15 was selected for the investigation. A standard aerodynamics-type model was used, but modified to accommodate the blowing ports and tubing to provide the tangential blowing sources. Three blowing positions were employed in the tests; namely, the wing root location , the gun bump location, and the nose. The nominal tails used in aerodynamics tests were removed and replaced with special tails for this testing. The left hand side (LHS) tail was replaced by a scaled flexible tail, designed to replicate, at this scale, the first several natural vibration modes of the full size tail. This tail was instrumented with pressure transducers, root bending and torsion strain gauge bridges, and accelerometers at the tip. The other tail (RHS) was replaced by a relatively rigid tail and equipped with pressure transducers. The flexible tail instrumentation provided data on oscillatory root bending and torsion moments, tip acceleration, and pressures. The rigid tail instrumentation provided data on oscillatory pressures without influence of tail flexibility and vibration.

Tests were conducted in the SARL wind tunnel at Wright Patterson Air Force Base during Fall 1995, and were sponsored by AFRL under an IPT effort. A three volume report [1]-[3] was prepared under the IPT and is divided as: (a) Volume I-Test Results, Discussion, and Correlation, (b) Volume II- Response Data, and (c) Volume III - Oscillatory Pressure Data. A buffet bibliography has been included to aid other investigators. Flow visualization tests were run, and are partially documented in [4].

TEST FACILITY

The SARL is a modern wind tunnel with a high contraction ratio, open circuit, operation capable of Mach Numbers up to 0.55. It is fully equipped for flutter, aerodynamics, buffet, and loads testing . The Tunnel test section is approximately 10 ft. high by 7 ft. wide and 15 ft. in length, and has 2 ft. flats at the wall and side intersections, making an octagonal-type cross section. Relatively large models can be tested. An automated sting can be pitched and yawed rather rapidly at a given elevation, and has variable rates of motion. The sting elevation can be varied. A large portion of the viewing wall is high quality Plexiglas, providing excellent viewing and allows use of Laser sheet illumination. Data acquisition equipment is available to capture data taken from a wide range of instrumentation. Data can be digitized for rapid data reduction, both insitu and post test. Online data is recorded through a MicoVAX III computer connected to a software controlled, 120 channel

multiplexer and connected to a 13 bit 100,000 samples per second, auto ranging, AC to DC converter. Balance channel signals, discrete pressure transducer data, strain gauge signals, and accelerometer signals were fed through Dynamic brand amplifier/bridge conditioners. Additionally, a Metrum dynamic data recorder was used for the bending and torsion and acceleration data for the flexible tail. A majority of the dynamic data taken was reduced post test by digital data reduction methods using a VAX 11780 computer for most of this work. Some specific data reduction and analysis was carried out with a Micron Super PC computer. Fast Fourier transform methods were used to develop PSD and rms results for the data taken from the wind tunnel tests. The digitized data were fed to these computer programs, and used anti-aliasing filters and noise filtering to produce high quality data. The anti-aliasing filter was a 4 pole Chebysev, low pass type, set at 625 Hz.

MODEL

The wind tunnel model is shown in a planview drawing in Fig. 1 and indicates some details of the instrumentation. Fig. 2 is a photo of the model on the wind tunnel sting. Fig. 3 details the instrumentation on the flexible tail. The rigid tail is similar, except that it has no accelerometers and no strain gauges. The flexible tail was equipped with bending and torsion strain gauge bridges to measure root bending and root torsion moments, both static and oscillatory. Accelerometers were placed at the forward and aft areas of the tip of the flexible vertical tail to capture overall and bending and torsional motions there. The flexible tail was also equipped to measure static and oscillatory pressures, with pressure transducers located identically to those on the rigid tail, as shown in Fig. 3. The pressure pickups were placed on both faces of the tails so that, a pressure difference, ΔP, across the tail could be obtained at each location. Data acquired were digitized at a rate of 5 kHz samples per second per channel, and higher rates were compared to insure accuracy. Data were recorded with a Metrum RSR512 Digital Tape Recorder, with 32 Channels being recorded simultaneously.

The natural frequencies of the model flexible tail were measured by the model manufacturer, Dynamic Engineering Incorporated (DEI), and again by AFRL. These results are shown here along with Finite Element Analysis (FEM) results from DEI.

	AFRL Lab Test*	DEI Test**	DEI FEM	
	Hz.	Hz.	Hz.	
MODE 1	39.8	37.5	36.8	First Bend.
MODE 2	169.0	160.6	159.3	First Tors.
MODE 3	189.0	183.8	195.3	Second Bend.

* Tail clamped to fixture ** tail on model

The tangential blowing at the nose, the gun bump and at the wing root was done independently, and all combinations were used; namely, nose/wing, nose/gun, wing/gun, These flow injections were done simultaneously on both sides of the model, maintaining flow symmetry. Wing blowing pressures of 0, 45, and 65 psi were used. A blowing pressure of 87 psi at the gun location was used throughout the tests, while the pressure at the gun bump location was maintained at 65 psi for all cases.

DATA ACQUISITION AND REDUCTION

The data acquired were directly digitized for subsequent reduction, and some on line data were constantly monitored for check pointing to ensure that parameters were in range of

anticipated values. Oscillatory pressures, root bending moment, and root torsion moments were acquired and developed into PSD format and rms summary format to aid in tracking buffet effects versus angle attack and yaw angle for two values of dynamic pressure, 30 and 56 psf, and for blowing at the three positions (nose, wing and gun bump) and for various blowing pressures. A few pressure CSD's were determined to indicate typical behavior. Some acceleration data in PSD and rms forms were also included in the report in both volumes. The bulky data consisting of many PSD plots are shown in [2] and [3] while some typical PSD's are in [1]. The rms summary plots are in [1], in both dimensional and nondimensional forms, to enhance discussion. In [1] are also shown (a) rms root bending moments for the flexible tail, calculated from rms pressures, (b) coherence functions for selected pressure pick-ups, (c) and flexible tail bending acceleration data derived from the data from the accelerometers at the tip of the tail.

RESULTS

A large data base was accumulated in this test, and a list of variables is noted here; namely:

Test Variable
- Dynamic Pressure, Q, = 30, 56 psf
- Angle of Attack (AOA) , Alpha.. range of 0-32 deg
- Yaw angle(Beta)...0, -4, +4 deg
- Blowing pressures
  - No blowing (base cases)
  - Wing Blowing (WBP) of 45 and 65 psi
  - Gun Blowing (WBP) of 65 psi
  - Nose Blowing (NBP) of 87 psi

Measurands
- Flexible Tail
  - Oscillatory Root bending and torsion moments
  - Tip acceleration
  - Bending moment from pressure integration
  - Oscillatory Pressures
- Rigid Tail
  - Oscillatory Pressures

(Dimensional and nondimensional data forms are shown for these measurands)

Yaw is defined as positive when the right wing moves forward when viewing down onto the aircraft. Pitch, or angle of attack (AOA), is defined as positive when pitching the nose upwards. A right hand vector rule at the c.g. applies to yaw and pitch. Only positive angles of attack were used in these tests.

Fig. 4 typifies the influence of angle of attack (AOA) and yaw angle (beta) on root bending and torsion of the flexible tail, for the case with no blowing, for broadband data, for a Q of 56 psf. Note, bending is growing at the highest AOA, while torsion seems to have peaked and is reduced at that angle. For both bending and torsion below an AOA of 24-28 deg., the positive yaw tends to show less buffet effect, while negative yaw increases responses. This makes sense, since the vortex tends to trail directly backwards, and thus negative beta pushes the LHS tail into the vortex, while conversely positive beta does the opposite. Above 24-28 degrees, the yaw effects are mixed or even reversed indicating the vortex has grown much larger, likely fully burst. Similarly, Fig. 5 summarizes the influence of wing blowing

pressures (WBP) of 0,45,65 psi on flexible tail root bending and torsion moments versus AOA for the case of beta of 0 deg., for a Q of 56 psf. Note that only AOA's of 20 deg or higher were shown. While an influence of WBP is shown, mostly reducing response, a few points show the opposite. These data are for broadband response. Narrow band data corresponding to both Fig. 4 and 5, show similar, but some what different trends, depending on the yaw angle and depending whether torsion versus bending is considered, and further depending on the vibration mode. In the main report, [1]-[3], significant detail of these trends are given. The blowing from the gun bump(GBP) was the next most effective position, while blowing from the nose, (NBP) was the least effective. For tie-in, the data of Figs. 4 and 5 are those in Figs. 7-10 in the earlier Paper [4].

At approximately the time the earlier paper was released, a discovery was made that led to additional data reduction, and to revisiting calibrations, settings, etc. That is, while the bending and torsion response at the lower Q of 30 psf exhibited lower values than did responses for a Q of 56 psf, the ratio of the bending responses was not proportional to the Q ratio when the data was nondimensionalized. Fig. 6 shows the broadband bending and torsion responses of the flexible tail versus AOA at Beta of 0 for the two Q's. It is seen that the effect of lowering the dynamic pressure has the correct trend. However as seen in the next graph, Fig. 7, that is not entirely as thought to be. In the latter figure, the nondimensional bending and torsion moment coefficients, C_M and C_T are defined as C_M = BM/QSc and C_T = TM/QSc, where BM is bending moment, Q is dynamic pressure, S is tail area, c is the tail mean aerodynamic chord, and TM is the torsional moment. Note that when nondimensionalized, the scaled responses for bending show that the data for the lower Q are either too large, or vice-versa, the data for the larger Q are too small. The AOA trend for both Q's are the same. Note, the torsional responses do scale closely, and the trend at the lower Q show the same AOA peaking.

Simultaneously, the pressure data was more closely reviewed to see if there was any connection to these trends in moment data. Fig. 8 shows the designations of the pressure transducers, A-F on the flexible tail, and G-K on the rigid tail. Fig. 9 shows oscillatory pressure coefficients, $\Delta p/Q$ expressed in rms terms for no blowing. In the top half are data for Q of 56 psf, while data for Q of 30 psf are given in the lower half. Data for the flexible tail are on the left hand side, and data for the rigid tail are on the right hand side. Note that these coefficients seem to correlate with Q as they should, and that the peaking at the higher angles seems to be present for the larger pressure pick-ups. In Fig. 10 are similar data for the same case, but with a WBP of 45 psi. Here it is seen that the same trends and scaling seem to hold as when WBP = 0, with the overall pressure trends showing slight reductions from blowing.

Attempts were made to correlate the nondimensional data with data from the F/A-18 in [1], and a portion is repeated here. Fig 11 shows a comparison of nondimensional bending and torsion data with those from the F/A-18 Vertical Tail. Both wind tunnel model data scaled-up and flight test data are presented for the F/A-18, per [7]. The F-15 and F-18 data show good agreement overall, except that only the F-15 bending data does not peak and fall off as does the other data. In Fig. 12, the comparison between the F-15 Vertical Tail and the F/A-18 Stabilator is shown, with both scaled model data and flight data for the latter. Note that data for the F-18 stabilator follows those of the F-15 vertical tail nicely where available. Though the stabilator is a stiffer surface than is the F-15 Vertical Tail due to more stringent flutter requirements, their nondimensional data compares favorably. Also, the F-18 data

were nondimensionalized slightly differently, but the net effects are not appreciable. A more precise correlation would require that the basic data of all these cases be scaled to a more compatible configuration before nondimensionalizing per [5], but even then, there is no assurance of improved correlation. The F-18 basic data was not available to the Authors to do this.

CONCLUSIONS AND RECOMMENDATIONS

There was a definite influence of blowing on the vortical flows at the tails, and a definite, but mixed effect on the flexible tail response. Generally, buffet was reduced somewhat in most cases. Similarly, the effect of blowing was seen to be different for response data at various yaw angles; in some cases, blowing slightly increased response. Bending was effected in different ways than was torsion. Likewise the narrow band data surrounding the various tail vibration modes were effected differently than were broadband data. Generally torsional responses showed trends with angle of attack that were as expected from the Author's experiences. Bending showed no peaking in the AOA range investigated, which was not as expected. This could mean that bending might peak at higher angles beyond those investigated, else there may have been some influence of tunnel flow causing this trend. Acceleration data for bending showed peaking in the AOA range. Pressure data showed peaking, as did root bending moments calculated from the rms pressure data(done on both the flexible and rigid tails). Another oddity from the tests was that bending did not scale as closely as expected with the two dynamic pressures, while torsion did and the pressures did. While some calibration error was suspected initially, none was found even after extensive review of all processes. The blowing from the wing position was the most effective, blowing from the gun bump was the next most effective, while nose blowing was the least effective. The fact that the flows convected back to the tail areas as well as they did suggests that some type of Coanda Effect was occurring.

Based on the results, it is recommended that additional work be done with this approach, namely that the flow injection points be moved back to various stations approaching the tail root. The possibility of oscillating the flow pressure about some mean pressure value seems to be a likely candidate, especially if the pressure oscillations can be made at frequencies known to dominate the vortical flows. Transient effects are known to have some effect on buffet, and should be investigated with this model, as done with a generic model in [11]. Perhaps some in-flight case could be attempted to see if the same levels of induced flows would have the same quantitative effects while the aircraft is moving with less-than-the-stationary conditions of the wind tunnel model.

REFERENCES

1. Ferman, M. A. , and Turner, E. W., "An Experimental Investigation of Tangential Blowing to Reduce Buffet Response of the Vertical Tails of An F-15 Wind Tunnel Model, Vol. I- Test Results, Discussion, and Correlation," AFRL-VA-WP-1999-3018 , Jan. 1999
2. Ferman, M. A. , and Turner, E. W., An Experimental Investigation of Tangential Blowing to Reduce Buffet Response of the Vertical Tails of An F-15 Wind Tunnel Model, Vol. II - Detailed Test Data- Flexible Model Response," AFRL-VA-WP-1999-3019, Jan.1999
3. Ferman, M. A. , and Turner, E. W., "An Experimental Investigation of Tangential Blowing to Reduce Buffet Response of the Vertical Tails of An F-15 Wind Tunnel Model, Vol. III- Oscillatory Pressure Data, " AFRL-VA-WP-1999-3020, Jan. 1999
4. Huttsell, L. J., Tinapple, J. A., Weyer, R. M., "Investigation of Buffet Load Alleviation on

A Scaled Twin Tail Model", AGARD Report-R-822, AGARD SMP, Aalborg, Denmark, 14-15 Oct. 1997
5. Zimmerman, N. H., and Ferman, M. A., " Prediction of Tail Buffet Loads for Design Applications" USN Report, NADC 88043-60, July 1987
6. Zimmerman, N.H., Ferman, M.A., Yurkovich, R. N.,and Gerstenkorn, G., "Prediction of Tail Buffet Loads for Design Applications", 30 th SDM, Mobile, AL, 3-5 April 1989
7. Ferman, M. A., Patel, S., Zimmerman, N.H., And Gersternkorn, G., " A Unified Approach to Buffet Response of Fighter Aircraft Empennage", AGARD/NATO 70th SMP, Sorrento,Italy, 2-4 April 1990
8. Ferman, M.A., and Liguore, S. L., " Buffet Coupled Response of the HARV Thrust Vectoring Vane System", NASA High Angle of Attack Conference, Hampton, VA, Oct 1990
9. Washburn, A. E., Jenkins, L.N., and Ferman, M.A., " Experimental Investigation of Vortex-Fin Interaction", 31 Aersospaces Meeting, Reno, NV, 11-14 Jan 1993
10. Ferman, M.A., Liguore, S. L. Liguore, Colvin,B.L., Smith, C.M., "Composite Exoskin Doubler Extends F-15 Vertical Tail Fatigue Life", AIAA/ASME 34th SDM, La Jolla, CA, 19-21 April 1993
11. DIMA, C. " The Effects of Time Varying Maneuver Conditions on Empennage Buffet Response" MS Thesis, Parks College, St. Louis University, St. Louis, MO, Dec 1994

ACKNOWLEDGEMENTS

The Authors wish to acknowledge significant contributions of several people: (a) Mr. Dansen Brown, AFRL, WPAFB, OH who did the huge data reduction, (b)Mr. Jon Tinapple,AFRL, WPAFB,OH who ran the tunnel tests, and (c) Mr. Ken Juhl, a Student at Parks College, St. Louis University, who helped Dr. Ferman, with endless graphs and many calculations.

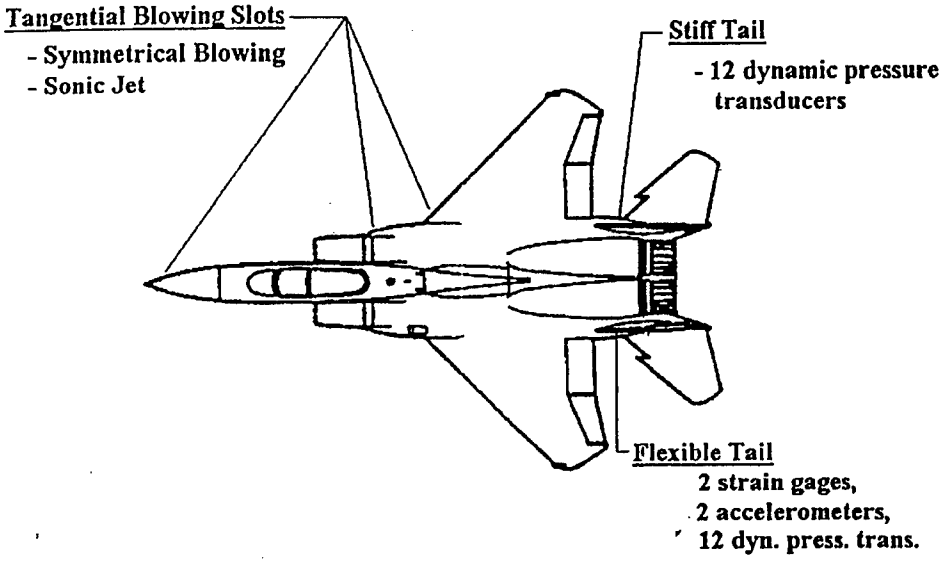

Figure 1 Planview of 4.7 % Wind Tunnel Model

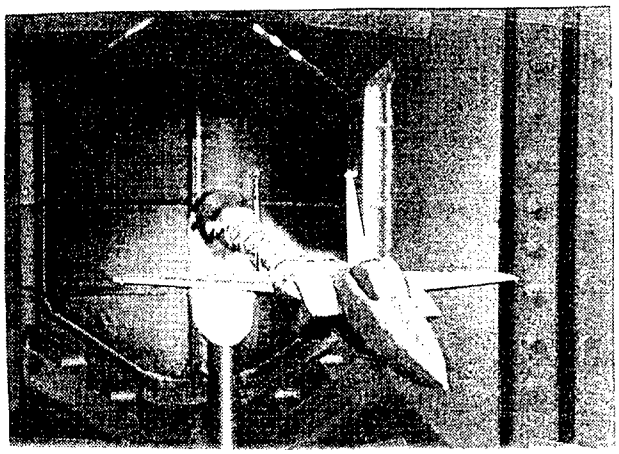

Figure 2 4.7 % Buffet Model in Wind Tunnel

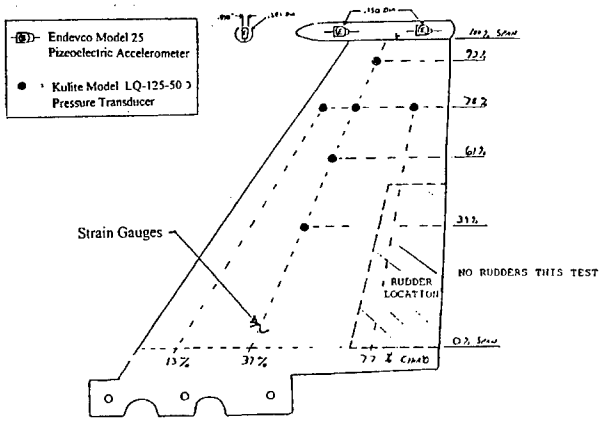

Figure 3 Instrumentation Layout on Flexible Vertical Tail

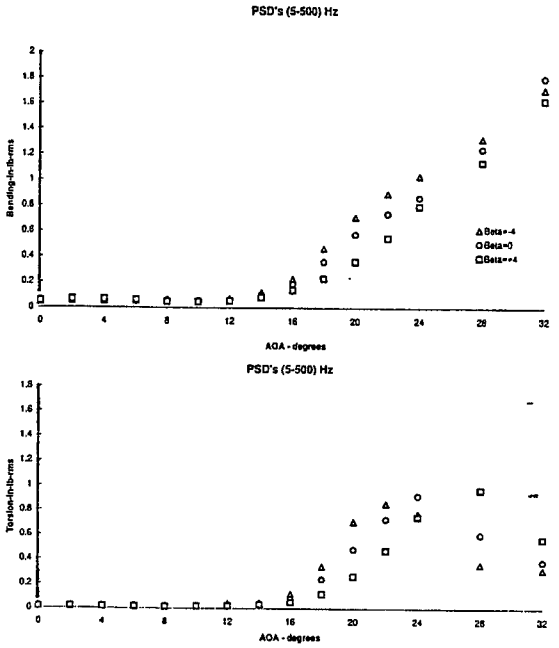

Figure 4 Flex. Tail Bending and Torsion Responses vs AOA
Q =56 psf, No Blowing

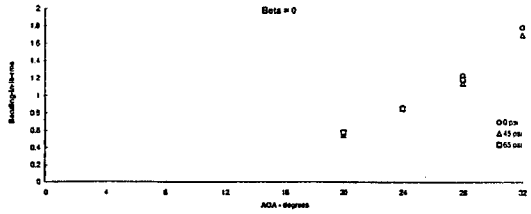

PSD'S 5-500 Hz.

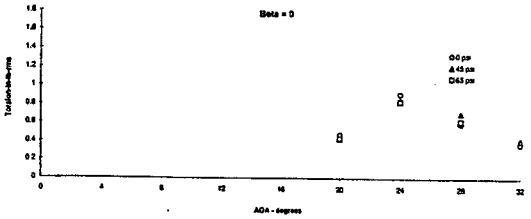

Figure 5 Flex. Tail Bending and Torsion Responses vs AOA
Q=56 psf, Wing Blowing Summary

F-1

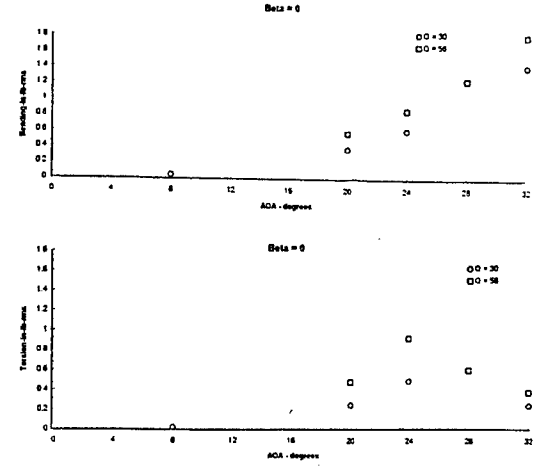

Figure 6 - Summary of Flex Tail Bending and Torsional Responses, WBP =0, Beta = 0 , Q= 56&30 psf

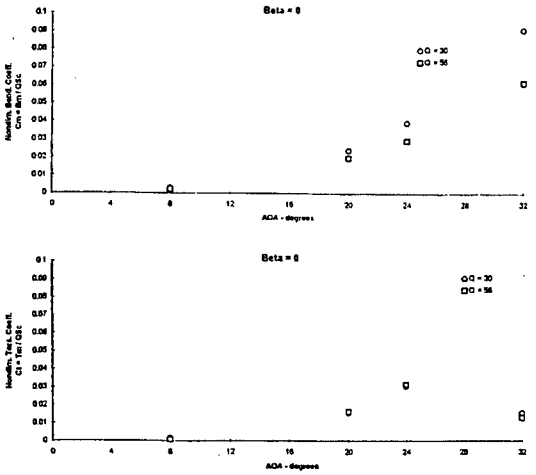

Figure 7- Summary of Flex Tail Nondimensional Bending and Torsional Responses, WBP=0, Beta = 0, Q= 56 & 30 psf

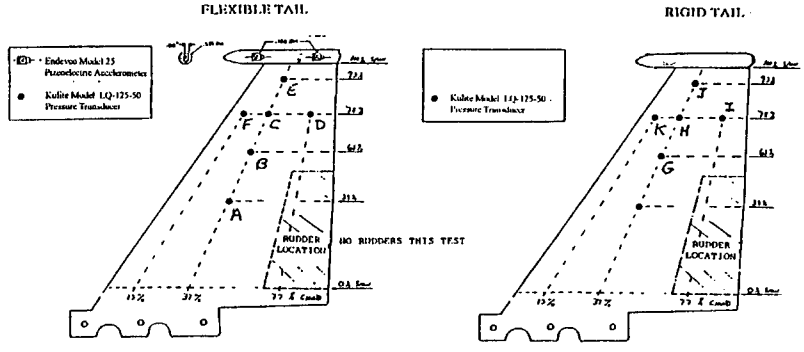

Figure 8 Pressure Pickups - Letter Identification

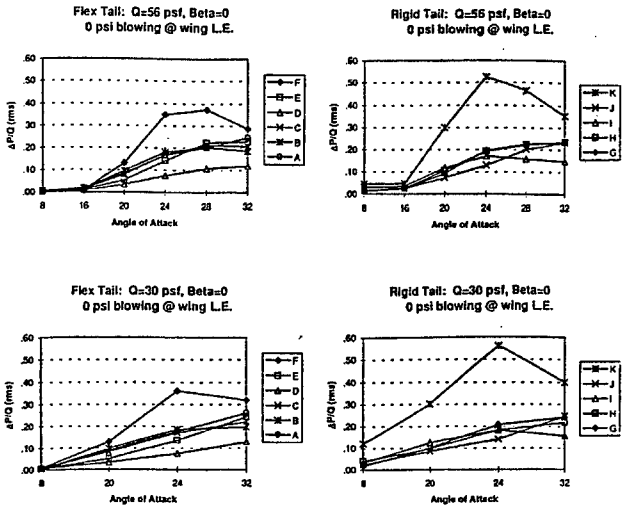

Figure 9 Oscillatory Pressure Coeff. vs. AOA
Q=30 & 56 psf, Beta = 0, WBP =0

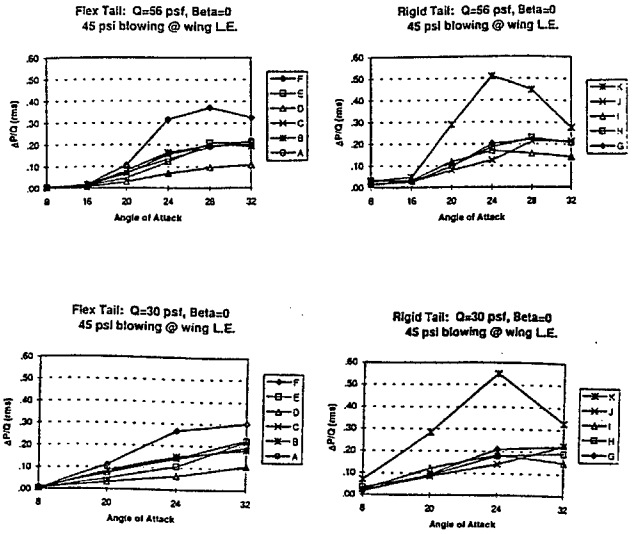

Figure 10 Oscillatory Pressure Coeff. vs. AOA
Q=30 & 56 psf, Beta = 0, WBP = 45 psi

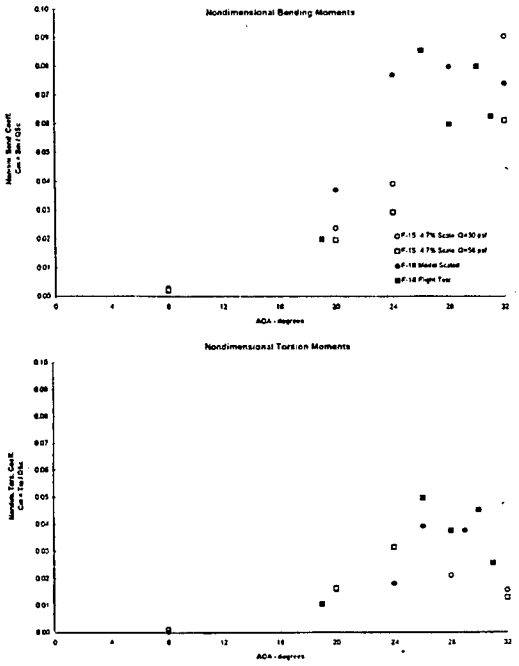

Figure 11 Correlation Between 4.7% Scale F-15 Vertical Tail and F/A-18 Vertical Tail

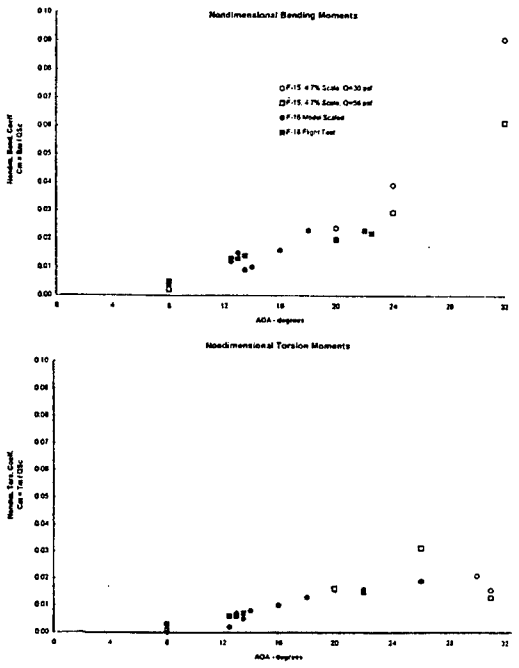

Figure 12 Correlation Between 4.7% Scale F-15 Vertical Tail and F/A-18 Stabilator

Development of a Transient Signal Analysis Method For Flutter Testing

by

J. Thomas vonHatten

Engineer/Scientist 4, The Boeing Company,

P. O. Box 516, St. Louis, MO 63166, USA

and

M. A. Ferman

Professor, Aerospace Engineering, Parks College of St. Louis University,

3540 Lindell Blvd., St. Louis, MO 63156, USA

Abstract

A device for recording and analyzing flutter model data has been developed for use in the St. Louis University-Parks College Low Speed Wind Tunnel (Parks LSWT). The Author developed this device as a Graduate Study Project in 1998 [1], with guidance from the Co-author. The objective was to devise and implement a computer-based data analysis tool to allow the observation of dynamic data from two separate inputs in real time, and to record the data during testing for post-test analysis of frequency and damping characteristics of a flutter model.

The device was constructed using LabVIEW® virtual instrument (VI) software, a package widely used in both industrial and educational settings, operating on a personal computer (PC) at the Parks LSWT facility. A flutter model was designed and tested to check the VI development. It was carefully designed to give a good database for these checks, and was carefully analyzed to insure proper behavior. Theory and tests compared well.

While the VI was directed toward flutter models, it can be used for other test applications, such as beam-vibration tests or tests using dynamic pressure transducers.

Background

Data acquired from wind tunnel testing of dynamically scaled models are of two basic types: visual and non-visual. The visual data are acquired by recording actual

model motions on film or videotape for post-run review and analysis. Frequently stroboscopic lights are used to emphasize these motions, if available. Non-visual data are acquired by recording instrumentation outputs from strain gages, accelerometers, and fiber-optic or selsyn devices, placed at various points on or in the model's structural components. These outputs can be manipulated for viewing by test personnel in "real-time" during the run, and are usually saved for post-test analysis.

Prior to this work, the capability to view and record non-visual dynamic flutter-model data was not present at the Parks LSWT. As a graduate research project, the author began an effort to devise a computer-based "virtual instrument" (VI) that would allow test personnel to view two separate dynamic flutter data channels in real-time, and to record data from these inputs as needed. In addition, the device would be able to automatically record data should a preset dynamic load limit (or other preselected criteria) be encountered on one or both of the input channels, such as when divergent flutter is encountered.

The Author also built, calibrated, and tested a segmented-wing flutter model to check the operation and usefulness of the VI being developed. The model used full-bridge strain-gage networks to measure wing root bending and torsion, and was installed on the Parks LSWT Flutter Fixture for testing. The Author performed this work during the Fall and Spring 1998 semesters at Parks College, with the guidance of the Co-author. The flutter fixture noted here was allow for flutter testing in the Parks LSWT, an existing (1993) development to allow for flutter testing in the Parks LSWT.

Method

Non-visual dynamic wind-tunnel data as described above are traditionally acquired and viewed as follows: (a) analog data are acquired from a measuring device (strain gage, accelerometer, etc.), (b) the input signal is amplified, (c) the amplified output signal is then sent to a viewing/recording device, such as a strip chart, that has been scaled by calibrating the measuring device. This allows the amplified output (also called a "total signal") to be viewed in real-time, giving an observer the chance to monitor the total forces experienced by one or more data inputs.

If viewing the "dynamic" component of the output signal is also desired, each output signal is split into two paths. One of these is passed through a low-pass filter to obtain a "steady-state" portion of the "total" output signal. This steady-state value is removed from the total signal, and the resulting dynamic signal is then displayed for viewing.

Generally, both the total and dynamic signals are almost always recorded for use in post-test analysis. Along with the dynamic data, one or more calibrated "sine wave" input signals are recorded along with steady state tunnel parameters, tunnel dynamic pressure and total temperature, so relationships between the test conditions and the test data can be determined.

The Virtual Instrument DYN_DATA.VI

The virtual instrument devised was noted as DYN_DATA.VI, and reads and processes dynamic input data from two channels. In this case, the data analyzed were the outputs of the bending and torsion strain gages of the wing model. The VI, its detailed description, and a detailed set of operating instructions are resident on the PC used at the Parks LSWT.

This VI was designed using National Instruments' LabVIEW® software package, at Parks College. Detailed information about this software is given in [2] and [3].

This LabVIEW® virtual instrument was designed to acquire data, send it out to virtual "strip charts" to allow the "total" signal to be viewed, split this signal, filter one side to get the "steady-state" component, subtract this from the other side, and view this on another virtual "strip chart" as the "AC-coupled" signal. The two "AC-coupled" signals could then be combined and fed to an oscilloscope display. The instrument function is described in greater detail in [1], and contains the instructions on how to use DYN_DATA.VI. Figure (1) is the detailed LabVIEW® wiring diagram of the instrument. Figure (2) is its "front panel", or what is displayed on the PC's CRT screen while the VI is in operation.

The VI reads all data received by the PC through its data acquisition unit. This VI is designed to record all the "total signal" data sent to the PC, so it is simpler and faster to record this entire data array. The VI then selects the data channels to be processed, and displayed to the user during testing. This means that measurements to compute tunnel dynamic pressure (and hence tunnel velocity), if available, are also

recorded, so post-test correlation between model behavior and tunnel speed (a primary concern in analyzing flutter data) can be performed.

Wind tunnel testing of flutter models can take relatively long periods of time. Even when only two input channels are being recorded, the amount of data obtained during a single run can quickly take up most of the storage space available in most desktop computers if recording is done continuously. With this in mind, the recording capability of the VI is "on-demand", with data being acquired as a series of "snapshots" by test personnel during the run. Before each tunnel run, a basic file name and recording length of each data snapshot is specified. A "dataset" value that is appended to the basic run file name is also specified, and can be changed during the run as desired. If the run dataset value is changed between data snapshots, a new file is written, with the proper data contained in the new file. If the dataset number is not changed between acquisitions, new data are appended onto the end of the file containing data already recorded under the existing file name. The data, once recorded, is easily found after the run ends, and can be displayed on commercially available PC spreadsheet software.

An "overscale" recording function that will automatically record a data snapshot if either data input reaches a predetermined static or dynamic limit is also available. This limit is determined by a pre-run calibration, which uses the channel "zero" and "span" features of the VI. The overscale "snapshot" file is given a special file name to make it stand out from the other data that might be taken during the run. If no overscale data is desired, this function may be overridden. All file naming, data "zeroes" and "spans", and file recording lengths are manually input through the front panel of the VI.

Test and VI Validation

The VI development and validation took place at the St. Louis University-Parks College Low Speed Wind Tunnel (Parks LSWT). The Parks LSWT is an open-return, solid-wall wind tunnel, with test section dimensions of 28"x40"x54" (0.7 m x 1.0 m x 1.4 m, H x W x L), and is capable of test section velocities of up to about 220 fps (67 m/s or 150 mph). Most aerodynamic test articles are mounted by some suitable means to a pyramidal-type external balance whose resolving center is in the center of the tunnel test section. Other test articles, such as flutter models or

pressure-instrumented test articles, can be fixed to a wall mount that replaces the left-hand window in the test section. This mount was developed at Parks College by the Co-author, and is described in [4] and [5]. The assembled wing model, as installed on the wall mount, is shown in Figure (3).

The SLU-Parks LSWT uses LabVIEW® as its primary data acquisition and display software, in conjunction with a Zenith Data Systems 486/66 MHz personal computer (PC). The LabVIEW® system at the Parks LSWT is used primarily to record data from the tunnel's external "pyramidal" six-component balance when it is used for aerodynamic force-and-moment testing. This raw data are input to a National Instruments SCXI signal conditioning/data multiplexing device, and output as a two-dimensional data array. The array is then sent to a multifunction data acquisition board (also manufactured by National Instruments) that is in the Parks LSWT PC. This board converts the multiplexed data from the SCXI to the PC in a form usable by LabVIEW®.

The test article used to validate this work was a segmented, flexible wing panel fabricated by the Author, and tested in the Parks LSWT. This wing model is shown in Figure (4). The design for this model was based on prior models successfully tested in the SLU-Parks LSWT, as listed in [4] and [5]. It consisted of five individual wooden wing sections mounted to a single, constant cross-section aluminum spar. Two full strain-gage bridge networks were mounted near the fixed end of the spar. One network was configured to measure spar root bending, and the other for spar root torsion. These gages were bonded to the spar using typical gage bonding techniques. The fixed end of the spar was designed and built to allow installation in the LSWT tunnel flutter mount without damaging the model's wiring harness.

A two-degree-of-freedom analysis of the model's flutter characteristics was also performed. This analysis was based on a coupling of the first bending and first torsional modes and frequencies, using the model's section masses and inertia values plus the "ideal" bending and torsional stiffness of an "ideal" spar of the same shape and material as the one in the model. This analysis used techniques described in [6], [7], and [8].

Test Results

Both "air-off" and "air-on" data were obtained from the model using DYN_DATA.VI as part of the validation of the VI. Air-off data were acquired both in a "bench-testing" condition away from the tunnel test section, and in an "installed" condition, mounted in the Parks LSWT test section on the flutter wall mount. Data acquisition was initiated, and then the test article was tapped lightly to excite it in bending, torsion, or a combination of the two. The recorded output levels from the test article were more than sufficient to allow the natural frequencies of the test article to be properly determined. The recorded data from each channel were analyzed both using a spreadsheet and a LabVIEW®-based spectral analyzer. The spectral analysis plots of these data are shown as Figures (5) and (6). These checks determined that the first and second bending frequencies of the test article were 3.5 Hz and 19.5 Hz, respectively, and that the first torsional frequency was 24.0 Hz.

The air-off data acquisition was also used to determine the maximum practical sampling rate for the VI as installed on the Parks LSWT PC, which are 500 samples per second. The best screen update rate is twice a second, with 250 new data samples being displayed during each update.

For "air-on" testing, data acquisition was in many ways similar to many other dynamic wind tunnel tests. For an individual data point, the tunnel speed was set and stabilized, and data were acquired. This cycle was repeated for increasing tunnel speeds until one of three events occurred: (a) a flutter point was encountered, at which time additional data were taken if possible, (b) it was apparent that the model would not tolerate any further speed increases from a structural standpoint, or (c)The tunnel speed limit was reached, precluding further testing until changes could be made to the model.

This is similar to a flutter testing technique described in [9], with some small changes as needed for use at the Parks LSWT.

A total of three air-on runs were made, each being terminated when the test article fluttered. In each case, the strip chart traces of the virtual instrument were of valuable use during each run. On-line observation of the "total-signal" traces allowed the model's angle of incidence to be properly trimmed during the first two runs, so that its spar was not subjected to bending due to steady-state air loads during

a run. Both the "total" and "dynamic" traces also showed output from both the bending and torsion bridges indicating cyclical motion at flutter. The Lissajous figure formed by the virtual oscilloscope took the shape of a circle, indicating that the bending and torsion outputs were in a 90-degree phase relationship to one another, also indicative of flutter.

Data were obtained at the flutter point of each run, after which both the run and VI operation were terminated manually. In order to guarantee that data at flutter would be acquired, the VI was operated with its overscale trigger off to prevent its premature shutdown during running. Both the flutter speed and frequency were highly repeatable for each run. The flutter speed was 41 miles miles/hr (18.3 m/sec) and the flutter frequency was determined to be 20.85 Hz. Figure (7) shows a spectral analysis for data acquired from the test article at flutter.

As part of the project, predictions for flutter speed and frequency of the test article were performed. The two-degree-of-freedom calculations made by the Author assumed a coupling of the first bending and first torsional modes to produce the flutter mechanism in the model, based on its mass properties and an "ideal" spar stiffness computed from its actual dimensions.

A comparison of the actual flutter data obtained during testing with the calculated (ideal) values is listed in Table (1), below.

Data Type	Flutter Speed mph (m/s)	Frequency (Hz)
Calculated	49 (22)	9.8
Measured	41 (18.3)	20.85

Table (1) - Flutter Data Comparison

The calculated and measured flutter speeds were relatively close, but it can be seen that their corresponding flutter frequencies were not. A three-degree-of freedom analysis of the "ideal" model, using methods described in [6] through [8] and including the second bending frequency, would likely reduce the difference

between the calculated and measured flutter frequencies, and bring their respective flutter velocities even closer together.

Additional Comments

The VI was designed to acquire and display flutter model dynamic response data for two data inputs. It can, however, be easily expanded to process, display, and record as many data inputs as desired, based on the performance and storage limitations of the desktop computer being used to run the VI. More-than-acceptable performance from the VI as developed was obtained when used with the Parks LSWT computer, a 486/66 MHz with internal video (VGA) capability. Current generation computers have CPU speeds of over 500 MHz, RAM storage levels approaching 1 megabyte, data bus speeds of 100 MHz, separate high-resolution video processor hardware, and 10-20 gigabyte high-speed data storage devices. These improvements in PC performance would allow for far greater data acquisition at higher sample rates and display capability using either the basic VI or an expanded version.

Since the data acquired and processed by this VI were obtained from two strain-gage bridge networks, the usefulness of the device need not be limited to dynamic flutter testing in wind tunnels. The basic VI can process data that is obtained from other types of simple structural testing, such as beam-vibration models. Expanded versions could be used to process information obtained from externally excited test articles to determine natural frequencies and mode shapes for various structures. Data obtained from dynamic pressure transducers, can also be treated similarly.

Conclusion

The goal of acquiring, viewing, and recording flutter model dynamic wind tunnel data in real-time or near-real-time in the Parks LSWT was achieved by developing and validating a Lab-VIEW®-based virtual instrument, DYN_DATA.VI. A flutter model developed for this project demonstrated the usefulness of this VI as a dynamic data acquisition instrument. In addition, the flutter speed of the model tested corresponded well with those calculated using a two-degree-of-freedom analysis. Dynamic data of the frequency levels common for low-speed flutter models (below 100 Hz) can be successfully acquired, observed, and recorded for post-run analysis. Dynamic data from beam-vibration models or dynamic pressure transducers can also

be easily read and recorded using this device. Expansion of this device to read and record data from more than its current two-channel capability can easily be accomplished, and is expected, given both the improvements in the capabilities and capacities of newer personal computers.

References

1. J. Thomas vonHatten, "A Report on The Development and Validation of Flutter Model Instrumentation in the St. Louis University - Parks College Low-Speed Wind Tunnel", St. Louis University, May 1998
2. Gary W. Johnson, "LabVIEW® Graphical Programming: practical applications in instrumentation and control", McGraw-Hill, 1994.
3. National Instruments, "LabVIEW®" Users Manual, January 1996 edition.
4. Ferman, M. A., Philippi, V., Aldersflugel, J., and Coffey, F., "Development of Aeroelastic and Flutter Testing Capability at Parks College", 1994 ASEE IL/IN Conference, Parks College, March 1994.
5. Ferman, M. A., and Aldersflugel, J., "An Investigation of Low Damping Flutter in the Parks College Low Speed Wind Tunnel", 1994 ASEE Conference, Purdue University, March 16-18, 1995.
6. Ferman, M. A., "Conceptual Flutter Techniques", MDC Report F322, USN Report, Contract NOw-66-0298-c, 10 February 1967.
7. Ferman, M. A., Flutter Class Notes, St. Louis University, 1965-1971.
8. Ferman, M. A., "Flutter and Aeroelasticity Class Notes", Parks College of St. Louis University, 1989-1992.
9. Alan Pope and John J. Harper, "Low-Speed Wind Tunnel Testing", John Wiley and Sons, Inc., 1966.

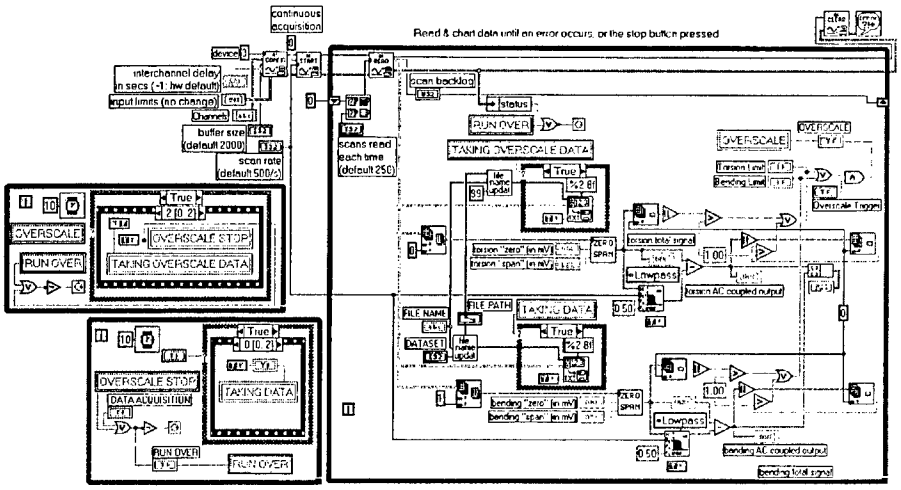

Figure 1 - The virtual instrument DYN_DATA.VI

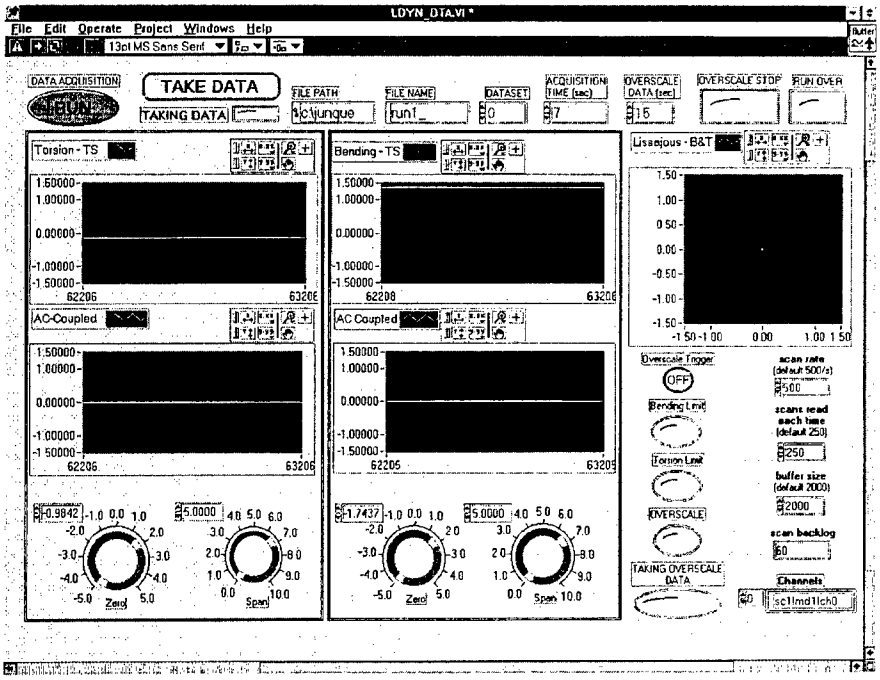

Figure 2 - The front panel for DYN_DATA.VI

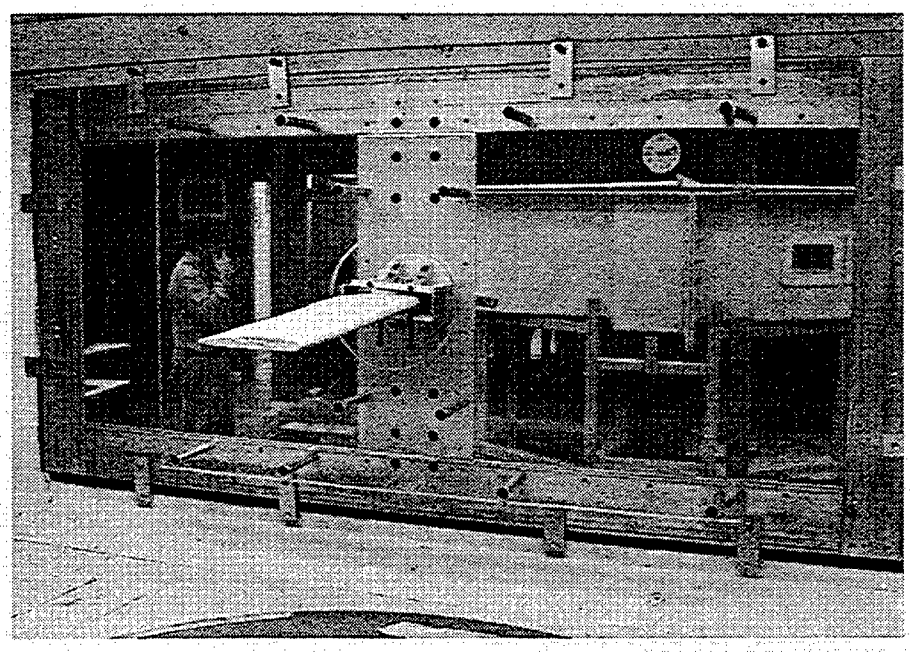

Figure 3 – The wing model installed on the Parks LSWT Flutter Wall Mount

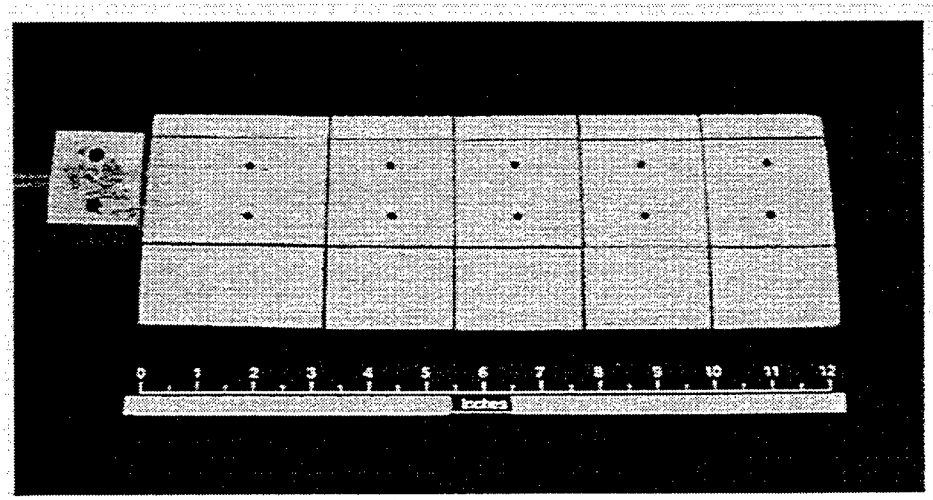

Figure 4 - The flutter wing used to validate DYN_DATA.VI

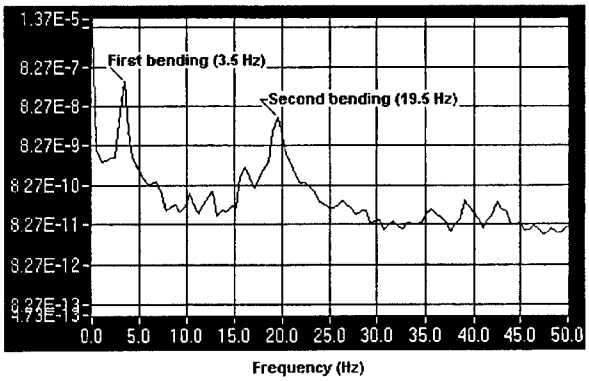

Figure 5 – Measured model bending frequencies (air-off)

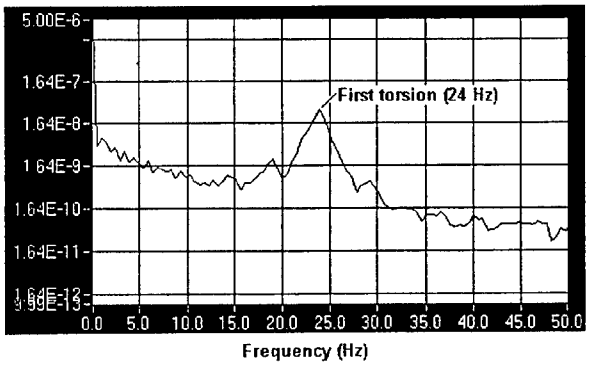

Figure 6 – Measured model torsion frequency (air-off)

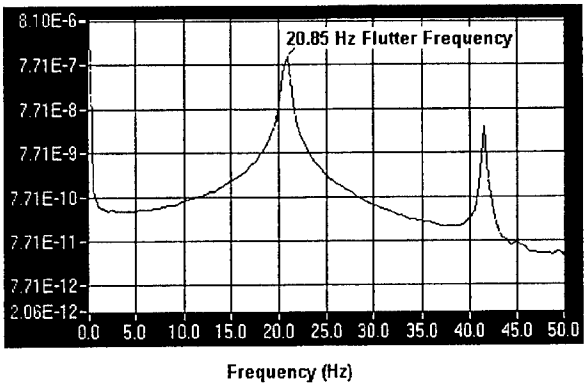

Figure 7 – Frequency of model at flutter onset (air-on, 41 mph)

Numerical Simulation of F/A-18 A/B/C/D Limit Cycle Oscillations (LCO) And An Active Oscillation Controller (AOC)

Professor - Dr. - Ing. Dale M. Pitt
The Boeing Company
St. Louis, MO 63166-0516

Professor - Dr. - Ing. David Manor
Parks College of Engineering and Aviation
St. Louis, MO 63103-1110

ABSTRACT

This paper outlines the use of standard linear aeroelastic analysis tools to develop a multi-input/multi-output (MIMO) state space model that can be used to simulate limit cycle oscillations (LCO) and consequently the design of a controller. A "closed loop" simulation was performed with a 16 Lb. LCO force providing the required lateral acceleration at the pilot seat. With the AOC actuated the response was decreased with the commanded aileron inputs from the AOC. The AOC was commanding an aileron deflection of ±0.15 degrees. This predicted value of aileron deflection agreed closely with the actual value measured during flight testing of ±0.2-0.4 degrees deflection. The simulated suppression qualitatively and quantitatively agreed with the flight test measured suppression.

INTRODUCTION

The F/A-18 model A/B/C/D is a combined fighter and attack aircraft. In the ground attack mode the aircraft carries a variety of stores on the four (two per wing) under-wing pylons. This model aircraft sometimes experiences undesirable oscillation at low altitudes and high speeds when carrying high pitch inertia stores on the outboard wing pylons inconjunction with an AIM-9 wing tip mounted missile. Figure 1 shows the aircraft in flight with stores on both the inboard and outboard pylons.

The oscillations are generally limit cycle in nature and produce an objectionable 5 to 6 Hz lateral acceleration at the pilot seat. The limit cycle oscillations are generally constant amplitude sinusoidal oscillations and are distinct from flutter where the amplitude of each successive oscillation increases until structural failure occurs. A time history trace of the pilot seat lateral acceleration measured during the flight test program is shown in Figure 2. These limit cycle oscillations

(LCO) have also been experienced by the F-16, Reference 1. The F/A-18 A/B LCO oscillation results in an unacceptable lateral acceleration at the pilot seat. Reference 2 states, " ... a structural-aerodynamic interaction mechanism is established which sustains the oscillations. The basic structural contributor to the

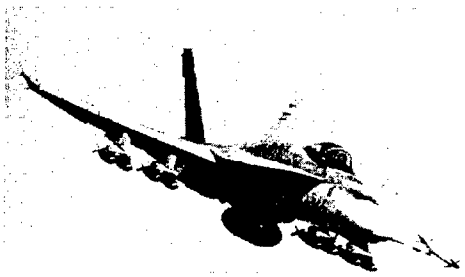

Figure 1.
Photograph of F/A-18 A/B/C/D Aircraft With External Stores

oscillation mechanism is the outboard pylon/store anti-symmetric pitch structural mode. These oscillations were characterized by anti-symmetric wing bending and torsion motion which coupled with the fuselage, primarily in the form of lateral bending."

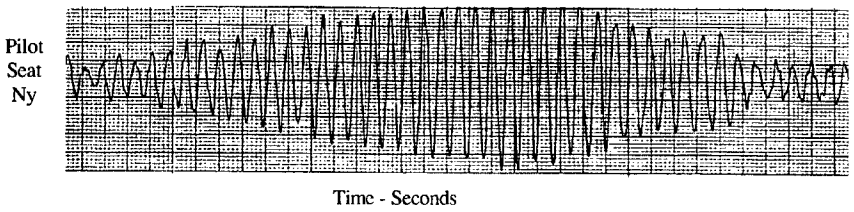

Figure 2.
Flight Test Time History

It was verified in flight-testing that the LCO was not classical flutter or Aeroserovoelasticly induced. The LCO severity is controlled more by Mach and load factor than by dynamic pressure, q. More details of the flight test can be found in References 1 and 2.

The standard linear aerodynamics, linear structural modeling and linear control laws are unable to predict the LCO. Much work has been

done to develop a non-linear analysis technique to predict LCO.[3-6] One technique uses Cunningham's trailing edge separation model. These models predict LCO, but as of yet have not been used to design a controller to suppress LCO. Some of the more recent efforts have focused on using linear theories to provide insight into the LCO phenomenna[7-8]. This paper joins the latter in that linear aeroelastic tools were employed to simulate LCO.

The problem LCO discovered during flight test was solved on the F/A-18 A/B/C/D aircraft by incorporating an "Active Oscillation Controller" (AOC) into the existing flight control system. The LCO frequency on the F/A-18 C/D was 5.6 Hz and was low enough that the oscillations could be controlled with the existing flight control system (FCS). The system commands anti-symmetric aileron motion based on the response of the flight control sensor package. Figure 3 is a reproduction from Reference 2 showing the ability of the AOC to reduce the LCO pilot seat response. One of the constraints imposed on the AOC design was to use only existing Flight Control System components; thus a software modification would incorporate the AOC. A generalized schematic of the AOC is shown in Figure 4. Extensive flight-testing was required to finalize the design of the AOC due to the limitations of the analytical tools[2].

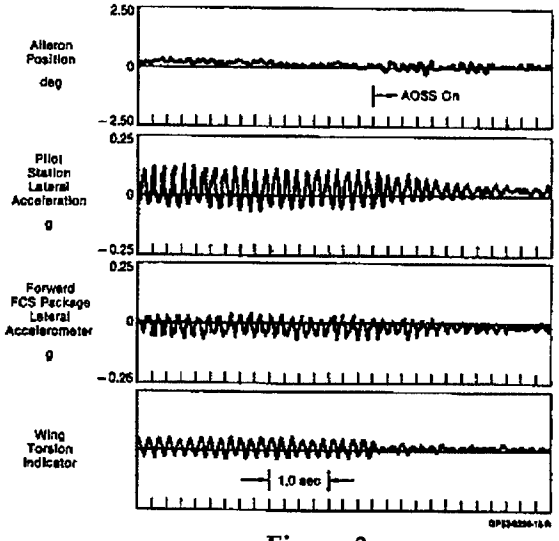

Figure 3.
AOC Flight Test Suppression Results

This paper outlines the use of standard linear aeroelastic analysis tools to develop a multi-input/multi-output (MIMO) State Space model that can be used to simulate LCO and consequently the design of a controller.

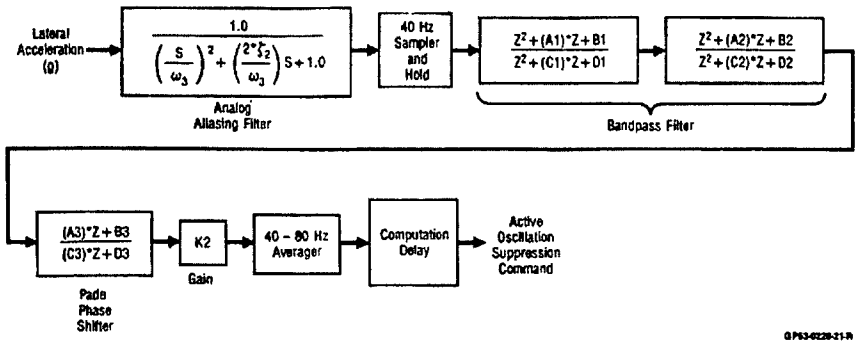

Figure 4.
Schematic of Active Oscillation Controller

Math Modeling

In this section the various mathematical models used in the analysis will be described. The F/A-18 aircraft was modeled structurally with a NASTRAN beam-rod model that has been correlated to Ground Vibration Test (GVT) results for various under wing stores. The stabilator and vertical tail flexibilities were also included in the dynamic NASTRAN model. This model yields accurate vibratory mode shapes, φ, and vibratory frequencies, ω. Grid points were added to the structural model to calculate the pilot seat and FCS Sensor lateral accelerometer responses. The plot of the model is shown in Figure 5. The beam-rod model was configured with the following external stores for this study: a 300-gallon external fuel tank on the inboard pylon and 2 MK-83 bombs on the outboard pylon.

The unsteady aerodynamics of the aircraft was represented using a linear doublet lattice computer code, N5KM[9]. The fuselage, wing, stabilator, and vertical tails were represented as lifting surfaces. A 3-dimensional plot of the Doublet Lattice model is shown in Figure 6.

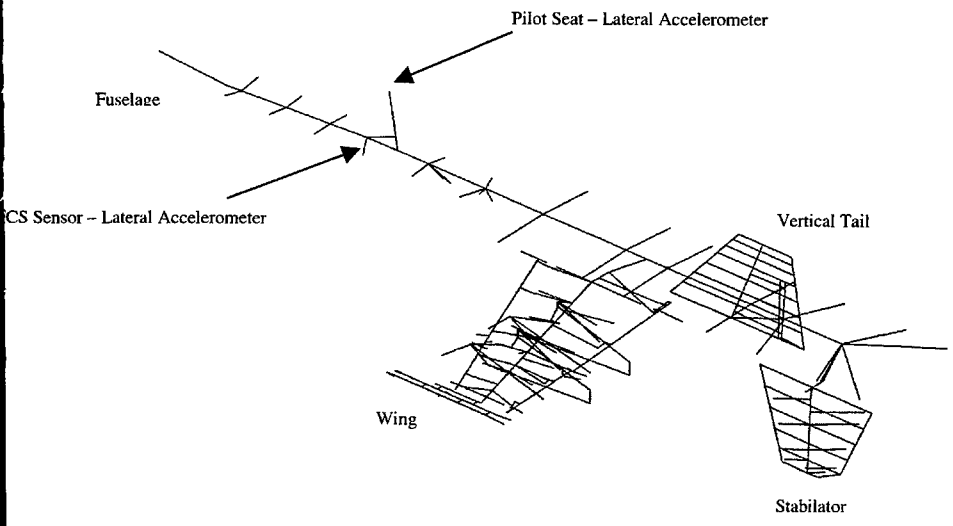

Figure 5
F/A-18 A/B/C/D Dynamic Beam Rod Model

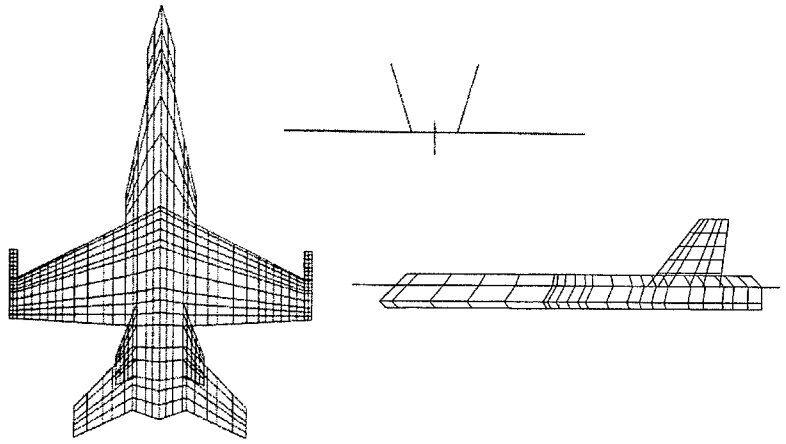

Figure 6.
F/A-18 A/B/C/D Unsteady Aerodynamic (Doublet Lattice) Model

The total degrees of freedom of the structural dynamic equations of motion for a flexible aircraft are greatly reduced by transforming the equations from physical coordinates, xyz, to modal coordinates, q. The unsteady aerodynamic forces on the aircraft, that results from the aircraft flexibility or vibrations, are also transformed from physical coordinates to modal coordinates. The NASTRAN vibratory mode shapes, φ, were combined with the unsteady Aerodynamic Influence Coefficient (AICs) to generate generalized aerodynamic forces at a series of reduced frequencies ($k=\omega b/V$; where ω=oscillatory frequency, b=semi-chord, and V=Velocity). These generalized aerodynamic forces were combined with the generalized mass, M, and generalized stiffness, K. Modal damping is expressed as structural damping, g, and is part of the complex stiffness term. The equation of motion for the flexible aircraft written in modal coordinates, q(t), is given in Equation 1.

$$M\ddot{q}(t) + K(1 + g\sqrt{j})q(t) = \frac{1}{2}\rho V^2 Q(k)q(t) \qquad [1]$$

Equation 1 is solved to assess the aeroelastic stability of the flexible aircraft. In this study a v-g-ω flutter solution was performed for this configuration at M=0.8 and sea level altitude. The flutter solution, Figure 7, indicated that for these conditions and configuration that the F/A-18 A/B/C/D flutter speed is greater than the maximum allowable flight envelope speed.

Because the aircraft structural modes are excited by the aircraft control surface deflections, the equations of motion are re-written to account for the aircraft control surface deflections. The control surface inertia effects, $[M_c]$, and aerodynamic effects, $Q_c(k)$ are include in Equation 2.

$$M\ddot{q}(t) + K(1 + g\sqrt{j})q(t) - \frac{1}{2}\rho V^2 Q(k)q(t) = -M_c\ddot{U}(t) - \frac{1}{2}\rho V^2 Q_c(k)U(t) \qquad [2]$$

The control surface unsteady aerodynamic force depends on dynamic pressure and reduced frequency, k. It was hypothesized that there was some non-linear aerodynamic force acting on the wing that was responsible for the LCO. Even though the major structural modes responsible for flutter are lightly damped at these flight conditions, a force, LCO force, could be applied at the wing tip to provide "simulated" LCO response at the wing and fuselage sensor package.

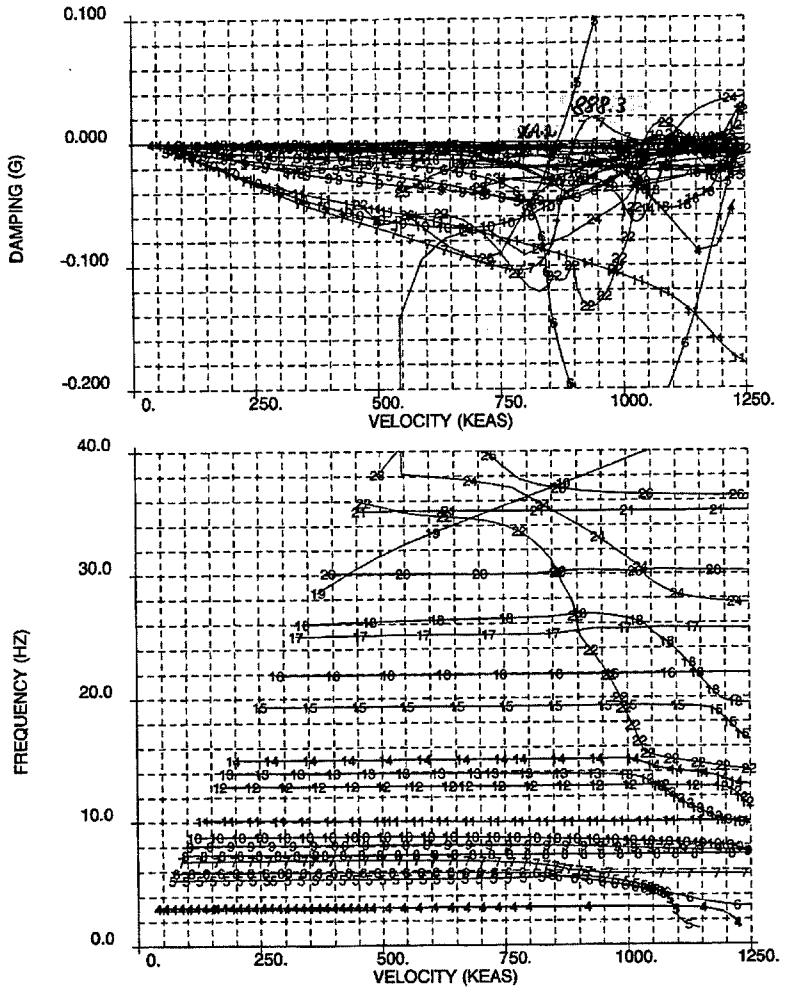

Figure 7.
V-g-ω Flutter Results For F/A-18 A/B/C/D
With LCO External Store Configuration

The equation of motion with the LCO force is shown below.

$$M\ddot{q}(t) + K(1+g\sqrt{j})q(t) - \frac{1}{2}\rho V^2 Q(k)q(t) = -M_c\ddot{U}(t) - \frac{1}{2}\rho V^2 Q_c(k)U(t) + F_{LCO}(t) \qquad [3]$$

A transient analysis of Equation 3 is required. A standard solution technique for linear differential equations is the use of Laplace transforms. The equation of the flexible aircraft for the LCO analysis in the Laplace domain is given by Equation 4.

$$[\, Ms^2 + K(1+g\sqrt{j}) \; - \frac{1}{2}\rho V^2 Q(s) \,]q(s) = [\; -M_c s^2 \; - \frac{1}{2}\rho V^2 Q_c(s) + F_{Lco} \,]u(s) \quad [4]$$

Equation 4 can be re-written as a transfer function, output/input. The output is the modal coordinates q and the input is u.

$$H(s) = \frac{q(s)}{u(s)} \quad [5]$$

The general solution technique for Equation 5 is to perform an inverse Laplace transform of both sides of the equation. The inverse Laplace transforms of Q(s) and $Q_c(s)$ do not exist, because they are tabulated matrix data which are a function of the Laplace transformed reduced frequencies. The modal transfer function in the Laplace domain is written as shown in Equation 6.

$$H_q(s) = [\, Ms^2 + K(1+g\sqrt{j}) \; - \frac{1}{2}\rho V^2 Q(s) \,]^{-1} \bullet [\; -M_c s^2 \; - \frac{1}{2}\rho V^2 Q_c(s) + F_{Lco} \,] \quad [6]$$

The modal transfer function is transformed to the physical coordinate system using the vibratory mode shapes, φ. The transfer function in the physical coordinates is given by Equation 7.

$$H(s) = \frac{y(s)}{u(s)} = \frac{\phi_c q(s)}{u(s)} = \phi_c H_q(s) \quad [7]$$

The transfer function is calculated over a series of frequencies, ω, or Laplace variables, $s=j\omega$. This process involves interpolating the tabulate unsteady aerodynamic terms of Q(s) and $Q_c(s)$, which are a function of $k=\omega b/V$, over the frequency range of interest, ω. A separate transfer function is calculated for each input-output pair. The desire is to develop a multi-input/ multi-output (MIMO) State Space model for the time domain transient analysis. The State Space Equations are written as:

$$\begin{aligned} \dot{x}(t) &= A\,x(t) + B\,u(t) \\ y(t) &= C\,x(t) + D\,u(t) \end{aligned} \quad [8]$$

The FAMUSS[10] aeroservoelastic (ASE) code was used to develop an equivalent State Space model, Equation 8, which accurately matches the original transfer function response, Equation 7. The transfer function frequency response for a MIMO state space model is shown in matrix form in Equation 9.

$$\hat{H}(s) = C[sI - A]^{-1}B + D \qquad [9]$$

FAMUSS uses a nonlinear optimization technique to determine the individual terms of the state matrices A, B, C, and D which best fits the transfer function response at each tabulated frequency, ω. The FAMUSS code was used to develop an anti-symmetric multi-input/multi-output aeroelastic model of the F-18. The model had two inputs: LCO force and aileron rotation. The model had two outputs: FCS sensor yaw response and pilot seat lateral response. The input and outputs are shown schematically in Figure 8. The ASE state space model is developed in FAMUSS by performing a series of non-linear curve fits to the respective transfer functions for the M=0.8 and 5000 foot altitude flight condition. The structural model used the 16 lowest vibratory modes and the ASE State Space model had 32 states. A comparison of the ASE state model fit with the lateral pilot seat response and lateral FCS sensor response due to anti-symmetric aileron rotation input is presented in Figure 9. The accuracy of the fit was $\pm$ 0.5 dB and the phase (not shown) was $\pm$ 2 degrees over the frequency range of 0 to 28 Hz. There is a peak response in the 5-6 Hz frequency range, thus the aileron is effective in reducing the response at the pilot seat for the 5.6 Hz LCO. Figure 10 is a comparison of the transfer function and ASE State Space model for the LCO force input. From this figure it can be seen that only 16 pounds of vertical force at 5.6 Hz applied at the wing tip is required to provide a $\pm$ 0.1g lateral acceleration at the pilot seat.

The Math Works Inc. software MATLAB® was used to perform a time history simulation of the F/A-18 LCO event. The State Space model was incorporated in the MATLAB® SIMULINK toolbox. A sinusoidal LCO input force results in LCO simulated response at the pilot seat and the FCS sensor package. An example of the simulated response at the pilot seat is shown in Figure 11. The simulated response shown in Figure 11 replicates the flight test response shown in Figure 2.

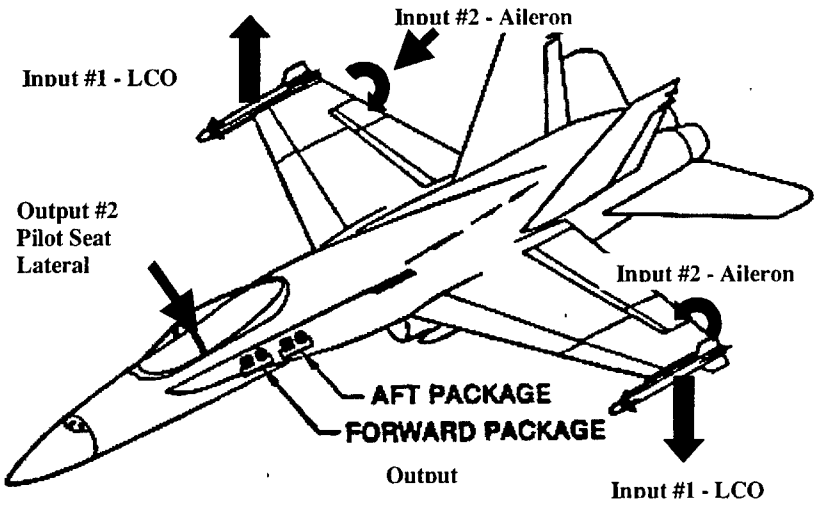

Figure 8.

Input-Output Idealization

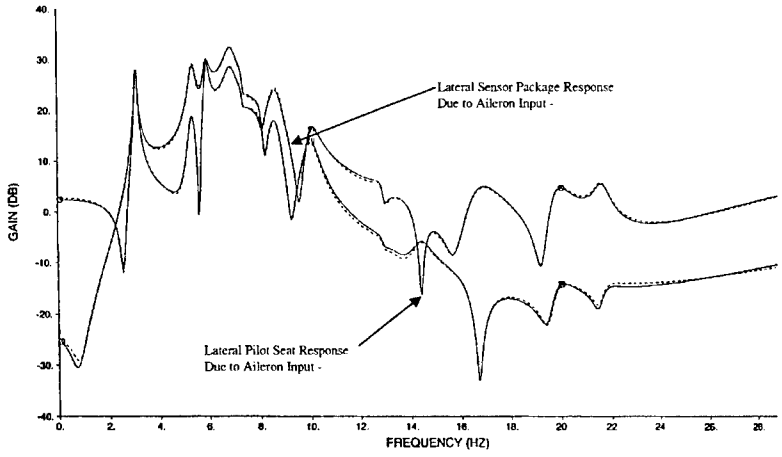

Figure 9.
Transfer Function Response – Aileron Input
M=0.8, H=5,000 Feet

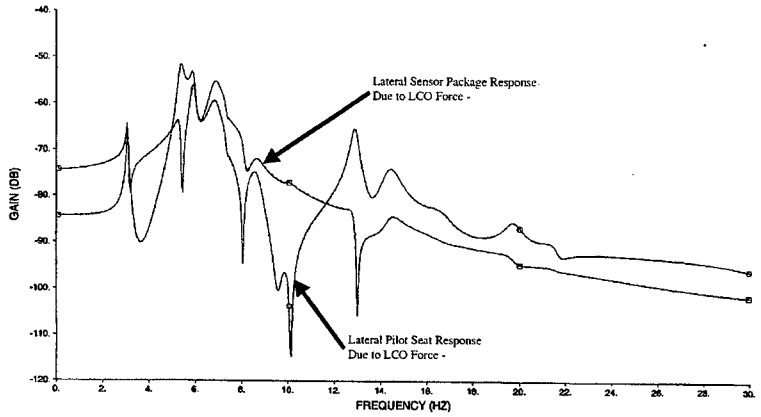

Figure 10.
Transfer Function Response – LCO Force Input
M=0.8, H=5,000 Feet

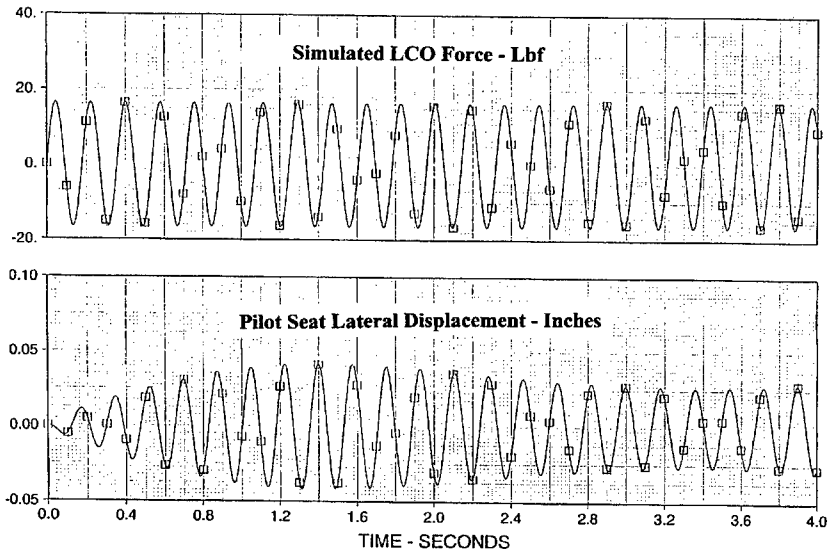

Figure 11.
Simulated LCO Response

A 16 pound 5.6 Hz anti-symmetric vertical force is applied at the wing tip to simulate the LCO force on the wing. This force produces a time history response at the pilot seat that replicates and matches measured flight test response levels.

The next step was to model the AOC system, block diagram shown in Figure 4, in MATLAB® SIMULINK. The simulated response of the AOC is compared to the actual response in Figure 12. The agreement is quite good. Note that only the gain response is shown in Figure 12, but that the phase angle response also agrees.

RESULTS

A "closed loop" simulation was performed with the 16 Lbs. LCO force providing the required lateral acceleration at the pilot seat. With the AOC actuated the response was decreased with the commanded aileron inputs from the AOC. The AOC was commanding an aileron deflection of ±0.15 degrees. This predicted value of aileron deflection agrees very well with the actual value measured during flight testing of ±0.2-0.4 degrees. Figure 13 is the time history of the F/A-18 A/B/C/D simulated LCO suppression. The simulated suppression of Figure 13 qualitatively and quantitatively agrees with the flight test measured suppression shown in Figure 3. A constant on gain and phase angle for the AOC in the simulation was required to adjust for "real world" effects.

Future plans call for the examination of different external store configurations. Flight test has shown that the current AOC does not improve ride quality to the extent desired for very heavy stores with high pitch inertia on the outboard pylon. The current technique, outlined in this paper, will also provide quantification of the LCO force required for different stores and different flight conditions. Future plans also provide for the design of a neural predictive controller that is adaptable to different store loading and flight conditions.

CONCLUSIONS

A new analytical procedure for simulating limit cycle oscillations for control system design and verification was developed. The technique develops a state space model of the flexible airframe and uses an oscillatory force at the wing tip to model the unsteady LCO force. The LCO force magnitude and frequency is tuned to match flight test measured pilot seat responses. The technique allows analytical

prediction of the control system actuation required to supress undesired dynamic responses.

REFERENCE

1. William, N.J., Limit Cycle Oscillation and Flight Flutter Testing, 21st Annual Symposium Proceedings, 1990 Society of Flight Test Engineers (SFTE), SFTE-CP-90H10, Aug 6-10, 1990.

2. Trame, L.W., Williams, L.E., and Yurkovich, R.N., Active Aeroelastic Oscillation Control on the F/A-18 Aircraft, Presented at the AIAA Guidance Navigation and Control Conference, 19-21 August 1985, Snowmass, CO

3. Cunningham, A. M., Jr. And Meijer, J. J,, "Semi-Empirical Unsteady Aerodynamics for Modeling Aircraft Limit Cycle Oscillations and Other Non-Linear Aeroelastic Problems", presented at the "International Forum on Aeroelasticity and Structural Dynamics, 1995", Manchester, U. K., 26-28 June 1995.

4. Meijer, J. J., Cunningham, A. M,, Jr., And Zwaan, R. J. , "A Semi-Empirical Approach to Predict Transonic Limit Cycle Oscillation Characteristics of Fighter Aircraft", 8* Aircraft/Stores Compatibility Symposium, Fort Walton Beach, Florida, 23-25 October 1990.

5. Meijer, J. J. and Cunningham, A. M., Jr., "Understanding and Development of a Prediction Method for Transonic Limit Cycle Oscillation Characteristics of Fighter Aircraft", AIAA Paper No. 92-4501, August 1992.

6. Meijer, J. J. and Cunningham, A.M., Jr., "A Semi-Empirical Non-Linear Aerodynamic to PredictTransonic LCO Characteristics of Fighter Aircraft", AIAA Paper No. 95-1340, April 1995.

7. Denegri Jr., C. M., and Cutchins, M.A., Evaluation of Classical Flutter Analyses for the Prediction of Limit Cycle Oscillations, AIAA Paper 97-1021

8. Chen, P.C., Sarhaddi, D., and Liu, D.D., Limit-Oscillation Studies of a Fighter with External Stores, AIAA-98-1727

9. Kalman, T.P., Giesing, J.P, Subsonic Steady and Oscillatory Aerodynamics for Multiple Interfering Wings and Bodies, McDonnell Douglas Report MDC-J7295, Volume I, Oct. 1976

10. Pitt, D.M., and Goodman, C.E., FAMUSS: A New Aeroservoelastic Modeling Tool, AIAA Paper 92-2395

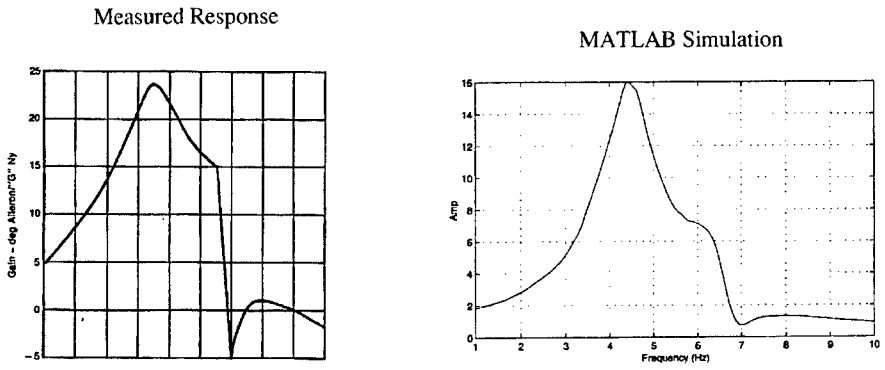

Figure 12.
Comparison of AOC Frequency Response
With MATLAB® Predicted Response

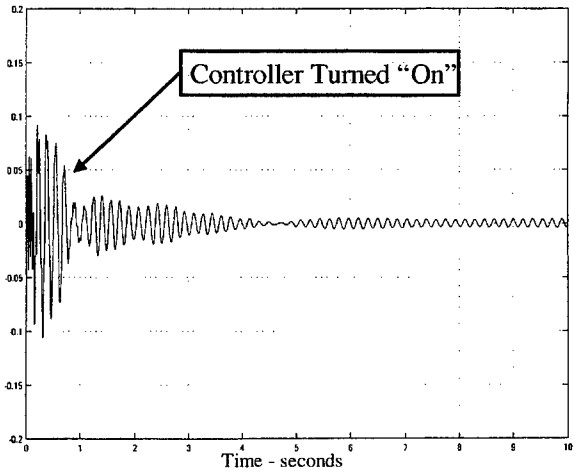

Figure 13.
F/A-18 Simulated Suppression of LCO

Coupled Flight Mechanics and Aeroelasticity

(The Effects of Quasi Steady Maneuvers on Supersonic Divergence and Flutter)

Dr James J. Olsen
Olsen Engineering Consulting
1186 Tralee Trail
Dayton, Ohio
USA 45430 - 1219

EMail: JamesJJOlsen@aol. com

Abstract

This paper reveals new insights into the coupled aeroelasticity and flight mechanics of flexible aircraft by obtaining and solving practical equations of motion for a flexible, maneuvering aircraft.

We obtain the general equations for general longitudinal/lateral motion of an accelerating, rotating, flexible vehicle. Rather than setting up the general problem in inertial coordinates and then transforming to body - fixed coordinates, we use the idea of "quasi coordinates". We establish a general form for Lagrange's equations in the non inertial, body - fixed coordinates, then reduce them to a special case of a "flat" airplane.

We illustrate the approach for two cases of increasing complexity: The first case of a "sprung" pendulum shows when rigid body angular velocities can be important as they approach the structural frequencies. The second case is a typical section airfoil on an accelerating, rotating fuselage in supersonic flight. It applies Lagrange's equations to the longitudinal problem in inertial coordinates, then transforms the equations to non inertial, body - fixed coordinates for solution. It also shows when rigid body rotations and longitudinal accelerations must be included in the flexibility equations.

1. Introduction

For many years there has been a search for a practical set of "unified" equations of motion that can be used in all of the disciplines of aerodynamics, structures and stability and control of flexible aircraft. Such an approach would allow the customary determination of the effects of structural flexibility on aircraft performance, stability and air loads. Also it would allow us to determine the effects of the "rigid body" motions on aeroelastic

characteristics such as trim, control - effectiveness, divergence and flutter. Further (and most importantly), it would allow all of those engineering problems to be treated by subsets of a single set of "unified" equations.

In most aircraft applications, the mutual coupling of rigid body and flexible motions is small because the vehicle angular velocities and structural frequencies are well separated. However, there have been examples of large aircraft where structural frequencies (say 2 Hz) approach the rigid body angular velocities (say 1 Hz). In other cases aerodynamic forces have driven the structural frequencies and the rigid body frequencies closer together.

To develop the necessary equations we must account for the fact that the aircraft's body - fixed coordinate system is not (in general) an inertial system. We develop a practical formulation to overcome that obstacle through the use of energy methods, Lagrange's equations and "quasi coordinates".

The equations become somewhat more complicated, and it is useful to examine them in three stages. First, some insight is available via a simplification which considers the rigid body velocities or accelerations merely as constant parameters. The rigid body motions alter the structural frequencies of vibration, thereby altering aeroelastic stability. In that case we refer to the rigid body motions as "quasi steady maneuvers". Second, a more exact approach is to specify the time dependent rigid body motions as functions of time (damped sinusoids) and then to recognize that the resulting flexibility equations resemble Mathieu's classical ordinary differential equation. Third, the ultimate procedure is always available - the simultaneous solution (perhaps numerically) of the fully coupled, non linear, rigid body and flexibility equations of motion in body - fixed coordinates.

2. Lagrange's Equations

If the inertial coordinates of a dynamic system can be represented in terms of N independent generalized coordinates:

$$X = X(q_i) \quad Y = Y(q_i) \quad Z = Z(q_i)$$

Lagrange's equations [1] can describe the motion of the system:

$$\frac{d}{dt}\left(\frac{\partial L}{\partial \dot{q}_i}\right) - \frac{\partial L}{\partial q_i} = Q_i$$

where:

L = Lagrangian, $T-U$

Q_i = Generalized Force

T = Kinetic Energy

U = Potential Energy

3. Quasi Coordinates and the General Motion of a Flexible Vehicle

We start with an inertial X,Y,Z coordinate system and a non inertial x,y,z system that can accelerate and rotate in the X,Y,Z system (Figure 1). The origin of the x,y,z system is located in the inertial system at:

$$X = X_0 = q_1 \quad Y = Y_0 = q_2 \quad Z = Z_0 = q_3$$

The orientation of the x,y,z system is given by the conventional sequence of Euler rotations:

$$\psi = q_4 \quad \theta = q_5 \quad \phi = q_6$$

Then inertial coordinates of a general point in x, y, z are:

$$\{X,Y,Z\} = \{q_1,q_2,q_3\} + [\tau]\{x,y,z\}$$

where $[\tau]$ is the usual Euler transformation [2], which is the product of three transformations that depend on the Euler angles:

$$[\tau] = [\tau_4][\tau_5][\tau_6]$$

$$[\tau_4] = \begin{bmatrix} c_4 & -s_4 & 0 \\ s_4 & c_4 & 0 \\ 0 & 0 & 1 \end{bmatrix} \quad [\tau_5] = \begin{bmatrix} c_5 & 0 & s_5 \\ 0 & 1 & 0 \\ -s_5 & 0 & c_5 \end{bmatrix} \quad [\tau_6] = \begin{bmatrix} 1 & 0 & 0 \\ 0 & c_6 & -s_6 \\ 0 & s_6 & c_6 \end{bmatrix}$$

$$s_i = \sin q_i \quad c = \cos q_i$$

We also write the "local" coordinates in terms of additional generalized coordinates $q_7, q_8 \cdots q_n$:

$$\{x,y,z\} = \sum_{i=7}^{n} \{x_i,y_i,z_i\} q_i(t)$$

to obtain the inertial coordinates in terms of the generalized coordinates:

$$\{X,Y,Z\} = \{q_1,q_2,q_3\} + [\tau] \sum_{i=7}^{n} \{x_i,y_i,z_i\} q_i(t)$$

In principle we could use the above expressions for the inertial coordinates to develop expressions for the kinetic energy, potential energy and generalized forces. Then we would obtain Lagrange's equations for the maneuvering, flexible system in terms of the

inertial translations q_1, q_2, q_3, the Euler angles q_4, q_5, q_6 and the flexible coordinates $q_7, q_8, \cdots q_n$. That would account for all of the inertia couplings that arise from the fact that the non inertial x, y, z system is accelerating and rotating in the inertial X, Y, Z system. We could solve those equations for the inertial coordinates and then transform the results to the non inertial translations along the body axes q_x, q_y, q_z and the instantaneous angular velocities $\omega_x, \omega_y, \omega_z$, using the transformations:

$$\{q_x, q_y, q_z\} = [\tau]^T \{q_1, q_2, q_3\}$$

$$\{\omega_x, \omega_y, \omega_z\} = [\alpha]\{\dot{q}_4, \dot{q}_5, \dot{q}_6\}$$

where

$$[\alpha] = \begin{bmatrix} -s_5 & 0 & 1 \\ c_5 s_6 & c_6 & 0 \\ c_5 c_6 & -s_6 & 0 \end{bmatrix}$$

The approach is mathematically correct, but tedious. It works easiest for special cases like rotation about one axis (where the time derivative of the appropriate Euler angle is indeed the angular velocity). However, it suffers from two inconveniences. First, the generalized coordinates q_1, q_2, q_3 are the translations in the directions of the inertial coordinates. We would like to replace them with the translations in directions of the non inertial, body - axis coordinates q_x, q_y, q_z . Second, the generalized coordinates are the Euler angles q_4, q_5, q_6. Their time derivatives $\dot{q}_4, \dot{q}_5, \dot{q}_6$ may not be the actual angular velocities of the x, y, z system for general motions. We would like to replace them with the angular velocities, $\omega_x, \omega_y, \omega_z$.

To overcome those inconveniences, the elegant and simple method of quasi coordinates is available due to Hamel [3] and Boltzmann [4]. The term "quasi coordinates" refers to the fact that since

$$\{\omega_x, \omega_y, \omega_z\} = [\alpha]\{\dot{q}_4, \dot{q}_5, \dot{q}_6\}$$

we cannot (in the general case of three dimensional motions) directly integrate the angular velocities to get the generalized coordinates. Whittaker [5] and Meirovitch [6] explain the method of quasi coordinates for the special case of rotational motions. Several others, among them Nayfeh and Mook [7], give applications. Actually all we are doing is performing the transformations before we apply Lagrange's equations, rather than after we get them.

The basic idea is that we want to write Lagrange's equations in a form that treats directly the body axis translations q_x, q_y, q_z and the true angular velocities $\omega_x, \omega_y, \omega_z$. We start with the usual form of Lagrange's equations in terms of the original, independent generalized coordinates $q_1, q_2 \cdots q_n$ and their time derivatives $\dot{q}_1, \dot{q}_2 \cdots \dot{q}_n$:

$$\frac{d}{dt}\left(\frac{\partial L}{\partial \dot{q}_i}\right) - \left(\frac{\partial L}{\partial q_i}\right) = Q_i$$

The Lagrangian can be written in the usual form in the original inertial coordinates:

$$L = L\begin{pmatrix} q_1, q_2, q_3, q_4, q_5, q_6, q_7, \cdots q_n; \\ \dot{q}_1, \dot{q}_2, \dot{q}_3, \dot{q}_4, \dot{q}_5, \dot{q}_6, \dot{q}_7, \cdots \dot{q}_n \end{pmatrix}$$

If we note that:

$$\{\dot{q}_4, \dot{q}_5, \dot{q}_6\} = [\beta]\{\omega_x, \omega_y, \omega_z\}$$

where

$$[\beta] = [\alpha]^{-1} = \begin{bmatrix} 0 & c_5^{-1} s_6 & c_5^{-1} c_6 \\ 0 & c_6 & -s_6 \\ 1 & t_5 s_6 & t_5 c_6 \end{bmatrix}$$

we can obtain the equivalent form of the Lagrangian in the quasi coordinates:

$$L = \tilde{L}\begin{pmatrix} q_x, q_y, q_z, q_4, q_5, q_6, q_7, \cdots q_n; \\ \dot{q}_x, \dot{q}_y, \dot{q}_z, \omega_x, \omega_y, \omega_z, \dot{q}_7, \cdots \dot{q}_n \end{pmatrix}$$

Then, following Whittaker [8] we can obtain the equations for:

Translation DOFs:

$$\frac{d}{dt}\begin{Bmatrix} \frac{\partial \tilde{L}}{\partial \dot{q}_x} \\ \frac{\partial \tilde{L}}{\partial \dot{q}_y} \\ \frac{\partial \tilde{L}}{\partial \dot{q}_z} \end{Bmatrix} - \begin{Bmatrix} \frac{\partial \tilde{L}}{\partial q_x} \\ \frac{\partial \tilde{L}}{\partial q_y} \\ \frac{\partial \tilde{L}}{\partial q_z} \end{Bmatrix} + [\Omega]\begin{Bmatrix} \frac{\partial \tilde{L}}{\partial \dot{q}_x} \\ \frac{\partial \tilde{L}}{\partial \dot{q}_y} \\ \frac{\partial \tilde{L}}{\partial \dot{q}_z} \end{Bmatrix} = [\tau]^T \begin{Bmatrix} Q_1 \\ Q_2 \\ Q_3 \end{Bmatrix}$$

Rotation DOFs:

$$\frac{d}{dt}\begin{Bmatrix} \frac{\partial \tilde{L}}{\partial \omega_x} \\ \frac{\partial \tilde{L}}{\partial \omega_y} \\ \frac{\partial \tilde{L}}{\partial \omega_z} \end{Bmatrix} - [\beta]^T \begin{Bmatrix} \frac{\partial \tilde{L}}{\partial q_4} \\ \frac{\partial \tilde{L}}{\partial q_5} \\ \frac{\partial \tilde{L}}{\partial q_6} \end{Bmatrix} + [\Omega]\begin{Bmatrix} \frac{\partial \tilde{L}}{\partial \omega_x} \\ \frac{\partial \tilde{L}}{\partial \omega_y} \\ \frac{\partial \tilde{L}}{\partial \omega_z} \end{Bmatrix} = [\beta]^T \begin{Bmatrix} Q_4 \\ Q_5 \\ Q_6 \end{Bmatrix}$$

Flexible DOFs remain the same form (except that we must use the modified Lagrangian $\tilde{L}$)

$$\boxed{\frac{d}{dt}\frac{\partial \tilde{L}}{\partial \dot{q}_i} - \frac{\partial \tilde{L}}{\partial q_i} = Q_i \quad for\ i \geq 7}$$

where:

$$[\Omega] = \begin{bmatrix} 0 & -\omega_z & \omega_y \\ \omega_z & 0 & -\omega_x \\ -\omega_y & \omega_x & 0 \end{bmatrix}$$

These are the equations of motion in terms of quasi coordinates. They are the fundamental advance which allows us to formulate a unified set of equations that can be used for the combined aerodynamics, structures and stability and control of flexible aircraft. They allow us to place the aeroelastic problem into the context, coordinate systems and notation that are used in flight mechanics and stability and control.

The complete development with all geometric nonlinearities can be found in Olsen [9, 10]. Here we specialize, for ease of illustration, to an essentially "flat" surface in the xy plane, Figure 2. We also assume mass symmetry about the y axis, x, y, z origin at the center of mass and perfectly known, perfectly orthogonal free - free vibration modes. Then with the usual definitions:

$\dot{q}_x = U$ velocity along the x axis

$\dot{q}_x = V$ velocity along the y axis

$\dot{q}_x = W$ velocity along the z axis

$\omega_x = P$ angular velocity about the x axis

$\omega_y = Q$ angular velocity about the y axis

$\omega_z = R$ angular velocity about the z axis

The equations of motion simplify to the usual rigid body equations and the modified flexible equations:

Translation DOFs

$$\begin{Bmatrix} \dot{U} \\ \dot{V} \\ \dot{W} \end{Bmatrix} + \begin{Bmatrix} WQ - VR \\ UR - WP \\ VP - UQ \end{Bmatrix} + g \begin{Bmatrix} s_5 \\ -c_5 s_6 \\ -c_5 c_6 \end{Bmatrix} = \frac{1}{M} \begin{Bmatrix} F_x \\ F_y \\ F_z \end{Bmatrix}$$

Rotation DOFs

$$\begin{Bmatrix} \dot{P} \\ \dot{Q} \\ \dot{R} \end{Bmatrix} + \begin{Bmatrix} QR \\ -PR \\ \frac{I_{xx}-I_{yy}}{I_{xx}+I_{yy}} PQ \end{Bmatrix} = \begin{Bmatrix} M_x/I_{yy} \\ M_y/I_{xx} \\ M_z/(I_{xx}+I_{yy}) \end{Bmatrix}$$

Flexible DOFs

$$\left\{\ddot{q}_i + \left[\omega_i^2 - \left(P^2 + Q^2\right)\right] q_i\right\} M_{ii} = Q_i$$

where

ω_i = natural frequency of the perfect ith mode

We can consider the solution to these coupled equations in four steps of increasing complexity:

a. Dealing only with the flexible equations, we could assume that the angular velocities P and Q are constant (quasi steady maneuvers). Then we could treat the flexible equations as if the effective structural frequency for any structural mode is just replaced by

$$\omega_i^2 \rightarrow \omega_i^2 - \left(P^2 + Q^2\right)$$

b. Dealing again with only the flexible equations, we could impose P and Q as (perhaps already known) functions of time. Then the flexible equations resemble Mathieu's equation.

c. We could numerically integrate the above linearized rigid and flexible equations of motion with linear or nonlinear aerodynamics on the RHS, perhaps from CFD. Once the analyst has committed to numerical methods for CFD and numerical integration of the equations of motion, there is very little additional labor to use the more comprehensive equations of motion above.

d. We could retain all of the geometric, structural and aerodynamic nonlinearities and numerically integrate the complete nonlinear rigid/flexible equations.

4. Example of Coupled Rigid - Flexible Motions, The "Sprung" Pendulum

Olsen [10] examined the case of the "sprung pendulum" which is free to rotate or oscillate about the origin, but which also contains a radial spring of linear stiffness k (Figure 3). If the "rigid body" motion is specified as a complete circular motion at a constant

angular velocity of ω (a quasi steady maneuver), the radial response acts as if the natural frequency in the radial direction is

$$\omega_{effective} = \sqrt{\frac{k}{m} - \omega^2} = \sqrt{\omega_0^2 - \omega^2}$$

If the "rigid body" motion is specified as an oscillation through an amplitude θ_0 with a constant frequency ω, then there are narrow unstable regions for frequency ratios (flex/rigid) near 1, 2,... n, Figure 4. Figure 5 shows time histories for a frequency ratio of 1. 1 and "rigid body" amplitudes of 0. 53, 0. 54 and 0. 55 radians for rigid body amplitudes up to 10 degrees. The oscillatory radial motion decays for a rigid body amplitude of 0. 53 radians and is unstable for 0. 54 and 0.55 radians.

5. Example of Coupled Rigid - Flexible Motions, A Typical Section Airfoil on a Accelerating, Rotating Fuselage

Olsen [10] developed the coupled rigid/flexible equations of motion for a typical section airfoil on an accelerating, rotating fuselage, Figure 6. He obtained the nonlinear equations in inertial coordinates, then defined the "apparent" body - fixed components of the vehicle's velocities and accelerations:

$$\dot{q}_x = \dot{q}_1 c_3 + \dot{q}_2 s_3 \qquad \dot{q}_y = \dot{q}_2 c_3 - \dot{q}_1 s_3$$

$$\ddot{q}_x = \ddot{q}_1 c_3 + \ddot{q}_2 s_3 \qquad \ddot{q}_y = \ddot{q}_2 c_3 - \ddot{q}_1 s_3$$

where the inertial coordinates are:

q_1 = inertial translation in the X direction

q_2 = inertial translation in the Y direction

q_3 = pitch rotation

q_x = translation along the body axis

q_y = translation normal to the body axis

The linearized flexibility equations, in body - fixed coordinates, (with damping added) were:

$$\begin{bmatrix} m_w & S_w \\ S_w & I_w \end{bmatrix} \begin{Bmatrix} \ddot{q}_4 \\ \ddot{q}_5 \end{Bmatrix} + \begin{bmatrix} c_4 & 0 \\ 0 & c_5 \end{bmatrix} \begin{Bmatrix} \dot{q}_4 \\ \dot{q}_5 \end{Bmatrix}$$

$$+ \left(\begin{bmatrix} k_4 & 0 \\ 0 & k_5 \end{bmatrix} - \dot{q}_3^2 \begin{bmatrix} m_w & S_w \\ S_w & -x_w S_w \end{bmatrix} - S_w (\ddot{q}_x + g s_3) \begin{bmatrix} 0 & 0 \\ 0 & 1 \end{bmatrix} \right) \begin{Bmatrix} q_4 \\ q_5 \end{Bmatrix}$$

$$\approx \begin{Bmatrix} Q_4 \\ Q_5 \end{Bmatrix} - \begin{bmatrix} m_w & m_w x_w + S_w \\ S_w & I_w + x_w S_w \end{bmatrix} \begin{Bmatrix} \ddot{q}_y \\ \ddot{q}_3 \end{Bmatrix} - g c_3 \begin{Bmatrix} m_w \\ S_w \end{Bmatrix} + \begin{bmatrix} k_4 & 0 \\ 0 & k_5 \end{bmatrix} \begin{Bmatrix} q_{4_{ref}} \\ q_{5_{ref}} \end{Bmatrix}$$

where:

q_4 = airfoil normal translation

q_5 = airfoil rotation

m_w = mass of the airfoil

S_w = mass unbalance

I_w = moment of inertia

In the case of mass balance, $S_w = 0$the and translation vibration equations acts with the "effective" translation stiffness

$$k_{4_{eff}} = k_4 - m_w \dot{q}_3^2 = k_4 \left[1 - \left(\frac{\dot{q}_3}{\omega_4} \right)^2 \right]$$

In the case of mass unbalance and $\dot{q}_3 = 0$, the torsion vibration equation acts with the "effective" torsion stiffness

$$k_5 - S_w \ddot{q}_x = k_5 \left(1 - \frac{\hat{x}_w}{\hat{r}_w^2} \frac{g}{c\omega_5^2} \frac{\ddot{q}_x}{g} \right)$$

In the remainder of this paper we examine the effects of fuselage pitch rate $\dot{q}_3$ and acceleration along the body axis $\ddot{q}_x$ on the structural vibrations and on supersonic flutter and divergence, assuming that the pitch rate and acceleration/deceleration are constant parameters (quasi steady maneuvers).

Vibrations - Figure 7 shows the coupled bending vibration frequency vs. the torsion axis for a pitch rate of 0.0 and 0. 5 times the uncoupled bending frequency $(\dot{q}_3 = 0.5\omega_4)$. The effect of positive or negative pitch rate is to uniformly reduce the coupled bending frequency. The effects of pitch rate on the coupled torsion frequency are quite small and are not presented.

Figures 8 and 9 show the coupled bending and torsion frequencies vs. the torsion axis for small acceleration or deceleration, $\frac{\dot{V}}{V\omega_{rb}} = \pm 0.01$. The effects are due to the product of the mass unbalance and the acceleration/deceleration. When the torsion axis is aft, acceleration reduces the bending and torsion frequencies significantly as well as their separation. When the torsion axis is forward, deceleration produces the same effects,

Supersonic Aeroelasticity - we use the piston theory of Ashley and Zartarian [11]. Figures 10 and 11 show the aeroelastic frequency and damping vs. the torsion axis for Mach 2 at an altitude of 60, 000 ft. Flutter (g = 0) occurs at for torsion axes between about 0. 52 and 0. 74 chord. Divergence occurs for the torsion axis behind 0. 45 chord.

Figures 12 and 13 show the relatively small effects of pitch rate and the more pronounced effects of acceleration/deceleration on flutter altitude for Mach 2 and a torsion axis of 0. 55 chord. The effect of pitch rate is slightly beneficial; it lowers the flutter altitude (increases the density). The effect of acceleration also is to lower the flutter altitude. The effect of deceleration is to raise the flutter altitude (decrease the density).

Figures 14 and 15 show the effects of pitch rate and acceleration/deceleration on divergence altitude for Mach 2 and a torsion axis of 0. 45 chord. Pitch rate slightly increases the divergence altitude (decreases the density). Likewise, acceleration increases the divergence altitude.

Time Dependent Rigid Body Motions - Rather than assume that the rigid body motions are constant parameters, we can outline a second approach which we will not implement here. We could assume representative forms for the time dependent rigid body motions and then plug them into the flexible equations of motion. We need the terms $\alpha, \dot{q}_3, \dot{q}_3^2, \ddot{q}_x, \ddot{q}_y$ and $\ddot{q}_3$. Following Etkin's [2] notation we can assume the time dependent forms for the oscillatory, damped speed, pitch angle and angle of attack, wherein each expression the terms a and b are assumed constants:

$$\dot{q}_x = u_0 + E(a_u S_1 + b_u C_1)$$

$$\theta = q_3 = \theta_0 + E(a_\theta S_1 + b_\theta C_1)$$

$$\alpha = \alpha_0 + E(a_\alpha S_1 + b_\alpha C_1)$$

where

$$S_n = \sin n\omega_{rb}t \quad C_n = \cos n\omega_{rb}t \quad E = e^{-\omega_{rb}\zeta_{rb}t}$$

ω_{rb} = assumed "rigid body" frequency

ζ_{rb} = assumed "rigid body" damping

Noting that $\dot{q}_y \approx \dot{q}_x \alpha$ and combining angles where possible, we obtain the "forcing terms" to be included in the equations of motion. The terms $\dot{q}_3^2, \ddot{q}_x$ appear on the LHS of the equation and influence stability:

$$\ddot{q}_x = \omega_{rb} E\left(a_{\ddot{q}_x} S_1 + b_{\ddot{q}_x} C_1\right)$$

$$\dot{q}_3^2 = \tfrac{1}{2}\omega_{rb}^2 E^2\left(K_{\dot{q}_3^2} + a^*_{\dot{q}_3^2} S_2 + b^*_{\dot{q}_3^2} C_2\right)$$

The major point is that terms $S_2 = \sin 2\omega_{rb}t$ and $C_2 = \cos 2\omega_{rb}t$ on the LHS introduce behavior like that of Mathieu's equation.

6. Summary, Conclusions

1. In the case of general motion of a flexible body, the combination of energy methods and quasi coordinates produces a practical set of equations that govern the aerodynamics, flight mechanics and structures problems of flexible aircraft. They allow the determination of the effects of structural flexibility on aircraft performance, stability and air loads and the effects of the "rigid body" motions on trim, aeroelastic control - effectiveness, divergence and flutter.

4. For the special case of the "flat airplane" with perfect mass distribution and perfect modes, a simple preliminary estimate of the effects of rigid body motions on flexible motions would be to replace all of the structural frequencies by:

$$\omega_i^2 \rightarrow \omega_i^2 - \left(P^2 + Q^2\right)$$

3. The "sprung pendulum" shows that a rigid body motion with constant angular velocity can reduce the "effective" natural frequencies. Using the resemblance to Mathieu's equation, we have seen that there is a coupling mechanism between the rigid body and flexible motions, even in the absence of aerodynamics. It appears that if a structural frequency is up to 1. 3 - 1. 5 times a rigid body frequency, then those coupling effects should be considered. In some cases ("slender" aircraft) the natural frequencies may already be in those ranges. In other cases (the X - 29) the aerodynamic forces drive some of the structural frequencies down toward the rigid body frequencies.

4. The airfoil on an accelerating/rotating fuselage shows that the effective bending stiffness is reduced by a constant pitch rate. It also shows that torsional stiffness is increased or decreased by constant acceleration/deceleration, depending on the sign of the unbalance. The results modify the divergence and flutter speeds and altitudes. If we impose the rigid body motions as forced, sinusoidal, damped motions - then terms appear in the differential equations which can produce additional instabilities, such as in Mathieu's equation.

7. References

1. Bisplinghoff, R. L., Ashley, H. and Halfman, R. L., Aeroelasticity, Addison - Wesley, Reading, Mass, 1955.

2. Etkin, B., Dynamics of Flight, Stability and Control, Wiley, New York, 1959.

3. Hamel, A., Zeitschrift fur Mathematiks und Physiks, 1904.

4. Boltzmann, R., Sitzungsberichte, Wien, 1902.

5. Whittaker, E. T., A Treatise on the Analytical Dynamics of Particles and Rigid Bodies, Dover Publications, New York, 1944.

6. Meirovitch, L., Methods of Analytical Dynamics, McGraw - Hill, New York, 1970.

7. Nayfeh, A. H. and Mook, D. T., Nonlinear Oscillations, Wiley, New York, 1979.

8. E. T. Whittaker; A Treatise on the Analytical Dynamics of Particles and Rigid Bodies, Dover Publications, New York, 1944.

9. Olsen, J. J., Coupled Flight Mechanics and Aeroelasticity - Some Effects of Aircraft Maneuvers on Aeroelastic Divergence and Flutter, 19th ICAS Congress, Los Angeles, Sept 1994.

10. Olsen, J. J., "Unified" Flight Mechanics and Aeroelasticity for Accelerating, Maneuvering, Flexible Aircraft, NATO/RTO/AVT Specialists' Meeting on Structural Aspects of Flexible Aircraft Control. Ottawa, Canada, Oct 1999.

11. Ashley, H. and Zartarian, G., Piston Theory, A New Aerodynamic Tool for the Aeroelastician, J. Aero. Sc., Vol 23, No. 6, June 1958.

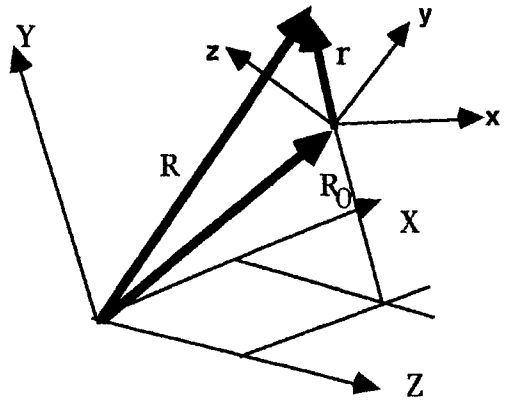

Figure 1. General Motion of a Flexible Vehicle

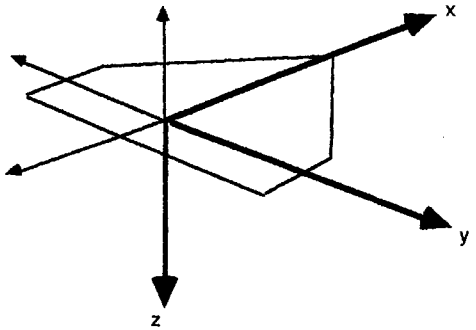

Figure 2. The "Flat" Airplane

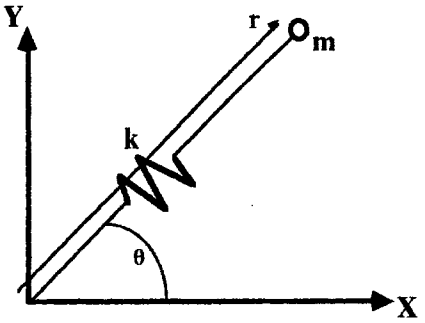

Figure 3. The Sprung Pendulum

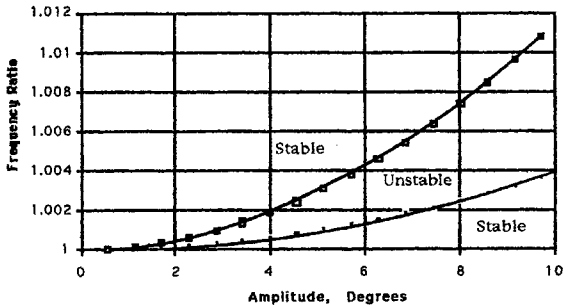

Figure 4. Instability Region for Frequency Ratios near 1

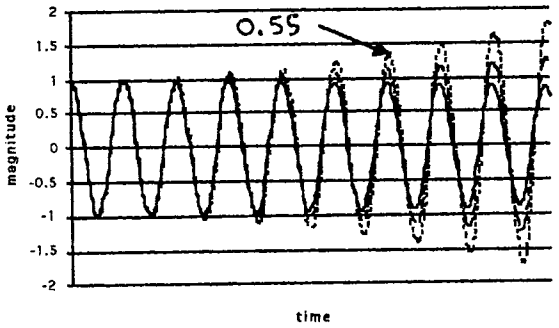

Figure 5. Time Histories for Frequency Ratio 1.1

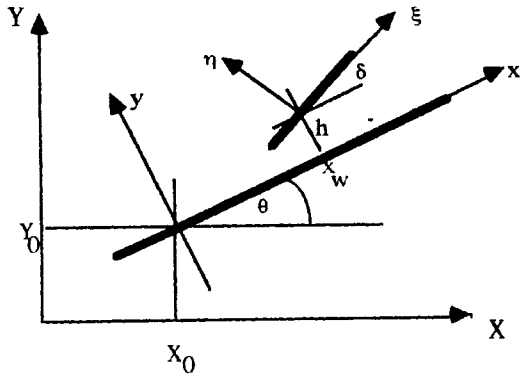

Figure 6. Airfoil on an Accelerating, Rotating Fuselage

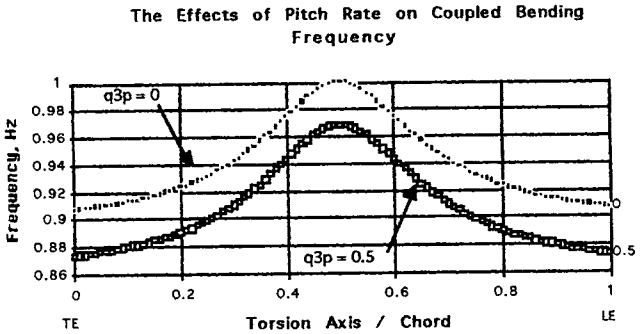

Figure 7. Effects of Pitch Rate on the Coupled Bending Frequency

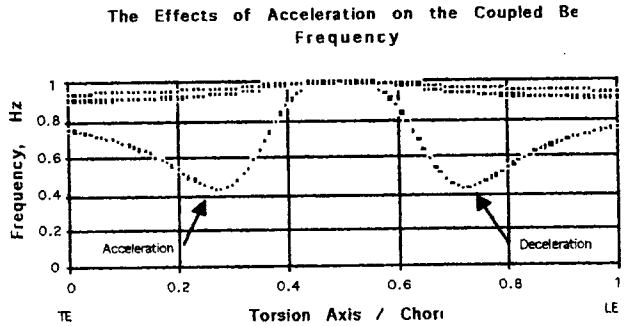

Figure 8. Effects of Acceleration on the Coupled Bending Frequency

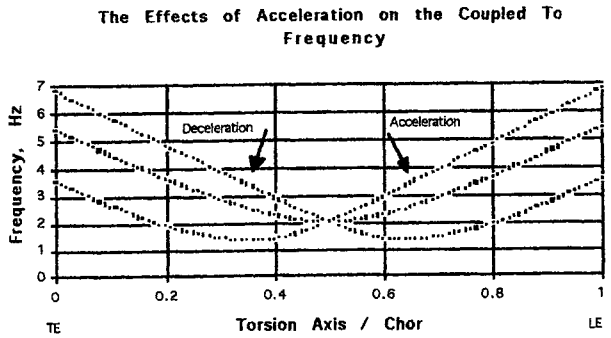

Figure 9. Effects of Acceleration on the Coupled Torsion Frequency

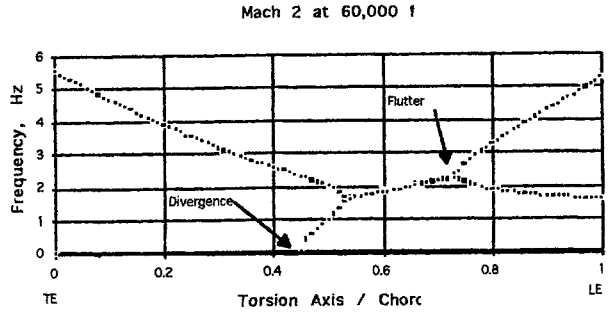

Figure 10. Aeroelastic Frequency vs. Torsion Axis, Mach 2 at 60,000 ft

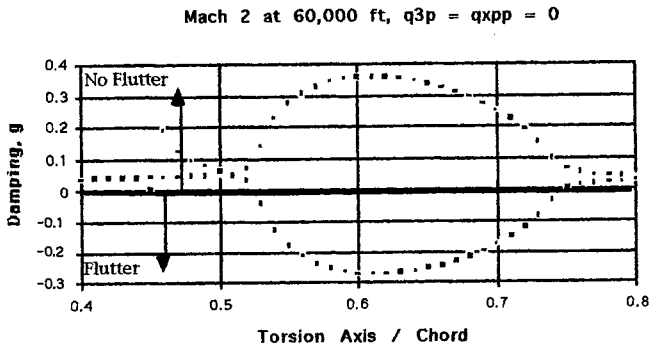

Figure 11. Aeroelastic Damping vs. Torsion Axis, Mach 2 at 60,000 ft

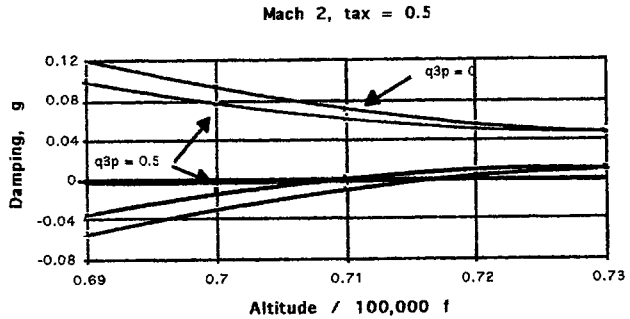

Figure 12. The Effects of Pitch Rate on Flutter Altitude, Mach 2, Torsion Axis at 55% Chord

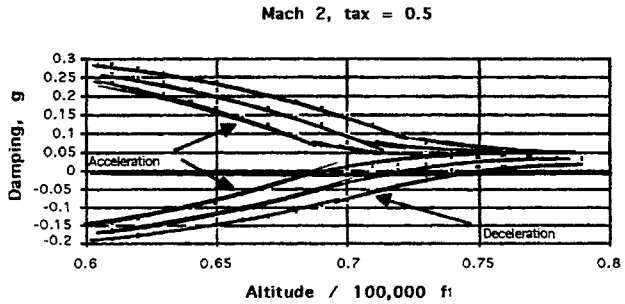

Figure 13. The Effects of Acceleration on Flutter Altitude, Mach 2, Torsion Axis at 0.55 Chord

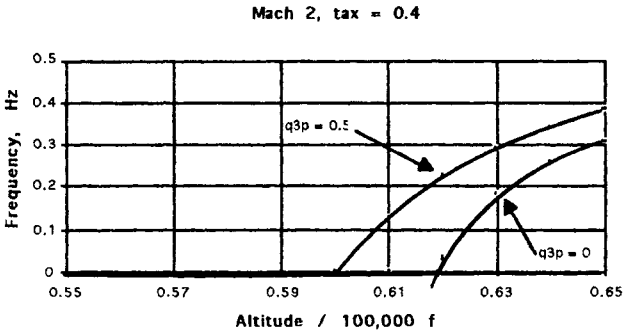

Figure 14. The Effects of Pitch Rate on Divergence Altitude, Mach 2, Torsion Axis at 0.45 Chord

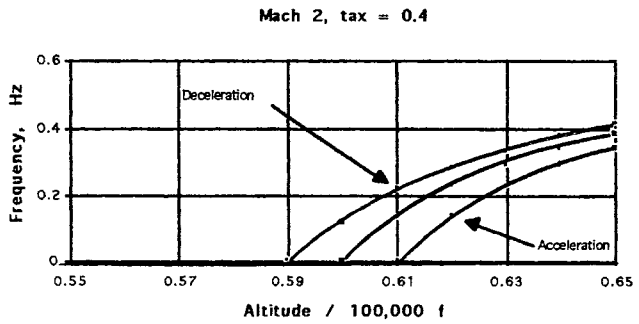

Figure 15. The Effects of Acceleration on Divergence Altitude, Mach 2, Torsion Axis at 0.45 Chord

GALLOPING OF BUNDLE CONDUCTORS

Q. Zhang, N. Popplewell and A.H. Shah
Faculty of Engineering, University of Manitoba
Winnipeg, Canada R3T 5V6

SUMMARY

A useful, design-oriented model is developed for a bundled electrical transmission line to study its galloping characteristics. The three degree-of-freedom model is adaptable because it incorporates mode shapes determined numerically by employing the finite element technique. On the other hand, it is quite computationally efficient because analytical expressions are used to investigate the initiation and steady-state (limit cycle) amplitudes of galloping. The model accommodates interactions of the vertical, horizontal and torsional movements, non-linear aerodynamic loads, a non-uniform ice geometry, distributed and discrete galloping control devices, and a variation of the wind along a span. Parametric studies are reported for single loop/span cases that assess the trends of the limit cycle amplitude with variations of the critical wind speed, wind speed above the critical wind speed, static tension and span length.

1. INTRODUCTION

High voltage transmission lines are often arranged in multi-conductors per phase to increase the power capacity of a circuit. They are often subjected to wind-induced vibrations. Galloping, which is a low frequency, high amplitude oscillation caused by a steady wind, happens more easily on a bundle conductor than on a single conductor [1]. Although considerable effort has been expended for many years to predict the galloping of a bundle conductor from that of a simpler

single conductor, the extrapolation has still not been resolved satisfactorily. One reason is that existing analytical and computational models are either oversimplified or they lack the efficiency needed to economically compute the effects of design changes in parameters [2-4] like the static tension, the span length and the number of conductors in a bundle or the result of a greater wind speed.

Most previous analytical studies of bundle conductors have been limited to a planar configuration [5–11]. However, field observations indicate that galloping often involves the simultaneous interaction of a horizontal motion with vertical and torsional movements [1]. Although a three degree-of-freedom (3DOF), analytical model has been formulated quite recently for a bundle conductor [12], a tedious time integration procedure was adopted and the aerodynamic forces were over simplified by their linearization. On the other hand, a more realistic, yet computationally efficient, 3DOF model has been developed in the last decade to determine the initiation conditions for galloping as well as the ensuing dynamic limit cycle motion but only for a single conductor [13, 14]. However, practically important non-uniformities arising, say, from icing variations or localized control devices like airflow spoilers or detuning pendulums cannot be accommodated. The aim of this paper is to overcome this deficiency and extend the single conductor approach to a bundle configuration having any number of conductors. Therefore, an adaptable but still computationally efficient 3DOF hybrid model is developed that uses finite element (FE) mode shapes, instead of their analytical counterparts, to construct the model and couple it to analytical expressions [14] to investigate the initiation and steady-state (limit-cycle) amplitude of galloping.

Only the commonly occurring bulk motion of a bundle line [1] is studied in which all the conductors move in phase in a single loop/span configuration. Then it is only necessary to consider, in detail, a reference curve that ficitiously connects the mass centers of the bundle's cross sections. In other words, the reference curve is analogous to a single conductor but its motion can be extrapolated to the individual conductors of a bundle. Results from parametric studies are presented for critical wind speeds, which are important to the initiation of galloping, as well as for limit cycle amplitudes at different wind speeds, static tensions and span lengths.

2. THE MODEL

Although an arbitrary number of conductors is considered, only a twin conductor bundle is illustrated in Fig. 1 (a) for simplicity. This figure presents the static positions of the two conductors that are produced by the conductors' weights and tensions as well as by the steady (side) wind and the accreted ice weight. Physical rigid spacers joining the conductors are illustrated as solid lines. Weightless, rigid fictitious spacers are introduced that periodically join the conductors to ensure that they essentially move together. Adjacent spans are always idealized by equivalent linear springs. Additional simplifying assumptions are:

1. Inertial and damping forces in the longitudinal direction, as well as the rotation of individual conductors about this direction, are neglected.
2. A line's sag-to-span ratio is small.
3. The rotation of the bundle about the reference curve is small and spacers are rigid.

4. No more than one mode per global direction is considered simultaneously.
5. The relative motion between the conductors of a bundle are neglected and the longitudinal motions of each of the conductors are presumed to be identical.

Items (1), (2), and (5) are the commonly made assumptions for the bulk motion of a bundle. The third item is reasonable in many cases because a bundle's torsional stiffness is much greater than that of a single conductor so that large rotations happen rarely. Item (4), on the other hand, presumes that the larger torsional stiffness of a bundle hardly changes the negligible coupling that is assumed for the single conductor for modes acting in the same direction. Limited comparisons with FE results suggest these simplifications are plausible for the cases considered later. Moreover, they noticeable reduce the computational effort.

3. EQUATIONS OF MOTION

The displacement at an arbitrary point (s, y, z) of a conductor is measured from that point's static position. It is given by

$$\begin{aligned} u_X(s,y,z,t) &= U(s,t) \\ v_Y(s,y,z,t) &= V(s,t) - z\Theta(s,t) \\ w_Z(s,y,z,t) &= W(s,t) - y\Theta(s,t). \end{aligned} \tag{1}$$

X, Y and Z are the global coordinates illustrated in Fig. 1(a) while x, y and z are the local coordinates shown Fig. 1(b). The latter are off-set from the global coordinates and their origin is located on the reference curve at the left support. The global displacement u_X, v_Y and w_Z has components whose direction is indicated by the corresponding suffix. On the other hand, s is the intrinsic coordinate which indicates the

distance that a cross section of the bundle is from the reference curve's origin. U, V and W are the global displacements of any point of the reference curve in the X, Y and Z directions, respectively. Θ is the rotation of the bundle about the reference curve and it is assumed to be small. If only one mode is considered in each direction, then U, V, W and Θ can be expressed as

$$\begin{aligned} U(s,t) &= q_u(t) f_u(s) \\ V(s,t) &= q_v(t) f_v(s) \\ W(s,t) &= q_w(t) f_w(s) \\ \Theta(s,t) &= q_\theta(t) f_\theta(s). \end{aligned} \tag{2}$$

The q_i and f_i, where $i = u,\ v,\ w,\ \theta$, are generalized coordinates and the associated mode shapes which are provided by a FE model, say.

By neglecting the inertial effects in the longitudinal direction, the total kinetic energy, T_k is given by

$$T_k = \frac{1}{2}\int_o^L \int_{A_T} \rho\left(\dot{v}_Y^2 + \dot{w}_Y^2\right) dA ds + \frac{1}{2}\sum_{k=1}^{p}\left[m_{sk}V^2(s_k,t) + m_{sk}W^2(s_k,t) + I_{sk}\Theta^2(s_k,t)\right] \tag{3}$$

where L is the total length of a line in a span; ρ is the mass density per unit volume over the iced bundle conductors' total cross-sectional area, A_T; m_{sk} and I_{sk} are the mass and the mass moment of inertia of the kth spacer, respectively; s_k is the intrinsic coordinate of the kth spacer's intersection with the reference curve; p is the number of spacers; and a dot superscript indicates differentiation with respect to time, t. The first order variation of the total strain energy for a bundle's bulk motion, δV_s, is [14]

$$\delta V_s = \sum_{i=1}^{n}\int_o^L \left[AE\delta\varepsilon_s\varepsilon_s + GJ\delta\varepsilon_\theta\varepsilon_\theta + T\delta\varepsilon_s + M_t\delta\varepsilon_\theta\right]_i ds \tag{4}$$

where n is the total number of conductors in a bundle. ε_s is the Lagrangian strain of the ith conductor, along s, T is the static tension in each conductor, M_t is a conductor's initial internal twisting moment that resists the external moment caused by an eccentric ice weight, A and GJ are the cross sectional area and the torsional rigidity of a bare conductor, respectively, and E is its modulus of elasticity.

The corresponding variation of the virtual work is

$$\delta W_{nc} = \int_0^L \left[F_y(s)\delta V + F_z(s)\delta W + F_\theta(s)\delta\Theta\right] ds - \delta q_a^T C_a^T \dot{q}_a. \qquad (5)$$

F_y, F_z and F_θ are the aerodynamic loads (per unit span length of the bundle) which act at the reference curve in the y, z and θ directions, respectively. C_a is an experimentally found damping matrix that depends upon ω_i and ξ_i, ξ_i (i = y, z, θ), the bundle's undamped, uncoupled natural frequencies and the measured damping ratios associated with the uncoupled vibrations in the direction indicated by a subscript. Finally, q_a is defined by

$$q_a^T = \left(q_u, q^T\right) where\ q^T = \left(q_v, q_w, q_\theta\right). \qquad (6)$$

By using a standard variational principle, equations (3) through (6) yield the three condensed equations of motion as

$$M\ddot{q} + C\dot{q} + Kq = F \qquad (7)$$

when the axial displacements are eliminated. The components of $F^T = \left(F_y F_z F_\theta\right)$ are

$$F_y = \frac{1}{2}\rho_{air} U_z^2 d\, C_y, F_z = \frac{1}{2}\rho_{air} U_z^2 d\, C_z, F_\theta = \frac{1}{2}\rho_{air} U_z^2 d^2\, C_\theta. \qquad (8)$$

Here ρ_{air} is the density of air, U_z is the steady side wind speed and d is the bare conductor's diameter. Furthermore,

$$C_y = f_{v\theta}\left(A_{y1}\alpha' + A_{y2}\alpha'^2 + A_{y3}\alpha'^3\right)$$

$$C_z = A_{z1}\alpha' + A_{z2}\alpha'^2 + A_{z3}\alpha'^3 \qquad (9)$$

$$C_\theta = A_{\theta 1}\alpha' + A_{\theta 2}\alpha'^2 + A_{\theta 3}\alpha'^3$$

where

$$f_{v\theta} = \frac{2}{L}\int_0^L f_v f_\theta ds, \qquad (10)$$

$$\alpha' = q_\theta - \frac{d}{2U_z}\dot{q}_\theta - \frac{f_{v\theta}}{U_z}\dot{q}_v, \qquad (11)$$

and

$$A_{ij} = \int_0^L a_{ij} f_\theta^{j+1} ds \qquad i = y,z,\theta, \qquad j = 1,2,3. \qquad (12)$$

The aerodynamic coefficients, a_{ij} , in equation (12) are obtained by curve fitting experimental, quasi-steady wind loads [15]. It is assumed that the aerodynamic interactions arising from the conductors of a bundle are negligible. This assumption is increasingly plausible as the separations between the conductors are enlarged beyond ten conductor diameters [3]. Then the aerodynamic forces and moments measured for an individual conductor can be merely summed at the reference curve. Details of the basic aerodynamic loads that correspond to the ice shape illustrated in Fig. 1(b), as well as the matrices M, C and K used in equation (7), are given in reference [14].

4. STABILITY ANALYSIS AND LIMIT CYCLES

The initial equilibrium solution (IES) of the linearized form of equation (7) gives an asymptotically stable, static configuration if all the eigenvalues have a negative real part. If, however, at least one of the eigenvalues crosses the real axis (a critical point) when a parameter increases, say U_z, then the IES becomes unstable and galloping may be

initiated. The critical wind speed, U_{zc}, is the value at which the IES just becomes unstable. Perturbation techniques are used to find new equilibrium states and periodic or quasi-periodic dynamic motions that may emerge from the critical point. Details are given in [11, 14].

5. NUMERICAL RESULTS

Numerical examples presume simple end supports, a single loop/span motion and a constant wind speed along a span. The finite element model [10] involves seven, three-node isoparametric elements along the reference curve, all interior nodes being joined by fictitious spacers. The wind's static angle of attack, θ_{static}, is taken invariably to be 40° because the single conductor satisfies the classical Den Hartog requirement for (a purely vertical) instability at this angle [1]. Ice accumulations on **each** connector are obtained from a short, single conductor sample placed in a freezing rain simulator [15]. The (C11) cross-section, illustrated in Fig. 1(b) resembles the D used in field trials to induce galloping [16]. Parameters of the icing and each individual conductor are summarized in Table 1. I is the centroidal inertial moment of a bare conductor, say i, whose centre is initially r_i from the reference curve; H is the static tension; e_y and e_z represent the eccentricity in the y and z directions, respectively, and $p = 0$. A_{ice} is the total cross-sectional area of an iced conductor and m is the corresponding mass per unit length. The parameters are selected so that the single loop/span, predominantly horizontal or vertical modes have virtually coincident (lowest) natural frequencies around 0.45 to 0.48Hz regardless of the number of conductors considered. Thus an internal resonance occurs, a situation that is conducive to galloping.

Fig. 2 (a) shows the variation in the reduced critical wind speed, $\overline{U}_{zc} = U_{zc} / fL_x$, and the nondimensional limit cycle amplitude, $\overline{A} = \sqrt{A_y^2 + A_z^2} / s_a$. A subscripted A indicates a component in the corresponding direction. The f is the lowest w_y, the predominantly vertical natural frequency; L_x is the horizontal span length; and s_a is the static sag at a line's mid-span. Fig. 2(a) indicates that $\overline{A}$ invariably decreases as $\overline{U}_{zc}$ increases, regardless of the number of conductors in a bundle. Therefore the greater "resistance" to the initiation of galloping, which is indicated by a higher $\overline{U}_{zc}$, appears to carry over to the dynamic limit cycle.

Fig. 2(b) gives the changes in $\overline{A}_y$ and $\overline{A}_z$ as the wind speed rises above the reduced critical wind speed, $\overline{U}_{zc}$. In this figure, the static horizontal tension is H = 30kN and L_x = 126m whereas $\overline{U}_z = U_z / fL_x$, $\overline{A}_y = A_y / s_a$ and $\overline{A}_z = A_z / s_a$. U_z varies from a steady 4 m/s to a steady 6 m/s. Not surprisingly, both $\overline{A}_y$ and $\overline{A}_z$ always grow as $\overline{U}_z$ and, hence, the wind's energy input to a line increases. As before, $\overline{A}_y$ is invariably much larger than $\overline{A}_z$. When galloping occurs, the number of conductors in a bundle hardly matters.

The effects of increasing the non-dimensional static horizontal tension, $\overline{H} = H / w$, and span length, L_x / s_a, are given in Figs. 2(c) and (d). Here w is the total weight of a bare conductor in one span. Both $\overline{A}_y$ and $\overline{A}_z$ invariably tend to grow as either $\overline{H}$ or L_x / s_a increases.

Moreover, Figs. 2 (c) and 2(d) are little different from the comparable situation observed in Fig. 2(b) for increasing $\overline{U}_z$.

6. CONCLUSIONS

Results for a particular ice shape and angle of attack to the wind suggest that the ratio of the limit cycle amplitude to the mid-span's static sag invariably decreases as the critical wind speed ratio increases, regardless of the number of conductors in a bundle. It also usually grows as the non-dimensional side wind speed (above the critical value), horizontal tension or span length increase – again, immaterial of the number of conductors.

7. ACKNOWLEDGMENTS

The financial support of Manitoba Hydro and the Natural Sciences and Engineering Research Council of Canada is acknowledged gratefully.

8. REFERENCES

1. Transmision Line Reference Book, Wind–induced conductor motion. 1979, EPRI, *Palo Alto, California*
2. Simpson, A., Determination of the natural frequencies of multiconductor overhead transmission lines. *Journal of Sound and Vibration*, 1974, 20 (4), 417-449.
3. Diana, G., Cheli, F., Manenti, A., Nicolini, P. and Tavano, F. Oscillation of bundle conductors in overhead lines due to turbulent wind. *IEEE Transaction on Power Delivery*, 1990, 5(4), 1910-1919.
4. Gawronski, K.E., Non-linear galloping of bundle-conductor transmission lines. *Ph.D thesis , Clarkson College of Technology*, 1977.

5. Richardson, A.S., Jr., Dynamic analysis of lightly iced conductor galloping in two degrees of freedom. *Proc. IEEE,* 1981, 128 (Pt. C) (4), 211-218.
6. Richardson, A.S., A study of galloping conductors on a 230 kv transmission line. *Electric Power System Research,* 1991, 21, 43-55.
7. Jones, K.F., Coupled vertical and horizontal galloping. *ASCE, Journal of Engineering Mechanics,* 1992, 118(1), 92-107.
8. Blevins, R.D., Flow – induced vibration (2nd edition). Van Nostrand Reinhold Co., New York, 1990.
9. Nakamura, Y. Galloping of bundled power line conductors. *Journal of Sound and Vibration,* 1980, 73 (3), 363-377.
10. Desai, Y.M., Yu, P., Popplewell, N. and Shah, A.H., Finite element modelling of transmission line galloping. *Computers and Structures,* 1995, 57 (3), 469-489.
11. Desai, Y.M., Yu, P., Popplewell, N. and Shah, A.H., Perturbation-based finite element analyses of transmission line galloping. *Journal of Sound and Vibration,* 1996, 191(4), 469-489.
12. Jianwei, W., Large vibrations of overhead electrical lines. *Ph.D thesis, Universite De Liege, Belgium,* 1996.
13. Yu, P., Shah, A.H. and Popplewell, N. Inertially coupled galloping of iced conductors. *Journal of Applied Mechanics, Trans. ASME,* 1992, 59 (1), 140-145.
14. Yu, P., Desai, Y.M., Shah, A.H. and Popplewell, N., Three-degree-of-freedom model for galloping (Parts I and II).ASCE, *Journal of Engineering Mechanics,* 1993, 119 (12), 2405-2448.
15. Stumpf, P., Determination of aerodynamics forces for iced single and twin-bundled conductors. *M.Sc. thesis, University of Manitoba, Winnipeg, Canada,* 1994.

16. Edwards, A.T. and Madeyski, A. , Progress report on the investigation of galloping of transmission line conductors. *Trans. AIEE*, 1956, 75(3), 666-686.

Table 1 Iced C11 Line Properties

Parameter	Data	Parameter	Data
d(m)	0.0286	A(mm^2)	423.24
E (N/m^2)	$4.78033*10^{10}$	m(kg/m)	2.379
GJ (Nm^2/rad)	101	ξ_y , ξ_z	$0.515*10^{-3}$
I(kg m)	$0.3334*10^{-3}$	ξ_θ	0.308
H (N)	30000	r_i (m)	0.2355
e_y (mm)	2.05	L_x (m)	125.88
e_z (mm)	–0.63	$\rho_{air}\left(kg/m^3\right)$	1.2929
A_{ice} (mm^2)	594.48	U_z (m/s)	4.0

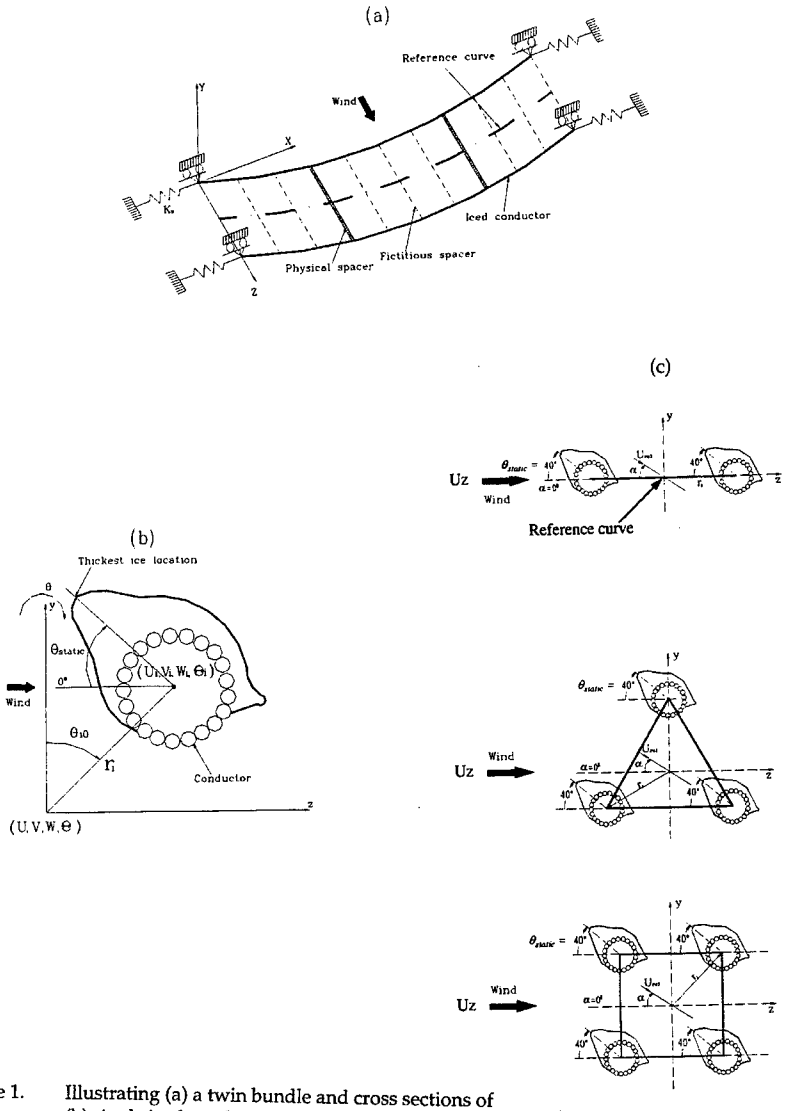

Figure 1. Illustrating (a) a twin bundle and cross sections of (b) single iced conductor and (c) two, three and four iced conductor bundles.

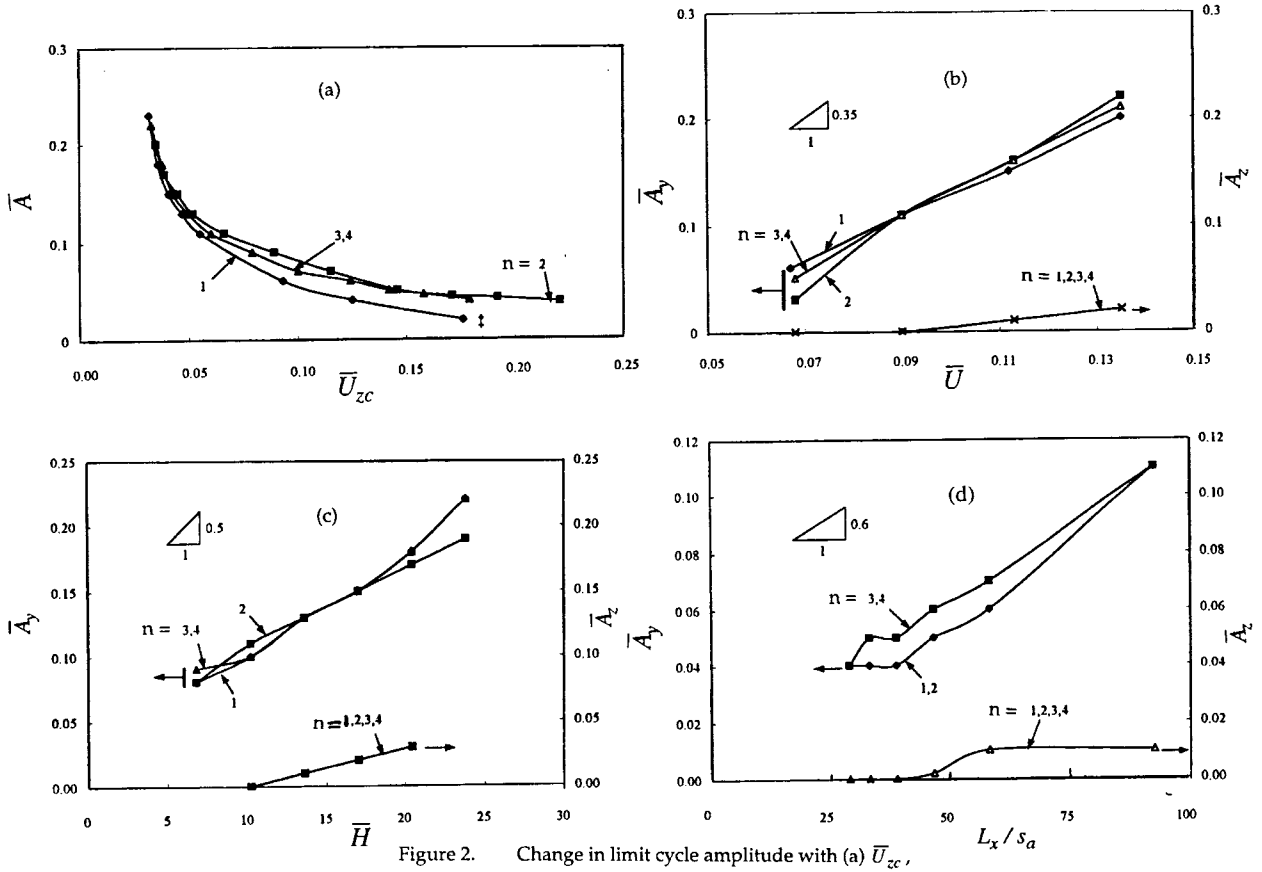

Figure 2. Change in limit cycle amplitude with (a) $\overline{U}_{zc}$, (b) $\overline{U}$, (c) $\overline{H}$ and (d) L_x / s_a.

WIND-INDUCED INSTABILITIES OF CURVED POLES

C. Zhang, N. Popplewell, P. Banerji*, A. Shah

Faculty of Engineering, University of Manitoba, Winnipeg, Manitoba
Canada R3T 5V6

ABSTRACT

The initiation of galloping is studied for a tapered pole in a steady wind. The aerodynamic coefficients associated with the wind load are obtained from scale model experiments. It is shown that galloping can occur at relatively low wind speeds of about 10 m/s (36 km/h). However, the initiation speed is very sensitive to the wind direction and structural damping. This analysis essentially confirms field observations.

1. INTRODUCTION

When an elastic structure like the light pole shown in Figure 1 or a traffic pole vibrates in a steady airflow, the flow relative to the pole also oscillates. The aerodynamic forces produced by this airflow can cause a growth in the amplitude of the pole's vibrations – a phenomenon called galloping. A comprehensive review of this phenomenon has been provided fairly recently [1].

A wind-induced, instability analysis requires a mix of an analytical formulation with an experimental determination of the wind effects. Experiments for cantilevered poles that involved a water table, tow tank and full scale field experiments [2] have shown that large vibrations are caused by galloping, not by pure vortex shedding. Furthermore, galloping was demonstrated to most likely occur in a steady wind of between 4.5 and 13.4 m/s when the wind's direction is within ±7.5° of the normal to a curved pole's plane of curvature. This

* Visiting Professor, Dept. of Civil Eng.
Indian Institute of Technology, Mumbai-400 076, India

situation, in which the $\bar{\alpha}_m$ shown in Figure 2 is within $\pm 7.5°$ *of* 90°, is considered exclusively here.

Fifteen three dimensional, three-node, curved beam elements [3] are used to analyze the wind-induced vibrations of the curved steel light pole shown full-scale in Figure 1. A 39 kg lamp may be located at node 31. The pole's cross-section is hexagonal and its other properties are given in Table 1. Critical wind speeds are calculated which correspond to the magnitude of a steady wind speed that is just large enough to initiate galloping. The effects of structural damping and small changes in the wind's direction are also investigated.

2. EQUATIONS OF MOTION

By using conventional theory, the equations of motion for the pole can be derived in the form:

$$[M]\{\ddot{Q}\}+[C]\{\dot{Q}\}+[K]\{Q\}=\{P\} \tag{1}$$

where $[M]$, $[C]$ and $[K]$ are the global structural mass, damping and stiffness matrices, respectively. The $\{Q\}$, $\{\dot{Q}\}$ and $\{\ddot{Q}\}$ are the nodal displacement, velocity and acceleration vectors, respectively. $\{P\}$ is the nodal load vector that is a function of the nodal displacements and velocities that, in turn, are functions of time for an aerodynamic load.

The structural mass and stiffness matrices are developed straightforwardly. Rayleigh damping, which has been found to be reasonable when the first couple of modes primarily contribute to the structural response, is used to define the structural damping matrix, $[C]$, as

$$[C]=a_{c0}\,[M]+a_{c1}\,[K]. \tag{2}$$

The a_{c0} and a_{c1} are constants. They can be evaluated from the modal damping ratios, typically the same value δ, in the first two structural modes having (circular) natural frequencies ω_1 *and* ω_2, say. Then

$$\begin{Bmatrix} a_{c^0} \\ a_{c^1} \end{Bmatrix} = \frac{2\delta}{\omega_1 + \omega_2} \begin{Bmatrix} \omega_1\omega_2 \\ 1 \end{Bmatrix}. \tag{3}$$

3. AERODYNAMIC EXPERIMENTS

Wind tunnel experiments are performed to obtain the aerodynamic coefficients of the wind load by applying a quasi-steady theory. Full-scale experiments could not be entertained due to the limited dimensions of the working cross-section of the available wind tunnel. Therefore, the tests are performed on geometrically similar but smaller models. According to the requirement for similarity [4], Reynolds number is kept approximately the same for both the model and full-scale poles. Because the taper of the pole considered is small (about 1:150), constant cross-sectional pole models (not tapered poles) are used for simplicity. As the maximum wind speed in the wind tunnel is about 32 m/s, and 4 m/s is at the lower end of the range of wind speeds observed to produce galloping in practice, a one-eighth scale for the model is realistic. However, solely one model at this scale is still too big to be placed in the wind tunnel. Consequently, a one-eighth-scale model has to be tested by using two separate components. One component corresponds to the combined curved-straight part shown as part *BE* in Figure 1. The other component is the straight part, *AB*. The interaction of the airflow between the two parts is assumed to be negligible. Wind tunnel tests using a wool tufted model suggest that this assumption is plausible.

The total drag force, P_D, shown in Figure 2(a) that acts on BE is defined along the wind's direction. The corresponding lift force, P_L, is vertical and the horizontal side force, P_S, is perpendicular to both P_D and P_L. These forces are usually given in terms of aerodynamic coefficients by:

$$\langle P_D \; P_L \; P_S \rangle = \frac{1}{2} \rho_{air} U^2_{wind} dL_{BE} \langle C_{DC} \; C_{LC} \; C_{SC} \rangle \tag{4}$$

where $\rho_{air} = 1.19 kg/m^3$ is the density of air, U_{wind} is the free stream air speed, and d is the dimension of the pole's cross-section normal to the wind. For convenience, d is taken as the distance between two opposite flat sides of the hexagonal cross-section. Furthermore, L_{BE} is the total outside peripheral length of the model's curved component, *BE*. The C_{DC}, C_{LC} and C_{SC} are the drag, lift and side force coefficients for *BE*. The rolling, yawing and pitching moments, M_R, M_Y *and* M_P respectively, are the corresponding moments about these three directions. They are given by:

$$\langle M_R \; M_Y \; M_P \rangle = \frac{1}{2} \rho_{air} U^2_{wind} d^2 L_{BE} \langle C_{MRC} \; C_{MYC} \; C_{MPC} \rangle \tag{5}$$

where C_{MRC} , C_{MYC} and C_{MPC} are the rolling, yawing and pitching moment coefficients for *BE*. Similarly, there are drag and side forces for the model's straight component, *AB*. However, the measured moments are negligible, regardless of the cross-section, so that only the forces per unit length are shown in Figure 2(b). They are given by:

$$\langle F_D \; F_S \rangle = \frac{1}{2} \rho_{air} U^2_{wind} d \langle C_D \; C_S \rangle \tag{6}$$

where C_D *and* C_S are the drag and side force coefficients for *AB*.

The aerodynamic forces and moments are non-dimensionalized to obtain the aerodynamic coefficients. Only the measured data for *BE* are shown in Figure 3. Other data can be found in [3]. In Figure 3, the wind speed is 31.4 m/s and the Reynolds number is 2.7×10^4 (i.e. in the subcritical range.). The reference angle, $\overline{\alpha}_m = 0^\circ$, for the curved model is taken to correspond to the position when part *ED* in Figure 2(a) is along the wind's direction and the wind blows from point *E* to point *D*. In addition, two opposite flat sides are perpendicular to the wind's direction at $\overline{\alpha}_m = 0°$ for both the curved and straight model. Theoretically, the data at $\overline{\alpha}_m = 0°$ and 360° should be the same. However, there are small differences in Figure 3 at these two angles which may arise from equipment drift. The drift is likely due to a temperature change during the wind tunnel experiments, even though the wind tunnel and its instrumentation were run for several hours before starting an experiment.

Next, because the measured aerodynamic coefficients for the curved component *BE* include the effects of the straight parts *BC* and *DE*, the aerodynamic coefficients for the purely curved part *CD* of the model are calculated by subtracting the effects of the straight parts from the measured coefficients. (See Ref [3] for details.) The results are designated $\overline{C}_D, \overline{C}_S$ *and* $\overline{C}_L$ for the forces and $\overline{C}_{MR}, \overline{C}_{MP}$ *and* $\overline{C}_{MY}$ for the moments. Only the positions around $\overline{\alpha}_m$ equal 90° are analyzed because the pole is most susceptible to gallop for that wind direction [2]. Note that an arrow is used in Figure 3 to highlight this particular orientation.

The effects on the aerodynamic coefficients of a lamp located at the tip of a pole are also investigated. In the experiment, a tubular

section (having a length of 20 mm, thickness 2 mm and an inside diameter equal to the model's cross-sectional dimension) is mounted coaxially at the tip of the curved pole model to simulate a lamp. The aerodynamic effect, however, is found to be small. On the other hand, because the wind speed in the wind tunnel could not be changed over a wide range, the effects of large changes in the Reynolds number could not be analyzed realistically.

4. AERODYNAMIC LOADS

The $\{P\}$ term in equation (1) is created by the wind load. Because the pole is so slender and its Reynolds number is in the subcritical range, it is reasonable to suppose that the airflow does not reattach to a downstream part of the pole at $\bar{\alpha}_m \approx 90°$. Indeed, the similar orientation of wool strands attached to the curved model suggested that the wind pressure is distributed quite uniformly over the model. Therefore, a uniform pressure assumption is adopted.

To determine the nodal forces arising from the airflow, the curved model is divided artificially into the three parts shown in Figure 2. The directions *X-Y-Z* given in Figure 2 correspond to the global coordinate system. $x-\zeta-\eta$ represent the local coordinate system for each part. The x *and* ζ directions are always defined along the tangential and normal directions of a pole's axis, respectively, and η is perpendicular to the $x-\zeta$ plane. The following derivations only give the details for determining the aerodynamic forces per unit length acting on the straight parts *AC* and *DE*. The extension to the curved part, *CD*, is detailed in [3].

Let the angle between the wind's direction and the structural (*X-Y*) plane be $90° \pm |\bar{\varepsilon}|$ where $|\bar{\varepsilon}|$ is a small offset angle. When $\bar{\varepsilon} = 0$, the

wind speed, U_{wind}, is along the η direction. Due to the pole's wind-induced dynamic rotation about the local x axis, Θ_x, the local coordinate plane $\zeta-\eta$, which corresponds to the pole's static configuration, instantaneously takes another orientation. Consequently, a vibrating pole experiences a relative wind, U_{rel}. The magnitude of U_{rel} and its direction, $\bar{\alpha}_V$, for the vertical part AC are given, with respect to the ζ-η system, as [3]:

$$U_{rel}^2 = \left(\dot{u} - U_{wind}\bar{\varepsilon}\right)^2 + \left(U_{wind} + \dot{v}\right)^2 \tag{7a}$$

and

$$\bar{\alpha}_v \approx \frac{\dot{u}}{U_{wind}} - \bar{\varepsilon} \tag{7b}$$

where the pole's velocities, $\dot{u}$ *and* $\dot{v}$ in the ζ *and* η directions, respectively, are assumed to be small in relation to the wind speed. The relative wind speed's magnitude and direction for the horizontal part DE is obtained by substituting $\bar{\varepsilon}=0$ in equation (7). The wind's instantaneous angle of attack, $\bar{\alpha}$, is:

$$\bar{\alpha} = \bar{\alpha}_v - \Theta_x \approx \frac{\dot{u}}{U_{wind}} - \Theta_x - \bar{\varepsilon}. \tag{8}$$

Equation (8) is used to find $\bar{\alpha}$ to determine the aerodynamic coefficients from the wind tunnel data. (Note, however, that the $\bar{\alpha}_m$ used in the experiment is $\bar{\alpha}_m = \bar{\alpha} - 90°$.) Moreover, $\bar{\alpha}$ and $\bar{\varepsilon}$ are taken to be positive in the clockwise direction (when viewed from above), whereas $\bar{\alpha}_v$ *and* Θ_x are positive in the counterclockwise direction.

The drag and side forces per unit length for part AC can be obtained from the aerodynamic coefficients by using equation (6)

where C_D *and* C_S are the drag and side force coefficients, respectively. The forces per unit length along AC's ζ *and* η directions are then computed by substituting data from equation (8) into

$$F_\zeta = -F_D \sin\bar{\alpha} - F_S \cos\bar{\alpha} \tag{9a}$$

as well as

$$F_\eta = F_D \cos\bar{\alpha} - F_S \sin\bar{\alpha} \tag{9b}$$

because Θ_x is found to be about a negligible 0.3° for a 13 m/s wind speed.

For the horizontal part *DE*, the lift force, F_L, is given by the same expression as that for F_S in equation (6). On the other hand, the forces per unit length for part *DE*, along its ζ *and* η directions, are:

$$F_\zeta = -F_D \sin\bar{\alpha} + F_L \cos\bar{\alpha} \tag{10a}$$

and

$$F_\eta = F_D \cos\bar{\alpha} + F_L \sin\bar{\alpha}. \tag{10b}$$

The element load vectors created by the distributed aerodynamic loading on the various parts of the light pole and the resulting $\{P\}$ can be obtained conventionally [3].

5. ANALYSIS OF INSTABILITY

The standard Newmark-β method is chosen to integrate the equations of motion. Then the critical wind speed, U_{crit}, can be found by gradually incrementing the wind speed, U_{wind}, in steps of 0.1 m/s to assess the convergence of the resulting temporal deflections at the pole's tip, for example. From a visual inspection, further increases in U_{wind} beyond U_{crit} make these deflections diverge. The critical wind speeds for the light pole, with and without a lamp, are presented in Figure 4 for small $\bar{\varepsilon}$ and different structural damping ratios. This

figure shows that, as expected, galloping is initiated at higher wind speeds if the structural damping is increased [1]. However, the lamp seemingly provides greater stability because initiation speeds are generally higher for a pole with a lamp. Furthermore, it can be seen that, in confirmation of field observations, the initiation of galloping is very sensitive to small changes in the wind's direction from the 90° orientation.

Deflection histories of the pole without a lamp are presented in Figure 5. They correspond to $\delta = 0, \bar{\varepsilon} = -0.5^0$ and a critical wind speed of 8.7 m/s in Figure 4(a). The tip deflection in the wind's direction (-v) predominates. It appears to be created mainly by the drag force [3]. Moreover, the two lowest frequency modes – one essentially in-plane, the other out-of-plane – dominate these deflections. Although the corresponding natural frequencies (1.79 and 1.82 Hz) are close, the modal coupling is negligible [3]. Hence, equation (3) appears reasonable.

6. CONCLUDING REMARKS

A study is presented to determine the wind-induced instabilities of curved poles. It is shown that galloping can occur at relatively low wind speeds of about 10 m/s, although the initiation speed is very sensitive to the wind's direction and the pole's structural damping.

7. ACKNOWLEDGEMENTS

The financial support of the Natural Sciences and Engineering Research Council of Canada is acknowledged gratefully.

8. REFERENCES

1. Parkinson, G.V., Phenomenon and modeling of flow-induced vibrations of bluff bodies. *Prog. Aerospace Sci.*, 1989, **26**, pp. 169-224.
2. McDonald, J.R., Mehta, K.C., Oler, W.W. and Pulipaka, N., Wind load effects on signs, luminaires and traffic signal structures. *Report No. 1303-F*, Texas Tech. University, Lubbock, USA, 1995.
3. Zhang, C., A curved beam element and its application to traffic poles. M.Sc. thesis, University of Manitoba, 1998.
4. Simiu, E. and Scanlan, R.H., *Wind Effects on Structures.* 2nd ed., John Wiley and Sons, New York, 1986.

Table 1 Properties of the steel light pole.

Young's modulus	200 GPa
Shear modulus	80 GPa
Density	7850 kg/m^3
Shear correction factor	0.5
d_A +	232 mm
d_B	154 mm
d_C	119.2 mm
d_D	82 mm
d_E	70 mm
h_{AB}	4.55 mm
h_{BE}	3.04 mm

+ Value of d (h) shown in Figure 1 at cross-section (component) designated by subsripted letter(s).

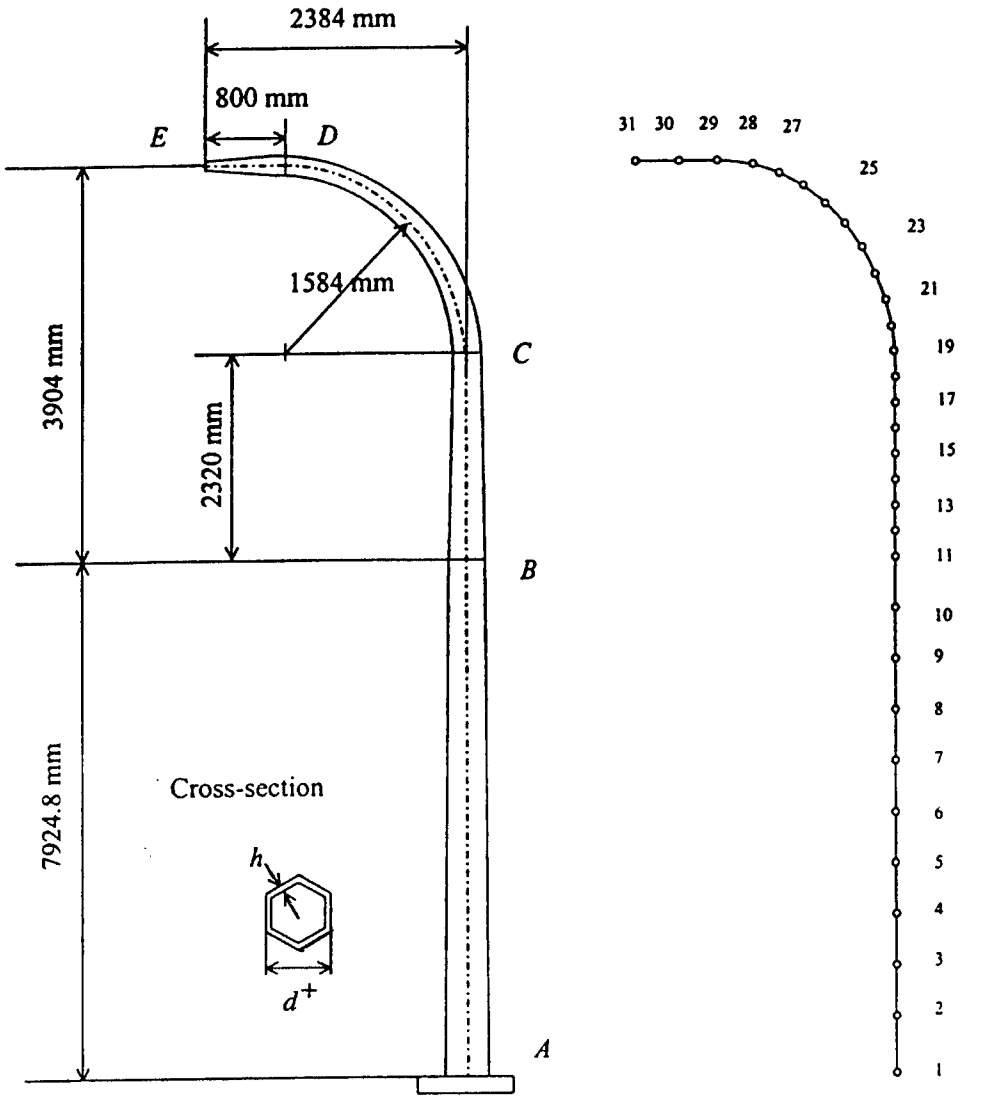

Figure 1 Showing the full-scale light pole and finite element nodes.
+ Perpendicular to wind when wind is perpendicular to plane ABE.

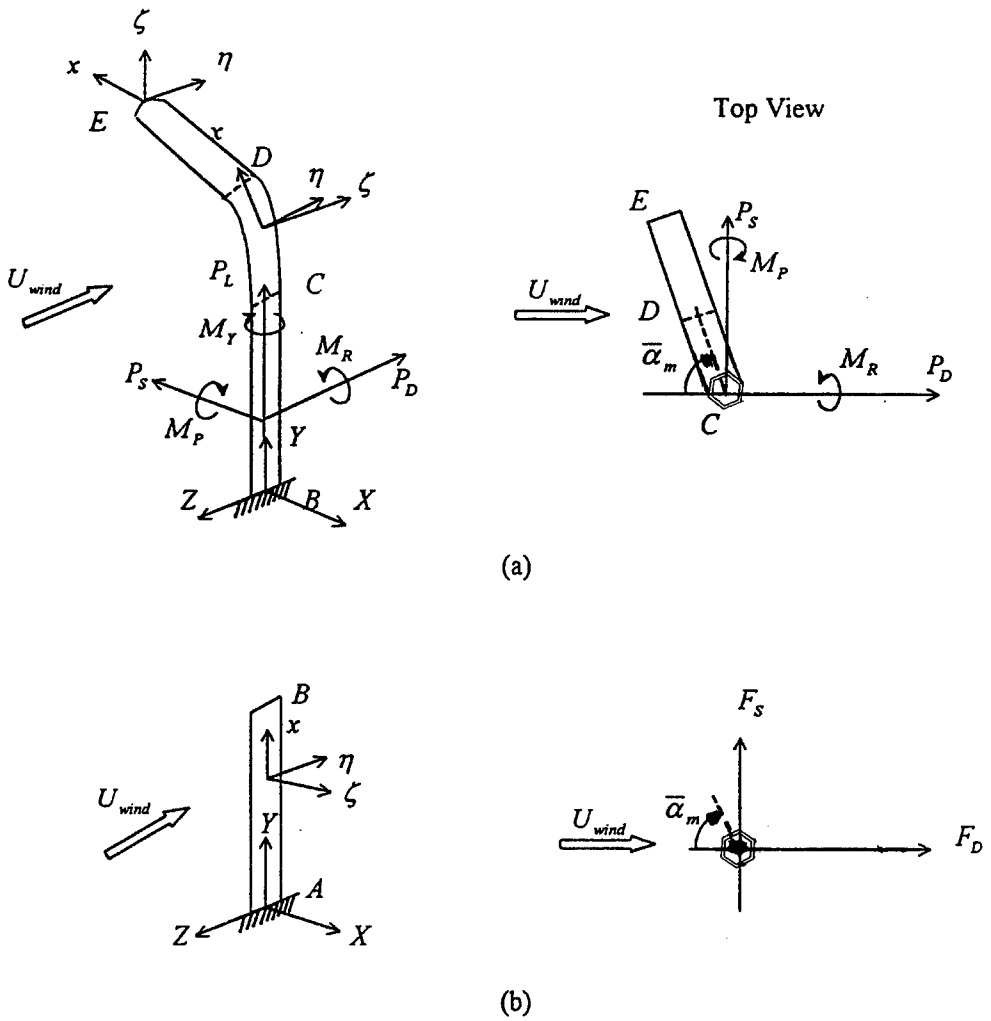

Figure 2 Schematic of the two components considered in the aerodynamic experiments, showing the global and local coordinate systems and (a) the total aerodynamic forces acting on the curved, rigid component *BE*; and (b) the aerodynamic forces per unit length on the straight, rigid component *AB*.

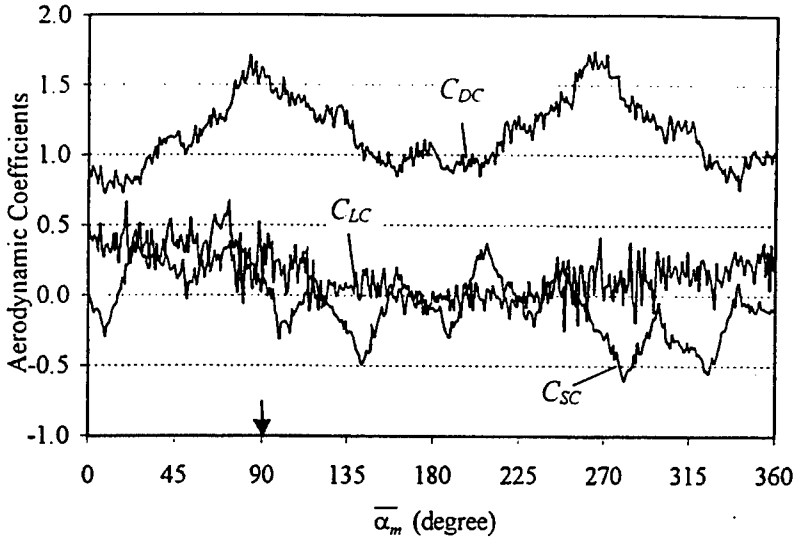

(a)

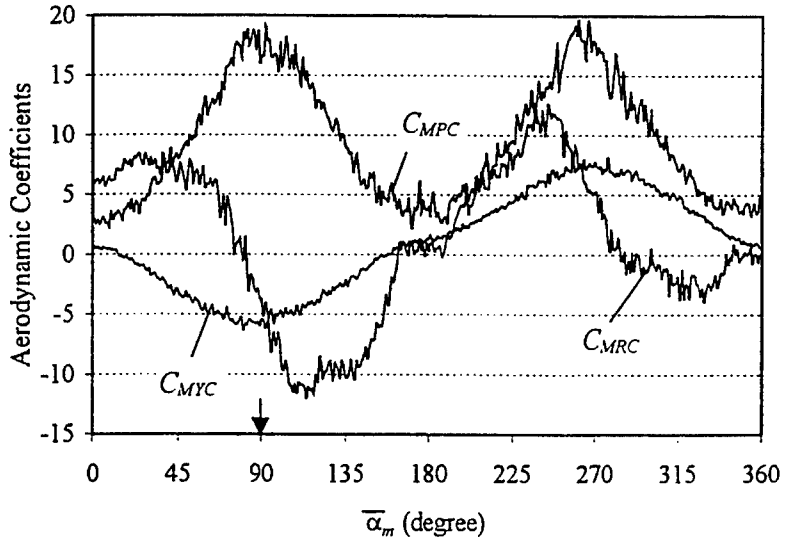

(b)

Figure 3 Measured aerodynamic coefficients for the model of the curved component *BE*

↓ Wind direction for analysis

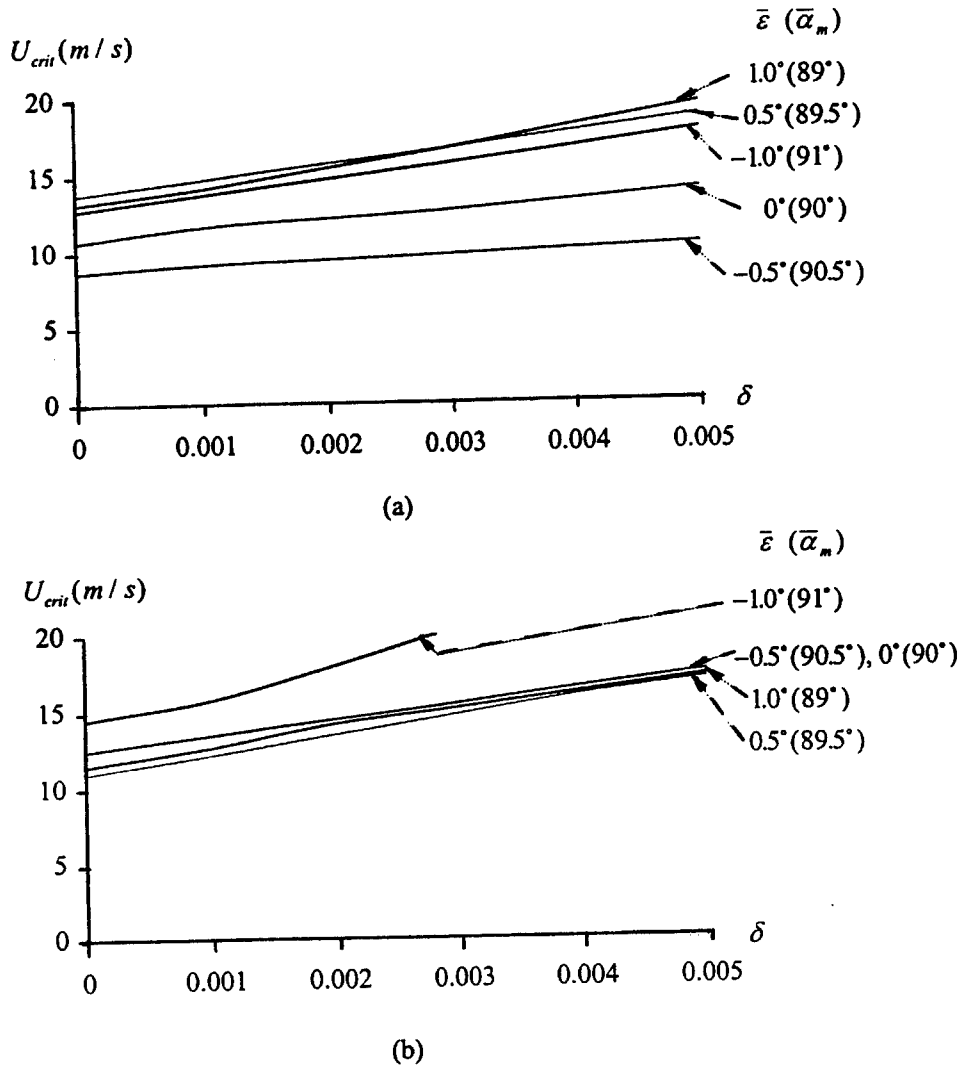

Figure 4 Critical wind speeds for a hexagonal light pole having different structural damping ratios, δ, and exposed to various wind directions, $\bar{\varepsilon}$. Showing (a) without a lamp and (b) with a lamp.

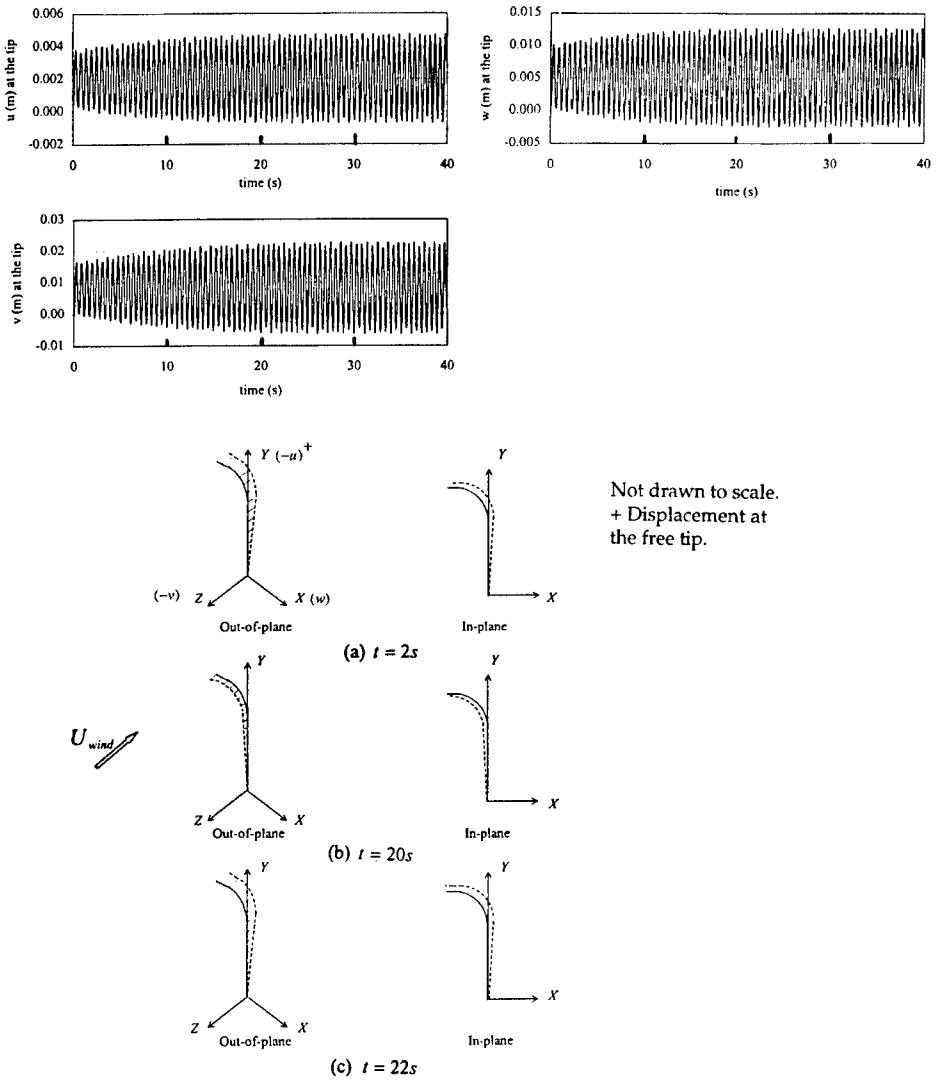

Figure 5 Deflection history at free tip of pole without a lamp when $\delta = 0, \bar{\varepsilon} = -0.5°$ *and* U_{wind} corresponds to the critical 8.7 m/s wind speed.

WORK IN PROGRESS

SOME NUMERICAL RESULTS OF ANALYTICAL SOLUTIONS FOR STEADY-STATE RESPONSE OF A BEAM WITH NONLINEAR BOUNDARY CONDITIONS

S. Aoki* and T. Watanabe**
* Department of Mechanical Engineering,
Tokyo Metropolitan College of Technology,
1-10-40, Higashi-Ohi, Shinagawa-ku, Tokyo, 140-0011, Japan
** Faculty of Education and Human Sciences,
Yamanashi University,
Takeda 4-4-37, Kofu-City 400-8510, Japan

ABSTRACT

This paper deals with the steady-state response of the beam with nonlinear boundary conditions, in which the system collides with the stop once in half period of its vibration. Considering the energy loss in a collision with a stop and the duration of collision, an analytical method of approximate solution for the beam which collides with the stop having quadrilateral hysteresis loop characteristics is presented. Some numerical results of the approximate solution are obtained.

INTRODUCTION

The steady-state response of continuous systems with nonlinear boundary conditions is of great importance in several engineering applications. Collision characteristics is one of the most important nonlinear characteristics. In the response analysis, the force of restitution is modeled as bilinear force-penetration characteristics in which stiffness increases during collision or the coefficient of restitution taken to be constant. However, in those models, energy loss or duration of collision are not considered.

In this paper, the force of restitution is modeled as quadrilateral hysteresis loop characteristics in order to consider the energy loss in a collision and the duration of collision[1]. An analytical method of solution for the response of the simply supported beam with nonlinear boundary conditions is presented.

The resonance curves are obtained and Some numerical results are compared with the other approximate solutions.

ANALYTICAL METHOD

A simplified dynamical model of the continuous system with symmetrical collision characteristics is shown in Fig.1. Namely, this model consists of a beam simply supported at one end, with amplitude constraint by the stops having quadrilateral hysteresis

loop characteristics as shown in Fig.2. In this case, the coefficient of restitution depends on the colliding velocity at the beam end.

Let ρ be the mass density, A the cross-sectional area, and EI the modulus of flexural rigidity. The equation of motion for transverse vibration of a beam with respect to relative displacement can be given as follows:

$$\frac{\partial^2 z}{\partial t^2}+\frac{EI}{\rho A}\frac{\partial^4 z}{\partial x^4}=y_0\omega^2\cos\omega t \tag{1}$$

A formal solution of Equation (1) can be expressed as follows:

$$z=-y_0\cos\omega t+\sum_{n=1}^{\infty}(A_n\cosh\lambda_n x+B_n\sinh\lambda_n x +C_n\cos\lambda_n x+D_n\sin\lambda_n x)\cos n\omega t \tag{2}$$

where A_n, B_n, C_n, D_n are constants to be determined in each particular case from the boundary conditions of the beam, where

$$\lambda_n^4 l^4=Z_1^4 n^2\Omega_1^2,\quad \Omega_1=\omega/\omega_1 \tag{3}$$

and

$$\omega_1=\frac{Z_1^2}{l^2}\sqrt{\frac{EI}{\rho A}},\quad Z_1=3.927 \tag{4}$$

In this paper, the steady-state vibration is dealt with. Once the vibration of the beam becomes steady and periodic, the force of restitution $f(z_l,\dot{z}_l)$ becomes also periodic and can be represented as a periodic function $g(\theta)$ of θ with the period 2π. The phase angle θ is defined as follows:

$$\theta=\omega t-\alpha \tag{5}$$

where α is the phase lag angle. The periodic function $g(\theta)$ must satisfy the conditions of the given characteristics of the force of restitution, which is to be written as the following equations:

$$f(z_l,\dot{z}_l)\begin{cases}\equiv g(\theta)=K_1(z_l-e_0), & -(\theta_1+\theta_2)\leqq\theta\leqq-\theta_2 \quad (\mathrm{I})\\ \equiv g(\theta)=K_1\delta_0+K_2(z_l-e_0-\delta_0), & -\theta_2\leqq\theta\leqq 0 \quad (\mathrm{II})\\ \equiv g(\theta)=K_3(z_l-z_{l3}), & 0\leqq\theta\leqq\theta_3 \quad (\mathrm{III})\\ \equiv g(\theta)=0, & \theta_3\leqq\theta\leqq\pi-(\theta_1+\theta_2) \quad (\mathrm{IV})\\ \equiv g(\theta)=K_1(z_l+e_0), & \pi-(\theta_1+\theta_2)\leqq\theta\leqq\pi-\theta_2 \quad (\mathrm{V})\\ \equiv g(\theta)=-K_1\delta_0+K_2(z_l+e_0+\delta_0), & \pi-\theta_2\leqq\theta\leqq\pi \quad (\mathrm{VI})\\ \equiv g(\theta)=K_3(z_l+z_{l3}), & \pi\leqq\theta\leqq\pi+\theta_3 \quad (\mathrm{VII})\\ \equiv g(\theta)=0, & \pi+\theta_3\leqq\theta\leqq 2\pi-(\theta_1+\theta_2) \quad (\mathrm{VIII})\end{cases} \tag{6}$$

where θ_1, θ_2 and θ_3 denote the range of θ as shown in Fig.3, and the period 2π is divided into 8 intervals (I ~ VIII).

Meanwhile, for half cycle of its vibration, the switching-over conditions from one to another intervals are expressed by

$$\theta=-(\theta_1+\theta_2),\ z_l=e_0 \quad (\mathrm{VIII}\rightarrow\mathrm{I}) \tag{7}$$

$$\theta=-\theta_2,\ z_l=e_0+\delta_0 \quad (\mathrm{I}\rightarrow\mathrm{II}) \tag{8}$$

$$\theta=0,\ \dot{z}_l=0,\ z_l=z_{l\max} \quad (\mathrm{II}\rightarrow\mathrm{III}) \tag{9}$$

$$\theta=\theta_3,\ z_l=z_{l3} \quad (\mathrm{III}\rightarrow\mathrm{IV}) \tag{10}$$

$g(\theta)$ is expanded into the Fourier series:

$$g(\theta)=\sum_{n=1,3,5,\ldots}^{\infty}(a_n\cos n\theta+b_n\sin n\theta) \tag{11}$$

and the nondimensional Fourier coefficients are defined as follows:

$$x_n=\frac{a_n}{k\Gamma},\ y_n=\frac{b_n}{k\Gamma}\quad (n=1,3,5,.....),\quad k=\frac{3EI}{l^3} \tag{12}$$

where Γ is the amplitude of the fundamental term of cosine part of z_l and displacement at the beam end ($x=l$). z_l is given as:

$$z_l=\Gamma[\cos\theta+\sum_{n=3,5,...}^{\infty} M_n x_n \cos n\theta + \sum_{n=3,5,...}^{\infty} M_n y_n(\sin n\theta-n\sin\theta)\}] \tag{13}$$

where

$$M_n=\frac{6\lambda_n l\sin\lambda_n l\sinh\lambda_n l}{Z_1^4 n^2\Omega_1^2(\cosh\lambda_n l\sin\lambda_n l-\sinh\lambda_n l\cos\lambda_n l)} \quad (n=1,3,5,.....) \tag{14}$$

Γ and the amplitude of sinusoidal excitation, y_0 are determined as:

$$\frac{\Gamma}{e_0}=\frac{y_0}{e_0}\frac{N_l}{\sqrt{(1-M_1x_1)^2+(\sum_{n=1,3,..}^{\infty} nM_n y_n)^2}} \tag{15}$$

$$\frac{y_0}{e_0}=\frac{\sqrt{(1-M_1x_1)^2+(\sum_{n=1,3,...}^{\infty} nM_n y_n)^2}}{N_l[\cos(\theta_1+\theta_2)+\sum_{n=3,5,...}^{\infty}\{M_n x_n\cos n(\theta_1+\theta_2) - M_n y_n\{\sin n(\theta_1+\theta_2)-n\sin(\theta_1+\theta_2)\}]} \tag{16}$$

where

$$N_l=\frac{\sin\lambda_1 l(1-\cosh\lambda_1 l)+\sinh\lambda_1 l(\cos\lambda_1 l-1)}{\cosh\lambda_1 l\sin\lambda_1 l-\sinh\lambda_1 l\cos\lambda_1 l} \tag{17}$$

From Eq.(6), an infinite set of simultaneous linear equations for x_n and y_n as an infinite number of unknowns are obtained. To improve the convergency of the resulting Fourier series $g(\theta)/k\Gamma$, a series transformation as follows is introduced. A new phase angle ϕ, and the angle θ_0 are given by

$$\phi=\theta+(\theta_1+\theta_2),\quad \theta_0=\theta_1+\theta_2+\theta_3 \tag{18}$$

and a new Fourier series for $g(\theta)/k\Gamma$ is approximated as follows:

$$\frac{g(\theta)}{k\Gamma}=\sum_{m=1}^{\infty}\xi_m\sin\frac{m\pi}{\theta_0}\phi\fallingdotseq\xi_0\sin\frac{\pi}{\theta_0}\phi\quad(0\leqq\phi\leqq\theta_0) \tag{19}$$

The relation between x_n, y_n and ξ_0 are given by

$$x_n=\frac{2}{\theta_0}\frac{\cos n(\theta_1+\theta_2)+\cos n\theta_3}{(\pi^2/\theta_0^2)-n^2}\xi_0\quad(n=1,3,5,.....) \tag{20}$$

$$y_n=-\frac{2}{\theta_0}\frac{\sin n(\theta_1+\theta_2)+\sin n\theta_3}{(\pi^2/\theta_0^2)-n^2}\xi_0\quad(n=1,3,5,.....) \tag{21}$$

ξ_0 is obtained by the following equation.

$$\xi_0=\frac{x_{11}}{1-c_{11}} \tag{22}$$

x_{11} and c_{11} are function with respect to θ_1, θ_2 and θ_3. $\cos\theta_2$

and $\cos\theta_3$ are expressed as:

$$\cos\theta_2=\cos(\theta_1+\theta_2)+\frac{\delta_0}{e_0}\cos(\theta_1+\theta_2) \tag{23}$$

$$\cos\theta_3=1-\frac{K_1}{K_3}\frac{\delta_0}{e_0}\cos(\theta_1+\theta_2)-\frac{K_1}{K_3}(1-\cos\theta_2) \tag{24}$$

Giving $\theta_1+\theta_2$, $\cos\theta_2$ and $\cos\theta_3$ are obtained from Eqs(23) and (24). And ξ_0 is obtained from Eq.(22). Then, y_0/e_0 is obtained from Eq. (16) and Γ/e_0 is obtained form Eq.(15). The amplitude of steady-state vibration at the beam end z_{1max}/e_0 is obtained from Eq.(13).

NUMERICAL EXAMPLES

Figure 4 shows resonance curve for the system with the amplitude Γ/e_0 of the beam end ($x=l$) versus the frequency ratio Ω_1 in which exciting ratio y_0/e_0 is taken to be 1.0 and nonlinear parameters $K_1/k=4$, $K_2/k=2$, $K_3/k=10$(n is 1 to 19 for x_n, y_n). Resonance curve is shown as a discontinuous line. Figure 5 shows resonance curve for the system with triangular hysteresis loop characteristics, $K_2/k=3$, $K_3/k=10$(n is 1 only for x_n, y_n), and then, in this case, resonance curve is shown as a continuous line.

CONCLUSIONS

An analytical method for the steady-state response of the beam simply supported at one end, colliding with the stop half period of its vibration at the other end has been proposed. Some numerical examples are shown.

REFERENCES

1. Aoki,S. and Watanabe,T., Forced vibration of a beam with a nonlinear support, Proceedings of the 6th International Conference on Recent Advances in Structural Dynamics, 1997, 2, 847-861

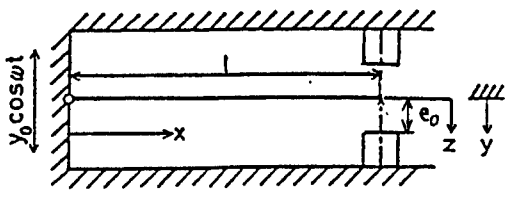

Fig.1 Analytical model

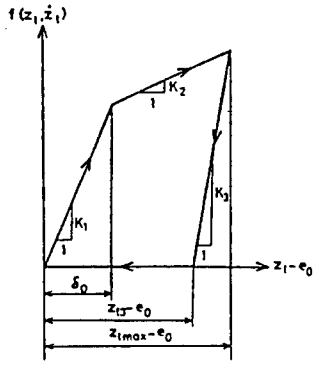

Fig.2 Hysteresis loop characteristics

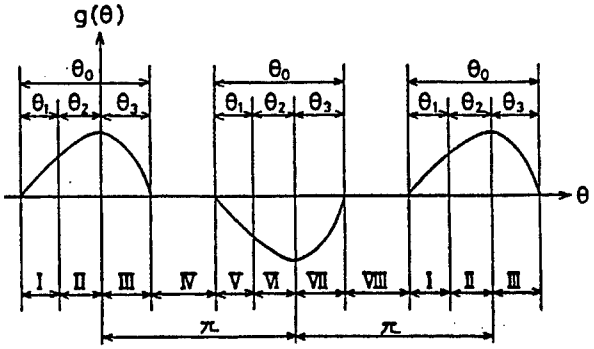

Fig.3 Waveform of force of restitution g(θ)

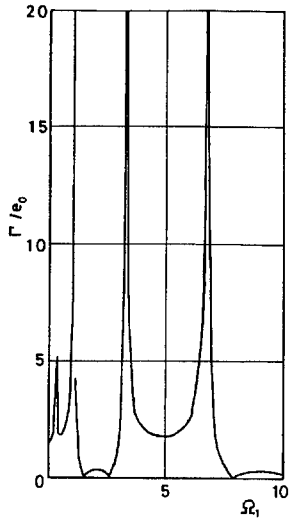

Fig.4 Resonance curve
($K_1/k=4$, $K_2/k=2$, $K_3/k=10$, $y_0/e_0=1.0$)

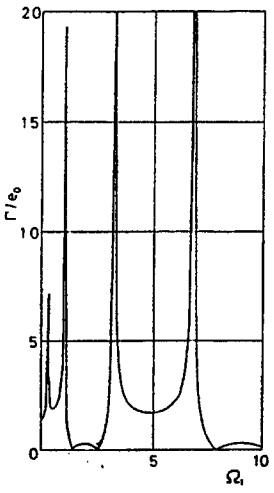

Fig.5 Resonance curve
($K_2/k=3$, $K_3/k=10$, $y_0/e_0=1.0$)

Nonlinear Vibration Control Based on An Artificial Neural Network Without Learning

Tatsu Aoki* and Shigeru Aoki**

* Department of Electrical Engineering, tatsu@tokyo-tmct.ac.jp
** Department of Mechanical Engineering, aoki@tokyo-tmct.ac.jp
Tokyo Metropolitan College of Technology
1 - 10 - 40 Higashi-Ohi, Shinagawa-ku, Tokyo 140-0011, Japan

Abstract

An Artificial Neural Network Method (ANNM) used for nonlinear vibration control systems is described. ANNM is a very efficient method in case that an analytical model of a plant is difficult to develop for their nonlinearity and measurement noise. A back propagation rule is usually adopted for their learning rule. Because iterations for learning become thousands or more, it is difficult to tune time-varying nonlinear systems in real-time.

Thus, in this paper ANNM where there is no need of learning is proposed for real-time tuning. The key methodology is that the weights of the hidden and output neuron are set to be the input and output pattern, respectively. Thus, the iterations for learning are not necessary. Applying this approach to the estimation of damping ratio of second-order systems, its availability was verified.

1. Introduction

In order to achieve an active vibration control based on a computer, we need to know a dynamic behavior of a controlled system, especially a damping ratio. However, it is difficult to measure a damping ratio from experimental data due to friction and measurement noise, which are generally time-varying parameters.

It is assumed that the multi layered feedforward neural network structure is employed. It is composed of three layers, namely input layer, hidden layer and output layer. Inputs, outputs, and teaching patterns for ANN are defined by on-off binary patterns. It is well known that ANN has the ability of associating an original pattern from an input pattern, which is disturbed by the noise and the nonlinearity.

In this paper, using this feature of ANN, the methodologies, which estimates a damping ratio of the second-order systems from the experimental data with the noise and the friction is proposed.

2. Proposal of new learning rule

ANN is composed of three layers, namely input layer, hidden layer and output layer, as shown in Figure 1.

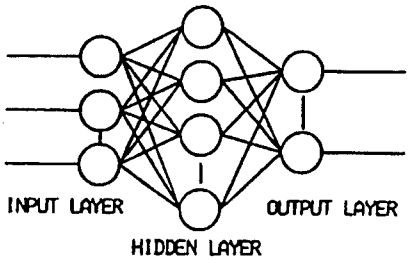

Figure 1 The structure of ANN

Input and output patterns of ANN are supposed to take only binary value, namely ± 1. Note that the usual binary numbers take the value of unity or zero. These patterns for ANN are developed by putting together binary numbers in time series. A back propagation rule(B.P.) is usually adopted for their learning rule. On the multilayer neural network, the effectiveness of B.P. has been confirmed[1]. Because the number of iterations becomes ten thousands or more, it is difficult to tune time-varying nonlinear systems in real-time. Also, there is a problem that the learning does not converge by the local minimum. In addition, information is dispersed and is expressed at the multiple neurones in B.P.. Therefore, the dispersion expression has advantages such as interpolation ability between information, robustness as the neuron is lacking. However, iterations for learning are necessary when we eliminate the part of memorized learning information and the learning data increases or decreases. On the other hand, by representing information in each hidden neurone, information can be localized. If the interpolation ability is provided in such method, it seems to be possible to improve the problem of B.P.. However, the expression efficiency is worse than that of B. P.. The weighing factors of each hidden neuron are set to be each learning pattern, as shown in Equation 1. When the input pattern is identical with the memorized pattern, the value of l takes the maximum value. As the difference between the input and output pattern increases, the value of l decreases from the maximum value. That is to say, the value of l shows the resemblance between patterns. According above, the detection neurone, which reacts only for the specific input pattern, is formed, as shown in Figure 2. By this detection neurone, the discrimination of EX-OR becomes possible.

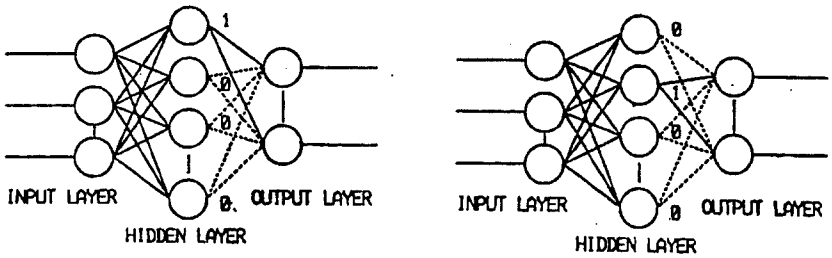

(a) (b)

Figure 2 Recognition of input pattern

The calculations of each neurone are shown in the following. The number of the input pattern elements is defined as n.

[1] Hidden neuron

$W_i^{hj} = X_i^j \cdot 2^i$ W_i^{hj}; Weight Learning rule

$$l = \frac{\sum_i W_i^{hj} \cdot X_i^j}{2^n}$$ X_i^j; Input (1)

$u_j^h = l - h$ h; Offset 0.9

$y_j = f_h(u_j^h)$ $f_h()$; Step function y_j; Output

[2] Output neuron

$W_k^{oj} = d_k^j$ W_k^{oj}; Weight

$u_k^o = \sum_j W_k^{oj} \cdot y_j$ d_k^j; Learning pattern (2)

$z_k = f_o(u_k^o)$ $f_o()$; Step function z_k; Output

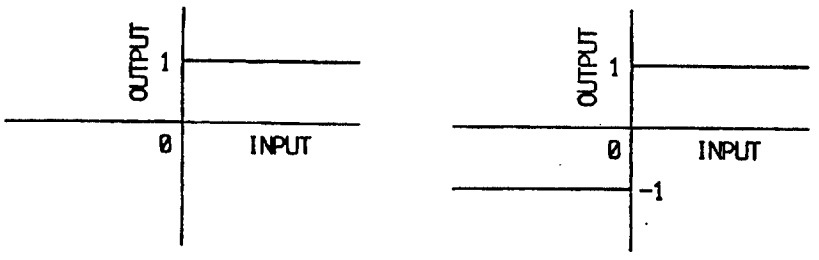

(a) $f_h()$; (b) $f_o()$;

Figure 3 Step function

In order to compare the proposed learning rule with B. P., a transformation of 7×7 alphabet patterns is considered. ANN is learned so that the next character is output, when a character is input, namely the pattern 'B' is output, when the pattern 'A' is input. In the local representation of the learning information, the number of hidden neurones is the same as that of the learning patterns. Since the number of learning patterns is 26 in this case, 26 hidden neurons are required. Thus, the necessary learning iterations are 26 times at the proposed method(F.V.Q.). On the other hand, the number of iterations becomes about 3000 times at B.P.. Next, compare the interpolation ability of the pattern. The patterns 'N' and 'O' are interpolated at Figure 4. Also, the proposed learning rule could powerfully distinguish the pattern, when the pattern had been disturbed by the noise, as it is shown in Figure 5. Thus, the availability of the proposed method was verified.

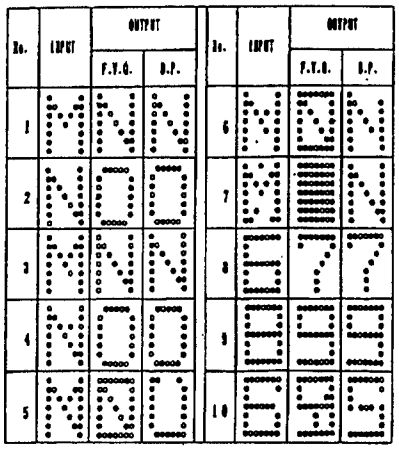

$f_h(x) = x \quad x \geq 0, \quad 0 \quad x < 0$

Figure 4 Interpolation ability

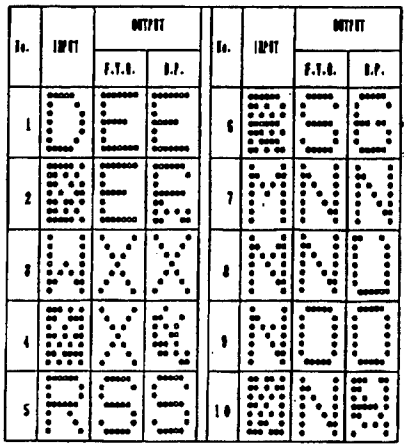

$f_h(x) = x^8 \quad x \geq 0, \quad 0 \quad x < 0$

Figure 5 Discrimination ability

3. Estimation of a damping ratio

The procedure is shown in the following. Second-order systems are considered as an illustration.

$$H(s) = \frac{\omega_n^2}{s^2 + 2\zeta\omega_n s + \omega_n^2} \tag{3}$$

Step 1

In making the damping ratio to be a parameter, the step response is measured. The amplitude normalizes as the relative amplitude for the step input. Time is normalized as a product of time and angular frequency.

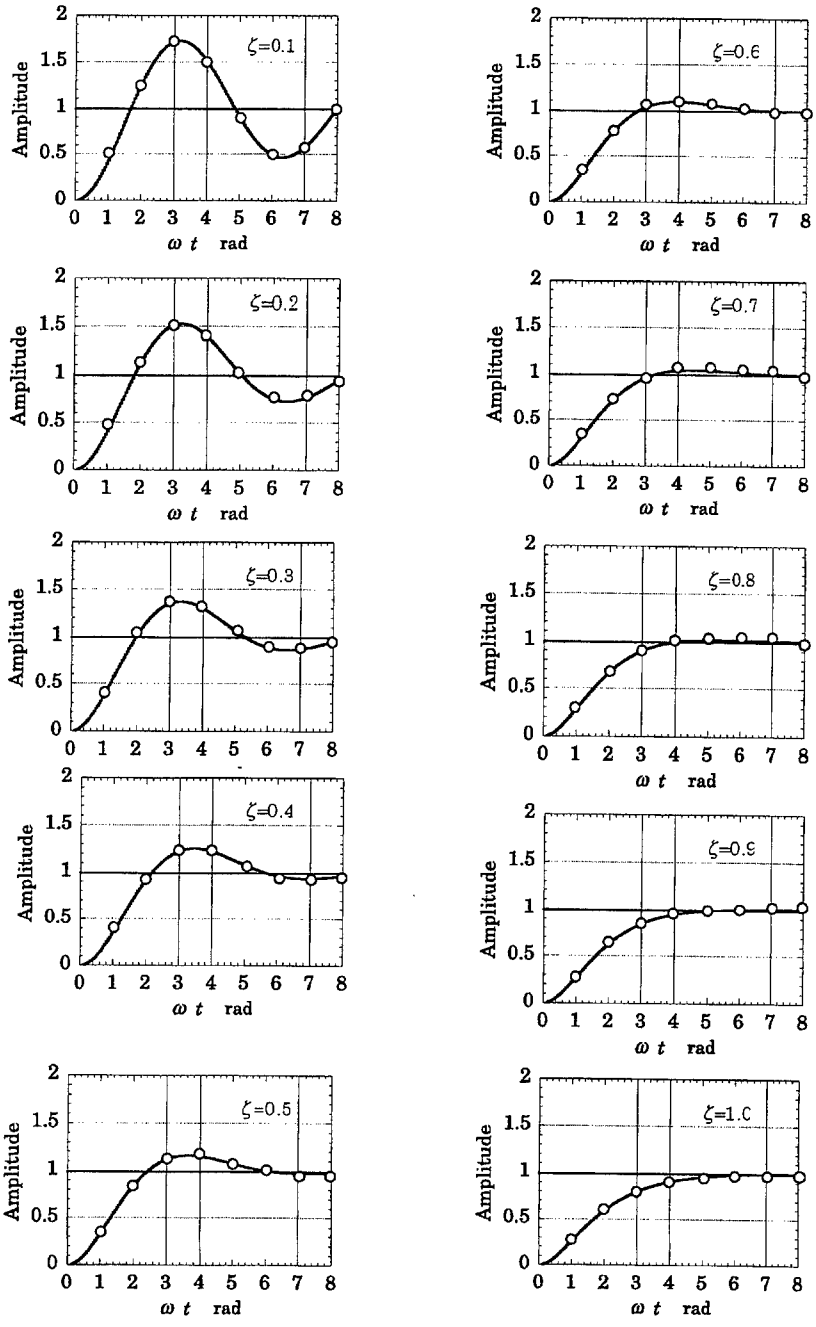

Figure 6 Step response

Step 3

The threshold of the amplitude set to be unity and the amplitude is discretized every one radian so that the number of the pattern elements is eight.

Table 1 The generation of the pattern

ζ	2^7	2^6		**Pattern**			2^1	2^0
0.1	-1	1	1	1	-1	-1	-1	1
0.2	-1	1	1	1	1	-1	-1	-1
0.3	-1	1	1	1	1	-1	-1	-1
0.4	-1	-1	1	1	1	-1	-1	-1
0.5	-1	-1	1	1	1	1	-1	-1
0.6	-1	-1	1	1	1	1	-1	-1
0.7	-1	-1	-1	1	1	1	-1	-1
0.8	-1	-1	-1	-1	1	1	1	-1
0.9	-1	-1	-1	-1	-1	-1	1	1
1	-1	-1	-1	-1	-1	-1	1	1

The number of learning patterns becomes eight from Table 1. Thus, eight hidden neurons are required. The block diagram of ANN is shown in Figure 7.

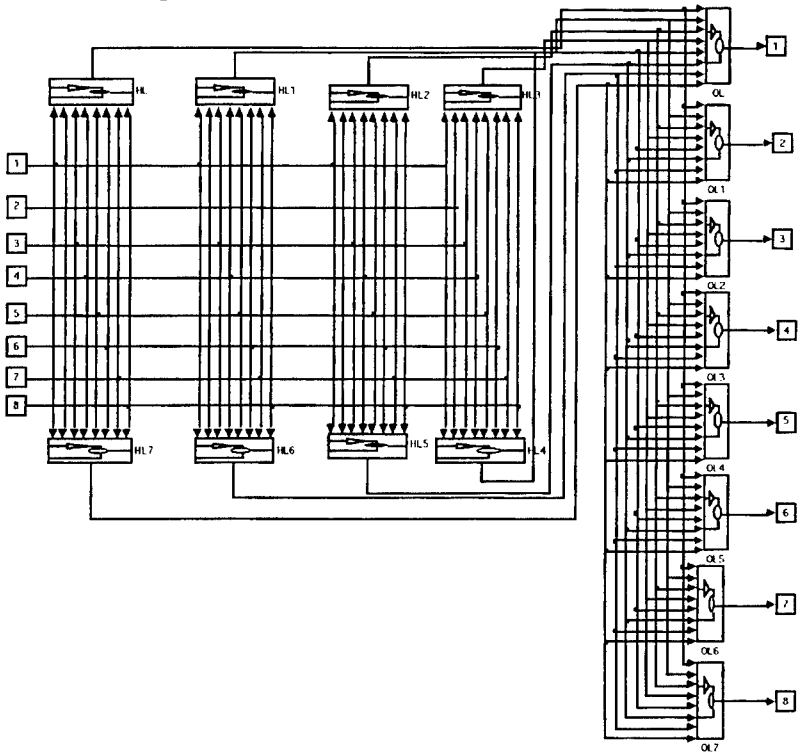

Figure 7 Schematic block diagram of ANN

4. Estimation results based on simulations

The actual and estimated value of the damping ratio is expressed in ζ and $\hat{\zeta}$, respectively.

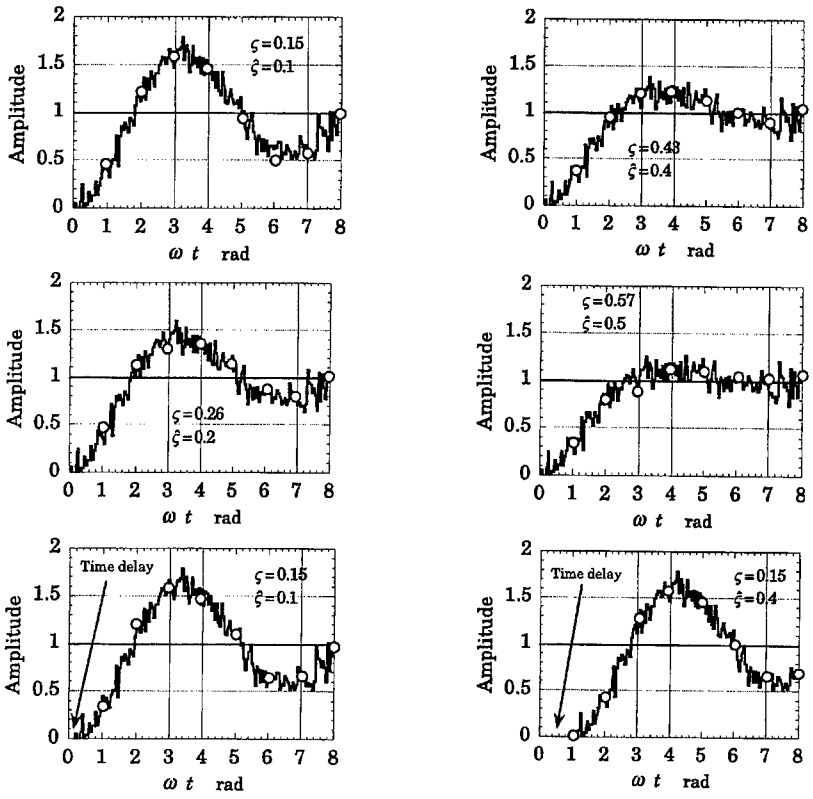

Figure 8 Simulation results

5. Conclusion and further consideration

It was verified that the damping ratio is accurately estimated by using ANN. In addition, a real-time active damping control is possible due to the proposed learning rule. When the time delay is introduced into the response by frictional force and backlash, the estimated error occurs. Therefor, the high resolution of the pattern will be necessary. Further work will include the following subject.

1) The determination of the optimum resolution of the pattern
2) The introduction of the estimation mode into the control loop
3) The determination of the vibration control law based on ANN

Reference

1. R. P. Lippmann, An introduction to Computing with Neural Nets, IEEE ASSP Magazine, 1988, 20, 4-22.

SELECTION OF OPTIMAL PARAMETERS FOR ACOUSTIC VIBRATION SUPPRESSORS

L. S. Kuravsky, S. N. Baranov

Russian Aviation Co, Research Group,

6 Leningradskoye Shosse, 125299 Moscow, Russia. E-mail: rusav@aha.ru

ABSTRACT

Presented is the technique to optimize characteristics of passive suppressors attached to the thin-walled structures subjected to some given excitation in acoustic frequency range. 1-df elastic oscillators as well as non-linear shock absorber are discussed. Structure behavior is represented via a set of ordinary differential equations resulted from natural mode decomposition. Panel response is determined by means of dynamic coding of numerical integration schemes in spreadsheets, with pressure fluctuations being represented as time-domain realizations of random processes with given spectra. Numerical optimization is used to get suppressor characteristics minimizing prescribed criteria expressed via parameters of interest in test points. Selected are the following suppressor parameters: partial frequencies, damping, positions, and clearances for moving (if any). Optimization technique for suppressing vibrations within a given frequency range, which is based on use of digital filters, is demonstrated. Examples of response estimations for wide-band acoustic load show that linear suppression systems have definite advantages with respect to examined non-linear ones.

INTRODUCTION

Suppression of vibration for thin-walled structures subjected to excitation in acoustic frequency range is a topical problem in designing modern aircraft. Results of its solution may be used for improvement of soundproofing characteristics, prolongation of structure service lifetime, etc. The dynamic suppression method is to attach additional devices to a structure, with special force influence on it being the case. The effect in question is realized by means of both redistribution of vibration energy from the structure to suppressors and increase in power dissipation [1]. This way differs from another approach, which uses insertion of additional kinematical connections (for example, fixing some structure points) and cannot be applied in series of situations because of design considerations.

Employment of reliable dynamic suppressors, which are simple in design, is an attractive and advantageous approach when high-level load is the case and other ways of solution fail because of aggressive environment (this situation occurs, for example, for air-intake panels).

Capabilities of suppressors are well studied for harmonic and narrow-band loads. The problem of their effectiveness in case of wide-band loads is not clarified sufficiently as uncertainty in proved selection of their characteristics is the case.

Under consideration in this paper is a technique for selection of optimal parameters of such attachments that may be applied for wide-band loads with given spectra. This technique is illustrated by an application to a panel suffered acoustic excitation. Effects of using one-degree-of-freedom elastic oscillators with fluid friction (Figure 1) as well as shock absorbers (Figure 2), analogous in design, are discussed. A series of computer experiments is presented to find out which parameters are important for dynamic suppression.

Since some hopes were connected with perspectives of application of non-linear devices, effects of non-linearities in suppressor characteristics were studied. Application of digital filters to ensure vibration suppression within the given frequency range was also under consideration.

MODELS AND METHOD

Dynamic behavior representation

Characteristic features of the presented technique are shown in Figure 3. Optimization process is based on dynamic representation of both a structure model and load. This representation constitutes some numerical integration scheme of differential equations, which describe the structure motion under study, and load time-domain realizations of interest, which are coded in a spreadsheet.

Dynamic behavior of a structure without any suppressors is represented by the following set of ordinary differential equations resulted from the Hamilton-Ostrogradsky principle after natural mode decomposition:

$$\ddot{\xi}_i + 2\varsigma_i\omega_i\dot{\xi}_i + \omega_i^2\xi_i = f_i(t), i = 1,\ldots, m$$

where $f_i(t) = \int_{\Sigma} Pu_i d\sigma$ - generalized force; $\xi_i(t)$ and $u_i(x)$ are corresponding normal coordinates and standardized natural mode shapes which are used to represent the displacement field for the surface Σ under study:

$$u(\bar{x},t) = \sum_{i=1}^{m} \xi_i(t)u_i(\bar{x});$$

$\bar{x}$ - coordinate vector of an arbitrary surface point; t is time; m - number of natural mode shapes taken into account in analysis; ζ_i - i-th dimensionless damping coefficient; ω_i - i-th natural frequency; $P(\bar{x},t)$ - load field.

Influence of dynamic suppressors is taken into account in the form of special terms added to the aforementioned differential equations and new differential equations supplementing the initial set. For example, a one-degree-of-freedom (1-df) elastic suppressor with fluid friction yields the following additional terms in the left parts of each of m equations forming the initial set:

$$\left[b_s\left[\dot{u}(\bar{x}_s,t) - \dot{y}_s(t)\right] + c_s\left[u(\bar{x}_s,t) - y_s(t)\right]\right]u_i(\bar{x}_s) -$$

and the complementary equation stated below:

$$m_s \ddot{y}_s(t) + b_s[\dot{y}_s(t) - \dot{u}(\bar{x}_s, t)] + c_s[y_s(t) - u(\bar{x}_s, t)] = 0,$$

where i - number of the equation, s - suppressor index, $y_s(t)$- suppressor displacement, $u(\bar{x}_s, t)$- displacement of the structure point adjoining to the suppressor, $\bar{x}_s$- coordinate vector of suppressor position, m_s- mass of the movable element, b_s- suppressor damping parameter, c_s- stiffness of elastic joint. The quantity $\omega_s = \sqrt{c_s / m_s}$ is called suppressor partial frequency.

During an optimization process, parameters of the attached suppressors (such as ω_s or b_s) are considered as optimized (free) variables.

Acoustic load

Representation of acoustic load realizations is based on the Corcos hypotheses that describe spatial-and-time correlation. The load is assumed to be a convective field of random forces defined by the following cross-spectral density of pressure fluctuations:

$$S_{P(M1),P(M2)}(f) = S_P(f) \times \exp\left[-\frac{|x_1 - x_2|}{r_x} - \frac{|y_1 - y_2|}{r_y} - \frac{j2\pi f(x_1 - x_2)}{U_k} \right],$$

where $S_P(f)$ is power spectral density of a homogeneous field; r_x, $r_y > 0$ are parameters of correlation scale; U_k is turbulence convection velocity (it is supposed that this velocity is directed along the x-axis); $Mi=(x_i,y_i)$, $i=1,2$ is a pair of arbitrary surface points; $j = \sqrt{-1}$.

This empirical formula was derived as generalization of results of experimental research. Power spectral density of the generalized force

$$S_{fi}(f) = \int\int_{\Sigma\Sigma} S_{P(M1),P(M2)}(f) u_i(x_1) u_i(x_2) d\sigma_1 d\sigma_2$$

may be expressed as $S_P(f)\varphi_i(u_i, r_x, r_y, U_k, f)$, where the quantities $\varphi_i(u_i, r_x, r_y, U_k, f)$ are calculated with the aid of the given natural mode shapes u_i and values of the other arguments (in the case of small damping, frequency f is assumed to be equal to $\omega_i/2\pi$).

The model in use is correct in the sense of convergence of a solution defined by the aforementioned set of ordinary differential equations, viz.: uniform convergence of the displacement power spectral density was proved when $m \to \infty$.

In solving the practical problems, parameters of loading pressure correlation, as a rule, are not defined. Only suppositions about the range of their values may be drawn in some particular situations. But even in these cases, the degree of their stability to the experiment conditions is unknown (in a real flight, for example, these conditions may be altered many times).

Therefore, simulation of two standard types of loading (so called homogeneous and aggressive fields) is implemented [2,3].

For a homogeneous field, it is assumed that pressure fluctuations influence all the structure points synchronously, i.e.:

$$S_{P(M1),P(M2)}(f) \equiv S_P(f).$$

An aggressive field for the given structure and given spectral density $S_P(f)$ (it is supposed to be the same for all structure points) is the loading with the parameters r_x, r_y and U_k which correspond to the greatest level of structure displacements. When correlation parameters are unknown, the response to an aggressive field is of topical practical interest since it is the most dangerous variant of behavior. The upper bound of this response may be obtained with the aid of the greatest absolute values of φ_i instead of these functions in expressions for power spectral densities of generalized forces. These absolute values, in its turn, may be replaced by the right parts of the following inequalities:

$$\left|\varphi_i\left(u_i, r_x, r_y, U_k, f\right)\right| \le \left[\int_\Sigma |u_i(x)| d\sigma\right]^2.$$

Time-domain realizations of load with power spectral density $S_P(f)$ are represented in the form of auto-regression processes. Auto-regression parameters are selected to get the acceptable form of a spectral density plot. This form is usually determined with available experimental data. If they are not complete or reliable, it is better to carry out the simulation for some extreme cases that are qualitatively differed: for example, a wide-band spectrum and some narrow-band ones, maximums of which are located in different parts of the frequency range under consideration. Comparison of the results obtained makes it possible to estimate how the structure dynamics depends on a spectrum form and to select the worst variant of its behavior.

Verification results for the aforementioned models of structure behavior and acoustic load were discussed in paper [4].

Computing natural modes

Description of the approach that was in use for computing natural modes of vibration ($u_i(x)$) was considered in paper [5]. This approach is called the method of correction by elastic connection insertion (the CECI method). It is suitable for stiffened, sandwich, and symmetrical composite panels including flat or curved ones. This method requires a variational formulation of a problem in terms of the Galerkin weak form or the Rayleigh-Ritz principle. The influence of stiffeners, anisotropy, or filling is described by special elastic and inertial operators which are added to the appropriate operators of some non-reinforced or hypothetical isotropic initial structure in the free vibration problem formulation.

The space of basis functions for the approximate solution is a set of initial structure natural mode shapes. As a rule, these shapes are determined

beforehand by any suitable numerical or analytical method. The original formulation is transformed to an algebraic eigenvalue problem, with a dimension being determined by the number of basis functions. As this dimension is much less than one in case of solution by the traditional finite element method, the presented approach is more economical with regard to the computation time and memory size in use.

Optimization procedure

The employed optimization procedure consists of two stages. On the preparatory stage, some optimization criterion that depends on the applied problem to be solved is formulated. This criterion is expressed in terms of accelerations, displacements, velocities or stresses in test points of interest. After that, some numerical integration scheme for the aforementioned differential equations (with a given acoustic load realization in their right parts) is coded to calculate structure response in the test points using a spreadsheet. Normal coordinates, which are exploited in the equations, are computed with some specified time step h from initial zero time point to the given specified upper time bound. Runge-Kutta methods [6] (or their equivalents) proved to be sufficient to get acceptable accuracy of solution. In particular, the modified Euler integration scheme of the second order may be used.

It is of vital importance that the spreadsheet supports dynamic links between cell contents. If one locates values of free variables and the time step h in the separate cells to which the cells containing formulas of the integration scheme in use are referred, all the solution will be automatically modified when these values are changed.

On the final stage, a multivariate optimization procedure to get suppressor characteristics yielding the best value of the prescribed criterion is run. The procedure of numerical non-linear optimization called the Generalized Reduced Gradient is used. Selected are the following characteristics: partial frequencies, damping, positions, and geometric parameters (if any). Suppressor masses are supposed to be fixed because of two reasons:

1) a designer usually has the choice among a discrete set of standard mass values;
2) optimization of free mass parameters tends to yield their extremely great values.

EXAMPLE OF APPLICATION

Structure and load parameters

The structure under study is simply supported steel sandwich rectangular panel with flute filling. Panel dimensions are 826×268×11.5 mm. Panel mass is 4.050 kg. Dimensionless damping was supposed to be 0.005 for all frequencies. Information on 5 structure natural modes is presented in Table 1.

Table 1. First natural frequencies and mode types of the structure under study.

Natural mode No.	**1**	**2**	**3**	**4**	**5**
Natural mode type	1:1	1:2	1:3	1:4	1:5
Natural frequency, Hz	609	765	1017	1378	1848

Test acoustic loads were represented by wide-band random processes of the same level (139.4 dB). Their power spectral densities are shown in Figure 4.

Problem formulations

Mean value for root-mean-square accelerations of 4 test points given in Figure 5 was considered as an optimization criterion. Characteristics of 2 and 3 vibration suppressors attached to the structure were optimized. It was supposed that masses of all suppressors were equal to 0.1 kg. Problem formulations that were under study are presented in Table 2. Both elastic and shock suppressors had fluid friction.

A shock suppressor (variant D-2) was a solid moving in a closed container filled with some viscous liquid. Shock response was simulated with the aid of a cubic polynomial response function with high rate of increase. Weak non-linearity (variant C-1) was also simulated by a free cubic term added to the linear response function.

Table 2. Variants of problem formulations.

Variant name	**Problem formulation**
A-1	2 identical elastic vibration suppressors with given positions; optimized are partial frequencies and damping of suppressors
A-2	2 identical elastic vibration suppressors; optimized are positions, partial frequencies and damping of suppressors
A-3, E-3	2 different elastic vibration suppressors; optimized are positions, partial frequencies and damping of suppressors; variants A-3 and E-3 differ in loads
A-4	3 different elastic vibration suppressors; optimized are positions, partial frequencies and damping of suppressors
B-3	Coincides with variant A-3 in which optimization is carried out for the frequency range from 0 to 1000 Hz only
B-3-H	Coincides with variant A-3 in which optimization is carried out for the frequency range above 1000 Hz only
C-1	Coincides with variant A-1 in which weak cubic non-linearity of the suppressor rigidity characteristic is assumed
D-2	2 identical shock vibration suppressors; optimized are positions, geometric parameter and damping of suppressors

Optimization results and their discussion

Summary of optimization output is presented in Tables 3 and 4 and Figure 5. Values of optimization criterion are expressed via a dimensionless acceleration

unit (g). The structure without suppressors is mentioned in the tables as an initial variant.

Table 3. Optimal criterion values and suppressor parameters.

Vari-ant	Crite-rion value, g	% of the initial variant	Partial frequencies, Hz			Damping parameter, kg/s		
Initial	82.27	100%	-	-		-	-	
A-1	17.50	21%	1099.6			363.2		
A-2	15.39	19%	958.6			359.3		
A-3	11.78	14%	836.7	1686.2		126.2	321.7	
A-4	9.94	12%	836.7	1686.2	837	126.2	321.7	586
B-3	3.90	-	615.7	805.7		536.8	88.6	
B-3-H	1.05	-	1220	1710		33.3	377.1	
C-1	17.47	21%	1099.6			363.1		
D-2	21.72	26%	-	-		780.8	780.8	
E-3	5.65	-	841.3	1640.1		130.1	349.3	

Table 4. Optimal positions of suppressors.

Variant	X_1, mm	Y_1, mm	X_2, mm	Y_2, mm	X_3, mm	Y_3, mm
Initial	-	-	-	-	-	-
A-1	120	200	120	400	-	-
A-2	134	242	134	423	-	-
A-3	134	228	142	408	-	-
A-4	134	232	158	416	133	541
B-3	134	409	134	132	-	-
B-3-H	134	249	134	317	-	-
C-1	120	200	120	400	-	-
D-2	134	245	134	406	-	-
E-3	134	227	134	409	-	-

One can see that application of 1-df elastic suppressors with proper partial frequencies and fluid friction parameters may result in considerable reduction of structure vibration level even if a wide-band load is the case. Reduced vibration levels in our example come up to 12-14% of the initial one. To illustrate this effect, Figure 6 presents power spectral densities of dimensionless accelerations in a test point for the initial and some modified (variant A-3) structure. Optimal partial frequencies of suppressors are close to certain natural frequencies of the initial structure. They are not equal exactly to each other as attachment of suppressors changes the initial system. Optimal positions of suppressors tend to be near antinodes of the most excited panel natural mode shapes. Sometimes these positions are interjacent for antinodes of different modes.

Table 3 and Figure 7 demonstrate how the increase in the number of free optimized parameters results in amplification of optimization effect. This outcome is evident, but it only concerns the parameters, which are significant for structure vibrations.

Comparison of problem formulations A-3 and E-3 shows that spectral forms of wide-band loads do not influence essentially the optimal partial frequencies, damping and positions of elastic suppressors. Thus, these parameters are determined mainly by the panel characteristics. Figure 8 gives corresponding response spectra.

Calculations revealed that addition of suppressors did not obligatory give rise to considerable decrease of panel vibrations. Table 3 and Figure 9 illustrate this fact. The observed effect may be explained by the situation in which optimal suppressor positions belong to different antinodes of the same natural mode shape.

Certain efforts were made to figure out whether suppressors with non-linear responses were able to reach greater effect than linear ones. Two types of the above-mentioned non-linearities were under study: a weak cubic term in the rigidity characteristic (variant C-1) and shock response (variant D-2).

Computer experiments for the given structure revealed vainness of such attempts. Variant C-1 yielded, in fact, the same output as variant A-1 (its linear analogue). The obtained cubic function was approximately equal to the former linear relation within the range of observed displacements.

Variant D-2 was obviously worse than analogous variant A-2 (see Table 3 and Figure 10). As to this case, it is necessary to note:

1) The optimization criterion is not sensitive with regard to shock characteristics (i. e. to the form of the response function after a contact);
2) The optimization criterion is not sensitive with regard to solid track length;
3) The optimization criterion is sensitive with regard to damping.

Thus, it may be concluded that suppression effect in variant D-2 is achieved due to energy dissipation only. (In case of variant A-2 the effect of antiresonance is also very significant.)

In some applications it is important to suppress vibrations in a given frequency range. The technique presented may be adopted to this request with the aid of digital filtration.

Digital filters are used to cut out a signal component in the frequency range of interest. Optimization criterion is formulated in respect to this component. A dynamic filtration scheme is coded in the spreadsheet together with the scheme of numerical integration. Parameters of digital filters were estimated according to traditional techniques [7].

Variants B-3 and B-3-H (see Table 3 and Figure 11) are included in the review to illustrate this way of optimization. The lowpass Butterworth filter of the second order and the bandpass sine filter of the sixth order were used for these cases correspondingly. Bandpass filtering seems to be more difficult in implementation with regard to computation time and spreadsheet size.

CONCLUSIONS

It has been demonstrated that considered dynamic representation of structure behavior makes it possible to carry out effective selection of optimal characteristics of passive suppressors attached to thin-walled structures

subjected to wide-band acoustic excitation. This representation is based on natural mode decomposition, dynamic coding of numerical integration schemes in spreadsheets, and multivariate numerical optimization yielding the best value of some prescribed criterion.

Presented examples show that application of 1-df elastic suppressors with proper partial frequencies and fluid friction parameters may result in considerable reduction of vibration level for a panel under acoustic load. Optimal partial frequencies of suppressors are close to certain natural frequencies of the initial structure. Optimal positions of suppressors tend to be near antinodes of the most excited panel natural mode shapes.

Increase in the number of free optimized parameters usually results in amplification of optimization effect. It was shown that addition of suppressors did not obligatory give rise to considerable decrease of panel vibrations. It may be explained by the situation in which optimal suppressor positions belong to different antinodes of the same natural mode shape.

Computer experiments comparing the effects of linear and non-linear responses revealed that non-linearities did not yield the improvement in suppression characteristics.

Availability of digital filtration for vibration suppression within the given frequency range was demonstrated.

The technique in question may be useful for experts solving the problems of airframe acoustic strength, on-board equipment damages, cabin soundproofing, etc.

REFERENCES

1. Zaschita ot Vibratsii i Udarov (Shock and Vibration Protection). In *Vibratsii v Tekhnike (Vibration in Engineering)*. Vol. 6, ed. K. V. Frolov, Mashinostroenie, Moscow, 1981 (in Russian).
2. Kuravsky, L. S., Baranov, S. N. and Vratchev, A. V., The DYSSAN Package: Principles of Implementation and Experience of Employment. In *Proc. 4th International Congress on Sound and Vibration* (St. Petersburg, Russia), 1996, **2**, 1237 – 1242.
3. Baranov, S. N., On the Approach to Modeling Dynamic Behavior of Thin-Walled Aircraft Structures under Acoustic Excitation. In *Proc. Asia-Pacific Vibration Conference'99* (Singapore). Vol. 1, 1999, pp. 42-47.
4. Baranov, S. N., Kuravsky, L .S., Vratchev, A. V. and Zhukov, K. P., Verification of the Mathematical Model for Prediction of Acoustic Vibrations of Aircraft Structures. In *Proc. INTERNOISE-98* (Christchurch, New Zealand), 1998.
5. Kuravsky, L. S., The Method of Correction by Elastic Connection Insertion in the Free-Vibration Problem for Thin-Walled Aircraft Structures. In *The Problems of Aeronautical Engineering*, series *Aircraft and Equipment Flight Tests. Airplanes and Helicopters*, LII publication, Zhukovsky, 1993, No.239, pp. 56-72 (in Russian).
6. Bakhvalov, N. S., *Chislennye Metody (Numerical Methods)*, Nauka, Moscow, 1975, pp. 447-459 (in Russian).
7. Otnes, R. K., Enochson, L., *Applied Time Series Analysis. Basic Techniques*, A Wiley-Interscience Publication, New York, 1978.

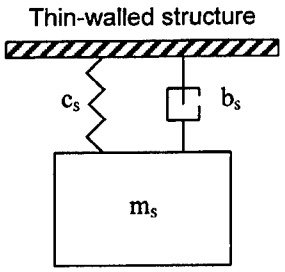

Figure 1. 1-df elastic suppressor with fluid friction.

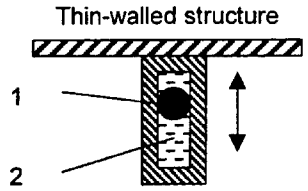

Figure 2. Shock absorber: 1 - moving body, 2 – liquid.

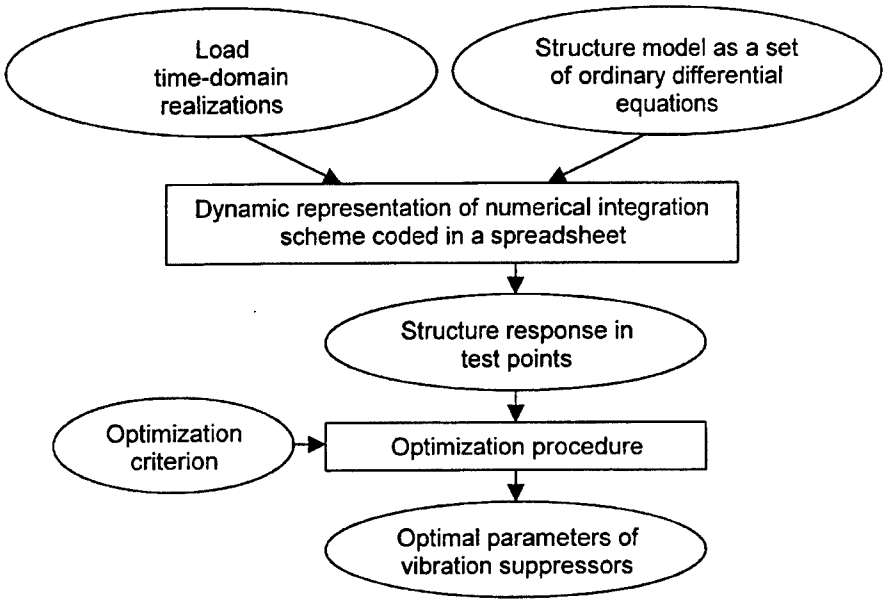

Figure 3. Diagram showing characteristic features of the optimization technique.

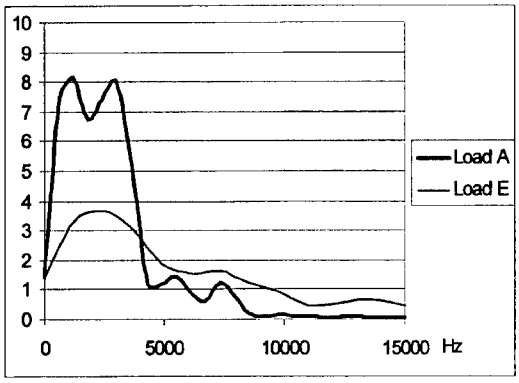

Figure 4. Power spectral densities of test loads (in Pa^2/Hz). Load E was used for variant E-3 only. Load A was used in all other cases.

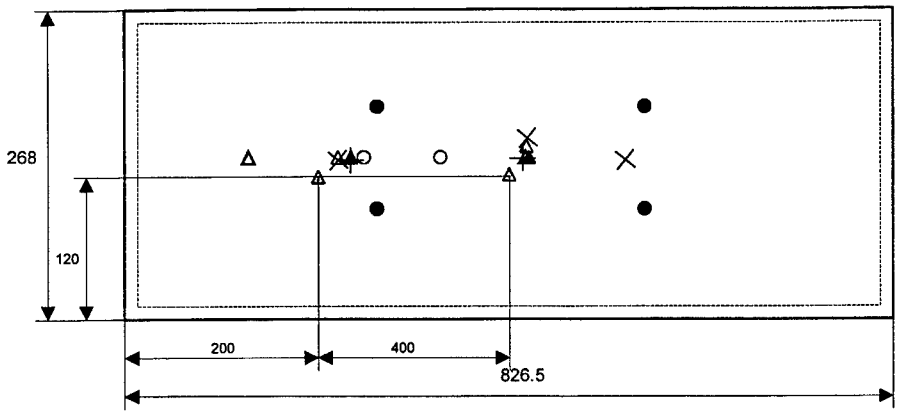

Figure 5. The panel under study and optimal positions of suppressors:

- △ - initial positions of suppressors (variants A-1, C-1),
- ▲ - optimal positions of suppressors (variant A-2),
- △ - optimal positions of suppressors (variant A-3, E-3),
- × - optimal positions of suppressors (variant A-4),
- △ - optimal positions of suppressors (variant B-3),
- ○ - optimal positions of suppressors (variant B-3-H),
- ┼ - optimal positions of suppressors (variant D-2),
- ● - test points (distances from the edges are equal to 1/3 and 2/3 of overall dimensions)

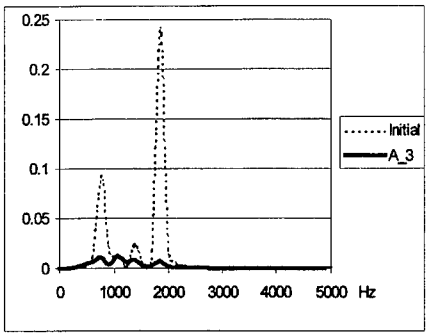

Figure 6. Power spectral densities of accelerations in a test point (in g^2/Hz): the initial structure vs variant A-3.

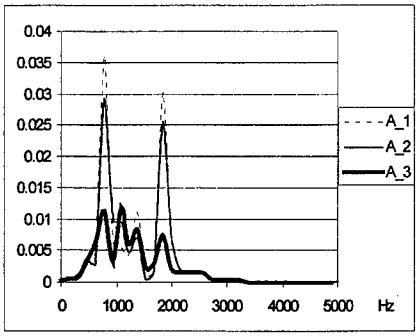

Figure 7. Power spectral densities of accelerations in a test point (in g^2/Hz): variants A-1and A-2 vs variant A-3.

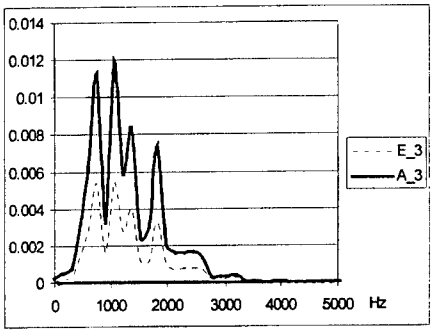

Figure 8. Power spectral densities of accelerations in a test point (in g^2/Hz): variant E-3 vs variant A-3.

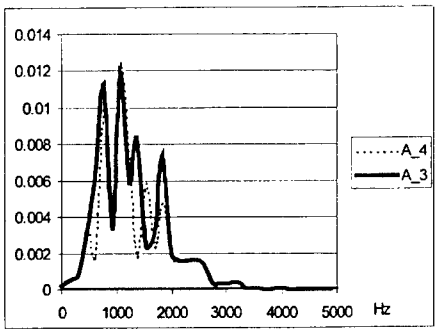

Figure 9. Power spectral densities of accelerations in a test point (in g^2/Hz): variant A-4 vs variant A-3.

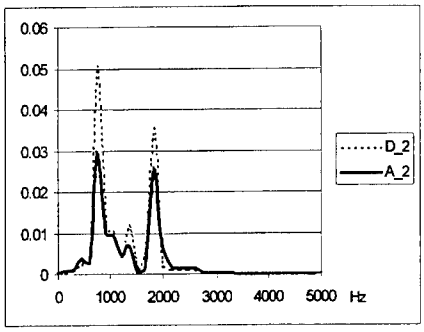

Figure 10. Power spectral densities of accelerations in a test point (in g^2/Hz): variant A-2 vs variant D-2.

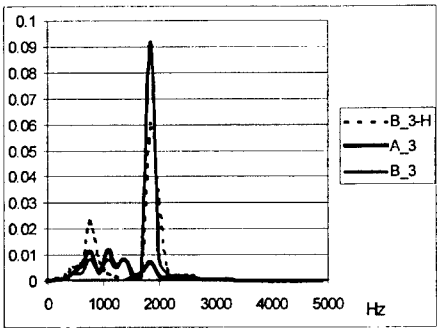

Figure 11. Power spectral densities of accelerations in a test point (in g^2/Hz): variants B-3 and B-3-H vs variant A-3.

PRACTISING ENGINEER'S APPROACH TO UNDERSTAND THE EFFECTS OF SHELL DYNAMICS ON NOISE RADIATION

Cuneyt Ozturk
Türk Elektrik Endüstrisi AS
Vibration and Acoustics Laboratory
Davutpasa, Litros yolu 1, Topkapı 34020
Istanbul, Turkey

Abstract

This study describes the endeavour of an engineer who is practising in industry, to investigate the effects of shell dynamics on noise radiation of a domestic refrigeration compressor. One of the objective of this study is to establish a guide for the practising engineer to approach the noise problem of the refrigeration compressor. The dynamic behaviour of the shell and its effects on the noise and vibration levels will be the subject of this paper.An experimental study that investigates the effect of varying shell geometry and the damping on its noise radiation is presented. It is shown that changing the geometry, which in effect changes the stiffness of the shell, has a major effect on the noise problem that we encounter. The damping that is introduced into one of the compressor shells by using polymer sandwiched between two steel plates, has no significant effect on the noise radiation while causing a noticeable drop in the vibration level of the shell. Experimental results will be presented that show the effects of curvature, the damping and possible reasons for these effects will be suggested. Preliminary considerations on design of the guide for practising engineers will be mentioned.

1 .Preliminary Investigation of the Shell Dynamics

A hermetic reciprocating compressor consists of a motor and pump unit and the hermetically surrounding shell, in which the motor-pump unit is suspended. Therefore, all the noise and vibration phenomena appear in and on the shell and unavoidably depend on the shell. The only way the vibration and acoustic energy escape from the motor pump unit is through the shell. This makes understanding the basics facts of the shell, extremely important for the noise control engineer to achieve the reduction of reciprocating compressor noise.

To understand these facts one should consider all the aspects of vibro-acoustic behaviour of the shell might begin with an understanding of the vibration and noise radiation spectra of the compressors and then of the

structure itself. The structural mechanics that might be modelled by discretizing the mass, spring and damping elements, may give a clue about the shell dynamics. Since most of the energy generally raises the specific frequencies of the shell modes, the investigation of the dynamic behaviour of the shell is essential in order to reach the goal. Noise control engineers are expected to direct their efforts towards the shell structure and the dynamics after observing discrete peaks that appear on the noise and vibration spectra of the reciprocating compressors. The effect of parametric changes in the model could provide noticeable variation on the noise and vibration levels. This study is part of continuing research and summarises the endeavours of a noise control engineer to understand the effects of shell structure and dynamics and the influence of parametric changes that shape the vibro acoustic behaviour of the shells. When the preliminary vibro acoustic measurements, on the three separate compressors are concluded, it is considered that the shell geometry and the dynamics might play a more important role then we first thought. Most of the energy that appears on the pumping harmonics might be released as a result of the variety of side effects, but provides significant excitation on the shell structure. The response of the shell on these excitations generally dependent on the shell material, shell structure and the inherent dynamic properties

Figure-1, shows the basic mechanism of the hermetic pumps and the shell geometry . The pump is suspended on the coil springs that stay in the oil sump. Figure-2, illustrates the spectra of the noise radiation and the mechanical vibrations when measured on the different compressors with different shell geometries and material, that separate them from each other.

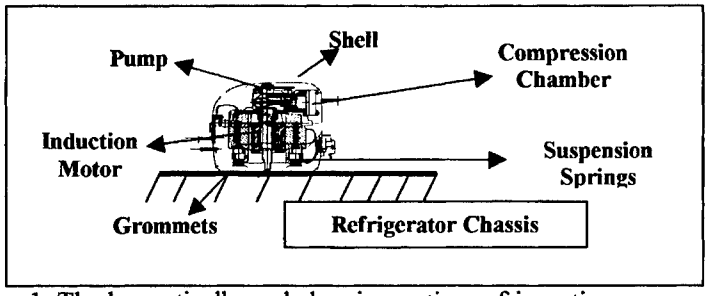

Figure-1, The hermetically sealed reciprocating refrigeration compressors.

When the noise generation mechanism and the energy sources are illustrated as shown on figure 3, the shell appears as the ultimate energy transformator that transmits the mechanical vibrations and cause noise radiation when the energy is converted. When the shell is considered as discrete model, shown in figure 4, it is considered that effect of the stiffened shell might be quite significant especially in the area that stays below the ring frequency, where the curvature help to avoid the excitations. When the fundamental differences are investigated between the noise and vibration spectra that appear as

illustrated on figure-2, it is seen that the basic differences generally appear below the ring frequencies that might provide direct excitations on the structure. differences are investigated between the noise and vibration spectra that appear as illustrated on figure-2, it is seen that the basic differences generally appear below the ring frequencies that might provide direct excitations on the structure.

2.Dynamics and the Effect of Stiffened geometry and material damping

Having established the preliminary features of the shell structure and its behaviour, further attempts are made to understand the effect of stiffened geometry and damped structure. The frequency responses of the different shell prototypes, produced with different geometries are obtained when impact testing is applied on the suspended shells. The results of the impact testing, noise and vibration measurements and number of tests that are designed to understand structural and cavity resonances, indicate that curvature of the shell might affect noise radiation more then the damping, which is provided, by using the polymer sandwiched composite steels. The compressor shell with less stiffened flat surfaces on the sides and a rounded cover shows significant radiation problem and higher emission levels when compared with stiffened surfaces of the curved geometry. When the similar geometry of curved shells are compared by using the different materials with different damping properties, it is shown that the influence of the damping on the emission levels could not be so significant, in contrast to the previous expectations. Figure-2 shows some results of our investigation with the different results obtained when shells with different geometry and damping are tested.

3.Some Clues for the Design Engineer

The engineer's approach to noise problem of reciprocating compressor . The understanding of basic facts of the problem should include the investigation on noise and vibration characteristics and modelling of vibro-acoustic behaviour. This modelling could be done either experimentally or by computing. The aspects of this approach is illustrated on figure-5. To date, we have seen that the shell might be stiffened with the curved surfaces. Properly rounded side surfaces might help in the efforts of achieving the required noise reduction. The effect of curvature can be investigated on prototypes and be modified properly by computing . But the application of damping should be carefully investigated before expecting significant changes in shell dynamics and radiation. In this continuing study, further investigation is considered on understanding the influence on the visco elastic damping, and why and how it could be effective on the shell radiation.

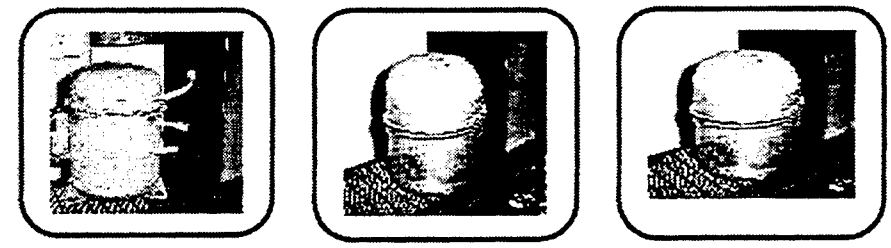

2-1a-Old Steel Shell | 2-1b-Composite Steel Shell | 2-1c-New Steel Shell

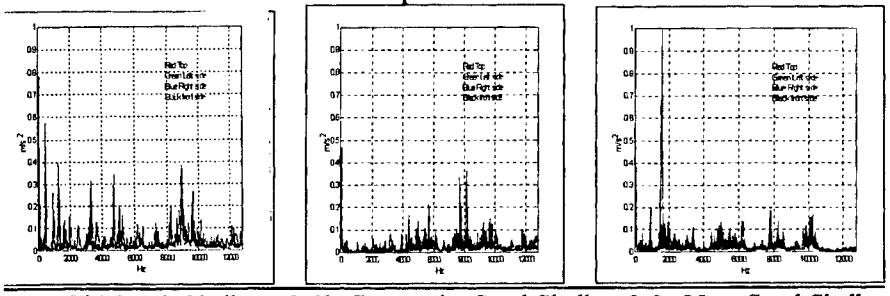

2-2a-Old Steel Shell vibration spectrum | 2-2b-Composite Steel Shell vibration spectrum | 2-2c-New Steel Shell vibration spectrum

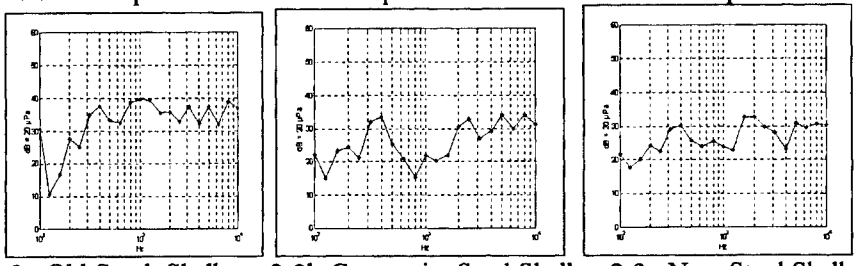

2-3a-Old Steel Shell noise spectrum | 2-3b-Composite Steel Shell noise spectrum | 2-3c-New Steel Shell noise spectrum

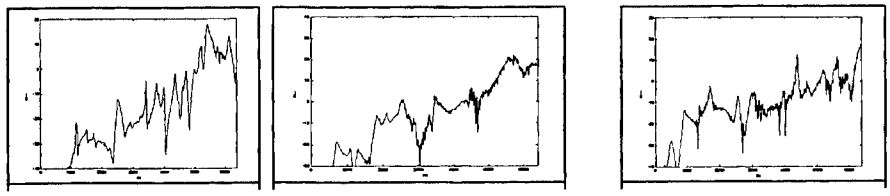

2-4a-Old Steel Shell Transfer function at point 2 | 2-4b-Composite Steel Shell Transfer function at point 2 | 2-4c-New Steel Shell Transfer function at point 2

Figure-2, The effect of shell curvature and damping on the noise and vibration levels of the compressors

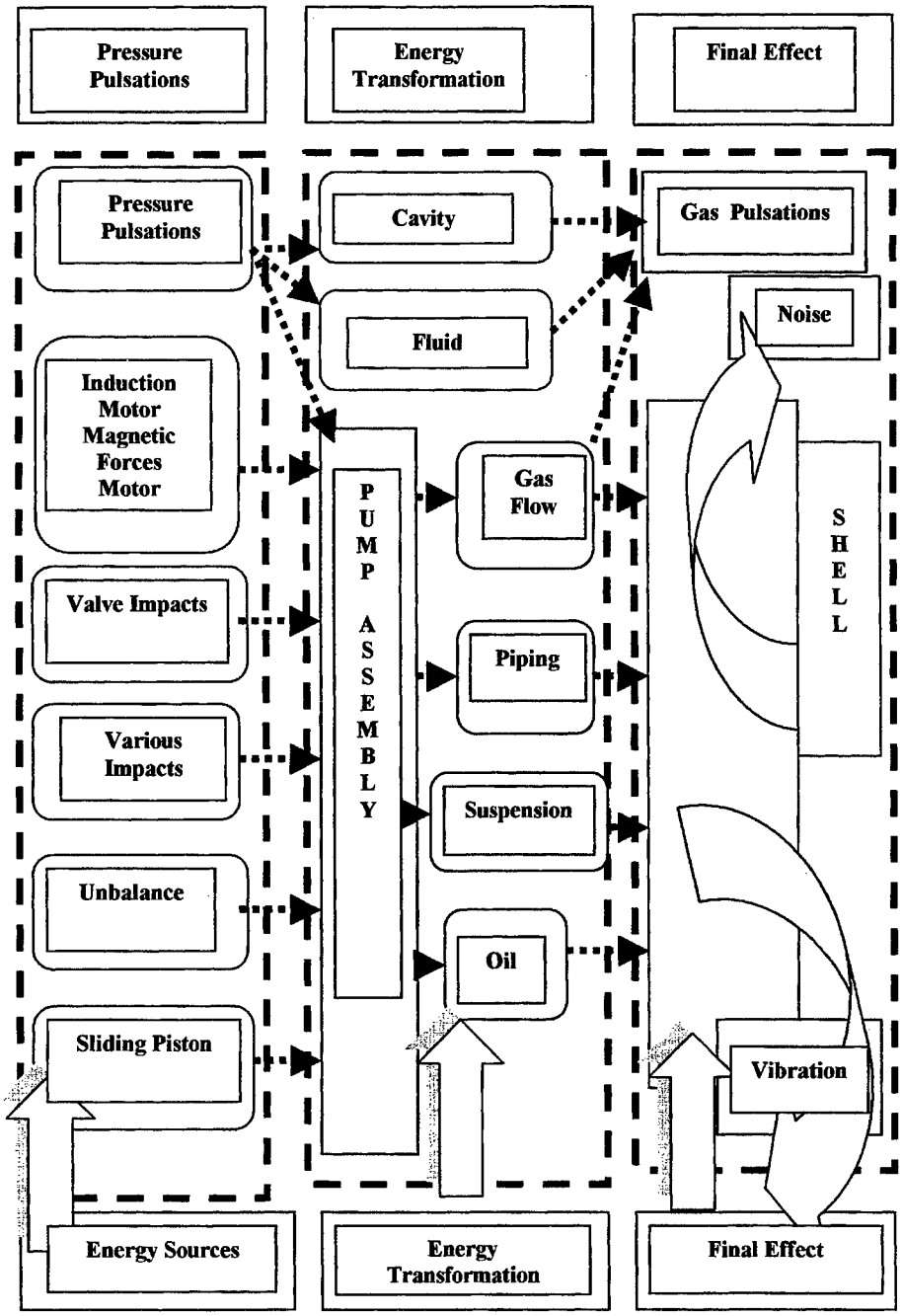

Figure-3, The noise generation mechanism, enery soruces and the transformation of the energy

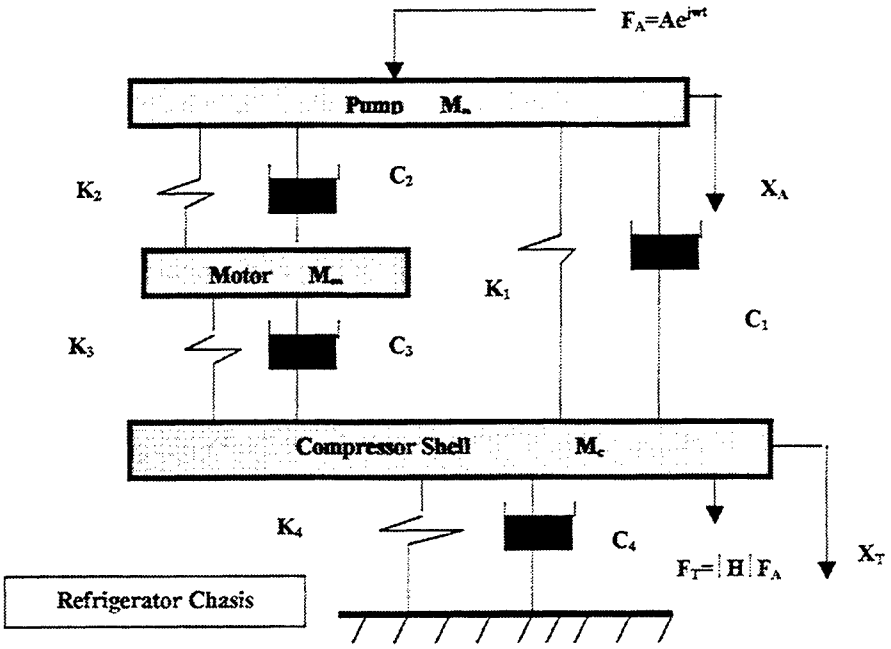

Figure-4, Lumped parameter model of the hermetically sealed reciprocating refrigeration compressors.

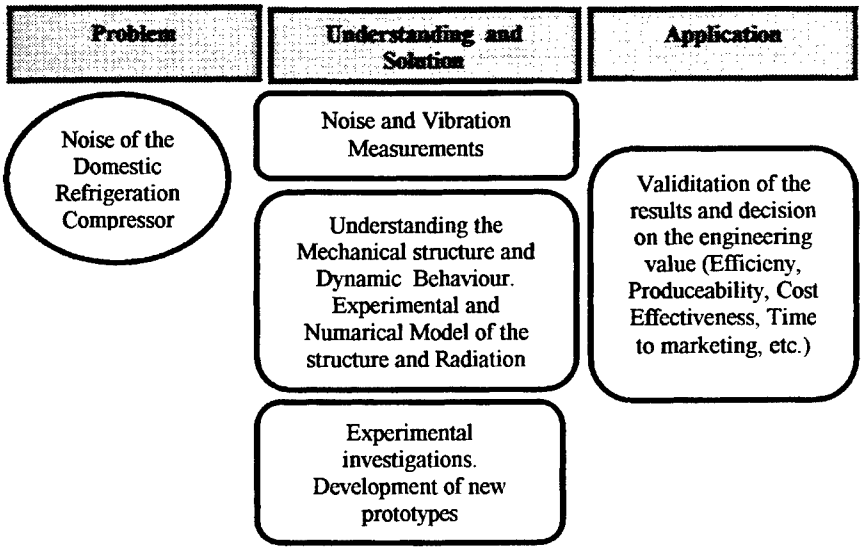

Figure-5 Practising engineer's approach to the noise problem of domestic refrigeration compressor noise problem. The approach should cover the model of vibro acoustic behaviour

Vibration Based Diagnostics of Combustion Process in Diesel Engines

Grover Zurita V.
Luleå University of Technology, Sweden
E-mail: Grover.Zurita@arb.luth.se

ABSTRACT

The main objective of this paper is to obtain combustion parameters, which can be use for engine diagnostics proposes. The main combustion parameters are the maximum cylinder pressure (p_{max}) and the derivative of the pressure rise ($dp/d\alpha$).
The based idea is to perform the reconstruction of the cylinder pressure by using the engine Transfer Function (TF) and the measured vibration response signal of the engine surface. The analysis is based on a non-linear method called real cepstrum and signal processing techniques. The TFs were adapted to slightly different situations such as other cylinders of the same engine, in particular where use can be made of symmetry.
A matrix with engine TFs for varying speed and load was obtained, this can be used as a data bank of TFs for reconstruction of the cylinder pressure at different operating conditions. An extensive analysis of the cycle to cycle variations was carried out, for both the measured and reconstructed cylinder pressure.

INTRODUCTION

The condition or operational monitoring of the diesel engines requires that all the signals related to the events of interest can be defined. In this paper the reconstruction of the cylinder pressure is focused. The cylinder pressure contains a lot of information about the performance of the combustion itself. The established method that is used to monitor the pressure pulse is to drill and machine a hole in each engine cylinder and insert a high pressure transducer. This is a very expensive and complicated method and is therefore only suitable for laboratory engines. Thus, there is a large need for a cheap and reliable method to measure the pressure pulse from the outside of the engine body. The cylinder pressure measurements are usually performed with the pressure transducer mounted flush to the cylinder wall in order to avoid resonances. In this type of measurements the cylinder transducer works in a harsh environment, making its life limited. Apart from being expensive, there is also very limited space for mounting transducers in the cylinder heads. Thus, there is a need to use transducers, i.e. accelerometers, attached to the engine surface for reliable and inexpensive measurements of cylinder pressure for performance and condition monitoring.
The engine is a complex structure and reconstruction of the cylinder pressure for engine diagnostics and control purposes is not straightforward. A working method has to be able to handle the wave dispersion, reverberation, and noise in the structure. In order to use vibration data to recover the cylinder pressure, more elaborated procedures are needed. The signal processing analysis is based on a non-linear method called real cepstrum.

The main objective of this paper is to obtain combustion parameters, which can be use for engine diagnostics proposes. The main combustion parameters are the maximum cylinder pressure (p_{max}) and the derivative of the pressure rise ($dp/d\alpha$).
A matrix with engine TFs was for varying speed and load was also obtained, this can be used as a data bank of TFs for reconstruction of the cylinder pressure at different operating conditions. An extensive analysis of the cycle to cycle variations was carried out, for both the measured and reconstructed cylinder pressure.
The cepstrum analysis technique was used for the analysis. Cepstral analysis is a non-linear signal processing technique with a variety of applications in areas such as speech and image processing. In

the recent years a great interest has focused to cepstral applications of machine diagnosis in reciprocating machines. The main advantage of this method compared to the other methods that the convolutions become an addition and the source and the transfer paths are easier to disjoint, see Equation 2. The Equation 2 is also called real complex .

$$P(\omega)=\frac{X(\omega)}{H(\omega)} \quad (1)$$

$$F^{-1}\{Log(P(\omega))\}=F^{-1}\{Log(X(\omega))\}-F^{-1}\{Log(H(\omega))\} \quad (2)$$

EXPERIMENTAL PROCEDURE AND MEASUREMENT SET-UP

The engine data recording was performed at the Scania acoustic laboratory in Södertälje (Sweden). The tests were carried out with 17 piezoelectric accelerometers, which were mounted firmly on the engine surface. An inductive magnetic sensor, which was connected to the flywheel, was used to locate the position of the piston in the cylinder. Two quartz pressure water-cooled transducers were used to make combustion pulse measurements. A needle lift was also used, in order to exactly detect the time of the injection fuel. All the acquisition signals, the 17 accelerometers, the two pressure transducers, the needle lift and the trigger signals were simultaneously digitized using a CADA-X (LMS) system and HP Paragon front-end.

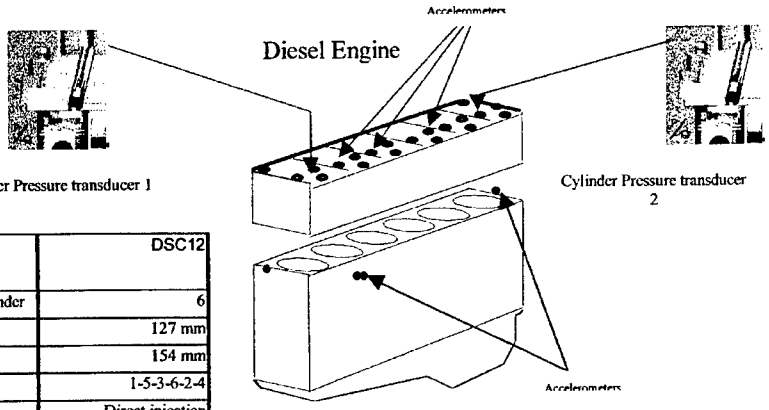

Engine Type	DSC12
Number of cylinder	6
Bore size	127 mm
Stroke length	154 mm
Fire order	1-5-3-6-2-4
Injection type	Direct injection

Figure 1: The measurement set-up and the engine data

The sampling frequency for all the experiments was 8192 Hz and the analyses were performed by post-processing in the signal processing toolbox of Mat-Lab.
The measurements were performed at three speeds (800, 1600, and 2000 rpm) and three loads (10%, 50% and 100% full load). In order to analyse only the interesting part of cylinder pressure and reduce the noise and the influence of the adjacent cylinders a combination of Hanning and uniform windows was used. The windowing technique was applied in order to reduce the leakage and the noise effects from the adjacent cylinders.

ANALYSIS AND RESULTS

The cylinder pressure time trace in engines offers a special challenge for diagnostic and control systems because of the broad range of frequencies in the signal and the effects of structural transmission on the signal. The cylinder pressure in the engines produce vibration signals that can be used for diagnostics and control, but because of the complexity and variability of the structural

transmissions, the procedure for using these vibrations is not straightforward. Fortunately, it appears like a robust procedure if carefully applied can overcome to some extent these difficulties. The analyses started with an extensive experimental study of cycle to cycle cylinder pressure variations, in order to define the standard deviations for each cylinder at different operating conditions. These results were used as reference values for the comparison between the measured and reconstructed cylinder pressures. A coherence analysis to find the best measurement points was also performed. These selected vibration responses for each cylinder were used in the subsequent analysis.

The data recording in search for the best measurement point was performed by measuring the vibration responses around the cylinder head and the cylinder pressures for each cylinder at a time. In order to determine the best measurement points, the coherence function between the cylinder pressure trace and the measurement points was measured. Fig 2a) shows the trigger signal, which was used in order to detect the position of the cylinder.

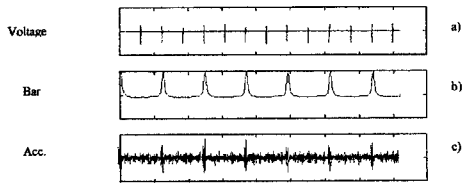

Figure 2 (a, b, c): The trigger signal, the cylinder pressure and the vibration response at 1600 rpm with constant load.

The cylinder head bolt vibration signals were found to be the most sensitive to changes in the cylinder pressure. The best responses for all cylinders were used for the subsequent studies.

Reconstruction of maximum cylinder pressure and cylinder pressure rise

The cylinder pressure and vibration data were conditioned before computing the transfer function, in order to reduce the influence of the noise contamination produced by many other sources in the engine. In order to reconstruct the pressure waveform starting from a vibration signal, it is first necessary to determine, once and for all, the TF between the vibrations and the cylinder pressure. This operation must be carried out for each cylinder with varying speed and load. To reduce the noise present in the cylinder pressure and vibration signals an averaging over 50 cycles was performed, see Equation 3.

$$\overline{H(Z)} = \frac{\sum_{i}^{50} P_i(Z)}{\sum_{i}^{50} Y_i(Z)} \qquad (3)$$

In order to validate the models, a new data set of 50 cylinder pressure cycles for each cylinder with varying running conditions were included in the analysis. The difference between the mean measured maximum cylinder pressures and the mean maximum reconstructed cylinder pressures for all the cylinders can be seen in Figure 3. This figure depicts the difference between the measured mean P_{max} and the mean reconstructed P_{rec}, the most accurate results have been obtained for 800 rpm at varying loads in the interval of 0.1 to 2.1 [%]. The results for 1600 rpm, and 2000 rpm were also accurate with a variation of 0.2 to 3.4 [%], and 0.1 to 3.3 [%], respectively.

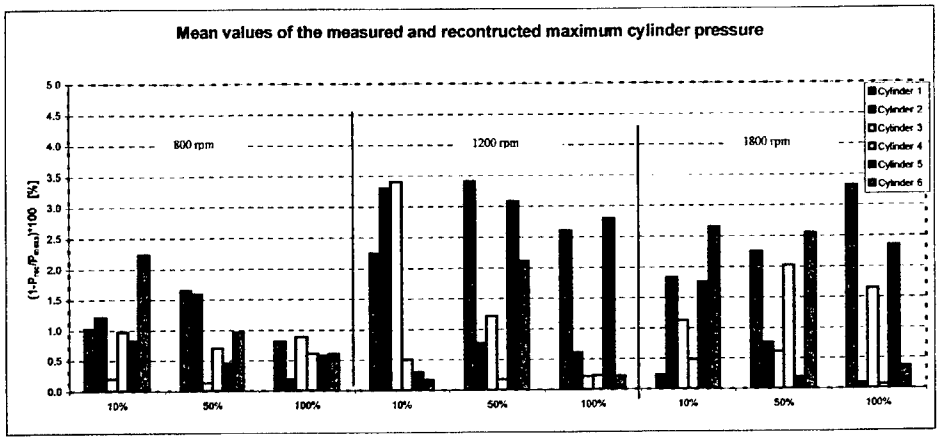

Figure 3: The comparison between the mean measured maximum cylinder pressures and the mean maximum reconstructed cylinder pressures for all the cylinders

The rapid pressure rise in diesel engines is recognised as an audible impulse noise, which is known as "knock". The knock is caused by the spontaneous combustion of a significant volume of fuel/air mixture and produces almost an instantaneous pressure rise locally in the combustion chamber. In order to determine the derivative of the pressure rise ($dp/d\alpha$), the highest rise rate of the combustion stage was calculated. Figure 4 shows the mean values of the difference between the measured and reconstructed $dp/d\alpha$. The best results were obtained for 800 rpm. The Min and Max variations for 800 rpm are 0.41% and -10.2 %. The Max and Min variations for 1600 rpm and 2000 rpm are, 5.4 to 20 %, and 2 and -19.3 %, respectively.

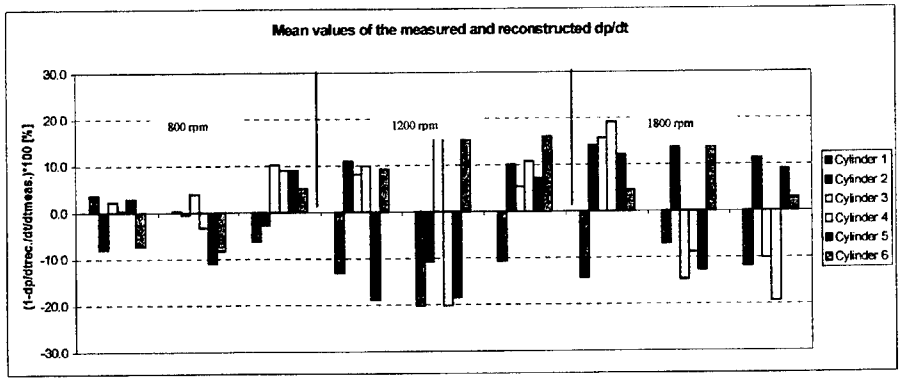

Figure 4. The difference between the mean measured cylinder pressure rise ($dp/d\alpha_{meas}$) and the mean reconstructed pressure rise (dp/dt_{rec}

The higher speeds show less accurate results. It has been difficult to obtain reliable precision at these speeds. It is hard to explain why, one reason could be that the valves have stronger influences

at higher speeds, another reason can be that the vibration signals smears with increasing speed frequencies, damping, and mode shapes.

CONCLUSIONS

- A matrix with engine frequency response functions for varying speed and loads was obtained. This matrix can be used later, as a data-bank of TFs which can track different operating conditions for the reconstruction of the cylinder pressure.

- The reconstruction of the cylinder pressures were satisfactorily performed for 800 rpm and 1600 rpm, although the results at 2000 rpm need to be improved in order to increase the accuracy.

FUTURE RESEARCH

- To exploit the method presented here for practical end-of-assembly diagnostics, it is necessary to verify that the estimated FRFs can work effectively on other engines of the same production run.
- The effects of the injection timing and the speed, on the engine structure transfer function will be further investigated, in order to increase the knowledge about the structure sensitivity due to these parameters.

REFERENCES

[1] R., Lyon: machinery Noise and Diagnostics ISBN0-409-90101-6

[2] R. B. Randall, Y. Ren and H. Ngu :, Diesel Engine cylinder pressure reconstruction, ISMA21-Noise and vibration and engineering, 1996

[3] Y. Gao, R. B. Randall, Reconstruction of diesel engine cylinder pressure using a time domain technique , Mechanical systems and signal processing, 1999.

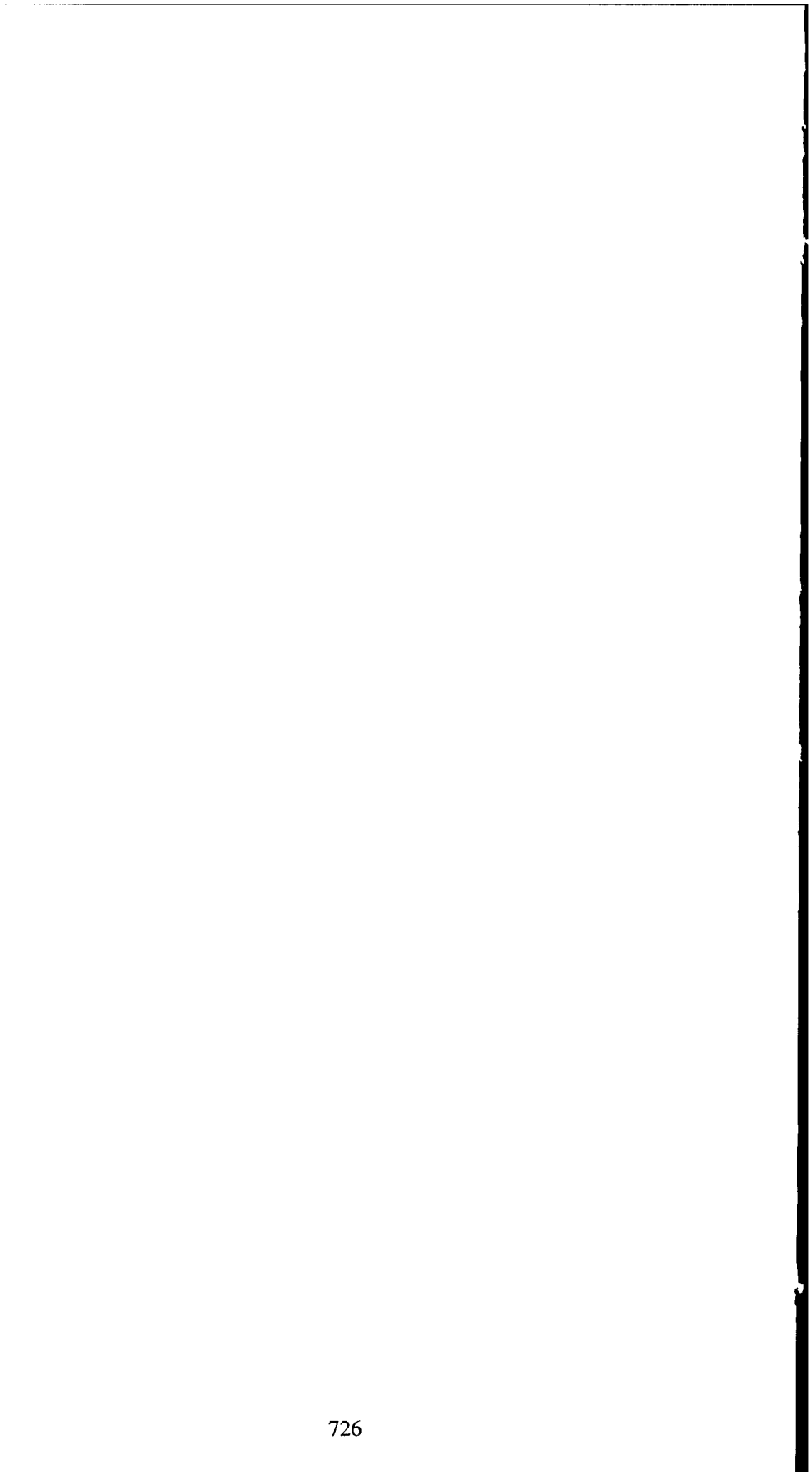

Acoustic actuator blanket for interior sound control

Thomas R. Howarth, James F. Tressler and Joseph A. Bucaro
Naval Research Laboratory, Washington, DC 20375-5350

and C. Garnett Horner and W. Eugene Robbins
NASA Langley Research Center, Hampton, VA 23681-0001

ABSTRACT

The Naval Research Laboratory (NRL) is currently developing techniques for the active noise control quieting of interior spaces. The conceptual approach to this effort is to develop an acoustic blanket that may be mounted either on the structure boundaries or hung from the wall in the interior free space. One of the most difficult aspects of this concept is the actuator subsystem. This particular component is the key to the system in that large displacement and acoustic output are required while maintaining lightweight and flexibility. These two needs are difficult to obtain as they are inconsistent with present technology capabilities. In an effort to accomplish these goals, NRL designed the actuator subsystem using the numerical analysis code PZFlex®. Upon satisfaction of the initial system actuator requirements, NRL worked with NASA's Langley Research Center (LaRC) to fabricate prototype blanket shells. This has required advanced fixturing and the use of an autoclave for formation of the specified actuator bubbles into the desired blanket configuration. After the actuator blanket shell was fabricated at LaRC, NRL then installed piezoelectric ceramic drivers into the shell. Both individual acoustic bubble shapes and a 30-cm by 30-cm section with four acoustic bubbles were evaluated for displacement using laser Doppler vibrometry (LDV). These same prototypes were also evaluated for acoustic sound pressure output using free field measurement techniques. This paper will discuss each of these steps as well as the direction for the final blanket configuration.

ACTUATOR BUBBLE CONCEPT

A sketch of the NRL bubble actuator blanket is shown in figures 1a (in cross-section) and 1b (viewed from the top). This actuator concept consists of a continuous network of piezoelectrically driven actuator subelements mechanically connected into a blanket-like configuration by means of a flexible backing. Each actuator subelement consists of a piezoelectric ring (the cross-hatched areas in figure 1a) which is electroded on its inner and outer walls and poled radially. The rings are mechanically coupled on the top and along the wall of the outer diameter to a thin flexible membrane or shell. The backing may be either rigidly attached to a wall, submarine/airplane hull, etc. or may be hung in the middle of a free space depending upon where the point of disturbance cancellation is desired.

When driven electrically, the piezoelectric ring either expands or contracts a small amount in the radial direction. This, in turn, causes the thin membrane or shell to displace a very large amount either downwards or upwards, respectively. In other words, the thin membrane acts as a mechanical transformer that enhances the radial mode of the piezoceramic ring and then acoustically couples this motion into sound and/or vibration.

The arrows in figure 1a show the case of a radially contracting ring causing an upward flexure in the membrane. The mechanical displacement, and hence, acoustic radiation emitted from the actuator, is thus orthogonal to the vibration mode direction of the piezoelectric.

DISPLACEMENT RESULTS

Displacement measurements were made on individual acoustic bubbles using a Vibration Measurement System (Model 1941, TSI® Incorporated, St. Paul, MN). This system is a non-contact system for detecting, monitoring, and measuring vibrations. Based on laser Doppler velocimetry (LDV) technology, the system operates by scattering monochromatic light from the surface of interest and measuring the Doppler shift of the light frequency caused by the motion of the surface. The shift is proportional to the surface velocity and consequently the surface displacement. The accuracy of the system is ± 0.4 dB.

During LDV measurements, the blanket was hung vertically in free space and then driven with a sinusoidal signal of 1 Volt (rms) over the frequency span 2 Hz to 2,000 Hz. Displacement measurements were made at discrete frequencies at 900 different points in a 30 X 30 square matrix over the piston-like radiating surface of the bubble.

Figure 2 shows the peak displacement as measured at the center of the acoustic bubble over the frequency range of 2 Hz to 3 kHz. The displacement profiles of four different individual bubble resonators is shown in the figure where the primary drum mode resonance of each bubble is evident. Bubbles A and C, as denoted in figure 1, both have two layers of KJ while bubbles B and D have three layers. Interestingly the bubble pairs with the same number of layers do not correspond exactly with each other although the trends are noted. These differences can be attributed to both the location with respect to the top mounting of the blanket and to some mutual impedance coupling effects between elements since the spacing of the elements is well within a half a wavelength.

The peak response is that of bubble A which is 16 μm (-96 dB//m/V) at 250 Hz while elements B (@ 270 Hz) and C (@335 Hz) are 10 μm (-100 dB//m/V) and bubble D is 6.3 μm (-104 dB//m/V) @ 396 Hz. These frequencies are still higher than the desired goal of 100 Hz and 200 Hz respectively but are indicative of the high output capability of the design approach.
In addition to the responses in the center of the bubble, scanning measurements of the complete bubble were also done and showed textbook drum head mode shapes.

SOUND MEASURMENT RESULTS

In addition to the displacement measurements, the actuator blanket was driven in the same arrangement using a microphone to record the sound output profile. The sound measurements were done in time and then an FFT was done to form a sound pressure level (SPL) versus frequency response.

Figure 3 shows the measured SPL for a 200 Volt (peak) drive with the microphone located 3 cm in front of bubble A. The response is in general agreement with the displacement response of figure 2 in which the peak drum mode response is shown to occur at approximately 250 Hz with an SPL of 118 dB.

CONCLUSIONS

The described actuator blanket has shown that it can deliver high tonal displacement and sound pressure levels at relatively low frequencies while maintaining a light weight and low profile package. On-going research includes redesigning the blanket to push the primary drum mode down to 100 Hz while increased bandwidth is being investigated through variation of the individual bubble designs and through advanced driver designs.

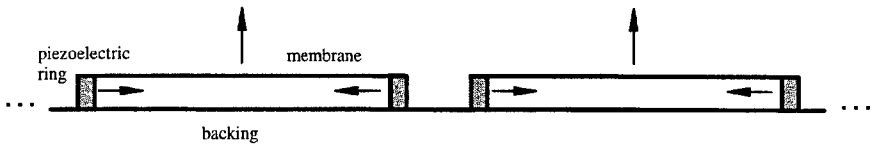

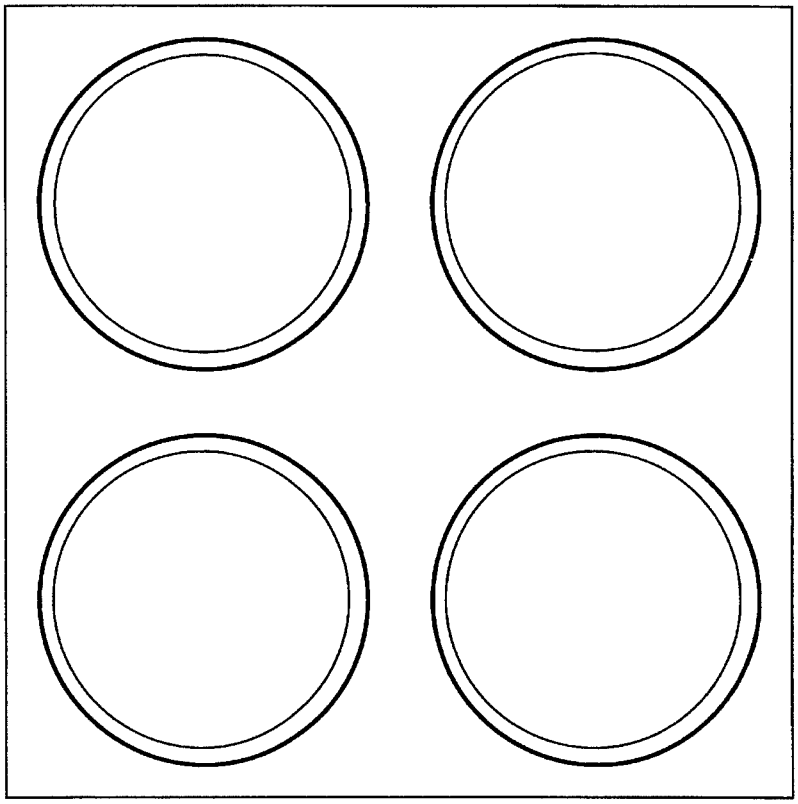

Figure 1: Sketch of the acoustic blanket showing the direction of vibration for the individual bubble drivers (top) and a 30-cm by 30-cm section of a two by two blanket (bottom). Bubble A is the top left element, bubble B is the top right element, bubble C is the bottom right element and bubble D is the bottom left element.

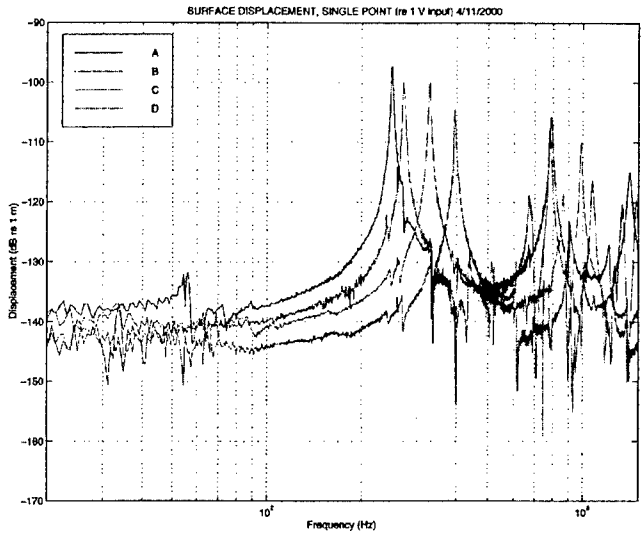

Figure 2: Displacement of the center of four individual bubble actuators for a 1 Volt (rms) drive as a function of frequency.

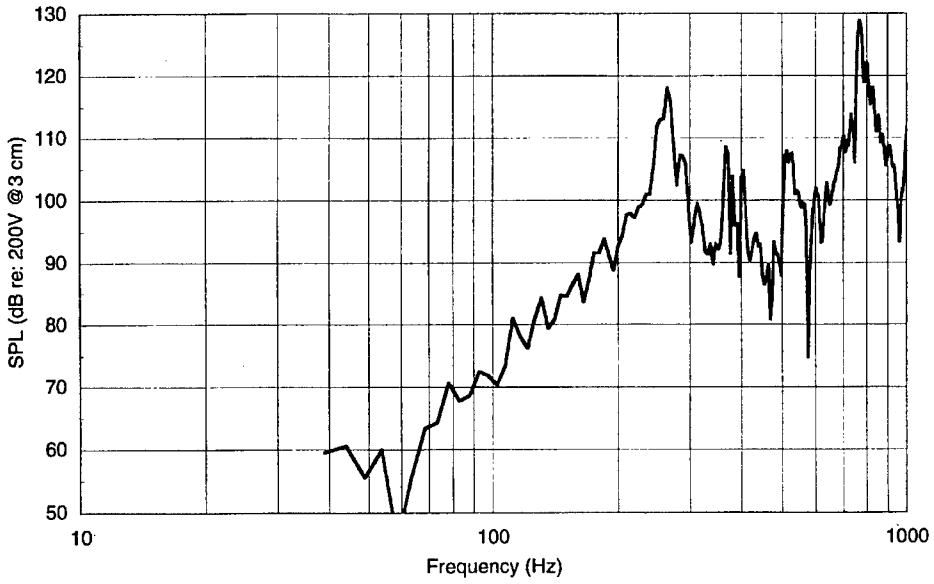

Figure 3: Measured sound pressure level of the center of individual bubble A for a 200 Volt (peak) drive as a function of frequency.